Graduate Texts in Physics

Marius Grundmann

The Physics of Semiconductors

An Introduction including Nanophysics and Applications

Second Edition

Graduate Texts in Physics

Graduate Texts in Physics

Graduate Texts in Physics publishes core learning/teaching material for graduate- and advanced-level undergraduate courses on topics of current and emerging fields within physics, both pure and applied. These textbooks serve students at the MS- or PhD-level and their instructors as comprehensive sources of principles, definitions, derivations, experiments and applications (as relevant) for their mastery and teaching, respectively. International in scope and relevance, the textbooks correspond to course syllabi sufficiently to serve as required reading. Their didactic style, comprehensiveness and coverage of fundamental material also make them suitable as introductions or references for scientists entering, or requiring timely knowledge of, a research field.

Series Editors

Professor William T. Rhodes
Florida Atlantic University
Department of Computer and Electrical Engineering and Computer Science
Imaging Science and Technology Center
777 Glades Road SE, Room 456
Boca Raton, FL33431, USA
E-mail: wrhodes@fau.edu

Professor H. Eugene Stanley
Boston University
Center for Polymer Studies
Department of Physics
590 Commonwealth Avenue, Room 204B
Boston, MA 02215, USA
E-mail: hes@bu.edu

Professor Richard Needs
Cavendish Laboratory
JJ Thomson Avenue
Cambridge CB3 0HE, UK
E-mail: rn11@cam.ac.uk

For further volumes:
http://www.springer.com/series/8431

Marius Grundmann

The Physics of Semiconductors

An Introduction Including Nanophysics and Applications

Second Edition

With 247 Figures

Prof. Dr. Marius Grundmann
Universität Leipzig
Inst. f. Experimentelle Physik II
AG Halbleiterphysik
Linnéstr. 5
04103 Leipzig
Germany
grundmann@physik.uni-leipzig.de

ISSN 1868-4513 e-ISSN 1868-4521
ISBN 978-3-642-13883-6 e-ISBN 978-3-642-13884-3
DOI 10.1007/978-3-642-13884-3
Springer Heidelberg Dordrecht London New York

Library of Congress Control Number: 2010936195

© Springer-Verlag Berlin Heidelberg 2010
This work is subject to copyright. All rights are reserved, whether the whole or part of the material is concerned, specifically the rights of translation, reprinting, reuse of illustrations, recitation, broadcasting, reproduction on microfilm or in any other way, and storage in data banks. Duplication of this publication or parts thereof is permitted only under the provisions of the German Copyright Law of September 9, 1965, in its current version, and permission for use must always be obtained from Springer. Violations are liable to prosecution under the German Copyright Law.
The use of general descriptive names, registered names, trademarks, etc. in this publication does not imply, even in the absence of a specific statement, that such names are exempt from the relevant protective laws and regulations and therefore free for general use.

Cover design: eStudio Calamar S.L., Heidelberg

Printed on acid-free paper

Springer is part of Springer Science+Business Media (www.springer.com)

To Michelle,
Sophia Charlotte
and Isabella Rose

Preface

Semiconductor electronics is commonplace in every household. Semiconductor devices have also enabled economically reasonable fiber-based optical communication, optical storage and high-frequency amplification and have recently revolutionized photography, display technology and lighting. Along with these tremendous technological developments, semiconductors have changed the way we work, communicate, entertain and think. The technological progress of semiconductor materials and devices is evolving continuously with a large worldwide effort in human and monetary capital. For students, semiconductors offer a rich, diverse and exciting field with a great tradition and a bright future.

This book introduces students to semiconductor physics and semiconductor devices. It brings them to the point where they can specialize and enter supervised laboratory research. It is based on the two semester semiconductor physics course taught at Universität Leipzig in its Master of Science physics curriculum. Since the book can be followed with little or no pre-existing knowledge in solid-state physics and quantum mechanics, it is also suitable for undergraduate students. For the interested reader some additional topics are included in the book that can be covered in subsequent, more specialized courses. The material is selected to provide a balance between aspects of solid-state and semiconductor physics, the concepts of various semiconductor devices and modern applications in electronics and photonics.

The first semester contains the fundamentals of semiconductor physics (Part I, Sects. 1–10) and selected topics from Part II (Sects. 11–19). Besides important aspects of solid-state physics such as crystal structure, lattice vibrations and band structure, semiconductor specifics such as technologically relevant materials and their properties, electronic defects, recombination, hetero- and nanostructures are discussed. Semiconductors with electric polarization and magnetization are introduced. The emphasis is put on inorganic semiconductors, but a brief introduction to organic semiconductors is given in Sect. 16. Dielectric structures (Sect. 18) serve as mirrors, cavities and microcavities and are a vital part of many semiconductor devices. Other sections give introductions to carbon-based nanostructures and transparent conductive oxides (TCOs). The third part (Part III – Sects. 20–23) is dedicated to semiconductor applications and devices that are taught in the second semester of the course. After a general and detailed discussion of

various diode types, their applications in electrical circuits, photodetectors, solar cells, light-emitting diodes and lasers are treated. Finally, bipolar and field-effect transistors including thin film transistors are discussed.

In the present text of the second edition a few errors and misprints of the first edition have been corrected. Many topics have been extended and are treated in more depth, e.g. dopant diffusion, partial dislocations, etching of semiconductors, double donors/acceptors, excess charge carrier profiles, direct transitions in germanium, alloy broadening, nanowires, recombination in organic semiconductors, depletion layers beyond the abrupt approximation, Schottky diodes with inhomogeneous barrier, multi-junction solar cells, quantum dot and organic LEDs, LED degradation, strained channel transistors, MOSFET scaling, memory concepts and thin film transistors. The two chapters on carbon-based nanostructures and transparent conductive oxides have been added.

The number of references has been doubled with respect to the first edition. The references have been selected to (i) cover important historical and milestone papers, (ii) direct to reviews and topical books for further reading and (iii) give access to current literature and up-to-date research. In Fig. 1, the almost 1500 references in this book are shown by year. Roughly three phases of semiconductor physics and technology can be seen. Before the realization of the first transistor in 1947, only a few publications are noteworthy. Then an intense phase of understanding the physics of semiconductors and developing semiconductor technology and devices based on bulk semiconductors (mostly Ge, Si, GaAs) followed. At the end of the 1970s, a new era began with the advent of quantum wells and heterostructures, and later nanostructures (nanotubes, nanowires and quantum dots) and new materials (e.g. organic semiconductors, nitrides or graphene).

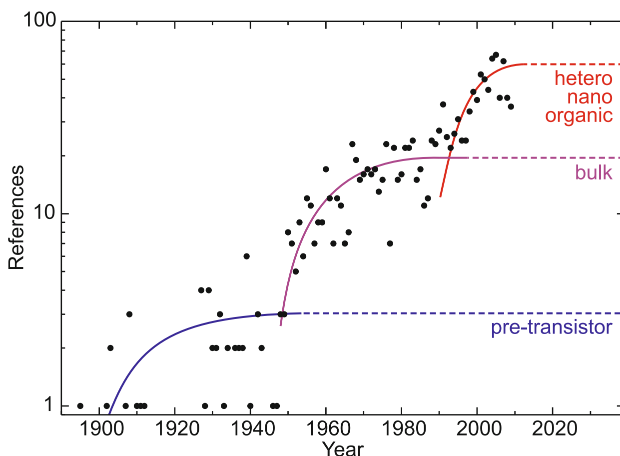

Fig. 1. Histogram of references in this book

I would like to thank several colleagues for their various contributions to this book, in alphabetical order (if no affiliation is given, from Universität Leipzig): Gabriele Benndorf, Klaus Bente, Rolf Böttcher, Matthias Brandt, Christian Czekalla, Christof Peter Dietrich, Pablo Esquinazi, Heiko Frenzel, Volker Gottschalch, Helena Hilmer, Axel Hoffmann (TU Berlin), Alois Krost (Otto-von-Guericke Universität Magdeburg), Alexander Lajn, Michael Lorenz, Thomas Nobis, Rainer Pickenhain, Hans-Joachim Queisser (Max-Planck-Institut für Festkörperforschung, Stuttgart), Bernd Rauschenbach (Leibniz-Institut für Oberflächenmodifizierung, Leipzig), Bernd Rheinländer, Heidemarie Schmidt, Mathias Schmidt, Rüdiger Schmidt-Grund, Matthias Schubert, Jan Sellmann, Oliver Stier (TU Berlin), Chris Sturm, Gerald Wagner, Holger von Wenckstern, Michael Ziese, and Gregor Zimmermann. Their comments, proof reading, experimental data and graphic material improved this work. Also, numerous helpful comments from my students on my lectures and the first edition of this book are gratefully acknowledged.

I am also indebted to many other colleagues, in particular to (in alphabetical order) Gerhard Abstreiter, Zhores Alferov, Levon Asryan, Günther Bauer, Manfred Bayer, Friedhelm Bechstedt, Dieter Bimberg, Fernando Briones, Immanuel Broser, Jürgen Christen, Laurence Eaves, Ulrich Gösele†, Alfred Forchel, Manus Hayne, Frank Heinrichsdorff, Fritz Henneberger, Detlev Heitmann, Robert Heitz†, Evamarie Hey-Hawkins, Evgeni Kaidashev, Eli Kapon, Nils Kirstaedter, Claus Klingshirn, Fred Koch, Jörg Kotthaus, Nikolai Ledentsov, Axel Lorke, Anupam Madhukar, Ingrid Mertig, Bruno Meyer, David Mowbray, Hisao Nakashima, Jörg Neugebauer, Mats-Erik Pistol, Fred Pollak, Volker Riede, Hiroyuki Sakaki, Lars Samuelson, Vitali Shchukin, Maurice Skolnick, Robert Suris, Volker Türck, Konrad Unger, Victor Ustinov, Leonid Vorob'jev, Richard Warburton, Alexander Weber, Eicke Weber, Peter Werner, Ulrike Woggon, Roland Zimmermann, Alex Zunger and Jesus Zúñiga-Pérez with whom I have worked closely, had enjoyable discussions with and who have posed questions that stimulated me.

Leipzig, April 2010 *Marius Grundmann*

Contents

1 Introduction ... 1
1.1 Timetable ... 1
1.2 Nobel Prize Winners ... 10
1.3 General Information ... 11

Part I Fundamentals

2 Bonds ... 19
2.1 Introduction ... 19
2.2 Covalent Bonds ... 19
2.2.1 Electron-Pair Bond ... 19
2.2.2 sp^3 Bonds ... 19
2.2.3 sp^2 Bonds ... 23
2.3 Ionic Bonds ... 25
2.4 Mixed Bonds ... 27
2.5 Metallic Bonding ... 30
2.6 van-der-Waals Bonds ... 30
2.7 Hamilton Operator of the Solid ... 32

3 Crystals ... 35
3.1 Introduction ... 35
3.2 Crystal Structure ... 35
3.3 Lattice ... 36
3.3.1 Unit Cell ... 36
3.3.2 Point Group ... 37
3.3.3 Space Group ... 39
3.3.4 2D Bravais Lattices ... 40
3.3.5 3D Bravais Lattices ... 40
3.3.6 Polycrystalline Semiconductors ... 45
3.3.7 Amorphous Semiconductors ... 45
3.4 Important Crystal Structures ... 47
3.4.1 Rocksalt Structure ... 47
3.4.2 CsCl Structure ... 48
3.4.3 Diamond Structure ... 48

3.4.4 Zincblende Structure . . . 49
3.4.5 Wurtzite Structure . . . 50
3.4.6 Chalcopyrite Structure . . . 51
3.4.7 Fluorite Structure . . . 53
3.4.8 Delafossite Structure . . . 54
3.4.9 Perovskite Structure . . . 55
3.4.10 NiAs Structure . . . 56
3.4.11 Further Structures . . . 56
3.5 Polytypism . . . 57
3.6 Reciprocal Lattice . . . 57
3.6.1 Reciprocal Lattice Vectors . . . 59
3.6.2 Miller Indices . . . 60
3.6.3 Brillouin Zone . . . 62
3.7 Alloys . . . 63
3.7.1 Random Alloys . . . 64
3.7.2 Phase Diagram . . . 66
3.7.3 Virtual Crystal Approximation . . . 68
3.7.4 Lattice Parameter . . . 68
3.7.5 Ordering . . . 69

4 Defects . . . 73
4.1 Introduction . . . 73
4.2 Point Defects . . . 73
4.2.1 Point Defect Types . . . 73
4.2.2 Thermodynamics . . . 74
4.2.3 Diffusion . . . 78
4.2.4 Dopant Distribution . . . 80
4.2.5 Large Concentration Effects . . . 84
4.3 Dislocations . . . 87
4.3.1 Dislocation Types . . . 88
4.3.2 Visualization of Dislocations by Etching . . . 92
4.3.3 Impurity Hardening . . . 94
4.4 Extended Defects . . . 95
4.4.1 Micro-cracks . . . 95
4.4.2 Stacking Faults . . . 95
4.4.3 Grain Boundaries . . . 97
4.4.4 Antiphase and Inversion Domains . . . 99
4.5 Disorder . . . 102

5 Mechanical Properties . . . 103
5.1 Introduction . . . 103
5.2 Lattice Vibrations . . . 103
5.2.1 Monoatomic Linear Chain . . . 103
5.2.2 Diatomic Linear Chain . . . 106
5.2.3 Lattice Vibrations of a Three-Dimensional Crystal . 110

5.2.4 Density of States . . . 112
5.2.5 Phonons . . . 114
5.2.6 Localized Vibrational Modes . . . 114
5.2.7 Phonons in Alloys . . . 116
5.2.8 Electric Field Created by Optical Phonons . . . 119
5.3 Elasticity . . . 122
5.3.1 Thermal Expansion . . . 122
5.3.2 Stress–Strain Relation . . . 122
5.3.3 Biaxial Strain . . . 127
5.3.4 Three-Dimensional Strain . . . 128
5.3.5 Substrate Bending . . . 130
5.3.6 Scrolling . . . 132
5.3.7 Critical Thickness . . . 133
5.4 Cleaving . . . 137

6 Band Structure . . . 139
6.1 Introduction . . . 139
6.2 Electrons in a Periodic Potential . . . 139
6.2.1 Bloch's Theorem . . . 139
6.2.2 Free-Electron Dispersion . . . 140
6.2.3 Kronig–Penney Model . . . 142
6.2.4 Lattice Vector Expansion . . . 144
6.2.5 Kramer's degeneracy . . . 147
6.3 Band Structure of Selected Semiconductors . . . 147
6.3.1 Silicon . . . 147
6.3.2 Germanium . . . 147
6.3.3 GaAs . . . 148
6.3.4 GaP . . . 149
6.3.5 GaN . . . 149
6.3.6 Lead Salts . . . 149
6.3.7 Chalcopyrites . . . 149
6.3.8 Delafossites . . . 151
6.3.9 Perovskites . . . 152
6.4 Alloy Semiconductors . . . 153
6.5 Amorphous Semiconductors . . . 155
6.6 Systematics of Semiconductor Band Gaps . . . 156
6.7 Temperature Dependence of the Band Gap . . . 158
6.8 Electron Dispersion . . . 161
6.8.1 Equation of Electron Motion . . . 161
6.8.2 Effective Mass of Electrons . . . 161
6.8.3 Polaron Mass . . . 165
6.8.4 Nonparabolicity of Electron Mass . . . 167
6.9 Holes . . . 168
6.9.1 Hole Concept . . . 168
6.9.2 Hole Dispersion Relation . . . 169
6.9.3 Valence-Band Fine Structure . . . 173

6.10 Strain Effect on the Band Structure . . . 176
6.10.1 Strain Effect on Band Edges . . . 176
6.10.2 Strain Effect on Effective Masses . . . 179
6.10.3 Interaction with a Localized Level . . . 179
6.11 Density of States . . . 179
6.11.1 General Band Structure . . . 179
6.11.2 Free-Electron Gas . . . 180

7 Electronic Defect States . . . 185
7.1 Introduction . . . 185
7.2 Fermi Distribution . . . 185
7.3 Carrier Concentration . . . 187
7.4 Intrinsic Conduction . . . 190
7.5 Shallow Defects . . . 193
7.5.1 Donors . . . 193
7.5.2 Acceptors . . . 202
7.5.3 Compensation . . . 206
7.5.4 Multiple Impurities . . . 208
7.5.5 Amphoteric Impurities . . . 210
7.5.6 High Doping . . . 211
7.6 Quasi-Fermi Levels . . . 215
7.7 Deep Levels . . . 216
7.7.1 Charge States . . . 217
7.7.2 Double Donors . . . 218
7.7.3 Double Acceptors . . . 219
7.7.4 Jahn–Teller Effect . . . 221
7.7.5 Negative-U Center . . . 221
7.7.6 DX Center . . . 224
7.7.7 EL2 Defect . . . 226
7.7.8 Semi-insulating Semiconductors . . . 227
7.7.9 Isoelectronic Impurities . . . 228
7.7.10 Surface States . . . 230
7.8 Hydrogen in Semiconductors . . . 231

8 Transport . . . 235
8.1 Introduction . . . 235
8.2 Conductivity . . . 236
8.3 Low-Field Transport . . . 238
8.3.1 Mobility . . . 238
8.3.2 Microscopic Scattering Processes . . . 239
8.3.3 Ionized Impurity Scattering . . . 239
8.3.4 Deformation Potential Scattering . . . 240
8.3.5 Piezoelectric Potential Scattering . . . 241
8.3.6 Polar Optical Scattering . . . 241
8.3.7 Dislocation Scattering . . . 241

8.3.8 Grain Boundary Scattering . . . 242
8.3.9 Temperature Dependence . . . 243
8.3.10 Doping Dependence . . . 243
8.3.11 Piezoresistivity . . . 246
8.4 Hall Effect . . . 247
8.5 High-Field Transport . . . 251
8.5.1 Drift-Saturation Velocity . . . 251
8.5.2 Negative Differential Resistivity . . . 252
8.5.3 Velocity Overshoot . . . 254
8.5.4 Impact Ionization . . . 254
8.6 High-Frequency Transport . . . 257
8.7 Diffusion . . . 257
8.8 Continuity Equation . . . 259
8.9 Heat Conduction . . . 259
8.10 Coupled Heat and Charge Transport . . . 261
8.10.1 Seebeck Effect . . . 261
8.10.2 Peltier Effect . . . 262

9 Optical Properties . . . 265
9.1 Spectral Regions and Overview . . . 265
9.2 Reflection and Diffraction . . . 266
9.3 Absorption . . . 268
9.4 Electron–Photon Interaction . . . 269
9.5 Band–Band Transitions . . . 271
9.5.1 Joint Density of States . . . 271
9.5.2 Direct Transitions . . . 272
9.5.3 Indirect Transitions . . . 274
9.5.4 Urbach Tail . . . 278
9.5.5 Intravalence-Band Absorption . . . 278
9.5.6 Amorphous Semiconductors . . . 279
9.5.7 Excitons . . . 280
9.5.8 Phonon Broadening . . . 283
9.5.9 Exciton Polariton . . . 285
9.5.10 Bound-Exciton Absorption . . . 288
9.5.11 Biexcitons . . . 290
9.5.12 Trions . . . 290
9.5.13 Burstein–Moss Shift . . . 291
9.5.14 Band Gap Renormalization . . . 292
9.5.15 Electron–Hole Droplets . . . 293
9.5.16 Two-Photon Absorption . . . 294
9.6 Impurity Absorption . . . 296
9.7 Free-Carrier Absorption . . . 299
9.8 Lattice Absorption . . . 303
9.8.1 Dielectric Constant . . . 304
9.8.2 Reststrahlenbande . . . 304

9.8.3 Polaritons . . . 304
9.8.4 Phonon–Plasmon Coupling . . . 307

10 Recombination . . . 309
10.1 Introduction . . . 309
10.2 Band–Band Recombination . . . 309
10.2.1 Spontaneous Emission . . . 309
10.2.2 Absorption . . . 311
10.2.3 Stimulated Emission . . . 311
10.2.4 Net Recombination Rate . . . 312
10.2.5 Recombination Dynamics . . . 313
10.2.6 Lasing . . . 314
10.3 Exciton Recombination . . . 315
10.3.1 Free Excitons . . . 315
10.3.2 Bound Excitons . . . 317
10.3.3 Alloy Broadening . . . 323
10.4 Phonon Replica . . . 326
10.5 Self-absorption . . . 330
10.6 Donor–Acceptor Pair Transitions . . . 331
10.7 Inner-Impurity Recombination . . . 331
10.8 Auger Recombination . . . 333
10.9 Band–Impurity Recombination . . . 335
10.9.1 Shockley-Read-Hall Kinetics . . . 335
10.9.2 Multilevel Traps . . . 339
10.10 Field Effect . . . 339
10.10.1 Thermally Activated Emission . . . 339
10.10.2 Direct Tunneling . . . 340
10.10.3 Assisted Tunneling . . . 340
10.11 Recombination at Extended Defects . . . 340
10.11.1 Surfaces . . . 340
10.11.2 Grain Boundaries . . . 341
10.11.3 Dislocations . . . 341
10.12 Excess-Carrier Profiles . . . 342
10.12.1 Generation at Surface . . . 343
10.12.2 Generation in the Bulk . . . 343

Part II Selected Topics

11 Heterostructures . . . 347
11.1 Introduction . . . 347
11.2 Heteroepitaxy . . . 347
11.2.1 Growth Methods . . . 347
11.2.2 Substrates . . . 348
11.2.3 Growth Modes . . . 351

11.2.4 Heterosubstrates . . . 352
11.2.5 Pseudomorphic Structures . . . 356
11.2.6 Plastic Relaxation . . . 356
11.2.7 Surfactants . . . 358
11.3 Energy Levels in Heterostructures . . . 359
11.3.1 Band Lineup in Heterostructures . . . 359
11.3.2 Quantum Wells . . . 361
11.3.3 Superlattices . . . 366
11.3.4 Single Heterointerface Between Doped Materials . . . 368
11.4 Recombination in Quantum Wells . . . 369
11.4.1 Thickness Dependence . . . 369
11.4.2 Broadening Effects . . . 370
11.4.3 Quantum Confined Stark Effect . . . 374
11.5 Isotope Superlattices . . . 375
11.6 Wafer Bonding . . . 377

12 External Fields . . . 379
12.1 Electric Fields . . . 379
12.1.1 Bulk Material . . . 379
12.1.2 Quantum Wells . . . 381
12.2 Magnetic Fields . . . 382
12.2.1 Free-Carrier Absorption . . . 383
12.2.2 Energy Levels in Bulk Crystals . . . 384
12.2.3 Energy Levels in a 2DEG . . . 386
12.2.4 Shubnikov–de Haas Oscillations . . . 387
12.3 Quantum Hall Effect . . . 389
12.3.1 Integral QHE . . . 389
12.3.2 Fractional QHE . . . 393
12.3.3 Weiss Oscillations . . . 394

13 Nanostructures . . . 397
13.1 Introduction . . . 397
13.2 Quantum Wires . . . 397
13.2.1 V-Groove Quantum Wires . . . 397
13.2.2 Cleaved-Edge Overgrowth Quantum Wires . . . 401
13.2.3 Nanowhiskers . . . 401
13.2.4 Nanobelts . . . 403
13.2.5 Quantization in Two-Dimensional Potential Wells . 404
13.3 Quantum Dots . . . 407
13.3.1 Quantization in Three-Dimensional Potential Wells . . . 407
13.3.2 Electrical and Transport Properties . . . 410
13.3.3 Self-assembled Preparation . . . 413
13.3.4 Optical Properties . . . 419

14 Polarized Semiconductors . . . 425
14.1 Introduction . . . 425
14.2 Spontaneous Polarization . . . 425
14.3 Ferroelectricity . . . 427
14.3.1 Materials . . . 428
14.3.2 Soft Phonon Mode . . . 428
14.3.3 Phase Transition . . . 429
14.3.4 Domains . . . 432
14.3.5 Optical Properties . . . 433
14.4 Piezoelectricity . . . 433
14.4.1 Piezoelectric Effect . . . 433
14.4.2 Zincblende Crystals . . . 434
14.4.3 Wurtzite Crystals . . . 435
14.4.4 Piezoelectric Effects in Nanostructures . . . 438

15 Magnetic Semiconductors . . . 441
15.1 Introduction . . . 441
15.2 Magnetic Semiconductors . . . 441
15.3 Diluted Magnetic Semiconductors . . . 442
15.4 Spintronics . . . 448
15.4.1 Spin Transistor . . . 448
15.4.2 Spin LED . . . 448

16 Organic Semiconductors . . . 451
16.1 Materials . . . 451
16.1.1 Small Organic Molecules, Polymers . . . 451
16.1.2 Organic Semiconductor Crystals . . . 451
16.2 Electronic Structure . . . 454
16.3 Doping . . . 456
16.4 Transport Properties . . . 457
16.5 Optical Properties . . . 457

17 Graphene and Carbon Nanotubes . . . 465
17.1 Graphene . . . 465
17.1.1 Structure . . . 465
17.1.2 Band Structure . . . 465
17.1.3 Electrical Properties . . . 468
17.1.4 Other Two-Dimensional Crystals . . . 472
17.2 Carbon Nanotubes . . . 473
17.2.1 Structure . . . 473
17.2.2 Band Structure . . . 474
17.2.3 Optical Properties . . . 475
17.2.4 Other Anorganic Nanotubes . . . 476

18 Dielectric Structures 481
18.1 Photonic Band Gap Materials 481
18.1.1 Introduction 481
18.1.2 General 1D Scattering Theory 481
18.1.3 Transmission of an N-Period Potential 483
18.1.4 The Quarter-Wave Stack 485
18.1.5 Formation of a 3D Band Structure 488
18.1.6 Disorder 491
18.1.7 Defect Modes 493
18.1.8 Coupling to an Electronic Resonance 497
18.2 Microscopic Resonators 500
18.2.1 Microdiscs 500
18.2.2 Purcell Effect 502
18.2.3 Deformed Resonators 503
18.2.4 Hexagonal Cavities 505

19 Transparent Conductive Oxide Semiconductors 511
19.1 Materials 511
19.2 Properties 512

Part III Applications

20 Diodes 519
20.1 Introduction 519
20.2 Metal–Semiconductor Contacts 520
20.2.1 Band Diagram in Equilibrium 520
20.2.2 Space-Charge Region 525
20.2.3 Schottky Effect 527
20.2.4 Capacitance 529
20.2.5 Current–Voltage Characteristic 532
20.2.6 Ohmic Contacts 543
20.2.7 Metal Contacts to Organic Semiconductors 546
20.3 Metal–Insulator–Semiconductor Diodes 548
20.3.1 Band Diagram for Ideal MIS Diode 548
20.3.2 Space-Charge Region 551
20.3.3 Capacitance 555
20.3.4 Nonideal MIS Diode 556
20.4 Bipolar Diodes 558
20.4.1 Band Diagram 558
20.4.2 Space-Charge Region 558
20.4.3 Capacitance 563
20.4.4 Current–Voltage Characteristics 565
20.4.5 Breakdown 575
20.4.6 Organic Semiconductor Diodes 580

20.5 Applications and Special Diode Devices . . . 582
20.5.1 Rectification . . . 582
20.5.2 Frequency Mixing . . . 584
20.5.3 Voltage Regulator . . . 586
20.5.4 Zener Diodes . . . 588
20.5.5 Varactors . . . 588
20.5.6 Fast-Recovery Diodes . . . 589
20.5.7 Step-Recovery Diodes . . . 590
20.5.8 pin-Diodes . . . 591
20.5.9 Tunneling Diodes . . . 592
20.5.10 Backward Diodes . . . 595
20.5.11 Gunn Diodes . . . 596
20.5.12 Heterostructure Diodes . . . 597

21 Light-to-Electricity Conversion . . . 599
21.1 Photocatalysis . . . 599
21.2 Photoconductors . . . 601
21.2.1 Introduction . . . 601
21.2.2 Photoconductivity Detectors . . . 601
21.2.3 Electrophotography . . . 603
21.2.4 QWIPs . . . 604
21.2.5 Blocked Impurity-Band Detectors . . . 608
21.3 Photodiodes . . . 610
21.3.1 Introduction . . . 610
21.3.2 pn Photodiodes . . . 611
21.3.3 pin Photodiodes . . . 613
21.3.4 Position-Sensing Detector . . . 615
21.3.5 MSM Photodiodes . . . 616
21.3.6 Avalanche Photodiodes . . . 623
21.3.7 Traveling-Wave Photodetectors . . . 625
21.3.8 Charge Coupled Devices . . . 627
21.3.9 Photodiode Arrays . . . 633
21.4 Solar Cells . . . 637
21.4.1 Solar Radiation . . . 637
21.4.2 Ideal Solar Cells . . . 638
21.4.3 Real Solar Cells . . . 643
21.4.4 Design Refinements . . . 643
21.4.5 Modules . . . 645
21.4.6 Solar-Cell Types . . . 646
21.4.7 Commercial Issues . . . 651

22 Electricity-to-Light Conversion . . . 653
22.1 Radiometric and Photometric Quantities . . . 653
22.1.1 Radiometric Quantities . . . 653
22.1.2 Photometric Quantities . . . 653

22.2 Scintillators 654
22.2.1 CIE Chromaticity Diagram 655
22.2.2 Display Applications 658
22.2.3 Radiation Detection 659
22.2.4 Luminescence Mechanisms 660
22.3 Light-Emitting Diodes 661
22.3.1 Introduction 661
22.3.2 Spectral Ranges 661
22.3.3 Quantum Efficiency 662
22.3.4 Device Design 663
22.3.5 White LEDs 668
22.3.6 Quantum Dot LED 671
22.3.7 Organic LED 672
22.4 Lasers 674
22.4.1 Introduction 674
22.4.2 Applications 676
22.4.3 Gain 678
22.4.4 Optical Mode 680
22.4.5 Loss Mechanisms 687
22.4.6 Threshold 688
22.4.7 Spontaneous Emission Factor 689
22.4.8 Output Power 690
22.4.9 Temperature Dependence 692
22.4.10 Mode Spectrum 694
22.4.11 Longitudinal Single-Mode Lasers 695
22.4.12 Tunability 697
22.4.13 Modulation 698
22.4.14 Surface-Emitting Lasers 703
22.4.15 Optically Pumped Semiconductor Lasers 707
22.4.16 Quantum Cascade Lasers 708
22.4.17 Hot-Hole Lasers 709
22.5 Semiconductor Optical Amplifiers 710

23 Transistors 713
23.1 Introduction 713
23.2 Bipolar Transistors 714
23.2.1 Carrier Density and Currents 715
23.2.2 Current Amplification 718
23.2.3 Ebers–Moll Model 719
23.2.4 Current–Voltage Characteristics 721
23.2.5 Basic Circuits 723
23.2.6 High-Frequency Properties 725
23.2.7 Heterobipolar Transistors 725
23.2.8 Light-Emitting Transistors 726
23.3 Field-Effect Transistors 727

23.4 JFET and MESFET 729
23.4.1 General Principle 729
23.4.2 Static Characteristics 730
23.4.3 Normally On and Normally Off FETs 733
23.4.4 Field-Dependent Mobility 734
23.4.5 High-Frequency Properties 736
23.5 MOSFETs 737
23.5.1 Operation Principle 737
23.5.2 Current–Voltage Characteristics 738
23.5.3 MOSFET Types 743
23.5.4 Complementary MOS 743
23.5.5 Large-Scale Integration 746
23.5.6 Tunneling FETs 753
23.5.7 Nonvolatile Memories 755
23.5.8 Heterojunction FETs 757
23.6 Thin-Film Transistors 763
23.6.1 Annealing of Amorphous Silicon 763
23.6.2 TFT Devices 765
23.6.3 OFETs 765

Part IV Appendices

A Tensors 769

B Space Groups 773

C Kramers–Kronig Relations 775

D Oscillator Strength 777

E Quantum Statistics 783

F The k · p Perturbation Theory 787

G Effective-Mass Theory 791

References 793

Index 843

Abbreviations

2DEG	two-dimensional electron gas
A	atomic mass ($A = 12$ for ^{12}C)
AAAS	American Association for the Advancement of Science
AB	antibonding (position)
ac	alternating current
ACS	American Chemical Society
AFM	atomic force microscopy
AIP	American Institute of Physics
AM	air mass
APD	antiphase domain
APD	avalanche photodiode
APS	American Physical Society
AR	antireflection
ARPES	angle-resolved photoemission spectroscopy
ASE	amplified spontaneous emission
AVS	American Vacuum Society (The Science & Technology Society)
BC	bond center (position)
bc	body-centered
bcc	body-centered cubic
BD	Blu-ray$^{\mathrm{TM}}$disc
BEC	Bose–Einstein condensation
BGR	band gap renormalization
CAS	calorimetric absorption spectroscopy
CCD	charge coupled device
CD	compact disc
CEO	cleaved-edge overgrowth
CIE	Commission Internationale de l'Éclairage
CIGS	Cu(In,Ga)Se_2 material
CIS	$CuInSe_2$ material
CL	cathodoluminescence

CMOS	complementary metal–oxide–semiconductor
CMY	cyan-magenta-yellow (color system)
CNT	carbon nanotube
COD	catastrophical optical damage
CPU	central processing unit
CRT	cathode ray tube
CSL	coincident site lattice
CVD	chemical vapor deposition
cw	continuous wave
CZ	Czochralski (growth)
DAP	donor–acceptor pair
DBR	distributed Bragg reflector
dc	direct current
DFB	distributed feedback
DH(S)	double heterostructure
DLTS	deep level transient spectroscopy
DMS	diluted magnetic semiconductor
DOS	density of states
DPSS	diode-pumped solid-state (laser)
DRAM	dynamic random access memory
DVD	digital versatile disc
EBL	electron blocking layer
EEPROM	electrically erasable programmable read-only memory
EHL	electron–hole liquid
EIL	electron injection layer
EL	electroluminescence
ELO	epitaxial lateral overgrowth
EMA	effective mass approximation
EML	emission layer
ELA	excimer laser annealing
EPR	electron paramagnetic resonance
ESR	electron spin resonance
EPROM	erasable programmable read-only memory
ESF	extrinsic stacking fault
ETL	electron transport layer
EXAFS	extended X-ray absorption fine structure
F_4-TCNQ	2,3,5,6-tetrafluoro-7,7,8,8-tetracyano-quinodimethane
fc	face-centered
fcc	face-centered cubic
FeRAM	ferroelectric random access memory
FET	field-effect transistor
FIR	far infrared

FKO	Franz–Keldysh oscillation
FLG	few layer graphene
FPA	focal plane array
FQHE	fractional quantum Hall effect
FWHM	full width at half-maximum
FZ	float-zone (growth)
Gb	Gigabit
GIZO	GaInZnO
GLAD	glancing-angle deposition
GRINSCH	graded-index separate confinement heterostructure
GSMBE	gas-source molecular beam epitaxy
GST	$Ge_2Sb_2Te_5$
HBL	hole blocking layer
HBT	heterobipolar transistor
hcp	hexagonally close packed
HCSEL	horizontal cavity surface-emitting laser
HEMT	high electron mobility transistor
HIGFET	heterojunction insulating gate FET
HIL	hole injection layer
HJFET	heterojunction FET
hh	heavy hole
HOPG	highly ordered pyrolithic graphite
HOMO	highest occupied molecular orbital
HR	high reflection
HRTEM	high-resolution transmission electron microscopy
HTL	hole transport layer
HWHM	half-width at half-maximum
IC	integrated circuit
IDB	inversion domain boundary
IEEE	Institute of Electrical and Electronics Engineers[1]
IF	intermediate frequency
IPAP	Institute of Pure and Applied Physics, Tokyo
IQHE	integral quantum Hall effect
IR	infrared
ISF	intrinsic stacking fault
ITO	indium tin oxide
JDOS	joint density of states
JFET	junction field-effect transistor
KKR	Kramers–Kronig relation

[1] Pronounced Eye-triple-E

KOH	potassium hydroxide
KTP	$KTiOPO_4$ material
LA	longitudinal acoustic (phonon)
LCD	liquid crystal display
LDA	local density approximation
LEC	liquid encapsulated Czochralski (growth)
LED	light-emitting diode
lh	light hole
LO	longitudinal optical (phonon), local oscillator
LPE	liquid phase epitaxy
LPCVD	low-pressure chemical vapor deposition
LPP	longitudinal phonon plasmon (mode)
LST	Lyddane–Sachs–Teller (relation)
LT	low temperature
LUMO	lowest unoccupied molecular orbital
LVM	local vibrational mode
MBE	molecular beam epitaxy
MEMS	micro-electro-mechanical system
MESFET	metal–semiconductor field-effect transistor
MIGS	midgap (surface) states
MILC	metal-induced lateral crystallization
MIOS	metal–insulator–oxide–semiconductor
MIR	mid-infrared
MIS	metal–insulator–semiconductor
MHEMT	metamorphic HEMT
ML	monolayer
MLC	multi-level cell
MMIC	millimeter-wave integrated circuit
MO	master oscillator
MODFET	modulation-doped FET
MOMBE	metalorganic molecular beam epitaxy
MOPA	master oscillator power amplifier
MOS	metal–oxide–semiconductor
MOSFET	metal–oxide–semiconductor field-effect transistor
MOVPE	metalorganic chemical vapor deposition
MQW	multiple quantum well
MRAM	magnetic random access memory
MRS	Materials Research Society
MS	metal–semiconductor (diode)
MSA	mobility spectral analysis
MSM	metal–semiconductor–metal (diode)
MTJ	magneto-tunneling junction
MWNT	multi-walled (carbon) nanotube

NDR	negative differential resistance
NEP	noise equivalent power
NIR	near infrared
NMOS	n-channel metal–oxide–semiconductor (transistor)
NTSC	national television standard colors
OLED	organic light emitting diode
OMC	organic molecular crystals
ONO	oxide/nitride/oxide
OPSL	optically pumped semiconductor laser
PA	power amplifier
PBG	photonic band gap
pc	primitive cubic
PCM	phase change memory
PFM	piezoresponse force microscopy
PHEMT	pseudomorphic HEMT
PL	photoluminescence
PLD	pulsed laser deposition
PLE	photoluminescence excitation (spectroscopy)
PMC	programmable metallization cell
PMMA	poly-methyl methacrylate
PMOS	p-channel metal–oxide–semiconductor (transistor)
PPC	persistent photoconductivity
PPLN	periodically poled lithium niobate
PV	photovoltaic
PWM	pulsewidth modulation
PZT	$PbTi_xZr_{1-x}O_3$ material
QCL	quantum cascade laser
QCSE	quantum confined Stark effect
QD	quantum dot
QHE	quantum Hall effect
QW	quantum well
QWIP	quantum-well intersubband photodetector
QWR	quantum wire
RAM	random access memory
RAS	reflection anisotropy spectroscopy
RF	radio frequency
RFID	radio frequency identification
RGB	red-green-blue (color system)
RHEED	reflection high-energy electron diffraction
RIE	reactive ion etching

RKKY	Ruderman–Kittel–Kasuya–Yoshida (interaction)
rms	root mean square
ROM	read-only memory
RRAM	resistance random access memory
SAGB	small-angle grain boundary
SAM	separate absorption and amplification (structure)
sc	simple cubic
SCH	separate confinement heterostructure
SdH	Shubnikov-de Haas (oscillation)
SEL	surface-emitting laser
SEM	scanning electron microscopy
SET	single-electron transistor, single electron tunneling
SGDBR	sampled grating distributed Bragg reflector
SHG	second-harmonic generation
si	semi-insulating
SIA	Semiconductor Industry Association
SIMS	secondary ion mass spectrometry
SL	superlattice
SLC	single-level cell
SLG	single layer graphene
s-o	spin-orbit (or split-off)
SOA	semiconductor optical amplifier
SPD	spectral power distribution
SPIE	International Society for Optical Engineering
SPS	short-period superlattice
sRGB	standard RGB
SRH	Shockley–Read–Hall (kinetics)
SSR	side-mode suppression ratio
STM	scanning tunneling microscopy
SWNT	single-walled (carbon) nanotube
TA	transverse acoustic (phonon)
TAS	thermal admittance spectroscopy
TCO	transparent conductive oxide
TE	transverse electric (polarization)
TED	transferred electron device
TFET	transparent FET, tunneling FET
TFT	thin film transistor
TEGFET	two-dimensional electron gas FET
TEM	transmission electron microscopy
TES	two-electron satellite
TF	thermionic field emission
TFT	thin-film transistor
TM	transverse magnetic (polarization)

TMAH	tetramethyl-ammonium-hydroxide
TMR	tunnel-magnetoresistance
TO	transverse optical (phonon)
TOD	turn-on delay (time)
TPA	two-photon absorption
TSO	transparent semiconducting oxide
UHV	ultrahigh vacuum
UV	ultraviolet
VCA	virtual crystal approximation
VCO	voltage-controlled oscillator
VCSEL	vertical-cavity surface-emitting laser
VFF	valence force field
VGF	vertical gradient freeze (growth)
VIS	visible
VLSI	very large scale integration
WGM	whispering gallery mode
WKB	Wentzel–Kramer–Brillouin (approximation or method)
WS	Wigner–Seitz (cell)
YSZ	Yttria-stabilized zirconia (ZrO_2)
X	exciton
XX	biexciton
XSTM	cross-sectional STM
Z	atomic number ($Z = 2$ for helium)
ZnPc	zinc-phthalocyanine

Symbols

α	Madelung constant, disorder parameter, linewidth enhancement factor
$\alpha(\omega)$	absorption coefficient
α_{m}	mirror loss
α_{n}	electron ionization coefficient
α_{p}	hole ionization coefficient
β	used as abbreviation for $e/(k_{\mathrm{B}}\,T)$, spontaneous emission coefficient
γ	broadening parameter, Grüneisen parameter
Γ	broadening parameter
$\gamma_1,\ \gamma_2,\ \gamma_3$	Luttinger parameters
δ_{ij}	Kronecker symbol
Δ_0	spin-orbit splitting
$\epsilon(\omega)$	dielectric function
ϵ_0	permittivity of vacuum
ϵ_{i}	dielectric constant of insulator
ϵ_{r}	relative dielectric function
ϵ_{s}	dielectric function of semiconductor ($= \epsilon_{\mathrm{r}}\,\epsilon_0$)
ϵ_{xy}	components of strain tensor
η	quantum efficiency
η_{d}	differential quantum efficiency
η_{ext}	external quantum efficiency
η_{int}	internal quantum efficiency
η_{w}	wall-plug efficiency
θ	angle
Θ_{D}	Debye temperature
Θ_{B}	typical phonon energy parameter
κ	imaginary part of index of refraction, heat conductivity
λ	wavelength
λ_{p}	plasma wavelength
μ	mobility
μ_0	magnetic susceptibility of vacuum
μ_{h}	hole mobility
μ_{n}	electron mobility

ν	frequency
Π	Peltier coefficient
π_{xy}	components of piezoresistivity tensor
ρ	mass density, charge density, resistivity
ρ_{xy}	components of resistivity tensor
σ	standard deviation, conductivity, stress, effective mass ratio
Σn	grain boundary type
σ_{n}	electron capture cross section
σ_{p}	hole capture cross section
σ_{P}	polarization charge
σ_{xy}	components of stress tensor, components of conductivity tensor
τ	lifetime, time constant
Θ_{D}	Debye temperature
ϕ	phase
χ	electron affinity, electric susceptibility
χ_{ex}	light extraction efficiency
χ_{sc}	electron affinity (of semiconductor)
$\chi(\mathbf{r})$	envelope wavefunction
ψ	angle
$\Psi(\mathbf{r})$	wavefunction
ω	angular frequency
Ω	interaction parameter

a	hydrostatic deformation potential
$\mathbf{a}$	acceleration
A	area
$\mathbf{A}$, A	vector potential
A^*	Richardson constant
a_0	(cubic) lattice constant
b	bowing parameter, deformation potential
$\mathbf{b}$	Burger's vector
B	bimolecular recombination coefficient, bandwidth
$\mathbf{B}$, B	magnetic field
c	velocity of light in vacuum, lattice constant (along c-axis)
C	capacitance, spring constant
C_{n}, C_{p}	Auger recombination coefficient
C_{ij}	elastic constants
d	distance, shear deformation potential
d_{i}	insulator thickness
D	density of states, diffusion coefficient
$\mathbf{D}$, D	displacement field
$D_{\mathrm{e}}(E)$	electron density of states
$D_{\mathrm{h}}(E)$	hole density of states
D_{n}	electron diffusion coefficient

D_{p}	hole diffusion coefficient
e	elementary charge
E	energy, electric field
$\mathbf{E}$, $\mathcal{E}$	electric field
E_{A}	energy of acceptor level
$E_{\mathrm{A}}^{\mathrm{b}}$	acceptor ionization energy
E_{C}	energy of conduction-band edge
E_{D}	energy of donor level, Dirac energy (in graphene)
$E_{\mathrm{D}}^{\mathrm{b}}$	donor ionization energy
E_{F}	Fermi energy
$E_{\mathrm{F_n}}$	electron quasi-Fermi energy
$E_{\mathrm{F_p}}$	hole quasi-Fermi energy
E_{g}	band gap
$\mathcal{E}_{\mathrm{m}}$	maximum electric field
E_{P}	energy parameter
E_{V}	energy of valence-band edge
E_{vac}	energy of vacuum level
E_{X}	exciton energy
$E_{\mathrm{X}}^{\mathrm{b}}$	exciton binding energy
f	oscillator strength
F	free energy
$\mathbf{F}$, F	force
$F(M)$	excess noise factor
F_{B}	Schottky barrier height
f_{e}	Fermi–Dirac distribution function
f_{i}	ionicity
F_{n}	electron quasi-Fermi energy
f_{p}	hole population
F_{p}	hole quasi-Fermi energy
F_{P}	Purcell factor
g	degeneracy, g-factor, gain
G	free enthalpy, generation rate
$\mathbf{G}$	vector of reciprocal lattice
g_{m}	transconductance
G_{th}	thermal generation rate
h	Planck constant
H	enthalpy
$\mathbf{H}$, H	magnetic field
$\mathcal{H}$	Hamiltonian
$\hbar$	$h/(2\pi)$
i	imaginary number
I	current
I_{s}	saturation current
I_{thr}	threshold current
j	current density, orbital momentum

j_{s}	saturation current density
j_{thr}	threshold current density
k	wavenumber, Boltzmann constant
$\mathbf{k}$	wavevector
k_{B}	Boltzmann constant
k_{F}	Fermi wavevector
l	angular orbital momentum
L	length of line element
$\mathbf{L}$	line vector (of dislocation)
L_{D}	diffusion length
L_{z}	quantum-well thickness
m	mass
m_0	free electron mass
m^*	effective mass
m_{c}	cyclotron mass
M	mass, multiplication factor
$\mathbf{M}$, M	magnetization
m_{e}	effective electron mass
m_{h}	effective hole mass
m_{j}	magnetic quantum number
m_{r}	reduced mass
n	electron concentration (in conduction band), ideality factor
$\mathbf{n}$	normal vector
$N(E)$	number of states
n^*	complex index of refraction ($= n_{\mathrm{r}} + \mathrm{i}\kappa$)
N_{A}	acceptor concentration
N_{c}	critical doping concentration
N_{C}	conduction-band edge density of states
N_{D}	donor concentration
n_{i}	intrinsic electron concentration
n_{if}	ideality factor due to image force effect
n_{r}	index of refraction (real part)
n_{s}	sheet electron density
N_{t}	trap concentration
n_{tr}	transparency electron concentration
n_{thr}	threshold electron concentration
N_{V}	valence-band edge density of states
p	pressure, free hole density
$\mathbf{p}$, p	momentum
P	power
$\mathbf{P}$, P	electric polarization
p_{cv}	momentum matrix element
p_{i}	intrinsic hole concentration
q	charge

$\mathbf{q}$, q	heat flow
Q	charge, quality factor, impurity-bound exciton localization energy
r	radius
$\mathbf{r}$	spatial coordinate
R	resistance, radius, recombination rate
R_λ	responsivity
$\mathbf{R}$	vector of direct lattice
r_H	Hall factor
R_H	Hall coefficient
s	spin
S	entropy, Seebeck coefficient, total spin, surface index, surface recombination velocity
S_{ij}	stiffness coefficients
t	time
t_ox	(gate) oxide thickness
T	temperature
u	displacement, cell-internal parameter
$u_{n\mathbf{k}}$	Bloch function
U	energy
$\mathbf{v}$, v	velocity
V	volume, voltage, potential
$V(\lambda)$	(standardized) sensitivity of human eye
V_a	unit-cell volume
V_bi	built-in voltage
v_g	group velocity
v_s	velocity of sound, drift-saturation velocity
v_th	thermal velocity
w	depletion-layer width
W_m	work function
X	electronegativity
Y	Young's module, CIE brightness parameter
Z	partition sum, atomic order number

Physical Constants

constant	symbol	numerical value	unit
speed of light in vacuum	c_0	2.99792458×10^{8}	$\mathrm{m\,s^{-1}}$
permeability of vacuum	μ_0	$4\pi \times 10^{-7}$	$\mathrm{N\,A^{-2}}$
permittivity of vacuum	$\epsilon_0 = (\mu_0 c_0^2)^{-1}$	$8.854187817 \times 10^{-12}$	$\mathrm{F\,m^{-1}}$
elementary charge	e	$1.60217733 \times 10^{-19}$	C
electron mass	m_e	$9.1093897 \times 10^{-31}$	kg
Planck constant	h	$6.6260755 \times 10^{-34}$	J s
	$\hbar = h/(2\pi)$	$1.05457266 \times 10^{-34}$	J s
	$\hbar$	6.582122×10^{-16}	eV s
Boltzmann constant	k_B	1.380658×10^{-23}	$\mathrm{J\,K^{-1}}$
		8.617385×10^{-5}	$\mathrm{meV\,K^{-1}}$
von-Klitzing constant	R_H	25812.8056	Ω
Rydberg constant		13.6056981	eV
Bohr radius	a_B	$5.29177249 \times 10^{-11}$	m

1 Introduction

The proper conduct of science
lies in the pursuit of Nature's puzzles,
wherever they may lead.
J.M. Bishop [1]

The historic development of semiconductor physics and technology began in the second half of the 19th century. Interesting discussions of the early history of the physics and chemistry of semiconductors can be found in treatises of G. Busch [2] and Handel [3]. The history of semiconductor industry can be followed in the text of Morris [4] and Holbrook et al. [5]. In 1947, the realization of the transistor was the impetus to a fast-paced development that created the electronics and photonics industries. Products founded on the basis of semiconductor devices such as computers (CPUs, memories), optical-storage media (lasers for CD, DVD), communication infrastructure (lasers and photodetectors for optical-fiber technology, high frequency electronics for mobile communication), displays (thin film transistors, LEDs), projection (laser diodes) and general lighting (LEDs) are commonplace. Thus, fundamental research on semiconductors and semiconductor physics and its offspring in the form of devices has contributed largely to the development of modern civilization and culture.

1.1 Timetable

In this section early important milestones in semiconductor physics and technology are listed.

1782
A. Volta – coins the phrase 'semicoibente' (semi-insulating) which was translated then into English as 'semiconducting' [6].

1821
T.J. Seebeck – discovery of semiconductor properties of PbS [7].

M. Grundmann, *The Physics of Semiconductors*, 2nd ed., Graduate Texts in Physics, DOI 10.1007/978-3-642-13884-3_1,
© Springer-Verlag Berlin Heidelberg 2010

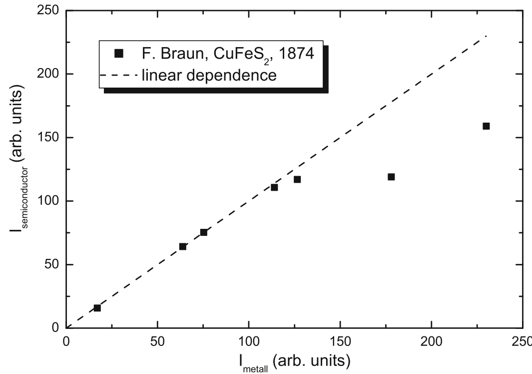

Fig. 1.1. Current through a silver–$CuFeS_2$–silver structure as a function of the current through the metal only, 1874. Data points are for different applied voltages. Experimental data from [12]

1833
M. Faraday – discovery of the temperature dependence of the conductivity of Ag_2S (negative $\mathrm{d}R/\mathrm{d}T$) [8].

1873
W. Smith – discovery of photoconductivity in selenium [9]. Early work on photoconductivity in Se is reviewed in [10, 11].

1874
F. Braun[1] – discovery of rectification in metal–sulfide semiconductor contacts [12], e.g. for $CuFeS_2$ and PbS. The current through a metal–semiconductor contact is nonlinear (as compared to that through a metal, Fig. 1.1), i.e. a deviation from Ohm's law. Braun's structure is similar to a MSM diode.

1876
W.G. Adams and R.E. Day – discovery of the photovoltaic effect in selenium [14].
W. Siemens – large response from selenium photoconductor [15], made by winding two thin platinum wires to the surface of a sheet of mica, and then covering the surface with a thin film of molten selenium. Resistance ratio between dark and illuminated by sunlight was larger than ten [15] and measured to 14.8 in [16].

1879
E.H. Hall – measurement of the transverse potential difference in a thin gold leaf on glass [17, 18]. Experiments were continued by his mentor H.A.

[1]F. Braun made his discoveries on metal–semiconductor contacts in Leipzig while a teacher at the Thomasschule zu Leipzig [13]. He conducted his famous work on vacuum tubes later as a professor in Strasbourg, France.

Rowland [19]. A detailed account of the discovery of the Hall effect is given in [20, 21].

1883
Ch. Fritts – first solar cell, based on an gold/selenium rectifier [16]. The efficiency was below 1%.

1901
J.C. Bose – point contact detector for electromagnetic waves based on galena (PbS) [22]. At the time, the term semiconductor was not introduced yet and Bose speaks about 'substances of a certain class (...) presenting a decreasing resistance to the passage of the electric current with an increasing impressed electromotive force'.

1906
G.W. Pickard – rectifier based on point contact (cat's whisker) diode on silicon [23–25]. Erroneously, the rectifying effect was attributed to a thermal effect, however, the drawing of the 'thermo-junction' (TJ in Fig. 1.2) developed into the circuit symbol for a diode (cmp. Fig. 20.56a).

1907
H.J. Round – discovery of electroluminescence investigating yellow and blue light emission from SiC [26].
K. Bädeker – preparation of metal (e.g. Cd, Cu) oxides and sulfides and also CuI from metal layers using a vapor phase transport method [27].[2]

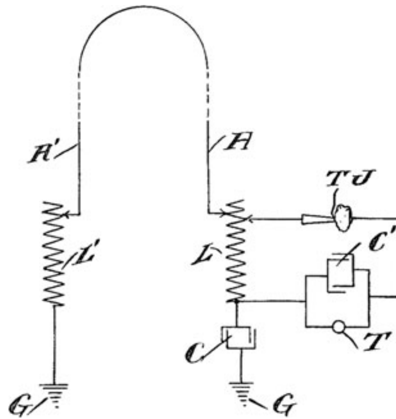

Fig. 1.2. Circuit diagram for a radio receiver with a point-contact diode (TJ). Adapted from [23]

[2]This work was conducted as Habilitation in the Physics Institute of Universität Leipzig. Bädeker became subsequently professor in Jena and fell in WW I. His scientific contribution to semiconductor physics is discussed in [28].

CuI is reported transparent ($\sim$ 200 nm thick films) with a specific resistivity of $\rho = 4.5 \times 10^{-2}\,\Omega\,\mathrm{cm}$, the first transparent conductor.[3] Also CdO (films of thickness 100–200 nm) is reported to be highly conductive, $\rho = 1.2 \times 10^{-3}\,\Omega\,\mathrm{cm}$, and orange-yellow in color, probably the first reported TCO (transparent conductive oxide). Anion deficiency in CuI causes insulating behavior.

1911
The term 'Halbleiter' (semiconductor) is introduced for the first time by J. Weiss [29] and J. Königsberger and J. Weiss [30]. Königsberger preferred the term 'Variabler Leiter' (variable conductor).

1925
J.E. Lilienfeld[4] – proposal of the metal-semiconductor field-effect transistor (MESFET) [33]) (Fig. 1.3). He was also awarded patents for a depletion mode MOSFET [34] and current amplification with nppn- and pnnp-transistors [35].

1927
A. Schleede, H. Buggisch – synthesis of pure, stoichiometric PbS, influence of sulphur excess and impurities [36].
A. Schleede, E. Körner – activation of luminescence of ZnS [37, 38].

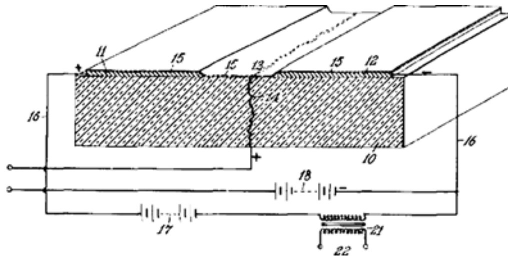

Fig. 1.3. Sketch of a field-effect transistor, 1926. From [33]

[3]CuI is actually a p-type transparent conductor; at that time the reverse sign of the Hall effect could not be interpreted as hole conduction yet although Bädeker considered positive charges [28].

[4]After obtaining his PhD in 1905 from the Friedrich-Wilhelms-Universität Berlin, J.E. Lilienfeld joined the Physics Department of University of Leipzig and worked on gas liquefaction and with Lord Zeppelin on hydrogen-filled blimps. In 1910 he became professor at the University of Leipzig where he mainly researched on X-rays and vacuum tubes. To the surprise of his colleagues he left in 1926 to join a US industrial laboratory [31, 32].

1928
F. Bloch – quantum mechanics of electrons in a crystal lattice, ‘Bloch functions’ [39].

1929
R. Peierls – explanation of positive (anomalous) Hall effect with unoccupied electron states [40, 41].

1931
W. Heisenberg – theory of hole (‘Löcher’) states [42].
R. de L. Kronig and W.G. Penney – properties of periodic potentials in solids [43].
A.H. Wilson – development of band-structure theory [44].
C. Zener – Zener tunneling [45].

1933
C. Wagner – excess (‘Elektronenüberschuss-Leitung’, n-type) and defect (‘Elektronen-Defektleitung’, p-type) conduction [46]. Anion deficiency in ZnO causes conducting behavior [47].

1936
J. Frenkel – description of excitons [48].

1938
B. Davydov – theoretical prediction of rectification in Cu_2O [49].
W. Schottky – theory of the boundary layer in metal–semiconductor contacts [50], being the basis for Schottky contacts and field-effect transistors.
N.F. Mott – metal–semiconductor rectifier theory [51].
R. Hilsch and R.W. Pohl – three-electrode crystal (KBr) [52].

1940
R.S. Ohl – Silicon-based photoeffect (solar cell, Fig. 1.4) [53] from a pn-junction formed within a slab of polycrystalline Si fabricated with directed solidification due to different distribution coefficients of p- and n-dopants (e.g. boron and phosphorus, cmp. Fig. 4.7b) (J. Scaff and H. Theurer) [54, 55].

1941
R.S. Ohl – Silicon rectifier with point contact [56] (Fig. 1.5), building on work from G.W. Pickard (1906) and using metallurgically refined and intentionally doped silicon (J. Scaff and H. Theurer) [54].

1942
K. Clusius, E. Holz and H. Welker – rectification in germanium [57].

1945
H. Welker – patents for JFET and MESFET [58].

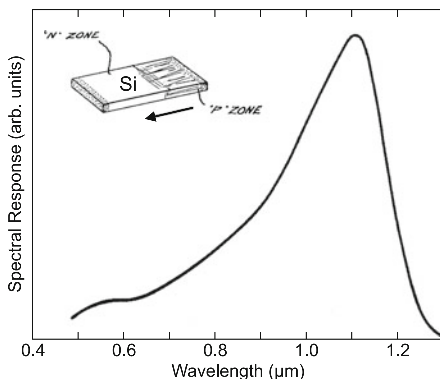

Fig. 1.4. Spectral response of silicon pn-junction photoelement, 1940. The *inset* depicts schematically a Si slab with built-in pn-junction formed during directed solidification (cmp. Fig. 4.7). The *arrow* denotes the direction of solidification. Adapted from [53]

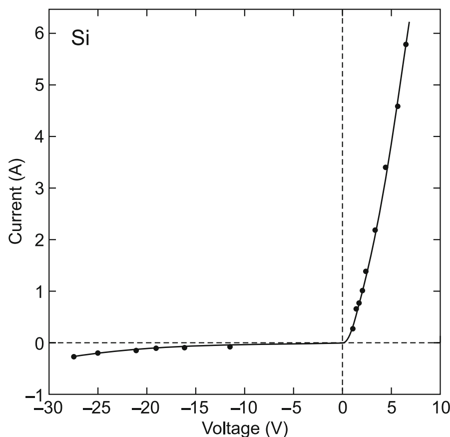

Fig. 1.5. Characteristics of a silicon rectifier, 1941. Adapted from [56]

1947
W. Shockley, J. Bardeen and W. Brattain fabricate the first (point contact) Transistor in the AT&T Bell Laboratories, Holmdel, NJ in an effort to improve hearing aids [59].[5] Strictly speaking the structure was a point-contact transistor. A 50-µm wide slit was cut with a razor blade into gold foil over a plastic (insulating) triangle and pressed with a spring on n-type germanium (Fig. 1.6a) [63]. The surface region of the germanium is p-type due to

[5]Subsequently, AT&T, under pressure from the US Justice Department's antitrust division, licensed the transistor for $25,000. This action initiated the rise of companies like Texas Instruments, Sony and Fairchild.

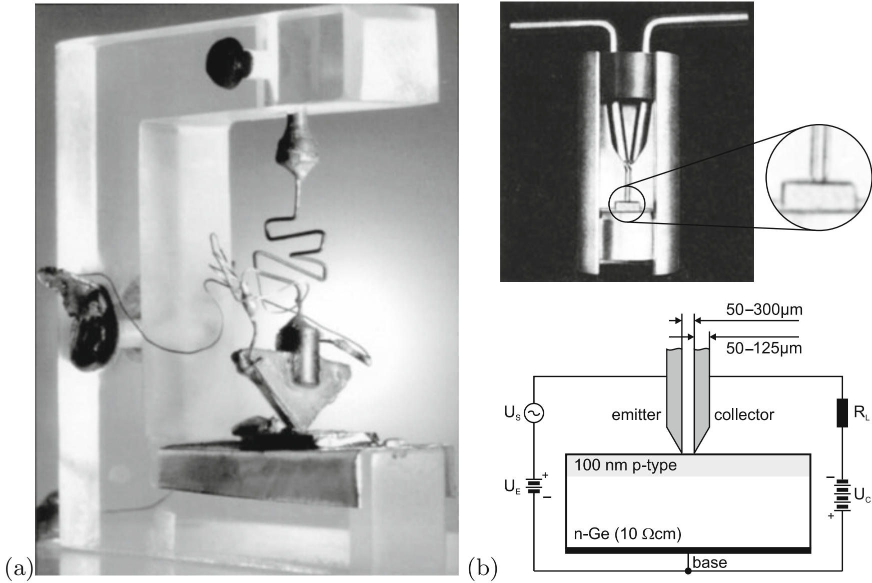

Fig. 1.6. (**a**) The first transistor, 1947 (length of side of wedge: 32 mm). (**b**) Cutaway model of a 1948 point contact transistor ('Type A') based on n-type bulk Ge ($n = 5 \times 10^{14}\,\mathrm{cm}^{-3}$) and common base circuit diagram. The surface region (∼ 100 nm depth) of the Ge is p-type due to surface states and represents an inversion layer. The two wires are made from phosphor bronze. Adapted from [61]

surface states and represents an inversion layer. The two gold contacts form emitter and collector, the large-area back contact of the germanium the base contact [61]. For the first time, amplification was observed [62]. Later models use two close point contacts made from wires with their tips cut into wedge shape (Fig. 1.6b) [61].[6] More details about the history and development of the semiconductor transistor can be found in [63], written on the occasion of the 50th anniversary of its invention.

1948
W. Shockley – invention of the bipolar (junction) transistor [64].

1952
H. Welker – fabrication of compound semiconductors [65–68]
W. Shockley – description of today's version of the (J)FET [69].

[6] The setup of Fig. 1.6b represents a common base circuit. In a modern bipolar transistor, current amplification in this case is close to unity (Sect. 23.2.2). In the 1948 germanium transistor, the reversely biased collector contact is influenced by the emitter current such that current amplification $\partial I_C/\partial I_E$ for constant U_C was up to 2–3. Due to the collector voltage being much larger than the emitter voltage, a power gain of ∼125 was reported [61].

1953
G.C. Dacey and I.M. Ross – first realization of a JFET [70].
D.M. Chapin, C.S. Fuller and G.L. Pearson – invention of the silicon solar cell at Bell Laboratories [71]. A single 2-cm^2 photovoltaic cell from Si, Si:As with an ultrathin layer of Si:B, with about 6% efficiency generated 5 mW of electrical power.[7] Previously existing solar cells based on selenium had very low efficiency (<0.5%).

1958
J.S. Kilby made the first integrated circuit at Texas Instruments. The simple 1.3 MHz RC-oscillator consisted of one transistor, three resistors and a capacitor on a $11 \times 1.7\,\mathrm{mm}^2$ Ge platelet (Fig. 1.7a). J.S. Kilby filed in 1959 for a US patent for miniaturized electronic circuits [72]. At practically the same time R.N. Noyce from Fairchild Semiconductors, the predecessor of INTEL, invented the integrated circuit on silicon using planar technology [73]. A detailed view on the invention of the integrated circuit can be found in [74]. Figure 1.7b shows a flip-flop with four bipolar transistors and five resistors. Initially, the invention of the integrated circuit[8] met scepticism because of concerns regarding yield and the achievable quality of the transistors and the other components (such as resistors and capacitors).

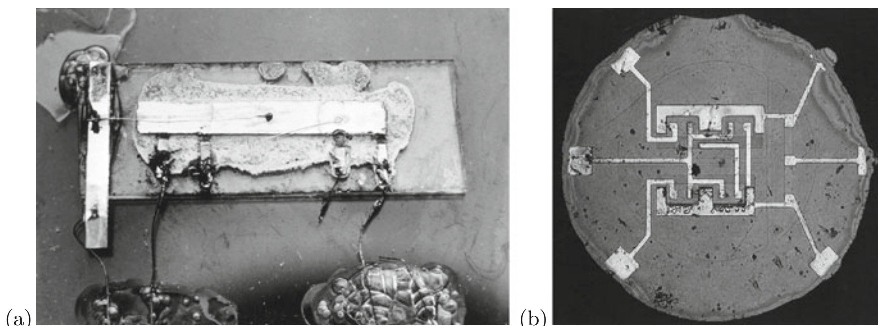

Fig. 1.7. (**a**) The first integrated circuit, 1958 (germanium, $11 \times 1.7\,\mathrm{mm}^2$). (**b**) The first planar integrated circuit, 1959 (silicon, diameter: 1.5 mm)

[7] A solar cell with 1 W power cost \$300 in 1956 (\$3 in 2004). Initially, 'solar batteries' were only used for toys and were looking for an application. H. Ziegler proposed the use in satellites in the 'space race' of the late 1950s.

[8] The two patents led to a decade-long legal battle between Fairchild Semiconductors and Texas Instruments. Eventually, the US Court of Customs and Patent Appeals upheld R.N. Noyce's claims on interconnection techniques but gave J.S. Kilby and Texas Instruments credit for building the first working integrated circuit.

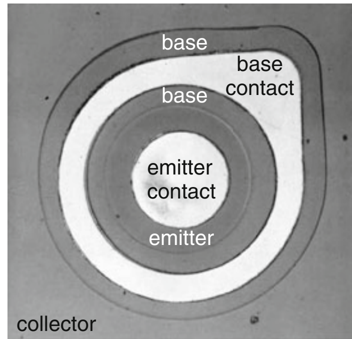

Fig. 1.8. Planar pnp silicon transistor, 1959. The contacts are Al surfaces (not bonded)

1959
J. Hoerni[9] and R. Noyce – first realization of a planar transistor (in silicon) (Fig. 1.8) [76–79].

1960
D. Kahng and M.M. Atalla – first realization of a MOSFET [80, 81].

1962
The first semiconductor laser on GaAs basis at 77 K at GE [82] and at IBM [83]. First visible laser diode [84].

1963
Proposal of a double heterostructure laser (DH laser) by Zh.I. Alferov [85] and H. Kroemer [86].
J.B. Gunn – discovery of the Gunn effect, the spontaneous microwave oscillations in GaAs and InP at sufficiently large applied electric field (due to negative differential resistance) [87].

1966
Zh.I. Alferov – report of the first DH laser on the basis of GaInP at 77 K [88].
C.A. Mead – proposal of the MESFET ('Schottky Barrier Gate FET') [89].

1967
W.W. Hooper and W.I. Lehrer – first realization of a MESFET [90].

1968
DH laser on the basis of GaAs/AlGaAs at room temperature, independently developed by Zh.I. Alferov [91] and I. Hayashi [92].
GaP:N LEDs with yellow-green emission (550 nm) and 0.3% efficiency [93].

[9]The Swiss born Jean Hoerni also contributed $12 000 for the building of the first school in the Karakoram Mountain area in Pakistan and has continued to build schools in Pakistan and Afghanistan as described in [75].

1968
SiC blue LED with efficiency of 0.005% [94].

1975
First monolithic microwave integrated circuit (MMIC) [95].

1995
S. Nakamura – blue GaN heterostructure LED with efficiency exceeding 10% [96].

1.2 Nobel Prize Winners

Several Nobel Prizes[10] have been awarded for discoveries and inventions in the field of semiconductor physics (Fig. 1.9).

1909
Karl Ferdinand Braun
'in recognition of his contributions to the development of wireless telegraphy'

1914
Max von Laue 'for his discovery of the diffraction of X-rays by crystals'

1915
Sir William Henry Bragg
William Lawrence Bragg
'for their services in the analysis of crystal structure by means of X-rays'

1946
Percy Williams Bridgman
'for the invention of an apparatus to produce extremely high pressures, and for the discoveries he made therewith in the field of high pressure physics'

1953
William Bradford Shockley
John Bardeen
Walter Houser Brattain
'for their researches on semiconductors and their discovery of the transistor effect'

1973
Leo Esaki
'for his experimental discoveries regarding tunneling phenomena in semiconductors'

1985
Klaus von Klitzing
'for the discovery of the quantized Hall effect'

[10] www.nobel.se

1998
Robert B. Laughlin
Horst L. Störmer
Daniel C. Tsui
'for their discovery of a new form of quantum fluid with fractionally charged excitations'

2000
Zhores I. Alferov
Herbert Kroemer
'for developing semiconductor heterostructures used in high-speed and opto-electronics'
Jack St. Clair Kilby
'for his part in the invention of the integrated circuit'

2009
Willard S. Boyle
George E. Smith
'for the invention of an imaging semiconductor circuit – the CCD sensor'

2010
Andre Geim
Konstantin Novoselov
'for groundbreaking experiments regarding the two-dimensional material graphene'

1.3 General Information

In Fig. 1.10, the periodic table of elements is shown. In Table 1.1 the physical properties of various semiconductors are summarized.

1909
Karl Ferdinand Braun
(1850–1918)

1914
Max von Laue
(1879–1960)

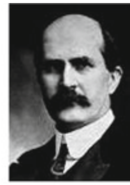
1915
Sir William Henry Bragg
(1862–1942)

1915
William Laurence Bragg
(1890–1971)

1946
Percy Williams Bridgman
(1882–1961)

1953
William B. Shockley
(1910–1989)

1953
John Bardeen
(1908–1991)

1953
Walter Hauser Brattain
(1902–1987)

1973
Leo Esaki
(*1925)

1985
Klaus von Klitzing
(*1943)

1998
Robert B. Laughlin
(*1930)

1998
Horst L. Störmer
(*1949)

1998
Daniel C. Tsui
(*1939)

2000
Zhores I. Alferov
(*1938)

2000
Herbert Kroemer
(*1928)

2000
Jack St. Clair Kilby
(1923–2005)

2009
Willard S. Boyle
(*1924)

2009
George E. Smith
(*1930)

2010
Andre Geim
(*1958)

2010
Konstantin Novoselov
(*1974)

Fig. 1.9. Winners of Nobel Prize in Physics and year of award with great importance for semiconductor physics

Fig. 1.10. Periodic table of elements. From [97]

Table 1.1. Physical properties of various semiconductors at room temperature. 'S' denotes the crystal structure (d: diamond, w: wurtzite, zb: zincblende, ch: chalcopyrite, rs: rocksalt)

	S	a_0 (nm)	E_g (eV)	m_e^*	m_h^*	ϵ_0	n_r	μ_e (cm^2/Vs)	μ_h (cm^2/Vs)
C	d	0.3567	5.45 (Γ)			5.5	2.42	2200	1600
Si	d	0.5431	1.124 (X)	0.98 (m_l) 0.19 (m_t)	0.16 (m_{lh}) 0.5 (m_{hh})	11.7	3.44	1350	480
Ge	d	0.6461	0.67 (L)	1.58 (m_l) 0.08 (m_t)	0.04 (m_{lh}) 0.3 (m_{hh})	16.3	4.00	3900	1900
α-Sn	d	0.64892	0.08 (Γ)	0.02				2000	1000
3C-SiC	zb	0.436	2.4			9.7	2.7	1000	50
4H-SiC	w	0.3073 (a) 1.005 (c)	3.26			9.6	2.7		120
6H-SiC	w	0.30806 (a) 1.5117 (c)	3.101			10.2	2.7	1140	850
AlN	w	0.3111 (a) 0.4978 (c)	6.2			8.5	3.32		
AlP	zb	0.54625	2.43 (X)	0.13		9.8	3.0	80	
AlAs	zb	0.56605	2.16 (X)	0.5	0.49 (m_{lh}) 1.06 (m_{hh})	12		1000	80
AlSb	zb	0.61335	1.52 X)	0.11	0.39	11	3.4	200	300
GaN	w	0.3189 (a) 0.5185 (c)	3.4 (Γ)	0.2	0.8	12	2.4	1500	

Table 1.1. (continued)

	S	a_0 (nm)	E_g (eV)	m_e^*	m_h^*	ϵ_0	n_r	μ_e (cm^2/Vs)	μ_h (cm^2/Vs)
GaP	zb	0.54506	2.26 (Γ)	0.13	0.67	10	3.37	300	150
GaAs	zb	0.56533	1.42 (Γ)	0.067	0.12 (m_{lh}) 0.5 (m_{hh})	12.5	3.4	8500	400
GaSb	zb	0.60954	0.72 (Γ)	0.045	0.39	15	3.9	5000	1000
InN	w	0.3533 (a) 0.5693 (c)	0.9 (Γ)						
InP	zb	0.58686	1.35 (Γ)	0.07	0.4	12.1	3.37	4000	600
InAs	zb	0.60584	0.36 (Γ)	0.028	0.33	12.5	3.42	22 600	200
InSb	zb	0.64788	0.18 (Γ)	0.013	0.18	18	3.75	100 000	1700
ZnO	w	0.325 (a) 0.5206 (c)	3.4 (Γ)	0.24	0.59	6.5	2.2	220	
ZnS	zb	0.54109	3.6 (Γ)	0.3		8.3	2.4	110	
ZnSe	zb	0.56686	2.58 (Γ)	0.17		8.1	2.89	600	
ZnTe	zb	0.61037	2.25 (Γ)	0.15		9.7	3.56		
CdO	rs	0.47	2.16						
CdS	w	0.416 (a) 0.6756 (c)	2.42 (Γ)	0.2	0.7	8.9	2.5	250	
CdSe	zb	0.650	1.73 (Γ)	0.13	0.4	10.6		650	
CdTe	zb	0.64816	1.50 (Γ)	0.11	0.35	10.9	2.75	1050	100

Table 1.1. (continued)

	S	a_0 (nm)	E_g (eV)	m_e^*	m_h^*	ϵ_0	n_r	μ_e (cm^2/Vs)	μ_h (cm^2/Vs)
MgO	rs	0.421	7.3						
HgS	zb	0.5852	2.0 (Γ)					50	
HgSe	zb	0.6084	−0.15 (Γ)	0.045		25		18 500	
HgTe	zb	0.64616	−0.15 (Γ)	0.029	0.3	20	3.7	22 000	100
PbS	rs	0.5936	0.37 (L)	0.1	0.1	170	3.7	500	600
PbSe	rs	0.6147	0.26 (L)	0.07 (m_{lh}) 0.039 (m_{hh})	0.06 (m_{lh}) 0.03 (m_{hh})	250		1800	930
PbTe	rs	0.645	0.29 (L)	0.24 (m_{lh}) 0.02 (m_{hh})	0.3 (m_{lh}) 0.02 (m_{hh})	412		1400	1100
$ZnSiP_2$	ch	0.54 (a) 1.0441 (c)	2.96 (Γ)	0.07					
$ZnGeP_2$	ch	0.5465 (a) 1.0771 (c)	2.34 (Γ)		0.5				
$ZnSnP_2$	ch	0.5651 (a) 1.1302 (c)	1.66 (Γ)						
$CuInS_2$	ch	0.523 (a) 1.113 (c)	1.53 (Γ)						
$CuGaS_2$	ch	0.5347 (a) 1.0474 (c)	2.5 (Γ)						
$CuInSe_2$	ch	0.5784 (a) 1.162 (c)	1.0 (Γ)						
$CuGaSe_2$	ch	0.5614 (a) 1.103 (c)	1.7 (Γ)						

Part I

Fundamentals

2 Bonds

2.1 Introduction

The positively charged atomic nuclei and the electrons in the atomic shells of the atoms making up the semiconductor (or any other solid) are in a binding state. Several mechanisms can lead to such cohesiveness. First, we will discuss the homopolar, electron-pair or covalent bond, then the ionic bond and subsequently the mixed bond. We will only briefly touch on the metallic bond and the van-der-Waals bond.

2.2 Covalent Bonds

Covalent bonds are formed due to quantum-mechanical forces. The prototype covalent bond is the bonding of the hydrogen molecule due to overlapping of the atomic shells. If several electron pairs are involved, directional bonds can be formed in various spatial directions, eventually making up a solid.

2.2.1 Electron-Pair Bond

The covalent bond of two hydrogen atoms in a H_2 molecule can lead to a reduction of the total energy of the system, compared to two single (distant) atoms (Fig. 2.1). For fermions (electrons have spin 1/2) the two-particle wavefunction of the two (indistinguishable) electrons A and B must be antisymmetric, i.e. $\Psi(A, B) = -\Psi(B, A)$ (Pauli principle). The wavefunction of each electron has degrees of freedom in real space ($\mathbf{r}$) and spin (σ), $\Psi(A) = \Psi_{\mathbf{r}}(A)\,\Psi_\sigma(A)$. The two-particle wavefunction of the molecule is non-separable and has the form $\Psi(A, B) = \Psi_{\mathbf{r}}(r_A, r_B)\,\Psi_\sigma(\sigma_A, \sigma_B)$. The binding state has a wavefunction with a symmetric orbital and antiparallel spins, i.e. $\Psi_{\mathbf{r}}(r_A, r_B) = \Psi_{\mathbf{r}}(r_B, r_A)$ and $\Psi_\sigma(\sigma_A, \sigma_B) = -\Psi_\sigma(\sigma_B, \sigma_A)$. The antisymmetric orbital with parallel spins is antibinding for all distances of the nuclei (protons).

2.2.2 sp^3 Bonds

Elements from group IV of the periodic system (C, Si, Ge, ...) have 4 electrons on the outer shell. Carbon has the electron configuration $1s^2 2s^2 2p^2$.

M. Grundmann, *The Physics of Semiconductors*, 2nd ed., Graduate Texts in Physics, DOI 10.1007/978-3-642-13884-3_2,

© Springer-Verlag Berlin Heidelberg 2010

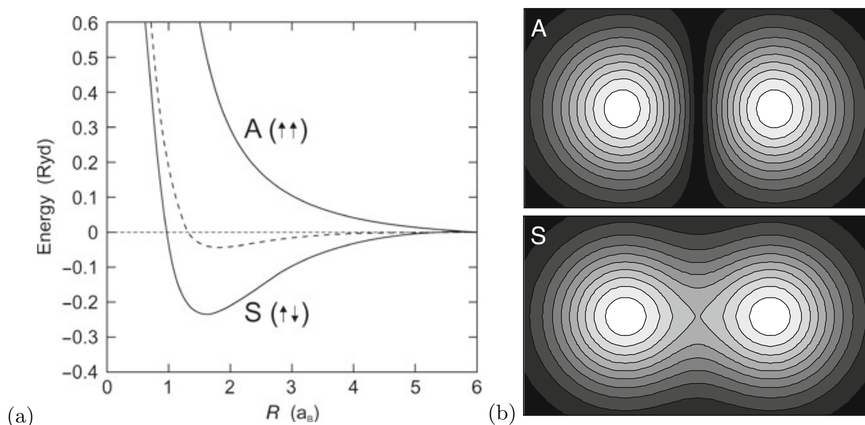

Fig. 2.1. Binding of the hydrogen molecule. (**a**) *Dashed line*: classical calculation (electrostatics), 'S', 'A': quantum-mechanical calculation taking into account Pauli's principle (S: symmetric orbital, antiparallel spins, A: antisymmetric orbital, parallel spins). The distance of the nuclei (protons) is given in units of the Bohr radius $a_B = 0.053$ nm, the energy is given in Rydberg units (13.6 eV). (**b**) Schematic contour plots of the probability distribution ($\Psi^* \Psi$) for the S and A states

For an octet configuration bonding to four other electrons would be optimal (Fig. 2.2). This occurs through the mechanism of sp^3 hybridization.[1] First, one electron of the ns^2np^2 configuration is brought into a p orbital, such that

Fig. 2.2. Octet, the favorite card game of the 'Atomis' (trying to reach octet configuration in a bond by swapping wavefunctions). The bubble says: 'Do you have a 2p?'. Reprinted with permission from [99], ©2002 Wiley-VCH

[1] It is debated in femtosecond chemistry whether the bond *really* forms in this way. However, it is a picture of overwhelming simplicity.

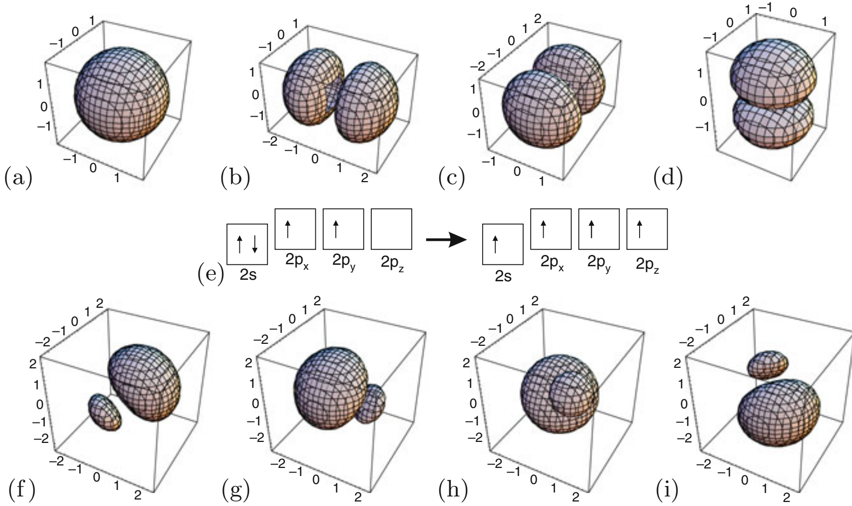

Fig. 2.3. (**a**) s orbital, (**b**,**c**,**d**) p_x, p_y and p_z orbital, (**e**) hybridization, (**f**,**g**,**h**,**i**) orbitals of the sp^3 hybridization: (**f**) $(s{+}p_x{+}p_y{+}p_z)/2$, (**g**) $(s{+}p_x{-}p_y{-}p_z)/2$, (**h**) $(s{-}p_x{+}p_y{-}p_z)/2$, (**i**) $(s{-}p_x{-}p_y{+}p_z)/2$

the outermost shell contains one s, p_x, p_y, and p_z orbital each (Figs. 2.3a–e). The energy necessary for this step is more than regained in the subsequent formation of the covalent bonds. The four orbitals can be reconfigured into four other wavefunctions, the sp^3 hybrids (Figs. 2.3f–i), i.e.

$$\Psi_{++++} = (s + p_x + p_y + p_z)/2 \tag{2.1a}$$

$$\Psi_{++--} = (s + p_x - p_y - p_z)/2 \tag{2.1b}$$

$$\Psi_{+-+-} = (s - p_x + p_y - p_z)/2 \tag{2.1c}$$

$$\Psi_{+--+} = (s - p_x - p_y + p_z)/2\,. \tag{2.1d}$$

These orbitals have a directed form along tetrahedral directions. The binding energy (per atom) of the covalent bond is large, for H–H 4.5 eV, for C–C 3.6 eV, for Si–Si 1.8 eV, and for Ge–Ge 1.6 eV. Such energy is, for *neutral* atoms, comparable to the ionic bond, discussed in the next section.

In Fig. 2.4a the energy of a crystal made up from silicon atoms is shown for various crystal structures[2] or phases (cf. Chap. 3). We note that the crystal energy of further silicon structures are discussed in [98]). The lattice constant with the lowest total energy determines the lattice spacing for each crystal structure. The thermodynamically stable configuration is the phase with the lowest overall energy for given external conditions.

The covalent bond of a group-IV atom to other group-IV atoms has a tetrahedral configuration with electron-pair bonds, similar to the hydrogen molecule bond. In Fig. 2.4b the energy states of the $n = 2$ shell for

[2]Hexagonal diamond is wurtzite structure with two identical atoms in the base.

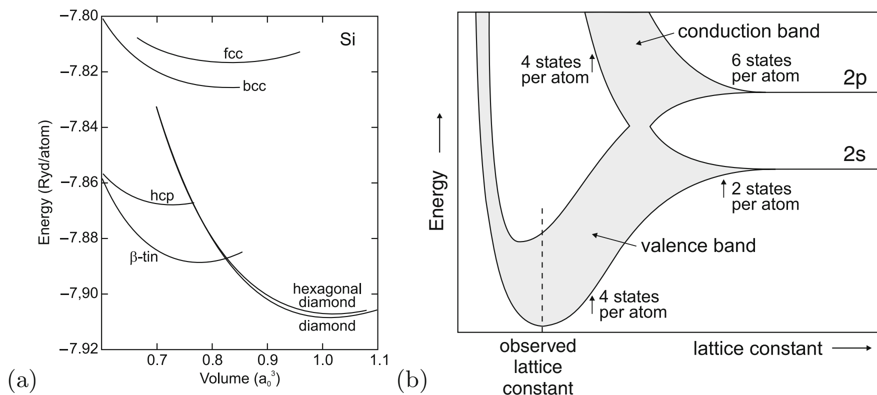

Fig. 2.4. (**a**) Energy per atom in silicon for various crystal structures. Adapted from [100]. (**b**) Electron energy levels in (diamond structure) carbon as a function of the distance of the atomic nuclei (schematic). Adapted from [101, 102]

tetrahedrally bonded carbon (diamond, see Sect. 3.4.3) are shown as a function of the distance from the nuclei. First, the energetically sharp states become a band due to the overlap and coupling of the atomic wavefunctions (cf. Sect. 6). The mixing of the states leads to the formation of the filled lower valence band (binding states) and the empty upper conduction band (antibinding states). This principle is valid for most semiconductors and is shown schematically also in Fig. 2.5. The configuration of bonding and antibinding p orbitals is depicted schematically in Fig. 2.6. The bonding and antibinding sp^3 orbitals are depicted in Figs. 2.7a,b and 2.13. We note that the energy of the crystal does not only depend on the distance from the nuclei but also on their geometric arrangement (crystal structure).

Per carbon atom there are (in the second shell) four electrons and four unoccupied states, altogether eight. These are redistributed into four states (filled) per atoms in the valence band and four states per atom (empty) in the conduction band. Between the top of the valence band and the bottom of the conduction band there is an energy gap, later called the *band gap* (cf. Chap. 6).

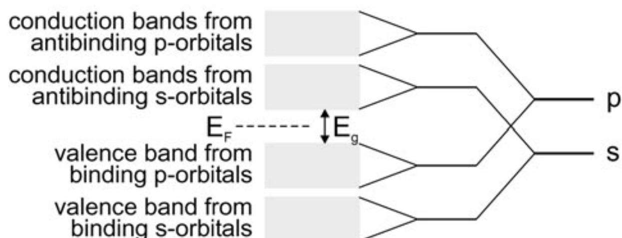

Fig. 2.5. Schematic of the origin of valence and conduction band from the atomic s and p orbitals. The band gap E_g and the position of the Fermi level E_F are indicated

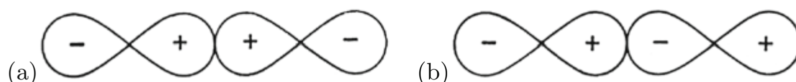

Fig. 2.6. Schematic representation of (**a**) bonding and (**b**) antibinding p orbitals. The *signs* denote the phase of the wavefunction

2.2.3 sp^2 Bonds

Organic semiconductors (see Chap. 16) are made up from carbon compounds. While for inorganic semiconductors the covalent (or mixed, cf. Sect. 2.4) bond with sp^3 hybridization is important, the organic compounds are based on the sp^2 hybridization. This bonding mechanism, which is present in graphite, is stronger than the sp^3-bond present in diamond. The prototype organic molecule is the benzene ring[3] (C_6H_6), shown in Fig. 2.8. The benzene ring is the building block for small organic molecules and polymers.

In the benzene molecule neighboring carbon atoms are bonded within the ring plane via the binding σ states of the sp^2 orbitals (Fig. 2.8a). The wavefunctions (Fig. 2.9) are given by (2.2a–c).

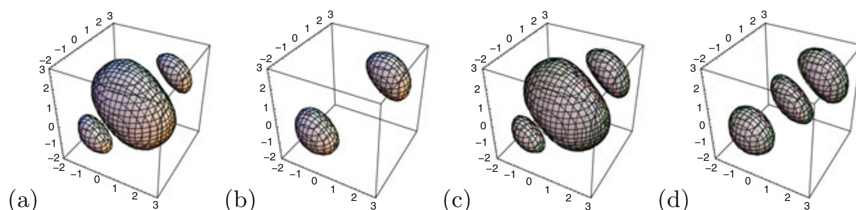

Fig. 2.7. Schematic representation of (**a**,**c**) bonding and (**b**,**d**) antibinding symmetric (**a**,**b**) and nonsymmetric (**c**,**d**) sp^3 orbitals

[3]Supposedly, the chemist Friedrich August Kekulé von Stadonitz had a dream about dancing carbon molecules and thus came up with the ring-like molecule structure [103]. Kekulé remembered: 'During my stay in Ghent, I lived in elegant bachelor quarters in the main thoroughfare. My study, however, faced a narrow side-alley and no daylight penetrated it.... I was sitting writing on my textbook, but the work did not progress; my thoughts were elsewhere. I turned my chair to the fire and dozed. Again the atoms were gamboling before my eyes. This time the smaller groups kept modestly in the background. My mental eye, rendered more acute by the repeated visions of the kind, could now distinguish larger structures of manifold conformation; long rows sometimes more closely fitted together all twining and twisting in snake-like motion. But look! What was that? One of the snakes had seized hold of its own tail, and the form whirled mockingly before my eyes. As if by a flash of lightning I awoke; and this time also I spent the rest of the night in working out the consequences of the hypothesis.'

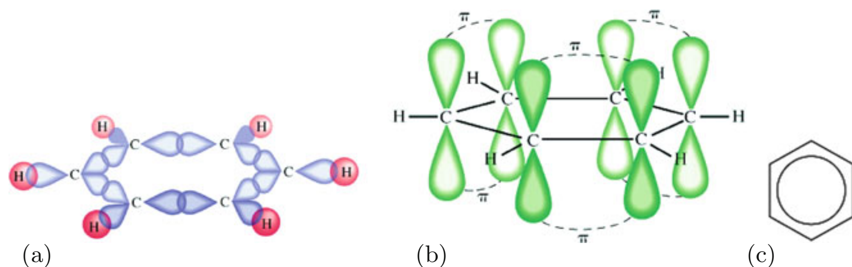

Fig. 2.8. Schematic representation of the (**a**) σ and (**b**) π bonds in benzene, (**c**) schematic symbol for benzene

$$\Psi_1 = (\mathrm{s} + \sqrt{2}\,\mathrm{p}_x)/\sqrt{3} \tag{2.2a}$$

$$\Psi_2 = (\mathrm{s} - \sqrt{1/2}\,\mathrm{p}_x + \sqrt{3/2}\,\mathrm{p}_y)/\sqrt{3} \tag{2.2b}$$

$$\Psi_3 = (\mathrm{s} - \sqrt{1/2}\,\mathrm{p}_x - \sqrt{3/2}\,\mathrm{p}_y)/\sqrt{3}\,. \tag{2.2c}$$

The 'remaining' p_z orbitals do not directly take part in the binding (Fig. 2.8b) and form bonding (π, filled) and antibinding (π^*, empty) orbitals (see Fig. 2.10). The π and π^* states are delocalized over the ring. Between the highest populated molecular orbital (HOMO) and the lowest unoccupied molecular orbital (LUMO) is typically an energy gap (Fig. 2.11). The antibinding σ^* orbitals are energetically above the π^* states.

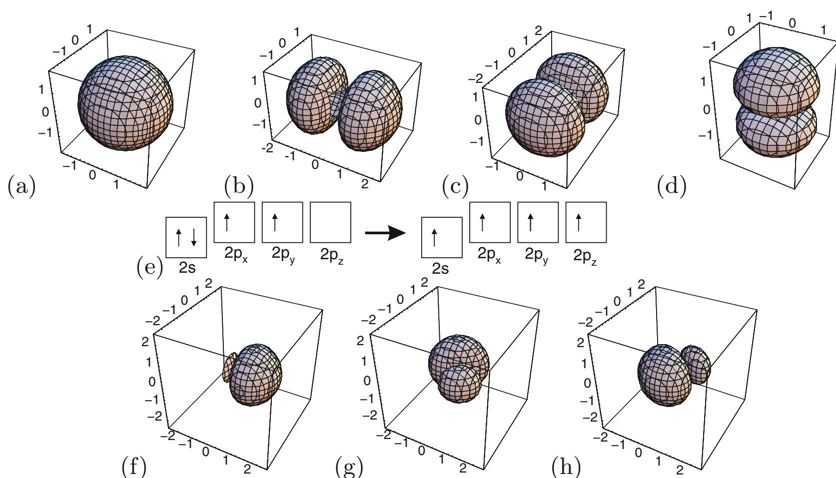

Fig. 2.9. (**a**) s orbital, (**b**,**c**,**d**) p_x, p_y and p_z orbital, (**e**) hybridization, (**f**,**g**,**h**) orbitals of the sp^2 hybridization: (**f**) $(\mathrm{s}+\sqrt{2}\,\mathrm{p}_x)/\sqrt{3}$, (**g**) $(\mathrm{s}-\sqrt{1/2}\,\mathrm{p}_x+\sqrt{3/2}\,\mathrm{p}_y)/\sqrt{3}$, (**h**) $(\mathrm{s}-\sqrt{1/2}\,\mathrm{p}_x-\sqrt{3/2}\,\mathrm{p}_y)/\sqrt{3}$

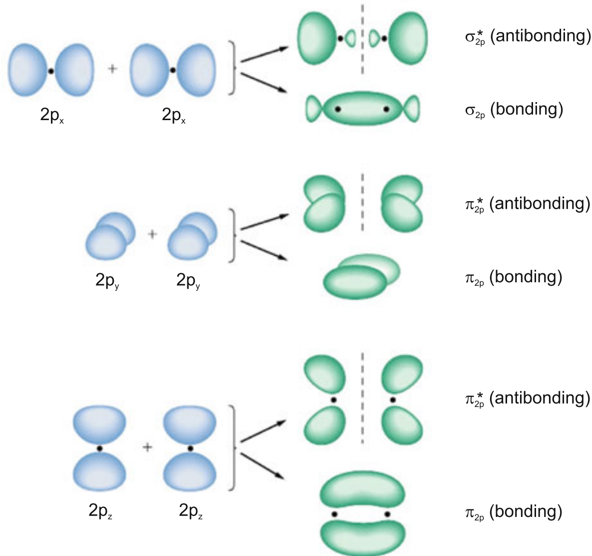

Fig. 2.10. Orbitals due to binding and antibinding configurations of various π orbitals

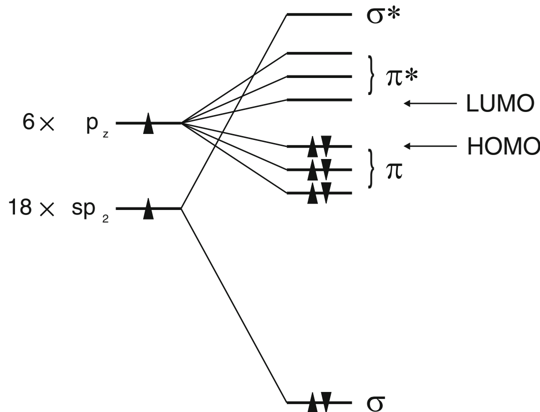

Fig. 2.11. Schematic energy terms of the benzene molecule

2.3 Ionic Bonds

Ionic crystals are made up from positively and negatively charged ions. The heteropolar or ionic bond is the consequence of the electrostatic attraction between the ions. However, the possibly repulsive character of next neighbors has to be considered.

For I–VII compounds, e.g. LiF or NaCl, the shells of the singly charged ions are complete: Li: $1s^2 2s^1 \rightarrow$ Li$^+$: $1s^2$, F: $1s^2 2s^2 2p^5 \rightarrow$ F$^-$: $1s^2 2s^2 2p^6$.

Compared to ions in a gas, a Na–Cl pair in the crystal has a binding energy of 7.9 eV that mostly stems from the electrostatic energy (Madelung energy). Van-der-Waals forces (cf. Sect. 2.6) only contribute 1–2%. The ionization energy of Na is 5.14 eV, the electron affinity of Cl is 3.61 eV. Thus the energy of the NaCl pair in the solid is 6.4 (=7.9−5.1+3.6) eV smaller than in a gas of neutral atoms.

The interaction of two ions with distance vector $\mathbf{r}_{ij}$ is due to the Coulomb interaction

$$U_{ij}^{\mathrm{C}} = \frac{q_i q_j}{4\pi\epsilon_0} \frac{1}{r_{ij}} = \pm \frac{e^2}{4\pi\epsilon_0} \frac{1}{r_{ij}} \tag{2.3}$$

and a repulsive contribution due to the overlap of (complete) shells. This contribution is typically approximated by a radially symmetric core potential

$$U_{ij}^{\mathrm{core}} = \lambda \, \exp(-\lambda/\rho) \tag{2.4}$$

that only acts on next neighbors. λ describes the strength of this interaction and ρ parameterizes its range.

The distance of ions is denoted as $r_{ij} = p_{ij} R$, where R denotes the distance of next neighbors and the p_{ij} are suitable coefficients. The electrostatic interaction of an ion with *all* its neighbors is then written as

$$U_{ij}^{\mathrm{C}} = -\alpha \, \frac{e^2}{4\pi\epsilon_0} \frac{1}{R} \,, \tag{2.5}$$

where α is the Madelung constant. For an attractive interaction (as in a solid), α is positive. It is given (calculated for the i-th ion) as

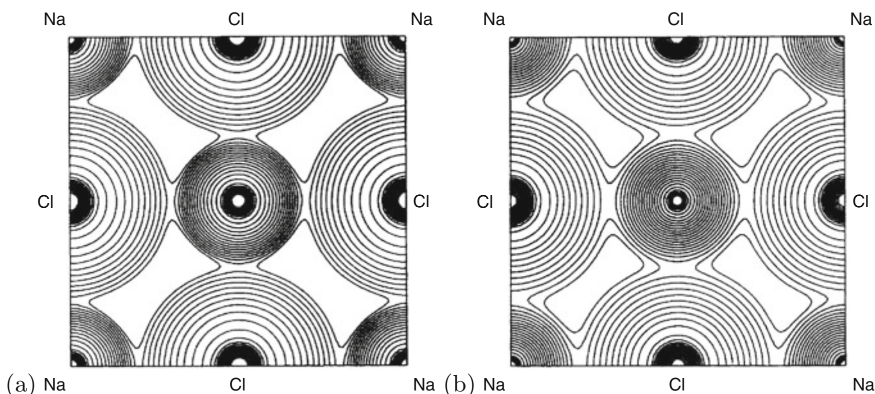

Fig. 2.12. (**a**) Experimental and (**b**) theoretical charge distribution in the (100) plane of NaCl. The lowest contour in the interstitial region corresponds to a charge density of 7 e/nm^3 and adjacent contours differ by $\sqrt{2}$. Differences are mainly due to the fact that the X-ray experiments have been made at room temperature. Adapted from [104]

$$\alpha = \sum_{ij} \frac{\pm 1}{p_{ij}} . \tag{2.6}$$

For a one-dimensional chain $\alpha = 2 \ln 2$. For the rocksalt (NaCl) structure (cf. Sect. 3.4.1) it is $\alpha \approx 1.7476$, for the CsCl structure (see Sect. 3.4.2) it is $\alpha \approx 1.7627$, and for the zincblende structure (see Sect. 3.4.4) it is $\alpha \approx 1.6381$. This shows that ionic compounds prefer the NaCl or CsCl structure. The charge distribution for NaCl is shown in Fig. 2.12. For tetragonal and orthorhombic structures, the Madelung constant has been calculated in [105].

2.4 Mixed Bonds

The group-IV crystals are of perfectly covalent nature, the I–VII are almost exclusively ionically bonded. For III–V (e.g. GaAs, InP) and II–VI compounds (e.g. CdS, ZnO) we have a mixed case.

The (screened) Coulomb potentials of the A and B atoms (in the AB compound) shall be denoted V_A and V_B. The origin of the coordinate system is in the center of the A and B atom (i.e. for the zincblende structure (cf. Sect. 3.4.4) at $(1/8, 1/8, 1/8)a$. The valence electrons then see the potential

$$V_{\mathrm{crystal}} = \sum_{\alpha} V_A(\mathbf{r} - \mathbf{r}_\alpha) + \sum_{\beta} V_B(\mathbf{r} - \mathbf{r}_\beta) , \tag{2.7}$$

where the sum α (β) runs over all A (B) atoms. This potential can be split into a symmetric (V_c, covalent) and an antisymmetric (V_i, ionic) part (2.8b), i.e. $V_{\mathrm{crystal}} = V_\mathrm{c} + V_\mathrm{i}$

$$\begin{aligned} V_\mathrm{c} = \frac{1}{2} \; \Big\{ & \sum_{\alpha} V_A(\mathbf{r} - \mathbf{r}_\alpha) + \sum_{\alpha} V_B(\mathbf{r} - \mathbf{r}_\alpha) \\ & + \sum_{\beta} V_B(\mathbf{r} - \mathbf{r}_\beta) + \sum_{\beta} V_A(\mathbf{r} - \mathbf{r}_\beta) \Big\} \end{aligned} \tag{2.8a}$$

$$\begin{aligned} V_\mathrm{i} = \frac{1}{2} \; \Big\{ & \sum_{\alpha} V_A(\mathbf{r} - \mathbf{r}_\alpha) - \sum_{\alpha} V_B(\mathbf{r} - \mathbf{r}_\alpha) \\ & + \sum_{\beta} V_B(\mathbf{r} - \mathbf{r}_\beta) - \sum_{\beta} V_A(\mathbf{r} - \mathbf{r}_\beta) \Big\} . \end{aligned} \tag{2.8b}$$

For homopolar bonds $V_\mathrm{i} = 0$ and the splitting between bonding and antibinding states is E_h, which mainly depends on the bond length l_{AB} (and the related overlap of atomic wavefunctions). In a partially ionic bond the orbitals are not symmetric along A–B, but the center is shifted towards the more electronegative material (Figs. 2.7c,d and 2.13).

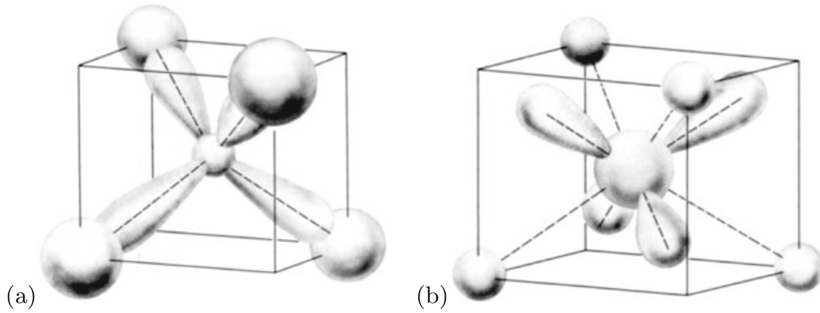

Fig. 2.13. Schematic representation of (**a**) bonding and (**b**) antibinding sp^3 orbitals. From [106]

The band splitting[4] between the (highest) bonding and (lowest) antibinding state E_{ba} is then written as

$$E_{\mathrm{ba}} = E_{\mathrm{h}} + \mathrm{i}C \,, \tag{2.9}$$

where C denotes the band splitting due to the ionic part of the potential and depends only on $V_A - V_B$. C is proportional to the difference of the electronegativities X of the A and B atoms, $C(A, B) = 5.75(X_A - X_B)$. A material thus takes a point in the (E_{h},C) plane (Fig. 2.14). The absolute value for the band splitting is given as $E_{\mathrm{ba}}^2 = E_{\mathrm{h}}^2 + C^2$.

The ionicity of the bond is described with the ionicity (after Phillips) f_{i}, defined as [108]

$$f_{\mathrm{i}} = \frac{C^2}{E_h^2 + C^2} \,. \tag{2.10}$$

The covalent part is $1 - f_{\mathrm{i}}$. In Table 2.1 the ionicity is given for a number of binary compounds. The ionicity can also be interpreted as the angle $\tan(\phi) = C/E_h$ in the (E_h,C) diagram. The critical value of $f_{\mathrm{i}} = 0.785$ for the ionicity separates quite exactly (for about 70 compounds) the 4-fold (diamond, zincblende and wurtzite) from the 6-fold (rocksalt) coordinated substances ($f_{\mathrm{i}} = 0.785$ is indicated by a dashed line in Fig. 2.14).

For ionic compounds, an effective ionic charge e^* is defined connecting the displacement $\mathbf{u}$ of negative and positive ions and the resulting polarization $\mathbf{P} = (e^*/2a^3)\,\mathbf{u}$ [109]. Connected with the ionicity is the so-called s-parameter, describing the change of the charge upon change of bond length b from its equilibrium value b_0 [110]

[4]This energy should not be confused with the *band gap* ΔE_{cv}, the energy separation of the highest valence-band state and the lowest conduction-band state. The energy splitting E_{ba} is the energy separation between the centers of the valence and conduction bands. Mostly, the term E_{g} is used for ΔE_{cv}.

Table 2.1. Ionicity f_i (2.10) for various binary compounds

C	0.0	AlAs	0.27	BeO	0.60	CuCl	0.75
Si	0.0	BeS	0.29	ZnTe	0.61	CuF	0.77
Ge	0.0	AlP	0.31	ZnO	0.62	AgI	0.77
Sn	0.0	GaAs	0.31	ZnS	0.62	MgS	0.79
BAs	0.002	InSb	0.32	ZnSe	0.63	MgSe	0.79
BP	0.006	GaP	0.33	HgTe	0.65	CdO	0.79
BeTe	0.17	InAs	0.36	HgSe	0.68	HgS	0.79
SiC	0.18	InP	0.42	CdS	0.69	MgO	0.84
AlSb	0.25	AlN	0.45	CuI	0.69	AgBr	0.85
BN	0.26	GaN	0.50	CdSe	0.70	LiF	0.92
GaSb	0.26	MgTe	0.55	CdTe	0.72	NaCl	0.94
BeSe	0.26	InN	0.58	CuBr	0.74	RbF	0.96

$$e^*(b) = e^*(b_0)\left(\frac{b}{b_0}\right)^s \approx e_0^*(1 + s\epsilon)\ , \tag{2.11}$$

ϵ being the strain of the bond length, $b/b_0 = 1 + \epsilon$. It seems justified to assume that $e^*(b_0)$ is always positive at the metal atom in III–V and II–VI compounds. The relation of s with the ionicity f_i is shown in Fig. 2.15 for various compound semiconductors.

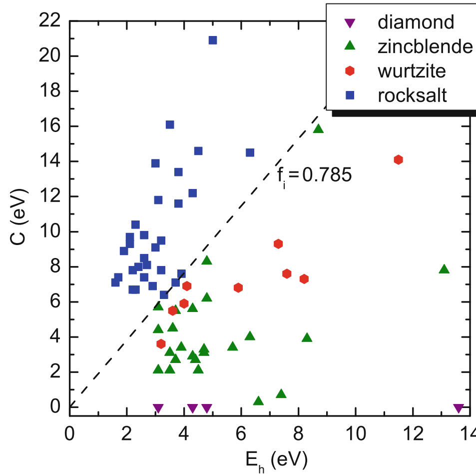

Fig. 2.14. Values of E_h and C for various $A^N B^{8-N}$ compounds. The *dashed line* $f_i = 0.785$ separates 4-fold from 6-fold coordinated structures. Most data taken from [107]

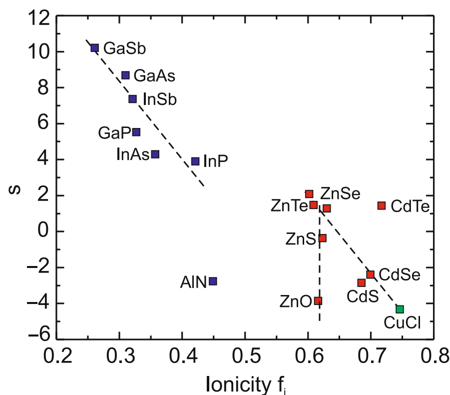

Fig. 2.15. s-Parameter as defined in (2.11) as a function of the ionicity f_i (2.10) for various compound semiconductors. *Dashed lines* are guides to the eye. Data from [111], value for CuCl from [110]

2.5 Metallic Bonding

In a metal, the positively charged atomic cores are embedded in a more or less homogeneous sea of electrons. The valence electrons of the atoms become the conduction electrons of the metal. These are freely moveable and at $T = 0\,\mathrm{K}$ there is no energy gap between filled and empty states. The bonding is mediated by the energy reduction for the conduction electrons in the periodic potential of the solid compared to free atoms. This will be clearer when the band structure is discussed (Chap. 6). In transition metals the overlap of inner shells (d or f) can also contribute to the bonding.

2.6 van-der-Waals Bonds

The van-der-Waals bond is a dipole bond that leads to bonding in the noble-gas crystals (at low temperature). Ne, Ar, Kr and Xe crystallize in the densely packed fcc lattice (cf. Sect. 3.3.5). He^3 and He^4 represent an exception. They do not solidify at zero pressure at $T = 0\,K$ due to the large zero-point energy. This quantum-mechanical effect is especially strong for oscillators with small mass.

When two neutral atoms come near to each other (distance of the nuclei R), an attractive dipole–dipole interaction $-AR^{-6}$ arises (London interaction) the van-der-Waals interaction. The quantum-mechanical overlap of the (filled) shells leads to a strong repulsion $+BR^{-12}$. Altogether, a binding energy minimum results for the Lennard–Jones potential V_LJ (see Fig. 2.16)

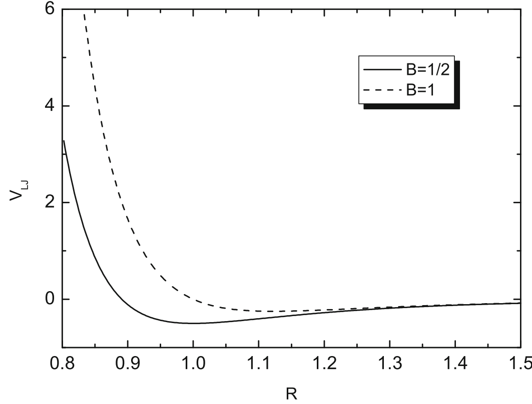

Fig. 2.16. Lennard–Jones potential (2.12) for $A = 1$ and two values of B

$$V_{\mathrm{LJ}}(R) = -\frac{A}{R^6} + \frac{B}{R^{12}} \ . \tag{2.12}$$

The energy minimum $E_{\min} = -A^2/(2B)$ is at $R = (2B/A)^{1/6}$.

The origin of the attractive dipole–dipole interaction can be understood from a one-dimensional (1D) model as follows: Two atoms are modeled by their fixed positively charged nuclei in a distance R and their negatively charged electron shells that are polarizable, i.e. can be displaced along one direction x. Additionally, we assume (two identical) 1D harmonic oscillators for the electron motion at the positions 0 and R. Then, the Hamilton operator H_0 of the system without interaction (R is very large)

$$H_0 = \frac{1}{2m}\, p_1^2 + C\, x_1^2 + \frac{1}{2m}\, p_2^2 + C\, x_2^2 \ . \tag{2.13}$$

The indices 1 and 2 denote the two electrons of atoms. x_1 and x_2 are the displacements of the electrons. Both harmonic oscillators have a resonance frequency $\omega_0 = \sqrt{C/m}$, and the zero-point energy is $\hbar\omega_0/2$.

Taking into account the Coulomb interaction of the four charges, an additional term H_1 arises

$$H_1 = \frac{e^2}{R} + \frac{e^2}{R + x_1 + x_2} - \frac{e^2}{R + x_1} - \frac{e^2}{R - x_2} \approx -\frac{2e^2}{R^3}\, x_1\, x_2 \ . \tag{2.14}$$

The approximation is valid for small amplitudes $x_i \ll R$. A separation of variables can be achieved by transformation to the normal modes

$$x_s = \frac{x_1 + x_2}{\sqrt{2}}, x_a = \frac{x_1 - x_2}{\sqrt{2}} \ . \tag{2.15}$$

Then we find

$$\begin{aligned} H &= H_0 + H_1 \\ &= \left[\frac{1}{2m} p_s^2 + \frac{1}{2}\left(C - \frac{2e^2}{R^3}\right) x_s^2\right] + \left[\frac{1}{2m} p_a^2 + \frac{1}{2}\left(C - \frac{2e^2}{R^3}\right) x_a^2\right] . \end{aligned} \tag{2.16}$$

This equation is the Hamiltonian of two decoupled harmonic oscillators with the normal frequencies

$$\omega_\pm = \sqrt{\left(C \pm \frac{2e^2}{R^3}\right) / m} \approx \omega_0 \left[1 \pm \frac{1}{2}\left(\frac{2e^2}{CR^3}\right) - \frac{1}{8}\left(\frac{2e^2}{CR^3}\right)^2 + \ldots\right] . \tag{2.17}$$

The coupled system thus has a lower (zero-point) energy than the uncoupled. The energy difference per atom is (in lowest order) proportional to R^{-6}.

$$\Delta U = \hbar\omega_0 - \frac{1}{2}(\omega_+ - \omega_-) \approx -\hbar\omega_0 \frac{1}{8}\left(\frac{2e^2}{CR^3}\right)^2 = -\frac{A}{R^6} . \tag{2.18}$$

The interaction is a true quantum-mechanical effect, i.e. the reduction of the zero-point energy of coupled oscillators.

2.7 Hamilton Operator of the Solid

The total energy of the solid, including kinetic and potential terms, is

$$\begin{aligned} H = &\sum_i \frac{\mathbf{p}_i^2}{2m_i} + \sum_j \frac{\mathbf{P}_j^2}{2M_j} \\ &+ \frac{1}{2}\sum_{j,j'} \frac{Z_j\, Z_{j'}\, e^2}{4\pi\epsilon_0\, |\mathbf{R}_j - \mathbf{R}_{j'}|} + \frac{1}{2}\sum_{i,i'} \frac{e^2}{4\pi\epsilon_0\, |\mathbf{r}_i - \mathbf{r}_{i'}|} \\ &- \sum_{i,j} \frac{Z_j\, e^2}{4\pi\epsilon_0\, |\mathbf{R}_j - \mathbf{r}_i|} , \end{aligned} \tag{2.19}$$

where $\mathbf{r}_i$ and $\mathbf{R}_i$ are the position operators and $\mathbf{p}_i$ and $\mathbf{P}_i$ are the momentum operators of the electrons and nuclei, respectively. The first term is the kinetic energy of the electrons, the second term is the kinetic energy of the nuclei. The third term is the electrostatic interaction of the nuclei, the fourth term is the electrostatic interaction of the electrons. In the third and fourth terms the summation over the same indices is left out. The fifth term is the electrostatic interactions of electrons and nuclei.

In the following, the usual approximations in order to treat (2.19) are discussed. First, the nuclei and the electrons tightly bound to the nuclei

(inner shells) are united with ion cores. The remaining electrons are the valence electrons.

The next approximation is the Born–Oppenheimer (or adiabatic) approximation. Since the ion cores are much heavier than the electrons (factor $\approx 10^3$) they move much slower. The frequencies of the ion vibrations are typically in the region of several tens of meV (phonons, cf. Sect. 5.2), the energy to excite an electron is typically 1 eV. Thus, the electrons always 'see' the momentary position of the ions, the ions, however, 'see' the electron motions averaged over many periods. Thus, the Hamiltonian (2.19) is split into three parts:

$$H = H_{\mathrm{ions}}(\mathbf{R}_j) + H_{\mathrm{e}}(\mathbf{r}_i, \mathbf{R}_{j0}) + H_{\mathrm{e-ion}}(\mathbf{r}_i, \delta\mathbf{R}_j) \; . \tag{2.20}$$

The first term contains the ion cores with their potential and the time-averaged contribution of the electrons. The second term is the electron motion around the ion cores at their averaged positions $\mathbf{R}_{j0}$. The third term is the Hamiltonian of the electron–phonon interaction that depends on the electron positions and the deviation of the ions from their average position $\delta\mathbf{R}_j = \mathbf{R}_j - \mathbf{R}_{j0}$. The electron–phonon interaction is responsible for such effects as electrical resistance and superconductivity.

3 Crystals

3.1 Introduction

The economically most important semiconductors have a relatively simple atomic arrangement and are highly symmetric. The symmetry of the atomic arrangement is the basis for the classification of the various crystal structures. Using group theory [112], basic and important conclusions can be drawn about the physical properties of the crystal, such as its elastic and electronic properties. The presence of highly symmetric planes is obvious from the crystal shape of the minerals and their cleavage behavior.

Polycrystalline semiconductors consist of grains of finite size that are structurally perfect but have various orientations. The grain boundaries are a lattice defect (see also Sect. 4.4.3). Amorphous semiconductors are disordered on the atomic scale, see Sect. 3.3.7.

3.2 Crystal Structure

The crystals are built up by the (quasi-) infinite periodic repetition of identical building blocks. This lattice (Bravais lattice) is generated by the three fundamental *translation* vectors $\mathbf{a}_1$, $\mathbf{a}_2$ and $\mathbf{a}_3$. These three vectors may not lie in a common plane. The lattice (Fig. 3.1) is the set of all points $\mathbf{R}$.

$$\mathbf{R} = n_1\,\mathbf{a}_1 + n_2\,\mathbf{a}_2 + n_3\,\mathbf{a}_3 \; . \tag{3.1}$$

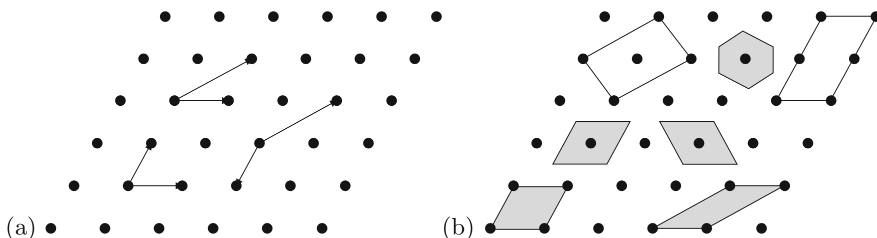

Fig. 3.1. (**a**) Two-dimensional lattice. It can be generated by various pairs of translation vectors. (**b**) Elementary cells of the lattice. Primitive elementary cells are *shaded*

M. Grundmann, *The Physics of Semiconductors*, 2nd ed., Graduate Texts in Physics, DOI 10.1007/978-3-642-13884-3_3,
© Springer-Verlag Berlin Heidelberg 2010

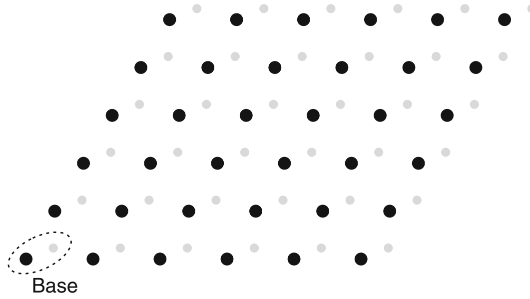

Fig. 3.2. Crystal structure, consisting of a lattice and a base

The crystal structure is made up by the lattice and the building block that is attached to each lattice point. This building block is called the base (Fig. 3.2). In the simplest case, e.g. for simple crystals like Cu, Fe or Al, this is just a single atom (monoatomic base). In the case of C (diamond), Si or Ge, it is a diatomic base with two identical atoms (e.g. Si–Si or Ge–Ge), in the case of compound semiconductors, such as GaAs or InP, it is a diatomic base with nonidentical atoms such as Ga–As or In–P. There exist far more involved structures, e.g. $NaCd_2$ where the smallest cubic cell contains 1,192 atoms. In protein crystals, the base of the lattice can contain 10,000 atoms.

In summary: Crystal structure = Lattice × Base.

3.3 Lattice

As described in Sect. 3.2 the lattice is spanned by three vectors $\mathbf{a}_i$. The lattice symmetry is decisive for the physical properties of the semiconductor. It is described by the appropriate groups of the symmetry operations.

3.3.1 Unit Cell

The choice of the vectors $\mathbf{a}_i$ making up the lattice is not unique (Fig. 3.1). The volume that is enclosed in the parallelepiped spanned by the vectors $\mathbf{a}_1$, $\mathbf{a}_2$ and $\mathbf{a}_3$ is called the *elementary cell*. A *primitive* elementary cell is an elementary cell with the smallest possible volume (Fig. 3.1b). In each primitive elementary cell there is exactly *one* lattice point. The coordination number is the number of next-neighbor lattice points. A primitive cubic (pc) lattice, e.g. has a coordination number of 6.

The typically chosen primitive elementary cell is the *Wigner–Seitz* (WS) cell that reflects the symmetry of the Bravais lattice best. The Wigner–Seitz cell around a lattice point R_0 contains all points that are closer to this lattice point than to any other lattice point. Since all points fulfill such a condition for some lattice point R_i, the Wigner–Seitz cells fill the volume completely.

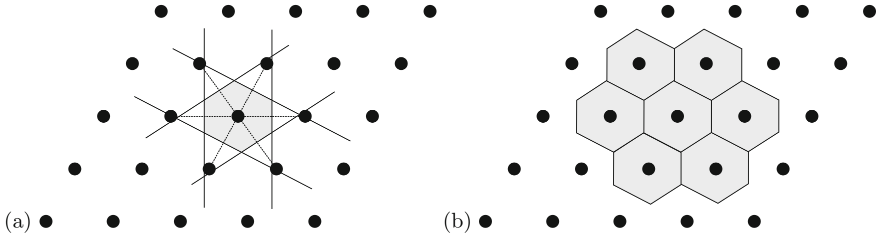

Fig. 3.3. (**a**) Construction of a two-dimensional Wigner–Seitz cell, (**b**) filling of space with WS cells

The boundary of the Wigner–Seitz cell is made up by points that have the same distance to R_0 and some other lattice point(s). The Wigner–Seitz cell around R_0 is constructed by drawing lines from R_0 to the next neighbors R_j, taking the point at half distance and erecting a perpendicular plane at $(R_j + R_0)/2$. The WS cell is the smallest polyhedra circumscribed by these planes. A two-dimensional construction is shown in Fig. 3.3.

3.3.2 Point Group

Besides the translation there are other operations under which the lattice is invariant, i.e. the lattice is imaged into itself. These are:

Identity. The neutral element of any point group is the identity that does not change the crystal. It is denoted as 1 (E) in international (Schönfließ) notation.

Rotation. The rotation around an axis may have a rotation angle of 2π, $2\pi/2$, $2\pi/3$, $2\pi/4$ or $2\pi/6$ or their integer multiples. The axis is then called n = 1-, 2-, 3-, 4- or 6-fold, respectively, and denoted as n (international notation) or C_n (Schönfließ). Objects with C_n symmetry are depicted in Fig. 3.4.

Mirror operation with respect to a plane through a lattice point. Different mirror planes are discerned (Fig. 3.5) (after Schönfließ) σ_h: a mirror plane perpendicular to a rotational axis, σ_v: a mirror plane that contains a rota-

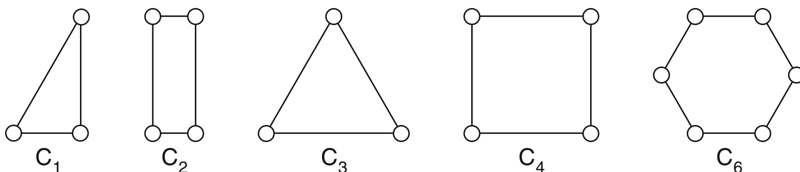

Fig. 3.4. Two-dimensional objects with perpendicular rotation axis C_n. Note that the *circles* do not exhibit σ_h symmetry with respect to the paper plane, i.e. they are different on the top and bottom side

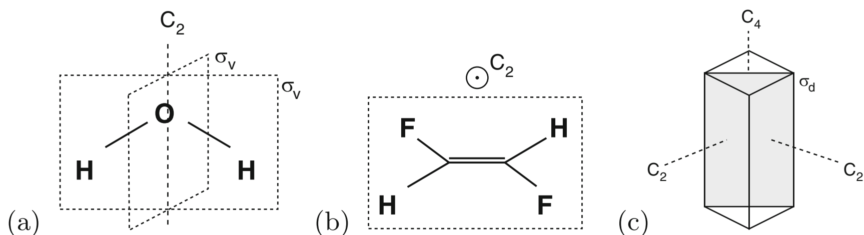

Fig. 3.5. Mirror planes: (**a**) σ_v (at H_2O molecule), (**b**) σ_h (at F_2H_2 molecule) and (**c**) σ_d

tional axis, and σ_d: a mirror plane that contains a rotational axis and bisects the angle between two C_2 axes. The international notation is $\bar{2}$.

Inversion. All points around the inversion center $\mathbf{r}$ are replaced by $-\mathbf{r}$. The inversion is denoted $\bar{1}$ (i) in international (Schönfließ) notation.

Improper rotation. The improper rotation S_n is a rotation C_n followed immediately by the inversion operation i denoted as $\bar{n}$ in international notation. There are $\bar{3}$, $\bar{4}$ and $\bar{6}$ and their powers. Only the combined operation $\bar{n}$ is a symmetry operation, while the individual operations C_n and i alone are not symmetry operations. In the Schönfließ notation the improper rotation is defined as $S_n = \sigma_{\mathrm{h}} C_n$, with σ_{h} being a mirror operation with a plane perpendicular to the axis of the C_n rotation, denoted as S_n. There are S_3, S_4 and S_6 and $\bar{3} = S_6^5$, $\bar{4} = S_4^3$ and $\bar{6} = S_3^5$. For successive applications, the S_n yield previously known operations, e.g. $S_4^2 = C_2$, $S_4^4 = E$, $S_6^2 = C_3$, $S_6^3 = i$, $S_3^2 = C_3^2$, $S_3^3 = \sigma_{\mathrm{h}}$, $S_3^4 = C_3$, $S_3^6 = E$. We note that formally S_1 is the inversion i and S_2 is the mirror symmetry σ. Objects with S_n symmetry are schematically shown in Fig. 3.6.

These symmetry operations form 32 *point groups*. These groups are shown (with their different notations and elements) in Table 3.1. The highest symmetry is the cubic symmetry $O_h = O \times i$. The tetraeder group T_d (methane molecule) is a subgroup of O_h.

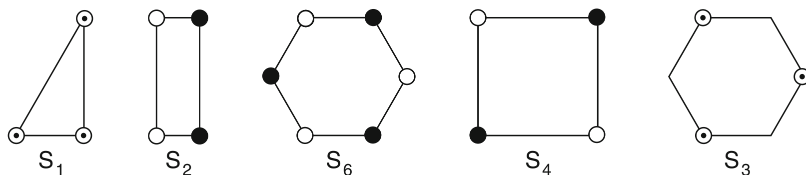

Fig. 3.6. Two-dimensional objects with perpendicular improper rotation axis S_n. Note that the *white* and *black circles* do not exhibit σ_h symmetry with respect to the paper plane, i.e. they are white on the top and black on the bottom. The *circles with a dot* in the center exhibit σ_h symmetry, i.e. they look the same from top and bottom

Table 3.1. The 32 point groups. N_{sg} denotes the number of space groups

System	Class		N_{sg}	Symmetry elements
	Inter-national	Schön-fließ		
triclinic	1	C_1	1	E
	$\bar{1}$	C_i	1	$E\ i$
monoclinic	m	C_s	3	$E\ \sigma_h$
	2	C_2	4	$E\ C_2$
	$2/m$	C_{2h}	6	$E\ C_2\ i\ \sigma_h$
orthorhombic	$2mm$	C_{2v}	9	$E\ C_2\ \sigma_v'\ \sigma_v''$
	222	D_2	22	$E\ C_2\ C_2'\ C_2''$
	mmm	D_{2h}	28	$E\ C_2\ C_2'\ C_2''\ i\ \sigma_h\ \sigma_v'\ \sigma_v''$
tetragonal	4	6	C_4	$E\ 2C_4\ C_2$
	$\bar{4}$	2	S_4	$E\ 2S_4\ C_2$
	$4/m$	6	C_{4h}	$E\ 2C_4\ C_2\ i\ 2S_4\ \sigma_h$
	$4mm$	10	C_{4v}	$E\ 2C_4\ C_2\ 2\sigma_v'\ 2\sigma_d$
	$\bar{4}2m$	12	D_{2d}	$E\ C_2\ C_2'\ C_2''\ 2\sigma_d\ 2S_4$
	422	12	D_4	$E\ 2C_4\ C_2\ 2C_2'\ 2C_2''$
	$4/mmm$	20	D_{4h}	$E\ 2C_4\ C_2\ 2C_2'\ 2C_2''\ i\ 2S_4\ \sigma_h\ 2\sigma_v'\ 2\sigma_h$
trigonal (rhombohedral)	3	C_3	4	$E\ 2C_3$
	$\bar{3}$	S_6	2	$E\ 2C_3\ i\ 2S_6$
	$3m$	C_{3v}	7	$E\ 2C_3\ 3\sigma_v$
	32	D_3	6	$E\ 2C_3\ 3C_2$
	$\bar{3}m$	D_{3d}	6	$E\ 2C_3\ 3C_2\ i\ 2S_6\ 3\sigma_d$
hexagonal	$\bar{6}$	C_{3h}	6	$E\ 2C_3\ \sigma_h\ 2S_3$
	6	C_6	1	$E\ 2C_6\ 2C_3\ C_2$
	$6/m$	C_{6h}	2	$E\ 2C_6\ 2C_3\ C_2\ i\ 2S_3\ 2S_6\ \sigma_h$
	$\bar{6}m2$	D_{3h}	6	$E\ 2C_3\ 3C_2\ \sigma_h\ 2S_3\ 3\sigma_v$
	$6mm$	C_{6v}	4	$E\ 2C_6\ 2C_3\ C_2\ 3\sigma_v\ 3\sigma_d$
	622	D_6	4	$E\ 2C_6\ 2C_3\ C_2\ 3C_2'\ 3C_2''$
	$6/mmm$	D_{6h}	4	$E\ 2C_6\ 2C_3\ C_2\ 3C_2'\ 3C_2''\ i\ 2S_3\ 2S_6\ \sigma_h\ 3\sigma_d\ 3\sigma_v$
cubic	23	T	5	$E\ 4C_3\ 4C_3^2\ 3C_2$
	$m3$	T_h	7	$E\ 4C_3\ 4C_3^2\ 3C_2\ i\ 8S_6\ 3\sigma_h$
	$\bar{4}3m$	T_d	8	$E\ 8C_3\ 3C_2\ 6\sigma_d\ 6S_4$
	432	O	6	$E\ 8C_3\ 3C_2\ 6C_2'\ 6C_4$
	$m3m$	O_h	10	$E\ 8C_3\ 3C_2\ 6C_2\ 6C_4\ i\ 8S_6\ 3\sigma_h\ 6\sigma_d\ 6S_4$

Important for surface symmetries, there are 10 two-dimensional point groups.

3.3.3 Space Group

The space group is formed by the combination of the elements of the point group with translations. The combination of a translation along a rotational axis with a rotation around this axis creates a screw axis n_m. In Fig. 3.7a, a so-called 4_1 screw axis is shown. The first index n indicates the rotation angle, i.e. $2\pi/n$, the second index indicates the translation, i.e. cm/n, c being

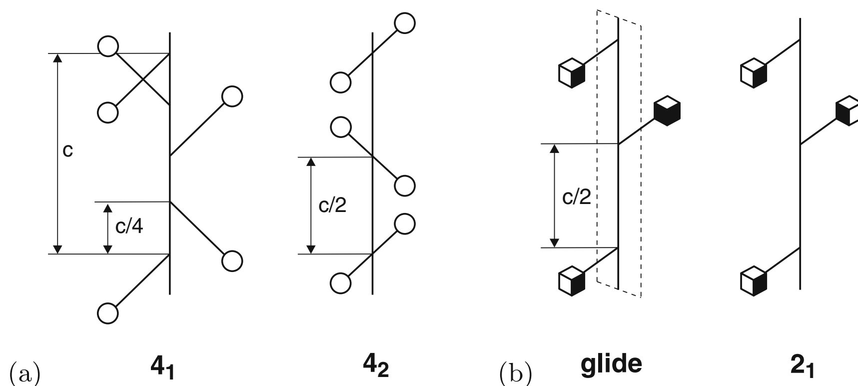

Fig. 3.7. (**a**) Schematic drawing of a 4_1 and 4_2 screw axis. (**b**) Schematic drawing of an axial glide reflection. The mirror plane is shown with dashed outline. Opposite faces of the cube have opposite color. For comparison a 2_1 screw axis is shown

the periodicity along the axis. There are eleven crystallographically allowed screw rotations.[1]

The combination of the mirror operation at a plane that contains a rotational axis with a translation along this axis creates a glide reflection (Fig. 3.7b). For an axial glide (or b-glide) the translation is parallel to the reflection plane. A diagonal glide (or d-glide) involves translation in two or three directions. A third type of glide is the diamond glide (or d-glide). There are 230 different space groups, listed in Appendix B. A detailed treatment can be found in [113].[2]

Important for surface symmetries, there are 17 two-dimensional space groups.

3.3.4 2D Bravais Lattices

There are five two-dimensional (2D) Bravais lattices (Fig. 3.8) which are distinct and fill all (2D) space. These are very important for the description of symmetries at surfaces. The 2D Bravais lattices are the square, hexagonal, rectangular and centered-rectangular lattice.

3.3.5 3D Bravais Lattices

In three dimensions, the operations of the point group results in fourteen 3D Bravais lattices (Fig. 3.9), that are categorized into seven crystal classes (trigonal, monoclinic, rhombic, tetragonal, cubic, rhombohedral and hexagonal).

---

[1] 2_1, 3_1, 3_2, 4_1, 4_2, 4_3, 6_1, 6_2, 6_3, 6_4, 6_5.

[2] One should in particular consider the pitfalls pointed out in Appendix 10 of this reference.

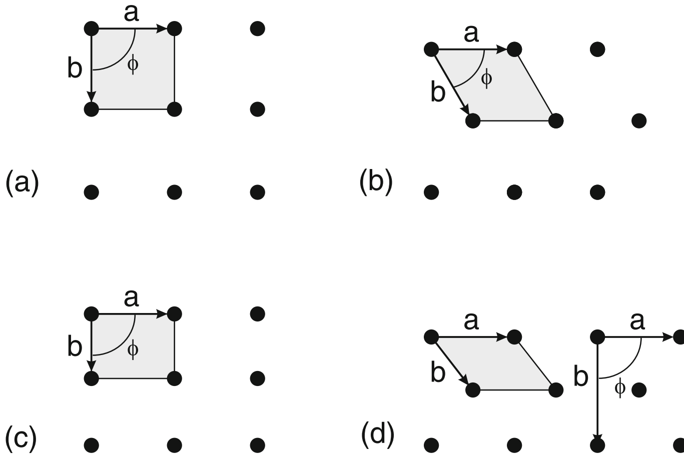

Fig. 3.8. The two-dimensional Bravais lattices with the primitive unit cells: (**a**) square lattice ($a = b$, $\phi = 90°$), (**b**) hexagonal lattice ($a = b$, $\phi = 60°$), (**c**) rectangular lattice ($a \neq b$, $\phi = 90°$), (**d**) centered-rectangular lattice ($a \neq b$, $\phi = 90°$, for the (nonprimitive) rectangular unit cell shown on the *right*)

These classes are discerned by the conditions for the lengths and the mutual angles of the vectors that span the lattice (Table 3.2). Some classes have several members. The cubic crystal can have a simple (sc), face-centered (fcc) or body-centered (bcc) lattice.

Table 3.2. Conditions for lengths and angles for the 7 crystal classes. Note that only the positive conditions are listed. The rhombohedral system is a special case of the trigonal class. Conditions for the trigonal and hexagonal classes are the same, however, trigonal symmetry includes a single C_3 or S_6 axis, while hexagonal symmetry includes a single C_6 or S_6^5 axis

System	#	lattice symbol	conditions for the usual unit cell
triclinic	1		none
monoclinic	2	s, c	$\alpha = \gamma = 90°$ or $\alpha = \beta = 90°$
orthorhombic	4	s, c, bc, fc	$\alpha = \beta = \gamma = 90°$
tetragonal	2	s, bc	$a = b$, $\alpha = \beta = \gamma = 90°$
cubic	3	s, bc, fc	$a = b = c$, $\alpha = \beta = \gamma = 90°$
trigonal	1		$a = b$, $\alpha = \beta = 90°$, $\gamma = 120°$
(rhombohedral)	1		$a = b = c$, $\alpha = \beta = \gamma$
hexagonal	1		$a = b$, $\alpha = \beta = 90°$, $\gamma = 120°$

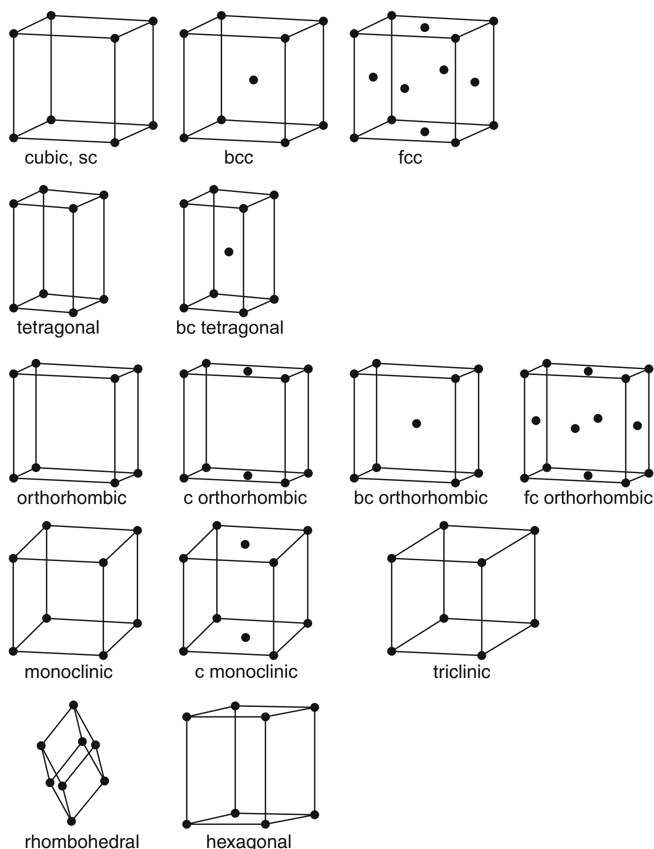

Fig. 3.9. The 14 three-dimensional Bravais lattices: cubic (sc: simple cubic, bcc: body-centered cubic, fcc: face-centered cubic), tetragonal (simple and body-centered), orthorhombic (simple, centered, body-centered and face-centered), monoclinic (simple and centered), triclinic, rhombohedral and hexagonal

In the following, some of the most important lattices, in particular those most relevant to semiconductors, will be treated in some more detail.

Cubic fcc and bcc Lattices

The primitive translation vectors for the cubic face-centered (fcc) and the cubic body-centered (bcc) lattice are shown in Fig. 3.10 and Fig. 3.11, respectively. Many metals crystallize in these lattices, e.g. copper (fcc) and tungsten (bcc).

In the fcc lattice, one lattice point sits in the center of each of the six faces of the usual cubic unit cell. The vectors spanning the primitive unit cell are

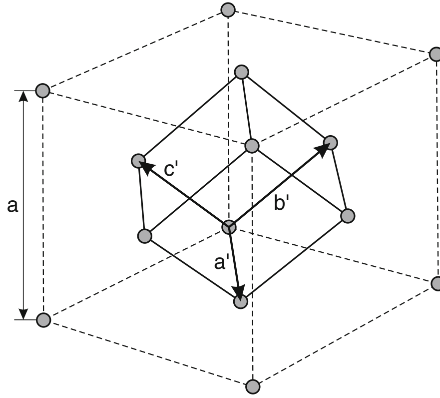

Fig. 3.10. Primitive translations of the fcc lattice. These vectors connect the origin with the face-center points. The primitive unit cell is the rhombohedron spanned by these vectors. The primitive translations $\mathbf{a}'$, $\mathbf{b}'$ and $\mathbf{c}'$ are given in (3.2). The angle between the vectors is 60°

$$\begin{aligned}
\mathbf{a}' &= \frac{a}{2}\left(\mathbf{e_x} + \mathbf{e_y}\right) \\
\mathbf{b}' &= \frac{a}{2}\left(\mathbf{e_y} + \mathbf{e_z}\right) \\
\mathbf{c}' &= \frac{a}{2}\left(\mathbf{e_x} + \mathbf{e_z}\right) \ .
\end{aligned} \tag{3.2}$$

In the bcc lattice, one extra lattice point sits at the intersection of the three body diagonals at $(\mathbf{a}_1 + \mathbf{a}_2 + \mathbf{a}_3)/2$. The vectors spanning the primitive unit cell are

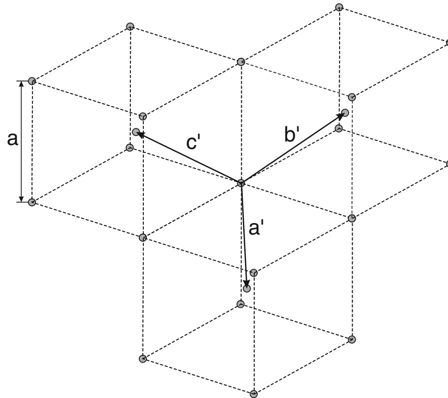

Fig. 3.11. Primitive translations of the bcc lattice. These vectors connect the origin with the lattice points in the cube centers. The primitive unit cell is the rhombohedron spanned by these vectors. The primitive translations $\mathbf{a}'$, $\mathbf{b}'$ and $\mathbf{c}'$ are given in (3.3). The angle between the vectors is $\approx 70.5°$

$$\mathbf{a}' = \frac{a}{2}\left(\mathbf{e_x} + \mathbf{e_y} - \mathbf{e_z}\right) \tag{3.3}$$
$$\mathbf{b}' = \frac{a}{2}\left(-\mathbf{e_x} + \mathbf{e_y} + \mathbf{e_z}\right)$$
$$\mathbf{c}' = \frac{a}{2}\left(\mathbf{e_x} - \mathbf{e_y} + \mathbf{e_z}\right) \ .$$

Hexagonally Close Packed Lattice (hcp)

The 2D hexagonal Bravais lattice fills a plane with spheres (or circles) with maximum filling factor. There are two ways to fill space with spheres and highest filling factor. One is the fcc lattice, the other is the hexagonally close packed (hcp) structure. Both have a filling factor of 74%.

For the hcp, we start with a hexagonally arranged layer of spheres (A), see Fig. 3.12. Each sphere has six next-neighbor spheres. This could, e.g., be a plane in the fcc perpendicular to the body diagonal. the next plane B is put on top in such a way that each new sphere touches three spheres of the previous layer. The third plane can now be added in two different ways: If the spheres of the third layer are vertically on top of the spheres of layer A, a plane A' identical to A has been created that is shifted from A along the stacking direction (normally called the c-axis) by

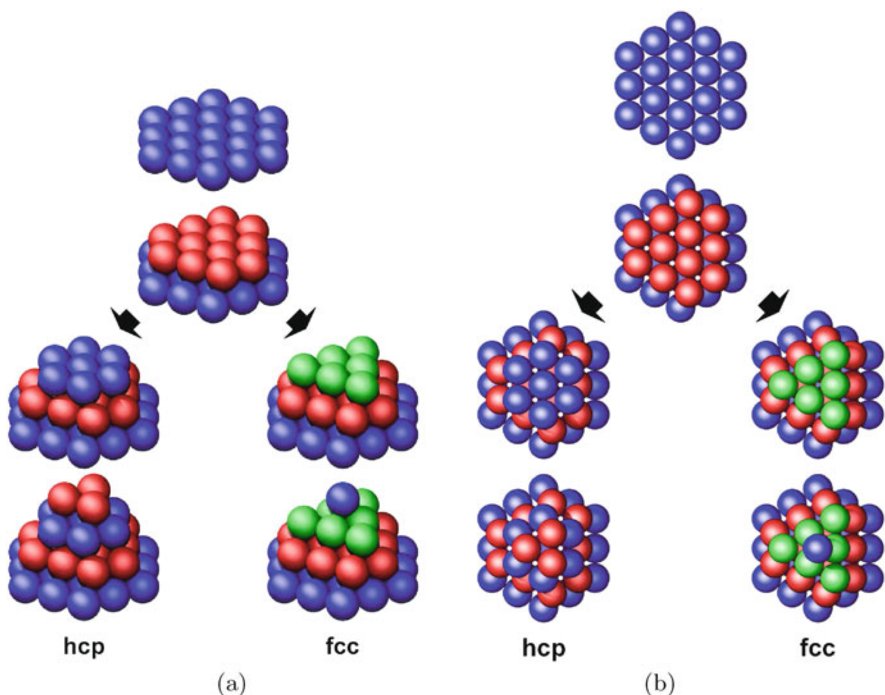

Fig. 3.12. Structure of the (**a**) hcp and (**b**) fcc lattice. For hcp the stacking (along the c-axis) is ABABAB..., for fcc (along the body diagonal) it is ABCABCABC...

$$c_{\mathrm{hcp}} = \sqrt{8/3}\, a \approx 1.633\, a \ . \tag{3.4}$$

The hcp stacking order is ABABAB... for hcp, the coordination number is 12. In the fcc structure, the third layer is put on the thus far unfilled positions and forms a new layer C. Only the forth layer is again identical to A and is shifted by

$$c_{\mathrm{fcc}} = \sqrt{6}\, a \approx 2.45\, a \ . \tag{3.5}$$

The fcc stacking order is ABCABCABC....

In the hexagonal plane of the fcc lattice (which will later be called a {111} plane) the distance between lattice points is $a = a_0/\sqrt{2}$, where a_0 is the cubic lattice constant. Thus $c = \sqrt{3}\, a_0$, just what is expected for the body diagonal.

For real materials with hexagonal lattice the ratio c/a deviates from the ideal value given in (3.4). Helium comes very close to the ideal value, for Mg it is 1.623, for Zn 1.861. Many hcp metals exhibit a phase transition to fcc at higher temperatures.

3.3.6 Polycrystalline Semiconductors

A polycrystalline material consists of crystal grains that are randomly oriented with respect to each other. Between two grains a (large-angle) grain boundary (see also Sect. 4.4.3) exists. An important parameter is the grain size and its distribution. It can be influenced via processing steps such as annealing. Polycrystalline semiconductors are used in cheap, large-area applications such as solar cells (e.g. polysilicon, $CuInSe_2$) or thin-film transistors (poly-Si) or as n-conducting contact material in MOS diodes (poly-Si) as shown in Fig. 3.13 (see also Fig. 20.26). Polycrystalline material can be fabricated from amorphous material using annealing procedures as discussed in Sect. 23.6.1 for silicon.

3.3.7 Amorphous Semiconductors

An amorphous material lacks the long-range order of the direct lattice. It is disordered on the atomic scale. Amorphous silicon is denoted as 'a-Si'.

The local quantum mechanics provides almost rigorous requirements for the bond length to next neighbors. The constraints for the bond angle are less strict. Covalently bonded atoms arrange in an open network with correlations up to the third and fourth neighbors. The short-range order is responsible for the observation of semiconductor properties such as an optical absorption edge and also thermally activated conductivity. In Fig. 3.14a a model of a continuous random network (with a bond-angle distortion of less than about 20%) of a-Si is depicted. The diameter d_{SR} of the short-range order region is related to the disorder parameter α via [114]

$$d_{\mathrm{SR}} = \frac{a}{2\alpha} \ , \tag{3.6}$$

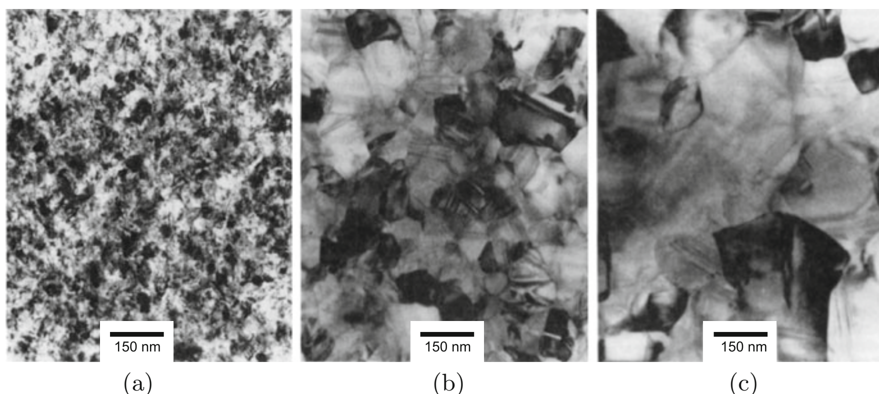

Fig. 3.13. Transmission electron micrographs of polycrystalline silicon (poly-Si). (**a**) As-deposited material from low-pressure chemical vapor deposition (LPCVD) at about 620°C, grain size is about 30 nm. (**b**) After conventional processing (annealing at 1150°C), average grain size is about 100 nm. (**c**) After annealing in HCl that provides enhanced point defect injection (and thus increased possibility to form larger grains), average grain size is about 250 nm. Adapted from [115]

where a is the next-neighbor interatomic distance. For a diamond structure it is related to the lattice constant by $a = \sqrt{3}\,a_0/4$.

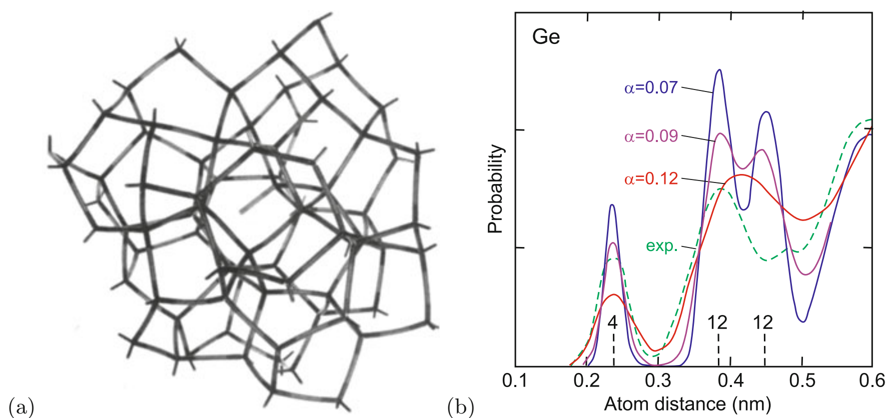

Fig. 3.14. (**a**) A continuous random network model of amorphous silicon containing a dangling bond in the center of the figure. Reprinted with permission from [116]. (**b**) Calculated radial atomic distribution functions of amorphous Ge (*solid lines*) for three different values of the disorder parameter α (3.6) as labeled and experimental result (*dashed line*). The positions of next, second-next and third-next neighbors are indicted by *vertical bars* with numbers of their multiplicity (4, 12, and 12). Adapted from [114]

Typically, a significant number of dangling bonds exists. Bonds try to pair but if an odd number of broken bonds exists locally, an unsaturated, dangling bond remains. This can be passivated by a hydrogen atom. Thus, the hydrogenation of amorphous semiconductors is very important. A hydrogen atom can also break an overlong (and therefore weak) bond, saturate one side and eventually leave a dangling bond.

Amorphous material can be (re-)crystallized into crystalline, mostly polycrystalline material upon annealing. This is technologically very important for a-Si (see Sect. 23.6.1).

3.4 Important Crystal Structures

Now the crystal structures that are important for semiconductor physics will be discussed. These are the rocksalt (PbS, MgO), diamond (C, Si, Ge), zincblende (GaAs, InP, ...) and wurtzite (GaN, ZnO, ...) structures.

3.4.1 Rocksalt Structure

The rocksalt (rs, NaCl, space group 225, $\mathrm{Fm\bar{3}m}$) structure (Fig. 3.15a) consists of a fcc lattice with the period a and a diatomic base in which the Cl atom is positioned at (0,0,0) and the Na atom at $(1/2,1/2,1/2)a$ with a distance $\sqrt{3}\,a/2$. Materials that crystallize (under normal conditions) in the rocksalt lattice are, e.g., KCl, KBr, PbS (galena), PbSe, PbTe, AgBr, MgO, CdO, MnO. AlN, GaN and InN undergo, under high pressure, a phase transition from the wurtzite into the rocksalt structure.

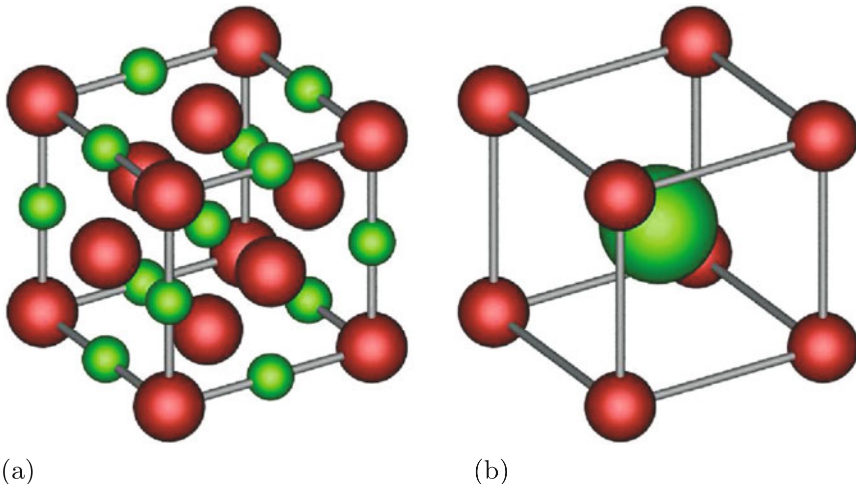

Fig. 3.15. (**a**) Rocksalt (NaCl) structure, (**b**) CsCl structure

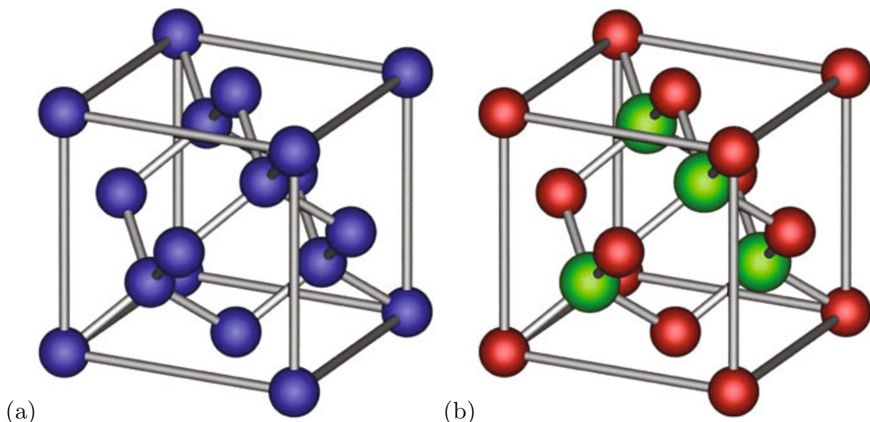

Fig. 3.16. (**a**) Diamond structure and (**b**) zincblende structure (*red spheres*: A atoms, *green spheres*: B atoms). The tetragonal bonds are indicated

3.4.2 CsCl Structure

The CsCl structure (space group 221, $Pm\bar{3}m$) (Fig. 3.15b) consists of a simple cubic lattice. Similar as for the rocksalt structure, the base consists of different atoms at (0,0,0) and $(1/2,1/2,1/2)a$. Typical crystals with CsCl-structure are TlBr, TlI, CuZn (β-brass), AlNi.

3.4.3 Diamond Structure

The diamond structure (C, space group 227, $Fd\bar{3}m$) (Fig. 3.16a) has the fcc lattice. The base consists of two identical atoms at (0,0,0) and $(1/4,1/4,1/4)a$. Each atom has a tetrahedral configuration. The packing density is only about 0.34. The materials that crystallize in the diamond lattice are C, Ge, Si and α-Sn. The diamond structure (point group O_h) has an inversion center, located between the two atoms of the base, i.e. at $(1/8,1/8,1/8)a$. The radii of the wavefunctions for various group-IV elements increases with the order number (Table 3.3), and accordingly increases the lattice constant.

Table 3.3. Radii of the wavefunctions in the diamond structure, r_s and r_p are related to s^1p^3, r_d to $s^1p^2d^1$ and lattice constant a_0

	r_s (nm)	r_p (nm)	r_d (nm)	a_0 (nm)
C	0.121	0.121	0.851	0.356683
Si	0.175	0.213	0.489	0.543095
Ge	0.176	0.214	0.625	0.564613

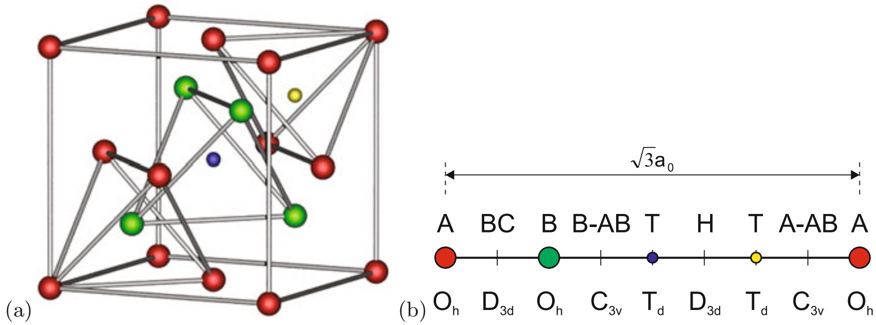

Fig. 3.17. (**a**) Unit cell of the zincblende structure with the indication of tetragonal symmetries. The position of the small *yellow* (*blue*) *sphere* is the tetrahedrally configured unoccupied positions of the A (B) sublattice, denoted with 'T' in part (**b**). (**b**) Line along ⟨111⟩ in the zincblende structure. The positions of the A and B atoms are denoted by *red* and *green circles* as labeled. Other positions are called the bond center ('BC'), antibonding ('AB') relative to A and B atoms ('A–AB', 'B–AB'), hexagonal ('H') and tetrahedral position ('T', *blue* and *yellow circles*). The point symmetries of the various locations are given in the *lower line*

In Fig. 3.17a the unit cell with tetragonal symmetry of three places along the ⟨111⟩ direction is shown. In Fig. 3.17b the arrangement of atoms along ⟨111⟩ is depicted. The symmetry along this line is at least C_{3v}. At the atoms sites it is O_h. The bond center (BC) and the hexagonal (H) position are a center of inversion and have D_{3d} symmetry. The unoccupied 'T' positions have T_d symmetry. High-pressure phases of silicon are already found in indentation experiments [117].

We note that α-Sn has little current importance. The diamond structure α–Sn phase is stable below 13.2°C. The addition of Ge inhibits the retransformation to metallic tin up to higher temperatures (e.g. 60°C for 0.75 weight percent Ge). The properties of gray tin are reviewed in [118].

3.4.4 Zincblende Structure

The zincblende (sphalerite, ZnS, space group 216, F$\bar{4}$3m) structure (Fig. 3.16b) has a fcc lattice with a diatomic base. The metal (A) atom is at $(0, 0, 0)$ and the nonmetal (B) atom is at $(1/4, 1/4, 1/4)a$. Thus the cation and anion sublattices are shifted with respect to each other by a quarter of the body diagonal of the fcc lattice. The atoms are tetrahedrally coordinated, a Zn atom is bonded to four S atoms and vice versa. However, no inversion center is present any longer (point group T_d). In the zincblende structure the stacking order of diatomic planes along the body diagonal is aAbBcCaAbBcC. . ..

Many important compound semiconductors, such as GaAs, InAs, AlAs, InP, GaP and their alloys (cf. Sect. 3.7), but also the II–VI compounds ZnS, ZnSe, ZnTe, HgTe and CdTe crystallize in the zincblende structure.

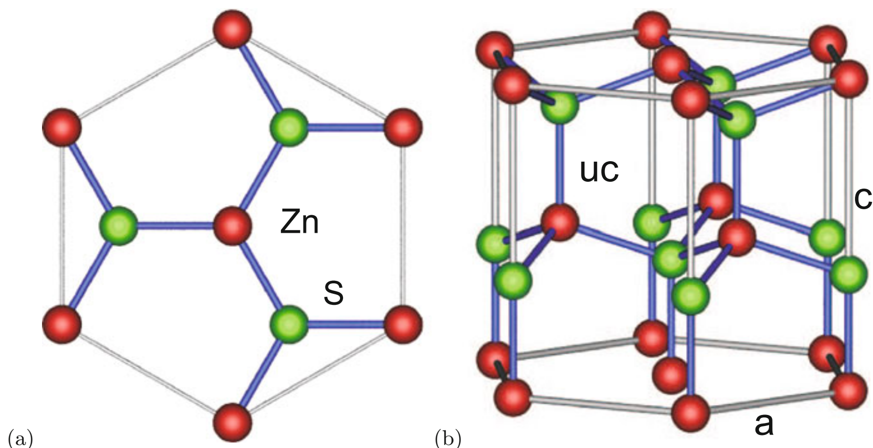

Fig. 3.18. (**a**) Top view (along the c-axis) and (**b**) side view of the wurtzite structure with the tetragonal bonds indicated. The top (bottom) surface of the depicted structure is termed the Zn-face, (00.1) (O-face, $(00.\bar{1})$)

Four-fold coordinated materials (zincblende and wurtzite) typically undergo a phase transition into 6-fold coordinated structures upon hydrostatic pressure [119]. For GaAs under pressure see [120].

3.4.5 Wurtzite Structure

The wurtzite structure (ZnS, space group 186, $P6_3mc$) is also called the hexagonal ZnS structure (because ZnS has both modifications). It consists (Fig. 3.18) of a hcp lattice with a diatomic base. The c/a ratio typically deviates from the ideal value $\zeta_0 = \sqrt{8/3} \approx 1.633$ (3.4) as listed in Table 3.4. The c-axis is a 6_3 screw axis.

The Zn atom is located at $(0, 0, 0)$, the S atom at $(0, 0, \sqrt{3/8})a$. This corresponds to a shift of $3/8\,c$ along the c-axis. This factor is called the cell-internal parameter u. For the ideal wurtzite structure it has the value $u_0 = 3/8 = 0.375$. For real wurtzite crystals u deviates from the ideal value,

Table 3.4. c/a ratio of various wurtzite semiconductors. Listed is $\xi = (c/a - \zeta_0)/\zeta_0$. Data based on [121]

material	ξ (%)	material	ξ(%)	material	ξ (%)	material	ξ (%)
AlN	−2.02	CdS	−0.61	CuBr	0.43	BeO	−0.61
GaN	−0.49	CdSe	−0.18	CuCl	0.55	ZnO	−1.9
InN	−1.35	CdTe	0.25	CuI	0.74	6H-SiC	0.49
ZnS	0.25	MgS	−0.80	AgI	0.12	BN	0.74
ZnSe	0.06	MgSe	−0.67	ZnTe	0.74	MgTe	−0.67

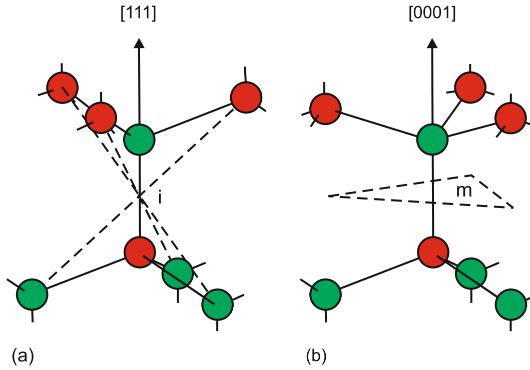

Fig. 3.19. Comparison of the tetragonal bonds in the (**a**) zincblende and (**b**) wurtzite structure (i: inversion center, m: symmetry plane)

e.g. for group-III nitrides $u > u_0$. The ZnS diatomic planes have a stacking order of aAbBaAbB... in the wurtzite structure.

In Fig. 3.19 the different local structural environment of the atoms in the zincblende and wurtzite structure is shown.

Many important semiconductors with large band gap crystallize in the wurtzite structure, such as GaN, AlN, InN [122], ZnO [123], SiC [124], CdS and CdSe.

3.4.6 Chalcopyrite Structure

The chalcopyrite [125] (ABC_2, named after 'fool's gold' $CuFeS_2$, space group 122, I$\bar{4}$2d) structure is relevant for I–III–VI_2 (with chalcogenide anions) and II–IV–V_2 (with pnictide anions) semiconductors such as, e.g., (Cu,Ag)-(Al,Ga,In)$(S,Se,Te)_2$ and (Mg,Zn,Cd)(Si,Ge,Sn)$(As,P,Sb)_2$. A nonmetallic anion atom ('C') is tetrahedrally bonded to two different types of cation atoms ('A' and 'B') as shown in Fig. 3.20. The local surrounding of each anion is identical, two of both the A and B atoms. The structure is tetragonal. The aspect ratio $\eta = c/(2a)$ deviates from its ideal value 1; typically $\eta < 1$ [126, 127].

If the C atom is in the tetrahedral center of the two A and two B atoms, the bond lengths R_{AC} and R_{BC} of the A–C and B–C bonds, respectively, are equal. Since the ideal A–C and B–C bond lengths d_{AC} and d_{BC} Are typically unequal, this structure is strained. The common atom C is therefore displaced along [100] and [010] such that it is closer (if $d_{\mathrm{AC}} < d_{\mathrm{BC}}$) to the pair of A atoms and further away from the B atoms. The displacement parameter is

$$u = \frac{1}{4} + \frac{R_{\mathrm{AC}}^2 - R_{\mathrm{BC}}^2}{a^2} \tag{3.7}$$

and it deviates from the ideal value $u_0 = 1/4$ for the zincblende structure as listed in Table 3.5 for a number of chalcopyrite compounds. In the chalcopyrite structure

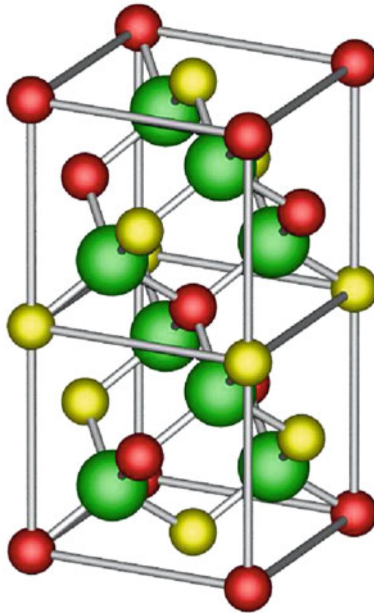

Fig. 3.20. Chalcopyrite structure, *red* and *yellow spheres* denote the metal species. The bigger *green spheres* represent the nonmetal anion

$$R_{\mathrm{AC}} = a\sqrt{u^2 + \frac{1+\eta^2}{16}} \tag{3.8a}$$

$$R_{\mathrm{BC}} = a\sqrt{\left(u - \frac{1}{2}\right)^2 + \frac{1+\eta^2}{16}} \,. \tag{3.8b}$$

Table 3.5. Lattice nonideality parameters η and u (from (3.9)) of various chalcopyrite compounds and their experimentally observed disorder stability (+/− indicates compound with/without order–disorder (D–O) transition, respectively). Data from [127]

	η	u	D–O		η	u	D–O
$CuGaSe_2$	0.983	0.264	+	$ZnSiAs_2$	0.97	0.271	−
$CuInSe_2$	1.004	0.237	+	$ZnGeAs_2$	0.983	0.264	+
$AgGaSe_2$	0.897	0.287	−	$CdSiAs_2$	0.92	0.294	−
$AgInSe_2$	0.96	0.261	+	$CdGeAs_2$	0.943	0.287	
$CuGaS_2$	0.98	0.264		$ZnSiP_2$	0.967	0.272	−
$CuInS_2$	1.008	0.236	+	$ZnGeP_2$	0.98	0.264	+
$AgGaS_2$	0.895	0.288	−	$CdSiP_2$	0.92	0.296	−
$AgInS_2$	0.955	0.262		$CdGeP_2$	0.939	0.288	−

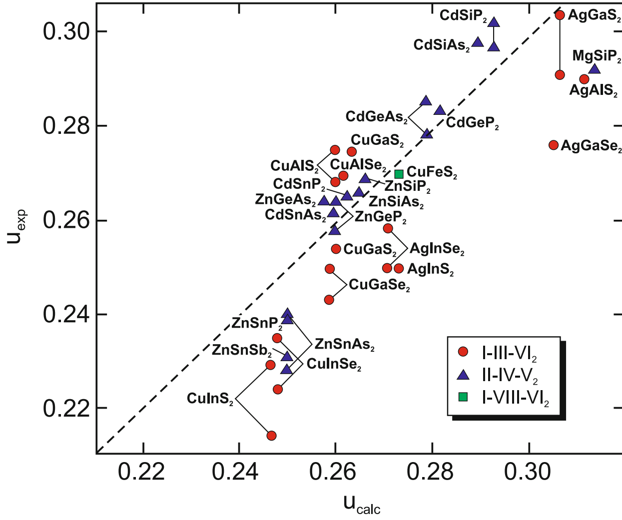

Fig. 3.21. Experimental values u_{exp} of the displacement parameter for various chalcopyrites vs. the calculated value u_{calc} according to (3.9). The *dashed line* indicates $u_{\mathrm{exp}} = u_{\mathrm{calc}}$. Adapted from [128]

The minimization of the microscopic strain yields (in first order) [128]

$$u \cong \frac{1}{4} + \frac{3}{8}\,\frac{d_{\mathrm{AC}}^2 - d_{\mathrm{BC}}^2}{d_{\mathrm{AC}}^2 + d_{\mathrm{BC}}^2}\;. \tag{3.9}$$

Compounds with $u > u_{\mathrm{c}}$, $u_{\mathrm{c}} = 0.265$ being a critical displacement parameter, (or $u < 1/2 - u_{\mathrm{c}} = 0.235$) are stable with regard to cation disorder [127]. In Fig. 3.21 the correlation of the calculated value for u according to (3.9) and the experimental values is shown.

3.4.7 Fluorite Structure

Named after the minerale fluorite (CaF_2, space group 225, Fm3m), this structure for binary ionic compounds occurs when the cation valence is twice the anion valence, e.g. for (cubic) ZrO_2 (zirconia) or HfO_2. The lattice is fcc with a triatomic base. At (0,0,0) is the cation (e.g. Zr^{4+}), the anions (e.g. O^{2-}) are at $(1/4, 1/4, 1/4)\,a$ (as in the zincblende structure) and $(3/4, 3/4, 3/4)\,a$ (Fig. 3.22). The anion atom positions are on a simple cubic lattice with lattice constant $a/2$. Zirconia can crystallize in various phases [129], the most prominent being the monoclinic, tetragonal and cubic phases. The cubic phase can be extrinsically stabilized using yttrium [130, 131] (YSZ, yttria-stabilized zirconia). Hafnium oxide has the remarkable property that the HfO_2/Si interface is stable and allows the fabrication of transistor gate oxides with high dielectric constant (see Sect. 23.5.5).

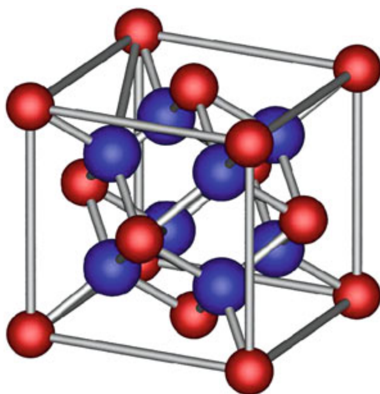

Fig. 3.22. Fluorite crystal structure, the cations are depicted as *red speheres*, the anions as *blue spheres*

3.4.8 Delafossite Structure

The I–III–O_2 materials crystallize in the trigonal delafossite ($CuFeO_2$, space group 166, $R\bar{3}m$) structure (Fig. 3.23). This structure is also called caswell-silverite ($NaCrS_2$). In Table 3.6 the lattice parameters of some delafossite compounds are given. The (Cu,Ag) (Al,Ga,In)O_2 materials are transparent conductive oxides (TCO). We note that Pt and Pd as group-I component

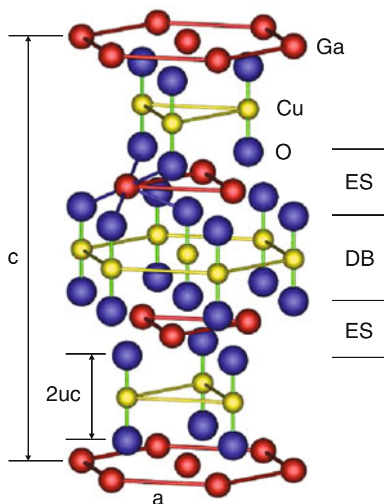

Fig. 3.23. Hexagonal unit cell of delafossite $CuGaO_2$. Oxygen atoms are bonded to the Cu in a dumbbell ('DB') configuration. In the edge-sharing ('ES') layer the Ga atoms are octahedrally configured as GaO_6

Table 3.6. Lattice parameters a, c, and u of some delafossite compounds. Theoretical values are shown with asterisk. Data from [132]

	a (nm)	c (nm)	u (nm)
$CuAlO_2$	0.2858	1.6958	0.1099
$CuGaO_2$	0.2980	1.7100	0.1073^*
$CuInO_2$	0.3292	1.7388	0.1056^*

create metal-like compounds because of the d^9 configuration as opposed to the d^{10} configuration of Cu and Ag.

3.4.9 Perovskite Structure

The perovskite structure (calcium titanate, $CaTiO_3$, space group 62, Pnma) (Fig. 3.24) is relevant for ferroelectric semiconductors (cf. Sect. 14.3). It is cubic with the Ca (or Ba, Sr) ions (charge state 2+) on the corners of the cube, the O ions (2−) on the face centers and the Ti (4+) in the body center. The lattice is simple cubic, the base is Ca at (0,0,0), O at (1/2,1/2,0), (1/2,0,1/2) and (0,1/2,1/2) and Ti at (1/2,1/2,1/2). The ferroelectric polarization is typically evoked by a shift of the negatively and positively charged ions relative to each other. $LaAlO_3$ (lanthanium aluminate) is available as substrate material (space group 226, Fm$\bar{3}$c [133]). Perovskites are also important for high temperature superconductivity.

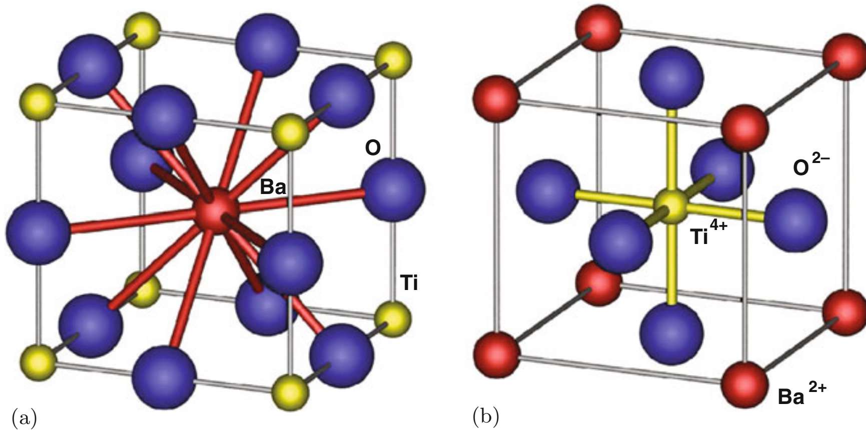

Fig. 3.24. Perovskite structure ($BaTiO_3$), (**a**) A cell with 12-fold (cuboctahedrally) configured Ba, (**b**) B cell with octahedrally configured Ti

3.4.10 NiAs Structure

The NiAs structure (space group 194, $P6_3/mmc$) (Fig. 3.25) is relevant for magnetic semiconductors, such as MnAs, and also occurs in the formation of Ni/GaAs Schottky contacts [134]. The structure is hexagonal. The arsenic atoms form a hcp structure and are trigonal prismatically configured with six nearest metal atoms. The metal atoms form hcp planes and fill all octahedral holes of the As lattice. For a cubic close packed, i.e. fcc, structure this would correspond to the rocksalt crystal. The stacking is ABACABAC... (A: Ni, B,C: As).

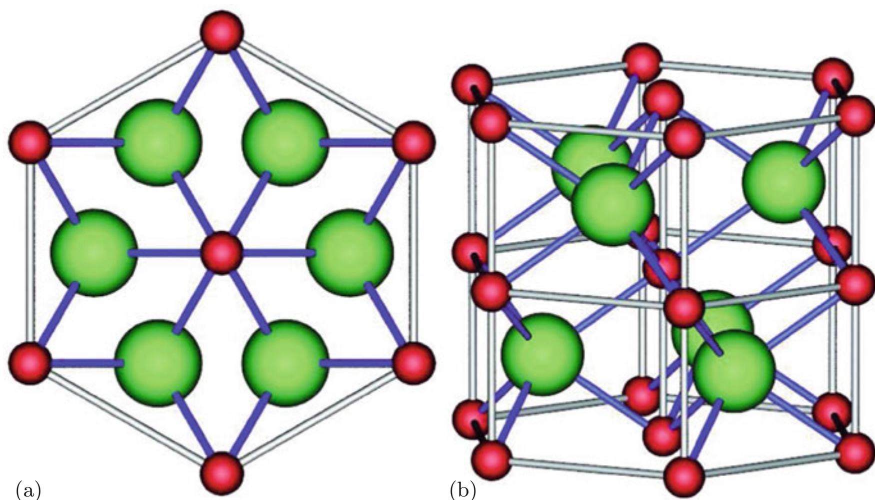

Fig. 3.25. NiAs structure, metal atoms: *dark grey*, chalcogenide atoms: *light grey*

3.4.11 Further Structures

There are many other crystal structures that have relevance for semiconductor materials. Among them are the

- corundum structure (Al_2O_3, space group 167, $R\bar{3}c$) occurring, e.g., for sapphire substrates used in epitaxy or for gallium oxide Ga_2O_3 (a multiphase material [135])
- spinel structure ($MgAl_2O_4$, space group 227, $Fd\bar{3}m$). A large variety of ternary compounds of type $A^{II}B^{III}{}_2C^{VI}{}_4$ crystallize in this structure, A: Mg, Cr, Mn, Fe, Co, Ni, Cu, Zn, Cd, Sn, B: Al, Ga, In, Ti, V, Cr, Mn, Fe, Co, Rh, Ni, and C: O, S, Se, Te. As an example $ZnGa_2O_4$ (zinc gallate) has received attention as interfacial layer in ZnO/GaAs epitaxy [136], luminescent material [137], and as ferromagnetic semiconductor [138].

ScAlMgO$_4$ (SCAM) is available as substrate material. Also $\mathrm{A^{VI}B^{II}{}_2C^{VI}{}_4}$ compounds exist, e.g. GeB$_2$O$_4$ (with B=Mg, Fe, Co, Ni)

- inverted spinel structure for $\mathrm{A^{II}B^{III}{}_2C^{VI}{}_4}$ compounds, e.g. for magnetite (Fe_3O_4), a material with high spin polarization, or $MgFe_2O_4$. Also $\mathrm{A^{VI}B^{II}{}_2C^{VI}{}_4}$ compounds exist in this structure, e.g. SnB$_2$O$_4$ (with B=Mg, Mn, Co, Zn), TiB$_2$O$_4$ (with B=Mg, Mn, Fe, Co, Zn), and VB$_2$O$_4$ (with B=Mg, Co, Zn)
- quartz (SiO_2) structures, α-quartz (space group 154, P3$_2$21) and β-quartz (space group 180, P6$_2$22)

Space does not permit to discuss these and other structures in more detail here. The reader should refer to textbooks on crystallography, e.g. [139, 140], and space groups [113, 142]. A good source for information and images of crystal structures on the web is [143].

3.5 Polytypism

In polytype materials the stacking order is not only hcp or fcc but takes different sequences, such as, e.g., ACBCABAC as the smallest unit cell along the stacking direction. A typical example is SiC, for which in addition to hcp and fcc 45 other stacking sequences are known. The largest primitive unit cell of SiC [124] contains 594 layers. Some of the smaller polytypes are shown in Fig. 3.26. In Fig. 3.27 cubic diamond crystallites and metastable hexagonal and orthorhombic phases (in silicon) are shown.

For the ternary alloy (cf. Sect. 3.7) $\mathrm{Zn}_{1-x}\mathrm{Cd}_x\mathrm{S}$ the numbers n_h of diatomic layers with hexagonal stacking (AB) and n_c of layers with cubic stacking (ABC) have been investigated. CdS has wurtzite structure and ZnS mostly zincblende structure. The hexagonality index α as defined in (3.10) is shown in Fig. 3.28 for $\mathrm{Zn}_{1-x}\mathrm{Cd}_x\mathrm{S}$

$$\alpha = \frac{n_\mathrm{h}}{n_\mathrm{h} + n_\mathrm{c}} \,. \tag{3.10}$$

3.6 Reciprocal Lattice

The reciprocal lattice is of utmost importance for the description and investigation of periodic structures, in particular for X-ray diffraction [144], surface electron diffraction, phonons and the band structure. It is the quasi-Fourier transformation of the crystal lattice. The crystal lattice is also called the *direct* lattice, in order to distinguish it from the reciprocal lattice.

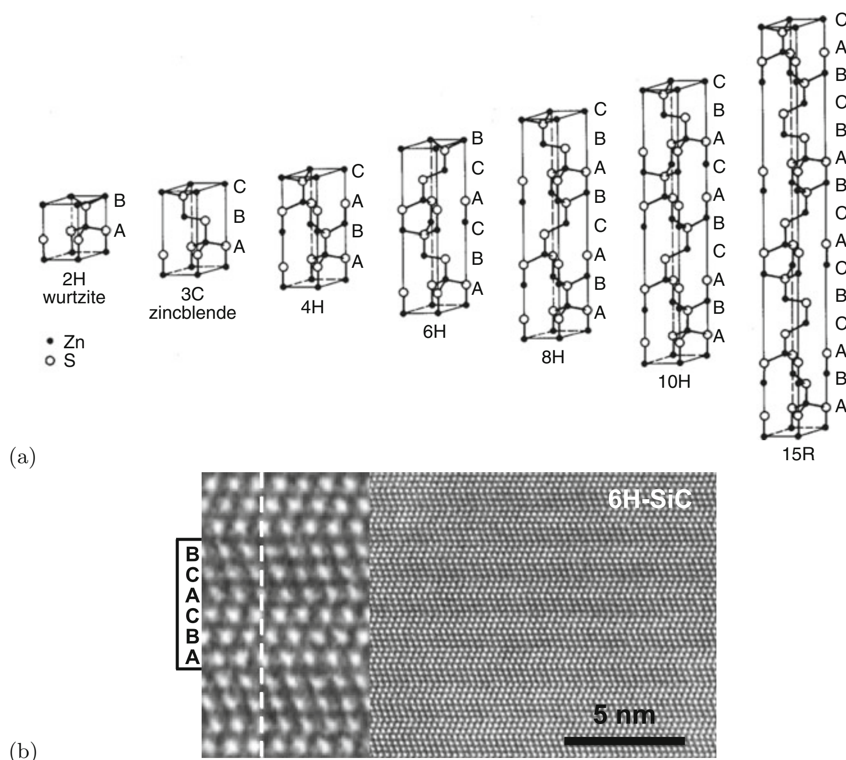

Fig. 3.26. (**a**) Polytypes of the zincblende and wurtzite lattice (found in SiC), the letters A, B and C denote the three possible positions of the diatomic layers (see Fig. 3.12). (**b**) High resolution TEM image of 6H-SiC. For the enlarged view on the left, the unit cell and the stacking sequence are indicated. Adapted from [145]

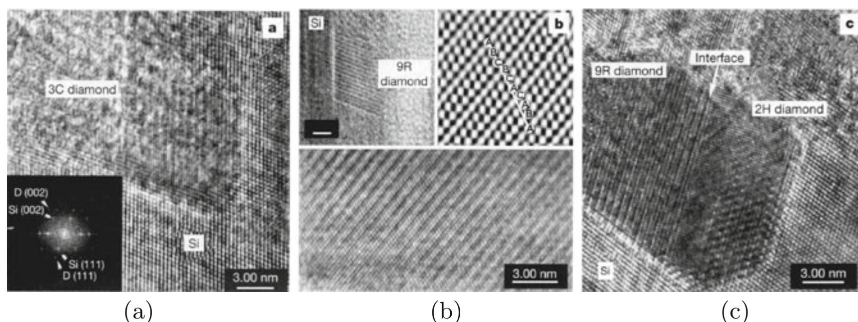

Fig. 3.27. Polytypes of diamond found in crystallites (metastable phases in silicon). (**a**) cubic type (3C) with stacking ABC, *inset* shows a diffractogram and the alignment of the C and Si lattice, (**b**) rhombohedral 9R crystallite with ABCB-CACABA stacking, (**c**) 9R phase with interface to a hexagonal 2H (AB stacking) phase. Reprinted with permission fromNature [146], ©2001 Macmillan Magazines Limited

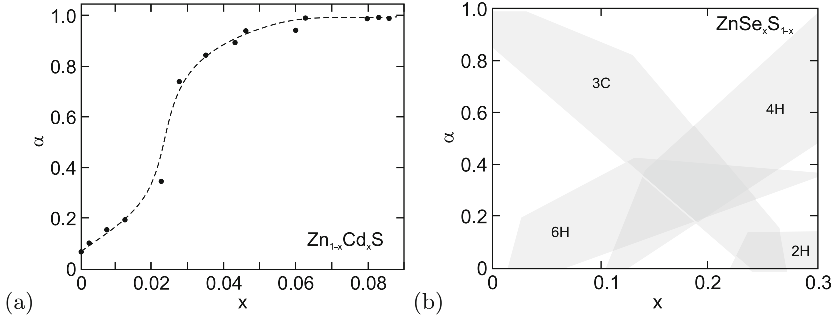

Fig. 3.28. (**a**) Hexagonality index α (3.10) of $\mathrm{Zn}_{1-x}\mathrm{Cd}_x\mathrm{S}$ for various ternary compositions. *Dashed line* is a guide to the eye. (**b**) Regions of different polytypes in $\mathrm{ZnSe}_x\mathrm{S}_{1-x}$. Adapted from [147]

3.6.1 Reciprocal Lattice Vectors

When $\mathcal{R}$ denotes the set of vectors of the direct lattice, the set $\mathcal{G}$ of the reciprocal lattice vectors is given by the condition[3]

$$\exp\left(\mathrm{i}\,\mathbf{G}\cdot\mathbf{R}\right) = 1 \tag{3.11}$$

for all $\mathbf{R} \in \mathcal{R}$ and $\mathbf{G} \in \mathcal{G}$. Therefore, for all vectors $\mathbf{r}$ and a reciprocal lattice vector $\mathbf{G}$

$$\exp\left(\mathrm{i}\,\mathbf{G}\cdot(\mathbf{r}+\mathbf{R})\right) = \exp\left(\mathrm{i}\,\mathbf{G}\cdot\mathbf{r}\right)\ . \tag{3.12}$$

Each Bravais lattice has a certain reciprocal lattice. The reciprocal lattice is also a Bravais lattice, since when $\mathbf{G}_1$ and $\mathbf{G}_2$ are two reciprocal lattice vectors, then this is obviously true also for $\mathbf{G}_1+\mathbf{G}_2$. For the primitive translation vectors $\mathbf{a}_1$, $\mathbf{a}_2$ and $\mathbf{a}_3$ of the direct lattice, the vectors $\mathbf{b}_1$, $\mathbf{b}_2$ and $\mathbf{b}_3$ that span the reciprocal lattice can be given directly as

$$\mathbf{b}_1 = \frac{2\pi}{V_a}\left(\mathbf{a}_2\times\mathbf{a}_3\right) \tag{3.13a}$$

$$\mathbf{b}_2 = \frac{2\pi}{V_a}\left(\mathbf{a}_3\times\mathbf{a}_1\right) \tag{3.13b}$$

$$\mathbf{b}_3 = \frac{2\pi}{V_a}\left(\mathbf{a}_1\times\mathbf{a}_2\right)\ , \tag{3.13c}$$

where $V_a = \mathbf{a}_1\cdot(\mathbf{a}_2\times\mathbf{a}_3)$ is the volume of the unit cell spanned by the vectors $\mathbf{a}_i$. The volume of the unit cell in the reciprocal space is $V_a^* = (2\pi)^3/V_a$.

The vectors $\mathbf{b}_i$ fulfill the conditions

$$\mathbf{a}_i\,\mathbf{b}_j = 2\pi\,\delta_{ij}\ . \tag{3.14}$$

[3]The dot product $\mathbf{a}\cdot\mathbf{b}$ of two vectors shall also be denoted as $\mathbf{ab}$.

Thus, it is clear that (3.11) is fulfilled. For an arbitrary reciprocal lattice vector $\mathbf{G} = k_1\mathbf{b}_1 + k_2\mathbf{b}_2 + k_3\mathbf{b}_3$ and a vector $\mathbf{R} = n_1\mathbf{a}_1 + n_2\mathbf{a}_2 + n_3\mathbf{a}_3$ in direct space we find

$$\mathbf{G} \cdot \mathbf{R} = 2\pi \, (n_1 \, k_1 + n_2 \, k_2 + n_3 \, k_3) \ . \tag{3.15}$$

The number in brackets is an integer. Additionally, we note that the reciprocal lattice of the reciprocal lattice is again the direct lattice. The reciprocal lattice of the fcc is bcc and vice versa. The reciprocal lattice of hcp is hcp (rotated by 30° with respect to the direct lattice).

For later, we note two important theorems. A (sufficiently well behaved) function $f(\mathbf{r})$ that is periodic with the lattice, i.e. $f(\mathbf{r}) = f(\mathbf{r}+\mathbf{R})$ can be expanded into a Fourier series with the reciprocal lattice vectors according to

$$f(\mathbf{r}) = \sum a_{\mathbf{G}} \, \exp\left(\mathrm{i}\, \mathbf{G} \cdot \mathbf{r}\right) \, , \tag{3.16}$$

where $a_{\mathbf{G}}$ denotes the Fourier component of the reciprocal lattice vector $\mathbf{G}$, $a_{\mathbf{G}} = \int_V f(\mathbf{r}) \exp\left(-\mathrm{i}\, \mathbf{G}\cdot\mathbf{r}\right) \mathrm{d}^3\mathbf{r}$. If $f(\mathbf{r})$ is lattice periodic, the integral given in (3.17) is zero unless $\mathbf{G}$ is a reciprocal lattice vector.

$$\int_V f(\mathbf{r}) \, \exp\left(-\mathrm{i}\, \mathbf{G}\cdot\mathbf{r}\right) \, \mathrm{d}^3\mathbf{r} = \begin{cases} a_{\mathbf{G}} \\ 0, \mathbf{G} \notin \mathcal{G} \end{cases} \ . \tag{3.17}$$

3.6.2 Miller Indices

A lattice plane is the set of all lattice points in a plane spanned by two independent lattice vectors $\mathbf{R_1}$ and $\mathbf{R_2}$. The lattice points on that plane form a two-dimensional Bravais lattice. The entire lattice can be generated by shifting the lattice plane along its normal $\mathbf{n} = (\mathbf{R_1} \times \mathbf{R_2})/|\mathbf{R_1} \times \mathbf{R_2}|$. The plane belongs to the reciprocal lattice vector $\mathbf{G_n} = 2\pi\mathbf{n}/d$, d being the distance between planes.

This correspondence between reciprocal lattice vectors and sets of planes allows the orientation of planes to be described in a simple manner. The shortest reciprocal lattice vector perpendicular to the plane is used. The coordinates with respect to the primitive translation vectors of the reciprocal space $\mathbf{b}_i$ form a triplet of integer numbers and are called Miller indices.

The plane described by $\mathbf{G_n} \cdot \mathbf{r} = A$ fulfills the condition for a suitable value of A. The plane intersects the axes $\mathbf{a}_i$ at the points $x_1\mathbf{a}_1$, $x_2\mathbf{a}_2$ and $x_3\mathbf{a}_3$. Thus we find $\mathbf{G_n} x_i \mathbf{a}_i = A$ for all i. From (3.15) follows $\mathbf{G_n} \cdot \mathbf{a}_1 = 2\pi h$, $\mathbf{G_n} \cdot \mathbf{a}_2 = 2\pi k$ and $\mathbf{G_n} \cdot \mathbf{a}_3 = 2\pi l$, where h, k and l are integers. The triplet of integer numbers (hkl), the reciprocal values of the axis intersections in the direct lattice, are the Miller indices. An example is shown in Fig. 3.29.

Planes are denoted as (hkl) with parentheses. The (outward) normal direction is denoted with $[hkl]$ (square brackets). A set of equivalent planes is denoted with curly brackets as $\{hkl\}$. For example, in the simple cubic lattice (100), (010), (001), (−1 00), (0−1 0) are (00−1) equivalent and are denoted

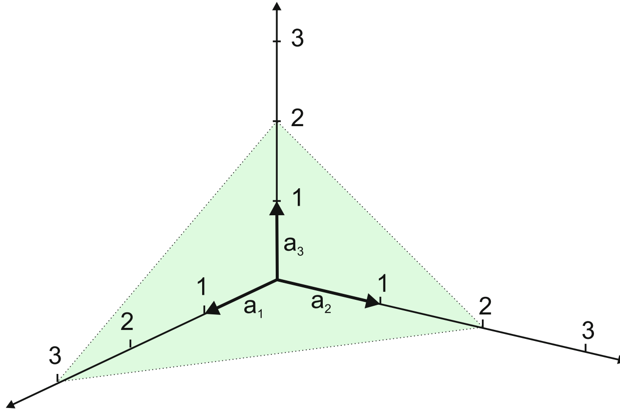

Fig. 3.29. The plane intersects the axes at 3, 2, and 2. The inverse of these numbers is 1/3, 1/2, and 1/2. The smallest integer numbers of this ratio form the Miller indices (233)

by $\{100\}$. $(-1\,00)$ can also be written as $(\bar{1}00)$. A set of equivalent directions is denoted with $\langle hkl \rangle$.

In a cubic lattice the faces of the cubic unit cell are $\{001\}$ and the planes perpendicular to the area (body) diagonals are $\{110\}$ ($\{111\}$) (Fig. 3.30). In the zincblende lattice the $\{111\}$ planes consist of diatomic planes with Zn and S atoms. It depends on the direction whether the metal or the nonmetal is on top. These two cases are denoted by A and B. We follow the convention

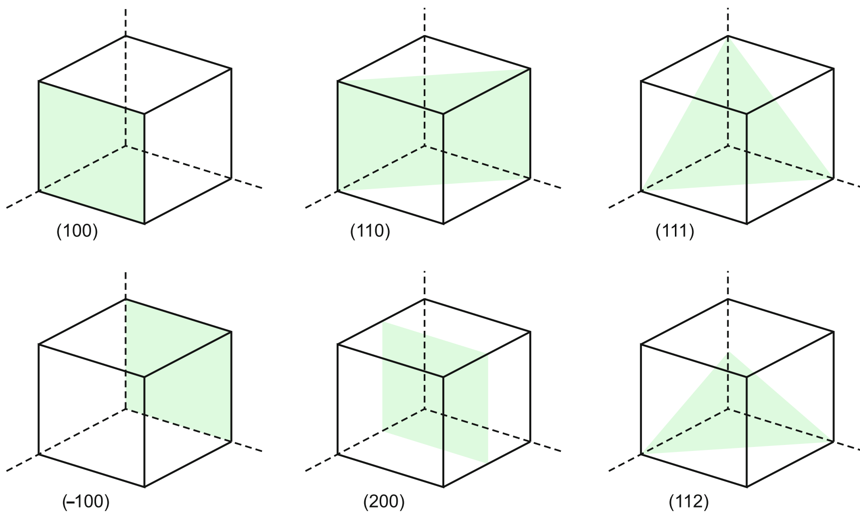

Fig. 3.30. Miller indices of important planes for the simple cubic (and fcc, bcc) lattice

that the (111) plane is (111)A and the metal is on top (as in Fig. 3.16b). For each change of sign the type changes from A to B and vice versa, e.g. (111)A, $(1\bar{1}1)$B and $(\bar{1}\bar{1}\bar{1})$B.

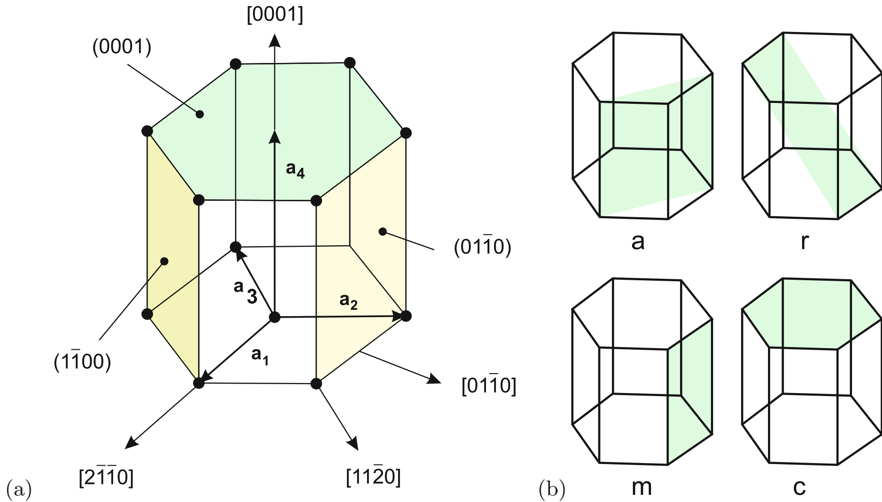

Fig. 3.31. (**a**) Miller indices for the wurtzite (or hcp) structure. (**b**) Orientation of the a-, r-, m-, and c-plane in the wurtzite structure

In the wurtzite lattice the Miller indices are denoted as $[hklm]$ (Fig. 3.31). Within the (0001) plane three indices hkl are used that are related to the three vectors $\mathbf{a}_1$, $\mathbf{a}_2$ and $\mathbf{a}_3$ (see Fig. 3.31a) rotated with respect to each other by 120°. Of course, the four indices are not independent and $l = -(h+k)$. The third (redundant) index can therefore be denoted as a dot. The c-axis [0001] is then denoted as [00.1]. Wurtzite (and trigonal, e.g. sapphire) substrates are available typically with a ([11.0]), r ([01.2]), m ([01.0]) and c ([00.1]) surface orientations (Fig. 3.31b).

3.6.3 Brillouin Zone

The Wigner–Seitz cell in reciprocal space is called the (first) Brillouin zone. In Fig. 3.32, the Brillouin zones for the most important lattices are shown. Certain points in the Brillouin zone are labeled with dedicated letters. The Γ point always denotes $\mathbf{k} = 0$ (zone center). Certain paths in the Brillouin zone are labeled with dedicated Greek symbols.

In the Brillouin zone of the fcc lattice (Si, Ge, GaAs, ...) the X point denotes the point at the zone boundary in [001] direction (at a distance $2\pi/a$ from Γ), K for [110] (at a distance $\sqrt{2}\,\pi/a$) and L for the [111] direction (at a distance $\sqrt{3}\,\pi/a$). The straight paths from Γ to X, K, and L are denoted as Δ, Σ, and Λ, respectively.

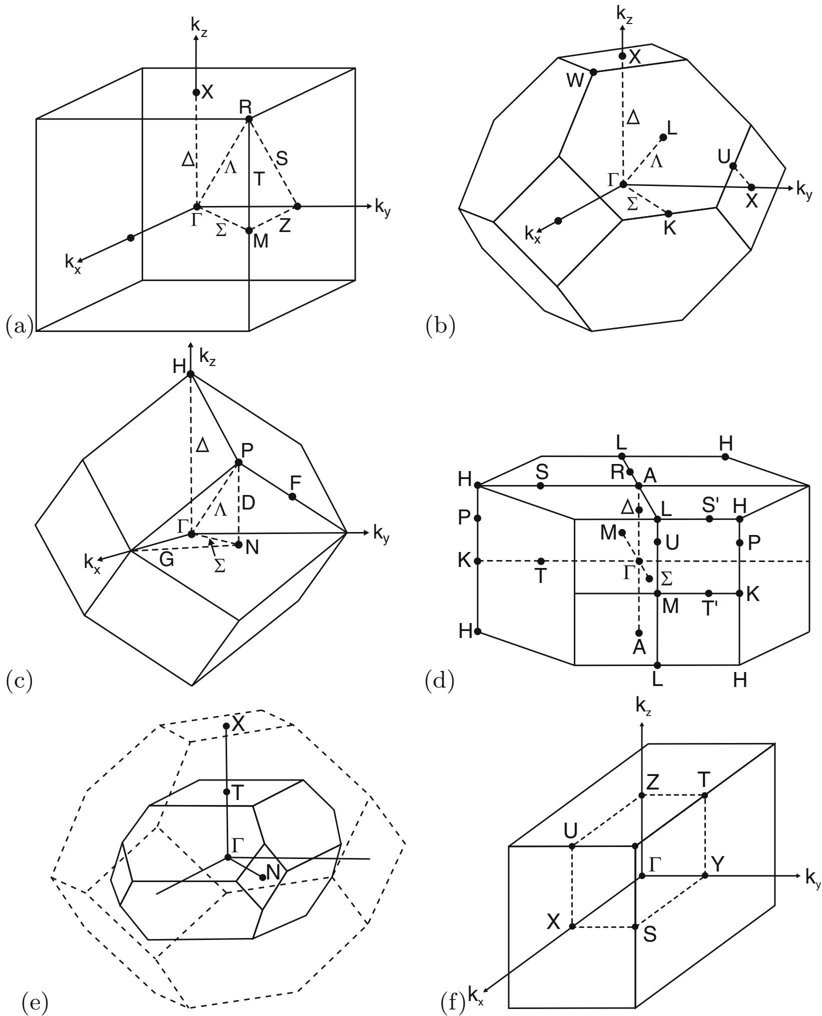

Fig. 3.32. Brillouin zones and special **k** points for the (**a**) primitive cubic (pc), (**b**) fcc, (**c**) bcc, and (**d**) hcp lattice. (**e**) Brillouin zone for chalcopyrite structure with fcc Brillouin zone shown as *dashed outline*. (**f**) Brillouin zone for orthorhombic lattice with one quadrant shown with *dashed lines*.

3.7 Alloys

When different semiconductors are mixed various cases can occur:

- The semiconductors are not miscible and have a so-called miscibility gap. They will tend to form clusters that build up the crystal. The formation of defects is probable.
- They form an ordered (periodic) structure that is called a superlattice.
- They form a random alloy.

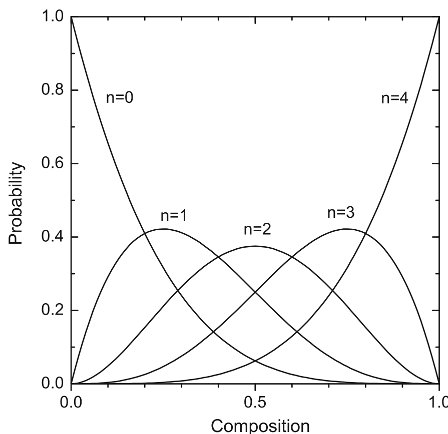

Fig. 3.33. Probability that a Si atom has n next-neighbor Ge atoms in a random Ge_xSi_{1-x} alloy

3.7.1 Random Alloys

Alloys for which the probability to find an atom at a given lattice site is given by the fraction of these atoms (i.e. the stoichiometry), independent of the surrounding, are called *random* alloys. Deviations from the random population of sites is termed *clustering*.

For a Ge_xSi_{1-x} alloy this means that any given atom site has the probability x to have a Ge atom and $1-x$ to have a Si atom. The probability p_n that a Si atom has n next-neighbor Ge atoms is

$$p_n = \binom{4}{n} x^n \, (1-x)^{4-n} \, , \tag{3.18}$$

and is depicted in Fig. 3.33 as a function of the alloy composition. The symmetry of the Si atom is listed in Table 3.7. If it is surrounded by four of the same atoms (either Ge or Si), the symmetry is T_d. If one atom is different

Table 3.7. Probability p_n (3.18) and symmetry of an A atom being surrounded by n B atoms in a tetrahedrally configured B_xA_{1-x} random alloy

n	p_n	symmetry
0	x^4	T_d
1	$4\,x^3\,(1-x)$	C_{3v}
2	$6\,x^2\,(1-x)^2$	C_{2v}
3	$4\,x\,(1-x)^3$	C_{3v}
4	$(1-x)^4$	T_d

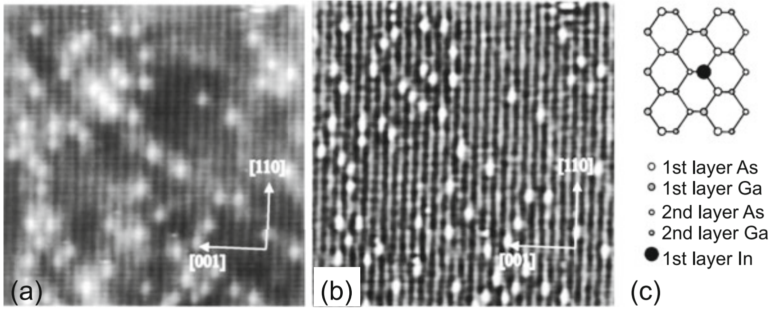

Fig. 3.34. (**a**) STM empty-state image ($17.5 \times 17.5\,\mathrm{nm}^2$) of the $(1\bar{1}0)$ surface of an MBE-grown $\mathrm{In_{0.05}Ga_{0.95}As}$ alloy on GaAs, (**b**) curvature-enhanced image. (**c**) Schematic atomic arrangement of the first and second atomic layer. Adapted from [148]

from the other three next neighbors, the symmetry is reduced to C_{3v} since one bond is singled out. For two atoms each the symmetry is lowest (C_{2v}).

In an alloy from binary compound semiconductors such as $\mathrm{Al}_x\mathrm{Ga}_{1-x}\mathrm{As}$ the mixing of the Al and Ga metal atoms occurs only on the metal (fcc) sublattice. Each As atom is bonded to four metal atoms. The probability that it is surrounded by n Al atoms is given by (3.18). The local symmetry of the As atom is also given by Table 3.7. For $\mathrm{AlAs}_x\mathrm{P}_{1-x}$ the mixing occurs on the nonmetal (anion) sublattice. If the alloy contains three atom species it is called a *ternary* alloy. In Fig. 3.34 the $(1\bar{1}0)$ surface (UHV cleave) of an $\mathrm{In_{0.05}Ga_{0.95}As}$ alloy is shown. Indium atoms in the first layer show up as brighter round dots [149]. Along the [001]-direction the positions are uncorrelated, along [110] an anti-correlation is found, corresponding to an effective repulsive pair interaction energy of 0.1 eV for the nearest neighbor In–In pairs along the [110]-direction due to strain effects [148].

If the binary end components have different crystal structure, the alloy shows a transition (or compositional transition range) from one structure to the other at a particular concentration. An example is the alloy between wurtzite ZnO and rocksalt MgO. The $\mathrm{Mg}_x\mathrm{Zn}_{1-x}\mathrm{O}$ alloy exhibits wurtzite structure up to about $x = 0.5$ and rocksalt structure for $x > 0.6$ [150].

If the alloy contains four atom species it is called *quaternary*. A quaternary zincblende alloy can have the mixing of three atom species on one sublattice, such as $\mathrm{Al}_x\mathrm{Ga}_y\mathrm{In}_{1-x-y}\mathrm{As}$ or $\mathrm{GaAs}_x\mathrm{P}_y\mathrm{Sb}_{1-x-y}$ or the mixing of two atom species on both of the two sublattices, such as $\mathrm{In}_x\mathrm{Ga}_{1-x}\mathrm{As}_y\mathrm{N}_{1-y}$.

The random placement of different atoms on the (sub)lattice in an alloy represents a perturbation of the ideal lattice and causes additional scattering (alloy scattering). In the context of cluster formation, the probability of an atom having a direct neighbor of the same kind on its sublattice is important. Given a $\mathrm{A}_x\mathrm{B}_{1-x}\mathrm{C}$ alloy, the probability p_S to find a single A atom surrounded by B atoms is given by (3.19a). The probability p_{D^1} to find a cluster of two neighbored A atoms surrounded by B atoms is given by (3.19b).

$$p_{\mathrm{S}} = (1-x)^{12} \tag{3.19a}$$

$$p_{\mathrm{D}^1} = 12\,x\,(1-x)^{18}\;. \tag{3.19b}$$

These formulas are valid for fcc and hcp lattices. For larger clusters [151, 152], probabilities in fcc and hcp structures differ.

3.7.2 Phase Diagram

The mixture A_xB_{1-x} with average composition x between two materials A and B can result in a single phase (alloy), a two-phase system (phase separation) or a metastable system. The molar free enthalpy ΔG of the mixed system is approximated by

$$\Delta G = \Omega\,x\,(1-x) + kT\,\left[x\,\ln(x) + (1-x)\,\ln(1-x)\right]\;. \tag{3.20}$$

The first term on the right-hand side of (3.20) is the (regular solution) enthalpy of mixing with the interaction parameter Ω, which can depend on x. The second term is the ideal configurational entropy based on a random distribution of the atoms. The function is shown for various ratios of kT/Ω in Fig. 3.35a. In an equilibrium phase diagram (see Fig. 3.35b) the system is above the binodal curve in one phase (miscible). On the binodal line $T_{\mathrm{b}}(x)$ in the (x, T) diagram the A- and B-rich disordered phases have equal chemical potentials, i.e. $\partial G/\partial x = 0$. For Ω independent of x the temperature T_{b} is given by (3.21a). A critical point is at the maximum temperature T_{mg} and concentration x_{mg} of the miscibility gap. For Ω independent of x it is given by $T_{\mathrm{mg}} = \Omega/2$ and $x_{\mathrm{mg}} = 1/2$. In the region below the spinodal boundary, the system is immiscible and phases immediately segregate (by spinodal decomposition). On the spinodal line $T_{\mathrm{sp}}(x)$ the condition $\partial^2 G/\partial x^2 = 0$ is fulfilled.

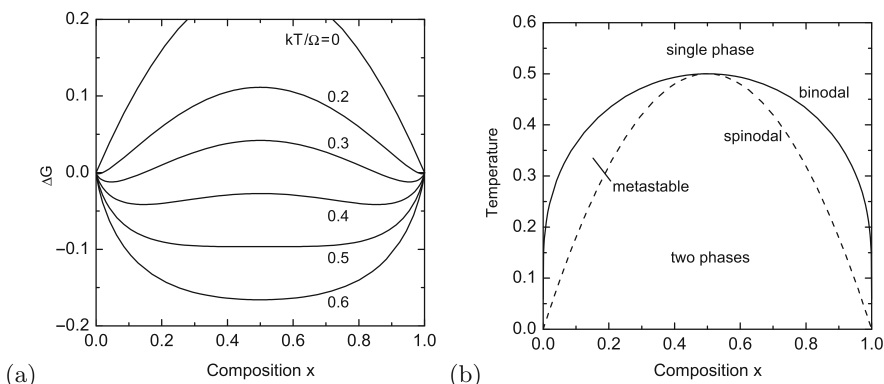

Fig. 3.35. (**a**) Free enthalpy ΔG of mixed binary system (3.20) in units of Ω for Ω =const. and various values of kT/Ω as labeled. (**b**) Schematic phase diagram for binary mixture. The temperature is given in units of Ω/k. The *solid* (*dashed*) denotes the binodal (spinodal) line

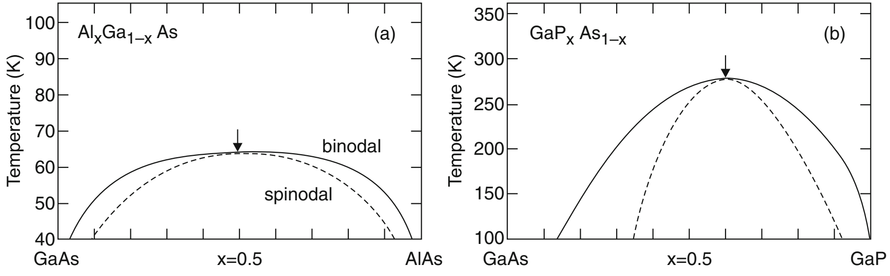

Fig. 3.36. Calculated phase diagrams for (**a**) $Al_xGa_{1-x}As$ and (**b**) GaP_xAs_{1-x}. The binodal (spinodal) curve is shown as *solid* (*dashed*) line. Adapted from [153]

For Ω independent of x the temperature T_{sp} is given by (3.21b). The region between the binodal and spinodal curves is the metastable region, i.e. the system is stable to small fluctuations of concentration or temperature but not for larger ones.

$$kT_b(x) = \Omega \frac{2x-1}{\ln(x) - \ln(1-x)} \tag{3.21a}$$

$$kT_{sp}(x) = 2\Omega\, x\,(1-x)\,. \tag{3.21b}$$

In Fig. 3.36 calculated diagrams for GaAs-AlAs and GaAs-GaP [153] are shown. The arrows denote the critical point. These parameters and the interaction parameters for a number of ternary alloys are given in Table 3.8. For example, for $Al_xGa_{1-x}As$ complete miscibility is possible for typical growth temperatures (>700 K), but for $In_xGa_{1-x}N$ the In solubility at a typical growth temperature of 1100 K is only 6% [154].

Table 3.8. Calculated interaction parameter $\Omega(x)$ (at $T = 800$ K, 1 kcal/mol= 43.39 meV), miscibility-gap temperature T_{mg} and concentration x_{mg} for various ternary alloys. Data for InGaN from [154], other data from [153]

alloy	T_{mg} (K)	x_{mg}	$\Omega(0)$ (kcal/mol)	$\Omega(0.5)$ (kcal/mol)	$\Omega(1)$ (kcal/mol)
$Al_xGa_{1-x}As$	64	0.51	0.30	0.30	0.30
GaP_xAs_{1-x}	277	0.603	0.53	0.86	1.07
$Ga_xIn_{1-x}P$	961	0.676	2.92	3.07	4.60
$GaSb_xAs_{1-x}$	1080	0.405	4.51	3.96	3.78
$Hg_xCd_{1-x}Te$	84	0.40	0.45	0.80	0.31
$Zn_xHg_{1-x}Te$	455	0.56	2.13	1.88	2.15
$Zn_xCd_{1-x}As$	605	0.623	2.24	2.29	2.87
$In_xGa_{1-x}N$	1505	0.50	6.32	5.98	5.63

3.7.3 Virtual Crystal Approximation

In the *virtual crystal approximation* (VCA) the disordered alloy AB_xC_{1-x} is replaced by an ordered binary compound AD with D being a 'pseudoatom' with properties that are configuration averaged over the properties of the B and C atoms, e.g. their masses or charges. Such an average is weighted with the ternary composition, e.g. the mass is $M_D = xM_B + (1-x)M_C$. For example, the A–D force constant would be taken as the weighted average over the A–B and A–C force constants.

3.7.4 Lattice Parameter

In the VCA for an alloy a new sort of effective atom is assumed that has an averaged bond length that depends linearly on the composition. Typically, Vegard's law (3.22), which predicts that the lattice constant of a ternary alloy $A_xB_{1-x}C$ depends linearly on the lattice constants of the binary alloys AC and BC, is indeed fulfilled

$$a_0(A_xB_{1-x}C) = a_0(BC) + x\,[a_0(AC) - a_0(BC)]\ . \tag{3.22}$$

In reality, the bond length of the AC and BC bonds changes rather little (Fig. 3.37a) such that the atoms in the alloy suffer a displacement from

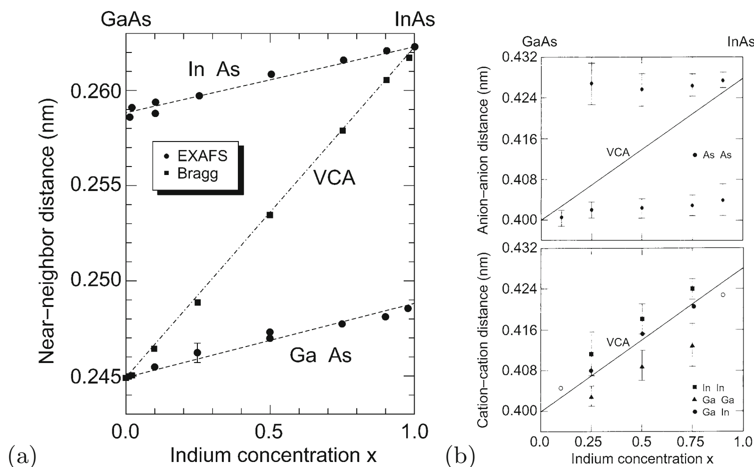

Fig. 3.37. (**a**) Near-neighbor distance ($\sqrt{3}a_0/4$) of $In_xGa_{1-x}As$ as measured by standard X-ray diffraction (Bragg reflection, *solid squares*) and VCA approximation (*dash-dotted line*). Near-neighbor Ga–As and In–As distances as determined by EXAFS (extended X-ray absorption fine structure, *solid squares*). *Dashed lines* are guides to the eye. Data from [155]. (**b**) Second-neighbor distances for $In_xGa_{1-x}As$ as determined from EXAFS, *top*: anion–anion distance (for As–As), *bottom*: cation–cation distance (for In–In, Ga–Ga, and Ga–In). *Solid lines* in both plots are the VCA ($a_0/\sqrt{2}$). Data from [156]

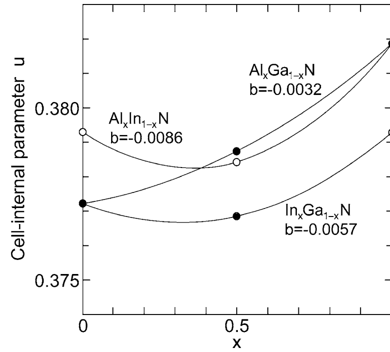

Fig. 3.38. Theoretical values ($T = 0\,\mathrm{K}$) for the cell-internal parameter u as a function of the composition for group-III nitride alloys. The *solid lines* are quadratic curves (bowing parameter b is shown) through the points for $x = 0$, 0.5, and 1.0. Data from [158]

their average position and the lattice is deformed on the nanoscopic scale. In a lattice of the type $In_xGa_{1-x}As$ the anions suffer the largest displacement since their position adjusts to the local cation environment. For $In_xGa_{1-x}As$ a bimodal distribution, according to the As–Ga–As and As–In–As configurations, is observed (Fig. 3.37b). The cation–cation second-neighbor distances are fairly close to the VCA.

While the average lattice parameter in alloys changes linearly with composition, the cell-internal parameter u (for wurtzite structures, see Sect. 3.4.5) exhibits a nonlinear behavior as shown in Fig. 3.38. Therefore physical properties connected to u, such as the spontaneous polarization, will exhibit a bowing.

3.7.5 Ordering

Some alloys have the tendency for the formation of a superstructure [160]. Growth kinetics at the surface can lead to specific adatom incorporation leading to ordering. For example, in $In_{0.5}Ga_{0.5}P$ the In and Ga atoms can be ordered in subsequent (111) planes (CuPt structure) instead of being randomly mixed (Fig. 3.39). This impacts fundamental properties such as the phonon spectrum or the band gap. CuPt ordering on (111) and $(\bar{1}\bar{1}1)$ planes is called $CuPt_A$, on $(\bar{1}11)$ and $(1\bar{1}1)$ planes $CuPt_B$ ordering. In Fig. 3.40, a TEM image of a $Cd_{0.68}Zn_{0.32}Te$ epilayer is shown with simultaneous ordering in the CuPt structure (doublet periodicity along $[1\bar{1}1]$ and $[\bar{1}11]$) and in the CuAu-I structure[4] (doublet periodicity along [001] and $[\bar{1}10]$). The geometry of different ordering types is shown in Fig. 3.41.

[4]The CuAu-I structure has tetragonal symmetry. There exists also the CuAu-II structure that is orthorhombic.

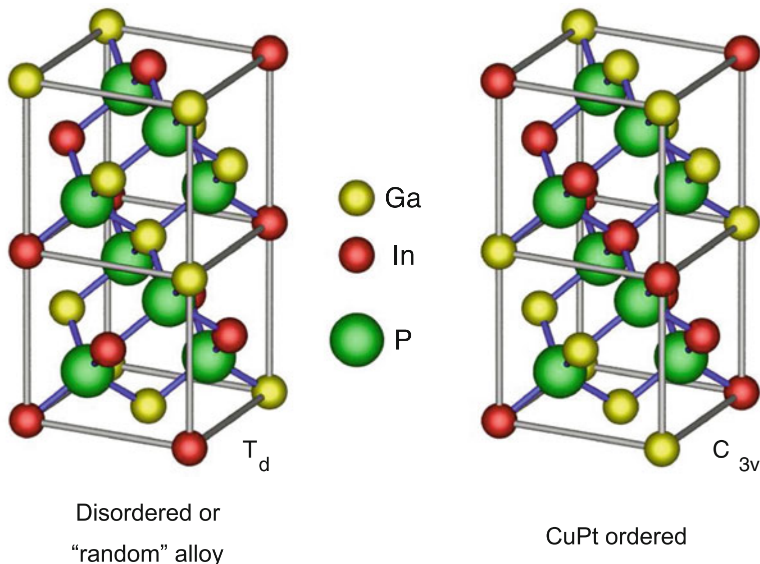

Fig. 3.39. CuPt-ordered ternary alloy $In_{0.5}Ga_{0.5}P$; the lattice symmetry is reduced from T_d to C_{3v}

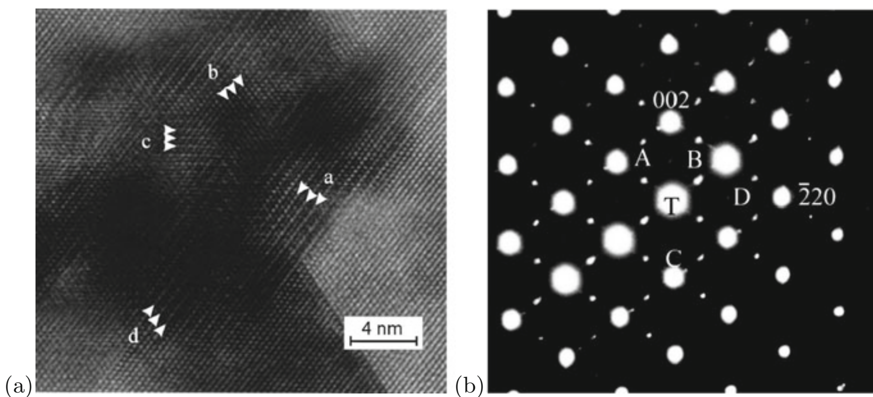

Fig. 3.40. (**a**) Cross-sectional transmission electron microscope image along the [110] zone axis of a $Cd_{0.68}Zn_{0.32}Te$ epilayer on GaAs showing ordered domains having a doublet periodicity on the {111} and {001} lattice planes. Two different {111} variants are labeled 'a' and 'b'. The doublet periodicity in the [001] is seen in the 'c' region. (**b**) Selected-area diffraction pattern along the [110] zone. Strong peaks are fundamental peaks of the zincblende crystal, weak peaks are due to CuPt ordering, labeled A and B, and CuAu-I ordering, labeled C and D. The latter are the weakest due to a small volume fraction of CuAu-ordered domains. Adapted from [159]

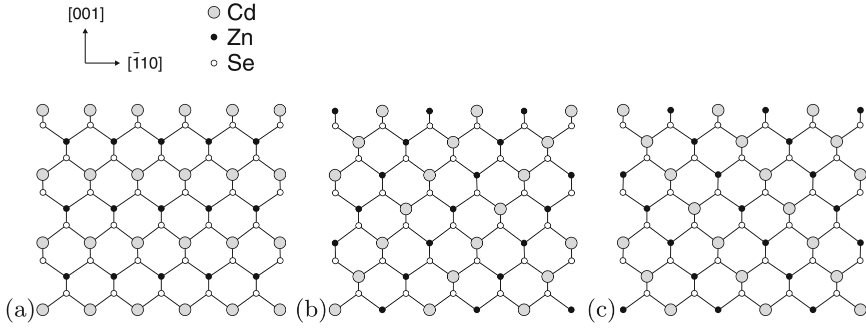

Fig. 3.41. Schematic diagrams of zincblende $Cd_xZn_{1-x}Te$ along [110] with (**a**) CuAu-I type ordering and (**b**,**c**) two types of the $CuPt_B$ type ordering. Doublet periodicity is along (**a**) [001] and [$\bar{1}$10], (**b**) [1$\bar{1}$1] and (**c**) [$\bar{1}$11]. Adapted from [159]

4 Defects

4.1 Introduction

In an ideal lattice each atom is at its designated position. Deviations from the ideal structure are called defects. In the following, we will briefly discuss the most common defects. The electrical activity of defects will be discussed in Sects. 7.5 and 7.7. For the creation (formation) of a defect a certain free enthalpy $G_{\mathrm{D}}^{\mathrm{f}}$ is necessary. At thermodynamical equilibrium a (point) defect density $\propto \exp\left(-G_{\mathrm{D}}^{\mathrm{f}}/kT\right)$ will always be present (cf. Sect. 4.2.2).

Point defects (Sect. 4.2) are deviations from the ideal structure involving essentially only one lattice point. The formation energy for line defects (Sect. 4.3) or area defects (Sect. 4.4) scales with $N^{1/3}$ and $N^{2/3}$, respectively, N being the number of atoms in the crystal. Therefore, these defects are not expected in thermodynamic equilibrium. However, the path into thermodynamical equilibrium might be so slow that these defects are metastable and must be considered quasi-frozen. There may also exist metastable point defects. By annealing the crystal, the thermodynamic equilibrium concentration might be re-established.

4.2 Point Defects

4.2.1 Point Defect Types

The simplest point defect is a vacancy V, a missing atom at a given atomic position. If an atom is at a position that does not belong to the crystal structure an interstitial I (or Frenkel defect) is formed. Depending on the position of the interstitial different types are distinguished. An interstitial atom that has the same chemical species as the crystal is called 'self-interstitial'.

If an atom site is populated with an atom of different order number Z, an impurity is present. An impurity can also sit on interstitial position. If the number of valence electrons is the same as for the original (or correct) atom, then it is an isovalent impurity and quasi fits into the bonding scheme. If the valence is different, the impurity adds extra (negative or positive) charge to the crystal bonds, which is compensated by the extra, locally fixed charge in the nucleus. This mechanism will be discussed in detail in the context of

M. Grundmann, *The Physics of Semiconductors*, 2nd ed., Graduate Texts in Physics, DOI 10.1007/978-3-642-13884-3_4,

© Springer-Verlag Berlin Heidelberg 2010

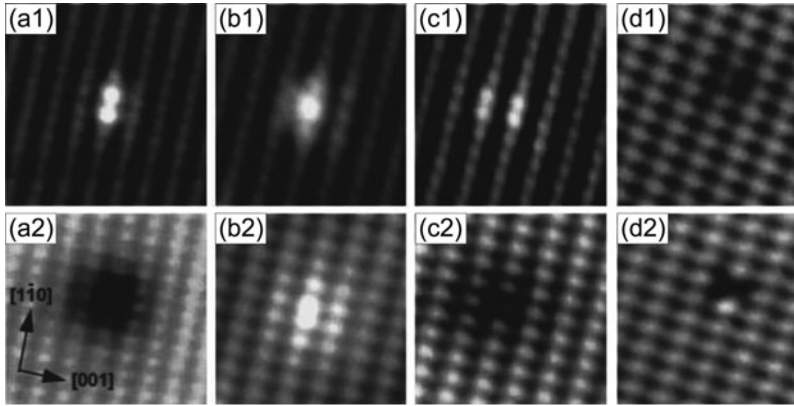

Fig. 4.1. Images of occupied (*upper frames*) and empty (*lower frames*) density of states of typical defects on Si-doped GaAs (110) surfaces. (**a1**, **a2**) show a Ga vacancy, (**b1**, **b2**) a $\mathrm{Si_{Ga}}$ donor, (**c1**, **c2**) a $\mathrm{Si_{As}}$ acceptor and (**d1**, **d2**) a $\mathrm{Si_{Ga}}$–$\mathrm{V_{Ga}}$ complex. Adapted from [160]

doping (Sect. 7). If in an AB compound an A atom sits on the B site, the defect is called an antisite defect A_B.

A Ga vacancy, a silicon impurity atom on Ga- and As-site and a $\mathrm{Si_{Ga}}$-vacancy complex at the (110) surface of Si doped GaAs are shown in Fig. 4.1 as observed with STM [160, 161]. Also antisite defects in GaAs can be observed with STM [162, 163].

A point defect is typically accompanied by a relaxation of the surrounding host atoms. As an example, we discuss the vacancy in Si (Fig. 4.2a). The missing atom leads to a lattice relaxation with the next neighbors moving some way into the void (Fig. 4.2b). The bond lengths of the next and second-next neighbor Si atoms around the neutral vacancy are shown in Fig. 4.2c. The lattice relaxation depends on the charge state of the point defect (Jahn–Teller effect) which is discussed in more detail in Sect. 7.7. In Fig. 4.2d the situation for the positively charged vacancy with one electron missing is shown. One of the two bonds is weakened since it lacks an electron. The distortion is therefore different from that for V^0. Also the (self-)interstitial is accompanied with a lattice relaxation as shown in Fig. 4.3 for a silicon interstitial at tetrahedral place. Self-interstitials in silicon and germanium are reviewed and compared in [164] for their various charge states.

Point defects can cluster. An example of five nearby vacancies in silicon, the so-called $\mathrm{V_5}$ cluster is shown in Fig. 4.4. A large number of clustered vacancies is equivalent to a void. Also impurities cluster (see Sect. 4.2.5).

4.2.2 Thermodynamics

For a given temperature, the free enthalpy G of a crystal (a closed system with regard to particle exchange)

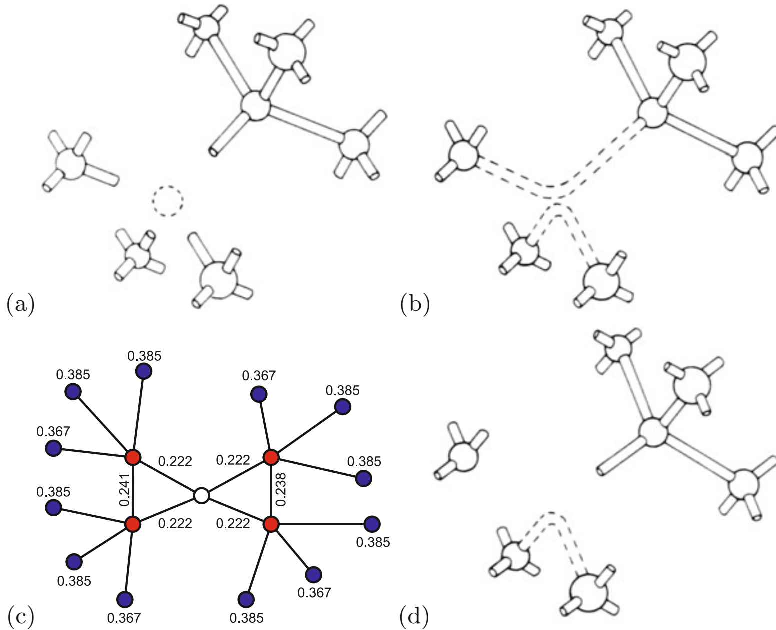

Fig. 4.2. (**a**) Schematic diamond lattice with vacancy, i.e. a missing Si atom without relaxation. (**b**) Si with neutral vacancy (V^0), lattice relaxation and formation of two new bonds. (**c**) Schematic diagram showing the (inward) relaxation of the neighbors around the neutral Si vacancy defect site (*empty circle*) calculated by an ab initio method. The distances of the outer shell of atoms (*red circles*) from the vacant site is labeled (in nm). The bond lengths of the two new bonds and the second-neighbor (*blue circles*) distance are also indicated. The bond length in bulk Si is 0.2352 nm, the second-neighbor distance 0.3840 nm. Adapted from [165]. (**d**) Si unit cell with positively charged vacancy (V^+). Parts (**a**,**b**,**d**) reprinted with permission from [166]

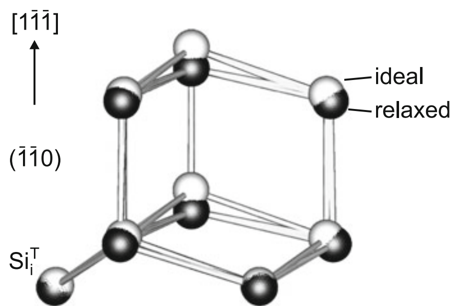

Fig. 4.3. Silicon tetrahedral interstitial Si_i^T and its next atoms in ideal (*white spheres*) and relaxed (*black spheres*) position. Adapted from [98]

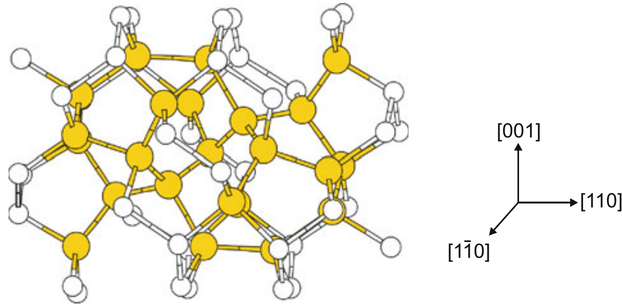

Fig. 4.4. Predicted configuration of the V_5-cluster (five vacancies) in silicon. *Yellow spheres* indicate more distorted atoms than the rest of the lattice atoms (*white spheres*). Adapted from [167]

$$G = H - TS \tag{4.1}$$

is minimum. H is the enthalpy and S the entropy. The enthalpy $H = E + pV$ is the thermodynamic potential for a system whose only external parameter is the volume V. It is used when the independent variables of the system are the entropy S and pressure p. The free enthalpy is used when the independent parameters are T and p. G_0 (H_0) is the free energy (enthalpy) of the perfect crystal. H^{f} is the formation enthalpy of an isolated defect. This could be, e.g., the enthalpy of a vacancy, created by bringing an atom from the (later) vacancy site to the surface, or an interstitial, created by bringing an atom from the surface to the interstitial site. In the limit that the n defects do not interact with each other, i.e. their concentration is sufficiently small, they can be considered independent and the enthalpy is given by

$$H = H_0 + n\, H^{\mathrm{f}} \ . \tag{4.2}$$

The increase of entropy due to increased disorder is split into the configurational disorder over the possible sites, denoted as S^{d}, and the formation entropy S_{f} due to localized vibrational modes. The total change ΔG of the free energy is

$$\Delta G = G - G_0 = n\,(H^{\mathrm{f}} - TS^{\mathrm{f}}) - TS^{\mathrm{d}} = n\,G^{\mathrm{f}} - TS^{\mathrm{d}} \ , \tag{4.3}$$

where $G^{\mathrm{f}} = H^{\mathrm{f}} - TS^{\mathrm{f}}$ denotes the free enthalpy of formation of a single isolated defect. In Table 4.1 experimental values for the formation entropy and enthalpy are given for several defects. Surprisingly, despite their fundamental importance in semiconductor defect physics, these numbers are not very well known and disputed in the literature.

The defect concentration is obtained by minimizing ΔG, i.e.

$$\frac{\partial \Delta G}{\partial n} = G^{\mathrm{f}} - T\,\frac{\partial S^{\mathrm{d}}}{\partial n} = 0 \ . \tag{4.4}$$

Table 4.1. Formation enthalpy H^{f} and entropy S^{f} of the interstitial (I) and vacancy (V) in Si and the Ga vacancy in GaAs. Data for Si from [168, 169], for GaAs from [170]

Material	defect	H^{f} (eV)	S^{f} (k_{B})
Si	I	3.2	4.1
Si	V	2.8	~ 1
GaAs	V_{Ga}	3.2	9.6

The entropy S^{d} due to disorder is given as

$$S^{\mathrm{d}} = k_{\mathrm{B}} \ln W \ , \tag{4.5}$$

where W is the complexion number, usually the number of distinguishable ways to distribute n defects on N lattice sites

$$W = \binom{N}{n} = \frac{N!}{n!\,(N-n)!} \ . \tag{4.6}$$

With Stirling's formula $\ln x! \approx x(\ln x - 1)$ for large x we obtain

$$\frac{\partial S^{\mathrm{d}}}{\partial n} = k_{\mathrm{B}} \left[\frac{N}{n} \ln \left(\frac{N}{N-n} \right) + \ln \left(\frac{N-n}{n} \right) \right] \ . \tag{4.7}$$

If $n \ll N$, $\partial N/\partial n = 0$ and the right side of (4.7) reduces to $k_{\mathrm{B}} \ln(N/n)$. The condition (4.4) reads $G^{\mathrm{f}} + k_{\mathrm{B}}T \ \ln(n/N)$, or

$$\frac{n}{N} = \exp\left(-\frac{G^{\mathrm{f}}}{k_{\mathrm{B}}T} \right) \ . \tag{4.8}$$

In the case of several different defects i with a degeneracy Z_i, e.g. a spin degree of freedom or several equivalent configurations, (4.8) can be generalized to

$$\frac{n_i}{Z_i\, N} = \exp\left(-\frac{G_i^{\mathrm{f}}}{k_{\mathrm{B}}T} \right) \ . \tag{4.9}$$

In [171] the equilibrium concentration of interstitials C_I^{eq} in silicon has been given as

$$C_I^{\mathrm{eq}} = \left(1.0 \times 10^{27}\,\mathrm{cm}^{-3}\right) \exp\left(-\frac{3.8\,\mathrm{eV}}{kT} \right) \ , \tag{4.10}$$

about $10^{14}\,\mathrm{cm}^{-3}$ at 1200°C. The vacancy concentration has been investigated in [172]. Around a temperature of 1200°C it is in the 10^{14}–$10^{15}\,\mathrm{cm}^{-3}$ range. Due to the reaction

$$0 \rightleftharpoons I + V \ , \tag{4.11}$$

a mass action law holds for the concentrations of interstitials and vacancies

$$C_I\, C_V = C_I^{\mathrm{eq}}\, C_V^{\mathrm{eq}} \ . \tag{4.12}$$

4.2.3 Diffusion

The diffusion of point defects is technologically very important, in particular for silicon as host material. Typically a dopant profile should be stable under following technological processing steps and also during device performance. Also defect annihilation is crucial after implantation processes. Diffusion of an interstitial I and a vacancy V to the same site is prerequisite for recombination of defects (so called *bulk process*) according to the scheme $I + V \rightarrow 0$. We note that the process $0 \rightarrow I + V$ is called *Frenkel pair process*.[1] Also the self-diffusion of silicon has been studied, e.g. using radioactively marked isotopes [171]. The diffusion of point defects including dopants in silicon has been reviewed in [173, 174]. Usually Fick's law is applied, stating how the flux J depends on the concentration gradient, for an interstitial it reads:

$$J_I = -D_I \nabla C_I \; , \tag{4.13}$$

D_I being the interstitial diffusion coefficient. For interstitials in Si it was found [171] that

$$D_I = 0.2 \, \exp\left(-\frac{1.2\,\mathrm{eV}}{kT}\right) \, \mathrm{cm^2/s} \; . \tag{4.14}$$

The diffusion of neutral vacancies occurs with [175]

$$D_V = 0.0012 \, \exp\left(-\frac{0.45\,\mathrm{eV}}{kT}\right) \, \mathrm{cm^2/s} \; . \tag{4.15}$$

The temperature dependent diffusion coefficients of point defects and dopants in silicon are shown in Fig. 4.5.

The self-diffusion coefficient of silicon has been determined from the annealing of isotope superlattices (Sect. 11.5) of sequence $^{28}\mathrm{Si}_n/^{30}\mathrm{Si}_n$, $n = 20$ to be [176]

$$D_{\mathrm{Si}}^{\mathrm{SD}} = \left[2175.4 \, \exp\left(-\frac{4.95\,\mathrm{eV}}{kT}\right) + 0.0023 \, \exp\left(-\frac{3.6\,\mathrm{eV}}{kT}\right)\right] \, \mathrm{cm^2/s} \; , \tag{4.16}$$

the first (second) term being due to interstitial (vacancy) mechanism, dominant for temperatures larger (smaller) than 900°C. The enthalpy in the exponent, e.g. $H_V = 3.6^{+0.3}_{-0.1}\,\mathrm{eV}$ [176], consists of the formation and migration enthalpies,

$$H_V = H_V^{\mathrm{f}} + H_V^{\mathrm{m}} \; . \tag{4.17}$$

Using the experimental value $H_V^{\mathrm{f}} = 2.8 \pm 0.3\,\mathrm{eV}$ [169] from Table 4.1, for the migration enthalpy a value around $H_V^{\mathrm{m}} \approx 0.8\,\mathrm{eV}$ is obtained.

[1] At higher temperatures a silicon atom can occasionally acquire sufficient energy from lattice vibrations to leave its lattice site and thus an interstitial and a vacancy are generated.

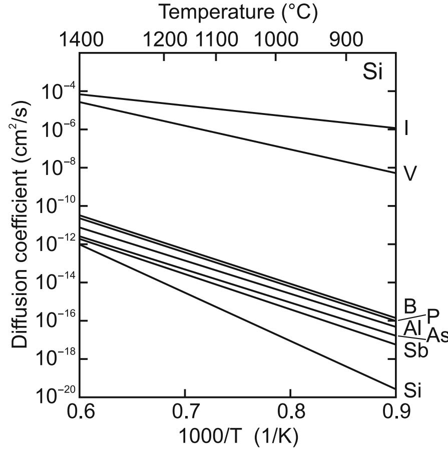

Fig. 4.5. The temperature dependent diffusion coefficient of Si interstitials I, vacancies V and various impurities in silicon. Also the self-diffusion coefficient, labeled with 'Si' is shown. Based on data from [173]

As an example for a dopant diffusion process that has been understood microscopically, we discuss here boron in silicon. In Fig. 4.6a the lowest-energy configuration of a boron-related defect in silicon is depicted, B_s–Si_i^T, i.e. boron on a substitutional site and a self-interstitial Si on the 'T' place with highest symmetry[2] (see Fig. 3.17). Due to its importance as an acceptor in Si, the configuration and diffusion of B in Si has found great interest [177–179]. The diffusion depends on the charge state of boron. The diffusion of positively charged boron has been suggested [179] to occur via the following route: The boron leaves its substitutional site and goes to the hexagonal site ('H') (Fig. 4.6b) with an activation energy of about 1 eV (Fig. 4.6d). It can then relax (~ 0.1 eV) without barrier to the tetrahedral 'T' position (Fig. 4.6c). The direct migration B_s–$Si_i^{T+} \rightarrow B_i^{T+}$ has a higher activation energy of 1.12 eV and is thus unlikely. The boron atom can then diffuse through the crystal by going from 'H' to 'T' to 'H' and so on (Fig. 4.6e). However, long-range diffusion seems to be not possible in this way because the kick-in mechanism will bring back the boron to its stable configuration. The pair diffusion mechanism for neutral boron B_s–$Si_i^T \rightarrow B_i^H \rightarrow B_s$–$Si_i^T$ via the hexagonal site has an activation energy of about 0.5 eV (Fig. 4.6d) while the path via B_i^T has a larger 0.9 eV barrier. The concentration dependence of the diffusion mechanism has been discussed in [180].

Similarly, indium diffusion in silicon has been investigated suggesting a minimum energy In_s–$Si_i^T \rightarrow In_i^T \rightarrow In_s$–$Si_i^T$ diffusion pathway via the

[2] The positive charge state is stable, the neutral charge state is metastable since the defect is a negative-U center (see Sect. 7.7.5).

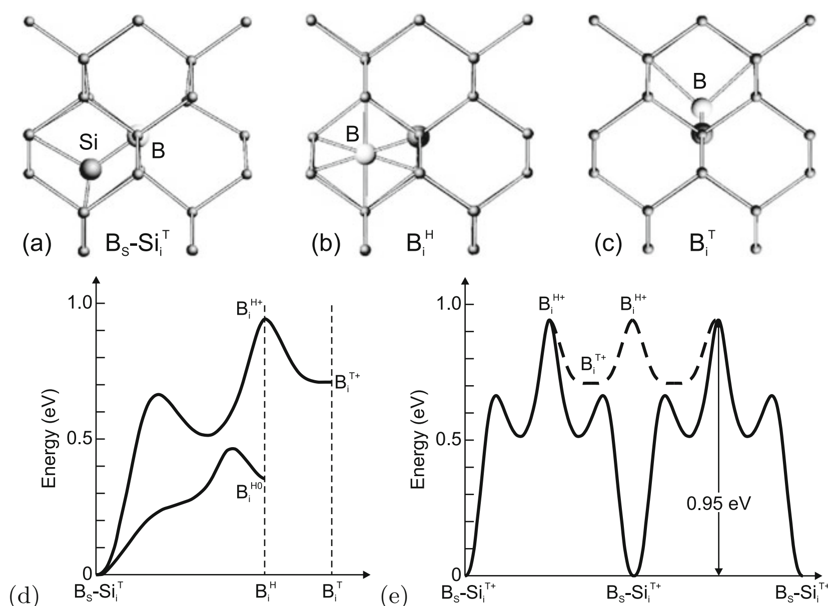

Fig. 4.6. Configurations of boron in Si: (**a**) Substitutional boron and Si self-interstitial at 'T' site (B_S–Si_i^T). Interstitial boron at (**b**) 'H' (B_i^H) and (**c**) 'T' site (B_i^T), each with the Si atoms on the Si lattice sites. The *large bright ball* represents the boron atom, *large* and *small dark balls* represent Si atoms. (**d**) Lowest energy barrier diffusion paths for positively charged and neutral B–Si states, total energy vs. configuration. (**e**) Two diffusion pathways for positively charged B–Si, kick-out (*dashed line*) and pair diffusion (*solid line*); the activation energy is labeled. Adapted from [179]

tetrahedral site with 0.8 eV activation energy [181]. Microscopic modeling has been reported also for diffusion of phosphorus [182].

4.2.4 Dopant Distribution

The introduction of impurities into a semiconductor (or other materials such as glasses) is termed *doping*. The unavoidable incorporation of impurities in the nominally pure (nominally undoped) material is called *unintentional* doping and leads to a residual or background impurity concentration. Several methods are used for doping and the creation of particular doping profiles (in depth or lateral). All doping profiles underly subsequent diffusion of dopants (Sect. 4.2.3).

Various methods of doping are used. A straightforward method of doping is the incorporation during crystal growth or epitaxy. For semiconductor wafers a homogeneous doping concentration is targeted, both laterally and along the rod from which the wafer is cut (Sect. 11.2.2). When a crystal is

grown from melt, containing a concentration c_0 of the impurity, the concentration in the solid is given by ('normal freezing' case [183–185])[3]

$$c(x) = c_0\, k\, (1-x)^{k-1} \; , \tag{4.18}$$

where $c(x)$ is the impurity concentration in the crystal at the freezing interface, x is the frozen melt fraction (ratio of solid mass to total mass, $0 \leq x \leq 1$). k is the *distribution coefficient* (or segregation coefficient) which is the fraction of impurities that is built into the crystal at the liquid–solid interface. Since the melt volume reduces during the solidification, the impurity concentration rises over time. For small distribution coefficients (4.18) can be approximated to

$$c(x) \approx c_0\, \frac{k}{1-x} \; , \tag{4.19}$$

An experimental example for Ge:In is shown in Fig. 4.7a.

In Table 4.2 the distribution coefficients for various impurities in Si, Ge and GaAs is given. The modification of distribution coefficients in SiGe alloys

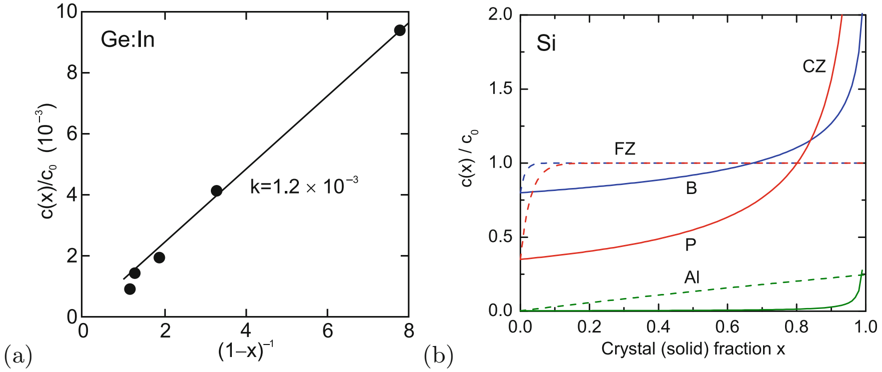

Fig. 4.7. (**a**) Relative concentration of indium along a CZ-grown germanium crystal. Absolute concentration is in the $10^{16}\,\mathrm{cm}^{-3}$ range. *Solid line* follows (4.19) with $k = 1.2 \times 10^{-3}$. *Symbols* are experimental data from [189]. (**b**) Impurity distribution (relative concentration $c(x)/c_0$) for CZ (4.18) (*solid lines*) and FZ (4.20) (*dashed lines*, $z = 0.01$) silicon crystals for B (*blue*), P (*red*), and Al (*green*). Distribution coefficients have been taken from Table 4.2. Note crossing of B and P lines and possibly associated change from p-type to n-type (cmp. Fig. 1.4)

[3] Mass preservation of the impurities can be written at any time $c_\mathrm{m}(1-x) + \int_0^x c(x')\,\mathrm{d}x' = c_0$, where c_m is the (remaining) concentration in the melt. At the beginning $c_\mathrm{m}(0) = c_0$. At the interface $c(x) = k\, c_\mathrm{m}(x)$. Putting this into the mass preservation, building $c'(x)$ and solving the resulting differential equation $c' = c(1-k)/(1-x)$ with $c(0) = k\, c_0$ leads to (4.18).

Table 4.2. Equilibrium distribution coefficients (at melting point) of various impurities in silicon, germanium and GaAs. Data for Si from [185, 188], for Ge from [189–192] and for GaAs from [192]

impurity	Si	Ge	GaAs
C	0.07	> 1.85	0.8
Si		5.5	0.1
Ge	0.33		0.03
N	7×10^{-4}		
O	≈ 1		0.3
B	0.8	12.2	
Al	2.8×10^{-3}	0.1	3
Ga	8×10^{-3}	0.087	
In	4×10^{-4}	1.2×10^{-3}	0.1
P	0.35	0.12	2
As	0.3	0.04	
Sb	0.023	3.3×10^{-3}	< 0.02
S	10^{-5}	$> 5 \times 10^{-5}$	0.3
Fe	6.4×10^{-6}	3×10^{-5}	2×10^{-3}
Ni	$\approx 3 \times 10^{-5}$	2.3×10^{-6}	6×10^{-4}
Cu	8×10^{-4}	1.3×10^{-5}	2×10^{-3}
Ag	$\approx 1 \times 10^{-6}$	10^{-4}	0.1
Au	2.5×10^{-5}	1.5×10^{-5}	
Zn	2.5×10^{-5}	6×10^{-4}	0.1

is discussed in [186]. Equilibrium values (k_{eq}) are obtained for 'slow' crystal growth. For finite growth rates, k becomes a function of the growth rate and is then called the *effective* distribution coefficient. For $k < 1$, $k_{\mathrm{eff}} > k_{\mathrm{eq}}$. k_{eff} approaches 1 for high growth rates, i.e. all impurities at the rapidly moving interface are incorporated.

(4.18) applies to Czrochalski growth where the crystal is pulled out of the melt [187]. In float-zone (FZ) growth [187] a polycrystalline rod is transformed into a crystalline one while a RF-heated and liquid 'float' zone is moved through the crystal. In this case the impurity distribution is given by[4]

$$c(x) = c_0 \left[1 - (1 - k) \, \exp\left(- \frac{k \, x}{z} \right) \right] \, , \tag{4.20}$$

[4]When the float zone moves through the crystal, the change of mass of impurities $m_{\mathrm{m}} = c_{\mathrm{m}} z$ in the liquid is $m'_{\mathrm{m}} = c_0 - k c_{\mathrm{m}}$. The first term stems from the melting of the polycrystalline part, the second from the solidification of the crystal. Solving the resulting differential equation $c'_{\mathrm{m}} = (c_0 - k c_{\mathrm{m}})/z$ with $c_{\mathrm{m}}(0) = c_0$ and using $c(x) = k c_{\mathrm{m}}(x)$ yields (4.20).

where x is the ratio of the crystal mass to the total mass, i.e. crystal, liquid and feed rod. z is the relative mass of the (liquid) float zone, i.e. the ratio of liquid mass to the total mass. The impurity distribution for CZ and FZ crystals is compared in Fig. 4.7b. Obviously the FZ process can create much more homogeneous profiles.[5]

Using epitaxy arbitrary doping profiles along the growth directions can be created by varying the impurity supply during growth. Impurities can be introduced through the surface of the material by diffusion from a solid or gas phase. In ion implantation [193] the impurity atoms are accelerated towards the semiconductor and deposited with a certain depth profile due to multiple scattering and energy loss events, depending on the acceleration voltage (increasing deposition depth with increasing voltage, Fig. 4.8a) and ion mass (decreasing deposition depth with increasing mass, Fig. 4.8b). The depth profile is often investigated using secondary ion mass spectrometry (SIMS) [194]. The profile also depends on the matrix material whose stopping power depends on its density and atomic mass. While an implantation depth of about 50 nm is reached for boron in silicon ($A \approx 28$) for 10 keV, 20 keV are necessary in germanium ($A \approx 72.6$) [195]. The mean path length[6] d_{m} depends also on the crystallographic direction (channeling effects, Fig. 4.9) [196]. A simulation of the interaction of ions and solids can be performed using the SRIM software [197, 198].

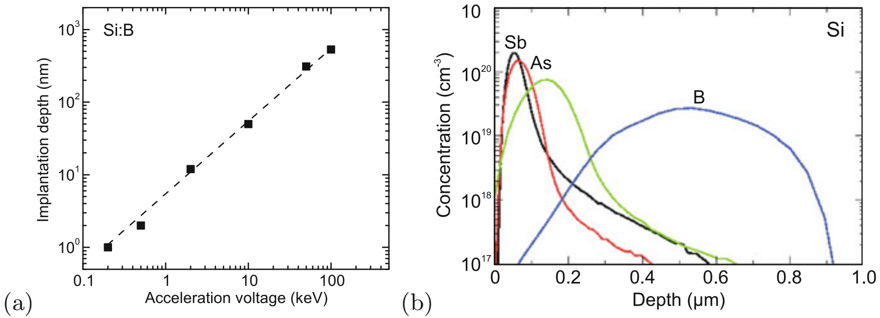

Fig. 4.8. (**a**) Depth of peak concentration of boron implanted in silicon for various acceleration voltages U. Data from various sources, for $U < 1$ keV from [199]. *Dashed line* is linear dependence. (**b**) Simulated depth profiles of impurity concentration for B, P, As, and Sb implanted into crystalline silicon with $U = 100$ keV and a dose of 10^{15} cm^{-2}. Adapted from [200]

[5] We note that during directed solidification of Si:(B,P) a pn-junction forms due to the different distribution coefficients of boron and phosphorus. This has been used in [53].

[6] The mean path length is the distance integrated along the ion trajectory until its direction deviates by more than 4° from the incident direction.

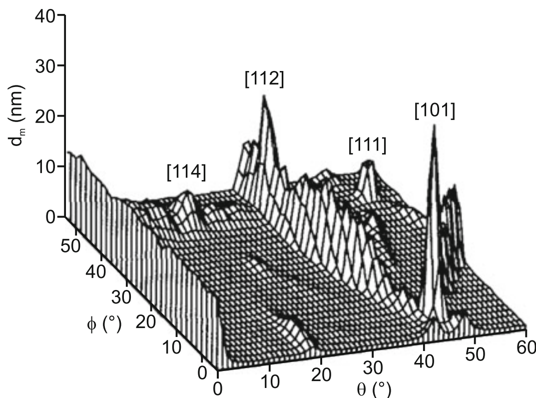

Fig. 4.9. Simulated mean path length as a function of implantation direction (azimuthal angle ϕ and polar angle θ) near [001] for 5 keV boron in silicon. The [001] channeling peak appears as a ridge at the *left side* of the plot ($\theta = 0$, any value of ϕ). Adapted from [196]

4.2.5 Large Concentration Effects

Lattice Constant

At high doping concentration, a noticeable effect on the lattice constant a_0 is found. For silicon the atom density[7] is $N_{\mathrm{Si}} = 5 \times 10^{22}\,\mathrm{cm}^{-3}$. A doping level of $N = 10^{19}\,\mathrm{cm}^{-3}$ corresponds thus to a dopant fraction of 0.02%. Such crystal could also be considered a very dilute alloy. About each $(N_{\mathrm{Si}}/N)^{1/3} \approx 17$-th atom in a given direction is a dopant.

The effect of high doping on the lattice constant is due to different ionic radius of the dopant and the hydrostatic deformation potential of the band edge occupied by the free carriers [201]. In a linear approach, the effect is summarized in the coefficient β via

$$\beta = \frac{1}{N} \frac{\Delta a_0}{a_0} \,. \tag{4.21}$$

The effect due to charge carriers on β is negative (positive) for p-doping (n-doping). Experimental data for Si, Ge, GaAs and GaP are compiled in [202, 203] and theoretically discussed. The effect is in the order of $\beta = \pm(1$–$10) \times 10^{-24}\,\mathrm{cm}^3$. For example, in the case of Si:B, the shrinkage of the lattice constant is mostly due to the charge carrier effect, for Si:P both effects almost cancel. In [204] it is shown that boron incorporation in silicon changes the lattice constant in various directions quite differently, e.g. d_{333} is shrank by 0.4% for a doping level of $10^{19}\,\mathrm{cm}^{-3}$ while the {620} lattice constant remains constant.

[7] Eight atoms per cubic unit cell of length $a_0 = 0.543\,\mathrm{nm}$.

Clustering

Typically a random distribution of dopants in the host is assumed (cmp. Sect. 3.7.1 on random alloys). The introduction of several impurities can lead to pairing effects, e.g. described for Se and B, Ga, Al or In in silicon [205]. A high concentration of a single impurity makes the existence of clusters, i.e. two or more neighboring dopant atoms, more probable. This effect has been extensively studied for B in Si [206], showing that several boron atoms with interstitials I form thermodynamically stable clusters, e.g. B_3I_2. This cluster forms from B_2I and BI with only 0.2 eV activation barrier [207] as shown in Fig. 4.10. The formation is limited by diffusion of the smaller clusters to the same site. The number of free carriers (here holes) released from such cluster is smaller than the number of boron atoms since it forms a deep acceptor [206]. This autocompensation mechanism is thus limiting the maximum achievable free carrier concentration due to doping and is technologically unfavorable. Reactions between boron atoms and silicon self-interstitials often lead to boron clustering in the peak region of an implantation profile and require detailed optimization of the annealing process [208].

Solubility Limit

The steady-state impurity solubility can be defined as the maximum concentration of impurity atoms in a crystal allowing thermodynamic balance between the crystal and another phase, e.g. a liquid phase, an extended defect or a precipitate. Precipitates are small inclusions of a second phase in a crystal, exhibiting a high concentration of 'gathered' impurities that cannot be solved in the crystal. Solubility limits for impurities in silicon have

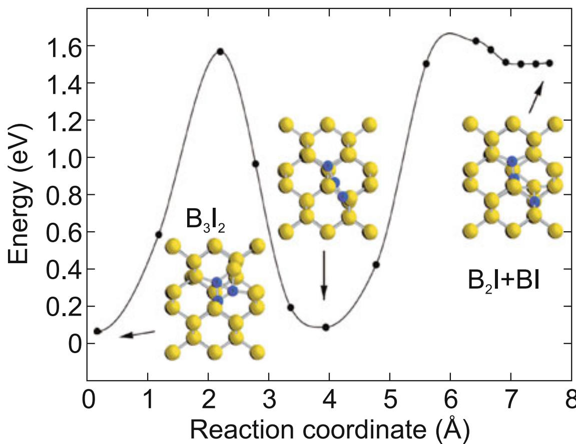

Fig. 4.10. Minimum energy path for the breakup of a B_3I_2 cluster into B_2I and BI. Silicon (boron) atoms are shown as *yellow* (*blue*) *spheres*. Adapted from [207]

Table 4.3. Maximum solubility N_s of some impurities creating shallow levels in silicon. Data for B, P, As, Sb from [215], other data from [212]

impurity	N_s (10^{20} cm^{-3})
B	4
P	5
As	4
Sb	0.7
Al	0.13
Cu	1.4×10^{-2}
Au	1.2×10^{-3}
Fe	3×10^{-4}

been first determined in [209] with a bulk of subsequent research [210] due to its practical relevance in device fabrication. The solubility limit for a few impurities in silicon are listed in Table 4.3. The temperature dependence is depicted in Fig. 4.11a. The solubility depends also on the present strain [211]. The simple empirical relation $x_s = 0.1\,k$ (Fig. 4.11b) between the maximum molar solubility x_s and the distribution coefficient k in silicon and germanium has been pointed out in [212].

A typical example for the formation of precipitates is Fe in InP, used for compensation of shallow donors in order to produce semi-insulating material (Sect. 7.7.8). The solubility of Fe in InP is fairly low, about $10^{17}\,\mathrm{cm}^{-3}$ at growth temperature [213]. In Fig. 4.12 a high-resolution TEM image of a

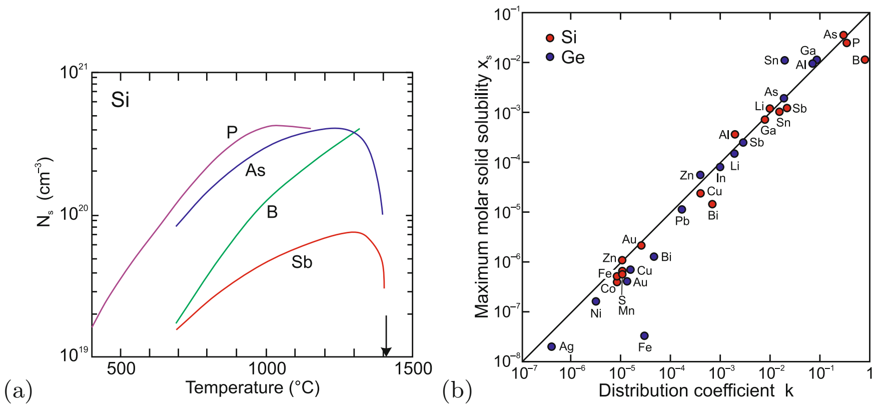

Fig. 4.11. (**a**) Steady-state solubility of impurities (P, As, B and Sb as labeled) in silicon. *Solid lines* are theoretical model matching various experimental data. *Arrow* denotes the melting point of silicon (1410°). Adapted from [210]. (**b**) Maximum molar solid solubility x_s vs. the distribution coefficient for various impurities in crystalline silicon and germanium. *Solid line* follows $x_s = 0.1\,k$. Adapted from [212]

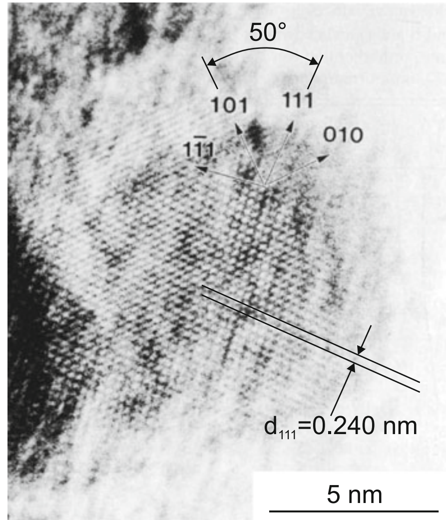

Fig. 4.12. High resolution TEM image of a FeP precipitate in iron-doped InP. Adapted from [214]

precipitate in InP doped with $3 \times 10^{18}\,\mathrm{cm}^{-3}$ Fe is shown. The precipitate exhibits a lattice constant of $d_{111} = 0.240\,\mathrm{nm}$ in [111]-direction, much different from that of InP ($d_{111}^{\mathrm{InP}} = 0.339\,\mathrm{nm}$). The angle between the [101] and [111] direction is 50° instead of 35° for InP. This is consistent with orthorhombic FeP [214]. Typically FeP and FeP_2 precipitates are found in highly Fe-doped InP [215].

4.3 Dislocations

Dislocations are line defects along which the crystal lattice is shifted by a certain amount. The vector along the dislocation line is called line vector **L**. A closed path around the dislocation core differs from that in an ideal crystal. The difference vector is called the Burger's vector **b**. Dislocation for which the Burger's vector is a vector of the lattice are called *full* dislocations. In contrast, dislocations with Burger's vectors that are not translation vectors of the lattice are called *partial* dislocations. The history of dislocation theory is described in [216].

Since the energy of a dislocation is proportional to $\mathbf{b}^2$, only dislocations with the shortest Burger's vector are stable. The plane spanned by **L** and **b** is called the *glide* plane. In Fig. 4.13 a high-resolution image of the atoms around a dislocation and the phase and amplitude of the (111) reflection are shown. The phase corresponds to the atomic columns, the amplitude to the displacement of the atoms at the dislocation core (see also Fig. 5.21).

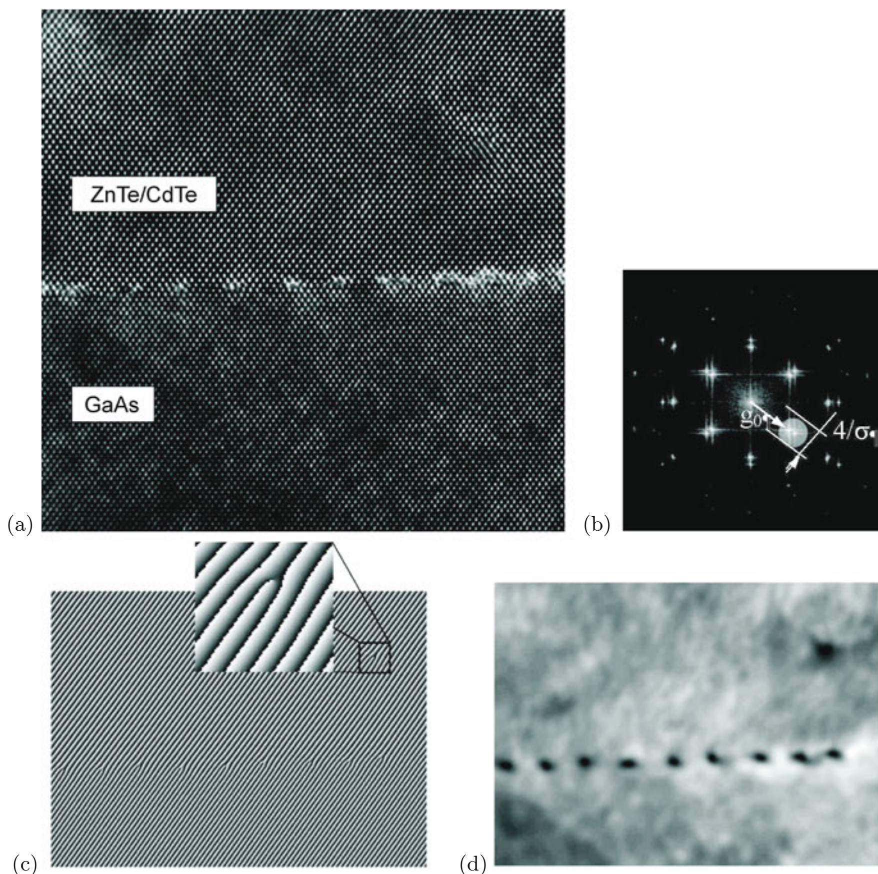

Fig. 4.13. (**a**) High-resolution transmission electron microscopy image (HRTEM) in the $\langle 110 \rangle$ projection of a network of misfit dislocations at a GaAs/CdTe/ZnTe interface. Substrate: GaAs (001), 2° off $\langle 110 \rangle$, ZnTe buffer layer is 2 monolayers thick. (**b**) Fourier transform with round mask around the (111) Bragg reflection. (**c**) Phase and (**d**) amplitude images for the mask from (**b**). From [217]

4.3.1 Dislocation Types

Edge Dislocations

For an *edge* dislocation (Fig. 4.14a) $\mathbf{b}$ and $\mathbf{L}$ are perpendicular to each other. An extra half-plane spanned by $\mathbf{L}$ and $\mathbf{b} \times \mathbf{L}$ is inserted.

Screw Dislocations

For a *screw* dislocation (Fig. 4.14b) $\mathbf{b}$ and $\mathbf{L}$ are collinear. The solid has been cut along a half-plane up to the dislocation line, shifted along $\mathbf{L}$ by the amount $\mathbf{b}$ and reattached.

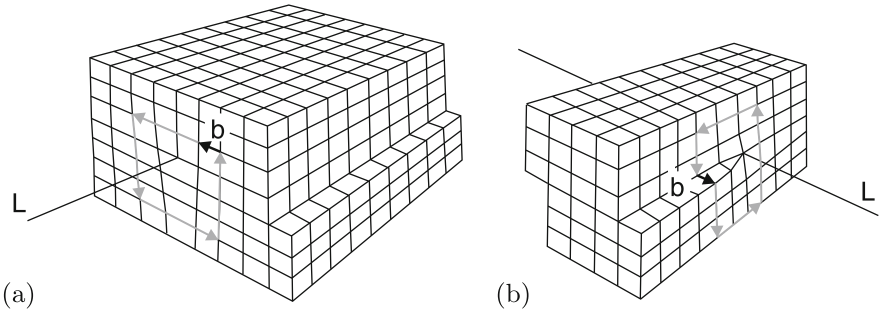

Fig. 4.14. Model of (**a**) an edge and (**b**) a screw dislocation. The line vector **L** and the Burger's vector **b** are indicated

Around the intersection of a screw dislocation with a surface, the epitaxial growth occurs, typically in the form of a growth spiral that images the lattice planes around the defect (Fig. 4.15).

60° Dislocations

The most important dislocations in the zincblende lattice (Fig. 4.16) have the line vector along $\langle 110 \rangle$. With the Burger's vector $a/2\ \langle 110 \rangle$ three different types of dislocations can be formed: edge, screw and 60° dislocations. The

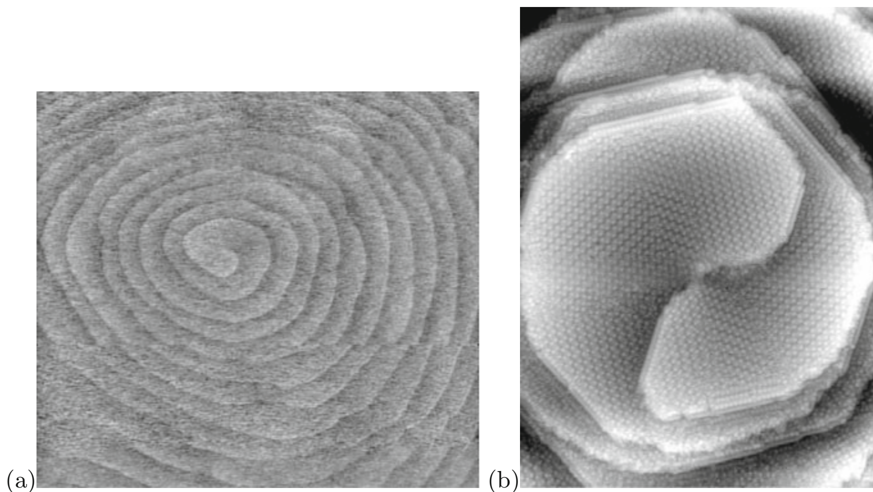

Fig. 4.15. (**a**) Atomic force microscopy image of growth spiral around a screw dislocation on a silicon surface; image width: 4 µm. (**b**) STM image (width: 75 nm) of a screw-type dislocation with a Burgers vector of [000-1] on the N-face of GaN. The reconstruction is c(6×12). The c(6×12) row directions correspond to $\langle \bar{1}100 \rangle$. Reprinted with permission from [218], ©1998 AVS

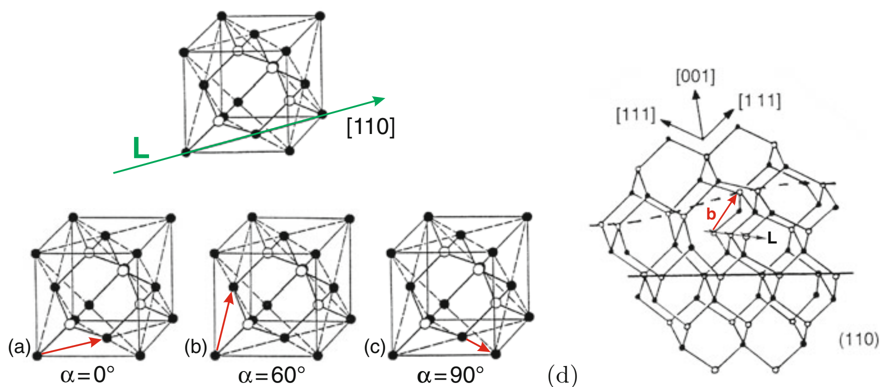

Fig. 4.16. Dislocations in the zincblende structure. The line vector is along [100]. The Burger's vector $a/2\,\langle 110\rangle$ can create an (**a**) edge dislocation, a (**b**) screw dislocation, and (**c**) a 60° dislocation. (**d**) Atomistic structure of a 60° dislocation

vicinity of the core of the latter is shown in more detail in Fig. 4.16d. We note that the atomistic structure of 60° dislocations is different for **L** along [110] and [−1 10]; depending on whether the cation or anion are in the core, they are labeled α or β dislocations.

Misfit Dislocations

When materials with different lattice constants are grown on top of each other, the strain can plastically relax via the formation of misfit dislocations. A typical network of such dislocations is shown in Fig. 4.17 for SiGe on Si.

Partial Dislocations

Partial dislocations, i.e. the Burger's vector is not a lattice vector, must necessarily border a two-dimensional defect, usually a stacking fault (Sect. 4.4.2). A typical partial dislocation in diamond or zincblende material is the Shockley partial dislocation (or just Shockley partial) with Burger's vector $b = (a_0/6)\,\langle 112\rangle$. Another important partial is the Frank partial with $b = (a_0/3)\,\langle 111\rangle$. A perfect dislocation can be dissociated into two partials. This is energetically favorable. As an example we consider the reaction (Fig. 4.18a)

$$\frac{1}{2}\,[\bar{1}01] \rightarrow \frac{1}{6}\,[\bar{1}\bar{1}2] + \frac{1}{6}\,[\bar{2}11]\ . \tag{4.22}$$

The length of the full dislocation is $a_0/\sqrt{2}$. The length of the Shockley partial is $a_0/\sqrt{6}$. Thus the energy $E = G\,b^2$ of the full dislocation is $E_1 = Ga_0^2/2$ and the sum of the energies of the partials is smaller, $E_2 = 2Ga_0^2/6 = Ga_0^2/3$. In Fig. 4.18b a TEM image of a Ge/Si interface with a Shockley partial is shown.

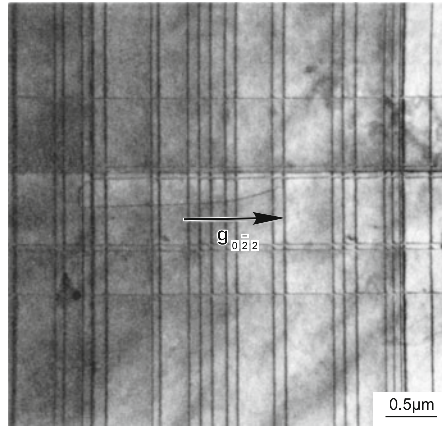

Fig. 4.17. Plan-view transmission electron microscopy image of a network of ⟨110⟩ dislocation lines in InGaAs on InP (001) with a lattice mismatch of about 0.1%. The TEM diffraction vector is $\mathbf{g} = [2\bar{2}0]$. Adapted from [219]

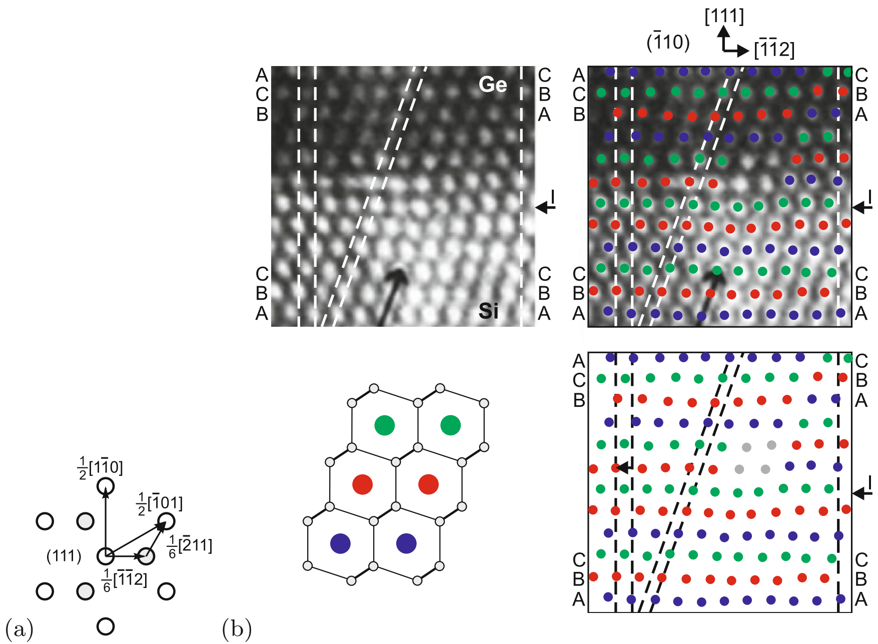

Fig. 4.18. (**a**) Graphical representation of the dislocation reaction of (4.22). (**b**) TEM image of the interface of a Ge/Si heterostructure with a $[\bar{2}11]/6$ Shockley partial dislocation. The image is overlayed with empty rod positions (as schematically shown in the *lower left* part of the figure) colored according to the stacking position (A: *blue*, B: *red*, C: *green*). The *arrows* labeled 'I' denote the position of the interface. Based on [221].

4.3.2 Visualization of Dislocations by Etching

Defects can be made visible using etching techniques. This is particularly popular for finding dislocations. Many etches are anisotropic, i.e. the etch velocity varies for different crystal directions. As an example the result of etching a silicon sphere in molten KOH and a germanium sphere in a HNO_3/HF solution are shown in Fig. 4.19. The remaining bodies exhibit those planes with low etching velocity. The etch velocity of various etch solutions has been investigated in detail in particular for silicon (Fig. 4.20).

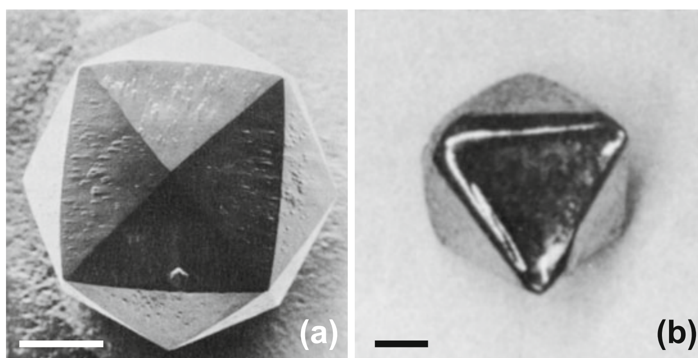

Fig. 4.19. (**a**) Resulting shape of Si sphere ('Lösungskörper') after 3 h at 100°C in molten KOH. (**b**) Resulting shape of Ge sphere after etching in HNO_3:HF:CH_3COOH, 35:30:35 weight percent. The octaedric form indicates {111} faces. Markers are 1 mm. Adapted from [222]

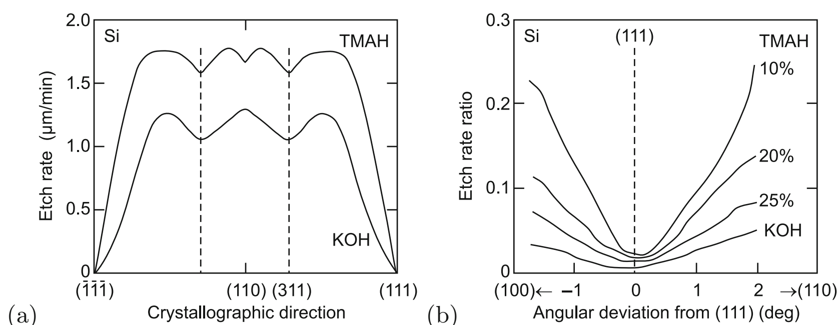

Fig. 4.20. (**a**) Etch rate of silicon for tetramethyl-ammonium-hydroxide (TMAH) water solution (25%) at 86°C and 40% KOH at 70°C as a function of crystallographic direction. (**b**) Detail of the anisotropy around the (111) direction for TMAH solutions with three different concentrations and 40% KOH, all at 86°C. Adapted from [223]

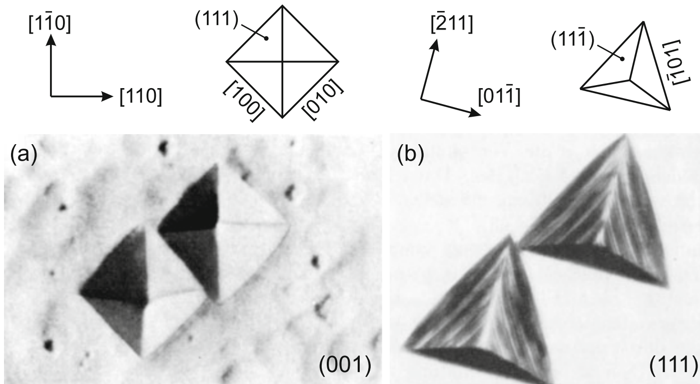

Fig. 4.21. Etch pits on germanium with (**a**) (001) and (**b**) (111) surface orientation. In both cases {111} facets are prepared by the etch. As etch in (**b**) a HNO_3/HF/CH_3COOH solution with $AgNO_3$ additive has been used. Width of the triangular etch pits is about 100 µm. Adapted from [224]

In a planar geometry, etch pits indicate the presence of dislocations, as shown in Fig. 4.21 for Ge of different orientation. The anisotropic etch prepares {111} planes. The dislocation core is at the intersection of the planes. In Fig. 4.22 hexagonal etch pits stretched along [1$\bar{1}$0] are developed by molten KOH [220]. The sides of the base are along [110], ⟨130⟩ and ⟨310⟩. The depth and width of the pits increases with increasing etching time. On the (00$\bar{1}$) surface, the orientation of the pits is rotated by 90° because of the polar [111]-axis of the zincblende structure [220]. Such etch pit develops at a dislocation

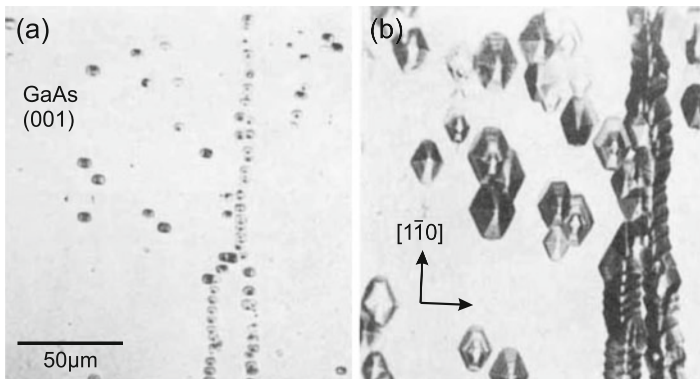

Fig. 4.22. Etch pits on GaAs (001) after (**a**) 3 min and (**b**) 10 min etch time in molten KOH at 300°C. Adapted from [220]

with Burger's vector $a/2\,[011]$ (inclined to the (001) surface) [225]. Other types of etch pits indicate dislocations with other Burger's vectors [225, 226]. Recipes how to wet chemically etch various semiconductors can be found in [222, 224, 227, 228]. Other etching techniques include dry processes such as plasma etching or reactive ion etching (RIE) [229–231].

4.3.3 Impurity Hardening

It has been found that the addition of impurities can lead to a substantial reduction of the dislocation density. This effect is known as impurity hardening and is caused by a hardening of the lattice due to an increase of the so-called critical resolved shear stress [232]. In Fig. 4.23 the dependence of the dislocation density in GaAs and InP is shown as a function of the carrier density that is induced by the incorporation of (electrically active) group-II or group-VI atoms (acceptors or donors, cf. Sect. 7.5). The high carrier concentration is unwanted when semi-insulating substrates (cf. Sect. 7.7.8) or low optical absorption (cf. Sect. 9.7) are needed. Thus the incorporation of isovalent impurities, such as In, Ga or Sb in GaAs and Sb, Ga or As in InP, has been investigated and found to be remarkably effective. Material containing such impurities in high concentration ($> 10^{19}\,\mathrm{cm}^{-3}$) must be considered a low-concentration alloy. The lattice constant is thus slightly changed, which can cause problems in the subsequent (lattice-mismatched) epitaxy of pure layers.

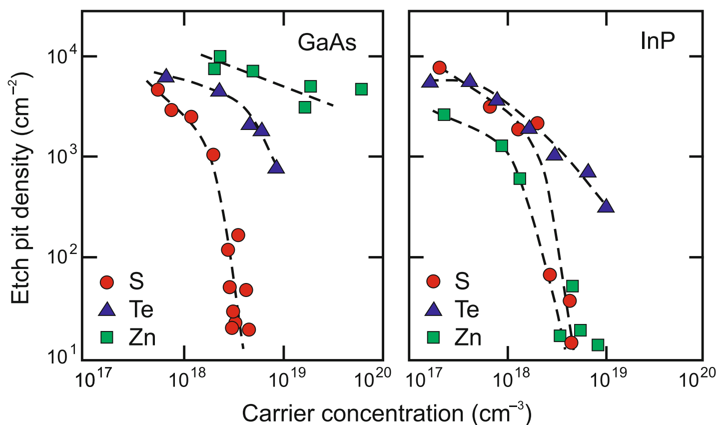

Fig. 4.23. Dislocation density (as revealed by etch pits) for GaAs and InP as a function of the carrier concentration for various concentrations of impurities (S, Te, and Zn). Adapted from [233].

4.4 Extended Defects

4.4.1 Micro-cracks

If the stress in a material becomes too big to be accommodated by dislocations, cracks may form to release strain energy.[8] In Fig. 4.24 an example is shown. In this case, micro-cracks have formed in a bulk mercury indium telluride crystal upon incorporation of residual stress and thermal stress during cooling of the material from growth temperature (about 1000 K) to room temperature. See also Fig. 11.10 for micro-cracks in an epitaxial layer.

4.4.2 Stacking Faults

The ideal stacking of (111) planes in the zincblende structure, ABCABC..., can be disturbed in various ways and creates area defects. If one plane is missing, i.e. the stacking is ABC*AC*ABC, an *intrinsic* stacking fault is present. If an additional plane is present, the defect is called an *extrinsic* stacking fault, i.e. ABCAB*A*CABC. An extended stacking fault in which the order of stacking is reversed is called a twin lamella, e.g. ABCABC*BACB*ABCABC. If two regions have inverted stacking order they are called twins and their joint interface is called a twin boundary, e.g. ...ABCABCAB*C*BACBACBA... (Fig. 4.27). The various types of stacking faults are shown in Fig. 4.25. In Fig. 4.26 a cross-sectional image of stacking faults in GaAs on Si is shown. They block each other and thus partially annihilate with increasing thickness.

A stacking fault is bounded by two partial dislocations (Sect. 4.3.1) formed by the dissociation of a perfect dislocation. A full (or *perfect*) dislocation with

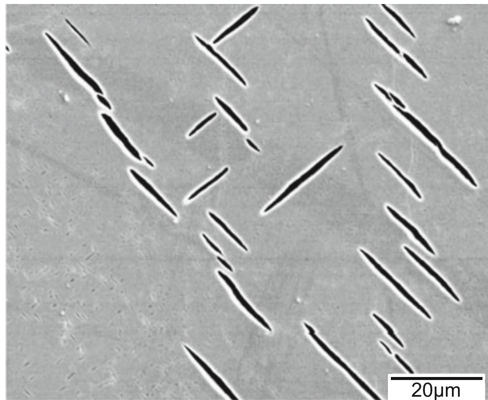

Fig. 4.24. Micro-cracks in a mercury indium telluride crystal. Adapted from [234]

[8]We note that in elasticity theory a *continuous* deformation is assumed. Obviously the separation (fracture) into two unstrained blocks is the lowest strain energy state of a stressed piece of material.

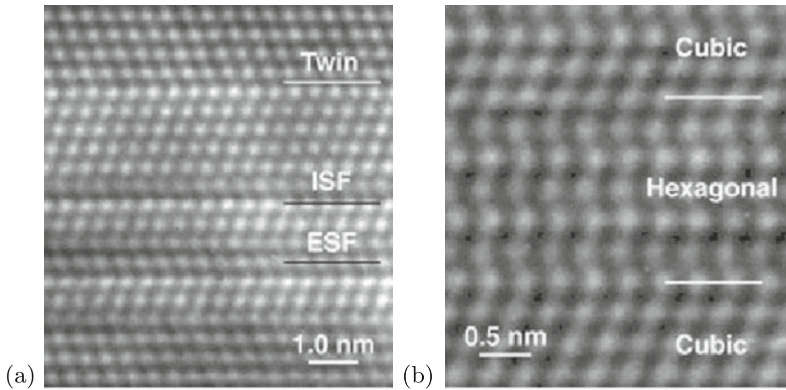

Fig. 4.25. HRTEM images of (**a**) thin-film silicon with intrinsic (labeled 'ISF') and extrinsic ('ESF') stacking faults and twin boundary ('Twin'). (**b**) Six monolayer thick hexagonal (wurtzite) CdTe layer in cubic (zincblende) CdTe. Stacking order (from *bottom to top*) is: ABCABABABABC... Reprinted with permission from [242]

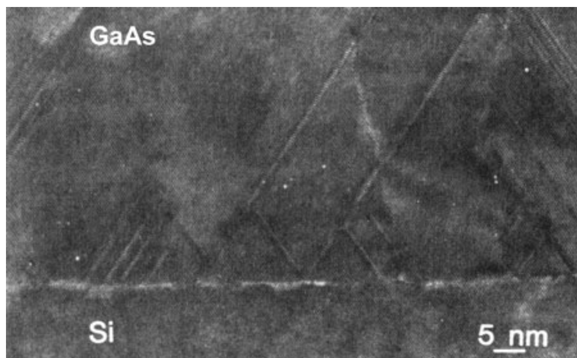

Fig. 4.26. Cross-sectional TEM image showing stacking faults in heteroepitaxial GaAs on Si. Adapted from [243]

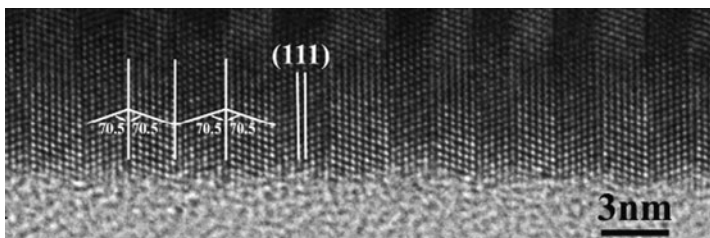

Fig. 4.27. High resolution TEM image of ZnS nanowire exhibiting periodical twin structures. Adapted from [244]

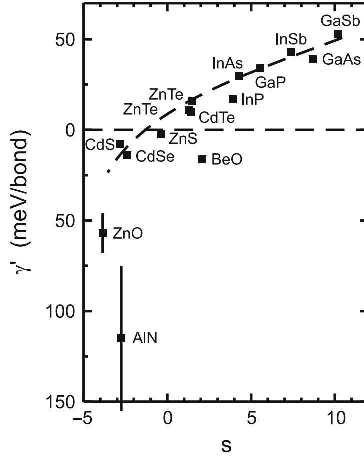

Fig. 4.28. Reduced stacking fault energy (stacking fault energy per bond) γ' for various compound semiconductors plotted as a function of the s-parameter. *Dashed line* is guide to the eye. Data from [111]

Burger's vector $a/2[110]$ in a III–V compound is dissociated into two Shockley partials according to (4.22) [235]. Since the dislocation energy is proportional to $|\mathbf{b}|^2$, the dissociation is energetically favored (see Sect. 4.3.1).

The stacking-fault energy in pure silicon is $\gamma = 47\,\mathrm{mJ\,m^{-2}}$ [236]. A similar value is found for Ge, $\gamma = 60\,\mathrm{mJ\,m^{-2}}$ [237] and undoped GaAs, $\gamma = 45\,\mathrm{mJ\,m^{-2}}$ [238]. In diamond a much larger value is found, $\gamma = 285\,\mathrm{mJ\,m^{-2}}$ [239]. Impurity incorporation typically reduces the stacking fault energy. The systematics of stacking fault energy for various III–V and II–VI compounds has been discussed [111, 240, 241]. It can be correlated with the s-parameter (2.11) as depicted in Fig. 4.28.

4.4.3 Grain Boundaries

The boundaries of crystal grains are called *grain boundaries*. They are defined by five parameters, three rotation angles (e.g. Euler angles) to describe how the orientation of grain II results from grain I and two parameters to define the boundary plane of the two grains in the coordinate system of reference grain I.

Such defects can have a large impact on the electric properties. They can act as barriers for transport or as carrier sinks. Details of their structure and properties can be found in [245, 246]. The two crystal grains meet each other with a relative tilt and/or twist. The situation is shown schematically in Fig. 4.29a for a small angle between the two crystals. A periodic pattern of dislocations forms at the interface that is called a small-angle grain boundary (SAGB) (Fig. 4.29b). In Fig. 4.30, experimental results for pure tilt SAGB are shown. The dislocation spacing is inversely proportional to the tilt angle θ. An image of a twist SAGB is shown in Fig. 4.31.

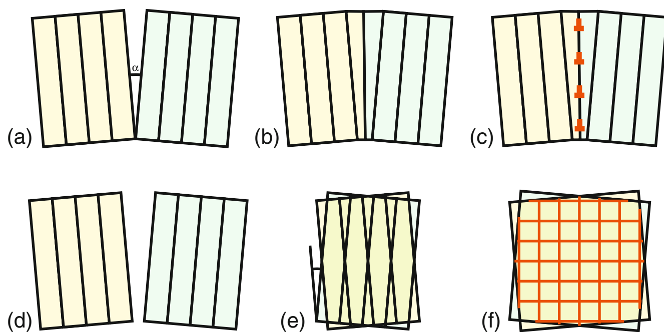

Fig. 4.29. Schemes of (**a**,**b**,**c**) pure tilt and (**d**,**e**,**f**) pure twist boundary, dislocation formation in (**c**) pure tilt and (**f**) twist boundaries

Fig. 4.30. (**a**) Scheme of a small-angle (pure tilt) grain boundary. (**b**) Model of edge dislocations in a {110} plane in Ge. (**c**) Relation of dislocation distance d and tilt angle θ for various small-angle grain boundaries in Ge. *Solid line* is relation $d = 4.0 \times 10^{-8}/\theta$. (**d**) Optical image of an etched (CP–4 etch) Ge sample with a small-angle grain boundary. Adapted from [249]. (**e**) HRTEM image of a small-angle grain boundary in Si with dislocations highlighted. From [250]

Fig. 4.31. Bright-field TEM image of pure twist boundary with network of pure twist dislocations fabricated by wafer bonding of two Si (001) surfaces with a relative twist. Adapted from [251]

Special large angle boundaries possess (for a certain angle) a *coincident site lattice* (CSL). Some of these grain boundaries have a low energy and are thus commonly observed. The ratio of lattice points of the CSL and the lattice unit cell is an odd integer number n; the corresponding grain boundary is then labeled Σn. SABG are also termed $\Sigma 1$. $\Sigma 3$ grain boundaries are always twin boundaries. An example with (111) grain boundary is schematically shown in an example in Fig. 4.32a. A $\Sigma 3$ (twin) boundary in silicon with $\{112\}$ grain boundary [247, 248] is depicted in Fig. 4.33 together with the atomic arrangement of the grain boundary itself. A $\Sigma 5$ (001) grain boundary is schematically shown in Fig. 4.32b; the special angle is $\theta = \arctan 3/4 \approx 36.87°$.

Real grain boundaries may not be flat, contain impurities or precipitates and even consist of a thin amorphous layer.

4.4.4 Antiphase and Inversion Domains

Antiphase domains occur when one part of the crystal is shifted with respect to another by an antiphase vector **p**. This does not form a twin. If the polar direction changes between two domains they are called inversion domains.

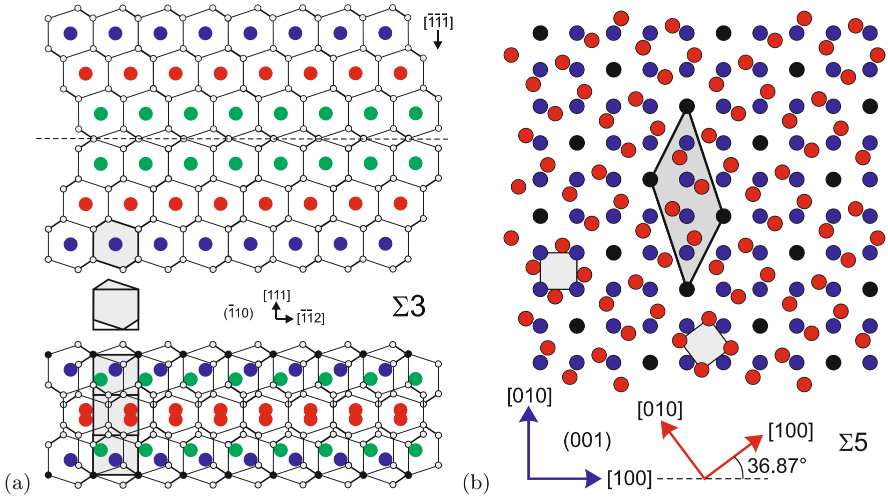

Fig. 4.32. (**a**) Schematic of $\Sigma 3\,(111)$ twin boundary in a diamond or zincblende structure (cmp. Fig. 4.27). The grain boundary is marked by a *dashed line* shown in side-view. The hexagonal and rectangular *grey boxes* have the same area. The lattice points of the coincident site lattice (CSL) are shown with *black circles* in the lower part of the figure. The unit cell of the CSL has three times the volume of the unit cell of the fcc lattice. (**b**) Schematic of a $\Sigma 5\,(001)$ grain boundary in a (simple) cubic crystal shown in plane-view. The *blue* and the *red* lattice are rotated by 36.86°, the lattice points of the CSL are shown in *black*. The unit cell of the CSL lattice (*dark grey*) has five times the volume of the cubic unit cell (*light grey*)

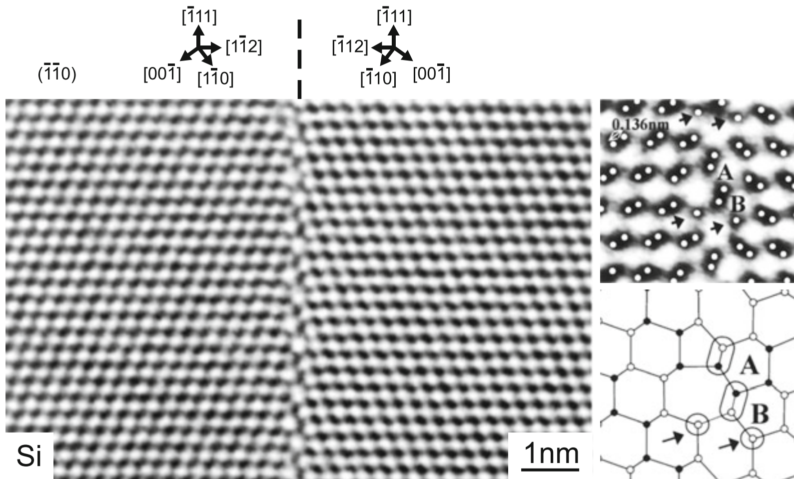

Fig. 4.33. TEM images in two magnifications of a $\Sigma 3\,\{112\}$ boundary in silicon together with a schematic of the atomic arrangement. Adapted from [248]

In the zincblende structure the [110] and $[\bar{1}10]$ directions are not equivalent. In one case there is a Zn-S lattice and in the other a S-Zn lattice. Both lattices vary by a 90° rotation or an inversion operation (which is not a symmetry operation of the zincblende crystal). If, e.g., a zincblende crystal is grown on a Si surface with monoatomic steps (Fig. 4.34), adjoint regions have a different phase; they are called antiphase domains (APD). The antiphase vector is $(0,0,1)a_0/4$. At the boundaries a two-dimensional defect, an antiphase domain boundary, develops. The APD boundary contains bonds between identical atom species. In Fig. 4.35, intertwinning APD boundaries are shown on the surface of InP layers on Si. The antiphase domains can be visualized with an anisotropic etch.

In Fig. 4.36a, inversion domains in iron-doped ZnO are shown. Between domains the direction of the c-axis is reversed. The iron is found preferentially in the inversion domain boundary (IDB) (Fig. 4.36b) and plays an important role in its formation [252].

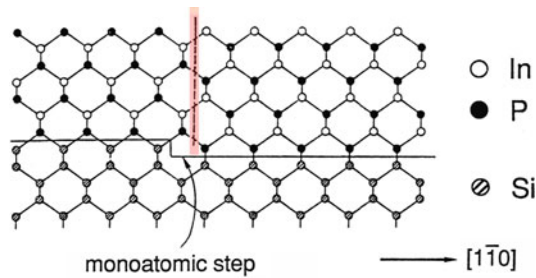

Fig. 4.34. Monoatomic step on the Si (001) surface and subsequent formation of an antiphase boundary in InP (zincblende)

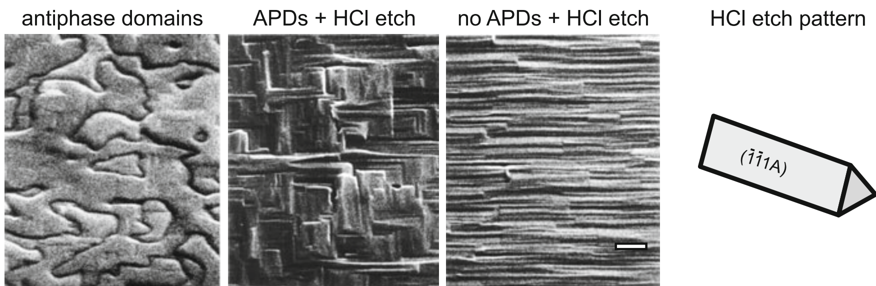

Fig. 4.35. Antiphase domains in InP on Si. HCl etchs InP anisotropically and prepares A planes. The etch patterns of layers with (without) APDs are crosshatched (linear). Adapted from [253]

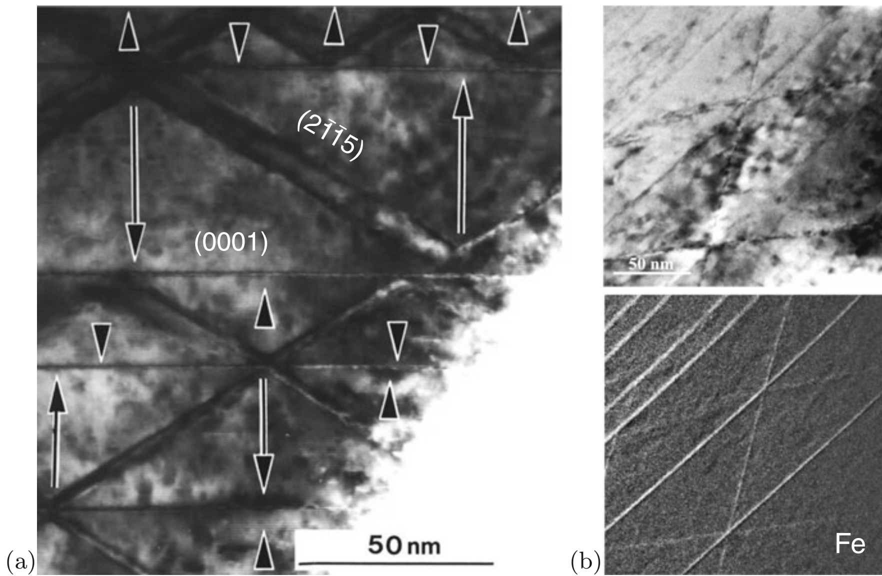

Fig. 4.36. Transmission electron microscopy of inversion domains in ZnO:Fe. (**a**) Inversion domains in iron-doped ZnO (ZnO:Fe_2O_3 =100:1). *Arrows* denote the orientation of the c-axis in the respective domains. (**b**) *Top*: bright field TEM, *bottom* Fe distribution from energy-filtered image. Adapted from [254]

4.5 Disorder

Disorder is a general term for deviations from the ideal structure on a microscopic scale. Examples are

- The presence of various isotopes of an element. This introduces disorder with regard to the mass of the atoms and impacts mostly phonon properties (see, e.g., Fig. 8.19).
- The occupation of lattice sites in alloys (Sect. 3.7) ranging from a random alloy, clustering to (partially) ordered phases.

5 Mechanical Properties

5.1 Introduction

The atoms making up the solid have an average position from which they can deviate since they are elastically bonded. The typical atomic interaction potential looks like the one shown in Fig. 2.1. The atoms thus perform a vibrational motion and the solid is elastic. The potential is essentially asymmetric, being steeper for small distances due to quantum-mechanical overlap of orbitals. However, for small amplitudes around the minimum a harmonic oscillator is assumed (harmonic approximation).

5.2 Lattice Vibrations

In the following we will discuss the dispersion relations for lattice vibrations, i.e. the connection between the frequency ν (or energy $h\nu = \hbar\omega$) of the wave and its wavelength λ (or k-vector $k = 2\pi/\lambda$). Acoustic and optical vibrations are introduced in one-dimensional models. A detailed treatment of the physics of lattice vibrations is given in [255].

5.2.1 Monoatomic Linear Chain

The essential physics of lattice vibrations can best be seen from a one-dimensional model that is called the linear chain. The mechanical vibrations will also be called *phonons*, although technically this term is reserved for the quantized lattice vibrations resulting from the quantum-mechanical treatment.

In the monoatomic linear chain the atoms of mass M are positioned along a line (x-axis) with a period (lattice constant) a at the positions $x_{n_0} = na$. This represents a one-dimensional Bravais lattice. The Brillouin zone of this system is $[-\pi/a, \pi/a]$.

The atoms will interact with a harmonic potential, i.e. the energy is proportional to the displacement $u_n = x_n - x_{n_0}$ to the second power. The total (mechanical) energy of the system is then:

$$U = \frac{1}{2} C \sum_n (u_n - u_{n+1})^2 \; . \tag{5.1}$$

M. Grundmann, *The Physics of Semiconductors*, 2nd ed., Graduate Texts in Physics, DOI 10.1007/978-3-642-13884-3_5,

© Springer-Verlag Berlin Heidelberg 2010

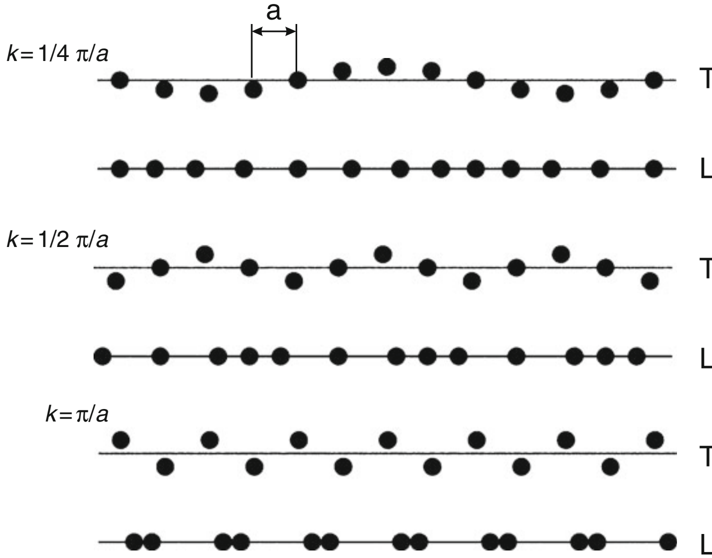

Fig. 5.1. Visualization of transverse ('T') and longitudinal ('L') waves in a linear monoatomic chain at different wavevectors

The model assumes that the mass points are connected via massless, ideal springs with a spring constant C. If $\phi(x)$ is the interaction energy between two atoms, C is given by $C = \phi''(a)$. Again, the harmonic approximation is only valid for small displacements, i.e. $u_n \ll a$. The displacement of the atoms can be along the chain (longitudinal wave) or perpendicular to the chain (transverse wave), see Fig. 5.1. We note that for these two types of waves the elastic constant C must not be the same.

When the sum in (5.1) has a finite number of terms ($n = 0, \ldots, N-1$), the boundary conditions have to be considered. There are typically two possibilities: The boundary atoms are fixed, i.e. $u_0 = u_{N-1} = 0$, the boundary conditions are periodic (Born–von Karman), i.e. $u_i = u_{N+i}$. If $N \gg 1$, the boundary conditions play no significant role anyway, thus those with the greatest ease for subsequent math are chosen. In solid-state physics typically periodic boundary conditions are used. Boundary phenomena, such as at surfaces, are then treated separately.

The equations of motion derived from (5.1) are

$$M\ddot{u}_n = F_n = -\frac{\partial U}{\partial u_n} = -C\left(2u_n - u_{n-1} - u_{n+1}\right) . \tag{5.2}$$

We solve for solutions that are periodic in time (harmonic waves), i.e. $u_n(x,t) = u_n \exp(-\mathrm{i}\omega t)$. Then the time derivative can be executed immediately as $\ddot{u}_n = -\omega^2 u_n$ and we obtain:

$$M\omega^2 \, u_n = C\left(2u_n - u_{n-1} - u_{n+1}\right) . \tag{5.3}$$

If, also, the solution is periodic in space, i.e. is a (one-dimensional) plane wave, i.e. $u_n(x,t) = v_0 \exp(\mathrm{i}(kx - \omega t))$ with $x = na$, we find from the periodic boundary condition $\exp(\mathrm{i}kNa) = 1$ and thus

$$k = \frac{2\pi}{a}\frac{n}{N},\ n \in \mathbf{N}\,. \tag{5.4}$$

It is important that, when k is altered by a reciprocal space vector, i.e. $k' = k + 2\pi n/a$, the displacements u_n are unaffected. This property means that there are only N values for k that generate independent solutions. These can be chosen as $k = -\pi/a, \ldots, \pi/a$, so that k lies in the Brillouin zone of the lattice. In the Brillouin zone there is a total number of N k values, i.e. one for each lattice point. The distance between adjacent k values is

$$\frac{2\pi}{Na} = \frac{2\pi}{L}\,, \tag{5.5}$$

L being the lateral extension of the system.

The displacements at the lattice points n and $n+m$ are now related to each other via

$$\begin{aligned} u_{n+m} &= v_0\, \exp(\mathrm{i}k(n+m)a) \\ &= v_0\, \exp(\mathrm{i}kna)\, \exp(\mathrm{i}kma) = \exp(\mathrm{i}kma)\, u_n\,. \end{aligned} \tag{5.6}$$

Thus, the equation of motion (5.3) reads

$$M\omega^2 u_n = C\,(2 - \exp(-\mathrm{i}ka) - \exp(\mathrm{i}ka))\, u_n\,. \tag{5.7}$$

Using the identity $\exp(\mathrm{i}ka)+\exp(-\mathrm{i}ka) = 2\cos(ka)$, we find the dispersion relation of the monoatomic linear chain (Fig. 5.2):

$$\omega^2(k) = \frac{4C}{M}\,\frac{1-\cos(ka)}{2} = \frac{4C}{M}\,\sin^2\left(\frac{ka}{2}\right)\,. \tag{5.8}$$

The solutions describe plane waves that propagate in the crystal with a phase velocity $c = \omega/k$ and a group velocity $v_g = \mathrm{d}\omega/\mathrm{d}k$

$$v_g = \sqrt{\frac{4C}{M}}\,\frac{a}{2}\,\cos\left(\frac{|k|a}{2}\right)\,. \tag{5.9}$$

In the vicinity of the Γ point, i.e. $k \ll \pi/a$ the dispersion relation is linear in k

$$\omega(k) = a\sqrt{\frac{C}{M}}\,|k|\,. \tag{5.10}$$

We are used to such linear relations for sound (and also light) waves. The phase and group velocity are the same and do not depend on k. Thus, such solutions are called *acoustic*. The sound velocity of the medium is given by $c_{\mathrm{s}} = a\sqrt{C/M}$.

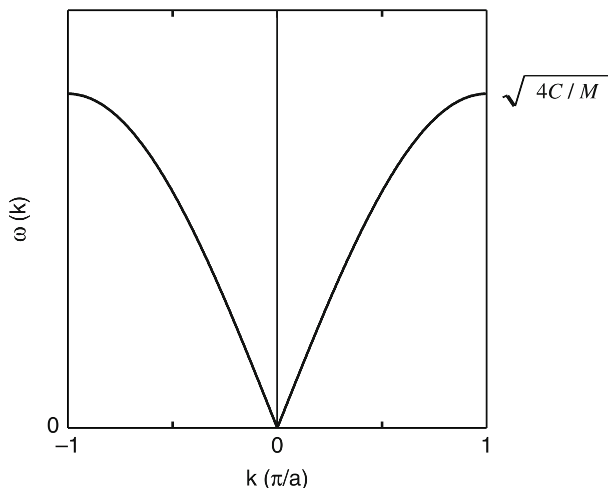

Fig. 5.2. Dispersion relation for a monoatomic linear chain

It is characteristic of the nonhomogeneous medium that, when k approaches the boundary of the Brillouin zone, the behavior of the wave is altered. For $k = \pi/a$ the wavelength is just $\lambda = 2\pi/k = 2a$, and thus samples the granularity of the medium. The maximum phonon frequency ω_m is

$$\omega_\mathrm{m} = \sqrt{\frac{4C}{M}} \; . \tag{5.11}$$

The group velocity is zero at the zone boundary, thus a standing wave is present.

Since the force constants of the longitudinal and transverse waves can be different, the dispersion relations are different. The transverse branch of the dispersion relation is 2-fold degenerate, unless the two directions that are perpendicular to x are not equivalent.

5.2.2 Diatomic Linear Chain

Now we consider the case that the system is made up from two different kinds of atoms (Fig. 5.3). This will be a model for semiconductors with a diatomic base, such as zincblende. We note that the diamond structure also needs to be modeled in this way, although both atoms in the base are the same.

The lattice will be the same and the lattice constant will be a. Alternating atoms of sort 1 and 2 with a relative distance of $a/2$ are on the chain. The displacements of the two atoms are labeled u_n^1 and u_n^2, both belonging to the lattice point n. The atoms have the masses M_1 and M_2. The force constants are C_1 (for the 1–2 bond within the base) and C_2 (for the 2–1 bond between different bases).

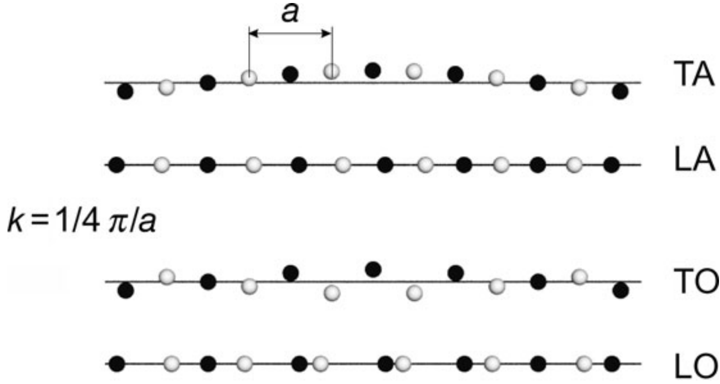

Fig. 5.3. Visualization of acoustic and optical waves in a diatomic linear chain

The total energy of the system is then given as

$$U = \frac{1}{2} C_1 \sum_n \left(u_n^1 - u_n^2\right)^2 + \frac{1}{2} C_2 \sum_n \left(u_n^2 - u_{n+1}^1\right)^2 \; . \tag{5.12}$$

The equations of motion are

$$M_1 \ddot{u}_n^1 = -C_1 \left(u_n^1 - u_n^2\right) - C_2 \left(u_n^1 - u_{n-1}^2\right) \tag{5.13a}$$
$$M_2 \ddot{u}_n^2 = -C_1 \left(u_n^2 - u_n^1\right) - C_2 \left(u_n^2 - u_{n+1}^1\right) \; . \tag{5.13b}$$

With the plane-wave ansatz $u_n^1(x,t) = v_1 \exp\left(\mathrm{i}(kna - \omega t)\right)$ and $u_n^2(x,t) = v_2 \exp\left(\mathrm{i}(kna - \omega t)\right)$ and periodic boundary conditions we find

$$0 = -M_1 \omega^2 v_1 + C_1 (v_1 - v_2) + C_2 (v_1 - v_2 \exp(-\mathrm{i}ka)) \tag{5.14a}$$
$$0 = -M_2 \omega^2 v_2 + C_1 (v_2 - v_1) + C_2 (v_2 - v_1 \exp(\mathrm{i}ka)) \; . \tag{5.14b}$$

These equations for v_1 and v_2 can only be solved nontrivially if the determinant vanishes, i.e.

$$\begin{aligned} 0 &= \begin{vmatrix} M_1 \omega^2 - (C_1 + C_2) & C_1 + \mathrm{e}^{-\mathrm{i}ka} C_2 \\ C_1 + \mathrm{e}^{\mathrm{i}ka} C_2 & M_2 \omega^2 - (C_1 + C_2) \end{vmatrix} \\ &= M_1 M_2 \omega^4 - (M_1 + M_2)(C_1 + C_2)\,\omega^2 + 2C_1 C_2 \left(1 - \cos(ka)\right) . \end{aligned} \tag{5.15}$$

Using the substitutions $C_+ = (C_1 + C_2)/2$, $C_\times = \sqrt{C_1 C_2}$, the arithmetic and geometrical averages, and accordingly for M_+ and $M_\times$, the solution is

$$\omega^2(k) = \frac{2C_\times}{\gamma M_\times} \left[1 \pm \sqrt{1 - \gamma^2 \frac{1 - \cos(ka)}{2}} \right] , \tag{5.16}$$

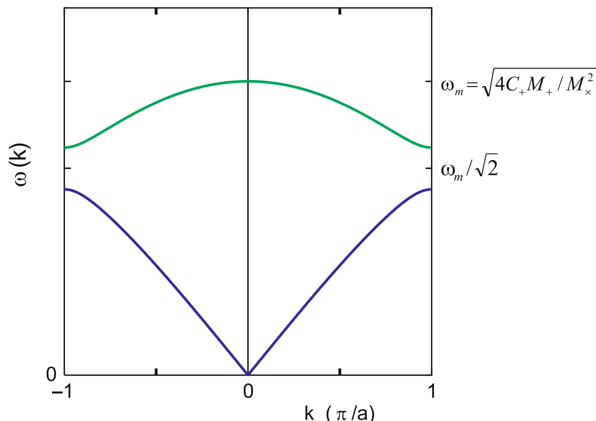

Fig. 5.4. Dispersion relation for a diatomic linear chain with acoustic (*blue*) and optical (*green*) branch

with

$$\gamma = \frac{C_\times M_\times}{C_+ M_+} \, . \tag{5.17}$$

The dispersion relation, as shown in Fig. 5.4, now has (for each longitudinal and transverse mode) two branches. The lower branch ('−' sign in (5.16)) is related to the acoustic mode; neighboring atoms have similar phase (Fig. 5.3). For the acoustic mode $\omega = 0$ at the Γ point and the frequency increases towards the zone boundary. The maximum phonon frequency ω_m is in the upper branch ('+' sign in (5.16)) at the zone center

$$\omega_\mathrm{m} = \sqrt{\frac{4C_\times}{\gamma M_\times}} = 2\sqrt{\frac{C_+ M_+}{M_\times^2}} \, . \tag{5.18}$$

The upper branch is called the optical mode (since it can interact strongly with light, see Sect. 9.8) and neighboring atoms have opposite phase. In the vicinity of the Γ point the dispersion of optical phonons is parabolic with negative curvature:

$$\omega(k) \cong \omega_\mathrm{m} \left[1 - \frac{1}{2} \left(\frac{\gamma a}{4} \right)^2 k^2 \right] \, . \tag{5.19}$$

Thus, four different vibrations exist that are labeled TA, LA, TO, and LO. Both the TA and TO branches are degenerate.

At the zone boundary (X point) a frequency gap exists. The gap center is at

$$\bar{\omega}_\mathrm{X} = \frac{\omega_\mathrm{m}}{\sqrt{2}} \, , \tag{5.20}$$

and the total width of the gap is

$$\Delta\omega_X = \omega_{\rm m}\sqrt{1-\gamma} = 2\sqrt{\frac{C_+ M_+ - C_\times M_\times}{M_\times^2}}\ . \tag{5.21}$$

The group velocity is zero for optical and acoustic phonons at $k = \pi/a$ and for optical phonons at the Γ point.

Usually two cases are treated explicitly: (i) atoms with equal mass ($M = M_1 = M_2$) and different force constants or (ii) atoms with unequal mass and identical force constants $C = C_1 = C_2$. For the case $C_1 = C_2$ and $M_1 = M_2$, $\gamma = 1$ and thus $\Delta\omega_X = 0$. Then the dispersion relation is the same as for the monoatomic chain, except that the k space has been folded since the actual lattice constant is now $a/2$.

$M_1 = M_2$

In this case, $M_+ = M_\times = M$ and the dispersion relation is

$$\omega^2 = \frac{2C_+}{M}\left[1 \pm \sqrt{1 - \frac{C_\times^2}{C_+^2}\frac{1-\cos(ka)}{2}}\,\right]\ . \tag{5.22}$$

At the zone boundary the frequencies for the acoustic and the optical branch are $\omega_{X,1} = \sqrt{2C_1/M}$ with $v_1 = v_2$ and $\omega_{X,2} = \sqrt{2C_2/M}$ with $v_1 = -v_2$, respectively (assuming $C_2 > C_1$). The motion for $k = \pi/a$ is phase shifted by 180° for adjacent bases. Additionally, for the acoustic branch the atoms of the base are in phase, while for the optical branch the atoms of the base are 180° out of phase. The vibration looks as if only one of the springs is strained.

$C_1 = C_2$

In this case, $C_+ = C_\times = C$ and the dispersion relation is

$$\omega^2 = \frac{2CM_+}{M_\times^2}\left[1 \pm \sqrt{1 - \frac{M_\times^2}{M_+^2}\frac{1-\cos(ka)}{2}}\,\right]\ . \tag{5.23}$$

At the zone boundary the frequencies for the acoustic and the optical branch are $\omega_{X,1} = \sqrt{2C/M_1}$ with $v_2 = 0$ and $\omega_{X,2} = \sqrt{2C/M_2}$ with $v_1 = 0$, respectively (assuming $M_2 < M_1$). In the vibration for $k = \pi/a$ thus only one atom species oscillates, the other does not move. Close to the Γ point the atoms are in phase in the acoustic branch, i.e. $v_1 = v_2$. For the optical branch, the frequency at the Γ point is given by $\omega = \sqrt{2C/M_{\rm r}}$ (with the reduced mass $M_{\rm r}^{-1} = M_1^{-1} + M_2^{-1} = 2M_+/M_\times^2$) and the amplitude ratio is given by the mass ratio: $v_2 = -(M_1/M_2)v_1$, i.e. the heavier atom has the smaller amplitude.

5.2.3 Lattice Vibrations of a Three-Dimensional Crystal

When calculations are executed for a three-dimensional crystal with a monoatomic base, there are $3N$ equations of motion. These are transformed to normal coordinates and represent 3 acoustic branches (1 LA phonon mode and 2 TA phonon modes) of the dispersion relation. In a crystal with a base with p atoms, there are also 3 acoustic branches and $3(p-1)$ optical branches. For a diatomic base (as in the zincblende structure) there are 3 optical phonon branches (1 LO phonon mode and 2 TO phonon modes). The total number of modes is $3p$. The dispersion $\omega(\mathbf{k})$ now has to be calculated for all *directions* of $\mathbf{k}$.

In Figs. 5.5 and 5.6, the phonon dispersion in silicon and GaAs is shown along particular lines in the Brillouin zone (cf. Fig. 3.32b). The main differences are: (i) the degeneracy of the acoustic and optical branch at the X point for the group-IV semiconductor is lifted for the III–V semiconductor due to the different mass of the constituents, (ii) the degeneracy of the LO and TO energies at the Γ point for the group-IV semiconductor is lifted for the III–V semiconductor due to the ionic character of the bond and the macroscopic electric field connected with the long-wavelength LO phonon (see Sect. 5.2.8).

We note that the degeneracy of the TA phonon is lifted for propagation along the $\langle 110 \rangle$ directions (Σ) because the two transverse directions $\langle 001 \rangle$ and $\langle 1\bar{1}0 \rangle$ are not equivalent.

In boron nitride the masses of the two constituents are so similar that no gap exists between acoustical and optical branches (Fig. 5.7). Also the

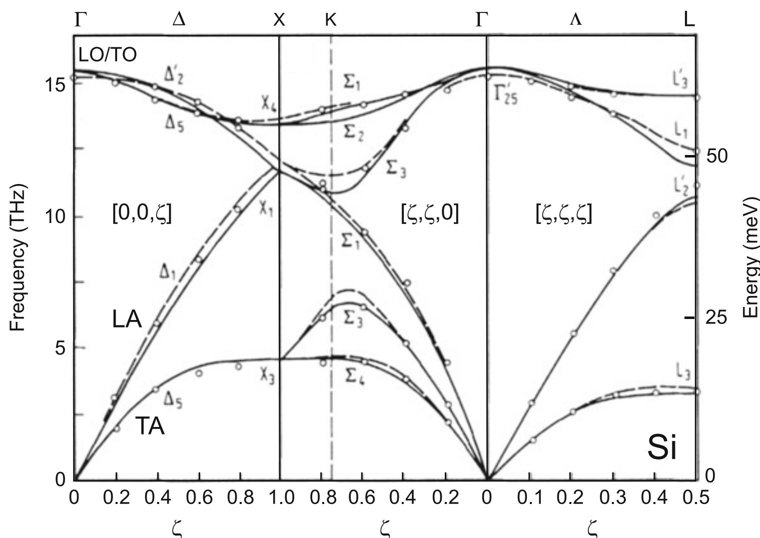

Fig. 5.5. Phonon dispersion in Si, experimental data and theory (*solid lines*: bond charge model, *dashed lines*: valence force field model). Adapted from [192]

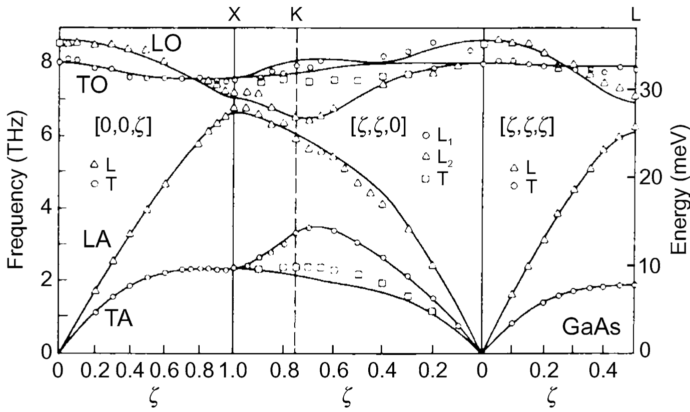

Fig. 5.6. Phonon dispersion in GaAs, experimental data and theory (*solid lines*, 14-parameter shell model). 'L' and 'T' refer to longitudinal and transverse modes, respectively. 'I' and 'II' (along $[\zeta,\zeta,0]$) are modes whose polarization is in the $(1,\bar{1},0)$ plane. Adapted from [256]

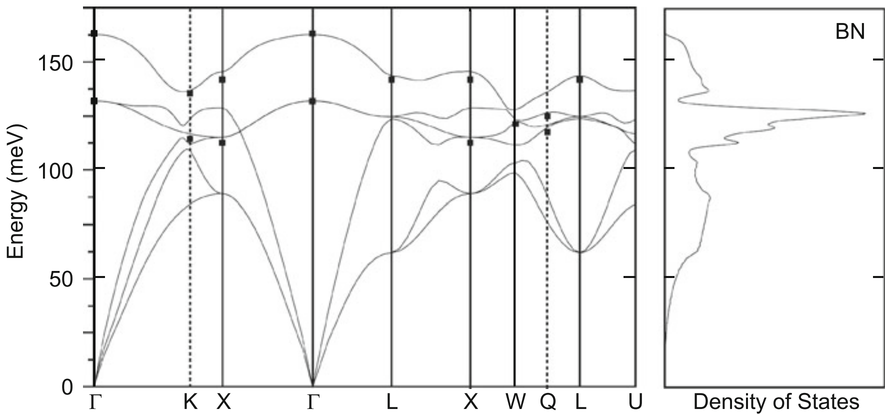

Fig. 5.7. Phonon dispersion in BN (*left panel*), experimental data (*symbols*) and theory (*solid lines*, first principles pseudopotential model). In the *right panel* the density of states is depicted. Adapted from [257]

density of states (averaged over the entire Brillouin zone) is depicted (see next Sect.).

The displacement of atoms is shown in Fig. 5.8 for the different phonon modes present in wurtzite crystals.

The dependence of the phonon frequency on the mass of the atoms ($\propto 1/\sqrt{M}$) can be demonstrated with the isotope effect, visualized for GaAs in Fig. 5.9. The dependence of the phonon frequencies on the stiffness of the

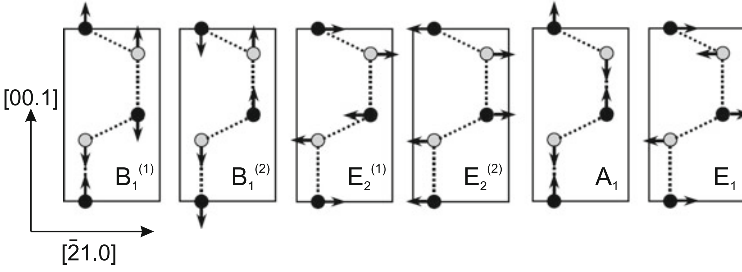

Fig. 5.8. Displacement of atoms for various phonon modes in wurtzite crystals. Adapted from [258]

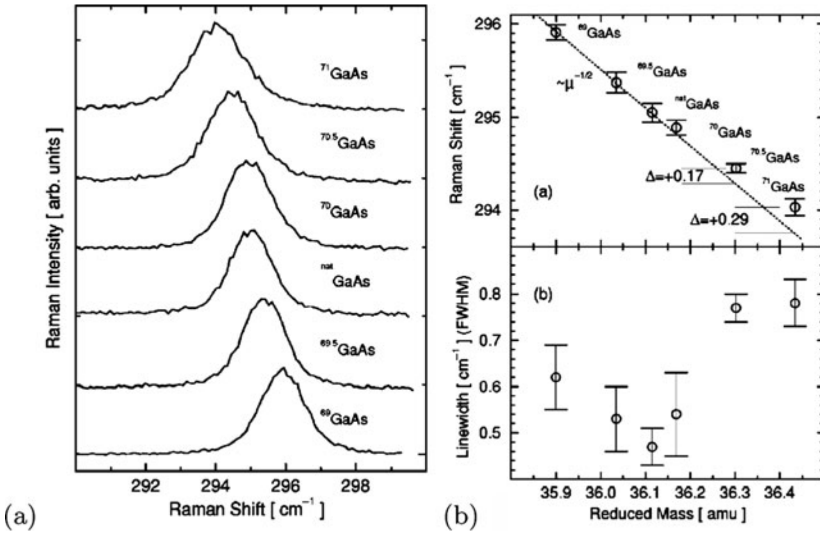

Fig. 5.9. (**a**) Raman spectra of GaAs with different isotope content as labeled. (**b**) Energy of optical phonons in GaAs with different isotope content [using the Raman spectra shown in (**a**)]. Reprinted with permission from [259], ©1999 APS

spring can be seen from Fig. 5.10; the smaller lattice constant provides the stiffer spring.

5.2.4 Density of States

The *density of states* (DOS) tells how many of the total $3pN$ modes are in a given energy interval. The states are spaced equally in **k**-space but not on the energy scale (see also Sect. 6.11). As a simple example, the number of states $N(E')$ from $E = 0$ up to $E = E'$ for the dispersion of the one-dimensional acoustic phonons (5.8) is given as

$$N(E') = k' \frac{N}{\pi/a} = \frac{L}{\pi} k' \; , \tag{5.24}$$

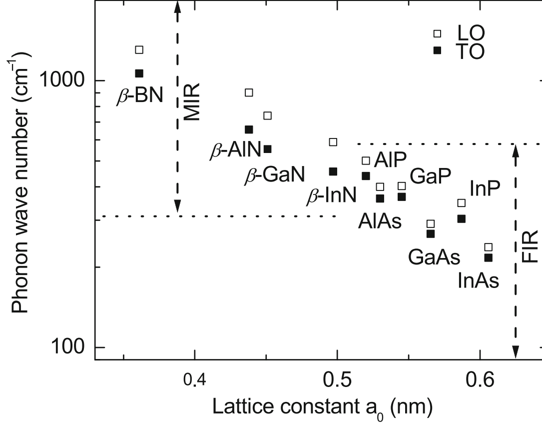

Fig. 5.10. Optical phonon frequencies (TO: *filled squares*, LO: *empty squares*) for a number of III–V compounds with different lattice constant a_0. 1 meV corresponds to 8.065 wave numbers (or cm^{-1}). Adapted from [260]

with the wave-vector k' fulfilling $E' = \hbar\omega(k')$. Using (5.8), we find for one polarization ($E_\mathrm{m} = \hbar\,\omega_\mathrm{m}$)

$$N(E) = \frac{2N}{\pi} \arcsin\left(\frac{E}{E_\mathrm{m}}\right) . \tag{5.25}$$

The DOS $D(E)$ is given by

$$D(E) = \frac{\mathrm{d}N(E)}{\mathrm{d}E} = \frac{2N}{\pi\,E_\mathrm{m}} \frac{1}{\sqrt{1-(E/E_\mathrm{m})^2}} . \tag{5.26}$$

Often the density of states is scaled by the (irrelevant) system size and given per atom (D/N) or per volume (D/L^3) (per length (D/L) in a one-dimensional system).

In a three-dimensional solid, (5.24) is modified to (for three degenerate polarizations)

$$N(E') = \frac{4\pi}{3} \frac{3}{(2\pi/L)^3} k'^3 , \tag{5.27}$$

taking into account all states within a sphere in **k**-space of radius k'. Assuming a linear dispersion $\omega = v_\mathrm{s}\,k$, we obtain

$$N(E) = \frac{V}{2\pi^2} \frac{E^3}{\hbar^3\,v_\mathrm{s}^3} . \tag{5.28}$$

This is also the base for Debye's law for the temperature dependence of the heat capacity.

5.2.5 Phonons

Phonons are the quantized quasi-particles of the lattice vibrations (normal modes). The energy of a phonon can take the discrete values of a harmonic oscillator

$$E_{ph} = \left(n + \frac{1}{2}\right) \hbar\omega \ , \tag{5.29}$$

where n denotes the quantum number of the state, which corresponds to the number of energy quanta $\hbar\omega$ in the vibration. The amplitude of the vibration can be connected to n via the following discussion. For the classical oscillation $u = u_0 \, \exp \mathrm{i}(kx - \omega t)$ the space and time average for the kinetic energy yields

$$E_{\rm kin} = \frac{1}{2} \rho V \overline{\left(\frac{\partial u}{\partial t}\right)^2} = \frac{1}{8} \rho V \omega^2 \, u_0^2 \ , \tag{5.30}$$

where ρ is the density and V the volume of the (homogeneous) solid. The energy of the oscillation is split in half between kinetic and potential energy. From $2E_{\rm kin} = E_{\rm ph}$ we find

$$u_0^2 = \left(n + \frac{1}{2}\right) \frac{4\hbar}{\rho V \omega} \ . \tag{5.31}$$

The number of phonons with which a vibrational mode is populated is thus directly related to the classical amplitude square.

Phonons act with a momentum $\hbar\mathbf{k}$, the so-called crystal momentum. When phonons are created, destroyed or scattered the crystal momentum is conserved, except for an arbitrary reciprocal-space vector $\mathbf{G}$. Scattering with $\mathbf{G} = 0$ is called a *normal* process, otherwise (for $\mathbf{G} \neq 0$) it is called an *umklapp* process.

5.2.6 Localized Vibrational Modes

A defect in the crystal can induce localized vibrational modes (LVM). The defect can be a mass defect, i.e. one of the masses M is replaced by $M_{\rm d}$, or the force constants in the neighborhood are modified to $C_{\rm d}$. A detailed treatment can be found in [261]. LVM are discussed, e.g., in [262–264].

First we consider the LVM for the one-dimensional, monoatomic chain. If the mass at lattice point $i = 0$ is replaced by $M_{\rm d} = M + \Delta M$ ($\epsilon_{\rm M} = \Delta M / M$), the displacements are given by $u_i = AK^{|i|}$, A being an amplitude, with

$$K = -\frac{1 + \epsilon_{\rm M}}{1 - \epsilon_{\rm M}} \ , \tag{5.32}$$

and the defect phonon frequency $\omega_{\rm d}$ is

$$\omega_{\rm d} = \omega_{\rm m} \sqrt{\frac{1}{1 - \epsilon_{\rm M}^2}} \ . \tag{5.33}$$

A real frequency is obtained for $|\epsilon_\mathrm{M}| < 1$. ω_d is then higher than the highest frequency of the bulk modes $\omega_\mathrm{m} = \sqrt{4C/M}$ (5.11). For $\epsilon_\mathrm{M} < 0$, i.e. the mass of the defect is smaller than the mass of the host atoms, K is negative and $|K| < 1$. Thus, the displacement can be written as

$$u_i \propto (-|K|)^{|i|} = (-1)^{|i|} \exp\left(+|i| \log|K|\right) . \tag{5.34}$$

The numerical value of the exponent is negative, thus the amplitude decreases exponentially from the defect and indeed makes a localized vibrational mode. For small mass $M_\mathrm{d} \ll M$ (5.33) yields approximately $\omega_\mathrm{d} = \sqrt{2C/M_\mathrm{d}}$. This approximation is the so-called one-oscillator model. Since typically the extension of the localized mode is only a few lattice constants, the picture of LVM remains correct for impurity concentrations up to $\sim 10^{18}$–$10^{20}\,\mathrm{cm}^{-3}$. For higher concentrations the concept of alloy modes has to be invoked (cf. Sect. 5.2.7).

For the case of group-III or -V substitutional impurities in group-IV semiconductors the change in force constants (treated below) can be neglected to some extent. For silicon ($M = 28$) and germanium ($M = 73$) the effect of various substitutions is shown in Fig. 5.11.

Now, additionally the force constants left and right of the defect are replaced by $C_\mathrm{d} = C + \Delta C$ ($\epsilon_\mathrm{C} = \Delta C/C$). The displacements are still given by $u_i = AK^{|i|}$, now with

$$K = -\frac{(1+\epsilon_\mathrm{M})\,(1+\epsilon_\mathrm{C})}{1-\epsilon_\mathrm{M}-2\epsilon_\mathrm{C}} . \tag{5.35}$$

An exponential decrease of the LVM amplitude occurs for negative K that is ensured for $\epsilon_\mathrm{M} + 2\epsilon_\mathrm{C} < 0$ (and $\epsilon_\mathrm{M} > -1$ and $\epsilon_\mathrm{C} > -1$). The defect

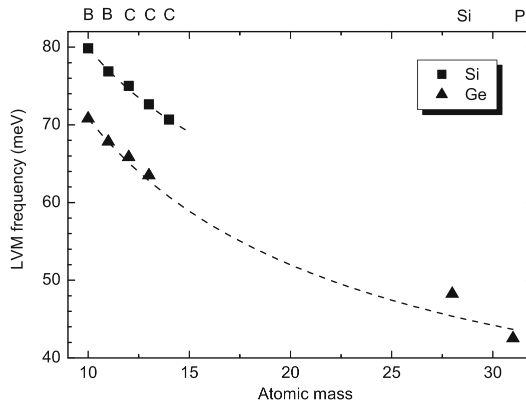

Fig. 5.11. Energy of local vibrational modes in Si and Ge. Experimental values at $T = 300\,\mathrm{K}$ (B in Ge: $T = 80\,\mathrm{K}$) taken from [261] and references therein and from [265] (C in Ge). The *dashed lines* are the mass dependence according to (5.33) scaled to the experimental frequency of the ^{10}B LVM

frequency is given by

$$\omega_\mathrm{d} = \omega_\mathrm{m} \sqrt{\frac{(1+\epsilon_\mathrm{C})\,(2+\epsilon_\mathrm{C}\,(3+\epsilon_\mathrm{M}))}{2(1+\epsilon_\mathrm{M})\,(2\epsilon_\mathrm{C}+1-\epsilon_\mathrm{M})}}\,. \tag{5.36}$$

We note that for $\epsilon_\mathrm{C} = 0$ (5.32) and (5.33) are recovered.

For a given mass defect, the change of frequency with ΔC is (in linear order, i.e. for $\epsilon_\mathrm{C} \ll 1$)

$$\frac{\partial \omega_\mathrm{d}(\epsilon_\mathrm{M}, \epsilon_\mathrm{C})}{\partial \epsilon_\mathrm{C}} = \frac{1 - 4\,\epsilon_\mathrm{M} - \epsilon_\mathrm{M}^2}{4(1-\epsilon_\mathrm{M})\,\sqrt{1-\epsilon_\mathrm{M}^2}}\,\epsilon_\mathrm{C}\,. \tag{5.37}$$

The linear coefficient diverges for $\epsilon_\mathrm{M} \to -1$. For ϵ_M between -0.968 and 0 the linear coefficient varies between 2 and 1/4. Therefore, a larger force constant ($\epsilon_\mathrm{C} > 0$) increases the LVM frequency of the defect, as expected for a stiffer spring.

In a binary compound the situation is more complicated. We assume here that the force constants remain the same and only the mass of the substitution atom M_d is different from the host. The host has the atom masses M_1 and M_2 with $M_1 < M_2$. Substitution of the heavy atom with a lighter one creates a LVM above the optical branch for $M_\mathrm{d} < M_2$. Additionally, a level in the gap between the optical and acoustic branch is induced. Such LVM is called a *gap mode*. Substitution of the lighter atom of the binary compound induces a LVM above the optical branch for $M_\mathrm{d} < M_1$. A gap mode is induced for $M_\mathrm{d} > M_1$. The situation for GaP is depicted in Fig. 5.12. LVM in GaAs have been reviewed in [262].

The energy position of a local vibrational mode is sensitive to the isotope mass of the surrounding atoms. In Fig. 5.13, a high-resolution ($0.03\,\mathrm{cm}^{-1}$) spectrum of the $^{12}\mathrm{C}_\mathrm{As}$ LVM in GaAs is shown together with a theoretical simulation. The various theoretical peak positions are given as vertical bars, their height indicating the oscillator strength. Five experimental peaks are obvious that are due to a total of nine different transitions. The C atom can experience five different surroundings (see Table 3.7) with the four neighbors being ^{69}Ga or ^{71}Ga. The natural isotope mix is an 'alloy' $^{69}\mathrm{Ga}_x{}^{71}\mathrm{Ga}_{1-x}\mathrm{As}$ with $x = 0.605$. The configurations with T_d symmetry contribute one peak each, the lowest (^{71}Ga surrounding) and highest (^{69}Ga surrounding) energy transitions. The configurations with C_{3v} and C_{2v} symmetry contribute each with 2 and 3 nondegenerate modes, respectively.

The vibrations of impurity complexes have been discussed in [267].

5.2.7 Phonons in Alloys

In an alloy of the type $\mathrm{AB}_{1-x}\mathrm{C}_x$ the phonon frequencies will depend on the ternary composition. For the binary end materials AB and AC clearly TO and LO frequencies exist. The simplest behavior of the alloy is the one-mode

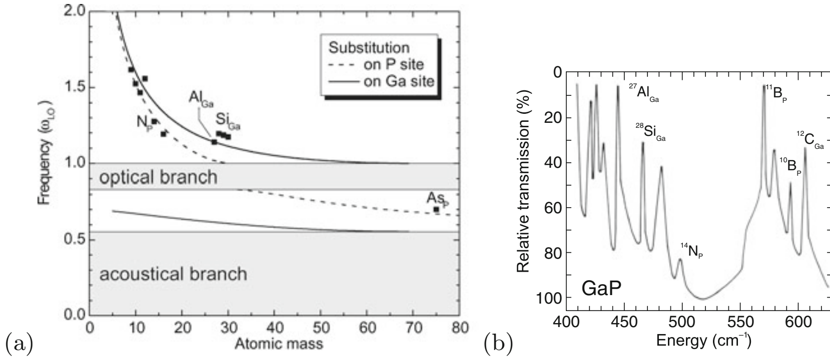

Fig. 5.12. (**a**) Numerical simulation of a linear chain model for GaP ($M_1 = 31$, $M_2 = 70$). Energy of local vibrational modes (*dashed* (*solid*) *line*): substitution on P (Ga) site) in units of the optical phonon frequency at Γ ($\omega_m = 45.4\,\text{meV}$). The *grey areas* indicate the acoustic and optical phonon bands. *Solid squares* are experimental data (from [261]), scaled to the theoretical curve for the $^{27}Al_{Ga}$ LVM frequency. (**b**) Differential transmission spectrum of GaP structure (nitrogen-doped layer on zinc-doped compensated substrate) against pure crystal ($T = 77\,\text{K}$). Data from [266]

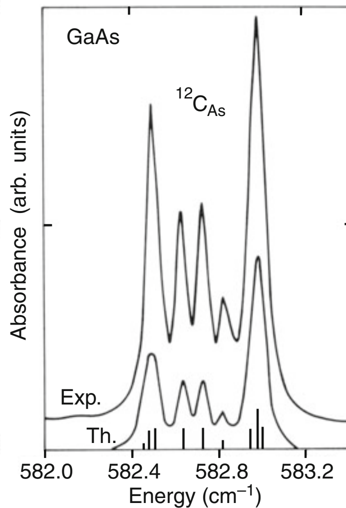

Fig. 5.13. Experimental (Exp., $T = 4.2\,\text{K}$, resolution $0.03\,\text{cm}^{-1}$) and theoretical (Th., artificial Lorentzian broadening) infrared spectra of LVM of $^{12}C_{As}$ in GaAs. The positions and oscillator strengths of the theoretical transitions involving different configurations with ^{69}Ga and ^{71}Ga isotopes are shown as *vertical bars*. Data from [262]

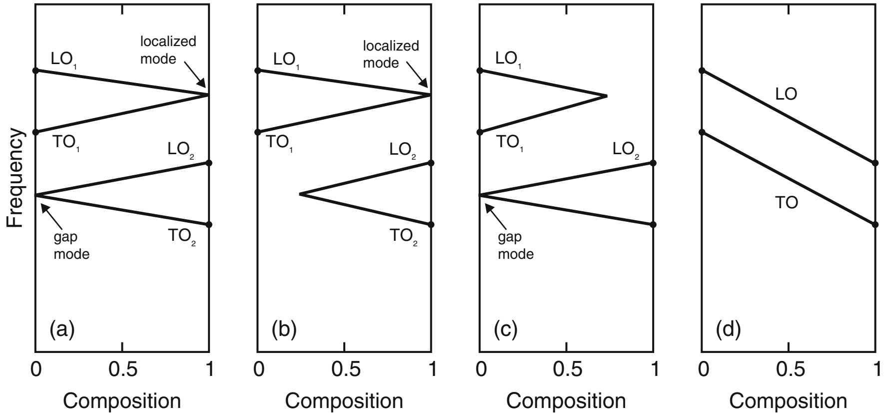

Fig. 5.14. Schematic behavior of phonon modes in an alloy. (**a**) Two-mode behavior with gap mode and localized mode, (**b**,**c**) mixed-mode behavior, (**b**) only localized mode allowed, (**c**) only gap mode allowed, (**d**) one-mode behavior with neither localized mode nor gap mode allowed

behavior (Fig. 5.14d) where the mode frequencies vary continuously (and approximately linearly) with the composition. The oscillator strength (LO–TO splitting, (9.64)) remains approximately constant. In many cases, the two-mode behavior is observed where the LO–TO gap closes (accompanied by decreasing oscillator strength) and a localized vibrational mode and a gap mode occur for the binary end materials (Fig. 5.14a). Also, a mixed-mode behavior (Fig. 5.14b,c) can occur.

The masses of the three constituent atoms will be M_A, M_B, and M_C. Without limiting the generality of our treatment, we assume $M_\mathrm{B} < M_\mathrm{C}$. From the considerations in Sect. 5.2.6 on LVM and gap modes, the condition

$$M_\mathrm{B} < M_\mathrm{A}, M_\mathrm{C} \tag{5.38}$$

for two-mode behavior can be deduced. This ensures a LVM of atom B in the compound AC and a gap mode of atom C in the compound AB. However, it turns out that this condition is not sufficient, e.g. $\mathrm{Na}_{1-x}\mathrm{K}_x\mathrm{Cl}$ fulfills (5.38) but exhibits one-mode behavior. From a modified REI[1] model (for $\mathbf{k} \sim 0$ modes) it has been deduced that

$$M_\mathrm{B} < \mu_\mathrm{AC} = \frac{M_\mathrm{A}\, M_\mathrm{C}}{M_\mathrm{A} + M_\mathrm{C}} < M_\mathrm{A}, M_\mathrm{C} \tag{5.39}$$

is a necessary and sufficient condition (unless the force constants between A–B and A–C are significantly different) for two-mode behavior [268]. A detailed discussion is given in [269]. Equation (5.39) is a stronger condition

[1] random element isodisplacement

Table 5.1. Atomic masses of the constituents of various ternary compounds, reduced mass μ_{AC} (5.39), fulfillment of the relation from (5.39) ('+': fulfilled, '−': not fulfilled) and experimental mode behavior ('2': two-mode, '1': one-mode)

alloy	A	B	C	M_{A}	M_{B}	M_{C}	μ_{AC}	rel.	modes
$\mathrm{GaP}_{1-x}\mathrm{As}_x$	Ga	P	As	69.7	31.0	74.9	36.1	+	2
$\mathrm{GaAs}_{1-x}\mathrm{Sb}_x$	Ga	As	Sb	69.7	74.9	121.8	44.3	−	1
$\mathrm{CdS}_{1-x}\mathrm{Se}_x$	Cd	S	Se	112.4	32.1	79.0	46.4	+	2
$\mathrm{Cd}_x\mathrm{Zn}_{1-x}\mathrm{S}$	S	Zn	Cd	32.1	65.4	112.4	25.0	−	1
$\mathrm{Mg}_x\mathrm{Zn}_{1-x}\mathrm{O}$	O	Mg	Zn	16.0	24.3	65.4	12.9	−	1

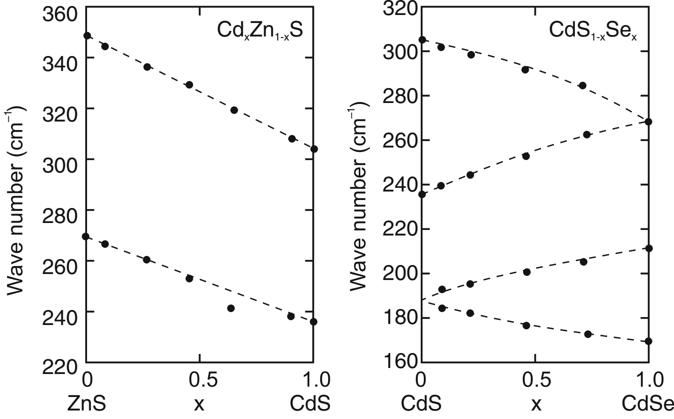

Fig. 5.15. Phonon energies of $\mathrm{Cd}_x\mathrm{Zn}_{1-x}\mathrm{S}$ and $\mathrm{CdS}_{1-x}\mathrm{Se}_x$ as a function of the ternary composition. Experimental data (*solid circles*) are from [268], *dashed lines* are guides to the eye

than the previous one (5.38). If (5.39) is not fulfilled the compound exhibits one-mode behavior. As an example, we show the mass relations for $\mathrm{CdS}_{1-x}\mathrm{Se}_x$ and $\mathrm{Cd}_x\mathrm{Zn}_{1-x}\mathrm{S}$ in Table 5.1 and the experimental phonon energies in Fig. 5.15. Also in Table 5.1 the masses for $\mathrm{GaP}_{1-x}\mathrm{As}_x$ ($\mathrm{GaAs}_{1-x}\mathrm{Sb}_x$) exhibiting two- (one-) mode behavior are shown.

5.2.8 Electric Field Created by Optical Phonons

Adjacent atoms oscillate with opposite phase in an optical phonon. If the bond has (partial) ionic character, this leads to a time-dependent polarization and subsequently to a macroscopic electric field. This additional field will influence the phonon frequencies obtained from a purely mechanical approach. We consider in the following the case $\mathbf{k} \approx 0$. The phonon frequency for TO and LO vibrations is given by

$$\omega_0 = \sqrt{\frac{2C}{M_\mathrm{r}}}\;, \tag{5.40}$$

where M_r is the reduced mass of the two different atoms (cf. Sect. 5.2.2). $\mathbf{u}$ is the relative displacement $\mathbf{u}_1 - \mathbf{u}_2$ of the two atoms in a diatomic base. When the interaction with the electric field $\mathbf{E}$ (which will be calculated self-consistently in the following) is considered, the Hamiltonian for the long-wavelength limit is given by [270]:

$$\hat{H}(\mathbf{p},\mathbf{u}) = \frac{1}{2}\left(\frac{1}{M_\mathrm{r}}\,\mathbf{p}^2 + b_{11}\,\mathbf{u}^2 + 2b_{12}\,\mathbf{u}\cdot\mathbf{E} + b_{22}\,\mathbf{E}^2\right)\;. \tag{5.41}$$

The first term is the kinetic energy ($\mathbf{p}$ stands for the momentum of the relative motion of the atoms 1 and 2 in the base, $\mathbf{p} = M_\mathrm{r}\dot{\mathbf{u}}$), the second the potential energy, the third the dipole interaction and the fourth the electric-field energy. The equation of motion for a plane wave $\mathbf{u} = \mathbf{u}_0 \exp\left[-\mathrm{i}(\omega t - \mathbf{k}\cdot\mathbf{r})\right]$ ($\ddot{\mathbf{u}} = -\omega^2\mathbf{u}$) yields

$$M_\mathrm{r}\,\omega^2\,\mathbf{u} = b_{11}\,\mathbf{u} + b_{12}\,\mathbf{E}\;. \tag{5.42}$$

Thus, the electric field is

$$\mathbf{E} = (\omega^2 - \omega_\mathrm{TO}^2)\,\frac{M_\mathrm{r}}{b_{12}}\,\mathbf{u}\;. \tag{5.43}$$

Here, the substitution $\omega_\mathrm{TO}^2 = b_{11}/M_\mathrm{r}$ was introduced that is consistent with (5.40) and $b_{11} = 2C$. ω_TO represents the mechanical oscillation frequency of the atoms undisturbed by any electromagnetic effects. Already now the important point is visible. If ω approaches ω_TO, the system plus electric field oscillates with the frequency it has without an electric field. Therefore the electric field must be zero. Since the polarization $\mathbf{P} = (\epsilon - 1)\epsilon_0\mathbf{E}$ is finite, the dielectric constant ϵ thus diverges.

The polarization is

$$\mathbf{P} = -\nabla_\mathbf{E}\hat{H} = -\left(b_{12}\,\mathbf{u} + b_{22}\,\mathbf{E}\right)\;. \tag{5.44}$$

The displacement field is

$$\mathbf{D} = \epsilon_0\,\mathbf{E} + \mathbf{P} = \epsilon_0\,\mathbf{E} - \left(b_{22} - \frac{b_{12}^2/M_\mathrm{r}}{\omega_\mathrm{TO}^2 - \omega^2}\right)\mathbf{E} = \epsilon_0\,\epsilon(\omega)\,\mathbf{E}\;. \tag{5.45}$$

Therefore, the dielectric function is

$$\epsilon(\omega) = \epsilon(\infty) + \frac{\epsilon(0) - \epsilon(\infty)}{1 - (\omega/\omega_\mathrm{TO})^2}\;. \tag{5.46}$$

Here, $\epsilon(\infty) = 1 - b_{22}/\epsilon_0$ is the high-frequency dielectric constant and $\epsilon(0) = \epsilon(\infty) + b_{12}^2/(b_{11}\epsilon_0)$ the static dielectric constant. The relation (5.46) is shown in Fig. 5.16.

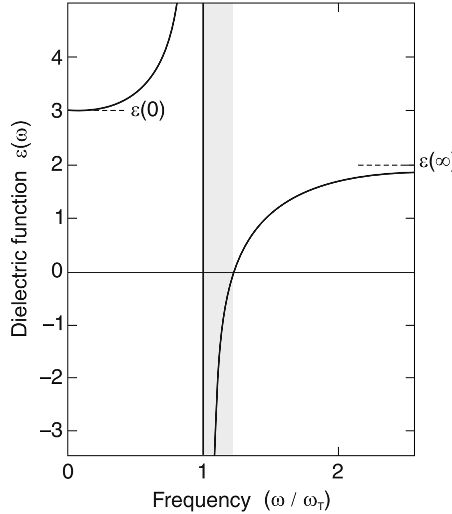

Fig. 5.16. Dielectric function according to (5.46) with $\epsilon(0) = 3$ and $\epsilon(\infty) = 2$ (without damping). *Grey area* denotes the region of negative ϵ

From the Maxwell equation $\nabla \cdot \mathbf{D} = 0$ for zero free charge we obtain the relation

$$\epsilon_0 \, \epsilon(\omega) \, \nabla \cdot \mathbf{E} = 0 \; . \tag{5.47}$$

Thus, either $\epsilon(\omega) = 0$ or $\nabla \cdot \mathbf{E} = 0$, i.e. $\mathbf{u}$ is perpendicular to $\mathbf{k}$. In the latter case we have a TO phonon and, neglecting retardation effects, using $\nabla \times \mathbf{E} = 0$ we find $\mathbf{E} = 0$ and therefore $\omega = \omega_{\mathrm{TO}}$, justifying our notation. In the case of $\epsilon(\omega) = 0$, we call the related frequency ω_{LO} and find the so-called Lyddane–Sachs–Teller (LST) relation

$$\frac{\omega_{\mathrm{LO}}^2}{\omega_{\mathrm{TO}}^2} = \frac{\epsilon(0)}{\epsilon(\infty)} \; . \tag{5.48}$$

This relation holds reasonably well for optically isotropic, heteropolar materials with two atoms in the basis, such as NaI and also GaAs. Since at high frequencies, i.e. $\omega \gg \omega_{\mathrm{TO}}$, only the individual atoms can be polarized, while for low frequencies the atoms can also be polarized against each other, $\epsilon(0) > \epsilon(\infty)$ and therefore also $\omega_{\mathrm{LO}} > \omega_{\mathrm{TO}}$. For GaAs, the quotient of the two phonon energies is 1.07. Using the LST relation (5.48), we can write for the dielectric function

$$\epsilon(\omega) = \epsilon(\infty) \left(\frac{\omega_{\mathrm{LO}}^2 - \omega^2}{\omega_{\mathrm{TO}}^2 - \omega^2} \right) \; . \tag{5.49}$$

The (long-wavelength) TO-phonon does not create a long-range electric field. Using $\nabla \cdot \mathbf{D} = 0$ and (5.45) and looking at the longitudinal fields, we have

$$\epsilon_0 \, \mathbf{E} = b_{12} \, \mathbf{u} + b_{22} \, \mathbf{E} \, . \tag{5.50}$$

This can be rewritten as

$$\mathbf{E} = -\omega_{\mathrm{LO}} \sqrt{\frac{M_{\mathrm{r}}}{\epsilon_0}} \sqrt{\frac{1}{\epsilon(\infty)} - \frac{1}{\epsilon(0)}} \, \mathbf{u} \propto -\mathbf{u} \, . \tag{5.51}$$

The (long-wavelength) LO-phonon thus creates a long-range electric field acting *against* the ion displacement and represents an additional restoring force. This effect is also consistent with the fact that $\omega_{\mathrm{LO}} > \omega_{\mathrm{TO}}$.

5.3 Elasticity

The elastic properties of the semiconductor are important if the semiconductor is subjected to external forces (pressure, temperature) or to lattice mismatch during heteroepitaxy.

5.3.1 Thermal Expansion

The lattice constant depends on temperature. The (linear) thermal expansion coefficient is defined as

$$\alpha(T_0) = \left. \frac{\partial a_0(T)}{\partial T} \right|_{T=T_0} \tag{5.52}$$

and is temperature dependent. The temperature dependence of α for silicon and germanium is shown in Fig. 5.17. α is approximately proportional to the heat capacity (C_{V}) except at low temperatures. The negative values are due to negative Grüneisen parameters [271]. These anharmonicity effects are discussed in detail in [255].

5.3.2 Stress–Strain Relation

In this section, we recall the classical theory of elasticity [272]. The solid is treated as a continuous medium (piecewise homogeneous) and the displacement vector is thus a continuous function $\mathbf{u}(\mathbf{r})$ of the spatial coordinates. When the spatial variation $\nabla \mathbf{u}$ of $\mathbf{u}$ is small, the elastic energy can be written as

$$U = \frac{1}{2} \int \frac{\partial u_l}{\partial x_k} \, C_{klmn} \, \frac{\partial u_n}{\partial x_m} \, \mathrm{d}^3 \mathbf{r} \, , \tag{5.53}$$

where C_{klmn} is the (macroscopic) tensor of the elastic coefficients. 21 components of this tensor can be independent. For crystals with cubic symmetry the number of independent constants is reduced to 3. An exchange $k \leftrightarrow l$ and $m \leftrightarrow n$ does not matter, only six indices have to be considered (xx, yy, zz, yz, xz, and xy). The strain components ϵ_{ij} are symmetrized according to

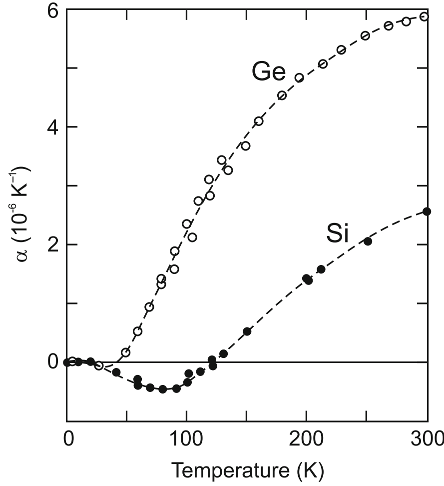

Fig. 5.17. Linear thermal expansion coefficient of silicon (*solid circles*) and germanium (*open circles*). Adapted from [271] based on experimental data from various sources. *Dashed lines* are guide to the eyes

$$\epsilon_{ij} = \frac{1}{2}\left(\frac{\partial u_j}{\partial x_i} + \frac{\partial u_i}{\partial x_j}\right) . \tag{5.54}$$

The strains ϵ_{xx} are along the main axes of the crystal as visualized in Fig. 5.18.

The stresses[2] σ_{kl} are then given by

$$\sigma_{kl} = C_{klmn}\,\epsilon_{mn} . \tag{5.55}$$

The inverse relation is mediated by the stiffness tensor **S**.

$$\epsilon_{kl} = S_{klmn}\,\sigma_{mn} . \tag{5.56}$$

Typically, the strain components e_{ij} or e_i are used with the convention $xx \rightarrow 1$, $yy \rightarrow 2$, $zz \rightarrow 3$, $yz \rightarrow 4$, $xz \rightarrow 5$, and $xy \rightarrow 6$:

$$e_{ij} = \epsilon_{ij}\,(2 - \delta_{ij}) . \tag{5.57}$$

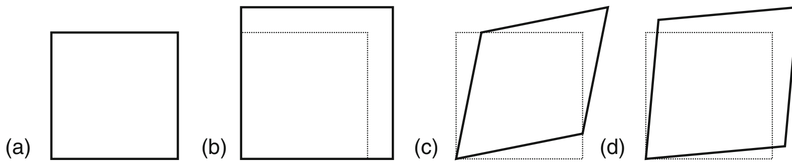

Fig. 5.18. Deformation of a square (**a**). (**b**) Pure hydrostatic deformation ($\epsilon_{xx} = \epsilon_{yy} = 0.2$, $\epsilon_{xy} = 0$), (**c**) pure shear deformation ($\epsilon_{xx} = \epsilon_{yy} = 0$, $\epsilon_{xy} = 0.2$), and (**d**) mixed deformation ($\epsilon_{xx} = \epsilon_{yy} = 0.1$, $\epsilon_{xy} = 0.1$)

Then, $\sigma_m = C_{mn} e_n$ with the C_{ij} being the elastic constants, i.e. $C_{11} = C_{1111}$, $C_{12} = C_{1122}$ and $C_{44} = C_{1212}$. The x, y, and z directions are the main axes of the cubic solid, i.e. the $\langle 100 \rangle$ directions. Then, we have explicitly

$$\begin{pmatrix} \sigma_1 \\ \sigma_2 \\ \sigma_3 \\ \sigma_4 \\ \sigma_5 \\ \sigma_6 \end{pmatrix} = \begin{pmatrix} C_{11} & C_{12} & C_{12} & 0 & 0 & 0 \\ C_{12} & C_{11} & C_{12} & 0 & 0 & 0 \\ C_{12} & C_{12} & C_{11} & 0 & 0 & 0 \\ 0 & 0 & 0 & C_{44} & 0 & 0 \\ 0 & 0 & 0 & 0 & C_{44} & 0 \\ 0 & 0 & 0 & 0 & 0 & C_{44} \end{pmatrix} \begin{pmatrix} e_1 \\ e_2 \\ e_3 \\ e_4 \\ e_5 \\ e_6 \end{pmatrix} . \tag{5.58}$$

Values for some semiconductors are given in Table. 5.2. The inverse relation is given by the matrix

$$\begin{pmatrix} S_{11} & S_{12} & S_{12} & 0 & 0 & 0 \\ S_{12} & S_{11} & S_{12} & 0 & 0 & 0 \\ S_{12} & S_{12} & S_{11} & 0 & 0 & 0 \\ 0 & 0 & 0 & S_{44} & 0 & 0 \\ 0 & 0 & 0 & 0 & S_{44} & 0 \\ 0 & 0 & 0 & 0 & 0 & S_{44} \end{pmatrix} , \tag{5.59}$$

with the stiffness coefficients in this notation given by

$$S_{11} = \frac{C_{11} + C_{12}}{(C_{11} - C_{12})\,(C_{11} + 2C_{12})} \tag{5.60a}$$

$$S_{12} = \frac{C_{12}}{-C_{11}^2 - C_{11}C_{12} + 2C_{12}^2} \tag{5.60b}$$

$$S_{44} = \frac{1}{C_{44}} . \tag{5.60c}$$

Table 5.2. Elastic constants of some cubic semiconductors at room temperature. ξ refers to (5.62) and is a measure for the isotropy, I_K refers to the Keating criterion (5.63). For MgO, the Keating criterion is not fulfilled because it has (six-fold coordinated) rocksalt structure and is thus not tetrahedrally bonded

Material	C_{11} (10^{10} Pa)	C_{12} (10^{10} Pa)	$2C_{44}$ (10^{10} Pa)	ξ	I_K
C	107.64	12.52	57.74	−1.3	1.005
Si	16.58	6.39	7.96	−0.56	1.004
Ge	12.85	4.83	6.68	−0.40	1.08
BN	82.0	19.0	48.0	−0.63	1.11
GaAs	11.9	5.34	5.96	−0.20	1.12
InAs	8.33	4.53	3.96	0.08	1.22
AlAs	12.05	4.686	5.94	−0.48	1.03
ZnS	10.46	6.53	4.63	0.30	1.33
MgO	29.7	15.6	9.53	−0.96	0.80

[2]The stress is a force per unit area and has the dimensions of a pressure.

We emphasize that in this convention (also called the *engineering* convention), e.g. $e_1 = \epsilon_{xx}$ and $e_4 = 2\epsilon_{yz}$. There is also another convention (the *physical* convention) without this factor of two; in this case the matrix in (5.58) contains the elements $2C_{44}$. Introducing

$$C_0 = 2C_{44} + C_{12} - C_{11} \ , \tag{5.61}$$

we note that for an isotropic material the isotropy parameter ξ is zero

$$\xi = \frac{C_0}{C_{44}} = 0 \ . \tag{5.62}$$

This isotropy condition is not obeyed by real semiconductors as shown in Table 5.2. Another relation, known as the Keating criterion [273, 274]

$$I_{\mathrm{K}} = \frac{2\,C_{44}\,(C_{11} + C_{12})}{(C_{11} - C_{12})\,(C_{11} + 3C_{12})} = 1 \tag{5.63}$$

stems from the consideration of bending and stretching of the tetrahedral bonds in the valence force field (VFF) model. It is closely fulfilled (Table 5.2), in particular for the covalent semiconductors.

If $C_0 \neq 0$, the Young's modulus ($\sigma_{\mathbf{nn}} = Y(\mathbf{n})\epsilon_{\mathbf{nn}}$) is nonspherical (see Fig. 5.19a for GaAs). Typically, the $\langle 100 \rangle$ directions are the softest. In terms of the Euler angles (Fig. A.1) the angular dependence of the stiffness constant S_{11} is (Fig. 5.19b,c)

$$\begin{aligned}\frac{S_{11}(\phi,\theta)}{S_{11}^0} = & \frac{C_{11} - C_{12}}{C_0 + C_{11} - C_{12}} + \frac{C_0(21C_{11} + 10C_{12})}{32(C_0 + C_{11} - C_{12})(C_{11} + C_{12})} \\ & + \frac{C_0(C_{11} + 2C_{12})}{32(C_0 + C_{11} - C_{12})(C_{11} + C_{12})} \\ & \times (4\cos 2\theta + 7\cos 4\theta + 8\cos 4\phi \sin^4\theta) \ ,\end{aligned} \tag{5.64}$$

where S_{11}^0 is the stiffness along the $\langle 100 \rangle$ directions as given in (5.60a). We note that the Young's modulus Y (Y of (5.65a) is equivalent to $1/S_{11}$ of (5.60a)) and the Poisson ratio ν used for isotropic materials[3] are related to the constants of cubic material by

$$Y = C_{11} - \frac{2\,C_{12}^2}{C_{11} + C_{12}} \tag{5.65a}$$

$$\nu = \frac{C_{12}}{C_{11} + C_{12}} \ . \tag{5.65b}$$

[3] We note that Y, ν and C_{ij} of typical materials are both positive. Materials with negative Poisson ratio are called *auxetic* [275, 277]. Also materials with negative compressibility are possible [278].

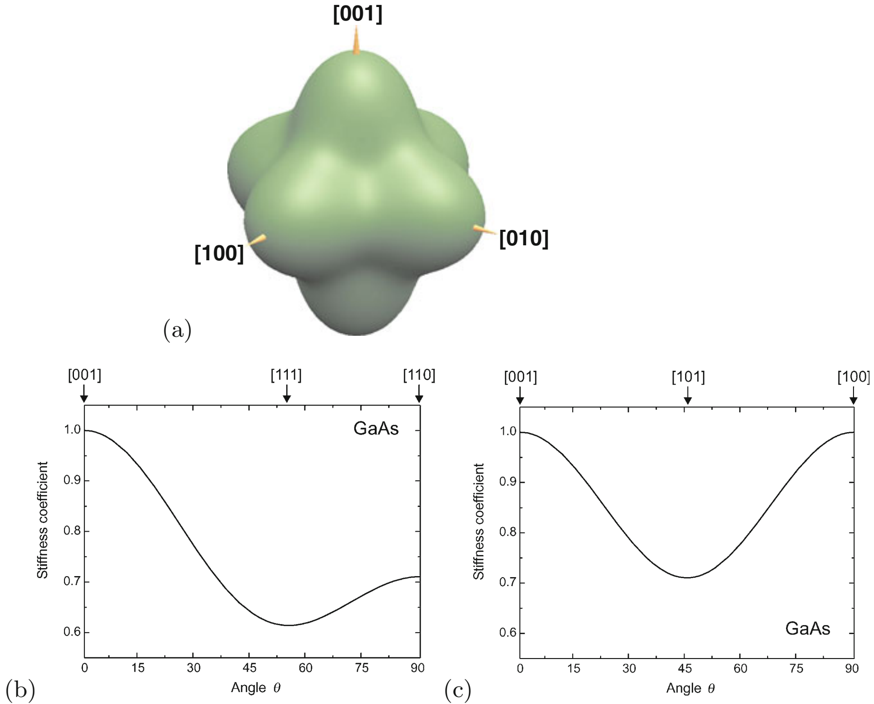

Fig. 5.19. The directional dependence of the inverse of the Young's modulus ($1/Y(\mathbf{n})$) for uniaxial stress (along the direction $\mathbf{n}$) in GaAs. (**a**) 3D view, arbitrary units, (**b**) dependence on polar angle θ in the (01–1) plane (for $\phi = \pi/4$, normalized to S_{11}), (**c**) dependence on polar angle θ in the (010) plane (for $\phi = 0$, normalized to S_{11})

For isotropic materials Lamé's constants λ and μ are also used. They are given by $C_{11} = \lambda + 2\mu$, $C_{12} = \lambda$ and $C_{44} = \mu$.

Beyond the dependence of the elastic constants on the bond length (as materialized in the phonon frequencies in Fig. 5.10), they depend on the ionicity. In Fig. 5.20, the elastic constants of various zincblende semiconductors are shown as a function of the ionicity f_{i}. The values for the elastic constants are normalized by e^2/a^4, a being the average nearest-neighbor distance.

For wurtzite crystals, five elastic constant are necessary for the stress–strain relation that reads

$$C_{ij} = \begin{pmatrix} C_{11} & C_{12} & C_{13} & 0 & 0 & 0 \\ C_{12} & C_{11} & C_{13} & 0 & 0 & 0 \\ C_{13} & C_{13} & C_{33} & 0 & 0 & 0 \\ 0 & 0 & 0 & C_{44} & 0 & 0 \\ 0 & 0 & 0 & 0 & C_{44} & 0 \\ 0 & 0 & 0 & 0 & 0 & \frac{1}{2}(C_{11} - C_{12}) \end{pmatrix} . \qquad (5.66)$$

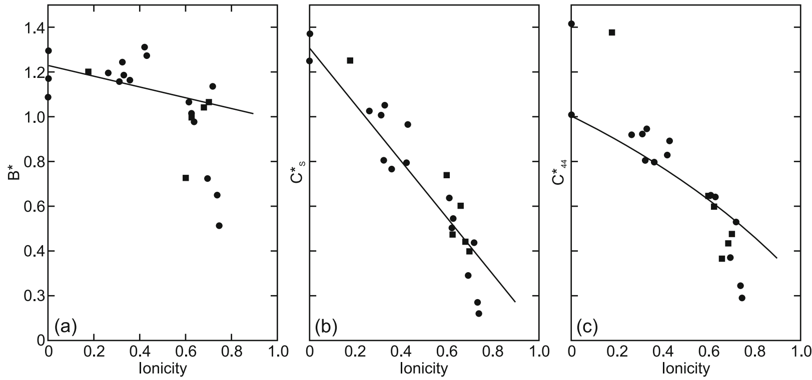

Fig. 5.20. Elastic constants as a function of ionicity for various semiconductors with diamond or zincblende (*circles*) and wurtzite (*squares*) structure. Constants are normalized by the modulus $C_0 = e^2/d^4$, d being the average nearest-neighbor distance. (**a**) Bulk modulus, $B^* = (C_{11} + 2C_{12})/(3C_0)$, (**b**, **c**) shear moduli, (**b**) $C^*_\mathrm{S} = (C_{11} - C_{12})/C_0$, (**c**) $C^*_{44} = C_{44}/C_0$. *Solid lines* are a simple model as discussed in [281]. Adapted from [279]

Table 5.3. Elastic constants of some wurtzite semiconductors. All values in units of 10^{10} Pa.

Material	C_{11}	C_{12}	C_{13}	C_{33}	C_{44}	Ref.
GaN	39.1	14.3	10.8	39.9	10.3	[284]
AlN	41.0	14.9	9.9	38.9	12.5	[285]
ZnS	12.4	6.02	4.55	14.0	2.86	[286]
ZnO	20.6	11.8	11.8	21.1	4.4	[287]

Experimental values for wurtzite materials are given in Table 5.3. The relation of the elastic tensor of wurtzite and zincblende materials, in particular viewed along the $\langle 111 \rangle$-direction has been discussed in [279, 280].

5.3.3 Biaxial Strain

In heteroepitaxy (cf. Sect. 11.2.5), a biaxial strain situation arises, i.e. layered material is compressed (or expanded in the case of tensile strain) in the interface plane and is expanded (compressed) in the perpendicular direction. Here, we assume that the substrate is infinitely thick, i.e. that the interface remains planar. Substrate bending is discussed in Sect. 5.3.5.

The simplest case is epitaxy on the (001) surface, i.e. $e_1 = e_2 = \epsilon_\parallel$. The component e_3 is found from the condition $\sigma_3 = 0$ (no forces in the z direction). All shear strains are zero. For zincblende material it follows

$$\epsilon_{\perp}^{100} = e_3 = -\frac{C_{12}}{C_{11}}\,(e_1 + e_2) = -\frac{2C_{12}}{C_{11}}\,\epsilon_{\parallel}\ . \tag{5.67}$$

For other crystallographic directions the formula is more involved [282]:

$$\epsilon_{\perp}^{110} = -\frac{2C_{12} - C_0/2}{C_{11} + C_0/2}\,\epsilon_{\parallel} \tag{5.68}$$

$$\epsilon_{\perp}^{111} = -\frac{2C_{12} - 2C_0/3}{C_{11} + 2C_0/3}\,\epsilon_{\parallel}\ . \tag{5.69}$$

In Fig. 5.21 the strain around misfit dislocations at a GaAs/CdTe heterointerface, as calculated from a TEM image (Fig. 4.13), is shown.

For wurtzite crystals and pseudomorphic growth along [00.1] the strain along the c-axis is given by

$$\epsilon_{\perp}^{0001} = -\frac{C_{13}}{C_{33}}\,(e_1 + e_2) = -\frac{2C_{13}}{C_{33}}\,\epsilon_{\parallel}\ , \tag{5.70}$$

where $\epsilon_{\perp} = (c - c_0)/c_0$ and $\epsilon_{\parallel} = (a - a_0)/a_0$.

5.3.4 Three-Dimensional Strain

The strain distribution in two-dimensional or three-dimensional objects such as quantum wires and dots (see also Sect. 13) is more complicated.

A simple analytical solution for the problem of a strained inclusion is only possible for isotropic material parameters [283].

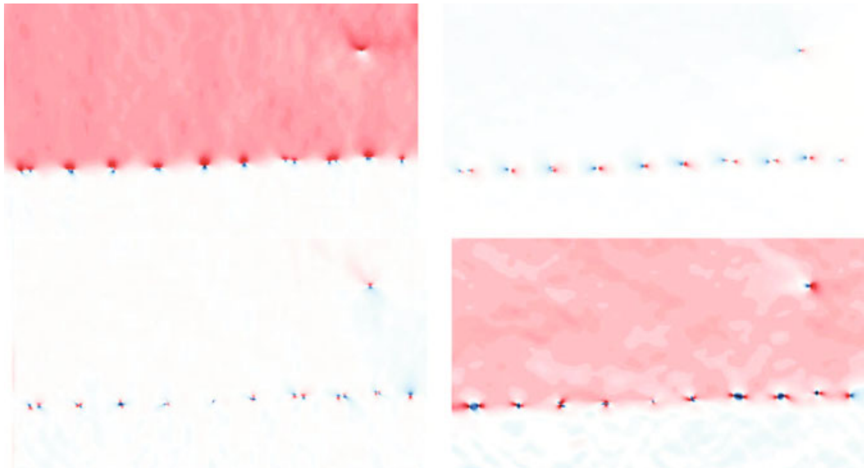

Fig. 5.21. Components $\begin{pmatrix} \epsilon_{xx} & \epsilon_{xz} \\ \epsilon_{zx} & \epsilon_{zz} \end{pmatrix}$ of the strain tensor (with respect to the GaAs lattice constant) of the dislocation array shown in Fig. 4.13, *red*/*blue*: positive/negative value, *white*: zero. From [217]

The solution for a sphere can be extended to yield the strain distribution of an inclusion of arbitrary shape. This scheme applies only for isotropic materials and identical elastic properties of the inclusion and the surrounding matrix. The solution will be given in terms of a surface integral of the boundary of the inclusion, which is fairly easy to handle. Several disconnected inclusions can be treated by a sequence of surface integrals.

The strain distribution for the inner and outer parts of a sphere with radius ρ_0 is given (in spherical coordinates) by

$$\epsilon_{\rho\rho}^{\text{in}} = \frac{2}{3}\,\epsilon_0\,\frac{1-2\nu}{1-\nu} = \epsilon_{\theta\theta}^{\text{in}} = \epsilon_{\phi\phi}^{\text{in}} \tag{5.71}$$

$$\epsilon_{\rho\rho}^{\text{out}} = \frac{2}{3}\,\epsilon_0\,\frac{1+\nu}{1-\nu}\left(\frac{\rho_0}{\rho}\right)^3 = -2\epsilon_{\theta\theta}^{\text{out}} = -2\epsilon_{\phi\phi}^{\text{out}}\ , \tag{5.72}$$

where ρ denotes the radius, ν the Poisson ratio, and ϵ_0 the relative lattice mismatch of the inclusion and the matrix. The radial displacements are

$$u_\rho^{\text{in}} = \frac{2}{3}\,\epsilon_0\,\frac{1-2\nu}{1-\nu}\rho \tag{5.73}$$

$$u_\rho^{\text{out}} = \frac{2}{3}\,\epsilon_0\,\frac{1-2\nu}{1-\nu}\,\rho_0^3\,\frac{1}{\rho^2}\ . \tag{5.74}$$

Dividing the displacement by the sphere's volume, we obtain the displacement per unit volume of the inclusion. From the displacement we can derive the stress σ_{ij}^0 per unit volume.

$$\sigma_{ii}^0 = \frac{1}{4\pi}\,\frac{Y\epsilon_0}{1-\nu}\,\frac{2x_i^2 - x_j - x_k}{\rho^5} \tag{5.75}$$

$$\sigma_{ij}^0 = \frac{3}{2}\,\frac{1}{4\pi}\,\frac{Y\epsilon_0}{1-\nu}\,\frac{x_i x_j}{\rho^5}\ , \tag{5.76}$$

where i, j and k are pairwise unequal indices. Due to the linear superposition of stresses, the stress distribution σ_{ij}^V for the arbitrary inclusion of volume V can be obtained by integrating over V

$$\sigma_{ij}^V = \int_V \sigma_{ij}^0\left(\mathbf{r} - \mathbf{r_0}\right)\mathrm{d}^3\mathbf{r}\ . \tag{5.77}$$

The strains can be calculated from the stresses.

When ϵ_0 is constant within V, the volume integral can be readily transformed into an integral over the surface ∂V of V using Gauss' theorem. With the 'vector potentials' $\mathbf{A}_{ij}$ we fulfill $\mathrm{div}\mathbf{A}_{ij} = \sigma_{ij}$.

$$\mathbf{A}_{ii} = -\frac{1}{4\pi}\,\frac{Y\epsilon_0}{1-\nu}\,\frac{x_i\mathbf{e}_i}{\rho^3} \tag{5.78}$$

$$\mathbf{A}_{ij} = -\frac{1}{2}\,\frac{1}{4\pi}\,\frac{Y\epsilon_0}{1-\nu}\,\frac{x_i\mathbf{e}_j + x_j\mathbf{e}_i}{\rho^3}\ . \tag{5.79}$$

Equation (5.79) is valid for the case $i \neq j$. $\mathbf{e}_i$ is the unit vector in the i-th direction. However, special care must be taken at the singularity $\mathbf{r} = \mathbf{r}_0$ if $\mathbf{r}_0$ lies within V because the stress within the 'δ-inclusion' is not singular (in contrast to the electrostatic analog of a δ-charge). Thus, we find

$$\sigma_{ij}^V(\mathbf{r}_0) = \oint_{\partial V} \mathbf{A}_{ij}\, \mathrm{d}\mathbf{S} + \delta_{ij} \frac{Y \epsilon_0}{1-\nu} \int_V \delta(\mathbf{r} - \mathbf{r_0})\, \mathrm{d}^3\mathbf{r}\ . \tag{5.80}$$

As an example, we show in Fig. 5.22 the numerically calculated strain components [288] (taking into account the different elastic properties of the dot and matrix materials) in the cross section of a pyramidal InAs quantum dot in a GaAs matrix on top of a two-dimensional InAs layer. The strain component ϵ_{zz} is positive in the 2D layer, as expected from (5.67). However, in the pyramid ϵ_{zz} exhibits a complicated dependence and even takes negative values at the apex.

5.3.5 Substrate Bending

If a lattice-mismatched layer is pseudomorphically grown on top of a substrate it suffers biaxial strain. For finite substrate thickness part of the strain will relax via substrate bending. If the substrate is circular, a spherical cap is formed. If the lattice constant of the film is larger (smaller) than that of the substrate, the film is under compressive (tensile) strain and the curvature is convex (concave) with respect to the outward normal given by the growth direction (Fig. 5.23a). Substrate bending can also be induced by a mismatch of the thermal expansion coefficients $\alpha_{\mathrm{th}}^{\mathrm{f}}$ and $\alpha_{\mathrm{th}}^{\mathrm{s}}$ of the film and substrate,

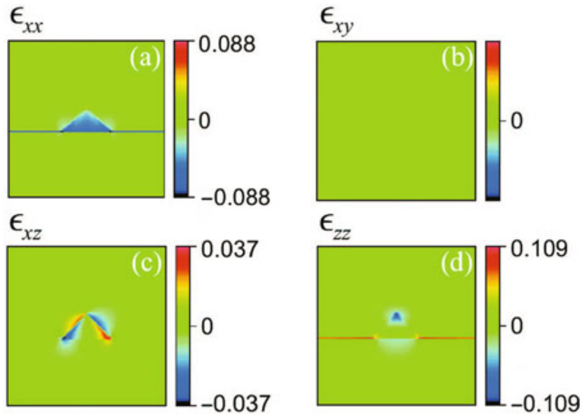

Fig. 5.22. Strain components in an InAs pyramid (quantum dot with {101} faces), embedded in GaAs. The cross section is through the center of the pyramid. The lattice mismatch between InAs and GaAs amounts to $\approx -7\%$. Reprinted with permission from [288], ©1995 APS

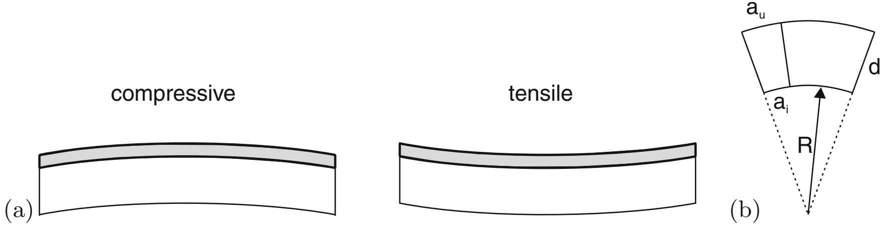

Fig. 5.23. (**a**) Schematic bending of a film/substrate system for compressive (*left*) and tensile (*right*) film strain. (**b**) Schematic deformation of curved film of thickness d. The lattice constants at the inner and outer surface are a_i and a_u, respectively.

respectively. If a film/substrate system is flat at a given temperature, e.g. growth temperature, a decrease of temperature, e.g. during cooling, will lead to compressive (tensile) strain if $\alpha_\mathrm{th}^\mathrm{f}$ is smaller (larger) than $\alpha_\mathrm{th}^\mathrm{s}$.

In a curved structure, the lattice constant in the tangential direction increases from a_i^t at the inner surface ($r = R = \kappa^{-1}$) to a_u^t at the outer surface ($r = R + d$). Thus, the tangential lattice constant varies with the radial position

$$a^\mathrm{t}(r) = a_\mathrm{i}^\mathrm{t}\,(1 + r\,\kappa)\ , \tag{5.81}$$

where d is the layer thickness (Fig. 5.23b). Therefore $a_\mathrm{u} = a_\mathrm{i}(1 + d/R)$. We note that (5.81) holds in all layers of a heterostructure, i.e. the film *and* the substrate.

The lattice constant in the radial direction a^r, however, depends on the lattice constant a_0 of the local material and is calculated from the biaxial strain condition, such as (5.67). The in-plane strain is $\epsilon_\| = (a^\mathrm{t} - a_0)/a_0$ (we assume a spherical cap with $\epsilon_\| = \epsilon_{\theta\theta} = \epsilon_{\phi\phi}$). For an isotropic material we find $a^\mathrm{r} = a_0\,(1+\epsilon_\perp)$ with $\epsilon_\perp = -2\nu\epsilon_\|/(1-\nu)$. The local strain energy density U is given by

$$U = \frac{Y}{1-\nu}\,\epsilon_\|^2\ . \tag{5.82}$$

The total strain energy per unit area U' of a system of two layers with lattice constants a_1, a_2, Young's moduli Y_1, Y_2 and thickness d_1, d_2 (we assume the same Poisson constant ν in both layers) is

$$U' = \int_0^{d_1} U_1\,\mathrm{d}r + \int_{d_1}^{d_2} U_2\,\mathrm{d}r\ . \tag{5.83}$$

The total strain energy needs to be minimized with respect to a_i and R in order to find the equilibrium curvature κ. We find

$$\begin{aligned}\kappa &= \frac{6a_1a_2(a_2-a_1)d_1d_2(d_1+d_2)Y_1Y_2}{a_2^3d_1^4Y_1^2 + \alpha Y_1Y_2 + a_1^3d_2^4Y_2^4}\\ \alpha &= a_1a_2d_1d_2\left[-a_2d_1(2d_1+3d_2) + a_1(6d_1^2+9d_1d_2+4d_2^2)\right]\ .\end{aligned} \tag{5.84}$$

For $a_2 = a_1\ (1+\epsilon)$ we develop κ to first order of ϵ and find ($\chi = Y_2/Y_1$) [289, 290]

$$\kappa = \frac{6\chi d_1 d_2 (d_1 + d_2)}{d_1^4 + 4\chi d_1^3 d_2 + 6\chi d_1^2 d_2^2 + 4\chi d_1 d_2^3 + \chi^2 d_2^4}\,\epsilon\,. \tag{5.85}$$

In the case of a substrate (d_s) with a thin epitaxial layer ($d_\mathrm{f} \ll d_\mathrm{s}$), the radius of curvature is approximately (Stoney's formula [290])

$$\kappa = 6\,\epsilon\,\frac{d_\mathrm{f}}{d_\mathrm{s}^2}\,\frac{Y_\mathrm{f}}{Y_\mathrm{s}}\,. \tag{5.86}$$

Conversely, if the radius of curvature is measured [292], e.g. optically, the film strain can be determined during epitaxy.

5.3.6 Scrolling

In some cases cylindrically scrolled structures are important, e.g. for thin-film flexible electronics, nanotubes and nanoscrolls. The scrolling of thin layers must be avoided by suitable strain management for thin layers that are lifted off from their substrate for transfer to somewhere else. If the film remains attached to its substrate, a scroll can be fabricated as schematically shown in Fig. 5.24. Such structures were first reported in [293]. The shape of such scroll is investigated in [294] without a priori assumptions on its shape.

If bending strain occurs only in *one* of the tangential directions, the energy density is given by

$$U = \frac{Y}{2(1-\nu^2)}\left(\epsilon_\mathrm{t}^2 + \epsilon_y^2 + 2\nu\,\epsilon_\mathrm{t}\,\epsilon_y\right)\,, \tag{5.87}$$

where ϵ_y is the strain in the unbent direction (cylinder axis) as shown in Fig. 5.25a. For a strained heterostructure made up from two layers the curvature is given by (calculated analogous to (5.85), $\chi = Y_2/Y_1$ [290])

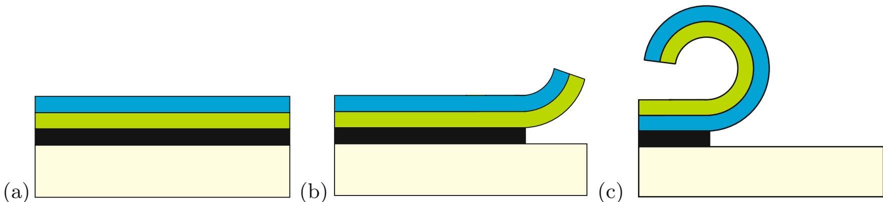

Fig. 5.24. Schematic representation of nanoscroll formation. (**a**) Strained heterostructure (*blue/green*) that is planar due to large substrate thickness, (**b**) starting removal of sacrificial layer (*black*), (**c**) release of thin film into nanoscroll geometry

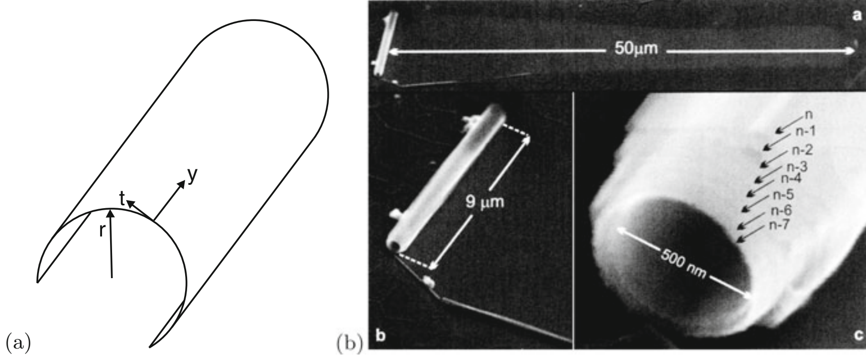

Fig. 5.25. (**a**) Schematic representation of a cylindrically rolled sheet with radial direction r, tangential direction t and direction along the cylinder axis y. (**b**) SEM images of multiwall InGaAs/GaAs nanoscroll rolled up over about 50 µm. Part (**b**) from [297]

$$\kappa = \frac{6(1+\nu)\chi d_1 d_2 (d_1 + d_2)}{d_1^4 + 4\chi d_1^3 d_2 + 6\chi d_1^2 d_2^2 + 4\chi d_1 d_2^3 + \chi^2 d_2^4}\, \epsilon\,, \tag{5.88}$$

which differs from (5.85) only by the factor $1+\nu$ in the nominator.

For cubic material and a (001) surface the energy is given as

$$U_{100} = \frac{C_{11} - C_{12}}{2C_{11}} \left[C_{11} \left(\epsilon_{\mathrm{t}}^2 + \epsilon_y^2 + C_{12} \left(\epsilon_{\mathrm{t}} + \epsilon_y \right)^2 \right) \right] \tag{5.89}$$

for a scrolling direction along $\langle 100 \rangle$. When the (001)-oriented film winds up along a direction $\langle hk0 \rangle$ having an angle ϕ with the [100] direction ($\phi = 45°$ for $\langle 110 \rangle$), the strain energy is given by (C_0 is given by (5.61))

$$U_\phi = U_{100} + C_0 \left(\frac{\epsilon_{\mathrm{t}} - \epsilon_y}{2} \right)^2 \sin^2(2\phi)\,. \tag{5.90}$$

The strain energy vs. bending radius ($= \kappa^{-1}$) is shown for a SiGe nanoscroll in Fig. 5.26. First, the relaxation along the cylinder axis plays a minor role. The smallest strain energy is reached for scrolling along $\langle 100 \rangle$, also yielding the smaller bending radius (larger curvature). Therefore, the film preferentially scrolls along $\langle 100 \rangle$. This explains the observed 'curl' behavior of scrolls winding up for $\phi \neq 0$ (Fig. 5.26b). The effect of surface strain needs to be included to yield improved quantitative agreement with experimental values of $\kappa(\epsilon, d)$ [295].

5.3.7 Critical Thickness

Strained epitaxial films are called pseudomorphic when they do not contain defects and the strain relaxes elastically, e.g. by tetragonal distortion.

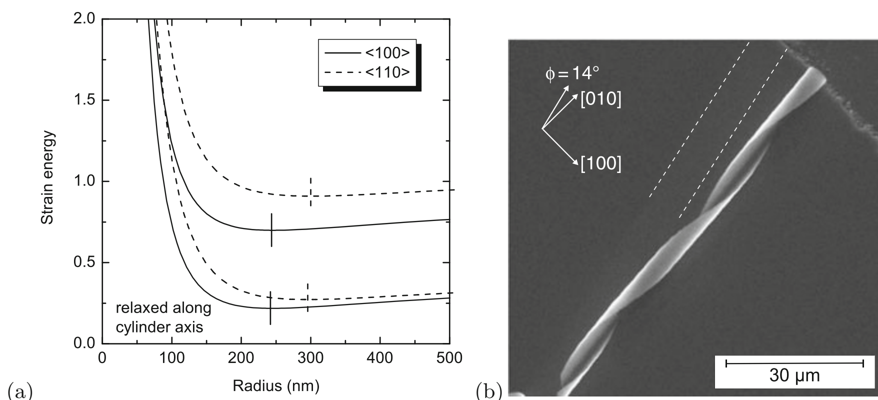

Fig. 5.26. (**a**) Strain energy (in units of the strain energy of the flat pseudomorphic layers) of a scroll of a 4-layer SiGe structure ($Si_{0.3}Ge_{0.7}$, $Si_{0.6}Ge_{0.4}$ and $Si_{0.8}Ge_{0.2}$, each 3 nm thick and a 1-nm Si cap) as a function of radius for winding directions along ⟨100⟩ and ⟨110⟩. *Top* (*bottom*) curves without (with complete) strain relaxation along the cylinder axis. *Vertical lines* indicate the positions of the respective energy minima [290]. (**b**) SEM image of curled InGaAs/GaAs nanoscroll rolled $\phi = 14°$ off ⟨100⟩. The stripe from which the film was rolled off is indicated by *white dashed lines*. Part (**b**) from [297]

When the layer thickness increases, however, strain energy is accumulated that will lead at some point to plastic relaxation via the formation of defects. In many cases, a grid of misfit dislocations forms at the interface (Figs. 4.17 and 5.27). The average distance p of the dislocations is related to the misfit

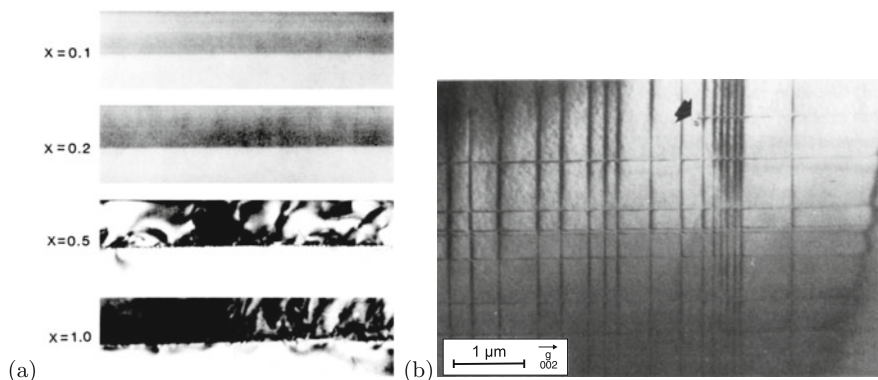

Fig. 5.27. (**a**) Series of cross-sectional TEM images of 100-nm thick Ge_xSi_{1-x} layers on Si(001) with different ternary compositions $x = 0.1$, 0.2, 0.5, and 1.0. The growth temperature was 550°C. The transition from commensurate to incommensurate growth is obvious. Adapted from [298]. (**b**) Plan view ⟨022⟩ TEM bright field image of a 250-nm $Ge_{0.15}Si_{0.85}$ layer on Si (001), annealed at about 700°C. The arrow denotes the position of a dislocation loop. Reprinted with permission from [299], ©1989 AVS

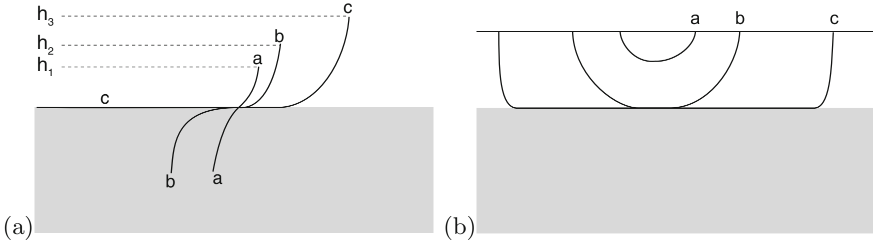

Fig. 5.28. Schematic formation of misfit dislocations by (**a**) elongation of a grown-in threading dislocation and (**b**) by the nucleation and growth of dislocation half-loops. (**a**) depicts a threading dislocation. Initially, for thickness h_1 the interface is coherent 'a', for larger thickness h_2 the interface is critical and the force of the interface on the dislocation is equal to the tension in the dislocation line, 'b'. For larger thickness, e.g. h_3, the dislocation line is elongated in the plane of the interface, 'c'. In (**b**) 'a' denotes a subcritical dislocation half-loop, 'b' depicts a half-loop being stable under the misfit stress and for 'c' the loop has grown under the misfit stress into a misfit dislocation line along the interface

$f = (a_1 - a_2)/a_2$ and the edge component $b_\perp$of the Burger's vector (for a 60° dislocation $b_\perp = a_0/\sqrt{8}$)

$$p = \frac{b_\perp}{f} \,. \tag{5.91}$$

Two mechanisms have been proposed for the formation of misfit dislocations (Fig. 5.28), the elongation of a grown-in threading dislocation [300] and the nucleation and growth of dislocation half-loops [301]. For the modeling of such systems a mechanical approach based on the forces on dislocations [300] or an energy consideration based on the minimum strain energy necessary for defect formation [301–303] can be followed. Both approaches have been shown to be equivalent [304] (if a periodic array of dislocations is considered). In [305] it was pointed out that the finite speed of plastic flow also has to be considered to explain experimental data. Temperature affects the observed critical thickness and a kinetic model is needed. Another way of introducing dislocations is the plastic relaxation at the edge of coherent strained islands (cmp. Fig. 13.26)

In the following, isotropic materials and identical elastic constants of substrate and thin film are assumed, following [304]. The interface plane is the (x,y)-plane, the growth direction is z. The energy E_d of a periodic dislocation array with period p and Burgers vector $\mathbf{b} = (b_1, b_2, b_3)$ is

$$\begin{aligned} E_\mathrm{d} &= \frac{Y}{8\pi(1-\nu^2)}\,\beta^2 \qquad (5.92)\\ \beta^2 &= \left[b_1^2 + (1-\nu)b_2^2 + b_3^2\right] \ln\left(\frac{p\left[1-\exp(-4\pi h/p)\right]}{2\pi q}\right) \\ &\quad + \left(b_1^2 - b_3^2\right)\frac{4\pi h}{p}\,\frac{\exp(-4\pi h/p)}{1-\exp(-4\pi h/p)} \end{aligned}$$

$$-\frac{1}{2}\left(b_1^2+b_3^2\right)\left(\frac{4\pi h}{p}\right)^2 \frac{\exp(-4\pi h/p)}{[1-\exp(-4\pi h/p)]^2}$$

$$+b_3^2\,\frac{2\pi h}{p}\,\frac{\exp(-2\pi h/p)}{1-\exp(-2\pi h/p)}\;,$$

where h is the film thickness and q denotes the cutoff length for the dislocation core, taken as $q=b$. The misfit strain including the relaxation due to dislocations with Burger's vectors $\mathbf{b}$ and $\hat{\mathbf{b}}$ in the two orthogonal interface $\langle 110\rangle$ directions $\mathbf{n}$ and $\hat{\mathbf{n}}$. We chose the coordinate system such that $\mathbf{n}=(1,0,0)$ and $\hat{\mathbf{n}}=(0,1,0)$ (the z direction remains). With respect to these axes the Burger's vectors are $\left(\pm\frac{1}{2},\frac{1}{2},\frac{1}{\sqrt{2}}\right)a_0/\sqrt{2}$. The misfit strain $\epsilon_{ij}^{\mathrm{m}}$ is reduced due to the dislocation formation to the 'relaxed' misfit strain $\epsilon_{ij}^{\mathrm{r}}$ with

$$\epsilon_{ij}^{\mathrm{r}}=\epsilon_{ij}^{\mathrm{m}}+\frac{b_i n_j+b_j n_i}{2p}+\frac{\hat{b}_i\hat{n}_j+\hat{b}_j\hat{n}_i}{2p}\;, \tag{5.93}$$

with an associated stress σ_{ij}. The strain energy E_{s} of the layer due to the relaxed misfit is then

$$E_{\mathrm{s}}=\frac{1}{2}\,h\,\sigma_{ij}\,\epsilon_{ij}^{\mathrm{r}} \tag{5.94}$$

$$\lim_{p\to\infty}E_{\mathrm{s}}=2h\,\frac{Y(1+\nu)}{1-\nu}\,f^2\;. \tag{5.95}$$

The total strain energy E is given by

$$pE=2E_{\mathrm{d}}+2E_{\mathrm{c}}+pE_{\mathrm{s}} \tag{5.96}$$

$$E_{\infty}=\lim_{p\to\infty}E\;, \tag{5.97}$$

with the core energy E_{c} of the dislocation that needs to be calculated with an atomistic model (not considered further here). This energy is shown in Fig. 5.29a for the material parameters of $Ge_{0.1}Si_{0.9}/Si(001)$ (misfit -0.4%) for various layer thicknesses as a function of $1/p$. This plot looks similar to that for a first-order phase transition (with $1/p$ as the order parameter). For a certain critical thickness h_{c1} the energy of the layer without any dislocation and the layer with a particular dislocation density p_1 are identical ($E-E_{\infty}=0$) and additionally $\partial E/\partial p|_{p=p_1}=0$. However, between $p\to\infty$ and $p=p_0$ there is an energy barrier. The critical thickness h_{c2} is reached when

$$\partial E/\partial p\;|_{p\to\infty}=0\;, \tag{5.98}$$

i.e. the energy decreases monotonically for increasing dislocation density up to the global energy minimum at a certain equilibrium dislocation spacing p_2. Equation (5.98) leads to the following implicit equation for the determination of h_{c2}:

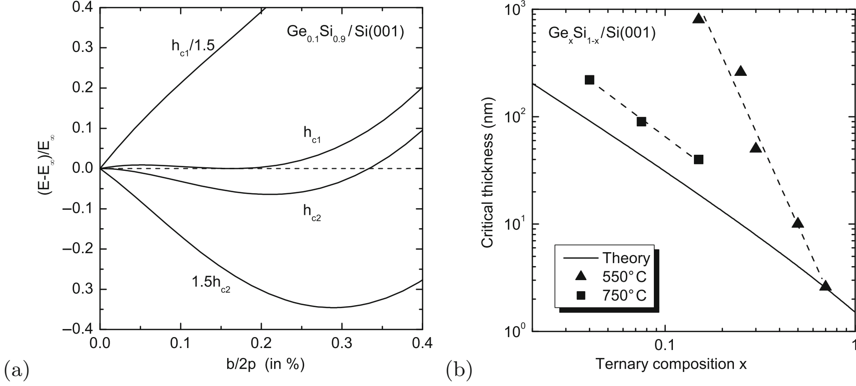

Fig. 5.29. (**a**) Theoretical calculation for the strain energy vs. inverse dislocation density for various thicknesses of $Ge_{0.1}Si_{0.9}$ layers on Si (001). The ordinate is $b/2p$, $b/2$ being the edge component of the Burgers vector and p being the dislocation spacing. The abscissa is the strain energy E scaled with E_∞ (5.97). (**b**) Critical thickness for Ge_xSi_{1-x} layers on Si (001). The *solid line* is theory (h_{c2}) according to (5.99). Data points are from [306] (*squares*, growth temperature of 750°C) and from [298] (*triangles* for growth temperature of 550°C)

$$h_{c2} = \frac{b\left[-16 + 3b^2 + 8(-4+\nu)\ln\left(2h_{c2}/q\right)\right]}{128\, f\pi\,(1+\nu)}\,, \tag{5.99}$$

with the length of the Burgers vector $b = a_0/\sqrt{2}$.

The theoretical dependence of h_{c2} for Ge_xSi_{1-x}/Si(001) with varying composition is shown in Fig. 5.29b together with experimental data. The critical thickness for a fairly high growth temperature is much closer to the energetic equilibrium than that deposited at lower temperature. This shows that there are kinetic limitations for the system to reach the mechanical equilibrium state. Also, the experimental determination of the critical thickness is affected by finite resolution for large dislocation spacing, leading generally to an overestimate of h_c.

In zincblende materials two types of dislocations are possible, α and β, with Ga- and As-based cores, respectively. They have $[\bar{1}10]$ and $[110]$ line directions for a compressively strained interface. The α dislocation has the larger glide velocity. Therefore, strain relaxation can be anisotropic with regard to the $\langle 110 \rangle$ directions for zincblende material, e.g. InGaAs/GaAs [307, 308].

5.4 Cleaving

The cleavage planes of the diamond structure are $\{111\}$ planes. It is easiest to break the bonds connecting the double layers in the $\langle 111 \rangle$ directions.

The cleavage planes of the zincblende structure are {110} planes. Due to the ionic character, breaking the bonds connecting the double layers in the ⟨111⟩ directions would leave charged surfaces, which is energetically unfavorable. The {100} planes contain only one sort of atom and would also leave highly charged surfaces. The {110} planes contain equal amounts of A and B atoms and are neutral.

Ideally, the cleaving plane is atomically flat or exhibits large monoatomically flat terraces. However, certain dopants in high concentrations, e.g. GaAs:Te, can induce a rough surface due to lattice distortion [309].

6 Band Structure

Silicon is a metal.
A.H. Wilson, 1931 [45]

6.1 Introduction

Valence electrons that move in the crystals feel a periodic potential

$$U(\mathbf{r}) = U(\mathbf{r} + \mathbf{R}) \tag{6.1}$$

for all vectors $\mathbf{R}$ of the direct lattice. The potential[1] is due to the effect of the ion cores and all other electrons. Thus a serious many-body problem is present. In principle, the band structure can be calculated from the periodic arrangements of the atoms and their atomic order number. We note that for some problems, e.g. the design of optimal solar cells, a certain band structure is known to be ideal and a periodic atomic arrangement, i.e. a material, needs to be found that generates the optimal band structure. This problem is called the *inverse band structure problem*.

6.2 Electrons in a Periodic Potential

6.2.1 Bloch's Theorem

First, we will deduce some general conclusions about the structure of the solution as a consequence of the periodicity of the potential. We first investigate the solution of a Schrödinger equation of the type

$$H\,\Psi(\mathbf{r}) = \left[-\frac{\hbar^2}{2m}\nabla^2 + U(\mathbf{r})\right]\Psi(\mathbf{r}) = E\,\Psi(\mathbf{r}) \tag{6.2}$$

for an electron. U will be periodic with the lattice, i.e. it will obey (6.1).

[1] In this book the form of the potential will never be explicitly given.

M. Grundmann, *The Physics of Semiconductors*, 2nd ed., Graduate Texts in Physics, DOI 10.1007/978-3-642-13884-3_6,

© Springer-Verlag Berlin Heidelberg 2010

Bloch's theorem says that the eigenstates Ψ of a one-particle Hamiltonian as in (6.2) can be written as the product of plane waves and a lattice-periodic function, i.e.

$$\Psi_{n\mathbf{k}}(\mathbf{r}) = A\, \mathrm{e}^{\mathrm{i}\mathbf{k}\mathbf{r}}\, u_{n\mathbf{k}}(\mathbf{r}) \ . \tag{6.3}$$

The normalization constant A is often omitted. If $u_{n\mathbf{k}}(\mathbf{r})$ is normalized, $A = 1/\sqrt{V}$, where V is the integration volume. The wavefunction is indexed with a quantum number n and the wavevector $\mathbf{k}$. The key is that the function $u_{n\mathbf{k}}(\mathbf{r})$, the so-called Bloch function, is periodic with the lattice, i.e.

$$u_{n\mathbf{k}}(\mathbf{r}) = u_{n\mathbf{k}}\,(\mathbf{r} + \mathbf{R}) \tag{6.4}$$

for all vectors $\mathbf{R}$ of the direct lattice. The proof is simple in one dimension and more involved in three dimensions with possibly degenerate wavefunctions, see [310].

If $E_{n\mathbf{k}}$ is an energy eigenvalue, then $E_{n\mathbf{k}+\mathbf{G}}$ is also an eigenvalue for all vectors $\mathbf{G}$ of the reciprocal lattice, i.e.

$$E_n(\mathbf{k}) = E_n\,(\mathbf{k} + \mathbf{G}) \ . \tag{6.5}$$

Thus the energy values are periodic in reciprocal space. The proof is simple, since the wavefunction (for $\mathbf{k} + \mathbf{G}$) $\exp\left(\mathrm{i}(\mathbf{k} + \mathbf{G})\mathbf{r}\right) u_{n(\mathbf{k}+\mathbf{G})}(\mathbf{r})$ is for $u_{n(\mathbf{k}+\mathbf{G})}(\mathbf{r}) = \exp\left(-\mathrm{i}\mathbf{G}\mathbf{r}\right) u_{n\mathbf{k}}(\mathbf{r})$ obviously an eigenfunction to $\mathbf{k}$.

A band structure along one $\mathbf{k}$-direction can be displayed in various zone schemes as depicted in Fig. 6.1. The most frequently used scheme is the *reduced* zone scheme. In three dimensions, the band structure is typically shown along particular paths in the Brillouin zone, as depicted, e.g., in Fig. 6.2c.

6.2.2 Free-Electron Dispersion

If the entire wavefunction (from (6.3)) obeys the Schrödinger equation (6.2), the Bloch function $u_{n\mathbf{k}}$ fulfills the equation

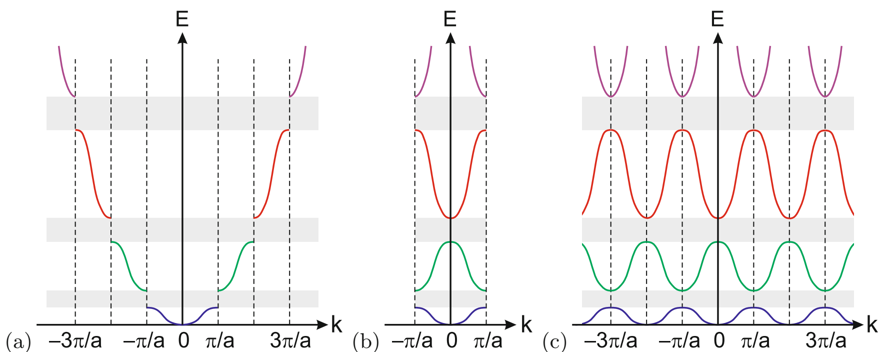

Fig. 6.1. Zone schemes for a band structure: (**a**) extended, (**b**) reduced and (**c**) repetitive zone scheme

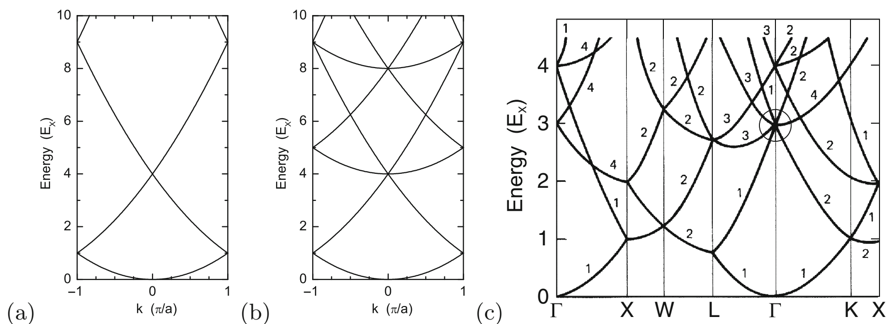

Fig. 6.2. Dispersion of free electrons (empty lattice calculation, $U = 0$, shown in the first Brillouin zone) in (**a**) a one-dimensional lattice ($\mathbf{G} = n\,2\pi/a$), (**b**) a simple cubic lattice ($\mathbf{G} = (h,k,l)\,2\pi/a$) and (**c**) in a fcc lattice. The energy is measured in units of the energy at the X-point, $E_X = (\hbar^2/2m)(2\pi/a)^2$. The *shaded circle* in (**c**) represents the region where the band gap develops for finite periodic potential $U \neq 0$

$$\left[-\frac{1}{2m}\,(\mathbf{p}+\mathbf{k})^2 + U(\mathbf{r})\right]\,u_{n\mathbf{k}}(\mathbf{r}) = E_{n\mathbf{k}}\,u_{n\mathbf{k}}(\mathbf{r})\;, \tag{6.6}$$

which is easy to see from $\mathbf{p} = -i\hbar\nabla$.

First, we discuss the simplest case of a periodic potential, $U \equiv 0$. This calculation is also called the *empty lattice* calculation. The solution of (6.6) is then just constant, i.e. $u_\mathbf{k} = c$ and $\Psi_\mathbf{k}(\mathbf{r}) = c\exp(\mathrm{i}\mathbf{k}\mathbf{r})$. The dispersion of the free electron is then given by

$$E(\mathbf{k}) = \frac{\hbar^2}{2m}\,\mathbf{k}^2\;, \tag{6.7}$$

where $\mathbf{k}$ is an arbitrary vector in the reciprocal space. $\mathbf{k}'$ is a vector from the Brillouin zone such that $\mathbf{k} = \mathbf{k}' + \mathbf{G}$ with a suitable reciprocal lattice vector $\mathbf{G}$. Because of (6.5) the dispersion relation can be written also as

$$E(\mathbf{k}) = \frac{\hbar^2}{2m}\,(\mathbf{k}' + \mathbf{G})^2\;, \tag{6.8}$$

where $\mathbf{k}'$ denotes a vector from the Brillouin zone. Thus, many branches of the dispersion relation arise from using various reciprocal lattice vectors in (6.8).

The resulting dispersion relation for the free electron is shown in Fig. 6.2a for a one-dimensional system ($\mathbf{k}'$ and $\mathbf{G}$ are parallel) and in Fig. 6.2b for the simple cubic lattice (in the so-called reduced zone scheme). In Fig. 6.2c, the (same) dispersion of the free electron is shown for the fcc lattice.

6.2.3 Kronig–Penney Model

The Kronig–Penney model [43] is a simple, analytically solvable model that visualizes the effect of the periodic potential on the dispersion relation of the electrons, i.e. the formation of a band structure.

A one-dimensional periodic hard-wall potential of finite height is assumed (Fig. 6.3a). The well width is a, the barrier width b and thus the period $P = a + b$. The potential is zero in the well (regions $(0, a) + nP$) and $+U_0$ in the barrier. The Schrödinger equation

$$-\frac{\hbar^2}{2m}\frac{\partial^2\Psi}{\partial x^2} + U(x)\,\Psi(x) = E\,\Psi(x) \tag{6.9}$$

has to be solved. The solutions for a single hard-wall potential well are well known. In the well, they have oscillatory character, i.e. $\Psi \propto \exp{(\mathrm{i}kx)}$ with real k. In the barrier, they have exponential character, i.e. $\Psi \propto \exp{(kx)}$ with real k. Thus we chose

$$\Psi(x) = A\exp{(\mathrm{i}Kx)} + B\exp{(-\mathrm{i}Kx)} \tag{6.10a}$$

$$\Psi(x) = C\exp{(\kappa x)} + D\exp{(-\kappa x)}\ . \tag{6.10b}$$

The wavefunction from (6.10a) is for the well between 0 and a with $E = \hbar^2 K^2/2m$. The wavefunction from (6.10b) is for the barrier between a and $a+b$ with $U_0 - E = \hbar^2\kappa^2/2m$. From the periodicity and Bloch's theorem the wavefunction at $x = -b$ must have the form $\Psi(-b) = \exp(-\mathrm{i}kP)\,\Psi(a)$, i.e. between the two wavefunctions is only a phase factor. The wavevector k of the Bloch function (plane-wave part of the solution) is a new quantity and must be carefully distinguished from K and κ.

Both K and κ are real numbers. As boundary conditions, the continuity of Ψ and Ψ' are used.[2] At $x = 0$ and $x = a$ this yields

$$A + B = C + D \tag{6.11a}$$

$$\mathrm{i}KA - \mathrm{i}KB = \kappa C - \kappa D \tag{6.11b}$$

$$A\exp(\mathrm{i}Ka) + B\exp(-\mathrm{i}Ka) = C\exp(\kappa a) + D\exp(-\kappa a) \tag{6.11c}$$

$$\mathrm{i}KA\exp(\mathrm{i}Ka) - \mathrm{i}KB\exp(-\mathrm{i}Ka) = \kappa C\exp(\kappa a) - \kappa D\exp(-\kappa a). \tag{6.11d}$$

The continuity of Ψ and Ψ' at $x = -b$ is used in the left sides of (6.11c,d).

A nontrivial solution arises only if the determinant of the coefficient matrix is zero. This leads (after some tedious algebra) to

$$\cos(kP) = \left[\frac{\kappa^2 - K^2}{2\kappa K}\right]\sinh(\kappa b)\,\sin(Ka) + \cosh(\kappa b)\,\cos(Ka)\ . \tag{6.12}$$

---

[2] Generally, Ψ'/m should be continuous, however, in the present example the mass is assumed constant throughout the structure.

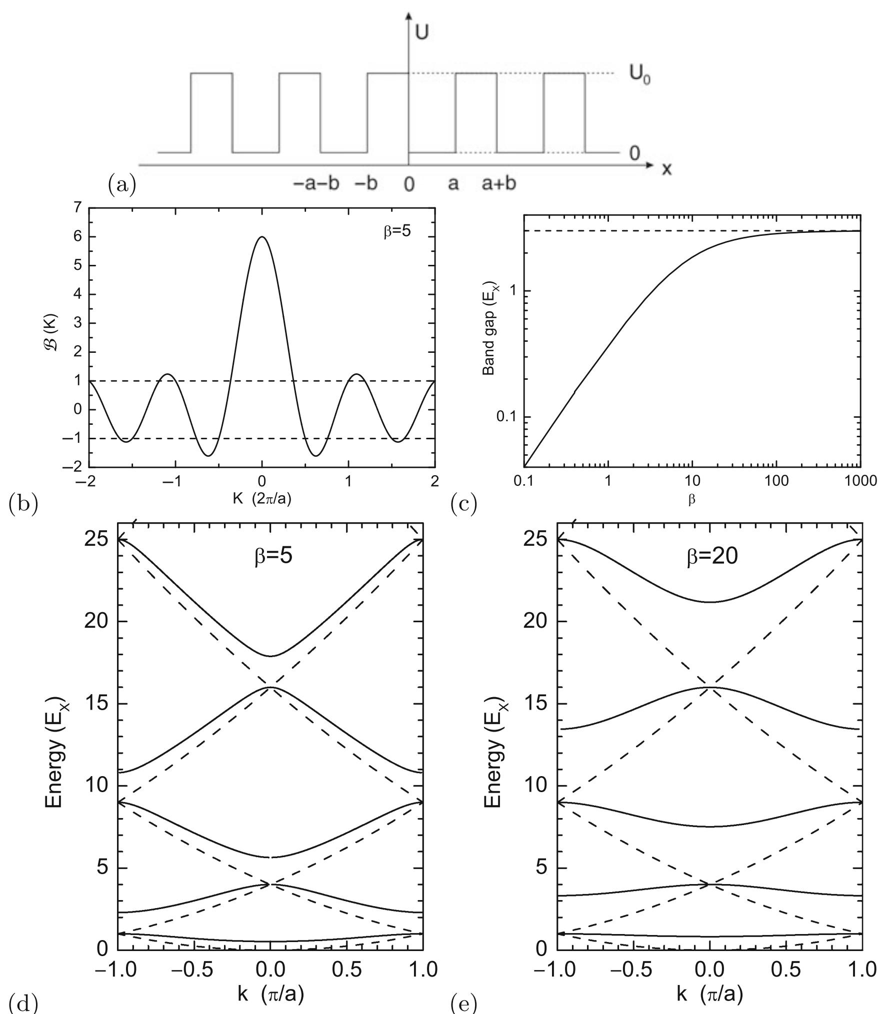

Fig. 6.3. (**a**) One-dimensional periodic hard-wall potential (Kronig–Penney model). (**b**) Transcendental function $\mathcal{B}(K)$ from (6.13) for $\beta = 5$. The *dashed lines* indicate the $[-1, 1]$ interval for which solutions exist for (6.13). (**c**) Band gap between first and second subband (in units of $E_\mathrm{X} = \hbar^2\pi^2/(2ma^2)$) as a function of β. For smaller β the band gap is $\propto \beta$. For thick barriers ($\beta \to \infty$) the band gap saturates towards $3E_\mathrm{X}$ as expected for uncoupled wells. (**d**, **e**) The resulting energy dispersion (in units of E_X) as a function of the superlattice wavevector k for (**d**) $\beta = 5$ and (**e**) $\beta = 20$ in (6.13). The *dashed lines* are the free-electron dispersion (for $\beta = 0$) (see Fig. 6.2a)

Further simplification can be reached by letting the barrier thickness $b \to 0$ and $U_0 \to \infty$. Then $P \to a$. The limit, however, is performed in such a way that the barrier 'strength' $U_0 b \propto \kappa^2 b$ remains constant and finite. Equation (6.12) then reads (for $\kappa b \to 0$: $\sinh(\kappa b) \to \kappa b$ and $\coth(\kappa b) \to 1$):

$$\cos(ka) = \beta \frac{\sin(Ka)}{Ka} + \cos(Ka) = \mathcal{B}(K) \; . \tag{6.13}$$

The coupling strength $\beta = \kappa^2 ba/2$ represents the strength of the barrier. Equation (6.13) only has a solution if the right side is in the interval $[-1, 1]$ (Fig. 6.3b). The function $\sin(x)/x$ oscillates with decreasing amplitude such that for sufficiently high values of Ka a solution can always be found. The resulting dispersion is shown in Fig. 6.3c. The dispersion is different from the free-electron dispersion and has several separated bands. The band gaps are related to the K values, i.e. energies for which (6.13) cannot be fulfilled. At the zone boundary ($k = \pi/a$) the bands are split and the tangent is horizontal ($\mathrm{d}E/\mathrm{d}k = 0$). The form of the dispersion is similar to the arccos function.

For large coupling between the potential wells (small β, $\beta \lesssim 1$) the band gap E_{12} between the first and the second subband at the X-point is $E_{12} = 4\beta/\pi^2 E_\mathrm{X}$ with $E_\mathrm{X} = \hbar^2\pi^2/(2ma^2)$. In this case, the width of the subbands is wide. For small coupling (large β) the band gap E_{12} converges towards $3E_\mathrm{X}$ as expected for decoupled potential wells with energy levels $E_n = E_\mathrm{X} n^2$ and the width of the bands is small.

6.2.4 Lattice Vector Expansion

General Wave Equation

In this section, we will discuss the solution of a general wave equation for electrons in a periodic potential. The solution is investigated particularly at the zone boundary. The potential U is periodic with the lattice (6.1). It can be represented as a Fourier series with the reciprocal lattice vectors (cf. (3.16)):

$$U(\mathbf{r}) = \sum_{\mathbf{G}} U_{\mathbf{G}} \exp\left(\mathrm{i}\mathbf{G}\mathbf{r}\right) \; . \tag{6.14}$$

Since U is a real function, $U_{-\mathbf{G}} = U^*_{\mathbf{G}}$. The deeper reason for the success of such an approach is that for typical crystal potentials, the Fourier coefficients decrease rapidly with increasing $\mathbf{G}$, e.g. for the unscreened Coulomb potential $U_{\mathbf{G}} \propto 1/G^2$. The wavefunction is expressed as a Fourier series (or integral) over all allowed (Bloch) wavevectors $\mathbf{K}$,

$$\Psi(\mathbf{r}) = \sum_{\mathbf{K}} C_{\mathbf{K}} \exp\left(\mathrm{i}\mathbf{K}\mathbf{r}\right) \; . \tag{6.15}$$

The kinetic and potential energy terms in the Schrödinger equation (6.6) are

$$\nabla^2 \Psi = -\sum_{\mathbf{K}} \mathbf{K}^2 \, C_{\mathbf{K}} \, \exp(\mathrm{i}\mathbf{K}\mathbf{r}) \tag{6.16a}$$

$$U\Psi = \sum_{\mathbf{G}} \sum_{\mathbf{K}} U_{\mathbf{G}} \, C_{\mathbf{K}} \, \exp(\mathrm{i}(\mathbf{G}+\mathbf{K})\,\mathbf{r}) \ . \tag{6.16b}$$

With $\mathbf{K}' = \mathbf{K} + \mathbf{G}$, (6.16b) can be rewritten as

$$U\Psi = \sum_{\mathbf{G}} \sum_{\mathbf{K}'} U_{\mathbf{G}} \, C_{\mathbf{K}'-\mathbf{G}} \, \exp(\mathrm{i}\mathbf{K}'\mathbf{r}) \ . \tag{6.17}$$

Now, the Schrödinger equation can be written as an (infinite) system of algebraic equations:

$$(\lambda_{\mathbf{K}} - E)\, C_{\mathbf{K}} + \sum_{\mathbf{G}} U_{\mathbf{G}} \, C_{\mathbf{K}-\mathbf{G}} = 0 \,, \tag{6.18}$$

with $\lambda_{\mathbf{K}} = \hbar^2 \, \mathbf{K}^2/(2m)$.

Approximate Solution at the Zone Boundary

The potential energy will have only one important Fourier coefficient U for the shortest reciprocal lattice vector $\mathbf{G}$. Also, we have $U_{-\mathbf{G}} = U_{\mathbf{G}}$. Thus, the (one-dimensional) potential has the form $U(x) = 2U\cos(Gx)$. We consider the solution at the zone boundary, i.e. in the vicinity of $\mathbf{K} = \mathbf{G}/2$. The kinetic energy is then the same for $\mathbf{K} = \pm\mathbf{G}/2$, i.e. $\lambda_{\mathbf{K}} = \lambda_{\mathbf{K}-\mathbf{G}} = (\hbar^2/2m)\,(G^2/4)$. $C_{\mathbf{G}/2}$ is an important coefficient of the wavefunction, thus $C_{-\mathbf{G}/2}$ will also be important. We will now limit the $\mathbf{K}$ vectors for the series of (6.15) to just these two. For the coefficient vector $\begin{pmatrix} C_{\mathbf{G}/2} \\ C_{-\mathbf{G}/2} \end{pmatrix}$ the determinant is

$$\begin{vmatrix} \lambda - E & U \\ U & \lambda - E \end{vmatrix} = (\lambda - E)^2 - U^2 = 0 \,, \tag{6.19}$$

with $\lambda = \lambda_{\mathbf{K}} = \lambda_{-\mathbf{K}} = (\hbar^2/2m)\,(G^2/4)$ for $\mathbf{K} = \mathbf{G}/2$. Thus the energy values are

$$E_{\pm} = \lambda \pm U = \frac{\hbar^2}{2m} \frac{G^2}{4} \pm U \ . \tag{6.20}$$

At the zone boundary, a splitting of the size $E_+ - E_- = 2U$ occurs. The center of the energy gap is given by the energy $\lambda_{\mathbf{K}}$ of the free-electron dispersion. The ratio of the coefficients is $C_{\mathbf{G}/2}/C_{-\mathbf{G}/2} = \mp 1$. The '$-$' solution of (6.20) (lower energy) is a standing cosine wave (Ψ_-), the '+' solution (Ψ_+) is a standing sine wave as visualized in Fig. 6.4. For the lower-energy (binding) state the electrons are localized at the potential minima, i.e. at the atoms, for the upper state (antibinding) the electrons are localized between the atoms. Both wavefunctions have the same periodicity since they belong to the same wavevector $\mathbf{K} = \mathbf{G}/2$. We note that the periodicity of Ψ is $2a$, while the periodicity of Ψ^2 is equal to the lattice constant a.

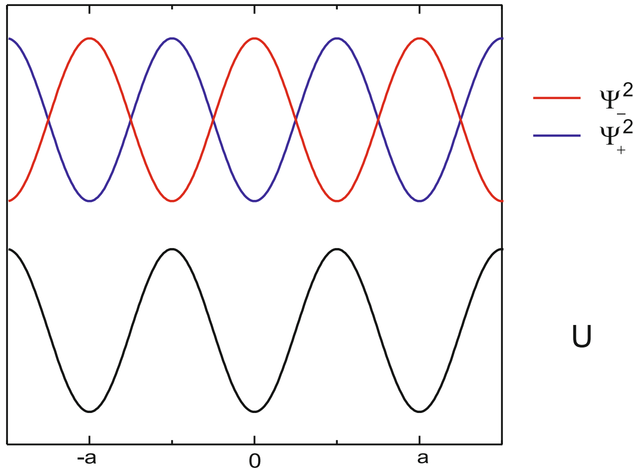

Fig. 6.4. Periodic potential U (one-dimensional cosine, *black*) and the squares of the wavefunctions Ψ_- (*red*) and Ψ_+ (*blue*) for the wavevector at the zone boundary, $K = G/2 = \pi/a$

Solution in the Vicinity of the Zone Boundary

In the vicinity of the zone boundary we rewrite (6.19) as

$$\begin{vmatrix} \lambda_{\mathbf{K}} - E & U \\ U & \lambda_{\mathbf{K}-\mathbf{G}} - E \end{vmatrix} = 0 \,. \tag{6.21}$$

We find two solutions

$$E_{\pm} = \frac{1}{2}\left(\lambda_{\mathbf{K}} + \lambda_{\mathbf{K}-\mathbf{G}}\right) \pm \left[\frac{1}{4}\left(\lambda_{\mathbf{K}} - \lambda_{\mathbf{K}-\mathbf{G}}\right)^2 + U^2\right]^{1/2} \,. \tag{6.22}$$

For $\mathbf{K}$ in the vicinity of the zone boundary these solutions can be developed. Therefore, we use the (small) distance from the zone boundary $\widetilde{\mathbf{K}} = \mathbf{K} - \mathbf{G}/2$. With $\lambda = (\hbar^2/2m)\,(G^2/4)$ we rewrite still exactly (6.22):

$$E_{\pm}\left(\widetilde{\mathbf{K}}\right) = \frac{\hbar^2}{2m}\left(\frac{1}{4}\mathbf{G}^2 + \widetilde{\mathbf{K}}^2\right) \pm \left[4\lambda\,\frac{\hbar^2\widetilde{\mathbf{K}}^2}{2m} + U^2\right]^{1/2} \,. \tag{6.23}$$

For small $\widetilde{\mathbf{K}}$ with $\frac{\hbar^2\mathbf{G}\widetilde{\mathbf{K}}}{2m} \ll |U|$, the energy is then approximately given by

$$E_{\pm}\left(\widetilde{\mathbf{K}}\right) \cong \lambda \pm U + \frac{\hbar^2\widetilde{\mathbf{K}}^2}{2m}\left(1 \pm \frac{2\lambda}{U}\right) \,. \tag{6.24}$$

Thus the energy dispersionin the vicinity of the zone boundary is parabolic. The lower state has a negative curvature, the upper state a positive curvature. The curvature is

$$m^* = m \frac{1}{1 \pm 2\lambda/U} \approx \pm m \frac{U}{2\lambda} , \tag{6.25}$$

and will be later related to the *effective mass*. The approximation in (6.25) is valid for $|U| \ll 2\lambda$. We note that in our simple model m^* increases linearly with increasing band gap $2U$ (see Fig. 6.23 for experimental data).

6.2.5 Kramer's degeneracy

$E_\mathrm{n}(\mathbf{k})$ is the dispersion in a band. The time-reversal symmetry (Kramer's degeneracy) implies

$$E_{\mathrm{n}\uparrow}(\mathbf{k}) = E_{\mathrm{n}\downarrow}(-\mathbf{k}) , \tag{6.26}$$

where the arrow refers to the direction of the electron spin. If the crystal is symmetric under inversion, we have additionally

$$E_{\mathrm{n}\uparrow}(\mathbf{k}) = E_{\mathrm{n}\uparrow}(-\mathbf{k}) . \tag{6.27}$$

With both time reversal and inversion symmetry the band structure fulfills

$$E_{\mathrm{n}\uparrow}(\mathbf{k}) = E_{\mathrm{n}\downarrow}(\mathbf{k}) . \tag{6.28}$$

6.3 Band Structure of Selected Semiconductors

In the following, the band structures of various important and prototype semiconductors are discussed. The band below the energy gap is called the valence band; the band above the gap is the conduction band. The band gap ΔE_cv, mostly denoted as E_g, is the energy separation between the highest valence-band state and the lowest conduction-band state. The maximum of the valence band is for most semiconductors at the Γ point.

6.3.1 Silicon

For silicon, an elemental semiconductor (Fig. 6.5a), the minimum of the conduction band is located close to the X point at $0.85\pi/a$ in the $\langle 100 \rangle$ direction. Thus, it is not at the same point in $\mathbf{k}$ space as the top of the valence band. Such a band structure is called *indirect*. Since there are six equivalent $\langle 100 \rangle$ directions, there are six equivalent minima of the conduction band.

6.3.2 Germanium

Germanium, another elemental semiconductor (Fig. 6.5b), also has an indirect band structure. The conduction minima are at the L point in the $\langle 111 \rangle$ direction. Due to symmetry there are eight equivalent conduction-band minima.

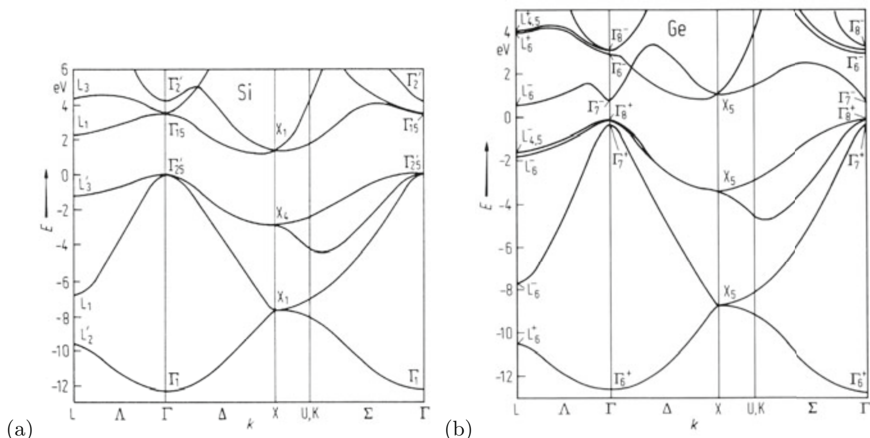

Fig. 6.5. Band structure of (**a**) silicon (indirect) and (**b**) germanium (indirect). In Si, the minima of the conduction band are in the ⟨100⟩ direction, for germanium in the ⟨111⟩ direction. From [192], based on [311]

6.3.3 GaAs

GaAs (Fig. 6.6a) is a compound semiconductor with a *direct* band gap since the top of the valence band and the bottom of the conduction band are at the same position in **k** space (at the Γ point). The next highest (local) minimum in the conduction band is close to the L point.

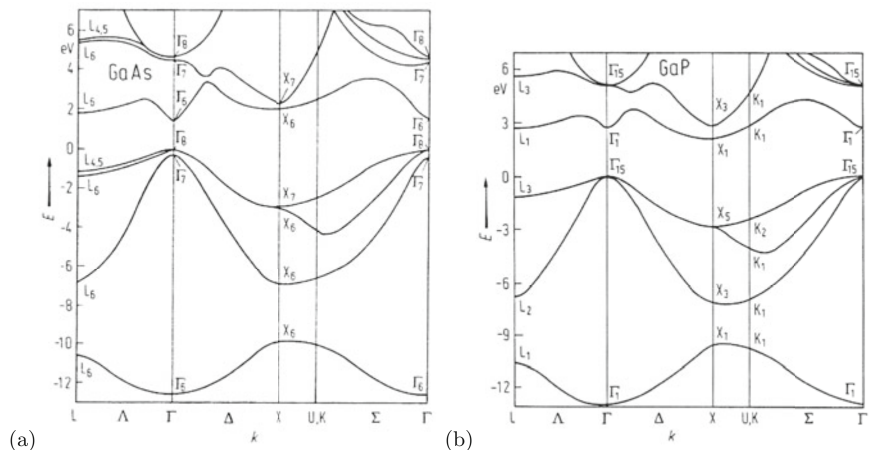

Fig. 6.6. Band structure of (**a**) GaAs (direct) and (**b**) GaP (indirect). For GaAs the minimum of the conduction band is at Γ, for GaP in the ⟨100⟩ direction. From [192], based on [311]

6.3.4 GaP

GaP (Fig. 6.6b) is an indirect compound semiconductor. The conduction-band minima are along the ⟨100⟩ directions.

6.3.5 GaN

GaN (Fig. 6.7) is a direct semiconductor that has wurtzite structure but can also occur in the metastable cubic (zincblende) phase.

6.3.6 Lead Salts

The band gap of PbS (Fig. 6.8), PbSe and PbTe is direct and located at the L point. The lead chalcogenide system shows the anomaly that with increasing atomic weight the band gap does not decrease monotonically. At 300 K, the band gaps are 0.41, 0.27 and 0.31 eV for PbS, PbSe and PbTe, respectively.

6.3.7 Chalcopyrites

The experimental band gaps of a number of chalcopyrite semiconductors are listed in Table 6.1. The band structures of $CuAlS_2$, $CuAlSe_2$, and $CuGaSe_2$ are compared in Fig. 6.9.

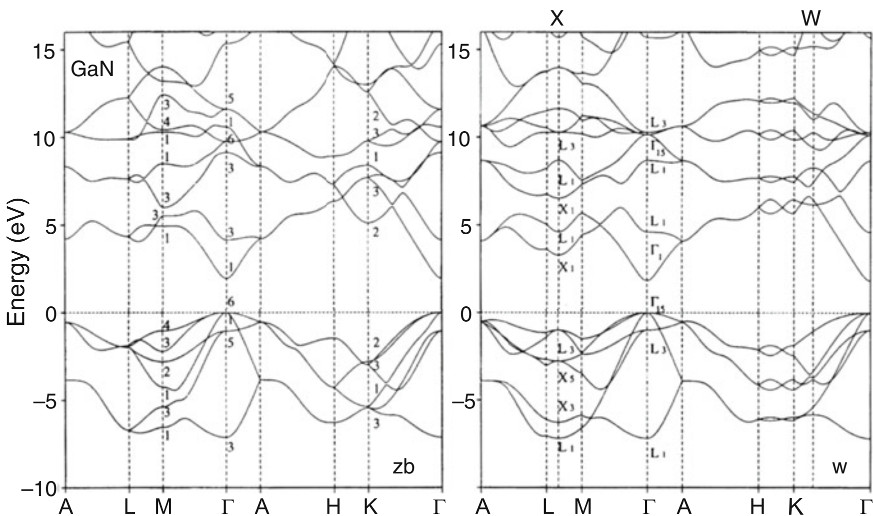

Fig. 6.7. Band structure of GaN (direct) in zincblende (zb) modification (*left*) and wurtzite (w) modification (*right*), both displayed in the wurtzite Brillouin zone to facilitate comparison

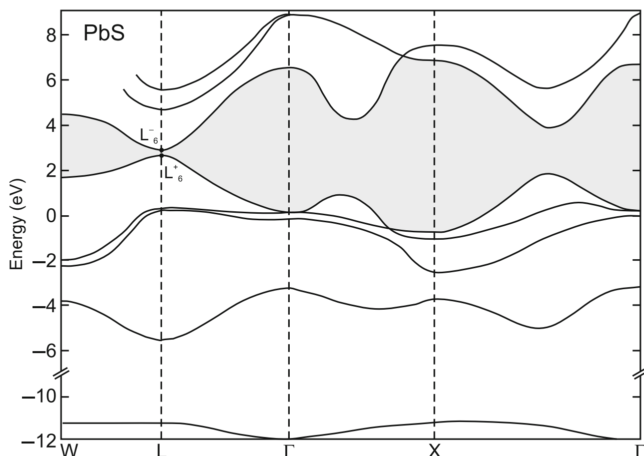

Fig. 6.8. Calculated band structure of PbS (direct). The energy gap is at the L point. The forbidden band is shown in *grey*. Adapted from [312]

Table 6.1. Band gaps of various chalcopyrite semiconductors

material	E_g (eV)		E_g (eV)		E_g (eV)
$CuAlS_2$	3.5	$CuGaS_2$	2.5	$CuInS_2$	1.53
$CuAlSe_2$	2.71	$CuGaSe_2$	1.7	$CuInSe_2$	1.0
$CuAlTe_2$	2.06	$CuGaTe_2$	1.23	$CuInTe_2$	1.0–1.15
$AgAlS_2$	3.13	$AgGaS_2$	2.55	$AgInS_2$	1.87
$AgAlSe_2$	2.55	$AgGaSe_2$	1.83	$AgInSe_2$	1.24
$AgAlTe_2$	2.2	$AgGaTe_2$	1.1–1.3	$AgInTe_2$	1.0
$ZnSiP_2$	2.96	$ZnGeP_2$	2.34	$ZnSnP_2$	1.66
$ZnSiAs_2$	2.12	$ZnGeAs_2$	1.15	$ZnSnAs_2$	0.73
$CdSiP_2$	2.45	$CdGeP_2$	1.72	$CdSnP_2$	1.17
$CdSiAs_2$	1.55	$CdGeAs_2$	0.57	$CdSnAs_2$	0.26

In Fig. 6.10, the theoretical band structure of GaN and its closest related chalcopyrite $ZnGeN_2$ are compared, both shown in the chalcopyrite (orthorhombic) Brillouin zone. The band gap of $ZnGeN_2$ is smaller than that of GaN and the difference of 0.4 eV is fairly well reproduced by the calculation[3] (giving 0.5 eV).

[3] Due to the local density approximation (LDA) the absolute values of the band gaps are too small by about 1 eV.

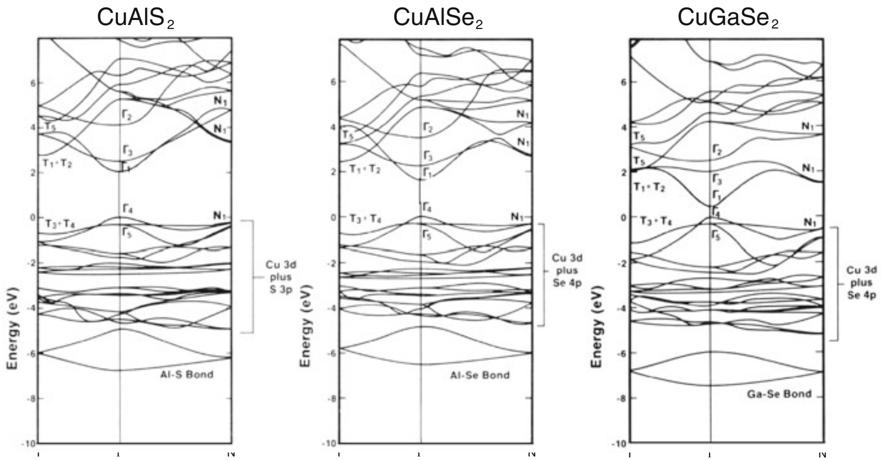

Fig. 6.9. Calculated band structures of $CuAlS_2$, $CuAlSe_2$, and $CuGaSe_2$. Absolute values of gaps are incorrect due to LDA. Adapted from [313]

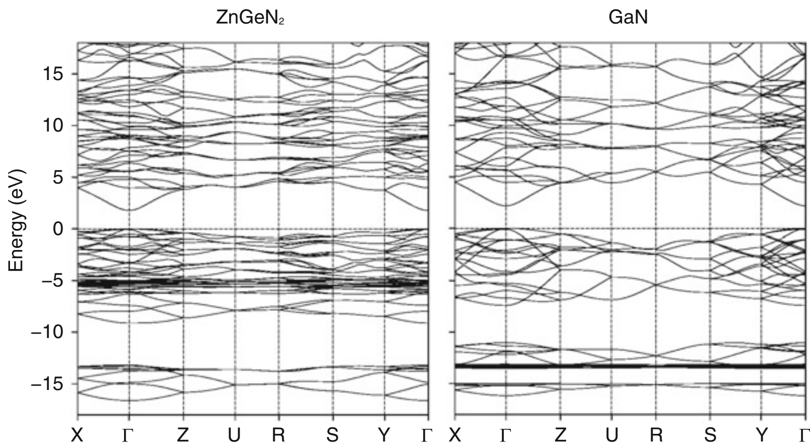

Fig. 6.10. Calculated (within LDA) band structures of $ZnGeN_2$ and its related III–V compound GaN, both displayed in the chalcopyrite (orthorhombic) Brillouin zone to facilitate comparison. Adapted from [314]

6.3.8 Delafossites

In Fig. 6.11, the theoretical band structures of the delafossites $CuAlO_2$, $CuGaO_2$, and $CuInO_2$ are shown. The maximum of the valence band is not at Γ but near the F point. The direct band gap at Γ decreases for the sequence Al $\rightarrow$ Ga $\rightarrow$ In, similar to the trend for AlAs, GaAs and InAs. The direct band gap at F and L, causing the optical absorption edge, increases, however (experimental values are 3.5, 3.6, and 3.9 eV).

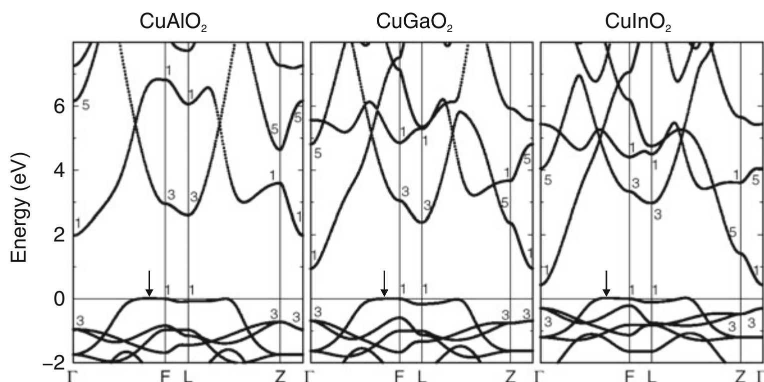

Fig. 6.11. Band structures of $CuAlO_2$, $CuGaO_2$, and $CuInO_2$, calculated with LDA (underestimating the absolute value of the band gaps). The *arrows* denote the maximum of the valence band that has been set to zero energy for each material. Adapted from [135]

6.3.9 Perovskites

The calculated band structure of $BaTiO_3$ in the tetragonal phase is shown in Fig. 6.12. The minimum of the conduction band is at the Γ point. The maximum of the valence band is not at the Γ point but at the M point. The band gap of the LDA[4] calculation is too small (2.2 eV) compared to the experimental value ~ 3.2 eV.

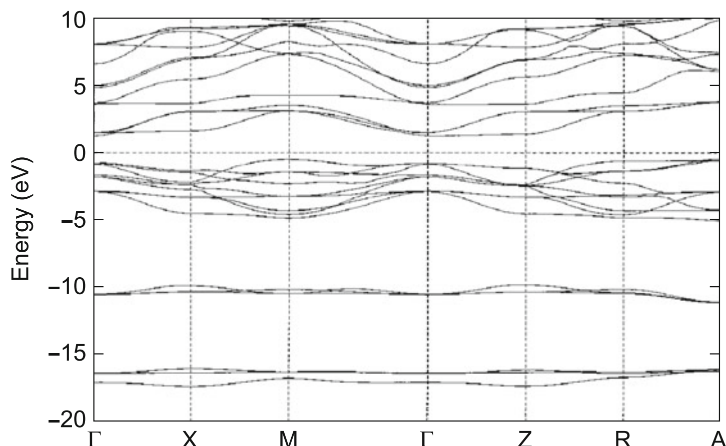

Fig. 6.12. Calculated energy band structure of $BaTiO_3$ along the major symmetry directions. The Fermi level (E_F) is set at zero energy. Adapted from [315]

[4]local density approximation

6.4 Alloy Semiconductors

In alloy semiconductors, the size of the band gap and the character of the band gap will depend on the composition. The dependence of the band gap on the ternary composition is mostly nonlinear and can usually be expressed with a bowing parameter b that is mostly positive. For a compound $A_xB_{1-x}C$ the band gap is written as

$$E_g(A_xB_{1-x}C) = E_g(BC) + x\,[E_g(AC) - E_g(BC)] - b\,x\,(1-x)\,. \tag{6.29}$$

Even on the virtual crystal approximation (VCA) level (Sect. 3.7.3) a nonzero bowing parameter b is predicted. However, a more thorough analysis shows that the bowing cannot be treated adequately within VCA and is due to the combined effects of volume deformation of the band structure with the alloy lattice constant, charge exchange in the alloy with respect to the binary end components, a structural contribution due to the relaxation of the cation–anion bond lengths in the alloy and a small contribution due to disorder [316].

The Si_xGe_{1-x} alloy has diamond structure for all concentrations and the position of the conduction-band minimum in **k**-space switches from L to X at about $x = 0.15$ (Fig. 6.13a). However, for all concentrations the band structure is indirect. The $In_xGa_{1-x}As$ alloy has zincblende structure for all compositions. The band gap is direct and decreases with a bowing parameter of $b = 0.6\,\text{eV}$ [317] (Fig. 6.13b). This means that for $x = 0.5$ the band gap is $0.15\,\text{eV}$ smaller than expected from a linear interpolation between GaAs and InAs, as reported by various authors [318].

If one binary end component has a direct band structure and the other is indirect, a transition occurs from direct to indirect at a certain composition. An example is $Al_xGa_{1-x}As$ where GaAs is direct and AlAs is indirect. For all concentrations the crystal has zincblende structure. In Fig. 6.13c, the Γ, L and X conduction-band minima for ternary $Al_xGa_{1-x}As$ are shown. Up to an aluminum concentration of $x = 0.4$ the band structure is direct. Above this value the band structure is indirect with the conduction-band minimum being at the X point. The particularity of $Al_xGa_{1-x}As$ is that the lattice constant is almost independent of x. For other alloys lattice match to GaAs or InP substrates is only obtained for specific compositions, as shown in Fig. 6.14.

If the two binary end components have different crystal structure, a phase transition occurs at a certain composition (range). An example is $Mg_xZn_{1-x}O$, where ZnO has wurtzite structure and MgO has rocksalt structure. The band gap is shown in Fig. 6.13d. In this case, each phase has its own bowing parameter.

All alloys of Fig. 6.13b–d have mixed cations. The band gap also varies upon anion substitution in a similar way as shown in Fig. 6.15 for ternary alloys with the cation Zn and the chalcogenides S, Se, Te and O.

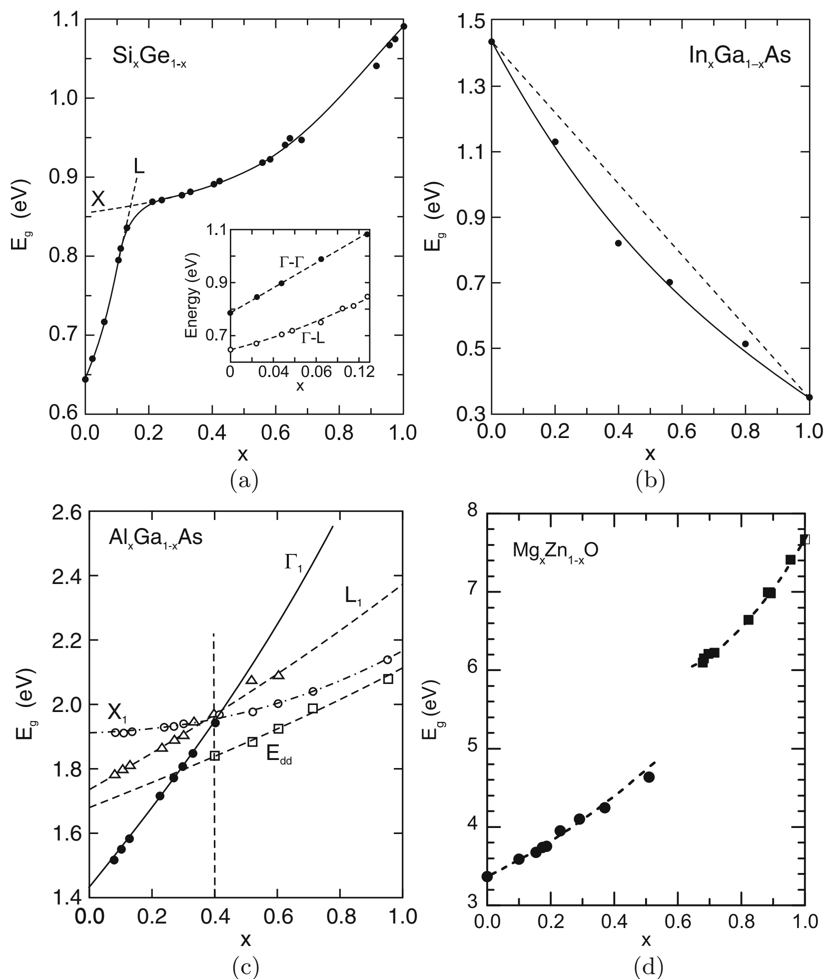

Fig. 6.13. (**a**) Band gap of Si_xGe_{1-x} alloy ($T = 296$ K) with a change from the conduction-band minimum at L (Ge-rich) to X. The *inset* depicts the transition energy of the indirect (Γ–L) and direct (Γ–Γ) absorption edge for low Si content. Adapted from [320]. (**b**) Band gap (at room temperature) of $In_xGa_{1-x}As$. The *solid line* is an interpolation with bowing ($b = 0.6$ eV) and the *dashed line* is the linear interpolation. Data from [317]. (**c**) Band gap (at room temperature) in the ternary system $Al_xGa_{1-x}As$. For $x < 0.4$ the alloy is a direct, for $x > 0.4$ an indirect, semiconductor. E_{dd} denotes the energy position of a deep donor (cf. Sect. 7.7.6). Adapted from [321]. (**d**) Band gap (at room temperature) in the ternary system $Mg_xZn_{1-x}O$. Data (from spectroscopic ellipsometry [322, 323]) are for hexagonal wurtzite phase (*circles*), and Mg-rich cubic rocksalt phase (*squares*). *Dashed lines* are fits to data with a different bowing parameter for each phase

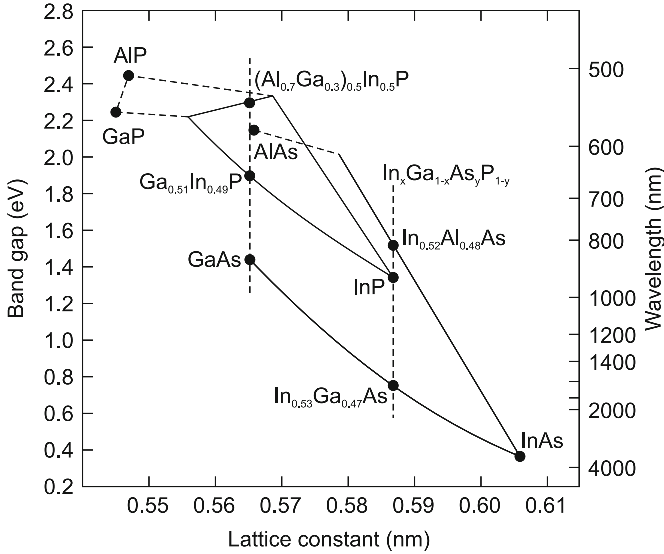

Fig. 6.14. Band gap vs. lattice constant for $Ga_xIn_{1-x}P$ and $Al_xIn_{1-x}P$ (lattice matched to GaAs) as well as for $In_xAl_{1-x}As$ and $In_xGa_{1-x}As$ alloys (lattice matched to InP)

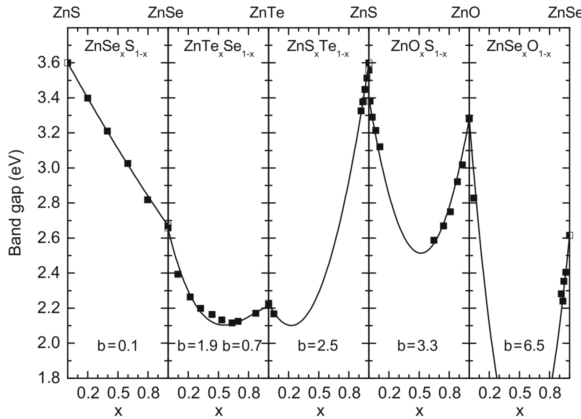

Fig. 6.15. Band gap of various Zn-based alloys. The *lines* are fits with (6.29), the bowing parameter b is labeled. Data for Zn(S,Se,Te) from [324], for Zn(O,Se/Te) from [325]

6.5 Amorphous Semiconductors

In a perfectly crystalline semiconductor the eigenenergies of the states in the bands are real. An amorphous semiconductor can be modeled using a spectrum of complex energies [319]. In Fig. 6.16 the band structure of

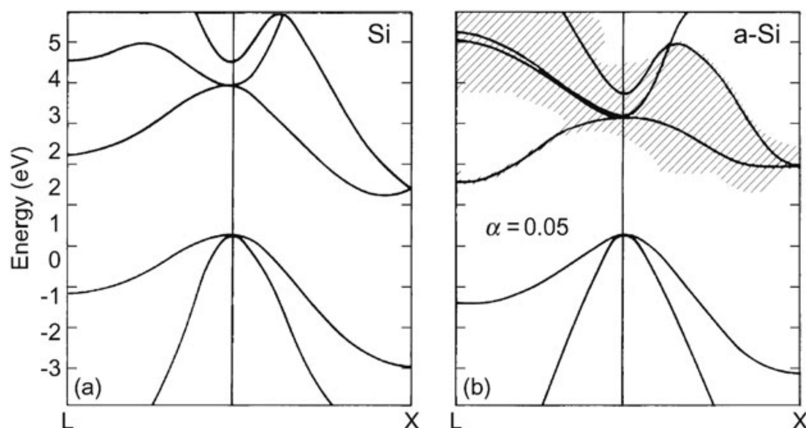

Fig. 6.16. (**a**) Calculated band structure of crystalline silicon. (**b**) Calculated band structure of amorphous silicon with $\alpha = 0.05$ (cf. (3.6)). The *solid lines* denote the real part of the energy, the *shaded areas* denote the regions with a width of twice the imaginary part of the energies centered around the real part. Adapted from [326]

crystalline silicon is shown next to that calculated for amorphous silicon with $\alpha = 0.05$.

6.6 Systematics of Semiconductor Band Gaps

The trends with regard to the size of the band gap for elemental, III–V and II–VI semiconductors can essentially be understood in terms of the bond strength and ionicity. In Fig. 6.17, the band gaps of many important

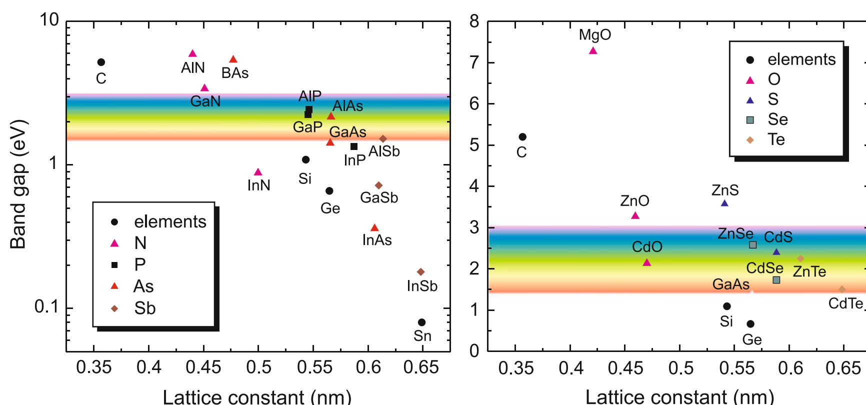

Fig. 6.17. Band gaps as a function of the lattice constant for various elemental, III–V and II–VI semiconductors. The lattice constant of wurtzite semiconductors has been recalculated for a cubic cell

semiconductors are shown as a function of the lattice constant. For elemental semiconductors, the band gap decreases with reduced bond strength, i.e. lattice constant (C→Si→Ge). A similar trend exists both for the III–V and the II–VI semiconductors.

For the same lattice constant, the band gap increases with increasing ionicity, i.e. IV–IV→III–V→II–VI. The best example is the sequence Ge→ GaAs→ZnSe for which all materials have almost the same lattice constant.

This behavior can be understood within the framework of a modified Kronig–Penney model [327] (Sect. 6.2.3). Double potential wells ($b/a = 3$) are chosen to mimic the diatomic planes along the ⟨111⟩ direction in the zincblende structure (Fig. 6.18a). Symmetric wells (depth P_0) are chosen to model covalent semiconductors and asymmetric wells with depths $P_0 \pm \Delta P$

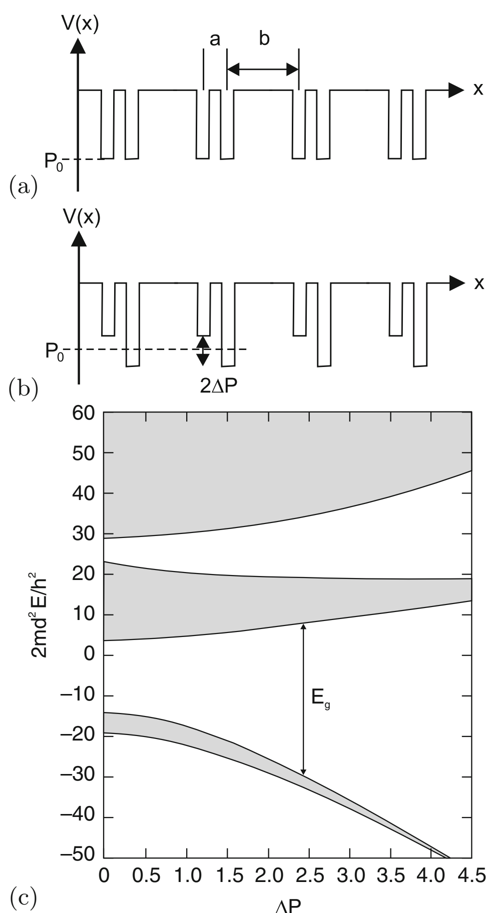

Fig. 6.18. Kronig–Penney model (along ⟨111⟩, $b/a = 3$) for a (**a**) IV–IV semiconductor and (**b**) for a III–V (or II–VI) semiconductor, (**c**) resulting band structure ($P_0 = -3$). d is the lattice constant ($b + a$). Adapted from [327]

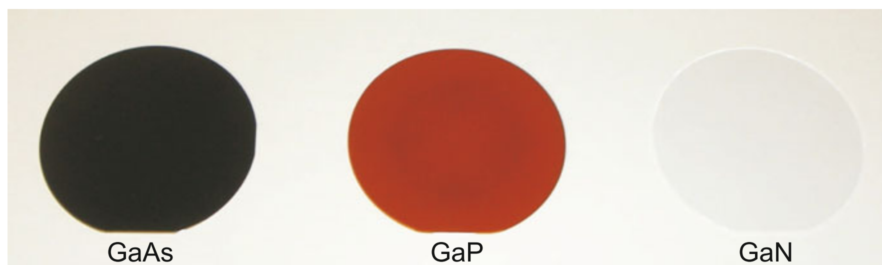

Fig. 6.19. Optical image of two inch wafers of GaAs (*left*), GaP (*center*) and ZnO (*right*). A GaN wafer would look like the ZnO wafer.

to model partially ionic semiconductors. Results are shown in Fig. 6.18a for $P_0 = -3$. With increasing asymmetry, i.e. ionicity, the band gap increases, mostly due to a downward shift of the valence band. The case of III–V (II–VI) semiconductors is reached for $\Delta P \approx 2$ (4).

In Fig. 6.19, the visual impression of 2" wafers of GaAs, GaP and GaN on white paper is shown. GaAs (and GaSb) is opaque since the band gap is below the visible spectral range. GaP has a band gap in the green and appears red, GaN has a band gap in the ultra-violet and thus appears transparent. As can be seen from Table. 6.2, the anion sequence Sb, As, P, and N leads to smaller lattice constant and higher ionicity.

We note that the band edge slightly depends on the isotope composition of the semiconductor [328]

Table 6.2. Comparison of band gap, lattice constant and ionicity of gallium–group V semiconductors for various anions. Lattice constant for GaN has been recalculated for a cubic cell.

anion	E_g (eV)	a_0 (nm)	f_i
N	3.4	0.45	0.50
P	2.26	0.545	0.33
As	1.42	0.565	0.31
Sb	0.72	0.61	0.26

6.7 Temperature Dependence of the Band Gap

The band gap typically decreases with increasing temperature (see Fig. 6.20 for Si and GaAs). The reasons for this are the change of electron–phonon interaction and the expansion of the lattice. The temperature coefficient may be written as

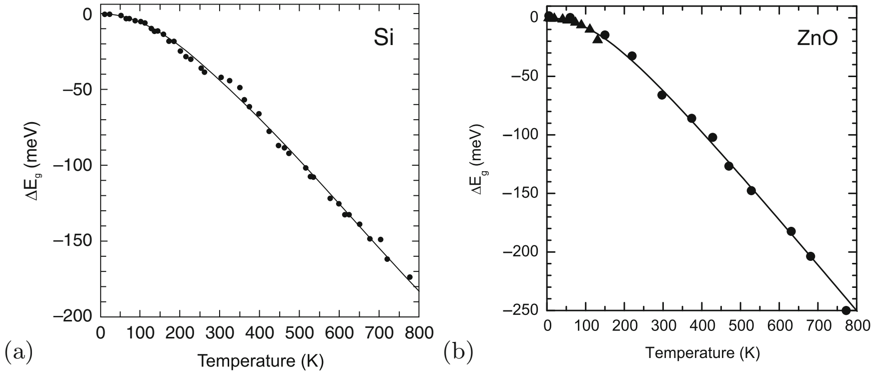

Fig. 6.20. Temperature dependence of the band gap of (**a**) Si (data from [331]) and (**b**) ZnO (experimental data from photoluminescence (*triangles*) and ellipsometry (*circles*)). The *solid lines* are fits with (6.33) and the parameters given in Table 6.3

$$\left(\frac{\partial E_{\mathrm{g}}}{\partial T}\right)_p = \left(\frac{\partial E_{\mathrm{g}}}{\partial T}\right)_V - \frac{\alpha}{\beta}\left(\frac{\partial E_{\mathrm{g}}}{\partial p}\right)_T , \tag{6.30}$$

where α is the volume coefficient of thermal expansion and β is the volume compressibility. A recommendable discussion of the thermodynamic role of the band gap as chemical potential for the mass action law (7.17), entropy contributions and its temperature dependence can be found in [329].

An anomaly is present for the lead salts (PbS, PbSe, PbTe) for which the temperature coefficient is positive (Fig. 6.21a). Theoretical calculations [330] show that both terms in (6.30) are positive for the lead salts. The L_6^+ and L_6^- levels (see Fig. 6.8) shift as a function of temperature in such a way that their separation increases (Fig. 6.21b).

For many semiconductors the temperature dependence can be described with the empirical, three-parameter Varshni formula [332],

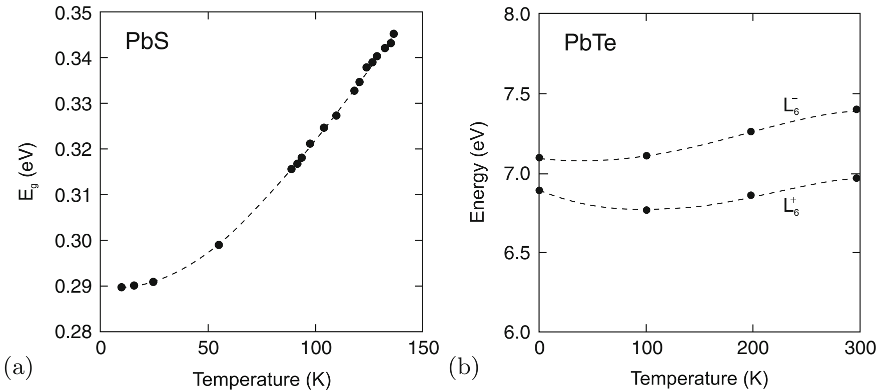

Fig. 6.21. (**a**) Band gap vs. temperature for PbS. (**b**) Theoretical position of L_6^+ and L_6^- as a function of temperature for PbTe. Adapted from [312]

$$E_g(T) = E_g(0) - \frac{\alpha T^2}{T + \beta} , \tag{6.31}$$

where $E_g(0)$ is the band gap at zero temperature. A more precise and physically motivated formula (based on a Bose–Einstein phonon model) has been given in [333]

$$E_g(T) = E_g(0) - 2\,\alpha_B\,\Theta_B \left[\coth\left(\frac{\Theta_B}{2T}\right) - 1\right] , \tag{6.32}$$

where α_B is a coupling constant and $k\Theta_B$ is a typical phonon energy; typical values are given in Table 6.3. This model reaches a better description of the fairly flat dependence at low temperatures. However, experimentally the dependence at low temperatures is rather quadratic.

The more elaborate model of [334] takes into account a more variable phonon dispersion, including optical phonons, and proposes the four-parameter formula

$$E_g(T) = E_g(0) - \alpha\,\Theta \left[\frac{1 - 3\Delta^2}{\exp(2/\gamma) - 1} + \frac{3\Delta^2}{2}\left(\sqrt[6]{1+\beta} - 1\right)\right] \tag{6.33}$$
$$\beta = \frac{\pi^2}{3(1+\Delta^2)}\gamma^2 + \frac{3\Delta^2 - 1}{4}\gamma^3 + \frac{8}{3}\gamma^4 + \gamma^6$$
$$\gamma = 2T/\Theta ,$$

where α is the high-temperature limiting magnitude of the slope (of the order of several 10^{-4} eV/K), Θ is an effective average phonon temperature and Δ is related to the phonon dispersion (typically between zero (Bose–Einstein model) and 3/4).

Table 6.3. Parameters for the temperature dependence of the band gap (6.32) and (6.33) for various semiconductors

	α (10^{-4} eV/K)	Θ (K)	Δ	α_B (10^{-4} eV/K)	Θ_B (K)
Si	3.23	446	0.51	2.82	351
Ge	4.13	253	0.49		
GaAs	4.77	252	0.43	5.12	313
InP	3.96	274	0.48		
InAs	2.82	147	0.68		
ZnSe	5.00	218	0.36		
ZnO	3.8	659	0.54		

6.8 Electron Dispersion

6.8.1 Equation of Electron Motion

The equation of motion for the electron in the band structure is no longer given by Netwon's law $\mathbf{F} = \mathrm{d}(m\mathbf{v})/\mathrm{d}t$ as in vacuum. Instead, the propagation of quantum-mechanical electron wave packets has to be considered. Their group velocity is given by ($v_\mathrm{g} = \partial\omega/\partial k$)

$$\mathbf{v} = \frac{1}{\hbar}\,\nabla_\mathbf{k} E(\mathbf{k})\;, \tag{6.34}$$

where $\nabla_\mathbf{k}$ is the gradient with respect to $\mathbf{k}$. Through the dispersion relation the influence of the crystal and its periodic potential on the motion enters the equation.

An electric field $\mathcal{E}$ acts on an electron during the time δt the work $\delta E = -e\mathcal{E}v_g\delta t$. This change in energy is related to a change in k via $\delta E = \mathrm{d}E/\mathrm{d}k\delta k = \hbar v_g \delta k$. Thus, we arrive at $\hbar\mathrm{d}k/\mathrm{d}t = -e\mathcal{E}$. For an external force we thus have

$$\hbar\frac{\mathrm{d}\mathbf{k}}{\mathrm{d}t} = -e\mathbf{E} = \mathbf{F}\;. \tag{6.35}$$

Thus, the crystal momentum $\mathbf{p} = \hbar\mathbf{k}$ takes the role of the momentum. A more rigorous derivation can be found in [310].

In the presence of a magnetic field $\mathbf{B}$ the equation of motion is:

$$\hbar\,\frac{\mathrm{d}\mathbf{k}}{\mathrm{d}t} = -e\,\mathbf{v}\times\mathbf{B} = -\frac{e}{\hbar}\,(\nabla_\mathbf{k} E)\times\mathbf{B}\;. \tag{6.36}$$

The motion in a magnetic field is thus perpendicular to the gradient of the energy, i.e. the energy of the electron does not change. It oscillates therefore on a surface of constant energy perpendicular to $\mathbf{B}$.

6.8.2 Effective Mass of Electrons

From the free-electron dispersion $E = \hbar^2k^2/(2m)$ the mass of the particle is inversely proportional to the curvature of the dispersion relation, i.e. $m = \hbar^2/(\mathrm{d}^2E/\mathrm{d}k^2)$. This relation will now be generalized for arbitrary dispersion relations. The tensor of the effective mass is defined as

$$(m^{*-1})_{ij} = \frac{1}{\hbar^2}\,\frac{\partial^2 E}{\partial k_i \partial k_j}\;. \tag{6.37}$$

The equation $\mathbf{F} = m^*\dot{\mathbf{v}}$ must be understood as a tensor equation, i.e. for the components of the force $F_i = m^*_{ij}a_j$. Force and acceleration must no longer be collinear. In order to find the acceleration from the force, the inverse of the effective-mass tensor must be used, $\mathbf{a} = (\mathbf{m}^*)^{-1}\,\mathbf{F}$.

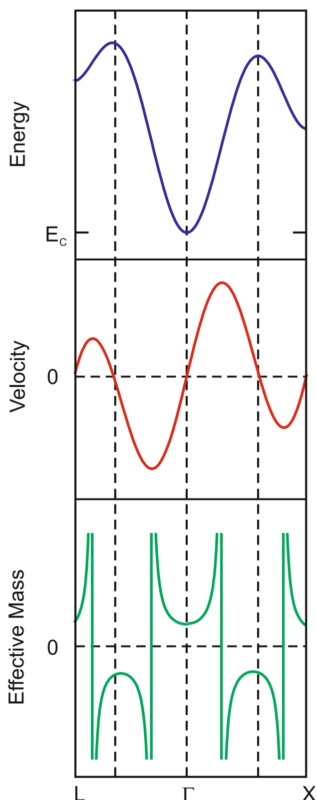

Fig. 6.22. Schematic diagram of the electron dispersion $E(\mathbf{k})$ in a typical semiconductor (*blue*) and corresponding carrier velocity ($\propto \partial E/\partial k$) (*red*) and effective mass ($\propto 1/(\partial^2 E/\partial k^2)$) (*green*)

In Fig. 6.22 the energy dispersion of the (lowest) conduction band in a typical semiconductor, the related electron velocity and the effective mass are shown schematically.

In (6.25) the ratio of the effective mass and the free-electron mass is of the order of $m^*/m \approx U/\lambda$, the ratio of the free particle energy and the band gap. For typical semiconductors, the width of the (valence) band is of the order of 20 eV, and the gap is about 0.2–2 eV. Thus, the effective mass is expected to be 10–100 times smaller than the free-electron mass. Additionally, the relation $m^* \propto E_\mathrm{g}$ is roughly fulfilled (Fig. 6.23).

From so-called $\mathbf{k}\cdot\mathbf{p}$ theory [331] (see Appendix F) the effective electron mass is predicted to be related to the momentum matrix element $\mathbf{p}_\mathrm{cv}$

$$\mathbf{p}_\mathrm{cv} = \langle c|\mathbf{p}|v\rangle = \int_{\Omega_0} u^*_{\mathrm{c},\mathbf{k}}(\mathbf{r})\,\mathbf{p}\,u_{\mathrm{c},\,\mathbf{k}}(\mathbf{r})\,\mathrm{d}^3\mathbf{r}\ , \tag{6.38}$$

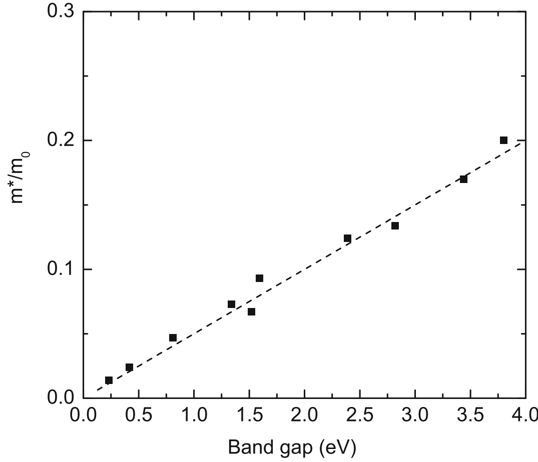

Fig. 6.23. Effective electron mass (in units of the free-electron mass m_0) as a function of the (low-temperature) band gap for several (direct band gap) semiconductors. The *dashed line* fulfills $m^*/m_0 = E_\mathrm{g}/20\,\mathrm{eV}$

with Ω_0 being the unit cell volume and the Bloch functions $|c\rangle$ and $|v\rangle$ of the conduction and valence band, respectively, given as

$$|c\rangle = u_{\mathrm{c},\mathbf{k}_\mathrm{c}}(\mathbf{r})\,\exp\left(\mathrm{i}\mathbf{k}_\mathrm{c}\mathbf{r}\right) \tag{6.39a}$$

$$|v\rangle = u_{\mathrm{v},\mathbf{k}_\mathrm{v}}(\mathbf{r})\,\exp\left(\mathrm{i}\mathbf{k}_\mathrm{v}\mathbf{r}\right)\ . \tag{6.39b}$$

Typically, the **k**-dependence of the matrix element is small and neglected. The momentum matrix element will also be important for optical transitions between the valence and conduction bands (Sect. 9.4). Other related quantities that are often used are the energy parameter E_P

$$E_\mathrm{P} = \frac{2\,|\mathbf{p}_\mathrm{cv}|^2}{m_0}\ , \tag{6.40}$$

and the bulk momentum matrix element M_b^2 that is given by

$$M_\mathrm{b}^2 = \frac{1}{3}\,|\mathbf{p}_\mathrm{cv}|^2 = \frac{m_0}{6}\,E_\mathrm{P}\ . \tag{6.41}$$

The electron mass is given by[5]

$$\begin{aligned}\frac{m_0}{m_\mathrm{e}^*} &= 1 + \frac{E_\mathrm{P}}{3}\left(\frac{2}{E_\mathrm{g}} + \frac{1}{E_\mathrm{g}+\Delta_0}\right) \\ &= 1 + E_\mathrm{P}\,\frac{E_\mathrm{g}+2\Delta_0/3}{E_\mathrm{g}\left(E_\mathrm{g}+\Delta_0\right)} \approx 1 + \frac{E_\mathrm{P}}{E_\mathrm{g}+\Delta_0/3} \approx \frac{E_\mathrm{P}}{E_\mathrm{g}}\ .\end{aligned} \tag{6.42}$$

[5] Δ_0 is the spin-orbit splitting discussed in Sect. 6.9.2.

Table 6.4. Longitudinal direction of effective mass ellipsoid, longitudinal and transverse effective electron mass in several semiconductors. Values for m_{l} and m_{t} in units of the free electron mass m_0

	long. dir.	m_{l}	m_{t}	$m_{\mathrm{l}}/m_{\mathrm{t}}$	Ref.
Si	{110}	0.98	0.19	5.16	[339]
Ge	{111}	1.59	0.082	19.4	[339]
ZnO	[00.1]	0.21	0.24	0.88	[340]
CdS	[00.1]	0.15	0.17	0.9	[341]

Comparison with the fit from Fig. 6.23 yields that E_{P} is similar for all semiconductors [336] and of the order of 20 eV (InAs: 22.2 eV, GaAs: 25.7 eV, InP: 20.4 eV, ZnSe: 23 eV, CdS: 21 eV).

In silicon there are six conduction-band minima. The surfaces of equal energy are schematically shown in Fig. 6.24c. The ellipsoids are extended along the $\langle 100\rangle$ direction because the longitudinal mass (along the Δ path) is larger than the transverse mass in the two perpendicular directions (Table 6.4). For example, the dispersion relation around the [100] minimum is then given as (k_x^0 denotes the position of the conduction-band minimum)

$$E(\mathbf{k}) = \hbar^2 \left(\frac{(k_x - k_x^0)^2}{2m_{\mathrm{l}}} + \frac{k_y^2 + k_z^2}{2m_{\mathrm{t}}} \right) . \tag{6.43}$$

For germanium surfaces of constant energy around the eight conduction-band minima in the $\langle 111\rangle$ directions are depicted in Fig. 6.24d. The longitudinal and the transverse masses are again different. For GaAs, the conduction-band dispersion around the Γ point is isotropic, thus the surface of constant energy is simply a sphere (Fig. 6.24a). In wurtzite semiconductors the conduction-band minimum is typically at the Γ point. The mass along the c-axis is typically smaller than the mass within the (00.1) plane [337] ($m_{\mathrm{l}}/m_{\mathrm{t}} \approx 0.9$ for ZnO [338]), see Fig. 6.24b. In [337] also an anisotropy within the (00.1) plane is predicted.

The directional dependence of the mass can be measured with cyclotron resonance experiments with varying direction of the magnetic field. In Fig. 6.25, the field **B** is in the (110) plane with different azimuthal directions. When the (static) magnetic field makes an angle θ with the longitudinal axis of the energy surface, the effective mass is given as [342]

$$\frac{1}{m^*} = \sqrt{\frac{\cos^2\theta}{m_{\mathrm{t}}^2} + \frac{\sin^2\theta}{m_{\mathrm{t}} m_{\mathrm{l}}}} . \tag{6.44}$$

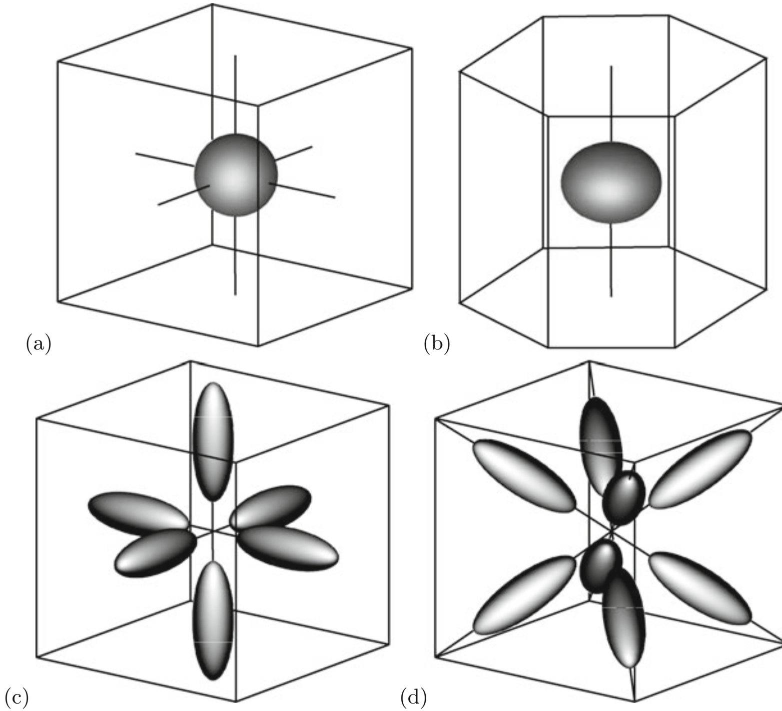

Fig. 6.24. Ellipsoids of constant energy in the vicinity of the conduction-band minima for (**a**) GaAs with isotropic minimum at Γ point, (**b**) ZnO with anisotropic minimum at Γ point (anisotropy exaggerated), (**c**) silicon with six equivalent anisotropic minima ($m_l/m_t = 5$ not to scale) along $\langle 100 \rangle$ and (**d**) germanium with eight equivalent anisotropic minima along $\langle 111 \rangle$. The cube indicates the $\langle 100 \rangle$ directions for the cubic materials. For the wurtzite material (part (**b**)) the vertical direction is along [00.1]

6.8.3 Polaron Mass

In an ionic lattice, the electron polarizes the ions and causes a change of their equilibrium position. When the electron moves, it must drag this ion displacement with it. This process it called the *polaronic* effect and requires additional energy [343, 344]. It leads to an increase of the electron mass to the 'polaron mass' m_p,[6]

$$m_p = m^* \left(1 + \frac{\alpha}{6} + 0.025\,\alpha^2 + \ldots\right) , \tag{6.45}$$

[6]For the calculation, many-particle theory and techniques are needed; the best solution is still given by Feynman's path integral calculation [344–346].

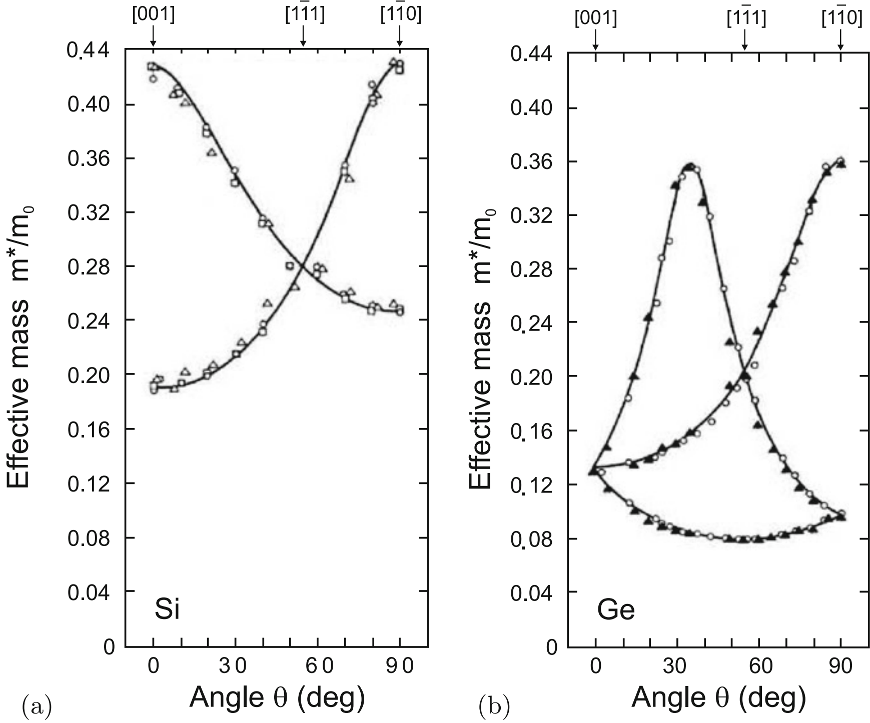

Fig. 6.25. Cyclotron mass (at $T = 4\,\mathrm{K}$) in (**a**) Si and (**b**) Ge for the magnetic field in the (110) plane and various azimuthal directions θ. Experimental data and fits (*solid lines*) using (6.44) with (**a**) $m_\mathrm{l} = 0.98$, $m_\mathrm{t} = 0.19$ and (**b**) $m_\mathrm{l} = 1.58$, $m_\mathrm{t} = 0.082$. Data from [339]

for $\alpha \leq 1$, with m^* being the band mass as defined in Sect. 6.8.2 and α the Fröhlich coupling constant[7]

$$\alpha = \frac{1}{2}\,\frac{e^2}{\hbar}\sqrt{\frac{2m^*}{\hbar\omega_\mathrm{LO}}}\left(\frac{1}{\epsilon_\infty} - \frac{1}{\epsilon_0}\right) . \tag{6.46}$$

Often, the polaron mass is given as $m_\mathrm{p} = m^*/(1 - \alpha/6)$ which is the result of perturbation theory [343] and an approximation to (6.45) for small α.

For large coupling parameter, $\alpha \gg 1$, the polaron mass is given by [345]

$$m_\mathrm{p} = m^*\,\frac{16}{81\,\pi^4}\,\alpha^4 . \tag{6.47}$$

[7]This constant is part of the matrix element in the Hamiltonian of the electron–phonon interaction and is related to the electric field created by LO phonons, as given in (5.51).

Table 6.5. Fröhlich coupling constant for various semiconductors. Data from [348]

GaSb	GaAs	GaP	GaN	InSb	InAs	InP	InN
0.025	0.068	0.201	0.48	0.022	0.045	0.15	0.24

3C-SiC	ZnO	ZnS	ZnSe	ZnTe	CdS	CdSe	CdTe
0.26	1.19	0.63	0.43	0.33	0.51	0.46	0.35

The energy of the electron is lowered due to the interaction with the lattice. The energy E_0 for $k = 0$ is given, relative to the uncoupled case, by

$$E_0 = -\left(\alpha + 0.0098\,\alpha^2 + \ldots\right)\,\hbar\omega_0 \quad , \alpha \leq 1 \tag{6.48a}$$

$$E_0 = -\left(2.83 + 0.106\,\alpha^2\right)\,\hbar\omega_0 \quad , \alpha \gg 1 \tag{6.48b}$$

Numerical results are reported in [347].

Polarons in semiconductors are typically 'large' or Fröhlich-type polarons, i.e. the coupling constant is small (Table 6.5). The dressing with phonons (as the ion displacement is called in a quantum-mechanical picture) is then only a perturbative effect and the number of phonons per electron ($\approx \alpha/2$) is small. If α becomes large ($\alpha > 1$, $\alpha \sim 6$), as is the case for strongly ionic crystals such as alkali halides, the polaron becomes localized by the electron–phonon interaction[8] and hopping occurs infrequently from site to site.

6.8.4 Nonparabolicity of Electron Mass

The dispersion around the conduction-band minimum is only parabolic for small **k**. The further away the wavevector is from the extremum, the more the actual dispersion deviates from the ideal parabola (see, e.g., Fig. 6.6). This effect is termed *nonparabolicity*. Typically, the energy increases less quickly with k than in the parabolic model. This can be described in a so-called two-level model with the dispersion relation

$$\frac{\hbar^2 k^2}{2m_0^*} = E\left(1 + \frac{E}{E_0^*}\right) , \tag{6.49}$$

where $E_0^* > 0$ parameterizes the amount of nonparabolicity (a parabolic band corresponds to $E_0^* = \infty$). The nonparabolic dispersion for GaAs is shown in Fig. 6.26a. The curvature is reduced for larger **k** and thus the effective mass

[8] One can think about it in the way that the electron strongly polarizes the lattice and digs itself a potential hole out of which it can no longer move.

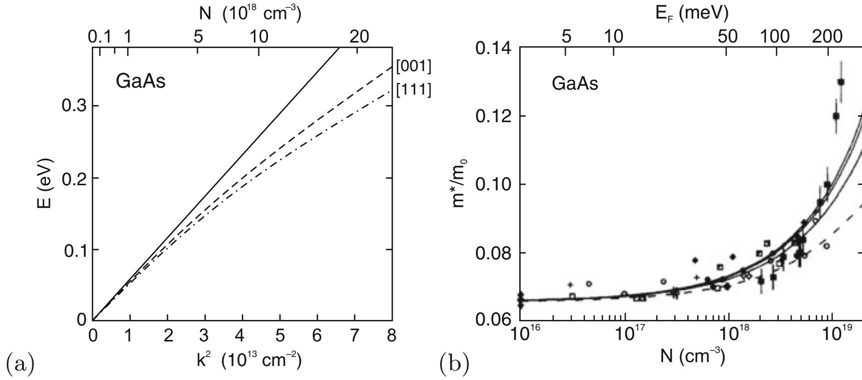

Fig. 6.26. (**a**) Dispersion relations for the conduction band of GaAs. The *solid line* is parabolic dispersion (constant effective mass). The *dashed* (*dash-dotted*) *line* denotes the dispersion for $\mathbf{k}$ along [001] ([111]) from a five-level $\mathbf{k} \cdot \mathbf{p}$ model (5LM). (**b**) Cyclotron resonance effective mass of electrons in GaAs as a function of the Fermi level (upper abscissa) and the corresponding electron concentration (lower abscissa). The *dashed line* is from a 2LM according to (6.50) with $E_0^* = 1.52\,\mathrm{eV}$. The *solid lines* are for a 5LM for the three principal directions of the magnetic field. The *symbols* represent experimental data from different sources. Data from [349]

is energy dependent and increases with the energy. Equation (6.49) leads to the energy-dependent effective mass

$$m^*(E) = m_0^* \left(1 + \frac{2E}{E_0^*}\right) , \tag{6.50}$$

where m_0^* denotes here the effective mass at $\mathbf{k} = 0$. Theory and experimental data for the effective electron mass of GaAs are shown in Fig. 6.26b.

6.9 Holes

6.9.1 Hole Concept

Holes are missing electrons in an otherwise filled band. A Schrödinger-type wave-equation for holes (unoccupied electron states) was derived by Heisenberg [42] to interpret Hall effect data. The hole concept is useful to describe the properties of charge carriers at the top of the valence band. The hole is a new quasi-particle whose dispersion relation is schematically shown in Fig. 6.27 in relation to the dispersion of electrons in the valence band.

The wavevector of the hole (filled circle in Fig. 6.27) is related to that of the 'missing' electron (empty circle in Fig. 6.27) by $k_\mathrm{h} = -k_\mathrm{e}$. The energy is $E_\mathrm{h}(k_\mathrm{h}) = -E_\mathrm{e}(k_\mathrm{e})$, assuming that $E_\mathrm{V} = 0$, otherwise $E_\mathrm{h}(k_\mathrm{h}) = -E_\mathrm{e}(k_\mathrm{e}) + 2E_\mathrm{V}$. The hole energy is larger for holes that are further away from the top

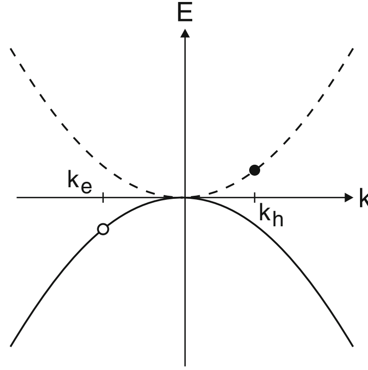

Fig. 6.27. Hole dispersion (*dashed line*) in relation to the electron dispersion in the valence band (*solid line*)

of the valence band, i.e. the lower the energy state of the missing electron. The velocity of the hole, $v_{\mathrm{h}} = \hbar^{-1}\mathrm{d}E_{\mathrm{h}}/\mathrm{d}k_{\mathrm{h}}$, is the same, $v_{\mathrm{h}} = v_{\mathrm{e}}$, and the charge is positive, $+e$. The effective mass of the hole is positive at the top of the valence band, $m_{\mathrm{h}}^* = -m_{\mathrm{e}}^*$. Therefore, the drift velocities of an electron and hole are opposite to each other. The resulting current, however, is the same.

6.9.2 Hole Dispersion Relation

The valence band at the Γ point is 3-fold degenerate. The band developed from the atomic (bonding) p states; the coupling of the spin $s = 1/2$ electrons with the orbital angular momentum $l = 1$ leads to a total angular momentum $j = 1/2$ and $j = 3/2$. The latter states are degenerate at Γ in zincblende bulk material and are called *heavy* holes (hh) for $m_j = \pm 3/2$ and *light* holes (lh) for $m_j = \pm 1/2$ due to their different dispersion (Fig. 6.28a). The two $(m_j = \pm{}^{/}2)$ states of the $j = 1/2$ state are split-off from these states by an energy Δ_0 due to spin-orbit interaction and are called *split-off* (s-o) holes. The spin-orbit interaction increases with increasing atomic order number Z of the anion since the electrons are located preferentially there (Fig. 6.29). A detailed discussion of the spin-orbit splitting in zincblende semiconductors is given in [350].

All three holes have different mass. In the vicinity of the Γ point the dispersion for heavy and light holes can be described with (+:hh, −:lh)

$$E(\mathbf{k}) = Ak^2 \pm \sqrt{B^2k^4 + C^2\left(k_{\mathrm{x}}^2k_{\mathrm{y}}^2 + k_{\mathrm{y}}^2k_{\mathrm{z}}^2 + k_{\mathrm{x}}^2k_{\mathrm{z}}^2\right)}\ . \tag{6.51}$$

For heavy and light holes there is a dependence of the dispersion, i.e. the mass, in the (001) plane. This effect, sketched in Fig. 6.28b, is called *warping*. The warping at the GaAs valence-band edge is shown in Fig. 6.30. (6.51) can also be expressed in terms of angular coordinates [351].

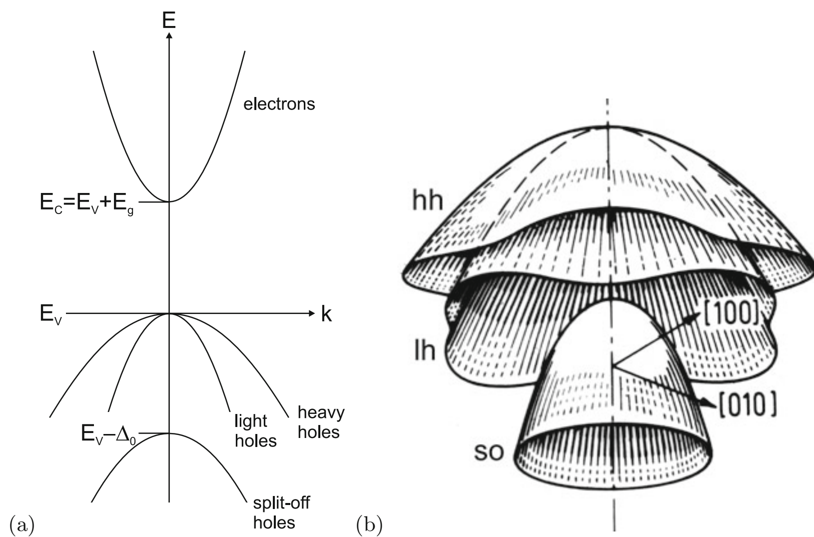

Fig. 6.28. (**a**) Simplified band structure with conduction band and three valence bands and (**b**) three-dimensional visualization (E vs. (k_x, k_y)) of the valence bands of Ge (including warping). Part (**b**) from [352]

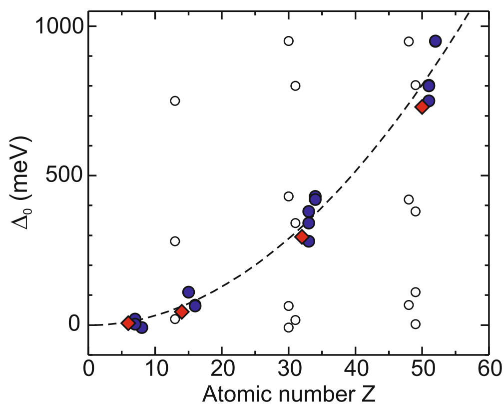

Fig. 6.29. Spin-orbit splitting Δ_0 for elemental (*diamonds*) and various III–V and II–VI (*circles*) semiconductors. The data are plotted as *empty* (*filled*) *circles* as a function of the cation (anion) order number. Obviously, Δ_0 correlates with the anion Z. The *dashed line* is proportional to Z^2.

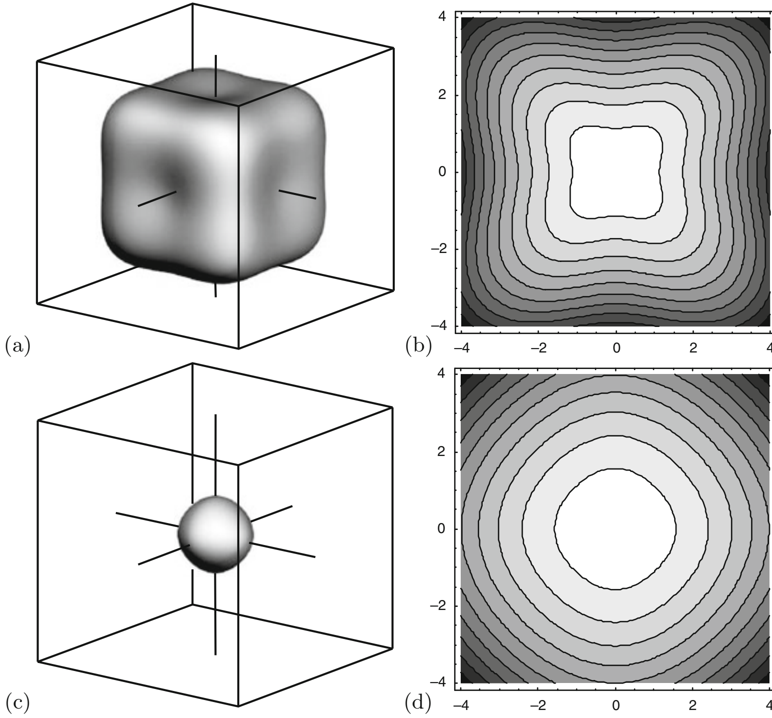

Fig. 6.30. Dispersion at the valence band edge of GaAs for (**a**,**b**) heavy holes and (**c**,**d**) light holes. (**a**,**c**) Constant energy surfaces and (**b**,**d**) isolines in the (k_x, k_y)-plane ((**b**) and (**d**) have different energy scales)

The s-o holes have the dispersion

$$E(\mathbf{k}) = -\Delta_0 + Ak^2 \; . \tag{6.52}$$

Values for A, B, C^2 and Δ_0 for a number of semiconductors are given in Table 6.6. The valence-band structure is often described with the Luttinger parameters γ_1, γ_2, and γ_3 that can be represented through A, B, and C via

$$\frac{\hbar^2}{2m_0}\gamma_1 = -A \tag{6.53a}$$

$$\frac{\hbar^2}{2m_0}\gamma_2 = -\frac{B}{2} \tag{6.53b}$$

$$\frac{\hbar^2}{2m_0}\gamma_3 = \frac{\sqrt{B^2 + C^2/3}}{2} \; . \tag{6.53c}$$

The mass of holes in various directions can be derived from (6.51). The mass along the [001] direction, i.e. $\hbar^2/\left(\partial^2 E(\mathbf{k})/\partial k_x^2\right)$ for $k_y = 0$ and $k_z = 0$, is

Table 6.6. Valence-band parameters (for (6.51)) A and B in units of $(\hbar^2/2m_0)$, C^2 in units of $(\hbar^2/2m_0)^2$, and Δ_0 in eV. From [192, 353, 354]

material	A	B	C^2	Δ_0
C	−4.24	−1.64	9.5	0.006
Si	−4.28	−0.68	24	0.044
Ge	−13.38	−8.5	173	0.295
GaAs	−6.9	−4.4	43	0.341
InP	−5.15	−1.9	21	0.11
InAs	−20.4	−16.6	167	0.38
ZnSe	−2.75	−1.0	7.5	0.43

$$\frac{1}{m_{\mathrm{hh}}^{100}} = \frac{2}{\hbar^2}(A+B) \tag{6.54a}$$

$$\frac{1}{m_{\mathrm{lh}}^{100}} = \frac{2}{\hbar^2}(A-B)\,. \tag{6.54b}$$

The anisotropy of hole masses has been investigated with cyclotron resonance experiments (Fig. 6.31). For θ being the angle between the magnetic

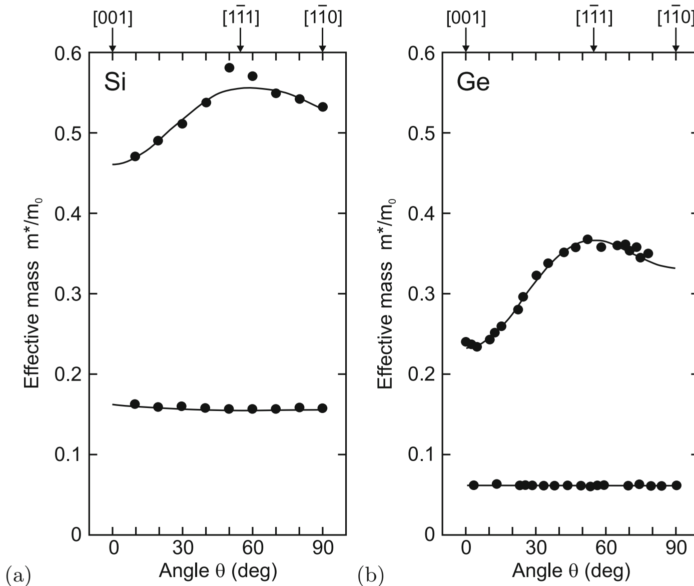

Fig. 6.31. Cyclotron resonance ($T = 4\,\mathrm{K}$) effective mass of (heavy and light) holes in (**a**) Si and (**b**) Ge for the magnetic field in the (110) plane and various azimuthal directions θ. Experimental data (*symbols*) and fits (*solid lines*) using (6.55). Adapted from [339]

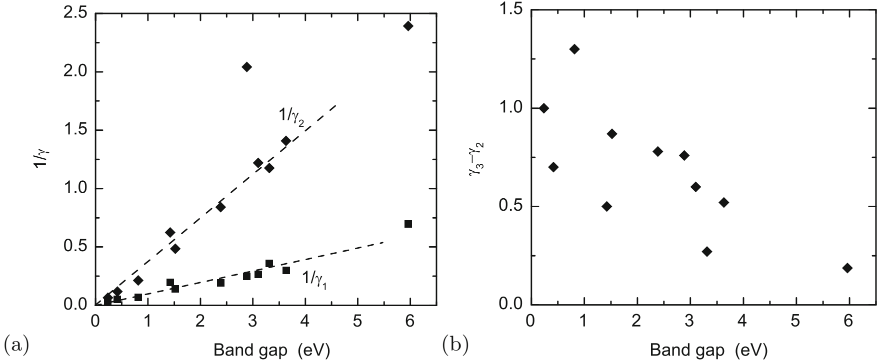

Fig. 6.32. Luttinger parameters for various III-V semiconductors vs. their band gap. (**a**) Inverse values of γ_1 (*squares*) and γ_2 (*diamonds*). *Dashed lines* are guides to the eyes. (**b**) $\gamma_3 - \gamma_2$ vs. band gap

field and the [001] direction, the effective heavy hole (upper sign) and light hole (lower sign) mass in cubic semiconductors is given by [339]

$$m^* = \frac{\hbar^2}{2} \frac{1}{A \pm \sqrt{B^2 + C^2/4}} \times \left\{ \frac{C^2 \, (1 - 3\cos^2\theta)^2}{64\sqrt{B^2 + C^2/4} \, \left[A \pm \sqrt{B^2 + C^2/4}\right]} + \ldots \right\} . \tag{6.55}$$

For $C^2 = 0$ the hole bands are isotropic, as is obvious from (6.51). In this case $\gamma_2 = \gamma_3$, the so-called spherical approximation. The average of the hole masses over all directions is

$$\frac{1}{m_{\mathrm{hh}}^{\mathrm{av}}} = \frac{2}{\hbar^2} \left(A + B \left[1 + \frac{2C^2}{15B^2} \right] \right) \tag{6.56a}$$

$$\frac{1}{m_{\mathrm{lh}}^{\mathrm{av}}} = \frac{2}{\hbar^2} \left(A - B \left[1 + \frac{2C^2}{15B^2} \right] \right) . \tag{6.56b}$$

Similar to the correlation of the electron mass with the band gap (Fig. 6.23), the Luttinger parameters are correlated with the band gap as shown in Fig. 6.32. The parameters $1/\gamma_1$ and $1/\gamma_2$ increase about linearly with E_{g}. The parameter $\gamma_3 - \gamma_2$, which is responsible for the valence band warping, decreases with increasing band gap.

6.9.3 Valence-Band Fine Structure

In Fig. 6.33, the schematic structure of the band edges for zincblende structure semiconductors is shown. The s-o holes in the zincblende structure are

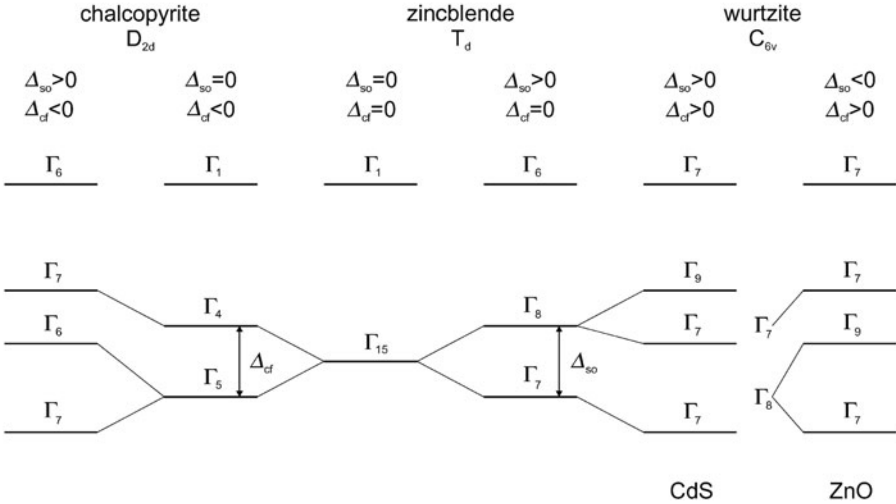

Fig. 6.33. Schematic band structure of zincblende and the valence-band splitting due to spin-orbit interaction Δ_{so} and crystal field splitting Δ_{cf} for chalcopyrites (typically $\Delta_{\mathrm{cf}} < 0$, see Fig. 6.34) and wurtzites. For the wurtzites the situation is schematically shown for CdS ($\Delta_{\mathrm{so}} = 67\,\mathrm{meV}$, $\Delta_{\mathrm{cf}} = 27\,\mathrm{meV}$) (or GaN) and ZnO ($\Delta_{\mathrm{so}} = -8.7\,\mathrm{meV}$, $\Delta_{\mathrm{cf}} = 41\,\mathrm{meV}$)

split-off due to the spin-orbit interaction Δ_{so}, the Γ_8 band is degenerate (heavy and light holes). Degeneracies for the holes are removed in the wurtzite and chalcopyrite structures by the additional crystal field splitting Δ_{cf} due to the anisotropy between the a- and c-axes. Typically, e.g. for CdS, the topmost valence band in the wurtzite structure has Γ_9 symmetry (allowed optical transitions only for $\mathbf{E} \perp \mathbf{c}$); an exception is ZnO for which the two upper bands are believed to be reversed. In the chalcopyrite structure optical transitions involving the Γ_6 band are only allowed for $\mathbf{E} \perp \mathbf{c}$. The three hole bands are usually labeled A, B, and C from the top of the valence band.

The energy positions of the three bands (with respect to the position of the Γ_{15} band) in the presence of spin-orbit interaction and crystal field splitting are given within the quasi-cubic approximation [355] by

$$E_1 = \frac{\Delta_{\mathrm{so}} + \Delta_{\mathrm{cf}}}{2} \tag{6.57a}$$

$$E_{2,3} = \pm\sqrt{\left(\frac{\Delta_{\mathrm{so}} + \Delta_{\mathrm{cf}}}{2}\right)^2 - \frac{2}{3}\,\Delta_{\mathrm{so}}\,\Delta_{\mathrm{cf}}}\;. \tag{6.57b}$$

In chalcopyrites the crystal field splitting is typically negative (Fig. 6.34). It is approximately linearly related to $1 - \eta$ (for $\eta = c/2a$ see Sect. 3.4.6).

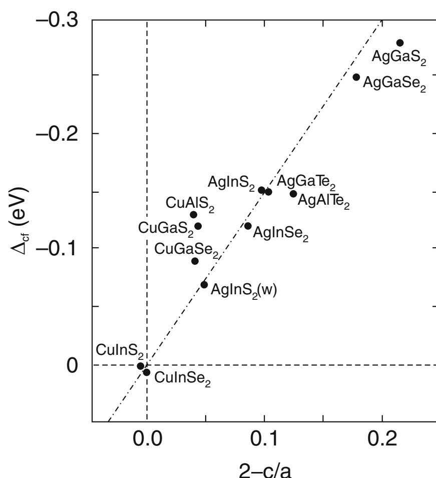

Fig. 6.34. Crystal field splitting Δ_{cf} for various chalcopyrite compounds vs. the tetragonal distortion $2-c/a = 2\,(1-\eta)$. *Dash-dotted line* represents $\Delta_{\mathrm{cf}} = 1.5\,b\,(2-c/a)$ for $b = 1\,\mathrm{eV}$. Data from [357]

In certain compounds the band gap can shrink to zero (zero-gap semiconductor, cf. Sect. 17.1.2) and even become negative in the sense that the Γ_6 symmetry (conduction) band is below the valence-band edge (Fig. 6.35). For the zero-gap case, the dispersion of some bands is linear (cmp. Sect. 17.1.2);

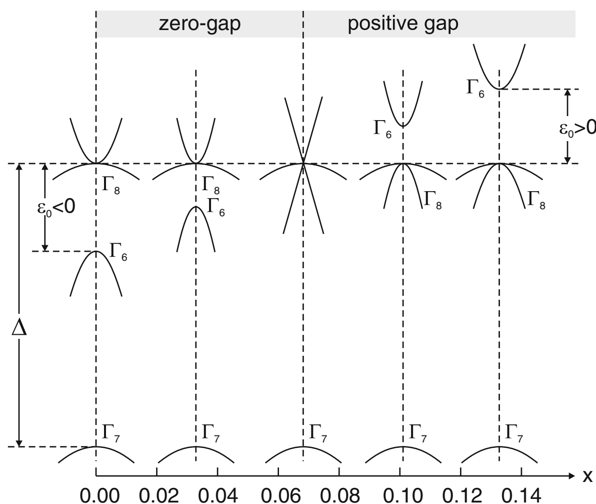

Fig. 6.35. Schematic band structure of zincblende with vanishing energy gap for the ternary compounds $\mathrm{Mn}_x\mathrm{Hg}_{1-x}\mathrm{Te}$. Note the linear dispersion for the zero-gap case at $x \approx 0.07$

this corresponds to a very strong non-parabolicity. The dielectric function of zero-gap semiconductors is discussed in [356].

6.10 Strain Effect on the Band Structure

A mechanical strain (or equivalently stress) causes changes in the bond lengths. Accordingly, the band structure is affected. These effects have been exhaustively treated in [358, 359]. For small strain, typically $\epsilon \lesssim 0.01$ the shift of the band edges is linear with the strain, for large strain it becomes nonlinear [360]. Often homogeneous strain is assumed, the effect of inhomogeneous strain is discussed in [361].

6.10.1 Strain Effect on Band Edges

In a direct-gap zincblende material the position of the conduction-band edge is only affected by the hydrostatic component of the strain

$$E_{\mathrm{C}} = E_{\mathrm{C}}^0 + a_{\mathrm{c}} \left(\epsilon_{\mathrm{xx}} + \epsilon_{\mathrm{yy}} + \epsilon_{\mathrm{zz}}\right) = E_{\mathrm{C}}^0 + a_{\mathrm{c}}\,\mathrm{Tr}(\epsilon) \;, \tag{6.58}$$

where $a_{\mathrm{c}} < 0$ is the conduction-band hydrostatic deformation potential and E_{C}^0 is the conduction-band edge of the unstrained material. Similarly, the valence-band edge is

$$E_{\mathrm{V}} = E_{\mathrm{V}}^0 + a_{\mathrm{v}}\,\mathrm{Tr}(\epsilon) \;, \tag{6.59}$$

where $a_{\mathrm{v}} > 0$ is the valence-band hydrostatic deformation potential. Therefore the band gap increases by

$$\Delta E_{\mathrm{g}} = a\,\mathrm{Tr}(\epsilon) = a\,\left(\epsilon_{\mathrm{xx}} + \epsilon_{\mathrm{yy}} + \epsilon_{\mathrm{zz}}\right) \;, \tag{6.60}$$

with $a = a_{\mathrm{c}} - a_{\mathrm{v}}$. Such linear behavior upon hydrostatic pressure has been found for many semiconductors and is shown in Fig. 6.36a for $\mathrm{Ga_{0.92}In_{0.08}As}$. The anomaly for N-doping is discussed below in Sect. 6.10.3. In Fig. 6.37 the dependence of the direct and indirect gaps of GaAs is shown. The dependence of the direct gap on pressure is non-linear, that on the density is linear [362].

Biaxial and shear strains affect the valence bands and lead to shifts and splitting of the heavy and light holes at the Γ point:

$$\begin{aligned} E_{\mathrm{v,hh/lh}} &= E_{\mathrm{v}}^0 \pm E_{\epsilon\epsilon} \\ E_{\epsilon\epsilon}^2 &= b^2/2\left[\left(\epsilon_{\mathrm{xx}} - \epsilon_{\mathrm{yy}}\right)^2 + \left(\epsilon_{\mathrm{yy}} - \epsilon_{\mathrm{zz}}\right)^2 + \left(\epsilon_{\mathrm{xx}} - \epsilon_{\mathrm{zz}}\right)^2\right] \\ &\quad + d^2\left[\epsilon_{\mathrm{xy}}^2 + \epsilon_{\mathrm{yz}}^2 + \epsilon_{\mathrm{xz}}^2\right] \;, \end{aligned} \tag{6.61a}$$

where E_{v}^0 denotes the bulk valence-band edge. b and d are the optical deformation potentials. For compressive strain the heavy-hole band is above the light-hole band. For tensile strain there is strong mixing of the bands (Fig. 6.38).

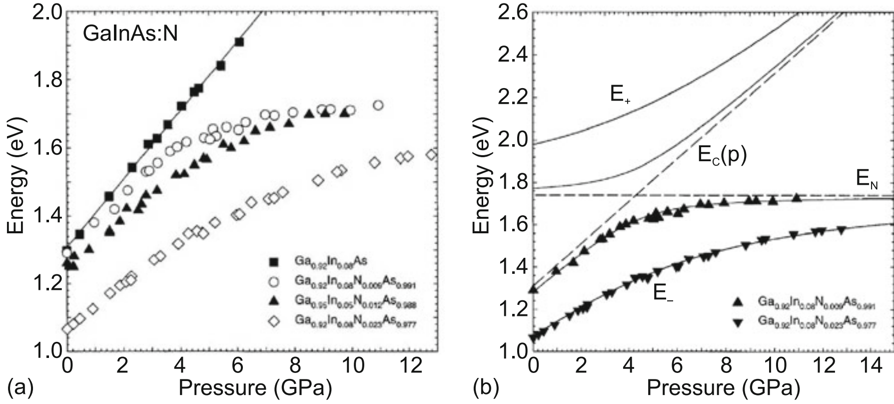

Fig. 6.36. (**a**) Dependence of the band gap of $Ga_{0.92}In_{0.08}As$ alloy (*squares*) and nitrogen-doped GaInAs on (compressive) hydrostatic pressure, determined by photomodulated transmission at $T = 295\,K$. (**b**) Pressure dependence of band gap for two GaInAsN samples together with model calculation (6.65). The coupling parameter is $V = 0.12\,eV$ (0.4 eV) for a nitrogen content of 0.9% (2.3%). Adapted from [363]

In Table 6.7 the deformation potentials for some III–V semiconductors are listed. Typical values are in the eV regime. In a wurtzite crystal, five deformation potentials are needed that are termed a and D_1–D_4 [364, 365].

In Si and Ge, three deformation potentials, termed a, b, d, are needed for the valence band and two for each conduction band minimum, Ξ_u and

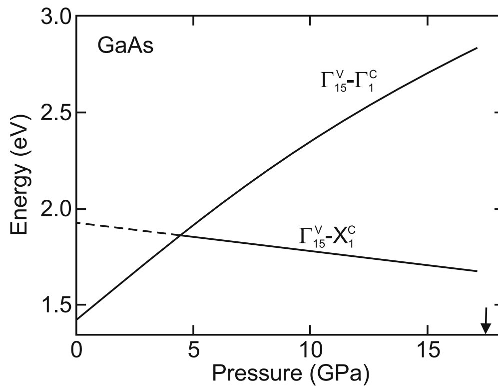

Fig. 6.37. Dependence of the direct Γ_{15}^{V}–Γ_{1}^{C} and indirect Γ_{15}^{V}–X_{1}^{C} band gap of GaAs ($T = 300\,K$) on pressure. *Solid lines* are interpolations of experimental data, *dashed line* is extrapolation to $p = 0$. The crossing of the direct and indirect band gap occurs at 4.2 GPa. The *arrow* denotes the pressure of the phase transition from zincblende to an orthorhombic structure around 17 GPa. Adapted from [362]

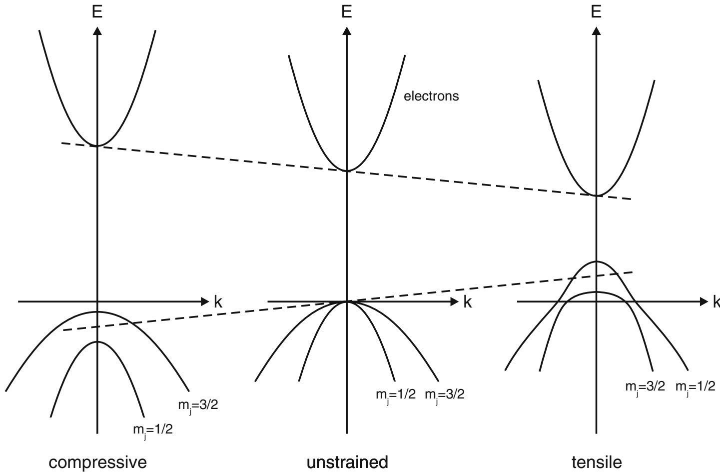

Fig. 6.38. Schematic band structure of GaAs in unstrained state (*center*) and under compressive and tensile biaxial strain as labeled. *Dashed lines* indicate shift of band edges due to hydrostatic part of strain

Table 6.7. Deformation potentials for some III–V semiconductors. All values in eV.

material	a	b	d
GaAs	−9.8	−1.7	−4.6
InAs	−6.0	−1.8	−3.6

Ξ_{d} [366]. The energy position of the i-th conduction-band edge (with unit vector $\mathbf{a}_i$ pointing to the valley) is

$$E_{\mathrm{C},i} = E^0_{\mathrm{C},i} + \Xi_{\mathrm{d}}\,\mathrm{Tr}(\boldsymbol{\epsilon}) + \Xi_{\mathrm{u}}\,\mathbf{a}_i\,\boldsymbol{\epsilon}\,\mathbf{a}_i \,, \tag{6.62}$$

where $E^0_{\mathrm{C},i}$ denotes the energy of the unstrained conduction-band edge. The deformation potentials for Si and Ge are given in Table 6.8.

Table 6.8. Deformation potentials for silicon and germanium. All values in eV from [367]

material	$\Xi_{\mathrm{d}}^{(\Delta)}$	$\Xi_{\mathrm{u}}^{(\Delta)}$	$\Xi_{\mathrm{d}}^{(\mathrm{L})}$	$\Xi_{\mathrm{u}}^{(\mathrm{L})}$	a	b	d
Si	1.1	10.5	−7.0	18.0	2.1	−2.33	−4.75
Ge	4.5	9.75	−4.43	16.8	2.0	−2.16	−6.06

6.10.2 Strain Effect on Effective Masses

In the presence of strain the band edges are shifted (cf. Sect. 6.10). Since the electron mass is related to the band gap, it is expected that the mass will also be effected. In the presence of hydrostatic strain ϵ_H the electron mass is [368] (cf. to (6.42) for $\epsilon_\mathrm{H} \to 0$)

$$\frac{m_0}{m_\mathrm{e}^*} = 1 + \frac{E_\mathrm{P}}{E_\mathrm{g} + \Delta_0/3} \left[1 - \epsilon_\mathrm{H} \left(2 + \frac{3a}{E_\mathrm{g} + \Delta_0/3} \right) \right] , \tag{6.63}$$

with a being the hydrostatic deformation potential and $\epsilon_\mathrm{H} = \mathrm{Tr}(\epsilon)$. In [368], formulas are also given for biaxial and shear strain and also for hole masses. Since the effective mass enters the mobility, the electrical conductivity depends on the stress state of the semiconductor (piezoresistivity, see Sect. 8.3.11).

6.10.3 Interaction with a Localized Level

The normal dependence of the band gap on hydrostatic pressure is linear and given by (6.60). GaInAs containing nitrogen exhibits a remarkable deviation from this behavior as shown in Fig. 6.36a. This is due to the interaction of the continuum states of the conduction band with the electron level of the isoelectronic nitrogen impurity (Sect. 7.7.9) E_N, being within the conduction band. For GaAs it is 0.2 eV above the conduction band edge E_C. This phenomenon has been investigated theoretically within microscopic detail [369]. Within a simple two-level model, the coupling of the pressure-dependent conduction band edge E_M and the nitrogen level can be obtained from solving the eigenwert equation

$$\begin{vmatrix} E - E_\mathrm{C} & V \\ V & E - E_\mathrm{N} \end{vmatrix} = 0 , \tag{6.64}$$

V being the coupling constant. The determinant vanishes for

$$E_\pm = \frac{1}{2} \left(E_\mathrm{C} + E_\mathrm{N} \pm \sqrt{(E_\mathrm{C} - E_\mathrm{N})^2 + 4V^2} \right) . \tag{6.65}$$

Here the weak pressure dependence of E_N is neglected for simplicity. This model can explain the pressure dependence of the band gap of GaInAs:N fairly well [363] (Fig. 6.36b). The coupling parameter V is in the order of a few 0.1 eV. In photomodulated reflection also the E_+ levels can be observed.

6.11 Density of States

6.11.1 General Band Structure

The dispersion relation yields how the energy of a (quasi-) particle depends on the **k** vector. Now we want to know how many states are at a given energy.

This quantity is called the *density of states* (DOS) and is written as $D(E)$. It is defined in an infinitesimal sense such that the number of states between E and $E+\delta E$ is $D(E)\delta E$. In the vicinity of the extrema of the band structure many states are at the same energy such that the density of states is high.

The dispersion relation of a band will be given as $E = E(\mathbf{k})$. If several bands overlap, the densities of state of all bands need to be summed up. The density of states at the energy $\tilde{E}$ for the given band is

$$D\left(\tilde{E}\right) \mathrm{d}E = 2 \int \frac{\mathrm{d}^3\mathbf{k}}{(2\pi/L)^3}\, \delta(\tilde{E} - E(\mathbf{k}))\ , \tag{6.66}$$

where, according to (5.5), $(2\pi/L)^3$ is the $\mathbf{k}$-space volume for one state. The factor 2 is for spin degeneracy. The integral runs over the entire $\mathbf{k}$-space and selects only those states that are at $\tilde{E}$. The volume integral can be converted to a surface integral over the isoenergy surface $S\left(\tilde{E}\right)$ with $E(\mathbf{k}) = \tilde{E}$. The volume element $\mathrm{d}^3\mathbf{k}$ is written as $\mathrm{d}^2S\mathbf{k}_\perp$. The vector $\mathbf{k}_\perp$ is perpendicular to $S\left(\tilde{E}\right)$ and proportional to $\nabla_\mathbf{k}E(\mathbf{k})$, i.e. $\mathrm{d}E = |\nabla_\mathbf{k}E(\mathbf{k})|\mathrm{d}\mathbf{k}_\perp$.

$$D\left(\tilde{E}\right) = 2 \int_{S(\tilde{E})} \frac{\mathrm{d}^2S}{(2\pi/L)^3}\, \frac{1}{|\nabla_\mathbf{k}E(\mathbf{k})|}\ . \tag{6.67}$$

In this equation, the dispersion relation is explicitly contained. At band extrema the gradient diverges, however, in three dimensions the singularities are integrable and the density of states takes a finite value. The corresponding peak is named a van-Hove singularity. The concept of the density of states is valid for all possible dispersion relations, e.g. for electrons, phonons or photons.

The density of states for the silicon band structure (see Fig. 6.5a) is shown in Fig. 6.39. If disorder is introduced, the density of states is modified as shown in Fig. 6.40 for amorphous germanium. The defects, as compared to the perfect lattice, introduced states in the band gap and generally wash out the sharp features from the crystalline DOS.

6.11.2 Free-Electron Gas

In M dimensions, the energy states of a free-electron gas are given as

$$E(\mathbf{k}) = \frac{\hbar^2}{2m^*} \sum_{i=1}^{M} k_i^2\ . \tag{6.68}$$

The k_i can take the values $\pm\pi n/L$ (in the first Brillouin zone) with $n \leq N$, N being the number of unit cells in one dimension. These values are equidistant in $\mathbf{k}$-space. Each M-dimensional $\mathbf{k}$-point takes a volume of $(2\pi/L)^M$. The number of states $N(E_\mathrm{F})$ up to the energy $E_\mathrm{F} = \frac{\hbar^2}{2m}k_\mathrm{F}^2$ (later used as Fermi energy E_F and Fermi vector k_F) is

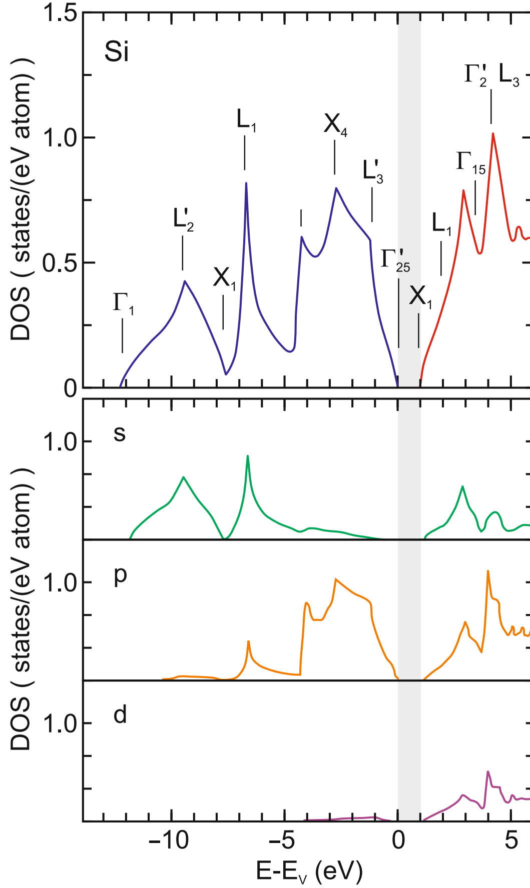

Fig. 6.39. Density of states in the silicon valence- (*blue*) and conduction-band (*red*) as obtained from theoretical calculation using empirical pseudopotentials. *Grey* regions denotes the band gap. Critical points (cf. Fig. 6.5a) are labeled. In the lower three graphs, the DOS is decomposed into contributions from different angular momentum states (s (*green*), p (*orange*) and d (*purple*)). *Top part* adapted from [370], *bottom part* adapted from [98]

$$N(E_{\mathrm{F}}) = \frac{2}{(2\pi/L)^M} \int_{\mathbf{k}=0}^{|\mathbf{k}|=k_{\mathrm{F}}} \mathrm{d}^M k \ . \tag{6.69}$$

The factor 2 is for spin degeneracy, the integration runs over M dimensions. The density of states is the derivative

$$D(E) = \frac{\mathrm{d}N}{\mathrm{d}E} \ . \tag{6.70}$$

In the following, the density of states for $M = 3, 2, 1$ and zero dimensions is derived. A visualization is given in Fig. 13.1.

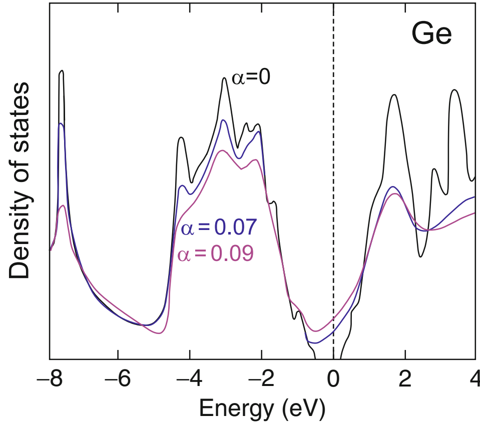

Fig. 6.40. Theoretical calculation for the density of states of amorphous Ge models as obtained for various degrees of disorder α (3.6). $\alpha = 0.09$ corresponds to a mean short-range order distance of about 2.4 lattice constants (cmp. Fig. 3.14b). Adapted from [114]

$M = 3$

This case relates to bulk material in which electrons are free to move in all three dimensions. Performing the integral (6.69) for $M = 3$ yields

$$N^{3\mathrm{D}} = \frac{V}{3\pi^2} k_\mathrm{F}^3 = \frac{V}{3\pi^2} \left(\frac{2mE_\mathrm{F}}{\hbar^2} \right)^{3/2} . \tag{6.71}$$

Therefore, k_F and E_F are given by

$$k_\mathrm{F} = \left(\frac{3\pi^2 N}{V} \right)^{1/3} \tag{6.72}$$

$$E_\mathrm{F} = \frac{\hbar^2}{2m^*} \left(\frac{3\pi^2 N}{V} \right)^{2/3} , \tag{6.73}$$

and the density of states in three dimensions is

$$D^{3\mathrm{D}}(E) = \frac{V}{2\pi^2} \left(\frac{2m^*}{\hbar^2} \right)^{3/2} \sqrt{E} . \tag{6.74}$$

$M = 2$

This case is important for thin layers in which the electron motion is confined in one direction and free in a plane. Such structures are called quantum wells (see Sect. 11.3.2). We find for the 2D density of states (for each subband over which it is not summed here, including spin degeneracy)

$$N^{2D} = \frac{A}{2\pi} k_F^2 = \frac{A}{\pi} \frac{m^*}{\hbar^2} E \,, \tag{6.75}$$

where A is the area of the layer. The density of states is thus constant and given by

$$D^{2D}(E) = \frac{A}{\pi} \frac{m^*}{\hbar^2} \,. \tag{6.76}$$

$M = 1$

The case $M = 1$ describes a quantum wire in which the electron motion is confined in two dimensions and free in only one dimension. For this case, we find for a wire of length L

$$N^{1D} = \frac{2L}{\pi} k_F = \frac{2L}{\pi} \left(\frac{2m^* E}{\hbar^2} \right)^{1/2} \,. \tag{6.77}$$

The density of states becomes singular at $E = 0$ and is given by (for one subband)

$$D^{1D}(E) = \frac{L}{\pi} \left(\frac{2m^*}{\hbar^2} \right)^{1/2} \frac{1}{\sqrt{E}} \,. \tag{6.78}$$

$M = 0$

In this case electrons have no degrees of freedom, as, e.g., in a quantum dot, and each state has a δ-like density of states at each of the quantized levels.

7 Electronic Defect States

Über Halbleiter sollte man nicht arbeiten,
das ist eine Schweinerei,
wer weiß ob es überhaupt Halbleiter gibt.[1]
W. Pauli, 1931 [371]

7.1 Introduction

One cm^3 of a semiconductor contains about 5×10^{22} atoms. It is practically impossible to achieve perfect purity. Typical low concentrations of impurity atoms are in the 10^{12}–$10^{13}\,cm^{-3}$ regime. Such a concentration corresponds to a purity of 10^{-10}, corresponding to about one alien in the world's human population. In the beginning of semiconductor research the semiconductors were so impure that the actual semiconducting properties could only be used inefficiently. Nowadays, thanks to large improvements in high-purity chemistry, the most common semiconductors, in particular silicon, can be made so pure that the residual impurity concentration plays no role in the physical properties. However, the most important technological step for semiconductors is *doping*, the controlled incorporation of impurities, in order to manage the semiconductor's conductivity. Typical impurity concentrations used in doping are 10^{15}–$10^{20}\,cm^{-3}$. A milestone in the understanding of doping and the spreading of semiconductor technology was the 1950 textbook by Shockley [372].

7.2 Fermi Distribution

In thermodynamic equilibrium, the distribution function for electrons is given by the Fermi–Dirac distribution (Fermi function) $f_e(E)$ (cf. Sect. E)

[1] One should not work on semiconductors. They are a mess. Who knows whether semiconductors exist at all.

M. Grundmann, *The Physics of Semiconductors*, 2nd ed., Graduate Texts in Physics, DOI 10.1007/978-3-642-13884-3_7,

© Springer-Verlag Berlin Heidelberg 2010

$$f_{\mathrm{e}}(E) = \frac{1}{\exp\left(\frac{E-E_{\mathrm{F}}}{kT}\right) + 1} , \tag{7.1}$$

where k (or k_{B}) denotes the Boltzmann constant, T is the temperature, and E_{F} is the Fermi level, which is called the chemical potential μ in thermodynamics. The Fermi distribution is shown in Fig. 7.1 for various parameters. The distribution function gives the probability that a state at energy E is populated in thermodynamic equilibrium. For $E = E_{\mathrm{F}}$ the population is 1/2 for all temperatures. At (the unrealistic case of) $T = 0$, the function makes a step from 1 (for $E < E_{\mathrm{F}}$) to 0.

The high-energy tail of the Fermi distribution, i.e. for $E - E_{\mathrm{F}} \gg kT$, can be approximated by the Boltzmann distribution:

$$f_{\mathrm{e}}(E) \cong \exp\left(-\frac{E - E_{\mathrm{F}}}{kT}\right) . \tag{7.2}$$

If the Boltzmann distribution is a good approximation, the carrier distribution is called *nondegenerate*. If the Fermi distribution needs to be invoked,

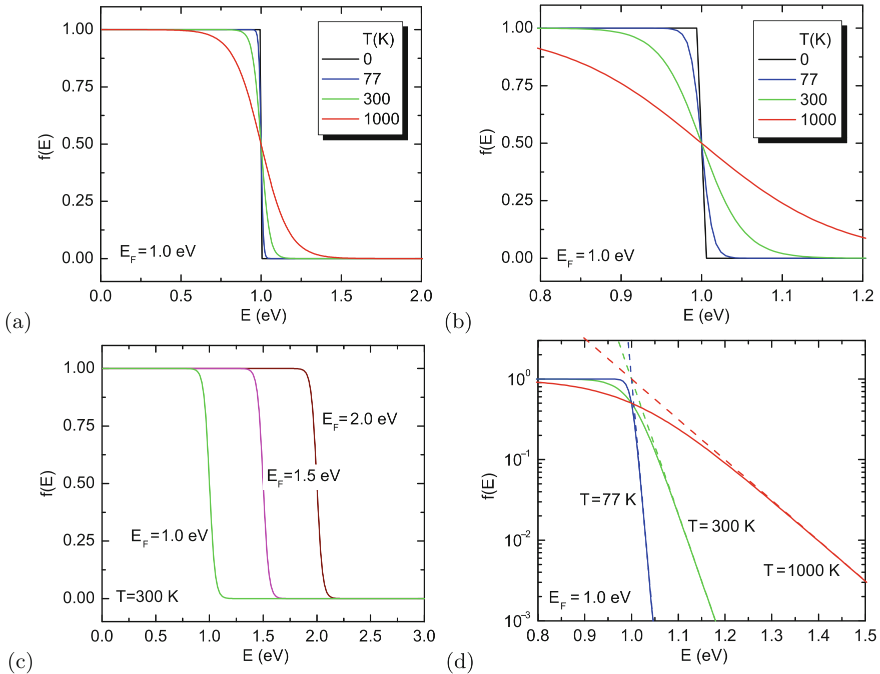

Fig. 7.1. Fermi function for (**a**,**b**) different temperatures (for $E_{\mathrm{F}} = 1.0\,\mathrm{eV}$) and (**c**) for different chemical potentials (for $T = 300\,\mathrm{K}$). (**d**) Fermi function (*solid lines*) compared with Boltzmann approximation (*dashed lines*) for various temperatures and $E_{\mathrm{F}} = 1.0\,\mathrm{eV}$ on semilogarithmic plot

the carrier ensemble is called *degenerate*. If the Fermi level is within the band the ensemble is highly degenerate.

7.3 Carrier Concentration

Generally, the density of electrons in the conduction band is given by

$$n = \int_{E_C}^{\infty} D_e(E)\, f_e(E)\, \mathrm{d}E\ , \tag{7.3}$$

and accordingly the density of holes in the valence band is

$$p = \int_{-\infty}^{E_V} D_h(E)\, f_h(E)\, \mathrm{d}E\ . \tag{7.4}$$

The energy of the top of the valence band is denoted by E_V, the bottom of the conduction band as E_C. The distribution function for holes is $f_h = 1 - f_e$. Thus,

$$f_h(E) = 1 - \frac{1}{\exp\left(\frac{E-E_F}{kT}\right) + 1} = \frac{1}{\exp\left(-\frac{E-E_F}{kT}\right) + 1}\ . \tag{7.5}$$

If several hole bands (hh, lh, so) are considered, the same distribution is valid for all hole bands in thermal equilibrium.

We assume parabolic band edges, i.e. effective masses m_e and m_h for electrons and holes, respectively. The density of states in the conduction band (per unit volume) is given (for $E > E_C$) as (cf. (6.74))

$$D_e(E) = \frac{1}{2\pi^2}\left(\frac{2m_e}{\hbar^2}\right)^{3/2}\sqrt{E - E_C}\ . \tag{7.6}$$

If, in the previous consideration the Boltzmann approximation cannot be applied, i.e. at high temperatures or for very small band gaps, the integral over Df cannot be explicitly (or analytically) evaluated. In this case the Fermi integral is needed that is defined[2] as

$$F_n(x) = \frac{2}{\sqrt{\pi}} \int_0^{\infty} \frac{y^n}{1 + \exp(y - x)}\, \mathrm{d}y\ . \tag{7.7}$$

In the present case of bulk materials $n = 1/2$. For large negative argument, i.e. $x < 0$ and $|x| \gg 1$, $F_{1/2}(x) \cong \sqrt{\pi}/2\exp(x)$, which is the Boltzmann approximation. $F_{1/2}(0) = 0.67809\ldots \approx 2/3$. For large argument, i.e. $x \gg 1$, $F_{1/2}(x) \approx 2/3x^{3/2}$. Such fairly simple approximations are plotted in Fig. 7.2

[2]Equation (7.7) is restricted to $n > -1$. A form without restriction is $\mathcal{F}_n(x) = \frac{1}{\Gamma(n+1)} \int_0^{\infty} \frac{y^n}{1+\exp(y-x)}\mathrm{d}y$. The factor $2/\sqrt{\pi}$ is often omitted but must be then added explicitly in, e.g., (7.8).

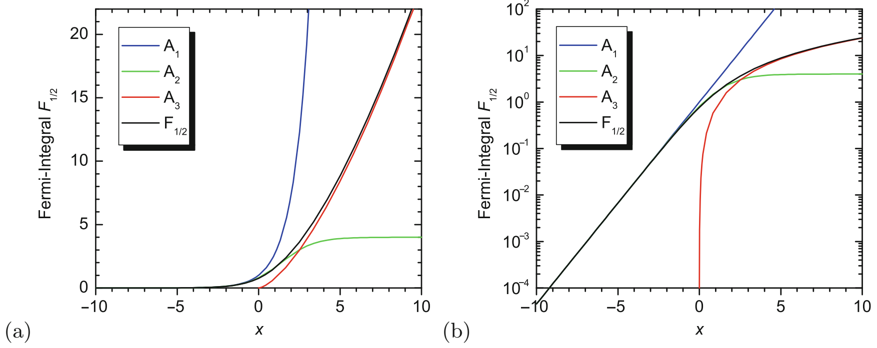

Fig. 7.2. Fermi integral $\hat{F}_{1/2} = (\sqrt{\pi}/2)F_{1/2}$ with approximations in three regions of the argument: $A_1(x) = (\sqrt{\pi}/2)\exp(x)$ for $x < 2$, $A_2(x) = (\sqrt{\pi}/2)(1/4+\exp(-x))^{-1}$ for $-2 < x < 2$, $A_3(x) = 2/3x^{3/2}$ for $x > 2$. (**a**) linear, (**b**) semilogarithmic plot

in comparison with the Fermi integral. For computations, analytical [373–375] or numerical approximations [376, 377] are used.

The derivative of the Fermi integral is given by $F_n'(x) = nF_{n-1}(x)$, $n > 0$. For $n = 0$, i.e. a two-dimensional system, the integral can be executed explicitly, $F_0(x) = \ln[1 + \exp(x)]$.

With the Fermi integral $F_{1/2}$ (7.15) and (7.16) then have the following expressions for the free-carrier densities:

$$n = N_{\mathrm{C}}\, F_{1/2}\left(\frac{E_{\mathrm{F}} - E_{\mathrm{C}}}{kT}\right) \tag{7.8}$$

$$p = N_{\mathrm{V}}\, F_{1/2}\left(-\frac{E_{\mathrm{F}} - E_{\mathrm{V}}}{kT}\right) , \tag{7.9}$$

with

$$N_{\mathrm{C}} = 2\left(\frac{m_{\mathrm{e}} kT}{2\pi\,\hbar^2}\right)^{3/2} \tag{7.10}$$

$$N_{\mathrm{V}} = 2\left(\frac{m_{\mathrm{h}} kT}{2\pi\,\hbar^2}\right)^{3/2} , \tag{7.11}$$

where N_{C} (N_{V}) is called the conduction-band (valence-band) edge density of states. If the conduction-band minimum is degenerate, a factor g_{v} (valley degeneracy) must be included, i.e. $g_{\mathrm{v}} = 6$ for Si and $g_{\mathrm{v}} = 8$ for Ge ($g_{\mathrm{v}} = 1$ for GaAs). This factor is typically included in the mass used in (7.10) that then becomes the density of states mass $m_{\mathrm{d,e}}$. If the conduction-band minimum has cylindrical symmetry in **k**-space, such as for Si and Ge, the mass that has to be used is

$$m_{\mathrm{d,e}} = g_{\mathrm{v}}^{2/3}\left(m_{\mathrm{t}}^2 m_{\mathrm{l}}\right)^{1/3} . \tag{7.12}$$

In the case of a degeneracy of the valence band, the states of several bands need to be summed for N_V. In bulk material, typically the heavy and light hole bands are degenerate at the Γ point. If the split-off band is not populated because of insufficient temperature, the valence-band edge density of states is given by

$$N_\mathrm{V} = 2\left(\frac{kT}{2\pi\hbar^2}\right)^{3/2}\left(m_\mathrm{hh}^{3/2} + m_\mathrm{lh}^{3/2}\right) . \tag{7.13}$$

Alternatively, the mass m_h in (7.11) can be taken as the density of states hole mass

$$m_\mathrm{d,h} = (m_\mathrm{hh}^{3/2} + m_\mathrm{lh}^{3/2})^{2/3} . \tag{7.14}$$

Values of $N_\mathrm{C,V}$ for Si, Ge and GaAs are given in Table 7.1.

Now, we assume that the Boltzmann approximation (7.2) can be used, i.e. the probability that a band state is populated is $\ll 1$. Then, the integral (7.3) can be executed analytically and the concentration n of electrons in the conduction band is given as

$$n = 2\left(\frac{m_\mathrm{e}kT}{2\pi\hbar^2}\right)^{3/2}\exp\left(\frac{E_\mathrm{F}-E_\mathrm{C}}{kT}\right) = N_\mathrm{C}\exp\left(\frac{E_\mathrm{F}-E_\mathrm{C}}{kT}\right) . \tag{7.15}$$

For the Boltzmann approximation and a parabolic valence band, the density of holes is given by

$$p = 2\left(\frac{m_\mathrm{h}kT}{2\pi\hbar^2}\right)^{3/2}\exp\left(-\frac{E_\mathrm{F}-E_\mathrm{V}}{kT}\right) = N_\mathrm{V}\exp\left(-\frac{E_\mathrm{F}-E_\mathrm{V}}{kT}\right) . \tag{7.16}$$

The product of the electron and hole density is

$$\begin{aligned} n\,p &= N_\mathrm{V}\,N_\mathrm{C}\exp\left(-\frac{E_\mathrm{C}-E_\mathrm{V}}{kT}\right) = N_\mathrm{V}\,N_\mathrm{C}\exp\left(-\frac{E_\mathrm{g}}{kT}\right) \\ &= 4\left(\frac{kT}{2\pi\hbar^2}\right)^{3}(m_\mathrm{d,e}\,m_\mathrm{d,h})^{3/2}\exp\left(-\frac{E_\mathrm{g}}{kT}\right) . \end{aligned} \tag{7.17}$$

Table 7.1. Band gap, intrinsic carrier concentration, conduction band and valence-band edge density of states at $T = 300\,\mathrm{K}$ for various semiconductors

	E_g (eV)	n_i (cm^{-3})	N_C (cm^{-3})	N_V (cm^{-3})
InSb	0.18	1.6×10^{16}		
InAs	0.36	8.6×10^{14}		
Ge	0.67	2.4×10^{13}	1.04×10^{19}	6.0×10^{18}
Si	1.124	1.0×10^{10}	7.28×10^{19}	1.05×10^{19}
GaAs	1.43	1.8×10^{6}	4.35×10^{17}	5.33×10^{18}
GaP	2.26	2.7×10^{0}		
GaN	3.3	$\ll 1$		

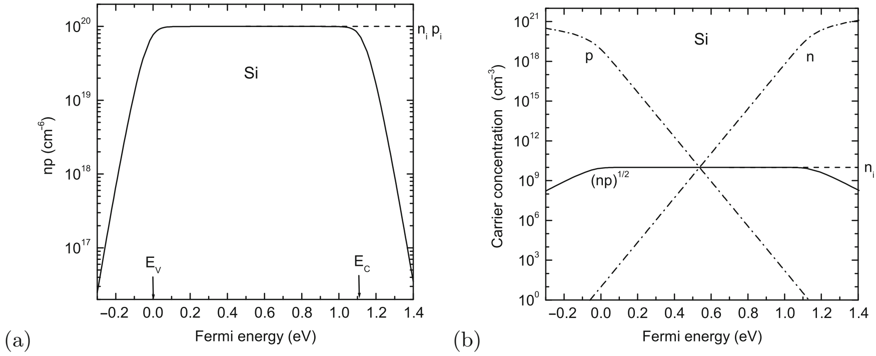

Fig. 7.3. (**a**) np for silicon at $T = 300\,\mathrm{K}$ as a function of the position of the Fermi level. The valence-band edge E_V is chosen as $E = 0$. np is constant for the range of Fermi energies given by (7.18) ($4kT \approx 0.1\,\mathrm{eV}$). (**b**) n, p and $\sqrt{np}$ as a function of the Fermi level

Thus, the product np is *independent* of the position of the Fermi level, as long as the Boltzmann approximation is fulfilled, i.e. the Fermi level is not in the vicinity of one of the band edges within several kT:

$$E_\mathrm{V} + 4kT < E_\mathrm{F} < E_\mathrm{C} - 4kT\ . \tag{7.18}$$

The relation (7.17) is called the mass-action law.

In Fig. 7.3, the product np is shown for silicon over a wide range of Fermi energies. If E_F is within the band gap, np is essentially constant. If the Fermi level is in the valence or conduction band, np decreases exponentially.

7.4 Intrinsic Conduction

First, we consider the conductivity of the intrinsic, i.e. an ideally pure, semiconductor. At $T = 0$ all electrons are in the valence band, the conduction band is empty and thus the conductivity is zero (a completely filled band cannot conduct current). Only at finite temperatures do the electrons have a finite probability to be in a conduction-band state and to contribute to the conductivity. Due to neutrality, the electron and hole concentrations in the intrinsic semiconductors are the same, i.e. each electron in the conduction band comes from the valence band,

$$-n + p = 0\ , \tag{7.19}$$

or $n_\mathrm{i} = p_\mathrm{i}$. Therefore

$$\begin{aligned} n_\mathrm{i} = p_\mathrm{i} &= \sqrt{N_\mathrm{V}\, N_\mathrm{C}}\, \exp\left(-\frac{E_\mathrm{g}}{2kT}\right) \\ &= 2\left(\frac{kT}{2\pi\hbar^2}\right)^{3/2} (m_\mathrm{e} m_\mathrm{h})^{3/4} \exp\left(-\frac{E_\mathrm{g}}{2kT}\right)\ . \end{aligned} \tag{7.20}$$

The mass-action law

$$n\,p = n_{\rm i}\,p_{\rm i} = n_{\rm i}^2 = p_{\rm i}^2 \tag{7.21}$$

will be essential also for doped semiconductors. The intrinsic carrier concentration is exponentially dependent on the band gap (Fig. 7.4). Thus, in thermodynamic equilibrium intrinsic wide-gap semiconductors have much smaller electron concentrations than intrinsic small-gap semiconductors (see Table 7.1). The intrinsic carrier concentration of Si has been determined to be (within 1%, T in K)

$$n_{\rm i}^{\rm Si} = 1.640 \times 10^{15}\, T^{1.706} \exp\left(-\frac{E_{\rm g}(T)}{2kT}\right) \tag{7.22}$$

for temperatures between 77 and 400 K [378, 379].

As we will see later in Part II, many semiconductor devices rely on regions of low conductivity (depletion layers) in which the carrier concentration is small. Since the carrier concentration cannot be smaller than the intrinsic concentration ($n + p \geq 2n_{\rm i}$), an increase of temperature leads to increasing ohmic conduction in the depletion layers and thus to a reduction or failure of device performance. The small band gap of Ge leads to degradation of bipolar device performance already shortly above room temperature. For silicon, intrinsic conduction limits operation typically to temperatures below about 300°C. For higher temperatures, as required for devices in harsh environments, such as close to motors or turbines, other semiconductors with wider band gaps need to be used, such as GaN, SiC or even diamond.

From the neutrality condition for the intrinsic semiconductor (7.19) and (7.15) and (7.16), the Fermi level of the intrinsic semiconductor can be determined as

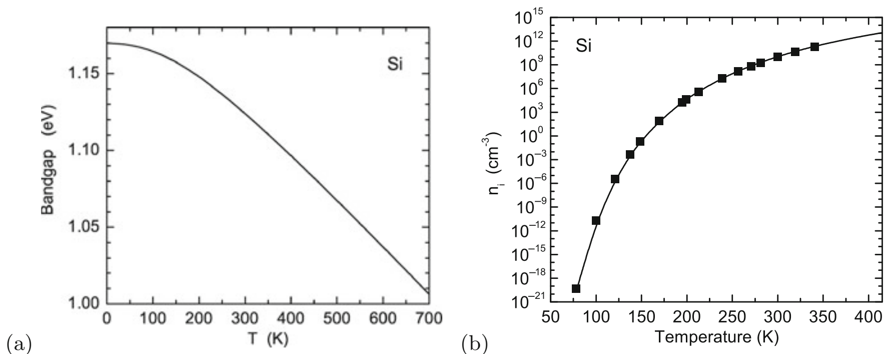

Fig. 7.4. (**a**) Band gap of silicon vs. temperature. (**b**) Intrinsic carrier concentration of silicon vs. temperature. *Solid line* is (7.22) using $E_{\rm g} = 1.204\,{\rm eV} - (2.73 \times 10^{-4}\,{\rm eV/K})\,T$ [380], *symbols* are experimental data from [381]

$$E_{\mathrm{F}} = \frac{E_{\mathrm{V}} + E_{\mathrm{C}}}{2} + \frac{kT}{2} \ln\left(\frac{N_{\mathrm{V}}}{N_{\mathrm{C}}}\right) = \frac{E_{\mathrm{V}} + E_{\mathrm{C}}}{2} + \frac{3}{4} kT \ln\left(\frac{m_{\mathrm{h}}}{m_{\mathrm{e}}}\right) . \quad (7.23)$$

Since the hole mass is perhaps a factor of ten larger than the electron mass, the second term has the order of kT. Thus, for typical semiconductors where $E_{\mathrm{g}} \gg kT$, the intrinsic Fermi level, denoted by E_{i}, is close to the middle of the band gap, i.e. $E_{\mathrm{i}} \approx (E_{\mathrm{C}} + E_{\mathrm{V}})/2$.

The situation for an intrinsic semiconductor is schematically shown in Fig. 7.5b.

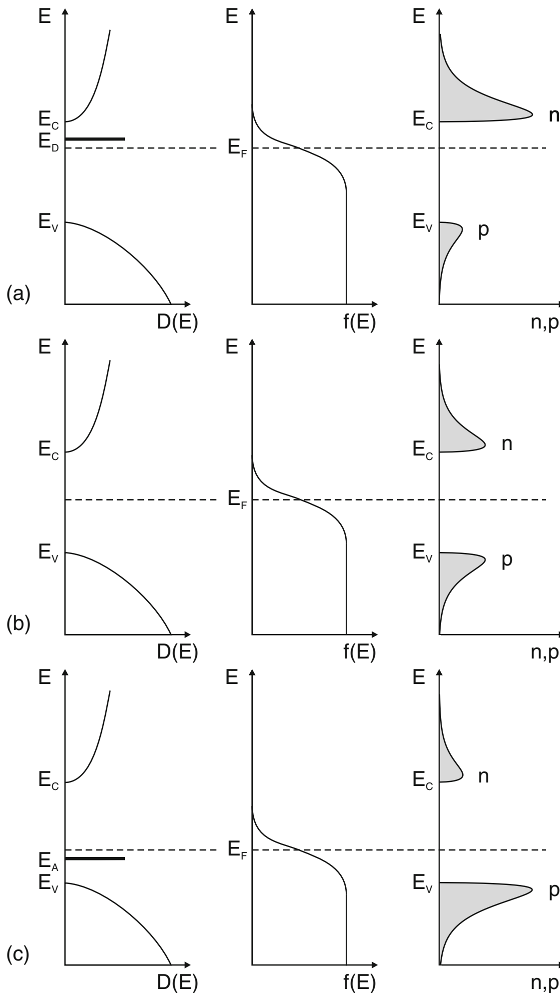

Fig. 7.5. Density of states (*left column*), Fermi distribution (*center column*) and carrier concentration (*right column*) for (**a**) n-type, (**b**) intrinsic and (**c**) p-type semiconductors in thermal equilibrium

7.5 Shallow Defects

The electronic levels of a defect or an impurity can be within the forbidden gap of the bulk host material. These levels can be close to the band edges or rather in the middle of the band gap. In 1930 electrical conduction of semiconductors was attributed solely to impurities [382]. However 'chemically pure' substances become conductive upon deviation from stoichiometry, e.g. historically found for changes in the anion concentration and conductivity in CuI [27] (p-type) and ZnO [47] (n-type).

In Fig. 7.6, the positions of the energy levels of a variety of impurities are shown for Ge, Si and GaAs. An impurity for which the long-range Coulomb part of the ion-core potential determines the energetic level is termed a *shallow* impurity. The extension of the wavefunction is given by the Bohr radius. This situation is in contrast to a *deep* level where the short-range part of the potential determines the energy level. The extension of the wavefunction is then of the order of the lattice constant.

We will consider first a group-IV semiconductor, Si, and (impurities) dopants from the groups III and V of the periodic system. When these are incorporated on a lattice site (with tetrahedral bonds), there is one electron too few (group III, e.g. B) or one electron too many (group V, e.g. As). The first case is called an *acceptor*, the latter a *donor*. The doping of III–V semiconductors is detailed in [383].

7.5.1 Donors

Silicon doped with arsenic is denoted as Si:As. The situation is schematically shown in Fig. 7.7. The arsenic atom has, after satisfying the tetrahedral bonds, an extra electron. This electron is bound to the arsenic atom via the Coulomb interaction since the ion core is positively charged compared to the silicon cores. If the electron is ionized, a fixed positive charge remains at the As site.

Without being in the silicon matrix, an arsenic atom has an ionization energy of 9.81 eV. However, in the solid the Coulomb interaction is screened by the dielectric constant of the material, typically ϵ_r is of the order of 10 for typical semiconductors. Additionally, the mass is renormalized (effective mass) by the periodic potential to a value that is smaller than the free-electron mass. Within effective-mass theory (Appendix G) Bohr's theory of the hydrogen problem is scaled with the (isotropic) effective mass m_e^* and the dielectric constant ϵ_r, the binding energy (ionization energy) E_D^b of the electron to the shallow donor is (relative to the continuum given by the conduction-band edge E_C)

$$E_\mathrm{D}^b = \frac{m_\mathrm{e}^*}{m_0} \frac{1}{\epsilon_\mathrm{r}^2} \frac{m_0 e^4}{2(4\pi\epsilon_0\hbar)^2} . \tag{7.24}$$

Fig. 7.6. Energetic position (ionization energy labeled in meV) of various impurities (A: acceptor, D: donor) in (**a**) Ge, (**b**) Si and (**c**) GaAs. Based on [384]

The absolute energy position of the level is $E_\mathrm{D} = E_\mathrm{C} - E_\mathrm{D}^b$. The first factor in the right side of (7.24) is the ratio of effective and free-electron mass, typically 1/10, the second factor is typically 1/100. The third factor is the ionization energy of the hydrogen atom, i.e. the Rydberg energy of 13.6 eV. Thus, the binding energy in the solid is drastically reduced by about 10^{-3} to the 10 meV regime. The excited states of the hydrogen-like spectrum can also be investigated experimentally (Sect. 9.6).

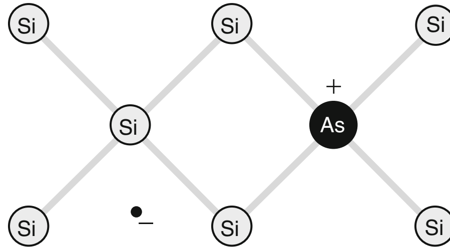

Fig. 7.7. Arsenic impurity in silicon. Arsenic donates one electron, and a fixed positive charge remains

The extension of the wavefunction of the electron bound to the fixed ion is given by the Bohr radius

$$a_{\mathrm{D}} = \frac{m_0}{m_{\mathrm{e}}^*} \epsilon_{\mathrm{r}} \, a_{\mathrm{B}} \ , \tag{7.25}$$

where $a_{\mathrm{B}} = 0.053$ nm denotes the hydrogen Bohr radius. For GaAs $a_{\mathrm{D}} = 10.3$ nm. For semiconductors with a nonisotropic band minimum, such as Si, Ge or GaP, an 'elliptically deformed' hydrogen problem with the masses m_{l} and m_{t} has to be treated [385].

An impurity that fulfills (7.24) is called an *effective-mass* impurity. For silicon we find, from (7.24), a donor binding energy of 6 meV. Using the correct tensor of the effective masses, the result for the effective-mass donor binding energy is 9.05 meV. Some experimentally observed values are summarized in Table 7.2. Different impurities can have quite similar binding energies. They can be distinguished, e.g., by electron spin resonance (ESR). At low temperatures the electron is localized on the impurity and the hyperfine interaction with the nucleus can be resolved in ESR. In Fig. 7.8 data are shown for As and P in germanium. The multiplets distinguish the nuclear spins $I = 3/2$ for arsenic (^{75}As) and $I = 1/2$ for phosphorus (^{31}P) [386].

For GaAs, the effective-mass donor has a binding energy of 5.715 meV, which is closely fulfilled for several chemical species (Table 7.3). In GaP, experimental values deviate considerably from the effective mass donor (59 meV).

Table 7.2. Binding energies $E_{\mathrm{D}}^{\mathrm{b}}$ of Li and group-V donors in elemental semiconductors. Data for carbon from [387]. All values in meV

	Li	N	P	As	Sb
C		1700	≈ 500		
Si	33		45	49	39
Ge	9.3		12.0	12.7	9.6

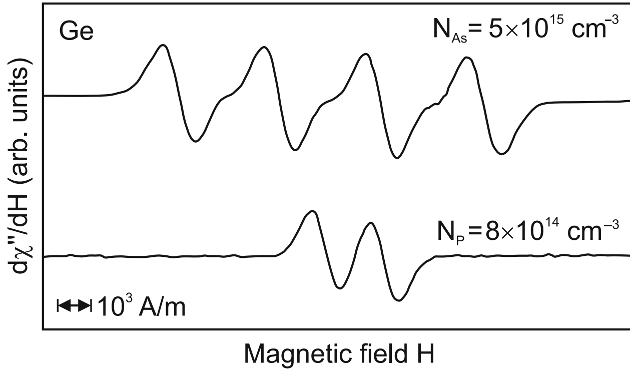

Fig. 7.8. Electron spin resonance signal from As and P in Ge with the magnetic field **H** parallel to [100], $T \approx 1.3\,\mathrm{K}$. Adapted from [386]

Table 7.3. Binding energies E_D^b of donors in GaAs (data from [388]), GaP (data from [389]) and GaN (low concentration limits, data from [390, 391]). All values in meV

	V site		III site	
GaAs	S	5.854	C	5.913
	Se	5.816	Si	5.801
	Te	5.786	Ge	5.937
GaP	O	897	Si	85
	S	107	Ge	204
	Se	105	Sn	72
	Te	93		
GaN	O	39	Si	22

The donors are typically distributed statistically (randomly) in the solid. Otherwise their distribution is called clustered. The concentration of donors is labeled N_D and usually given in cm^{-3}.

The concentration of donors populated with an electron (neutral donors) is denoted by N_D^0, the concentration of ionized donors (positively charged) is N_D^+. Other conventions in the literature label the concentrations N_1 and N_0, respectively:

$$N_1 = N_\mathrm{D}^0 = N_\mathrm{D}\, f_\mathrm{e}(E_\mathrm{D}) \tag{7.26a}$$

$$N_0 = N_\mathrm{D}^+ = N_\mathrm{D}\,(1 - f_\mathrm{e}(E_\mathrm{D}))\;, \tag{7.26b}$$

with $f_\mathrm{e}(E_\mathrm{D}) = [1 + \exp(E_\mathrm{D} - E_\mathrm{F})]^{-1}$. For the sum of these quantities the condition

$$N_\mathrm{D} = N_\mathrm{D}^+ + N_\mathrm{D}^0 \tag{7.27}$$

holds.

The ratio of the two concentrations is first given as (caveat: this formula will be modified below)

$$\frac{N_\mathrm{D}^0}{N_\mathrm{D}^+} = \frac{N_1}{N_0} = \frac{f}{1-f} = \exp\left(\frac{E_\mathrm{F} - E_\mathrm{D}}{kT}\right) . \tag{7.28}$$

Now, the degeneracy of the states has to be considered. The donor charged with one electron has a 2-fold degeneracy $g_1 = 2$ since the electron can take the spin up and down states. The degeneracy of the ionized (empty) donor is $g_0 = 1$. Additionally, we assume here that the donor cannot be charged with a second electron (cmp. Sect. 7.7.2). Due to Coulomb interaction, the energy level of the possible N_D^- state is in the conduction band. Otherwise, a multiply charged center would be present. We also do not consider excited states of N_D^0 that might be in the band gap as well. In the following, we will continue with $\hat{g}_\mathrm{D} = g_1/g_0 = 2$ as suggested in [392].[3] We note that the definition of the degeneracy factor for donors (and acceptors, see (7.45)) is not consistent in the literature as summarized in [393]. Considering now the degeneracy, (7.28) is modified to

$$\frac{N_\mathrm{D}^0}{N_\mathrm{D}^+} = \frac{N_1}{N_0} = \hat{g}_\mathrm{D} \exp\left(\frac{E_\mathrm{F} - E_\mathrm{D}}{kT}\right) . \tag{7.29}$$

This can be understood from thermodynamics (cf. Sect. 4.2.2), a rate analysis or simply the limit $T \to \infty$.

The probabilities f^1 and f^0 for a populated or empty donor, respectively, are

$$f^1 = \frac{N_1}{N_\mathrm{D}} = \frac{1}{\hat{g}_\mathrm{D}^{-1} \exp\left(\frac{E_\mathrm{D} - E_\mathrm{F}}{kT}\right) + 1} \tag{7.30a}$$

$$f^0 = \frac{N_0}{N_\mathrm{D}} = \frac{1}{\hat{g}_\mathrm{D} \exp\left(-\frac{E_\mathrm{D} - E_\mathrm{F}}{kT}\right) + 1} . \tag{7.30b}$$

First, we assume that no carriers in the conduction band stem from the valence band (no intrinsic conduction). This will be the case at sufficiently low temperatures when $N_\mathrm{D} \gg n_\mathrm{i}$. Then the number of electrons in the conduction band is equal to the number of ionized donors, i.e.

$$\begin{aligned} n = f^0 N_\mathrm{D} = N_0 &= \frac{N_\mathrm{D}}{1 + \hat{g}_\mathrm{D} \exp\left(\frac{E_\mathrm{F} - E_\mathrm{D}}{kT}\right)} \\ &= \frac{n}{n + n_1} N_\mathrm{D} = \frac{1}{1 + n_1/n} N_\mathrm{D} , \end{aligned} \tag{7.31}$$

[3] We do not agree with the treatment of the conduction band valley degeneracy in [392] for the donor degeneracy factor for Ge and Si.

with $n_1 = (N_{\rm C}/\hat{g}_{\rm D}) \exp\left(-E_{\rm D}^b/kT\right)$. The neutrality condition is

$$-n + N_{\rm D}^+ = -n + N_0 = 0\ . \tag{7.32}$$

Thus the equation (n is given by (7.15))

$$N_{\rm C} \exp\left(\frac{E_{\rm F} - E_{\rm C}}{kT}\right) - \frac{N_{\rm D}}{1 + \hat{g}\ \exp\left(\frac{E_{\rm F} - E_{\rm D}}{kT}\right)} = 0 \tag{7.33}$$

needs to be solved to obtain the Fermi level.[4] The result is

$$E_{\rm F} = E_{\rm C} - E_{\rm D}^b + kT\ \ln\left[\frac{\left[1 + 4\hat{g}_{\rm D}\,\frac{N_{\rm D}}{N_{\rm C}}\exp\left(\frac{E_{\rm D}^b}{kT}\right)\right]^{1/2} - 1}{2\hat{g}_{\rm D}}\right]\ . \tag{7.34}$$

For $T \to 0$ the Fermi level is, as expected, in the center between the populated and unpopulated states, i.e. at $E_{\rm F} = E_{\rm C} - E_{\rm D}^b/2$. In Fig. 7.9a the position of the Fermi is shown for a donor with 45 meV binding energy in Si. For low temperatures the solution can be approximated as (dashed curve in Fig. 7.9b)

$$E_{\rm F} \cong E_{\rm C} - \frac{1}{2}E_{\rm D}^b + \frac{1}{2}kT\ \ln\left(\frac{N_{\rm D}}{\hat{g}_{\rm D} N_{\rm C}}\right)\ . \tag{7.35}$$

The freeze-out of carriers in n-type silicon has been discussed in detail in [394], taking into account the effects of the fine structure of the donor states. We

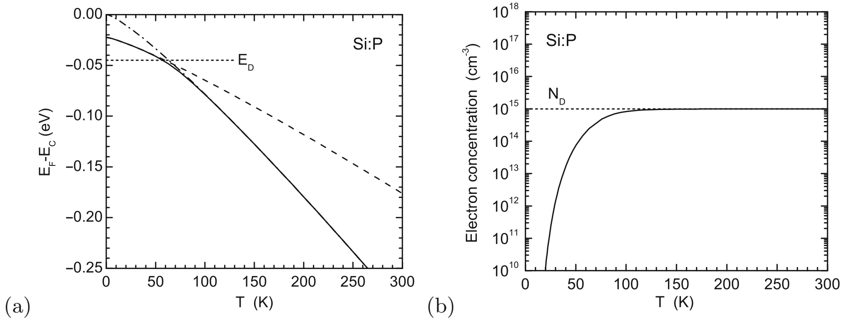

Fig. 7.9. (**a**) Position of the Fermi level in Si:P ($N_{\rm D} = 10^{15}\,{\rm cm}^{-3}$, $E_{\rm D}^b = 45\,{\rm meV}$, no acceptors) as a function of temperature *without* consideration of intrinsic carriers. Zero energy refers to the (temperature-dependent, Table 6.3) conduction-band edge $E_{\rm C}$ with approximative solutions for low (*dashed line*, (7.35)) and high (*dash-dotted line*, (7.36)) temperatures. (**b**) Corresponding density of conduction-band electrons as a function of temperature

[4]As usual, the Fermi level is determined by the global charge neutrality, see also Sect. 4.2.2.

note that the fairly high donor binding energy in silicon leads to freeze-out of carriers at about 40 K and is thus limiting for the low-temperature performance of devices. Ge has smaller donor ionization energies and subsequently a lower freeze-out temperature of 20 K. For n-type GaAs, conductivity is preserved down to even lower temperatures.

We note that the freeze-out of carriers involves the recombination of free electrons with the ionized donors. This aspect is considered in Sect. 10.9. Microscopically this process is equal to the emission of a (far infrared) photon [395, 396]. Similarly the release of an electron from the donor is due to the absorption of a photon.

For higher temperatures, when the electron density saturates towards N_{D}, the approximate solution is (dash-dotted curve in Fig. 7.9a)

$$E_{\mathrm{F}} \cong E_{\mathrm{C}} + kT \,\ln\left(\frac{N_{\mathrm{D}}}{N_{\mathrm{C}}}\right) \,. \tag{7.36}$$

The electron density n is given (still in the Boltzmann approximation) by

$$\begin{aligned} n &= N_{\mathrm{C}} \,\exp\left(-\frac{E_{\mathrm{D}}^b}{kT}\right) \frac{\left[1 + 4\hat{g}_{\mathrm{D}} \,\frac{N_{\mathrm{D}}}{N_{\mathrm{C}}} \,\exp\left(\frac{E_{\mathrm{D}}^b}{kT}\right)\right]^{1/2} - 1}{2\hat{g}_{\mathrm{D}}} \\ &= \frac{2N_{\mathrm{D}}}{1 + \left[1 + 4\hat{g}_{\mathrm{D}} \,\frac{N_{\mathrm{D}}}{N_{\mathrm{C}}} \,\exp\left(\frac{E_{\mathrm{D}}^b}{kT}\right)\right]^{1/2}} \,. \end{aligned} \tag{7.37}$$

The theoretical electron density as a function of temperature is shown in Fig. 7.9b. It fits very well to experimental data for gallium doped germanium [397] as shown in Fig. 7.10 (Arrhenius plot, $\ln n$ vs. $1/T$).

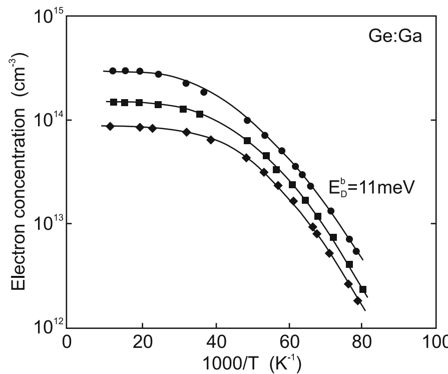

Fig. 7.10. Electron concentration as a function of temperature for three different Ge:Ga samples in the 10^{14} cm^{-3} doping regime. *Solid lines* are fits to the data with a donor binding energy of 11 meV. Adapted from [397]

For low temperatures, the solution (7.38) is close to

$$n \cong \sqrt{\frac{N_\mathrm{D} N_\mathrm{C}}{\hat{g}_\mathrm{D}}} \exp\left(-\frac{E_\mathrm{D}^b}{2kT}\right) = \sqrt{n_1 \, N_\mathrm{D}} \; . \tag{7.38}$$

For high temperatures, $n \cong N_\mathrm{D}$. This regime is called *exhaustion* or *saturation* since all possible electrons have been ionized from their donors. We note that even in this case $np = n_\mathrm{i} p_\mathrm{i}$ holds, however, $n \gg p$.

While the characteristic energy for the ionization of electrons from donors is E_D^b, at high enough temperatures electrons are transferred also from the valence band into the conduction band. Thus, in order to make the above consideration valid for all temperatures, the intrinsic conduction also has to be considered. The neutrality condition (still in the absence of any acceptors) is

$$-n + p + N_\mathrm{D}^+ = 0 \; . \tag{7.39}$$

Using (7.15) and $p = n_\mathrm{i}^2/n$, the equation

$$N_\mathrm{C} \exp\left(\frac{E_\mathrm{F} - E_\mathrm{C}}{kT}\right) - \frac{n_\mathrm{i}^2}{N_\mathrm{C} \exp(\frac{E_\mathrm{F} - E_\mathrm{C}}{kT})} - \frac{N_\mathrm{D}}{1 + \hat{g}_\mathrm{D} \exp(\frac{E_\mathrm{F} - E_\mathrm{D}}{kT})} = 0 \tag{7.40}$$

needs to be solved. The result is

$$E_\mathrm{F} = E_\mathrm{C} - E_\mathrm{D}^b + kT \, \ln \left[\frac{\frac{\beta}{\gamma} + \frac{\gamma}{N_\mathrm{C}^2} - 1}{3\hat{g}_\mathrm{D}} \right] \; , \tag{7.41}$$

with

$$\gamma = \left(\frac{-N_\mathrm{C}^4 \alpha + \sqrt{(N_\mathrm{C}^4 \alpha)^2 - 4(N_\mathrm{C}^2 \beta)^3}}{2} \right)^{1/3} \tag{7.42}$$

$$\beta = N_\mathrm{C}^2 + 3\hat{g}_\mathrm{D} N_\mathrm{C} N_\mathrm{D} \exp\left(\frac{E_\mathrm{D}}{kT}\right) + 3\hat{g}_\mathrm{D}^2 n_\mathrm{i}^2 \exp\left(\frac{2E_\mathrm{D}}{kT}\right)$$

$$\alpha = 2N_\mathrm{C}^2 + 9\hat{g}_\mathrm{D} N_\mathrm{C} N_\mathrm{D} \exp\left(\frac{E_\mathrm{D}}{kT}\right) - 18\hat{g}_\mathrm{D}^2 n_\mathrm{i}^2 \exp\left(\frac{2E_\mathrm{D}}{kT}\right) \; .$$

The temperature-dependent position of the Fermi level is shown in Fig. 7.11.

The carrier concentration is given by

$$n = N_\mathrm{C} \, \exp\left(-\frac{E_\mathrm{D}^b}{kT}\right) \frac{\frac{\beta}{\gamma} + \frac{\gamma}{N_\mathrm{C}^2} - 1}{3\hat{g}_\mathrm{D}} \; , \tag{7.43}$$

with α, β and γ having the same meaning as in (7.41). The three important regimes are the intrinsic conduction at high temperatures when $n_\mathrm{i} \gg N_\mathrm{D}$, the exhaustion at intermediate temperatures when $n_\mathrm{i} \ll N_\mathrm{D}$ and $kT > E_\mathrm{D}$, and finally the freeze-out regime for $kT \ll E_\mathrm{D}$ at low temperatures when the electrons condense back into the donors. The three regimes can be seen in the experimental data of Fig. 8.5a for donors (n-Ge) and Fig. 7.15 for acceptors (p-Ge).

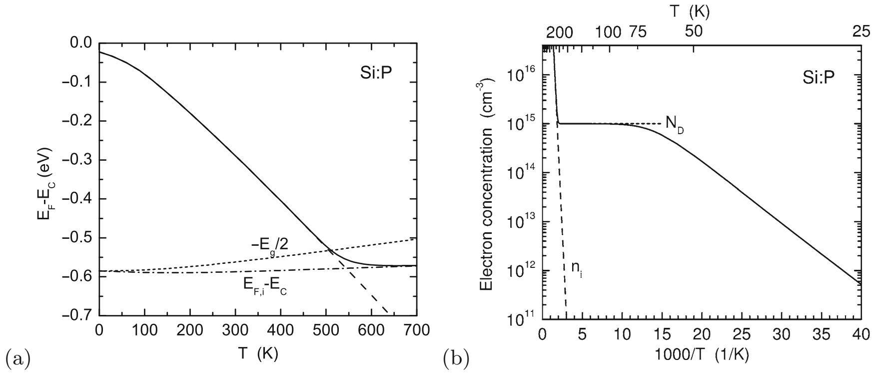

Fig. 7.11. (**a**) Position of the Fermi level in Si:P ($N_\mathrm{D} = 10^{15}\,\mathrm{cm}^{-3}$, $E_\mathrm{D}^b = 45\,\mathrm{meV}$, no acceptors) as a function of temperature. The temperature dependence of the band gap (as given in Table 6.3) has been taken into account. Zero energy refers to the conduction-band edge for all temperatures. The *dotted curve* shows $E_\mathrm{g}/2$. The *dashed* (*dash-dotted*) *line* shows the low- (high-) temperature limit according to (7.35) and (7.23), respectively. (**b**) Corresponding electron concentration as a function of temperature. The *dashed line* shows the intrinsic carrier density

A similar plot as in Fig. 7.11a is shown in Fig. 7.12. With increasing temperature the Fermi level shifts from close to the band edge towards the band center. At higher doping the shift begins at higher temperatures.

The electronic states of individual donors can be directly visualized by scanning tunneling microscopy (STM) as shown in Fig. 7.13 for Si:P. For small negative bias, tunneling occurs through the charged dopant that is

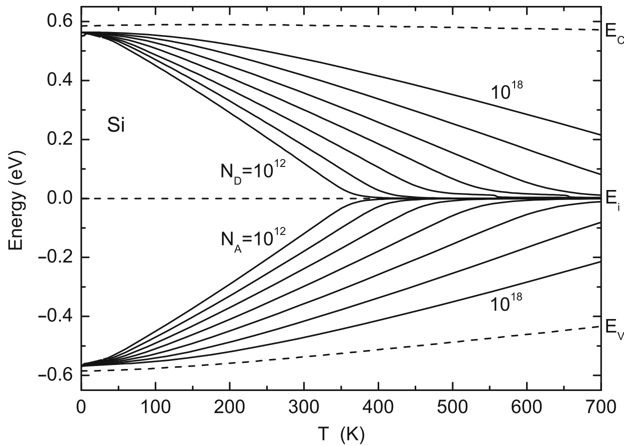

Fig. 7.12. Fermi level in silicon as a function of temperature for various doping levels (n-type and p-type) of $10^{12}, 10^{13}, \ldots, 10^{18}\,\mathrm{cm}^{-3}$. The intrinsic Fermi level is chosen as zero energy for all temperatures. The (temperature-dependent) conduction and valence band edges are shown as *dashed lines*

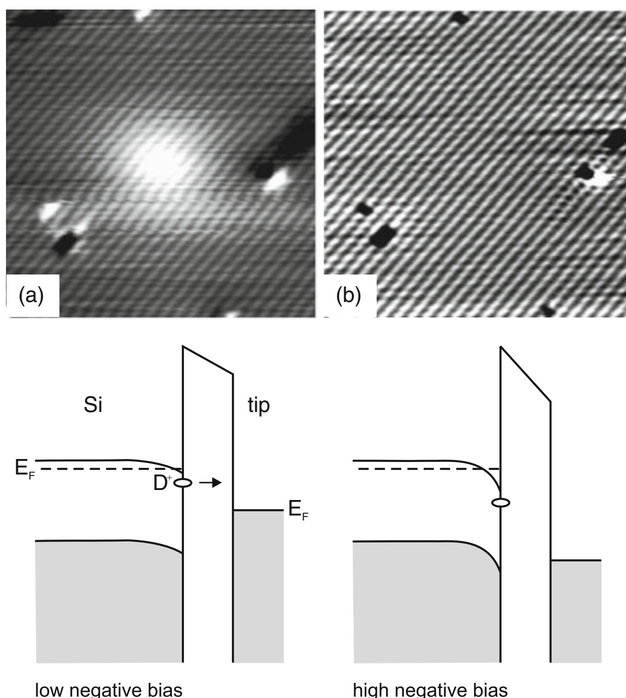

Fig. 7.13. Filled-state image of a phosphorus atom underneath a Si (001) surface at a tunneling current of 110 pA. The doping level is $5\times10^{17}\,\text{cm}^{-3}$. (**a**) Sample bias -0.6 V, (**b**) sample bias -1.5 V between Si:P and tip. Image sizes are $22\times22\,\text{nm}^2$. Reprinted with permission from [400], ©2004 APS. *Lower row*: Schematic band diagrams for the two bias situations

located within the first three monolayers. At high negative bias the large contribution from the filled valence band masks the effect of the donor. This image, however, shows that the contrast attributed to the dopant atom is not due to surface defects or absorbates.

7.5.2 Acceptors

A group-III atom in Si has one electron too few for the tetrahedral bond. Thus, it 'borrows' an electron from the electron gas (in the valence band) and thus leaves a missing electron (termed hole) in the valence band (Fig. 7.14). The energy level is in the gap close to the valence-band edge. The latter consideration is made in the electron picture. In the hole picture, the acceptor ion has a hole and the hole ionizes (at sufficient temperature) into the valence band. After ionization the acceptor is charged negatively. Also, for this system a Bohr-like situation arises that is, however, more complicated than for donors because of the degeneracy of the valence bands and their warping.

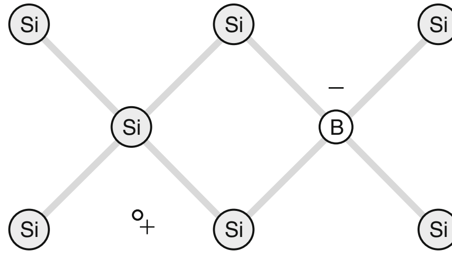

Fig. 7.14. Boron impurity in silicon. Boron accepts one electron and a fixed negative charge remains

Table 7.4. Binding energies E_A^b of group-III acceptors in elemental semiconductors. Data for diamond from [398, 399]. All values in meV

	B	Al	Ga	In
C	369			
Si	45	57	65	16
Ge	10.4	10.2	10.8	11.2

In Table 7.4 the acceptor binding energies E_A^b for group-III atoms in C, Ge and Si are listed. The absolute acceptor energy is given as $E_A = E_V + E_A^b$. In Table 7.5 acceptor binding energies are listed for GaAs, GaP and GaN.

Table 7.5. Binding energies E_A^b of acceptors in GaAs, GaP and GaN (low concentration values, data from [403, 404]). All values in meV

	V site		III site	
GaAs	C	27	Be	28
	Si	34.8	Mg	28.8
	Ge	40.4	Zn	30.7
	Sn	167	Cd	34.7
GaP	C	54	Be	57
	Si	210	Mg	60
	Ge	265	Zn	70
			Cd	102
GaN	C	230	Mg	220
	Si	224	Zn	340
			Cd	550

While in GaAs some acceptors are close to the effective mass value of 27 meV, in GaP the deviation from the effective mass value ≈50 meV is large.

When the conductivity is determined by holes or electrons, the material is called p-type or n-type, respectively. We note that some metals also show hole conduction (e.g. Al). However, for metals the conductivity type is fixed, while the same semiconductor can be made n- or p-type with the appropriate doping.

The acceptor concentration is denoted by N_A. The concentration of neutral acceptors is N_A^0, the concentration of charged acceptors is N_A^-. Of course

$$N_\mathrm{A} = N_\mathrm{A}^0 + N_\mathrm{A}^- \,. \tag{7.44}$$

The ratio of the degeneracy of the (singly) filled and empty acceptor level is $\hat{g}_\mathrm{A}$. In Ge $\hat{g}_\mathrm{A} = 4$ since the localized hole wave function may be formed in EMA with four Bloch wave functions (heavy and light holes) [401]. For Si with its small split-off energy (Table 6.6) $\hat{g}_\mathrm{A} = 6$ according to [402]. For doubly ionized acceptors, e.g. Zn in Si and Ge (see Sect. 7.7.3), the more shallow level ($\mathrm{Zn}^- \to \mathrm{Zn}^0$) has $\hat{g}_\mathrm{A} = 6/4 = 1.5$ in Ge [402]. A more general discussion of the degeneracy factor for multiply charged acceptors can be found in [392, 405]. Similar to the considerations for electrons and donors we have

$$\frac{N_\mathrm{A}^0}{N_\mathrm{A}^-} = \hat{g}_\mathrm{A} \, \exp\left(-\frac{E_\mathrm{F} - E_\mathrm{A}}{kT}\right) \,. \tag{7.45}$$

The population of the acceptor levels is given by

$$N_\mathrm{A}^- = \frac{N_\mathrm{A}}{1 + \hat{g}_\mathrm{A} \, \exp\left(-\frac{E_\mathrm{F} - E_\mathrm{A}}{kT}\right)} \,. \tag{7.46}$$

The formulas for the position of the Fermi level and the hole density are analogous to those obtained for electrons and donors and will not be explicitly given here. The analogue to Fig. 7.11b is shown for data on p-doped Ge [406] in Fig. 7.15. The acceptor activation energy is 11 meV which could be due to various impurities (cf. Table 7.4). The different impurities (B, Al, Ga) can be distinguished by photothermal ionization spectroscopy [406] (cmp. Sect. 9.6).

In Fig. 7.12, the temperature dependence of the Fermi level is included for p-type Si. With increasing temperature the Fermi level shifts from the valence-band edge (For $T = 0$, $E_\mathrm{F} = E_\mathrm{V} + E_\mathrm{A}^b/2$) towards the middle of the band gap (intrinsic Fermi level).

Also, the wavefunction at acceptors can be imaged using scanning tunneling microscopy [407]. In [408] images of ionized and neutral Mn in GaAs have been reported (Fig. 7.16b). The tunneling I–V characteristics are shown in Fig. 7.16a. At negative bias, the acceptor is ionized and appears spherically symmetric due to the effect of the A^- ion Coulomb potential on the valence-band states. At intermediate positive voltages, tunneling is through the neutral state. The wavefunction of A^0 looks like a bow-tie due to the

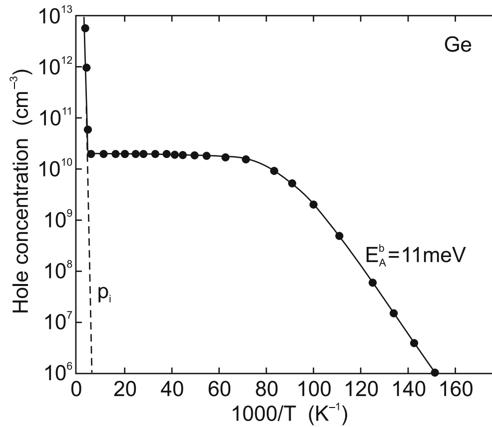

Fig. 7.15. Carrier concentration as a function of temperature for p-type Ge. The net shallow level concentration is $2 \times 10^{10}\,\mathrm{cm}^{-3}$. *Solid line* is fit to the data, the *dashed line* indicates the intrinsic hole concentration p_i. Adapted from [406]

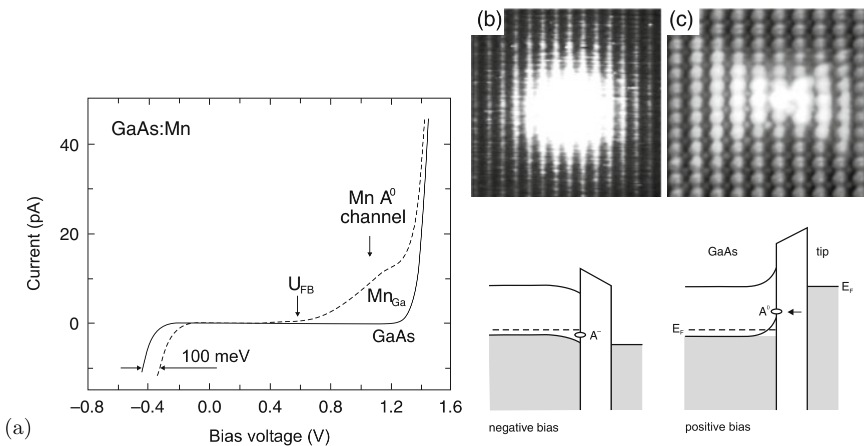

Fig. 7.16. (**a**) Tunneling I–V characteristic of GaAs:Mn sample. *Solid* (*dashed*) line is for pure GaAs (subsurface Mn on Ga site). U_FB denotes the simulated flat-band voltage. Adapted from [408]. (**b**,**c**) STM images of a Mn atom underneath a GaAs (110) surface. The doping level is $3 \times 10^{18}\,\mathrm{cm}^{-3}$. (**b**) Sample bias $-0.7\,\mathrm{V}$, (**c**) sample bias $+0.6\,\mathrm{V}$. Below the images are schematic band diagrams of GaAs:Mn and tip. Image sizes are (**b**) $8 \times 8\,\mathrm{nm}^2$ and (**c**) $5.6 \times 5\,\mathrm{nm}^2$. Reprinted with permission from [408], ©2004 APS. *Lower row* under parts (**a**,**b**): Schematic band diagrams for the two bias situations

admixture of d-wavefunctions [409]. The Mn atom is presumably in the third subsurface atomic layer. At even higher positive bias the contrast due to the dopant is lost because the image is dominated by a large tunneling current from the tip to the empty conduction band.

7.5.3 Compensation

When donors *and* acceptors are simultaneously present, some of the impurities will compensate each other. Electrons from donors will recombine with holes on the acceptors. Depending on the quantitative situation the semiconductor can be n- or p-type. This situation can be invoked by intentional doping with donors or acceptors or by the unintentional background of donors (acceptors) in p-doped (n-doped) material. Also the formation of pairs, exhibiting a new defect level different from the single donor or single acceptor, has been described, e.g. for Se and B in silicon [205].

The charge-neutrality condition (now finally in its most general form) reads

$$-n + p - N_{\mathrm{A}}^{-} + N_{\mathrm{D}}^{+} = 0 \, . \tag{7.47}$$

We will now discuss the case of the presence of donors and acceptors, but limit ourselves to sufficiently low temperatures (or wide band gaps) such that the intrinsic carrier density can be neglected. We assume Boltzmann statistics and assume here $N_{\mathrm{D}} > N_{\mathrm{A}}$. Then it is a very good approximation to use $N_{\mathrm{A}}^{-} = N_{\mathrm{A}}$ since there are enough electrons from the donors to recombine with (and thus compensate) all acceptors. Under the given assumptions regarding the temperature $p = 0$ and the material is n-type. Thus, in order to determine the position of the Fermi level, the charge-neutrality condition

$$n + N_{\mathrm{A}} - N_{\mathrm{D}}^{+} = 0 \tag{7.48}$$

must be solved (compare to (7.33))

$$N_{\mathrm{C}} \, \exp\left(\frac{E_{\mathrm{F}} - E_{\mathrm{C}}}{kT}\right) + N_{\mathrm{A}} - \frac{N_{\mathrm{D}}}{1 + \hat{g}\,\exp(\frac{E_{\mathrm{F}} - E_{\mathrm{D}}}{kT})} = 0 \, . \tag{7.49}$$

We rewrite (7.48) and find $N_{\mathrm{D}} - N_{\mathrm{A}} - n = N_{\mathrm{D}}^{0} = N_{\mathrm{D}}^{+}\,\hat{g}_{\mathrm{D}}\,\exp\left(\frac{E_{\mathrm{F}} - E_{\mathrm{D}}}{kT}\right)$ using (7.29). Using again (7.48) and also (7.15), (7.49) can be written as

$$\frac{n\,(n + N_{\mathrm{A}})}{N_{\mathrm{D}} - N_{\mathrm{A}} - n} = \frac{N_{\mathrm{C}}}{\hat{g}_{\mathrm{D}}} \, \exp\left(-\frac{E_{\mathrm{D}}^{\mathrm{b}}}{kT}\right) \, , \tag{7.50}$$

a form given in [410]. Analogously for compensated p-type material

$$\frac{p\,(p + N_{\mathrm{D}})}{N_{\mathrm{A}} - N_{\mathrm{D}} - p} = \frac{N_{\mathrm{V}}}{\hat{g}_{\mathrm{A}}} \, \exp\left(-\frac{E_{\mathrm{A}}^{\mathrm{b}}}{kT}\right) \tag{7.51}$$

holds.

The solution of (7.49) is

$$E_F = E_C - E_D^b + kT \ln \left[\frac{\left[\alpha^2 + 4\hat{g}_D \frac{N_D - N_A}{N_C} \exp\left(\frac{E_D^b}{kT}\right)\right]^{1/2} - \alpha}{2\hat{g}_D} \right] \quad (7.52)$$

$$\alpha = 1 + \hat{g}_D \frac{N_A}{N_C} \exp\left(\frac{E_D^b}{kT}\right) = 1 + \frac{N_A}{\beta}$$

$$\beta = \frac{N_C}{\hat{g}} \exp\left(-\frac{E_D^b}{kT}\right) .$$

The carrier density is best obtained from (7.50)

$$n = \sqrt{(N_A - \beta)^2 + 4N_D\,\beta} - \frac{N_A + \beta}{2} . \quad (7.53)$$

For $N_A = 0$ we have $\alpha = 1$ and (7.34) is reproduced, as expected. For $T = 0$ the Fermi energy lies at $E_F = E_D$ since the donor level is *partially* filled ($N_D^0 = N_D - N_A$). For low temperatures the Fermi level is approximated by

$$E_F \cong E_C - E_D^b + kT \ln\left(\frac{N_D/N_A - 1}{\hat{g}_D}\right) . \quad (7.54)$$

The corresponding carrier density at low temperatures is

$$n = \frac{N_C}{\hat{g}_D} \exp\left(-\frac{E_D^b}{kT}\right)\left(\frac{N_D}{N_A} - 1\right) . \quad (7.55)$$

For higher temperatures (7.38) holds approximately for $n > N_A$; the slope is now given by $E_D^b/2$ as in the uncompensated case (Fig. 7.17b). For

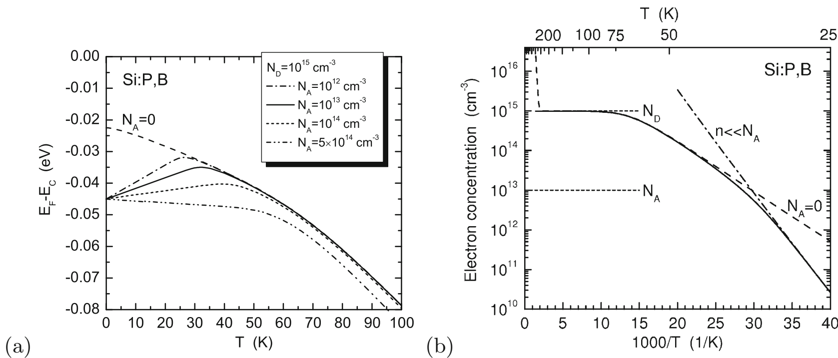

Fig. 7.17. (**a**) Position of Fermi level in partially compensated Si:P,B ($N_D = 10^{15}\,\mathrm{cm}^{-3}$, $E_D^b = 45\,\mathrm{meV}$, $E_A^b = 45\,\mathrm{meV}$, *solid line*: $N_A = 10^{13}\,\mathrm{cm}^{-3}$, *dashed line*: $N_A = 0$, *dash-dotted line*: $N_A = 10^{12}\,\mathrm{cm}^{-3}$, *short-dashed line*: $N_A = 10^{14}\,\mathrm{cm}^{-3}$, *dash-double dotted line*: $N_A = 5 \times 10^{14}\,\mathrm{cm}^{-3}$) as a function of temperature. (**b**) Corresponding electron concentration for $N_A = 10^{13}\,\mathrm{cm}^{-3}$ as a function of temperature (neglecting intrinsic carriers), *dashed line* for $N_A = 0$ according to (7.38), *dash-dotted line* approximation for $n \ll N_A$ as in (7.55)

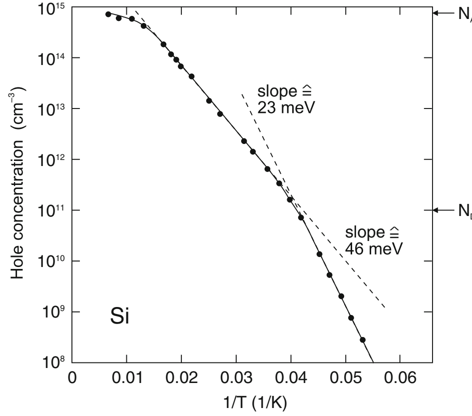

Fig. 7.18. Hole density in p-type silicon ($N_\mathrm{A} = 7.4 \times 10^{14}\,\mathrm{cm}^{-3}$, $E^b_\mathrm{A} = 46\,\mathrm{meV}$ (probably boron) and partial compensation with $N_\mathrm{D} = 1.0 \times 10^{11}\,\mathrm{cm}^{-3}$). Adapted from [411]

sufficiently high temperatures in the exhaustion regime (but still $n_\mathrm{i} < n$) the electron density is given by

$$n \cong N_\mathrm{D} - N_\mathrm{A}\ . \tag{7.56}$$

At even higher temperatures the electron density will be determined by the intrinsic carrier concentration. Only in this case $p \neq 0$!

An experimental example is shown in Fig. 7.18 for partially compensated p-Si (with $N_\mathrm{D} \ll N_\mathrm{A}$). The change of slope around $p \approx N_\mathrm{D}$ is obvious.

If donors are added to a p-type semiconductor, first the semiconductor remains p-conducting as long as $N_\mathrm{D} \ll N_\mathrm{A}$. If the donor concentration becomes larger than the acceptor concentration, the conductivity type switches from p- to n-conduction. If the impurities are exhausted at room temperature, the lowest carrier concentration is reached for $N_\mathrm{D} = N_\mathrm{A}$. Such a scenario is shown for p-type $\mathrm{In}_x\mathrm{Ga}_{1-x}\mathrm{As}_{1-y}\mathrm{N}_y$ doped with various concentrations of Si in Fig. 7.19. At high Si incorporation, the number of charge carriers saturates due to autocompensation (see Sect. 7.5.5) and the formation of Si precipitates. Since the ionization energies of donors and acceptors are typically different, the situation for $N_\mathrm{D} \approx N_\mathrm{A}$ needs, in general, to be investigated carefully and will depend on the temperature.

7.5.4 Multiple Impurities

If more than one donor species is present, (7.49) can be generalized, e.g. for the case of two donors D1 and D2 in the presence of compensating acceptors,

$$n + N_\mathrm{A} - \frac{N_\mathrm{D1}}{1 + \hat{g}_1 \exp(\frac{E_\mathrm{F} - E_\mathrm{D1}}{kT})} - \frac{N_\mathrm{D2}}{1 + \hat{g}_2 \exp(\frac{E_\mathrm{F} - E_\mathrm{D2}}{kT})} = 0\ . \tag{7.57}$$

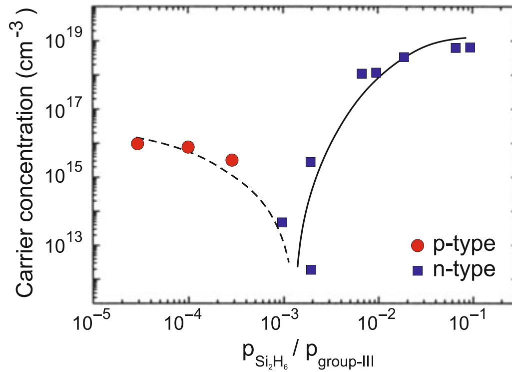

Fig. 7.19. Carrier concentration and conductivity type (*red circles*: p, *blue squares*: n) for MOVPE-grown $In_xGa_{1-x}As_{1-y}N_y$ layers on GaAs (001) (layer thickness $\approx 1\,\mu m$, $x \approx 5\%$, $y \approx 1.6\%$) doped with different amounts of silicon. The ordinate is the ratio of the partial pressures of disilane and the group-III precursors (TMIn and TMGa) in the gas phase entering the MOVPE reactor. *Lines* are guides to the eye. Experimental data from [414]

This case is treated in [412]. Simple high and low temperature approximations can be found where the trap with the larger and smaller activation energy, respectively, dominates. The case for multiple acceptors (and compensating donors) is treated analogously. As detailed in [413], the function dn/dE_F has a maximum at the donor level position; this can be used to visualize the contribution of several donors (with sufficiently different binding energies) from $n(T)$ as measured by Hall effect (Fig. 7.20).

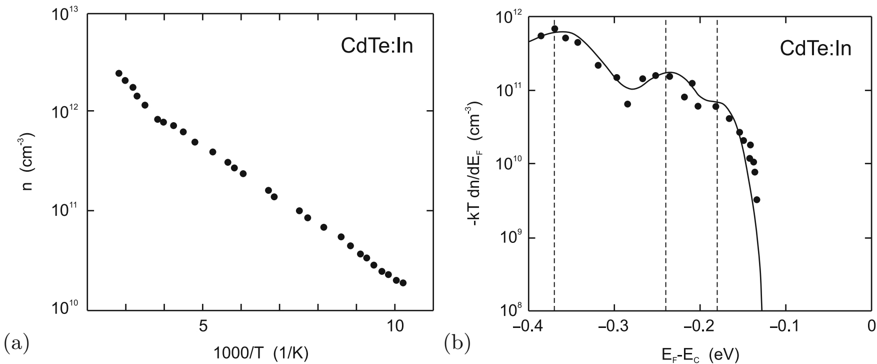

Fig. 7.20. (**a**) Electron concentration vs. temperature as determined from Hall effect for a CdTe sample doped with indium. (**b**) $-kT\,dn/dE_F$, as determined from the experimental Hall data (*symbols*). The *solid line* is theory for three donor levels ($E_{D1} = E_C - 0.37\,eV$, $N_{D1} = 2.5 \times 10^{12}\,cm^{-3}$; $E_{D2} = E_C - 0.24\,eV$, $N_{D2} = 7.0 \times 10^{11}\,cm^{-3}$; $E_{D3} = E_C - 0.18\,eV$, $N_{D3} = 2.5 \times 10^{11}\,cm^{-3}$) whose energy positions are indicated by *dashed lines*. Adapted from [413]

7.5.5 Amphoteric Impurities

If an impurity atom can act as a donor and acceptor it is called amphoteric. This can occur if the impurity has several levels in the band gap (such as Au in Ge or Si). In this case, the nature of the impurity depends on the position of the Fermi level. Another possibility is the incorporation on different lattice sites. For example, carbon in GaAs is a donor if incorporated on the Ga-site. On the As-site carbon acts as an acceptor.

Thus, e.g., crystal growth kinetics can determine the conductivity type. In Fig. 7.21 the conductivity due to carbon background is shown for GaAs grown using MOVPE under various growth conditions. At high (low) arsine partial pressure incorporation of carbon on As-sites is less (more) probable, thus the conductivity is n-type (p-type). Also, growth on different surfaces can evoke different impurity incorporation, e.g., n-type on (001) GaAs and p-type on (311)A GaAs, since the latter is Ga-stabilized.

The charge density at an impurity nucleus can be investigated via the isomer shift as determined by Mössbauer spectroscopy [416, 417]. The incorporation of the isotope ^{119}Sn can be controlled in III-V compounds to be on cation or anion site as donor or acceptor, respectively. This is accomplished by introducing ^{119}In or ^{119}Sb on group-III and group-V site, respectively, both decaying into ^{119}Sn without leaving their lattice site. The isomer shifts of ^{119}Sn in various III-V compounds are shown in Fig. 7.22. In [417] it is concluded from these data that the tin donor is formed by a positive tin ion and the electron charge transfer to its neighboring (group-V) atoms is rather small. For tin as an acceptor, for the present conditions an ionized, i.e. negatively charged acceptor, the isomer shift follows closely the trend from

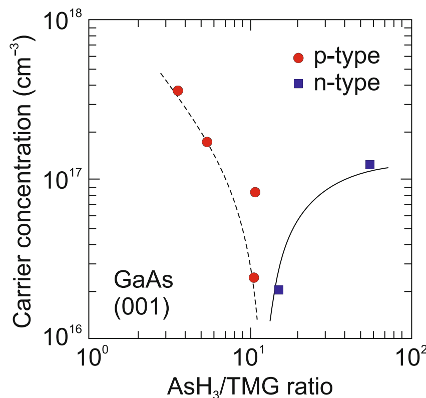

Fig. 7.21. Background doping of GaAs due to carbon in MOVPE for different ratios of the partial pressures of AsH_3 and TMG (trimethylgallium). The conductivity type (*blue squares*: n-type, *red circles*: p-type) depends on the incorporation of C from CH_3 radicals on Ga- or As-site. *Lines* are guides to the eye. Experimental data from [415]

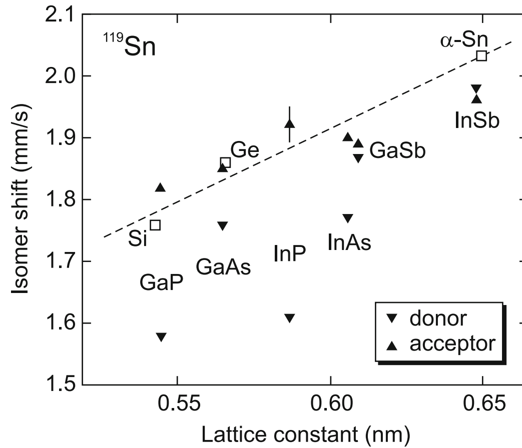

Fig. 7.22. Isomer shift (relative to $CaSnO_3$) of ^{119}Sn in various group-IV and III-V compound semiconductors as labeled. *Dashed line* is trend from isoelectronic substitution. Experimental data from [417]

substitution in group-IV semiconductors. Therefore four electrons form the tetrahedral bond, while the extra electron is located rather at the (positively charged) group-III next neighbors and not in the impurity cell. The difference to the point charge Coulomb distribution is called central-cell correction.

Deviation from the ideal stoichiometry introduces point defects that can be electrically active and change conductivity type and carrier concentration. In the case of $CuInSe_2$, excess Cu could go on interstitial positions or promote selenium vacancies, both leading to n-type behavior. This material is particularly sensitive to deviations from ideal stoichiometry for both Cu/In ratio (Fig. 7.23) and Se deficiency [418].

7.5.6 High Doping

For low doping concentrations, the impurity atoms can be considered to be decoupled. At low temperature, only hopping from one impurity to the next is possible due to thermal emission or tunneling and the semiconductor becomes an insulator.

With increasing concentration, the distance between impurities decreases and their wavefunctions can overlap. Then, an impurity band develops (Fig. 7.24). A periodic arrangement of impurity atoms would result in well-defined band edges as found in the Kronig–Penney model. Since the impurity atoms are randomly distributed, the band edges exhibit tails. For high doping, the impurity band overlaps with the conduction band. In the case of compensation, the impurity band is not completely filled and contains (a new type of) holes. In this case, conduction can take place within the impurity band even at low temperature, making the semiconductor a metal. This

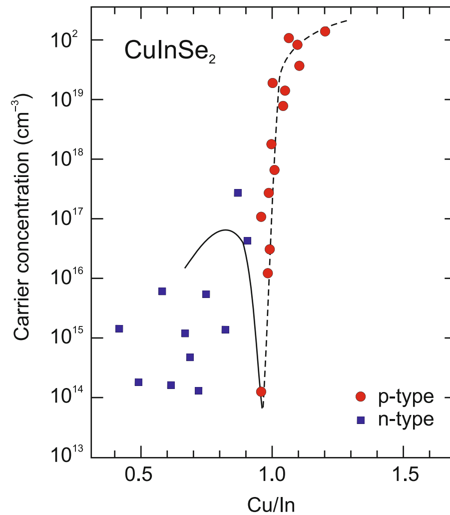

Fig. 7.23. Carrier concentration and conductivity type (*blue squares*: n-type, *red circles*: p-type) as a function of stoichiometry for $CuInSe_2$ thin films. *Lines* are guides to the eye. Experimental data from [418]

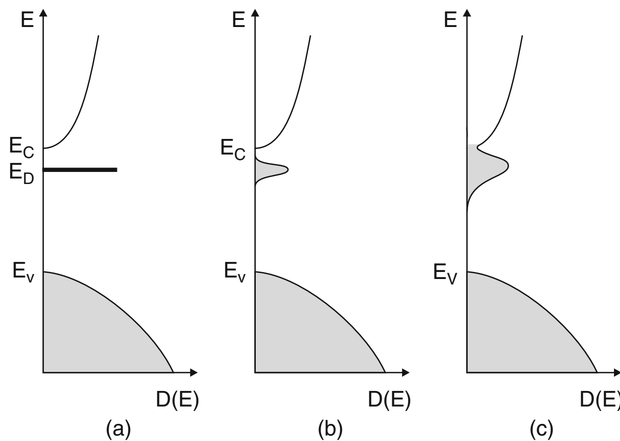

Fig. 7.24. Principle of the formation of a (donor) impurity band. (**a**) Small doping concentration and sharply defined impurity state at E_D, (**b**) increasing doping and development of an impurity band that (**c**) widens further and eventually overlaps with the conduction band for high impurity concentration. The *shaded areas* indicate populated states at $T = 0\,\mathrm{K}$

metal–insulator transition has been discussed by Mott [419]. Examples for highly doped semiconductors are transparent conductive oxides (Sect. 19), the contact layer for an ohmic contact (Sect. 20.2.6) or the active layers in a tunneling diode (Sect. 20.5.9). The physics, properties and preparation of highly doped semiconductors are treated in detail in [420].

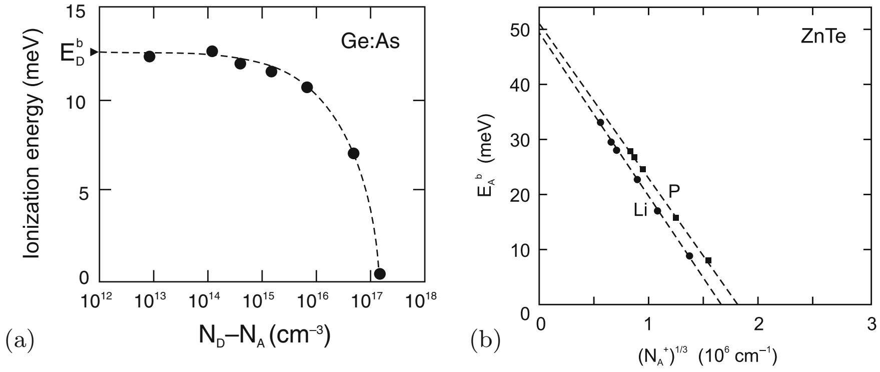

Fig. 7.25. (**a**) Donor ionization energy in n-type Ge for various doping concentrations. *Dashed line* is a guide to the eye. The arrow labeled $E_{\mathrm{D}}^{\mathrm{b}}$ denotes the low-concentration limit (cf. Table 7.2). Experimental data from [421]. (**b**) Acceptor ionization energy for ZnTe:Li and ZnTe:P as a function of the third root of the ionized acceptor concentration. Data from [422]

The formation of the impurity band leads to a reduction of the impurity ionization energy as known from (7.24). Typical results are shown in Fig. 7.25a for n-type Ge [421] and Fig. 7.25b for p-type ZnTe [422]. At the critical doping concentration of $N_{\mathrm{c}} = 1.5 \times 10^{17}$, the activation energy for the carrier concentration disappears. Similar effects have been observed for Si [423] and GaAs [424]. The freeze-out of the carrier concentration (see Fig. 7.9) disappears as shown in Fig. 7.26. Critical doping concentrations are listed in Table 7.6. The decrease of the ionization energy E^{b} (donor or acceptor) follows the dependence [421, 423]

$$E^{\mathrm{b}} = E_0^{\mathrm{b}} - \alpha\, N_{\mathrm{i}}^{1/3} = E_0^{\mathrm{b}} \left[1 - \left(\frac{N_{\mathrm{i}}}{N_{\mathrm{c}}}\right)^{1/3}\right] , \tag{7.58}$$

where N_{i} is the concentration of ionized dopants.

The critical density can be estimated from the Mott criterion when the distance of the impurities becomes comparable to their Bohr radius (7.25)

$$2a_{\mathrm{D}} = \frac{3}{2\pi}\, N_{\mathrm{c}}^{1/3} . \tag{7.59}$$

The pre-factor $3/(2\pi)$ stems from the random distribution of impurities and disappears for a periodic arrangement. The Mott criterion is (rewriting (7.59))

$$a_{\mathrm{D}}\, N_{\mathrm{c}}^{1/3} \approx 0.24 . \tag{7.60}$$

For GaAs with $a_{\mathrm{D}} = 10.3\,\mathrm{nm}$, the criterion yields $N_{\mathrm{c}} = 1.2 \times 10^{16}\,\mathrm{cm}^{-3}$, in agreement with experiment.

The achievable maximum concentration of electrically active dopants is limited by the concentration dependence of the diffusion coefficient, Coulomb

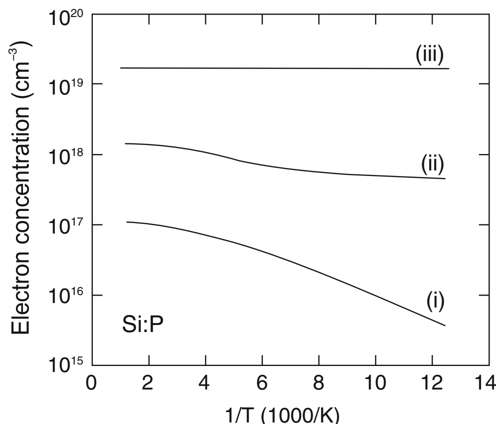

Fig. 7.26. Electron concentration vs. inverse temperature for Si:P for three different doping concentrations ((i): $1.2 \times 10^{17}\,\mathrm{cm}^{-3}$, (ii): $1.25 \times 10^{18}\,\mathrm{cm}^{-3}$, (iii): $1.8 \times 10^{19}\,\mathrm{cm}^{-3}$). Experimental data from [423]

Table 7.6. Critical doping concentration for various semiconductors (at room temperature)

material	type	$N_\mathrm{c}\,(\mathrm{cm}^{-3})$	Ref.
C:B	p	2×10^{20}	[399]
Ge:As	n	1.5×10^{17}	[421]
Si:P	n	1.3×10^{18}	[423]
Si:B	p	6.2×10^{18}	[423]
GaAs	n	1.0×10^{16}	[424]
GaP:Si	n	6×10^{19}	[426]
GaP:Zn	p	2×10^{19}	[427]
GaN:Si	n	2×10^{18}	[428]
GaN:Mg	p	4×10^{20}	[403]
$\mathrm{Al_{0.23}Ga_{0.77}N}$:Si	n	3.5×10^{18}	[429]
ZnTe:Li	p	4×10^{18}	[422]
ZnTe:P	p	6×10^{18}	[422]
ZnO:Al	n	8×10^{18}	[430]

repulsion, autocompensation and the solubility limit [383]. In Table 7.7 the maximum carrier concentrations for GaAs with various dopants are listed. As an example we show the Ga-doping of epitaxial ZnO layers on sapphire in Fig. 7.27. Under slightly Zn-rich (O-polar) conditions the growth mode is two-dimensional and the carrier concentration increases linearly with the Ga concentration, $n \approx c_{\mathrm{Ga}}$, up to high values in the $10^{20}\,\mathrm{cm}^{-3}$ range. For O-rich

Table 7.7. Maximum electrically active doping concentration for GaAs

material	type	N_c (cm^{-3})	Ref.
GaAs:Te	n	2.6×10^{19}	[431]
GaAs:Si	n	1.8×10^{19}	[432]
GaAs:C	p	1.5×10^{21}	[433]
GaAs:Be	p	2×10^{20}	[434]

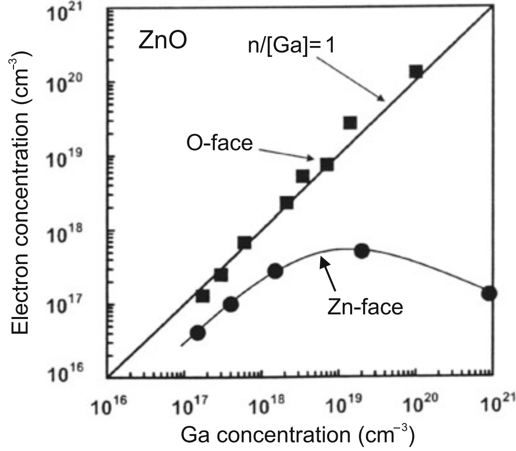

Fig. 7.27. Electron concentration as a function of gallium concentration in MBE grown ZnO:Ga on sapphire for the two different polarities. Adapted from [425]

(Zn-polar) conditions the growth mode changes to three-dimensional growth and the activation ratio of Ga donors becomes low [425].

7.6 Quasi-Fermi Levels

The carrier concentrations were given by (7.8) and (7.9). So far, we have only considered semiconductors in thermodynamic equilibrium for which $np = n_i^2$. In a nonequilibrium situation, e.g. for external excitation or carrier injection in a diode, the electron and hole densities can each take arbitrary values, in principle. In particular, np will no longer be equal to n_i^2 and there is no Fermi level constant throughout the structure. In this case, however, quasi-Fermi levels F_n and F_p for electrons and holes, respectively, are defined via

$$n(\mathbf{r}) = N_C\, F_{1/2}\left(\frac{F_n(\mathbf{r}) - E_C}{kT}\right) \tag{7.61a}$$

$$p(\mathbf{r}) = N_V\, F_{1/2}\left(-\frac{F_p(\mathbf{r}) - E_V}{kT}\right) . \tag{7.61b}$$

A quasi-Fermi level is sometimes called imref[5] and can also be denoted as E_{F_n} or E_{F_p}. We emphasize that the quasi-Fermi levels are *only* a means to describe the local carrier density in a logarithmical way. The quasi-Fermi levels can be obtained from the density via

$$F_n = E_C + kT \ln\left(\frac{n}{N_C}\right) \tag{7.62a}$$

$$F_p = E_V - kT \ln\left(\frac{p}{N_V}\right) . \tag{7.62b}$$

The quasi-Fermi levels do not imply that the carrier distribution is actually a Fermi distribution. This is generally no longer the case in thermodynamical nonequilibrium. However, in 'well-behaved' cases the carrier distribution in nonequilibrium can be approximated locally as a Fermi distribution using a local quasi-Fermi level and a local temperature, i.e.

$$f_e(\mathbf{r}, E) \cong \frac{1}{\exp\left(\frac{E - F_n(\mathbf{r})}{kT(\mathbf{r})}\right) + 1} . \tag{7.63}$$

Using the quasi-Fermi levels, np is given by

$$n(\mathbf{r})\, p(\mathbf{r}) = n_i^2 \exp\left(\frac{F_n(\mathbf{r}) - F_p(\mathbf{r})}{kT}\right) . \tag{7.64}$$

We note that for an inhomogeneous semiconductor or a heterostructure (cf. Sect. 11), n_i may also depend on the spatial position. In the case of thermodynamic equilibrium the difference of the quasi-Fermi levels is zero, i.e. $F_n - F_p = 0$ and $F_n = F_p = E_F$.

7.7 Deep Levels

For deep levels the short-range part of the potential determines the energy level. The long-range Coulomb part will only lead to a correction. The term 'deep level' implies that the level is within the band gap and close to the band edges. However, some deep levels (in the sense of the potential being determined by the ion core) have energy levels close to the band edges or even within a band. Details can be found in [166, 435–438].

The wavefunction is strongly localized. Thus, it cannot be composed of Bloch functions, as has been done for the shallow levels for the effective-mass impurity. The localization in $\mathbf{r}$ space leads to a delocalization in $\mathbf{k}$ space. Examples are Si:S, Si:Cu or InP:Fe, GaP:N, ZnTe:O. Deep levels can also be due to intrinsic defects such as vacancies or antisite defects.

[5] W. Shockley had asked E. Fermi for permission to use his name reversed. Fermi was not too enthusiastic but granted permission.

Due to the larger distance to the band edges, deep levels are not efficient at providing free electrons or holes. Quite the opposite, they rather capture free carriers and thus lead to a reduction of conductivity. Centers that can capture electrons *and* holes lead to nonradiative recombination of electrons through the deep level into the valence band (see also Sect. 10). This can be useful for the fabrication of semi-insulating layers with low carrier concentration and fast time response of, e.g., switches and photodetectors.

While the electronic properties of deep levels can be readily characterized, the microscopic origin is not immediately apparent. Next to theoretical modeling of defects and correlation with experimental results, paramagnetic hyperfine interactions have proven useful to identify the microscopic nature of various defects [439].

7.7.1 Charge States

The level can have different charge states depending on the occupancy of the levels with electrons. The energy position within the gap varies with the charge state due to the Coulomb interaction. Also, the lattice relaxation around the defect depends on the charge state and modifies the energy level.

The localized charge q_{d} at the defect is the integral over the change $\Delta\rho$ of the charge density compared to the perfect crystal over a sufficiently large volume V_∞ around the defect

$$q_{\mathrm{d}} = \int_{V_\infty} \Delta\rho(\mathbf{r})\,\mathrm{d}^3\mathbf{r} = \frac{n\,e}{\epsilon_{\mathrm{r}}}\ . \qquad (7.65)$$

In semiconductors, the charge $q_{\mathrm{d}}\epsilon_{\mathrm{r}}$ is an integer multiple of the elementary charge. The defect is said to be in the n-th charge state. Each charge state has a certain stable atomic configuration $\mathbf{R}_n$. Each charge state has a ground state and excited states that can each have different stable atomic configurations.

Now, we discuss how the concentration of the various charge states depends on the position of the Fermi level. The overall constraint of global charge neutrality determines the chemical potential of the electron, i.e. the Fermi level in Fermi–Dirac statistics. We use the approximation that the concentration of defects is so small that the mutual interaction of defects becomes negligible.

As an example, we treat the possible reaction $V^0 \rightleftharpoons V^+ + e^-$, where V^0 denotes a neutral vacancy and V^+ is a positively charged vacancy, created by the ionization of an electron from the vacancy into the conduction band. The free energy G depends on the numbers n_0 of neutral and n_+ of positively charged vacancies. The minimum condition is met by

$$\mathrm{d}G = \frac{\partial G}{\partial n_0}\,\mathrm{d}n_0 + \frac{\partial G}{\partial n_+}\,\mathrm{d}n_+ = 0\ . \qquad (7.66)$$

The neutrality constraint is $\mathrm{d}n_0 + \mathrm{d}n_+ = 0$ and therefore the minimum condition reads

$$\frac{\partial G}{\partial n_0} = \frac{\partial G}{\partial n_+} \, . \tag{7.67}$$

For noninteracting defects and using (4.9) we write

$$\frac{\partial G}{\partial n_0} = G^{\rm f}(V^0) + kT \, \ln\left(\frac{n_0}{N_0}\right) \tag{7.68a}$$

$$\frac{\partial G}{\partial n_+} = \frac{\partial G(V^+)}{\partial n_+} + \frac{\partial G(e^-)}{\partial n_+} = G^{\rm f}_{V^+} + kT \, \ln\left(\frac{n_+}{N_+}\right) + \mu_{\rm e^-} \, , \tag{7.68b}$$

where $N_0 = NZ_0$ and $N_+ = NZ_+$ are the number of available sites, given by the number N of atomic sites and including possible internal degeneracies Z_0 and Z_+, respectively. Degeneracy factors of deep levels are not a simple subject [402] and , e.g., the degeneracy factors of Au donor and acceptor levels in Si are under discussion [440–442]. $G_{\rm f}$ denotes the free enthalpy of formation of the respective defect, as in (4.3). We have written the free enthalpy of the separated pair V^+ and e^- as the sum $G(V^+) + G(e^-)$. $\mu_{\rm e^-} = \partial G(e^-)/\partial n_+$ is (by definition) the chemical potential of the electron, i.e. the Fermi energy $E_{\rm F}$ of Fermi–Dirac statistics.[6] From (7.68a,b) we find for the ratio of the concentrations of defects $c_0 = n_0/N$ and $c_+ = n_+/N$

$$\frac{c_0}{c_+} = \frac{Z_+}{Z_0} \, \exp\left(-\frac{G^{\rm f}_{V^+} - G^{\rm f}_{V^0} + E_{\rm F}}{kT}\right) = \frac{Z_+}{Z_0} \, \exp\left(\frac{E_{\rm t}(V^0) - E_{\rm F}}{kT}\right) \, , \tag{7.69}$$

where the trap level energy (for the particular charge transition), $E_{\rm t}(V^0) = G^{\rm f}_{V^0} - G^{\rm f}_{V^+}$, is the free enthalpy of ionization of V^0. We note that c_0 can be obtained from (4.9) and $E_{\rm F}$ is determined by the charge-neutrality condition.

As example experimental data on the charge transition $\mathrm{Fe}^0 \rightleftharpoons \mathrm{Fe}^+ + \mathrm{e}^-$ of interstitial iron (in tetrahedral position, Fig. 7.28a, cmp. Fig. 3.17) in silicon is shown. The concentration of Fe^0 is tracked via the EPR signal from the neutral $S = 1$ state[7] with g-factor $g = 2.07$ [443]. For n-type samples the iron is in neutral state and the maximum EPR signal is found. For strongly p-type samples, the Fermi energy is below the trap level and all iron is in Fe^+ state, yielding no EPR signal at the given g-factor. From the investigation of various silicon samples with different doping levels and consequently different position of the Fermi level, the trap (deep donor) energy is found to be $E_{\rm V} + 0.375\,\mathrm{eV}$ as indicated in Fig. 7.28b.

7.7.2 Double Donors

An impurity that has two extra electrons available after bonding in the matrix may give rise to a double donor. Typical examples are substitutional

[6] The chemical potential in a one-component system is $\mu = \partial G/\partial n = G/n$. In a multicomponent system it is, for the i-th component, $\mu_i = \partial G/\partial n_i \neq G/n_i$.

[7] The electron configuration is $3\mathrm{d}^8$ with two paramagnetic electrons. Under uniaxial stress along [100] the EPR line splits into a doublet. [443] Further details can be found in [444].

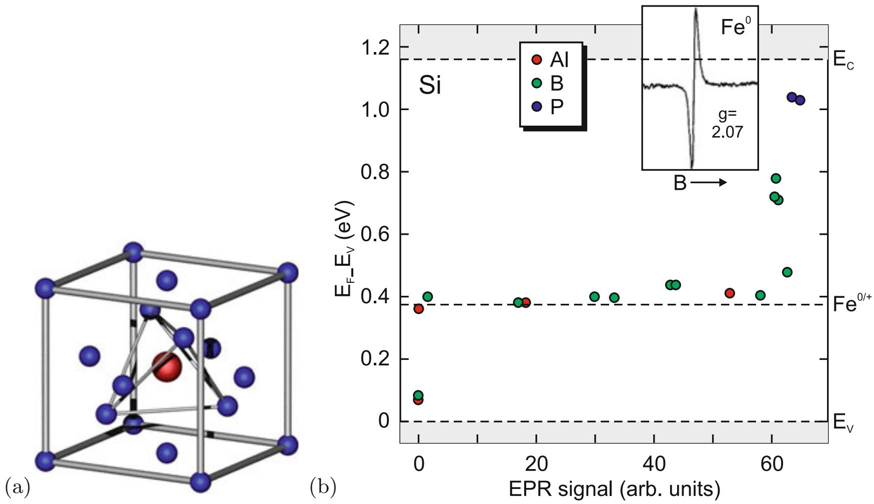

Fig. 7.28. (**a**) Silicon cubic unit cell with an interstitial iron atom (*red*) at tetrahedral site. (**b**) EPR intensity (at $T = 95\,\mathrm{K}$ from interstitial iron in neutral state, Fe^0 with $S = 1$) vs. Fermi level position for iron-doped silicon with varying Fermi level due to different amounts of shallow impurity levels from to Al, B and P as labeled. The *shaded areas* indicate the valence and conduction band. The *dashed line* at $E_\mathrm{t} = E_\mathrm{V} + 0.375\,\mathrm{eV}$ indicates the trap level. The *inset* shows a typical EPR spectrum of Fe^0. Adapted from [445], *inset* adapted from [446]

chalcogenide atoms (S, Se or Te) in silicon [447] and germanium [448], interstitial impurities such as $\mathrm{Mg_i}$ in Si [449], or group-V atoms on a group-III site in a III–V compound (antisite defect), such as $\mathrm{P_{Ga}}$ in GaP [450] or $\mathrm{As_{Ga}}$ in GaAs [451].

The double donor is similar to a He atom. Due to the repulsive Coulomb interaction of the two electrons on the neutral double donor, the (single) ionization energy of D^0 is smaller than of D^+. For He and He^+ the ratio of ionization energies is 0.45; for chalcogenides in Si and Ge similar ratios have mostly been found (Table 7.8).

The degeneracy factors for a double donor have been discussed in [392]. Typically, the degeneracy factor for the ionization of the double donor $\mathrm{D}^0 \rightarrow \mathrm{D}^+$ is $\hat{g}_\mathrm{D} = g_2/g_1 = 1/2$ and for the ionization $\mathrm{D}^+ \rightarrow \mathrm{D}^{++}$ is $\hat{g}_\mathrm{D} = g_1/g_0 = 2/1 = 2$.

7.7.3 Double Acceptors

In analogy to double donor defects, double acceptors can introduce up to two holes into the valence band. A typical example is Zn in silicon [452], exhibiting its ‘normal’ acceptor level $(\mathrm{Zn}^0/\mathrm{Zn}^-)$ at $E_\mathrm{V}+0.31\,\mathrm{eV}$. In moderately n-doped silicon another level $(\mathrm{Zn}^-/\mathrm{Zn}^{2-})$ is observed at $E_\mathrm{C} - 0.55\,\mathrm{eV}$, when the n-doping is sufficient to partially compensate the Zn and supply one electron

Table 7.8. Binding energies (to conduction band) of double donor chalcogenide impurities in Si and Ge. All energies in meV, data from [447, 448]

host	state	S	Se	Te
Si	D^0	318	307	199
	D^+	612	589	411
Ge	D^0	280	268	93
	D^+	590	512	330

for each Zn atom but not two ($2N_{Zn} > N_D > N_{Zn}$). A similar situation has been observed for Zn in germanium, exhibiting the levels $E_V + 0.03\,eV$ and $E_V + 0.09\,eV$ [453]. In Fig. 7.29 three different Ge:Zn samples are compared. If the additional Sb donor concentration ($N_D \approx 3.4 \times 10^{16}\,cm^{-3}$) is larger than $2N_{Zn}$ ($N_{Zn} \approx 1.2 \times 10^{16}\,cm^{-3}$), the sample is n-type (upper curve). The slope is similar to the Ge:Sb donor binding energy (Table 7.2). If compensation with donors is weak ($N_{Zn} > N_D$, middle curve) first the shallow donor level with 0.03 eV activation energy is activated and subsequently the deeper one with 0.09 eV activation energy, creating p-conduction with a saturated

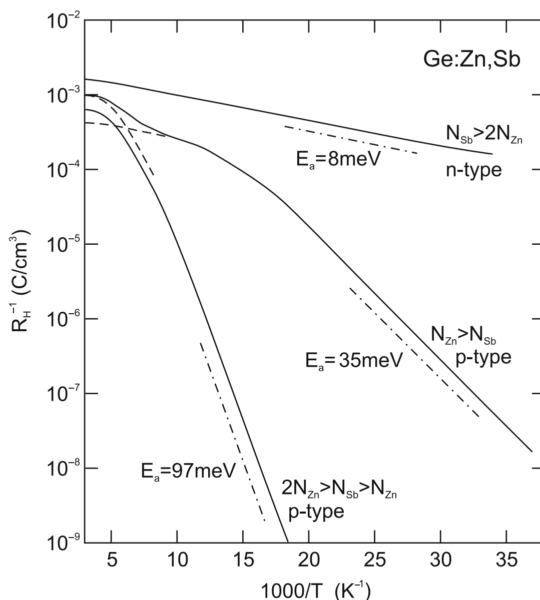

Fig. 7.29. Inverse (absolute) Hall coefficient (cmp. Sect. 8.4) R_H^{-1}, i.e. charge concentration, for three Ge:Zn samples with different degree of compensation with Sb donors as labeled. The *dash-dotted lines* indicate typical slopes. The *dashed lines* sketch the $Zn^0 \rightarrow Zn^-$ and the $Zn^- \rightarrow Zn^{--}$ processes. Adapted from [453]

hole density of $p \approx 2N_\mathrm{A} - N_\mathrm{D} > N_\mathrm{Zn}$ (negative Hall coefficient). The two individual activation processes are sketched as dashed lines in Fig. 7.29. If the Sb concentration is larger than N_Zn but smaller than $2N_\mathrm{Zn}$, the shallow acceptor level is filled with electrons, leaving still the only partially filled deeper acceptor level available for ionization (lower curve). In this case the sample is still p-type, but the saturation hole density is $p \approx 2N_\mathrm{A} - N_\mathrm{D} < N_\mathrm{Zn}$. The degeneracy factors for Zn in Si and Ge have been discussed in [402].

7.7.4 Jahn–Teller Effect

The lattice relaxation can reduce the symmetry of the defect. Many defects, such as a vacancy, a tetrahedral interstitial or an impurity, occupy initially tetrahedral sites in the zincblende structure. The lattice relaxation reduces the symmetry, e.g. to tetragonal or trigonal, and therefore causes initially degenerate levels to split. Such splitting is called the static Jahn–Teller effect [435, 454]. The energy change in terms of the atomic displacement Q can be denoted (using perturbation theory for the simplest, nondegenerate case) as $-I\,Q$ ($I > 0$). Including the elastic contribution with a force constant C, the energy of a configuration Q is

$$E = -I\,Q + \frac{1}{2}\,C\,Q^2 \,. \tag{7.70}$$

The stable configuration Q_min, for which the energy is minimal (E_min), is therefore given by

$$Q_\mathrm{min} = \frac{I}{C} \tag{7.71a}$$

$$E_\mathrm{min} = -\frac{I^2}{2C} \,. \tag{7.71b}$$

Several equivalent lattice relaxations may exist, e.g. a 3-fold minimum for remaining C_{3v} symmetry. The energy barrier between them has a finite height. Therefore, e.g. at sufficient temperature, the defect can switch between different configurations and eventually again becomes isotropic (dynamic Jahn–Teller effect). The experimental observation depends on the relation between the characteristic time of the experiment and the reorientation time constant of the defect.

7.7.5 Negative-U Center

We explain the principle of a so-called negative-U center [455] for the Si vacancy [456] (cf. Fig. 4.2). It was first proposed by Anderson to explain the properties of amorphous chalcogenide glasses [457]. Many defectsin semi-

conductors exhibit negative-U behavior, e.g. also the boron interstitial in Si [456, 458]. Coulomb energy and the Jahn–Teller effect compete for the position of the occupancy level for different charge states. U refers to the additional energy upon charging of the defect with an additional electron. The Coulomb repulsion of electrons leads to an *increase* of the energy, i.e. positive U, which has been calculated to be 0.25 eV for the Si vacancy [459] for all charge states. The occupation level (cf. Sect. 4.2.2) $E_0(1,2)$ (the index 0 indicates effects only due to many-electron Coulomb interaction), separating the domination of V^{++} and V^{+} (Fig. 7.30) is 0.32 eV above the valence-band edge. Therefore, the occupation level $E_0(0,1)$ is expected to lie at about 0.57 eV about E_V.

The Jahn–Teller effect may lead to a splitting of the otherwise 4-fold degenerate states of the vacancy. A detailed experimental study using hyperfine interactions can be found in [460]. The schematic level diagram for the Jahn–Teller splitting is shown in Fig. 7.31. The V^{++} state (A_1 is always populated with two electrons) is resonant with the valence band. The T_2 state lies in the band gap. When the Jahn–Teller effect (now on the T_2 state) is included, the energies of the different charge states depend on the configuration coordinate (a mostly tetragonal distortion in the case of the Si vacancy).

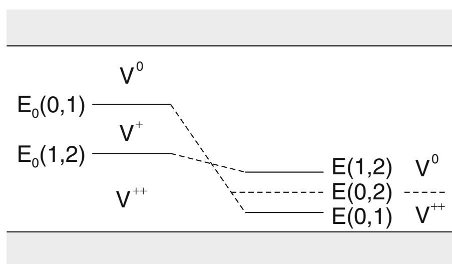

Fig. 7.30. Charge states of the vacancy in silicon. *Left*: level scheme without lattice relaxation, *right*: level scheme including the Jahn–Teller effect. For a Fermi level below (above) $E(0,2)$ the charge state V^{++} (V^0) is dominant

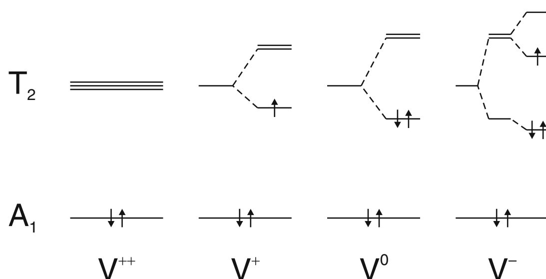

Fig. 7.31. Jahn–Teller splitting for different charge states of the vacancy. A_1 and T_2 refer to irreducible representations of the T_d point symmetry group. A_1 is nondegenerate and therefore does not exhibit a Jahn–Teller effect. T_2 is triply degenerate. The arrows represent electrons and their spin orientation

$$E_{V^0} = E(0,Q) = E(0,Q=0) - 2IQ + \frac{1}{2}CQ^2 \quad (7.72a)$$

$$E_{V^+} = E(1,Q) = E(1,Q=0) - IQ + \frac{1}{2}CQ^2 \quad (7.72b)$$

$$E_{V^{++}} = E(2,Q) = E(2,Q=0) + \frac{1}{2}CQ^2 \,. \quad (7.72c)$$

For the $n = 2$ state the T_2 gap state is empty and thus no degeneracy and Jahn–Teller term arises. For $n = 1$ there is a linear Jahn–Teller term. The occupation with two electrons (V^0) causes an approximately twice as large Jahn–Teller splitting for the $n = 0$ state. The force constant is assumed to be independent of the charge state. The energies for the minimum configurations $Q^n_{\min}$ are therefore

$$E(0, Q^0_{\min}) = E(0,Q=0) - 4\,\frac{I^2}{2C} \quad (7.73a)$$

$$E(1, Q^1_{\min}) = E(1,Q=0) - \frac{I^2}{2C} \quad (7.73b)$$

$$E(2, Q^2_{\min}) = E(2,Q=0) \,. \quad (7.73c)$$

The Jahn–Teller energy $E_{\mathrm{JT}} = I^2/2C$ lowers the position of the occupancy levels E_0 calculated with Coulomb terms only. The occupancy levels *including* the Jahn–Teller contribution are therefore given as

$$E(1,2) = E_0(1,2) - E_{\mathrm{JT}} \quad (7.74a)$$

$$E(0,1) = E_0(0,1) - 3\,E_{\mathrm{JT}} \,. \quad (7.74b)$$

For the vacancy in silicon the Jahn–Teller energy E_{JT} is about 0.19 eV. Thus the $E(1,2)$ level is lowered from 0.32 eV to 0.13 eV. The E(0,1) occupancy level, however, is reduced from 0.57 eV to 0.05 eV [456, 461] (see Fig. 7.30). The occupancy level $E(0,2)$ is in the middle between $E(0,1)$ and $E(1,2)$.

The relative concentrations of the three charge states are determined by (7.69) (degeneracy and entropy terms have been neglected)

$$\frac{c(V^{++})}{c(V^+)} = \exp\left(\frac{E(1,2) - E_{\mathrm{F}}}{kT}\right) \quad (7.75a)$$

$$\frac{c(V^{+})}{c(V^0)} = \exp\left(\frac{E(0,1) - E_{\mathrm{F}}}{kT}\right) \,. \quad (7.75b)$$

Therefore, V^{++} dominates if $E_{\mathrm{F}} < E(0,1)$ and V^0 dominates for $E_{\mathrm{F}} > E(1,2)$. In the intermediate range $E(0,1) < E_{\mathrm{F}} < E(1,2)$ we know from (7.75a,b) that V^+ is dominated by V^0 and V^{++}. However, at this point it is not clear whether V^{++} or V^0 dominates overall. The ratio of the concentrations of V^{++} and V^0 is given by

$$\frac{c(V^{++})}{c(V^0)} = \exp\left(\frac{E(1,2) + E(0,1) - 2E_{\mathrm{F}}}{kT}\right) = e^2\,\exp\left(\frac{E(0,2) - E_{\mathrm{F}}}{kT}\right) \,. \quad (7.76)$$

The occupancy level $E(0,2)$ is thus given as

$$E(0,2) = \frac{1}{2}\,[E(0,1) + E(1,2)]\ , \tag{7.77}$$

and is shown in Fig. 7.30. V^{++} dominates if $E_\mathrm{F} < E(0,2)$ and V^0 dominates for $E_\mathrm{F} > E(0,2)$. V^+ is, for no position of the Fermi level, the dominating charge state of the Si vacancy. We note that for n-doped Si the V^- and V^{--} can also be populated. The population of the V^0 state with an extra electron introduces another Jahn–Teller splitting (Fig. 7.31) that has trigonal symmetry.

Generally, the Jahn–Teller effect can make the addition of an electron cause an effectively negative charging energy; in this case the center is termed a negative-U center. We note that the single vacancy in germanium is not a negative-U center due to smaller Jahn–Teller distortion and smaller electron-lattice coupling [462].

7.7.6 DX Center

The DX center is a deep level that was first investigated for n-doped (e.g. Si-doped) $\mathrm{Al}_x\mathrm{Ga}_{1-x}\mathrm{As}$. It dominates the transport properties of the alloy for $x > 0.22$. For smaller Al concentrations and GaAs the DX level lies in the conduction band. DX-type deep levels have also been found for other alloys and dopants, e.g. GaAsP:S.

It is experimentally found that the capture process of electrons into the DX center is thermally activated. The capture energy E_c depends on the AlAs mole fraction (Fig. 7.32). The (average) barrier for electron capture has a minimum of 0.21 eV for $x \approx 0.35$, near the crossover point between direct

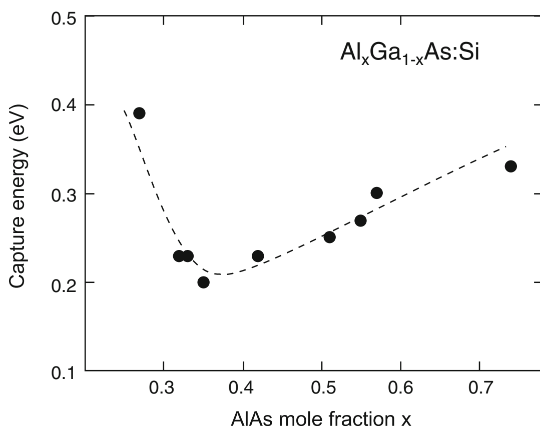

Fig. 7.32. Energy barrier for electron capture E_c at the Si-DX center in $\mathrm{Al}_x\mathrm{Ga}_{1-x}\mathrm{As}$ for various compositions. Experimental data from [463]

and indirect band gap (cf. Fig. 6.13). For lower Al concentrations, the capture barrier increases to 0.4 eV for $x = 0.27$; for $x > 0.35$ the capture barrier increases to about 0.3 eV for x around 0.7 [463]. The barrier for thermally releasing carriers from the DX center has been determined to be about 0.43 eV, independent of the Al mole fraction [463].

Carriers can be removed from the DX center by optical absorption of photons with energy larger than about 1.2 eV. If carriers are removed by optical excitation at low temperatures the (re-)capture is so slow ($\sigma < 10^{-30}\,\mathrm{cm}^2$) that the carriers remain in the conduction band and cause persistent photoconductivity (PPC). The PPC is only reduced upon increasing the sample temperature. The concentration of the DX center is about the same as the net doping concentration.

The properties of the DX center are reviewed in [464, 465]. So far, no definite microscopic model of the DX center has been agreed on. Lang [466] proposed that the DX center involves a donor and an unknown defect (probably a vacancy). It probably involves large lattice relaxation as in the configuration coordinates model of Fig. 7.33 where the donor binding energy E_D^b with respect to the conduction-band minimum, the barrier for electron capture E_c, the barrier for electron emission E_e and the optical ionization energy E_o are labeled. The donor binding energy is measured with Hall effect (cf. Sect. 8.4) at temperatures sufficient to overcome the capture and emission barriers, the emission barrier is measured with deep level transient spec-

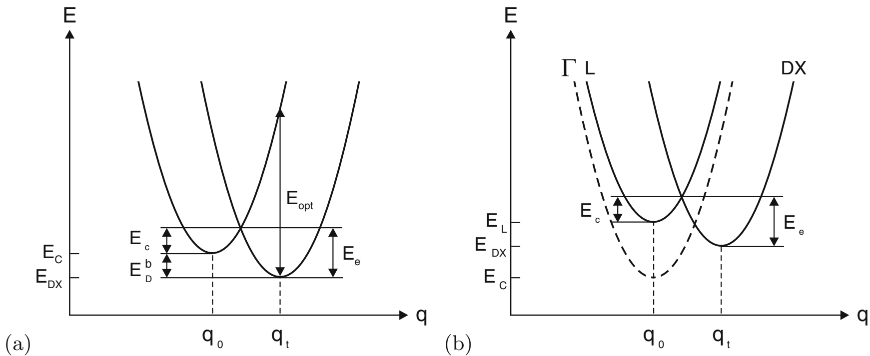

Fig. 7.33. (**a**) Schematic configuration coordinate diagram for the DX level with large lattice relaxation. q_0 is the configuration of the empty defect, q_t is the configuration of the filled defect. The donor binding energy E_D^b, the barrier for electron capture E_c, the barrier for electron emission E_e and the optical ionization energy E_o are labeled. E_C denotes the conduction-band edge. We note that in AlGaAs the DX level is associated with the L conduction band (see Fig. 6.13). (**b**) Schematic configuration coordinate diagram for the DX level in $\mathrm{Al_{0.14}Ga_{0.86}As}$ with the DX level being degenerate with the (Γ-related) conduction band

troscopy (DLTS). The capture barrier manifests itself in PPC experiments. We note that the DX center is related to the L-conduction band. For small Al mole fraction, the DX level is degenerate with the Γ-related conduction band (see Fig. 7.33b).

Theoretical models and experimental evidence hint at a vacancy-interstitial model for the Si-DX center [467]. The donor (Si) is displaced along the $\langle 111 \rangle$ direction from the Ga substitution site. The displacement is predicted to be 0.117 nm and the distorted geometry can be viewed as a Ga vacancy and a Si interstitial. The charge state of the (filled) DX center is proposed to be a two-electron negative-U state.

7.7.7 EL2 Defect

The EL2 defect is a deep donor in GaAs. It is not related to impurities but occurs for intrinsic material, in particular grown under As-rich conditions. It has physical properties similar to the DX center. The bleaching of absorption due to EL2, i.e. the optical removal of electrons from the defect at low temperatures, is shown in Fig. 7.34. The microscopic model [468] describes the EL2 defect as an arsenic antisite defect, i.e. an arsenic atom on a Ga site, As_{Ga}. In the charged state the arsenic atom is displaced from the lattice position and a complex of a Ga vacancy (symmetry T_{3d}) and an interstitial As (symmetry C_{3v}) with 0.14 nm displacement along $\langle 111 \rangle$ forms (V_{Ga}-As_i). The charged state is filled with two electrons.

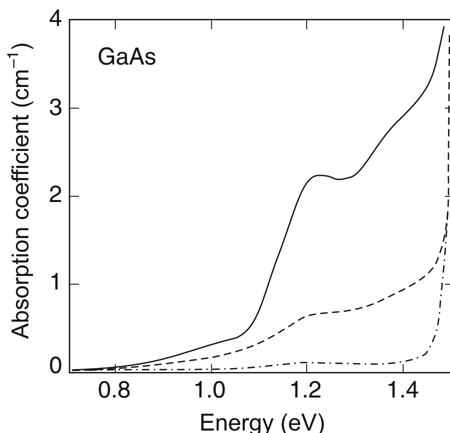

Fig. 7.34. Absorption spectrum of GaAs at low temperatures (T = 10 K) when cooled in the dark (*solid line*). The *dashed* (*dash-dotted*) *line* is the absorption after illuminating the sample for 1 min (10 min) with white light, leading to quenching of the EL2-related absorption. Adapted from [471]

7.7.8 Semi-insulating Semiconductors

Semiconductors with high resistivity (10^7–$10^9\,\Omega\,\mathrm{cm}$) are called semi-insulating ('s.i.' or 'si'). Semi-insulating substrates are needed for high-speed devices. The high resistivity should stem from a small free-carrier density at finite temperature and not from a small mobility due to poor crystal quality. For sufficiently wide band gap, the intrinsic carrier concentration is small and such pure material is semi-insulating, e.g. GaAs with $n_\mathrm{i} = 1.47 \times 10^6\,\mathrm{cm}^{-3}$ and $5.05 \times 10^8\,\Omega\,\mathrm{cm}$ [469]. Since shallow impurities are hard to avoid, another route is used technologically. Impurities that form deep levels are incorporated in the semiconductor in order to compensate free carriers. For example, a deep acceptor compensates all electrons if $N_\mathrm{A} > N_\mathrm{D}$. Since the acceptor is deep ($E_\mathrm{A}^\mathrm{b} \gg kT$), it does not release holes for reasonable temperatures. Examples of suitable impurities for compensation of electrons are Si:Au [470], GaAs:Cr [472] and InP:Fe [473]. A deep donor, e.g. InP:Cr [474], is necessary to compensate p-type conductivity.

Figure 7.35a shows the terms of Fe in InP [475, 476]. An overview of transition metals in III–V semiconductors can be found in [477]. The electron configuration of neutral Fe atoms is $3\mathrm{d}^6 4\mathrm{s}^2$ (cf. Table 15.2). The Fe is incorporated on the In site and thus has a Fe^{3+} state as a neutral acceptor (A^0). The Fe^{3+} state has the electron configuration $3\mathrm{d}^5$. The arrow in Fig. 7.35a represents the capture of an electron from the conduction band or from a shallow donor. The charge state of the Fe becomes Fe^{2+} (charged acceptor, A^-) with the electron configuration $3\mathrm{d}^6$. The cubic crystal field (T_d

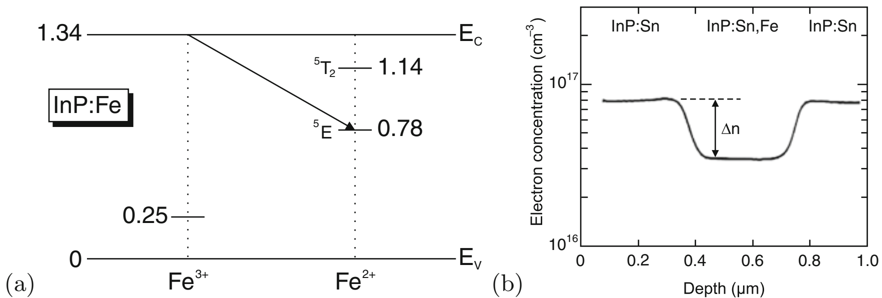

Fig. 7.35. (**a**) Schematic band diagram of InP with levels of Fe impurities in the 3+ and 2+ charge states at low temperature. All energies are given in eV. The *arrow* denotes capture of an electron (from the conduction band or a shallow donor) on the deep acceptor. Compare this figure also with Figs. 9.34 and 10.24. (**b**) Depth profile of electron concentration in an InP:Sn/InP:Sn,Fe/InP:Sn structure. The change $\Delta n \approx 4.5 \times 10^{16}\,\mathrm{cm}^{-3}$ of electron concentration is due to the compensation by Fe and corresponds to the chemical iron concentration determined by SIMS, $[\mathrm{Fe}]=4.9 \times 10^{19}\,\mathrm{cm}^{-3}$. Part (**b**) adapted from [481]

symmetry) splits this ^{5}D Fe state[8] into two terms [478] that exhibit further fine structure [476]. The large thermal activation energy of 0.64 eV found in the Hall effect on semi-insulating InP:Fe [473] corresponds to the energy separation of the ^{5}E level and the conduction band.

The maximum electron concentration that can be compensated in this way is limited by the solubility of Fe in InP [479], about 1×10^{17} cm^3. Higher Fe incorporation leads to the formation of Fe (or FeP) precipitates and degrades the crystal quality. Only a fraction of the incorporated Fe may then be electrically active and contribute to the compensation. The maximum electrically active Fe concentration is found to be 5–6×10^{16} cm^{-3} [480]. The compensation can be directly visualized via the depth profile of the electron concentration in a n-si-n structure (Fig. 7.35b). The poor thermal stability of Fe, i.e. high diffusion coefficient, has evoked proposals for more stable dopants such as InP:Ru [482].

7.7.9 Isoelectronic Impurities

Isoelectronic impurities, generally represent a deep level with a short range potential. The isoelectronic trap introduces a bound state for an electron or a hole. Once a carrier has been captured, the defect becomes charged. The other carrier type is then easily trapped, forming a bound exciton (Sect. 10.3.2). The theory of isoelectronic impurities is outlined in [483]. A detailed theoretical treatment of N in GaAs and GaP is given in [369].

In GaP:N, an electron is spatially localized on the N impurity. Most of the wave function is at the X-point. The nitrogen-bound electron level in GaP (A_1 symmetry) is close to the conduction band edge and within the band gap. Important for the energy position is the lattice relaxation, leading to an inward relaxation of the surrounding Ga atoms (Fig. 7.37). Due to the spatial localization of the wave function it is delocalized in k-space (Fig. 7.36a) and obtains a sizeable component at the Γ-point, facilitating zero-phonon absorption from the valence band. This effect is present only when the lattice relaxation around the impurity is considered; without relaxation the Γ-component is zero, with relaxation about 1% [369]. The Γ-component of the wave-function is larger for localization at an isoelectronic impurity than at a shallow donor such as sulfur [484]. This way a large oscillator strength for optical transitions occurs (Sect. 9.5.10, 10.3.2). The wavefunction of an isolated single N impurity and a neighboring N–N pair (NN_1) in GaP are shown in Fig. 7.36b.

Isolated nitrogen impurities in (unstrained) GaAs introduce states only within the conduction band (Fig. 7.37). The reason is that the GaAs conduction band edge is further from the vacuum level than that of GaP (see Fig. 11.14). Only the NN_1 and NN_4 pair levels are theoretically expected to

[8]The notation is ^{2S+1}J (multiplicity), with S being the total spin and J being the total angular momentum.

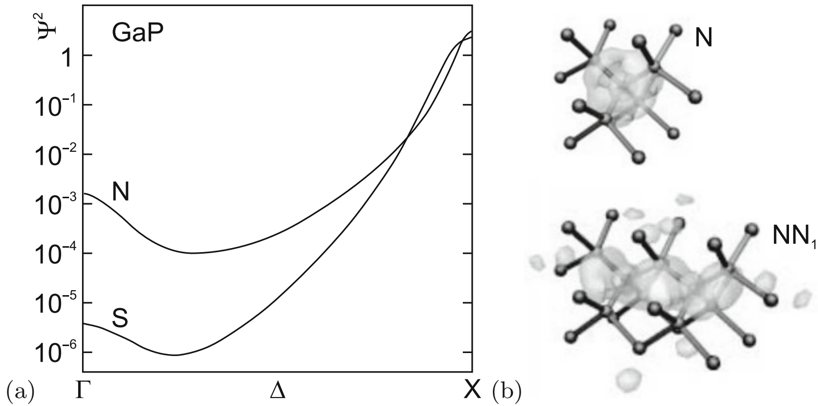

Fig. 7.36. (**a**) Model calculation of the wave-vector dependence of the probability density of an electron bound to a 10 meV deep isoelectronic trap (N) and to a 100 meV deep shallow donor (S) in GaP. Adapted from [484]. (**b**) Wavefunction (isosurface at 20% of maximum) of isolated nitrogen (N) and neighboring N–N pair (NN_1) in GaP. Adapted from [369]

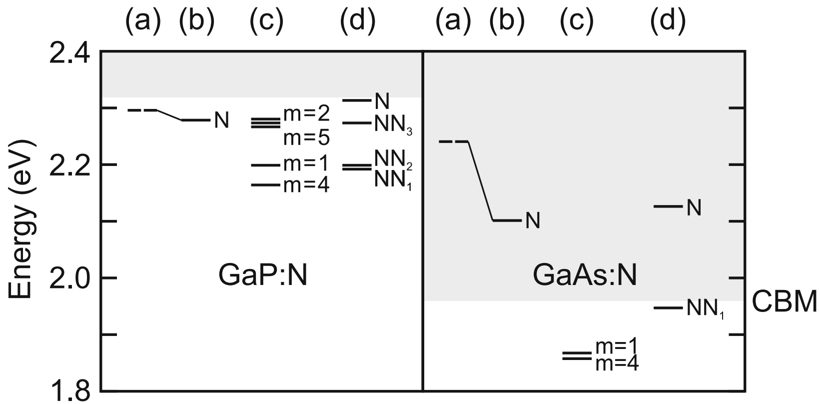

Fig. 7.37. Energy levels of nitrogen impurity states in GaP (*left*) and GaAs (*right*). The energy scale is relative to the bulk GaP valence band maximum, the conduction band minima (CBM) are thus shown relative to the vacuum level. The conduction band is shown in *grey*. For both materials, (a) denotes the isolated N impurity level calculated *without* lattice relaxation (*dashed line*), and (b) *with* lattice relaxation. (c) denotes the position of N–N pair levels, m denoting the neighbor. (d) shows selected experimental data. NN_1 denotes the direct neighbor NN-pair. The other NN_n follow the usual nomenclature as in [490]. Data taken from [369]

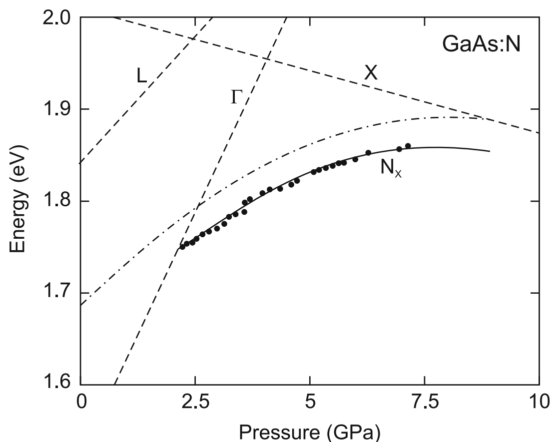

Fig. 7.38. Pressure dependence of the energy of excitons bound to isolated nitrogen impurities in GaAs (*circles*), measured from the top of the GaAs valence band. The *dashed lines* are the pressure dependent GaAs bulk band gaps (cmp. Fig. 6.37). The *solid* (*dash-dotted*) *line* is a theoretical model for the nitrogen-bound exciton (electron) level. Adapted from [487]

be within the GaAs band gap. The index denotes the n-th neighbor position. The NN_1 level has been experimentally observed [485, 486]. The isolated nitrogen impurity level is forced into the GaAs band gap upon hydrostatic pressure [486, 487] (Fig. 7.38). Further levels deeper within the band gap are due to clusters containing more than two nitrogen atoms.

7.7.10 Surface States

The investigation of (semiconductor) surfaces is a large field with sophisticated methods that allow real-space imaging with atomic resolution by scanning probe microscopy and highly depth resolved electronic studies. The surface represents first of all a break in the periodic crystal potential and thus a defect of the bulk crystal. The unsatisfied bonds partly rearrange, e.g. by building dimers, forming a surface reconstruction or remain as dangling bonds. The surface exhibits a surface density of states. Such states can lie in the band gap and capture electrons, leading to recombination and a depletion layer. In this book, we will not get into details of semiconductor surface physics and refer the reader to [488].

As an example of the formation of electronic states at surface defects we show in Fig. 7.39 the comparison of topography and work function (measured by Kelvin probe force microscopy [489]) at a surface step on a GaP(110) surface that has been prepared by cleaving in-situ in ultrahigh vacuum (UHV). The depletion-type band bending of the surface is about 0.4 eV. The further increase of the position of the vacuum level at the step edge shows the pres-

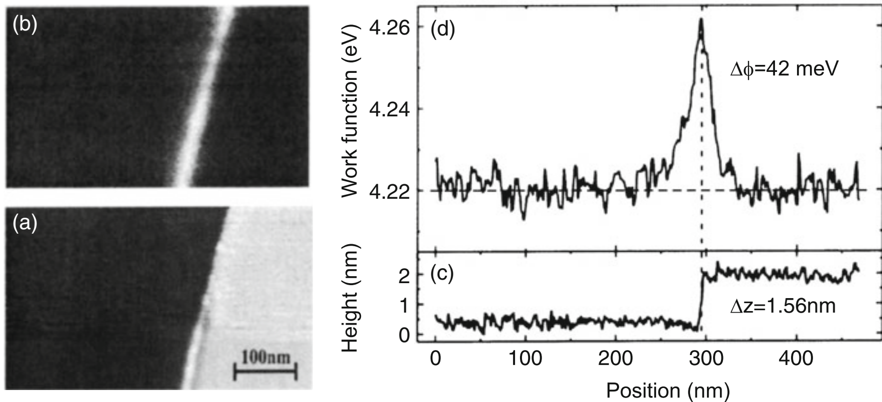

Fig. 7.39. Image of (**a**) topography ($\Delta z = 2.8\,\mathrm{nm}$) and (**b**) work function ($\Delta\phi =$ 4.21–4.26 eV) of a surface step along [111] on a n-GaP(110) surface cleaved in UHV. Adapted from [489]. (**c**) and (**d**) show the corresponding linescans. Adapted from [489]

ence of trap states in the band gap causing the conduction band to bend upwards (cf. Sect. 20.2.1). Modeling of the effect shows that the charge density at the surface is $6 \times 10^{11}\,\mathrm{cm}^{-2}$ and at the step edge $1.2 \times 10^{6}\,\mathrm{cm}^{-1}$.

7.8 Hydrogen in Semiconductors

The role of hydrogen in semiconductors was first recognized in studies of ZnO [491]. It is now clear that hydrogen plays an important role in the passivation of defects. As a 'small' atom, it can attach easily to dangling bonds and form an electron-pair bond. Thus, surfaces, grain boundaries, dislocations and shallow (donor and acceptor) and deep impurity levels become passivated. A good overview and many details of the physics and technological use of hydrogen in semiconductors can be found in [492, 493]. The hydrogen must be typically introduced as atomic species into semiconductors, e.g. from a plasma in the vicinity of the surface or by ion irradiation.

With regard to silicon it is important to note that the Si–H bond is stronger than the Si–Si bond. Thus a silicon surface under atomic hydrogen exhibits Si–H termination rather than Si–Si dimers [494]. Due to the stronger bond, the hydrogenation leads to an increase of the silicon band gap, which can be used for surface passivation [495], leading to reduced reverse diode current.

The hydrogen concentration in amorphous Si (a-Si) can be as high as 50% [496]. Electronic grade a-Si contains typically 10–30 atomic % hydrogen and is thus rather a silicon–hydrogen alloy.

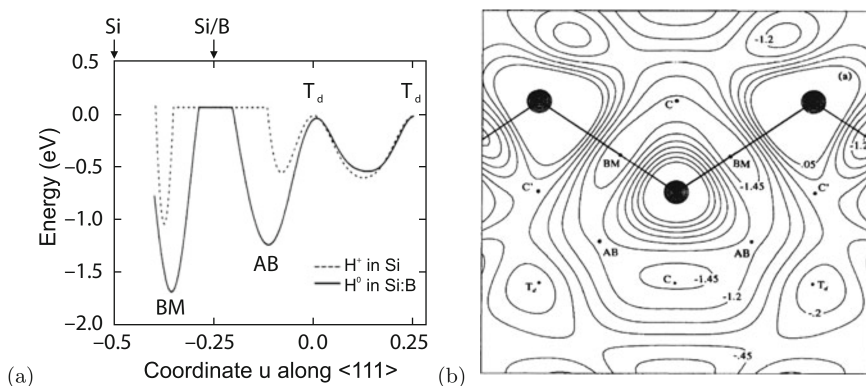

Fig. 7.40. (**a**) Energy for positions u of the hydrogen atom along the $\langle 111 \rangle$ direction for H^+ in pure Si (Si atom at $u = -0.25$) and neutral hydrogen (B atom at $u = -0.25$). u is measured in units of $\sqrt{3}a_0$. For all positions of the hydrogen atom the positions of the other atoms have been relaxed in the calculation. Data from [521]. (**b**) Adiabatic potential energy in the (110) plane for hydrogen in Si:B. 'BM' denotes the bond minimum site (high valence electron density), C and C' are equivalent for pure Si. Reprinted with permission from [497], ©1989 APS

Hydrogen in crystalline silicon occupies the bond-center interstitial position (see Fig. 3.17b) as shown in Fig. 7.40a. The complexes formed by hydrogen with shallow acceptors and donors have been studied in detail. It is now generally accepted that for acceptors (e.g. boron) in silicon the hydrogen is located close to the bond-center position of the Si–B pair (BM, bond minimum) as sketched in Fig. 7.41a. The boron atom forms an electron-pair bond with three silicon atoms of the tetrahedra, the fourth silicon bonds to the hydrogen atom. The complex therefore no longer acts as an acceptor. The silicon atoms and the acceptor relax their positions. The adiabatic potential energy surface of hydrogen in Si:B is shown in Fig. 7.40b. The hydrogen can sit on four equivalent sites (BM) along the $\langle 111 \rangle$ directions of the initial $B\text{–}Si_4$ tetrahedron. This reduces the symmetry, e.g. of H–B vibrations [498]. The energetic barrier for the hydrogen orientation has been determined to be 0.2 eV theoretically [497] for a hydrogen motion along the path BM–C–BM in Fig. 7.40b. Stress (along [100] and [112]) reduces the symmetry and leads to splitting of the local vibrational modes, now showing axial symmetry [499]. However, this preferential orientation disappears with an activation energy of 0.19 eV, close to the theoretical value.

Hydrogen has experimentally been found to also passivate shallow donors. The microscopic configuration is sketched in Fig. 7.41b. The hydrogen atom sits on the Si–AB (antibonding) position and forms an electron-pair bond with the silicon atom. The donor, e.g. phosphorus, is left with a double-filled p-orbital (lone pair) whose level is in the valence band and thus no longer contributes to conductivity. Molecular hydrogen can passivate the so-called A

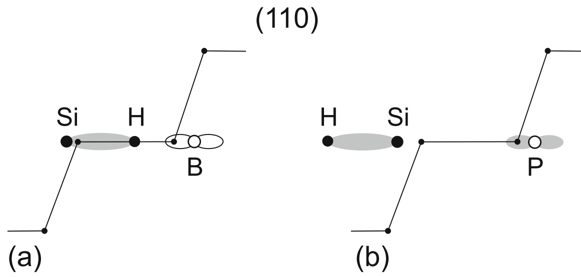

Fig. 7.41. Schematic model for hydrogen in silicon forming a complex with (**a**) a shallow acceptor (boron, empty orbital) and (**b**) a shallow donor (phosphorus, double-filled orbital)

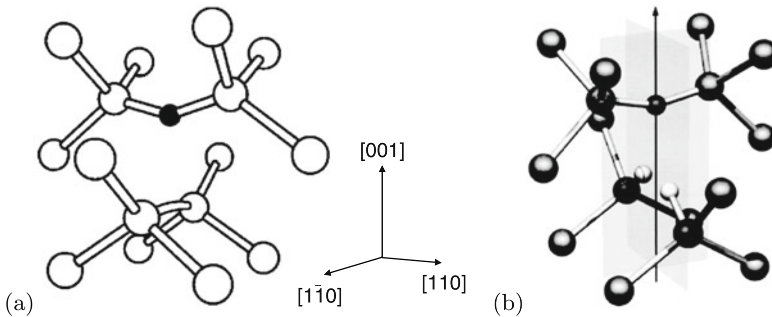

Fig. 7.42. (**a**) Structure of the V–O complex (A center) in silicon. The *black sphere* represents the oxygen atom. Reprinted with permission from [501], ©2004 APS. (**b**) Calculated ground-state structure for the V–O–H_2 center in silicon. Oxygen is over the C_2 axis, and the two *white* spheres represent hydrogen. Reprinted with permission from [500], ©2000 APS

center in Si, an oxygen–vacancy complex [500]. The atomistic configuration of the V–O–H_2 complex is shown in Fig. 7.42. The deep double donor S in Si with a level at 0.3 eV below the conduction-band edge can also be passivated by two hydrogen atoms [502].

8 Transport

8.1 Introduction

Charge and heat energy can be transported through the semiconductor in the presence of appropriate (generalized) forces. Such a force can be an electric field or a temperature gradient. Both transport phenomena are coupled since electrons can transport energy and charge through the crystal. First, we will treat the charge transport as a consequence of a gradient in the Fermi level, then the heat transport upon a temperature gradient and finally the coupled system, i.e. the Peltier and Seebeck effects.

Practically all important semiconductor devices are based on the transport of charge, such as diode, transistor, photodetector, solar cell and laser.

Carriers move in the semiconductor driven by a gradient in the Fermi energy. We distinguish

- drift, as a consequence of an electric field $\mathbf{E}$,
- diffusion, as a consequence of a concentration gradient ∇n or ∇p.

In inhomogeneous semiconductors for which the position of the band edges is a function of position, another force occurs. This will not be treated here, since later (cf. Sect. 11) it will be included as an additional, internal electric field.

Many semiconductor properties, such as the carrier concentration and the band gap, depend on the temperature. Thus, device properties will also depend on temperature. During operation of a device typically heat is generated, e.g. by Joule heating due to finite resistivity. This heat leads to an increase of the device temperature that subsequently alters the device performance, mostly for the worse. Ultimately, the device can be destroyed. Thus cooling of the device, in particular of the active area of the device, is essential. Mostly the thermal management of device heating limits the achievable performance (and lifetime) of the device. In high-power devices quite high energy densities can occur, e.g. the facet of a high-power semiconductor laser has to withstand an energy density beyond $10\,\mathrm{MW\,cm^{-2}}$.

M. Grundmann, *The Physics of Semiconductors*, 2nd ed., Graduate Texts in Physics, DOI 10.1007/978-3-642-13884-3_8,

© Springer-Verlag Berlin Heidelberg 2010

8.2 Conductivity

Under the influence of an electric field the electrons accelerate according to (cf. (6.35))

$$\mathbf{F} = m^* \frac{\mathrm{d}\mathbf{v}}{\mathrm{d}t} = \hbar \frac{\mathrm{d}\mathbf{k}}{\mathrm{d}t} = q\,\mathbf{E} = -e\,\mathbf{E}\,. \tag{8.1}$$

In the following, q denotes a general charge, while e is the (positive) elementary charge. After the time δt the $\mathbf{k}$ vector of all conduction electrons (and the center of the Fermi sphere) has been shifted by $\delta\mathbf{k}$

$$\delta\mathbf{k} = -\frac{e\,\mathbf{E}}{\hbar}\,\delta t\,. \tag{8.2}$$

In the absence of scattering processes this goes on further (similar to an electron in vacuum). This regime is called *ballistic* transport. In a (periodic) band structure, the electron will perform a closed cycle as indicated in Fig. 8.1. Such motion is called a Bloch oscillation. However, in a bulk crystal the period T of such an oscillation $e\mathcal{E}T/\hbar = 2\pi/a_0$ is of the order of 10^{-10} s for $\mathcal{E} = 10^4$ V/cm. This time is much longer than a typical scattering time of 10^{-14} s. Thus, in bulk material the Bloch electron cannot reach the zone boundary. However, in artificial superlattices (cf. Sect. 11) with larger periodicity (≈ 10 nm), high electric fields ($\approx \mathcal{E} = 10^6$ V/cm) and high quality (reduced collision time) such motion is possible. We note that in the absence of scattering, electrons also perform a periodic oscillation in a magnetic field (cyclotron motion).

In a real semiconductor, at finite temperatures, impurities, phonons and defects (finally also the surface) will contribute to scattering. In the relaxation-time approximation it is assumed that the probability for a scattering event, similar to friction, is proportional to the (average) carrier velocity. The average relaxation time τ is introduced via an additional term $\dot{\mathbf{v}} = -\mathbf{v}/\tau$ that sums up all scattering events. Thus, the maximum velocity that can be reached in a static electric field is given by (steady-state velocity)

$$\mathbf{v} = -\frac{e\,\mathbf{E}\,\tau}{m^*}\,. \tag{8.3}$$

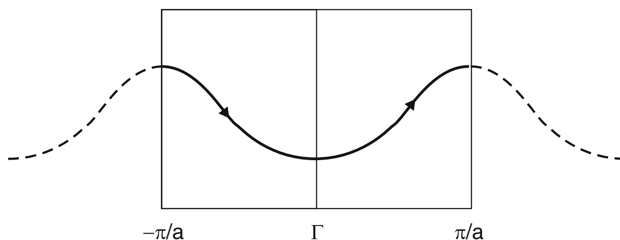

Fig. 8.1. Schematic representation of a Bloch oscillation

The current density per unit area is then linear in the field, i.e. fulfills Ohm's law

$$\mathbf{j} = nq\mathbf{v} = \frac{ne^2\,\mathbf{E}\,\tau}{m^*} = \sigma\,\mathcal{E}\;. \tag{8.4}$$

The conductivity σ in the relaxation-time approximation is given by

$$\sigma = \frac{1}{\rho} = \frac{ne^2\tau}{m^*}\;. \tag{8.5}$$

The specific resistivity is the inverse of the conductivity. Metals have a high conductivity (see Table 8.1), e.g. for Cu at room temperature $\sigma = 5.8 \times 10^5\,\Omega^{-1}\,\mathrm{cm}^{-1}$. At low temperatures (4 K) the conductivity is even a factor of 10^5 higher. The mean free path $d = \tau\,v_\mathrm{F}$ is

$$d = \frac{\sigma\,m^* v_\mathrm{F}}{n\,e^2}\;, \tag{8.6}$$

Table 8.1. Conductivity at room temperature for various metals, semiconductors, insulators and liquids

material	σ ($\Omega^{-1}\,\mathrm{cm}^{-1}$)
Ag	6.25×10^5
Al	3.6×10^5
Au	4.35×10^5
Cu	5.62×10^5
Fe	1.1×10^5
Pt	1.02×10^5
Ge pure ($N_\mathrm{D} \sim 10^{13}\,\mathrm{cm}^{-3}$)	10^{-2}
Ge ($N_\mathrm{D} \sim 10^{15}\,\mathrm{cm}^{-3}$)	1
Ge ($N_\mathrm{D} \sim 10^{17}\,\mathrm{cm}^{-3}$)	2×10^1
Ge ($N_\mathrm{D} \sim 10^{18}\,\mathrm{cm}^{-3}$)	2×10^2
Si pure	4.5×10^{-6}
Si:As ($N_\mathrm{D} \sim 3 \times 10^{19}\,\mathrm{cm}^{-3}$)	4×10^2
Si:B ($N_\mathrm{A} \sim 1.5 \times 10^{19}\,\mathrm{cm}^{-3}$)	1.2×10^2
GaAs pure	1.4×10^{-7}
ZnO:Al (highly doped)	$\approx 1 \times 10^4$
pentacene	10^{-8} – 10^{-4}
SiO_2	$\approx 10^{-15}$
Al_2O_3	$\approx 10^{-16}$
H_2O pure	4×10^{-8}
hexane	$\approx 10^{-18}$

v_F being the Fermi velocity ($E_F = m^* v_F^2/2$). For copper, $d = 3$ mm at low temperature (and thus susceptible to the sample geometry) while at room temperature the mean free path is only about 40 nm. However, this becomes an issue when the metal line width and height of interconnects in integrated circuits approaches this length scale [503] (see Sect. 23.5.5).

In semiconductors, the carrier concentration depends strongly on the temperature. At zero temperature the conductivity is zero. Also, the scattering processes and thus the relaxation time constant exhibit a temperature dependence. The conductivity spans a large range from insulating to almost metallic conduction (see Table 8.1).

8.3 Low-Field Transport

First we consider only *small* electric fields. The real meaning of this will only become clear in Sect. 8.5 on high-field transport. In the low-field regime the velocity is proportional to the electric field.

8.3.1 Mobility

The mobility is defined (scalar terms) as

$$\mu = \frac{v}{\mathcal{E}} . \tag{8.7}$$

By definition, it is a negative number for electrons and positive for holes. However, the numerical value is usually given as a positive number for both carrier types. In an intrinsic semiconductor the mobility is determined by scattering with phonons. Further scattering is introduced by impurities, defects or alloy disorder. The conductivity is (8.4)

$$\sigma = q\, n\, \mu \tag{8.8}$$

for each carrier type. The mobility in the relaxation time approximation is

$$\mu = \frac{q\, \tau}{m^*} . \tag{8.9}$$

and the conductivity thus

$$\sigma = \frac{q^2 n \tau}{m^*} . \tag{8.10}$$

In the presence of both electrons and holes,

$$\sigma = -en\mu_n + ep\mu_p , \tag{8.11}$$

where μ_n and μ_p are the mobilities for electrons and holes, respectively. In the relaxation-time approximation these are given by $\mu_n = -e\tau_n/m_e^*$ and $\mu_p = e\tau_p/m_p^*$.

Table 8.2. Mobilities of electrons and holes at room temperature for various semiconductors

material	$-\mu_n$ (cm^2/Vs)	μ_p (cm^2/Vs)
Si	1300	500
Ge	4500	3500
GaAs	8800	400
GaN	300	180
InSb	77,000	750
InAs	33,000	460
InP	4600	150
ZnO	230	8

As a unit, usually cm^2/Vs is used. While Cu at room temperature has a mobility of 35 cm^2/Vs, semiconductors can have much higher values. In two-dimensional electron gases (cf. Sect. 11), the mobility can reach several 10^7 cm^2/Vs at low temperature (Fig. 11.29). In bulk semiconductors with small band gap, a high electron mobility is caused by its small effective mass. Some typical values are given in Table 8.2.

8.3.2 Microscopic Scattering Processes

The relaxation time constant summarizes all scattering mechanisms. If the relaxation times τ_i of various processes are independent, the Matthiesen rule can be used to obtain the mobility ($\mu_i = q\tau_i/m^*$)

$$\frac{1}{\mu} = \sum_i \frac{1}{\mu_i} \ . \tag{8.12}$$

The different scattering mechanisms have quite different temperature dependences such that the mobility is a rather complicated function of temperature. In [504] the various mechanisms determining the low and high-field transport properties of (cubic) semiconductors are reviewed.

8.3.3 Ionized Impurity Scattering

Theoretically, this problem is treated similar to Rutherford scattering. A screened Coulomb potential is assumed, as the scattering potential

$$V(r) = -\frac{Ze}{4\pi\epsilon_0\epsilon_r}\frac{1}{r}\exp\left(-\frac{r}{l_D}\right) \ , \tag{8.13}$$

where L_D is the screening length. The problem has been treated classically by Conwell and Weisskopf [505] and quantum mechanically by Brooks [506]

and Herring. An expression for the mobility that encompasses the Conwell–Weisskopf and Brooks–Herring results is derived in [507]. Further details are given in [508, 509]. For the mobility it is found that

$$\mu_{\text{ion.imp.}} = \frac{2^{7/2}(4\pi\epsilon_0\epsilon_{\text{r}})^2}{\pi^{3/2}Z^2e^3\sqrt{m^*}} \frac{(kT)^{3/2}}{N_{\text{ion}}} \frac{1}{\ln(1+b) - b/(1+b)} , \tag{8.14}$$

with $b = 4k^2l_{\text{D}}^2 = 8m^*E(l_{\text{D}}/\hbar)^2$.

8.3.4 Deformation Potential Scattering

Acoustic phonons with small wavevector, i.e. a wavelength large compared to the unit cell, can have TA or LA character. The TA phonons represent a shear wave (with zero divergence), the LA phonons are a compression wave (with zero rotation). The LA is a plane wave of displacement $\delta\mathbf{R}$ parallel to the k-vector $\mathbf{q}$,

$$\delta\mathbf{R} = \mathbf{A}\,\sin\left(\mathbf{q}\cdot\mathbf{R} - \omega t\right) \,. \tag{8.15}$$

The strain tensor is given by

$$\epsilon_{ij} = \frac{1}{2}\left(\mathbf{q}_i\,\mathbf{A}_j + \mathbf{q}_j\,\mathbf{A}_i\right)\,\cos\left(\mathbf{q}\,\mathbf{R} - \omega t\right) \,. \tag{8.16}$$

It has a diagonal form $\epsilon_{ij} = \mathbf{q}_i\mathbf{A}_j$ for $\mathbf{q}$ and $\omega \to 0$. Therefore, the LA phonon creates an oscillatory volume dilatation (and compression) with amplitude $\mathbf{q}\cdot\mathbf{A}$. This volume modulation affects the position of the band edges. For the conduction-band edge the energy change is related to the volume change by the hydrostatic deformation potential $E_{\text{ac.def.}} = V\partial E_{\text{C}}/\partial V$. Since the modulation is small compared to the energy of the charge carriers, it is mostly an elastic scattering process. The Hamilton operator for the LA scattering is

$$\hat{H} = E_{\text{ac.def.}}\,(\mathbf{q}\cdot\mathbf{A}) \,. \tag{8.17}$$

The size of the LA amplitude is given by the number of phonons in the mode that is given by the Bose–Einstein distribution, $N_{\text{ph}}(\hbar\omega) = \left[\exp\left(\frac{\hbar\omega}{kT}\right)\right]^{-1}$. The mobility due to acoustic deformation potential scattering is found to be

$$\mu_{\text{ac.def.}} = \frac{2\sqrt{2\pi}e\hbar^4c_{\text{l}}}{3m^{*5/2}E^2_{\text{ac.def.}}}\left(\frac{1}{kT}\right)^{3/2} , \tag{8.18}$$

where $c_{\text{l}} = \rho c_{\text{s}}^{\text{LA}}$, ρ being the density and c_{s} being the sound velocity. The acoustical deformation potential scattering is therefore important at high temperatures. It is dominating in nonpolar semiconductors (Ge, Si) at high temperatures (typically at and above room temperature).

8.3.5 Piezoelectric Potential Scattering

In piezoelectric crystals (see Sect. 14.4), i.e. crystals that show an electric polarization upon strain, certain acoustic phonons lead to piezoelectric fields. In GaAs, with $\langle 111 \rangle$ being the piezoelectric directions, this is the case for shear waves. In strongly ionic crystals, e.g. II–VI semiconductors, the piezoelectric scattering can be stronger than the deformation potential scattering. The mobility due to piezoelectric potential scattering is

$$\mu_{\text{pz.el.}} = \frac{16\sqrt{2\pi}}{3} \frac{\hbar \epsilon_0 \epsilon_{\text{r}}}{m^{*3/2} e K^2} \left(\frac{1}{kT} \right)^{1/2} , \tag{8.19}$$

with $K = \frac{e_{\text{p}}^2/c_{\text{l}}}{\epsilon_0 \epsilon_{\text{r}} + e_{\text{p}}^2/c_{\text{l}}}$, e_{p} being the piezoelectric coefficient.

8.3.6 Polar Optical Scattering

LO phonons are connected with an electric field antiparallel to the displacement (5.51). In the scattering mechanism the absorbed or emitted phonon energy $\hbar\omega_0$ is comparable to the thermal energy of the carriers. Therefore, the scattering is inelastic and the relaxation-time approximation does not work. The general transport theory is complicated. If the temperature is low compared to the Debye temperature, $T \ll \Theta_{\text{D}}$

$$\mu_{\text{pol.opt.}} = \frac{e}{2m^* \alpha \omega_0} \exp\left(\frac{\Theta_{\text{D}}}{T} \right) , \tag{8.20}$$

where $\alpha = \frac{1}{137} \sqrt{\frac{m^* c^2}{2k\Theta_{\text{D}}}} \left(\frac{1}{\epsilon(\infty)} - \frac{1}{\epsilon(0)} \right)$ is the dimensionless polar constant.

8.3.7 Dislocation Scattering

Dislocations can contain charge centers and thus act as scattering centers [510]. This has been first demonstrated for n-Ge crystals that have been deformed [511, 512]. The deformation has introduced acceptor-type defects reducing the mobility in particular at low temperatures (similar to ionized impurity scattering). The mobility due to dislocation scattering in an n-type semiconductor is given by [513, 514]

$$\mu_{\text{disl.}} = \frac{30\sqrt{2\pi}\epsilon^2 d^2 (kT)^{3/2}}{N_{\text{disl}}\, e^3 f^2 L_{\text{D}} \sqrt{m^*}} \propto \frac{\sqrt{n}}{N_{\text{disl}}} T , \tag{8.21}$$

d being the average distance of acceptor centers along the dislocation line, f their occupation rate, N_{disl} the area density of dislocations and $L_{\text{D}} = (\epsilon kT/(e^2 n))^{1/2}$ the Debye screening length. The relation $\mu \propto \sqrt{n}/N_{\text{disl}}$ has been confirmed for various n-type GaN samples [515].

8.3.8 Grain Boundary Scattering

The lowering of mobility due to transport across grain boundaries is an important effect in polycrystalline materials, such as poly-silicon for solar cells or thin film transistors [516–519]. Grain boundaries contain electronic traps whose filling depends on the doping of the bulk of the grains. Charges will be trapped in the grain boundaries and a depletion layer will be created.[1] At low doping the grains are fully depleted and all free carriers are trapped in the grain boundaries. This means low conductivity, however, no electronic barrier to transport exists. At intermediate doping, traps are partially filled and the partial depletion of the grain leads to the creation of an electronic barrier ΔE_{b} (Fig. 8.2a) hindering transport since it must be overcome via thermionic emission. At high doping the traps are completely filled and the barrier vanishes again. Accordingly the mobility goes through a minimum as a function of the doping concentration (Fig. 8.2b) [516]. In [520] these data have been modeled with a 20 nm grain size, the value found in [516] from TEM analysis.

The expression for the limitation of the mobility due to scattering at grain boundaries is given by [519, 521]

$$\mu_{\mathrm{GB}} = \frac{e L_{\mathrm{G}}}{\sqrt{8 m^* \pi k}} \, T^{-1/2} \exp\left(-\frac{\Delta E_{\mathrm{b}}}{kT}\right) , \tag{8.22}$$

where L_{G} is the grain size.

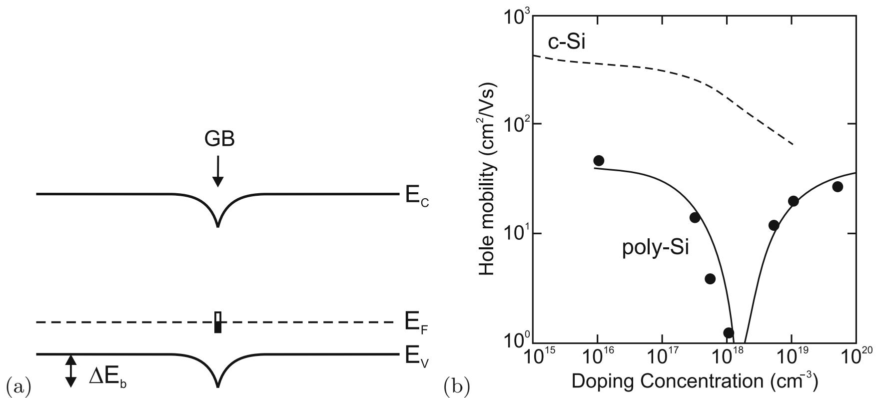

Fig. 8.2. (**a**) Electronic barrier (ΔE_{b}) for (hole) transport at a grain boundary (GB). (**b**) Average hole mobility in poly-silicon, experimental data (*symbols*) and theoretical model (*solid line*). The dependence for monocrystalline silicon is shown for comparison as *dashed line*. Adapted from [516]

[1] The following arguments may only be followed once the concept of depletion layers and band bending is understood, see Sect. 20.2.1.

8.3.9 Temperature Dependence

The sum of all scattering processes leads to a fairly complicated temperature dependence of the mobility $\mu(T)$. In covalent semiconductors (Si, Ge) the most important processes are the ionized impurity scattering ($\mu \propto T^{3/2}$) at low temperatures and the deformation potential scattering ($\mu \propto T^{-3/2}$) at high temperatures (Fig. 8.3a). In polar crystals (e.g. GaAs) at high temperatures the polar optical scattering is dominant (Fig. 8.3b).

In Fig. 8.4 the electron mobility of bulk and thin-film ZnO is compared. Since ZnO is polar the mobility at room temperature is limited by polar optical phonon scattering. In the thin film, grain-boundary scattering (Sect. 8.3.8) additionally occurs and limits the mobility.

Since the carrier concentration increases with increasing temperature and the mobility decreases, the conductivity has a maximum, typically around 70 K (see Fig. 8.5). At very high temperature, when intrinsic conduction starts, σ shows a strong increase due to the increase in n.

8.3.10 Doping Dependence

The mobility decreases with increasing dopant concentration as shown in Figs. 8.3a and 8.6. Thus, for bulk material high carrier density and high mobility are contrary targets. A solution will be provided with the concept of *modulation* doping where the dopants and the (two-dimensional) carrier gas will be spatially separated (cf. Sect. 11.3.4).

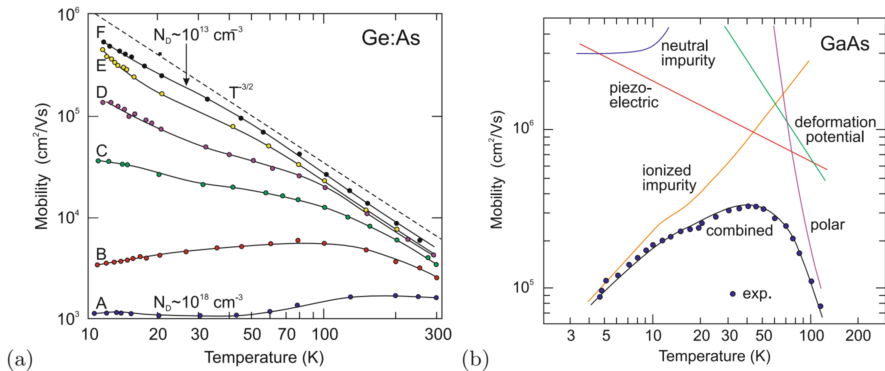

Fig. 8.3. (**a**) Temperature dependence of the electron mobility in n-doped Ge (for various doping levels from $N_D \approx 10^{18}$ for sample A to $10^{13}\,\mathrm{cm}^{-3}$ for sample F in steps of a factor of ten). *Dashed line* indicates $T^{-3/2}$ dependence of deformation potential scattering, *solid lines* are guides to the eye. Adapted from [421]. (**b**) $\mu_n(T)$ for n-type GaAs ($N_D \approx 5 \times 10^{13}\,\mathrm{cm}^{-3}$, $N_A \approx 2 \times 10^{13}\,\mathrm{cm}^{-3}$). *Solid lines* are theoretical mobilities for various scattering mechanisms and combined mobility according to (8.12). Adapted from [522]

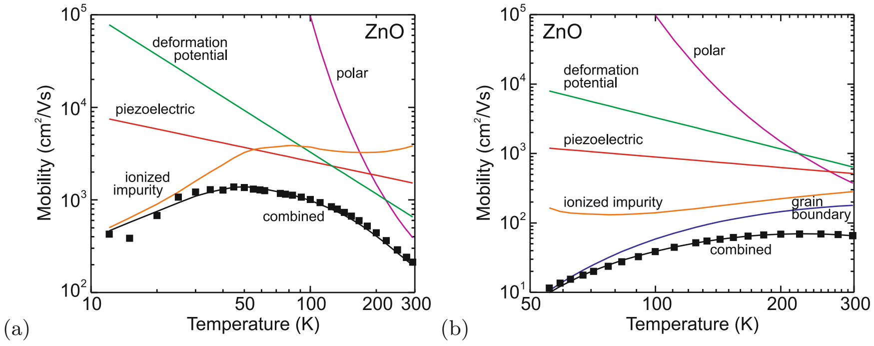

Fig. 8.4. Temperature dependence of the electron mobility in n-type (**a**) bulk ZnO and (**b**) a PLD-grown ZnO thin film on sapphire. In the latter, grain-boundary scattering is limiting the mobility. *Squares* are experimental data, *solid lines* are theoretical mobilities for various scattering mechanisms and combined mobility according to (8.12). Experimental data from [523]

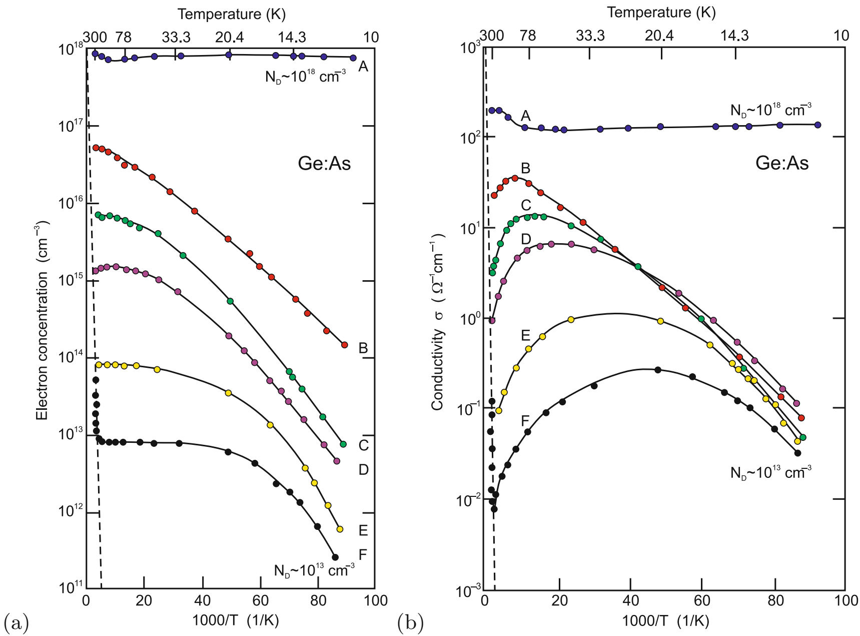

Fig. 8.5. (**a**) Carrier concentration and (**b**) conductivity of n-type Ge as a function of temperature. The doping level varies from $N_{\mathrm{D}} \approx 10^{13}$ to 10^{18} (samples A–F as in Fig. 8.3a where the mobility of the same samples is shown). The *dashed lines* are for intrinsic Ge. The *solid lines* are guides to the eye. Adapted from [421]

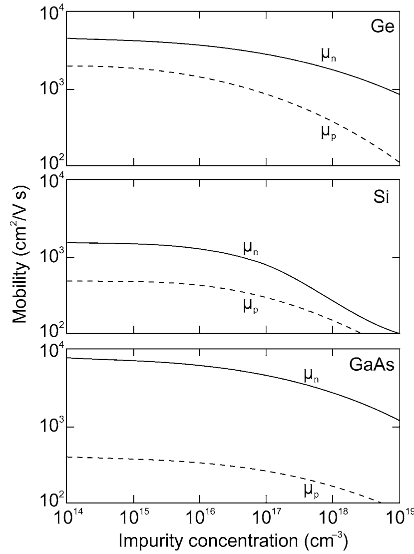

Fig. 8.6. Room-temperature mobility as a function of dopant concentration for Ge, Si, and GaAs. *Solid lines* (*dashed lines*) represent the electron (hole) mobility. Adapted from [384]

The primary reason of the decrease of mobility with increasing doping level is the increasing role of ionized impurity scattering. At high doping level, it becomes more important at room temperature than phonon scattering [524]. The mobility of carriers in silicon with very high carrier concentrations is depicted in Fig. 8.7.

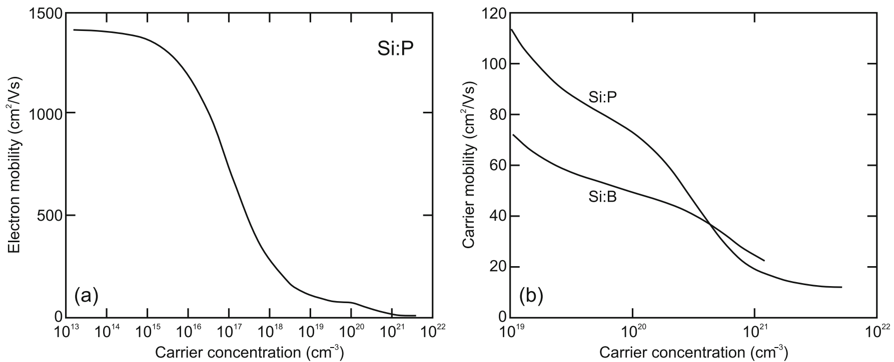

Fig. 8.7. (**a**) Electron mobility in Si:P at room temperature over a wide range of carrier concentrations. (**b**) Electron mobility in Si:P and hole mobility in Si:B for various high carrier concentrations. Adapted from [525]

8.3.11 Piezoresistivity

The dependence of resistivity on stress or strain is known as piezoresistive effect, first described in [526]. It is a consequence of the modification of the band structure upon stress and the change of effective masses (Sect. 6.10.2). In a cubic material, the resistivity ρ_i for transport in cartesian direction i changes compared to the unstrained state in a phenomenological description according to

$$\frac{\Delta\rho_i}{\rho_i} = \pi_{ij}\,\sigma_j \;, \tag{8.23}$$

where $\boldsymbol{\pi}$ is the piezoresistivity tensor (8.24) and the σ_j form the six-component stress tensor (5.58),

$$\boldsymbol{\pi} = \begin{pmatrix} \pi_{11} & \pi_{12} & \pi_{12} & 0 & 0 & 0 \\ \pi_{12} & \pi_{11} & \pi_{12} & 0 & 0 & 0 \\ \pi_{12} & \pi_{12} & \pi_{11} & 0 & 0 & 0 \\ 0 & 0 & 0 & \pi_{44} & 0 & 0 \\ 0 & 0 & 0 & 0 & \pi_{44} & 0 \\ 0 & 0 & 0 & 0 & 0 & \pi_{44} \end{pmatrix} . \tag{8.24}$$

Values for the piezoelectric coefficients are given in Table 8.3 for Si, Ge and GaAs.

The piezoelectric effect has been discussed in detail [527] and modeled for p-type Si [528]. We shall only give a simple example which is particularly relevant for advanced CMOS design (Sect. 23.5.5); the directional dependence of the piezoresistive coefficient of silicon is shown for uniaxial stress within in the (001) plane in Fig. 8.8. Uniaxial tensile stress increases hole resistivity along $\langle 110 \rangle$ stress directions, compressive stress thus increases hole conductivity.

Table 8.3. Piezoresistivity coefficients (in $10^{-11}\,\mathrm{Pa}^{-1}$) for Si, Ge and GaAs at room temperature

material	ρ (Ω cm)	π_{11}	π_{12}	π_{44}	Ref.
p-Si	7.8	6.6	−1.1	138.1	[526]
n-Si	11.7	−102.2	53.4	−13.6	[526]
p-Ge (Ge:Ga)	15.0	−10.6	5.0	98.6	[526]
n-Ge (Ge:As)	9.9	−4.7	−5.0	−137.9	[526]
p-GaAs	$\sim 10^{-3}$	−12.0	−0.6	46	[529]
n-GaAs	$\sim 10^{-3}$	−3.2	−5.4	−2.5	[529, 530]

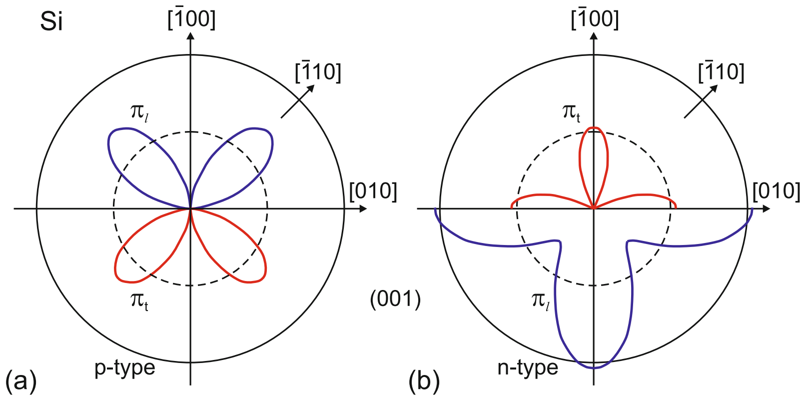

Fig. 8.8. Piezoresistive coefficient for current parallel (perpendicular) to the stress π_l as *blue lines*(π_t, *red lines*) for uniaxially stressed Si (001) at room temperature, (**a**) for p-type Si, (**b**) for n-type Si. The *upper* (*lower*) halves of the graphs show positive (negative) values of the piezoresistive coefficient, i.e. resistivity increases (decreases) with tensile stress. The *solid circle* indicates the value of $|\pi| = 10^{-9}\,\mathrm{Pa}^{-1}$, the *dashed circle* half that value. Adapted from [531]

8.4 Hall Effect

An electrical current along the x (longitudinal) direction in a perpendicular magnetic field $\mathbf{B} = (0, 0, B)$ along z induces an electric field $\mathcal{E}_y$ along the transverse (y) direction. The charge accumulation is due to the Lorentz force. The related transverse voltage is called the Hall voltage and the resistivity $\rho_{xy} = \mathcal{E}_\dagger / j_x$ the Hall resistivity [17, 20, 21]. For the Hall geometry see Fig. 8.9. For thin-film samples typically the van-der-Pauw geometry (Fig. 8.10) and method is used [532–534].

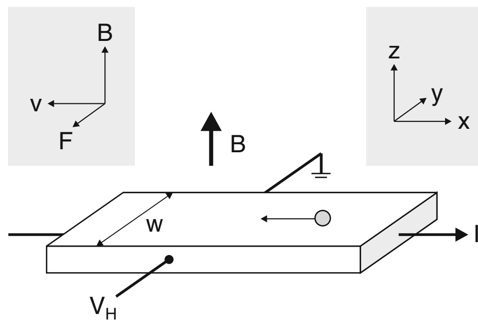

Fig. 8.9. Scheme of the Hall-effect geometry. The movement of one electron in the longitudinal electric current I is shown schematically. The coordinate system (x, y, z) and the directions of the magnetic field **B**, the drift velocity of an electron **v** and the resulting Lorentz force **F** are given. The transverse field $\mathcal{E}_y$ is given by V_H/w

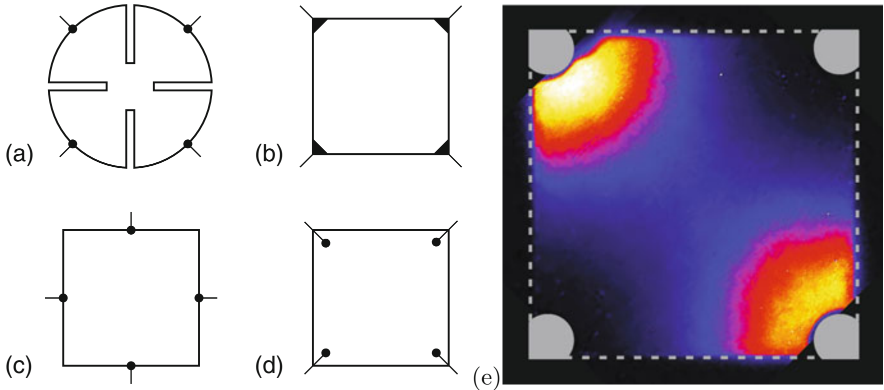

Fig. 8.10. (**a**–**d**) Geometry for van-der-Pauw Hall measurements. (**a**) Best geometry (cloverleaf), (**b**) acceptable square geometry with small contacts on the corners, (**c**,**d**) not recommended geometries with contacts on the edge centers or inside the square, respectively. (**e**) Current distribution, as visualized by lock-in thermography [535], in epitaxial ZnO layer on sapphire with Hall geometry as in part (**b**). *Grey dashed line* indicates the outline of the $10 \times 10\,\mathrm{mm}^2$ substrate, *grey areas* indicate gold ohmic contacts

The steady-state equation of motion is

$$m^* \frac{\mathbf{v}}{\tau} = q\,(\mathbf{E} + \mathbf{v} \times \mathbf{B})\ . \tag{8.25}$$

We note that this equation of motion is also valid for holes, given the convention of Sect. 6.9.1, i.e. positive charge. With the cyclotron frequency $\omega_\mathrm{c} = qB/m^*$ the conductivity tensor is ($\mathbf{j} = qn\mathbf{v} = \boldsymbol{\sigma}\,\mathbf{E}$)

$$\boldsymbol{\sigma} = \begin{pmatrix} \sigma_{xx} & \sigma_{xy} & 0 \\ \sigma_{yx} & \sigma_{yy} & 0 \\ 0 & 0 & \sigma_{zz} \end{pmatrix} \tag{8.26a}$$

$$\sigma_{xx} = \sigma_{yy} = \sigma_0\,\frac{1}{1+\omega_\mathrm{c}^2\tau^2} = \sigma_0\,\frac{1}{1+\mu^2B^2} \tag{8.26b}$$

$$\sigma_{xy} = -\sigma_{yx} = \sigma_0\,\frac{\omega_\mathrm{c}\tau}{1+\omega_\mathrm{c}^2\tau^2} = \sigma_0\,\frac{\mu B}{1+\mu^2B^2} \tag{8.26c}$$

$$\sigma_{zz} = \sigma_0 = \frac{q^2 n\tau}{m^*} = qn\mu\ . \tag{8.26d}$$

Perpendicular to the magnetic field, the conductivity (σ_{zz}) is given by (8.10). If only one type of carrier (charge q, density n) is considered, the condition $j_y = 0$ leads to $\mathcal{E}_y = \mu B \mathcal{E}_x$ and $j_x = \sigma_0 \mathcal{E}_x$. The Hall coefficient is defined as $R_\mathrm{H} = \mathcal{E}_y/(j_x\,B)$ or more precisely as

$$R_\mathrm{H} = \frac{\rho_{xy}}{B}\ , \tag{8.27}$$

where the resistivity tensor $\boldsymbol{\rho}$ is the inverse of the conductivity tensor $\boldsymbol{\sigma}$,

$$\boldsymbol{\rho} = \boldsymbol{\sigma}^{-1} = \begin{pmatrix} \rho_{xx} & \rho_{xy} & 0 \\ \rho_{yx} & \rho_{yy} & 0 \\ 0 & 0 & \rho_{zz} \end{pmatrix} \tag{8.28a}$$

$$\rho_{xx} = \rho_{yy} = \frac{\sigma_{xx}}{\sigma_{xx}^2 + \sigma_{xy}^2} \tag{8.28b}$$

$$\rho_{xy} = -\rho_{yx} = \frac{\sigma_{xy}}{\sigma_{xx}^2 + \sigma_{xy}^2} \tag{8.28c}$$

$$\rho_{zz} = \frac{1}{\sigma_{zz}} = \frac{1}{\sigma_0} \; . \tag{8.28d}$$

For a single type of carriers, the Hall coefficient is therefore given by

$$R_{\mathrm{H}} = \frac{\mu}{\sigma_0} = \frac{1}{q\,n} \; . \tag{8.29}$$

It is negative (positive) for electron (hole) conduction. We note that electrons and holes are deflected in the same y-direction by the magnetic field and collect at the same electrode. Thus the Hall effect allows the determination of the carrier density.[2]

If both types of carriers are present simultaneously, the conductivity is given by the sum of electron and hole conductivity (8.11),

$$\boldsymbol{\sigma} = \boldsymbol{\sigma}_{\mathrm{e}} + \boldsymbol{\sigma}_{\mathrm{h}} \; . \tag{8.30}$$

The Hall constant (8.27) is then

$$R_{\mathrm{H}} = \frac{1}{e} \frac{-n\mu_{\mathrm{e}}^2(1+\mu_{\mathrm{h}}^2B^2) + p\mu_{\mathrm{h}}^2(1+\mu_{\mathrm{e}}^2B^2)}{n^2\mu_{\mathrm{e}}^2(1+\mu_{\mathrm{h}}^2B^2) - 2np\mu_{\mathrm{e}}\mu_{\mathrm{h}}(1+\mu_{\mathrm{e}}\mu_{\mathrm{h}}B^2) + p^2\mu_{\mathrm{h}}^2(1+\mu_{\mathrm{e}}^2B^2)} \; . \tag{8.31}$$

Under the assumption of small magnetic fields,[3] i.e. $\mu B \ll 1$, the Hall coefficient is

$$R_{\mathrm{H}} = \frac{1}{e}\left[\frac{-n\mu_{\mathrm{e}}^2 + p\mu_{\mathrm{h}}^2}{(-n\mu_{\mathrm{e}} + p\mu_{\mathrm{h}})^2} + \frac{np(-n+p)\mu_{\mathrm{e}}^2\mu_{\mathrm{h}}^2(\mu_{\mathrm{e}} - \mu_{\mathrm{h}})^2}{(-n\mu_{\mathrm{e}} + p\mu_{\mathrm{h}})^4}\,B^2 + \ldots\right] \; . \tag{8.32}$$

For small magnetic field this can be written as

$$R_{\mathrm{H}} = \frac{1}{e}\frac{p - n\beta^2}{(p - n\beta)^2} \; , \tag{8.33}$$

with $\beta = \mu_{\mathrm{e}}/\mu_{\mathrm{h}} < 0$. For large magnetic fields, i.e. $\mu B \gg 1$, the Hall coefficient is given by

[2] Using the Hall effect, the net *free* charge carrier concentration is determined. We note that the concentration of *fixed* charges in semiconductors can be investigated by depletion layer spectroscopy (Sect. 20.2.4).

[3] We note that for a mobility of $10^4\,\mathrm{cm}^2/\mathrm{Vs}$, μ^{-1} is a field of $B = 1\,\mathrm{T}$.

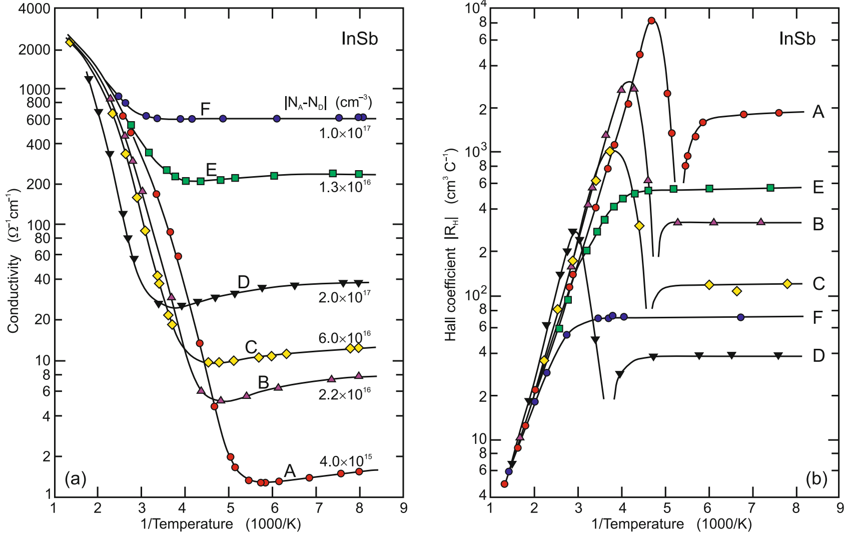

Fig. 8.11. (**a**) Conductivity and (**b**) absolute value of the Hall coefficient vs. inverse temperature for four p-doped (A–D) and two n-doped (E, F) InSb samples. The doping levels are given in (**a**). Adapted from [536]

$$R_{\mathrm{H}} = \frac{1}{e} \frac{p-n}{(p+n)^2} \ . \tag{8.34}$$

In Fig. 8.11, the absolute value of the Hall coefficient for InSb samples with different doping concentrations is shown. The p-doped samples exhibit a reverse of the sign of the Hall coefficient upon increase of temperature when intrinsic electrons contribute to the conductivity. The zero in R_{H} occurs for $n = p\,\mu_{\mathrm{h}}^2/\mu_{\mathrm{e}}^2 = n_{\mathrm{i}}/|\beta|$. For high temperatures, the Hall coefficient for n- and p-doped samples is dominated by the electrons that have much higher mobility (Table 8.2).

In the derivation of the Hall coefficient we had assumed that all carriers involved in the transport have the same properties, in particular that they are subject to the same scattering time. This assumption is generally not the case and we need to operate with the ensemble average of the discussed quantities. The ensemble average of an energy-dependent quantity $\zeta(E)$ over the (electron) distribution function $f(E)$ is denoted as $\langle\zeta\rangle$ and is given as[4]

$$\langle\zeta\rangle = \frac{\int \zeta(e) f(E) \mathrm{d}E}{\int f(E) \mathrm{d}E} \ . \tag{8.35}$$

[4]For this consideration it is assumed that the energy dependence is the decisive one. Generally, averaging may have to be performed over other degrees of freedom as well, such as the spin or, in the case of anisotropic bands, the orbital direction.

In particular $\langle\tau\rangle^2$ is now different from $\langle\tau^2\rangle$. Considering the equation $\langle\mathbf{j}\rangle = \langle\boldsymbol{\sigma}\rangle\,\mathbf{E}$ for the ensemble averaged current densities we find (for one type of carrier, cf. (8.29))

$$R_{\mathrm{H}} = \frac{1}{q\,n}\,r_{\mathrm{H}}\ , \tag{8.36}$$

with the so-called *Hall factor* r_{H} given by

$$\begin{aligned} r_{\mathrm{H}} &= \frac{\gamma}{\alpha^2 + \omega_{\mathrm{c}}^2\gamma^2} \\ \alpha &= \left\langle \frac{\tau}{1+\omega_{\mathrm{c}}^2\tau^2} \right\rangle \\ \gamma &= \left\langle \frac{\tau^2}{1+\omega_{\mathrm{c}}^2\tau^2} \right\rangle\ . \end{aligned} \tag{8.37}$$

The Hall factor depends on the scattering mechanisms and is of the order of 1. For large magnetic fields the Hall factor approaches 1. For small magnetic fields we have

$$R_{\mathrm{H}} = \frac{1}{q\,n}\,\frac{\langle\tau^2\rangle}{\langle\tau\rangle^2}\ . \tag{8.38}$$

The mobility calculated from (cf. (8.26d)) $\sigma_0 R_{\mathrm{H}}$ is called the *Hall mobility* μ_{H} and is related to the mobility via

$$\mu_{\mathrm{H}} = r_{\mathrm{H}}\,\mu\ . \tag{8.39}$$

It is assumed so far that the free carrier density and mobility are homogeneous in the volume of current transport. Also multi-layer models can be fitted to experimental Hall data. In a two-layer model, contributions from bulk and surface conduction can be separated. The magnetic field dependence of $\boldsymbol{\sigma}$ can be used to separate contributions of carriers with different density and mobility (including its sign) without assumptions and obtain the mobility spectrum $s(\mu)$ (MSA, mobility spectral analysis),

$$\sigma_{xx} = \int_{-\infty}^{\infty} s(\mu)\,\frac{1}{1+\mu^2B^2}\,\mathrm{d}\mu \tag{8.40a}$$

$$\sigma_{xy} = \int_{-\infty}^{\infty} s(\mu)\,\frac{\mu B}{1+\mu^2B^2}\,\mathrm{d}\mu\ , \tag{8.40b}$$

(8.40c)

as a generalization of (8.30), (8.26b) and (8.26c) [537, 538].

8.5 High-Field Transport

8.5.1 Drift-Saturation Velocity

In the case of small electric fields the scattering events are elastic. The drift velocity is linearly proportional to the electric field. The average thermal energy is close to its thermal value $3kT/2$.

The scattering efficiency, however, is reduced already at moderate fields. Then, the electron temperature becomes larger than the lattice temperature. If the carrier energy is large enough it can transfer energy to the lattice by the emission of an optical phonon. This mechanism is very efficient and limits the maximum drift velocity. Such behavior is non-ohmic. The limiting value for the drift velocity is termed the *drift-saturation velocity*. It is given by [539]

$$v_\mathrm{s} = \sqrt{\frac{8}{3\pi}} \sqrt{\frac{\hbar\omega_\mathrm{LO}}{m^*}} \,. \tag{8.41}$$

This relation can be obtained from an energy-balance consideration. The energy gain per unit time in the electric field is equal to the energy loss by the emission of an optical phonon.

$$q\,\mathbf{v}\cdot\mathbf{E} = \frac{\hbar\omega_\mathrm{LO}}{\tau} \,, \tag{8.42}$$

where τ is the typical relaxation time constant for LO phonon emission. Together with (8.3) we find (8.42) except for the pre-factor, which is close to 1. The exact pre-factor results from a more exact quantum-mechanical treatment. For Ge the drift-saturation velocity at room temperature is 6×10^6 cm/s, for Si it is 1×10^7 cm/s (Fig. 8.12a). The carrier velocity also depends on the crystallographic direction [540].

8.5.2 Negative Differential Resistivity

In GaAs there is a maximum drift velocity of about 2×10^7 cm/s and following a reduction in velocity with increasing field (1.2×10^7 cm/s at 10 kV/cm, 0.6×10^7 cm/s at 200 kV/cm) as shown in Fig. 8.12a. This regime, above

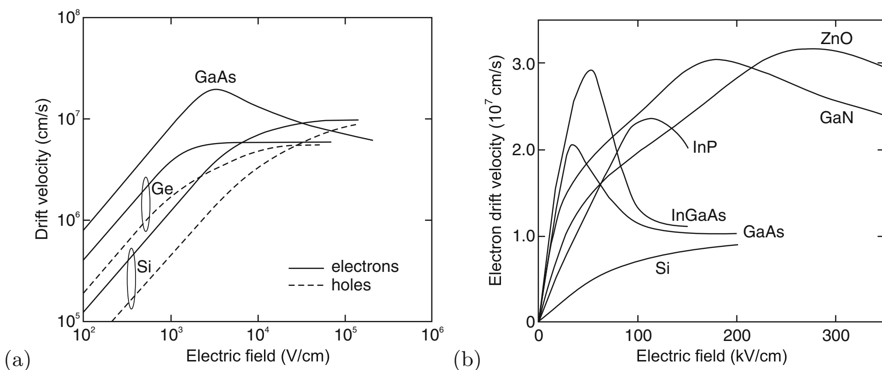

Fig. 8.12. Drift velocity at room temperature as a function of applied electric field for (**a**) high-purity Si, Ge, and GaAs on a double-logarithmic plot and (**b**) on linear plots for Si [543], Ge [544], GaAs [469], InP [545], InGaAs [546], GaN and ZnO [547]

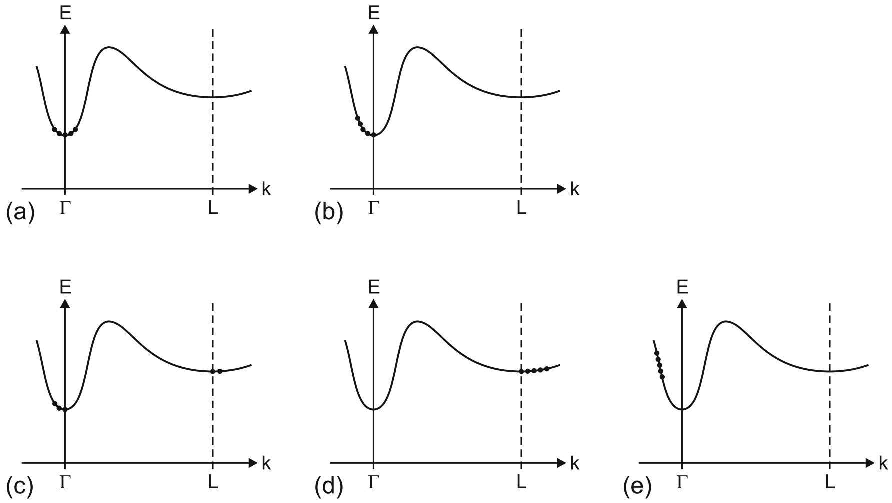

Fig. 8.13. Charge-carrier distribution in a multivalley band structure (e.g. GaAs, InP) for (**a**) zero, (**b**) small ($E < E_{\mathrm{a}}$), (**c**) intermediate and (**d**) large ($E > E_{\mathrm{b}}$) field strength. The situation shown in (**e**) is reached temporarily during velocity overshoot (see also Fig. 8.15)

the threshold field of $\mathcal{E}_{\mathrm{T}} = 3.2\,\mathrm{kV/cm}$ in GaAs, is called *negative differential resistivity* (NDR) and was predicted in [541]. This phenomenon can be used in microwave oscillators, e.g. the Gunn element (Sect. 20.5.11).

The effect occurs in a multivalley band structure (see Fig. 8.13, for values cf. Table 8.4), e.g. in GaAs or InP, when the carrier energy is high enough to scatter (Fig. 8.13c,d) from the Γ minimum (small mass and high mobility) into the L valley (large mass and low mobility) [542].

The temperature dependence of the saturation velocity is shown in Fig. 8.14. With increasing temperature the saturation velocity decreases since the coupling with the lattice becomes stronger.

Table 8.4. Material parameters for multivalley bandstructure of GaAs and InP. ΔE denotes the energetic separation of the two lowest valleys of the conduction band, $\mathcal{E}_{\mathrm{T}}$ the threshold field for NDR and v_{P} the peak velocity (at $\mathcal{E}_{\mathrm{T}}$). Most values from [548]

material	E_{g} (eV)	ΔE (eV)	$\mathcal{E}_{\mathrm{T}}$ (kV/cm)	v_{P} (10^7 cm/s)	lower valley (Γ) m^* (m_0)	lower valley (Γ) μ_{n} ($\mathrm{cm^2/Vs}$)	upper valley (L) m^* (m_0)	upper valley (L) μ_{n} ($\mathrm{cm^2/Vs}$)
GaAs	1.42	0.36	3.2	2.2	0.068	≈ 8000	1.2	≈ 180
InP	1.35	0.53	10.5	2.5	0.08	≈ 5000	0.9	≈ 100

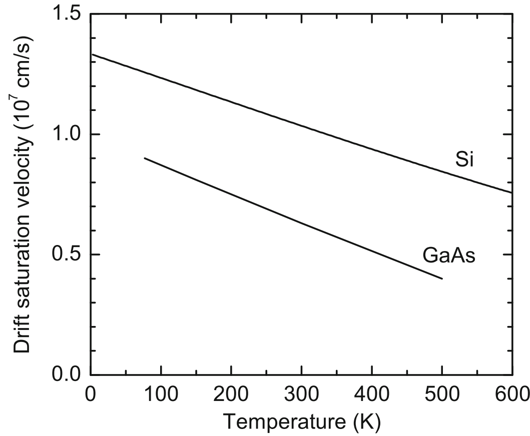

Fig. 8.14. Temperature dependence of the saturation velocity for Si (following $v_\mathrm{s} = v_{\mathrm{s}_0}(1 + 0.8\exp(T/600\,K))^{-1}$ with $v_{\mathrm{s}_0} = 2.4 \times 10^7$ cm/s from [543]) and GaAs [469, 550, 551]

8.5.3 Velocity Overshoot

When the electric field is switched on, the carriers are at first in the $\varGamma$ minimum (Fig. 8.13a). Only after a few scattering processes are they scattered into the L minimum. This means that in the first moments transport occurs with the higher mobility of the lowest minimum (Fig. 8.13e). The velocity is then larger than the (steady-state) saturation velocity in a dc field. This phenomenon is called *velocity overshoot* and is a purely dynamic effect (Fig. 8.15). Velocity overshoot in GaN is discussed in [549]. It is an important effect in small transistors.

8.5.4 Impact Ionization

If the energy gain in the field is large enough to generate an electron–hole pair, the phenomenon of impact ionization occurs. The energy is $\propto v^2$. Momentum and energy conservation apply. Thus, at small energies (close to the threshold for impact ionization) the vectors are short and collinear to fulfill momentum conservation. At higher energy, larger angles between the velocity vectors of the impact partners can also occur. If the process is started by an electron (Fig. 8.16a) the threshold energy is given by

$$E_\mathrm{e}^\mathrm{thr} = \frac{2m_\mathrm{e} + m_\mathrm{hh}}{m_\mathrm{e} + m_\mathrm{hh}} E_\mathrm{g} \ . \tag{8.43}$$

The threshold for impact ionization triggered by a s-o hole (shown schematically in Fig. 8.16b) is

$$E_\mathrm{h}^\mathrm{thr} = \left[1 + \frac{m_\mathrm{so}(1 - \varDelta_0/E_\mathrm{g})}{2m_\mathrm{hh} + m_\mathrm{e} - m_\mathrm{so}}\right] E_\mathrm{g} \ . \tag{8.44}$$

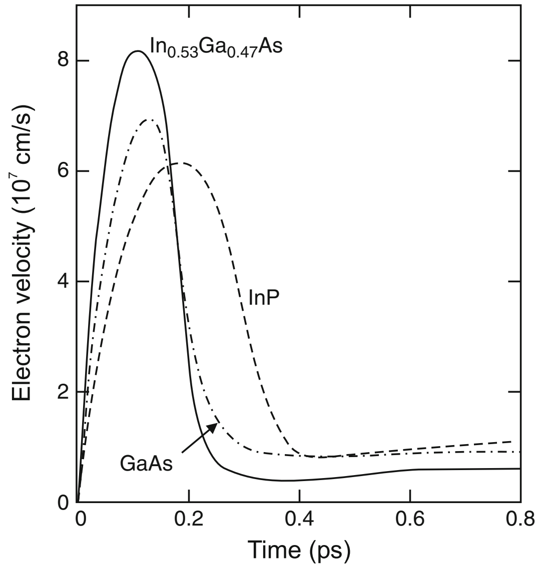

Fig. 8.15. Time dependence of the electron velocity at room temperature upon a step-like electric field (40 kV/cm) for GaAs (*dash-dotted line*), InP (*dashed line*) and $In_{0.53}Ga_{0.47}As$ (*solid line*)

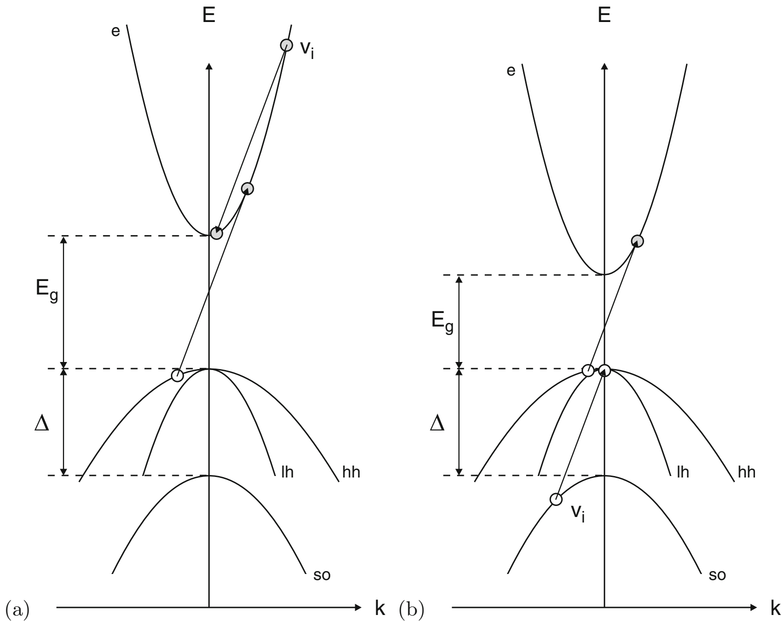

Fig. 8.16. Electron and hole transitions for impact ionization close to the threshold energy. Ionization is triggered by (**a**) an electron and (**b**) a split-off hole of velocity v_i

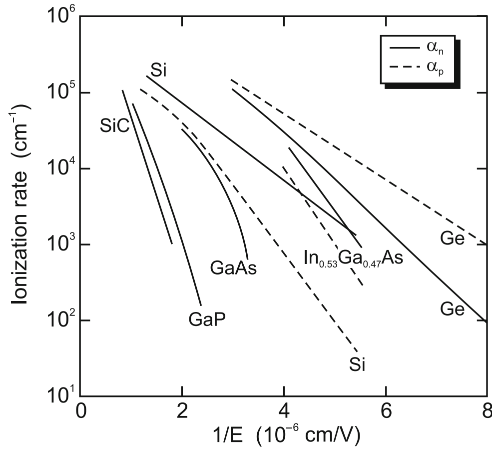

Fig. 8.17. Impact ionization rates for electrons and holes as a function of the inverse electric field for Si, Ge and other compound semiconductors at 300 K. Adapted from [384]

The generation rate G of electron–hole pairs during impact ionization is given by

$$G = \alpha_{\mathrm{n}} n v_{\mathrm{n}} + \alpha_{\mathrm{p}} p v_{\mathrm{p}} \ , \tag{8.45}$$

where α_{n} is the electron ionization coefficient. It describes the generation of electron–hole pairs per incoming electron per unit length. α_{p} denotes the hole ionization coefficient. The coefficients depend strongly on the applied electric field. They are shown in Fig. 8.17. They also depend on the crystallographic direction.

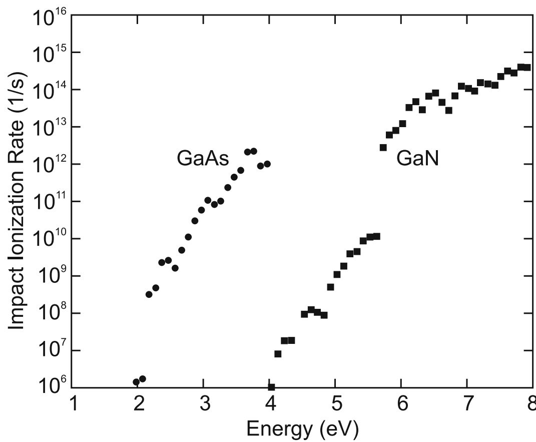

Fig. 8.18. Averaged rates for electron initiated impact ionization in GaAs (*circles*) and GaN (*squares*). Adapted from [552]

The energy dependence of the electron initiated impact ionization rate has been calculated in [552] for GaAs, GaN and ZnS considering details and anisotropy of the band structure. The rates averaged over the Brillouin zone are compared in Fig. 8.18. Because of the large band gap of GaN, impact ionization can only be generated by electrons in higher conduction bands. The sharp increase of ionization rate for GaN around 5.75 eV correlates with a large valence band DOS from hole states at the zone boundary.

8.6 High-Frequency Transport

The above consideration pertained to dc (or slowly varying) fields. Now, we consider an ac field. It accelerates the carriers but at the same time the dissipative force in the relaxation-time approximation is present, i.e. (for electrons)

$$m^* \dot{\mathbf{v}} = -e\mathbf{E} - m^* \frac{\mathbf{v}}{\tau} \, . \tag{8.46}$$

For a harmonic field $\mathcal{E} \propto \exp(-\mathrm{i}\omega t)$ the complex conductivity ($\mathbf{j} = \sigma \mathbf{E} = nq\mathbf{v}$) is

$$\sigma = \frac{ne^2\tau}{m^*} \frac{1}{1 - \mathrm{i}\omega\tau} = \frac{ne^2}{m^*} \frac{\mathrm{i}}{\omega + \mathrm{i}\gamma} \, , \tag{8.47}$$

with $\gamma = 1/\tau$ being the damping constant. Splitting into real and imaginary parts yields

$$\sigma = \frac{ne^2\tau}{m^*} \left(\frac{1}{1+\omega^2\tau^2} + \mathrm{i} \frac{\omega\tau}{1+\omega^2\tau^2} \right) \, . \tag{8.48}$$

For small frequencies ($\omega \to 0$) the dc conductivity from (8.5) is recovered, i.e. $\sigma = ne^2\tau/m^*$. For high frequencies ($\omega\tau \gg 1$)

$$\sigma = \frac{ne^2\tau}{m^*} \left(\frac{1}{\omega^2\tau^2} + \mathrm{i} \frac{1}{\omega\tau} \right) \, . \tag{8.49}$$

8.7 Diffusion

A gradient of a particle concentration n leads to a particle current proportional to $-\nabla n$. This diffusion law (Fick's law) corresponds microscopically to a random walk. The gradients of the semiconductor carrier densities ∇n or ∇p thus lead to electron and hole currents, respectively:

$$\mathbf{j}_\mathrm{n} = eD_\mathrm{n} \nabla n \tag{8.50a}$$

$$\mathbf{j}_\mathrm{p} = -eD_\mathrm{p} \nabla p \, . \tag{8.50b}$$

The coefficients D_n and D_p are called the electron and hole diffusion coefficient, respectively. Thus the total electron and hole currents in the presence of an electric field $\mathbf{E}$ and diffusion are

$$\mathbf{j}_{\rm n} = -e\mu_{\rm n} n\,\mathbf{E} + eD_{\rm n}\,\nabla n \tag{8.51a}$$
$$\mathbf{j}_{\rm p} = e\mu_{\rm p} p\,\mathbf{E} - eD_{\rm p}\,\nabla p\;. \tag{8.51b}$$

This relation can also be deduced more generally from the gradient of the Fermi level as

$$\mathbf{j}_{\rm n} = -e\mu_{\rm n} n\,\mathbf{E} - n\mu_{\rm n}\,\nabla E_{\rm F} \tag{8.52a}$$
$$\mathbf{j}_{\rm p} = e\mu_{\rm p} p\,\mathbf{E} - p\mu_{\rm p}\,\nabla E_{\rm F}\;. \tag{8.52b}$$

Using (7.8) and (7.9) for the concentrations (valid also in the case of degeneracy) and using $\mathrm{d}F_j(x)/\mathrm{d}x = F_{j-1}(x)$ we obtain

$$\mathbf{j}_{\rm n} = -e\mu_{\rm n} n\,\mathbf{E} - kT\mu_{\rm n}\frac{F_{1/2}(\eta)}{F_{-1/2}(\eta)}\,\nabla n \tag{8.53a}$$
$$\mathbf{j}_{\rm p} = e\mu_{\rm p} p\,\mathbf{E} - kT\mu_{\rm p}\frac{F_{1/2}(\zeta)}{F_{-1/2}(\zeta)}\,\nabla p\;, \tag{8.53b}$$

with $\eta = (E_{\rm F} - E_{\rm C})/kT$ and $\zeta = -(E_{\rm F} - E_{\rm V})/kT$. If the pre-factor of the density gradient is identified as the diffusion coefficient we find the (generalized) so-called 'Einstein relations' ($\beta = e/(kT)$) [410, 553]:

$$D_{\rm n} = -\beta^{-1}\mu_{\rm n}\frac{F_{1/2}(\eta)}{F_{-1/2}(\eta)} \tag{8.54a}$$
$$D_{\rm p} = \beta^{-1}\mu_{\rm p}\frac{F_{1/2}(\zeta)}{F_{-1/2}(\zeta)}\;. \tag{8.54b}$$

Useful analytical approximations have been discussed in [554]. We note that, e.g., (8.54a) can also be written as [555, 556]

$$D_{\rm n} = -\beta^{-1}\mu_{\rm n}\,n\,\frac{\partial\eta}{\partial n}\;. \tag{8.55}$$

In the case of nondegeneracy, i.e. when the Fermi level is within the band gap and not closer than about $4kT$ to the band edges, the equation simplifies to $D = \frac{kT}{q}\mu$, i.e. the 'regular' Einstein-relations,

$$D_{\rm n} = -\beta^{-1}\mu_{\rm n} \tag{8.56a}$$
$$D_{\rm p} = \beta^{-1}\mu_{\rm p}\;. \tag{8.56b}$$

In this case, (8.51a,b) read

$$\mathbf{j}_{\rm n} = -e\mu_{\rm n} n\,\mathbf{E} - kT\mu_n\,\nabla n \tag{8.57a}$$
$$\mathbf{j}_{\rm p} = e\mu_{\rm p} p\,\mathbf{E} - kT\mu_p\,\nabla p\;. \tag{8.57b}$$

We recall that both diffusion coefficients are positive numbers, since $\mu_{\rm n}$ is negative. Generally, the diffusion coefficient depends on the density. A Taylor series of the Fermi integral yields

$$D_{\rm n} = -\beta^{-1}\mu_{\rm n}\left[1 + 0.35355\left(\frac{n}{N_{\rm C}}\right) - 9.9\times10^{-3}\left(\frac{n}{N_{\rm C}}\right)^2 + \ldots\right]\;. \tag{8.58}$$

8.8 Continuity Equation

The balance equation for the charge is called the continuity equation. The temporal change of the charge in a volume element is given by the divergence of the current and any source (generation rate G), e.g. an external excitation, or drain (recombination rate U). Details about recombination mechanisms are discussed in Sect. 10. Thus, we have

$$\frac{\partial n}{\partial t} = G_{\mathrm{n}} - U_{\mathrm{n}} - \frac{1}{q}\,\nabla\cdot\mathbf{j}_{\mathrm{n}} = G_{\mathrm{n}} - U_{\mathrm{n}} + \frac{1}{e}\,\nabla\cdot\mathbf{j}_{\mathrm{n}} \tag{8.59a}$$

$$\frac{\partial p}{\partial t} = G_{\mathrm{p}} - U_{\mathrm{p}} - \frac{1}{e}\,\nabla\cdot\mathbf{j}_{\mathrm{p}}\ . \tag{8.59b}$$

In the case of nondegeneracy we find, using (8.51ab)

$$\frac{\partial n}{\partial t} = G_{\mathrm{n}} - U_{\mathrm{n}} - \mu_{\mathrm{n}} n\,\nabla\cdot\mathbf{E} - \mu_{\mathrm{n}}\,\mathbf{E}\,\nabla n + D_{\mathrm{n}}\Delta n \tag{8.60a}$$

$$\frac{\partial p}{\partial t} = G_{\mathrm{p}} - U_{\mathrm{p}} - \mu_{\mathrm{p}} p\,\nabla\cdot\mathbf{E} - \mu_{\mathrm{p}}\,\mathbf{E}\,\nabla p + D_{\mathrm{p}}\Delta p\ . \tag{8.60b}$$

In the case of zero electric field these read

$$\frac{\partial n}{\partial t} = G_{\mathrm{n}} - U_{\mathrm{n}} + D_{\mathrm{n}}\Delta n \tag{8.61a}$$

$$\frac{\partial p}{\partial t} = G_{\mathrm{p}} - U_{\mathrm{p}} + D_{\mathrm{p}}\Delta p\ , \tag{8.61b}$$

and if the stationary case also applies:

$$D_{\mathrm{n}}\Delta n = -G_{\mathrm{n}} + U_{\mathrm{n}} \tag{8.62a}$$

$$D_{\mathrm{p}}\Delta p = -G_{\mathrm{p}} + U_{\mathrm{p}}\ . \tag{8.62b}$$

8.9 Heat Conduction

We consider here the heat transport [557] due to a temperature gradient. The heat flow $\mathbf{q}$, i.e. energy per unit area per time in the direction $\hat{\mathbf{q}}$, is proportional to the local gradient of temperature. The proportionality constant κ is called, heat conductivity,

$$\mathbf{q} = -\kappa\,\nabla T\ . \tag{8.63}$$

In crystals, the heat conductivity can depend on the direction and thus κ is generally a tensor of rank 2. In the following, κ will be considered as a scalar quantity. The quite generally valid Wiedemann–Franz law connects the thermal and electrical conductivities

$$\kappa = \frac{\pi^2}{3} \left(\frac{k}{e} \right)^2 T\sigma \ . \tag{8.64}$$

The balance (continuity) equation for the heat energy Q is

$$\nabla \cdot \mathbf{q} = -\frac{\partial Q}{\partial t} = -\rho C \frac{\partial T}{\partial t} + A \ , \tag{8.65}$$

where ρ denotes the density of the solid and C the heat capacity. A denotes a source or drain of heat, e.g. an external excitation. Combining (8.63) and (8.65), we obtain the equation for heat conductivity

$$\Delta T = \frac{\rho C}{\kappa} \frac{\partial T}{\partial t} - \frac{A}{\kappa} \ , \tag{8.66}$$

which simply reads $\Delta T = 0$ for a stationary situation without sources.

The random mixture of various atoms in natural elements represents a perturbation of the perfectly periodic lattice. Since the mass of the nuclei varies, in particular lattice vibrations will be perturbed. Thus we expect an effect on the heat conductivity. In Fig. 8.19, the thermal conductivity of crystals from natural Ge and enriched ^{74}Ge are compared [558], the latter having, as expected, the higher heat conductivity, i.e. less scattering. The thermal conductivity of isotopically pure ^{28}Si thin films has been measured to be 60% greater than natural silicon at room temperature and at least 40% greater at 100°C, a typical chip operating temperature [559, 560].

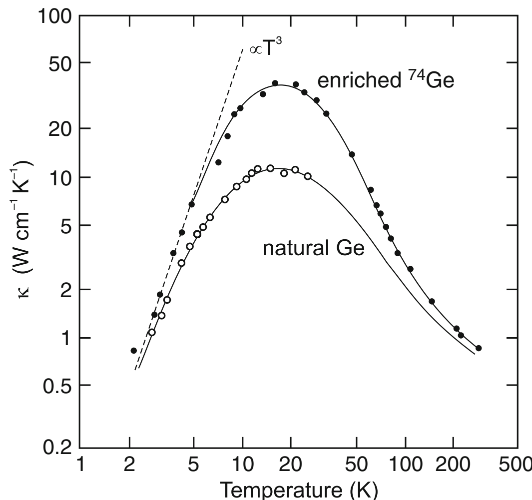

Fig. 8.19. Thermal conductivity of Ge vs. temperature. The enriched Ge consists of 96% ^{74}Ge while the natural isotope mix is 20% ^{70}Ge, 27% ^{72}Ge, 8% ^{73}Ge, 27% ^{74}Ge and 8% ^{76}Ge. The *dashed line* shows the $\kappa \propto T^3$ dependence at low temperatures (Debye's law). Adapted from [558]

8.10 Coupled Heat and Charge Transport

The standard effect of coupled charge and heat transport is that a current heats its conductor via Joule heating. However, more intricate use of thermoelectric effects can also be employed to cool certain areas of a device. For further details see [561, 562].

For the analysis of coupled charge and heat transport we first sum the electric field and the concentration gradient to a new field $\hat{\mathbf{E}} = \mathbf{E} + \nabla E_\mathrm{F}/e$. Then, the heat flow and charge current are

$$\mathbf{j} = \sigma\, \hat{\mathbf{E}} + L\, \nabla T \tag{8.67}$$

$$\mathbf{q} = M\, \hat{\mathbf{E}} + N\, \nabla T\ , \tag{8.68}$$

where $\hat{\mathbf{E}}$ and ∇T are the stimulators for the currents. From the experimental point of view there is interest to express the equations in $\mathbf{j}$ and ∇T since these quantities are measurable. With new coefficients they read

$$\hat{\mathbf{E}} = \rho\, \mathbf{j} + S\, \nabla T \tag{8.69}$$

$$\mathbf{q} = \Pi\, \mathbf{j} - \kappa\, \nabla T\ , \tag{8.70}$$

where ρ, S and Π are the specific resistance, thermoelectric power and Peltier coefficient (transported energy per unit charge), respectively. The relations with the coefficients σ, L, M, and N are given by

$$\rho = \frac{1}{\sigma} \tag{8.71a}$$

$$S = -\frac{L}{\sigma} \tag{8.71b}$$

$$\Pi = \frac{M}{\sigma} \tag{8.71c}$$

$$\kappa = \frac{M L}{\sigma} - N\ . \tag{8.71d}$$

8.10.1 Seebeck Effect

Assume a semiconductor with a temperature gradient and in an open circuit, i.e. $\mathbf{j} = 0$. Then a field $\hat{\mathbf{E}} = S \nabla T$ will arise. This effect is called the thermoelectric or Seebeck effect. The voltage can be measured and used to determine the temperature at one end if the temperature at the other end is known. Electrons and holes have different sign of the thermoelectric coefficient (see Fig. 8.20). A famous relation from irreversible thermodynamics connects it to the Peltier coefficient via

$$S = \frac{\Pi}{T}\ . \tag{8.72}$$

With the Seebeck effect the conductivity type of a semiconductor can be determined. If the cold substrate is grounded, the sign of the voltage at a hot

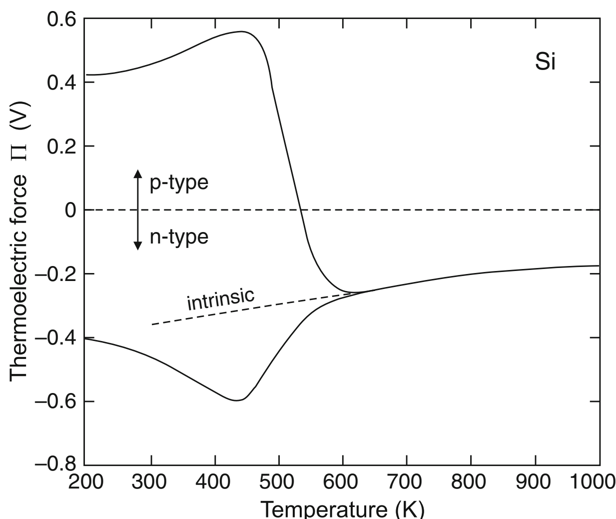

Fig. 8.20. Thermoelectric force Π of n- and p-silicon as a function of temperature. Adapted from [563]

solder tip pressed (carefully) on the surface of the semiconductor yields the conductivity type, n-type (p-type) for a negative (positive) voltage. However, the semiconductor should not be heated so strongly that intrinsic conduction arises.

8.10.2 Peltier Effect

In a semiconductor with a temperature gradient a current flow will be allowed now (short circuit). The current leads via the charge transport also to a heat (or energy) transport. This effect is called the Peltier effect. The Peltier coefficient is negative (positive) for electrons (holes). The total amount of energy P that is transported consists of the generation term and the loss due to transport:

$$P = \mathbf{j} \cdot \hat{\mathbf{E}} - \nabla \cdot \mathbf{q} \,. \tag{8.73}$$

With (8.69) and (8.70) we find

$$P = \frac{\mathbf{j} \cdot \mathbf{j}}{\sigma} + S\, \mathbf{j} \cdot \nabla T - \Pi\, \nabla \cdot \mathbf{q} + \kappa\, \Delta T \,. \tag{8.74}$$

The first term is Joule heating, the second term is Thomson heating. The third exists only when carriers are generated or when they recombine. The fourth term is the heat conduction. In the Thomson term $S\,\mathbf{j} \cdot \nabla T$ heat is generated in an n-type semiconductor if $\mathbf{j}$ and ∇T are in the same direction. This means that electrons that move from the hotter to the colder part transfer energy to the lattice. The effect can be used to construct a thermoelectric

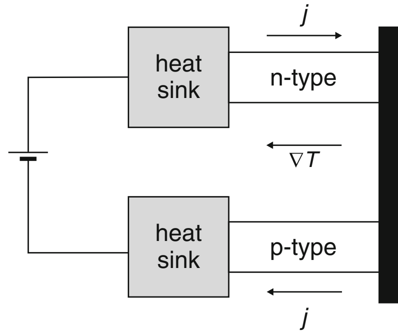

Fig. 8.21. Schematic Peltier cooler. The heat sinks (*grey*) and the cold junction (*black*) on the left are metals that make ohmic contacts with the semiconductors. The current flow is such that electrons move through the n-type semiconductor from right to left

cooler, as shown in Fig. 8.21, that generates a temperature difference due to a current flow. For optimal performance σ should be large to prevent excess Joule heating and κ should be small such that the generated temperature difference is not rapidly equalized.

9 Optical Properties

The interaction of semiconductors with light is of decisive importance for photonic and optoelectronic devices as well as for the characterization of semiconductor properties.

9.1 Spectral Regions and Overview

When light hits a semiconductor first reflection, transmission and absorption are considered, as for any dielectric material. The response of the semiconductor largely depends on the photon energy (or wavelength) of the light. In Table 9.1 an overview of the electromagnetic spectrum in the optical range is shown. The energy and wavelength of a photon are related by[1] $E = h\nu = hc/\lambda$, i.e.

$$E\,[\mathrm{meV}] = \frac{1240}{\lambda\,[\mathrm{nm}]}\ . \tag{9.1}$$

Table 9.1. Spectral ranges with relevance to semiconductor optical properties

Range		wavelengths	energies
deep ultraviolet	DUV	< 250 nm	> 5 eV
ultraviolet	UV	250–400 nm	3–5 eV
visible	VIS	400–800 nm	1.6–3 eV
near infrared	NIR	800 nm–2 µm	0.6–1.6 eV
mid-infrared	MIR	2–20 µm	60 meV–0.6 eV
far infrared	FIR	20–80 µm	1.6–60 meV
THz region	THz	> 80 µm	< 1.6 meV

[1] The exact numerical value in (9.1) is 1239.84.

M. Grundmann, *The Physics of Semiconductors*, 2nd ed., Graduate Texts in Physics, DOI 10.1007/978-3-642-13884-3_9,

© Springer-Verlag Berlin Heidelberg 2010

9.2 Reflection and Diffraction

From Maxwell's equations and the boundary conditions at a planar interface between two media with different index of refraction for the components of the electric and magnetic fields the laws for reflection and diffraction are derived. We denote the index of refraction as n and also n_r in the following. The interface between two media with refractive indices n_1 and n_2 is depicted in Fig. 9.1. In the following we assume first that no absorption occurs.

Snellius' law for the angle of diffraction is

$$n_1 \sin\phi = n_2 \sin\psi \; . \tag{9.2}$$

When the wave enters the denser medium, it is diffracted towards the normal. If the wave propagates into the less-dense medium (reversely to the situation shown in Fig. 9.1), a diffracted wave occurs only up to a critical angle of incidence

$$\sin\phi_\mathrm{TR} = \frac{n_2}{n_1} \; . \tag{9.3}$$

For larger angles of incidence, total internal reflection occurs and the wave remains in the denser medium. Thus, the angle in (9.3) is called the critical angle for total reflection. For GaAs and air the critical angle is rather small, $\phi_\mathrm{TR} = 17.4°$.

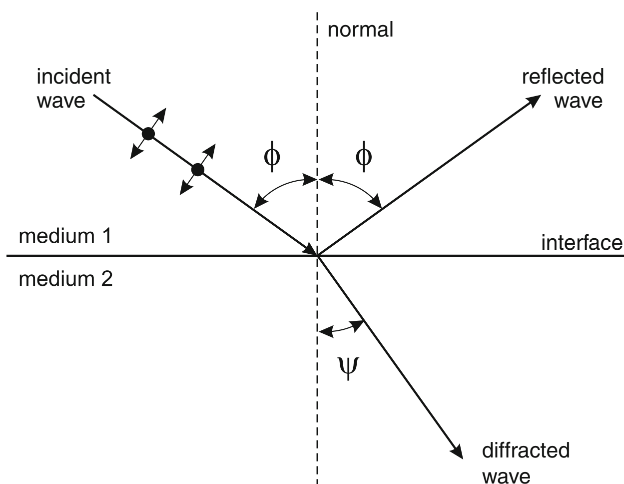

Fig. 9.1. Reflection and diffraction of an electromagnetic wave at the transition between medium '1' and '2', $n_2 > n_1$. The polarization plane is defined by the surface normal and the k-vector of the light (plane of incidence). The parallel ('p') polarized wave (TM-wave, electric field vector oscillates in the plane) is shown as '$\leftrightarrow$'; perpendicular ('s') polarization (TE-wave, electric field vector is perpendicular to plane) is depicted as '·'

The reflectance depends on the polarization (Fresnel formulas). The index 'p' ('s') denotes parallel polarized/TM (perpendicular polarized/TE) waves.

$$R_{\mathrm{p}} = \left(\frac{\tan(\phi - \psi)}{\tan(\phi + \psi)} \right)^2 \tag{9.4}$$

$$R_{\mathrm{s}} = \left(\frac{\sin(\phi - \psi)}{\sin(\phi + \psi)} \right)^2 . \tag{9.5}$$

The situation for GaAs and air is shown for both polarization directions and unpolarized radiation in Fig. 9.2 for a wave going into and out of the GaAs.

When the reflected and the diffracted wave are perpendicular to each other, the reflectance of the p-polarized wave is zero. This angle is the Brewster angle ϕ_{B},

$$\tan \phi_{\mathrm{B}} = \frac{n_2}{n_1} . \tag{9.6}$$

If a wave has vertical incidence from vacuum on a medium with index of refraction n_{r}, the reflectance is given (both polarizations are degenerate) as

$$R = \left(\frac{n_{\mathrm{r}} - 1}{n_{\mathrm{r}} + 1} \right)^2 . \tag{9.7}$$

For GaAs, the reflectance for vertical incidence is 29.2%.

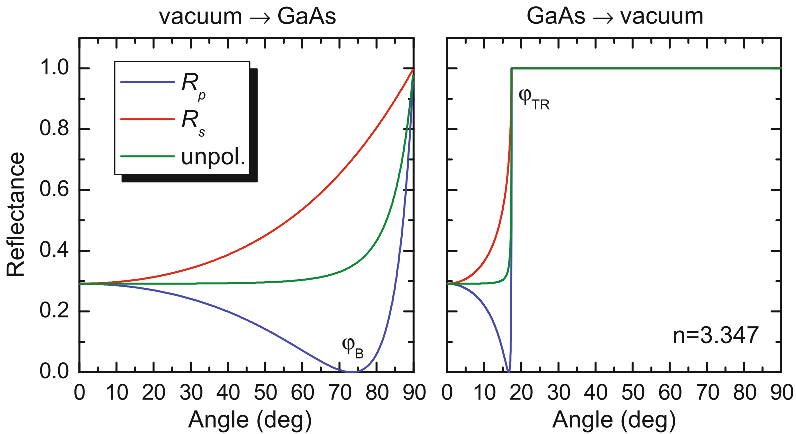

Fig. 9.2. Reflectance of the GaAs/vacuum interface (close to the band gap, $n_{\mathrm{r}} = 3.347$) for radiation from vacuum/air (*left panel*) and from the GaAs (*right panel*), respectively, as a function of incidence angle and polarization

9.3 Absorption

In the absorption process, energy is transferred from the electromagnetic field to the semiconductor. In the case of a linear absorption process, when the probability of light absorption is proportional to the incoming intensity, the decrease of intensity in the absorbing medium is exponential (Lambert–Beer's law [564, 565]),[2]

$$I(x) = I(0) \exp -\alpha x \, . \tag{9.8}$$

The quantity α is the *absorption coefficient*, its reverse the absorption depth. The spectral dependence $\alpha(E)$, the absorption spectrum, contains the information of the possible absorption processes, their energy, momentum and angular momentum selection rules, and their strength (oscillator strength).

In Fig. 9.3 a schematic absorption spectrum of a semiconductor is depicted. The transition of electrons from the valence to the conduction band is at the band gap energy. The band gaps of Si, Ge, GaAs, InP, InAs, InSb are in the IR, those of AlAs, GaP, AlP, InN in the VIS, those of GaN and ZnO in the UV, MgO and AlN are in the deep UV. The Coulomb correlation of electrons and holes leads to the formation of excitons that leads to absorption below the band gap. The typical exciton binding energy is in the range of 1–100 meV (see Fig. 9.16). Optical transitions from valence-band electrons into donors and from electrons on acceptors into the conduction band lead to band–impurity absorption. In the region from 10–100 meV the interaction with lattice vibrations (phonons) leads to absorption if the phonons are infrared active. Further in the FIR are transitions from impurities to the closest

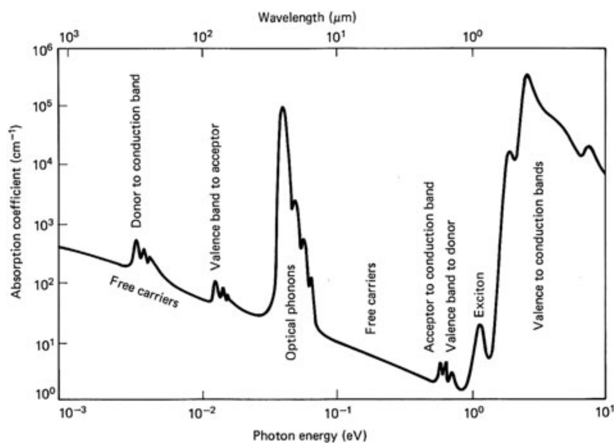

Fig. 9.3. Schematic absorption spectrum of a typical semiconductor. From [566]

[2] In [565], the absorption coefficient μ was defined via $I(d)/I(0) = \mu^d$, i.e. $\mu = \exp -\alpha$.

band edge (donor to conduction and acceptor to valence band). A continuous background is due to free-carrier absorption.

If absorption is considered, the reflectance (9.7) needs to be modified. Using the complex index of refraction $n^* = n_\mathrm{r} + \mathrm{i}\kappa$, it is given as

$$R = \left| \frac{n^* - 1}{n^* + 1} \right|^2 = \frac{(n_\mathrm{r} - 1)^2 + \kappa^2}{(n_\mathrm{r} + 1)^2 + \kappa^2} \ . \tag{9.9}$$

The absorption constant κ is related to the absorption coefficient of the plane wave (damping of $\mathbf{E}^2$) by

$$\alpha = 2 \frac{\omega}{c} \kappa = \frac{4\pi}{\lambda} \kappa = 2\, k\, \kappa \ . \tag{9.10}$$

Here, k and λ denote the respective values in vacuum.

9.4 Electron–Photon Interaction

The absorption process is quantum mechanically described by the coupling of electrons and photons. The process is described with time-dependent perturbation theory. If $\mathbf{H}_\mathrm{em}$ is the perturbation operator (electromagnetic field), the transition probability per time w_fi for electrons from (unperturbed) state 'i' (initial) to state 'f' (final) is given (with certain approximations) by Fermi's golden rule

$$w_\mathrm{fi}(\hbar\omega) = \frac{2\pi}{\hbar} \left| H'_\mathrm{fi} \right|^2 \delta(E_\mathrm{f} - E_\mathrm{i} - \hbar\omega) \ , \tag{9.11}$$

where $\hbar\omega$ is the photon energy, E_i (E_f) is the energy of the initial (final) state. H'_fi is the matrix element

$$H'_\mathrm{fi} = \langle \Psi_\mathrm{f} \,|\mathbf{H}'|\, \Psi_\mathrm{i} \rangle \ , \tag{9.12}$$

where Ψ_i (Ψ_f) are the wavefunctions of the unperturbed initial (final) state.

$\mathbf{A}$ is the vector potential for the electromagnetic field, i.e. $\mathbf{E} = -\dot{\mathbf{A}}$, $\mu\mathbf{H} = \nabla \times \mathbf{A}$, $\nabla \cdot \mathbf{A} = 0$ (Coulomb gauge). The Hamiltonian of an electron in the electromagnetic field is

$$\mathbf{H} = \frac{1}{2m} \left(\hbar\mathbf{k} - q\mathbf{A} \right)^2 \ . \tag{9.13}$$

When terms in $\mathbf{A}^2$ are neglected (i.e. two-photon processes), the perturbation Hamiltonian is thus

$$\mathbf{H}_\mathrm{em} = -\frac{q}{m} \mathbf{A}\mathbf{p} = \frac{\mathrm{i}q\hbar}{m} \mathbf{A} \cdot \nabla \approx q\, \mathbf{r} \cdot \mathbf{E} \ . \tag{9.14}$$

The latter approximation is valid for small wavevectors of the electromagnetic wave and is termed the *electric dipole approximation*.

In order to calculate the dielectric function of the semiconductor from its band structure we assume that $\mathbf{A}$ is weak and we can apply (9.11). The transition probability R for the photon absorption rate at photon energy $\hbar\omega$ is then given by[3]

$$R(\hbar\omega) = \frac{2\pi}{\hbar} \int_{\mathbf{k}_\mathrm{c}} \int_{\mathbf{k}_\mathrm{v}} \left|\langle c|\mathbf{H}_\mathrm{em}|v\rangle\right|^2 \delta\left(E_\mathrm{c}(\mathbf{k}_\mathrm{c}) - E_\mathrm{v}(\mathbf{k}_\mathrm{v}) - \hbar\omega\right) \mathrm{d}^3\mathbf{k}_\mathrm{c}\, \mathrm{d}^3\mathbf{k}_\mathrm{v} \,, \tag{9.15}$$

with the Bloch functions $|c\rangle$ and $|v\rangle$ of the conduction and valence band, respectively, as given in (6.39b).

The vector potential is written as $\mathbf{A} = A\hat{\mathbf{e}}$ with a unit vector $\hat{\mathbf{e}}$ parallel to $\mathbf{A}$. The amplitude is connected to the electric-field amplitude $\mathcal{E}$ via

$$A = -\frac{\mathcal{E}}{2\omega} \left[\exp\left(\mathrm{i}(\mathbf{qr} - \omega t)\right) + \exp\left(-\mathrm{i}(\mathbf{qr} - \omega t)\right)\right] \,. \tag{9.16}$$

In the electric-dipole approximation the momentum conservation $\mathbf{q}+\mathbf{k}_\mathrm{v} = \mathbf{k}_\mathrm{c}$, $\mathbf{q}$ being the momentum of the light wave is approximated by $\mathbf{k}_\mathrm{v} = \mathbf{k}_\mathrm{c}$. The matrix element is then given by

$$\left|\langle c|\mathbf{H}_\mathrm{em}|v\rangle\right|^2 = \frac{e^2\,|A|^2}{m^2} \left|\langle c|\hat{\mathbf{e}} \cdot \mathbf{p}|v\rangle\right|^2 \,, \tag{9.17}$$

with

$$\langle c\,|\hat{\mathbf{e}} \cdot \mathbf{p}|v\rangle|^2 = \frac{1}{3} \left|\mathbf{p}_\mathrm{cv}\right|^2 = M_\mathrm{b}^2 \,, \tag{9.18}$$

and the momentum matrix element $\mathbf{p}_\mathrm{cv}$ given in (6.38). A $\mathbf{k}$-independent matrix element $|\mathbf{p}_\mathrm{cv}|^2$ is often used as an approximation. In Fig. 9.4 the matrix elements for valence to conduction band transitions in GaN are shown as a function of $\mathbf{k}$.

In terms of the electric-field amplitude $\mathcal{E}(\omega)$ the transition probability is

$$R(\hbar\omega) = \frac{2\pi}{\hbar} \left(\frac{e}{m\omega}\right)^2 \left|\frac{\mathcal{E}(\omega)}{2}\right|^2 \left|\mathbf{p}_\mathrm{cv}\right|^2 \int_{\mathbf{k}} \delta\left(E_\mathrm{c}(\mathbf{k}) - E_\mathrm{v}(\mathbf{k}) - \hbar\omega\right) \mathrm{d}^3\mathbf{k} \,. \tag{9.19}$$

If the integration over $\mathbf{k}$ is restricted to those values allowed in unit volume, the power that is lost from the field in unit volume is given by $R\hbar\omega$. The dielectric function $\epsilon = \epsilon_\mathrm{r} + \mathrm{i}\epsilon_\mathrm{i}$ is given by

$$\epsilon_\mathrm{i} = \frac{1}{4\pi\epsilon_0} \left(\frac{2\pi e}{m\omega}\right)^2 \left|\mathbf{p}_\mathrm{cv}\right|^2 \int_{\mathbf{k}} \delta\left(E_\mathrm{c}(\mathbf{k}) - E_\mathrm{v}(\mathbf{k}) - \hbar\omega\right) \mathrm{d}^3\mathbf{k} \tag{9.20a}$$

$$\epsilon_\mathrm{r} = 1 + \int_{\mathbf{k}} \frac{e^2}{\epsilon_0 m \omega_\mathrm{cv}^2} \frac{2|\mathbf{p}_\mathrm{cv}|^2}{m\hbar\omega_\mathrm{cv}} \frac{1}{1 - \omega^2/\omega_\mathrm{cv}^2} \mathrm{d}^3\mathbf{k} \,, \tag{9.20b}$$

[3] Here we assume that the valence-band states are filled and the conduction-band states are empty. If the conduction-band states are filled and the valence-band states are empty, the rate is that of stimulated emission.

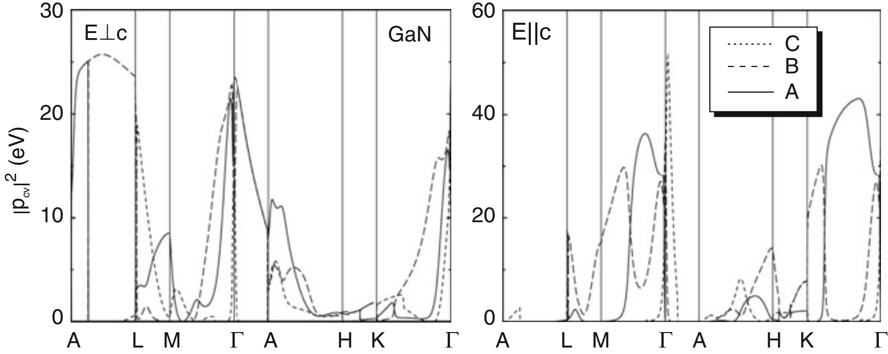

Fig. 9.4. Theoretical momentum matrix elements $|p_{\rm cv}|^2$ along high-symmetry directions in the Brillouin zone (see Fig. 3.32d) for transitions between valence and conduction bands in GaN and light polarized perpendicular (*left panel*) and parallel (*right panel*) to the *c*-axis. The transitions are A: Γ_9(A)→ $\Gamma_{7\rm c}$, B: Γ_7(B)→ $\Gamma_{7\rm c}$, C: Γ_7(C)→ $\Gamma_{7\rm c}$ (see Fig. 6.33). Adapted from [567]

with $\hbar\omega_{\rm cv} = E_{\rm c}(\mathbf{k}) - E_{\rm v}(\mathbf{k})$. The second equation has been obtained via the Kramers–Kronig relations[4] (see Appendix C).

Comparison with (D.7) yields that the oscillator strength of the band–band absorption is given by

$$f = \frac{e^2}{\epsilon_0 m \omega_{\rm cv}^2} \frac{2|\mathbf{p}_{\rm cv}|^2}{m\hbar\omega_{\rm cv}} , \tag{9.21}$$

with

$$N_{\rm cv} = \frac{2|\mathbf{p}_{\rm cv}|^2}{m\hbar\omega_{\rm cv}} \tag{9.22}$$

being the classical 'number' of oscillators with the frequency $\omega_{\rm cv}$.

9.5 Band–Band Transitions

9.5.1 Joint Density of States

The strength of an allowed optical transitions between valence and conduction bands is proportional to the joint density of states (JDOS) $D_{\rm j}(E_{\rm cv})$ (cf. (6.66), (6.67) and (9.20a))

$$D_{\rm j}(E_{\rm cv}) = 2 \int_{S(\tilde{E})} \frac{{\rm d}^2 S}{(2\pi/L)^3} \frac{1}{|\nabla_{\mathbf{k}} E_{\rm cv}|} , \tag{9.23}$$

[4]The real and imaginary parts of the dielectric function are generally related to each other via the Kramers–Kronig relations.

where E_{cv} is an abbreviation for $E_{\mathrm{c}}(\mathbf{k}) - E_{\mathrm{v}}(\mathbf{k})$ and d^2S is a surface element of the constant energy surface with $\tilde{E} = E_{\mathrm{cv}}$. The spin is assumed to generate doubly degenerate bands and accounts for the pre-factor 2. Singularities of the JDOS (*van-Hove singularities* or *critical points*) appear where $\nabla_{\mathbf{k}} E_{\mathrm{cv}}$ vanishes. This occurs when the gradient for both bands is zero or when both bands are parallel. The latter generates particularly large JDOS because the condition is valid at many points in **k**-space.

Generally, the (three-dimensional) energy dispersion $E(\mathbf{k})$ around a three-dimensional critical point (here developed at $\mathbf{k} = 0$) can be written as

$$E(\mathbf{k}) = E(0) + \frac{\hbar^2 k_{\mathrm{x}}^2}{2m_{\mathrm{x}}} + \frac{\hbar^2 k_{\mathrm{y}}^2}{2m_{\mathrm{y}}} + \frac{\hbar^2 k_{\mathrm{z}}^2}{2m_{\mathrm{z}}} \,. \tag{9.24}$$

The singularities are classified as M_0, M_1, M_2 and M_3 with the index being the number of masses m_i in (9.24) that are negative. M_0 (M_3) describes a minimum (maximum) of the band separation. M_1 and M_2 are saddle points. For a two-dimensional **k**-space there exist M_0, M_1 and M_2 points (minimum, saddle point and maximum, respectively). For a one-dimensional **k**-space there exist M_0 and M_1 points (minimum and maximum, respectively). The functional dependence of the JDOS at the critical points is summarized in Table 9.2. The resulting shape of the dielectric function is visualized in Fig. 9.5.

9.5.2 Direct Transitions

Transitions between states at the band edges at the Γ point are possible (Fig. 9.6). The **k** conservation requires (almost) vertical transitions in the $E(\mathbf{k})$ diagram because the length of the light **k** vector, $k = 2\pi/\lambda$, is much

Table 9.2. Functional dependence of the joint density of states for critical points in 3, 2 and 1 dimensions. E_0 denotes the energy (band separation) at the critical point, C stands for a constant value. The type of critical point is given (min.: minimum, saddle: saddle point, max.: maximum)

Dim.	label	type	D_{j} for $E < E_0$	D_{j} for $E > E_0$
3D	M_0	min.	0	$\sqrt{E - E_0}$
	M_1	saddle	$C - \sqrt{E_0 - E}$	C
	M_2	saddle	C	$C - \sqrt{E - E_0}$
	M_3	max.	$\sqrt{E_0 - E}$	0
2D	M_0	min.	0	C
	M_1	saddle	$-\ln(E_0 - E)$	$-\ln(E - E_0)$
	M_2	max.	C	0
1D	M_0	min.	0	$\sqrt{E - E_0}$
	M_1	max.	$\sqrt{E_0 - E}$	0

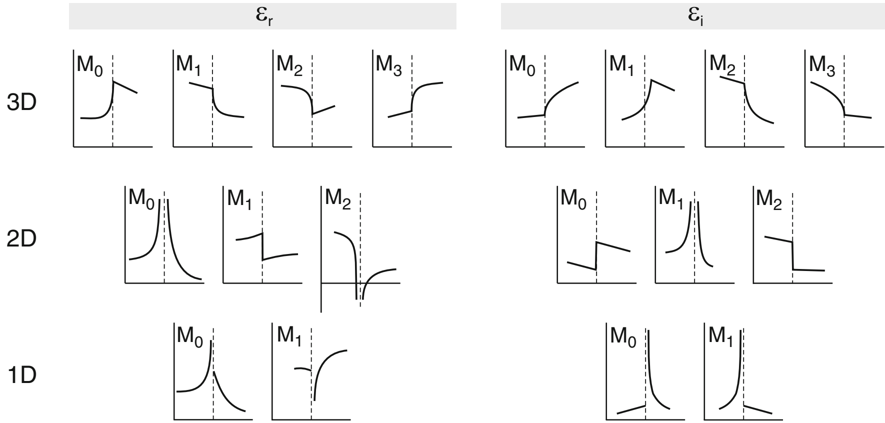

Fig. 9.5. Shape of the real (*left panel*) and imaginary (*right panel*) parts of the dielectric function in the vicinity of critical points in 3, 2 and 1 dimensions (for labels see Table 9.2). The *dashed line* in each graph indicates the energy position of the critical point E_0. Adapted from [568]

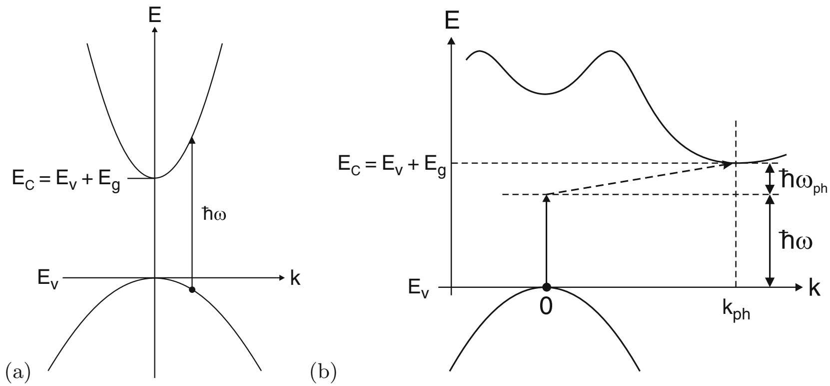

Fig. 9.6. (**a**) Direct optical transition and (**b**) indirect optical transitions between valence and conduction bands. The photon energy is $\hbar\omega$. The indirect transition involves a phonon with energy $\hbar\omega_{\rm ph}$ (here: phonon absorption) and wavevector $k_{\rm ph}$

smaller than the size of the Brillouin zone $|k| \leq \pi/a_0$. The ratio of the lengths of the **k** vectors is $\sim 2a_0/\lambda$ and typically about 10^{-3} for NIR wavelengths.

For parabolic bands, i.e. bands described with an energy-independent effective mass, the absorption coefficient is (M_0 critical point)

$$\alpha \propto \sqrt{E - E_{\rm g}} \, . \tag{9.25}$$

The absorption spectrum of GaAs is shown in Fig. 9.7a for photon energies close to the band gap. The rapid increase, typical for direct semiconductors,

is obvious. At low temperatures, however, the absorption lineshape close to the band gap is dominated by an excitonic feature, discussed in Sect. 9.5.7.

Due to the increasing density of states, the absorption increases with the photon energy (Fig. 9.7c). At 1.85 eV there is a step in the absorption spectrum of GaAs due to the beginning of the contribution of transitions between the s-o hole band and the conduction band (see $E_0 + \Delta_0$ transition in Fig. 9.7e). When bands go parallel, i.e. with the same separation, in the $E(\mathbf{k})$ diagram, the absorption processes contribute at the same transition energy. In this way higher peaks in the absorption spectrum due to the E_1 or E_0' transitions originate as indicated in the band structure in Fig. 9.7e.

The selection rules for transitions from valence to conduction band must take into account the angular momentum and spin states of the wavefunctions. The optical transitions are circularly polarized as shown in Fig. 9.8. A lifting of the energetic degeneracies of these states occurs, e.g. by magnetic fields or spatial confinement.

9.5.3 Indirect Transitions

In an indirect band structure the missing k difference (across the Brillouin zone) between valence- and conduction-band state needs to be provided by a second particle. A phonon can provide the momentum and additionally contributes a small amount of energy $\hbar\omega_{\mathrm{ph}}$. There are several steps in the absorption spectrum due to various involved phonons (or combinations of them). At low temperature ($T = 1.6$ K, Fig. 9.9) phonons can only be generated and the absorption starts at energies *above* the band gap. At higher temperatures (typically above 40 K [569], Fig. 9.9), acoustical phonons assisting the optical absorption transition can also be absorbed from the crystal; in this case due to energy conservation the absorption starts already at an energy $E_{\mathrm{g}} - \hbar\omega_{\mathrm{ph}}$ *below* the band gap. At even higher temperatures (> 200 K, Fig. 9.9), also optical phonons can be absorbed.

The two-particle process is less probable than the direct absorption that only involves one photon. The perturbation calculation yields an absorption coefficient with a quadratic dependence on energy (9.26) [570]. However, the strength close to the band gap is about 10^{-3} smaller than for the direct transition.

$$\alpha \propto (E - E_{\mathrm{g}} \pm \hbar\omega_{\mathrm{ph}})^2 \, . \tag{9.26}$$

An 11-parameter formula based on terms like (9.26) can describe the room temperature absorption spectrum of silicon in the visible with a precision of a few percent [573].

The absorption spectra close to the absorption edge are shown for GaP (Fig. 9.9) and Si (Fig. 9.10a). According to (9.26), the plot of $\sqrt{\alpha}$ vs. energy (Macfarlane-Roberts plot [574]) yields a straight line beyond the spectral region of phonon effects. The complicated form close to the (indirect) gap energy is due to the contribution of different phonons. The phonon energies

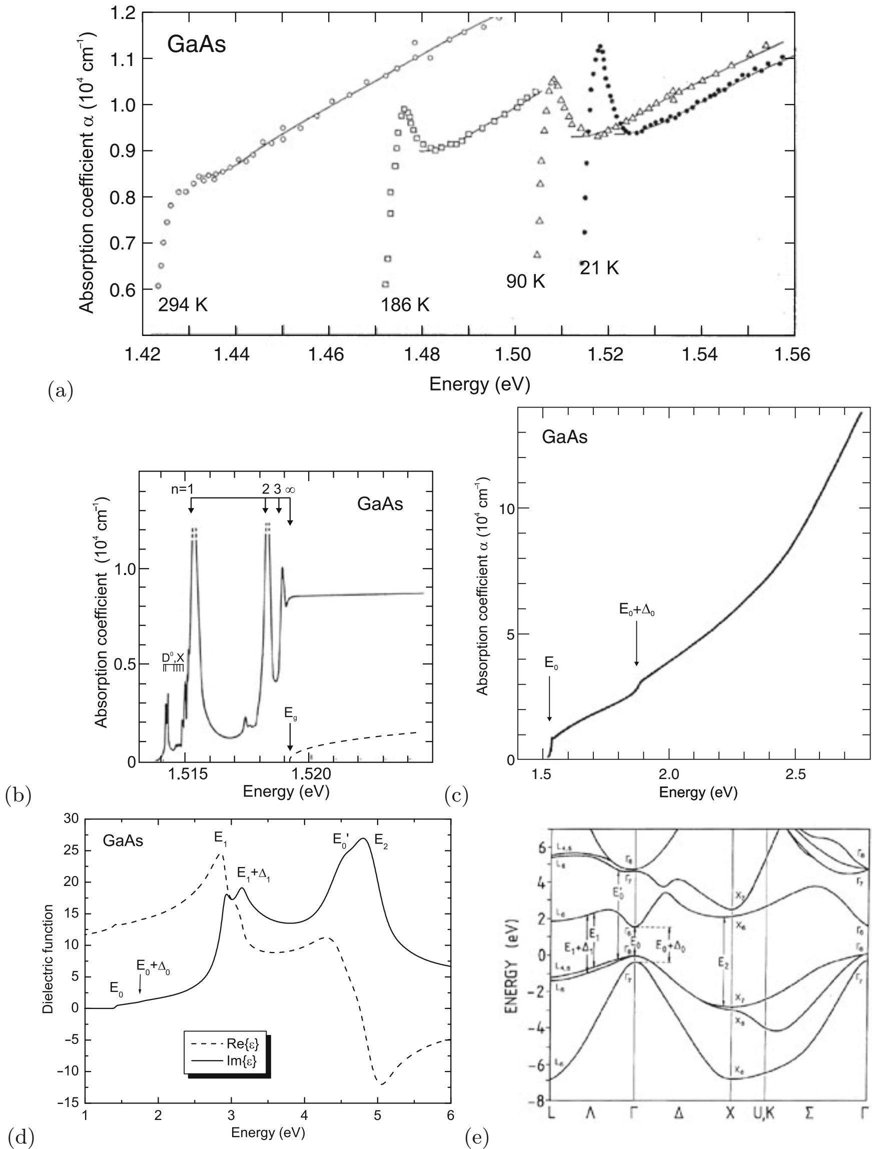

Fig. 9.7. (**a**) Absorption of GaAs close to the band gap at different temperatures. Adapted from [571]. (**b**) High-resolution absorption spectrum of highly pure GaAs at $T = 1.2\,\mathrm{K}$ in the exciton region. *Dashed line* is theory without excitonic correlation. Adapted from [572]. (**c**) Absorption spectrum of GaAs at $T = 21\,\mathrm{K}$ in the vicinity of the band gap. Adapted from [571]. (**d**) Complex dielectric function of GaAs at $T = 300\,\mathrm{K}$, *dashed* (*solid*) *line*: real (imaginary) part of dielectric constant. Peak labels relate to transitions shown in part (**e**). (**e**) Band structure of GaAs with band gap transition (E_0) and higher transitions ($E_0 + \Delta_0$, E_1, $E_1 + \Delta_1$, E_0', and E_2) indicated

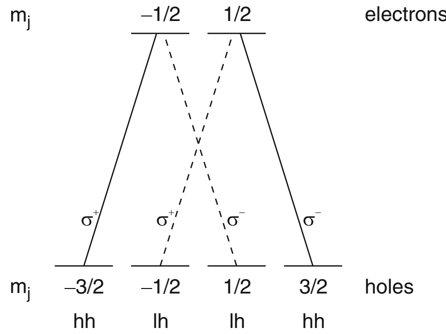

Fig. 9.8. Optical selection rules for band–band transitions in bulk material

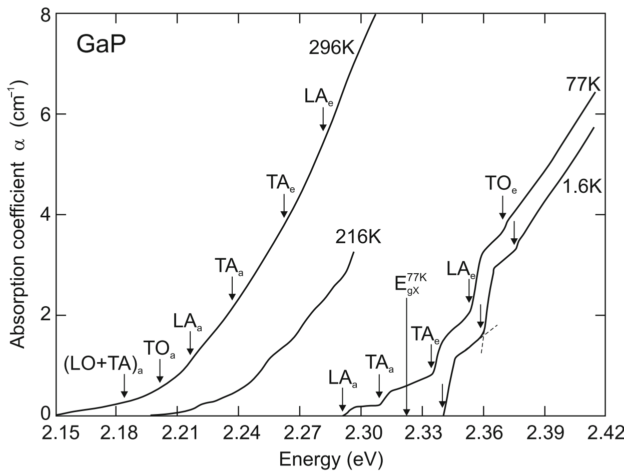

Fig. 9.9. Absorption edge of GaP at various temperatures. The index 'e' ('a') indicates phonon emission (absorption) during the optical absorption process. The theoretical excitonic gap (E_{gX}) at $T = 77\,\mathrm{K}$ is indicated Adapted from [569]

found to contribute to the silicon absorption edge [575] agree with the TA and TO energy at the X minimum [576] (Fig. 9.10b). Also multiple phonons can contribute (Fig. 9.9). The momentum conservation can also be achieved by impurity scattering or electron-electron scattering [577].

We note also that the indirect semiconductors have an optical transition between Γ valence- and conduction-band states. However, this transition is at higher energies than the fundamental band gap, e.g. for Si ($E_{\mathrm{g}} = 1.12\,\mathrm{eV}$) at $3.4\,\mathrm{eV}$ (see Fig. 6.5a). In Fig. 9.11, the absorption scheme for indirect and direct absorption processes starting with an electron at the top of the valence band is shown together with an experimental absorption spectrum for Ge with the direct transition ($\Gamma_8 \rightarrow \Gamma_7$) at $0.89\,\mathrm{eV}$, $0.136\,\mathrm{eV}$ above the fundamental band gap.

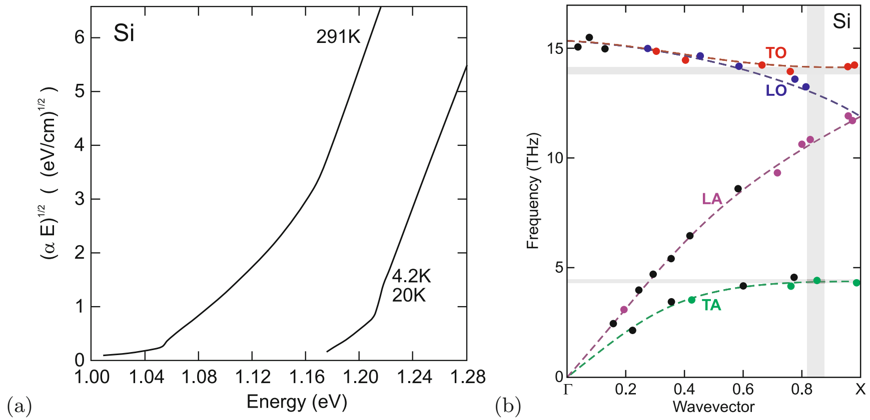

Fig. 9.10. (**a**) Absorption edge of Si at two different temperatures. Adapted from [575]. (**b**) Phonon energies in silicon along [001] obtained from neutron scattering (*black*: unidentified, *green*: TA, *purple*: LA, *blue*: LO, *red*: TO). The *vertical grey bar* indicates the position of the conduction band minimum, the *horizontal grey bars* the energies of the phonons observed at the indirect optical absorption edge. The *dark grey* overlap areas indicate that TO and TA phonons contribute. Adapted from [576]

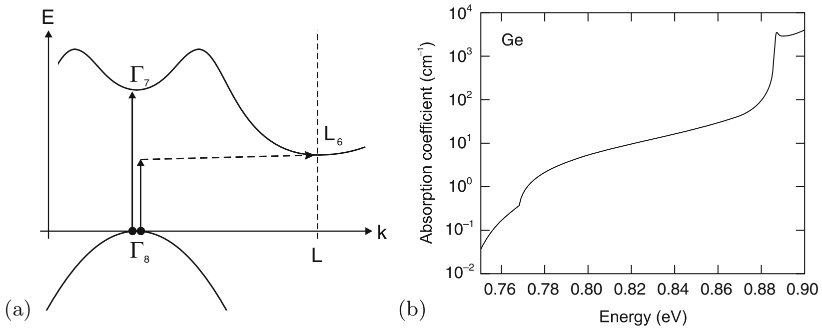

Fig. 9.11. (**a**) Scheme of indirect and direct optical transitions starting at the top of the valence band in Ge. Vertical *solid lines* represent the involved photon, the horizontal *dashed line* the involved phonon. (**b**) Experimental absorption spectrum of Ge ($T = 20\,$K). Adapted from [575]

In Fig. 9.12, the absorption edge of $BaTiO_3$ is shown. An indirect transition with an increase of (weak) absorption $\propto E^2$ and an indirect gap of $E_\mathrm{i} = 2.66\,$eV and a direct transition with an increase of (strong) absorption $\propto E^{1/2}$ and a direct gap of $E_\mathrm{d} = 3.05\,$eV are observed. These transitions could be due to holes at the M (indirect gap) and Γ (direct gap) points (cf. Sect. 6.3.9), respectively.

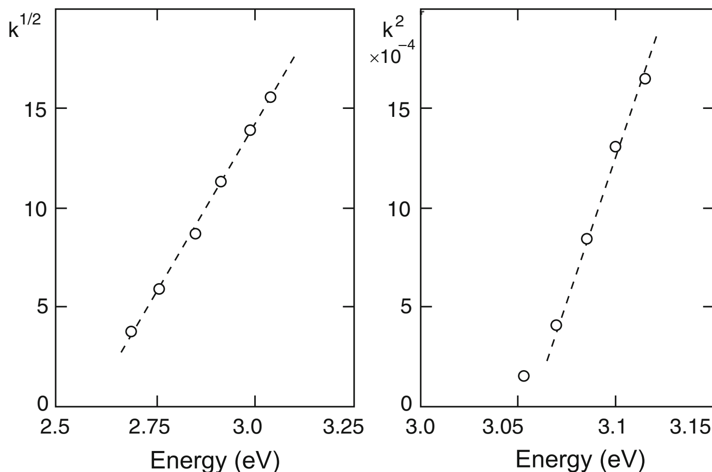

Fig. 9.12. Absorption of $BaTiO_3$ at room temperature. Experimental data (*circles*) from [578] with fits (*dashed lines*) $\propto E^2$ and $\propto E^{1/2}$, respectively

9.5.4 Urbach Tail

Instead of the ideal $(E - E_g)^{1/2}$ dependence of the direct band-edge absorption, often an exponential tail is observed (see Fig. 9.13). This tail is called the Urbach tail [579] and follows the functional dependence

$$\alpha(E) = \alpha_g \exp\left(\frac{E - E_g}{E_0}\right) , \tag{9.27}$$

where E_0 is the characteristic width of the absorption edge, the so-called Urbach parameter.

The Urbach tail is attributed to transitions between band tails below the band edges. Such tails can originate from disorder of the perfect crystal, e.g. from defects or doping, and the fluctuation of electronic energy bands due to lattice vibrations. The temperature dependence of the Urbach parameter E_0 is thus related to that of the band gap as discussed in [581, 582].

9.5.5 Intravalence-Band Absorption

Besides optical interband transitions between the valence and the conduction band there are also optical transitions within the valence band. In p-type material holes from the valence-band edge can undergo absorption and end up in the split-off hole band (Fig. 9.14a). Such intravalence-band absorption occurs at photon energies close to Δ_0 as shown in Fig. 9.14b for p-type GaAs:Zn. Also, hh $\rightarrow$ lh transitions are possible.

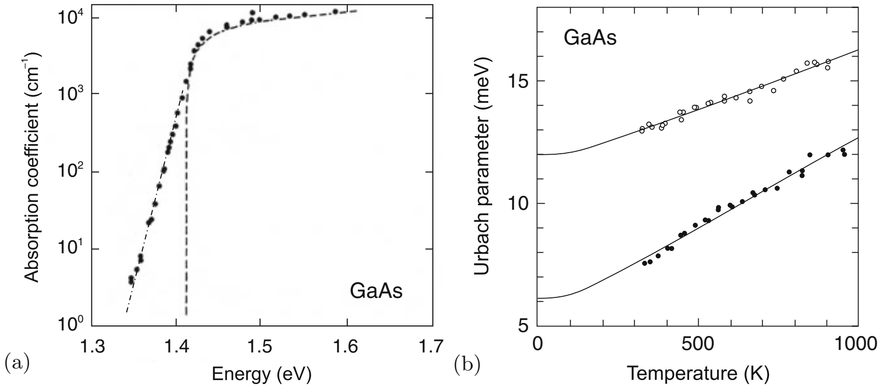

Fig. 9.13. (**a**) Experimental absorption spectrum (*circles*) of GaAs at room temperature on a semilogarithmic plot. The exponential tail below the band gap is called the Urbach tail (the *dash-dotted* line corresponds to $E_0 = 10.3\,\mathrm{meV}$ in (9.27)). The *dashed line* is the theoretical dependence from (9.25). Adapted from [580]. (**b**) Temperature dependence of Urbach parameter E_0 for two GaAs samples. Experimental data for undoped (*solid circles*) and Si-doped ($n = 2 \times 10^{18}\,\mathrm{cm}^{-3}$, *empty circles*) GaAs and theoretical fits (*solid lines*) with one-phonon model. Adapted from [581]

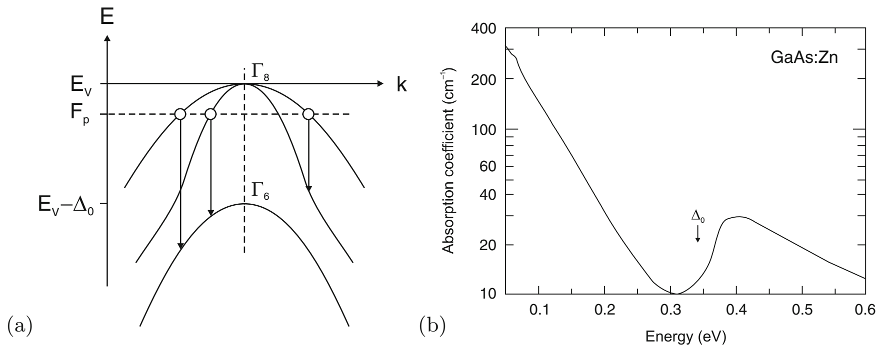

Fig. 9.14. (**a**) Schematic optical transitions within the valence band. Holes (*empty circles*) are shown to start at the hole quasi-Fermi level, transitions are from left to right: 'hh → s-o', 'lh → s-o' and 'hh → lh'. (**b**) Experimental absorption spectrum of GaAs:Zn with $p = 2.7 \times 10^{17}\,\mathrm{cm}^{-3}$ at $T = 84\,\mathrm{K}$. The absorption above the split-off energy Δ_0 is due to the hh/lh → s-o process. Adapted from [583]

9.5.6 Amorphous Semiconductors

The sharp features in the dielectric function due to critical points in the band structure of crystalline semiconductors are washed out in amorphous material. As an example the spectra of the imaginary part of the dielectric function for crystalline (trigonal) and amorphous selenium are shown in Fig. 9.15.

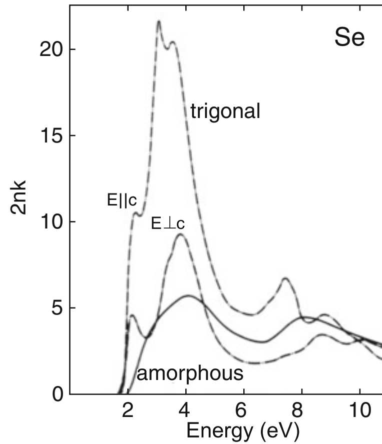

Fig. 9.15. Imaginary part of the dielectric function of amorphous (*solid line*) and crystalline (trigonal) selenium (*dash-dotted lines* for two different polarization directions). From [584]

9.5.7 Excitons

An electron in the conduction band and a hole in the valence band form a hydrogen-like state due to the mutual Coulomb interaction. Such a state is called an exciton. The center-of-mass motion is separated and has a dispersion $E = \frac{\hbar^2}{2M}\mathbf{K}^2$, where $M = m_\mathrm{e} + m_\mathrm{h}$ is the total mass and $\hbar\mathbf{K}$ is the center-of-mass momentum

$$\mathbf{K} = \mathbf{k}_\mathrm{e} + \mathbf{k}_\mathrm{h} \ . \tag{9.28}$$

The relative motion yields hydrogen-like quantized states $E_n \propto n^{-2}$ $(n \geq 1)$:

$$E_\mathrm{X}^n = -\frac{m_\mathrm{r}^*}{m_0}\,\frac{1}{\epsilon_\mathrm{r}^2}\,\frac{m_0 e^4}{2(4\pi\epsilon_0\hbar)^2}\,\frac{1}{n^2} \ , \tag{9.29}$$

where m_r^* denotes the reduced effective mass $m_\mathrm{r}^{*-1} = m_\mathrm{e}^{*-1} + m_\mathrm{h}^{*-1}$. The third factor is the atomic Rydberg energy (13.6 eV). The exciton binding energy $E_X^b = -E_X^1$ is scaled by $\frac{m^*}{m_0}\frac{1}{\epsilon_\mathrm{r}^2} \approx 10^{-3}$. A more detailed theory of excitons beyond the simple hydrogen model presented here, taking into account the valence-band structure, can be found in [585] for direct and [586] for indirect cubic and in [587] for wurtzite semiconductors. The exciton binding energies for various semiconductors are listed in Table 9.3 and shown in Fig. 9.16a vs. the band gap.

The radius of the exciton is

$$r_\mathrm{X}^n = n^2\,\frac{m_0}{m_\mathrm{r}^*}\,\epsilon_\mathrm{r}\,a_\mathrm{B} \ , \tag{9.30}$$

Table 9.3. Exciton (E_X^b) and biexciton (E_{XX}^b, see Sect. 9.5.11) binding energies in various bulk semiconductors. Values for 10 nm GaAs/15 nm $Al_{0.3}Ga_{0.7}As$ quantum well (QW) are taken from [588]

Material	E_X^b (meV)	E_{XX}^b (meV)	E_{XX}^b/E_X^b
GaAs	4.2		
GaAs QW	9.2	2.0	0.22
ZnSe	17	3.5	0.21
GaN	25	5,6	0.22
CdS	27	5.4	0.20
ZnS	37	8.0	0.22
ZnO	59	15	0.25

where $a_B = 0.053$ nm denotes the hydrogen Bohr radius.[5] The Bohr radius of the exciton is $a_X = r_X^1$ (14.6 nm for GaAs, ~ 2 nm for ZnO). The exciton moves with the center-of-mass **K**-vector through the crystal. The complete dispersion is (see Fig. 9.16b)

$$E = E_g + E_X^n + \frac{\hbar^2}{2M}\mathbf{K}^2 \ . \tag{9.31}$$

The oscillator strength of the exciton states decays $\propto n^{-3}$. The absorption due to excitons is visible in Fig. 9.7a for GaAs at low temperatures. If inhomogeneities are present, typically only the $n = 1$ transition is seen. How-

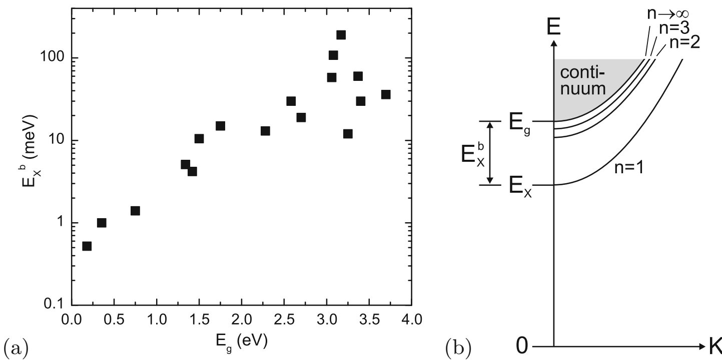

Fig. 9.16. (**a**) Exciton binding energy vs. band gap for various semiconductors. (**b**) Schematic dispersion of excitonic levels. The K-vector refers to the center-of-mass motion

[5] Cf. (7.25); an electron bound to a donor can be considered as an exciton with an infinite hole mass.

ever, under special conditions also higher transitions of the exciton Rydberg series are seen (e.g. $n = 2$ and 3 in Fig. 9.7b).

The exciton concept was introduced first for absorption in Cu_2O [589]. The $J = 1/2$ absorption spectrum ('yellow series') is shown in Fig. 9.17. In this particular material both the valence and conduction bands have s character, thus the 1s transition of the exciton is forbidden and the np transitions are observed in normal (one-photon) absorption. Only with two-photon absorption can the s (and d) transitions also be excited.

The scattering (unbound) states of the exciton [590] for $E > E_{\mathrm{g}}$ contribute to absorption above the band gap. The factor by which the absorption spectrum is changed is called the Sommerfeld factor. For bulk material it is

$$S(\eta) = \eta \, \frac{\exp(\eta)}{\sinh(\eta)} \, , \tag{9.32}$$

with $\eta = \pi \left(\frac{E_X^b}{E - E_{\mathrm{g}}} \right)^{1/2}$. The change of the absorption spectrum due to the Coulomb correlation is shown in Fig. 9.18. There is a continuous absorption between the bound and unbound states. At the band gap there is a finite absorption ($S(E \to E_{\mathrm{g}}) \to \infty$). The detail to which exciton peaks can be resolved depends on the spectral broadening.

In Fig. 9.19 the energy separations of the A-, B-, and C-excitons in GaN are shown [365]. Thus, the ordering of the valence bands depends on the strain state of the semiconductor.

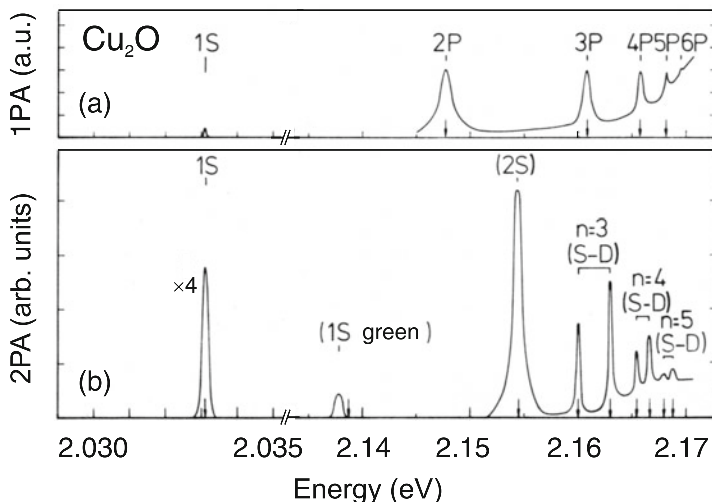

Fig. 9.17. One-photon (*top*) and two-photon (*bottom*) absorption spectra of Cu_2O at $T = 4.2\,\mathrm{K}$. *Arrows* denote theoretical peak positions. Adapted from [592]

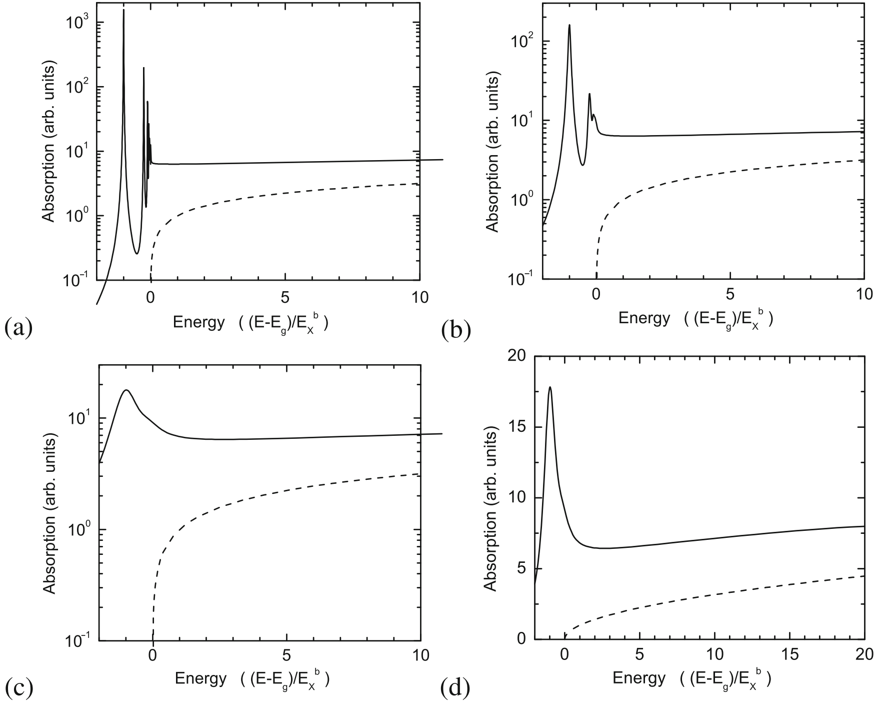

Fig. 9.18. Modification of the absorption edge of a direct transition by excitonic effects for different spectral (Lorentzian) broadening ($\propto (E^2 + \Gamma^2/4)^{-1}$), (**a**) $\Gamma = 0.01E_X^b$, (**b**) $\Gamma = 0.1E_X^b$, (**c**) $\Gamma = E_X^b$. (**d**) is (**c**) in linear scale. *Dashed lines* are electron–hole plasma absorption according to (9.25)

9.5.8 Phonon Broadening

The scattering with phonons and the related dephasing leads to homogeneous broadening $\Gamma_{\rm hom}$ of absorption (and recombination) lines. Acoustic and optical phonons contribute to the broadening according to the dependence [591]

$$\Gamma_{\rm hom}(T) = \Gamma_0 + \gamma_{\rm AC}\, T + \gamma_{\rm LO}\, \frac{1}{\exp(\hbar\omega_{\rm LO}/kT) - 1}\,, \tag{9.33}$$

where $\hbar\omega_{\rm LO}$ is the optical phonon energy and the last factor is the Bose function (E.22). Γ_0 is a temperature-independent contribution, $\Gamma_0 = \Gamma(T = 0)$. The increasing broadening with increasing temperature is obvious, e.g., in absorption spectra (Fig. 9.20a). In Fig. 9.20b experimental data for GaAs, ZnSe and GaN are assembled. The data have been fitted with (9.33); the resulting phonon broadening parameters are listed in Table 9.4.[6] The optical

[6]Such parameter can be directly determined from spectroscopic broadening (as in [594]) or a time-resolved measurement of the decay of the coherent polarization

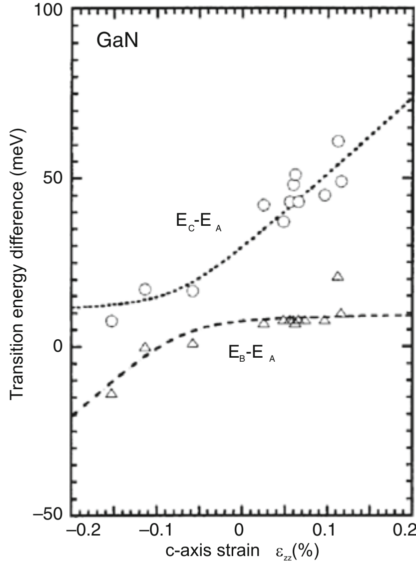

Fig. 9.19. Theoretical dependency (*lines*) for the the differences of the C-line and A-line as well as B-line and A-line exciton transition energies in GaN as a function of the *c*-axis strain. *Symbols* are experimental data from [598]. Adapted from [365]

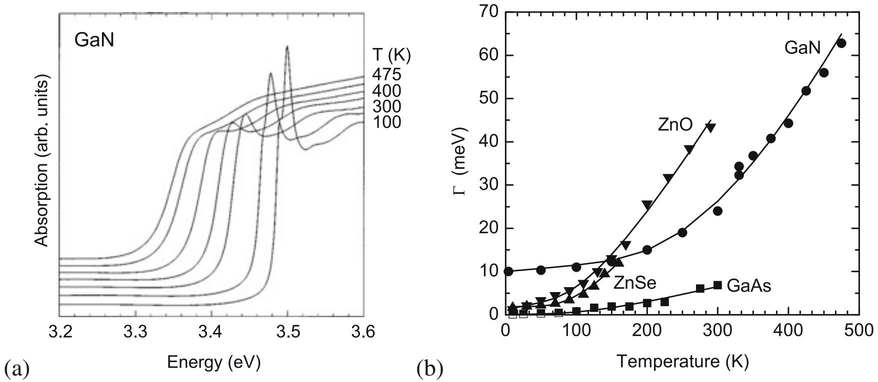

Fig. 9.20. (**a**) Absorption spectra of GaN bulk (0.38 µm thick epilayer on sapphire) for various temperatures $T = 100$, 200, 300, 350, 400, 450, and 475 K. Adapted from [594] (**b**) Homogeneous broadening as a function of temperature, *symbols* are experimental data, *solid lines* are fits, rf. Table 9.4

(four-wave mixing) as in [595]. In the latter, the decay constant of the dephasing T_2 is related to the decay constant τ of the FWM-signal by $T_2 = 2\tau$ for homogeneous broadening. The Fourier transform of $\exp -t/(2\tau)$ is a Lorentzian of the type $\propto ((E - E_0)^2 + \Gamma^2/4)^{-1}$ with $\Gamma = 1/\tau$ being the FWHM.

Table 9.4. Phonon broadening parameters (FWHM) of various bulk semiconductors. Values from fits with (9.33) to experimental data for GaAs [596], ZnSe [595], GaN [594], ZnO [597] (phonon energy fitted) as shown in Fig. 9.21b

Material	$\hbar\omega_{\mathrm{LO}}$ (meV)	Γ_0 (meV)	γ_{AC} (µeV/K)	γ_{LO} (meV)
GaAs	36.8	0	4 ± 2	16.8 ± 2
ZnSe	30.5	1.9	0 ± 7	84 ± 8
GaN	92	10	15 ± 4	408 ± 30
ZnO	33	1.2	32 ± 26	96 ± 24

transitions in polar semiconductors exhibit stronger coupling to optical phonons. The phonon coupling parameters from different measurements on GaN are discussed and compared in [593].

9.5.9 Exciton Polariton

Electrons and holes are particles with spin 1/2. Thus, the exciton can form states with total spin $S = 0$ (para-exciton, singlet) and $S = 1$ (ortho-exciton, triplet). The exchange interaction leads to a splitting of these states, the singlet being the energetically higher. The singlet state splits into the longitudinal and transverse exciton with respect to the orientation of the polarization carried by the Bloch functions and the center-of-mass motion $\mathbf{K}$ of the exciton. Dipole transitions are only possible for singlet excitons (bright excitons). The triplet excitons couple only weakly to the electromagnetic field and are thus also called dark excitons.

The coupling of these states to the electromagnetic field creates new quasiparticles, the exciton polaritons [599, 600]. The dielectric function of the exciton (with background dielectric constant ϵ_{b}) is

$$\epsilon(\omega) = \epsilon_{\mathrm{b}} \left[1 + \frac{\beta}{1 - (\omega^2/\omega_{\mathrm{X}})^2} \right] \cong \epsilon_{\mathrm{b}} \left[1 + \frac{\beta}{1 - (\omega^2/\omega_{\mathrm{T}})^2 + \hbar\, K^2/(M\, \omega_{\mathrm{T}})} \right] , \tag{9.34}$$

where β is the oscillator strength and the energy is $\hbar\omega_{\mathrm{X}} = \hbar\omega_{\mathrm{T}} + \hbar^2\, K^2/2M$. $\hbar\omega_{\mathrm{T}}$ is the energy of the transverse exciton at $K = 0$. With this dispersion the wave dispersion must be fulfilled, i.e.

$$c^2\, k^2 = \omega^2\, \epsilon(\omega) , \tag{9.35}$$

where k is the k vector of the light that needs to be $k = K$ due to momentum conservation. The dependence of the dielectric function on k is called *spatial dispersion* [601]. Generally, up to terms in k^2 it is written as

$$\epsilon(\omega) = \epsilon_{\mathrm{b}} \left[1 + \frac{\beta}{1 - (\omega^2/\omega_0)^2 + D\, k^2} \right] . \tag{9.36}$$

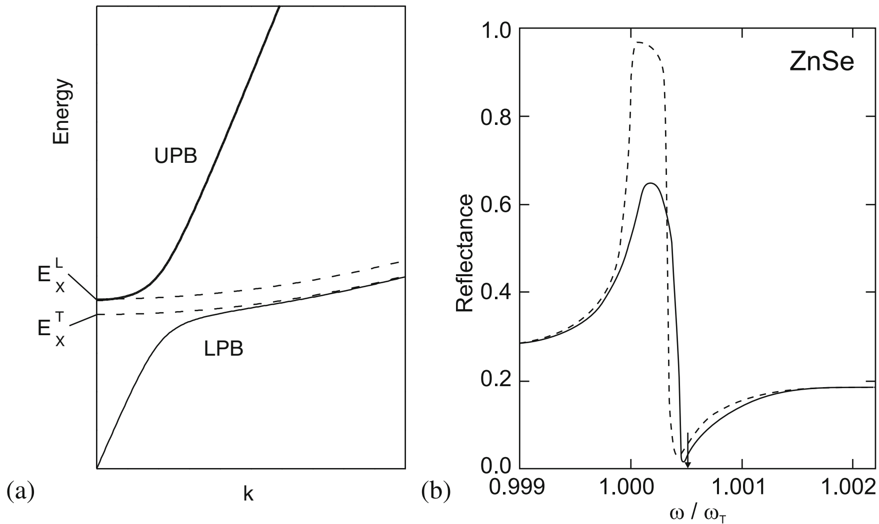

Fig. 9.21. (**a**) Schematic dispersion of exciton polaritons. The lower polariton branch ('LPB') is at small k photon-like, at large k exciton-like. The upper branch ('UPB') is exciton-like at small k and photon-like at larger k. The limit of the UPB for $k \to 0$ is the energy of the longitudinal exciton. The *dashed lines* represent the pure exciton dispersions. (**b**) Theoretical effect of spatial dispersion on the reflectance at the fundamental exciton resonance at normal incidence for ZnSe material parameters ($\hbar\omega_{\mathrm{T}}$ =2.8 eV, $\beta = 1.0 \times 10^{-3}$ and a background dielectric constant of $\epsilon_{\mathrm{b}} = 8.1$, damping was set to $\Gamma = 10^{-5}\omega_{\mathrm{T}}$). The arrow denotes the position of ω_{L}. The *solid* (*dashed*) *line* is with (without) spatial dispersion for $\hat{D} = 0.6 \times 10^{-5}$ ($\hat{D} = 0$). Data from [601]

The term k^2 with curvature D (for the exciton polariton $D = \hbar/(M\,\omega_{\mathrm{T}})$) plays a role in particular when $\omega_{\mathrm{T}}^2 - \omega^2 = 0$. For $\mathbf{k} \neq 0$ even a cubic material is anisotropic. The dimensionless curvature $\hat{D} = Dk'^2$ should fulfill $\hat{D} = \hbar/(Mc) \ll 1$ in order to make k^4 terms unimportant. For exciton polaritons[7] typically $\hat{D} = \hbar\omega_{\mathrm{T}}/(m\,c^2) \approx 2 \times 10^{-5}$ for $\hbar\omega_{\mathrm{T}} = 1\,\mathrm{eV}$ and $m^* = 0.1$.

From (9.35) together with (9.36) two solutions result:

$$2\omega^2 = c^2k^2 + (1 + \beta + Dk^2)\omega_0^2 \pm \left[-4c^2k^2(1 + Dk^2)\omega_0^2 + (c^2k^2 + (1 + \beta + Dk^2)\omega_0^2)^2\right]^{1/2} . \tag{9.37}$$

The two branches are shown schematically in Fig. 9.21a. Depending on the k value they have a photonic (linear dispersion) or excitonic (quadratic

[7]The dependence of the optical-phonon energies on k is typically too small to make spatial dispersion effects important. According to (5.19) $\hat{D} = -(a_0\omega_{\mathrm{TO}}/4c)^2 \approx 4 \times 10^{-11}$ for typical material parameters (lattice constant $a_0 = 0.5\,\mathrm{nm}$, TO phonon frequency $\omega_{\mathrm{TO}} = 15\,\mathrm{THz}$).

dispersion) character. The anticrossing behavior at $k' \approx \omega_\mathrm{T}/c$ (for $\hbar\omega_\mathrm{T} = 1\,\mathrm{eV}$ $k' \approx 0.5 \times 10^{-5}\,\mathrm{cm}^{-1}$) creates a bottleneck region in the lower polariton branch. This name stems from the small emission rate of acoustic phonons (i.e. cooling) in that region, as predicted in [602] and experimentally found, e.g. in CdS [603]. The polaritons decay into a photon when they hit the surface. The effect of the oscillator strength of the dispersion is shown in Fig. 9.22 for two-exciton resonance. In the case of several excitons (9.36) reads

$$\epsilon(\omega) = \epsilon_\mathrm{b} \left[1 + \sum_{i=1}^{n} \frac{\beta_i}{1 - (\omega^2/\omega_{0,i})^2 + D_i\, k^2} \right] . \tag{9.38}$$

For $k = 0$ either $\omega = 0$ (lower polariton branch) or $\epsilon(\omega_\mathrm{L}) = 0$. For the latter we find from (9.36)

$$\omega_\mathrm{L} = \sqrt{1+\beta}\,\omega_\mathrm{T} . \tag{9.39}$$

Therefore, the energy splitting ΔE_LT, mostly denoted as Δ_LT, between the L- and T-exciton energy given by

$$\Delta E_\mathrm{LT} = \hbar(\omega_\mathrm{L} - \omega_\mathrm{T}) = \left[\sqrt{1+\beta} - 1 \right] \hbar\omega_\mathrm{T} \approx \frac{1}{2}\,\beta\,\hbar\omega_\mathrm{T} \tag{9.40}$$

is proportional to the exciton oscillator strength (for experimental values see Table 9.5). We note that if (D.9) is used for the dielectric function, β in (9.40) needs to be replaced by $\beta/\epsilon_\mathrm{b}$.

The effect of spatial dispersion on the reflection at the fundamental exciton resonance is depicted in Fig. 9.21b. For non-normal incidence an additional feature due to the longitudinal wave is observed for p-polarization [601].

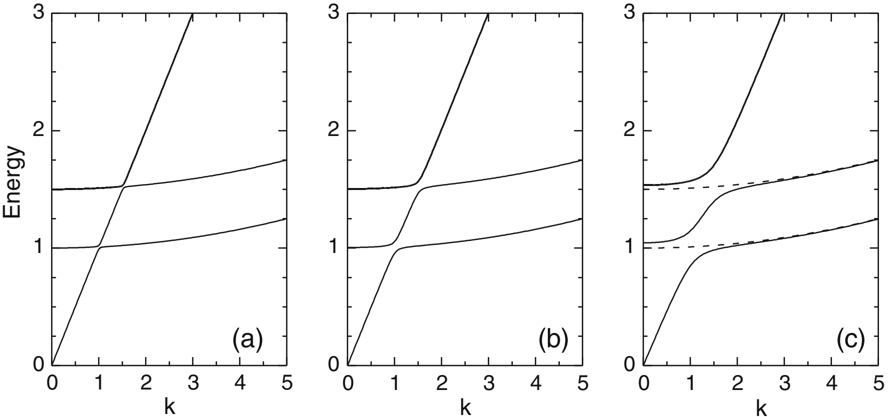

Fig. 9.22. Schematic polariton dispersion for a two-exciton resonance (curvature of exciton dispersion greatly exaggerated, $\hat{D} = 10^{-2}$) at $\omega_{\mathrm{T},1} = 1$ and $\omega_{\mathrm{T},2} = 1.5$ for three different oscillator strengths (**a**) $f = 10^{-3}$, (**b**) $f = 10^{-2}$, (**c**) $f = 10^{-1}$. The *dashed lines* in (**c**) represent the pure exciton dispersions

Table 9.5. Exciton energy (low temperature), LT splitting and exciton polariton oscillator strength for various semiconductors. Values for ZnO from [606], values for GaAs from [607], all other values from [608]

	CdS A	CdS B	ZnO A	ZnO B	ZnSe	GaN A	GaN B	GaAs
$\hbar\omega_{\mathrm{T}}$ (eV)	2.5528	2.5681	3.3776	3.3856	2.8019	3.4771	3.4816	1.5153
Δ_{LT} (meV)	2.2	1.4	1.45	5	1.45	1.06	0.94	0.08
β (10^{-3})	1.7	1.1	0.9	3.0	1.0	0.6	0.5	0.11

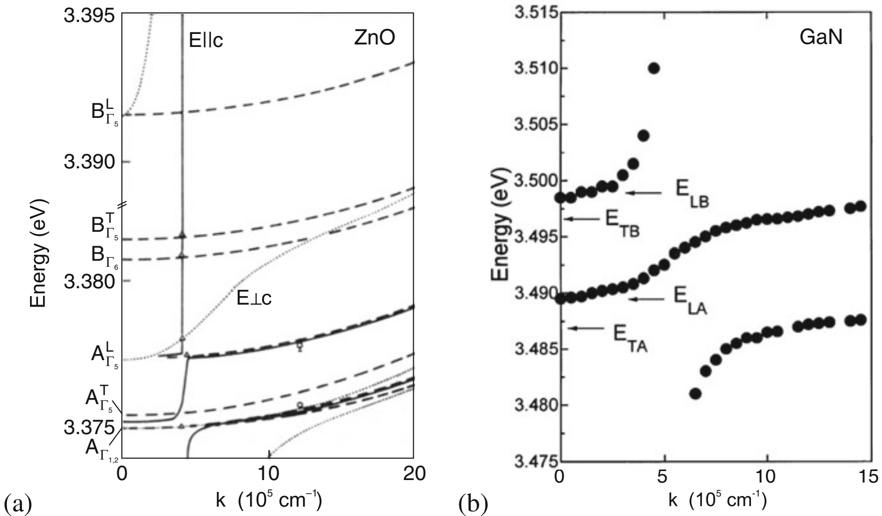

Fig. 9.23. (**a**) Exciton polariton dispersion ($\mathbf{k} \perp c$) of ZnO with experimental data ($T = 1.8$ K). *Solid* (*dotted*) *lines* are for polaritons with $\mathbf{E} \parallel c$ ($\mathbf{E} \perp c$). The *dashed lines* refer to excitons. Adapted from [609]. (**b**) Exciton polariton dispersion ($T = 2$ K) in GaN (on sapphire) for $\mathbf{E} \perp c$. Reprinted from [610], ©1998, with permission from Elsevier, originally in [611]

For a detailed discussion additional effects due to anisotropy in wurtzite crystals, an exciton free layer at the semiconductor surface, additional boundary conditions and damping need to be considered [604, 605]. The polariton dispersions of ZnO and GaN are shown in Fig. 9.23.

9.5.10 Bound-Exciton Absorption

Excitons can localize at impurities or inhomogeneities. Such excitons are called *bound excitons*. Here, the absorption due to such complexes is discussed. The recombination is discussed in Sect. 10.3.2. In GaP:N excitons are bound to isoelectronic N impurities (substituting P), resulting in the 'A'

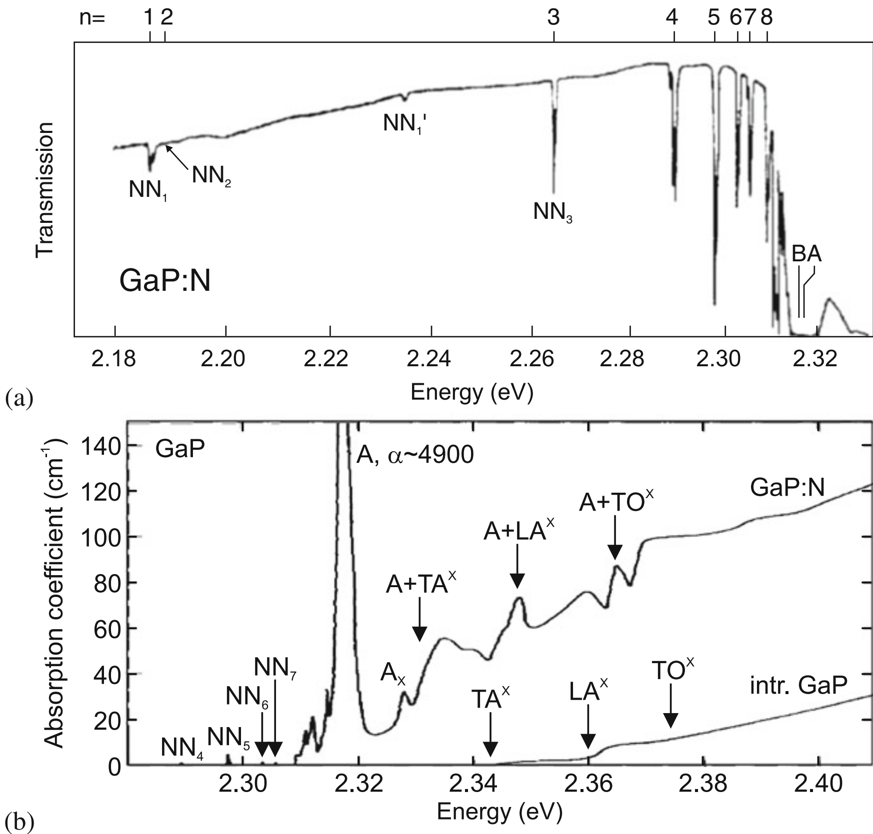

Fig. 9.24. (**a**) Transmission spectrum of GaP:N with a nitrogen concentration of about $10^{19}\,\mathrm{cm}^{-3}$ at 1.6 K (thickness: 1.1 mm). n is indicated for the first eight transitions due to excitons bound to nitrogen pairs. NN_n' indicate phonon replica. The 'A' line denotes the position of the transition due to excitons bound to a single nitrogen atom (observable for samples with low N doping). The 'B' line is forbidden and due to the $J = 2$ exciton. Adapted from [490]. (**b**) Absorption spectra of N-doped ($N_\mathrm{N} = 7 \times 10^{18}\,\mathrm{cm}^{-3}$) and intrinsic GaP ($T = 2\,\mathrm{K}$). Adapted from [484]

line at 2.3171 eV (at $T = 4.2\,\mathrm{K}$). The absorption due to A excitons is well resolved in the spectrum of Fig. 9.24b. At sufficiently high nitrogen doping, there exist nitrogen pairs, i.e. a complex where a nitrogen impurity has a second nitrogen impurity in the vicinity. The pairs are labeled NN_n. It was believed that the second nitrogen atom is in the n-th shell around the first one. However, the proper level assignment is probably different in the view of modern theory [369]. Also clusters with more than two nitrogen atoms may exist. NN_1 is a prominent level and relates to a N–Ga–N complex having 12 equivalent sites for the second N atom on the next neighbor anion site. The

Table 9.6. Index of nitrogen pairs NN_n and energy separation ΔE of bound-exciton transitions from the free-exciton line for $n = 1 \ldots 10$ and the 'A' line

n	1	2	3	4	5	6	7	8	9	10	∞ (A)
ΔE (meV)	143	138	64	39	31	25	22	20	18	17	11

transitions due to excitons bound to NN_n, as shown in Fig. 9.24a, give a series of lines (see Table 9.6) that fulfill $\lim_{n \to \infty} NN_n = A$. Although GaP has an indirect band structure, the absorption coefficient of N-related transitions is large, about $10^5\,cm^{-1}$ for a nitrogen doping level of $10^{19}\,cm^{-3}$.[8] This is due to the fact that the electron spatially localized at the nitrogen isoelectronic trap (Sect. 7.7.9) has a sizeable $k = 0$-component of its wave-function (Fig. 7.36), leading to a large transition probability with Γ-point holes with an oscillator strength of 0.09 [612].

9.5.11 Biexcitons

Similar to two hydrogen atoms forming a hydrogen molecule, two excitons can also form a bound complex, the biexciton involving two electrons and two holes. The biexciton binding energy is defined as

$$E_{XX}^{b} = 2\,E_X - E_{XX}\ . \tag{9.41}$$

Biexcitons are binding in bulk material. Accordingly, the biexciton recombination or absorption occurs at lower energy than that of the exciton. Values of the biexciton binding energy are listed in Table 9.3 for various semiconductors. The ratio of biexciton and exciton binding energies is fairly constant about 0.2. In semiconductors with small exciton binding energy, such as GaAs, biexcitons are hard to observe in bulk material but show up in heterostructures that provide additional carrier confinement (see also Sect. 13.3.4). While the exciton density increases linearly with external excitation, the density of biexcitons increases quadratically.

9.5.12 Trions

The complexes 'eeh' and 'ehh' are called trions. Also, the notation X^- and X^+ is common. X^- is typically stable in bulk material but hard to observe. In quantum wells or dots, trions are easier to observe. In quantum dots excitons with higher charge, e.g. X^{2-}, have also been observed (see Fig. 13.34).

[8] Also the recombination (Sect. 10.3.2) is efficient and allows green GaP:N and yellow GaAsP:N light emitting diodes.

9.5.13 Burstein–Moss Shift

In the discussion so far it has been assumed that all target states in the conduction band are empty. In the presence of free carriers the absorption is modified by the

- change of the distribution function
- many-body effects (band gap renormalization)

The latter is discussed in the next section. For a degenerate electron distribution all states close to the conduction-band edge are populated. Thus a transition from the valence band cannot take place into such states. This shift of the absorption edge to higher energies is called the Burstein–Moss shift [613, 614].

k-conserving optical transitions between parabolic hole and electron bands have the dependence

$$E = E_{\mathrm{g}} + \frac{\hbar^2 k^2}{2m_{\mathrm{e}}^*} + \frac{\hbar^2 k^2}{2m_{\mathrm{h}}^*} = E_{\mathrm{g}} + \frac{\hbar^2 k^2}{2m_{\mathrm{r}}} \; , \tag{9.42}$$

where m_{r} is the reduced mass of electron and hole. About $4kT$ below the Fermi level all levels in the conduction band are populated (Fig. 9.25). Thus the k value at which the absorption starts is given as

$$\hat{k} = \sqrt{\frac{2m_{\mathrm{r}}}{\hbar^2} \left(E_{\mathrm{F}} - E - 4kT\right)} \; . \tag{9.43}$$

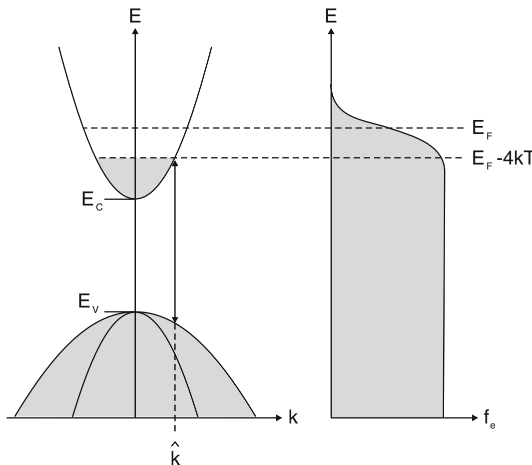

Fig. 9.25. Principle of Burstein–Moss shift. *Left panel*: Schematic band structure with completely filled electron states shown in *grey*. The k-vector for the lowest photon energy optical absorption process is indicated as $\hat{k}$. *Right panel*: Electron distribution function for a degenerate electron gas with Fermi level in the conduction band

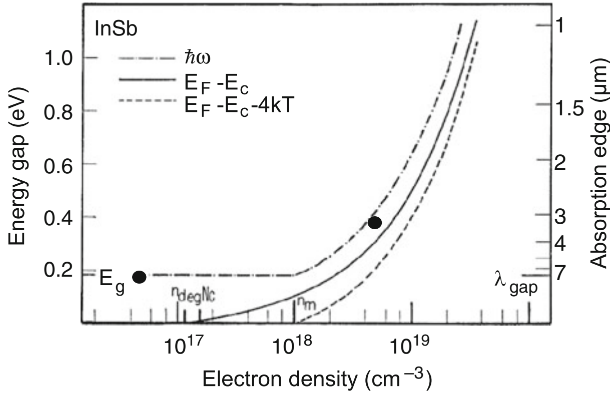

Fig. 9.26. Burstein–Moss effect at InSb ($E_\mathrm{g} = 0.18\,\mathrm{eV}$) at room temperature. Theoretical dependence and data points for intrinsic InSb and $5 \times 10^{18}\,\mathrm{cm}^{-3}$ n-type. Data from [613]

Besides the energy shift in the conduction band, the corresponding energy shift in the valence band $\hbar k^2/(2m_\mathrm{h})$ must be considered. Thus, the Burstein–Moss shift of the absorption edge is

$$\Delta E = \hbar\omega - E_\mathrm{g} = (E_\mathrm{F} - 4kT - E_\mathrm{C}) \left(1 + \frac{m_\mathrm{e}}{m_\mathrm{h}}\right) . \tag{9.44}$$

The relation between n and the Fermi level is given by (7.8). If $E_\mathrm{F} - E_\mathrm{C} \gg kT$ the Fermi integral can be approximated by $\frac{2}{\sqrt{\pi}} \left(\frac{E_\mathrm{F}-E_\mathrm{C}}{kT}\right)^{3/2}$. Using (7.10) for N_C, the Burstein–Moss shift can be written for this case as

$$\Delta E = n^{2/3} \frac{h^2}{8m_\mathrm{e}} \left(\frac{3}{\pi}\right)^{2/3} \left(1 + \frac{m_\mathrm{e}}{m_\mathrm{h}}\right) \approx 0.97 \frac{h^2}{8m_\mathrm{r}} n^{2/3} . \tag{9.45}$$

Originally, the Burstein–Moss shift was evoked to explain the absorption shift in InSb with varying carrier concentration (Fig. 9.26).

9.5.14 Band Gap Renormalization

The band structure theory has been developed so far for small carrier densities. If the carrier density is large the interaction of free carriers has to be considered. The first step was exciton formation. However, at high temperatures (ionization) and at large carrier density (screening) the exciton is not stable. Exchange and correlation energy leads to a decrease of the optical absorption edge that is called *band gap renormalization* (BGR).

An effect due to significant carrier density is to be expected when the density is of the order of the exciton volume, i.e. $n \sim a_\mathrm{B}^{-3}$. For $a_\mathrm{B} \sim 15\,\mathrm{nm}$ (GaAs) this means $n \sim 3 \times 10^{17}\mathrm{cm}^{-3}$. The dimensionless radius r_s is defined via

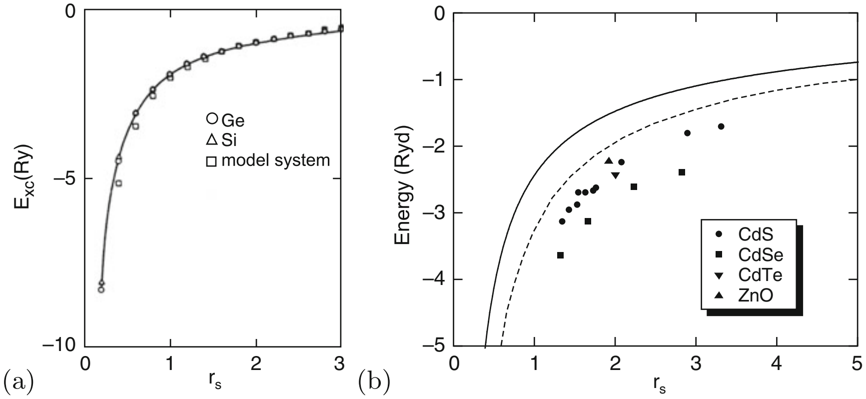

Fig. 9.27. (**a**) Theoretical exchange and correlation energies in units of the exciton Rydberg energy as a function of the dimensionless variable r_s for Ge, Si and a model system (with one isotropic conduction and valence band each). The *solid line* is a fit according to (9.47). Adapted from [615]. (**b**) Band gap renormalization in terms of the excitonic Rydberg for various II–VI semiconductors. *Solid line* is the relation according to (9.47), *dashed line* is the dependence predicted in [619] for $T = 30$ K. Data are compiled in [620]

$$\frac{4\pi}{3}\, r_s^3 = \frac{1}{n\, a_B^3} \,. \tag{9.46}$$

The sum of exchange and correlation energies E_{xc} is found to be mostly independent of material parameters [615] (Fig. 9.27a) and follows the form

$$E_{xc} = \frac{a + b\, r_s}{c + d\, r_s + r_s^2} \,, \tag{9.47}$$

with $a = -4.8316$, $b = -5.0879$, $c = 0.0152$ and $d = 3.0426$. Thus the density dependence of the band gap at small carrier density is $\propto n^{1/3}$. Experimental data for a number of II–VI semiconductors roughly follow such a dependence (Fig. 9.27b).

In Fig. 9.28, a theoretical calculation of the absorption spectrum of bulk GaAs for various carrier densities (n=p) [616] is shown. With increasing density, the excitonic resonance broadens and vanishes. The shape approaches the electron–hole plasma shape. The absorption edge shifts to smaller energies. At high carrier density, the absorption becomes negative in a spectral range before absorption sets in. In this spectral region, the material exhibits gain and an incoming light wave is amplified (cmp. Sect. 10.2.6).

9.5.15 Electron–Hole Droplets

At low temperature and high density, electron–hole pairs in Ge and Si can undergo a phase transition into a liquid state. This electron–hole liquid (EHL)

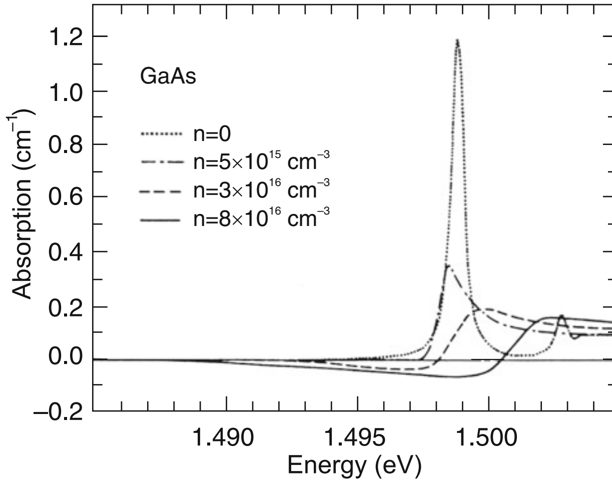

Fig. 9.28. Absorption of GaAs (low temperature, $T = 10\,\mathrm{K}$) as a function of the electron–hole density n (theory). Adapted from [616]

was suggested in [617] and is a Fermi liquid exhibiting the high conductivity of a metal and the surface and density of a liquid. The condensation is due to exchange interaction and correlation. The formation is fostered by the band structure of Ge [618] and the long lifetime of carriers in the indirect band structure. In unstressed Ge typically a cloud of electron–hole droplets with diameter in the µm range exists. The phase diagram is shown in Fig. 9.29a. In suitably stressed Ge electron–hole droplets with several hundred µm diameter form around the point of maximum shear strain in inhomogeneously strained crystals, as shown in Fig. 9.29b. The pair density in such a liquid is of the order of $10^{17}\,\mathrm{cm}^{-3}$.

We note that the metallic EHL state hinders observation of the Bose–Einstein condensation (BEC) of (bosonic) excitons. The light-exciton mass offers a high condensation temperature in the 1 K range (compared to the mK range for atoms). Recent experiments with spatially indirect excitons in coupled quantum wells lead towards BEC [624, 625]. A sufficiently long lifetime ensures cooling of the excitons close to the lattice temperature. Another potential candidate for BEC are long-living excitons (ms-range) in Cu_2O [626]. The condensation of polaritons (cf. Sect. 9.5.9) in microcavities to well-defined regions of **k**-space has been discussed in [627] and compared to bosonic condensation in bulk.

9.5.16 Two-Photon Absorption

So far, only absorption processes that involve one photon have been considered. The attenuation of the intensity I of a light beam (of frequency ω_0) along the z direction can be written as

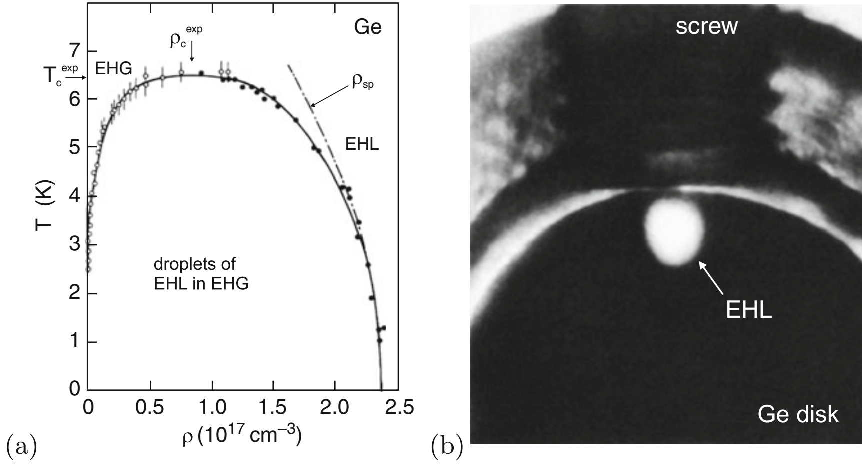

Fig. 9.29. (**a**) Temperature–density phase diagram of electrons and holes in Ge. The regions of electron–hole gas (EHG) and liquid (EHL) and the droplet phase are labeled. *Solid line* is theoretical calculation, *symbols* are experimental data from [621]. The *dash-dotted line* denoted $\rho_{\rm sp}$ is the experimentally obtained temperature dependence of the liquid density due to single-particle excitations. $\rho_{\rm c}^{\rm exp}$ and $T_{\rm c}^{\rm exp}$ denote the experimental critical density and temperature, respectively. Adapted from [622]. (**b**) Photographic image of radiative recombination (at 1.75 µm wavelength) from a 300-µm diameter droplet of electron–hole liquid (EHL) in a stressed (001) Ge disk (diameter 4 mm, thickness 1.8 mm) at $T = 2$ K. The stress is applied from the top by a nylon screw along a ⟨110⟩ direction. Adapted from [623], reprinted with permission, ©1977 APS

$$\frac{\mathrm{d}I}{\mathrm{d}z} = -\alpha\, I - \beta\, I^2 \,, \tag{9.48}$$

where α is due to the (linear) absorption coefficient (and possibly scattering) and β is the two-photon absorption coefficient. A two-photon process can occur in two steps, e.g. via a midgap level, which is not considered any further here. Here, we consider two-photon absorption (TPA) via the population of a state at $2\hbar\omega_0$ higher energy than the initial state with a nonlinear optical process. The TPA coefficient is related to the nonlinear third-order electric dipole susceptibility tensor [629] χ_{ijkl}. Within the two-band approximation theory predicts [630]

$$\beta \propto (2\hbar\omega_0 - E_{\rm g})^{3/2} \ . \tag{9.49}$$

The exponent 3/2 is indeed found experimentally, as shown in Fig. 9.30 for GaAs. The strength of absorption depends on the relative orientation of the light polarization with respect to the main crystallographic directions, e.g. TPA for polarization along ⟨110⟩ is about 20% larger than for the ⟨100⟩ orientation.

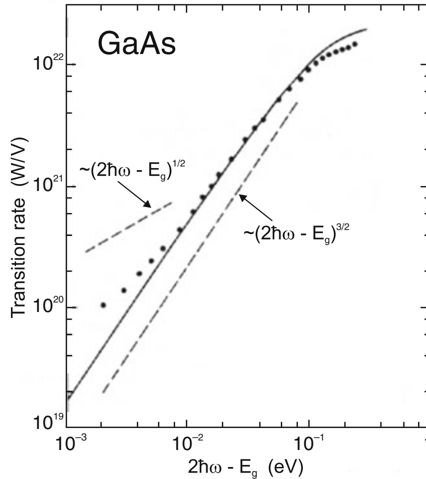

Fig. 9.30. Experimental (*dots*) two-photon absorption of GaAs ($T = 4\,\mathrm{K}$) as a function of the difference of the double-photon energy $2\hbar\omega$ from the GaAs band edge E_g. The *solid line* is a theoretical calculation, the *dashed lines* represent slopes with exponent 1/2 and 3/2, respectively. Adapted from [628]

9.6 Impurity Absorption

Charge carriers bound to shallow impurities exhibit a hydrogen-like term scheme

$$E_n = \frac{m^*}{m_0} \frac{1}{\epsilon_\mathrm{r}^2} \frac{1}{n^2} \times 13.6\,\mathrm{eV} \ , \tag{9.50}$$

with the ionization limit E_∞ being the conduction (valence) band edge for donors (acceptors), respectively. They can be excited by light to the nearest band edge. Such absorption is typically in the FIR region and can be used for photodetectors in this wavelength regime. The optical absorption cross section of impurity absorption can be related to the carrier capture cross section [395, 396].

The actual transition energies can deviate from (9.50) due to deviation of the potential close to the impurity from the pure Coulomb potential. Such an effect is known as the chemical shift or central cell correction (cf. Sect. 7.5.5) and is characteristic of the particular impurity. In GaAs such shifts are small ($\sim 100\,\mu\mathrm{eV}$) [632].

The term scheme for P in Si is shown in Fig. 9.31a. The ground state (1s) is split because of a reduction of the tetrahedral symmetry due to intervalley coupling. The anisotropic mass at the X-valley in Si causes the p states (and states with higher orbital momentum) to split into p_0 and $\mathrm{p}_\pm$ states. Such an effect is absent in a direct semiconductor with an isotropic conduction-band minimum such as GaAs (Fig. 9.32). Optical transitions between the

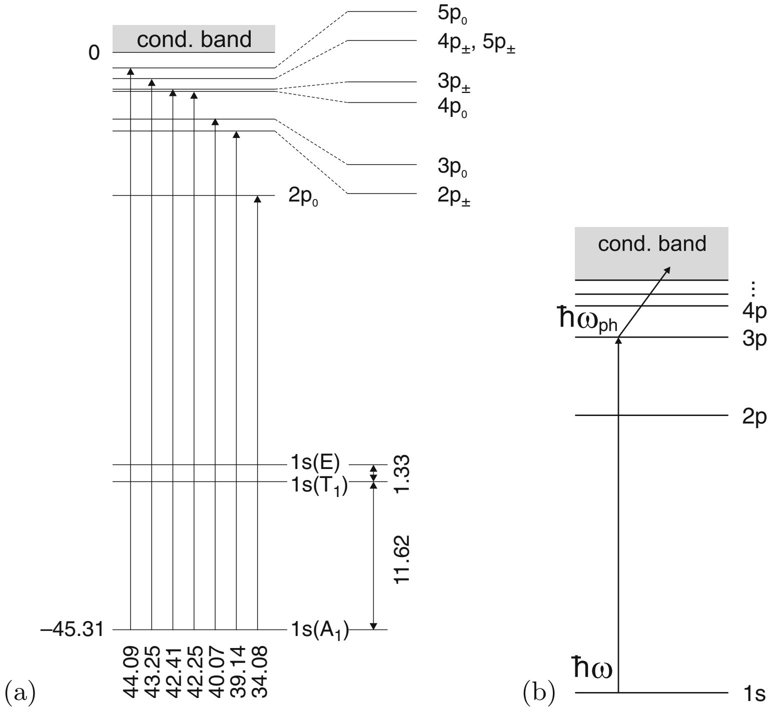

Fig. 9.31. (**a**) Term scheme of phosphorus donor in silicon, all energies in meV. After [631]. (**b**) Schematic sequence for photothermal ionization, here absorption of a photon with $\hbar\omega = E_{3\mathrm{p}} - E_{1\mathrm{s}}$ and subsequent absorption of a phonon with energy $\hbar\omega_{\mathrm{ph}} \geq E_{\infty} - E_{3\mathrm{p}}$

1s and various p states can be directly observed in absorption, e.g. for Si:P in [634]. These transitions are also observed in photoconductivity because the missing energy to the ionization into the continuum is supplied by a phonon at finite temperature (photothermal ionization) (Fig. 9.31b) [631]. The splitting of the 2p transition in Fig. 9.32a is the chemical shift due to different donors incorporated in the GaAs (Si, Sn, and Pb). Peak broadening is mostly due to Stark broadening due to neighboring charged impurities. The application of a magnetic field induces Zeeman-like splittings and increases the sharpness of the peaks. The peak width can be further increased by illuminating the sample with light having a higher energy than the band gap. The additional charge carriers neutralize charged impurities and allow higher resolution (Fig. 9.32b).

In Fig. 9.33 absorption spectra of highly doped n-type GaAs are shown. For doping concentrations larger than the critical concentration of $\sim 1 \times 10^{16}\,\mathrm{cm}^{-3}$ (cf. Table 7.6) significant broadening is observed due to the formation of an impurity band.

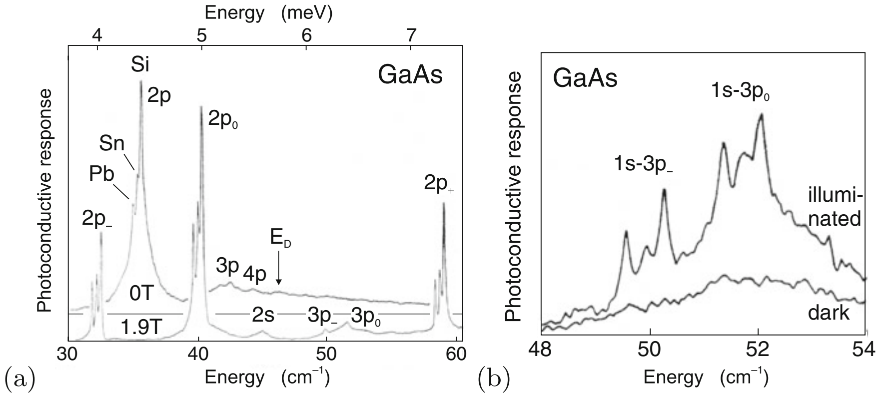

Fig. 9.32. (**a**) Far-infrared photoconductivity response (Lyman-type s→p series) of not intentionally doped GaAs with residual donors Pb, Sn, and Si, $N_A = 2.6 \times 10^{13}\,\mathrm{cm}^{-3}$, $N_D - N_A = 8 \times 10^{12}\,\mathrm{cm}^{-3}$. The *upper* (*lower*) curve is for a magnetic field of 0 (1.9) T. Measurement temperature is 4.2 K. (**b**) Photoconductive response of a (different) GaAs sample with the same impurities ($N_D = 1 \times 10^{13}\,\mathrm{cm}^{-3}$) with (*upper curve*) and without (*lower curve*) illumination with above-bandgap light ($B = 1.9\,\mathrm{T}$, $T = 4.2\,\mathrm{K}$). Adapted from [633]

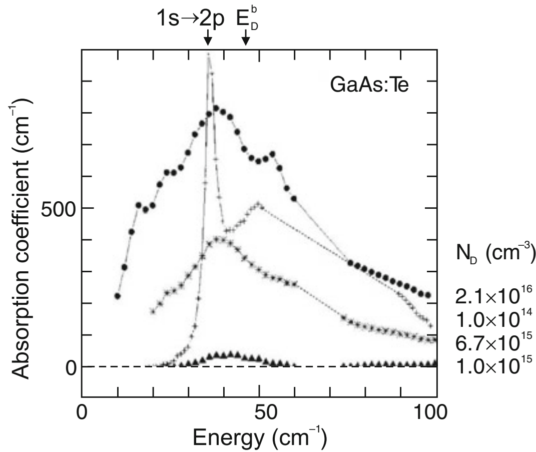

Fig. 9.33. Low-temperature ($T = 1.35\,\mathrm{K}$) absorption spectra of highly doped n-type GaAs:Te with doping concentrations as labeled (*circles*: $N_D = 2.1 \times 10^{16}\,\mathrm{cm}^{-3}$, *stars*: 6.7×10^{14}, *triangles*: 1.0×10^{15}). A sharp photoconductivity spectrum (in arbitrary units) from low-doped GaAs:Te (*crosses*, $N_D = 1.0 \times 10^{14}\,\mathrm{cm}^{-3}$) is shown for comparison (cf. Fig. 9.32a). The energy of the 1s→2p transition and the donor binding energy (onset of continuum absorption) are indicated. Adapted from [636]

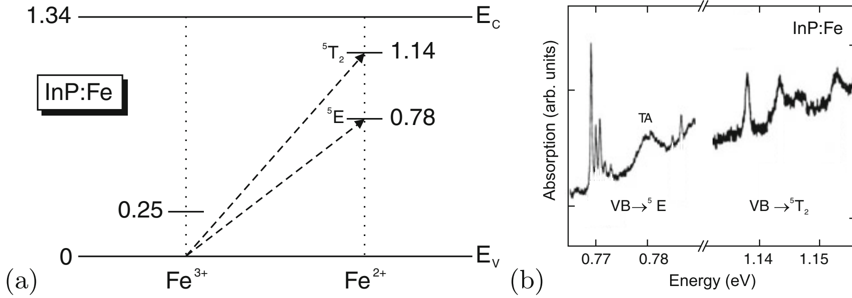

Fig. 9.34. (**a**) Schematic band diagram of InP with levels of Fe impurities in the 3+ and 2+ charge states at low temperature. All energies are given in eV. The *arrows* denote the optical transition of a valence-band electron to the Fe center, $\mathrm{Fe}^{3+} + \hbar\omega \rightarrow \mathrm{Fe}^{2+} + h$. (**b**) Calorimetric absorption spectra (at $T = 1.3\,\mathrm{K}$) of InP:Fe, $[\mathrm{Fe}]=5 \times 10^{16}\,\mathrm{cm}^{-3}$. Part (**b**) adapted from [476]

The absorption of deep levels is typically in the infrared. In Fig. 9.34a the possible optical absorption processes involving the Fe levels in InP (cf. Sect 7.7.8) during the charge transfer $\mathrm{Fe}^{3+} \rightarrow \mathrm{Fe}^{2+}$ are shown. These transitions and their fine structure (Fig. 9.34b) have been observed in calorimetric absorption spectroscopy (CAS) experiments [476].

In Fig. 9.35 the photoconductivity of Si:Mg is shown. The sharp peaks are due to transitions of interstitial, singly ionized Mg, Mg_i^+ [635]. Mg in Si is a double donor [449] (see Sect. 7.7.2). Above the ionization limit of about 256 meV, the peaks are replicated, shifted by the LO phonon energy of 59.1 meV. However, now they rather appear as dips. This behavior is typical for a discrete state interacting with a continuum, also called Fano resonance [637, 638] with its characteristic lineshape, going *below* the continuum level.

9.7 Free-Carrier Absorption

A time-dependent electric field accelerates the charge carriers. The excess energy is subsequently transferred to the lattice via scattering with phonons. A review of the effect of free carriers on optical properties can be found in [639]. In the relaxation-time approximation energy is relaxed with a time constant τ. Thus energy is absorbed from the electromagnetic wave and dissipated.

The complex conductivity (8.48) is given by

$$\sigma^* = \sigma_\mathrm{r} + \mathrm{i}\sigma_\mathrm{i} = \frac{ne^2\tau}{m^*}\left(\frac{1}{1+\omega^2\tau^2} + \mathrm{i}\frac{\omega\tau}{1+\omega^2\tau^2}\right) . \tag{9.51}$$

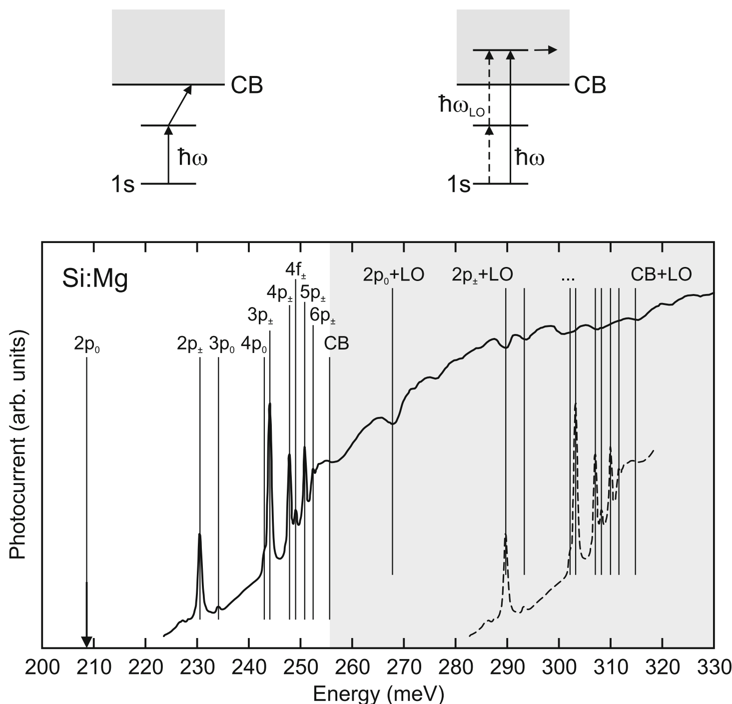

Fig. 9.35. Photocurrent spectrum of Si:Mg. Transitions are due to Mg_i^+ from its 1s state to excited states as labeled and indicated by *vertical lines*. CB denotes the conduction band edge (ionization limit). Above the CB edge (*shaded area*) phonon-assisted absorption occurs (Fano resonances). For comparison the absorption spectrum below CB is shown shifted by the phonon energy (*dashed line*). Above the plot, the transition mechanisms (photothermal ionization and Fano resonance) are schematically shown. Adapted from [635]

We note that a static magnetic field introduces birefringence as discussed in more detail in Sect. 12.2.1. The wave equation for the electric field is

$$\nabla^2 \mathbf{E} = \epsilon \mu_0 \ddot{\mathbf{E}} + \sigma \mu_0 \dot{\mathbf{E}} \ . \tag{9.52}$$

For a plane wave $\propto \exp\left[\mathrm{i}(\mathbf{kr} - \omega t)\right]$ the wavevector obeys

$$k = \frac{\omega}{c} \sqrt{\epsilon_\mathrm{r} + \mathrm{i} \frac{\sigma^*}{\epsilon_0 \omega}} \ , \tag{9.53}$$

where $c = (\epsilon_0 \mu_0)^{-1/2}$ is the velocity of light in vacuum, ϵ_r is the background dielectric constant (for large ω).

The part $\boldsymbol{\epsilon}_\mathrm{FC}$ of the dielectric tensor due to free carriers is

$$\boldsymbol{\epsilon}_\mathrm{FC} = \frac{\mathrm{i}}{\epsilon_0 \omega} \boldsymbol{\sigma}^* \ . \tag{9.54}$$

The complex index of refraction is

$$n^* = n_{\mathrm{r}} + \mathrm{i}\kappa = \sqrt{\epsilon_{\mathrm{r}} + \mathrm{i}\frac{\sigma^*}{\epsilon_0 \omega}} \,. \tag{9.55}$$

Taking the square of this equation yields

$$n_{\mathrm{r}}^2 - \kappa^2 = \epsilon_{\mathrm{r}} + \mathrm{i}\,\frac{\sigma_{\mathrm{i}}}{\epsilon_0 \omega} = \epsilon_{\mathrm{r}} - \frac{ne^2}{\epsilon_0 m^*}\,\frac{\tau^2}{1+\omega^2\tau^2} \tag{9.56a}$$

$$2n_{\mathrm{r}}\,\kappa = \frac{\sigma_{\mathrm{r}}}{\epsilon_0 \omega} = \frac{ne^2}{\epsilon_0 \omega m^*}\,\frac{\tau}{1+\omega^2\tau^2} \,. \tag{9.56b}$$

The absorption coefficient is related to κ by (9.10). For the case of higher frequencies, i.e. $\omega\tau \gg 1$, the absorption is

$$\alpha = \frac{n\,e^2}{\epsilon_0 c n_{\mathrm{r}} m^* \tau}\,\frac{1}{\omega^2} \,. \tag{9.57}$$

The absorption decreases with increasing frequency. For semiconductors it is particularly important in the mid- and far-infrared regions when carriers are present due to doping or thermal excitation. In Fig. 9.36a absorption spectra of n-type Ge for various doping concentrations are shown. The absorption coefficient in the transparency regime varies proportionally to $\lambda^2 \propto \omega^{-2}$ as predicted in (9.57). A more detailed discussion of the energy dependence of free carrier absorption can be found in [640]. In Fig. 9.36b the absorption coefficient due to free carrier absorption at fixed wavelength is shown as a function of dopant concentration.[9] The slope is slightly overlinear, indicating a weak dependence $\tau(n)$.

The index of refraction is given by (also for $\omega\tau \gg 1$)

$$n_{\mathrm{r}}^2 = \epsilon_{\mathrm{r}} - \frac{ne^2}{\epsilon_0 m^* \omega^2} + \kappa^2 = \epsilon_{\mathrm{r}}\left[1 - \left(\frac{\omega_{\mathrm{p}}}{\omega}\right)^2\right] + \frac{\epsilon_{\mathrm{r}}^2}{4n_{\mathrm{r}}^2}\left(\frac{\omega_{\mathrm{p}}}{\omega}\right)^4 \frac{1}{\omega^2\tau^2} \tag{9.58}$$

$$\approx \epsilon_{\mathrm{r}}\left[1 - \left(\frac{\omega_{\mathrm{p}}}{\omega}\right)^2\right] \,,$$

where

$$\omega_{\mathrm{p}} = \sqrt{\frac{ne^2}{\epsilon_{\mathrm{r}}\epsilon_0 m^*}} \tag{9.59}$$

is the plasma frequency. The approximation is valid for small absorption and when $(\omega\tau)^{-2}$ can be neglected. A graphical representation is given in Fig. 9.37a. For coupling to electromagnetic waves (still $\omega\tau \gg 1$)

[9] Even at low temperature, $n \approx N_{\mathrm{D}}$ since $N_{\mathrm{D}} \gg N_{\mathrm{c}}$ (cf. [421] and Sect. 7.5.6).

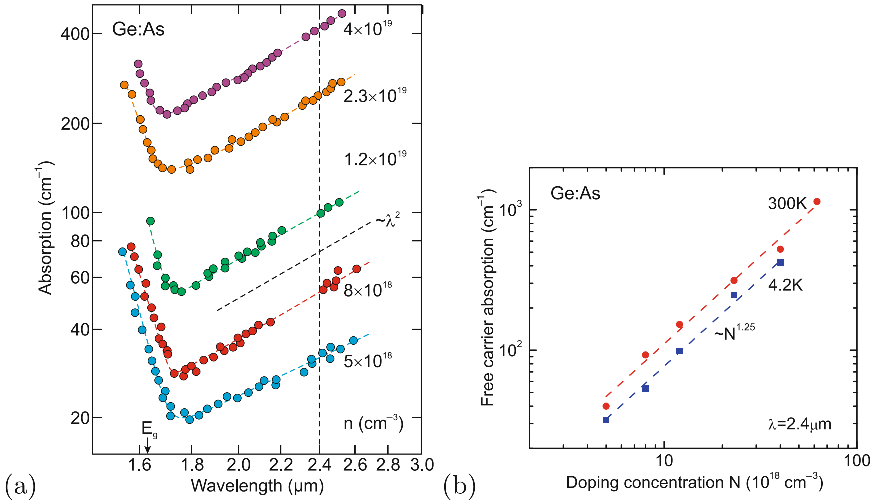

Fig. 9.36. (**a**) Optical absorption spectra (at $T = 4.2\,\mathrm{K}$) of n-type Ge for various As dopant concentrations as labeled. The *arrow* denotes the band edge of undoped Ge, the *vertical dashed line* the energy for which the free carrier absorption is measured in part (**b**). The inclined *dashed line* visualizes the slope $\propto \lambda^2$. *Curved dashed lines* are guides to the eye. Adapted from [577]. (**b**) Free carrier absorption at $\lambda = 2.4\,\mu\mathrm{m}$ as determined from part (**a**) of the figure (*blue squares*) as a function of As dopant concentration. Additionally data at 300 K (*red circles*) from the same samples are included [577]. The *dashed lines* visualizes the slope $\propto N_{\mathrm{D}}^{1.25}$

$$\epsilon(\omega) = \epsilon_{\mathrm{r}} \left[1 - \left(\frac{\omega_{\mathrm{p}}}{\omega} \right)^2 \right] = \frac{c^2\,k^2}{\omega^2} \tag{9.60}$$

must be fulfilled. It follows that the dispersion relation in the presence of free carriers (Fig. 9.37b) is

$$\omega^2 = \omega_{\mathrm{p}}^2 + \frac{c^2\,k^2}{\epsilon_{\mathrm{r}}^2}\ . \tag{9.61}$$

For $\omega > \omega_{\mathrm{p}}$, $\epsilon > 0$, thus waves can propagate. For $\omega < \omega_{\mathrm{p}}$, however, the dielectric constant is negative, i.e. $\epsilon < 0$. For such frequencies waves are exponentially damped and cannot propagate or penetrate a layer. This effect can be used in a plasmon waveguide. The expected dependence of the plasmon wavelength on the carrier density $\lambda_{\mathrm{p}} = 2\pi c/\omega_{\mathrm{p}} \propto n^{-1/2}$ is depicted in Fig. 9.38 for GaAs. For semiconductors the plasmon frequency is in the mid-or far-infrared spectral region.[10]

[10]The much higher free-electron density in metals shifts the plasma frequency to the UV, explaining the reflectivity of metals in the visible and their UV transparency.

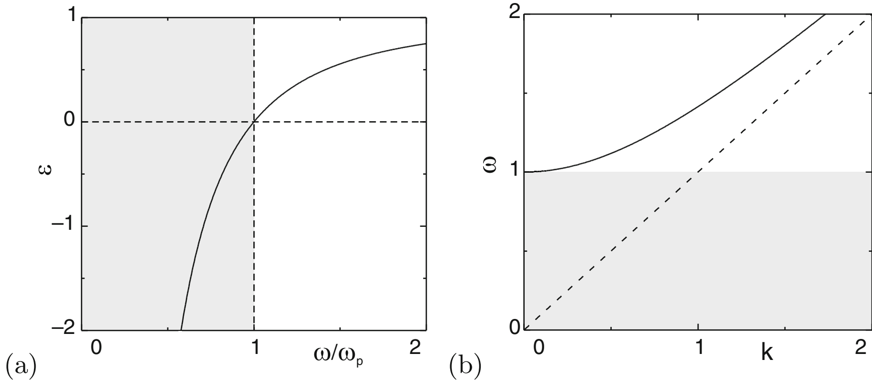

Fig. 9.37. (**a**) Dielectric constant for plasmon oscillations. *Shaded area* represents region of attenuation (negative ϵ). (**b**) Dispersion relation (k in units of ω_p/c, ω in units of ω_p) in the presence of free carriers (9.61, for $\epsilon_\mathrm{r} = 1$). *Shaded area* represents forbidden frequency range for propagating solutions. *Dashed line* is photon dispersion $\omega = ck$

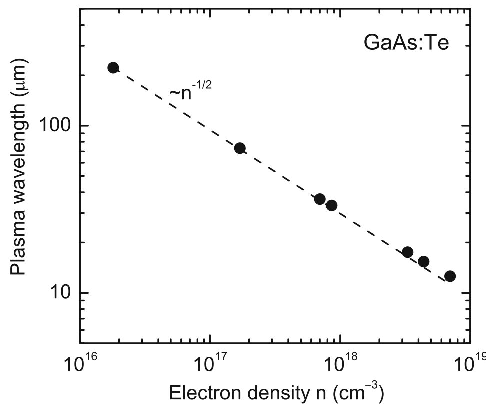

Fig. 9.38. Plasma wavelength λ_p for n-type GaAs with various electron concentrations due to different doping levels. *Filled circles*: experimental values, *dashed line*: $n^{-1/2}$ dependence; the deviation is due to nonparabolicity of the electron mass (cf. Fig. 9.42b). Data from [641]

9.8 Lattice Absorption

While there is no interaction of optical phonons and (infrared) light in Si and Ge due to crystal structure symmetry [642], strong effects are present for compound semiconductors. A review can be found in [643].

9.8.1 Dielectric Constant

The dielectric constant (with damping parameter $\varGamma$) in the vicinity of the optical phonon energies is given by (cf. (5.49))

$$\epsilon(\omega) = \epsilon(\infty) \left(\frac{\omega_{\mathrm{LO}}^2 - \omega^2 - \mathrm{i}\omega\varGamma}{\omega_{\mathrm{TO}}^2 - \omega^2 - \mathrm{i}\omega\varGamma} \right) . \tag{9.62}$$

The dispersion relation (without damping) can be written as

$$\epsilon(\omega) = \epsilon(\infty) + \frac{\epsilon(0) - \epsilon(\infty)}{1 - (\omega/\omega_{\mathrm{LO}})^2} = \epsilon(\infty) \left[1 + \frac{f}{1 - (\omega/\omega_{\mathrm{LO}})^2} \right] . \tag{9.63}$$

Thus the oscillator strength (compare with (D.10)) is $f = \frac{\epsilon(0)-\epsilon(\infty)}{\epsilon(\infty)}$. With the LST relation (5.48) the oscillator strength is

$$f = \frac{\omega_{\mathrm{LO}}^2 - \omega_{\mathrm{TO}}^2}{\omega_{\mathrm{TO}}^2} \approx 2 \frac{\omega_{\mathrm{LO}} - \omega_{\mathrm{TO}}}{\omega_{\mathrm{TO}}} , \tag{9.64}$$

and thus proportional to the splitting $\varDelta_{\mathrm{LT}} = \omega_{\mathrm{LO}} - \omega_{\mathrm{TO}}$ between the longitudinal and transverse optical phonon frequency. The approximation in (9.64) is valid for $\varDelta_{\mathrm{LT}} \ll \omega_{\mathrm{TO}}$.

The oscillator strength increases with the ionicity, i.e. the electronegativity difference of the atoms in the base (Fig. 9.39). Additionally, the oscillator strength depends on the reduced mass and the high-frequency polarizability; this can be seen, e.g., for the series of the Zn compounds that all have similar ionicity. For the series of the nitrides, the mass effect is small since the reduced mass is dominated by the light N mass.

9.8.2 Reststrahlenbande

The absorption of electromagnetic radiation by optical phonons is governed by the dielectric function that has been derived in (9.62). For small damping, i.e. $\varGamma \ll \varDelta_{\mathrm{LT}}$, the dielectric constant is negative between ω_{TO} and ω_{LO}. From $\epsilon_{\mathrm{r}} = n_{\mathrm{r}}^2 - \kappa^2$ it follows that κ^2 is much larger than n_{r}^2. Therefore, the reflectance (9.9) will be close to 1. This energy range is the so-called *reststrahlenbande*. This term stems from multiple reflections in this wavelength regime that suppresses neighboring spectral regions and thus achieves a certain monochromatization in the far-infrared spectral region. Within the semiconductor the absorption is large in the reststrahlenbande (Fig. 9.40).

9.8.3 Polaritons

The coupled propagation of phonons and electromagnetic radiation is related to the equation (without phonon damping)

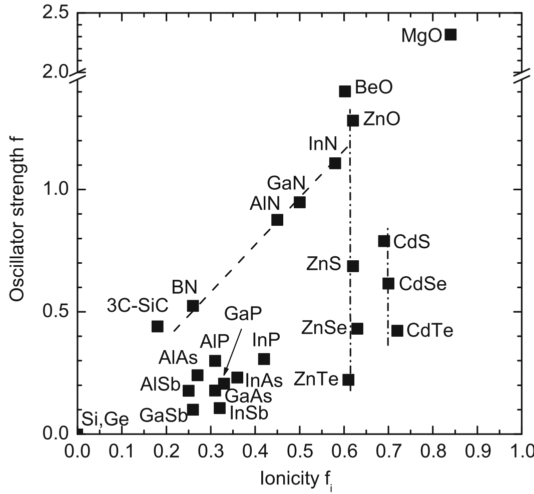

Fig. 9.39. Lattice absorption oscillator strength f from (9.64) for various elemental, III–V and II–VI semiconductors as a function of their ionicity f_i (cf. Table 2.1). *Dashed line* is linear dependence on ionicity for similar (reduced) mass, *dash-dotted lines* are guides to the eye for similar ionicity and varying mass

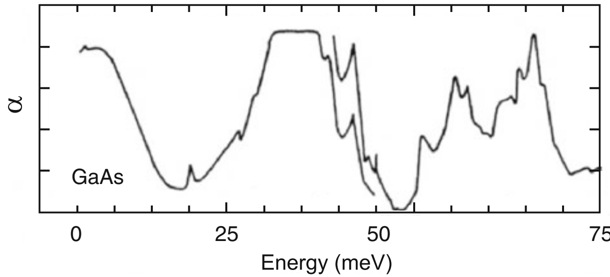

Fig. 9.40. Far-infrared absorption of GaAs. In the region around 35 meV is the reststrahlenbande with high absorption due to optical phonons. Adapted from [192], based on [644]

$$\epsilon(\omega) = \epsilon(\infty)\left(\frac{\omega_{\mathrm{LO}}^2 - \omega^2}{\omega_{\mathrm{TO}}^2 - \omega^2}\right) = \frac{c^2\,k^2}{\omega^2}\,. \tag{9.65}$$

There are two branches of propagating waves (real k):

$$\omega^2 = \frac{1}{2}\left(\omega_{\mathrm{LO}}^2 + \frac{c^2k^2}{\epsilon(\infty)}\right) \pm \sqrt{\frac{1}{4}\left(\omega_{\mathrm{LO}}^2 + \frac{c^2k^2}{\epsilon(\infty)}\right)^2 - \left(\frac{c^2k^2\omega_{\mathrm{TO}}^2}{\epsilon(\infty)}\right)^2}\,. \tag{9.66}$$

For $k = 0$ we find the solutions $\omega = \omega_{\mathrm{LO}}$ and $\omega = kc/\sqrt{\epsilon(0)}$. For large k we find $\omega = \omega_{\mathrm{TO}}$ and $\omega = kc/\sqrt{\epsilon(\infty)}$. These solutions are shown in Fig. 9.41.

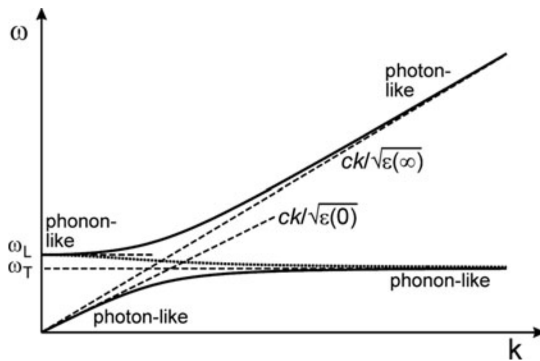

Fig. 9.41. Dispersion of the polariton. The *dotted line* displays the dispersion for a purely imaginary wavevector with the absolute value k

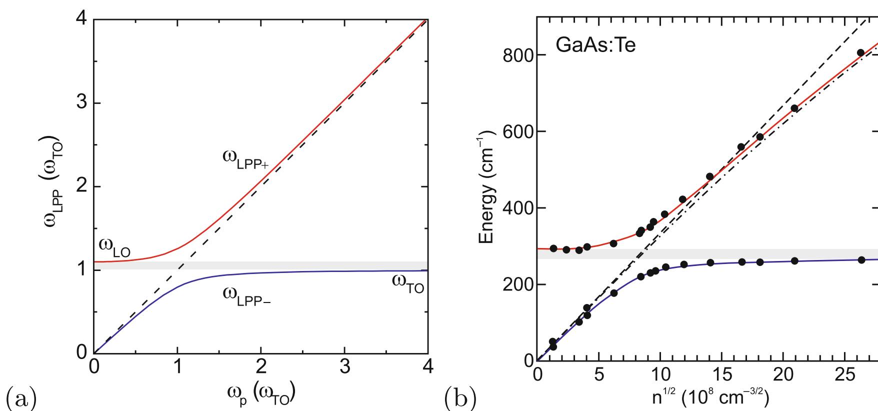

Fig. 9.42. (**a**) Frequency of the coupled longitudinal-phonon plasmon (LPP) modes (lower (upper) polariton branch in *blue* (*red*))as a function of the plasma frequency. *Dashed line* shows uncoupled plasmon frequency ($\omega = \omega_\mathrm{p}$), *grey area* indicates spectral region between TO and LO modes. (**b**) Experimental data on the polariton energies in n-type GaAs with different carrier concentration $\omega_\mathrm{p} \propto \sqrt{n\, m^*}$ (9.59). *Dashed* (*dash-dotted*) *line* is plasmon frequency ω_p without (with) consideration of conduction band non-parabolicity (cf. Fig. 6.26b). Data from [641, 645]

Both branches have a phonon- and a photon-like part. The coupled state between the phonon and the photon field is called the (phonon-) polariton.

In the interval $[\omega_\mathrm{TO}, \omega_\mathrm{LO}]$ the wavevector is purely imaginary, i.e. $k = \mathrm{i}\tilde{k}$ with real $\tilde{k}$. For this case there is only one solution that is also depicted in Fig. 9.41,

$$\omega^2 = \frac{1}{2}\left(\omega_\mathrm{LO}^2 + \frac{c^2\tilde{k}^2}{\epsilon(\infty)}\right) + \sqrt{\frac{1}{4}\left(\omega_\mathrm{LO}^2 + \frac{c^2\tilde{k}^2}{\epsilon(\infty)}\right)^2 + \left(\frac{c^2\tilde{k}^2\omega_\mathrm{TO}^2}{\epsilon(\infty)}\right)^2} \,. \quad (9.67)$$

9.8.4 Phonon–Plasmon Coupling

The coupling of phonons and plasmons in the spectral region of the reststrahlenbande leads to the development of two new branches, the longitudinal phonon plasmon modes (LPP+ and LPP−), in the common dispersion. The dielectric function is

$$\epsilon(\omega) = \epsilon(\infty)\left(1 + \frac{\omega_{\mathrm{LO}}^2 - \omega^2}{\omega_{\mathrm{TO}}^2 - \omega^2} - \frac{\omega_{\mathrm{p}}^2}{\omega^2}\right) . \tag{9.68}$$

For $\epsilon(\omega) = 0$ for $k = 0$ (coupling to photons) the two solutions $\omega_{\mathrm{LPP+}}$ and $\omega_{\mathrm{LPP-}}$ do not cross as a function of ω_{p} (Fig. 9.42),

$$\omega_{\mathrm{LPP\pm}} = \frac{1}{2}\left[\omega_{\mathrm{LO}}^2 + \omega_{\mathrm{p}}^2 \pm \sqrt{(\omega_{\mathrm{LO}}^2 + \omega_{\mathrm{p}}^2)^2 - 4\omega_{\mathrm{TO}}^2\omega_{\mathrm{p}}^2}\right] . \tag{9.69}$$

For small plasma frequencies $\omega_{\mathrm{LPP+}} = \omega_{\mathrm{LO}}$, i.e. the optical phonons couple to the electromagnetic field without change. Also $\omega_{\mathrm{LPP-}} = \omega_{\mathrm{p}}$. For large carrier density, i.e. $\omega_{\mathrm{p}} \gg \omega_{\mathrm{LO}}$, we find $\omega_{\mathrm{LPP-}} = \omega_{\mathrm{TO}}$ and $\omega_{\mathrm{LPP+}} = \omega_{\mathrm{p}}$. Thus, the carriers have effectively screened the electric field of the phonon that had led to the increase of the TO to the LO frequency.

10 Recombination

10.1 Introduction

In thermodynamic nonequilibrium excess charges can be present in the semiconductor. They can be created by carrier injection through contacts, an electron beam or the absorption of light with wavelength smaller than the band gap. After the external excitation is turned off, the semiconductor will return to the equilibrium state. The relaxation of carriers into energetically lower states (and energy release) is called recombination. The term stems from the electron recombining with the hole created after absorption of a photon. However, there are other recombination mechanisms. A dedicated textbook is [646].

In the simplest picture an excitation generates carriers with a rate G (carriers per unit volume and unit time). In the steady state (after all turn-on effects) a constant excess charge n carrier density is present. Then the generation exactly compensates the recombination processes. The principle of detailed balance even says that each microscopic process is balanced by its reverse process. If the time constant of the latter is τ, n is given by $n = G\tau$. This follows from the steady-state solution $\dot{n} = 0$ of

$$\frac{\mathrm{d}n}{\mathrm{d}t} = G - \frac{n}{\tau} \; . \tag{10.1}$$

10.2 Band–Band Recombination

The band–band recombination is the relaxation from an electron in the conduction band into the valence (the empty state there is the hole). In a direct semiconductor, electrons can make an optical transition between the bottom of the conduction band to the top of the valence band. In an indirect semiconductor, this process is only possible with the assistance of a phonon and is thus much less probable.

10.2.1 Spontaneous Emission

We consider the spontaneous recombination of an electron of energy E_{e} and a hole of energy E_{h} (Fig. 10.1a). $C(E_{\mathrm{e}}, E_{\mathrm{h}})$ is a constant proportional to

M. Grundmann, *The Physics of Semiconductors*, 2nd ed., Graduate Texts in Physics, DOI 10.1007/978-3-642-13884-3_10,

© Springer-Verlag Berlin Heidelberg 2010

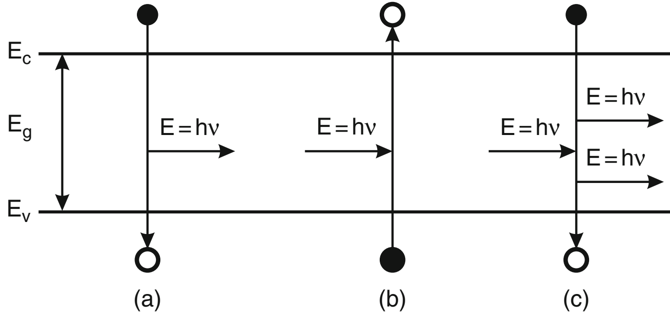

Fig. 10.1. Processes of band–band recombination: (**a**) spontaneous emission, (**b**) absorption and (**c**) stimulated emission. A *full* (*empty*) *circle* represents an occupied (unoccupied) electron state

the matrix element of the optical transition (cf. Sect. 9.4). The spontaneous recombination rate r_{sp} at photon energy $E \geq E_{\mathrm{C}} - E_{\mathrm{V}} = E_{\mathrm{g}}$ is (assuming energy conservation, i.e. $E = E_{\mathrm{e}} - E_{\mathrm{h}}$, but without k-conservation in a dense plasma [647]),

$$
\begin{aligned}
r_{\mathrm{sp}}(E) = & \int_{E_{\mathrm{C}}}^{\infty} \mathrm{d}E_{\mathrm{e}} \int_{-\infty}^{E_{\mathrm{V}}} \mathrm{d}E_{\mathrm{h}}\, C(E_{\mathrm{e}}, E_{\mathrm{h}}) \\
& \times D_{\mathrm{e}}(E_{\mathrm{e}})\, f_{\mathrm{e}}(E_{\mathrm{e}})\, D_{\mathrm{h}}(E_{\mathrm{h}})\, f_{\mathrm{h}}(E_{\mathrm{h}})\, \delta(E - E_{\mathrm{e}} + E_{\mathrm{h}}) \\
= & \int_{E_{\mathrm{C}}}^{E+E_{\mathrm{V}}} \mathrm{d}E_{\mathrm{e}}\, C(E_{\mathrm{e}}, E_{\mathrm{e}} - E) \\
& \times D_{\mathrm{e}}(E_{\mathrm{e}})\, f_{\mathrm{e}}(E_{\mathrm{e}})\, D_{\mathrm{h}}(E_{\mathrm{e}} - E)\, f_{\mathrm{h}}(E_{\mathrm{e}} - E)\ ,
\end{aligned}
\tag{10.2}
$$

where f_{h} denotes the hole occupation $f_{\mathrm{h}} = 1 - f_{\mathrm{e}}$.

The lineshape of the band–band recombination with k-conservation[1] is proportional to the joint density of states (9.23) and the Fermi distribution function. At small excitation and at low doping it can be approximated by the Boltzmann distribution function and the lineshape is given as

$$
I(E) \propto \sqrt{E - E_{\mathrm{g}}}\, \exp\left(-\frac{E}{kT}\right)\ . \tag{10.3}
$$

An experimental spectrum is shown in Fig. 10.2 together with a fit according to (10.3). The expected FWHM of the peak is $1.7954\,kT$, which is about 46 meV at $T = 300$ K.

The recombination rate in indirect semiconductors is small since the transition is phonon-assisted. For silicon, an internal quantum efficiency in the 10^{-6}-range has been reported [648]. For germanium, the direct transition is

[1]Excitonic effects are neglected here, e.g. for temperatures $kT \gg E_{\mathrm{X}}^{\mathrm{b}}$. Such effects are discussed in Sect. 10.3.

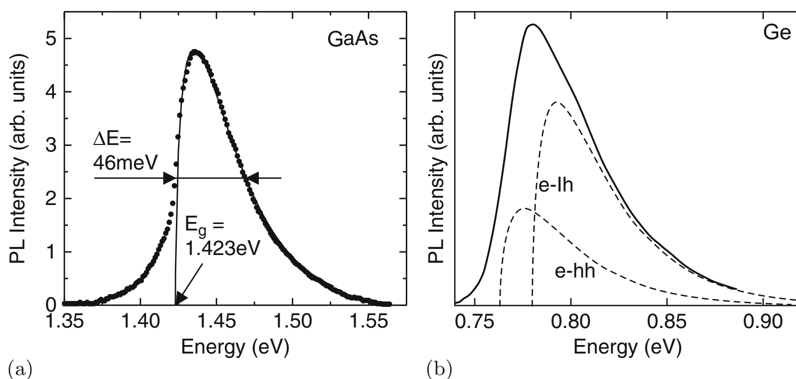

Fig. 10.2. (**a**) Photoluminescence spectrum of an undoped LPE-grown epitaxial GaAs layer at room temperature and low cw ($\lambda = 647\,\mathrm{nm}$) excitation density ($10\,\mathrm{W/cm^2}$). The *solid line* is a lineshape fit with (10.3) and E_g =1.423 eV and $T = 293\,\mathrm{K}$. (**b**) Room temperature, direct (e_Γ–h_Γ) recombination from heavily n-doped ($10^{19}\,\mathrm{cm}^{-3}$) germanium (1 µm thick Ge layer on silicon (001)) with biaxial (thermal) tensile strain. The strain-split valence band edge (Fig. 6.38) causes the e–hh and e–lh transitions (individual contributions with lineshape according to (10.3) shown as *dashed lines*) to occur at different energies. Adapted from [649]

energetically fairly close to the fundamental, indirect L–Γ band edge transition (Fig. 9.11). The energy difference can be reduced from its bulk value of 136 meV by tensile strain. Additionally, the direct transition can be favored by heavily n-doping and filling the L conduction band minimum states (see Sect. 9.5.13). In this case, direct recombination from the conduction band Γ-minimum can be observed [649] and the effective energy difference has been lowered to about 100 meV.

10.2.2 Absorption

A similar consideration is made for the absorption process (Fig. 10.1b). An electron is transferred upon light absorption from a valence-band state (occupied) to a conduction-band state that must be empty. The coefficient is B_1. Also, the process is proportional to the light intensity, represented by the density of occupied photon states $N_{\mathrm{ph}}(E)$,

$$r_{\mathrm{abs}}(E) = \int_{E_{\mathrm{C}}}^{E+E_{\mathrm{V}}} \mathrm{d}E_{\mathrm{e}}\; B_1(E_{\mathrm{e}}, E_{\mathrm{e}} - E) \times D_{\mathrm{e}}(E_{\mathrm{e}})\,(1 - f_{\mathrm{e}}(E_{\mathrm{e}}))\,D_{\mathrm{h}}(E_{\mathrm{e}} - E)\,(1 - f_{\mathrm{h}}(E_{\mathrm{e}} - E))\,N_{\mathrm{ph}}(E)\;. \tag{10.4}$$

10.2.3 Stimulated Emission

In this case, an incoming photon 'triggers' the transition of an electron in the conduction band into an empty state in the valence band. The emitted

photon is in phase with the initial photon (Fig. 10.1c). The rate is (with coefficient B_2):

$$r_{\mathrm{st}}(E) = \int_{E_{\mathrm{C}}}^{E+E_{\mathrm{V}}} \mathrm{d}E_{\mathrm{e}}\; B_2(E_{\mathrm{e}}, E_{\mathrm{e}} - E) \times D_{\mathrm{e}}(E_{\mathrm{e}})\, f_{\mathrm{n}}(E_{\mathrm{e}})\, D_{\mathrm{h}}(E_{\mathrm{e}} - E)\, f_{\mathrm{p}}(E_{\mathrm{e}} - E)\, N_{\mathrm{ph}}(E)\ . \tag{10.5}$$

10.2.4 Net Recombination Rate

In thermodynamical equilibrium the rates fulfill

$$r_{\mathrm{sp}}(E) + r_{\mathrm{st}}(E) = r_{\mathrm{abs}}(E)\ . \tag{10.6}$$

The population functions are Fermi functions with quasi-Fermi levels F_{n} and F_{p}. The photon density is given by Planck's law and the Bose–Einstein distribution (Appendix D)

$$N_{\mathrm{ph}} = N_0\, \frac{1}{\exp\left(E/kT\right) - 1}\ . \tag{10.7}$$

The pre-factor is $N_0 = \hbar\omega^3 n_{\mathrm{r}}^2/(\pi^2 c^3)$. Since for absorption and stimulated emission the same quantum-mechanical matrix element is responsible, $B_1 = B_2$. The detailed balance (10.6) yields

$$C(E_1, E_2) = B_1(E_1, E_2)\, N_{\mathrm{ph}} \left[\exp\left(\frac{E - (F_{\mathrm{n}} - F_{\mathrm{p}})}{kT}\right) - 1\right]\ . \tag{10.8}$$

In thermodynamic equilibrium, i.e. $F_{\mathrm{n}} = F_{\mathrm{p}}$,

$$C(E_1, E_2) = N_0\, B_1(E_1, E_2) = B\ . \tag{10.9}$$

If the constant B, the bimolecular recombination coefficient, is independent of the energy E, the integration for the net recombination rate R can be executed analytically and we find

$$\begin{aligned} r_{\mathrm{B}} &= \int_{E_{\mathrm{g}}}^{\infty} \left[r_{\mathrm{sp}}(E) + r_{\mathrm{st}}(E) - r_{\mathrm{abs}}(E)\right] \mathrm{d}E \\ &= B\, n\, p \left[1 - \exp\left(-\frac{F_{\mathrm{n}} - F_{\mathrm{p}}}{kT}\right)\right]\ . \end{aligned} \tag{10.10}$$

In thermodynamic equilibrium, of course, $r_{\mathrm{B}} = 0$. The recombination rate Bnp is then equal to the thermal generation rate G_{th}

$$G_{\mathrm{th}} = B\, n_0 p_0\ . \tag{10.11}$$

The bimolecular recombination rate typically used in Shockley–Read–Hall (SRH) [650, 651] kinetics is

Table 10.1. Bimolecular recombination coefficient at room temperature for a number of semiconductors. Data for GaN from [653], Si from [654], SiC from [655], other values from [656]

Material	B (cm^3/s)
GaN	1.1×10^{-8}
GaAs	1.0×10^{-10}
AlAs	7.5×10^{-11}
InP	6.0×10^{-11}
InAs	2.1×10^{-11}
4H-SiC	1.5×10^{-12}
Si	1.1×10^{-14}
GaP	3.0×10^{-15}

$$r_\mathrm{B} = B\,(np - n_0 p_0)\;. \tag{10.12}$$

Values for the coefficient B are given in Table 10.1. In the case of carrier injection, np is larger than in thermodynamical equilibrium, i.e. $np > n_0\,p_0$, and the recombination rate is positive, i.e. light is emitted. If the carrier density is smaller than in thermodynamical equilibrium, e.g. in a depletion region, absorption is larger than emission. This effect is also known as 'negative luminescence' [652] and plays a role particularly at elevated temperatures and in the infrared spectral region.

10.2.5 Recombination Dynamics

The carrier densities n and p, are decomposed into the densities n_0 and p_0 in thermodynamic equilibrium and the excess-carrier densities δn and δp, respectively

$$n = n_0 + \delta n \tag{10.13a}$$

$$p = p_0 + \delta p\;. \tag{10.13b}$$

Here, only neutral excitations are considered, i.e. $\delta n = \delta p$. Obviously the time derivative fulfills $\frac{\partial n}{\partial t} = \frac{\partial\,\delta n}{\partial t}$, and correspondingly for the hole density. The equation for the dynamics

$$\dot{n} = \dot{p} = -Bnp + G_\mathrm{th} = -B(np - n_0 p_0) = -B(np - n_\mathrm{i}^2) \tag{10.14}$$

can be written as

$$\frac{\partial\,\delta p}{\partial t} = -B\,(n_0\;\delta p + p_0\;\delta n + \delta n\;\delta p)\;. \tag{10.15}$$

The general solution of (10.15) is given by

$$\delta p(t) = \frac{(n_0 + p_0)\, \delta p(0)}{[n_0 + p_0 + \delta p(0)]\, \exp\left[Bt(n_0 + p_0)\right] - \delta p(0)} \,. \tag{10.16}$$

In the following, we discuss some approximate solutions of (10.15). First, we treat the case of a small (neutral) excitation, i.e. $\delta n = \delta p \ll n_0, p_0$. The dynamic equation is in this case

$$\frac{\partial\, \delta p}{\partial t} = -B\,(n_0 + p_0)\, \delta p \,. \tag{10.17}$$

Then the decay of the excess-carrier density is exponential with a time constant (lifetime) τ given by

$$\tau = \frac{1}{B\,(n_0 + p_0)} \,. \tag{10.18}$$

In an n-type semiconductor additionally $n_0 \gg p_0$, and thus the minority carrier lifetime τ_p is

$$\tau_p = \frac{1}{B\, n_0} \,. \tag{10.19}$$

If the nonequilibrium carrier densities are large, i.e. $n \approx p \gg n_0, p_0$, e.g. for strong injection, the kinetics obeys

$$\frac{\partial\, \delta p}{\partial t} = -B\,(\delta p)^2 \,, \tag{10.20}$$

and the transient has the form

$$\delta p(t) = \frac{\delta p(0)}{1 + B\, t\, \delta p(0)} \,, \tag{10.21}$$

where $\delta p(0)$ is the excess hole density at time $t = 0$. Such a decay is called *hyperbolic* and the recombination is bimolecular. The exponential decay time is formally $\tau^{-1} = B\delta p(t)$ and is thus time and density dependent. A detailed discussion of minority carrier lifetime is given in [657].

10.2.6 Lasing

The net rate for stimulated emission and absorption is

$$r_{\mathrm{st}}(E) - r_{\mathrm{abs}}(E) = \left[1 - \exp\left(\frac{E - (F_{\mathrm{n}} - F_{\mathrm{p}})}{kT}\right)\right] \tag{10.22}$$

$$\times \int_{E_{\mathrm{C}}}^{E+E_{\mathrm{V}}} \mathrm{d}E_{\mathrm{e}}\, B\, D_{\mathrm{e}}(E_{\mathrm{e}})\, f_{\mathrm{e}}(E_{\mathrm{e}})\, D_{\mathrm{h}}(E_{\mathrm{e}} - E)\, f_{\mathrm{h}}(E_{\mathrm{e}} - E)\, N_{\mathrm{ph}}(E) \,.$$

The net rate at photon energy $E = \hbar\omega$ is only larger than zero (i.e. dominating stimulated emission) when

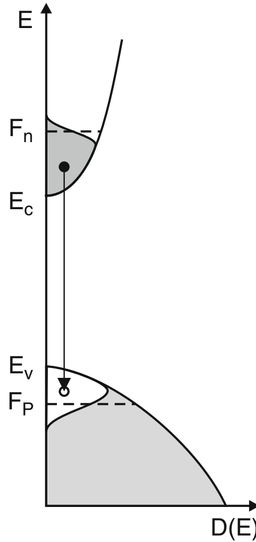

Fig. 10.3. Charge-carrier distribution during inversion, necessary for lasing. *Shaded areas* are populated with electrons. A stimulated transition between an electron and a hole is indicated

$$F_\mathrm{n} - F_\mathrm{p} > E \geq E_\mathrm{g} \; . \qquad (10.23)$$

When the difference of the quasi-Fermi levels is larger than the band gap, the carrier population is inverted, i.e. close to the band edges the conduction-band states are more strongly populated with electrons than the valence-band states, as shown in Fig. 10.3. An incoming optical wave of energy E will then be net amplified by stimulated emission. Equation (10.23) is also called the thermodynamic laser condition. We note that lasing requires further conditions as discussed in Sect. 22.4.

10.3 Exciton Recombination

10.3.1 Free Excitons

The observation of free-excitons is limited for semiconductors with a small exciton binding energies (such as in GaAs) to low temperatures. However, for large exciton binding energy, recombination from free-excitons is observed even at room temperature, as shown in Fig. 10.4 for ZnO.

A low temperature recombination spectrum of silicon is shown in Fig. 10.5. In pure silicon, phonon-assisted exciton recombination (cmp. Sect. 10.4) is observed involving acoustic (I^TA) and optical (I^TO) phonons. The weakly observed no-phonon line (I^0) is forbidden in perfect Si.

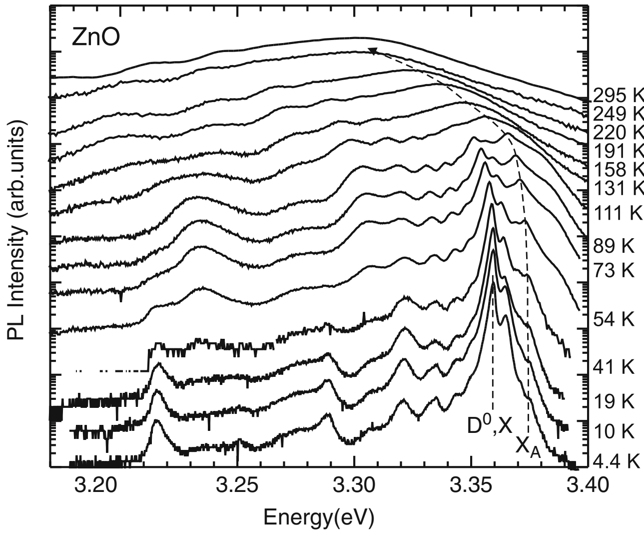

Fig. 10.4. Temperature-dependent luminescence spectra of a ZnO thin film (on sapphire). At low temperatures, the spectra are dominated by donor-bound exciton transitions (Al^0,X)). The *vertical dashed line* indicates the low-temperature position of the donor-bound exciton transition (D^0,X). The *curved dashed line* visualizes the energy position of the free-exciton transition (X_A) that becomes dominant at room temperature

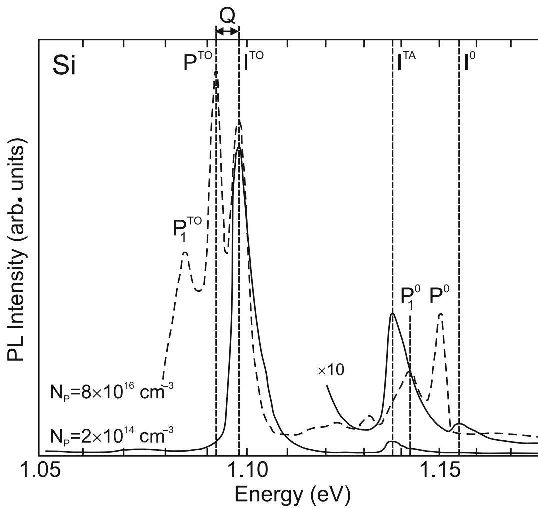

Fig. 10.5. Low temperature recombination spectra from silicon with low (*solid lines*) and sizeable (*dashed line*) phosphorus dopant concentration. Spectrum for $N_P = 2 \times 10^{14}\,\mathrm{cm}^{-3}$ ($N_P = 8 \times 10^{16}\,\mathrm{cm}^{-3}$) taken at 26 K (15 K). Transitions in pure Si are label with 'I', transitions involving P donors are labeled with 'P'. Q indicates the dissociation energy of the bound exciton. Adapted from [658]

10.3.2 Bound Excitons

Excitons can localize at impurities, defects or other potential fluctuations and subsequently recombine [659, 660]. Excitons can be bound to neutral or ionized donors and acceptors impurities. Also they can be bound to isoelectronic impurities, the most prominent example being N in GaP [661] (cmp. Sect. 9.5.10) or isoelectronic clusters [662]. The recombination of excitons localized in quantum wells (Sect. 11.4) and quantum dots (Sect. 13.3.4) is discussed later.

The transition energy $\hbar\omega$ of an exciton bound to a neutral impurity is

$$\hbar\omega = E_{\mathrm{g}} - E_{\mathrm{X}}{}^{\mathrm{b}} - Q \; , \tag{10.24}$$

where Q is the binding (or localization) energy of the exciton to the impurity. A transition involving an exciton bound to a neutral donor is denoted (D^0,X); correspondingly (D^+,X), also denoted as (h,D^0), and (A^0,X). Values for donor-bound excitons in various semiconductors are listed in Table 10.2. The (D^0,X) complex is stable for $0 < \sigma = m_{\mathrm{e}}^*/m_{\mathrm{h}}^* < 0.43$ according to [663]. The (D^+,X) peak can occur on the low- or high-energy side of the (D^0,X) recombination. Whether $Q^* < Q$ or $Q^* > Q$ depends on σ being smaller or larger than 0.2, respectively [663], and is fulfilled for many semiconductors, e.g. GaAs, GaN, CdS, and ZnSe.

Table 10.2. Localization energy Q (Q^*) of excitons on selected impurities (ionized impurities, D^+ or A^-, respectively) in various semiconductors. σ is the ratio of effective electron and hole (polaron) masses. EMD: effective mass donor.

host	donor	Q (meV)	Q^* (meV)	Q^*/Q	σ	Ref.
GaAs	EMD	0.88	1.8	2.0	0.28	[668]
	Zn	8.1	31.1	3.8		[669]
GaN	EMD	6.8	11.2	1.6	0.36	[670]
	Mg	20				[671]
AlN	Si	16				[671]
	Mg	40				
CdS	EMD	6.6	3.8	0.6	0.17	[672]
ZnSe	Al	4.9	5.4	1.1	0.27	[673, 674]
	Ga	5.1	6.6	1.3		
	In	5.4	7.5	1.4		
ZnO	Al	15.5	3.4	0.21	0.3	[675]
	Ga	16.1	4.1	0.25		
	In	19.2	8.5	0.44		

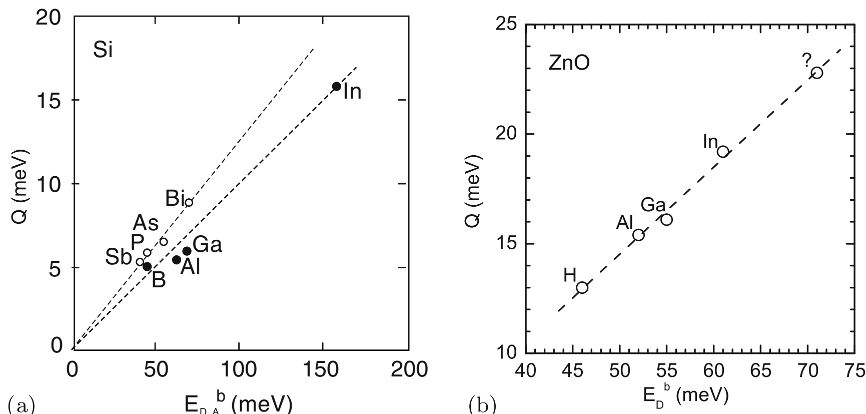

Fig. 10.6. Energy Q required to remove an exciton from a neutral impurity (10.24) as a function of the ionization energy $E_{\mathrm{D}}^{\mathrm{b}}$ (*open circles*) or $E_{\mathrm{A}}^{\mathrm{b}}$ (*solid circles*) of the involved impurity in (**a**) silicon (experimental data from [664]) and (**b**) ZnO (experimental data from [665])

Recombination in silicon due to excitons involving phosphorus donors is depicted in Fig. 10.5. The $(\mathrm{D}^0,\mathrm{X})$ transition in SI:P is labeled ‘P^0’ ($Q = 6\,\mathrm{meV}$). Other P-related transitions are discussed in [658]. In Si, the binding energy to the impurity is about one tenth of the binding energy of the impurity (Haynes’s rule [659, 664]), i.e. $Q/E_{\mathrm{D}}^{\mathrm{b}}$ and $Q/E_{\mathrm{A}}^{\mathrm{b}} \approx 0.1$ (Fig. 10.6a). In GaP the approximate relations $Q = 0.26E_{\mathrm{D}}^{\mathrm{b}} - 7\,\mathrm{meV}$ and $Q = 0.056E_{\mathrm{A}}^{\mathrm{b}} + 3\,\mathrm{meV}$ have been found [661]. For donors in ZnO, the relation $Q = 0.365E_{\mathrm{D}}^{\mathrm{b}} - 3.8\,\mathrm{meV}$ holds (Fig. 10.6b) [665]. In Fig. 10.7, the recombination spectrum of GaAs:C is shown that exhibits recombination from excitons bound to the acceptor (carbon) and shallow donors. The exciton is more strongly bound to an ionized donor (D^+) than to a neutral donor.

Varying the concentration of a specific impurity and observing the corresponding change in the intensity of the $(\mathrm{D}^0,\mathrm{X})$ transition allows to identify the chemical species to which the exciton is bound. This can be achieved via the comparison of different samples or more elegantly by introducing radioactive isotopes. This is shown in Fig. 10.8 for In in ZnO; the $(^{111}\mathrm{In}^0,\mathrm{X})$ transition disappears with the characteristic time constant close to that (97 h) of the nuclear decay of ^{111}In into stable ^{111}Cd. However, in such experiments it should be considered that the decay product and accompanying high-energy radiation can create new electronic and structural defects, respectively.

The peak labeled $(\mathrm{D}^0,\mathrm{X})_{2\mathrm{s}}$ in Fig. 10.7 is called a two-electron satellite (TES) [666]. High-resolution spectra of the TES in GaAs [388, 667] are shown in Fig. 10.9a. The TES recombination is a $(\mathrm{D}^0,\mathrm{X})$ recombination that leaves the donor in an excited state as schematically shown in Fig. 10.9b. Therefore a hydrogen-like series with $n = 2, 3, \ldots$ is observed with energies

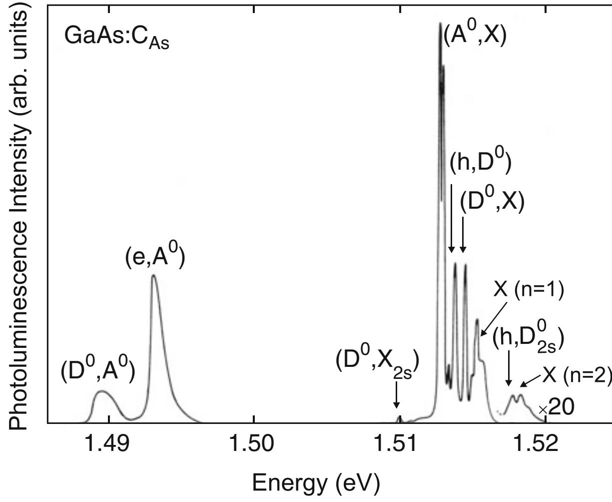

Fig. 10.7. Photoluminescence spectrum ($T = 2\,\mathrm{K}$, $D = 10\,\mathrm{mW\,cm^{-2}}$) of GaAs:C$_{\mathrm{As}}$ ($N_{\mathrm{A}} = 10^{14}\,\mathrm{cm^{-3}}$) with donor- and acceptor-related bound-exciton recombination around 1.512 eV, (e,A^0), (h,D^0) and (D^0,A^0) pair and free-exciton recombination. Adapted from [668]

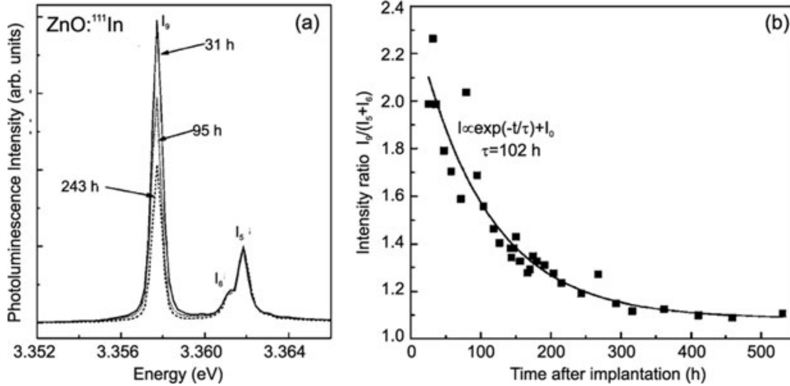

Fig. 10.8. (**a**) Low-temperature photoluminescence spectrum of ZnO implanted with ^{111}In featuring the so-called I$_9$-line. Spectra are recorded at various times after implantation as labeled. (**b**) Intensity of I$_9$-line as a function of time. Adapted from [678]

$$E^n_{\mathrm{TES}} = E_{(\mathrm{D^0,X})} - E^{\mathrm{b}}_{\mathrm{D}} \left(1 - \frac{1}{n^2}\right) . \tag{10.25}$$

The effect of isotope disorder on the sharpness and splitting of impurity states has been investigated in [676, 677]. The recombination of excitons

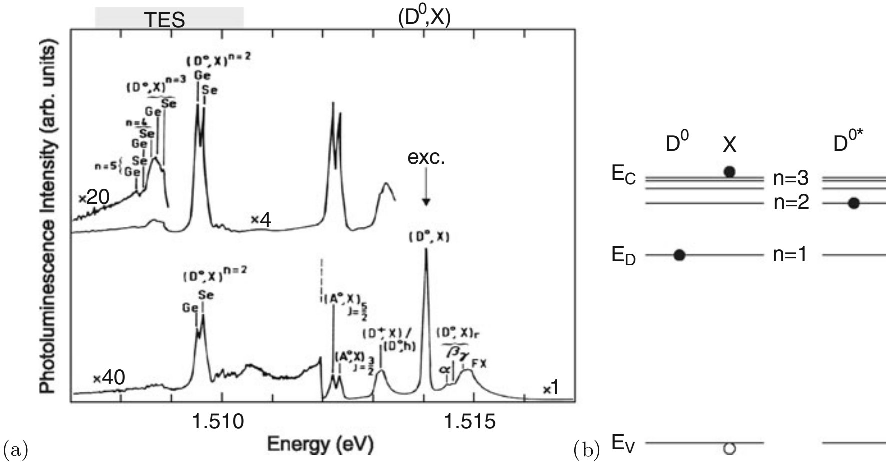

Fig. 10.9. (**a**) Photoluminescence spectrum ($T = 1.5\,\mathrm{K}$, $D = 50\,\mathrm{mW\,cm^{-2}}$) of high-purity GaAs with two donors (Ge and Se/Sn). The lower spectrum has been excited 6 meV above the band gap, the upper spectrum has been resonantly excited with the laser set to the (D^0,X) transition and exhibits $n = 2, 3, 4$, and 5 TES transitions. α,β,γ denote excited (hole rotational) states of the (D^0,X) complex. Adapted from [667]. (**b**) Schematic representation of the $n = 2$ TES process, *left*: initial, *right*: final state

bound to Al, Ga and In in natural silicon (92.23% ^{28}Si, 4.67% ^{29}Si, 3.10% ^{30}Si) is split into three lines due to the valley-orbit splitting [679] of electron states at the band minimum (Fig. 10.10). Each of these (A^0,X) lines is split by $0.01\,\mathrm{cm}^{-1}$ for Si:Al due to a symmetry reduction of the 4-fold degenerate A^0 ground state, as observed in the presence of applied axial strain or an electric field. The comparison to spectra from enriched ^{28}Si shows that the observed splitting without external perturbation is due to isotope disorder that causes random strains and splits the A^0 ground state into two doublets [677] (Fig. 10.10). Similarly, the (unsplit) phosphorus-induced (D^0,X) transition in enriched Si is found to be much sharper ($< 40\,\mu\mathrm{eV}$) than in natural Si ($330\,\mu\mathrm{eV}$) [676]. At higher resolution, a hyperfine splitting of 485 neV due to the ^{31}P nuclear spin $I = 1/2$ ($2 \times 10^{12}\,\mathrm{cm}^{-3}$) in isotopically pure (99.991%) ^{28}Si ($I = 0$) is observed for the (P^0,X) recombination [680]. In a magnetic field, the Zeeman-split lines have a FWHM of about 150 neV.

In Fig. 10.11 the recombination of excitons bound to the N isoelectronic impurity in lowly doped GaP is shown. The efficient recombination of nitrogen-bound electrons with holes at the Γ point is due to the wavefunction component of the localized electron at $k = 0$ [484] (Fig. 7.36). The decay time of the A exciton is about 40 ns [681] and thus larger than the typical lifetime of excitons in direct semiconductors (ns-range). The forbidden B exciton has a much longer lifetime of $4\,\mu\mathrm{s}$ [681].

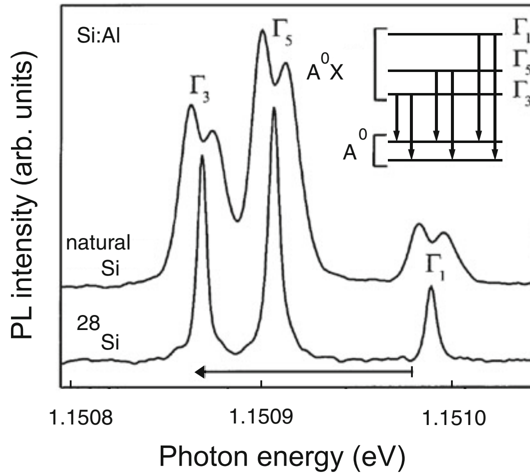

Fig. 10.10. High-resolution photoluminescence (PL) spectra of (A^0,X) recombination in natural and ^{28}Si-enriched silicon doped with aluminum ($T = 1.8$ K). The ^{28}Si PL spectrum is shifted up in energy by 0.114 meV, as indicated by the arrow, to compensate for the shift in band gap. The *inset* shows a level scheme for the recombination in natural silicon. Adapted from [677], reprinted with permission, ©2002 APS

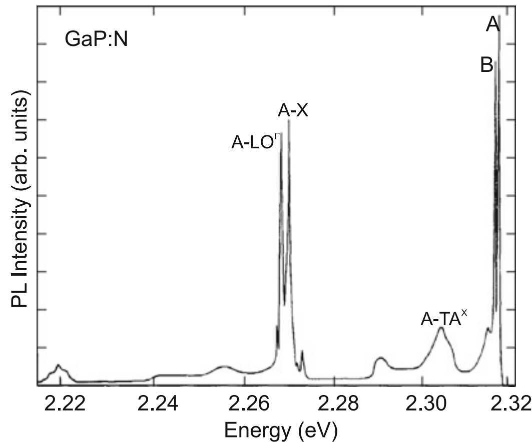

Fig. 10.11. Photoluminescence spectrum ($T = 4.2$ K) of GaP:N ($N_{\mathrm{N}} \approx 5 \times 10^{16}\,\mathrm{cm}^{-3}$). The A exciton is bound to an isolated nitrogen impurity, cmp. to Fig. 9.24. Adapted from [484]

In the case of In in GaAs it has been found that down to the regime of $N_{\mathrm{In}} < 10^{19}\,\mathrm{cm}^{-3}$ the indium does not act as a substitutional isoelectronic impurity but still fully participates in the composition of a pseudo-binary system (Sect. 6.4). Recombination from excitons bound to single indium

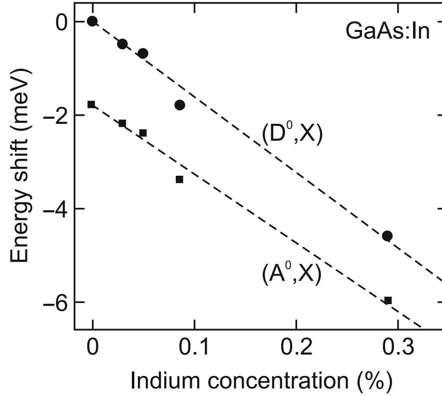

Fig. 10.12. Spectral position of neutral donor- and acceptor-bound exciton photoluminescence transition ($T = 2\,\mathrm{K}$) in GaAs doped with different amounts of indium relative to the donor-bound exciton luminescence in pure GaAs (1.5146 eV). Adapted from [682]

atoms or In–In pairs could not be found. The energy shift of donor- and acceptor-bound excitons in the dilute limit (Fig. 10.12) follows the band-gap dependence established for larger indium concentrations. The non-occurrence of localization effects is attributed to the small effective electron mass in InAs [369].

The luminescence intensity $I(T)$ of bound exciton lines is quenched with increasing temperature due to ionization of the excitons from the impurities. The temperature dependence can be modeled using the relation [683]

$$\frac{I(T)}{I(T=0)} = \frac{1}{1 + C\,\exp(-E_\mathrm{A}/kT)}\,, \tag{10.26}$$

E_A being the thermal activation energy and C a pre-factor. Often the activation energy is found equal to the localization energy, $E_\mathrm{A} = Q$ (Fig. 10.13, cmp. Table 10.2). If several processes contribute, additional exponential terms can be added with further activation energies. For acceptor-bound excitons in GaAs two processes are found to contribute, the ionization from the impurity into a free exciton ($E_\mathrm{A}^1 \approx Q$) and into an electron-hole pair ($E_\mathrm{A}^2 \approx Q + E_\mathrm{X}^\mathrm{b}$) [683].

So far *single* excitons bound to a center have been discussed. Also bound exciton *complexes* [684] containing up to six excitons have been observed at sufficient excitation density, e.g. for substitutional boron [685] or phosphorus [686] and interstitial Li [687] in silicon. In a multi-valley semiconductor several electrons are available to form bound excitons which follow approximately a shell model and exhibit further fine structure.

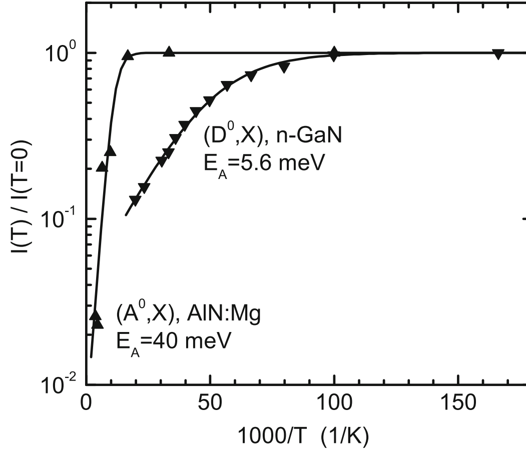

Fig. 10.13. (Temperature dependent PL intensity of (D^0,X) in GaN and (A0,X) in AlN:Mg recombination. *Solid lines* are fits with (10.26). Data from [671, 688]

10.3.3 Alloy Broadening

The bound-exciton recombination peak in a binary compound is spectrally fairly sharp (Sect. 10.3.2), even in the presence of isotope disorder (Fig. 10.10). In an alloy (see Sect. 3.7), the random distribution of atoms (with different atomic order number Z) causes a significant broadening effect of the luminescence (and absorption) line, the so-called *alloy broadening* [689, 690]. As an example, we treat $\mathrm{Al}_x\mathrm{Ga}_{1-x}\mathrm{As}$. The exciton samples, at different positions of the lattice, different coordinations of Ga and Al atoms. If the experiment averages over these configurations, an inhomogeneously broadened line is observed.

The cation concentration c_c for the zincblende lattice is given as $c_\mathrm{c} = 4/a_0^3$, for the wurtzite lattice as $c_\mathrm{c} = 4/(\sqrt{3}\, a^2 c)$. For example, $c_\mathrm{c} = 2.2 \times 10^{22}\,\mathrm{cm}^{-3}$ for $\mathrm{Al}_x\mathrm{Ga}_{1-x}\mathrm{As}$ in the entire composition range $0 \leq x \leq 1$ since the lattice constant does not vary significantly, and $c_\mathrm{c} = 4.2 \times 10^{22}\,\mathrm{cm}^{-3}$ for wurtzite $\mathrm{Mg}_x\mathrm{Zn}_{1-x}\mathrm{O}$ [691]. In a random alloy, the probability $p(N)$ to find exactly N Ga atoms in a given volume V (with a total of $c_\mathrm{c}V$ cations) is given by the binomial distribution

$$p(N) = \binom{c_\mathrm{c} V}{N} x^N \, (1-x)^{c_\mathrm{c} V - N} \,. \tag{10.27}$$

The sampling volume for a luminescence event is the exciton volume (cf. (9.30)) that is given for the free-exciton (in 1s hydrogen state) as [689, 692]

$$V_\mathrm{ex} = 10\,\pi\, a_\mathrm{X}^3 = 10\,\pi \left(\frac{m_0}{m_\mathrm{r}^*} \, \epsilon_\mathrm{s} \, a_\mathrm{B} \right)^3 \,. \tag{10.28}$$

One should note that due to the variation of the involved material parameters $V_{\rm ex}$ depends itself on x. In GaAs there are about 1.2×10^6 cations in the exciton volume. In $\mathrm{Al}_x\mathrm{Ga}_{1-x}\mathrm{As}$, there are on average $x c_{\rm c} V_{\rm ex}$ Al atoms in the exciton volume. The fluctuation is given by the standard deviation of the binomial distribution [692]

$$\sigma_{\rm x}^2 = \frac{x\,(1-x)}{c_{\rm c}\,V_{\rm ex}}\ . \tag{10.29}$$

The corresponding energetic broadening (full width at half-maximum) of the spectral line is given by $\varDelta_{\rm E} = 2.36\,\sigma$ with

$$\sigma = \frac{\partial E_{\rm g}}{\partial x}\,\sigma_{\rm x} = \frac{\partial E_{\rm g}}{\partial x}\sqrt{\frac{x(1-x)}{c_{\rm c} V_{\rm ex}}}\ . \tag{10.30}$$

We note that instead of the quantum mechanically correct factor $10\,\pi$ [689, 692], often the factor $4\pi/3$ [690] is used, resulting in larger theoretical broadening.

Experimental data for $\mathrm{Cd}_x\mathrm{Se}_{1-x}$ in Fig. 10.14a are consistent with (10.30). The theoretical dependence (10.30) is shown in Fig. 10.14b also for $\mathrm{Al}_x\mathrm{Ga}_{1-x}\mathrm{As}$ together with experimental data and found to disagree [693]. Since the exciton volume is much smaller (cf. Sect. 9.5.7) than in $\mathrm{Al}_x\mathrm{Ga}_{1-x}\mathrm{As}$, alloy broadening in $\mathrm{Mg}_x\mathrm{Zn}_{1-x}\mathrm{O}$ is much larger for a given for given x.

The spectral broadening due to alloy disorder masks the fine structure of recombination lines near the band edge present for binary semiconductors. Often for all temperatures only a single recombination line appears for alloys. Spectra for three different $\mathrm{Mg}_x\mathrm{Zn}_{1-x}\mathrm{O}$ alloys are shown in Fig. 10.15(a). The increasing inhomogeneous broadening is obvious, causing a single peak for $x > 0.03$. The temperature dependence of the peak positions is shown

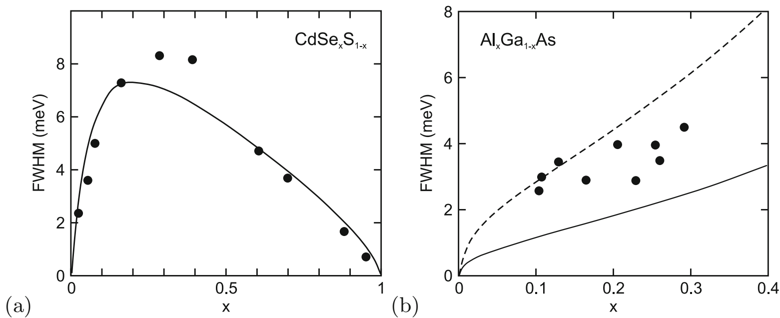

Fig. 10.14. (**a**) Spectral width of the photoluminescence from $\mathrm{CdS}_x\mathrm{Se}_{1-x}$ alloys. *Solid line* is theory according to (10.30). Adapted from [689]. (**b**) Spectral width of the bound exciton recombination in $\mathrm{Al}_x\mathrm{Ga}_{1-x}\mathrm{As}$ with various Al content within the direct-bandgap regime. *Solid line* is (10.30) with (10.28), *dashed line* with pre-factor $4\pi/3$ instead of $10\,\pi$. Adapted from [693].

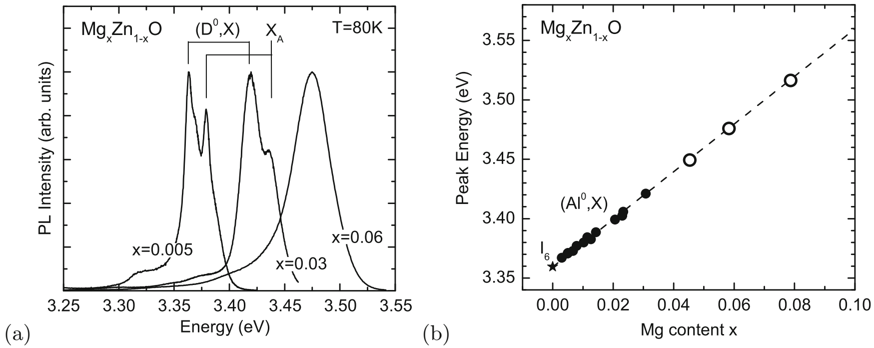

Fig. 10.15. (**a**) Photoluminescence spectra ($T = 80\,$K, scaled) of three $Mg_xZn_{1-x}O$ alloy layers on sapphire with three different Mg-contents, $x = 0.005$, $x = 0.03$, and $x = 0.06$ as labeled. The energy positions of (D^0,X) and X_A peaks are marked. Adapted from [694]. (**b**) Peak energy of the photoluminescence spectrum ($T = 2\,$K) of ZnO (I_6-line, *star*) and various $Mg_xZn_{1-x}O$ alloys (*circles*). For $x \leq 0.03$ (*filled circles*) the (D^0,X) recombination peak (Al donor) can be spectrally separated from the free exciton (X_A) recombination. For the samples with higher Mg content (*empty circles*) a single recombination peak is present at all temperatures. The *dashed line* is a linear least square fit for the alloys with $0 \leq x \leq 0.03$, showing that also for $x > 0.03$ the low temperature recombination peak is due to donor-bound excitons. Adapted from [695]

in Fig. 10.16 for the same samples. For $x = 0.005$ the bound exciton (Al-donor) (D^0,X) and free exciton (X_A) recombination lines can still be resolved despite the inhomogeneous broadening of $\sigma = 2.6\,$meV. At low temperature the luminescence intensity is dominated by (D^0,X) recombination, at room temperature by free exciton (X_A) recombination. Both peaks are present at low temperatures and exhibit a red-shift with increasing temperatures due to the shrinking of the band gap (Fig. 10.16(a)). The (D^0,X) peak vanishes at about 180 K due to ionization of the excitons from the donors ($Q \approx 15\,$meV, similar as in pure ZnO).

For larger Mg-content of $x = 0.03$ the two peaks can still mostly be separated ($\sigma = 6.0\,$meV). The (D^0,X) energy position shows a small dip (about 2 meV) due to exciton localization in the alloy disorder potential (arrow in Fig. 10.16b). At low temperatures excitons are frozen in local potential minima and have a non-thermal (non-Boltzmann) population. With increasing temperature they can overcome energy barriers and thermalize, leading to a shift of the recombination peak to lower energies. Further increase of temperature populates higher levels and leads to a shift of the recombination peak to higher energies. Superimposed is the red-shift due to the band gap shrinkage. This so-called “S”-shape effect of $E(T)$ is discussed in Sect. 11.4 in detail with regard to exciton localization in a quantum well disorder potential.

For $x = 0.06$ only a single photoluminescence peak is observed for the alloy ($\sigma = 8.5\,$meV). The (D^0,X) peak is the dominant for the $Mg_xZn_{1-x}O$

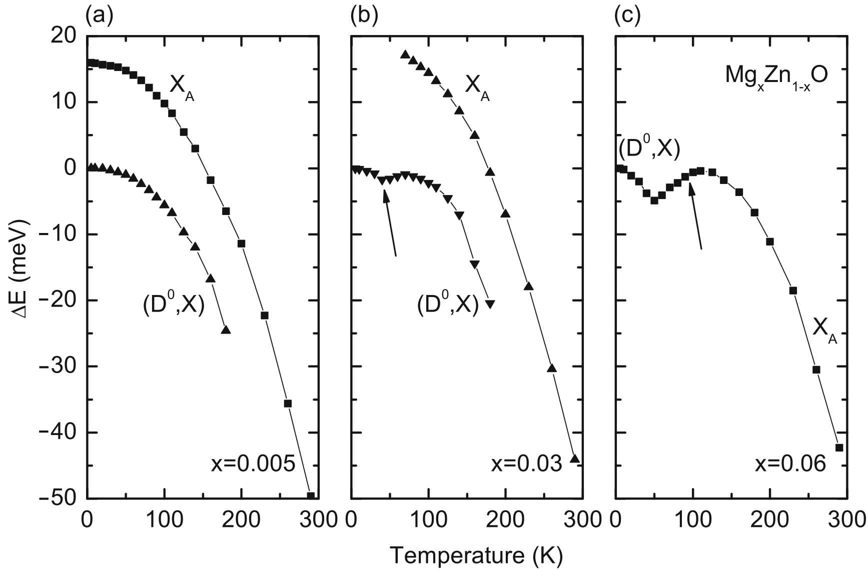

Fig. 10.16. Temperature dependence of the shift of energy position of (D^0,X) and X_A photoluminescence peak in $Mg_xZn_{1-x}O$ alloys with three different Mg-contents, (**a**) $x = 0.005$, (**b**) $x = 0.03$, (**c**) $x = 0.06$. The energy positions are given relative to the low temperature position of the respective (D^0,X) peaks. Adapted from [694]

alloys at low temperatures even in the presence of large alloy broadening (Fig. 10.15(b)). The peak changes its nature from (D^0,X) at low temperatures to X_A at room temperature. In between, first exciton thermalization (red-shift) in the disorder potential and subsequently exciton ionization from the donors (blue-shift, arrow in Fig. 10.16(c)) are observed [694]. Such exciton ionization from impurities has also been observed for AlGaN:Si [429, 696].

10.4 Phonon Replica

The momentum selection rule for free-exciton recombination allows only excitons with $\mathbf{K} \approx 0$ (for $\mathbf{K}$, cf. (9.28)) to recombine. The fine structure of this recombination is connected to polariton effects (cf. Sect. 9.5.9). Excitons with large $\mathbf{K}$ can recombine if a phonon or several phonons are involved [697] that provide the necessary momentum $\mathbf{q} = \mathbf{K}_1 - \mathbf{K}_2$, with $\mathbf{K}_1$ ($\mathbf{K}_2$) being the wavevector of the initial (intermediate) exciton state (Fig. 10.17). A so-called *zero-phonon* line at energy E_0 is then accompanied by *phonon replica* below E_0 at integer multiples (at low temperature) of the (LO) phonon energy $\hbar\omega_{\mathrm{ph}}$

$$E_n = E_0 - n\,\hbar\omega_{\mathrm{ph}} \; . \tag{10.31}$$

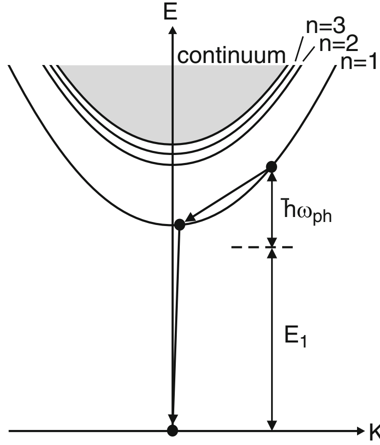

Fig. 10.17. Schematic representation of 1 LO exciton scattering of an exciton at $\mathbf{K} \neq 0$ to an intermediate state with $\mathbf{K} \approx 0$ and subsequent radiative decay. $\hbar\omega$ represents the phonon energy and E_1 the energy of the emitted photon

Phonon replicas have been observed in many polar semiconductors such as CdS [698] and ZnSe [699]. A sequence of such phonon replica, as observed in GaN [700], is depicted in Fig. 10.18a.

The lineshape of the n-th phonon-assisted line is proportional to the exciton population at a given excess energy, which is proportional to the density of states and the Boltzmann distribution function [701]

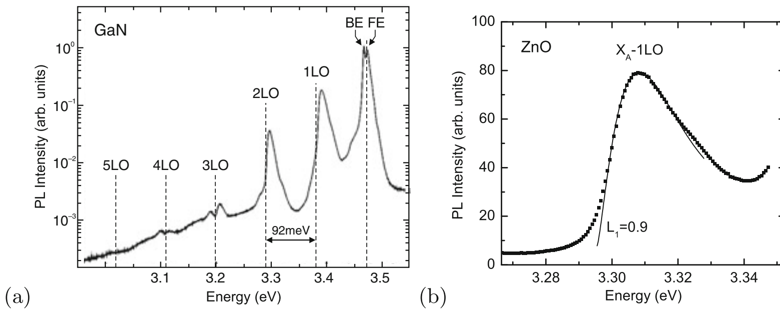

Fig. 10.18. (**a**) Photoluminescence spectrum of GaN (grown on SiC substrate) at $T = 50\,\mathrm{K}$. In addition to emission from free (FE) and bound (BE) excitons several phonon replica (labeled as 1LO–5LO) are observed. *Vertical dashed lines* indicate energy positions of multiple LO-phonon energies ($\hbar\omega_{\mathrm{LO}} = 92\,\mathrm{meV}$) below the FE peak. Adapted from [700]. (**b**) Photoluminescence spectrum of 1LO phonon-assisted recombination peak at $T = 103\,\mathrm{K}$ (from the data of Fig. 10.4). Data points (*dots*) and lineshape fit (*solid line*) according to (10.32) with the parameters $L_1 = 0.9$ and $E_1 = 3.2955\,\mathrm{eV}$ (and background)

$$I_n(E_{\rm ex}) \propto \sqrt{E_{\rm ex}}\, \exp\left(-\frac{E_{\rm ex}}{kT}\right) w_n(E_{\rm ex})\ . \tag{10.32}$$

Here, $E_{\rm ex}$ represents the exciton kinetic energy. The factor $w_n(E_{\rm ex})$ accounts for the **q**-dependence of the matrix element. It is typically expressed as

$$w_n(E_{\rm ex}) \propto E_{\rm ex}^{L_n}\ . \tag{10.33}$$

Accordingly, the energy separation ΔE_n of the energy of the peak maximum of phonon replica from E_0 is given by

$$\Delta E_n = E_n - E_0 = n\,\hbar\omega_{\rm ph} + \left(L_n + \frac{1}{2}\right) kT\ . \tag{10.34}$$

It is found theoretically that $L_1 = 1$ and $L_2 = 0$ [718]. These relations are approximately fulfilled for GaN [702]. A lineshape fit for the 1 LO phonon-assisted transition in ZnO is shown in Fig. 10.18b.

In Fig. 10.19a the 'green band' emission of ZnO is shown as presented in [703]. This band is mostly attributed to a Cu impurity; recently, evidence has grown from isotope decay and annealing studies that it is related to the zinc vacancy [704] (Fig. 10.19b). The zero phonon line is followed by many replica with a maximum at about 6 LO phonons. The intensity I_N of the N-th replica is given by [705, 706]

$$I_N \propto \exp(-S)\, \frac{S^N}{N!}\ , \tag{10.35}$$

where S is the so-called Huang–Rhys parameter. In [704], a coupling parameter of $S = 6.9$ has been determined.

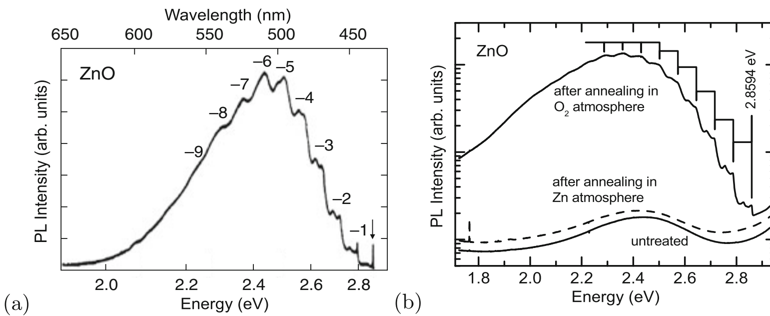

Fig. 10.19. (**a**) Luminescence spectrum of ZnO in the visible. The *arrow* denotes the zero-phonon line at 2.8590 eV. The numbers of the phonon replica are labeled. Adapted from [703]. (**b**) Luminescence spectra (*solid lines*) of a ZnO bulk crystal before ('untreated') and after annealing in O_2 atmosphere at $T = 1073$ K. After annealing in Zn atmosphere at the same temperature, the green band disappears again (*dashed line*). From [704]

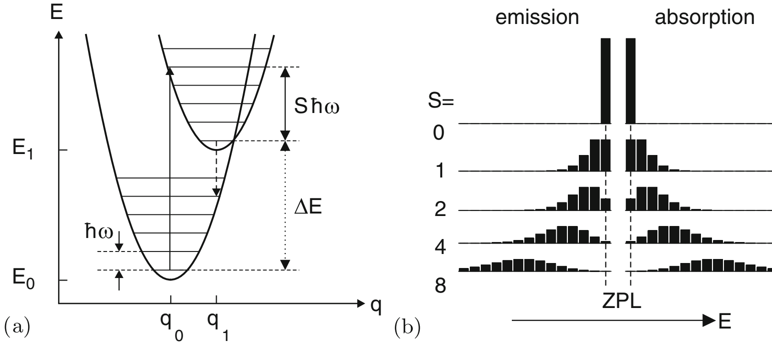

Fig. 10.20. (**a**) Configuration diagram of two states that differ in their configuration coordinate by $\delta q = q_1 - q_0$. Both are coupled to phonons of energy $\hbar\omega$. The absorption maximum (*solid vertical line*) and emission maximum (*dashed vertical line*) are shifted with respect to the zero-phonon line (*dotted vertical line*) with energy $E_1 - E_0$. The Huang–Rhys parameter is $S \sim 4$. (**b**) Intensity of zero-phonon line ('ZPL') and phonon replica (10.35) for emission and absorption processes with different values of the Huang–Rhys parameter S as labeled

Equation (10.35) is obtained from the consideration of transitions in the configuration diagram [705, 707] (Fig. 10.20), using the Born–Oppenheimer approximation. Here the electronic wavefunctions are separated from the vibrational wavefunctions, leading to the Franck–Condon principle, that optical transitions occur with the positions of the nuclei fixed and thus vertical in the configuration diagram Fig. 10.20. Assuming low temperatures, only the lowest state is (partially) occupied. The Huang–Rhys parameter, the average number of phonons involved in the transition, is related to the displacement $\delta q = q_1 - q_0$ of the two configurations

$$S = \frac{C\,\delta q^2}{2\hbar\omega_{\mathrm{ph}}}\,, \tag{10.36}$$

where C is the 'spring constant' of the parabola, $C = \mathrm{d}^2E/\mathrm{d}q^2$.

For small $S \ll 1$, we are in the weak coupling regime and the zero-phonon line is the strongest. In the strong coupling regime, $S > 1$, the maximum is (red-) shifted from the zero-phonon line. We note that in absorption, phonon replica occur on the high-energy side of the zero-phonon absorption. For large S the peak intensities are close to a Gaussian. The correspondence of emission and absorption is nicely seen for excitons on isoelectronic oxygen traps in ZnTe [708]. The oxygen is on substitutional Te site. Up to seven phonon replica are visible in Fig. 10.21 around the zero-phonon or A-line with a separation of about 26 meV, the optical phonon energy in ZnTe. The Huang-Rhys parameter is about 3–4. Other peaks are due to acoustic phonons.

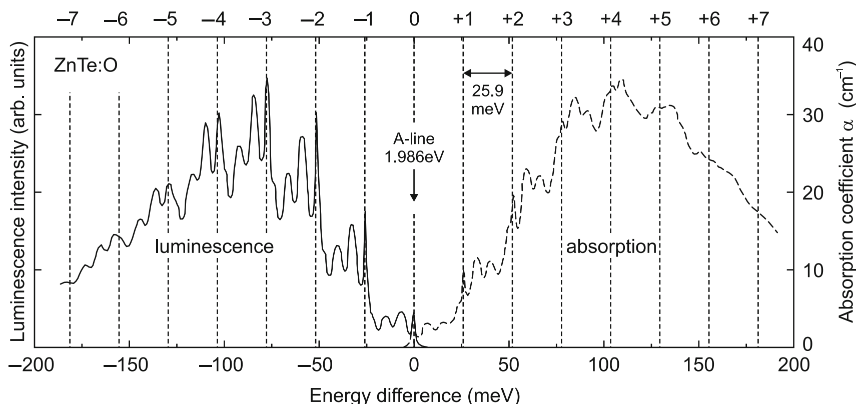

Fig. 10.21. Photoluminescence (*solid line*) and absorption (*dashed line*) spectra of excitons bound to substitutional oxygen in ZnTe at $T = 20\,\mathrm{K}$. The energy position is relative to the A-line at 1.9860 eV. The *vertical dashed lines* have a separation of 25.9 meV. Adapted from [708]

10.5 Self-absorption

Luminescence that is emitted within the semiconductor can be (re-)absorbed before it may reach the surface and can leave the crystal. This effect is called self-absorption. It is particularly strong for radiation with an energy where the absorption $\alpha(\hbar\omega)$ is high, i.e. above the band gap of a direct semiconductor. Similarly to the penetration depth $1/\alpha$ for radiation entering the crystal, emission approximately occurs only from a layer of such thickness. For typical values of α in the range of $10^5\,\mathrm{cm}^{-1}$, the 'skin' of the semiconductor that emits light with energy above the band gap is 100 nm. For light at the low energy side of the band gap or with energy within the band gap (deep levels), the emission depth can be much larger.

After re-absorption, the energy has another chance to relax non-radiatively, thus reducing the quantum efficiency. Alternatively it can be reemitted, either at the same energy or at a lower energy. Possibly several re-absorption processes occur before a photon eventually leaves the semiconductor ('photon recycling'). Such processes are important in LED structures where photon extraction has to be optimized (Sect. 22.3.4). Emission on phonon replica (Sect. 10.4) is red-shifted from the energy range of strong absorption and thus suffers no (or only little) self-absorption. This can be seen from the spectrum of a thick ZnO crystal excited homogeneously (via two-photon absorption with a red Ruby laser), Fig. 10.22. The zero phonon line (at E_{X}), originating from the $\approx 100\,\mathrm{nm}$ skin of the samples and being by far the strongest in thin films (Fig. 10.4), is practically absent and emission on the phonon replica collected from the entire volume dominates the spectrum.

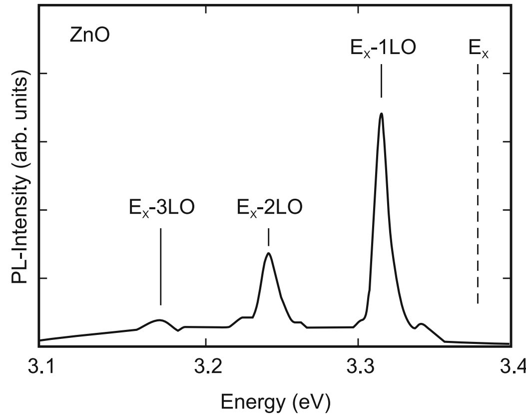

Fig. 10.22. Photoluminescence spectrum (at $T = 55\,\mathrm{K}$) from bulk ZnO excited homogeneously via two-photon excitation by a Q-switched ruby laser (pulse width 40 ns). Adapted from [709]

10.6 Donor–Acceptor Pair Transitions

Optical transitions can occur between neutral donors and acceptors. The (spatially indirect) donor–acceptor pair (DAP) recombination is present in (partially) compensated semiconductors and follows the scheme $D^0A^0 \rightarrow D^+A^-eh \rightarrow D^+A^- \; + \; \gamma$, where γ is a photon with the energy $\hbar\omega$. The energy of the emitted photon is given by

$$\hbar\omega = E_{\mathrm{g}} - E_{\mathrm{D}}^{\mathrm{b}} - E_{\mathrm{A}}^{\mathrm{b}} + \frac{1}{4\pi\epsilon_0}\,\frac{e^2}{\epsilon_{\mathrm{r}}R}\;, \tag{10.37}$$

where R is the distance between the donor and the acceptor for a specific pair. Since R is discrete, the DAP recombination spectrum consists of several discrete lines. If the donor and acceptor occupy the same sublattice, e.g. O and C both substituting P sites in GaP, the spatial distance of the donor and acceptor is $R(n) = a_0\sqrt{n/2}$, where a_0 is the lattice constant and n is an integer. However, for certain 'magic' numbers $n = 14, 30, 46, \ldots$ no lattice points exist and therefore the corresponding lines are missing (labeled 'G' in Fig. 10.23). No such gaps exist in DA spectra where donors and acceptors occupy different sublattices, e.g. GaP:O,Zn (see also Fig. 10.23). In this case, the spatial separation is given by $R(n) = a_0\sqrt{n/2 - 5/16}$. If significant broadening is present, the lines are washed out and a donor–acceptor pair band forms.

10.7 Inner-Impurity Recombination

The transitions of electrons between different states of an impurity level can be nonradiative or radiative. As an example, the radiative transition of elec-

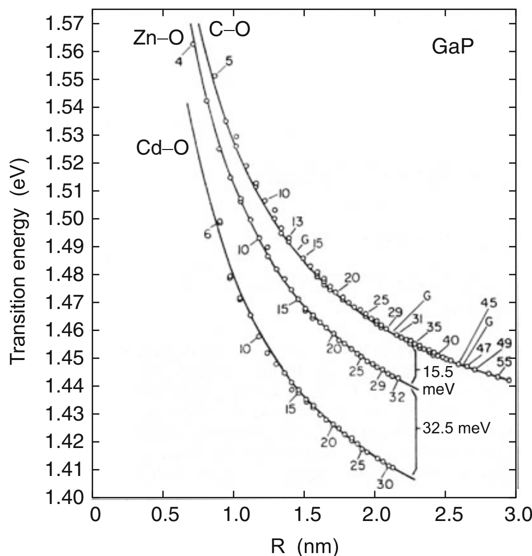

Fig. 10.23. Transition energies in GaP ($T = 1.6$ K) of the donor–acceptor recombination involving the deep oxygen donor and C, Zn, and Cd acceptors, respectively. The lines follow (10.37) for $E_g^{\rm GaP} = 2.339$ eV, $\epsilon_r = 11.1$ and $(E_D^b)_O = 893$ meV, $(E_A^b)_C = 48.5$ meV, $(E_A^b)_{Zn} = 64$ meV, and $(E_A^b)_{Cd} = 96.5$ meV. Predicted missing modes for GaP:C,O are labeled with 'G'. Adapted from [710]

trons in the Fe^{2+} state in InP ${}^5T_2 \rightarrow {}^5E$ (Fig. 10.24) and its fine structure were observed first in [711] at around 0.35 eV.

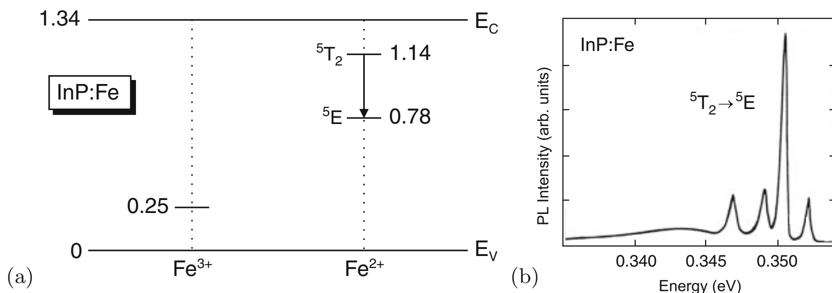

Fig. 10.24. (**a**) Schematic band diagram of InP with levels of Fe impurities in the 3+ and 2+ charge states at low temperature. All energies are given in eV. The *arrow* denotes the optical transition from an excited Fe^{2+} state to the Fe^{2+} ground state. (**b**) Photoluminescence spectrum (at $T = 4.2$ K) of InP:Fe sample with [Fe]=$5 \times 10^{16}\,\mathrm{cm}^{-3}$. Part (**b**) adapted from [712]

10.8 Auger Recombination

In competition with the radiative, bimolecular recombination is the Auger recombination (Fig. 10.25). In the Auger process, the energy that is released during the recombination of an electron and hole is not emitted with a photon but, instead, transferred to a third particle. This can be an electron (eeh, Fig. 10.25a) or a hole (hhe, Fig. 10.25b). The energy is eventually transferred nonradiatively from the hot third carrier via phonon emission to the lattice. The probability for such process is $\propto n^2p$ if two electrons are involved and $\propto np^2$ if two holes are involved. The Auger process is a three-particle process and becomes likely for high carrier density, either through doping, in the presence of many excess carriers, or in semiconductors with small band gap. Auger recombination is the inverse of the impact ionization (cf. Sect. 8.5.4). Phonon-assisted Auger recombination relaxes the momentum conservation rule for the involved charge carriers at the cost of an additional particle being involved in the scattering process. It has been pointed out that this process is dominating in bulk material [713] and quantum wells [714].

In thermodynamic equilibrium the rates for Auger recombination and thermal Auger generation must be equal, thus

$$G_{\mathrm{th}} = C_{\mathrm{n}}\, n_0^2\, p_0 + C_{\mathrm{p}}\, n_0\, p_0^2\ , \tag{10.38}$$

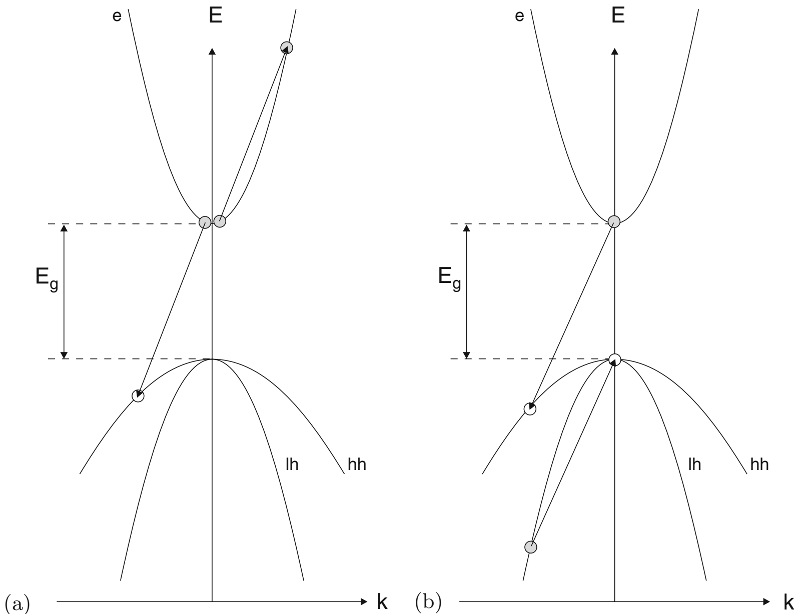

Fig. 10.25. Schematic representation of Auger recombination. An electron recombines with a hole and transfers the energy to (**a**) another electron in the conduction band, (**b**) another electron in the valence band

Table 10.3. Auger recombination coefficients for some semiconductors. Data for InSb from [715], SiC from [655], others from [656]

material	C_n (cm^6/s)	C_p (cm^6/s)
4H-SiC	5×10^{-31}	2×10^{-31}
Si, Ge	2.8×10^{-31}	9.9×10^{-32}
GaAs, InP	5.0×10^{-30}	3.0×10^{-30}
InSb	1.2×10^{-26}	

where C_n and C_p denote the Auger recombination coefficients. The equation for the dynamics in the presence of excess carriers (if solely Auger recombination is present) is given as

$$\frac{\partial\, \delta n}{\partial t} = G_{th} - R = -C_n\,(n^2\,p - n_0^2\,p_0) - C_p\,(n\,p^2 - n_0\,p_0^2)\ . \tag{10.39}$$

The Auger recombination rate typically used in SRH kinetics is

$$r_{Auger} = (C_n\,n + C_p\,p)\,(np - n_0 p_0)\ . \tag{10.40}$$

Typical values for the Auger recombination coefficients are given in Table 10.3.

In Fig. 10.26a the electron lifetime in heavily p-doped InGaAs (lattice matched to InP) is shown [716]. It follows $\tau_n^{-1} = C_p\,N_A^2$ as expected from (10.39) for p-type material. The Auger process in silicon has been discussed

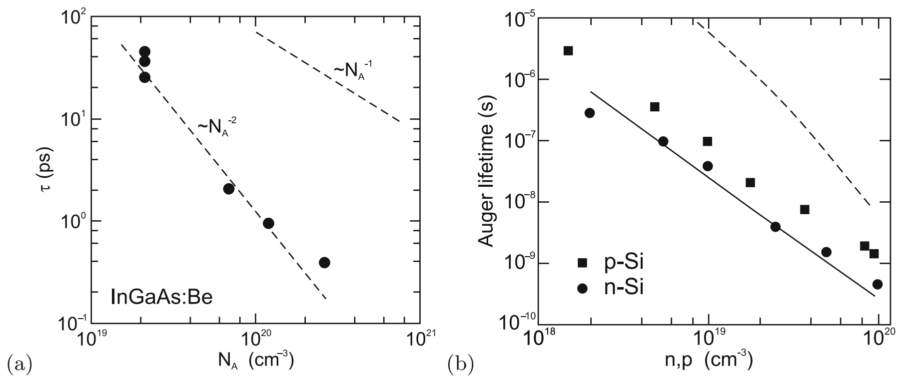

Fig. 10.26. (**a**) Experimental values of the electron lifetime in heavily p-doped InGaAs on InP at room temperature. The *dashed lines* show dependencies of Auger ($\propto N_A^{-2}$, $C_p = 8.1 \times 10^{-29}\,cm^{-6}\,s^{-1}$) and band-band recombination ($\propto N_A^{-1}$, $B = 1.43 \times 10^{-10}\,cm^{-3}\,s^{-1}$). Adapted from [716]. (**b**) Experimental Auger lifetimes in p-type (*squares*) and n-type (*circles*) silicon at 300 K. The *dashed* (*solid*) *line* is theory for p-type (n-type) material. Adapted from [717]

in detail [711]. In Fig. 10.26b experimental data for n-type and p-type Si are summarized. Auger theory can predict the lifetimes in n-type material. The predicted rate in p-type material is too small, thus a phonon-assisted process is evoked [711].

10.9 Band–Impurity Recombination

A very important recombination process is the capture of carriers by impurities. This process is in competition with all other recombination processes, e.g. the radiative recombination and the Auger mechanism. The band–impurity recombination is the inverse process to the carrier release from impurities and intimately related to carriers statistics (Sect. 7). It is particularly important at low carrier densities, for high dopant concentration and in indirect semiconductors since for these the bimolecular recombination is slow. This process is generally considered to be non-radiative since no photons close to the band edge are emitted.[2]

10.9.1 Shockley-Read-Hall Kinetics

The theory of capture on and recombination involving impurities is called Shockley–Read–Hall (SRH) kinetics [650, 651]. An example of radiative band–impurity recombination (of the type shown in Fig. 10.27a) is shown in Fig. 10.7 for the (e,A^0) recombination at the carbon acceptor in GaAs.

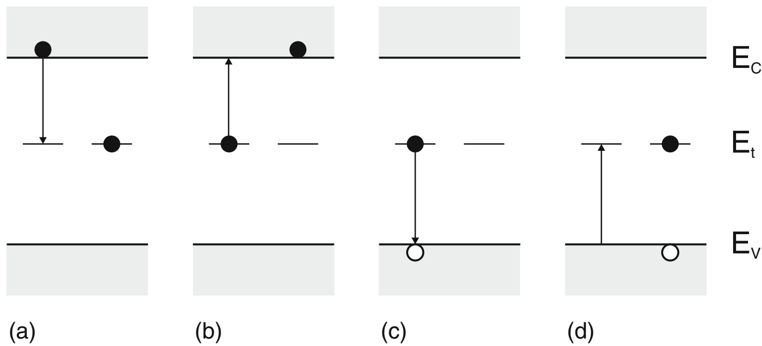

Fig. 10.27. Band-to-impurity processes at an impurity with one level (*left*: initial, *right*: final state in each part): (**a**) electron capture (from conduction band), (**b**) electron emission (into conduction band), (**c**) hole capture (from valence band), (**d**) hole emission (into valence band). The *arrows* indicate the transition of the electron

[2] Depending on the energetic depth of the trap, mid or far infrared photons can be emitted.

We consider electron traps [718] (see Fig. 10.27) with a concentration N_t with an energy level E_t. In thermodynamic equilibrium they have an electron population

$$f_\mathrm{t}^0 = \frac{1}{\exp\left(\frac{E_\mathrm{t}-E_\mathrm{F}}{kT}\right)+1} \;, \tag{10.41}$$

where f_t is the nonequilibrium population of the trap. Then the capture rate r_c is proportional to the unoccupied traps and the electron concentration, $r_\mathrm{c} \propto nN_\mathrm{t}(1-f_\mathrm{t})$. The proportionality factor has the form $v_\mathrm{th}\sigma_\mathrm{n}$, where v_th is the thermal velocity $v_\mathrm{th} = \sqrt{3kT/m^*} \approx 10^7$ cm/s and σ_n is the capture cross section that is of atomic scale, typically $\sim 10^{-15}\mathrm{cm}^2$. The capture cross section can be related to the optical absorption cross section [395, 396].

In order to make the following calculation more transparent, we put the effective-mass ratio $\sqrt{m_0/m^*}$ into σ in the following and thus have the same thermal velocity $v_\mathrm{th} = \sqrt{3kT/m_0}$ for electrons and holes. The capture rate of electrons is

$$r_\mathrm{c} = v_\mathrm{th}\,\sigma_\mathrm{n}\,n\,N_\mathrm{t}\,(1-f_\mathrm{t}) \;. \tag{10.42}$$

The emission rate from filled traps is

$$g_\mathrm{c} = e_\mathrm{n}\,N_\mathrm{t}\,f_\mathrm{t} \;, \tag{10.43}$$

where e_n denotes the emission probability. In a similar way, the emission and capture rates for holes can be written:

$$r_\mathrm{v} = v_\mathrm{th}\,\sigma_\mathrm{p}\,p\,N_\mathrm{t}\,f_\mathrm{t} \tag{10.44}$$

$$g_\mathrm{v} = e_\mathrm{p}\,N_\mathrm{t}\,(1-f_\mathrm{t}) \;. \tag{10.45}$$

In thermodynamical equilibrium, capture and generation rates are equal, i.e. $r_\mathrm{c} = g_\mathrm{c}$ and $r_\mathrm{v} = g_\mathrm{v}$. Thus, the emission probability is

$$e_\mathrm{n} = v_\mathrm{th}\,\sigma_\mathrm{n}\,n_0\,\frac{1-f_\mathrm{t}^0}{f_\mathrm{t}^0} \;. \tag{10.46}$$

Using $\frac{1-f_\mathrm{t}^0}{f_\mathrm{t}^0} = \exp\left(\frac{E_\mathrm{t}-E_\mathrm{F}}{kT}\right)$, (7.15) and (7.16) the emission probabilities can be written as

$$e_\mathrm{n} = v_\mathrm{th}\,\sigma_\mathrm{n}\,n_\mathrm{t} \tag{10.47}$$

$$e_\mathrm{v} = v_\mathrm{th}\,\sigma_\mathrm{p}\,p_\mathrm{t} \;, \tag{10.48}$$

with

$$n_\mathrm{t} = N_\mathrm{C}\,\exp\left(\frac{E_\mathrm{t}-E_\mathrm{C}}{kT}\right) \tag{10.49}$$

$$p_\mathrm{t} = N_\mathrm{V}\,\exp\left(-\frac{E_\mathrm{t}-E_\mathrm{V}}{kT}\right) \;. \tag{10.50}$$

We note that (cf. (7.20)) $n_\mathrm{t}\, p_\mathrm{t} = n_0\, p_0$.

The temperature dependence of the thermal velocity is $\propto T^{1/2}$, the temperature dependence of the band-edge density of states is $\propto T^{3/2}$ (7.10) and (7.13). Thus, the temperature dependence of the emission rate

$$r_\mathrm{c} = g_\mathrm{c} = v_\mathrm{th}\, \sigma_\mathrm{n}\, N_\mathrm{t}\, N_\mathrm{C}\, \exp\left(\frac{E_\mathrm{t} - E_\mathrm{C}}{kT}\right) f_\mathrm{t} \tag{10.51}$$

is (apart from the exponential term) $\propto T^2$ if σ is temperature independent.

Charge conservation requires $r_\mathrm{c} - r_\mathrm{v} = g_\mathrm{c} - g_\mathrm{v}$. From this we obtain the population function in nonequilibrium:

$$f_\mathrm{t} = \frac{\sigma_\mathrm{n} n + \sigma_\mathrm{p} p}{\sigma_\mathrm{n}\,(n + n_\mathrm{t}) + \sigma_\mathrm{p}\,(p + p_\mathrm{t})}\ . \tag{10.52}$$

The recombination rate $r_{\mathrm{b-i}}$ of the band–impurity recombination is then

$$\begin{aligned} r_{\mathrm{b-i}} = -\frac{\partial \delta n}{\partial t} &= r_\mathrm{c} - g_\mathrm{c} \\ &= \frac{\sigma_\mathrm{n}\, \sigma_\mathrm{p}\, v_\mathrm{th}\, N_\mathrm{t}}{\sigma_\mathrm{n}\,(n + n_\mathrm{t}) + \sigma_\mathrm{p}\,(p + p_\mathrm{t})}\,(np - n_0 p_0)\ . \end{aligned} \tag{10.53}$$

Using the ‘lifetimes’

$$\tau_{n_0} = (\sigma_\mathrm{n} v_\mathrm{th} N_\mathrm{t})^{-1} \tag{10.54}$$

$$\tau_{p_0} = (\sigma_\mathrm{p} v_\mathrm{th} N_\mathrm{t})^{-1}\ , \tag{10.55}$$

this is typically written as

$$r_{\mathrm{b-i}} = \frac{1}{\tau_{n_0}(n + n_\mathrm{t}) + \tau_{p_0}(p + p_\mathrm{t})}\,(np - n_0 p_0)\ . \tag{10.56}$$

For an n-type semiconductor the Fermi level is above E_t and the traps are mostly full. Thus hole capture is the dominating process. The equation for the dynamics simplifies to

$$\frac{\partial \delta p}{\partial t} = -\frac{p - p_0}{\tau_{p_0}}\ . \tag{10.57}$$

Thus, an exponential decay with minority-carrier lifetime τ_{p_0} (or τ_{n_0} for p-type material) occurs.

A recombination center is most effective when it is close to the middle of the band gap (midgap level). The condition $\partial r_{\mathrm{b-i}}/\partial E_\mathrm{t} = 0$ leads to the trap energy $E_\mathrm{t}^\mathrm{max}$ with the maximum recombination rate being located at

$$E_{\mathrm{t}}^{\max} = \frac{E_{\mathrm{C}} + E_{\mathrm{V}}}{2} - kT \, \ln \left(\frac{\sigma_{\mathrm{n}} \, N_{\mathrm{C}}}{\sigma_{\mathrm{p}} \, N_{\mathrm{V}}} \right) \, . \tag{10.58}$$

The curvature $\partial^2 r_{\mathrm{b-i}} / \partial E_{\mathrm{t}}^2$ at $E_{\mathrm{t}}^{\max}$ is proportional to $-(np - n_0 p_0)$ and thus indeed is negative in the presence of excess carriers. However, the maximum can be fairly broad.

The SRH kinetic presented here is valid for low densities of recombination centers. A more detailed discussion and a more general model can be found in [719].

A typical example for a recombination center is gold in silicon. The minority carrier lifetime decreases from 2×10^{-7} s to 2×10^{-10} s upon increase of the Au concentration from 10^{14} to 10^{17} cm^{-3}. The incorporation of recombination centers is an important measure for the design of high-frequency devices [720]. Due to importance in silicon technology the recombination properties of many metals in silicon have been investigated, in particular Fe-contamination and the role of FeB-complexes [721–723].

A reduction in minority-carrier lifetime can also be achieved by irradiation with high-energy particles and the subsequent generation of point defects with energy levels at midgap.

In Fig. 10.28 various data on minority carrier lifetime in silicon are compiled. Over some doping range, a dependence of the lifetime $\propto N^{-1}$ as in (10.54) prevails. For doping beyond the 10^{19} cm^{-3} range, Auger recombination (Sect. 10.8) with $\tau \propto N^{-2}$ is dominant. A more detailed discussion can be found in [724, 725]. Generally the lifetimes are temperature dependent [726] as expected from (10.54).

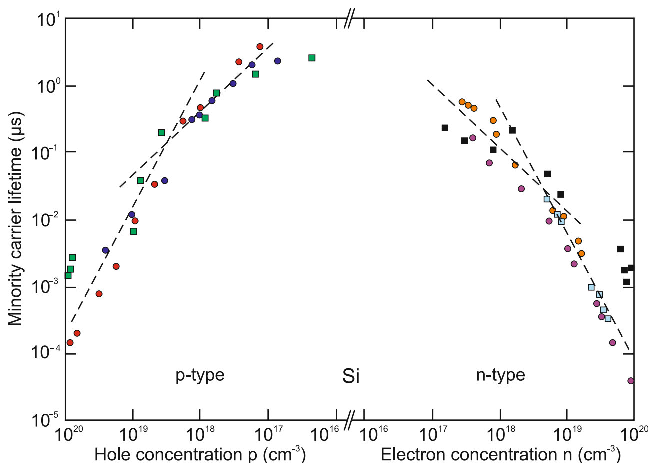

Fig. 10.28. Minority carrier lifetime at room temperature as a function of majority carrier concentration in n-type and p-type silicon. The *dashed lines* have the slopes N^{-1} and N^{-2}. Data from [725]

10.9.2 Multilevel Traps

Traps with multiple levels in the band gap have generally similar but more complicated dynamics as compared to single-level traps. Lifetimes are an average over negatively and positively charged states of the trap.

10.10 Field Effect

The emission of electrons from a trap is thermally activated with an ionization energy $E_\mathrm{i} = E_\mathrm{C} - E_\mathrm{t}$. If the trap is in a strong electric field $\mathcal{E}$, the emission probability can change. An acceptor-like trap after removal of the electron is neutral and its potential is short range. A donor has a long-range Coulomb potential after ionization. In an electric field, these potentials are modified as visualized in Fig. 10.29. Various additional processes can now occur.

10.10.1 Thermally Activated Emission

For the δ-like potential the ionization energy remains unchanged. For the Coulomb potential the barrier in the field direction is lowered by

$$\Delta E_\mathrm{i} = e\sqrt{\frac{e\mathcal{E}}{\pi\epsilon_0\epsilon_r}}\,. \tag{10.59}$$

The emission probability is increased in the field by $\exp(\Delta E_\mathrm{i}/kT)$. This effect is called the Poole–Frenkel effect [727] and can be quite important. For silicon and $\mathcal{E} = 2\times10^5$ V/cm and $\Delta E_\mathrm{i} = 100$ meV a 50-fold increase of emission rate results at room temperature.

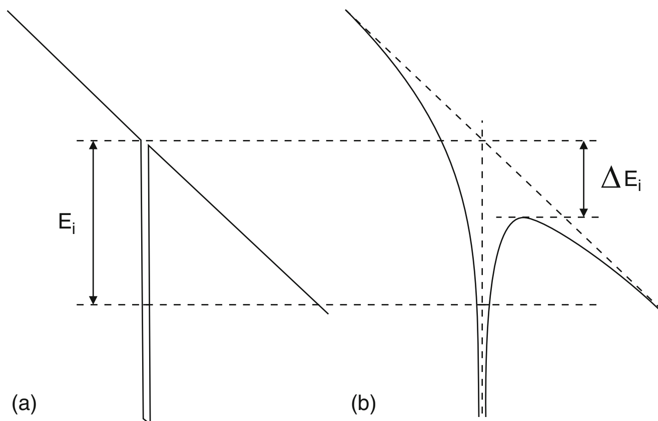

Fig. 10.29. Field effect at (**a**) a δ-like potential and (**b**) a Coulomb potential

10.10.2 Direct Tunneling

Carriers can tunnel from the trap level through the barrier in the field direction into the conduction band. This process is temperature independent. The transmission factor of a barrier is (in WKB approximation) proportional to $\exp[-(2/\hbar) \int \sqrt{2m[V(x)-E]}\, \mathrm{d}E]$. The emission probability for a triangular barrier is then

$$e_{\mathrm{n}} = \frac{e\mathcal{E}}{4\sqrt{2m^* E_{\mathrm{i}}}} \exp\left(-\frac{4\sqrt{2m^*}\, E_{\mathrm{i}}^{3/2}}{3e\hbar\,\mathcal{E}}\right) . \tag{10.60}$$

In the case of a Coulomb-like potential the argument of the exponent in (10.60) needs to be multiplied by a factor $1 - (\Delta E_{\mathrm{i}}/E_{\mathrm{i}})^{5/3}$ with ΔE_{i} from (10.59).

10.10.3 Assisted Tunneling

In a thermally assisted tunneling process the electron on the trap level is first excited to a virtual level $E_{\mathrm{t}} + E_{\mathrm{ph}}$ by phonon absorption and then tunnels out of the trap (photon-assisted tunneling). From the energetically higher level the tunneling rate is higher. The probability is proportional to $\exp{(E_{\mathrm{ph}}/kT)}$. The additional energy can also be supplied by a photon (photon-assisted tunneling).

10.11 Recombination at Extended Defects

10.11.1 Surfaces

A surface is typically a source of recombination, e.g. by midgap levels induced by the break of crystal symmetry. The recombination at surfaces is modeled as a recombination current

$$j_{\mathrm{s}} = -e\, S\, (n_{\mathrm{s}} - n_0) \ , \tag{10.61}$$

where n_{s} is the carrier density at the surface and S is the so-called *surface recombination velocity*.

The surface recombination velocity for GaAs is shown in Fig. 10.30. For InP, if the surface Fermi level is pinned close to midgap, the surface recombination velocity increases from $\sim 5 \times 10^{-3}$ cm/s for a doping level of $n \sim 3 \times 10^{15}\,\mathrm{cm}^{-3}$ to $\sim 10^6$ cm/s for a doping level of $n \sim 3 \times 10^{18}\,\mathrm{cm}^{-3}$ [728]. For Si, the surface recombination rate depends on the treatment of the surface and lies in the range between 10–10^4 cm/s [729, 730]. The Si-SiO_2 interface can exhibit $S \leq 0.5$ cm/s. Time-resolved measurements and detailed modeling for Si have been reported in [731].

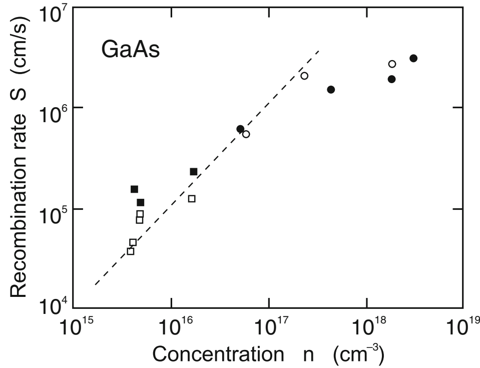

Fig. 10.30. Surface recombination velocity for GaAs as a function of n-type doping concentration. Different experimental points correspond to different surface treatment methods. *Dashed line* is a guide to the eye. Experimental data from [732]

10.11.2 Grain Boundaries

Grain boundaries can be a source of non-radiative recombination. This is technologically important for solar cells made from polycrystalline silicon (cf. Sect. 21.4.6). The grain boundary can be understood as an inner surface in the crystal. Modelling of recombination at a grain boundary can be done using an interface recombination velocity [733, 734] or considering deep traps [735]. The minority carrier lifetime decreases with decreasing grain boundary area A (Fig. 10.31a). The carrier loss at a grain boundary can be imaged directly via the efficiency of the collection of an electron beam induced current (EBIC) as shown in Fig. 10.31b. The minority carrier lifetime is only unaffected when the average distance to a grain boundary is much larger than the minority carrier diffusion length, $\sqrt{A} \gg L_{\mathrm{D}}$, otherwise the entire grain volume is subject to non-radiative recombination.

10.11.3 Dislocations

Also dislocations typically act as recombination centers, sometimes called carrier sinks. In Fig. 10.32 it can be seen that the minority carrier lifetime depends on the dislocation density n_{d} and follows a $\tau^{-1} \propto n_{\mathrm{d}}$ law, as if each dislocation is a recombination center [736]. The non-radiative recombination makes dislocations appear as 'dark line defects' in luminescence imaging [737]. In [738] also the decrease of carrier lifetime around (misfit) dislocations has been imaged. The effect of dislocations on the radiative recombination efficiency depends on the diffusion length [738].

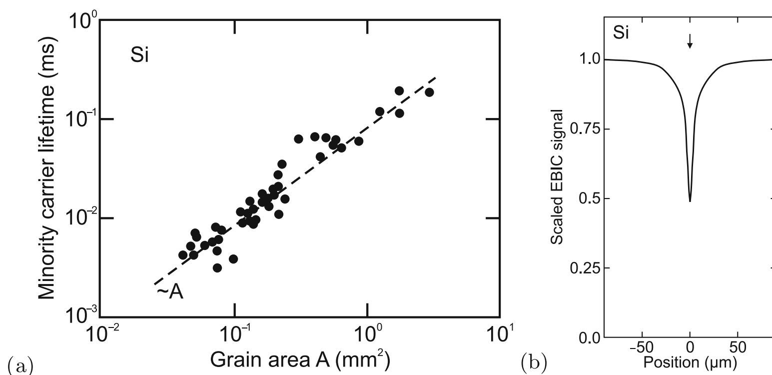

Fig. 10.31. (**a**) Minority carrier lifetime in (p-type) silicon as a function of grain boundary size. The *dashed line* has the slope $\propto A$. Data from [739]. (**b**) Linescan of the electron beam induced current (EBIC) perpendicular to a single grain boundary in silicon. The arrow denotes the position of the grain boundary. Compiled from [740]

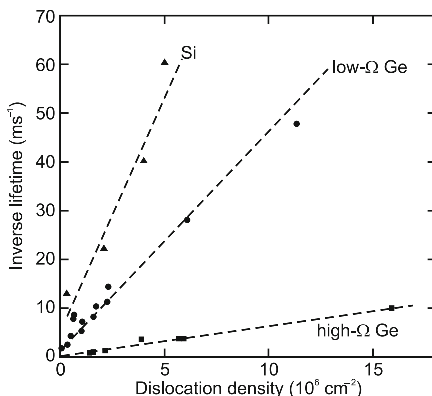

Fig. 10.32. Inverse minority carrier lifetime in n-type silicon (40 Ω cm), low resistivity Ge (3–5 Ω cm) and high resistivity Ge (30–40 Ω cm). Data from [736]

10.12 Excess-Carrier Profiles

In this section, some typical excess-carrier profiles (in one-dimensional geometry) are discussed that arise from certain excitation conditions. The excess-carrier density Δp (here holes in an n-type semiconductor, i.e. $\Delta p = p_\mathrm{n} - p_{\mathrm{n}_0}$) is determined by the diffusion equation (cf. (8.62a))

$$D_\mathrm{p} \frac{\partial^2 \Delta p}{\partial x^2} + \frac{\Delta p}{\tau_\mathrm{p}} = -G(x) \; . \tag{10.62}$$

10.12.1 Generation at Surface

First, the generation of excess carriers in a semi-infinite piece of semiconductor shall occur only at the surface at $x = 0$. The generation is zero everywhere else and the excitation is incorporated via the boundary condition $\Delta p(x = 0) = \Delta p_0$. The general solution for the homogeneous equation (10.62), i.e. $G = 0$, is

$$\Delta p(x) = C_1 \exp\left(-\frac{x}{L_\mathrm{p}}\right) + C_2 \exp\left(\frac{x}{L_\mathrm{p}}\right) , \tag{10.63}$$

with the diffusion length $L_\mathrm{p} = \sqrt{D_\mathrm{p}\tau_\mathrm{p}}$. Taking the boundary condition $\Delta p(x \to \infty) = 0$ the solution is

$$\Delta p(x) = \Delta p_0 \exp\left(-\frac{x}{L_\mathrm{p}}\right) . \tag{10.64}$$

In order to connect Δp_0 with the total generation rate per unit area G_tot, we calculate

$$G_\mathrm{tot} = \int_0^\infty \frac{\Delta p(x)}{\tau_\mathrm{p}}\, \mathrm{d}x = \frac{\Delta p_0\, L_\mathrm{p}}{\tau_\mathrm{p}} = \Delta p_0 \sqrt{\frac{D_\mathrm{p}}{\tau_\mathrm{p}}} . \tag{10.65}$$

10.12.2 Generation in the Bulk

Now, a generation rate following (9.8), realistic for photodiodes and solar cells, is considered,

$$G(x) = G_0 \exp(-\alpha x) , \tag{10.66}$$

i.e. due to light absorption with the (wavelength-dependent) absorption coefficient α. The total generation rate is

$$G_\mathrm{tot} = \int_0^\infty G(x)\, \mathrm{d}x = \frac{G_0}{\alpha} . \tag{10.67}$$

The total generation rate is equal to the number of photons per second Φ_0 that enter the semiconductor.

The solution of (10.62) is the sum of the homogeneous solution (10.63) and a particular solution that is given by

$$\Delta p(x) = C \exp(-\alpha x) . \tag{10.68}$$

The constant C is determined to be

$$C = \frac{G_0\, \tau_\mathrm{p}}{1 - \alpha^2 L_\mathrm{p}^2} . \tag{10.69}$$

Therefore, the solution is

$$\Delta p(x) = C_1 \exp\left(-\frac{x}{L_p}\right) + C_2 \exp\left(\frac{x}{L_p}\right) + \frac{G_0\,\tau_p}{1-\alpha^2 L_p^2}\exp(-\alpha x)\ . \tag{10.70}$$

Using again $\Delta p(x \to \infty) = 0$ (leading to $C_2 = 0$) and a recombination velocity S at the front surface, i.e.

$$-e\,S\,\Delta p_0 = -e\,D_p \left.\frac{\partial \Delta p}{\partial x}\right|_{x=0}\ . \tag{10.71}$$

The solution is given as

$$\Delta p(x) = \frac{G_0\,\tau_p}{1-\alpha^2 L_p^2}\left[\exp(-\alpha x) - \frac{S+\alpha D_p}{S+D_p/L_p}\exp\left(-\frac{x}{L_p}\right)\right]\ . \tag{10.72}$$

For vanishing surface recombination, $S = 0$, the solution is (Fig. 10.33)

$$\Delta p(x) = \frac{G_0\,\tau_p}{1-\alpha^2 L_p^2}\left[\exp(-\alpha x) - \alpha L_p \exp\left(-\frac{x}{L_p}\right)\right]\ . \tag{10.73}$$

For $\alpha L_p \gg 1$, (10.64) is recovered. This dependence is the excess-carrier profile if the absorption is strong, which is a tendency for short wavelengths. The current at the surface, $j(x=0) \propto \nabla\,\Delta p$, is zero.

In the case of very strong surface recombination, $S \to \infty$, (10.72) becomes

$$\Delta p(x) = \frac{G_0\,\tau_p}{1-\alpha^2 L_p^2}\left[\exp(-\alpha x) - \exp\left(-\frac{x}{L_p}\right)\right]\ , \tag{10.74}$$

with $\Delta p(0) = 0$ (Fig. 10.33). The current at the surface is ($D\,\tau_p = L_p^2$)

$$j(x=0) = -e\,D\left.\frac{\partial \Delta p}{\partial x}\right|_{x=0} = -e\,\frac{G_0\,L_p}{1+\alpha L_p} = -e\,\Phi_0\,\frac{\alpha\,L_p}{1+\alpha L_p}\ . \tag{10.75}$$

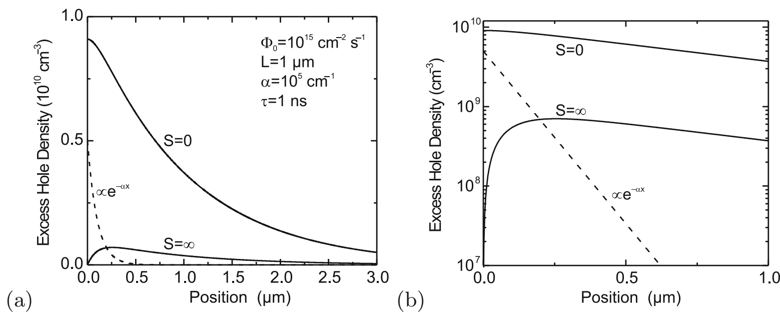

Fig. 10.33. Excess carrier density profile (10.72) in (**a**) linear and (**b**) semi-logarithmic plot for $S = 0$ and $S = \infty$. Other parameters are given in panel (**a**)

Part II

Selected Topics

11 Heterostructures

11.1 Introduction

Heterostructures consist of (at least two) different materials. The geometry of the interfaces between the two materials can be complicated. The simplest case is a planar interface, i.e. a layered system. A metal–semiconductor junction is generally a heterostructure. However, we will use the term mostly for structures of various semiconductors. Most of the heterostructures discussed here are epitaxial, i.e. fabricated by the successive epitaxy of the various layers on a substrate. Another method to fabricate heterostructures of different (and dissimilar) materials is wafer bonding that is briefly discussed in Sect. 11.6.

Many modern semiconductor devices rely on heterostructures, such as the heterobipolar transistor (HBT), the high electron mobility transistor (HEMT), lasers and nowadays also light-emitting diodes. Shockley had already considered heterostructures in his 1951 patent for pn-junctions. For the development and the realization of heterostructures H. Kroemer and Zh.I. Alferov were awarded the 2000 Physics Nobel Prize. The properties of charge carriers in layers that are part of heterostructures can be quite different from those in bulk material, e.g. extremely high mobility, high radiative recombination efficiency or novel states of matter, as revealed in the quantum Hall effects.

11.2 Heteroepitaxy

11.2.1 Growth Methods

Since the thickness of layers in the active part of heterostructures has to be controlled to monolayer precision and the thickness of layers can go down to the single monolayer range, special growth methods have been developed. Among these molecular beam epitaxy (MBE [741]), chemical vapor deposition (CVD [742, 743]) and metalorganic vapor phase epitaxy (MOVPE [744]) are the most common for Si, Ge, III–V and II–VI semiconductors. In particular, oxide semiconductors are also fabricated with pulsed laser deposition

M. Grundmann, *The Physics of Semiconductors*, 2nd ed., Graduate Texts in Physics, DOI 10.1007/978-3-642-13884-3_11,
© Springer-Verlag Berlin Heidelberg 2010

(PLD [745]). Liquid phase epitaxy (LPE [746]) used to be very important for the fabrication of LEDs but has lost its role largely to MOVPE.

MBE is performed in an ultrahigh vacuum (UHV) chamber, pumped by getter pumps and cryo-shrouds. The source materials are evaporated from effusion cells and directed towards the heated substrate. If the source materials are supplied as a gas stream, the method is called gas-source MBE (GSMBE). If metalorganic compounds are used as precursors, the method is denoted as MOMBE. The atoms impinge on the substrate with thermal energy and are first physisorbed. After diffusion on the surface they either desorb or they are chemisorbed, i.e. incorporated into the crystal. In order to obtain high spatial homogeneity of material properties such as composition, thickness and doping, the substrate is rotated during deposition.

During CVD and MOVPE the heated substrate is in a gaseous environment. The transport gas is typically H_2, N_2 or O_2. Precursor materials are hydrides such as silane, germane, arsine or phosphine (SiH_4, GeH_4, AsH_3, PH_3) and (for MOVPE) metalorganic compounds, such as, e.g. trimethylgallium (TMG). Due to the toxicity of the hydrides, alternative, i.e. less-toxic and less-volatile compounds are used, such as TBAs ($(CH_3)_3CAsH_2$). The crystal growth occurs after pyrolysis and catalysis of the compounds close to or on the substrate surface. All remaining C and H atoms (and whatever else that is not incorporated into the crystal) leave the reactor and are neutralized and stopped in a scrubber.

In-situ monitoring is of importance to obtain information about the growth process while it is underway. Using the information in a feedback loop it is possible to achieve in-situ control of the process, e.g. for precise determination of growth rates or layer thickness. Techniques are RHEED (reflection high-energy electron diffraction) [747] (only for UHV systems) and RAS (reflection anisotropy spectroscopy) [748, 749].

11.2.2 Substrates

Thin-film epitaxy is mostly performed on wafers, i.e. thin circular slices of substrate material. The most common substrate materials are Si (currently up to 400 mm diameter [750, 751]), Ge (also up to 300 mm [752]), GaAs (up to 6 inch), InP (up to 4 inch) and sapphire (up to 6 inch). Typical wafer thickness is 300–500 μm. Also, very thin, flexible Si wafers (8–10 μm) have been developed [753]. A wafer is cut from a large single cylindrical crystal that is fabricated with suitable growth techniques such as Czochralski (CZ) growth (1918) modified by Teal and Little [754]. In CZ growth the crystal is pulled from a seed crystal out of a melt of previously polycrystalline, pure or doped material. All dislocations stop in the narrow neck between the seed and the main body of the cylinder. The diameter of the crystal is controlled by the pulling rate and the heating power. For the growth of III–V compound semiconductors liquid encapsulated CZ (LEC) growth has been developed to counteract the high volatility of the growth-V component.

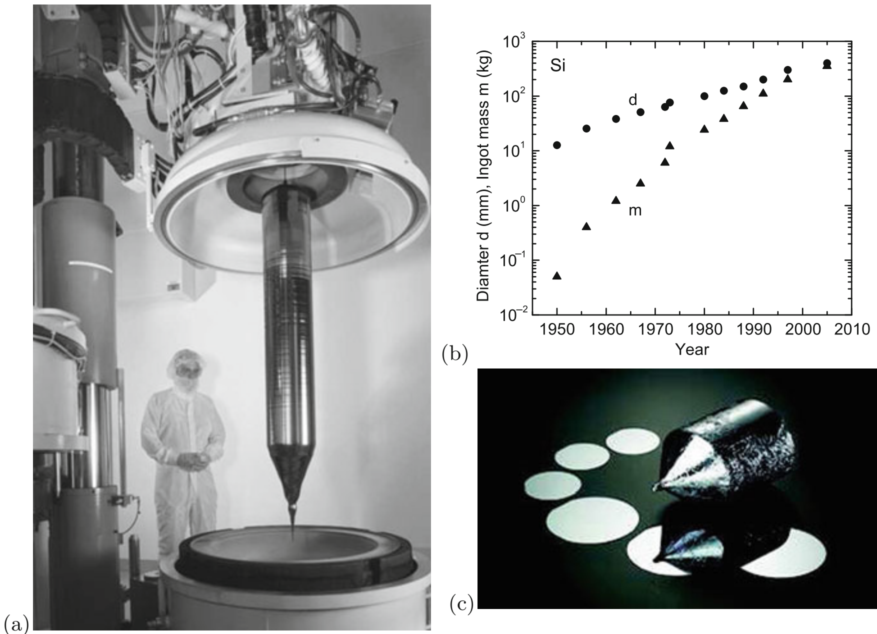

Fig. 11.1. (**a**) Silicon single crystal for 300-mm diameter wafers after opening of the crucible. From [757] with permission. (**b**) Historic development (first year of larger production) of silicon wafer diameter and ingot mass. Data from [751]. (**c**) GaAs single crystal (boule) for 4-inch wafers and some cut and polished wafers

During LEC growth the melt is completely covered with molten boric oxide (B_2O_3). The keys to optimization of the crystal growth process are numerical modeling and computer control. In Fig. 11.1a,c a large CZ silicon crystal and a smaller LEC GaAs crystal (boule) are shown. Over time wafer size and ingot mass have increased remarkably (Fig. 11.1b). For details on other important fabrication methods for bulk crystals, including float-zone (FZ [755]) or vertical gradient freeze (VGF), we refer to the literature [756]. Significant expertise is necessary for cutting, grinding and polishing (lapping) wafers for epitaxy.

For semiconductors, the wafer is marked with *flats* to indicate orientation and doping. In Fig. 11.2 the standard flats are shown for (100)- and (111)-oriented material. The primary (major) flat (OF, orientation flat) defines the crystallographic orientation[1] is longer than the secondary (minor) flat which defines the conductivity type (IF, identification flat). For a 4-inch (100 mm) diameter wafer the OF is 32 and the IF 12 mm long. The front surface, on which the epitaxy is performed, typically undergoes an elaborate cleaning

[1]In the 'US' flat definition, the primary flat is the (011) surface, in the 'EJ' definition, the primary flat is (011).

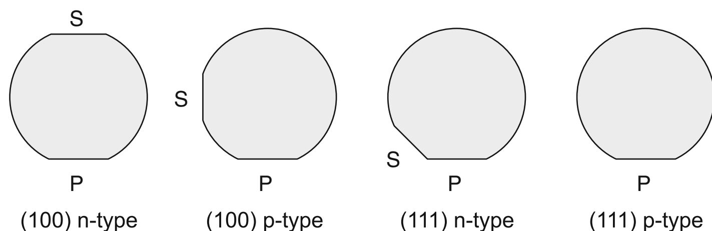

Fig. 11.2. Schematic semiconductor wafer geometry for various orientations and doping with the primary (P) and secondary (S) flats indicated

and polishing process. Silicon processes [758] are based on the RCA cleaning procedure [759] and the related Shiraki etch [760] and can achieve clean, atomically flat surfaces [761]. III-V semiconductors are typically prepared using a polishing etch [762, 763], often solutions containing bromine. It is possible to create compound semiconductor surfaces that exhibit large, essentially monoatomically flat terraces between individual surface steps. Polishing or other surface damage can also be removed prior to epitaxy with thermal (Fig. 11.3) or ion beam treatments.

One prerequisite for making high-quality heterostructures with thin layers is a flat surface. Even if the polished substrate is not perfect, flat interfaces can be achieved with the growth of appropriate superlattice buffer layers

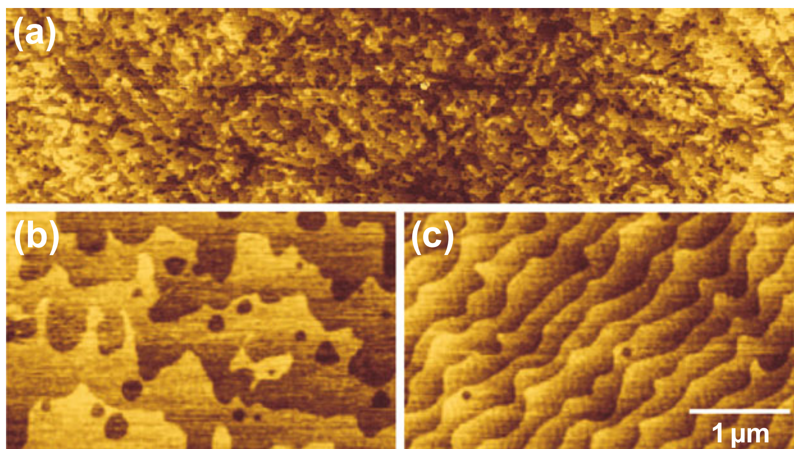

Fig. 11.3. (**a**) AFM images of an as-received ZnO wafer, exhibiting small terraces and nm deep scratches from polishing. (**b**, **c**) Two ZnO $(000\bar{1})$ wafers with vicinal surfaces after thermal treatment (1000 °C for 2 h in O_2), exhibiting atomically flat terraces with $c/2$ monoatomic step heights. Two different substrates with different off-cut (misorientation direction and angle) are shown. Adapted from [764]

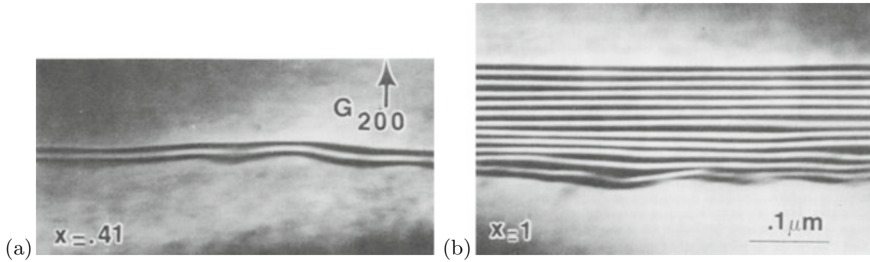

Fig. 11.4. Cross-sectional TEM of MBE-grown $Al_xGa_{1-x}As$/GaAs heterostructures for (**a**) $x = 0.41$ and (**b**) $x = 1.0$. Using an AlAs/GaAs superlattice an excellent flattening of substrate roughness is achieved. From [765]

(Fig. 11.4). Roughness can exist on all length scales and is typically investigated using atomic force microscopy scans.

High throughput demands and the advent of multi-wafer reactors make prior cleaning and etching procedures tedious. For this purpose, substrates for well-developed material systems are offered 'epiready'. Epiready wafers are often covered with a very thin protective film that can be released using a thermal treatment at or below typical growth temperature in the growth reactor immediately prior to epitaxy. The protective film separates the polished semiconductor wafer from the ambient. Examples are a few monolayers of arsenic on GaAs or two monolayers GaN on SiC. However, the suitability of a purchased substrate may depend on the duration and conditions of its storage.

11.2.3 Growth Modes

The growth of a material A on a material B can occur via three fundamental growth modes (Fig. 11.5), the layer-by-layer or Frank-van der Merwe (FvdM) growth mode [766], the island or Volmer-Weber (VW) growth mode [767] and the Stranski-Krastanow (SK) growth mode [768]. In [768] the possibility of island formation on an initially flat heteroepitaxial surface was proposed for the growth of lattice-*matched* ionic crystals that have different charges. The term SK growth is now typically used in lattice-*mismatched* heteroepitaxy for the island formation (and related relaxation of strain energy, cmp. Fig. 13.26)

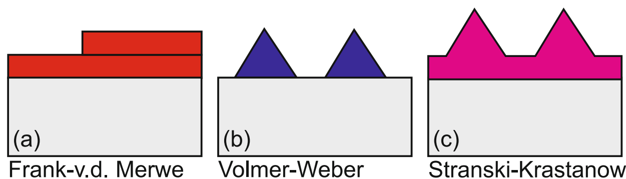

Fig. 11.5. Schematic of the three different fundamental epitaxial growth modes

on an initially two-dimensional layer (wetting layer).[2] Also growth of islands *relaxed* by misfit dislocations in strained heteroepitaxy has been termed SK growth [774].

The growth mode is determined by the relation of the free energies (per area) of the surface σ_s, interface σ_i and film σ_f. Wetting of the substrate and growth of a coherent film (FvdM-growth) occurs for

$$\sigma_\mathrm{s} > \sigma_\mathrm{i} + \sigma_\mathrm{f} \ . \tag{11.1}$$

If the inequality has the opposite sign, Volmer-Weber or Stranski-Krastanow growth occurs. Additionally the strain energy of the film must be considered. The SK growth generally occurs when there is wetting of the substrate but layer strain is unfavorable and leads to islanding.

Layer-by-layer growth typically involves nucleation of two-dimensional islands and 'filling' of the remaining monolayer before the next one is started. Another growth mode resulting in smooth epitaxial layers is step-flow growth where adatoms are incorporated mainly at step edges. A more detailed discussion can be found in [770]. Further details on crystal growth can be found in [771].

11.2.4 Heterosubstrates

If homosubstrates are not available or very expensive, semiconductors are grown on dissimilar substrates, e.g. GaN and ZnO on sapphire (Al_2O_3) or SiC.[3] In many cases, the integration of III–V- or II–VI-based semiconductors for optoelectronic applications on silicon for electronic devices is desirable, such as GaAs/Si, InP/Si, GaN/Si or ZnO/Si. For such combinations the epitaxial relationship, i.e. the alignment of the crystallographic directions of both materials, which can have different space groups, has to be considered [773]. Some examples are given in Table 11.1. In Fig. 11.6, X-ray diffraction data are shown from a ZnO layer on *c*-oriented sapphire. The hexagonal ZnO lattice is rotated by 30° with respect to the trigonal sapphire lattice. In the case of growth of ZnO on Si(111) an amorphous SiO_2 layer forms at the interface such that the crystallographic information of the substrate is lost. The ZnO grains exhibit random in-plane orientation (Fig. 11.7).

The initial growth steps can determine the orientation in polar materials. GaN directly grown on *c*-Al_2O_3 grows with N-face orientation (see Fig. 3.18). The high surface mobility of Ga allows nitrogen to take its preferred position in the first atomic layer. Even under Ga-rich conditions the N atoms can kick-off the Ga from its favorite site on the surface. If an AlN buffer is used the strong bond between Al and oxygen leads to an Al atomic layer at the

[2] This is the growth mode of self-assembled epitaxial quantum dots as discussed in Sect. 13.3.3.

[3] For ZnO, homosubstrates have recently been produced with 3-inch diameter [772].

Table 11.1. Epitaxial relationship for various film/substrate combinations, ZnO on *c*-, *a*- and *r*-sapphire and Si(111)

ZnO	Al_2O_3 [00.1]	ZnO	Al_2O_3 [11.0]	ZnO	Al_2O_3 [$\bar{1}$0.2]	ZnO	Si [111]
[00.1] [11.0]	[00.1] [01.0]	[00.1] [11.0]	[11.0] [00.1]	[11.0] [00.1]	[10.2] [01.1]	[00.1] [21.0]	[111] [110]

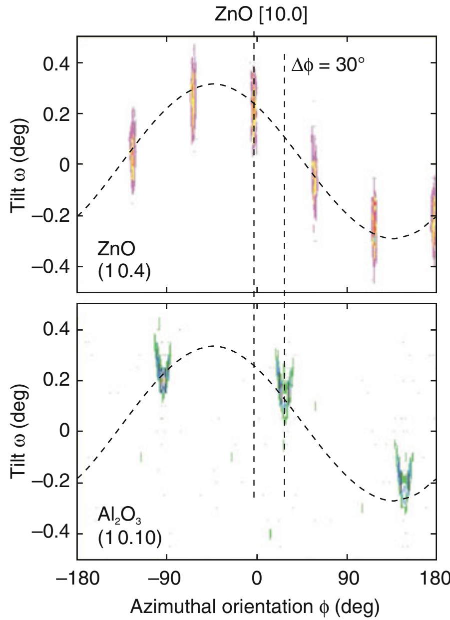

Fig. 11.6. X-ray diffraction intensity from the asymmetric ZnO (10.4) (*upper panel*) and the sapphire (10.10) (*lower panel*) reflections as a function of the azimuthal sample orientation (rotation angle ϕ around the [00.1] axis). The peaks appear at different tilt angles ω due to an overall tilt of the mounted sample (*dashed sinusoidal lines*). The ZnO [00.1] axis is not tilted with respect to the sapphire [00.1] direction

interface and subsequent GaN grows with a Ga-face [774]. On a sapphire substrate with lateral AlN patterns, laterally orientation-modulated GaN can be grown (Fig. 11.8). At the juncture of the phases an inversion domain boundary forms [775].

The nucleation and the initial film growth are important and determine the film quality. Several techniques have been developed to overcome common problems. A typical strategy is the growth of a low-temperature nucleation

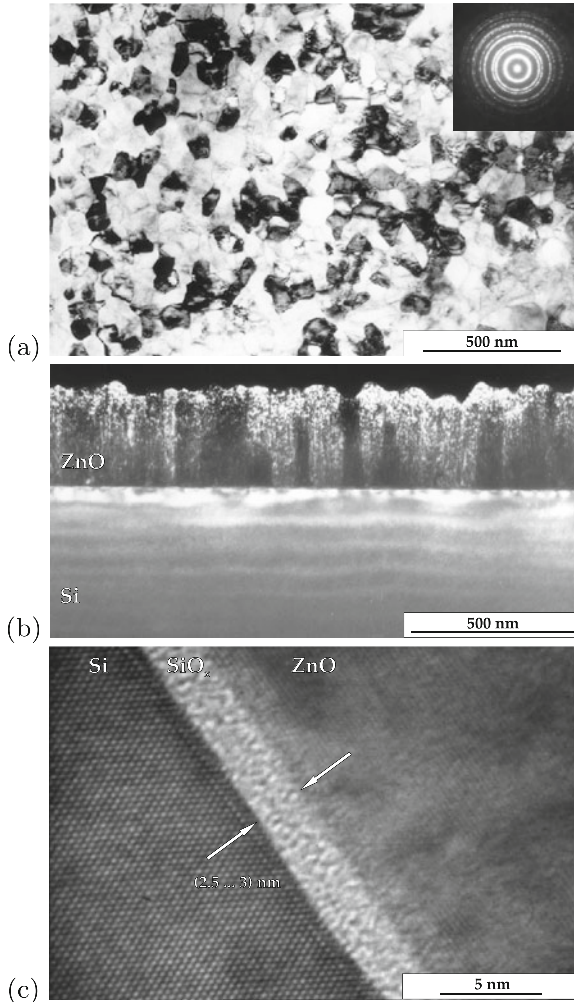

Fig. 11.7. (**a**) Plan-view TEM image (*inset*: electron diffraction diagram averaged over several grains) of ZnO on Si(111). (**b**) Cross-sectional TEM of the same sample. (**c**) High-resolution cross-sectional image of the ZnO/SiO_2/Si interface region. Adapted from [776]

layer. The defect density can be reduced in parts of the structure using epitaxial lateral overgrowth (ELO) [777]. The defects thread only from the limited contact area of the layer with the substrate and the part of the layer away from the mask ('wing') is free of defects (Fig. 11.9).

The cracking (Sect. 4.4.1) of thick films during cooling due to the mismatch of the thermal expansion coefficients (Fig. 11.10) can be avoided by the introduction of suitable stress-relaxing layers [779, 780].

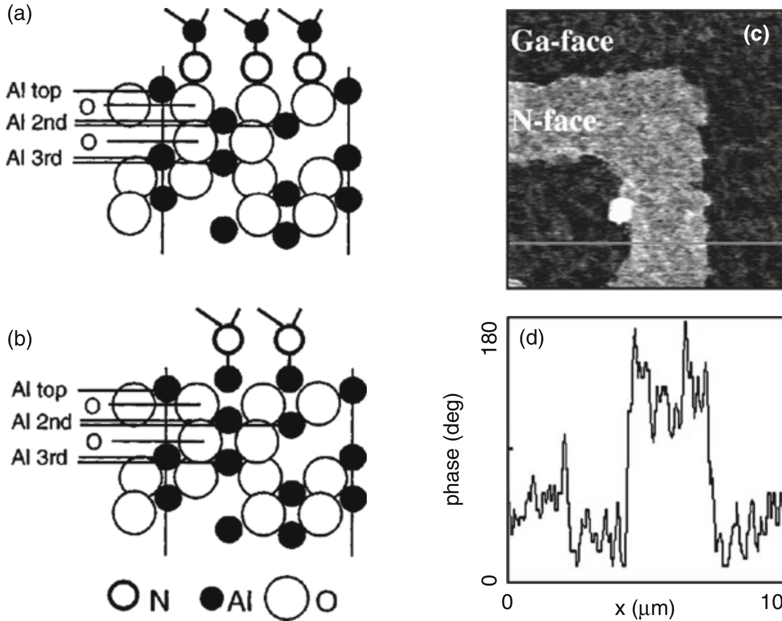

Fig. 11.8. Side view of the heterointerfaces between AlN and *c*-oriented sapphire with nitrogen (**a**) and Al (**b**) being the first layer. Adapted from [774]. (**c**) Phase image of piezoresponse force microscopy (PFM) of lateral polarity GaN heterostructure and (**d**) linescan of phase signal along *white line* in part (**c**). Adapted from [778], part (**c**) reprinted with permission, ©2002 AIP

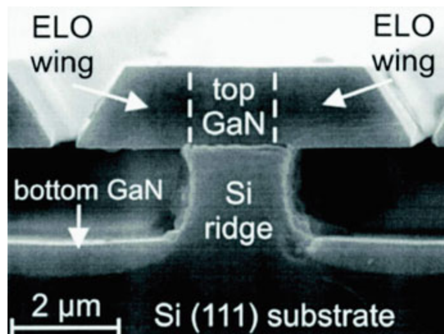

Fig. 11.9. SEM cross-sectional image of GaN grown on a structured Si(111) substrate. The laterally grown wings extend about 2.5 μm over the grooves. The thickness of the GaN layer is 0.5 μm on the bottom of the grooves, while it is 1.4 μm on top of the ridges. Reprinted with permission from [777], ©2001 AIP

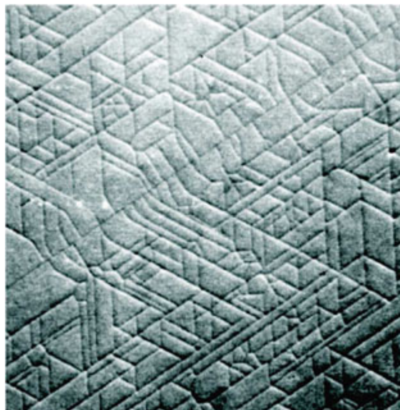

Fig. 11.10. 1×1 mm^2 top view with a differential interference contrast microscope of a 1.3-µm thick GaN layer grown on Si(111). Reproduced with permission from [779], ©2000 IPAP

11.2.5 Pseudomorphic Structures

Heterostructures can generally be made from any sequence of materials. However a mismatch in lattice constant (or a different crystal structure) leads to strains and stresses that are of the order of 10^3 atmos for strains of 1% ($\sigma \sim C\epsilon$, $C \approx 5 \times 10^{10}$ Pa) as discussed in Sect. 5.3.3. The total strain energy is $\propto C\epsilon^2$. Above a critical thickness $h_c \propto \epsilon^{-1}$ (cf. Sect. 5.3.7) defects, e.g. misfit dislocations (relaxing strain with their edge components), are generated (Sect. 11.2.6). There are a number of semiconductor combinations that are lattice matched and thus can be grown with arbitrary thickness. $Al_xGa_{1-x}As$ is closely lattice matched to GaAs for all Al concentrations. See Fig. 6.15 for lattice-matched pairs, e.g. $In_{0.53}Ga_{0.47}As$/InP. Often, thin layers of lattice-mismatched materials with thickness smaller than the critical thickness are used.

For many device applications the ability to grow pseudomorphic layers thicker than the critical layer thickness would be beneficial. The use of compliant substrates was proposed in [781] to meet this demand. A recent review on compliant substrate technologies can be found in [782]. Schemes to accommodate part of the mismatch strain in the substrate include the use of cantilevered membranes, silicon-on-insulator, twist bonding, glass bonding or trenched substrates. In this sense also nanowhiskers (Sect. 13.2.3) represent a compliant substrate, enabling the growth of coherent (laterally confined) layers thicker than the critical thickness of a 2D layer (cmp. Fig. 13.9).

11.2.6 Plastic Relaxation

Above the critical thickness, a film will relax plastically by forming misfit dislocations. The cross-hatch pattern at the surface due to misfit dislocations

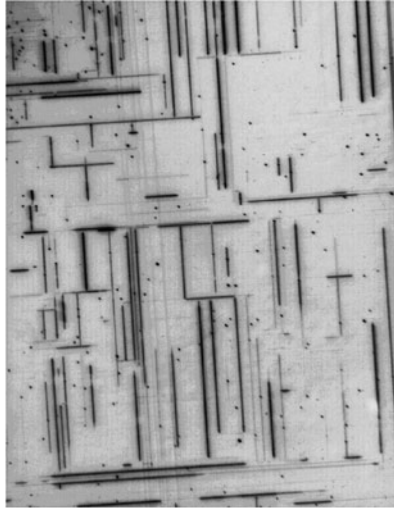

Fig. 11.11. Optical image of the surface of a supercritical, plastically relaxed $In_xGa_{1-x}As$ film on GaAs. Image width is about 1 mm. The cross-hatch pattern is due to misfit dislocations along [110] and $[1\bar{1}0]$. A pseudomorphic layer would exhibit no contrast under the given conditions

is shown in Fig. 11.11. A TEM image of an array of misfit dislocations can be found in Fig. 5.27b.

The strain relaxation in mismatched heteroepitaxy can be determined experimentally via the wafer curvature of the heterostructure (Sect. 5.3.5). Data for the thickness dependent relaxation $\epsilon(d)$ of $In_{0.15}Ga_{0.85}As$ on GaAs (mismatch $\approx 1\%$) are shown in Fig. 11.12. Growth interruptions lead to larger

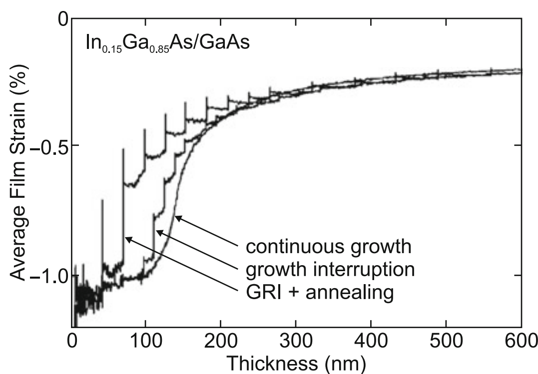

Fig. 11.12. Average film strain (measured in-situ via substrate curvature) of $In_{0.15}Ga_{0.85}As$/GaAs grown at 450°C as a function of film thickness (determined from growth time × deposition rate). Relaxation for three different growth modes are shown (as labeled): continuous growth, employment of several growth interruptions (GRI) and GRI with annealing step (to 550°). Adapted from [783]

relaxation at smaller thickness. Therefore relaxation at early times or small thickness (above h_c) is kinetically hindered, i.e., the available dislocation density and glide velocity are not sufficient to relieve the strain. At large thickness the strain does not go to zero (saturation regime) and the film remains in a metastable, incompletely relaxed state as discussed in more detail in [783].

11.2.7 Surfactants

The condition (11.1) allows layer-by-layer growth (cf. Sect. 11.2.3), i.e. the substrate surface free energy is higher than the than the total of interface and film surface free energy. This makes wetting energetically favorable. For two elements A and B, one of them must have the lower surface free energy. If A can be grown on B in Frank-van der Merwe (or Stranksi-Krastanow) growth mode, then (11.1) does not hold for B on A and the growth will occur in Volmer-Weber mode, i.e. with islands. This is a serious problem for the growth of embedded layers of the type A–B–A. If the embedded film grows well, the capping does not and vice versa.

In the case of Ge on Si, Ge has the lower surface free energy than Si. Ge grows on Si in Stranski-Krastanow mode [784] (Fig. 11.13a). Si grows both on Ge(001) and Ge/Si(001) in a Volmer-Weber mode [785] causing severe problems for the fabrication of Si/Ge/Si quantum wells or superlattices. A substantial modification of growth mode can be achieved by using a third element C as a capping layer, saturating surface bonds. It lowers the surface free energy of both materials A and B, thus favoring wetting of the substrate. Such element C is called *surfactant* (surface-active species) [786, 787]. Typical examples are As [786] or Sb [221] on Si and Ge (Fig. 11.13b). Also the sur-

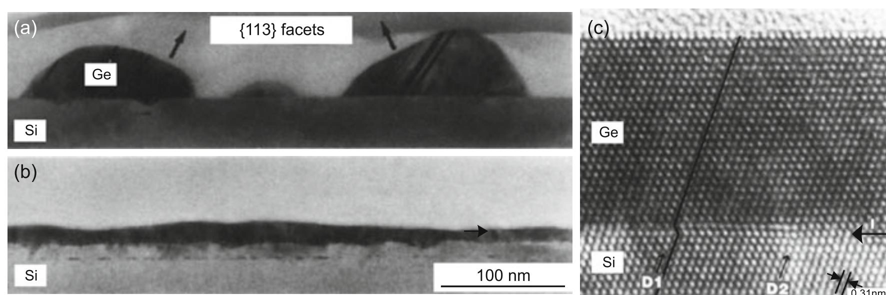

Fig. 11.13. (**a**, **b**) 10 nm thick Ge layer on Si (100) deposited at room temperature with MBE and annealed up to 770°C without (**a**) and with (**b**) Sb surfactant. Adapted from [791]. (**c**) Cross-section TEM image of a heterostructure of 70 monolayers germanium on Si (111), grown by MBE with Sb surfactant. The *horizontal arrow* labeled 'I' denotes the position of the interface. The *arrows* labeled 'D1' and 'D2' denote the positions of partial dislocations (cmp. Fig. 4.18). Adapted from [221]

factant modifies defect nucleation and can lead to defect-free epitaxial Ge/Si layers (Fig. 11.13c). Surfactants have also been described for the growth of compound semiconductors, e.g. In [788] or Sb [789, 790] for GaAs.

11.3 Energy Levels in Heterostructures

11.3.1 Band Lineup in Heterostructures

In heterostructures, semiconductors with different band gaps are combined. The relative position of conduction and valence band (band alignment) is determined by the electron affinities χ as shown in Fig. 11.14. For a semiconductor, the electron affinity is the (positive) energy difference between vacuum level and conduction band edge. It can lead to different types of heterostructures. In Fig. 11.15, the band alignment for type-I and type-II heterostructures are shown. In the type-I structure (straddled band lineup) the lower conduction-band edge and the higher valence-band edge are both in the material with smaller band gap. Thus, electrons and holes will localize there. In the type-II structure a staggered lineup is present and electrons and holes will localize in different materials. The technologically most relevant are type-I structures.

In a type-I heterostructure, the conduction- and valence-band discontinuities are given, respectively, by

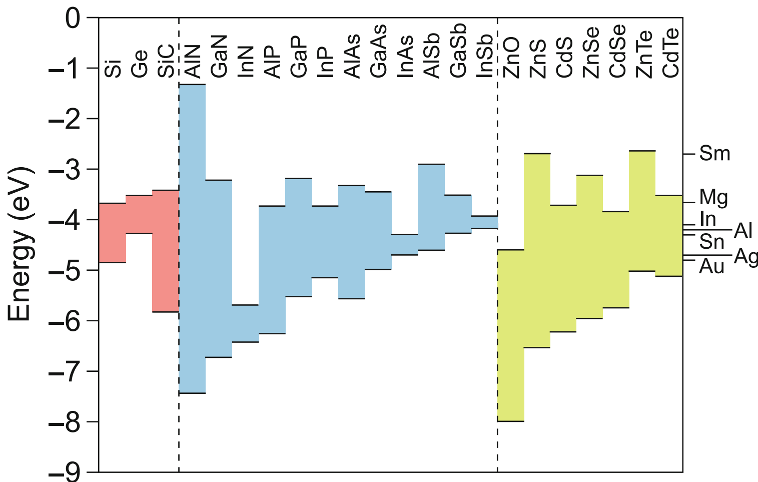

Fig. 11.14. Position of conduction and valence-band edges for a variety of semiconductors (relative to a common vacuum level at $E = 0\,\mathrm{eV}$). Based on values from [792]. On the right hand side the work functions of several metals are shown for comparison

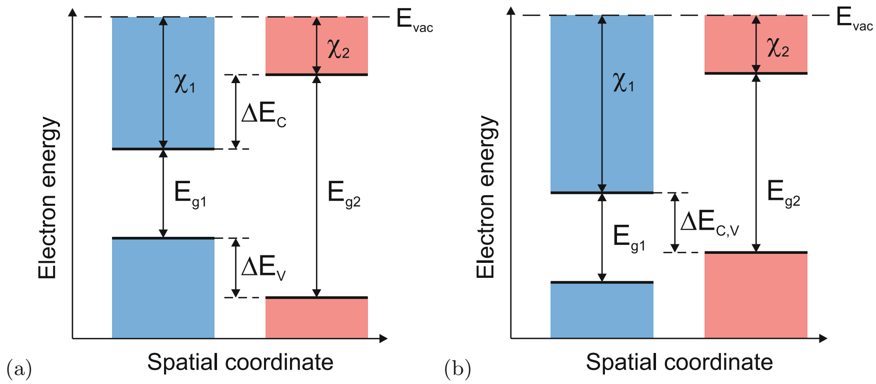

Fig. 11.15. Position of band edges (band alignment) in (**a**) type-I and (**b**) type-II heterostructure

$$\Delta E_{\mathrm{C}} = \chi_1 - \chi_2 \tag{11.2a}$$

$$\Delta E_{\mathrm{V}} = (\chi_1 + E_{\mathrm{g}_1}) - (\chi_2 + E_{\mathrm{g}_2}) \; . \tag{11.2b}$$

Depending on the layer sequence of high- and low-bandgap materials various configurations, as shown in Fig. 11.16 have obtained special names, such as single heterointerface, quantum well (QW), multiple quantum well (MQW), superlattice (SL). In the extreme case the layer is only one monolayer thick (Fig. 11.17) and the concept of layer and interface blurs. Such atomically precise layer sequences are mastered nowadays for a variety of material systems such as AlGaAs/GaAs/InAs, InP/InGaAs, Si/SiGe and also $BaTiO_3/SrTiO_3$.

The design of heterostructures to fulfill a certain device functionality or to have certain physical properties is called 'band gap engineering'.

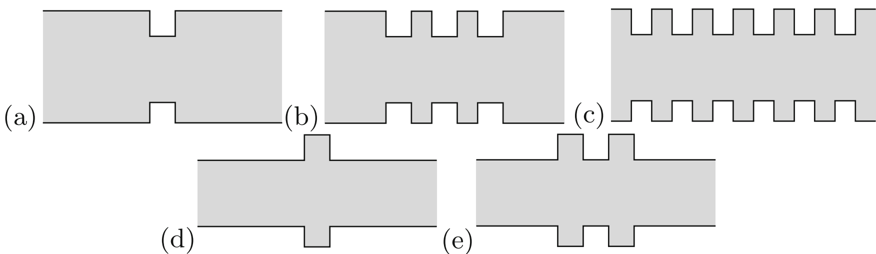

Fig. 11.16. Heterostructures with different layer sequences (band gap engineering). (**a**) quantum well (QW), (**b**) multiple quantum well (MQW), (**c**) superlattice (SL), (**d**) single-barrier tunneling structure, (**e**) double-barrier tunneling structure

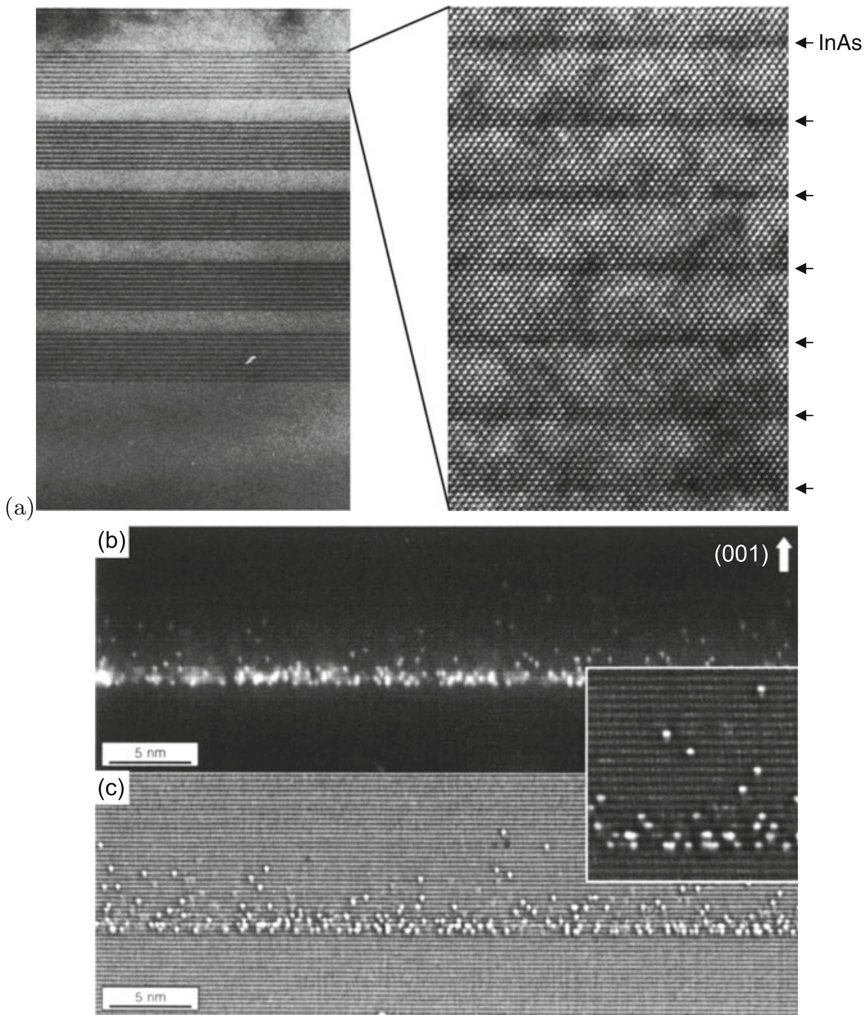

Fig. 11.17. Ultrathin heterostructures: (**a**) Cross-sectional TEM of a MOVPE-grown short-period superlattice (SPS) of InAs layers in $GaAs_{1-x}N_x$). In high resolution (*right image*), the individual rows of atoms can be seen. From [793]. (**b**, **c**) Cross-section STM image of 2 ML InAs on GaAs; the segregation of In into the top layer is visible atom by atom. Adapted from [794]

11.3.2 Quantum Wells

The energy in a single quantum well of thickness L_z (along the growth direction z) can be calculated with the quantum-mechanical particle-in-a-box model. In the envelope function approximation (Appendix G) the wavefunc-

tion is written as a product of the Bloch function and the envelope function $\chi(z)$.

$$\Psi^{\mathrm{A,B}}(\mathbf{r}) = \exp\left(\mathrm{i}\mathbf{k}_{\perp}\mathbf{r}\right)\, u_{n\mathbf{k}}(\mathbf{r})\chi_n(z) \ , \tag{11.3}$$

where 'A' and 'B' denote the two different materials. The envelope function χ fulfills, approximately, the one-dimensional Schrödinger-type equation,

$$\left(-\frac{\hbar^2}{2m^*}\frac{\partial^2}{\partial z^2} + V_{\mathrm{c}}(z)\right)\, \chi_n(z) = E_n\, \chi_n(z) \ , \tag{11.4}$$

where m^* denotes the effective mass. V_{c} is the confinement potential determined by the band discontinuities. Typically, $V_{\mathrm{c}} = 0$ in the well and $V_0>0$ outside in the barrier. E_n are the resulting energy values of the quantized levels. In the case of infinite barriers ($V_0 \rightarrow \infty$, Fig. 11.18a) the boundary conditions $\chi(0) = \chi(L_z) = 0$ yield

$$E_n = \frac{\hbar^2}{2m^*}\left(\frac{n\pi}{L_z}\right)^2 \tag{11.5}$$

$$\chi_n(z) = A_n\, \sin\left(\frac{n\pi}{L_z}\, z\right) \ , \tag{11.6}$$

where E_n is called the confinement energy. For finite barrier height (Fig. 11.18b) the calculation leads to a transcendental equation. The wavefunction tunnels into the barrier. While for infinite barrier height the lowest level diverges for $L_z \rightarrow 0$, for finite barrier height $E_1 \rightarrow V_0$.

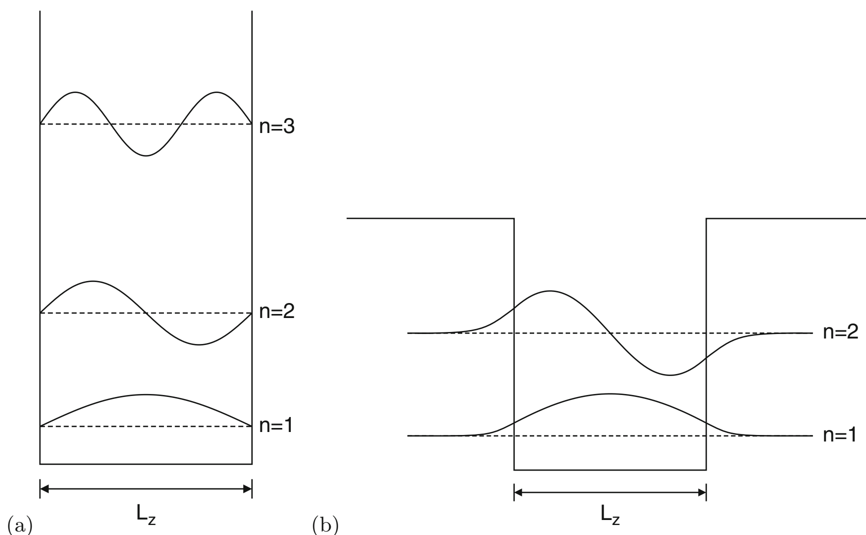

Fig. 11.18. Schematic energy levels and wavefunctions in (**a**) a potential well with infinite barriers, and (**b**) for finite barrier height

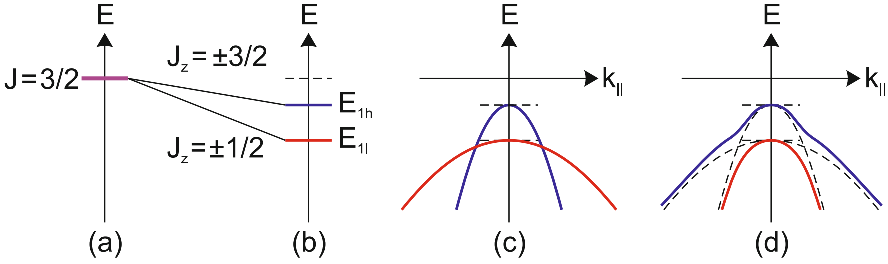

Fig. 11.19. Schematic representation of the development of hole levels in a quantum well: (**a**) degenerate bulk levels at Γ, (**b**) splitting at the subband edge (due to different quantized values of k_z), (**c**) in-plane dispersion (mass reversal), (**d**) anticrossing behavior. Based on [765]

In the plane the carriers are still free and have a two-dimensional dispersion. Thus, each quantized level contributes $m^*/(\pi\hbar^2)$ to the density of states at each subband edge E_n.

For holes, the situation is a little more complicated than that for electrons (Fig. 11.19). First, the degeneracy of heavy and light holes is lifted since their mass enters the confinement energy. The effective hole masses along the z direction, i.e. those that enter (11.4), are

$$\frac{1}{m_{\mathrm{hh}}^z} = \gamma_1 - 2\gamma_2 \tag{11.7a}$$

$$\frac{1}{m_{\mathrm{lh}}^z} = \gamma_1 + 2\gamma_2 \; . \tag{11.7b}$$

The light holes have the higher quantization energy. The angular momentum is quantized along the z direction. The transverse masses for the dispersion in the interface plane are

$$\frac{1}{m_{\mathrm{hh}}^{xy}} = \gamma_1 + \gamma_2 \tag{11.8a}$$

$$\frac{1}{m_{\mathrm{lh}}^{xy}} = \gamma_1 - \gamma_2 \; . \tag{11.8b}$$

Now the heavy hole, i.e. the $J_z = \pm\frac{3}{2}$ state, has the smaller mass and the light hole ($J_z = \pm\frac{1}{2}$) the larger (Fig. 11.19c). However, this consideration is only an approximation since the lifting of degeneracy and the dispersion have to be treated on the same level. Higher terms of the perturbation calculation lead to band mixing and remove the band crossing that seems to originate from the situation at the Γ point. In reality, the bands show anticrossing behavior and are strongly deformed. The hole dispersion in a superlattice and the anticrossing behavior is shown in Fig. 11.20.

Experimentally observed transition energies in quantum wells of varying thickness are shown in Fig. 11.21 and are in good agreement with the theoret-

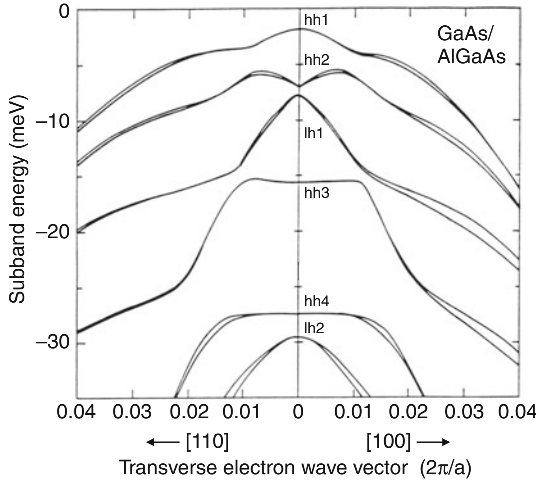

Fig. 11.20. Hole dispersion in a 68-ML GaAs/71 ML $Al_{0.25}Ga_{0.75}As$ superlattice (numerical calculation). The double curves originate from a lifting of time-reversal symmetry at $\mathbf{k} \neq 0$. Reprinted with permission from [796], ©1985 APS

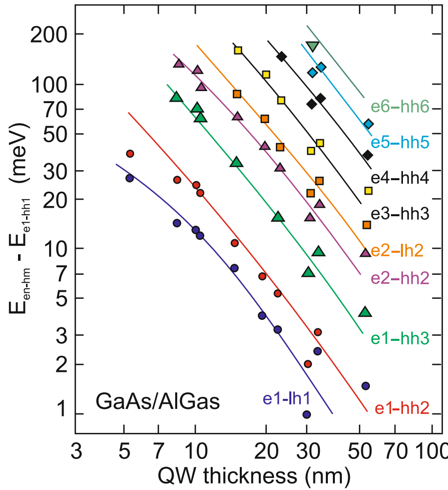

Fig. 11.21. Observed electron–hole transitions (energy difference to the first e–h transition from excitation spectroscopy) in GaAs/AlGaAs quantum wells of varying thickness. *Symbols* are experimental data, *solid lines* are theoretical model. Data from [797]

ical calculation. We note that for infinite barriers optical transitions are only allowed between confined electron and hole states with the same quantum number n. For finite barriers this selection rule becomes relaxed, and other

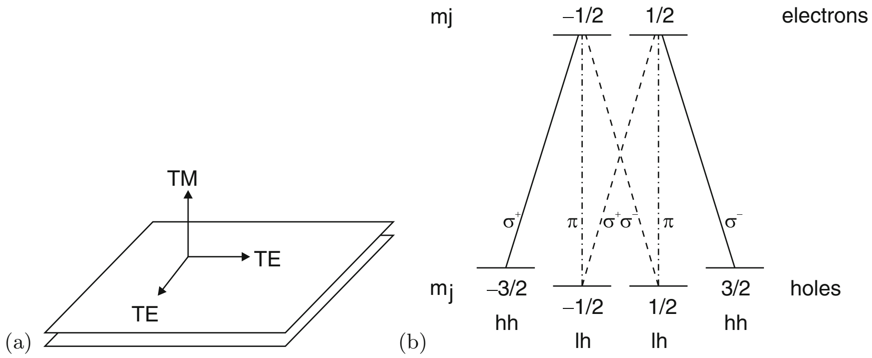

Fig. 11.22. (**a**) Directions of electric-field vector relative to the quantum-well plane for TE and TM polarization. (**b**) Optical selection rules for band–band transitions in a quantum well. If the (in-plane averaged) relative strength of the e–hh transitions (*solid lines*) is 1, the relative strength of the TE-polarized e–lh transitions (*dashed lines*) is 1/3 and that of the TM-polarized e–lh transitions (*dash-dotted lines*) is 4/3

transitions become partially allowed, e.g. e_1–hh_3. The optical matrix element from the Bloch part of the wavefunction, which was isotropic for (cubic) bulk material (9.18), is anisotropic for quantum wells. TE (TM) polarization is defined with the electromagnetic field in (perpendicular to) the plane of the quantum well (Fig. 11.22a). At the subband edge, i.e. for in-plane wavevector $k_{||} = 0$ the matrix elements for the various polarizations and propagation directions are given in Table 11.2. The matrix elements averaged over all in-

Table 11.2. Squared momentum matrix elements $|\langle c|\hat{\mathbf{e}} \cdot \mathbf{p}|v\rangle|^2$ in a quantum well for various propagation directions in units of M_b^2. The quantum-well normal is along **z**

	propagation	$\hat{\mathbf{e}}_\mathrm{x}$ (TE)	$\hat{\mathbf{e}}_\mathrm{y}$ (TE)	$\hat{\mathbf{e}}_\mathrm{z}$ (TM)
	x	–	1/2	0
e–hh	**y**	1/2	–	0
	z	1/2	1/2	–
	x	–	1/6	2/3
e–lh	**y**	1/6	–	2/3
	z	1/6	1/6	–
	x	–	1/3	1/3
e–so	**y**	1/3	–	1/3
	z	1/3	1/3	–

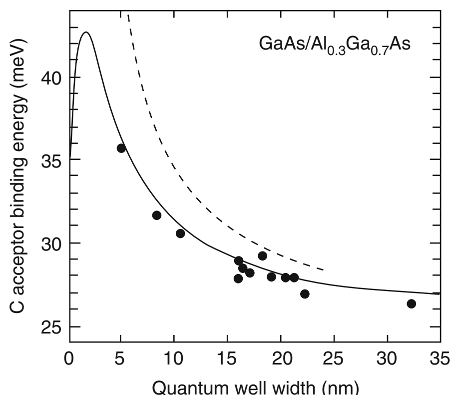

Fig. 11.23. Experimental values for the acceptor binding energy in GaAs/$Al_{0.3}Ga_{0.7}$As quantum wells (*solid circles*) from [798] as a function of well width. *Solid line* is theory (variational calculation) for the well-center acceptor including top four valence bands and finite barriers, *dashed line* is hydrogen-like model with infinite barrier height. Adapted from [799]

plane directions for TE-polarization are $3/2M_{\mathrm{b}}^2$ ($1/2M_{\mathrm{b}}^2$) for the electron to heavy (light) hole transition. For TM polarization the values are 0 and $2M_{\mathrm{b}}^2$, respectively [795]. The optical selection rules are shown in Fig. 11.22 (see Fig. 9.8 for bulk material). For propagation along the quantum-well plane, the ratio between the strength of the TE polarized e–hh and e–lh transitions is 3:1.

The confinement potential squeezes charge carriers bound to impurities closer to the ion. Therefore, the binding energy increases as shown in Fig. 11.23. This behavior can be modeled theoretically with good precision. It makes a difference whether the impurity is located at the center or the interface of the quantum well.

The confinement potential also squeezes electrons and holes in the exciton closer together and thus increases their Coulomb interaction. The binding energy of the quantum-well exciton is thus larger than in bulk material and depends on the well width (Fig. 11.24). In the simple hydrogen-like model with infinite barriers the exciton binding energy is 4 times the bulk binding energy in the limit $L_{\mathrm{z}} \rightarrow 0$. In a realistic calculation the effect of different dielectric constants in the well and barrier (image charge effect) need to be considered.

11.3.3 Superlattices

In a superlattice, the barrier thickness is so small that carriers can tunnel in neighboring wells or, in other terms, that there exists a significant wavefunction overlap between adjacent wells. This leads to a band structure (Fig. 11.25), similar to the Kronig–Penney model (Sect. 6.2.3). For the

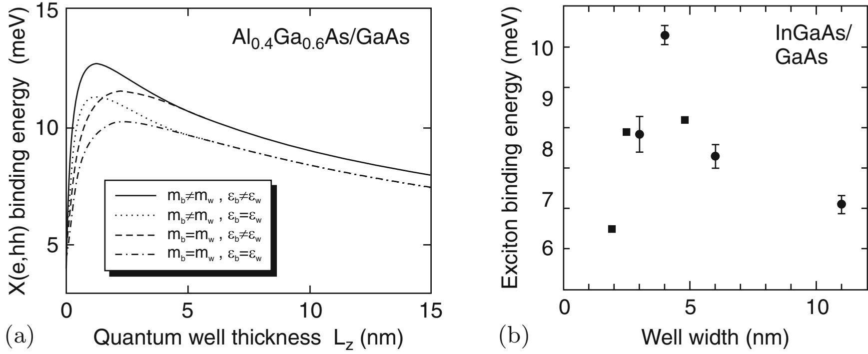

Fig. 11.24. (**a**) Theoretical (variational) calculation (*solid line*) of the heavy-hole exciton binding energy vs. QW thickness in a GaAs/$Al_{0.4}Ga_{0.6}$As quantum well (using also different approximations, *other lines*). Adapted from [800]. (**b**) Experimental exciton binding energy in In_xGa_{1-x}As/GaAs quantum wells of different thickness. *Circles*: data and error bars from [801], x unspecified, *squares*: data from [802], $x = 0.18$

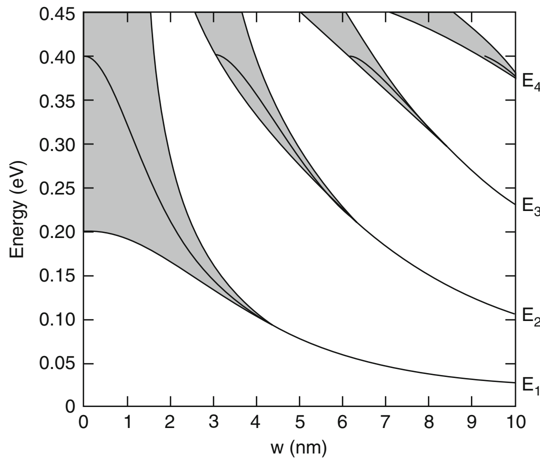

Fig. 11.25. Band structure of a superlattice with a potential depth of 0.4 eV and well and barrier width w ($L_{\mathrm{QW}} = L_{\mathrm{barr}}$). Adapted from [803]

superlattice the bands are called minibands, the gaps are called minigaps. The density of states does not make a step at the subband edge but follows an arccos function. The modification of the density of states, as seen in the absorption spectrum, are shown in Fig. 11.26 for 1, 2, 3 and 10 coupled wells.

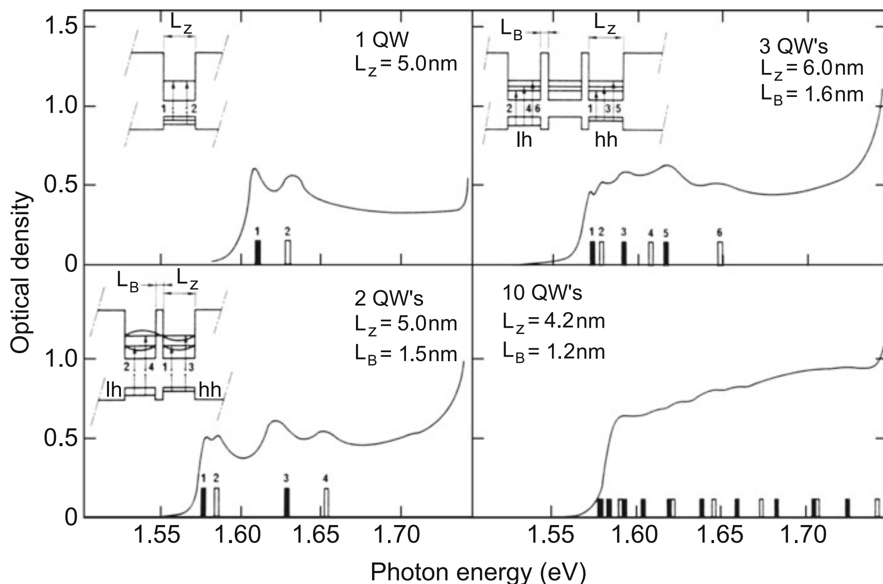

Fig. 11.26. Absorption spectra of a single, double, triple and ten coupled quantum wells. Theoretically predicted transitions with heavy (light) holes are labeled with *filled* (*empty*) *bars* at their respective transition energies. Adapted from [804]

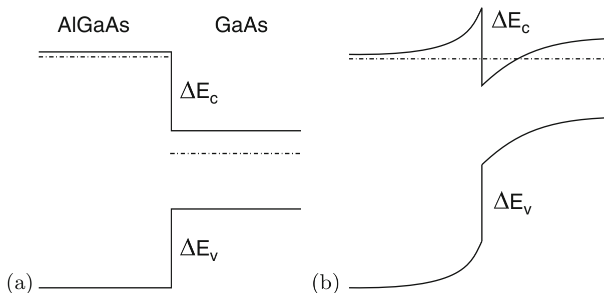

Fig. 11.27. Schematic formation of a triangular potential well in a n-AlGaAs/n-GaAs heterostructure, (**a**) before and (**b**) after equilibration of Fermi levels

11.3.4 Single Heterointerface Between Doped Materials

We consider a single heterointerface between n-doped materials. As an example we take n-AlGaAs/n-GaAs (Fig. 11.27). First, we consider the materials without contact, forming a type-I structure. In thermodynamic equilibrium the system must have a constant Fermi level. Thus, charge is transferred from the region close to the interface from AlGaAs to GaAs. This results in the formation of a triangular potential well in the GaAs close to the interface. A two-dimensional electron gas (2DEG) forms in this potential well

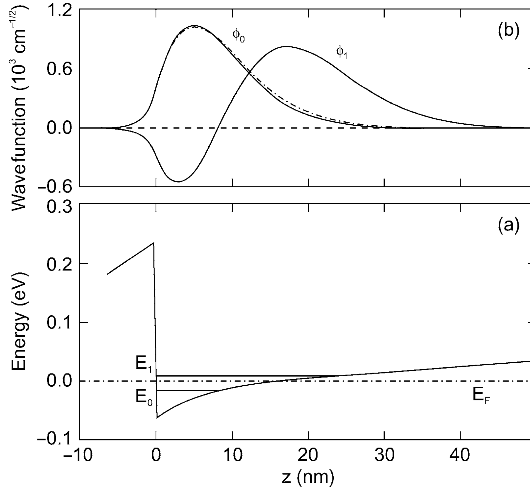

Fig. 11.28. (**a**) Conduction-band edge at a GaAs/$Al_{0.3}Ga_{0.7}As$ heterointerface ($T = 0$ K) with two confined states at E_0 and E_1 marked with *solid horizontal lines*. In the GaAs channel there are 5×10^{11} cm^{-2} electrons. The barrier height is 300 meV, $N_D^{GaAs} = 3 \times 10^{14}$ cm^{-3}. The position of the Fermi level E_F is at $E = 0$ and indicated with a *dash-dotted line*. (**b**) Envelope wavefunctions ϕ_0 and ϕ_1 of the two confined states, *dash-dotted line*: calculation without exchange and correlation for state at E_0. Adapted from [806]

(Fig. 11.28). The charge transfer in thermodynamic equilibrium adjusts the band bending and the charge density (quantized levels in the well) in such a way that they are self-consistent. The Poisson equation and the Schrödinger equation are simultaneously fulfilled. Numerically, both equations are iteratively solved and the solution is altered until it is self-consistent, i.e. it fulfills both equations.

If the region of the 2DEG is not doped, the electron gas exists without any dopant atoms and ionized impurity scattering no longer exists. This concept is called *modulation doping*. Mobilities up to 3.1×10^7 cm^2/Vs have been realized (Fig. 11.29). The theoretical limits of mobility in a 2DEG at modulation-doped AlGaAs/GaAs heterointerfaces are discussed in detail in [805].

11.4 Recombination in Quantum Wells

11.4.1 Thickness Dependence

The energy of exciton recombination in quantum wells is blue-shifted with respect to that in bulk material due to the quantum-confinement energies of electrons and holes (Fig. 11.30). The electron–hole recombination lineshape in quantum wells is given by the product of the joint density of states and the

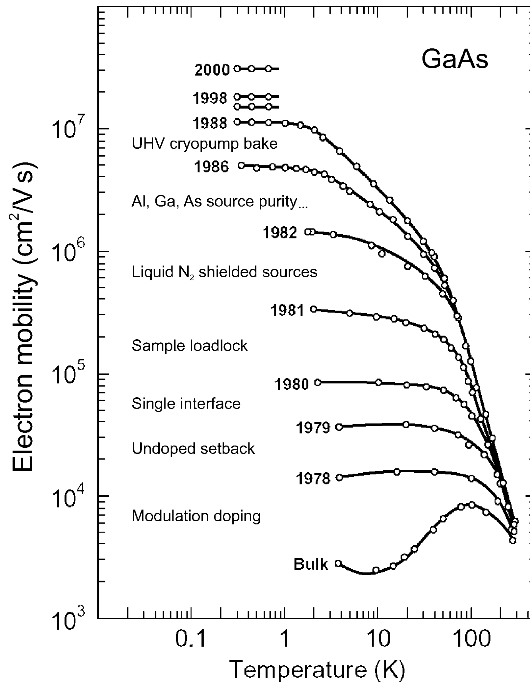

Fig. 11.29. Progress in the achievement of high electron mobility in GaAs, annotated with the technical innovation responsible for the improvement. Adapted from [808]

Boltzmann function (when Boltzmann statistics apply). The JDOS is given by a step function (Heavyside function $H(E)$).

$$I(E) \propto H(E - E_{11}) \exp\left(-\frac{E}{kT}\right) , \tag{11.9}$$

where $E_{11} = E_{\mathrm{g}} + E_{\mathrm{e1}} + E_{\mathrm{h1}}$ represents the energy of the E1–H1 subband edge as shown in Fig. 11.30. An experimental spectrum (Fig. 11.31a) shows that excitonic effects influence the recombination lineshape even at room temperature [807].

11.4.2 Broadening Effects

Many-Body Effects

At high carrier densities when the electron (quasi-) Fermi level is above the electron subband edge, the spectrum broadens and reflects the Fermi–Dirac distribution (Fig. 11.31b). At low temperatures a many-body effect, multiple electron–hole scattering with electrons at the Fermi edge, leads to an additional peak, termed *Fermi-edge singularity* that is discussed in [809].

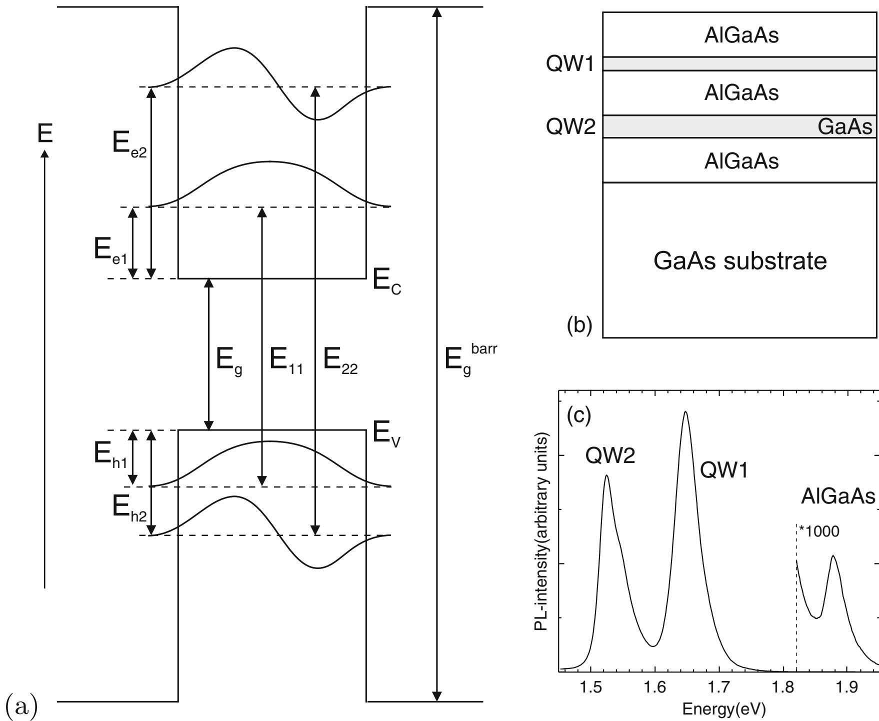

Fig. 11.30. (**a**) Schematic energy diagram of a quantum well with confined electron (e1, e2) and hole (h1, h2) states and recombination between them at energies E_{11} and E_{22}. (**b**) Schematic sample structure with two GaAs/Al$_x$Ga$_{1-x}$As quantum wells with thicknesses 3 nm and 6 nm. (**c**) Photoluminescence spectrum ($T = 300$ K) of the structure from part (**b**). A small amount of barrier luminescence appears at 1.88 eV, according to $x = 0.37$ (cf. Fig. 6.13c)

Homogeneous Broadening

The temperature dependence of the homogeneous broadening of quantum well luminescence has been investigated in [810]. It follows the dependence of the broadening known from bulk material (Sect. 9.5.8) with similar values for the LO broadening parameter. In Fig. 11.32a the reflectance spectra for different temperatures of a 17 nm GaAs/Al$_{0.3}$Ga$_{0.7}$As QW are shown. The optical phonon broadening parameter for various well widths is shown in Fig. 11.32b and coincides with the bulk value.

Inhomogeneous Broadening

Inhomogeneous broadening affects the recombination lineshape. Since the interfaces of the QW are not ideally flat, the exciton averages over different

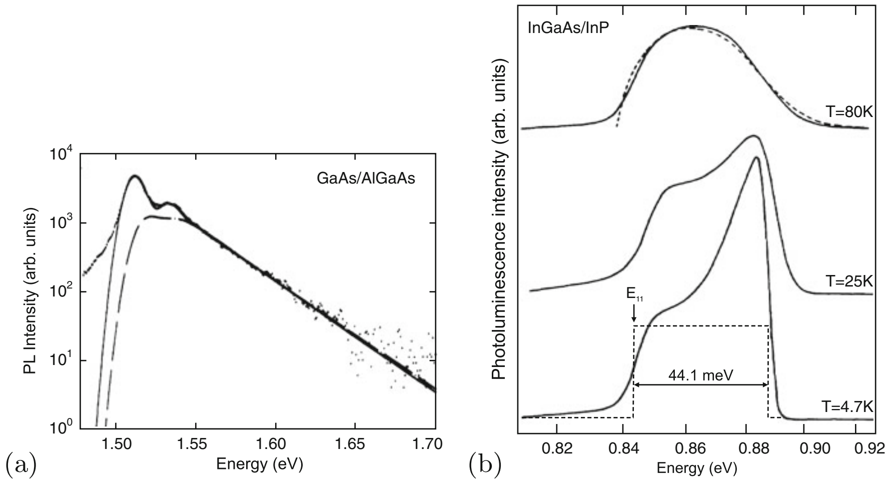

Fig. 11.31. (**a**) Photoluminescence spectrum of a 5-nm GaAs/AlGaAs quantum well at $T = 300\,\mathrm{K}$. The *solid* (*dashed*) line is fit with (without) excitonic effects. The two peaks are due to transitions involving heavy and light holes. Adapted from [808]. (**b**) Photoluminescence spectra at three different temperatures as labeled of a 10-nm modulation-doped InGaAs/InP quantum well with an electron sheet density $n_{\mathrm{s}} = 9.1 \times 10^{11}\,\mathrm{cm}^{-2}$. The electron quasi-Fermi level is $F_{\mathrm{n}} - (E_{\mathrm{C}} + E_{\mathrm{e1}}) = 44.1\,\mathrm{meV}$ from the subband edge. The *dashed line* in the $T = 80\,\mathrm{K}$ spectrum is the lineshape from JDOS and a Fermi–Dirac distribution without enhancement at the Fermi edge. Adapted from [809]

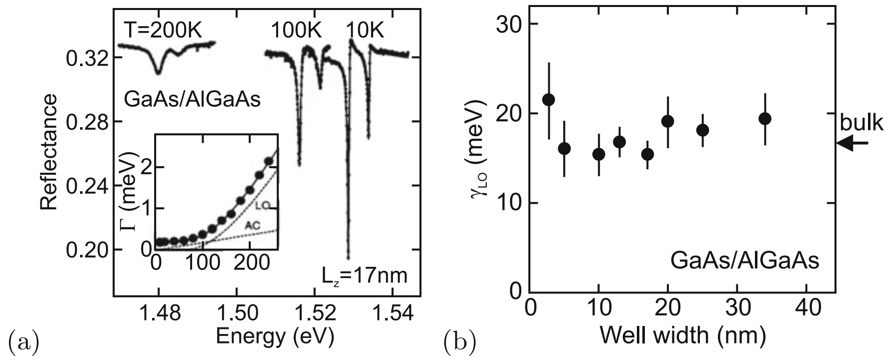

Fig. 11.32. (**a**) Reflectance spectra at various temperatures from a 17 nm thick GaAs/$\mathrm{Al_{0.3}Ga_{0.7}As}$ quantum well. The *inset* shows the temperature dependence of the homogeneous linewidth. (**b**) LO phonon broadening parameter (FWHM) for various quantum well widths. Adapted from [810]

quantum-well thicknesses within its volume. Also, e.g. for the GaAs/AlGaAs system, the wavefunction in the (binary) quantum well tunnels into the barrier, the amount depending on the QW width, and there 'sees' the alloy broadening (see Sect. 10.3.3). The problem of exciton dynamics in a potential with random fluctuations has been treated in detail [811, 812].

A simplified picture is as follows: At low temperatures the excitons populate preferentially the potential minima. A simple lineshape[4] of the QW absorption or joint density of states is given by a step function (cf. Table 9.2) at the QW band edge E_0. The inhomogeneous broadening has a Gaussian probability distribution $p(\delta E) \propto \exp[-(\delta E)^2/2\sigma^2)]$ with δE being the deviation from the QW band edge $\delta E = E - E_0$. The resulting lineshape is given by the convolution of the Gaussian with the unperturbed absorption spectrum yielding an error-function-like spectrum[5] as shown in Fig. 11.33a.

For complete thermalization the level population is given by the Boltzmann function. The recombination spectrum is given by the product of the absorption spectrum (or JDOS) and the Boltzmann function. It is (red-) shifted with respect to E_0 by about[6]

$$\Delta E(T) = -\frac{\sigma^2}{kT} = \gamma(T)\,kT\,. \tag{11.10}$$

This shift between emission and absorption is also called the Stokes shift.

Within their lifetime, limited at least by radiative recombination, the excitons are typically unable to reach the energy position required by the Boltzmann function, but only a local minimum. Thus, their thermalization may be incomplete due to insufficient lateral diffusion. This effect is particularly important at low temperatures when thermal emission into adjacent deeper potential minima is suppressed. In this case, the red-shift is smaller than expected from (11.10). A numerical simulation [811] yields such behavior of the energy position of the recombination line as shown in Fig. 11.33b. Simultaneously, the width of the recombination spectrum also exhibits a minimum (Fig. 11.33c). These findings are in agreement with experiments [813, 814]. An analytical model for temperature dependent exciton localization in the presence of disorder has been given in [815], yielding a value $0 \leq \gamma \leq \gamma_0 = (\sigma/kT)^2$ in (11.10).

A potential fluctuation can localize an exciton laterally at low temperatures [821] and behave like a quantum dot (cf. Sect. 13.3)). Localized and delocalized excitons are separated by a boundary called the mobility edge [816]. The transition between the two regimes is a Mott transition [817].

[4] neglecting excitonic enhancement

[5] The error function is defined as $\mathrm{erf}(x) = (2/\sqrt{\pi}) \int_0^z \exp -t^2\,\mathrm{d}t$.

[6] Formula (11.10) is exact for the product of a Gaussian and the Boltzmann function.

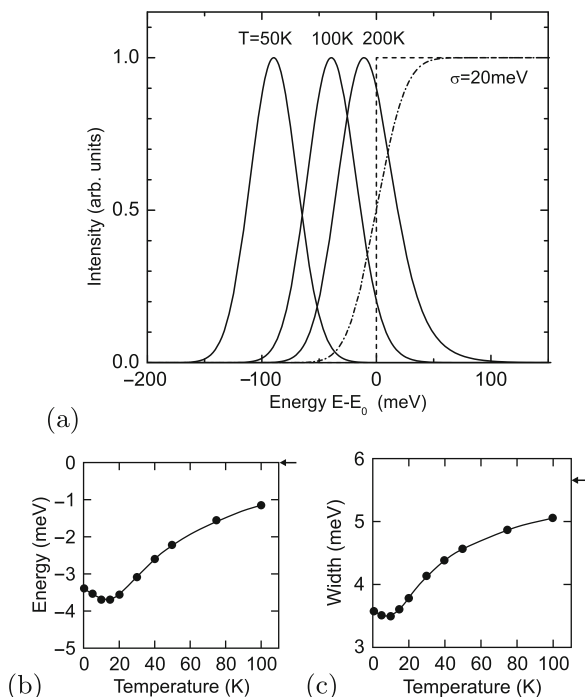

Fig. 11.33. (**a**) Recombination spectra (*solid lines*, scaled to same height) of a model quantum well for different temperatures as labeled and complete thermalization, *dashed* (*dash-dotted*) *line* is unperturbed (inhomogeneously broadened by $\sigma = 20\,\mathrm{meV}$) shape of the QW absorption edge. The energy scale is relative to the energy position of the unperturbed QW absorption edge at E_0. (**b**) Theoretical energy position and (**c**) linewidth of exciton recombination from a model disordered quantum well. The high-temperature limits are marked by *arrows*. Parts (**b**, **c**) adapted from [811]

Monolayer Growth Islands

Under certain growth conditions, quantum wells with piecewise very flat interfaces can be fabricated. The thickness difference between such regions (with lateral extension in the µm range) is an integer monolayer. Accordingly, the recombination spectrum yields several, typically two or three, discrete lines (Fig. 11.34).

11.4.3 Quantum Confined Stark Effect

The quantum confined Stark effect (QCSE, Sect. 12.1.2) in quantum wells shifts energy levels when electric fields are present along the width of the quantum well. A strong effect exists for pyro- and piezoelectric material combinations such as *c*-axis oriented (In,Ga)N/(Al,Ga)N [818, 819] or

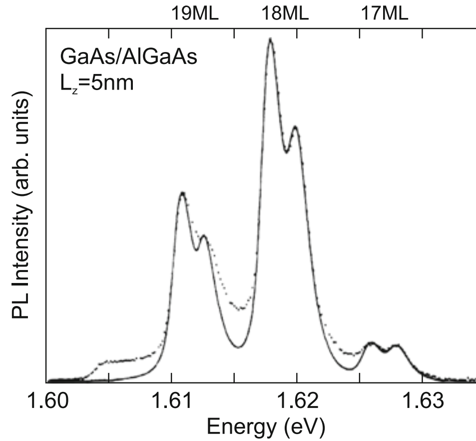

Fig. 11.34. Photoluminescence spectrum ($T = 2\,\mathrm{K}$) (*dots*) of GaAs/AlGaAs quantum well grown by MBE with 120 s growth interruptions. Recombination is due to excitons in islands of 19, 18, and 17 monolayers ($a_0/2$) height. The *solid line* is a lineshape fit including lifetime broadening ($\Gamma = 1.34\,\mathrm{meV}$) and residual inhomogeneous broadening ($\sigma = 0.04\,\mathrm{meV}$) due to AlGaAs barrier alloy fluctuations. Note that the energy separation of the peaks is much larger than kT. The peak doublet structure is discussed in [807]. Adapted from [807]

(Cd,Zn)O/(Mg,Zn)O [820, 821] quantum wells due to the built-in electric field (cf. Sect. 14.2). The QCSE induced red-shift is larger in thicker quantum wells and goes beyond the bulk band gap of the quantum well material (Fig. 11.35b). Also the wavefunction overlap is reduced with increasing well width, leading to an increase of the radiative recombination lifetime as shown in Fig. 11.35. The pyroelectric field and the related modification of lifetime are absent in quantum wells grown on non-polar directions such as [11.0] (Fig. 11.35a).

11.5 Isotope Superlattices

A special type of heterostructure is the modulation of the isotope content. The first kind of heterostructures made like this were $^{70}\mathrm{Ge}_n/^{74}\mathrm{Ge}_n$ symmetric superlattices [822]. Figure 11.36 shows phonon energies determined from Raman spectroscopy for various layer numbers n. The modes are classified by $^{70}\mathrm{LO}_m$ and $^{74}\mathrm{LO}_m$ denoting the material in which the amplitude is maximal and m being the number of maxima in that medium.[7] Such modes are visualized in Fig. 11.37a for a $^{69}\mathrm{GaP}_{16}/^{71}\mathrm{GaP}_{16}$ superlattice. Theoretical mode energies as a function of the superlattice period are shown in Fig. 11.37b.

[7]Only modes with odd m are Raman-active.

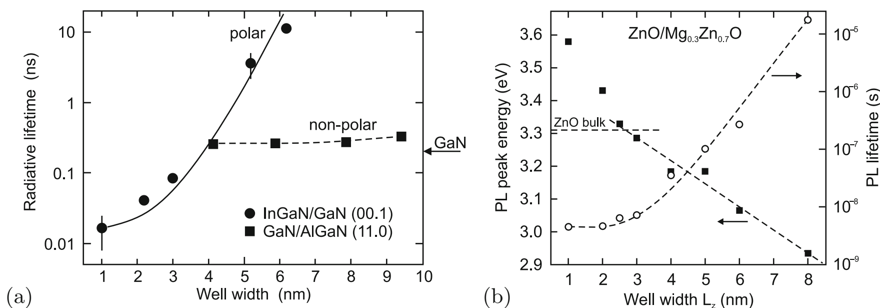

Fig. 11.35. (**a**) Radiative lifetime of electron-hole pairs in polar [00.1]-oriented $In_{0.2}Ga_{0.8}N/GaN$ (*circles*) and non-polar [11.0]-oriented $GaN/Al_{0.2}Ga_{0.8}N$ (*squares*) quantum wells of varying thickness. Experimental data are shown in *symbols*. The *solid line* is the (scaled) theoretical dependence of the electron-hole overlap for InGaN/GaN QWs. The *dashed line* is guide to the eyes. The *arrow* denotes the recombination time constant in bulk GaN. Adapted from [823, 824]. (**b**) Low temperature PL peak recombination energy (*solid squares*) for $ZnO/Mg_{0.3}Zn_{0.7}O$ quantum wells for various well widths L_z (barrier width $L_B = 5$ nm). *Dashed line* indicates dependence for internal field of 0.9 MV/cm, *horizontal dashed line* indicates recombination energy in ZnO bulk. Carrier lifetime determined from PL (*circles*), *dashed line* is guide to the eyes. Adapted from [821]

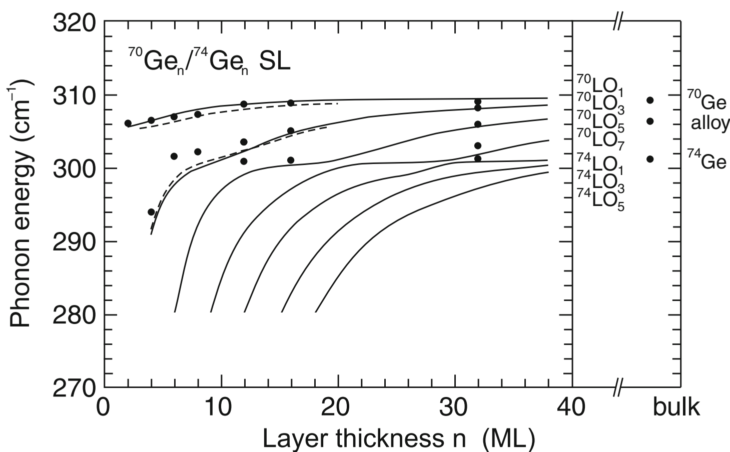

Fig. 11.36. Measured (*full circles*) and theoretical (*solid lines*) confined LO phonon energies in $^{70}Ge_n/^{74}Ge_n$ superlattices vs. the layer thickness (number of monolayers) n. The *dashed lines* represent a calculation that considers intermixing at the interfaces. On the right, the energies of bulk modes for isotopically pure ^{70}Ge and ^{74}Ge are shown together with that of an $^{70}Ge_{0.5}{}^{70}Ge_{0.5}$ alloy. Adapted from [822]

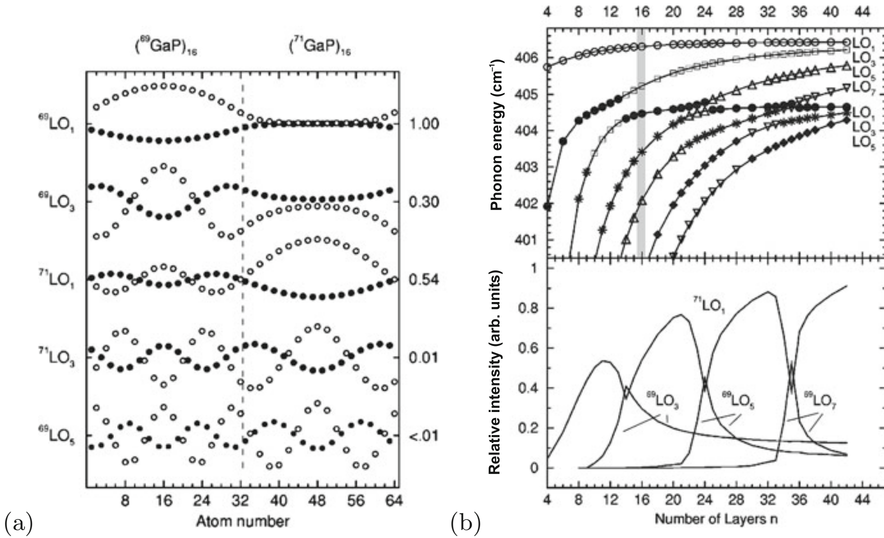

Fig. 11.37. (**a**) Atomic displacements [Ga (*filled dots*) and P (*open circles*)] of odd-index LO modes in a $^{69}Ga_{16}P/^{71}Ga_{16}P$ superlattice unit cell. These modes have even parity with respect to midlayer planes, which are at atom numbers 16 and 48 in this example. The labels on the left identify the predominant character of the mode, those on the right give the relative Raman intensities with respect to that of the $^{69}LO_1$ mode. The tick marks on the vertical axis indicate zero displacement of the respective mode. (**b**) *Upper panel*: Energies and characters of odd-index LO phonon modes in GaP isotope SLs as calculated within the planar bond charge model for the case of ideal interfaces. $^{69}LO_m$ modes are shown as *open symbols*; $^{71}LO_m$ modes as *full symbols*. The *shaded area* marks $n = 16$ for which the atomic displacements of the modes are shown in part (**a**). *Lower panel*: Calculated intensities of the modes relative to that of the $^{69}LO_1$ phonon mode. Adapted from [259], reprinted with permission, ©1999 APS

11.6 Wafer Bonding

Wafer bonding is a fairly recently developed method to join different and dissimilar materials. Two wafers of the respective materials are put together face to face and are adequately fused. The idea is to not only 'glue' the wafers together with a sticky (and compliant) organic material, but to form strong atomic bonds between the two materials with possibly a perfect interface. In some cases, the interface needs to allow charge-carrier transport through it. Less stringent conditions need to be met for photon transport.

Mechanical deficiencies such as surface roughness, dust particles and the like must be avoided in the wafer-bonding process since they result in voids. Several methods have been developed for bonding various materials [825, 826]. Such processes are successful for large substrate sizes. With proper process-

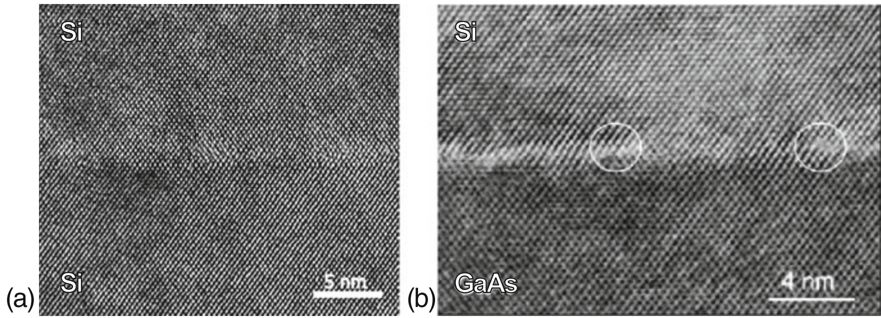

Fig. 11.38. High-resolution TEM images of wafer-bonded (**a**) Si-Si and (**b**) GaAs-Si interfaces. *White circles* indicate the position of misfit dislocations. Part (**a**) reprinted from [827], ©2003, with permission from Elsevier. Part (**b**) reprinted with permission from [828], ©1998 AIP

ing, ideal interfaces can be created, as shown in Fig. 11.38. Such structures, if made between a p-doped and a n-doped semiconductor, show diode characteristics.

12 External Fields

The energy levels of the solid and its optical and electronic properties depend on external electric and magnetic fields. In high magnetic fields and at low temperatures the quantum Hall effects give evidence for new states of matter in many-body systems.

12.1 Electric Fields

12.1.1 Bulk Material

The center-of-mass motion of the exciton is not influenced by an electric field. The Hamilton operator for the relative motion of an electron–hole pair of reduced mass μ along z in the presence of an electric field $\mathcal{E}$ along the z direction is

$$\hat{H} = -\frac{\hbar^2}{2\mu}\,\Delta - e\,\mathcal{E}\,z\;. \tag{12.1}$$

Here, the Coulomb interaction, leading to the formation of bound exciton states, is neglected. In the plane perpendicular to the field (here the z direction) the solutions for the relative motion are just plane waves.

In the electric field the bands are tilted (Fig. 12.1), i.e. there is no longer an overall band gap. Accordingly, the wavefunctions are modified and have exponential tails in the energy gap.

After separation of the motion in the (x,y) plane the Schrödinger equation for the motion in the z direction is

$$\left(-\frac{\hbar^2}{2\mu}\frac{\mathrm{d}^2}{\mathrm{d}z^2} - e\mathcal{E}z - E_z\right)\phi(z) = 0\;, \tag{12.2}$$

which is of the type

$$\frac{\mathrm{d}^2 f(\xi)}{\mathrm{d}\xi^2} - \xi\, f(\xi) = 0\;, \tag{12.3}$$

with $\xi = \frac{E_z}{\Theta} - z\left(\frac{2\mu e}{\hbar^2}\mathcal{E}\right)^{1/3}$ and the optoelectronic energy $\Theta = \left(\frac{e^2\mathcal{E}^2\hbar^2}{2\mu}\right)^{1/3}$. The solution of (12.3) is given by the Airy function Ai (cf. Fig. 12.2):

M. Grundmann, *The Physics of Semiconductors*, 2nd ed., Graduate Texts in Physics, DOI 10.1007/978-3-642-13884-3_12,

© Springer-Verlag Berlin Heidelberg 2010

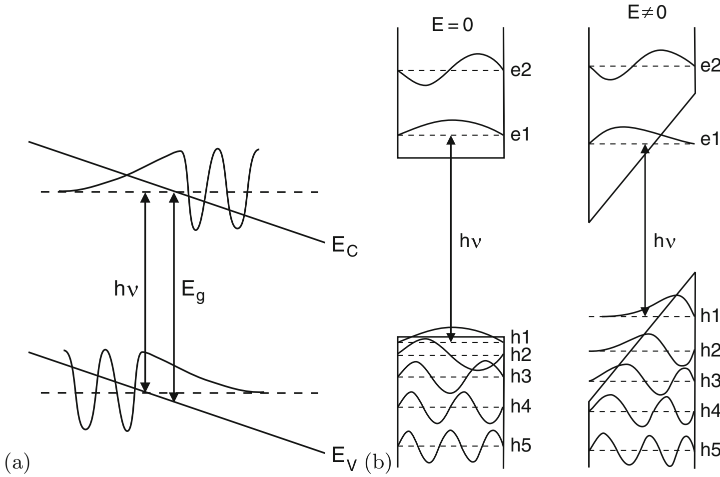

Fig. 12.1. Impact of an electric field on (**a**) bulk material (tilt of bands) and (**b**) a quantum well (quantum confined Stark effect, QCSE)

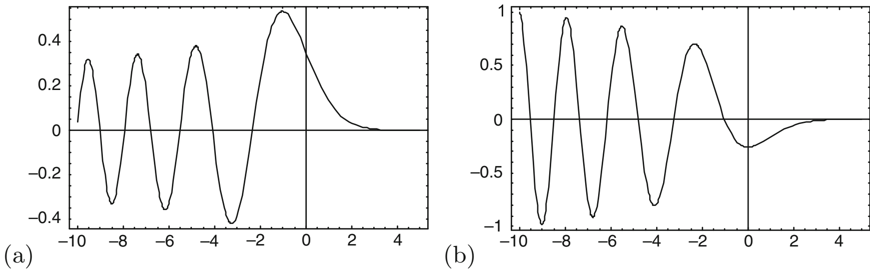

Fig. 12.2. (**a**) Airy function Ai(x), (**b**) Ai'(x)

$$\phi_{E_z}(\xi) = \frac{\sqrt{e\mathcal{E}}}{\Theta} \, Ai(\xi) \, . \tag{12.4}$$

The pre-factor guaranties the orthonormality (with regard to the E_z). The absorption spectrum is then given by

$$\alpha(\omega, E) \propto \frac{1}{\omega} \sqrt{\Theta} \, \pi \left[Ai'^2(\eta) - \eta \, Ai^2(\eta) \right] \, , \tag{12.5}$$

with $\eta = (E_\mathrm{g} - E)/\Theta$ and $Ai'(x) = \mathrm{d}Ai(x)/\mathrm{d}x$.

Optical transitions below the band gap become possible that are photon-assisted tunneling processes. The below-bandgap transitions have the form of an exponential tail. Additionally, oscillations develop above the band gap, the so-called Franz–Keldysh oscillations (FKO) (Fig. 12.3a).

The absorption spectrum scales with the optoelectronic energy Θ. The energy position of the FKO peaks E_n is periodic with ($\nu \sim 0.5$)

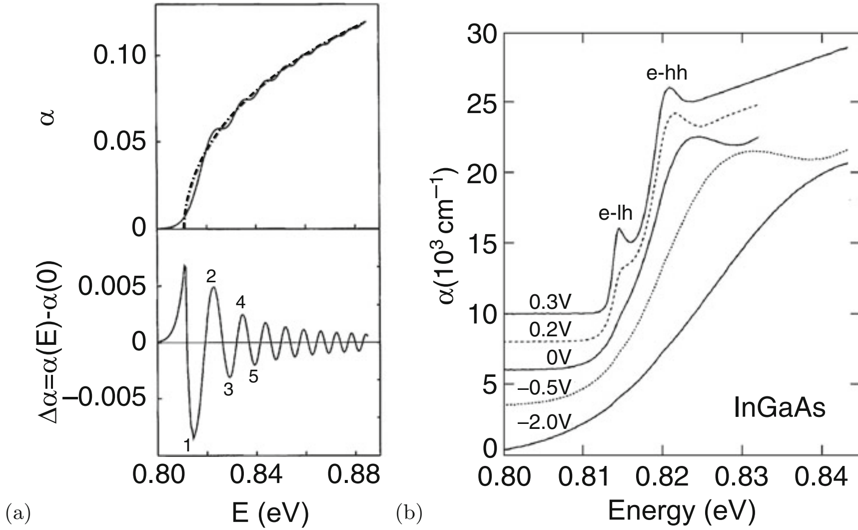

Fig. 12.3. (**a**) Theoretical absorption (*top panel*) with (*solid line*) and without (*dash-dotted line*) electric field for a volume semiconductor (without Coulomb interaction) and theoretical change of absorption (*bottom panel*). (**b**) Experimental absorption spectra of InGaAs on InP at $T = 15\,\mathrm{K}$ for various applied voltages as labeled. Adapted from [829]

$$(E_n - E_\mathrm{g})^{3/2} \propto (n - \nu)\,\mathcal{E}\,\sqrt{\mu}\,. \tag{12.6}$$

A nonperiodicity can indicate a nonparabolicity of the mass. For a given mass the electric field strength can be determined. Well-pronounced oscillations are only present for homogeneous fields.

Experimental spectra show additionally the peaks due to excitonic correlation (Fig. 12.3b) at low field strength. At higher fields the FKO evolve and the amplitude of the excitonic peaks decreases because the excitons are ionized in the field.

12.1.2 Quantum Wells

In a quantum well an electric field along the confinement direction (z direction) causes electrons and holes to shift their mean position to opposite interfaces (Fig. 12.1b). However, excitons are not ionized due to the electric field. With increasing field (for both field directions) the energy position of the absorption edge and the recombination energy is reduced. This is the quantum confined Stark effect (QCSE). Corresponding experimental data are shown in Fig. 12.4i–v. The shift depends quadratically on the electric field since the exciton has no permanent dipole moment (mirror symmetry of the quantum well). Thus, only the second-order Stark effect is present (as for the hydrogen atom) in which the field first induces a dipole $\mathbf{p} = \alpha\mathbf{E}$. This

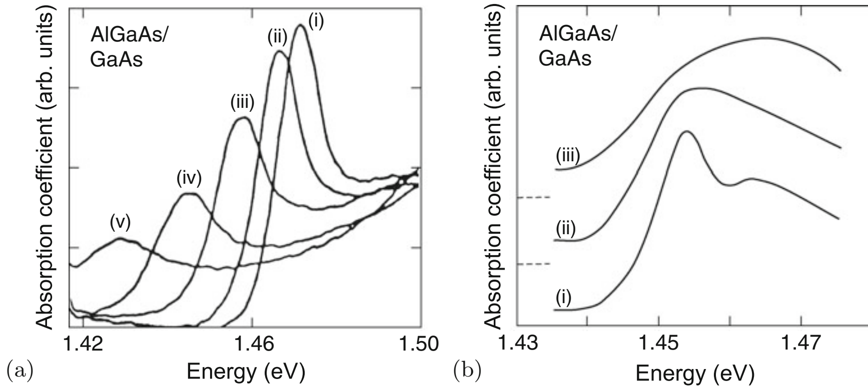

Fig. 12.4. Impact of electric fields on the absorption spectrum of $n \times$ (9.5 nm GaAs/9.8 nm $Al_{0.32}Ga_{0.68}As$) multiple quantum well structures. (**a**): Electric field along the [001] growth direction ($n = 50$), (**i**)–(**v**): $\mathcal{E} = 0$, 0.6, 1.1, 1.5, and 2×10^5 V/cm. (**b**): Electric field within the interface plane (n=60), (**i**,**ii**,**iii**): $\mathcal{E} = 0$, 1.1, and $2{\times}10^5$ V/cm. Adapted from [830]

dipole interacts with the field with an energy $E = -\mathbf{p} \cdot \mathbf{E} = -\alpha \mathbf{E}^2$. The carrier separation in opposite sides of the quantum well (Fig. 12.4b) leads to a reduced overlap of the electron and hole wavefunctions and subsequently to an increased recombination lifetime (see Fig. 11.35).

If the field is within the quantum-well interface plane, the field leads to the ionization of excitons without shift of the energy position. The loss of the excitonic peak is visualized in the spectra in Fig. 12.4a–c.

12.2 Magnetic Fields

In magnetic fields, electrons (or holes) perform a cyclotron motion with frequency $\omega_c = eB/m^*$, i.e. a motion perpendicular to the magnetic field on a line of constant energy in **k**-space. This line is the intersection of a plane perpendicular to the magnetic field and the respective isoenergy surface in **k**-space. For semiconductors with anisotropic mass, such as Si and Ge, the quantum theory of cyclotron resonance has been given in [831]. The physics of semiconductors in magnetic fields is covered in detail in [832].

The ballistic cyclotron motion can only occur between two scattering events. Thus, a significantly long path along the cyclotron trajectory (classically speaking) and the connected magnetotransport properties are only possible when

– $\omega_c \tau \gg 1$, i.e. when the average scattering time τ is sufficiently large. This requires high mobility.

– the magnetic field is sufficiently strong and the temperature sufficiently low, i.e. $\hbar\omega_c \gg kT$, such that thermal excitations do not scatter electrons between different Landau levels.
– the cyclotron path is free of geometric obstructions.

An external magnetic field also produces a splitting of the spin states. For the electron, the energy splitting ΔE is given by

$$\Delta E = g_e^* \, \mu_B \, B \,, \tag{12.7}$$

where B is the magnetic-field amplitude and g_e^* the (effective) electron g-factor. This value differs from the free-electron value in vacuum of $g_e = 2.0023$ due to the presence of spin-orbit interaction (see Sect. 12.2.2). Values for g_e^* at low carrier density and low temperatures are 2 for Si, 1.2 for InP and ZnSe, -1.65 for CdTe, -0.44 for GaAs, -15 in InAs, and -50 for InSb. In [833] the temperature dependence of g_e^* in GaAs, InP and CdTe is also measured and discussed. The electron g-factor increases in thin GaAs/AlGaAs quantum wells [834].

12.2.1 Free-Carrier Absorption

The absorption of free carriers was treated in Sect. 9.7 without the presence of a static magnetic field. Solving (8.25) for a static magnetic field $\mathbf{B} = \mu_0 \mathbf{H}$ with $\mathbf{H} = H\,(h_x, h_y, h_z)$ and a harmonic electric field $\mathbf{E} \propto \exp(-\mathrm{i}\omega t)$ yields for the dielectric tensor (cf. (9.54))

$$\epsilon = \frac{\mathrm{i}}{\epsilon_0 \omega}\, \sigma \,, \tag{12.8}$$

by comparing $\mathbf{j} = \sigma \mathbf{E} = qN\mathbf{v}$

$$\epsilon(\omega) = -\omega_p^{*2} \left[(\omega^2 + \mathrm{i}\omega\gamma)\mathbf{1} - \mathrm{i}\omega_c \begin{pmatrix} 0 & -h_z & h_y \\ h_z & 0 & -h_z \\ -h_y & h_z & 0 \end{pmatrix} \right]^{-1} \,, \tag{12.9}$$

where $\mathbf{1}$ denotes the (3 by 3) unity matrix and $\gamma = 1/\tau = m^*\mu/q$ is the damping parameter with μ representing the optical carrier mobility. The (unscreened) plasma frequency is given by

$$\omega_p^{*2} = n\, \frac{e^2}{\epsilon_0 m^*} \,. \tag{12.10}$$

The free-carrier cyclotron frequency is

$$\omega_c = e\, \frac{\mu_0 \, H}{m^*} \,. \tag{12.11}$$

If the effective mass is treated as a tensor, $1/m^*$ is replaced by $\mathbf{m}^{*-1}$ in (12.10) and (12.11). For zero magnetic field the classical Drude theory for one carrier species is recovered (cf. (9.56a))

$$\epsilon(\omega) = -\frac{\omega_{\mathrm{p}}^{*2}}{\omega(\omega + \mathrm{i}\gamma)} \, . \tag{12.12}$$

With the magnetic field perpendicular to the sample surface, i.e. $\mathbf{B} = \mu_0(0, 0, H)$ the magneto-optic dielectric tensor simplifies to (cf. (8.26d))

$$\epsilon(\omega) = \frac{-\omega_{\mathrm{p}}^{*2}}{\omega^2} \begin{pmatrix} \tilde{\epsilon}_{xx} & \mathrm{i}\tilde{\epsilon}_{xy} & 0 \\ -\mathrm{i}\tilde{\epsilon}_{xy} & \tilde{\epsilon}_{xx} & 0 \\ 0 & 0 & \tilde{\epsilon}_{zz} \end{pmatrix} \tag{12.13a}$$

$$\tilde{\epsilon}_{xx} = \frac{1 + \mathrm{i}\gamma/\omega}{(1 + \mathrm{i}\gamma/\omega)^2 - (\omega_{\mathrm{c}}/\omega)^2} \tag{12.13b}$$

$$\tilde{\epsilon}_{zz} = \frac{1}{(1 + \mathrm{i}\gamma/\omega)} \tag{12.13c}$$

$$\tilde{\epsilon}_{xy} = \frac{\omega_{\mathrm{c}}/\omega}{(1 + \mathrm{i}\gamma/\omega)^2 - (\omega_{\mathrm{c}}/\omega)^2} \, . \tag{12.13d}$$

The in-plane component ϵ_{xx} provides information about ω_{p}^* and γ, i.e. n and μ, the effective mass, are known. Additionally, the antisymmetric tensor component ϵ_{xy} is linear in the cyclotron frequency and provides q/m. This subtle but finite birefringence depends on the strength (and orientation) of the magnetic field and can be experimentally determined in the infrared using magneto-ellipsometry [835, 836]. Such 'optical Hall effect' experiment allows the determination of the carrier density n, the mobility μ, the carrier mass[1] m^* and the sign of the carrier charge $\mathrm{sgn}(q)$ with optical means. The electrical Hall effect (Sect. 8.4) can reveal n, μ and $\mathrm{sgn}(q)$ but cannot reveal the carrier mass.

12.2.2 Energy Levels in Bulk Crystals

In a 3D electron gas (the magnetic field is along z, i.e. $\mathbf{B} = B[0, 0, 1]$) the motion in the (x, y) plane is described by Landau levels. Quantum mechanically they correspond to levels of a harmonic oscillator. The magnetic field has no impact on the motion of electrons along z, such that in this direction a free dispersion relation $\propto k_z^2$ is present. The energy levels are given as

$$E_{nk_z} = \left(n + \frac{1}{2}\right) \hbar\omega_{\mathrm{c}} + \frac{\hbar^2}{2m} k_z^2 \, . \tag{12.14}$$

Thus, the states are on concentric cylinders in $\mathbf{k}$-space (Fig. 12.5a). The populated states of the 3D electron gas (at 0 K) lie within the Fermi vector

[1] We note that mobility and effective mass defined and measured in this way may be referred to as 'optical'. Other definitions and approaches to the mobility or effective mass may give different results.

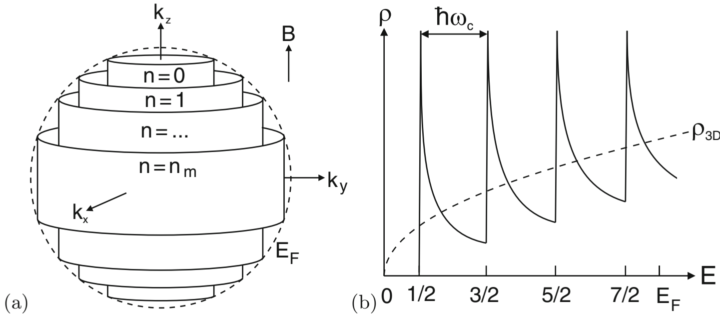

Fig. 12.5. 3D electron gas in an external magnetic field. (**a**) Allowed states in **k**-space for magnetic field along the z direction. (**b**) Density of states (DOS) ρ vs. energy (in units of $\hbar\omega_c$). *Dashed line* is three-dimensional DOS without magnetic field. Based on [765]

of length k_F. For the 3D system the density of states at the Fermi energy is a square root function of the Fermi energy (6.74). In the presence of a magnetic field the density of states diverges every time that a new cylinder (with a one-dimensional density of states, (6.78)) touches the Fermi surface at E_F. In real systems, the divergence will be smoothed, however, a pronounced peak or the periodic nature of the density of states is often preserved.

The period is given by the number n_m of cyclotron orbits (Landau levels) within the Fermi surface.

$$\left(n_m + \frac{1}{2}\right) \hbar\omega_c = E_F \; . \tag{12.15}$$

If the number of carriers is constant, the density of states at the Fermi energy at varying magnetic field varies periodically with $1/B$. From the conditions $\left(n_m + \frac{1}{2}\right) \hbar \frac{eB_1}{m} = E_F$ and $\left(n_m + 1 + \frac{1}{2}\right) \hbar \frac{eB_2}{m} = E_F$ with $\frac{1}{B_2} = \frac{1}{B_1} + \frac{1}{\Delta B}$ we find

$$\frac{1}{\Delta B} = \frac{e\hbar}{m^* E_F} \; . \tag{12.16}$$

This periodicity is used to determine experimentally, e.g., the properties of the Fermi surface in metals using the Shubnikov–de Haas oscillations (of the magnetoresistance) or the de Haas–van Alphén effect (oscillation of the magnetic susceptibility).

Equation (12.14) needs to be extended to account for the splitting (12.7) of the Landau level due to the electron spin. According to [837] the electron Landau level energy can be written as

$$E_n = \left(n + \frac{1}{2}\right) \frac{\hbar e B}{m^*(E)} \pm g_e^*(E) \mu_B B \; , \tag{12.17}$$

with energy dependent effective mass and g-factor

$$\frac{1}{m^*(E)} = \frac{1}{m^*(0)} \frac{E_g(E_g + \Delta_0)}{3E_g + 2\Delta_0} \left(\frac{2}{E + E_g} + \frac{1}{E + E_g + \Delta_0} \right) \quad (12.18a)$$

$$g_e^*(E) = g_e^*(0) \frac{E_g(E_g + \Delta_0)}{\Delta_0} \left(\frac{1}{E + E_g} - \frac{1}{E + E_g + \Delta_0} \right) \quad (12.18b)$$

The band edge value $m^*(0)$ of the effective mass is given by (6.42) and that of the g-factor by

$$g_e^*(0) = 2 \left[1 - \frac{2\Delta_0}{3E_g(E_g + \Delta_0)} E_P \right] . \quad (12.19)$$

For large spin-orbit splitting, the value of the g-factor deviates strongly from 2 and becomes negative.

12.2.3 Energy Levels in a 2DEG

In a 2D electron gas (2DEG), e.g. in a quantum well or a potential well at a modulation-doped heterointerface, a free motion in z is not possible and k_z is quantized. The energy levels (for each 2D subband) are only given by the cyclotron energy (Fig. 12.6a). The density of states is a sequence of δ-like peaks (Fig. 12.6b). Each peak contributes (degeneracy $\hat{g}$ of a Landau level) a total number of

$$\hat{g} = \frac{eB}{h} \quad (12.20)$$

states (per unit area without spin degeneracy and without the degeneracy of the band extremum). In reality, disorder effects lead to an inhomogeneous

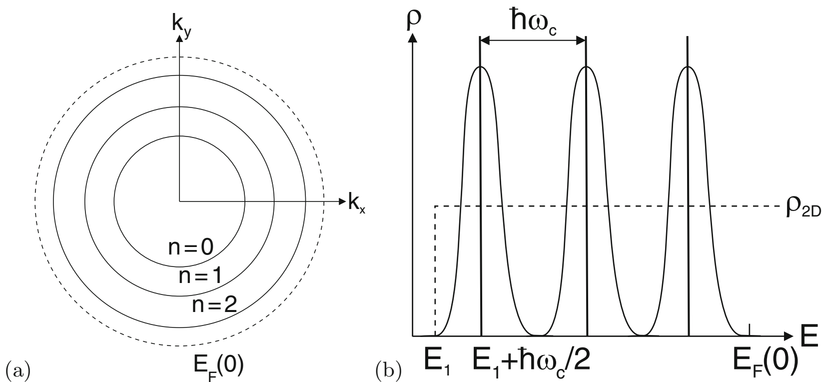

Fig. 12.6. 2D electron gas in an external magnetic field. (**a**) Allowed states in **k**-space. (**b**) Density of states (DOS) ρ vs. energy. *Dashed line* is two-dimensional DOS without magnetic field. *Thick vertical lines*: δ-like DOS without broadening, *curves*: broadened DOS. Based on [765]

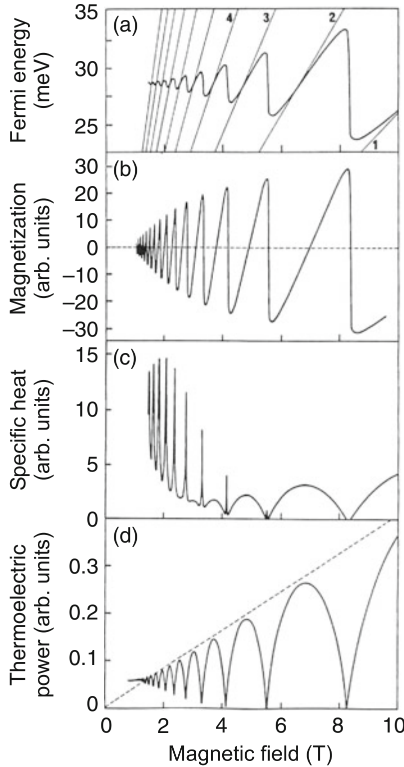

Fig. 12.7. Oscillatory (theory, $T = 6\,\mathrm{K}$) behavior of a 2DEG (GaAs/AlGaAs) in a magnetic field: (**a**) Fermi level, (**b**) magnetization, (**c**) specific heat, (**d**) thermoelectric power. A Gaussian broadening of 0.5 meV was assumed. Adapted from [765, 838]

broadening of these peaks. The states in the tails of the peaks correspond to states that are localized in real space.

Also, in a 2D system several physical properties exhibit an oscillatory behavior as a function of Fermi level, i.e. with varying electron number, and as a function of the magnetic field at fixed Fermi energy, i.e. at fixed electron number (Fig. 12.7).

12.2.4 Shubnikov–de Haas Oscillations

From the 2D density of states (per unit area including spin degeneracy) $D^{2\mathrm{D}}(E) = m^*/\pi\hbar^2$ the sheet density of electrons n_s can be expressed as a function of the Fermi level (at $T = 0\,\mathrm{K}$ without spin degeneracy)

$$n_\mathrm{s} = \frac{m^*}{2\pi\hbar^2}\,E_\mathrm{F}\;. \tag{12.21}$$

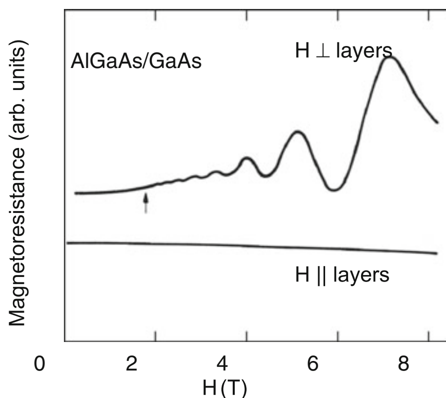

Fig. 12.8. Shubnikov–de Haas oscillations at a modulation-doped AlGaAs/GaAs heterostructure with a 2DEG, $n = 1.7 \times 10^{17}\,\mathrm{cm}^{-2}$ and $\mu = 11\,400\,\mathrm{cm}^2/\mathrm{Vs}$. Data from [839]

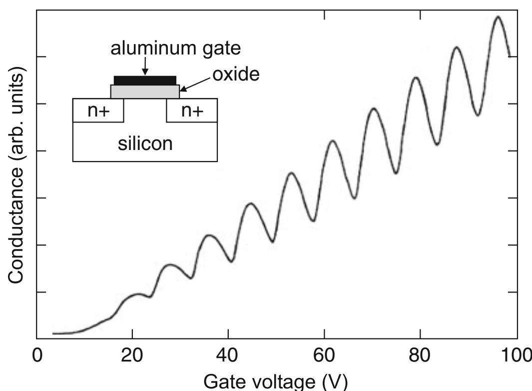

Fig. 12.9. Shubnikov–de Haas oscillations of a 2DEG at the (100) surface of p-type silicon (100 Ω cm) at a magnetic field of 33 kOe and $T = 1.34\,\mathrm{K}$. The *inset* shows schematically the contact geometry. Data from [840]

Using (12.16) we thus find (without spin degeneracy, without valley degeneracy), that the period of $1/B$ is $\propto n_\mathrm{s}$:

$$\frac{1}{\Delta B} = \frac{e}{h}\,\frac{1}{n_\mathrm{s}}\,. \tag{12.22}$$

The carrier density of a 2DEG can therefore be determined from the oscillations of magnetoresistance, and is proportional to the density of states at the Fermi level (Shubnikov–de Haas effect). A corresponding measurement with varying field and fixed electron density is shown in Fig. 12.8. The periodicity with $1/B$ is obvious. Since only the component of the magnetic field

perpendicular to the layer affects the (x, y) motion of the carriers, no effect is observed for the magnetic field parallel to the layer.

In another experiment the carrier density was varied at constant field (Fig. 12.9). The electron density in an inversion layer in p-type silicon is (linearly) varied with the gate voltage of a MOS (metal–oxide–semiconductor) structure (inset in Fig. 12.9, for MOS diodes cf. Sect. 23.5). In this experiment, the Fermi level was shifted through the Landau levels. The equidistant peaks show that indeed each Landau level contributes the same number of states.

12.3 Quantum Hall Effect

In high magnetic fields, at low temperatures and for high-mobility, 2D electron gases exhibit a deviation from the classical behavior. We recall that the classical Hall effect (i.e. considering the Lorentz force, classical Drude theory), the generation of a field $\mathcal{E}_y$ perpendicular to a current flow j_x (cf. Sect. 8.4), was described with the conductivity tensor σ (here, for the (x, y)-plane only)

$$\sigma = \frac{\sigma_0}{1+\omega_c^2\tau^2}\begin{pmatrix} 1 & \omega_c\tau \\ -\omega_c\tau & 1 \end{pmatrix} \tag{12.23a}$$

$$\sigma_{xx} = \sigma_0 \frac{1}{1+\omega_c^2\tau^2} \to 0 \tag{12.23b}$$

$$\sigma_{xy} = \sigma_0 \frac{\omega_c\tau}{1+\omega_c^2\tau^2} \to \frac{ne}{B} \, , \tag{12.23c}$$

where σ_0 is the zero-field conductivity $\sigma_0 = ne^2\tau/m^*$ (8.5). The arrows denote the limit for $\omega_c\tau \to \infty$, i.e. large fields. The resistivity tensor $\rho = \sigma^{-1}$ is given by

$$\rho = \begin{pmatrix} \rho_{xx} & \rho_{xy} \\ -\rho_{xy} & \rho_{xx} \end{pmatrix} \tag{12.24a}$$

$$\rho_{xx} = \frac{\sigma_{xx}}{\sigma_{xx}^2+\sigma_{xy}^2} \to 0 \tag{12.24b}$$

$$\rho_{xy} = \frac{-\sigma_{xy}}{\sigma_{xx}^2+\sigma_{xy}^2} \to -\frac{B}{ne} \, . \tag{12.24c}$$

12.3.1 Integral QHE

Experiments yield strong deviations from the linear behavior of the transverse resistivity $\rho_{xy} = \mathcal{E}_y/j_x = BR_\mathrm{H}$ with the Hall coefficient $R_\mathrm{H} = -1/(ne)$ with increasing magnetic field is observed at low temperatures for samples with high carrier mobility, i.e. $\omega_c\tau \gg 1$ (Fig. 12.10). In Fig. 12.11a,b, Hall bars are shown for 2DEGs in silicon metal–oxide–semiconductor field-effect

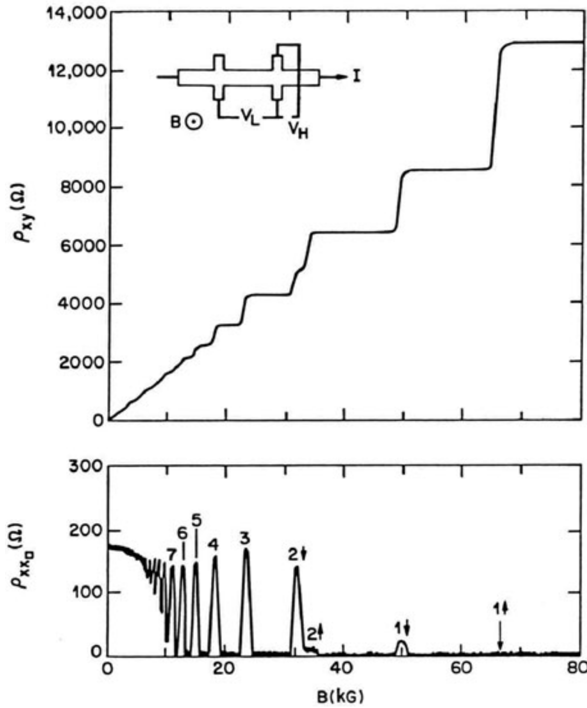

Fig. 12.10. Hall resistivity ρ_{xy} and longitudinal resistivity ρ_{xx} for a modulation-doped GaAs/AlGaAs heterostructure ($n = 4 \times 10^{11}\,\mathrm{cm}^{-2}$, $\mu = 8.6 \times 10^4\,\mathrm{cm}^2/\mathrm{Vs}$) at 50 mK as a function of magnetic field (10 kG=1 T). The numbers refer to the quantum number and spin polarization of the Landau level involved. The inset shows schematically the Hall bar geometry, V_L (V_H) denotes the longitudinal (Hall) voltage drop. Reprinted with permission from [841], ©1982 APS

transistor (Si-MOSFET) electron inversion layers and at GaAs/AlGaAs heterostructures, respectively.

The Hall resistivity exhibits extended Hall plateaus with resistivity values that are given by

$$\rho_{xy} = \frac{1}{i}\,\frac{h}{e^2}\,, \tag{12.25}$$

i.e. integer fractions of the quantized resistance $\rho_0 = h/e^2$ =25812.807... Ω, which is also called the von-Klitzing constant. In Fig. 12.10, a spin splitting is seen for the $n = 1$ Landau level (and a small one for the $n = 2$). We note that the topmost Hall plateau is due to the completely filled $n = 0$ Landau level; the resistance is $\rho_0/2$ due to the spin degeneracy of 2.

The integral quantum Hall effect, first reported in [843, 844], and the value for ρ_0 are found for a wide variety of samples and conditions regarding sample temperature, electron density or mobility of the 2DEG and the materials of the heterostructure.

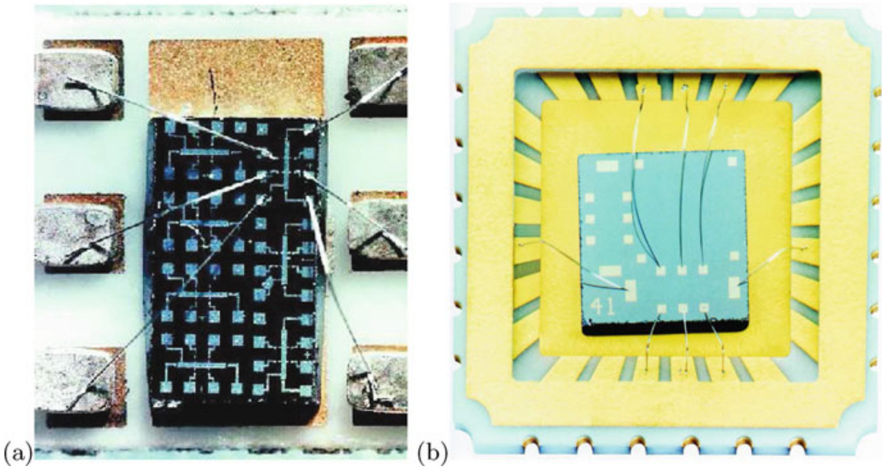

Fig. 12.11. (**a**) Silicon MOS (metal–oxide–semiconductor) structure of K. v. Klitzing's et al. original experiments. (**b**) GaAs/AlGaAs heterostructure sample grown with molecular beam epitaxy for QHE measurements, chip carrier and bond wires. Reprinted with permission from [842]

Within the plateau the resistivity is well defined within 10^{-7} or better up to 4×10^{-9}. A precise determination allows for a new normal for the unit Ohm [845, 846], being two orders of magnitude more precise than the realization in the SI system, and an independent value for the fine-structure constant $\alpha = \frac{e^2}{\hbar c} \frac{1}{4\pi\epsilon_0}$. At the same time, the longitudinal resistivity, starting from the classical value for small magnetic fields, exhibits oscillations and eventually it is zero for the plateaus in ρ_{xy}. For ρ_{xx} values of $10^{-10}\,\Omega/\Box$ have been measured, which corresponds to $10^{-16}\,\Omega$/cm for bulk material, a value three orders of magnitude smaller than for any nonsuperconductor.

The interpretation of the quantum Hall effect(s) is discussed in [847] among many other treatises. The simplest explanation is that the conductivity is zero when a Landau level is completely filled and the next is completely empty, i.e. the Fermi level lies between them. The temperature is small, i.e. $kT \ll \hbar\omega_\mathrm{c}$, such that no scattering between Landau levels can occur. Thus no current, similar to a completely filled valence band, can flow. The sheet carrier density n_s is given by counting the i filled Landau levels (degeneracy according to (12.20)) as

$$n_\mathrm{s} = i \frac{eB}{h} \,. \tag{12.26}$$

In the transverse direction energy dissipation takes place and the Hall resistivity $\rho_{xy} = B/(n_\mathrm{s} e)$ takes the (scattering-free) values given in (12.25).

However, this argument is too simple as it will not explain the extension of the plateaus. As soon as the system has one electron more or less, the Fermi energy will (for a system with δ-like density of states) be located in the

upper or lower Landau level, respectively. Then, the longitudinal conductivity should no longer be zero and the Hall resistivity deviates from the integer fraction of ρ_0.

Therefore (in the localization model) an inhomogeneous (Gaussian) broadening of the density of states is assumed. Additionally, the states in the tails of the distribution are considered nonconducting, i.e. localized, while those around the peak are considered conductive. This mobility edge is schematically shown in Fig. 12.12a–c.

When the Fermi level crosses the density of states of the broadened Landau level (upon increase of the magnetic field), it first populates localized states and ρ_{xx} remains at zero. When the Fermi level crosses the delocalized, conducting states, the longitudinal conductivity shows a peak and the Hall

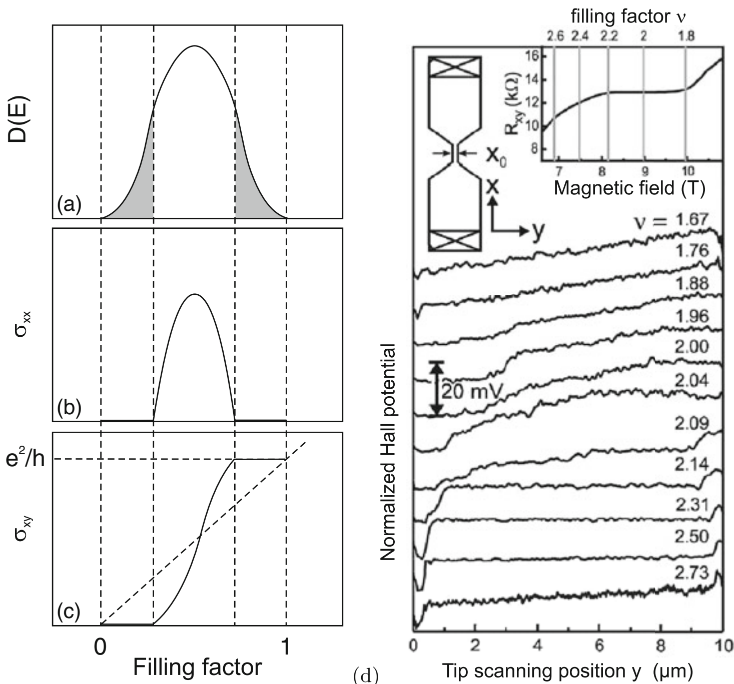

Fig. 12.12. (**a**) Density of states $D(E)$, (**b**) longitudinal conductivity σ_{xx} and (**c**) Hall conductivity σ_{xy} for a Landau level as a function of the filling factor $\mu = n/d$, where n is the electron density and d the degeneracy of the level. In (**a**) the filling factor relates via the position of the Fermi level to an energy scale. The *grey areas* in (**a**) denote localized states. The *slanted dashed line* in (**c**) has a slope of ne/B. Adapted from [850]. (**d**) Normalized Hall potential profile for different magnetic fields around filling factor $\nu = 2$. The overall voltage drop corresponds to 20 mV. The *insets* show the sample geometry and transport data. The 2DEG is from a GaAs/$Al_{0.33}Ga_{0.67}$As modulation-doped heterostructure, $n_s = 4.3 \times 10^{11}\,\text{cm}^{-2}$, $\mu = 5 \times 10^5\,\text{cm}^2/\text{Vs}$, $T = 1.4\,\text{K}$. Adapted from [851]

conductivity increases from the plateau value by e^2/h to the next plateau. When the Fermi level lies within the upper nonconducting states, the Hall resistivity remains constant in the next plateau. For the sample in Fig. 12.10 it has been estimated that 95% of the Landau level states are localized [841].

In the localization model it is still astonishing that the samples exhibit the step of e^2/h in the conductivity as if *all* electrons on the Landau level contribute to conduction, cf. (12.26). According to the calculations in [848] the Hall current lost by the localized states is compensated by an extra current by the extended states. The behavior of the electrons in the quantum Hall regime ('quantum Hall liquid') can be considered similar to that of an incompressible fluid where obstructions lead the fluid to move with increased velocity. Nevertheless, the single particle picture seems to be insufficient to model the IQHE.

Another model for the explanation of the QHE, supported now with plenty of experimental evidence, is the edge state model where quantized one-dimensional conductivity of edge channels, i.e. the presence of conductive channels along the sample boundaries, is evoked [849]. Due to depletion at the boundary of the sample, the density of the 2DEG varies at the edge of the sample and 'incompressible' stripes develop for which $\partial\mu/\partial n_{\mathrm{s}} \rightarrow \infty$. When the filling factor is far from an integer, the Hall voltage is found to vary linearly across the conductive channel and the current is thus homogeneous over the sample (Fig. 12.12d). In the Hall plateau, the Hall voltage is flat in the center of the channel and exhibits drops at the edges, indicating that the current flows along the boundary of the sample (edge current) [851] in agreement with predictions from [852]. Although the current pattern changes with varying magnetic field, the Hall resistivity remains at its quantized value.

The most fundamental arguments for the explanation of the IQHE come from gauge invariance and the presence of a macroscopic quantum state of electrons and magnetic flux quanta [853]. This model holds as long as there are any extended states at all.

12.3.2 Fractional QHE

For very low temperatures and in the extreme quantum limit, novel effects are observed when the kinetic energy of the electrons is smaller than their Coulomb interaction. New quantum Hall plateaus are observed at various fractional filling factors $\nu = p/q$. We note that the effects of the fractional quantum Hall effect (FQHE) in Fig. 12.13 mostly arise for magnetic fields beyond the $n = 1$ IQHE plateau. The filling factor $\nu = n/(eB/h)$ is now interpreted as the number of electrons per magnetic flux quantum $\phi_0 = h/e$.

The effects of the FQHE cannot be explained by single-electron physics. The plateaus at fractional fillings ν occur when the Fermi energy lies within a highly degenerate Landau (or spin) level and imply the presence of energy gaps due to many-particle interaction and the result of correlated 2D electron motion in the magnetic field.

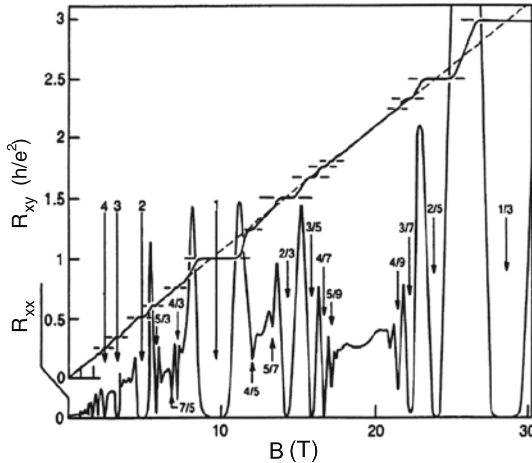

Fig. 12.13. Hall resistance R_{xy} and magnetoresistance R_{xx} of a two-dimensional electron system (GaAs/AlGaAs heterostructure) of density $n = 2.33 \times 10^{11}\,\mathrm{cm}^{-2}$ at a temperature of 85 mK, vs. magnetic field B. Numbers identify the filling factor ν, which indicates the degree to which the sequence of Landau levels is filled with electrons. Plateaus are due to the integral ($\nu = i$) quantum Hall effect (IQHE) and fractional ($\nu = p/q$) quantum Hall effect (FQHE). Adapted from [854], reprinted with permission, ©1990 AAAS

A decisive role is played by the magnetic flux quanta. The presence of the magnetic field requires the many-electron wavefunction to assume as many zeros per unit area as there are flux quanta penetrating it. The decay of the wavefunction has a length scale of the magnetic length $l_0 = \sqrt{\hbar/(eB)}$. Since the magnetic field implies a 2π phase shift around the zero, such an object is also termed a *vortex*, being the embodiment of the magnetic flux quanta in the electron system. Such a vortex represents a charge deficit (compared to a homogeneous charge distribution) and thus electrons and vortices attract each other. If a vortex and an electron are placed onto each other, considerable Coulomb energy is gained. At $\nu = 1/3$, there are three times more vortices than there are electrons, each vortex representing a charge deficit of $1/3\,e$. Such a system is described with many-particle wavefunctions, such as the Laughlin theory for $\nu = 1/q$ [853] and novel quasi-particles called *composite fermions* [855, 856] for other fractional fillings. For further reading we refer readers to [857] and references therein.

12.3.3 Weiss Oscillations

In Fig. 12.14, measurements are shown for a Hall bar in which an array of antidots (in which no conduction is possible) has been introduced by dry etching. The antidot size is 50 nm (plus depletion layer) and the period is

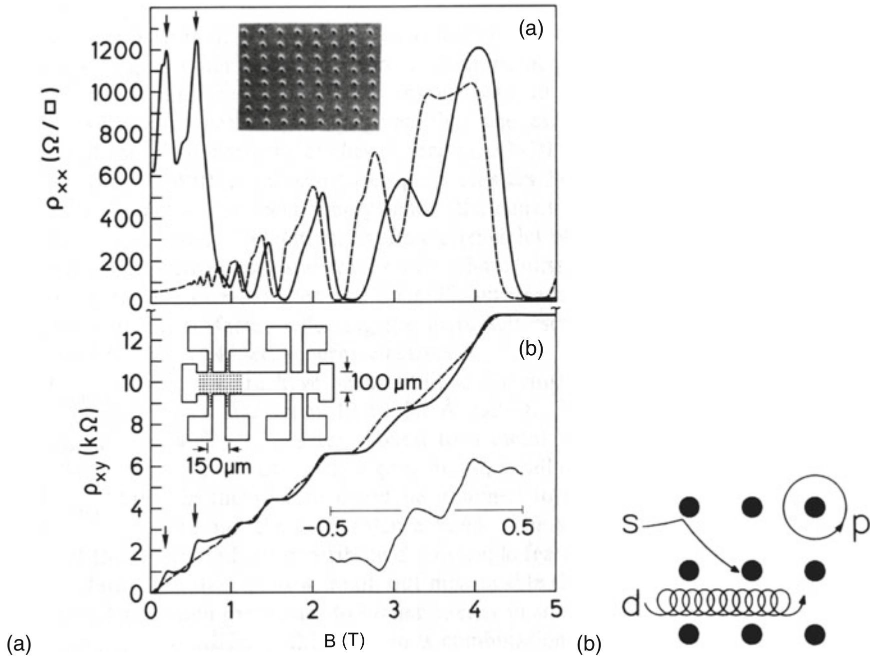

Fig. 12.14. Weiss oscillations: (**a**) magnetoresistance and (**b**) Hall resistance of an antidot lattice (*inset* in (**a**) with pattern (*solid lines*) and without pattern (*dashed lines*) at $T = 1.5$ K. (**b**) Schematic of the different orbits: ('p': pinned, 'd': drifting, 's': scattered). Reprinted with permission from [858], ©1991 APS

300 nm. These obstructions for the cyclotron motion lead to a modification of the magnetotransport properties.

Before etching of the antidot array the 2DEG has a mean free path length of 5–10 μm at 4 K for the mobility of $\approx 10^6$ cm^2/Vs. At low magnetic fields there is a strong deviation of the Hall resistivity from the straight line to which the QHE levels converge. Similarly, ρ_{xx} shows a strong effect as well.

These effects are related to commensurability effects between the antidot lattice and the cyclotron resonance path. When the cyclotron orbit is equal to the lattice period, electrons can fulfill a circular motion around one antidot (pinned orbit, Fig. 12.14b) that leads to a reduction of conductivity. At high fields, drifting orbits for which the cyclotron orbit is much smaller than the lattice period occur. At small fields, scattering orbits also contribute for which the cyclotron radius is large and the electron has antidots from time to time. Resonances in the Hall resistivity have been found due to pinned orbits enclosing 1, 2, 4, 9 or 21 antidots.

13 Nanostructures

The principles of physics,
as far as I can see,
do not speak against the possibility
of maneuvering things atom by atom.
R.P. Feynman, 1959 [859]

13.1 Introduction

When the structural size of functional elements enters the size range of the de Broglie matter wavelength, the electronic and optical properties are dominated by quantum-mechanical effects. The most drastic impact can be seen from the density of states (Fig. 13.1).

The quantization in a potential is ruled by the Schrödinger equation with appropriate boundary conditions. These are simplest if an infinite potential is assumed. For finite potentials, the wavefunction leaks out into the barrier. Besides making the calculation more complicated (and more realistic), this allows electronic coupling of nanostructures. Via the Coulomb interaction, a coupling is even given if there is no wavefunction overlap. In the following, we will discuss some of the fabrication techniques and properties of quantum wires (QWR) and quantum dots (QD). In particular for the latter, several textbooks can also be consulted [860, 861].

13.2 Quantum Wires

13.2.1 V-Groove Quantum Wires

Quantum wires with high optical quality, i.e. high recombination efficiency and well-defined spectra, can be obtained by employing epitaxial growth on corrugated substrates. The technique is shown schematically in Fig. 13.2. A V-groove is etched, using, e.g., an anisotropic wet chemical etch, into a GaAs substrate. The groove direction is along [110]. Even when the etched pattern is not very sharp on the bottom, subsequent growth of AlGaAs sharpens

M. Grundmann, *The Physics of Semiconductors*, 2nd ed., Graduate Texts in Physics, DOI 10.1007/978-3-642-13884-3_13,
© Springer-Verlag Berlin Heidelberg 2010

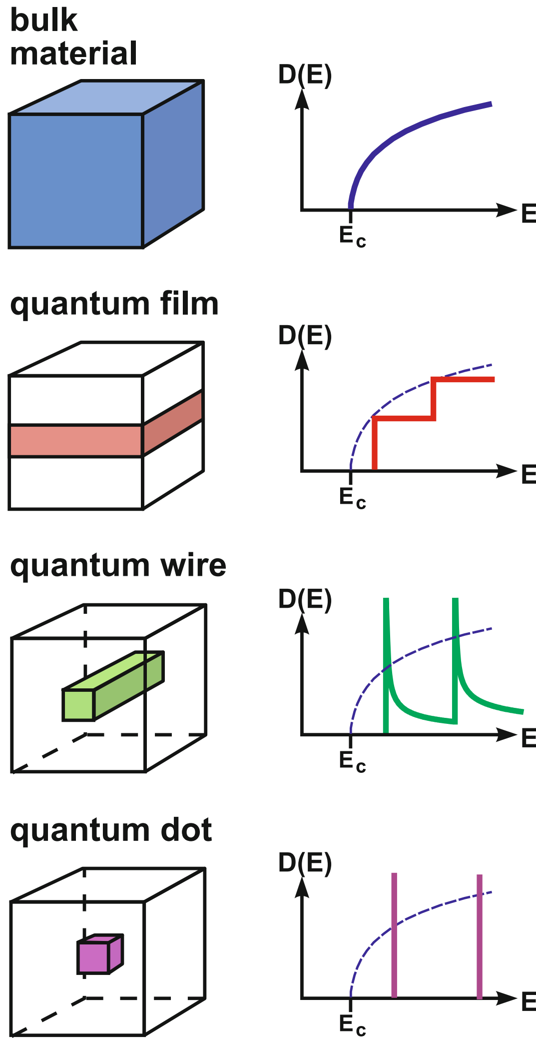

Fig. 13.1. Schematic geometry and density of states for 3D, 2D, 1D and 0D electronic systems

the apex to a self-limited radius ρ_l of the order of 10 nm. The side facets of the groove are {111}A. Subsequent deposition of GaAs leads to a larger upper radius $\rho_u > \rho_l$ of the heterostructure. The GaAs QWR formed in the bottom of the groove is thus crescent-shaped as shown in Fig. 13.3. A thin GaAs layer also forms on the side facets (sidewall quantum well) and on the top of the ridges. Subsequent growth of AlGaAs leads to a resharpening of the V-groove to the initial, self-limited value ρ_l. The complete resharpening after a sufficiently thick AlGaAs layer allows vertical stacking of crescent-

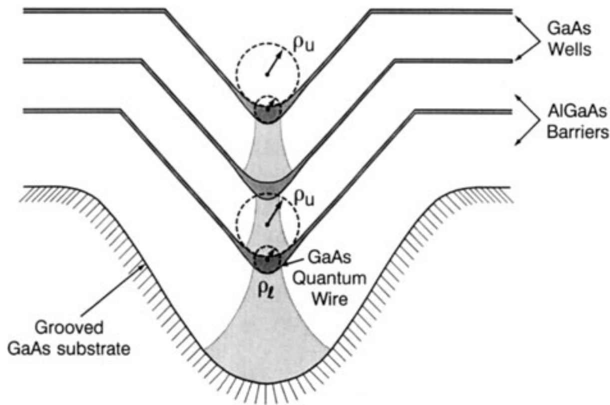

Fig. 13.2. Schematic cross section of a GaAs/AlGaAs heterostructure grown on a channeled substrate, illustrating the concept of self-ordered quantum-wire fabrication. Adapted from [862]

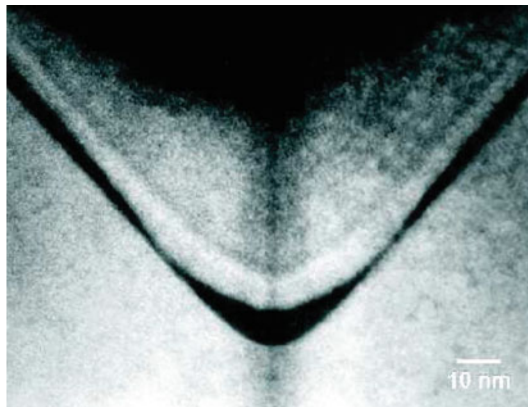

Fig. 13.3. Transmission electron microscopy cross-sectional image of a crescent-shaped single GaAs/AlGaAs quantum wire. From [863]

shaped QWRs of virtually identical size and shape, as shown in Fig. 13.4. In this sense, the self-limiting reduction of the radius of curvature and its recovery during barrier-layer growth leads to self-ordering of QWR arrays whose structural parameters are determined solely by growth parameters. The lateral pitch of such wires can be down to 240 nm.

To directly visualize the lateral modulation of the band gap, a lateral cathodoluminescence (CL) linescan perpendicular across the wire is displayed in Fig. 13.5. In Fig. 13.5a, the secondary electron (SE) image of the sample

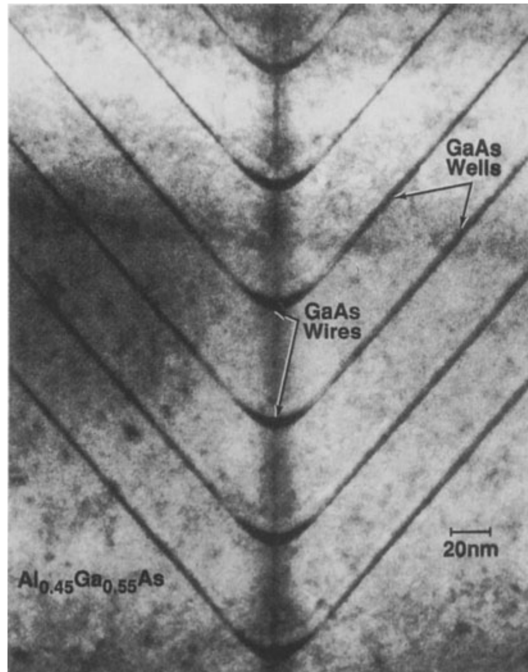

Fig. 13.4. TEM cross-sectional image of a vertical stack of identical GaAs/AlGaAs crescent-shaped QWRs. From [862]

from Fig. 13.3 is shown in plan view. The top ridge is visible in the upper and lower parts of the figure, while in the middle the sidewalls with the QWR in the center are apparent. In Fig. 13.5b, the CL spectrum along a linescan perpendicular to the wire (as indicated by the white line in Fig. 13.5a) is displayed. The x-axis is now the emission wavelength, while the y-axis is the lateral position along the linescan. The CL intensity is given on a logarithmic scale to display the full dynamic range. The top QW shows almost no variation in band gap energy ($\lambda = 725$ nm); only directly at the edge close to the sidewall does a second peak at lower energy ($\lambda = 745$ nm) appear, indicating a thicker region there. The sidewall QW exhibits a recombination wavelength of 700 nm at the edge to the top QW, which gradually increases to about 730 nm at the center of the V-groove. This directly visualizes a linear tapering of the sidewall QW from about 2.1 nm thickness at the edge to 3 nm in the center. The QWR luminescence itself appears at about 800 nm.

After fast capture from the barrier into the QWs and, to a much smaller extent corresponding to its smaller volume, into the QWR, excess carriers will diffuse into the QWR via the adjacent sidewall QW and the vertical QW. The tapering of the sidewall QW induces an additional drift current.

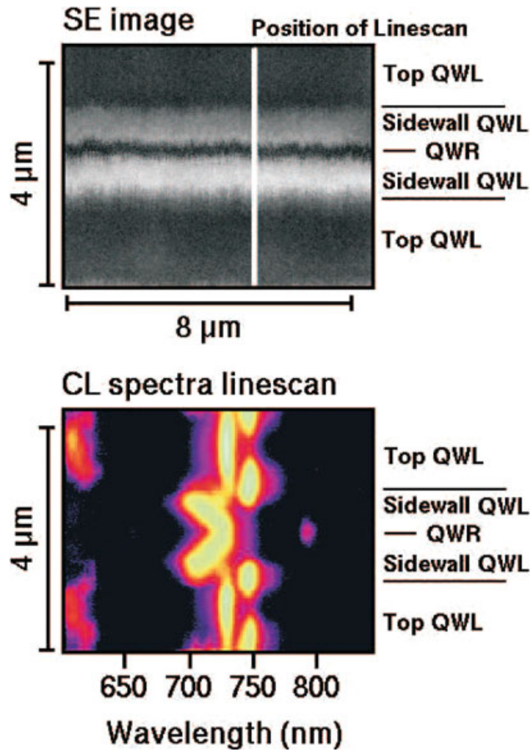

Fig. 13.5. (**a**) Plan-view SE image of single QWR (sample A), showing top and sidewall with QWR in the center. The *white line* indicates the position of the linescan on which the CL spectra linescan (**b**) has been taken at $T = 5\,\mathrm{K}$. The CL intensity is given on a logarithmic grey scale to display the full dynamic range as a function of wavelength and position along the *white line* in (**a**). From [863]

13.2.2 Cleaved-Edge Overgrowth Quantum Wires

Another method to create quantum wires of high structural perfection is cleaved-edge overgrowth (CEO) [864], shown schematically in Fig. 13.6. First, a layered structure is grown (single or multiple quantum wells or superlattice). Then, a {110} facet is fabricated by cleaving (in vacuum) and epitaxy is continued on the cleaved facet. At the junctures of the {110} layer and the original quantum wells QWRs form. Due to their cross-sectional form they are also called *T-shaped* QWRs. A second cleave and another growth step allow fabrication of CEO quantum dots [865, 866] (Fig. 13.6c).

13.2.3 Nanowhiskers

Whiskers are primarily known as thin metal spikes and have been investigated in detail [867]. Semiconductor whiskers can be considered as (fairly short) quantum wires. They have been reported for a number of materials, such as

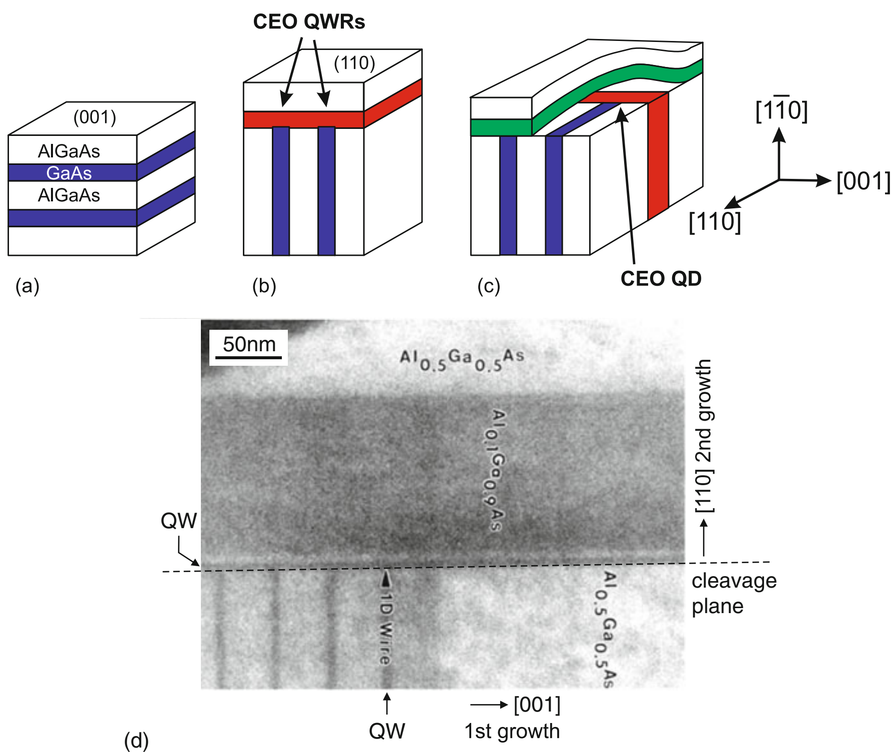

Fig. 13.6. Principle of CEO quantum wires and 2-fold CEO quantum dots. Part (**a**) depicts a layered structure (quantum wells or superlattice, *blue*), (**b**) describes the growth on the cleaved facet used for fabrication of quantum wires. In (**c**) a second cleave and growth on top of the plane allows the fabrication of quantum dots. From [865]. (**d**) Cross-sectional TEM image of CEO GaAs/AlGaAs quantum wires. Two quantum wells (QW) and the QWR at their junction are labeled. The first epitaxy was from left to right. The second epitaxy step was on top of the cleavage plane (*dashed line*) in the upward direction. Adapted from [866], reprinted with permission, ©1997 APS

Si, GaAs, InP and ZnO [868]. A field of ZnO whiskers is shown in Fig. 13.7. If heterostructures are incorporated along the whisker axis [869], quantum dots or tunneling barriers can be created (Fig. 13.8). The nanocrystal can also act as a nanolaser [870, 871]. In ZnO nanowhiskers the conversion of mechanical energy into electrical energy has been demonstrated [872] based on the piezoelectric effect (Sect. 14.4).

The critical thickness h_c in nanowire heterostructure is strongly modified from the 2D situation (Sect. 5.3.7). Based on the strain distribution of a misfitted slab in a cylindrical wire [875] the dependence of critical thickness on the nanowhisker radius r was developed [876, 877]. For given misfit ϵ there is a critical radius r_c for which h_c is infinite for $r < r_c$ (Fig. 13.9).

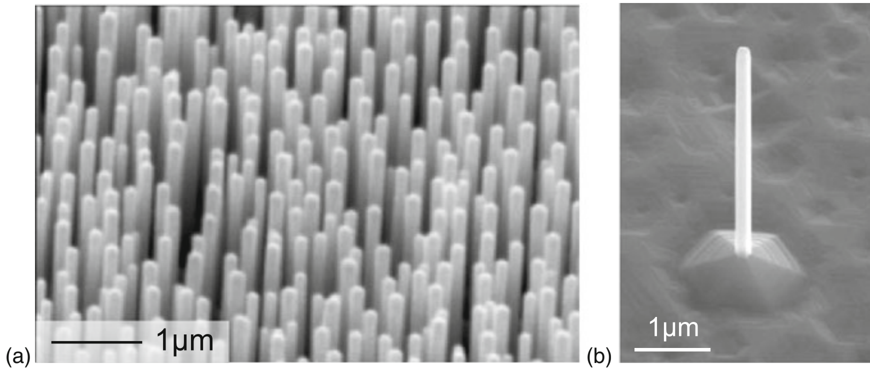

Fig. 13.7. (**a**) Array of ZnO nanowhiskers on sapphire, fabricated using thermal evaporation. Adapted from [873]. (**b**) Single, free-standing ZnO nanowire fabricated using PLD. Adapted from [874]

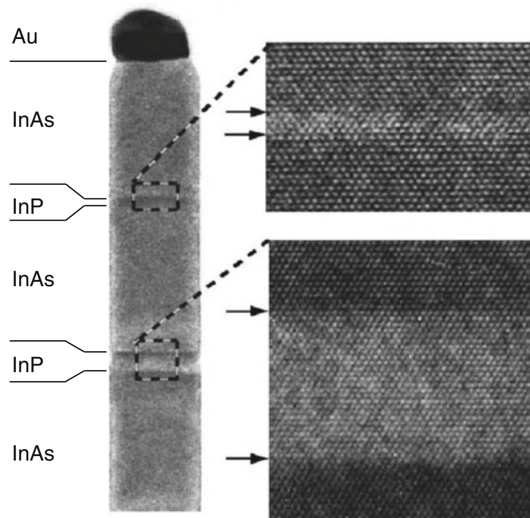

Fig. 13.8. TEM image of a part of an InAs whisker 40 nm in diameter that contains InP barriers. The zooms show sharp interfaces. On top of the whisker is a gold droplet from the so-called vapor–liquid–solid growth mechanism. The whisker axis is [001], the viewing direction is [110]. Adapted from [869], reprinted with permission, ©2002 AIP

13.2.4 Nanobelts

A number of belt-shaped nanostructures has been reported [868]. These are wire-like, i.e. very long in one dimension. The cross-section is rectangular with a high aspect ratio. In Fig. 13.10a ZnO nanobelts are shown. The wire direction is $[2\bar{1}.0]$. The large surface is (00.1), the thickness of the belt extends in [01.0]-direction. High resolution transmission microscopy (Fig. 13.10b) shows

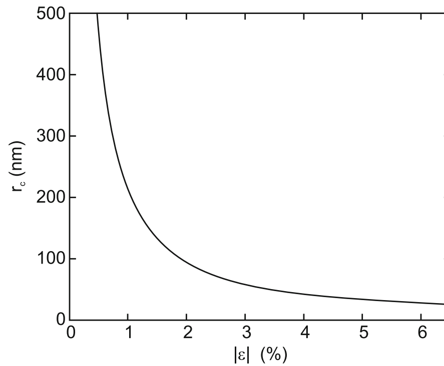

Fig. 13.9. Critical radius r_c above which an infinitely thick layer with misfit ϵ grows coherently on a cylindrical nanowire (relaxation by 60° dislocations, $b = 0.4$ nm, $\nu = 1/3$). Adapted from [877]

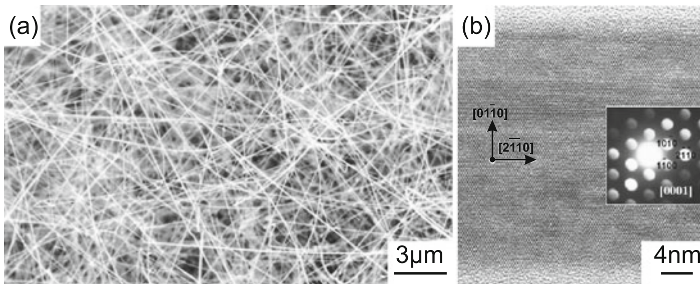

Fig. 13.10. (**a**) SEM image of an ensemble of ZnO nanobelts. (**b**) HRTEM image of a single ZnO nanobelt, viewing direction is [00.1]. The *inset* shows the diffraction pattern. Adapted from [878]

that these structures are defect-free. The pyroelectric charges on the ZnO (0001) surfaces (Sect. 14.2) lead to the formation of open (Fig. 13.11c) spirals. Closed spirals (Fig. 13.11a) occur if the short dimension is along [00.1] and alternating charges become compensated in a 'slinky'-like ring (Fig. 13.11b).

13.2.5 Quantization in Two-Dimensional Potential Wells

The motion of carriers along the quantum wire is free. In the cross-sectional plane the wavefunction is confined in two dimensions. The simplest case is for constant cross section along the wire. However, generally the cross section along the wire may change and therefore induce a potential variation along the wire. Such potential variation will impact the carrier motion along the longitudinal direction. Also, a twist of the wire along its axis is possible.

In Fig. 13.12, the electron wavefunctions in a V-groove GaAs/AlGaAs QWR are shown. Further properties of V-groove QWRs have been reviewed

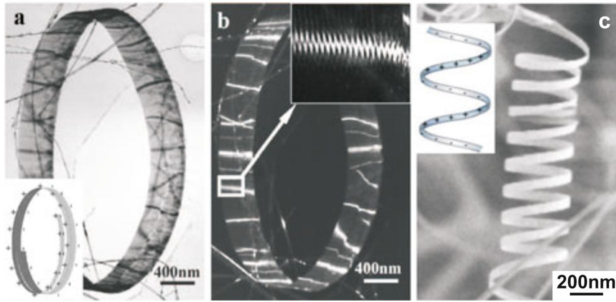

Fig. 13.11. (**a**) Bright field and (**b**) dark field TEM image of a ZnO nanoring formed by the 'slinky'-like growth of a nanobelt. (**c**) SEM image of an open ZnO nanospiral. The *insets* in (**a**, **c**) show schematically the surface charge distribution. Adapted from [879]

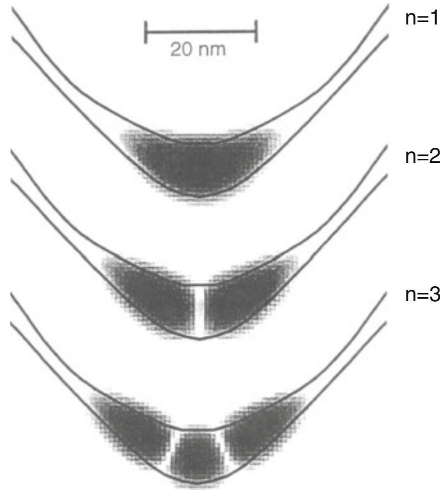

Fig. 13.12. Electron wavefunctions ($|\Psi|^2$ on logarithmic grey scale) for the first three confined levels for the QWR of Fig. 13.3. From [863]

in [880]. In Fig. 13.13, the excitonic electron and hole wavefunctions are shown for a (strained) T-shaped QWR.

In Fig. 13.14a the atomic structure of a very thin ZnO nanowhisker with a cross-section consisting of seven hexagonal unit cells is shown. The theoretical one-dimensional band structure [881] is shown in Fig. 13.14b together with the charge density of the lowest conduction band state (LUMO) and the highest valence band state (HOMO). The band gap is generally too small because of the LDA method used.[1] In [881] also the properties of nanowires

[1] The LDA in [881] yields $E_{\mathrm{g}} = 0.63\,\mathrm{eV}$ for the bulk ZnO band gap; its experimental value is 3.4 eV.

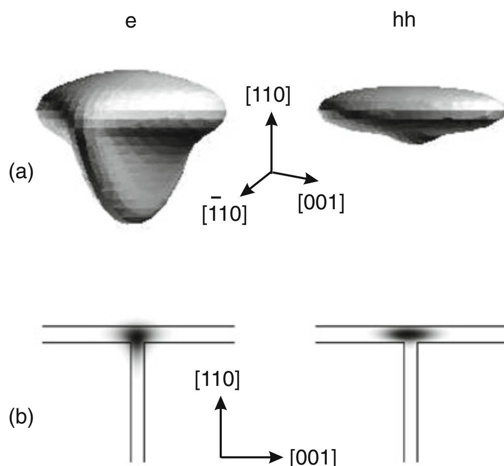

Fig. 13.13. (**a**) Three-dimensional view of the electron and (heavy) hole part of the excitonic wavefunction in a 4 nm × 5 nm T-shaped $In_{0.2}Ga_{0.8}As/GaAs$ QWR. The orbitals correspond to 70% probability inside. (**b**) Cross section through the electron and hole orbitals in their center along the wire direction. Reprinted with permission from [882], ©1998 APS

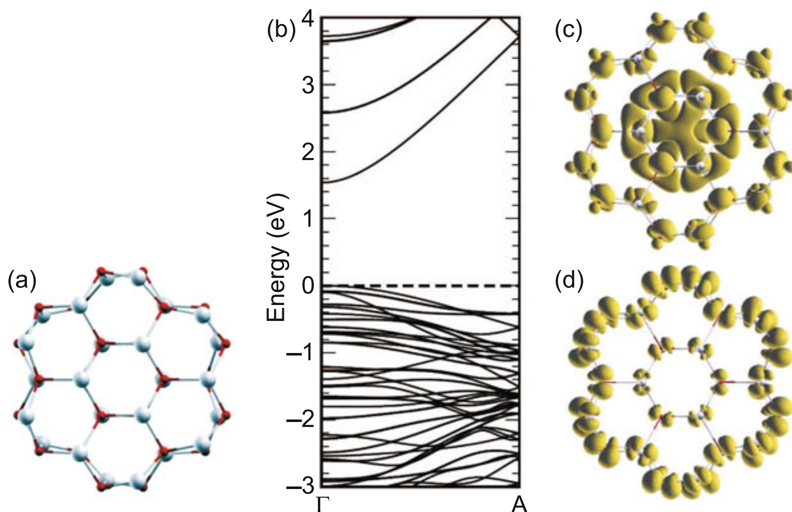

Fig. 13.14. (**a**) Atomic arrangement of a 1 nm wide ZnO nanowire. (**b**) Theoretical band structure and charge density of the (**c**) lowest conduction band and (**d**) highest valence band state. Adapted from [881]

with various diameters are compared. The HOMO at Γ lies only 80 meV above the top of valence band of bulk ZnO, and its position changes little with the wire diameter. It is mainly composed by surface oxygen 2p like dangling bonds (Fig. 13.14d). The LUMO ((Fig. 13.14c)) is delocalized in the whole nanowire, indicating that it is a bulk state. The delocalized distribution is also responsible for the large dispersion of the LUMO from Γ to A. The energy of the LUMO increases substantially with decreasing diameter due to the radial confinement.

13.3 Quantum Dots

13.3.1 Quantization in Three-Dimensional Potential Wells

The solutions for the d-dimensional ($d = 1$, 2, or 3) harmonic oscillator, i.e. the eigenenergies for the Hamiltonian

$$\hat{H} = \frac{\mathbf{p}^2}{2m} + \sum_{i=1}^{d} \frac{1}{2} m \, \omega_0^2 \, x_i^2 \tag{13.1}$$

are given by

$$E_n = \left(n + \frac{d}{2} \right) \hbar\omega_0 \; , \tag{13.2}$$

with $n = 0, 1, 2, \ldots$. More detailed treatments can be found in quantum-mechanics textbooks.

Next, we discuss the problem of a particle in a centrosymmetric finite potential well with different masses m_1 in the dot and m_2 in the barrier. The Hamiltonian and the potential are given by

$$\hat{H} = \nabla \frac{\hbar^2}{2m} \nabla + V(r) \tag{13.3}$$

$$V(r) = \begin{cases} -V_0 & , r \leq R_0 \\ 0 & , r > R_0 \end{cases} \; . \tag{13.4}$$

The wavefunction can be separated into radial and angular components $\Psi(\mathbf{r}) = R_{nlm}(r) \; Y_{lm}(\theta, \phi)$, where Y_{lm} are the spherical harmonic functions. For the ground state ($n = 1$) the angular momentum l is zero and the solution for the wavefunction (being regular at $r = 0$) is given by

$$R(r) = \begin{cases} \frac{\sin(kr)}{kr} & , r \leq R_0 \\ \frac{\sin(kR_0)}{kR_0} \exp\left(-\kappa(r - R_0)\right) & , r > R_0 \end{cases} \tag{13.5a}$$

$$k^2 = \frac{2m_1(V_0 + E)}{\hbar^2} \tag{13.5b}$$

$$\kappa^2 = -\frac{2m_2 E}{\hbar^2} \; . \tag{13.5c}$$

From the boundary conditions that both $R(r)$ and $\frac{1}{m}\frac{\partial R(r)}{\partial r}$ are continuous across the interface at $r = R_0$, the transcendental equation

$$kR_0 \cot(kR_0) = 1 - \frac{m_1}{m_2}(1 + \kappa R_0) \tag{13.6}$$

is obtained. From this formula the energy of the single particle ground state in a spherical quantum dot can be determined. For a given radius, the potential needs a certain strength $V_{0,\min}$ to confine at least one bound state; this condition can be written as

$$V_{0,\min} < \frac{\pi^2 \hbar^2}{8 m^* R_0^2} \tag{13.7}$$

for $m_1 = m_2 = m^*$. For a general angular momentum l, the wavefunctions are given by spherical Bessel functions j_l in the dot and spherical Hankel functions h_l in the barrier. Also, the transcendental equation for the energy of the first excited level can be given:

$$kR_0 \cot(kR_0) = 1 + \frac{k^2 R_0^2}{\frac{m_1}{m_2}\frac{2+2\kappa R_0+\kappa^2 R_0^2}{1+\kappa R_0} - 2} . \tag{13.8}$$

In the case of infinite barriers ($V_0 \to \infty$), the wavefunction vanishes outside the dot and is given by (normalized)

$$R_{nml}(r) = \sqrt{\frac{2}{R_0^3}} \frac{j_l(k_{nl} r)}{j_{l+1}(k_{nl} R_0)} , \tag{13.9}$$

where k_{nl} is the n-th zero of the Bessel function j_l, e.g. $k_{n0} = n\pi$. With two-digit precision the lowest levels are determined by

k_{nl}	$l=0$	$l=1$	$l=2$	$l=3$	$l=4$	$l=5$
$n=0$	3.14	4.49	5.76	6.99	8.18	9.36
$n=1$	6.28	7.73	9.10	10.42		
$n=2$	9.42					

The $(2l+1)$ degenerate energy levels E_{nl} are ($V_0 = \infty$, $m = m_1$):

$$E_{nl} = \frac{\hbar^2}{2m}\frac{k_{nl}^2}{R_0^2} . \tag{13.10}$$

The 1s, 1p, and 1d states have smaller eigenenergies than the 2s state.

A particularly simple solution is given for a cubic quantum dot of side length a_0 and infinite potential barriers. One finds the levels $E_{n_x n_y n_z}$:

$$E_{n_x n_y n_z} = \frac{\hbar^2}{2m} \pi^2 \frac{n_x^2 + n_y^2 + n_z^2}{a_0^2} , \tag{13.11}$$

with n_x, n_y, $n_z = 1, 2, \ldots$. For a sphere, the separation between the ground and first excited state is $E_1 - E_0 \approx E_0$, for a cube and a two-dimensional harmonic oscillator it is exactly E_0. For a three-dimensional harmonic oscillator this quantity is $E_1 - E_0 = 2E_0/3$.

For realistic quantum dots a full three-dimensional simulation of strain, piezoelectric fields and the quantum-mechanical confinement must be performed [883, 884]. In Fig. 13.15, the lowest four electron and hole wavefunctions in a pyramidal InAs/GaAs quantum dot (for the strain distribution see Fig. 5.22 and for the piezoelectric fields see Fig. 14.16) are shown. The figure shows that the lowest hole states have dominantly heavy-hole character and contain admixtures of the other hole bands. The wavefunction in such quantum dots can be imaged using scanning tunneling microscopy [885].

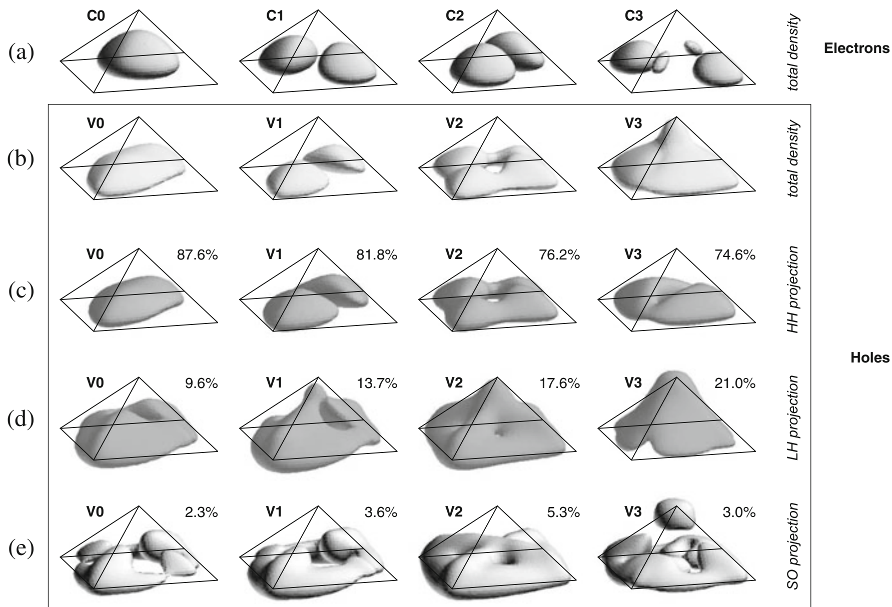

Fig. 13.15. Isosurface plots (25% of maximum value) of the total probability densities (**a**,**b**) and valence-band projections (**c**)–(**e**) of bound electron (**a**) and hole (**b**)–(**e**) states in a model pyramidal InAs/GaAs quantum dot with base length $b = 11.3$ nm. The percentages are the integrals of the projections to the bulk heavy, light and split-off hole bands, respectively, and the isosurfaces show the corresponding projection shapes. For each valence-band state the difference from 100% is the integral $\int_{-\infty}^{\infty} |\psi_{s\uparrow}|^2 + |\psi_{s\downarrow}|^2 \mathrm{d}^3\mathbf{r}$ of the s-type (conduction band) Bloch function projection (not shown). Reprinted with permission from [886]

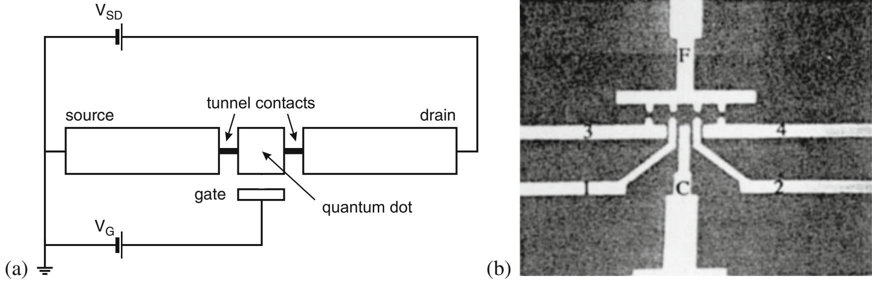

Fig. 13.16. (**a**) Schematic drawing of a quantum dot with tunnel contacts and gate electrode. (**b**) Realization with an in-plane gate structure. The distance between 'F' and 'C' (gate electrode) is 1 µm. Electron transport occurs from a 2DEG between 3/F to 4/F through the quantum points contacts 1/3 and 2/4. Part (**b**) reprinted with permission from [887]

13.3.2 Electrical and Transport Properties

The classical electrostatic energy of a quantum dot with capacitance C that is capacitively coupled to a gate (Fig. 13.16) at a bias voltage V_g is given by

$$E = \frac{Q^2}{2C} - Q\,\alpha\,V_\mathrm{g}\ , \tag{13.12}$$

where α is a dimensionless factor relating the gate voltage to the potential of the island and Q is the charge of the island.

Mathematically, minimum energy is reached for a charge $Q_\mathrm{min} = \alpha C V_\mathrm{g}$. However, the charge has to be an integer multiple of e, i.e. $Q = Ne$. If V_g has a value, such that $Q_\mathrm{min}/e = N_\mathrm{min}$ is an integer, the charge cannot fluctuate as long as the temperature is low enough, i.e.

$$kT \ll \frac{e^2}{2C}\ . \tag{13.13}$$

Tunneling into or out of the dot is suppressed by the Coulomb barrier $e^2/2C$, and the conductance is very low. Analogously, the differential capacitance is small. This effect is called *Coulomb blockade*. Peaks in the tunneling current (Fig. 13.17b), conductivity (Fig. 13.17a) and the capacitance occur, when the gate voltage is such that the energies for N and $N+1$ electrons are degenerate, i.e. $N_\mathrm{min} = N + \frac{1}{2}$. The expected level spacing is

$$e\,\alpha\,\Delta V_\mathrm{g} = \frac{e^2}{C} + \Delta\epsilon_N\ , \tag{13.14}$$

where $\Delta\epsilon_N$ denotes the change in lateral (kinetic) quantization energy for the added electron. e^2/C will be called the charging energy in the following. A variation of the source–drain voltage (for a given gate voltage) leads to a so-called Coulomb staircase since more and more channels of conductivity

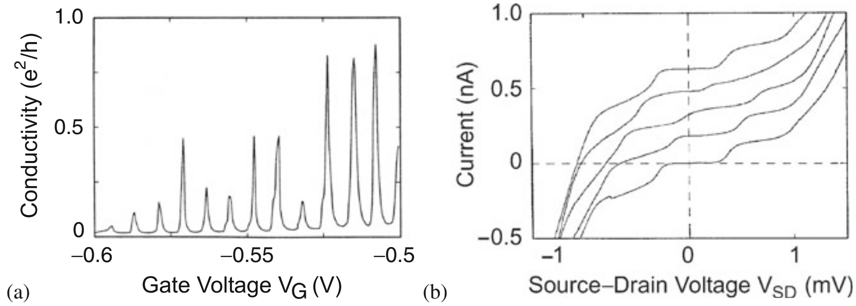

Fig. 13.17. (**a**) Conductivity (Coulomb oscillations) and (**b**) current–voltage diagram at different gate voltages (Coulomb staircase, shifted vertically for better readability) of a tunnel junction with a quantum dot as in Fig. 13.16. Adapted from [887]

contribute to the current through the device (Fig. 13.18). Single electron tunneling (SET) is investigated with respect to metrology for a novel ampere standard [845].

A lot of research so far has been done on lithographically defined systems where the lateral quantization energies are small and smaller than the Coulomb charging energy. In this case, periodic oscillations are observed, especially for large N. A deviation from periodic oscillations for small N and

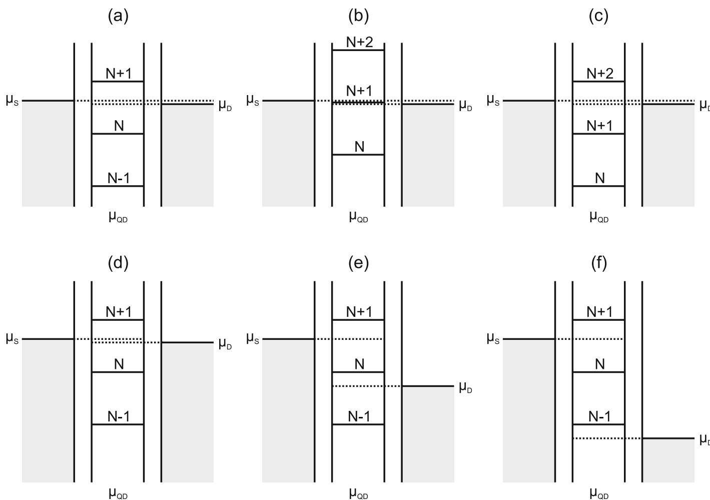

Fig. 13.18. Chemical potentials of source and drain and of a quantum dot in between them. (**a**), (**b**), and (**c**) show the sequence for a variation of the gate voltage and visualize the origin of the Coulomb oscillations (see Fig. 13.17a). (**d**), (**e**) and (**f**) visualize a variation of the source–drain voltage and the origin of the Coulomb staircase (cf. Fig. 13.17b)

a characteristic shell structure (at $N = 2$, 6, 12) consistent with a harmonic oscillator model ($\hbar\omega_0 \approx 3\,\mathrm{meV}$) has been reported for $\approx$ 500-nm diameter mesas (Fig. 13.19b,c). In this structure, a small mesa has been etched and contacted (top contact, substrate back contact and side gate). The quantum dot consists of a 12-nm $\mathrm{In_{0.05}Ga_{0.95}As}$ quantum well that is laterally constricted by the 500-nm mesa and vertically confined due to 9- and 7.5-nm thick $\mathrm{Al_{0.22}Ga_{0.68}As}$ barriers (Fig. 13.19a). By tuning the gate voltage, the number of electrons can be varied within 0 and 40. Measurements are typically carried out at a sample temperature of 50 mK.

In the sample shown in Fig. 13.20, self-assembled QDs are positioned in the channel under a split-gate structure. In a suitable structure, tunneling through a single QD is resolved.

In small self-assembled quantum dots single-particle level separations can be larger than or similar to the Coulomb charging energy. Classically, the capacitance for a metal sphere of radius R_0 is given as

$$C_0 = 4\pi\,\epsilon_0\,\epsilon_{\mathrm{r}}\,R_0\ , \tag{13.15}$$

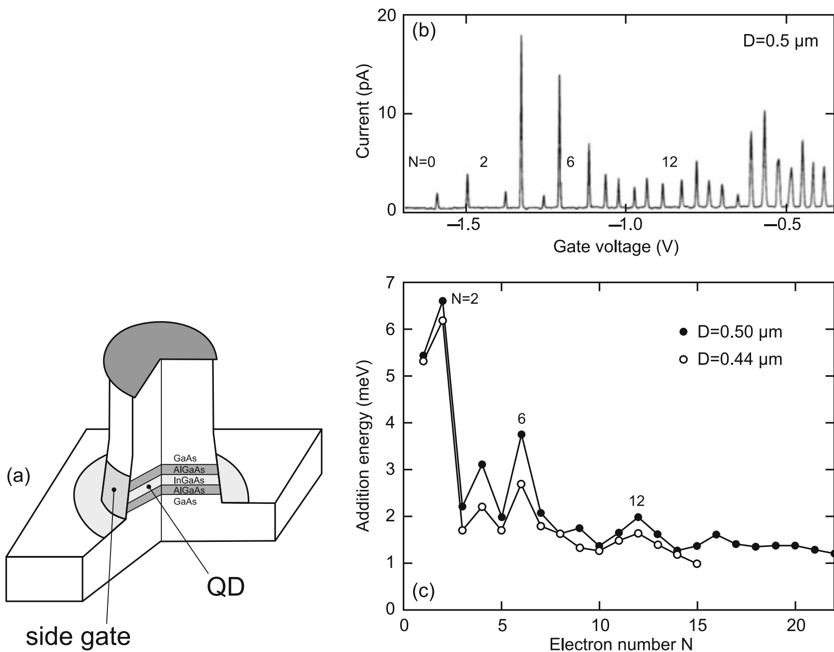

Fig. 13.19. (**a**) Schematic sample geometry for side-gated $\mathrm{In_{0.05}Ga_{0.95}As/Al_{0.22}Ga_{0.68}As}$ disk-shaped quantum dot. (**b**) Coulomb oscillations in the current vs. gate voltage at $B = 0\,\mathrm{T}$ observed for a $D = 0.5\,\mu\mathrm{m}$ disk-shaped dot. (**c**) Addition energy vs. electron number for two different dots with $D = 0.50$ and $0.44\,\mu\mathrm{m}$. Adapted from [888]

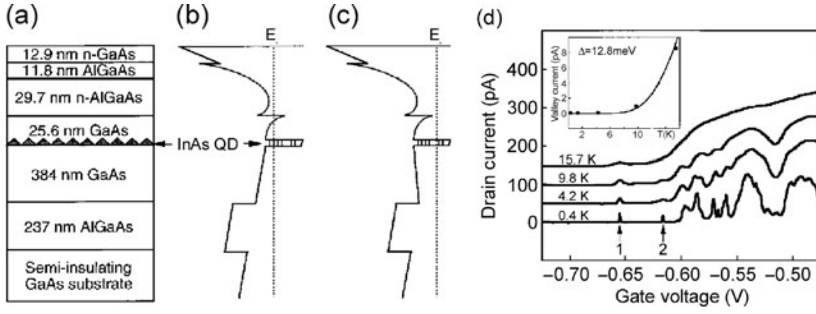

Fig. 13.20. (**a**) Schematic layer sequence of epitaxial structure comprising a n-AlGaAs/GaAs heterointerface with a two-dimensional electron gas and a layer of InAs/GaAs quantum dots. (**b**) and (**c**) are corresponding band diagrams with no gate bias and gate voltage below the critical value, respectively. (**d**) Experimental dependence of drain current on gate voltage in a split-gate structure at a drain source voltage of 10 µV. *Inset*: Dependence of valley current on temperature (*squares*) with theoretical fit. Reprinted with permission from [889], ©1997 AIP

e.g. $C_0 \approx 6\,\text{aF}$ for $R_0 = 4\,\text{nm}$ in GaAs, resulting in a charging energy of 26 meV. Quantum mechanically, the charging energy is given in first-order perturbation theory by

$$E_{21} = \langle 00|W_{\text{ee}}|00\rangle = \iint \Psi_0^2(\mathbf{r}_\text{e}^1)\, W_{\text{ee}}(\mathbf{r}_\text{e}^1, \mathbf{r}_\text{e}^2)\, \Psi_0^2(\mathbf{r}_\text{e}^2)\, \text{d}^3\mathbf{r}_\text{e}^1\, \text{d}^3\mathbf{r}_\text{e}^2 \,, \tag{13.16}$$

where W_{ee} denotes the Coulomb interaction of the two electrons and Ψ_0 the ground state (single particle) electron wavefunction. The matrix element gives an upper bound for the charging energy since the wavefunctions will rearrange to lower their overlap and the repulsive Coulomb interaction. For lens-shaped InAs/GaAs quantum dots with radius 25 nm a charging energy of about 30 meV has been predicted.

13.3.3 Self-assembled Preparation

The preparation methods for QDs split into top-down (lithography and etching) and bottom-up (self-assembly) methods. The latter achieve typically smaller sizes and require less effort (at least concerning the machinery).

Artificial Patterning

Using artificial patterning, based on lithography and etching (Fig. 13.21), quantum dots of arbitrary shape can be made (Fig. 13.22). Due to defects introduced by high-energy ions during reactive ion etching the quantum efficiency of such structures is very low when they are very small. Using wet-chemical etching techniques the damage can be significantly lowered but not completely avoided. Since the QDs have to compete with other structures that can be made structurally perfect, this is not acceptable.

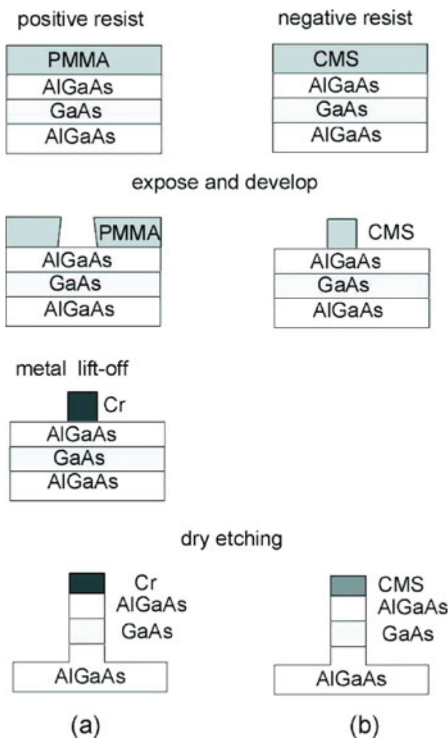

Fig. 13.21. Lithography and etching techniques for the fabrication of semiconductor structures

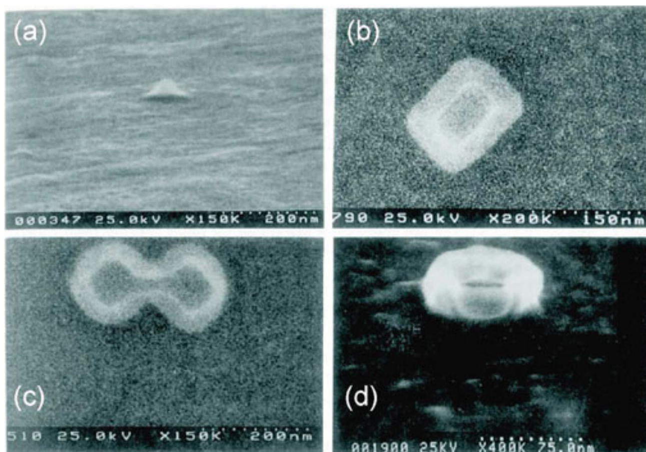

Fig. 13.22. Quantum dots of various shapes created by lithography and etching techniques. From [890]

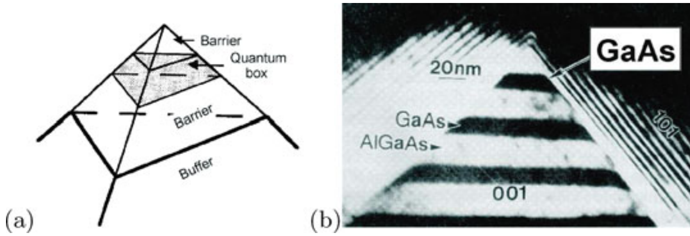

Fig. 13.23. (**a**) Schematic representation of growth on top of a predefined template, (**b**) cross-sectional TEM of quantum dot formation at the apex. Reprinted with permission from [891], ©1992 MRS

Template Growth

Template growth is another technique for the formation of nanostructures. Here, a mesoscopic structure is fabricated by conventional means. The nanostructure is created using size-reduction mechanisms, e.g. faceting, (Fig. 13.23). This method can potentially suffer from low template density, irregularities of the template, and problems of reproducibility.

Colloids

Another successful route to nanocrystals is the doping of glasses with subsequent annealing (color filters). When nanocrystals are prepared in a sol-gel process, the nanoparticles are present as a colloid in wet solution (Fig. 13.24). With the help of suitable stabilizing agents they are prevented from sticking to each other and can be handled in ensembles and also individually.

Mismatched Epitaxy

The self-assembly (or self-organization) relies on strained heterostructures that achieve energy minimization by island growth on a wetting layer (Stranski-Krastanow growth mode, see Sect. 11.2.3 and [860]). Additional ordering

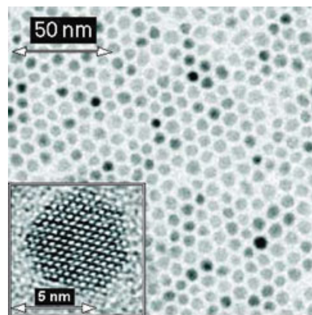

Fig. 13.24. CdSe colloidal nanoparticles. From [892]

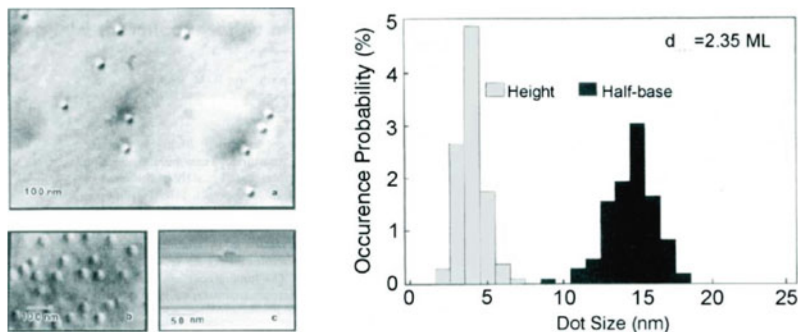

Fig. 13.25. Self-organized formation of InGaAs/GaAs quantum dots during epitaxy. *Left*: Plan-view and cross-sectional transmission electron micrographs. *Right*: Histogram of vertical and lateral size of the quantum dots. Reprinted with permission from [897], ©1993 AIP

mechanisms [893, 894] lead to ensembles that are homogeneous in size[2] [895] and shape [896] (Fig. 13.25).

When a thin layer of a semiconductor is grown on top of a flat substrate with different lattice constant, the layer suffers a tetragonal distortion (Sect. 5.3.3). Strain can only relax along the growth direction (Fig. 13.26). If the strain energy is too large (highly strained layer or large thickness), plastic relaxation via dislocation formation occurs. If there is island geometry, strain can relax in all three directions and about 50% more strain energy can relax,

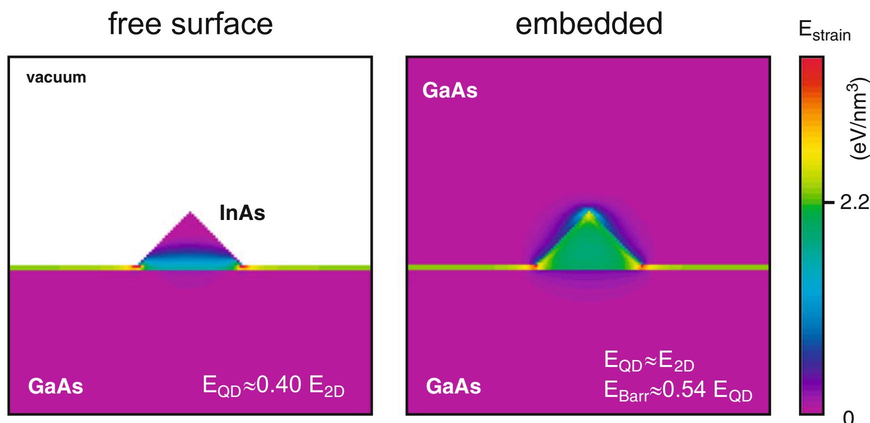

Fig. 13.26. Distribution of strain energy for (*left*) uncapped island and (*right*) island embedded in host matrix. Numerical values are for InAs/GaAs

[2]The ordering in size is remarkable. Typically Ostwald ripening (due to the Gibbs-Thomson effect; smaller droplets have larger vapor pressure and dissolve, larger droplets accordingly grow) occurs in an ensemble of droplets or nuclei. In the case of strained QDs, surface energy terms stabilize a certain QD size.

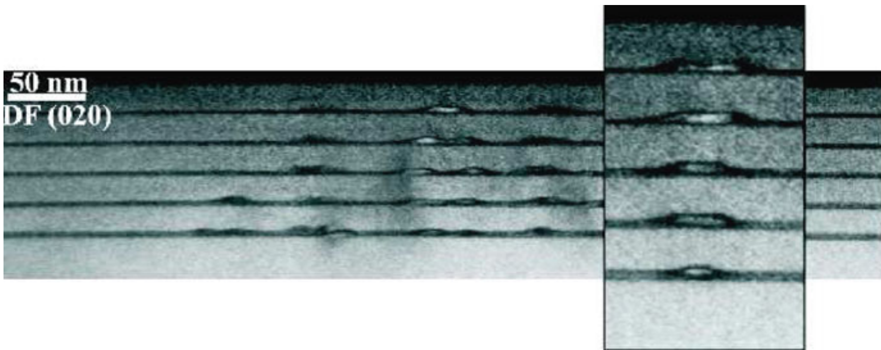

Fig. 13.27. Cross-sectional TEM image of a stack of five layers of quantum dots. Due to strain effects, vertical arrangement is achieved

thus making this type of relaxation energetically favorable. When the island is embedded in the host matrix, the strain energy is similar to the 2D case and the matrix becomes strained (metastable state).

When such QD layers are vertically stacked, the individual quantum dots grow on top of each other (Fig. 13.27) if the separation is not too large (Fig. 13.29). This effect is due to the effect of the underlying QD. In the case of InAs/GaAs (compressive strain), the buried QD stretches the surface above it (tensile surface strain). Thus, atoms impinging in the next QD layer find a smaller strain right on top of the buried QDs. In STM images of the cross section through (XSTM) such a stack (Fig. 13.28) individual indium atoms are visible and the shape can be analyzed in detail [898].

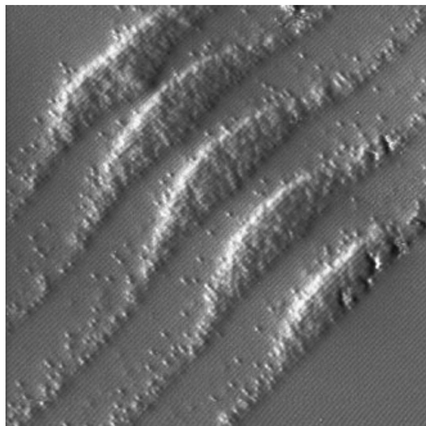

Fig. 13.28. Cross-sectional STM image of a stack of five InAs quantum dots in a GaAs matrix. Individual In atoms can be observed in-between the wetting layers and the quantum dots. Each quantum dot layer was formed by growing 2.4 ML of InAs. The intended distance between the quantum dot layers was 10 nm. Image size is $55 \times 55\,\mathrm{nm}^2$. Reprinted with permission from [898], ©2003 AIP

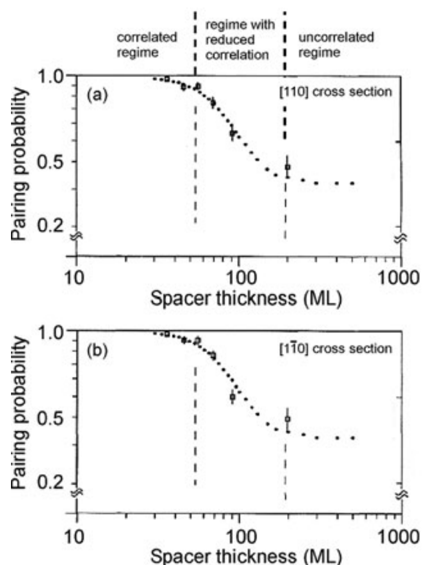

Fig. 13.29. Experimentally observed pairing probability in MBE-grown stacks of InAs/GaAs quantum dots as a function of the spacer-layer thickness. Data are taken from (**a**) (110) and (**b**) (1–10) cross-sectional TEM images. The *filled circles* are fit to data from theory of correlated island formation under strain fields. Reprinted with permission from [899], ©1995 APS

The vertical arrangement can lead to further ordering since a homogenization in lateral position takes place. If two QDs in the first layers are very close, their strain fields overlap and the second layer 'sees' only one QD.

The lateral (in-plane) ordering of the QDs with respect to each other occurs in square or hexagonal patterns and is mediated via strain interaction through the substrate. The interaction energy is fairly small, leading only to short-range in-plane order [893] as shown in Fig. 13.30. The in-plane ordering can be improved up to the point that regular one- or two-dimensional arrays form or individual quantum dots are placed on designated positions using directed self-assembly [860]. Among others, dislocation networks buried under the growth surface of the nanostructure, surface patterning and modification have been used to direct the QD positioning.

Ion-Beam Erosion

During the erosion of a surface with low-energy ion beam sputtering ordered patterns of dots appear [900–903]. Isotropic [904] and hexagonal [900, 902] (Fig. 13.31) near-range ordering has been observed. The pattern formation mechanism is based on the morphology-dependent sputter yield and further mechanisms of mass redistribution [905]. Also linear patterns have been reported [906].

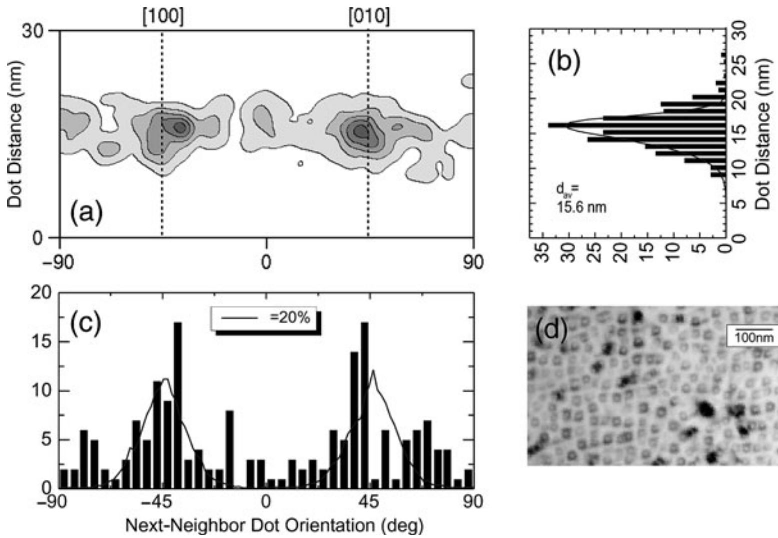

Fig. 13.30. Lateral ordering of QD array. (**d**) Plan-view TEM of QD array on which the statistical evaluation is based. (**a**) Two-dimensional histogram of QDs as a function of the nearest-neighbor distance and direction, (**b**,**c**) projections of part (**a**). *Solid lines* in (**b**) and (**c**) are theory for square array with $\sigma = 20\%$ deviation from ideal position. Adapted from [860] and [894]

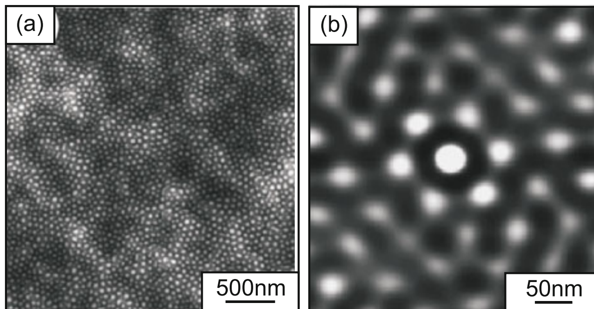

Fig. 13.31. (**a**) AFM image of a Si (001) substrate after 960 min of ion sputtering (1.2 keV Ar^+, normal incidence). (**b**) Two-dimensional autocorrelation function from a $400 \times 400\,\mathrm{nm}^2$ area of image in part (**a**). Adapted from [902]

13.3.4 Optical Properties

The optical properties of QDs are related to their electronic density of states. In particular, optical transitions are allowed only at discrete energies due to the zero-dimensional density of states.

Photoluminescence from a single QD is shown in Fig. 13.32. The δ-like sharp transition is strictly true only in the limit of small carrier numbers ($\ll 1$ exciton per dot on average) since otherwise many-body effects come into play

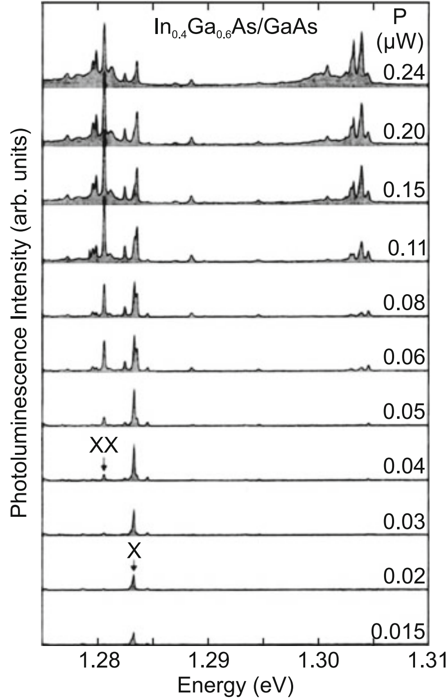

Fig. 13.32. Optical emission spectra ($T = 2.3\,\mathrm{K}$) of a single InGaAs/GaAs quantum dot at different laser excitation levels P as labeled. The single exciton (X) and biexciton (XX) lines are indicated. Adapted from [911]

that can encompass recombination from charged excitons or multiexcitons. At very low excitation density the recombination spectrum consists only of the one-exciton (X) line. With increasing excitation density small satellites on either side of the X-line develop that are attributed to charged excitons (trions) X^+ and X^-. On the low-energy side, the biexciton (XX) appears. Eventually, the excited states are populated and a multitude of states contribute with rich fine structure. In bulk material the biexciton (Sect. 9.5.11) is typically a bound state, i.e. its recombination energy E_{XX} is lower than that of the exciton E_{X}. A similar situation is present in Fig. 13.32. It was pointed out in [907] that in QDs the biexciton recombination energy can also be *larger* than the exciton recombination energy. In [908] the modification of the QD confinement potential of InAs/GaAs QDs by annealing was reported. The exciton binding energy (E_{X}-E_{XX}) is tuned from positive ('normal') to negative values upon annealing (Fig. 13.33).

The charging state of the exciton can be controlled in a field-effect structure. The recombination energy is modified due to Coulomb and exchange effects with the additional carriers. In charge-tunable quantum dots [909] and rings [910] exciton emission has been observed in dependence of the

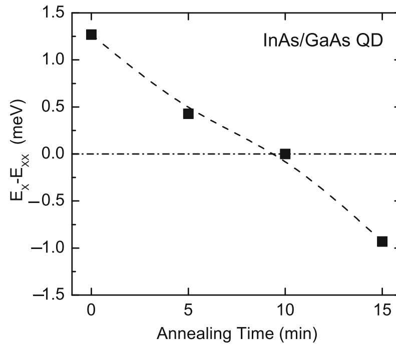

Fig. 13.33. Biexciton binding energy determined for a single InAs/GaAs quantum dot for various annealing times. Data from [908]

number of additional electrons. The electron population can be controlled in a Schottky-diode-like structure through the manipulation of the Fermi level with the bias voltage. At high negative bias all charge carriers tunnel out of the ring and no exciton emission is observed. A variation of the bias then leads to an average population with $N = 1, 2, 3, \ldots$ electrons. The recombination of additional laser-excited excitons depends (due to the Coulomb interaction) on the number of the electrons present (Fig. 13.34). The singly negatively charged exciton X^- is also called a trion.

The interaction of a spin with an exciton in a CdTe quantum dot has been observed in [912]. If the CdTe quantum dot is pure, a single line arises. If the dot contains a single Mn atom, the exchange interaction of the exciton

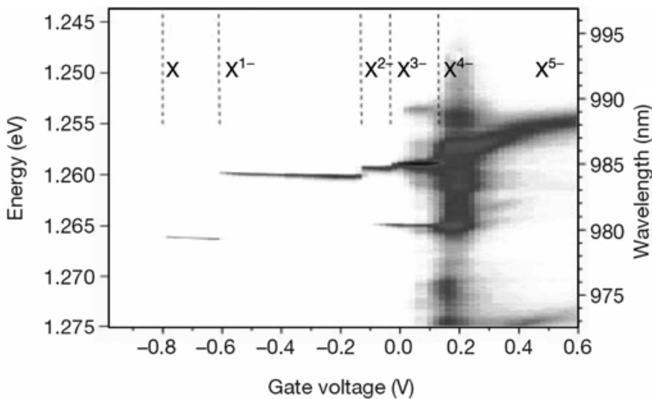

Fig. 13.34. Luminescence of charged excitons from a single quantum ring at $T = 4.2\,\mathrm{K}$ vs. the bias voltage with which the number of electrons in the quantum dot N is tuned from zero to $N>3$. Adapted from [910], reprinted with permission from Nature, ©2000 Macmillan Magazines Limited

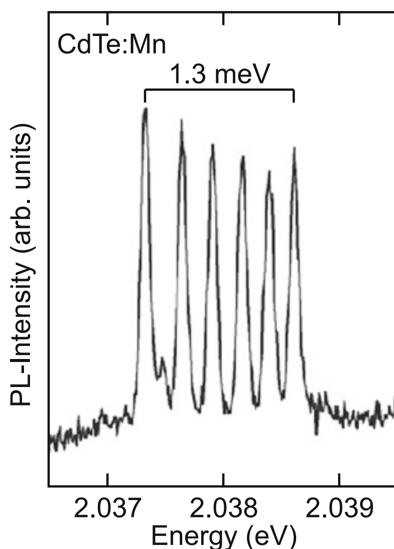

Fig. 13.35. Photoluminescence spectrum of a single CdTe/ZnSe quantum dot containing a single Mn atom ($T = 5\,\mathrm{K}$).

with the Mn $S = 5/2$ spin leads to a six-fold splitting of the exciton line (Fig. 13.35. In an external magnetic field a splitting into a total of twelve lines due to Zeeman effect at the Mn spin is observed.

In a QD ensemble, optical transitions are inhomogeneously broadened due to fluctuations in the QD size and the size dependence of the confinement

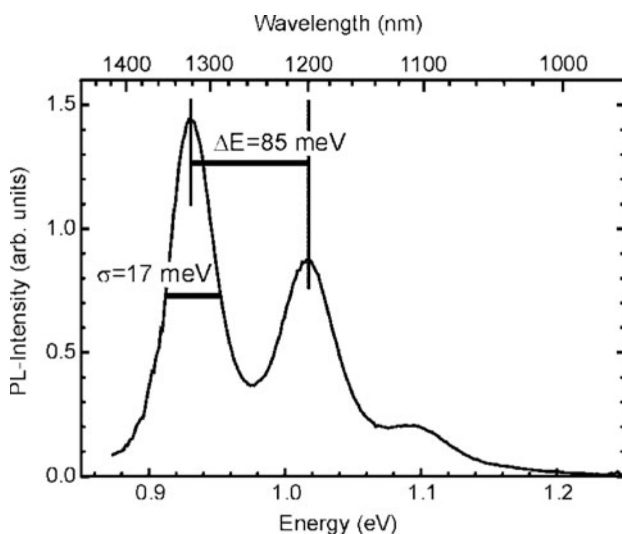

Fig. 13.36. Ensemble photoluminescence spectrum ($T = 293\,\mathrm{K}$, excitation density $500\,\mathrm{W/cm^2}$) of InAs/GaAs QDs

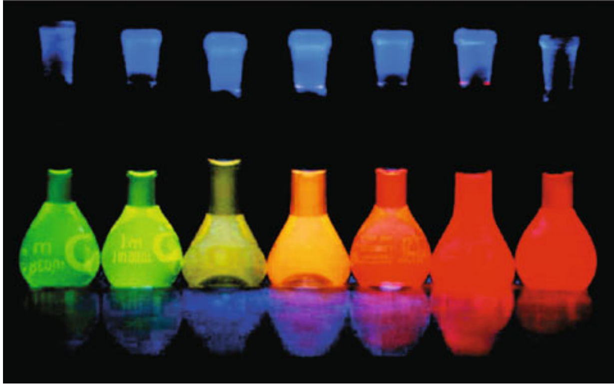

Fig. 13.37. Luminescence (under UV excitation) from flasks of colloidal CdTe quantum dots with increasing size (from left to right). From [892]

energies (Fig. 13.36). Interband transitions involving electrons and holes suffer from the variation of the electron and hole energies:

$$\sigma_E \propto \left(\left| \frac{\partial E_\mathrm{e}}{\partial L} \right| + \left| \frac{\partial E_\mathrm{h}}{\partial L} \right| \right) \delta L \, . \tag{13.17}$$

A typical relative size inhomogeneity of σ_L/L of 7% leads to several tens of meV broadening. Additional to broadening due to different sizes fluctuations of the quantum dot shape can also play a role. The confinement effect leads to an increase of the recombination energy with decreasing quantum-dot size. This effect is nicely demonstrated with colloidal quantum dots of different size as shown in Fig. 13.37.

14 Polarized Semiconductors

14.1 Introduction

Semiconductors can have an electric polarization. Such polarization can be induced by an external electric field (Fig. 14.1a). This phenomenon, i.e. that the semiconductor is dielectric, has been discussed already in Sect. 9. In this chapter, we discuss pyroelectricity, i.e. a spontaneous polarization without an external field (Fig. 14.1b), ferroelectricity,[1] i.e. pyroelectricity with a hysteresis (Fig. 14.1c) and piezoelectricity, i.e. a polarization due to external stress.

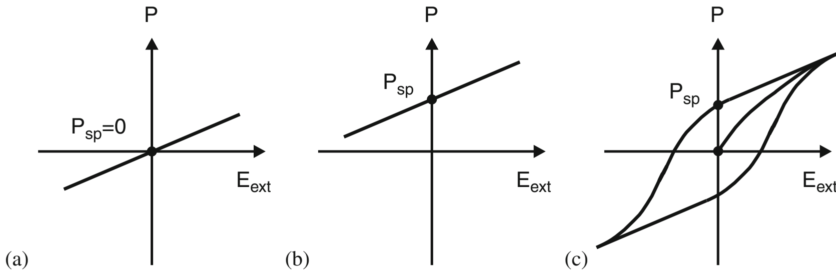

Fig. 14.1. Schematic representation of the polarization vs. external electric field dependence for (**a**) dielectric, (**b**) pyroelectric and (**c**) ferroelectric semiconductors

14.2 Spontaneous Polarization

The reason for a spontaneous polarization P_{sp} (without external electric field) is the static, relative shift of positive and negative charges in the unit cell. For a slab of semiconductor material (thus ignoring depolarization effects present in other geometries), the polarization causes polarization charges

[1] Ferromagnetic semiconductors are discussed in Sect. 15. We note that there exist so called *multiferroic* materials that possess more than one ferroic property [913, 914].

M. Grundmann, *The Physics of Semiconductors*, 2nd ed., Graduate Texts in Physics, DOI 10.1007/978-3-642-13884-3_14,

© Springer-Verlag Berlin Heidelberg 2010

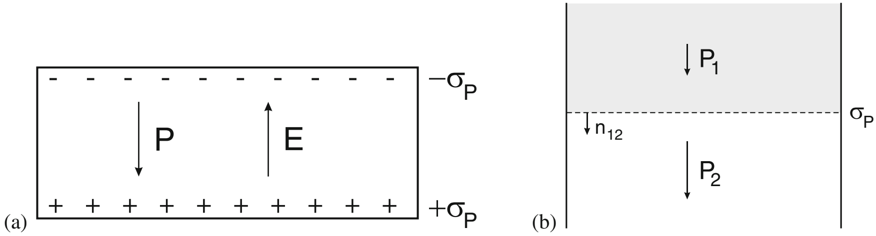

Fig. 14.2. (**a**) Surface polarization charges σ_P on a slab of semiconductor material with polarization. The electric field is given by $\mathbf{E} = -\mathbf{P}/\epsilon_0$. (**b**) Polarization charge σ_P at an interface between two semiconductors with different polarization. In the depicted situation σ is negative

located at the upper and lower surfaces (Fig. 14.2a). The polarization vector $\mathbf{P}$ points from the negative to the positive charge. The electric field due to the polarization charges has the opposite direction. In the absence of free charges, the Maxwell equation $\nabla \cdot \mathbf{D} = 0$ yields for piecewise constant fields at a planar interface (Fig. 14.2b) $(\mathbf{D}_2 - \mathbf{D}_1) \cdot \mathbf{n}_{12} = 0$ where $\mathbf{n}_{12}$ is the surface normal pointing from medium 1 to medium 2. Therefore, the polarization charge $\sigma_P = \epsilon_0 \nabla \cdot \mathbf{E}$ is given by

$$\sigma_P = -(\mathbf{P}_2 - \mathbf{P}_1) \cdot \mathbf{n}_{12} \, . \tag{14.1}$$

Polarization charges develop at interfaces where the polarization is discontinuous, e.g. an interface between two semiconductors with different spontaneous polarization. Vacuum (at a surface) represents a special case with $\mathbf{P} = 0$.

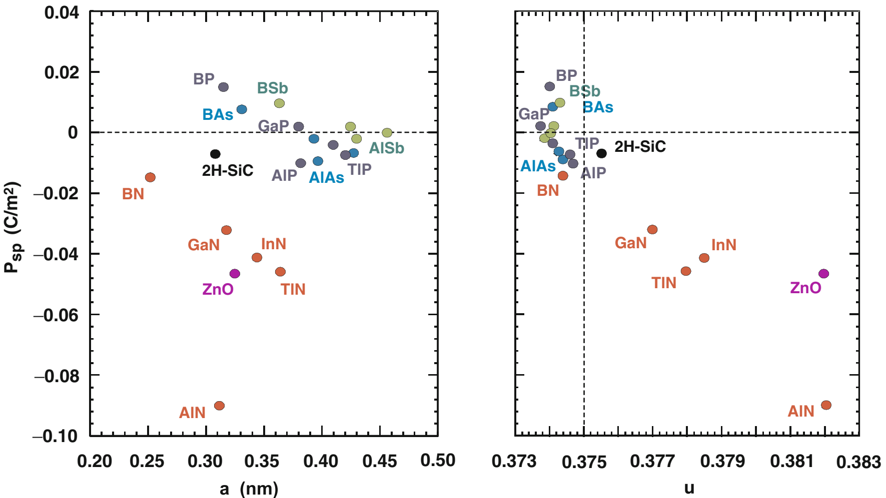

Fig. 14.3. Spontaneous polarization P_{sp} for various semiconductors as a function of the lattice constant a (*left*) and the cell-internal parameter u (*right*). Based on [918]

For cubic zincblende structure semiconductors, P_{sp} is typically fairly small. The anisotropy of the wurtzite structure allows for sizeable effects. The main cause is the nonideality of the cell-internal parameter u (Fig. 14.3) (cf. Sect. 3.4.5).

14.3 Ferroelectricity

Ferroelectric semiconductors exhibit a spontaneous polarization in the ferroelectric phase and zero spontaneous polarization in the paraelectric phase. As a function of temperature, the ferroelectric material undergoes a phase transition from the high-temperature paraelectric phase into the ferroelectric phase. There can be further phase transitions between different ferroelectric phases that differ in the direction of the polarization. The literature until 1980 is summarized in [915]. A more recent treatment can be found in [916, 917].

$PbTiO_3$ has perovskite structure (cf. Sect. 3.4.9). It exhibits a phase transition at $T_{\mathrm{C}} = 490\,°\mathrm{C}$ from the cubic into the (ferroelectric) tetragonal phase as shown in Fig. 14.4a. Mostly the cell symmetry changes, while the cell volume remains almost constant. A more complicated situation arises for $BaTiO_3$. At 120 °C the transition into the ferroelectric phase occurs (Fig. 14.4b) that is tetragonal with the polarization in the [100] direction. At −5 °C and −90 °C transitions occur into an orthorhombic and a rhombohedral (trigonal) phase, respectively. The largest polarization is caused by a displacement of the negatively (O) and positively (Ba, Ti) charged ions of

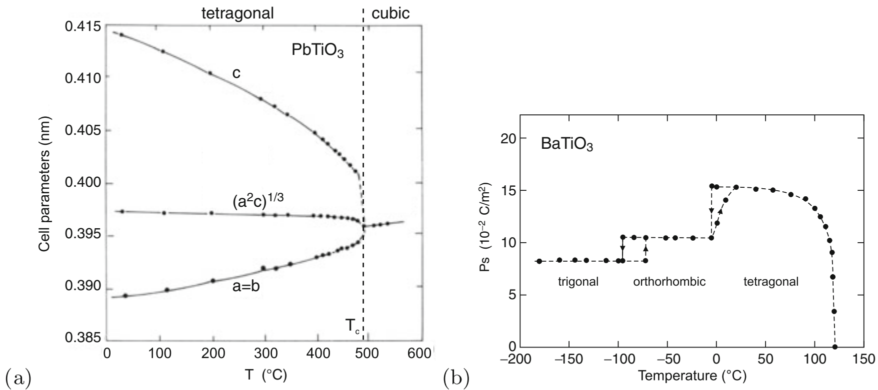

Fig. 14.4. (**a**) Cell parameters of $PbTiO_3$ as a function of temperature. Adapted from [921]. (**b**) Phase transitions of $BaTiO_3$ as a function of temperature. The spontaneous polarization P_{S} points along ⟨100⟩, ⟨110⟩ and ⟨111⟩ in the tetragonal (C_{4v}), orthorhombic (C_{2v}) and trigonal (C_{3v}, rhombohedral) phase, respectively. Adapted from [922]

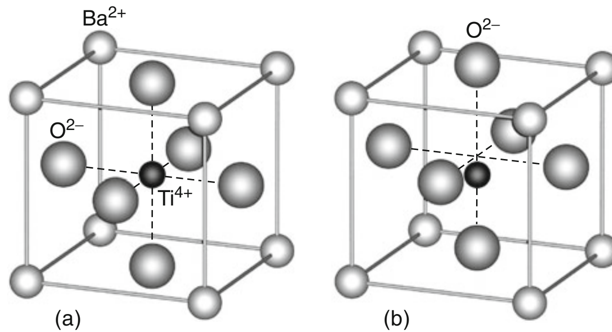

Fig. 14.5. (**a**) Crystal structure of $BaTiO_3$ (see Fig. 3.24). (**b**) Schematic tetragonal deformation below the Curie temperature, generating a dipole moment

the unit cell by $\delta \approx 0.02\,\mathrm{nm}$ (Fig. 14.5). Such an origin of the spontaneous polarization is called a *displacement* transition.[2]

14.3.1 Materials

A large class of ferroelectric semiconductors are of the type ABO_3, where A stands for a cation with larger ionic radius and B for an anion with smaller ionic radius. Many ferroelectrics have perovskite ($CaTiO_3$) structure. They are $A^{2+}B^{4+}O_3^{2-}$, e.g. (Ba,Ca,Sr) (Zi,Zr)O_3 or $A^{1+}B^{5+}O_3^{2-}$, e.g. (Li,Na,K) (Nb,Ta)O_3. Ferroelectrics can also be alloyed. Alloying in the B component yields, e.g. $PbTi_xZr_{1-x}O_3$ also called PZT. PZT is widely used for piezoelectric actuators. Also, alloying in the A component is possible, e.g. $Ba_xSr_{1-x}TiO_3$.

Another class of ferroelectrics are $A^{V}B^{VI}C^{VII}$ compounds, such as SbSI, SbSBr, SbSeI, BiSBr. These materials have a width of the forbidden band in the $\sim 2\,\mathrm{eV}$ range. A further class of ferroelectric semiconductors are $A_2^{V}B_3^{VI}$ compounds, such as Sb_2S_3.

14.3.2 Soft Phonon Mode

The finite displacement of the sublattices in the ferroelectric means that the related lattice vibration has no restoring force. The displacement is, however, finite due to higher-order terms (anharmonicity). Thus, for $T \to T_C$ $\omega_{TO} \to 0$.

[2]The widely accepted model for such ferroelectric is that the basic displacement occurs into the $\langle 111 \rangle$-direction at low temperature. The three higher symmetry phases at higher temperature are the result of 2 (orthorhombic), 4 (tetragonal) or 8 (cubic) allowed $\langle 111 \rangle$ orientations which make the macroscopically averaged polarization appear in $\langle 110 \rangle$- or $\langle 100 \rangle$-direction or vanishing altogether, respectively [919, 920].

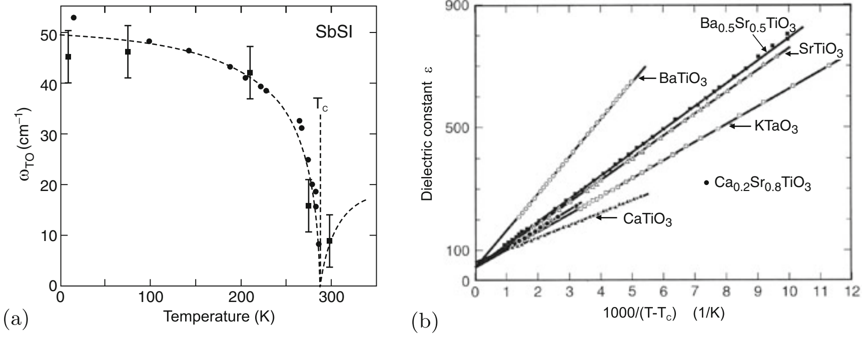

Fig. 14.6. (**a**) Decrease of the transverse phonon mode of SbSI close to the Curie temperature of $T_C = 288\,K$. The *dashed curved line* represents a $|T - T_C|^{1/2}$ dependence. Adapted from [923]. (**b**) Dielectric constant of various perovskites vs. $1/(T - T_C)$ in the paraelectric phase ($T > T_C$). Adapted from [924]

Such a mode is called a *soft phonon mode*. The decrease of the phonon frequency is shown in Fig. 14.6a for SbSI.

From the LST relation (5.48), it follows that the static dielectric function must increase strongly. The increase is $\propto (T - T_C)^{-1}$ (Fig. 14.6b).

14.3.3 Phase Transition

In the case of ferroelectrics, the order parameter for the Ginzburg–Landau theory of phase transitions is the spontaneous polarization P. The free energy F of the ferroelectric crystal is written in terms of the free energy of the paraelectric phase F_0 and is expanded in powers of P (here up to P^6) as

$$F = F_0 + \frac{1}{2}\,\alpha\,P^2 + \frac{1}{4}\,\beta\,P^4 + \frac{1}{6}\,\gamma\,P^6\,. \tag{14.2}$$

In this equation, we have neglected effects due to charge carriers, an external electric field or external stresses and we assume homogeneous polarization. In order to obtain a phase transition, it has to be assumed that α has a zero at a certain temperature T_C and we assume (expanding only to the linear term)

$$\alpha = \alpha_0\,(T - T_C)\,. \tag{14.3}$$

Second-Order Phase Transition

For modeling a second-order phase transition, we set $\gamma = 0$. Thus, the free energy has the form (Fig. 14.7a)

$$F = F_0 + \frac{1}{2}\,\alpha\,P^2 + \frac{1}{4}\,\beta\,P^4\,. \tag{14.4}$$

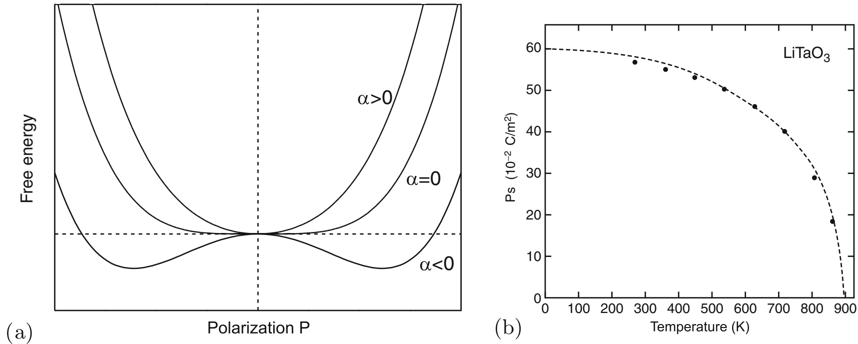

Fig. 14.7. (**a**) Schematic plot of the free energy vs. spontaneous polarization for a second-order phase transition. $\alpha > 0$ ($\alpha < 0$) corresponds to the paraelectric (ferroelectric) phase. (**b**) Spontaneous polarization of $LiTaO_3$ as a function of temperature exhibiting a second-order phase transition. The *dashed line* is theory with suitable parameters. Adapted from [925]

The equilibrium condition with regard to the free energy yields a minimum for

$$\frac{\partial F}{\partial P} = \alpha\, P + \beta\, P^3 = 0 \tag{14.5a}$$

$$\frac{\partial^2 F}{\partial P^2} = \alpha + 3\,\beta\, P^2 > 0\,. \tag{14.5b}$$

Equation (14.5a) yields two solutions. $P = 0$ corresponds to the paraelectric phase. $P^2 = -\alpha/\beta$ is the spontaneous polarization in the ferroelectric phase. The condition from (14.5b) yields that $\alpha > 0$ in the paraelectric phase, while $\alpha < 0$ in the ferroelectric phase. Also, $\beta > 0$ below the Curie temperature (β is assumed to be temperature independent in the following). Using (14.3), the polarization is given as (Fig. 14.7b)

$$P^2 = \frac{\alpha_0}{\beta}\,(T - T_{\mathrm{C}})\,. \tag{14.6}$$

Therefore, the entropy $S = -\frac{\partial F}{\partial T}$ and the discontinuity ΔC_{p} of the heat capacity $C_{\mathrm{p}} = T\left(\frac{\partial S}{\partial T}\right)_{\mathrm{p}}$ at the Curie point T_{C} are given by

$$S = S_0 + \frac{\alpha_0^2}{\beta}\,(T - T_{\mathrm{C}}) \tag{14.7a}$$

$$\Delta C_{\mathrm{p}} = \frac{\alpha_0^2}{\beta}\,T_{\mathrm{C}}\,, \tag{14.7b}$$

with $S_0 = -\frac{\partial F_0}{\partial T}$ being the entropy of the paraelectric phase. This behavior is in accordance with a second-order phase transition with vanishing latent heat

(continuous entropy) and a discontinuity of the heat capacity. The dielectric function in the paraelectric phase is $\propto 1/\alpha$ and in the ferroelectric phase $\propto -1/\alpha$. The latter relation is usually written as the Curie–Weiss law

$$\epsilon = \frac{C}{T - T_C} \,. \tag{14.8}$$

First-Order Phase Transition

When the P^6 term is included in (14.2) ($\gamma \neq 0$), a first-order phase transition is modeled. However, in order to obtain something new, compared to the previous consideration, now $\beta < 0$ (and $\gamma > 0$) is necessary. The dependence of the free energy on P is schematically shown in Fig. 14.8a for various values of α. The condition $\frac{\partial F}{\partial P} = 0$ yields

$$\alpha\, P + \beta\, P^3 + \gamma\, P^5 = 0 \,, \tag{14.9}$$

with the solutions $P = 0$ and

$$P^2 = -\frac{\beta}{2\gamma}\left(1 + \sqrt{1 - \frac{4\alpha\gamma}{\beta^2}}\right) \,. \tag{14.10}$$

For a certain value of α, i.e. at a certain temperature $T = T_1$, the free energy is zero for $P = 0$ *and* also for another value $P = P_0$ (second curve from the top in Fig. 14.8a). From the condition

$$\frac{1}{2}\,\alpha(T_1)\,P_0^2 + \frac{1}{4}\,\beta P_0^4 + \frac{1}{6}\,\gamma\,P_0^6 = 0 \,, \tag{14.11}$$

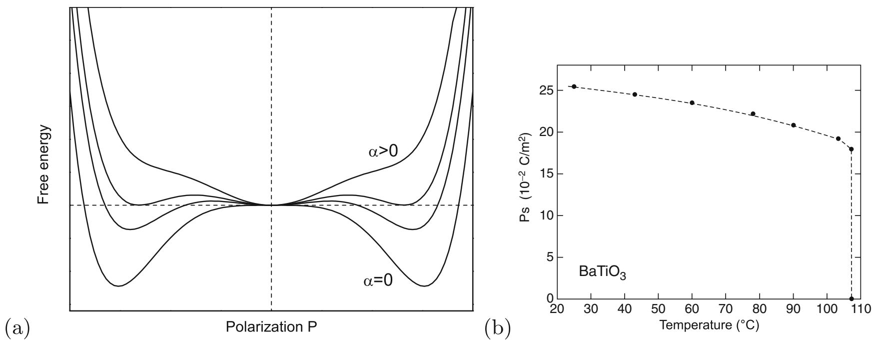

Fig. 14.8. (**a**) Schematic plot of the free energy vs. spontaneous polarization for a first-order phase transition. The lowest curve is for $\alpha = 0$, the others are for $\alpha > 0$. (**b**) Spontaneous polarization in $BaTiO_3$ as a function of temperature exhibiting a first-order phase transition. The *dashed line* is a guide to the eye. Adapted from [926]

the values for P_0 and α at the transition temperature $T = T_1$ are given by

$$P_0^2 = = -\frac{3}{4}\frac{\beta}{\gamma} \tag{14.12a}$$

$$\alpha(T_1) = \frac{3}{16}\frac{\beta^2}{\gamma} > 0\,. \tag{14.12b}$$

The schematic dependence of P at the phase transition temperature T_1 is depicted in Fig. 14.8b.

For $T \leq T_1$ the absolute minimum of the free energy is reached for finite polarization $P > P_0$. However, between $F(P = 0)$ and the minimum of the free energy an energy barrier (second lowest curve in Fig. 14.8) is present for T close to T_1. The energy barrier disappears at the Curie–Weiss temperature T_0. At the phase transition temperature, the entropy has a discontinuity

$$\varDelta S = \alpha_0\, P_0^2\,, \tag{14.13}$$

that corresponds to a latent heat $\varDelta Q = T\varDelta S$. Another property of the first-order phase transition is the occurrence of hysteresis in the temperature interval between T_1 and T_0

$$\varDelta T \approx T_1 - T_0 = \frac{1}{4\alpha_0}\frac{\beta^2}{\gamma}\,, \tag{14.14}$$

in which an energy barrier is present to hinder the phase transition. For decreasing temperature, the system tends to remain in the paraelectric phase. For increasing temperature, the system tends to remain in the ferroelectric phase. Such behavior is observed for $BaTiO_3$, as shown in Fig. 14.4b.

14.3.4 Domains

Similar to ferromagnets, ferroelectrics form domains with different polarization directions in order to minimize the total energy by minimizing the field energy outside the crystal. The polarization can have different orientations, 6 directions for P along $\langle 100\rangle$ (tetragonal phase), 12 directions for P along $\langle 110\rangle$ (orthorhombic phase) and 8 directions for P along $\langle 111\rangle$ (rhombohedral phase). In Fig. 14.9, such domains are visualized for $BaTiO_3$. Due to the restricted geometry, domain formation in thin films is different from that in bulk material.

Domains can also be artificially created by so-called poling. The ferroelectric semiconductor is heated to the paraelectric phase. With electrodes, appropriate electric fields are applied and the material is cooled. The polarization is then frozen in the ferroelectric phase. The domains of a periodically poled structure in $LiNbO_3$ (PPLN) are shown in Fig. 14.10b. The nonlinear optical properties in such structures can be used for efficient second harmonic generation (SHG).

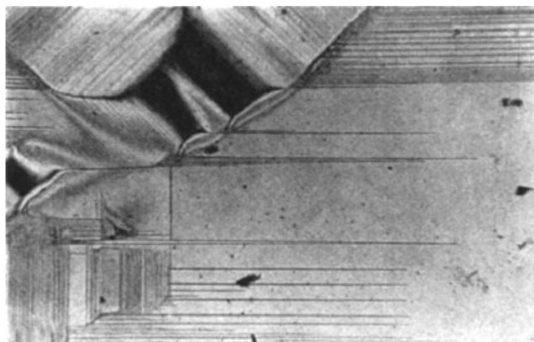

Fig. 14.9. Ferroelectric domains in a $BaTiO_3$ single crystal visualized by birefringence contrast. Reprinted with permission from [927], ©1949 APS

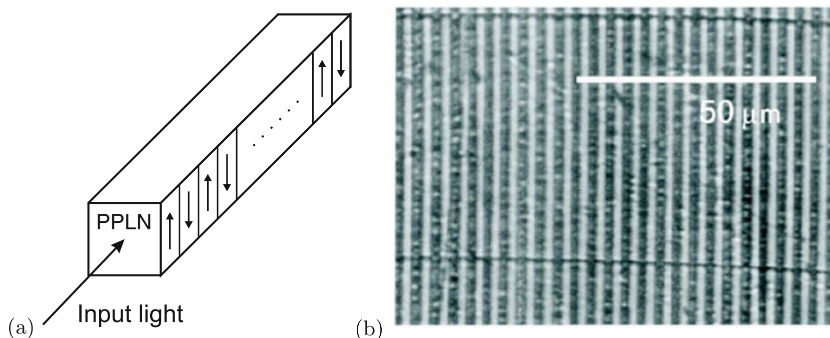

Fig. 14.10. (**a**) Scheme of PPLN (periodically poled lithium niobate), *arrows* denote the direction of spontaneous polarization. (**b**) Polarization microscopy image (vertical stripes are domains, horizontal dark lines are scratches)

14.3.5 Optical Properties

The first-order phase transition of $BaTiO_3$ manifests itself also in a discontinuity of the band gap (Fig. 14.11). The coefficient $\partial E_g/\partial T$ for the temperature dependence of the band gap is also different in the para- and ferroelectric phases.

14.4 Piezoelectricity

14.4.1 Piezoelectric Effect

External stress causes atoms in the unit cell to shift with respect to each other. In certain directions, such a shift can lead to a polarization. Generally, all ferroelectric materials are piezoelectric. However, there are piezoelectric

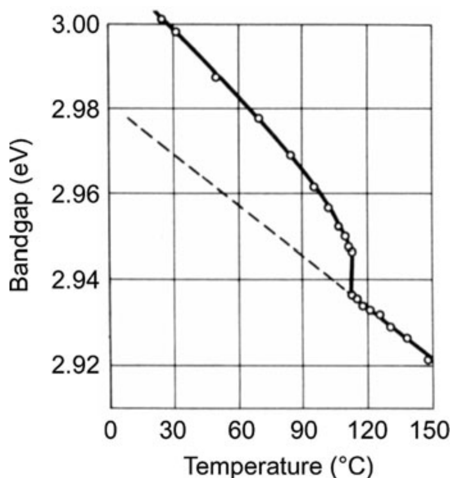

Fig. 14.11. Temperature dependence of the band gap in $BaTiO_3$ (for polarized light with $\mathbf{E} \perp c$). Experimental data from [928]

materials that are not ferroelectric, e.g. quartz, GaAs and GaN. Piezoelectricity can occur only when no center of inversion is present. Thus, e.g., GaAs is piezoelectric along $\langle 111 \rangle$, but Si is not. Also, the cubic perovskite structure (in the paraelectric phase) is not piezoelectric. Generally, the piezoelectric polarization is related to the strains via the tensor e_{ijk} of the piezoelectric modules

$$P_i = e_{ijk}\, \epsilon_{jk} \ . \tag{14.15}$$

14.4.2 Zincblende Crystals

In zincblende semiconductors, the polarization (with respect to $x = [100]$, $y = [010]$, $z = [001]$) is due to shear strains only and is given as

$$\mathbf{P}_{\mathrm{pe}} = 2e_{14} \begin{pmatrix} \epsilon_{yz} \\ \epsilon_{xz} \\ \epsilon_{xy} \end{pmatrix} . \tag{14.16}$$

The values of e_{14} for various zincblende compound semiconductors are listed in Table 14.1. We note that the sign of e_{14} reverses from negative in cubic III–V to positive in cubic II–VI semiconductors. This non-trivial behavior involves strain effects on ionic and electronic polarization and ionicity as discussed in [110, 929]. The coefficient e_{33}, the equivalent to e_{14} in wurtzite semiconductors (see below), is positive for III–V and II-VI semiconductors.

The strain in pseudomorphic heterostructures (cf. Sect. 5.3.3) can cause piezoelectric polarization in a piezoelectric semiconductor. In zincblende, the main effect is expected when the growth direction is along [111] and the strain

Table 14.1. Piezoelectric coefficients (in $\mathrm{C\,m^{-2}}$) for various zincblende and wurtzite semiconductors. Data from [929], for GaN from [932] (theoretical value), AlN [933]

zincblende				wurtzite	
A–B	e_{14}	A–B	e_{14}	A–B	e_{33}
InSb	−0.123	CdTe	0.054	CdSe	0.35
InAs	−0.078	ZnSe	0.049	CdS	0.44
GaSb	−0.218	ZnS	0.254	ZnS	0.27
GaAs	−0.277			ZnO	1.10
AlSb	−0.118			BeO	0.092
				GaN	0.58
				AlN	1.55

has a purely shear character. In this case, the polarization is in the [111] direction, i.e. perpendicular to the interface ($P_\perp$). For the [001] growth direction, no piezoelectric polarization is expected. For the [110] growth direction, the polarization is found to be parallel to the interface ($P_\|$). The situation is shown for various orientations of the growth direction in Fig. 14.12.

14.4.3 Wurtzite Crystals

In wurtzite crystals, the piezoelectric polarization (with respect to $x =$ [2–1.0], $y =$ [01.0], $z =$ [00.1]) is given by

$$\mathbf{P}_{\mathrm{pe}} = \begin{pmatrix} 2e_{15}\epsilon_{yz} \\ 2e_{15}\epsilon_{xz} \\ e_{31}(\epsilon_{xx} + \epsilon_{yy}) + e_{33}\epsilon_{zz} \end{pmatrix} . \tag{14.17}$$

Values of e_{33} for several wurtzite semiconductors are listed in Table 14.1.

The polarization (along c) for biaxial strain in heteroepitaxy (5.70) on the [00.1] surface is

$$P_{\mathrm{PE}} = 2\epsilon_\| \left(e_{31} - \frac{C_{13}}{C_{33}} e_{33} \right) , \tag{14.18}$$

where $\epsilon_\| = (a - a_0)/a_0$ is the in-plane strain. The dependence of the magnitude for GaN on the in-plane strain is shown in Fig. 14.13 together with the polarization for uniaxial stress along [00.1] and hydrostatic strain. In the latter two cases, the polarization is smaller.

The difference of spontaneous polarization of the constituent materials in heterostructures and piezoelectric effects in strained quantum wells lead to

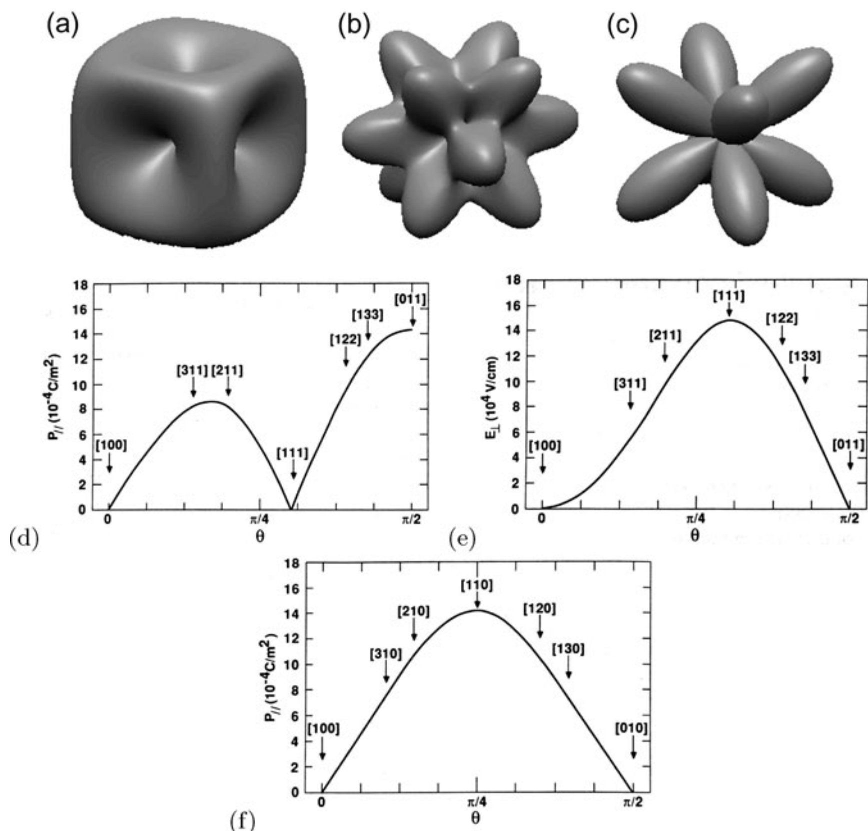

Fig. 14.12. Three-dimensional view of the (**a**) total, (**b**) longitudinal and (**c**) transverse polarization in uniaxially compressed GaAs. Reprinted with permission from [930], ©1994 APS. (**d**) Transverse polarization $P_{\parallel}$ (parallel to the interface) and (**e**) longitudinal electric field $E_{\perp}$ (perpendicular to the interface) in the InGaAs layer of a GaAs/$\mathrm{In_{0.2}Ga_{0.8}As}$ superlattice with joint in-plane lattice constant (obtained from energy minimization, 1.4% lattice mismatch, the InGaAs is under compressive and the GaAs under tensile strain). The layer thicknesses of the GaAs and InGaAs layers are identical. The quantities are shown for various orientations of the growth direction. The vector of the growth direction varies in the (01–1) plane ($\phi = \pi/4$) with polar angle θ reaching from [100] (0°) over [111] to [011] (90°). Image (**f**) depicts the transverse polarization $P_{\parallel}$ ($P_{\perp} = 0$ in this geometry) for growth directions in the (001) plane ($\phi = 0$). Parts (**d**,**e**,**f**) reprinted with permission from [931], ©1988 AIP

quantum confined Stark effect (QCSE, Sect. 12.1.2). The spatial separation of electrons and holes leads to a larger radiative lifetime (Fig. 11.35) and thus reduced radiative recombination rate in the presence of nonradiative channels, an effect unwanted in light emitting diodes. In particular nitride based LEDs grown along the c-direction are prone to this effect. Therefore

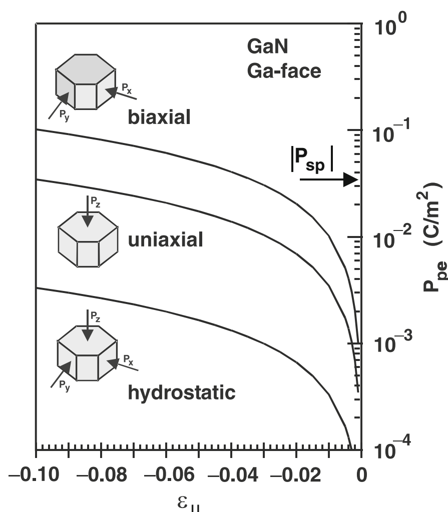

Fig. 14.13. Piezoelectric polarization P_{pe} in GaN (Ga-face) vs. in-plane strain $\epsilon_{\|} = (a - a_0)/a_0$ for biaxial, uniaxial and hydrostatic strain. The value of the spontaneous polarization P_{sp} is indicated by an *arrow*. From [934]

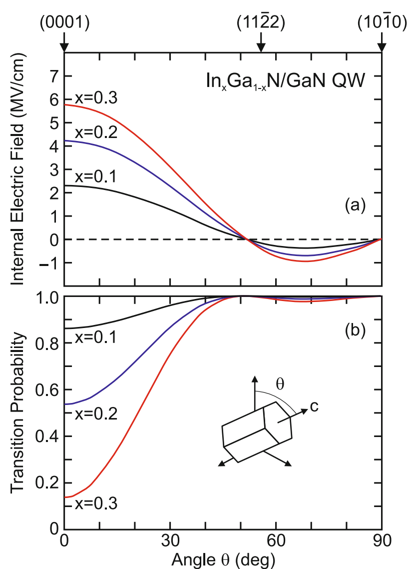

Fig. 14.14. (**a**) Internal electric field and (**b**) transition probability for electron-hole pairs in $\mathrm{In}_x\mathrm{Ga}_{1-x}\mathrm{N}$/GaN quantum well ($L_{\mathrm{w}} = 3\,\mathrm{nm}$) for three different indium contents x as labeled. θ denotes the angle between the c-axis and the normal of the interface plane (see *inset*). Based on [938]

growth on nonpolar surfaces such as $(1\bar{1}00)$ (m-plane) and $(11\bar{2}0)$ (a-plane) has been investigated [935, 936]. However, crystal quality for these growth planes seems limited.

An alternative route are 'semipolar' planes, e.g. $(10\bar{1}\bar{1})$ or $(11\bar{2}2)$ [937], with at least reduced polarization effects. The $(11\bar{2}2)$-plane is tilted 56° from the c-axis, close to the theoretically predicted zero of the internal electric field for InGaN/GaN quantum wells [938] (Fig. 14.14). Promising experimental results have been published on semipolar growth, especially for InGaN/GaN on $(11\bar{2}2)$-oriented GaN substrates [939].

14.4.4 Piezoelectric Effects in Nanostructures

The strain distribution around zincblende strained quantum wires [930] and quantum dots [288] contains shear components and thus generates piezoelectric fields. In Fig. 14.15, the electric field and potential due to the piezoelectric charges are shown for a strained $In_{0.2}Ga_{0.8}As$/GaAs quantum wire. In Fig. 14.16, the piezoelectric charges and potential are shown for the quantum dot from Fig. 5.22. The piezoelectric potential has quadrupole character and

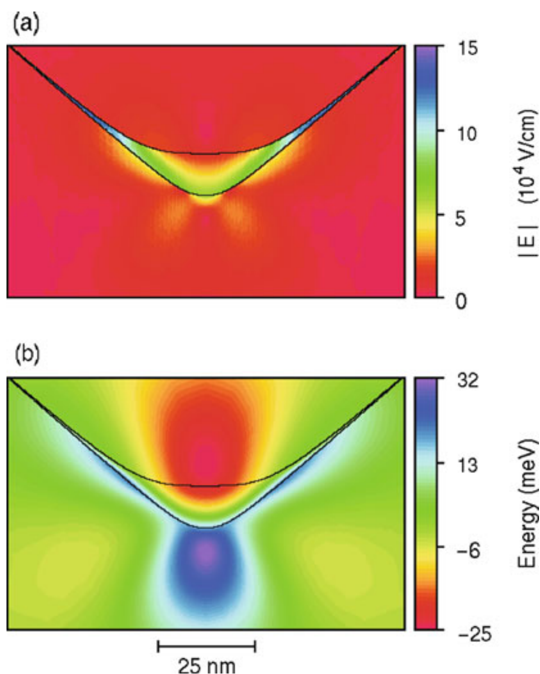

Fig. 14.15. (**a**) Electric field and (**b**) additional confinement potential for electrons due to piezoelectric charges for a strained $In_{0.2}Ga_{0.8}As$/GaAs quantum wire. Reprinted with permission from [930], ©1994 APS

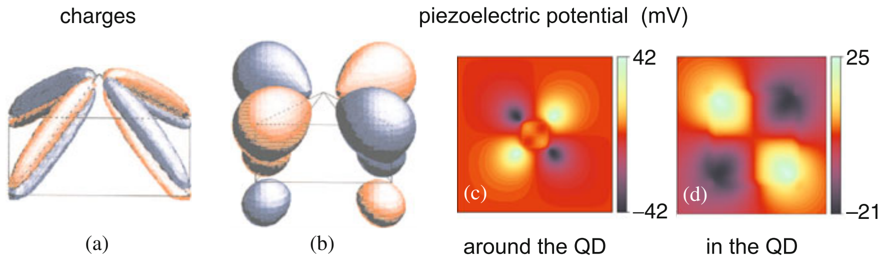

Fig. 14.16. (**a**) Piezoelectric charges and (**b**)–(**d**) resulting Coulomb potential for InAs/GaAs quantum dot with base length $b = 12\,\mathrm{nm}$. (**a**) Isosurfaces corresponding to volume charges $\pm 0.3\,\mathrm{e\,nm^{-3}}$. (**b**) Isosurfaces for the Coulomb potential at $\pm 30\,\mathrm{meV}$. (**c**,**d**) Cross section through the Coulomb potential somewhat above the wetting layer in two different magnifications, (**d**) is a zoom into (**c**). The InAs/GaAs interface is visible in (**d**) due to the image charge effect. Parts (**a**) and (**b**) reprinted with permission from [288], ©1995 APS

thus reduces the symmetry of the QD (to C_{2v}) [288].[3] Piezoelectric effects are particularly important in wurtzite nanostructures [940].

[3]The strain distribution has C_{2v} symmetry for a square-based pyramid for zincblende materials. The energy levels and wavefunctions are more strongly impacted by the piezoelectric effects than by the strain asymmetry [883, 884].

15 Magnetic Semiconductors

15.1 Introduction

Magnetic semiconductors exhibit spontaneous magnetic order. Even ferromagnetism, important for spin polarization, as needed in spinelectronics (also called spintronics), can occur below the Curie temperature that is characteristic of the material. Magnetic semiconductors can be binary compounds such as EuTe (antiferromagnetic) or EuS (ferromagnetic). Another class of magnetic semiconductors contains paramagnetic ions in doping concentration (typically $< 10^{21}\,\mathrm{cm}^{-1}$) or alloy concentration x (typically $x \geq 0.1\%$). Such materials are termed *diluted magnetic semiconductors* (DMS). The incorporation of the magnetic atoms leads first to conventional alloy effects, such as the modification of the lattice constant, the carrier concentration or the band gap. The status of the field up to the mid-1980s can be found in [941], mostly focused on II–VI DMS. A review of work on III–V based materials for spintronics, mostly GaAs:Mn, can be found in [942]. A 2003 review of wide band gap ferromagnetic semiconductors is given in [943].

15.2 Magnetic Semiconductors

In a magnetic semiconductor, one sublattice is populated with paramagnetic ions. The first two ferromagnetic semiconductors discovered were $CrBr_3$ [944] in 1960 and EuO [945] one year later. Europium monoxide has an ionic $Eu^{2+}O^{2-}$ character, such that the electronic configuration of europium is $[Xe]4f^7 5d^0 6s^0$ and that of oxygen is $1s^2 2s^2 2p^6$. Some properties of europium chalcogenides [946] are summarized in Table 15.1.

EuO can be modeled as a Heisenberg ferromagnet with dominant nearest- and next-nearest Eu–Eu interactions [947]. The Heisenberg exchange parameters J_1 and J_2 for these four compounds are shown in Fig. 15.1. In the nearest-neighbor interaction J_1 a 4f electron is excited to the 5d band, experiences an exchange interaction with the 4f spin on a nearest neighbor and returns to the initial state. This mechanism generally leads to ferromagnetic exchange. The next-nearest-neighbor interaction J_2 is weakly ferromagnetic (EuO) or antiferromagnetic (EuS, EuSe, EuTe). In the superexchange

M. Grundmann, *The Physics of Semiconductors*, 2nd ed., Graduate Texts in Physics, DOI 10.1007/978-3-642-13884-3_15,

© Springer-Verlag Berlin Heidelberg 2010

Table 15.1. Material properties of Eu chalcogenides. 'F' ('AF') denotes ferromagnetic (antiferromagnetic) order. T_N (T_C) denotes the Néel (Curie) temperature. Data collected in [948]

material	E_g (eV)	magnetic order	T_N, T_C (K)
EuO	1.12	F	69.3
EuS	1.65	F	16.6
EuSe	1.8	AF	4.6
		F	2.8
EuTe	2.00	AF	9.6

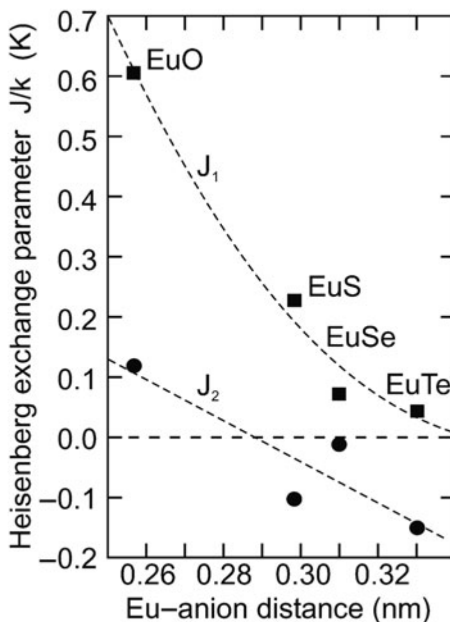

Fig. 15.1. Heisenberg nearest (J_1, *squares*) and next-nearest (J_2, *circles*) exchange parameters (in units of $J_{1,2}/k_B$) for the Eu chalcogenides vs. the Eu–anion distance. *Dashed lines* are guides to the eye. Experimental data from [948]

process, electrons are transferred from the anionic p states to the 5d states of the Eu^{2+} cations, resulting in an antiferromagnetic coupling.

15.3 Diluted Magnetic Semiconductors

In Table 15.2, the transition metals and their electron configurations are summarized. The 3d transition metals are typically used for magnetic impurities in DMS due to their partially filled 3d shell. Due to Hund's rule, the spins on

Table 15.2. 3d, 4d and 5d transition metals and their electron configurations. Note that Hf^{72} has an incompletely filled 4f-shell with $4f^{14}$

Sc^{21}	Ti^{22}	V^{23}	Cr^{24}	Mn^{25}	Fe^{26}	Co^{27}	Ni^{28}	Cu^{29}	Zn^{30}
3d	$3d^2$	$3d^3$	$3d^5$	$3d^5$	$3d^6$	$3d^7$	$3d^8$	$3d^{10}$	$3d^{10}$
$4s^2$	$4s^2$	$4s^2$	4s	$4s^2$	$4s^2$	$4s^2$	$4s^2$	4s	$4s^2$
Y^{39}	Zr^{40}	Nb^{41}	Mo^{42}	Tc^{43}	Ru^{44}	Rh^{45}	Pd^{46}	Ag^{47}	Cd^{48}
4d	$4d^2$	$4d^4$	$4d^5$	$4d^6$	$4d^7$	$4d^8$	$4d^{10}$	$4d^{10}$	$4d^{10}$
$5s^2$	$5s^2$	5s	5s	5s	5s	5s	–	5s	$5s^2$
La^{57}	Hf^{72}	Ta^{73}	W^{74}	Re^{75}	Os^{76}	Ir^{77}	Pt^{78}	Au^{79}	Hg^{80}
5d	$5d^2$	$5d^3$	$5d^4$	$5d^5$	$5d^6$	$5d^7$	$5d^9$	$5d^{10}$	$5d^{10}$
$6s^2$	$6s^2$	$6s^2$	$6s^2$	$6s^2$	$6s^2$	$6s^2$	6s	6s	$6s^2$

the 3d shell are filled in parallel for the first five electrons up to half filling (in order to allow the electrons to get out of their way in real space). Thus, the atoms have a sizeable spin and a magnetic moment. The spin of Mn is $S = 5/2$. Most transition metals have a $4s^2$ configuration that makes them isovalent in II–VI compounds. We note that Zn has a complete 3d shell and thus no net spin. In Fig. 15.2, an overview of the crystallographic properties is given for Mn-alloyed II–(Se,S,Te,O) based DMS [949] (DMS with Se, S, and Te have been discussed in [950]).

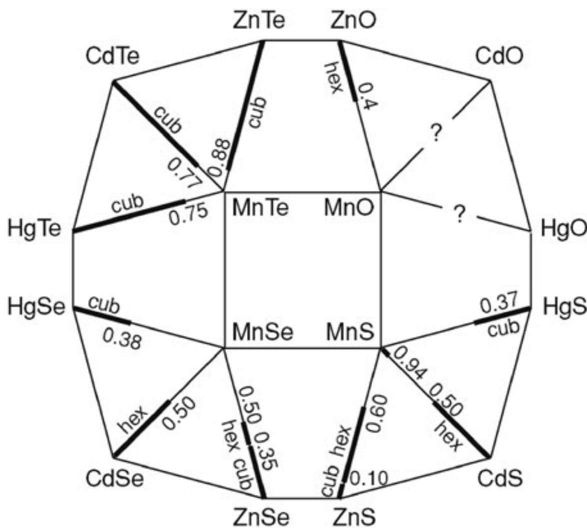

Fig. 15.2. Diagrammatic overview of $A^{II}_{1-x}Mn_xB^{VI}$ alloys and their crystal structures. The *bold lines* indicate ranges of the molar fraction x for which homogeneous crystal phases form. 'Hex' and 'Cub' indicate wurtzite and zincblende, respectively. From [949]

As an example, the properties of $Hg_{1-x}Mn_xTe$ are discussed. This alloy is semiconducting (positive band gap ϵ_0) for $x > 0.075$ and a zero-gap material (negative interaction gap ϵ_0) for smaller Mn concentration (cf. Fig. 6.35). The transitions between the Γ_6 and Γ_8 bands can be determined with magnetoabsorption spectra in the infrared [951]. In Fig. 15.3a, the magnetic field dependence of transition energies between different Landau levels is shown that can be extrapolated to yield the interaction gap. The interaction gap is shown in Fig. 15.3b as a function of the Mn concentration.

For small Mn concentrations, the DMS behaves like a paramagnetic material. For larger concentrations, the Mn atoms have increasing probability to be directly neighbored by another Mn atom and suffer superexchange interaction (cf. Eq. (3.19b)). At a certain critical concentration x_c, the cluster size becomes comparable with the size of the sample. If interaction up to the first, second or third neighbor are taken into account for a fcc lattice, the critical concentrations are given by x_c =0.195, 0.136, and 0.061, respectively [952]. The nearest-neighbor interaction between Mn atoms in such DMS

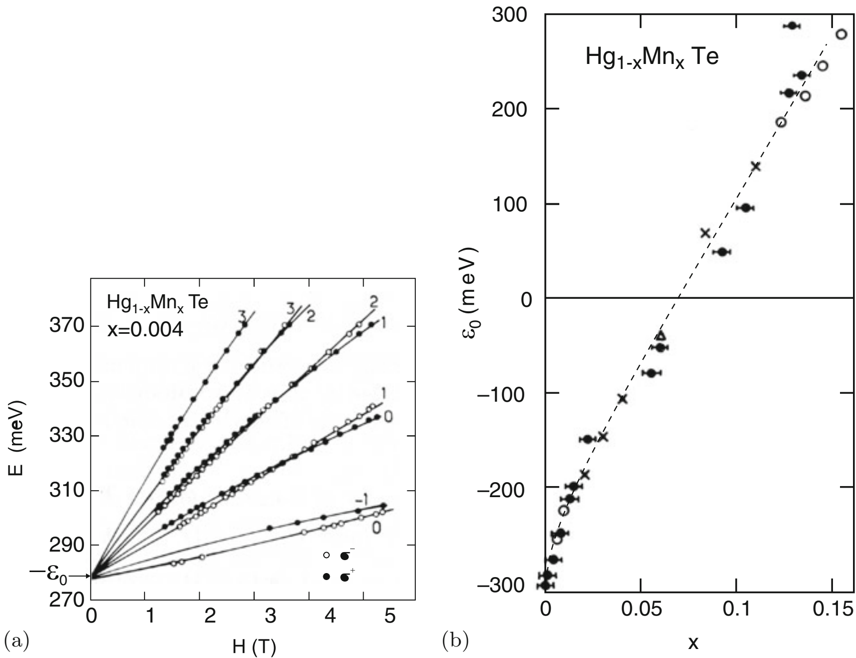

Fig. 15.3. (**a**) Energies of $\Gamma_6 \rightarrow \Gamma_8$ transitions vs. magnetic field for $Hg_{0.996}Mn_{0.004}Te$ at $T = 2$ K. *Symbols* are experimental values for two polarization directions as indicated. Numbers denote quantum numbers of transitions. *Solid lines* are theoretical fits. (**b**) Interaction gap vs. Mn concentration for $Hg_{1-x}Mn_xTe$ at $T = 4.2$ K. Various *symbols* represent data from different authors and methods. *Dashed line* is a guide to the eye. Adapted from [951]

as (Zn,Cd,Hg)Mn(S,Se,Te) was found to be antiferromagnetic,[1] i.e. neighboring spins are aligned antiparallel. Due to frustration of antiferromagnetic long-range order on a fcc lattice, an antiferromagnetic spin glass forms. The transition temperature T_C between the paramagnetic and spin-glass phases of $Hg_{1-x}Mn_xTe$ is shown in Fig. 15.4.

In III–V compounds, the 3d transition metals represent an acceptor if incorporated on the site of the group-III element as, e.g., in the much investigated compound $Ga_{1-x}Mn_xAs$. This material will be used in the following to discuss some properties of magnetic semiconductors. It seems currently well understood and has a fairly high Curie temperature of $T_C \approx 160$ K. Ferromagnetism in a diluted magnetic semiconductor is believed to be caused by indirect exchange through itinerant charge carriers. The ferromagnetic coupling can be invoked by the Ruderman–Kittel–Kasuya–Yoshida (RKKY) interaction, i.e. the spins of the paramagnetic ions are aligned via interaction with the free carriers in the semiconductor. A related concept is the double exchange[2] [953–955] in which carriers move in a narrow Mn-derived d-band (for d-wave character see Fig. 7.16c). Such a mechanism was first invoked for PbSnMnTe [956]. Later, ferromagnetism was discovered in InMnAs [957] and GaMnAs [958]. In (In,Ga)MnAs a Mn ion (spin up) spin polarizes the surrounding hole gas (spin down), which has been supplied from the Mn acceptors. This mechanism lowers the energy of the coupled system. The interaction

$$H = -\beta \, N_0 \, x \, S \, s \tag{15.1}$$

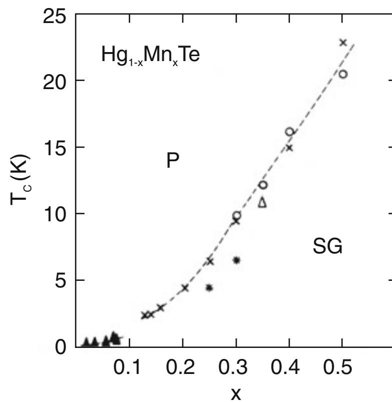

Fig. 15.4. Magnetic phase diagram of $Hg_{1-x}Mn_xTe$, 'P' ('SG') denotes the paramagnetic (spin glass) phase. Various *symbols* represent data from different authors and methods. *Dashed line* is a guide to the eye. Adapted from [951]

[1] Such superexchange leads to antiferromagnetic interaction if the bond angle is 'close' to 180°.

[2] This model is also called the Zener model.

between the Mn d-shell electrons ($S = 5/2$) and the p-like free holes ($s = 1/2$) is facilitated by p–d hybridization of the Mn states. N_0 denotes the concentration of cation sites in the $A_{1-x}Mn_xB$ alloys. The coupling via electrons is much weaker (coupling coefficient α). The holes interact with the next Mn ion and polarize it (spin up), thus leading to ferromagnetic order. The ferromagnetic properties are evident from the hysteresis shown in Fig. 15.6a. Without the carrier gas such interaction is not present and the material is only paramagnetic. Theoretical results for the Curie temperature of various p-type semiconductors are shown in Fig. 15.5. Generally, the quest for higher Curie temperatures (well above room temperature) is underway and wide band gap materials such as GaN or ZnO doped with transition metals have shown some encouraging results. Mn-substituted chalcopyrite semiconductors are analyzed theoretically in [959] and are predicted to exhibit less-stable ferromagnetism than III–V semiconductors of comparable band gap.

The carrier density and thus magnetic properties in a DMS can be controlled in a space-charge region (cf. Sect. 20.2.2) as demonstrated in [960]. In Fig. 15.6, results are shown for hydrogen- (deuterium-) passivated GaMnAs that exhibits ferromagnetism as 'as-grown' thin film. The deuterium is incorporated in similar concentration as the Mn, assumes a back-bond position (forming a H–As–Mn complex) and compensates the hole gas from the Mn (cf. Sect. 7.8). The low-temperature conductivity drops nine orders of magnitude [961]. Such material displays only paramagnetic behavior. An optimal Mn concentration for ferromagnetic $Ga_{1-x}Mn_xAs$ is around $x = 0.05$. For smaller Mn concentrations, the hole density is too small and the Curie

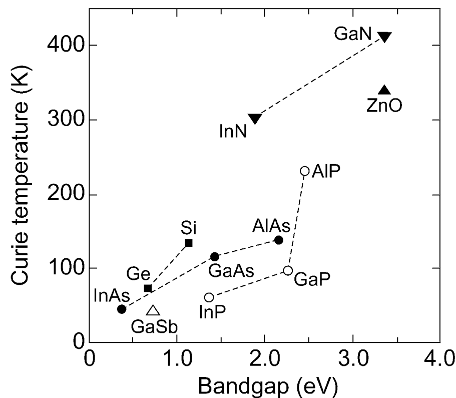

Fig. 15.5. Computed values of the Curie temperature T_C for various p-type semiconductors plotted vs. the band gap (*dashed lines* are guides to the eye). All materials contain 5% Mn on the cation sublattice and a hole concentration of $p = 3.5 \times 10^{20}\,\text{cm}^{-3}$. Values for T_C taken from [955]

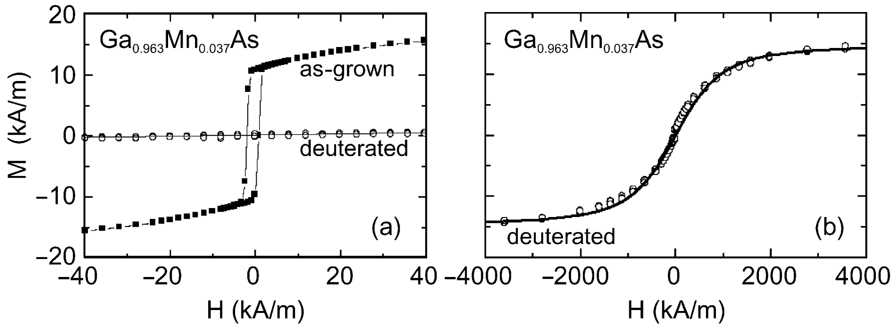

Fig. 15.6. Magnetization M vs. magnetic field H for $Ga_{0.963}Mn_{0.037}As$ at low temperature. (**a**) Comparison of as-grown (*full squares*) and deuterated (*open circles*) thin film with magnetic field in the layer plane at $T = 20\,K$. (**b**) Magnetization of the deuterated sample at $T = 2\,K$ for larger magnetic fields. *Solid line* is Brillouin function for $g = 2$ and $S = 5/2$. Adapted from [961]

temperature drops; for larger Mn concentrations, the structural properties of the alloy degrade (phase separation into GaAs and MnAs.[3])

Magnetic hysteresis has been found in nearly compensated Mn-doped ZnO [962, 963] (Fig. 15.7). Such material is interesting due to its small spin-orbit coupling. The exchange mechanism is under debate.

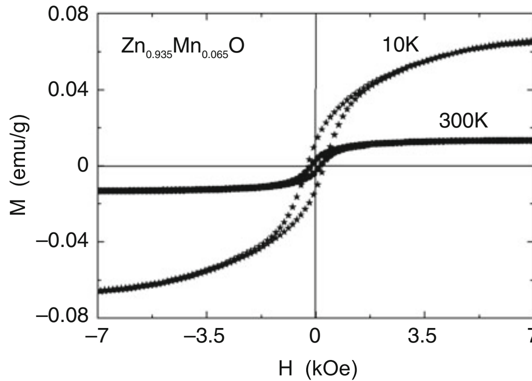

Fig. 15.7. Magnetization M vs. magnetic field H for $Zn_{0.935}Mn_{0.065}O$ thin film at $T = 10$ and $300\,K$. A hysteresis is obvious for both temperatures

[3] MnAs is a ferromagnetic metal. MnAs clusters can be a problem since they create ferromagnetic properties but not in the way the DMS is supposed to work.

15.4 Spintronics

Spintronics (as opposed to electronics) is an emerging field that uses the electron *spin* rather than its *charge* for transport, processing and storage of information. Prototype devices are the spin transistor and the spin LED. A crucial point is spin injection, i.e. the creation of (highly) spin-polarized currents. It remains to be seen whether spintronics can be developed to its theoretically envisioned potential and will play a commercially important role in the course of microelectronics. The spin degree of freedom also promises potential for quantum information processing due to its weak coupling to charge and phonons and the resulting long dephasing time.

15.4.1 Spin Transistor

In this device (for regular transistors cf. Chap. 23), spin-polarized electrons are injected from contact 1, transported through a channel and detected in contact 2 (Fig. 15.8). During the transport, the spin rotates (optimally by π) such that the electrons cannot enter contact 2 that has the same magnetization as contact 1. The spin rotation is caused by spin-orbit interaction due to the electric field under the gate contact. This effect is called the Rashba effect and is purely relativistic [964]. As channel material, a semiconductor with strong spin-orbit coupling such as InAs or (In,Ga)Sb is preferable. However, the use of narrow-gap semiconductors and the increase of spin scattering at elevated temperatures [965] make the realization of such a transistor at room temperature difficult.

15.4.2 Spin LED

In a spin LED (for LEDs see Sect. 22.3), the injection of spin-polarized carriers into the active layer leads to circularly polarized luminescence. The

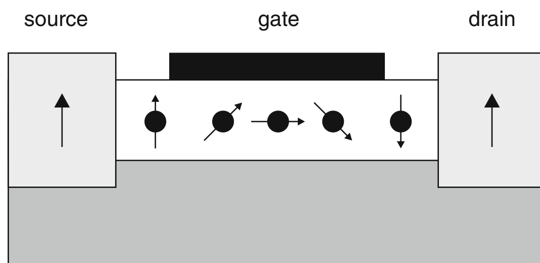

Fig. 15.8. Scheme of spin transistor after the proposal of [966]. Source and drain are ferromagnets with their magnetization shown schematically as arrows. The channel under the gate transports electrons whose spin rotates in the electric field under the gate

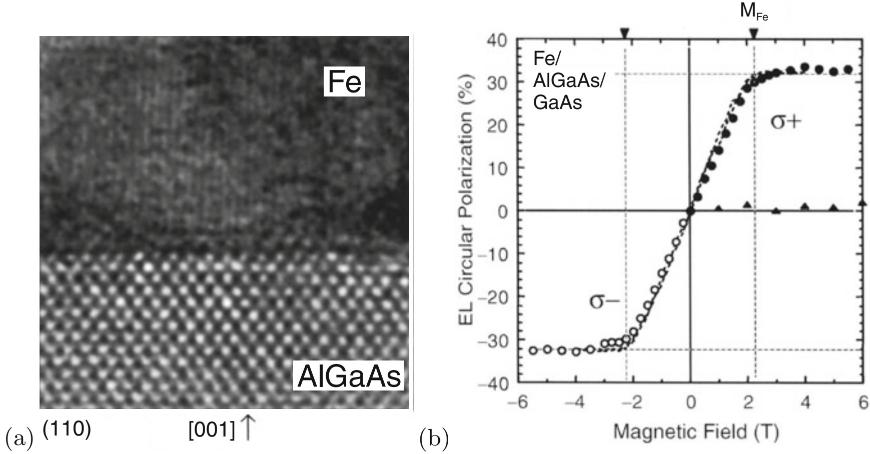

Fig. 15.9. (**a**) Transmission electron microscopy image of the (110) cross section of the Fe/AlGaAs interface of a spin LED. The *vertical lines* in Fe are the (110) planes with 0.203 nm distance. (**b**) Magnetic-field dependence of the circular polarization ratio P_σ at $T = 4.5\,\mathrm{K}$ (15.2) (*filled* and *empty* circles) and the out-of-plane component of the Fe-film magnetization (*dashed line*, scaled to the maximum of P_σ). Reproduced from [968] by permission of the MRS Bulletin

spin alignment can be achieved with semimagnetic semiconductors grown on top of the active layer or via spin injection from a ferromagnetic metal into the semiconductor (for metal–semiconductor junctions cf. Sect. 20.2). In Fig. 15.9a, a Fe/AlGaAs interface is shown.

Ideally, the spin-polarized electrons from the ferromagnetic metal tunnel into the semiconductor and transfer to the recombination region. Subsequently, the emission is circularly polarized (Fig. 11.22b). The degree of circular polarization is

$$P_\sigma = \frac{I_{\sigma+} - I_{\sigma-}}{I_{\sigma+} + I_{\sigma-}} \,, \tag{15.2}$$

with $I_{\sigma\pm}$ being the intensity of the respective polarization. The degree of polarization depends on the magnetization of the metal. For the saturation magnetization of Fe, the maximum polarization is about 30% at $T = 4.5\,\mathrm{K}$ (Fig. 15.9b) [967]. The interface and its structural nonideality of the interface presumably prevent the spin injection from being 100% efficient [968].

16 Organic Semiconductors

Organic semiconductors are based on carbon compounds. The main structural difference from inorganic semiconductors is the bond based on sp^2 hybridization (cf. Sect. 2.2.3) as present in benzene (and graphite). Diamond, although consisting of 100% carbon, is not considered an organic semiconductor. We note that carbon can form further interesting structures based on sp^2 bonds, such as carbon nanotubes (Sect. 17.2), (single or few layer) graphene sheets (Sect. 17.1) rolled up to form cylinders, or fullerenes, e.g. soccer-ball-like molecules such as C_{60}.

In the 1980 Handbook on Semiconductors only a good ten pages were devoted to organic semiconductors [969]. Now several textbooks are available [970, 971] for a much more detailed treatment than given here.

16.1 Materials

16.1.1 Small Organic Molecules, Polymers

The prototype organic molecule is the benzene molecule with its ring-like structure (Fig. 2.8).

There is a large number of organic, semiconducting molecules that differs by the number of benzene rings (Fig. 16.1), the substitution of carbon atoms by nitrogen or sulfur (Fig. 16.2a,b), the polymerization (Fig. 16.2c) or the substitution of hydrogen atoms by side groups (Fig. 16.2d). Since PPV is insoluble, typically derivatives such as MEH-PPV[1] [972] that are soluble in organic solvents are used. Compared to benzene, the substitution of one carbon atom by nitrogen (pyridine) represents doping with one electron. In Fig. 16.3, the most important building blocks of organic molecules are shown.

16.1.2 Organic Semiconductor Crystals

Small organic molecules can crystallize into solids, so-called *organic molecular crystals* (OMC), due to van-der-Waals interaction. In Fig. 16.4a, the monoclinic unit cell of an anthracene crystal [973] is shown as an example.

[1] 2-ethoxy,5-(2'-ethyl-hexyloxy)-1,4-phenylene vinylene

M. Grundmann, *The Physics of Semiconductors*, 2nd ed., Graduate Texts in Physics, DOI 10.1007/978-3-642-13884-3_16,
© Springer-Verlag Berlin Heidelberg 2010

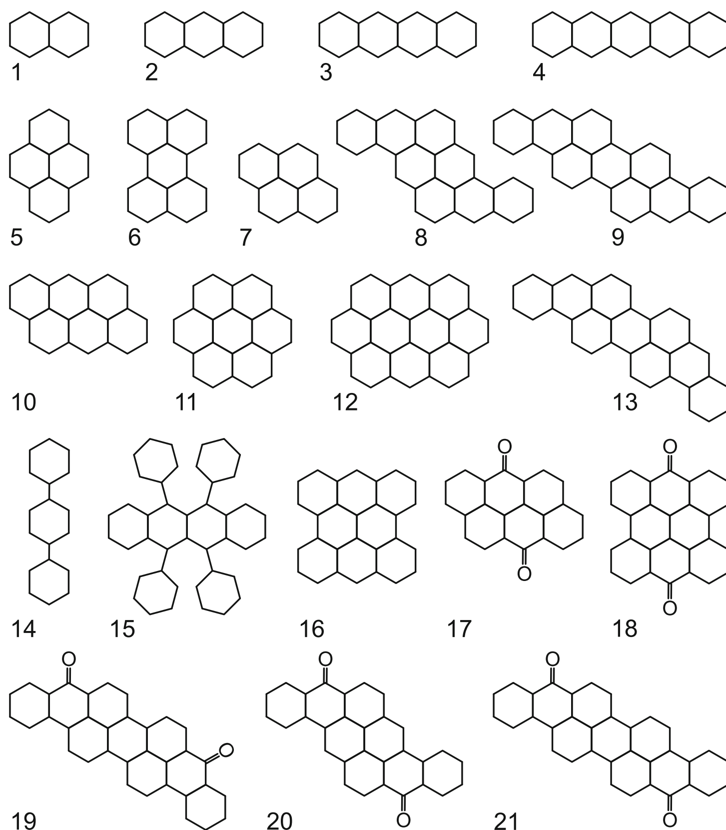

Fig. 16.1. Various organic compounds: 1: naphthalene, 2: anthracene, 3: tetracene, 4: pentacene, 5: pyrene, 6: perylene, 7: chrysene, 8: pyranthrene, 9: isoviolanthrene, 10: anthanthrene, 11: coronene, 12: ovalene, 13: violanthrene, 14: p-terphenyl, 15: rubrene, 16: m-dinaphthanthrene, 17: anthanthrone, 18: m-dinaphthanthrone, 19: violanthrone, 20: pyranthrone, 21: isoviolanthrone

Also tetracene and pentacene (Fig. 16.4b) have this layered 'herringbone' structure. A comparison of the unit cells of oligoacene crystals is given in Table 16.1.

Crystal growth of single crystal OMC is achieved with a variety of methods, among them sublimation, Bridgman- and Czochralski-type methods [974, 975], vapor phase growth [976, 977] or from solution [978, 979]. Single organic molecular crystals exhibit intrinsic material properties. The practical use of organic semiconductors involves thin films, e.g. in LEDs (OLED, Sect. 22.3.7) and transistors (OFET, Sect. 23.6.3). Thin films of organic molecules are typically disordered and their performance parameters are inferior to that of OMCs.

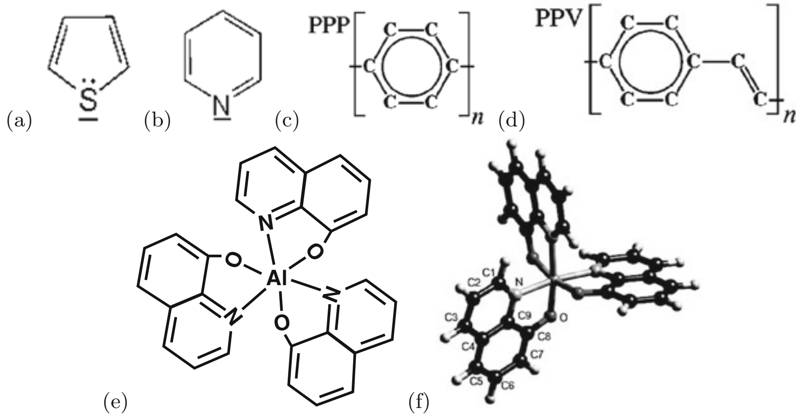

Fig. 16.2. Organic compounds: (**a**) thiophene, (**b**) pyridine, (**c**) poly-(p-phenyl), (**d**) poly-(p-phenylvinyl), (**e**) Alq_3 (tris-(8-hydroxyquinolate)-aluminum) and (**f**) a three-dimensional view of the Alq_3 molecule. Part (**f**) reprinted with permission from [980], ©1998 AIP

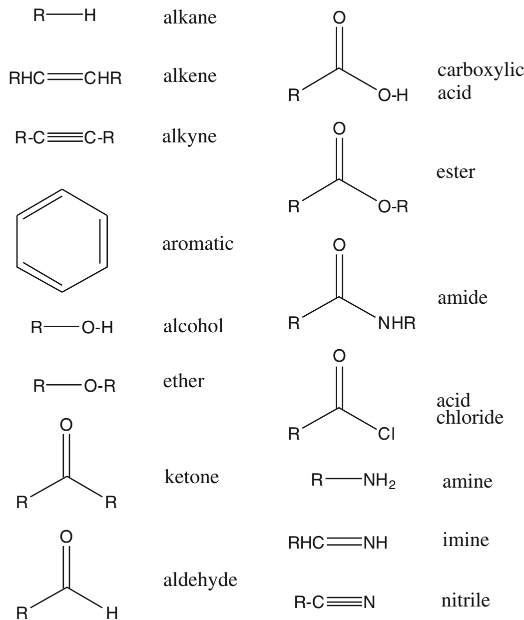

Fig. 16.3. Building blocks of organic molecules, 'R'=alkyl group, i.e. CH_3 (methyl-), CH_3CH_2 (buthyl-), ...

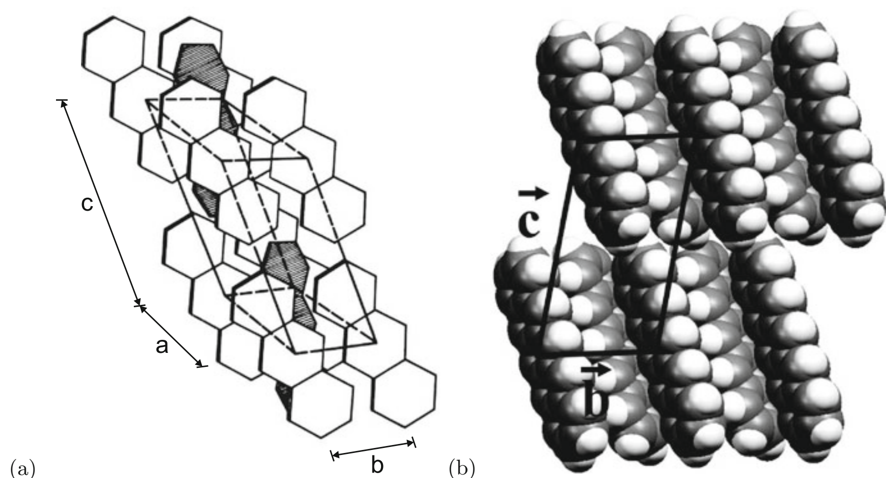

Fig. 16.4. (a) Monoclinic unit cell (for size see Table 16.1) of anthracene crystal. (b) Two herringbone layers of pentacene in a projection onto the bc plane of the triclinic unit cell. Adapted from [982]

Table 16.1. Properties of oligoacene crystals. Melting point and unit cell parameters. Data from [983]

property	naphthalene	anthracene	tetracene	pentacene
melting point (°C)	80	217	357	> 300°C
crystal system	monoclinic	monoclinic	triclinic	triclinic
a (nm)	0.824	0.856	0.798	0.793
b (nm)	0.600	0.604	0.614	0.614
c (nm)	0.866	1.116	1.357	1.603
α (°)	90	90	101.3	101.9
β (°)	122.9	124.7	113.2	112.6
γ (°)	90	90	87.5	85.8

16.2 Electronic Structure

The p_z orbitals in benzene are partially filled and there is an energy gap between HOMO and LUMO (Fig. 2.11). A similar consideration is valid for polymers. The coupling of orbitals along the polymer chain leads to broadening of the π and π^* states into a (filled) valence and an (empty) conduction band, respectively (Fig. 16.5). The HOMO and LUMO positions of various organic semiconductors are shown in Fig. 16.6 relative to the vacuum level (cmp. Fig. 11.14 for inorganic semiconductors). The HOMO is also known

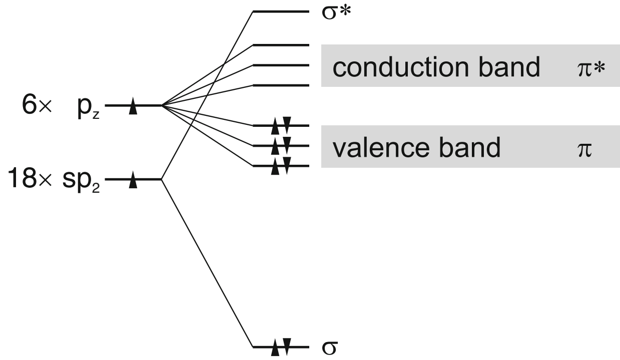

Fig. 16.5. Schematic band structure of a polymer originating from the states of the benzene molecule (see Fig. 2.11)

as *ionization energy* (IE), the LUMO as *electron affinity* (EA). With layered organic semiconductors heterostructures can be built, e.g. to design recombination pathways (recombination layer, electron blocking layers (EBL) and hole blocking layers (HBL)). For electron injection and electron extraction (hole injection) contacts, metals with appropriate work function (in connection with a possible interface dipole layer) have to be used. More details on injection and extraction contacts to organic semiconductors are discussed in Sect. 20.2.7.

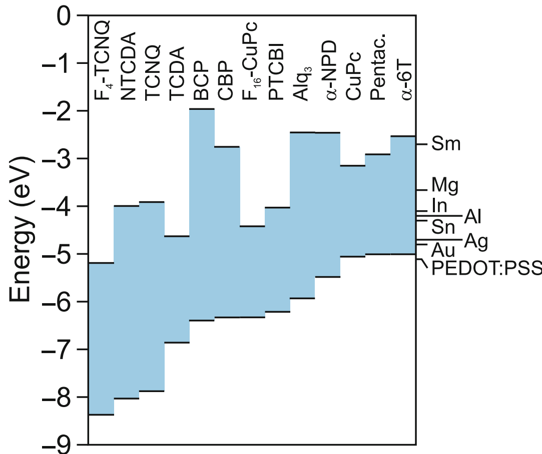

Fig. 16.6. Position of HOMO and LUMO for a variety of organic semiconductors (relative to a common vacuum level at $E = 0\,\mathrm{eV}$). Based on values from [983]. On the right hand side the work functions of several metals are shown for comparison

16.3 Doping

The doping of organic semiconductors can be achieved by

- partial oxidation or reduction of the organic molecule,
- substitution of atoms in the organic molecule,
- mixing of the matrix with 'dopant' molecules.

The systematic shift of the Fermi level with dopant concentration has been reported in [985]. Typically, the conductivity increases superlinearly with the doping concentration (Fig. 16.7a), an effect discussed in detail in [986]. While the mobility remains constant, the thermal activation energy E_a for carriers decreases with increasing doping (Fig. 16.7b) due to electrostatic interaction [421, 987], an effect already discussed in Sect. 7.5.6. The activation energy in the dilute limit $E_{a,0}$ is modified to (cmp. (7.58))

$$E_a = E_{a,0} - \beta N_D^{1/3} . \tag{16.1}$$

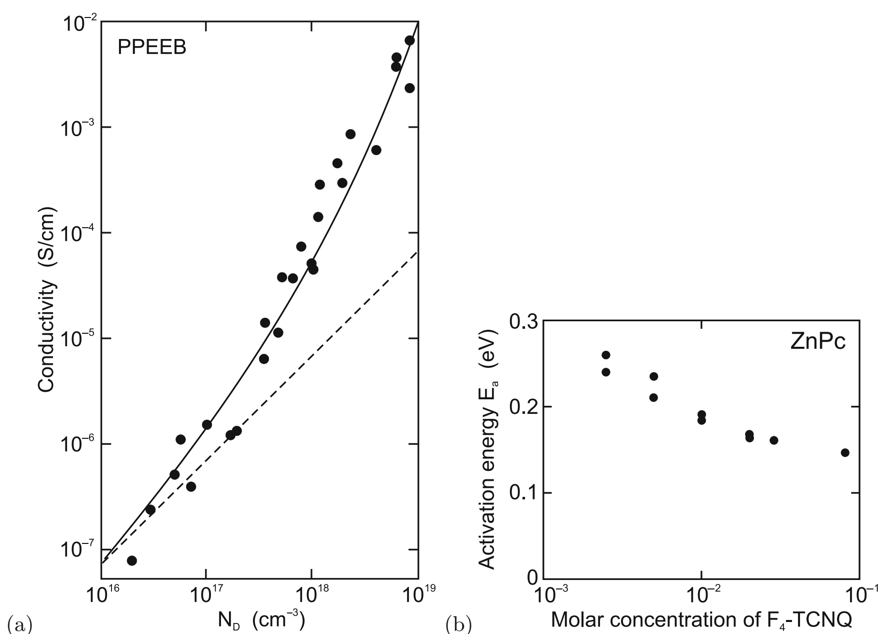

Fig. 16.7. (**a**) Conductivity (at 0.9 V/µm) vs. dopant concentration N_D for PPEEB films. Experimental data (*circles*) and fit (*solid line*) according to (16.1) with activation energy $E_{a,0} = 0.23$ eV and $\beta = 6.5 \times 10^{-8}$ eV cm ($\mu = 0.2\,cm^2/Vs$). *Dashed line* denotes linear relation between conductivity and N_D. Adapted from [984]. (**b**) Thermal activation energy E_a of carriers (holes) in ZnPc:F_4-TCNQ as a function of the molar dopant concentration. Adapted from [985]

16.4 Transport Properties

Transport in organic semiconductors is characterized by

- strong polaronic effects,
- hopping conduction,
- low mobility, low drift saturation velocity.

The interaction of charges with lattice deformations leads to the formation of polarons [988]. In organic materials these are often 'small', i.e. the extension of the deformation is on atomic scale. Such self-trapping of charges reduces their mobility. Two charges can share the same deformation (bipolaron) or oppositely charged polarons can attract (similar to an exciton). If these charges are on the same (neighboring) polymer chain, the polaron is called intrachain (interchain).

The conductivity within a molecule, e.g. a long polymer chain, and the conductivity between different molecules have to be distinguished. The conduction between different molecules occurs via *hopping*. Typically, the conductivity is thermally activated according to

$$\sigma = \sigma_0 \exp\left(-\frac{E_\mathrm{a}}{kT}\right) , \tag{16.2}$$

where E_a is an energy of the order of 1 eV. Such activation also pertains to the mobility alone, e.g. $E_\mathrm{a} = 0.48\,\mathrm{eV}$ for PPV [989].

The maximum low-field mobility of many crystalline organic semiconductors at room temperature is around $1\,\mathrm{cm}^2/\mathrm{Vs}$ with a weak temperature dependence [990]. Such mobility is much smaller than that of crystalline silicon AND rather comparable to that of amorphous silicon. Improved purity and handling of organic semiconductors has allowed to achieve intrinsic material properties (Fig. 16.8). The mobility increases at low temperatures, e.g. below 100 K in naphthalene [991]. This has been attributed to the freeze-out of phonons and the transition from hopping to band transport. The drift velocity at higher fields shows saturation but the values, even at low temperature, are much smaller than in silicon (Fig. 16.9). An analytical model for the described main features of transport in organic semiconductors has been given in [992].

16.5 Optical Properties

Organic molecules can emit light efficiently and are thus useful for light emitters. For the photo-physics of organic materials it is essential to recall the molecular physics of singlet and triplet states. In the singlet (triplet) state, the total spin quantum number of the unpaired electrons is $S = 0$ ($S = 1$). A simple energy scheme includes a ground state S_0 and excited singlet (S_1)

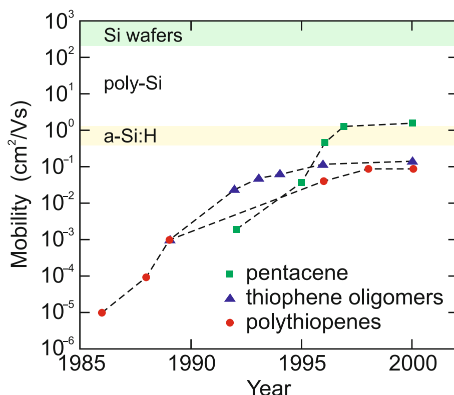

Fig. 16.8. Historic development of the experimentally achieved mobility of organic semiconductors at room temperature

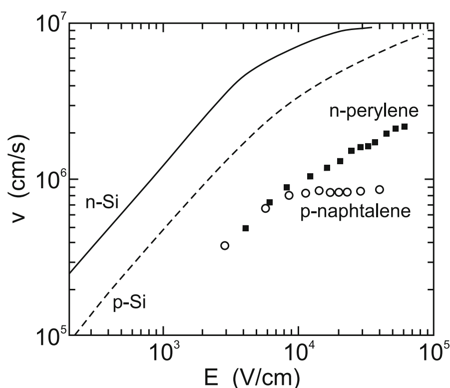

Fig. 16.9. Carrier velocity in ultrapure and highly perfect single crystals of (n-conducting) perylene at $T = 30\,\mathrm{K}$ and (p-conducting) naphthalene at $T = 4.3\,\mathrm{K}$. For comparison electron (hole) velocity in silicon at room temperature is shown as *solid* (*dashed*) line. Adapted from [975]

and triplet (T_1) states. The recombination transition $\mathrm{S}_1 \rightarrow \mathrm{S}_0$ is allowed and its lifetime short. Such luminescence is termed 'fluorescence'. Recombination from the triplet state is forbidden or at least very slow ('phosphorescence').

As an example for a small organic molecule, the fluorescence lifetime of Alq_3 is about 12 ns [993]. The triplet lifetime is in the 10 µs range [994]. Luminescence and absorption spectra of Alq_3 are shown in Fig. 16.10. The luminescence peak is redshifted with respect to the absorption edge due to the Frank-Condon principle (Fig. 10.20). The density of excited (empty) states of the Alq_3 molecule is shown in Fig. 16.11 together with the orbitals associated with the four prominent states. The lowest orbital is the LUMO and leads to the visible luminescence of the Alq_3 in the red.

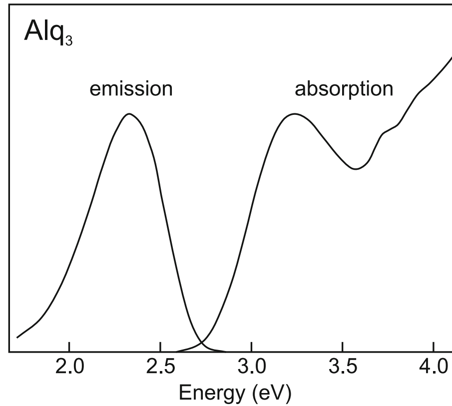

Fig. 16.10. Luminescence and absorption spectra of Alq_3 (vapor-deposited 150 nm thin film on a quartz substrate) at room temperature. Adapted from [995]

In Fig. 16.12a, the photoluminescence (PL) and absorption of a polymer, poly-thiophene are shown. The recombination is below the band gap of 2.1–2.3 eV on an excitonic level at 1.95 eV. There are several phonon replica whose separation of 180 meV corresponds to the C–C stretching mode. The PL excitation (PLE) spectrum of poly-thiophene demonstrates that the PL at 1.83 eV can be excited via the exciton level. The theoretical band structure of poly-thiophene is shown in Fig. 16.13a. The Brillouin zone is one-dimensional. The situation I corresponds to a single molecular chain, the situation II pertains to the chain embedded in a medium with a dielectric constant $\epsilon = 3$. The predicted band gaps are 3.6 eV and 2.5 eV, respectively. The exciton binding energy is about 0.5 eV. The exciton is a Frenkel exciton that has

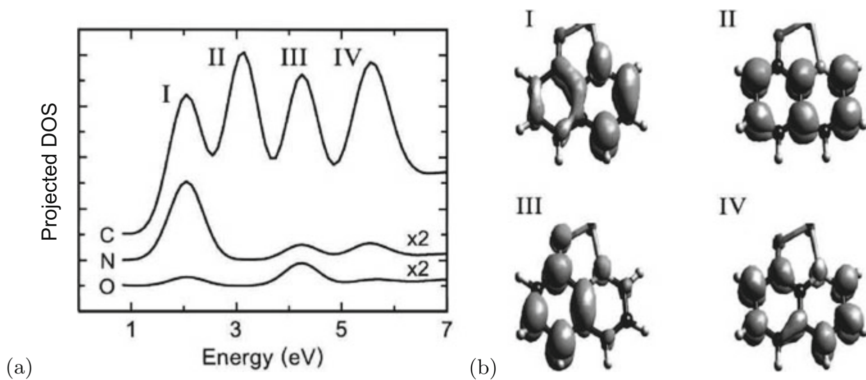

Fig. 16.11. (**a**) Projected density of states (for C, N, and O) of excited states in an Alq_3 molecule. The origin of the energy axis is the HOMO level. (**b**) Orbitals for the four states labeled I–IV in (**a**). Reprinted with permission from [980], ©1998 AIP

a small extension and is localized. The high binding energy is favorable for radiative recombination since the exciton is stable at room temperature. For photovoltaic applications, it is unfavorable since it has to be overcome in order to separate electrons and holes (after absorption). Generally, intrachain excitons (as here) and interchain excitons, where electron and the hole are localized on different chains, are distinguished.

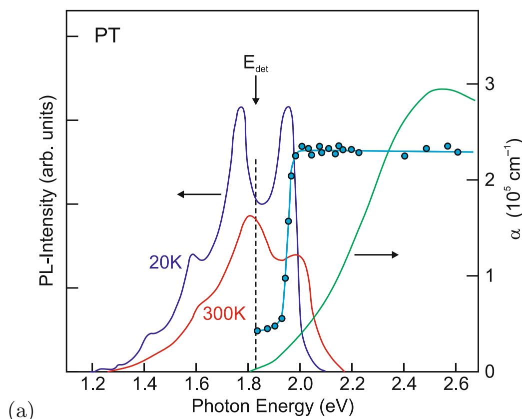

Fig. 16.12. Photoluminescence (PL) spectra at $T = 20$ and 300 K and absorption spectrum (*green line*) of poly-thiophene. The *vertical dashed line* denotes the detection energy ($E_{\mathrm{det}} = 1.83\,\mathrm{eV}$) of the PL excitation (PLE) spectrum (*blue circles*) ($T = 20\,\mathrm{K}$). Adapted from [996]

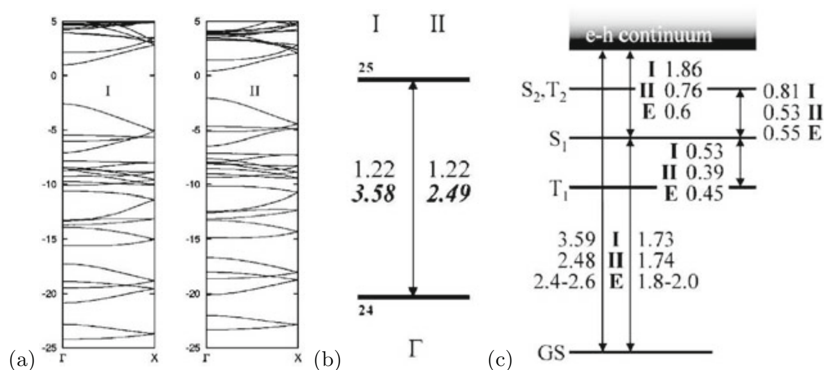

Fig. 16.13. (**a**) Band structure of poly-thiophene ('I': naked chain, 'II': chain in a dielectric medium ($\epsilon = 3$)), (**b**) single-particle energies and band gap, (**c**) exciton levels ('E': experimental values). Reprinted with permission from [997], ©2002 APS

Collection of carriers in the 'dark' triplet state poses a problem limiting the quantum efficiency to 25% in a simple model [998]. Harvesting luminescence from *all* exciton states would yield significantly higher efficiencies than is possible in purely fluorescent materials (or devices).

A successful route is the use of a phosphorescent guest material. Radiative transitions from triplet states become partially allowed when the excited singlet and triplet states are mixed. This is typically achieved in metalorganic molecules with heavy metal atoms, providing large spin-orbit interaction effects [1001, 1002]. Most prominently Ru-, Pt- and Ir-containing compounds are used, e.g. *fac* tris(2-phenylpyridine) iridium [$Ir(ppy)_3$] in 4,4'-N,N'-dicarbazole-biphenyl [CBP] (Fig. 16.14a,b) [1000]. The luminescence spectrum of $Ir(ppy)_3$ is shown in Fig. 16.14d. The radiative decay constant of the $Ir(ppy)_3$ triplet state is about 800 ns and observable if energy transfer from the host triplet state is exotherm ($\Delta G = G_{\mathrm{G}} - G_{\mathrm{H}} < 0$ [994], see Fig. 16.15a) and fast. This is the case for CBP:$Ir(ppy)_3$ (Fig. 16.15b), $\Delta G \approx -0.2$ eV. Actually, reverse transfer from $Ir(ppy)_3$ to CBP seems responsible for some loss in luminescence efficiency and the decrease in phosphorescent lifetime from 800 ns to 400 ns. In the case of N,N'-diphenyl-N,N'-bis(3-methylphenyl)-[1,1'-biphenyl]-4,4'-diamine [TDP] (Fig. 16.14c) host, the triplet energy transfer to the phosphorent $Ir(ppy)_3$ guest is endotherm ($\Delta G \approx +0.1$ eV) and represents the rate limiting step [994]. In this case the

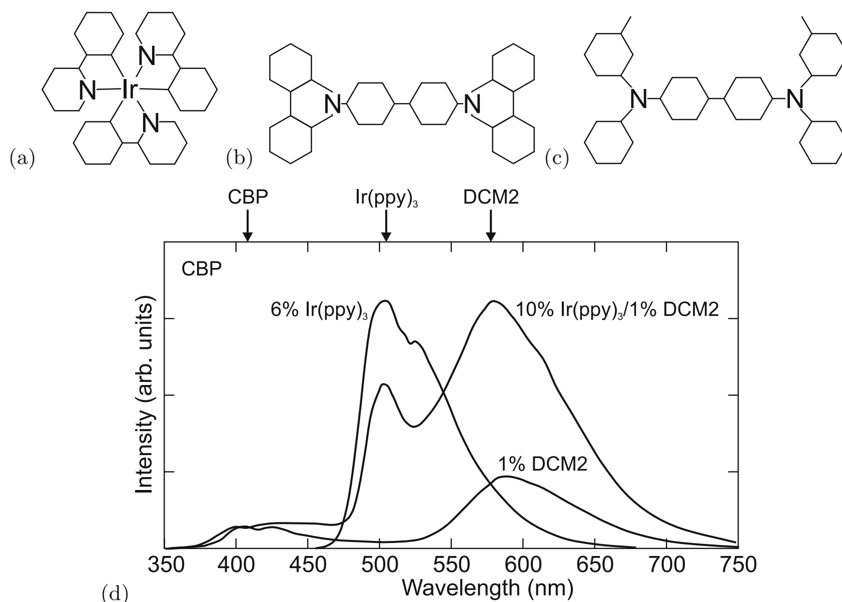

Fig. 16.14. Molecular structure of (**a**) $Ir(ppy)_3$, (**b**) CBP and (**c**) TDP (see text). (**d**) Electroluminescence spectra (at room temperature) of CBP:6% $Ir(ppy)_3$, CBP:10% $Ir(ppy)_3$/1%DCM2 and CBP:2%DCM2. Based on data from [999, 1000]

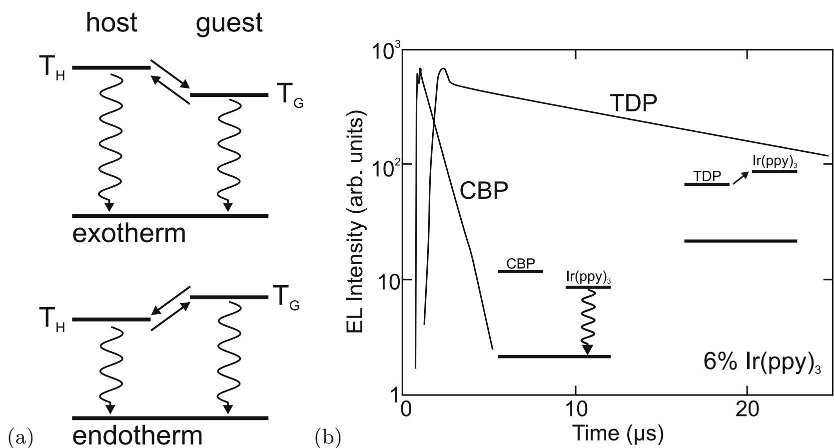

Fig. 16.15. (**a**) Schematic term diagram of host (T_H) and guest (T_G) triplet states. *Straight arrows* denote energy transfer between triplet states, *wiggly arrows* denote radiative transitions to the (singlet) ground state. (**b**) Electroluminescence transients (at room temperature, detected in the range 500–560 nm [cmp. Fig. 16.14b]) of CBP:6% Ir(ppy)$_3$ ($\tau \approx 1\,\mu$s) and TDP:6% Ir(ppy)$_3$ ($\tau \approx 15\,\mu$s). *Insets*: term schemes with arrow denoting the rate limiting step. Based on data from [994]

recombination of Ir(ppy)$_3$ has a decay constant of about 15 µs (Fig. 16.15b). The thermal activation character is confirmed by even longer decay times at low temperatures ($\tau \approx 80\,\mu$s at $T = 200\,$K) [994]. Endothermic transfer allows to pump a blue guest phosphor without a blue host material.

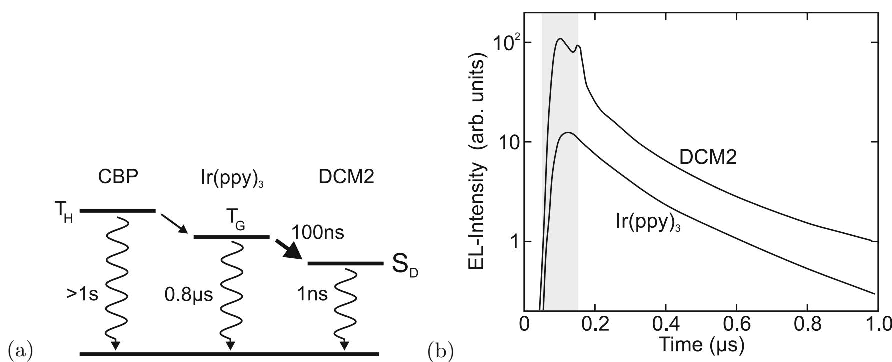

Fig. 16.16. (**a**) Schematic term scheme of CBP:Ir(ppy)$_3$/DCM2 and energy transfer and recombination paths (cmp. spectrum in Fig. 16.14). The rate constants are shown for various processes, the rate limiting step is shown with a *bold arrow*. (**b**) Electroluminescence transients after 100 ns excitation pulse (*grey area*) of Ir(ppy)$_3$ and DCM2 luminescence from CBP:10% Ir(ppy)$_3$/1% DCM2. Based on data from [999]

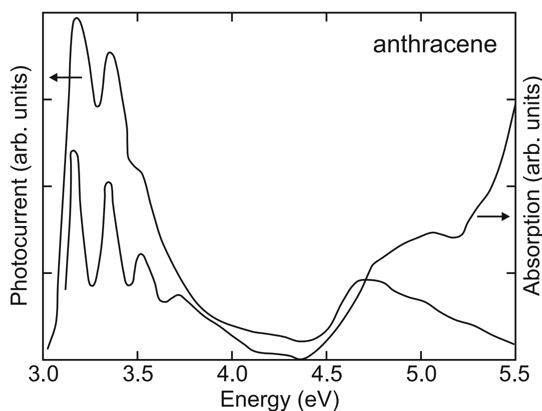

Fig. 16.17. Photoconductivity and absorption spectrum of anthracene

Further, subsequent Förster energy transfer [1003] from the guest triplet state to a fast and efficient singlet state (S_D) of a fluorescent dye is possible, e.g. from CBP:Ir(ppy)$_3$ to DCM2 [999]. The transient lifetime of pure DCM2 is about 1 ns. In a mixture of CBP:10% Ir(ppy)$_3$/1% DCM2 the luminescence of DCM2 appears with the same 100 ns decay constant as that of Ir(ppy)$_3$ (Fig. 16.16b). This decay constant (rate limiting step, see Fig. 16.16a) corresponds to the energy transfer depleting the triplet state of Ir(ppy)$_3$ to DCM2 and is much faster than the pure Ir(ppy)$_3$ radiative lifetime.

The photoconductivity of organic semiconductors is typically related to their absorption spectrum as shown for anthracene in Fig. 16.17.

17 Graphene and Carbon Nanotubes

17.1 Graphene

17.1.1 Structure

Graphene is a single sheet of carbon atoms in hexagonal arrangement. The carbon bond length is $d_{\mathrm{C-C}} = 0.142\,\mathrm{nm}$ (Fig. 17.1). It can be prepared from graphite via micromechanical cleavage, i.e. mechanical exfoliation (repeated peeling) of small mesas of highly oriented pyrolytic graphite [1004, 1005]. Graphite is a stacked arrangement of such graphene sheets (Fig. 17.2a) held together by van-der-Waals forces as shown in Fig. 17.2b. The carbon atoms bond in-plane via sp^2 hybridization. Organic molecules such as, e.g., anthracene or coronene (Fig. 16.1) can be understood as molecular-size pieces of such two-dimensional graphene sheet with hydrogen saturating the outside, broken bonds. In literature single layer graphene sheets (SLG) and few-layer graphene (FLG) sheets are distinguished. Ideally such two-dimensional crystal is infinitely extended, e.g. for band structure calculations. Real crystals have a boundary (surface) which is topologically a line or very thin sidewall. The mechanical properties of graphene are discussed in [1006].

The phonon dispersion of graphene is shown in Fig. 17.3. For the ZA and ZO modes the displacement is perpendicular to the graphene plane (out-of plane modes).

17.1.2 Band Structure

A single layer of graphene is a zero-gap semiconductor (cf. Fig. 6.35) which shows a linear photon-like spectrum

$$E = \hbar\, k\, c_* \tag{17.1}$$

around the Fermi energy at the K point (Fig. 17.4a). This point is also called Dirac point. The important bands close to the Fermi level stem from the π-orbitals. The linear dispersion around the K point is similar to that of relativistic particles without rest mass. The electrons in graphene are of course not really massless, their velocity (6.34) being $v = c_* \approx 10^6\,\mathrm{m/s}$, about 300 times smaller than the speed of light [1007, 1008].

M. Grundmann, *The Physics of Semiconductors*, 2nd ed., Graduate Texts in Physics, DOI 10.1007/978-3-642-13884-3_17,
© Springer-Verlag Berlin Heidelberg 2010

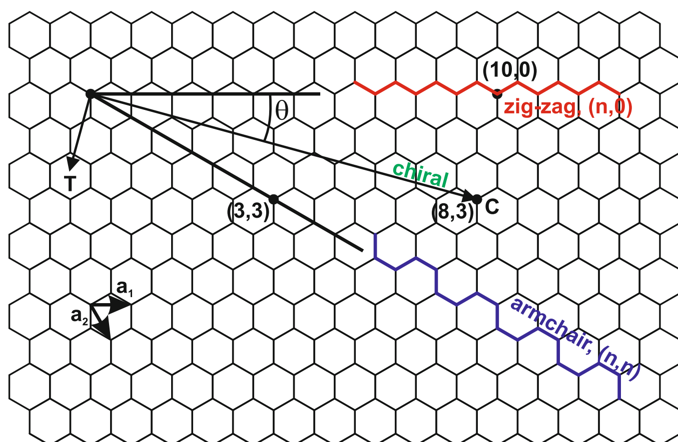

Fig. 17.1. Schematic atomic arrangement in graphene; the C–C bond length is $d_{\mathrm{C-C}} = 0.142\,\mathrm{nm}$. Several vectors for making carbon nanotubes (cf. Sect. 17.2) are shown

In the simplest tight-binding approximation, the band structure is given as

$$E(\mathbf{k}) = \pm T \sqrt{1 + 4\cos\left(\frac{\sqrt{3}ak_y}{2}\right)\cos\left(\frac{ak_x}{2}\right) + 4\cos^2\left(\frac{ak_x}{2}\right)}\,, \qquad (17.2)$$

where a is the lattice constant and $T \approx 3\,\mathrm{eV}$ is the next-neighbor hopping energy [1010]. In the meantime more elaborate tight-binding schemes have

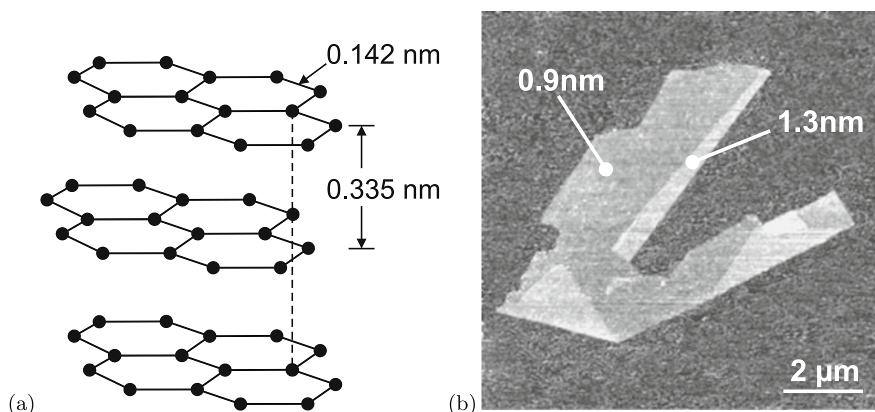

Fig. 17.2. (**a**) Schematic layer structure of graphite with bond length and layer distance labelled. (**b**) AFM image of graphene on oxidized silicon. The height of two areas relative to the background is labelled. Adapted from [1009]

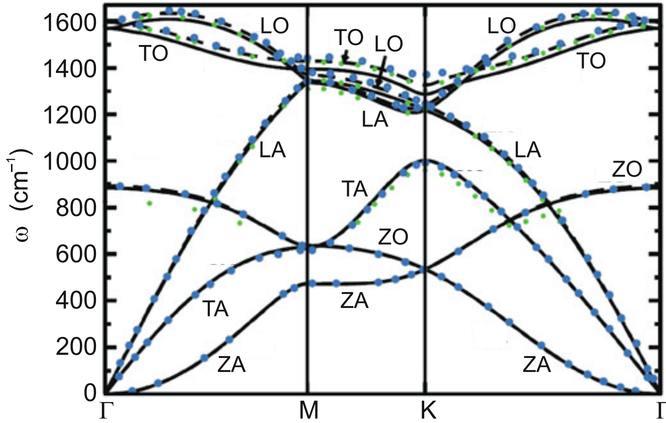

Fig. 17.3. Phonon dispersion in graphene. *Symbols* are experimental data from various methods. *Dashed lines* is DFT-LDA theory, *solid lines* GGA. Adapted from [1013]

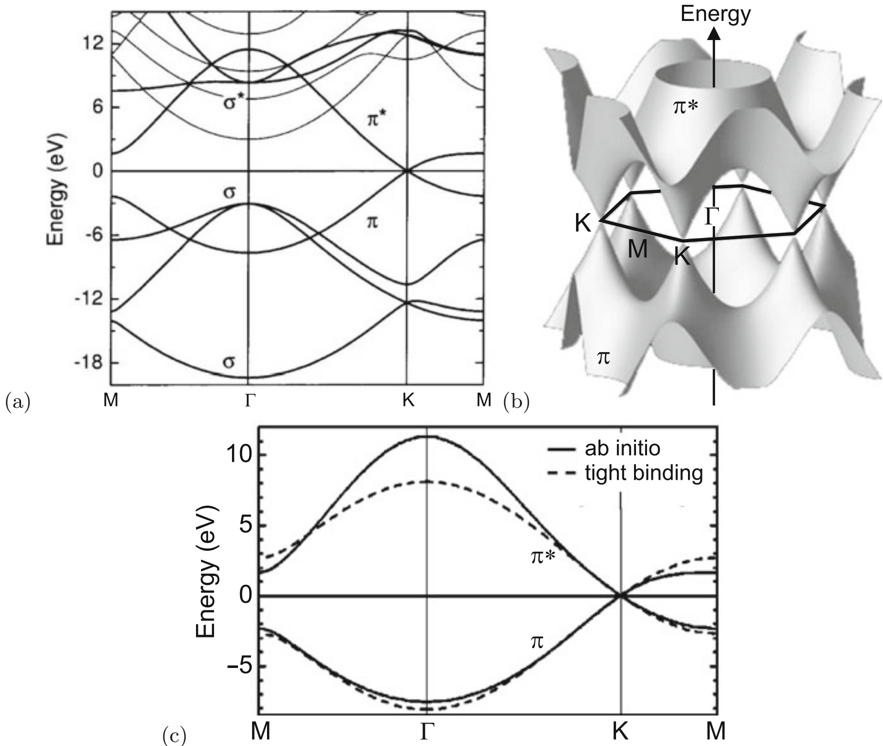

Fig. 17.4. (**a**) Band structure of graphene from first principles. (**b**) Three-dimensional representation $E(k_x, k_y)$ of the π-bands of graphene. (**c**) Band structure of graphene with only π-bands shown, *solid* lines are ab-initio calculation, *dashed lines* are calculated with tight-binding approximation. Adapted from [1012]

been reported [1011, 1012] as shown in Fig. 17.4b. The two-dimensional band structure is visualized in Fig. 17.4c. Such band structure has been directly confirmed experimentally [1014] as shown in Fig. 17.5a–e. The distortion of the band structure with increasing electron concentration (Fig. 17.5e–h) from the conical bands is due to strong electron-electron, electron-phonon, and electron-plasmon coupling effects [1014].

The band structure of FLG has been theoretically analysed in [1015]. For bilayers experimental data on the band structure can be found in [1016]. Subtle differences exist for different stacking orders of the graphene sheets. Bulk graphite shows a semimetallic behavior with a band overlap of about 41 meV. For more than ten graphene layers the difference with the band overlap in bulk graphite is less than 10%.

17.1.3 Electrical Properties

The Shubnikov-de Haas (SdH) oscillations from a graphene sheet exhibit a behavior [1008]

$$\frac{1}{\Delta B} = \frac{4e}{h} \frac{1}{n_{\rm S}} , \tag{17.3}$$

which corresponds to (12.22) for a two-dimensional electron system and a spin- and valley-degeneracy[1] of two. The cyclotron mass has been determined from the temperature dependence of the SdH oscillations to be proportional[2] to $\sqrt{n}$ (Fig. 17.6). The cyclotron mass is generally related [1017] to the area $S(E) = \pi k^2$ in k-space of the orbits at the Fermi energy via

$$m_{\rm c} = \frac{\hbar^2}{2\pi} \frac{\partial S(E)}{\partial E} \tag{17.4}$$

With the linear dispersion (17.1) we can write (17.4) as

$$m_{\rm c} = \frac{\hbar^2}{2\pi} \frac{2\pi E}{\hbar^2 c_*^2} = \frac{E}{c_*^2} . \tag{17.5}$$

For the linear energy dispersion (17.1) the number of states up to energy $E_{\rm F}$ is (with a degeneracy of 4)

$$N(E_{\rm F}) = 4 \frac{\pi k_{\rm F}^2}{(2\pi/L)^2} = A \frac{4\pi E_{\rm F}^2}{h^2 c_*^2} , \tag{17.6}$$

where A is the system area. Therefore we have (at low temperature) with (17.5)

$$n_{\rm S} = \frac{4\pi}{h^2} \frac{E_{\rm F}^2}{c_*^2} \propto m_{\rm c}^2 , \tag{17.7}$$

[1] Each of the six valleys at the K points is shared by three Brillouin zones.

[2] In a parabolic dispersion as in (12.21), the cyclotron mass is independent of n.

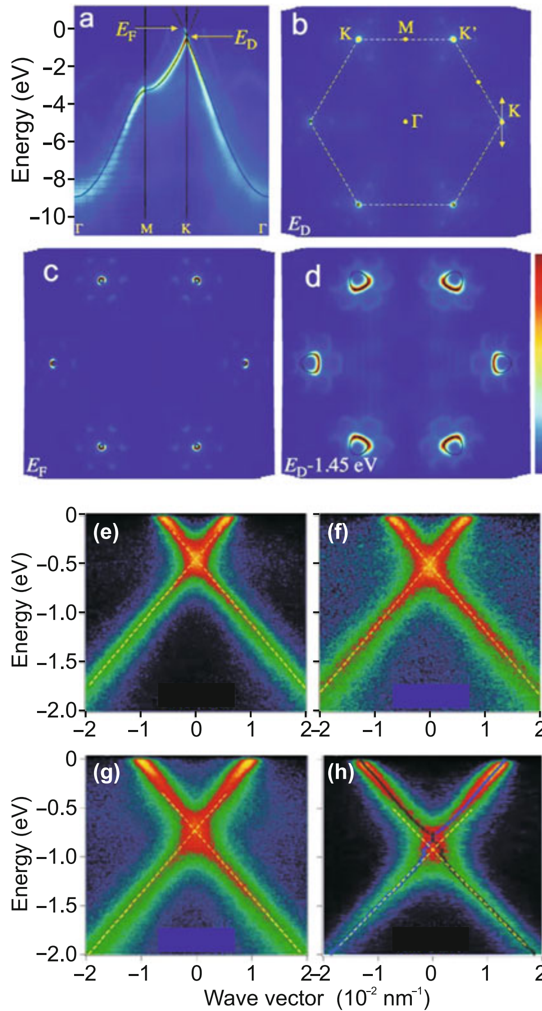

Fig. 17.5. Experimental bandstructure of graphene (on (0001) 6H-SiC) as determined from ARPES. (**a**) Energy distribution of states as a function of momentum along principal directions in the Brillouin zone. The single-orbital tight-binding model (17.2) with $T = 2.82\,\mathrm{eV}$ is shown as *solid lines*. The Fermi level is shifted by $0.435\,\mathrm{eV}$ due to doping. (**b**) Constant energy map of the states at binding energy corresponding to the Dirac energy E_D; the boundary of the Brillouin Zone boundary is superimposed as *dashed line*. The arrow at the K point indicates the directions over which the data in (**e**–**h**) were acquired. (**c**, **d**) Constant energy maps at the Fermi energy ($E_\mathrm{F} = E_\mathrm{D} + 0.45\,\mathrm{eV}$) and $E_\mathrm{D} - 1.5\,\mathrm{eV}$, respectively. (**e**–**h**) Experimental energy bands along the line through the K point parallel to Γ–M direction as indicated in (**b**). The *dashed lines* are an extrapolation of the lower bands below the Dirac crossing energy, which are observed not to pass through the upper bands (above E_D), suggesting the kinked shape of the bands around E_D. The sheet electron density is $n_\mathrm{S} = 1.1$, 1.5, 3.7, and $5.6 \times 10^{13}\,\mathrm{cm}^{-2}$ for (**e**)–(**h**), respectively, due to increased doping upon potassium adsorption. Adapted from [1014]

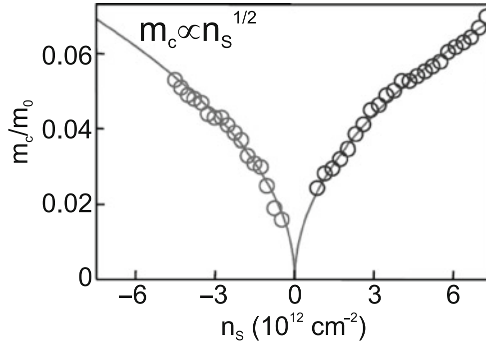

Fig. 17.6. Cyclotron mass in graphene as a function of the sheet electron concentration n_S (negative values relate to hole concentration, $E_\mathrm{F} < E_\mathrm{D}$). Adapted from [1008]

as determined experimentally. Therefore the behavior of the SdH oscillations confirms the linear dispersion relation. The experimental value for the velocity is $c_* \approx 10^6$ m/s. From (17.7) the density of states (per area and energy) around the Dirac point increases linearly with energy,

$$D(E) = \frac{8\pi}{h^2\,c_*^2}\,E\;. \tag{17.8}$$

The carrier density in a graphene sheet can be controlled via the field effect. The graphene is positioned on an insulator/semiconductor structure, typically SiO_2/Si (cf. Sect. 20.3). The carrier density is then related to the applied (gate) voltage V_g via (20.73) and (20.75), i.e.

$$n_\mathrm{S} = \frac{\epsilon_\mathrm{i}\,V_\mathrm{g}}{e\,d}\;, \tag{17.9}$$

where d is the thickness of the insulator and ϵ_i its dielectric constant. By applying positive (negative) bias electron (holes) can be induced in the sheet. The electron and hole densities depend on the Fermi energies[3]

$$n_\mathrm{S} = \frac{8\pi}{h^2\,c_*^2}\int_{E_\mathrm{D}}^{\infty} \frac{E-E_\mathrm{D}}{1+\exp\left[(E-E_\mathrm{F})/kT\right]}\,\mathrm{d}E \tag{17.10a}$$

$$p_\mathrm{S} = \frac{8\pi}{h^2\,c_*^2}\int_{-\infty}^{E_\mathrm{D}} \frac{-(E-E_\mathrm{D})}{1+\exp\left[-(E-E_\mathrm{F})/kT\right]}\,\mathrm{d}E \tag{17.10b}$$

as visualized in Fig. 17.7. These relations cannot be inverted to obtain $E_\mathrm{F}(n,p)$ analytically. The total charge carrier density is $\rho_\mathrm{S} = e(p_\mathrm{S} - n_\mathrm{S})$.

The Hall effect (Fig. 17.8) shows the expected ambipolar dependence according to (8.33) which takes the form

[3] Here we assume the linear dispersion for all thermally populated states.

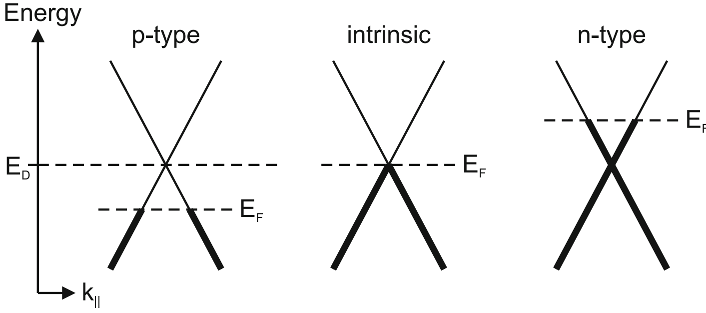

Fig. 17.7. Band structure of graphene with various positions of the Fermi energy E_F in relation to the Dirac energy E_D. States occupied with electrons are shown with in *bold*

$$R_H = \frac{1}{e} \frac{p_S - n_S}{(n_S + p_S)^2} \tag{17.11}$$

for equal electron and hole mobilities.[4]

From Hall effect measurements the mobility has been determined to be about $10^4\,\mathrm{cm^2/Vs}$, independent of temperature between 10 and 100 K, and the same for electrons and holes. This value, however, is much smaller than the in-plane mobility of about $10^6\,\mathrm{cm^2/Vs}$ at 4.2 K in high quality samples of

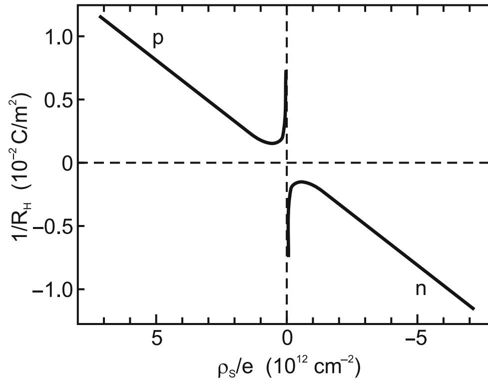

Fig. 17.8. Hall coefficient ($T = 10\,\mathrm{K}$) for a graphene sheet as a function of the free carrier sheet density $\rho_S/e = p_S - n_S$ (positive values indicate p-type). Data shown as *solid lines* from [1008]

[4]Including sign, $\mu_h = -\mu_e$. For $T = 0$ and $E_F = E_D$, $n_S = p_S = 0$ and thus $1/R_H$ should be zero. For finite temperatures there is always $n_S > 0$ and $p_S > 0$, even for $E_F = E_D$. Thus $1/R_H \propto 1/(p_S - n_S)$ diverges at $\rho_S = e(p_S - n_S) = 0$ with a change of sign.

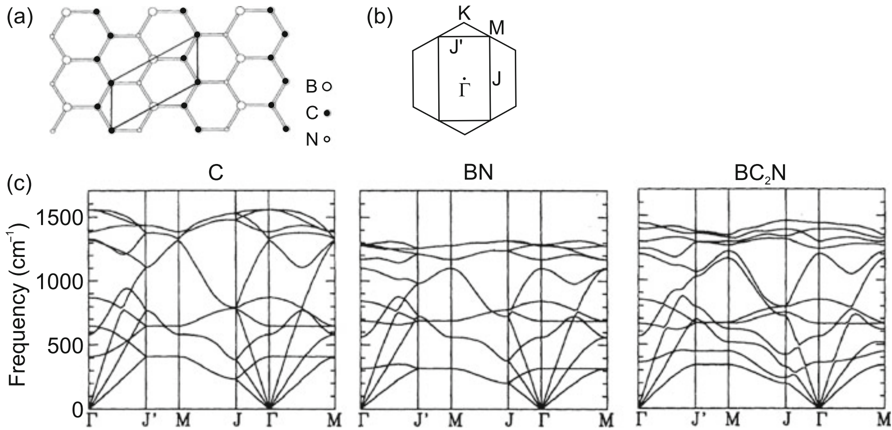

Fig. 17.9. (**a**) Crystal structure of BC_2N. (**b**) Brillouin zone of BC_2N (*rectangle*) and C, BN (*hexagon*). (**c**) Phonon dispersion of graphene (C) and BN- and BC_2N-sheets. Adapted from [1024]

highly ordered pyrolithic graphite (HOPG) [1018]. In suspended graphene a mobility of $2.3 \times 10^5\,\mathrm{cm}^2/\mathrm{Vs}$ has been found, limited by finite sample size [1019]. Thus in graphene layers on a solid surface extrinsic effects such as charge traps, interfacial phonons, ripples or fabrication residue seem to limit the carrier mobility.

The QHE has been observed in graphene [1008], reportedly up at room temperature [1020]. The plateaus $(4e^2/h)(n + 1/2)$ correspond to unusual half-integer filling, the first plateau occurring at $2e^2/h$, as has been also suggested from theory, and related to the 'pseudospin'. Another consequence of the Dirac-like behavior of the fermions in graphene is the presence of finite maximum resistivity $\rho_{\max} = h/4e^2 = 6.45\,\mathrm{k}\Omega$ even at low temperature and $E_\mathrm{F} = E_\mathrm{D}$. It is due to the fact that localization effects, leading to insulating behavior, are strongly suppressed. Then each carrier keeps a mean free path in the order of its Fermi wavelength.

The Klein paradox [1021, 1022], the efficient tunneling of Dirac particles through high and thick barriers seems accessible in transport experiments with graphene [1023].

17.1.4 Other Two-Dimensional Crystals

Two-dimensional crystals have been reported also for other materials such as BN, MoS_2, $NbSe_2$, $Bi_2Sr_2CaCu_2O_x$ [1005]. The phonon spectra of graphene, BN- and BC_2N-sheets are compared in Fig. 17.9. The spectrum of BC_2N is similar to the superposition of the C and BN spectra [1024].

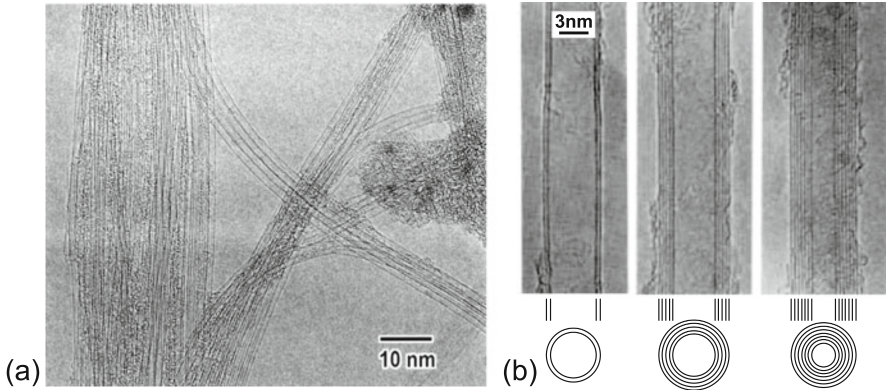

Fig. 17.10. (**a**) TEM image of single-walled carbon nanotubes (SWNT). (**b**) TEM images of various multi-walled carbon nanotubes (MWNT). Adapted from [1025].

17.2 Carbon Nanotubes

17.2.1 Structure

A carbon nanotube (CNT) is a part of a graphene sheet rolled up to form a cylinder. They were first described as multi-walled nanotubes by Iijima [1025] in 1991 (Fig. 17.10b) and in their single-walled form (Fig. 17.10a) in 1993 [1026]. Reviews can be found in [1011, 1027].

The chirality and diameter of a nanotube are uniquely described by the chiral vector

$$\mathbf{c}_\mathrm{h} = n_1\,\mathbf{a}_1 + n_2\,\mathbf{a}_2 \equiv (n_1, n_2)\ , \tag{17.12}$$

where $\mathbf{a}_1$ and $\mathbf{a}_2$ are the unit vectors of the graphene sheet. The chiral vector denotes two crystallographic equivalent sites which are brought together along the circumference of the nanotube. The possible vectors are visualized in Fig. 17.1 for $-30° \leq \theta \leq 0°$. The fiber diameter is given by

$$d = \frac{|\mathbf{c}_\mathrm{h}|}{\pi} = \frac{a}{\pi}\left(n_1^2 + n_1 n_2 + n_2^2\right)\ , \tag{17.13}$$

with the graphene lattice constant $a = \sqrt{3}\,d_{\mathrm{C-C}} = 0.246\,\mathrm{nm}$. Ab-initio calculations show that the diameter becomes a function of the chiral angle below 0.8 nm; deviations from (17.13) are below 2% for tube diameters $d > 0.5\,\mathrm{nm}$ [1028]. The $(n, 0)$ tubes ($\theta = 0$) are termed 'zig-zag' and an example is depicted in Fig. 17.11b. Nanotubes with $\theta = \pm\pi/6$, i.e. of the (n, n) (and $(2n, -n)$) type, are called 'armchair'. All others are termed 'chiral'.

The extension along the wire axis is large compared to the diameter. The tip of a nanotube is part of a buckminster-fullerene type molecule (Fig. 17.12). When the nanotube if formed by rolling a single sheet of graphene (SLG),

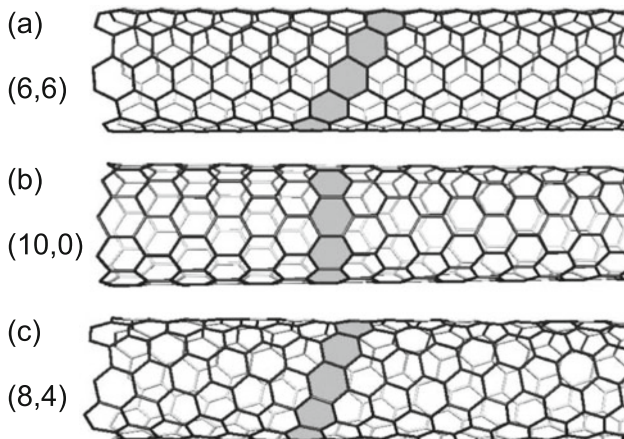

Fig. 17.11. Structure of different types of carbon nanotubes that have similar diameter of 0.8 nm. (**a**) Armchair (6,6), (**b**) zigzag (8,0) and (**c**) chiral symmetry. Adapted from [1027]

a single-walled nanotube (SWNT) is formed. A FLG sheet creates a multi-walled nanotube (MWNT). For small number of layers they are called double-walled, triple-walled and so forth.

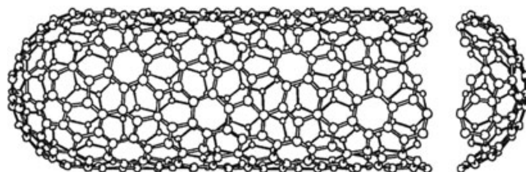

Fig. 17.12. A chiral nanotube (chiral vector is (10,5), $\theta = -19.11°$) with hemispherical caps at both ends based on an icosahedral C_{140} fullerene. The tube diameter is 1.036 nm. Adapted from [1029]

The mechanical strength of carbon nanotubes is very large. For SWNT Young's moduli of 10^3 GPa have been found experimentally [1030] in agreement with theoretical predictions [1031].

17.2.2 Band Structure

In carbon nanotubes there is some mixing of the $\pi(2p_z)$ and $\sigma(2s$ and $2p_z)$ carbon orbitals due to the radial curvature. This mixing is, however, small and can be neglected near the Fermi level [1032]. The band structure of a nanotube is mainly determined by zone-folding of the graphene band structure. The vector along the (infinitely extended) wire k_z is continuous. The vector $k_\perp$

around the nanotube is discrete with the periodic boundary condition

$$\mathbf{c}_{\mathrm{h}} \cdot \mathbf{g}_{\perp} = 2\pi \, m \; , \tag{17.14}$$

where m is an integer. The distance of allowed $k_{\perp}$-values is (5.5)

$$\Delta k_{\perp} = \frac{2\pi}{\pi \, d} = \frac{2}{d} \; . \tag{17.15}$$

The character of the nanotube band structure depends on how the allowed k-values lie relative to the graphene Brillouin zone and its band structure. This is visualized in Fig. 17.13. For the case of an armchair tube (n, n), as shown in Fig. 17.13a, the K-point of the graphene band structure always lies on an allowed k-point. Therefore, the nanotube is metallic, i.e. zero-gap, as seen in the bandstructure in Fig. 17.13b. The Dirac point is between Γ and X. For a zig-zag nanotube, the k-space is shown in Fig. 17.13c for a (6,0) nanotube. The corresponding band structure for a (6,0) nanotube is also metallic (Fig. 17.13d) with the Dirac point at the Γ point.

In Fig. 17.14c the band structure of another metallic (12,0) zig-zag nanotube is shown. However, only for ($3m$,0) the K-point is on an allowed state and thus the tube metallic. For the other cases, as shown for the k-space of a (8,0) nanotube in Fig. 17.14b, this is not the case. The corresponding band structure (Fig. 17.14c for (13,0)) has a gap and thus the nanotube is a semiconductor. Generally, the condition for a nanotube to be metallic is with an integer m

$$n_1 - n_2 = 3 \, m \; . \tag{17.16}$$

There are two semiconducting 'branches' with $\nu = (n_1 - n_2) \bmod 3 = \pm 1$. The tubes with $\nu = +1$ have a small band gap, those with $\nu = -1$ have a larger band gap.

The density of states is a series of one-dimensional DOS, proportional to $\sqrt{E}$ (6.78). It is compared in Fig. 17.15 for a metallic and a semiconducting nanotube. Within 1 eV from the Fermi energy the DOS can be expressed in an universal term [1033].

17.2.3 Optical Properties

Optical transitions occur with high probability between the van-Hove singularities of the DOS. The theoretical absorption spectrum of a (10,0) nanotube is shown in Fig. 17.16.

In an ensemble of nanotubes various types and sizes occur. The transition energies of all possible nanotubes sorted by diameter are assembled in the Kataura plot (Fig. 17.17a). Experimental data are shwon in Fig. 17.17b. The two branches of semiconducting nanotubes $\nu = \pm 1$ yield different transition energies. The overall dependence of the transition energy follows a $1/d$-law.

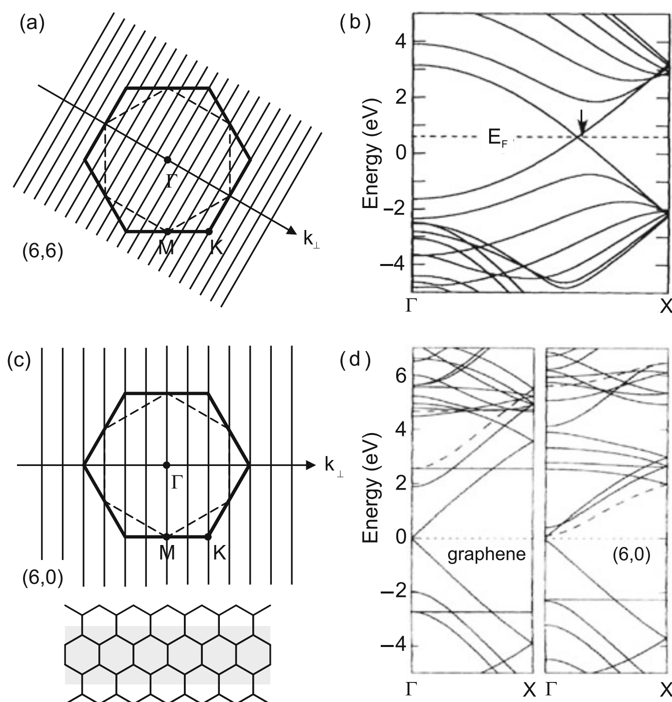

Fig. 17.13. (**a**) Brillouin zone of the graphene lattice (*bold* line) and allowed k-values for a (6,6) armchair nanotube. (**b**) Band structure of a (6,6) carbon nanotube. Adapted from [1034]. (**c**) Brillouin zone of the graphene lattice (*bold* line) and allowed k-values for a (6,0) zig-zag carbon nanotube. In the *lower part* the real space structure is visualized. (**d**) Band structure of graphene (*left*) and a (6,6) nanotube (*right*). Adapted from [1035].

17.2.4 Other Anorganic Nanotubes

Structures similar to carbon nanotubes have been reported for BN [1036, 1037]. A boron nitride nanotube is a cylindrically rolled part of a BN sheet. BN tubes are always semiconducting (Fig. 17.18) and have a band gap beyond 5 eV similar to hexagonal BN which is mostly independent on chirality and diameter [1038]. Thus, while carbon nanotubes appear black since they absorb within 0–4 eV, BN is transparent (or white if scattering). For high energies larger than 10 eV C and BN tubes are quite similar since they are isoelectronic and the high-lying unoccupied states are less sensitive to the difference in the nuclear charges than the states at and below the Fermi energy [1039].

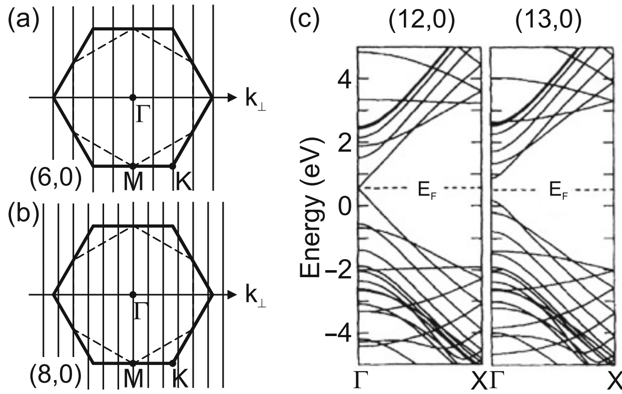

Fig. 17.14. (**a**, **b**) Brillouin zone of the graphene lattice (*bold* line) and allowed k-values for a (**a**) (6,0) and a (**b**) (8,0) zig-zag nanotube. (**c**) Band structures of a (12,0) metallic and (13,0) semiconducting armchair carbon nanotube. Adapted from [1034]

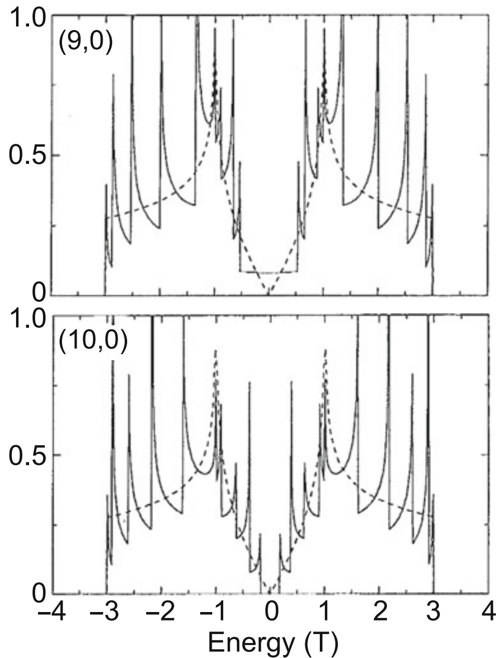

Fig. 17.15. Density of states for a (9,0) metallic and (10,0) semiconducting zig-zag carbon nanotube within the tight-binding approximation (17.2). The energy scale is given in units of the tight-binding parameter $T \approx 3\,\text{eV}$. The *dashed lines* are the DOS of graphene. Adapted from [1029]

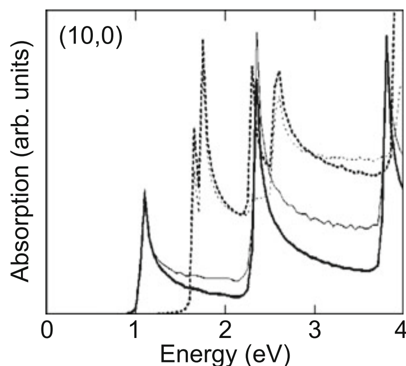

Fig. 17.16. Calculated absorption spectra for a (semiconducting) (10,0) carbon nanotube for parallel (*solid line*) and perpendicular (*dotted line*) polarization. The *thick* (*thin*) lines are calculated with (without) the matrix element included. Adapted from [1040]

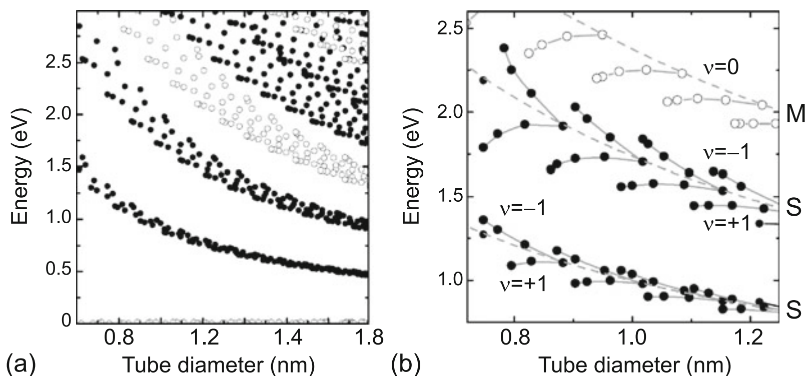

Fig. 17.17. (**a**) Theoretical transition energies of semiconducting (*filled symbols*) and metallic (*open symbols*) carbon nanotubes as a function of tube diameter (Kataura plot). Energies are calculated from van-Hove singularities in the JDOS within the third-order tight-binding approximation [1012]. (**b**) Experimental Kataura plot for the first two semiconducting (S, *closed symbols*) and the first metallic (M, *open symbols*) transition. *Dashed lines* connect the (near-to) armchair tubes; *full lines* connect tubes in a branch, $\nu = (n_1 - n_2) \bmod 3$. Data from photoluminescence [1041] and resonant Raman scattering [1042]. Adapted from [1043]

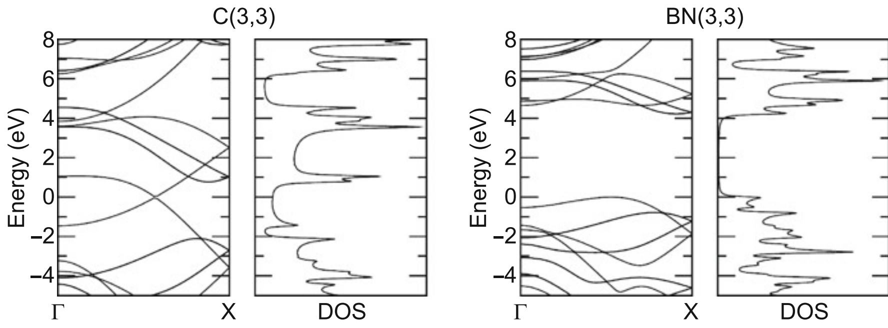

Fig. 17.18. Band structure and density of states (DOS) of C(3,3) and BN(3,3) nanotubes, calculated with DFT-LDA. Adapted from [1039]

18 Dielectric Structures

18.1 Photonic Band Gap Materials

Layered structures of dielectric materials with different index of refraction are used as optical elements such as filters or reflection and anti-reflection coatings [1044]. In this section we discuss the use of such concepts in one-, two- and three-dimensional photonic band gap materials.

18.1.1 Introduction

A structure with a so-called *photonic* band gap (PBG) exhibits an energy range (color range) in which photons cannot propagate in any direction. In the photonic band gap, there are no optical modes, no spontaneous emission and no vacuum (zero-field) fluctuations. We recollect that spontaneous emission is not a necessary occurrence: Looking at Fermi's golden rule (9.11) for the transition probability integrated over all final states

$$w(E) = \frac{2\pi}{\hbar}\,|M|^2\,\rho_{\mathrm{f}}(E)\;, \tag{18.1}$$

we see that the decay rate depends on the density ρ_{f} of final states at energy E. In the case of spontaneous emission, this is the (vacuum) density D_{em} of electromagnetic modes (per energy per volume) that varies $\propto \omega^2$:

$$D_{\mathrm{em}}(E) = \frac{8\pi}{(hc)^3}\,E^2\;. \tag{18.2}$$

In a homogeneous optical medium c must be replaced with c/n.

If the band gap of a PBG is tuned to the electronic gap of a semiconductor, the spontaneous emission, and also induced emission, can be suppressed. Thus, one mode has to be left by 'doping' the structure. In this mode all emission will disappear and an efficient single-mode (monochromatic) LED or 'zero-threshold' laser could be built. A schematic comparison of the band structure of electrons and photons is given in Fig. 18.1.

18.1.2 General 1D Scattering Theory

The formation of a photonic band gap in a one-dimensional dielectric can be calculated to a large extent analytically and thus with direct insight. Let

M. Grundmann, *The Physics of Semiconductors*, 2nd ed., Graduate Texts in Physics, DOI 10.1007/978-3-642-13884-3_18,

© Springer-Verlag Berlin Heidelberg 2010

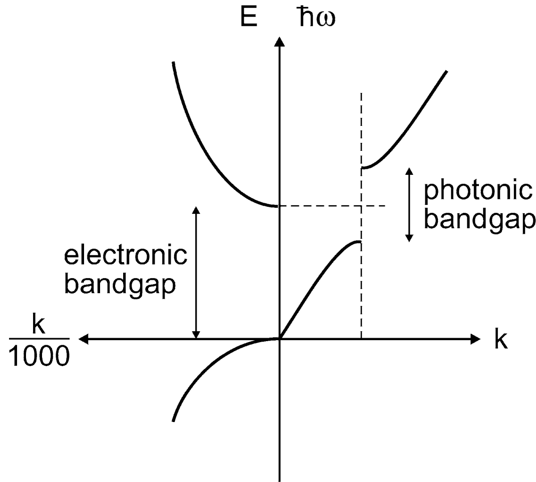

Fig. 18.1. *Right*: electromagnetic dispersion with a forbidden gap at the wavevector of the periodicity. *Left*: Electron-wave dispersion typical of a direct-gap semiconductor. When the photonic band gap straddles the electronic band gap, electron–hole recombination into photons is inhibited since the photons have no place to go (zero final density of states)

$n(x)$ be the spatially varying index of refraction (no losses or nonlinear optical effects). The one-dimensional wave equation (Helmholtz equation) reads for the electric field $\mathcal{E}$

$$\frac{\partial^2 \mathcal{E}(x)}{\partial x^2} + n^2(x) \frac{\omega^2}{c^2} \mathcal{E}(x) = 0 \,. \tag{18.3}$$

A comparison with a one-dimensional Schrödinger equation

$$\frac{\partial^2 \Psi(x)}{\partial x^2} - \frac{2m}{\hbar^2} \left[V(x) - E\right] \Psi(x) = 0 \tag{18.4}$$

shows that the Helmholtz equation corresponds to the quantum-mechanical wave equation of zero external potential V and a spatially modulated mass, i.e. a case that is usually not considered.

Let us consider now the amplitude a_k of the k eigenvector. The eigenvalue is then ω_k. The one-dimensional mode density $\rho(\omega)$ (per energy and per unit length) is

$$\rho(\omega) = \frac{\mathrm{d}k}{\mathrm{d}\omega} \,, \tag{18.5}$$

which is the inverse of the group velocity.

We follow one-dimensional scattering theory as presented in [1045]. At this point we do not rely on any specific form of $n(x)$ (Fig. 18.2a). The (complex) transmission coefficient t for any index structure is

$$t = x + \mathrm{i}y = \sqrt{T}\,\exp(\mathrm{i}\phi) \,, \tag{18.6}$$

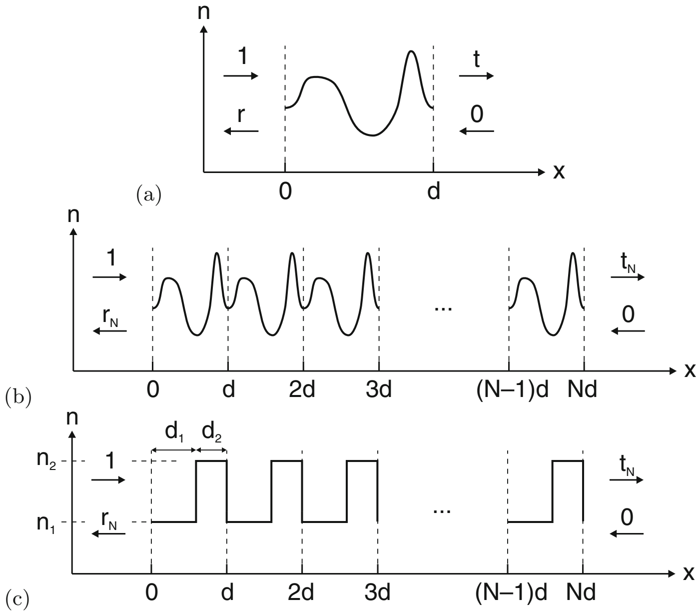

Fig. 18.2. 1D scattering problem: (**a**) General scattering of an index of refraction distribution, (**b**) N-period stack, (**c**) two-layer (quarter-wave) stack

where $\tan\phi = y/x$. ϕ is the total phase accumulated during propagation through the structure. It can be written as the product of the physical thickness of the structure d and the effective wave number k. Hence we have the dispersion relation

$$\frac{\mathrm{d}}{\mathrm{d}\omega}\tan(kd) = \frac{\mathrm{d}}{\mathrm{d}\omega}\left(\frac{y}{x}\right) . \tag{18.7}$$

Evaluating the derivative we find

$$\frac{1}{\cos^2(kd)}\, d\, \frac{\mathrm{d}k}{\mathrm{d}\omega} = \frac{y'x - x'y}{x^2} , \tag{18.8}$$

where the prime denotes derivation with respect to ω. Using the relation $\cos^2\theta = (1 + \tan^2\theta)^{-1}$, we obtain the general expression

$$\rho(\omega) = \frac{\mathrm{d}k}{\mathrm{d}\omega} = \frac{1}{d}\,\frac{y'x - x'y}{x^2 + y^2} . \tag{18.9}$$

18.1.3 Transmission of an *N*-Period Potential

Now, the behavior of N periods of a given index distribution $n(x)$ within a thickness d of one period (Fig. 18.2b) is investigated. The scattering matrix $\mathbf{M}$ connects the intensity at $x = 0$ with that at $x = d$. We use the column

vector $\mathbf{u} = \begin{pmatrix} u^+ \\ u^- \end{pmatrix}$ containing the right- and left-going waves (labeled '+' and '−', respectively), $u^\pm = f^\pm \exp(\pm \mathrm{i}kx)$,

$$\mathbf{u}(0) = \mathbf{M}\,\mathbf{u}(d)\ . \tag{18.10}$$

Using the boundary conditions $\mathbf{u}(0) = (1, r)$ and $\mathbf{u}(d) = (t, 0)$, we find that $\mathbf{M}$ has the structure

$$\mathbf{M} = \begin{pmatrix} 1/t & r^*/t^* \\ r/t & 1/t^* \end{pmatrix}\ . \tag{18.11}$$

The conservation of energy requires that $\det \mathbf{M} = (1 - R)/T = 1$. The eigenvalue equation for $\mathbf{M}$ is

$$\mu^2 - 2\mu\,\mathrm{Re}(1/t) + 1 = 0\ . \tag{18.12}$$

The two eigenvalues $\mu^\pm$ are related by $\mu^+\,\mu^- = \det \mathbf{M} = 1$. If we consider an infinite, periodic structure, we know from Bloch's theorem that the eigenvector varies between unit cells only via a phase factor, i.e. $|\mu| = 1$. Therefore, the eigenvalues can be written as

$$\mu^\pm = \exp(\pm \mathrm{i}\beta)\ , \tag{18.13}$$

where β corresponds to the Bloch phase of a hypothetical infinite periodic structure. This phase β should not be confused with ϕ defined earlier, which is associated with the unit cell transmission. We find the condition

$$\mathrm{Re}(1/t) = \cos\beta \tag{18.14}$$

for the Bloch phase. Since every matrix obeys its own eigenvalue equation, we have also ($\mathbf{1}$ being the unity matrix)

$$\mathbf{M}^2 - 2\mathbf{M}\cos\beta + \mathbf{1} = 0\ . \tag{18.15}$$

By induction one can show that the N-period case has the scattering matrix

$$\mathbf{M}^N = \mathbf{M}\,\frac{\sin(N\beta)}{\sin\beta} - \mathbf{1}\,\frac{\sin((N-1)\beta)}{\sin\beta}\ . \tag{18.16}$$

The solution for the finite period case can be written in terms of the Bloch phase of the infinite potential. The transmission and reflection of the N-period system are given by

$$\frac{1}{t_n} = \frac{1}{t}\,\frac{\sin(N\beta)}{\sin\beta} - \frac{\sin((N-1)\beta)}{\sin\beta} \tag{18.17a}$$

$$\frac{r_n}{t_n} = \frac{r}{t}\,\frac{\sin(N\beta)}{\sin\beta}\ . \tag{18.17b}$$

The transmission of intensity can be written as ($T = t^* t$)

$$\frac{1}{T_N} = 1 + \frac{\sin^2(N\beta)}{\sin^2\beta}\left[\frac{1}{T} - 1\right] . \tag{18.18}$$

Again, up to this point no specific distribution of the index of refraction within the unit cell has been specified.

From (18.17a), a general formula for the mode density $\rho_N(\omega)$ of the N-stack can be obtained as [1045]

$$\rho_N = \frac{1}{Nd}\frac{\frac{\sin(2N\beta)}{2\sin\beta}\left[\eta' + \frac{\eta\xi\xi'}{1-\xi^2}\right] - \frac{N\eta\xi'}{1-\xi^2}}{\cos^2(N\beta) + \eta^2\left[\frac{\sin(N\beta)}{\sin\beta}\right]^2} , \tag{18.19}$$

where $\xi = x/T = \cos\beta$ and $\eta = y/T$.

18.1.4 The Quarter-Wave Stack

A quarter-wave stack, also known as a Bragg mirror, exhibits a one-dimensional photonic band gap. One period consists of two regions with thickness and index of refraction (d_1, n_1) and (d_2, n_2), respectively (Fig. 18.2c). In the quarter-wave stack each region has an optical thickness of $\lambda/4$ (the wave accumulates in each region a phase of $\pi/2$) for a particular wavelength λ_0 or (midgap) frequency ω_0. Thus, the condition reads

$$n_1 d_1 = n_2 d_2 = \frac{\lambda_0}{4} = \frac{\pi}{2}\frac{c}{\omega_0} . \tag{18.20}$$

Using the Fresnel formulas, the transmission of an arbitrary two-layer cell is

$$t = \frac{T_{12}\,\exp(\mathrm{i}(p+q))}{1 + R_{12}\,\exp(2\mathrm{i}q)} , \tag{18.21}$$

where $p = n_1 d_1 \omega/c$ and $q = n_2 d_2 \omega/c$ are the phases accumulated in the two layers, respectively. The values of T_{12} and R_{12} are given as

$$T_{12} = \frac{4 n_1 n_2}{(n_1 + n_2)^2} \tag{18.22a}$$

$$R_{12} = \frac{(n_1 - n_2)^2}{(n_1 + n_2)^2} . \tag{18.22b}$$

For the quarter-wave stack ($p = q = \pi/2$), we obtain for (18.21)

$$t = \frac{T_{12}\,\exp(\mathrm{i}\pi\tilde{\omega})}{1 + R_{12}\,\exp(\mathrm{i}\pi\tilde{\omega})} , \tag{18.23}$$

where $\tilde{\omega} = \omega/\omega_0$ is the frequency scaled to the midgap value.

The transmission of a single two-layer cell is

$$T = \frac{T_{12}^2}{1 - 2R_{12}\cos(\pi\tilde{\omega}) + R_{12}^2} , \tag{18.24}$$

and the Bloch phase is given by

$$\cos\beta = \xi = \frac{\cos(\pi\tilde{\omega}) - R_{12}}{T_{12}} \tag{18.25a}$$

$$\eta = \frac{\sin(\pi\tilde{\omega})}{T_{12}} . \tag{18.25b}$$

For the N-period quarter-wave stack the transmission is given by

$$T_N = \frac{1 + \cos\beta}{1 + \cos\beta + 2(R_{12}/T_{12})\sin^2(N\beta)} . \tag{18.26}$$

A band gap forms. Within the band gap, the density of modes is lowered, at the edges it is enhanced (Figs. 18.3 and 18.4). The transmission at midgap decreases $\propto (n_i/n_j)^{2N}$, where $n_i < n_j$.

In the limit of large N the complete width $\Delta\tilde{\omega}$ of the band gap is implicitly given by

$$\cos\left(\frac{\pi}{2}\Delta\tilde{\omega}\right) = 1 - 2\left(\frac{n_1 - n_2}{n_1 + n_2}\right)^2 . \tag{18.27}$$

If $|n_1 - n_2| \ll n_1 + n_2$, we find

$$\Delta\tilde{\omega} \approx \frac{4}{\pi}\,\frac{|n_1 - n_2|}{n_1 + n_2} . \tag{18.28}$$

The principle of the quarter-wave stack is scalable to frequencies other than visible light.[1] In Fig. 18.5 the reflectance of various quarter-wave stacks from yttria-stabilized zirconia (YSZ [1046], high index material, Fig. 18.6a) and Al_2O_3 are shown [1047]. The different design wavelengths have been achieved solely by varying the layer thicknesses.

In Fig. 18.6b the three Bragg mirrors from Fig. 18.5 with $N = 15.5$ pairs are replotted in relative frequency units $\tilde{\omega}$. The spectra look very similar; subtle differences in the width of the reflectance band are due to slightly larger index contrast at higher design energy (cmp. Fig. 18.6a). The width of the gap is approximately $\Delta\tilde{\omega} \approx 0.18$ in agreement with (18.28).

As further example, a Mo/Si Bragg mirror with a period of 6.7 nm is shown in Fig. 18.7. Such a mirror works in the extreme UV and is used for soft X-ray optics, possibly in advanced lithography systems. Dielectric thin films can also be designed for anti-reflection coatings, edge filters or pass and stop band filters as detailed in [1044].

[1] This is a general property of Maxwell's equations which do not contain a specific length scale.

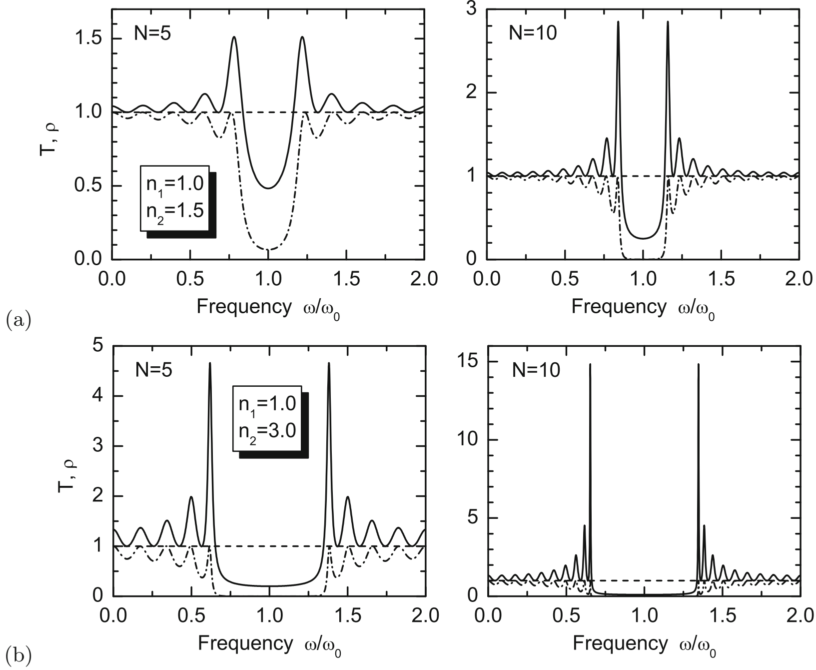

Fig. 18.3. Quarter-wave stack with indices of refraction (**a**) n_1, n_2 = 1.0, 1.5 and (**b**) 1.0, 3.0. *Solid lines*: dimensionless density of modes ρ_N (18.19), *dashed lines*: transmission T_N (18.26) for two different numbers of pairs $N = 5$ (*left panels*) and 10 (*right panels*) vs. the dimensionless frequency $\tilde{\omega}$

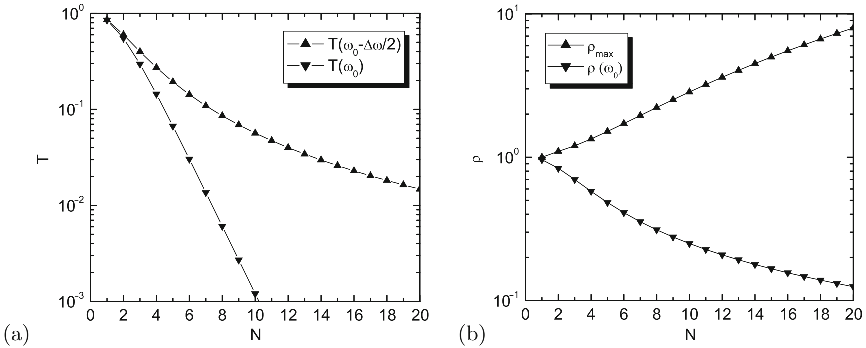

Fig. 18.4. Quarter-wave stack with indices of refraction n_1, n_2 = 1.0, 1.5: (**a**) Transmission T_N at midgap ($\tilde{\omega} = 1$, *down triangles*) and at the band edge ($\tilde{\omega} = 1 - \Delta\tilde{\omega}/2$, *up triangles*) vs. number of pairs N. (**b**) Dimensionless density of modes ρ_N at maximum near the band edge and at midgap vs. number of pairs N

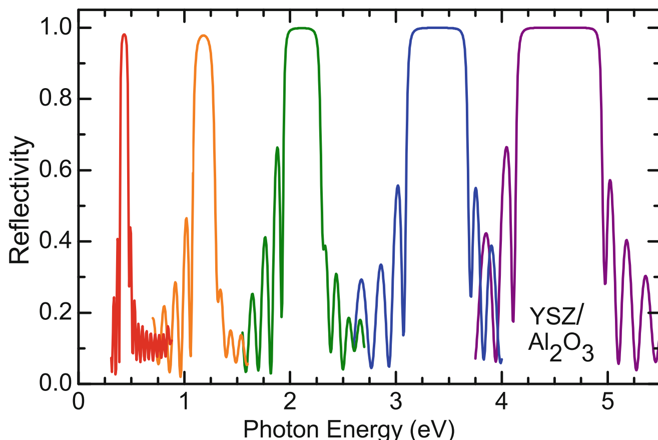

Fig. 18.5. Reflectance of various Bragg mirrors from YSZ/Al_2O_3 grown by pulsed laser deposition on sapphire. The different layer thicknesses result in the design energies 0.43 eV (N = 10.5, R_{max} = 0.9812, *red*), 1.19 eV (N = 10.5, R_{max} = 0.9779, *orange*), 2.11 eV (N = 15.5, R_{max} = 0.99953, *green*), 3.39 eV (N = 15.5, R_{max} = 0.99946, *blue*) and 4.54 eV (N = 15.5, R_{max} = 0.99989, *purple*)

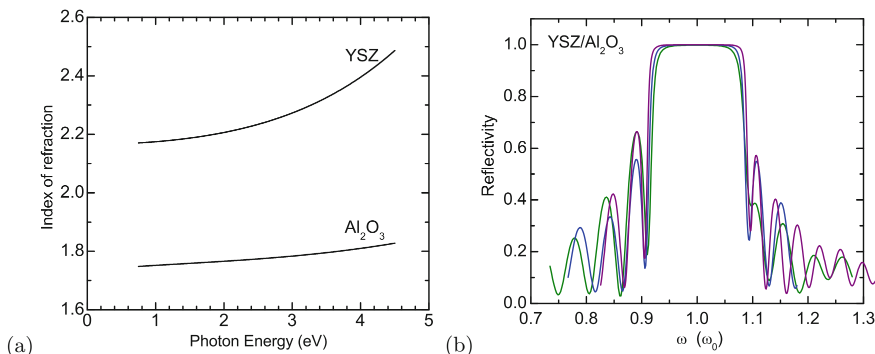

Fig. 18.6. (**a**) Index of refraction of YSZ and Al_2O_3 as a function of photon energy. (**b**) Reflectance spectra of the 2.11 eV, 3.39 eV and 4.54 eV Bragg mirrors of Fig. 18.5 replotted as a function of the scaled frequency $\tilde{\omega} = \omega/\omega_0$

18.1.5 Formation of a 3D Band Structure

For other applications, e.g. waveguides with minimized footprint, 3D (or at least 2D) photonic band gap structures are needed. Details can be found in dedicated textbooks [1048–1050]. In [1051] planar, cylindrical and spherical Bragg mirrors are discussed.

Since we want a photonic band gap that is present for *all* directions of propagation, a Brillouin zone with a shape close to a sphere is preferable. Then, the main directions are at similar k-values (Fig. 18.8). One of the best

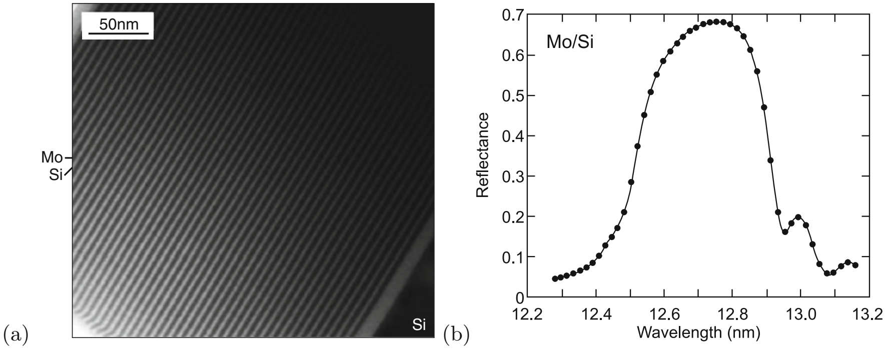

Fig. 18.7. (**a**) Cross-sectional TEM of Mo/Si superlattice with 2.7 nm Mo and 4.0 nm Si (period: 6.7 nm) on Si(001) substrate. From [1052]. (**b**) Reflection spectrum for a SL with period of 6.5 nm and 88.5° angle of incidence. Data points are shown as *circles*, the *solid line* is a fit with a period of 6.45 nm. Adapted from [1053]

suited is the fcc lattice. Since the L point is centered at ≈14% lower frequency than the X point, the forbidden gaps for different directions must be, however, sufficiently wide to create a forbidden frequency band overlapping at all points along the surface of the Brillouin zone. For example, the bcc lattice has a Brillouin zone that is less symmetric than that of the fcc lattice (see Fig. 3.32) and thus is less suited for the creation of an omnidirectional photonic band gap. However, the photonic band gap must not arise above the first band, relaxing problems due to asymmetry of the Brillouin zone (cf. Table 18.1).

Maxwell's equations (zero charge density) for monochromatic waves $\propto \exp(\mathrm{i}\omega t)$

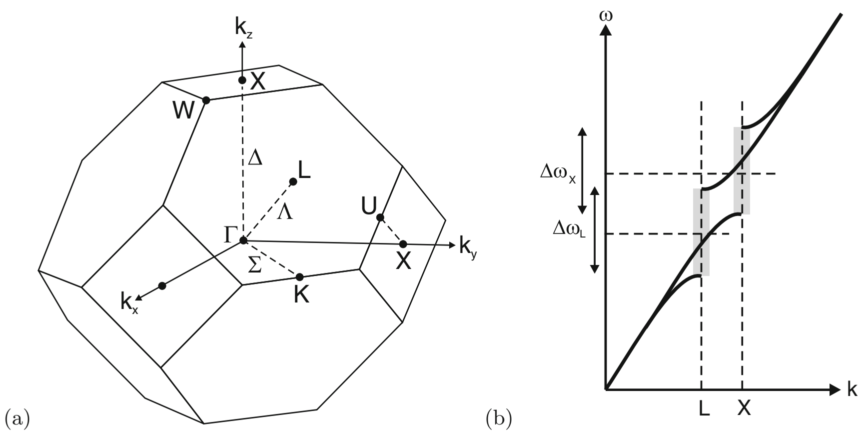

Fig. 18.8. The face-centered cubic Brillouin zone (**a**) in reciprocal space. Schematic forbidden gaps (**b**) at the L and X points

Table 18.1. Various photonic band gap structures and some of their properties. The band gap is between the n-th and $(n+1)$-th band, $\Delta\tilde{\omega}$ is given for air/silicon ($\epsilon \approx 12$).

name	crystal type	n	$\Delta\tilde{\omega}$ (%)	Ref.
diamond	diamond	2	29	[1054]
yablonovite	fcc	2	19	[1058]
woodpile	fc tetragonal	2	20	[1059]
spirals	sc	4	17	[1060]
square-spirals	tetragonal	4	24	[1055]
layered 3D	bc orthorhombic	4	23	[1061]
inverted scaffold	sc	5	7	[1062]
inverse opal	fcc	8	4.25	[1063]
inverse hcp	hcp	16	2.8	[1064]

$$\nabla \cdot \mathbf{D} = 0 \tag{18.29a}$$

$$\nabla \times \mathbf{E} = \mathrm{i}\frac{\mu\omega}{c}\mathbf{H} \tag{18.29b}$$

$$\nabla \times \mathbf{H} = \mathrm{i}\frac{\omega}{c}\mathbf{D} \tag{18.29c}$$

$$\nabla(\mu\mathbf{H}) = 0 \, , \tag{18.29d}$$

together with $\mathbf{D}(\mathbf{r}) = \epsilon(\mathbf{r})\mathbf{E}(\mathbf{r})$ and $\mu = 1$ they are combined into the wave equation

$$\nabla \times \left[\epsilon^{-1}(\mathbf{r}) \, \nabla \times \mathbf{H}(\mathbf{r})\right] + \frac{\omega^2}{c^2}\,\mathbf{H}(\mathbf{r}) = 0 \, . \tag{18.30}$$

This equation is numerically solved for planar waves with wavevector $\mathbf{k}$.

In the following, results are shown for various structures. In a fcc lattice of air spheres in a dielectric medium with $n = 3.6$ (a typical semiconductor), no band gap can be achieved (Fig. 18.9a), only a pseudogap (Fig. 18.9b) appears.

In a diamond lattice (two fcc lattices shifted by 1/4 $\langle 111 \rangle$), a complete photonic band gap is possible [1054] (Fig. 18.10). Recently, a periodic array of spirals (Fig. 18.11) has been predicted to exhibit a large photonic band gap [1055]. Glancing-angle deposition [1056] (GLAD) is a way to realize such structures. Another method to fabricate structures with arbitrary geometry within a material is two-photon lithography or two-photon holography. Another path to PBG structures are so-called inverted opals. First, a close-packed structure of spheres, e.g. monodisperse silica spheres, is fabricated by sedimentation or self-assembly. The gaps are filled with a high-index medium and the template is subsequently removed, e.g. by etching or dissolving. The resulting structure is shown in Fig. 18.12a. Such a structure has a photonic band gap (Fig. 18.12b) if the refractive index is sufficiently high (> 2.85) [1057]. The band gap in this case is between the 4th and 5th band.

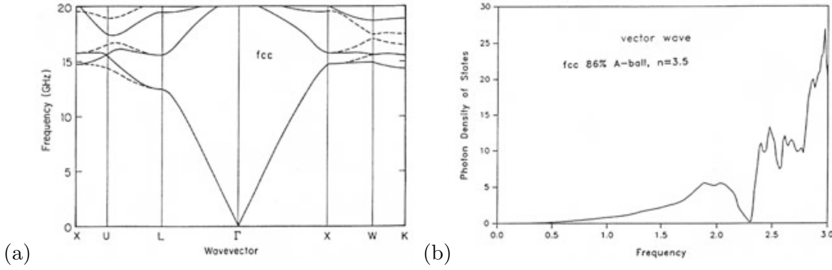

Fig. 18.9. (**a**) Calculated photonic band gap structure of a fcc dielectric structure composed of air spheres in a dielectric background of refractive index $n = 3.5$. The filling ratio is 86% air and 14% dielectric material. *Dotted* and *solid lines* represent coupling to s- and p-polarized light, respectively. Reprinted with permission from [1054], ©1990 APS. (**b**) Density of states for the band structure of part (**a**)

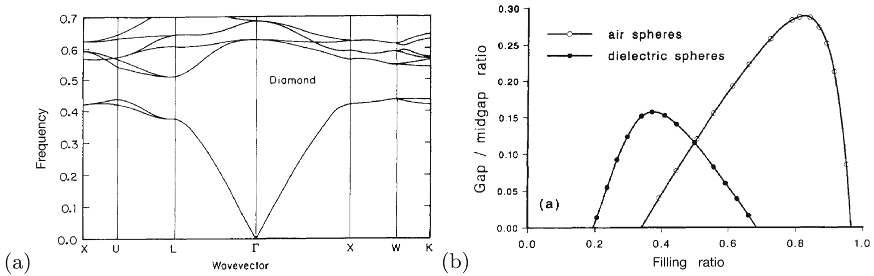

Fig. 18.10. (**a**) Calculated photonic band structure for a diamond dielectric structure consisting of overlapping air spheres in a dielectric material with $n = 3.6$. Filling ratio of air is 81%. The frequency is given in units of c/a, a being the cubic lattice constant of the diamond lattice and c being the velocity of light. (**b**) Gap-to-midgap frequency ratio for the diamond structure as a function of filling ratio for dielectric spheres $n = 3.6$ in air (*solid circles*) and air spheres in dielectric n. Optimal case: air spheres with 82% filling ratio. Reprinted with permission from [1054], ©1990 APS

Table 18.1 offers a compilation of various PBG structures and their properties.

18.1.6 Disorder

A real photonic band gap structure deviates from the ideal, perfectly periodic system by slight variations of the position and possibly also the size of the dielectric 'atoms'. This is schematically shown in Fig. 18.13a. The difference between the real and ideal structure is a (bipolar) spatial distribution of $\Delta\epsilon(\mathbf{r})$ which acts as a source of scattering and hence exponential attenuation of coherent beams propagating through photonic crystals over lengths l, named the '(extinction) mean free path'. After propagating over such distance l, a

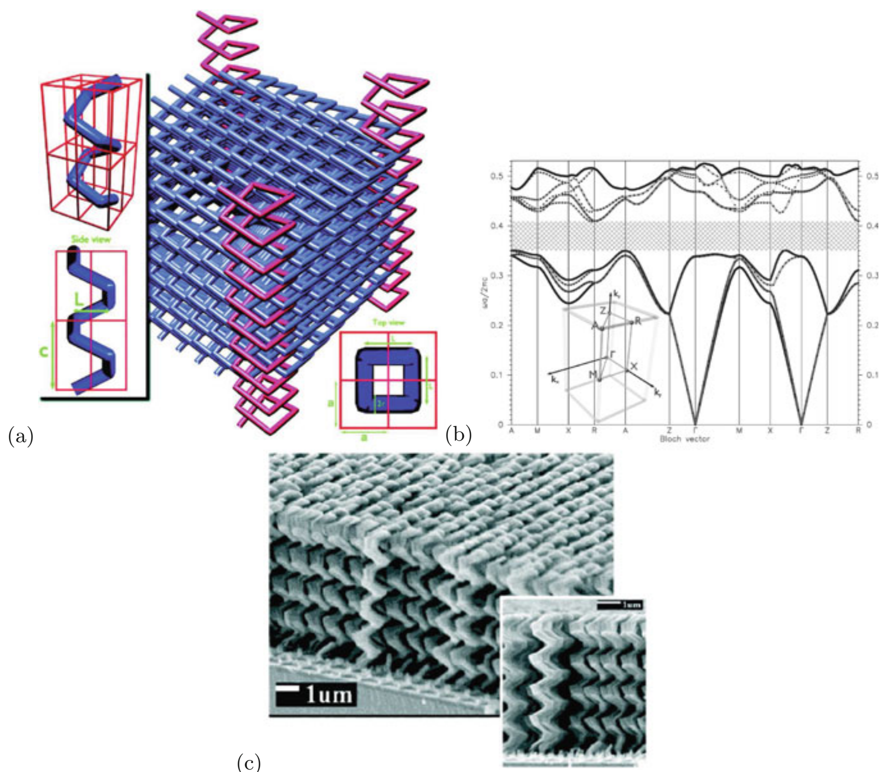

Fig. 18.11. (**a**) Tetragonal square-spiral photonic crystal. The crystal shown here has a solid filling fraction of 30%. For clarity, spirals at the corners of the crystal are highlighted with a different shade and height. The tetragonal lattice is characterized by lattice constants a and b. The geometry of the square spiral is illustrated in the insets and is characterized by its width, L, cylinder radius, r, and pitch, c. The *top left inset* shows a single spiral coiling around four unit cells. (**b**) Band structure for the direct structure crystal characterized by $[L,C,r]=[1.6,1.2,0.14]$ and a spiral filling factor $f_{\text{spiral}} = 30\%$. The lengths are given in units of a, the lattice constant. The width of the PBG is 15.2% relative to the center frequency for background dielectric constant $\epsilon_{\text{b}} = 1$ and spiral dielectric constant $\epsilon_{\text{s}} = 11.9$. The positions of high-symmetry points are illustrated in the *inset*. Reprinted with permission from [1055], ©2001 AAAS. (**c**) Oblique and edge views of a tetragonal square spiral structure grown using the GLAD (glancing-angle deposition) process. Reprinted with permission from [1056], ©2002 ACS

light beam is converted to a diffuse glow that corrupts the functionality of any photonic integrated circuit. Experimentally for opals a mean free path consistent with 5% fabrication accuracy has been found (Fig. 18.13b). For such disorder and a lattice constant $a \approx \lambda$, the mean free path is about only 10 wavelengths, $l \approx 10\lambda$.

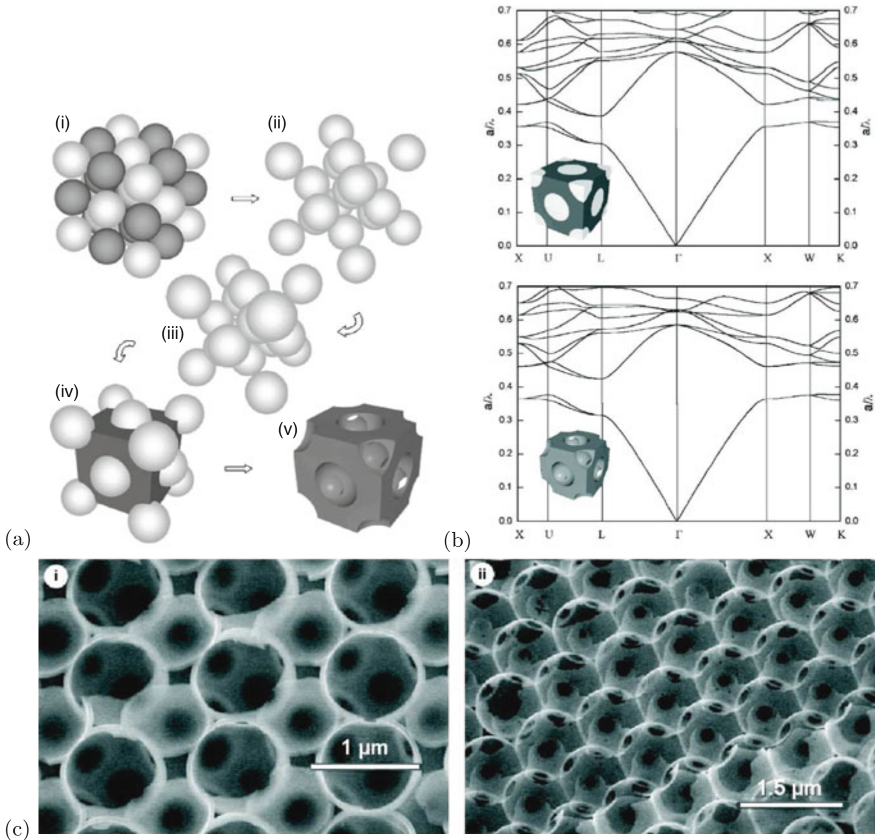

Fig. 18.12. (**a**) Cartoon showing, in five steps, the fabrication of an inverse diamond structure with a full photonic band gap. First, (i) a mixed body-centered cubic lattice is assembled (ii) after which the latex sublattice is removed; (iii) then the structure is sintered to a filling fraction of ∼50% after that (iv) silicon or germanium infiltration takes place and finally (v) silica elimination. (**b**) Photonic band diagrams of (upper panel) a silicon/silica composite diamond opal and (lower panel) made of air spheres in silicon resulting from the removal of the silica spheres from the former. The filling fraction for silicon is 50%. The inset shows the corresponding real space structures. Reprinted with permission from [1065], ©2001 AIP. (**c**) SEM images of internal facets of silicon inverse opal: (i) (110) facet, (ii) (111) facet. Adapted from [1066], reprinted with permission from Nature, ©2000 Macmillan Magazines Limited

18.1.7 Defect Modes

Similar to a perfect periodic atomic arrangement leading to the formation of the electronic band structure, a perfectly periodic dielectric structure leads to the photonic band structure. As we know from semiconductor physics, much of the interesting physics and numerous applications lie in defect modes, i.e.

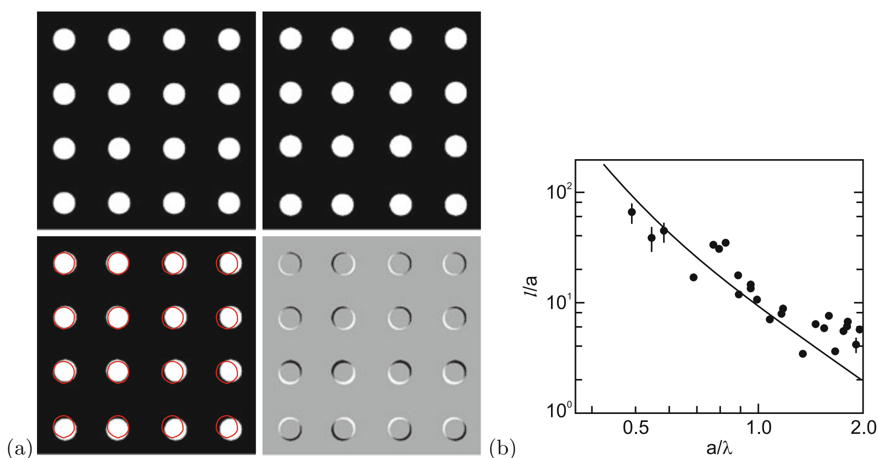

Fig. 18.13. (**a**) Schematic photonic band gap structure with perfect (*upper left*) and disordered (*upper right*) periodicity. In the *lower left* panel the disordered structure is overlayed with the ideal structure (*red circles*). In the *lower right* panel, the difference between ideal and disordered structure is shown. (**b**) Optical mean free path in an opal photonic band gap structure for various lattice constants. *Solid line* is theory for 5% fabrication accuracy. Adapted from [1067]

localized electronic states due to doping and recombination at such centers. The equivalent in PBG structures are point defects (one unit missing) or line defects (a line of units, straight, bend or with sharp angles, missing). Such defects create localized states, i.e. regions for light localization. In the case of line defects we deal with waveguides that can be conveniently designed and could help to reduce the size of photonic and optoelectronic integrated circuits.

1D Model

We revisit our 1D scattering theory and create now a 'defect'. A simple defect is the change of the width of the center n_2-region in a quarter-wave stack. For the numerical example, we choose $N = 11$, $n_1 = 1$, $n_2 = 2$.

In Fig. 18.14, the transmission curves are shown for the undisturbed quarter-wave stack and the microcavity with $n_2\, d_2^{\rm center} = 2\lambda_0/4 = \lambda_0/2$. A highly transmissive mode at $\omega = \omega_0$ arises that is quite sharp with $\Delta\omega = 3 \times 10^{-4}$. Thus, the quality factor Q, also called the Q-factor or finesse,

$$Q = \frac{\omega_0}{\Delta\omega} \,, \tag{18.31}$$

with ω_0 being the resonance frequency and $\Delta\omega$ being the linewidth, is 3.3×10^3 in this case.

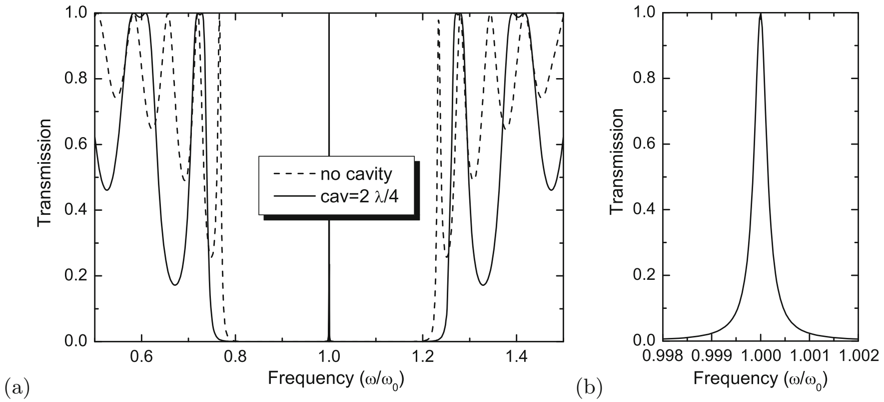

Fig. 18.14. Defect mode in 1D photonic band gap: (**a**) Transmission of $N = 11$ quarter-wave stack exhibiting a photonic band gap ($n_1 = 1$, $n_2 = 2$) (*dashed line*) and of microcavity (*solid line*) with center n_2-region of width $\lambda_0/2$ (instead of $\lambda_0/4$). (**b**) Relative width of mode is about 3×10^{-4}

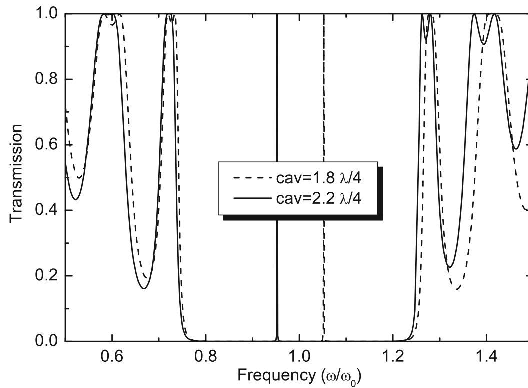

Fig. 18.15. Transmission of $N = 11$ quarter-wave stack ($n_1 = 1$, $n_2 = 2$) with center n_2-region of widths $1.8\,\lambda_0/4$ (*dashed line*) and $2.2\,\lambda_0/4$ (*solid line*)

If the thickness is varied (Fig. 18.15), the mode shifts away from the center. A similar scenario arises for higher-order $n_l/2$-cavities, e.g. $n_2 d_2^{\mathrm{center}} = 4\lambda_0/4 = \lambda_0$ (Fig. 18.16).

2D or 3D Defect Modes

An example of 2D waveguiding is shown in Fig. 18.17. Point defects can be used for high-finesse wavelength filtering. Emitters surrounded by a photonic band gap material with a defect mode can emit into the defect mode only, leading to spectrally filtered, highly directional emission.

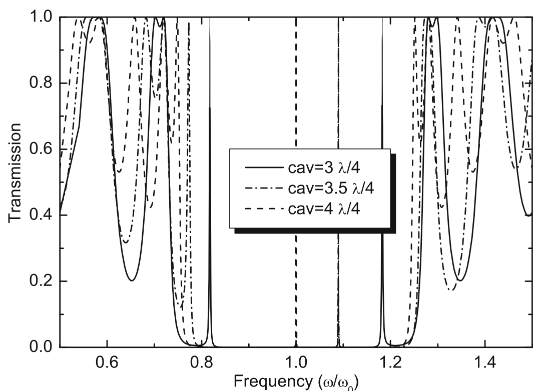

Fig. 18.16. Transmission of $N = 11$ quarter-wave stack ($n_1 = 1$, $n_2 = 2$) with center n_2-regions of widths $3\,\lambda_0/4$ (*solid line*), $3.5\,\lambda_0/4$ (*dash-dotted line*) and $4\,\lambda_0/4$ (*dashed line*)

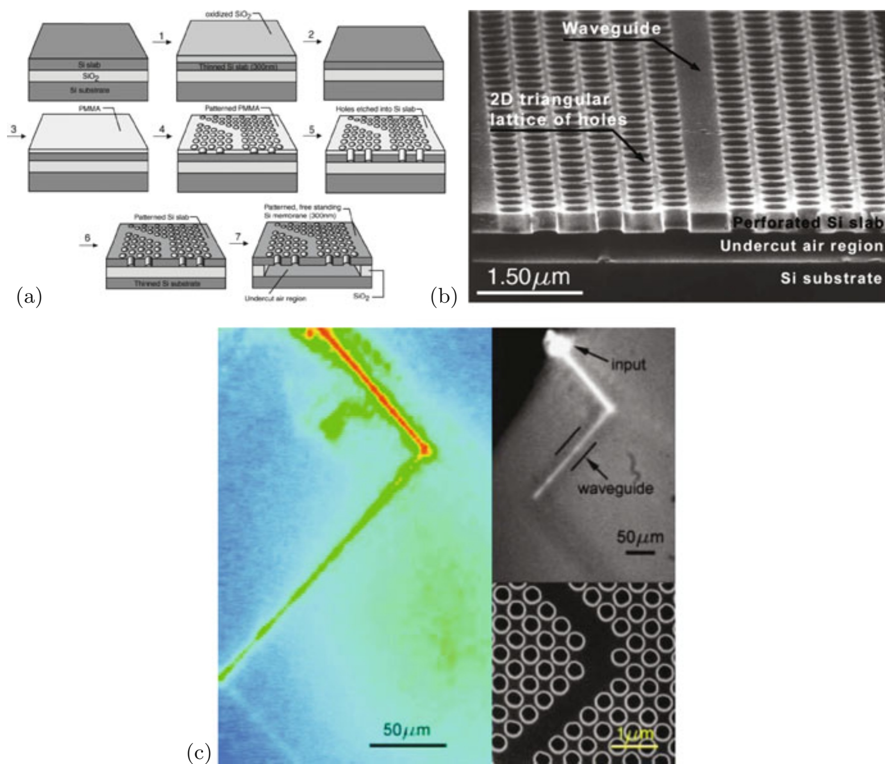

Fig. 18.17. 2D photonic band gap waveguide structure. (**a**) Fabrication principle, (**b**) SEM image of the structure, (**c**) light guiding at a 90° bend. Reprinted with permission from [1070], ©2000 AIP

18.1.8 Coupling to an Electronic Resonance

In a vertical-cavity surface-emitting laser (cf. Sect. 22.4.14), an optical defect mode in a 1D dielectric structure is coupled to an electronic excitation, such as an exciton in a quantum well or dot. In the simplest picture, the oscillator must emit its radiation into the cavity mode since other modes do not exist in the Bragg band. Thus, the emission energy is given and fixed by the cavity mode. However, the photon mode (field oscillator) and the electronic oscillator form a coupled system that generally must be described using quantum electrodynamics. Energy is periodically exchanged between the two oscillators with the Rabi frequency. An analogous phenomenon is investigated in the field of atom–cavity interactions. A necessary condition for the observation of such an oscillation is that the radiation energy remains long enough in the cavity that can be expressed as [1068, 1069] (cf. (18.37))

$$\alpha\, d \gg 1 - R \approx \pi/Q\;, \tag{18.32}$$

where α is the absorption coefficient of the electronic transition, d is the length of the absorbing medium, R is the reflectance of the cavity mirror and Q is the finesse of the cavity given in (18.31). This situation is called the *strong coupling* regime since it leads to anticrossing behavior of the cavity mode and electronic resonance. In the *weak coupling* regime for small absorption, the resonances cross (within their linewidth). For resonance, the emission intensity of the oscillator into the cavity mode is enhanced and its lifetime is reduced (Purcell effect), which is discussed in Sect. 18.2.2.

The transmission T of a Fabry–Perot cavity with two (equal and lossless) mirrors of transmission $T_\mathrm{m} = 1 - R_\mathrm{m}$ is given by

$$T(\omega) = \frac{T_\mathrm{m}^2\, \exp\left(-2L\alpha(\omega)\right)}{\left|1 - R_\mathrm{m}\, \exp\left(\mathrm{i}2n^* L\omega/c\right)\right|^2}\;, \tag{18.33}$$

with the complex index of refraction $n^* = n_\mathrm{r} + \mathrm{i}\kappa = \sqrt{\epsilon}$ and $\alpha = 2\omega\kappa/c$ (cf. (9.10)). For an empty cavity, i.e. a (small) background absorption α_B and a background index of refraction $n_\mathrm{r} = n_\mathrm{B}$, the resonances occur when the phase shift $2n_\mathrm{B}L\omega/c$ is an integer multiple of 2π, i.e. for

$$\omega_\mathrm{m} = m\,\frac{\pi c}{n_\mathrm{B} L}\;, \tag{18.34}$$

with $m \geq 1$ being a natural number. In the vicinity of the resonance, i.e. for $\omega = \omega_\mathrm{m} + \delta\omega$, we can expand $\exp\left(2n_\mathrm{B}L\omega/c\right) \approx 1 + \mathrm{i}2n_\mathrm{B}L\delta\omega/c$ and obtain from (18.33) a Lorentzian for the transmission

$$T(\omega) \approx \frac{T_\mathrm{m}^2 \exp\left(-2L\alpha(\omega)\right)}{\left|1 - R_\mathrm{m}(1 + \mathrm{i}2n_\mathrm{B}L\,\delta\omega/c)\right|^2} = \frac{(T_\mathrm{m}/R_\mathrm{m})^2 \exp\left(2L\alpha(\omega)\right)}{(\delta\omega)^2 + \gamma_\mathrm{c}^2}\;. \tag{18.35}$$

The frequency width (HWHM) γ_c of the empty-cavity resonance is given by

$$\gamma_{\rm c} = \frac{1-R'}{R'}\,\frac{c}{2n_{\rm B}L}\,, \tag{18.36}$$

where $R' = R_{\rm m}\exp(-2L\alpha)$. Thus, the decay rate (photon loss from the cavity) is proportional to $T_{\rm m} + \alpha_{\rm B}L$ if both terms are small. The quality factor of the cavity resonance m is given by

$$Q = \frac{\omega_{\rm m}}{2\gamma_{\rm c}} \approx \frac{m\pi}{1-R}\,. \tag{18.37}$$

Now, the electronic resonance is put into the cavity leading to a change in the dielectric function to (cf. (D.11))

$$\epsilon = n_{\rm B}^2\left[1+\frac{f}{1-(\omega^2+{\rm i}\omega\Gamma)/\omega_0^2}\right]\,, \tag{18.38}$$

where the index of refraction due to the electronic resonance is given by $n(\omega) = \sqrt{\epsilon}$ and (D.13a,b). For resonance of the cavity mode and the electronic oscillator, i.e. $\omega_{\rm m} = \omega_0$, the solution for the cavity resonance condition $2n_{\rm r}\omega L/c = m2\pi$ is obtained, using (18.34), from

$$n_{\rm r}(\omega) = m\frac{\pi c}{\omega L} = n_{\rm B}\frac{\omega_{\rm m}}{\omega}\,. \tag{18.39}$$

A graphical solution (Fig. 18.18a) yields three intersections of the left and right hands of (18.39). The very high absorption at the central solution ($\omega = \omega_0$) results in very low transmission. The other two solutions[2] yield the frequencies of the coupled normal mode peaks. For $f \ll 1$, we use (D.13a) in (18.39) and find for the splitting $\pm\Omega_0/2$ of the two modes

$$\Omega_0^2 = f\,\omega_0^2 - \Gamma^2\,. \tag{18.40}$$

This frequency is called the Rabi frequency. If the dielectric function of the oscillator is put into (18.33), the splitting is found to be

$$\Omega_0^2 = f\,\omega_0^2 - (\Gamma-\gamma_{\rm c})^2\,. \tag{18.41}$$

A splitting will only be observable if $\Omega_0 \gg \Gamma, \gamma_{\rm c}$. If the two resonances $\omega_{\rm c}$ and ω_0 are detuned by $\Delta = \omega_{\rm c} - \omega_0$, the splitting Ω of the transmission peaks shows the typical anticrossing behavior of two coupled oscillators

$$\Omega^2 = \Omega_0^2 + \Delta^2\,. \tag{18.42}$$

In the experiment, typically the electronic resonance remains fixed at ω_0 and the cavity resonance is detuned by variation of the cavity length across the wafer (Fig. 18.18b).

[2]These solutions only occur for sufficient oscillator strength $f > (\Gamma/\omega_0)^2$, i.e. in the strong coupling regime where $\Omega_0^2 > 0$. The absorption coefficient at ω_0 must be larger than $\Gamma n_\infty/c$.

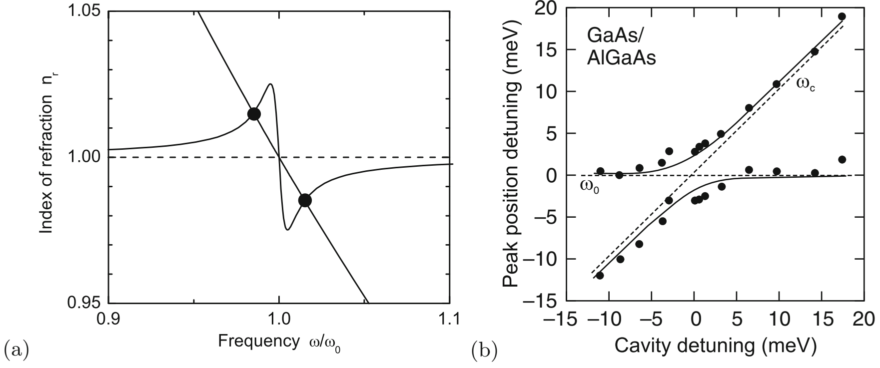

Fig. 18.18. (**a**) Graphical representation of (18.39) with the two solutions marked with *circles* for $n_\infty = 1$ (*dashed line*), $f = 10^{-3}$, $\Gamma/\omega_0 = 10^{-2}$ and $\omega_0 = \omega_\mathrm{m}$. (**b**) Reflectance peak positions (experimental data (*circles*) at $T = 5\,\mathrm{K}$) vs. cavity detuning $\omega_\mathrm{c} - \omega_0$ for a cavity with two GaAs/AlGaAs Bragg mirrors (24/33 pairs for the front/bottom mirror) and five embedded quantum wells whose resonances are closely matched. *Solid lines* are a theoretical fit according to (18.42) with $\Omega_0 = 4.3\,\mathrm{meV}$. The *dashed lines* show the electronic resonance ω_0 and the cavity resonance ω_c. Part (**b**) adapted from [1069]

A detailed theory of cavity polaritons is given in [1071]. The nonlinear optics of normal mode coupling in semiconductor microcavities is reviewed in [1072].

The in-plane dispersion of the cavity polaritons depends on the coupling strength. First, the photon dispersion is given by

$$E_\mathrm{ph}(\mathbf{k}) = \hbar\omega = \hbar ck = \hbar c\left(k_\parallel^2 + k_z^2\right)^{1/2} , \tag{18.43}$$

where $k_\parallel$ is the in-plane k-vector and k_z is given by the resonance condition, $k_z = \omega_m/c$ with (18.34),

$$k_z = m\,\frac{\pi}{n_\mathrm{B}L} . \tag{18.44}$$

Thus the dispersion relation is no longer linear as for freely propagating light.

For small $k_\parallel$ this leads to an (in-plane) effective photon 'rest mass', applying (6.37),

$$\frac{1}{m^*_\mathrm{ph}} = \frac{1}{\hbar^2}\,\frac{\partial^2 E_\mathrm{ph}}{\partial k^2} . \tag{18.45}$$

We find

$$m^*_\mathrm{ph} = \frac{\hbar k_z}{c} = \frac{\hbar\omega(k_\parallel = 0)}{c^2} . \tag{18.46}$$

Now we assume the electronic oscillator to be in resonance with the photon dispersion at $k_\parallel = 0$, i.e. $E_\mathrm{el} = \hbar\omega(k_\parallel = 0)$. The electronic resonance shall have vanishing dispersion for simplicity since the exciton mass is much

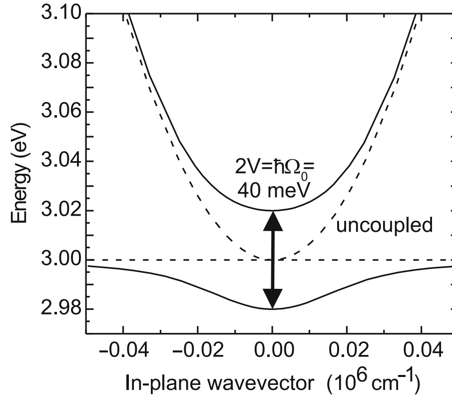

Fig. 18.19. Dispersion of cavity photon mode and electronic resonance at $E_{\mathrm{el}} = 3.0\,\mathrm{eV}$ (*dashed lines*) and coupled modes (*solid lines*) for $2V = 40\,\mathrm{meV}$

larger than (18.46). The eigenwert equation of the coupled system, resembling (6.64), is

$$\begin{vmatrix} E - E_{\mathrm{ph}} & V \\ V & E - E_{\mathrm{el}} \end{vmatrix} = 0 \,, \tag{18.47}$$

with two solutions, called the upper and lower cavity polariton branch, visualized in Fig. 18.19. Their splitting at $k_{\|} = 0$ is $2V$. Thus the coupling parameter $V = \hbar\Omega_0/2$ corresponds [1071] to the Rabi frequency (18.40). Experimental values for the splitting of 3–15meV in InAlGaAs based [1069, 1073–1076], 17–44meV in CdZnTeSe based [1077], 6–60meV in AlInGaN based [1078–1082] and 78 meV in ZnO based [1083] microcavities were found. It is possible to condensate cavity polaritons in the minimum of the dispersion around $k_{\|} = 0$ (Bose-Einstein condensation). In [1084] stimulated scattering and gain from cavity polaritons have been reported.

18.2 Microscopic Resonators

18.2.1 Microdiscs

A microdisc is a cylindrical resonator with a thickness d that is small compared to the radius R. It can be fabricated from semiconductors and semiconductor heterostructures using patterning and material-selective etching. With underetching a mostly free-standing disc can be made that resides on a post (Fig. 18.20).

The coordinate system is (ρ, ϕ, z) with the z direction being perpendicular to the disc area. Typically, the disc is so thin that there is only one node along z. Solving the wave equation in this geometry [1086], the modes are characterized by two numbers (m, l). m describes the number of zeros

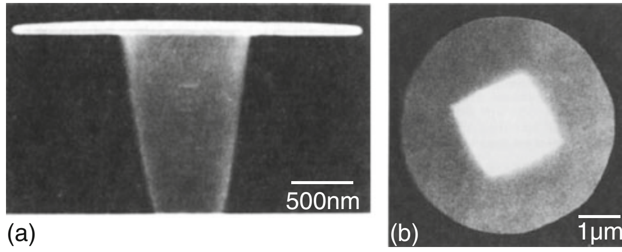

Fig. 18.20. (**a**) Side view of a 3-µm diameter disc containing one 10-nm InGaAs quantum well between 20-nm InGaAsP barriers standing on an InP pillar that has been selectively underetched using HCl. (**b**) Top view SEM image of a 5-µm diameter InGaAsP microdisc. The pedestal shape is a rhombus due to anisotropic etching of the HCl. Adapted from [1085], reprinted with permission, ©1992 AIP

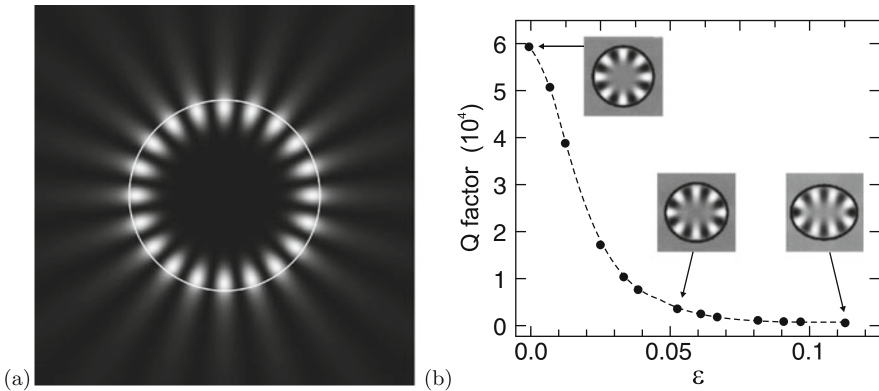

Fig. 18.21. (**a**) Field intensity for whispering gallery mode (10, 0) (TM-polarized) for a circle with 1 µm radius (shown as *white line*) and $n = 1.5$. The image size is $4 \times 4\,\mu\text{m}^2$. (**b**) Theoretical quality factor of a 2-µm InP microdisc as a function of the deformation parameter (18.49). The *insets* show (8,0) whispering gallery modes at a wavelength of 1.55 µm for $n = 3.4$. Part (**b**) adapted from [1088]

along the azimuthal direction ϕ with the field amplitude being proportional to $\exp(\pm i m \phi)$. Thus, except for $m = 0$, the modes are simply degenerate. Modes with $\mathcal{E}_\text{z} = 0$ are called TE modes. This is the preferred polarization of emission. The number l denotes the number of zeros in the radial direction. Only for modes with $|m| = 1$, is the intensity nonzero on the axis, i.e. for $\rho = 0$. All other modes have vanishing intensity in the disc center.

The light intensity in whispering gallery modes is preferentially concentrated along the circumference of the disc as shown in Fig. 18.21a. Since the light can only escape via evanescent waves, the light is well 'captured' in such a mode. The Q-factor (18.31) is extremely high and takes values of several 10^4. In order to couple light out of such a disc, deformed resonators, e.g. with

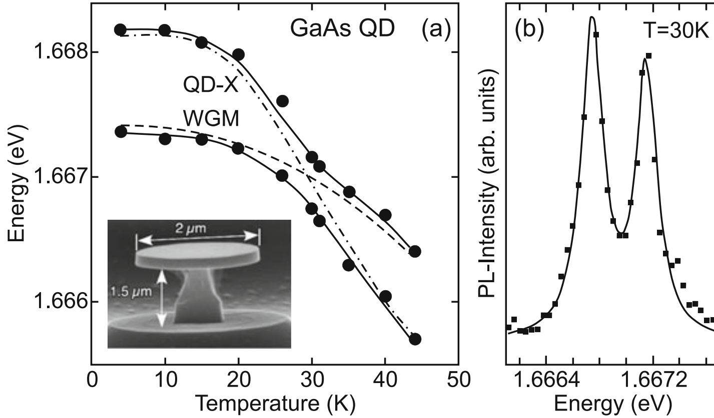

Fig. 18.22. Strong coupling of a single QD exciton (due to monolayer fluctuation in a 13 ML thick GaAs/$Al_{0.33}Ga_{0.67}As$ QW) with a WGM in a microdisk of 2 μm diameter (*inset*). (**a**) Anti-crossing of upper and lower peak for various temperatures. *Symbols* are data points, *solid lines* are theory considering coupling. The *dashed* (*dash-dotted*) line is the expected temperature shift of the WGM mode (exciton energy). (**b**) Photoluminescence spectrum at the anti-crossing point ($T = 30\,\mathrm{K}$). Experimental data (*squares*) and fit with two peaks (*solid line*). Adapted from [1089]

a defect in the form of protrusions [1087], were devised. Deformed resonators are discussed in more detail in the next section.

The strong coupling of a QD exciton to a whispering gallery mode is shown in Fig. 18.22 where anti-crossing behavior is observed at low temperatures. Tuning is achieved by temperature variation. Behavior of a similar system in the weak coupling regime is shown in Fig. 18.24.

18.2.2 Purcell Effect

According to Fermi's golden rule (18.1), the probability of an optical transition depends on the density of available optical modes (final states). If the density of modes is enhanced compared to its vacuum value (18.2) at a resonance of an optical cavity, the lifetime of the electronic state decreases by the Purcell factor [1091]

$$F_{\mathrm{P}} = \frac{3}{4\pi^2}\, Q\, \frac{(\lambda/n)^3}{V} \,, \tag{18.48}$$

where n is the refractive index of the medium, Q is the quality factor of the cavity resonance and V is the effective mode volume.[3] Experiments on the emission of quantum dots (that generally provide small absorption and

[3] V is given by the spatial integral of the vacuum field intensity for the cavity mode, divided by its maximum value.

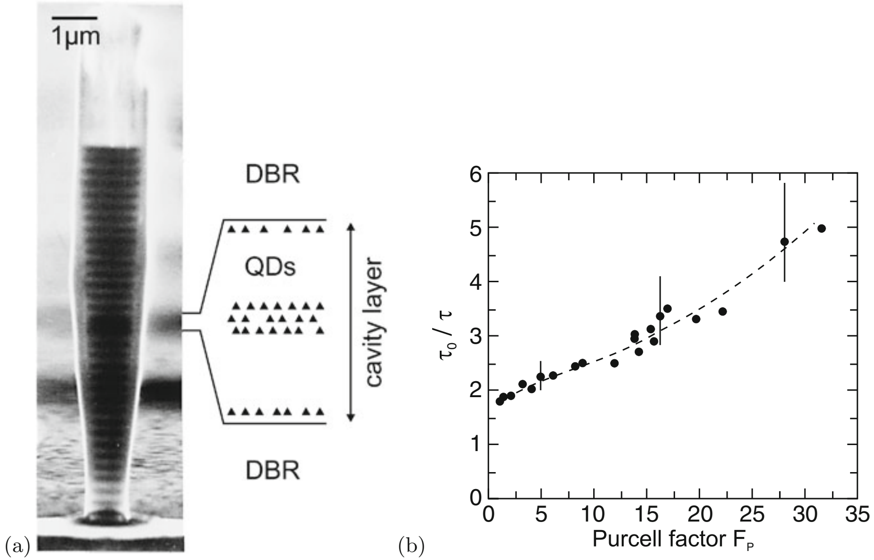

Fig. 18.23. (**a**) Micropillar with MBE-grown GaAs/AlAs DBRs and a cavity containing five layers of InAs quantum dots as indicated. The pillar has been prepared by reactive ion etching. Reprinted with permission from [1090], ©1998 APS. (**b**) Experimental decay time τ of on-resonance quantum dot luminescence scaled by off-resonance lifetime $\tau_0 = 1.1\,\mathrm{ns}$ (close to lifetime in a QD in bulk) for a variety of micropillars with different Purcell factors F_P. The *error bars* correspond to the measurement accuracy of the decay time ($\pm 70\,\mathrm{ps}$), the *dashed line* is a guide to the eye. Adapted from [1090]

thus allow for the weak coupling regime) in etched micropillars containing a microcavity (Fig. 18.23a) have shown that indeed the luminescence decay is faster for cavities with large Purcell factor (Fig. 18.23b) [1090]. The resonance of cavity mode and emitter leads to an enhanced emission intensity as shown in Fig. 18.24 for the exciton emission of a single quantum dot in a microdisc [1092].

18.2.3 Deformed Resonators

The whispering gallery modes in circular (or spherical) cavities are long-lived and emission goes into all angles. Light escape is based only on the exponentially slow process of evanescent leakage (neglecting disorder effects such as surface roughness). In order to overcome the isotropic light emission, the resonator needs to be deformed. This can be accomplished with an ellipsoidal shape, i.e.

$$r(\phi) = R\,[1 + \epsilon \cos \phi]\ , \tag{18.49}$$

where $1 + 2\epsilon$ is the aspect ratio of the ellipse. The increased radiation leads to a decrease of the Q-factor as shown in Fig. 18.21b. Also, a new decay

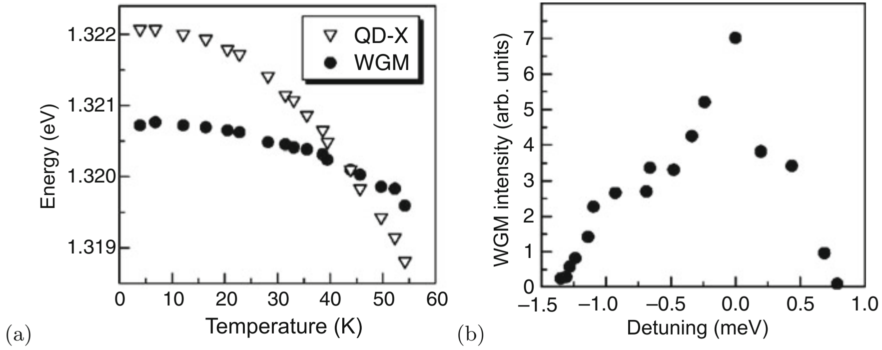

Fig. 18.24. (**a**) Temperature dependence of the energy positions of the whispering gallery mode (WGM) of a 5-µm diameter AlGaAs/GaAs microdisc ($Q = 6500$) and the single-exciton resonance of a single InAs quantum dot contained within the disc. (**b**) Intensity of WGM mode as a function of the detuning $E_{\mathrm{WGM}} - E_{\mathrm{QD-X}}$ from the QD single exciton resonance. The excitation density was 15 Wcm^{-2} for all data. Adapted from [1092]

process, refractive escape, becomes possible. A ray that is initially in a whispering gallery trajectory diffuses in phase space until finally an angle smaller than the critical angle for total reflection (9.3) is reached. The ray dynamics becomes partially chaotic [1093].

One other possible deformation of the circular disc geometry is a 'flattened quadrupole' as shown in Fig. 18.25a. This shape can be parameterized by a deformation parameter ϵ and the angle-dependent radius $r(\phi)$ given by

$$r(\phi) = R\,\left[1 + 2\epsilon\cos^2(2\phi)\right]^{1/2}\ . \tag{18.50}$$

For small deformation, the whispering gallery modes become chaotic and exhibit preferred emission along the long axis of the resonator (Fig. 18.25b). For larger deformations ($\epsilon \geq 0.14$), a stronger and qualitatively different directionality occurs in the shape of a bow-tie [1094] as shown in Fig. 18.25c. The optical laser power extracted from deformed resonators was found to increase exponentially with ϵ; for $\epsilon = 0.2$ it was 50 times larger than for the circular resonator.

Another modification that can be applied to the microdisc in order to increase outcoupling of light, is the spiral resonator [1095] as shown in Fig. 18.26a. The radius is parameterized by

$$r(\phi) = R\left[1 + \frac{\epsilon}{2\pi}\,\phi\right]\ . \tag{18.51}$$

The experimental emission pattern is displayed in Fig. 18.26b. It exhibits a maximum along the direction of the tangent at the radius step. The simulated near-field intensity of such an emission mode is shown in Fig. 18.26c. In a spiral laser, ray dynamics is also chaotic [1096].

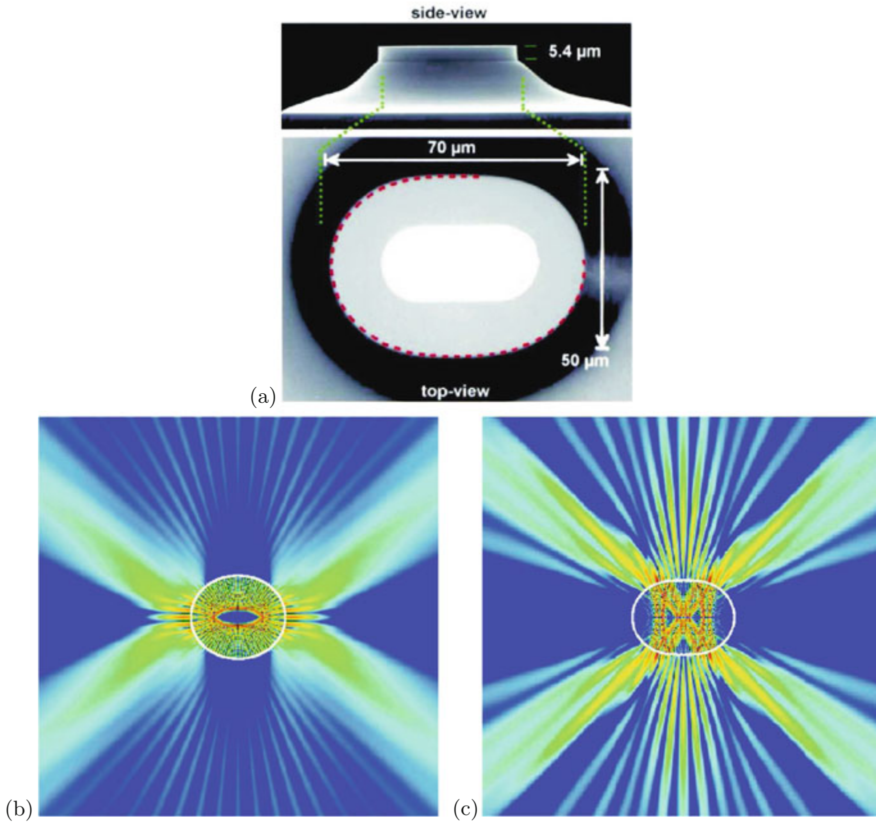

Fig. 18.25. (**a**) SEM image of a quadrupolar cylinder laser with deformation parameter $\epsilon \approx 0.16$ on a sloped InP pedestal. The *light grey area* in the top view is the electrical contact. (**b**) Simulated near-field intensity pattern of a chaotic whispering gallery mode for $\epsilon = 0.06$ and $n = 3.3$. (**c**) Simulated near-field intensity pattern of a bow-tie mode for $\epsilon = 0.15$. The length of the minor axis for (**b**) and (**c**) is $50\,\mu$m. Reprinted with permission from [1094], ©1998 AAAS

18.2.4 Hexagonal Cavities

Hexagonal cavities develop, e.g., in microcrystals of wurtzite semiconductors (with the c-axis along the longitudinal axis of the pillar). In Fig. 18.27a, a ZnO tapered hexagonal resonator (needle) is shown. Whispering gallery modes modulate the intensity of the green ZnO luminescence [1098].[4] In a simple plane-wave model, the resonance condition is given by

[4]We note that besides the green luminescence as in Fig. 10.19, an unstructured green band also occurs that is observed here. Its origin may be linked to the oxygen vacancy [1099].

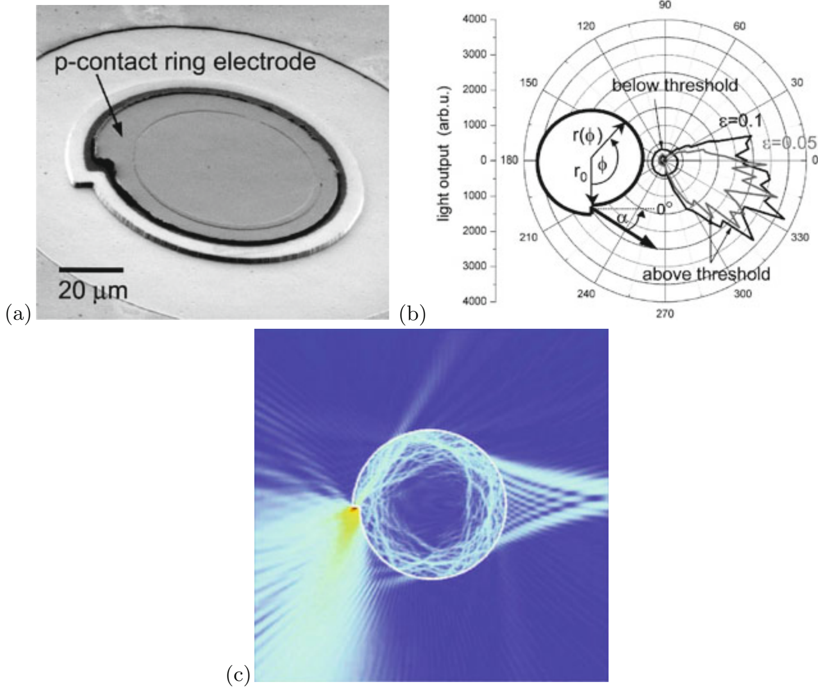

Fig. 18.26. (**a**) SEM image of a microcavity disc laser diode with a disc radius of 50 µm. The p-contact ring electrode defines the areas through which carriers are injected into the microdisc and where stimulated emission can take place. (**b**) Radial distribution of the light output from the spiral-shaped microdisc laser diode measured below and above threshold. The radius of the spiral microdisc was $r_0 = 250\,\mu\mathrm{m}$ and the deformation parameters were $\epsilon = 0.05$ (*grey*) and $\epsilon = 0.10$ (*black*). An emission beam at an angle of $\alpha = 0°$ corresponds to a direction normal to the notch surface as shown in the *inset*. Below the laser threshold, the emission pattern is essentially isotropic and independent of the deformation parameter. Above the threshold, directional emission is clearly observed with the emission direction at a tilt angle $\alpha \approx 25°$. The measured divergence angle of the far-field pattern is $\sim 75°$ for $\epsilon = 0.10$ and $\sim 60°$ for $\epsilon = 0.05$. Reprinted with permission from [1097], ©2004 AIP. (**c**) Simulated near-field intensity pattern of an emission mode with $nkR \approx 200$ for deformation $\epsilon = 0.10$. Reprinted with permission from [1095], ©2003 AIP

$$6R_{\mathrm{i}} = \frac{hc}{nE}\left[N + \frac{6}{\pi}\arctan\left(\beta\sqrt{3n^2-4}\right)\right] , \tag{18.52}$$

where R_{i} is the radius of the inner circle (Fig. 18.27d), n is the index of refraction, N is the mode number and β is given by $\beta_{\mathrm{TM}} = 1/n$ ($\beta_{\mathrm{TE}} = n$) for TM (TE) polarization, respectively. Due to birefringence, $n_{||}$ ($n_{\perp}$) has to be used as the index of refraction for TM (TE) polarization.

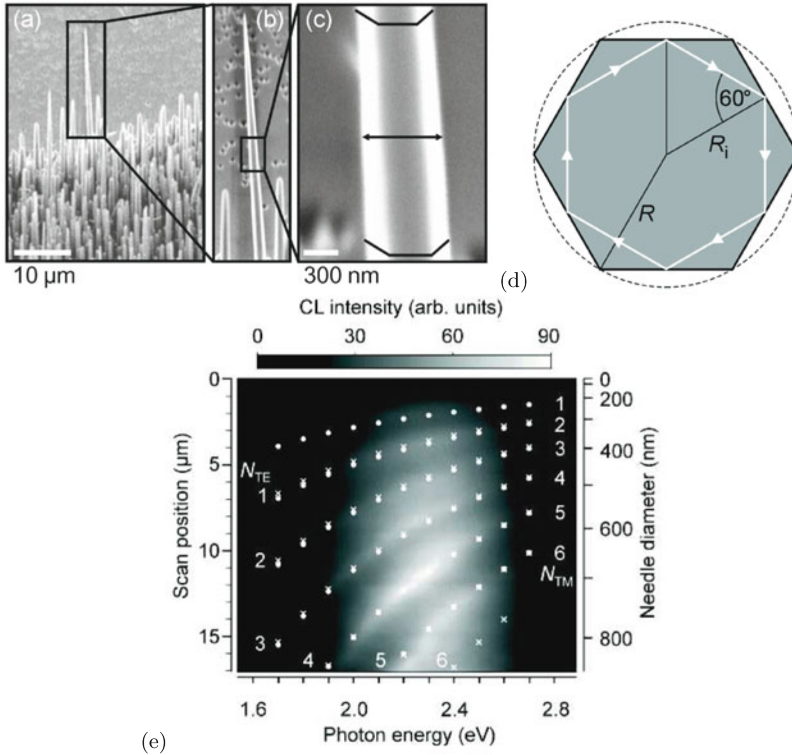

Fig. 18.27. (**a**)–(**c**) SEM images of ZnO nanoneedle fabricated by pulsed laser deposition. (**d**) Schematic geometry of cross-sectional plane. R_i (R) is the radius of the incircle (circumscribing circle). The circumference of the inscribed *white hexagon*, representing the path of a whispering gallery mode, has a length of $6R_i$. (**e**) Two-dimensional plot of spectra recorded along a linescan along the needle's longitudinal axis. The left vertical axis shows the linescan position x, the right one refers to the respective needle diameter D. The spectral maxima, i.e. the measured WGM energies, appear as bright belts going from the bottom left corner to the right upper one. With decreasing diameter, all resonances shift systematically to higher energies. The *white dots* give theoretical TM-resonance energy positions obtained from (18.52), *white crosses* give the same for TE-polarization. Reprinted with permission from [1098], ©2004 APS

A $N = 26$ whispering gallery mode of a hexagonal resonator is shown in Fig. 18.28c,d. The 6-fold symmetric emission stems from the edges of the hexagon. While whispering gallery resonators have typically mode numbers $N \gg 1$, in such hexagonal resonators the whispering gallery modes could be followed down to $N = 1$ [1098] as shown in Fig. 18.27a,b,e.

Under high optical pumping laser action occurs on the whispering gallery modes. The peak positions, close to the band gap in the spectral region of the electron-hole plasma, follow (18.52) [1101], as shown for various diameters in Fig. 18.29.

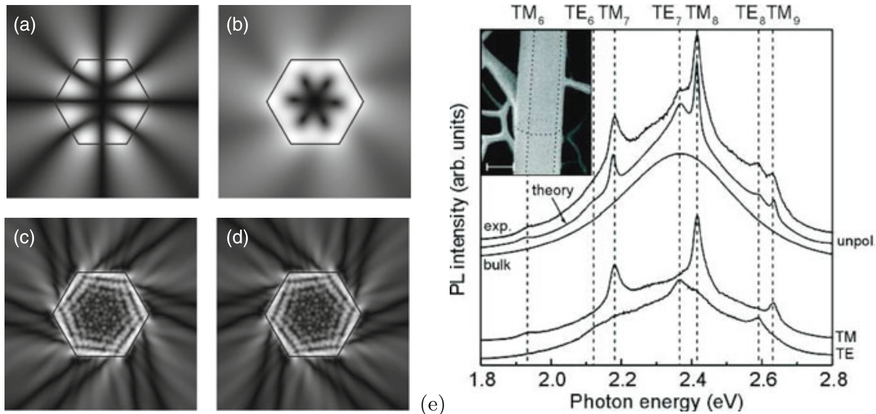

Fig. 18.28. Simulated near-field intensity pattern of modes in a cavity with hexagonal cross section (absolute value of electric field in linear grey scale): Modes ($N = 4$) with (**a**) symmetry $-a$ and (**b**) mode 4+ (nomenclature from [1100]) for $n = 2.1$ and $kR = 3.1553 - \mathrm{i}0.0748$. Modes (**c**) 26− and (**d**) 26+ for $n = 1.466$ and $kR = 22.8725 - \mathrm{i}0.1064$. The displayed modes have a chiral pattern. Emission originates mostly from the corners. (**e**) Micro-photoluminescence spectra of a single ZnO nanopillar. The three topmost curves are unpolarized. The curve labeled 'bulk' shows the unmodulated luminescence of the green luminescence in bulk. The line labeled 'exp.' shows the experimental μ-PL spectrum of the investigated nanopillar. The experimental spectra recorded for TM- and TE-polarization, respectively, are shown in the lowest two curves. The curve labeled 'theory' displays the theoretical luminescence spectra. *Dashed vertical lines* are guides to the eye referring to the spectral position of the dominating WGMs. The *inset* shows a SEM image of the investigated pillar, the scale bar has a length of 500 nm. The *dotted lines* show the position of the edges of the hexagonal resonator obtained from topography contrast

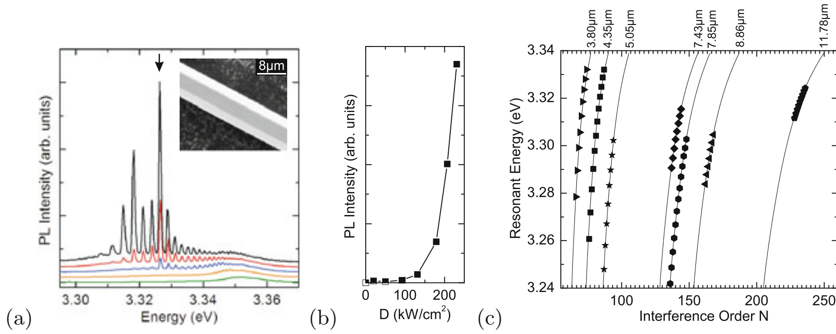

Fig. 18.29. (**a**) Photoluminescence spectra of a ZnO microwire with hexagonal cross section for various pump power densities (*lowest curve*: $D = 60\,\mathrm{kW/cm^2}$, *top curve*: $D = 250\,\mathrm{kW/cm^2}$) at $T = 10\,\mathrm{K}$. The inset shows the scanning electron microscopy image of a typical microwire ($d = 6.40\,\mu\mathrm{m}$). (**b**) Dependence of the emitted PL intensity of a selected lasing peak (denoted by an *arrow* in the spectrum in part (**a**)) on the excitation density D. *Lines* are guide to the eyes. (**c**) Dependence of the resonant energies on the interference order N for wires with different diameters as labeled on top of the graph. *Lines* are the predicted theoretical values calculated from (18.52) using diameter values obtained from SEM measurements; the *symbols* represent the experimentally observed peaks. Adapted from [1101]

19 Transparent Conductive Oxide Semiconductors

Transparent conductive oxides (TCO) are semiconductors that are simultaneous transparent and highly conductive. Therefore they can serve as transparent contacts, e.g. as a solar cell front contact or in display applications. The materials are typically fabricated in the form of thin films on glass, polymers or similar substrates and devices. The crystallographic structure is polycrystalline or amorphous. The first TCO investigated was CdO in pressed powder [1102] and thin film form [27]. The recent historic development of the resistivity of the most important TCO materials in the last 30 years is shown in Fig. 19.1. Further information on TCO films can be found in [1103–1105].

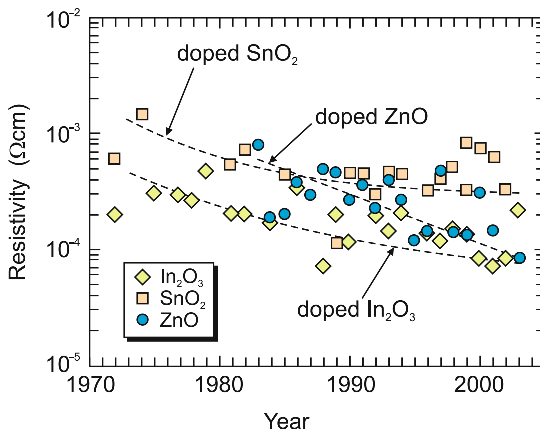

Fig. 19.1. Historical development of the resistivity of doped ZnO (*circles*), In_2O_3 (*squares*) and SnO_2 (*diamonds*) TCO films. Adapted from [1105]

19.1 Materials

Any wide-gap ($E_g > 3\,eV$) semiconductor that is conductive, e.g. due to intrinsic defects or by chemical impurities (doping), can be considered to be a TCO. Pratically only a few, non-toxic materials that can be easily deposited are of importance. The first TCO application was heating of air plane windows. As always in semiconductor technology, price drives the suitability for

M. Grundmann, *The Physics of Semiconductors*, 2nd ed., Graduate Texts in Physics, DOI 10.1007/978-3-642-13884-3_19,
© Springer-Verlag Berlin Heidelberg 2010

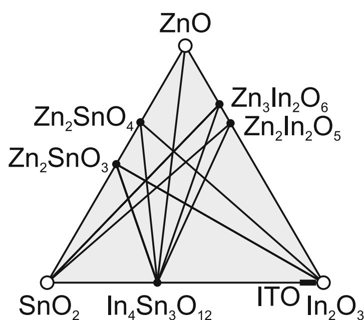

Fig. 19.2. Practical TCO materials

applications. This in particular true for TCO applications since they include large area devices such as solar cells, displays and also large glass panes for electromagnetic shielding and architectural heat and IR transparency management. Therefore large quantities of TCO are needed. The popular ITO (indium-tin-oxide) suffers from large indium price and potential indium scarcity, opening the field for aluminum-doped ZnO (ZAO) which is abundant. Possible other compounds including Cd are of no practical interest due to toxicity. Conductive GaN has not been considered due to its large processing temperatures. All practical TCO materials contain either Zn, Sn or In (Fig. 19.2). A number of TCO materials is reviewed in [1106]. TCO are mostly n-conducting. Also p-conducting TCOs have been reported [1107], but there has been so far no report on a practical transparent electrode.

The term ITO stands for a variety of Sn-doped indium oxide (In_2O_3) materials, the Sn content being typically in the 5–10% range but not strictly defined. The crystal structure of In_2O_3 [1108] is shown in Fig. 19.3. The effect of the replacement of indium by tin atoms in In_2O_3 on mechanical, electrical and optical properties of ITO has been calculated in [1109] using DFT. In Fig. 19.4 the band structures of pure In_2O_3 and $(Sn_{0.065}In_{0.935})_2O_3$ (one out of 16 indium atoms was replaced in the calculation) are compared [1110]. The fundamental band gap is slightly lowered, the high doping introduces a gigantic Burstein-Moss shift. Additionally another band gap opens that splits the lowest conduction band. Also the conduction mechanism in amorphous oxides has been discussed [1111].

19.2 Properties

The best conductivity of TCOs is in the range of $10^{-4}\,\Omega\,\mathrm{cm}$ for the specific resistivity. Such value is about three orders of magnitude smaller than that of metals. However, the TCO meanwhile is highly transparent in the visible region, while metals become transparent only in the UV region because of their high plasma frequency (cf. Sect. 9.7).

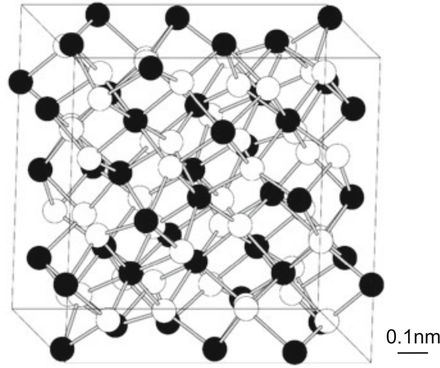

Fig. 19.3. The bixbyite crystal structure of indium oxide ($In_{32}O_{48}$) showing one unit cell where the indium and oxygen atoms are represented by the *full* and *empty circles*, respectively. Adapted from [1109]

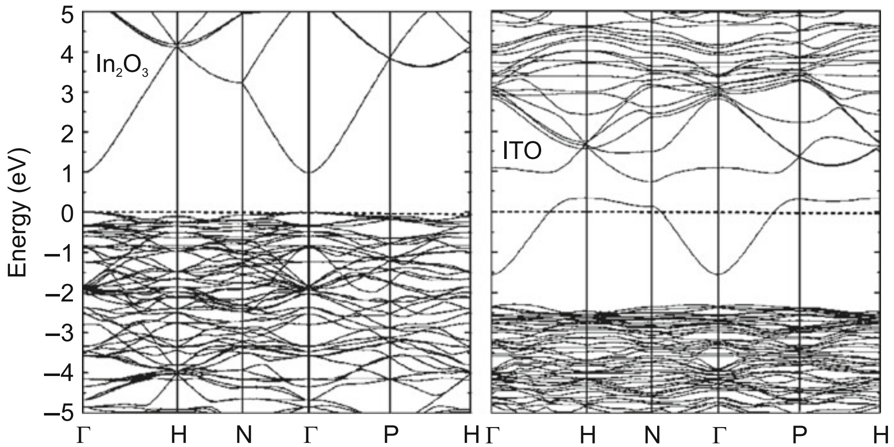

Fig. 19.4. Comparison of the band structure of In_2O_3 (*left*) and $(Sn_{0.065}In_{0.935})_2O_3$ (*right*). The position of the Fermi level is for both cases at $E = 0$. Adapted from [1110]

The conduction mechanism in ZnO:Al is band transport in a highly doped semiconductor. The carrier concentration is typically around $10^{21}\,cm^{-3}$. One of the best results is a (Hall) mobility of $47.6\,cm^2/Vs$, leading to a specific resistivity of $8.5 \times 10^{-5}\,\Omega\,cm$ [1112]. The mobility is limited by (doping level dependent) ionized impurity scattering (Sect. 8.3.3) as shown in Fig. 19.5 for various films. Also the mobility is correlated (Fig. 19.6) with scattering at structural defects such as grain boundaries [1113] (cf. Fig. 8.4). We note that the carrier mobility in a (polycrystalline) TCO is not very different from that in highly doped (crystalline) silicon (Fig. 8.7).

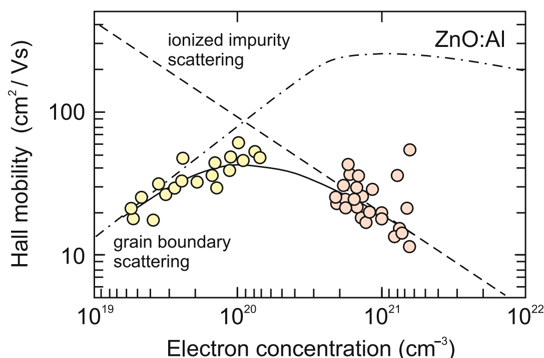

Fig. 19.5. Hall mobility for various ZnO:Al TCO thin films as a function of carrier (electron) concentration. The *dashed line* is the Brooks–Hering theory of ionized impurity scattering (taking into account non-parabolicity of the conduction band). The *dash-dotted* line is mobility in the presence of grain boundaries, the *solid line* is combined theory. *Symbols* are experimental data from two sets of samples. Adapted from [1105]

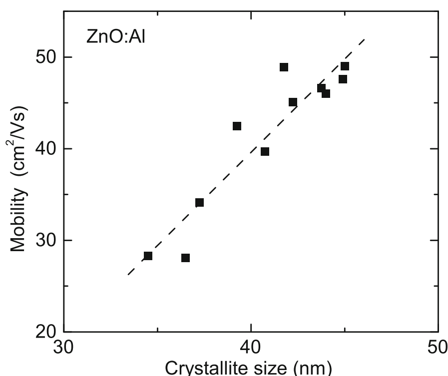

Fig. 19.6. Hall mobility of ZnO:Al films (of varying thickness) vs. the crystallite size. Experimental data (from [1105]) are shown as *symbols*. The *dashed line* is a guide to the eyes

Conductivity and transparency are, however, linked. The high doping of the TCO leads to shifts in the band gap (renormalization and Burstein-Moss shift), band tails and the like that can introduce absorption in the visible spectral region. Also the infrared transparency is related to the conductivity by free carrier absorption and the plasma edge (Sect. 9.7). With increasing carrier density, the plasma edge shifts into the visible spectral range (Fig. 19.7a), limiting the possible maximum carrier density to several 10^{21} cm^{-3}, the exact value depending on the carrier mass. In Fig. 19.7b the transparency spectra of two SnO_2 films with different conductivity are compared. The higher conductivity due to larger carrier concentration leads to reduced IR transparency.

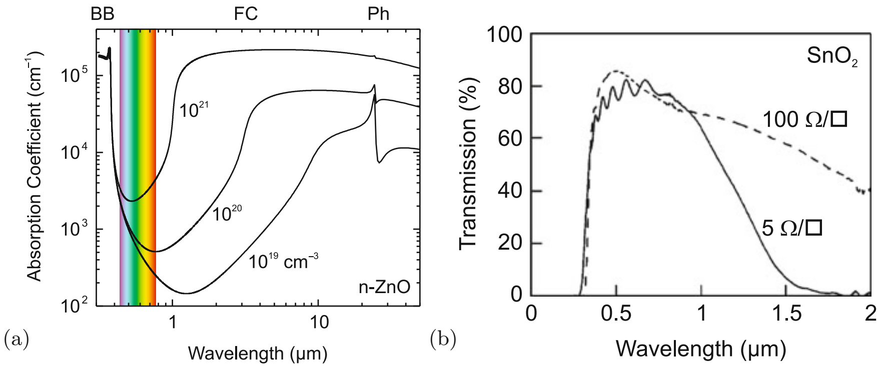

Fig. 19.7. (**a**) Absorption coefficient of n-type ZnO for various electron concentrations as labeled. Spectra synthesized from ellipsometric data of thin films. The visible spectral range is indicated. The contributing absorption processes are band-band transitions (BB), free carrier absorption (FC) and phonon-related absorption (Ph) as labeled. (**b**) Transparency vs. wavelength spectra of two SnO_2 films with different conductivity as labeled. Adapted from [1114]

Generally, the transmission of a TCO is limited by the band edge on the high energy side of the spectrum and the plasma edge on the low energy side of the spectrum. The limited carrier concentration due to the onset of free carrier absorption in the visible spectral range ($\sim 3 \times 10^{21}\,\mathrm{cm}^{-3}$) and the limited mobility in the presence of such high impurity concentration (max. $50\,\mathrm{cm}^2/\mathrm{Vs}$) restrict the minimum resistivity of a TCO (or any transparent conductor) to about $4 \times 10^{-5}\,\Omega\,\mathrm{cm}$ [1115].

Part III

Applications

20 Diodes

20.1 Introduction

One of the simplest[1] semiconductor devices is the diode. It is a so-called two-terminal device, i.e. a device with two leads. The most prominent property of a diode is the rectifying current–voltage (I–V) characteristic. This function was initially realized with vacuum tubes (Fig. 20.1); a heated filament emits electrons that are transferred through vacuum to the anode if it is on a positive potential. The semiconductor diode technology led to a tremendous miniaturization, integration with other devices (in planar technology) and cost reduction.

We distinguish[2] *unipolar* diodes, for which the *majority* carriers cause the effects (e.g. metal–semiconductor diodes), and *bipolar* diodes in which *minority* carriers play the decisive role, e.g. in the pn-junction diode.

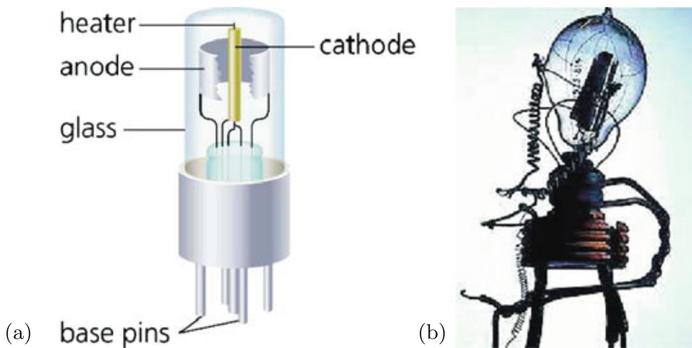

Fig. 20.1. (**a**) Schematic image of a vacuum diode. The electron current flows from the heated cathode to the anode when the latter is at a positive potential. (**b**) John A. Fleming's first diode 'valve', 1904

[1]The simplest device is a resistor made from a homogeneous piece of semiconductor, used, e.g., as a part of an integrated circuit or as a photoresistor as discussed in Sect. 21.2.

[2]This distinction is not only made for diodes but also for many other semiconductor devices such as transistors, see Sect. 23.

M. Grundmann, *The Physics of Semiconductors*, 2nd ed., Graduate Texts in Physics, DOI 10.1007/978-3-642-13884-3_20,

© Springer-Verlag Berlin Heidelberg 2010

20.2 Metal–Semiconductor Contacts

The metal–semiconductor contact was investigated in 1874 by F. Braun (see Sect. 1.1). For metal sulfides, e.g. $CuFeS_2$, he found nonohmic behavior. We remark here that we treat first metal–semiconductor contacts with rectifying properties. Later it becomes understandable that metal–semiconductor contacts can also be used as ohmic contacts, i.e. contacts with a very small contact resistance. Rectifying metal–semiconductor contacts are also called Schottky diodes. A very important variation are metal–insulator–semiconductor diodes for which an insulator, mostly an oxide, is sandwiched between the metal and the semiconductor. Such diodes are treated in Sect. 20.3. Reviews on Schottky diodes can be found in [1116–1120].

20.2.1 Band Diagram in Equilibrium

The metal and the semiconductor have generally different positions of the Fermi levels relative to the vacuum level. When the metal is in contact with the semiconductor, charges will flow in such a way that in thermodynamic equilibrium the Fermi level is constant throughout the structure.[3] In the following we treat two limiting cases: The contact of a metal with a semiconductor without any surface states (Schottky–Mott model) and a contact where the semiconductor has a very high density of surface states (Bardeen model).

The position of the Fermi level in the metal is given by the work function W_m that is shown in Fig. 20.2 for various metals (see also Table 20.1). The

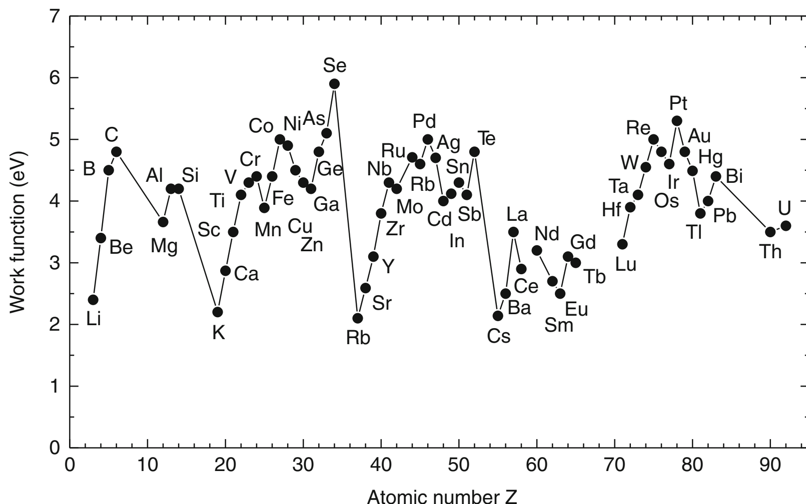

Fig. 20.2. Work function W_m of various metals

[3]This situation is similar to the heterostructure interface (Sect. 11.3.4), with the metal, however, having a very short screening length.

work function reflects the atomic shell structure; minima of the work function exist for group-I elements. The work function is the energy difference between the vacuum level (an electron is at rest in an infinite distance from the metal surface) and the metal Fermi level ($W_m > 0$). Since the electron density in the metal conduction band is very high, the position of the metal Fermi level does not change considerably when charge is exchanged between the metal and the semiconductor.

Since in a semiconductor the Fermi level depends strongly on the doping and temperature it is not useful to characterize the material itself. For semiconductors the electron affinity $\chi_{sc} = E_{vac} - E_C > 0$ is defined as the energy difference between the vacuum level and the conduction-band edge (see Fig. 11.14).

Ideal Band Structure

When the metal and the semiconductor are not in contact (Fig. 20.3a), the metal is characterized by its work function $W_m = E_{vac} - E_F$ and the semiconductor by its electron affinity χ_{sc}. First, we assume that $W_m > \chi_{sc}$. For an n-type semiconductor, the energy difference between the Fermi level and

Table 20.1. Values of the work function W_m of various metals

Z	element	W_m (eV)	Z	element	W_m (eV)	Z	element	W_m (eV)
3	Li	2.4	37	Rb	2.1	64	Gd	3.1
4	Be	3.4	38	Sr	2.59	65	Tb	3.0
5	B	4.5	39	Y	3.1	66	Dy	–
6	C	4.8	40	Zr	3.8	67	Ho	–
12	Mg	3.66	41	Nb	4.3	68	Er	–
13	Al	4.2	42	Mo	4.2	69	Tm	–
14	Si	4.2	44	Ru	4.71	70	Yb	–
19	K	2.2	45	Rh	4.6	71	Lu	3.3
20	Ca	2.87	46	Pd	5.0	72	Hf	3.9
21	Sc	3.5	47	Ag	4.7	73	Ta	4.1
22	Ti	4.1	48	Cd	4.0	74	W	4.55
23	V	4.3	49	In	4.12	75	Re	5.0
24	Cr	4.4	50	Sn	4.3	76	Os	4.8
25	Mn	3.89	51	Sb	4.1	77	Ir	4.6
26	Fe	4.4	52	Te	4.8	78	Pt	5.3
27	Co	5.0	55	Cs	2.14	79	Au	4.8
28	Ni	4.9	56	Ba	2.5	80	Hg	4.49
29	Cu	4.5	57	La	3.5	81	Tl	3.8
30	Zn	4.3	58	Ce	2.9	82	Pb	4.0
31	Ga	4.2	59	Pr	–	83	Bi	4.4
32	Ge	4.8	60	Nd	3.2	90	Th	3.5
33	As	5.1	62	Sm	2.7	92	U	3.6
34	Se	5.9	63	Eu	2.5			

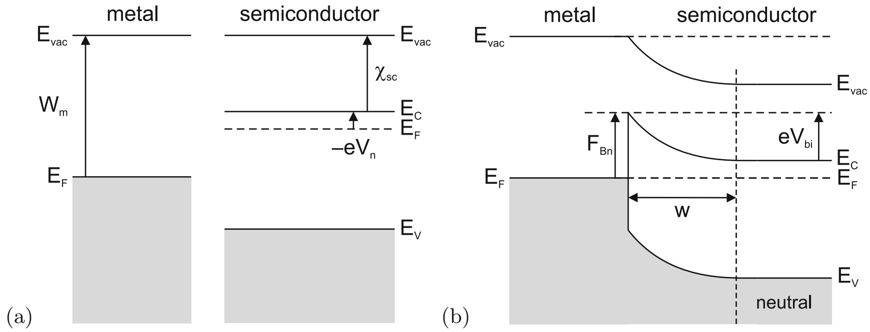

Fig. 20.3. Schematic band structure of a metal–semiconductor junction that is dominated by bulk properties of the semiconductor. (**a**) no contact, (**b**) metal and semiconductor in contact. w denotes the width of the depletion layer. Outside the depletion layer the semiconductor is neutral. $F_{\mathrm{B,n}}$ denotes the Schottky barrier height, V_{bi} denotes the built-in voltage (here $V_{\mathrm{bi}} > 0$)

the conduction band is denoted as $-eV_{\mathrm{n}} = E_{\mathrm{C}} - E_{\mathrm{F}}$ ($V_{\mathrm{n}} < 0$ for nondegenerate semiconductors). Thus, the position of the semiconductor Fermi level is given as

$$E_{\mathrm{F}} = E_{\mathrm{vac}} - \chi_{\mathrm{sc}} + eV_{\mathrm{n}} \ . \tag{20.1}$$

If the metal and semiconductor are brought into contact the Fermi levels will equilibrate. For the case of Fig. 20.3 ($E_{\mathrm{F,sc}} > E_{\mathrm{F,m}}$) electrons will flow from the semiconductor to the metal. The negative surface charge of the metal is compensated by a positive charge (due to D^+) in the semiconductor in the vicinity of the surface. Eventually a (Schottky) barrier of height[4] F_{Bn}

$$F_{\mathrm{Bn}} = W_{\mathrm{m}} - \chi_{\mathrm{sc}} \tag{20.2}$$

forms at the interface. The subscript 'n' stands for the contact on an n-type semiconductor. Surface/interface effects such as non-matching bonds, surface states, etc. are neglected at this point. In the semiconductor there exists a positively charged region that is called the *depletion layer* or space-charge region. Its extension (w in Fig. 20.3b) and properties will be discussed in Sect. 20.2.2. The space charge region in the metal is very thin due to the small screening length.

For a contact on a p-type semiconductor the barrier F_{Bp} (to the valence band) is (see Fig. 20.4d)

$$F_{\mathrm{Bp}} = E_{\mathrm{g}} - (W_{\mathrm{m}} - \chi_{\mathrm{sc}}) \ . \tag{20.3}$$

Between the surface of the metal and the bulk part of the semiconductor there is a potential drop

[4]We denote the energy barrier height with $F_{\mathrm{B}} = e\phi_{\mathrm{B}}$.

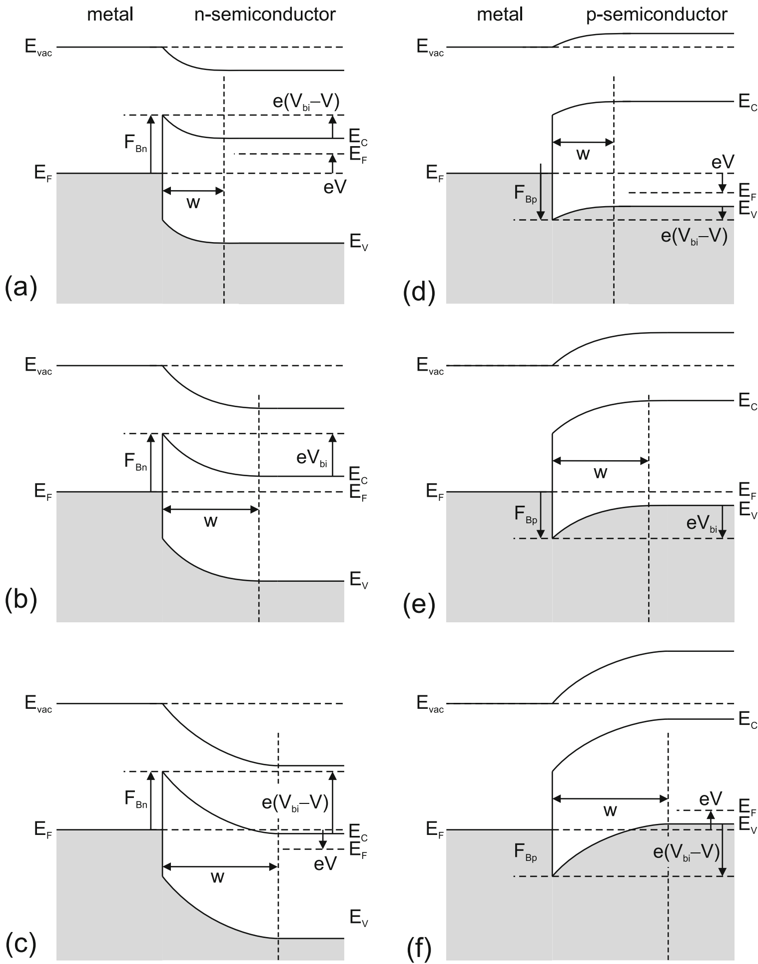

Fig. 20.4. Band structures of metal–semiconductor junctions for (**a**,**b**,**c**) an n-type semiconductor and (**d**,**e**,**f**) a p-type semiconductor (here $F_{\mathrm{Bp}} > 0$). (**b**,**e**) in thermodynamic equilibrium, (**a**,**d**) with forward bias ($V > 0$), (**c**,**f**) with reverse bias ($V < 0$)

$$V_{\mathrm{bi}} = \frac{F_{\mathrm{Bn}}}{e} + V_{\mathrm{n}} = \frac{W_{\mathrm{m}} - \chi_{\mathrm{sc}}}{e} + V_{\mathrm{n}} \, , \tag{20.4}$$

which is termed the built-in potential (or diffusion voltage). The exact form of the voltage drop, the so-called band bending, will be discussed in Sect. 20.2.2.

The surface index is defined as

$$S = \frac{\partial F_{\mathrm{Bn}}}{\partial W_{\mathrm{m}}} \, . \tag{20.5}$$

From the present consideration (20.2), the same semiconductor with metals of varying work function should result in $S = 1$.

Band Structure in the Presence of Surface States

Experimental data shown in Fig. 20.5a, however, show a different behavior with smaller slope. For GaAs, e.g., the barrier height is almost independent of the metal work function. Thus, a different model is needed for realistic Schottky diodes. A rule of thumb for the dominantly covalent semiconductors is that for n-type material the barrier height is 2/3 of the band gap and for p-type material 1/3 of the band gap, such that $E_C - E_F \approx 2E_g/3$ (Fig. 20.5b). Only for ionic semiconductors $S \approx 1$ holds (Fig. 20.5c) [1125].

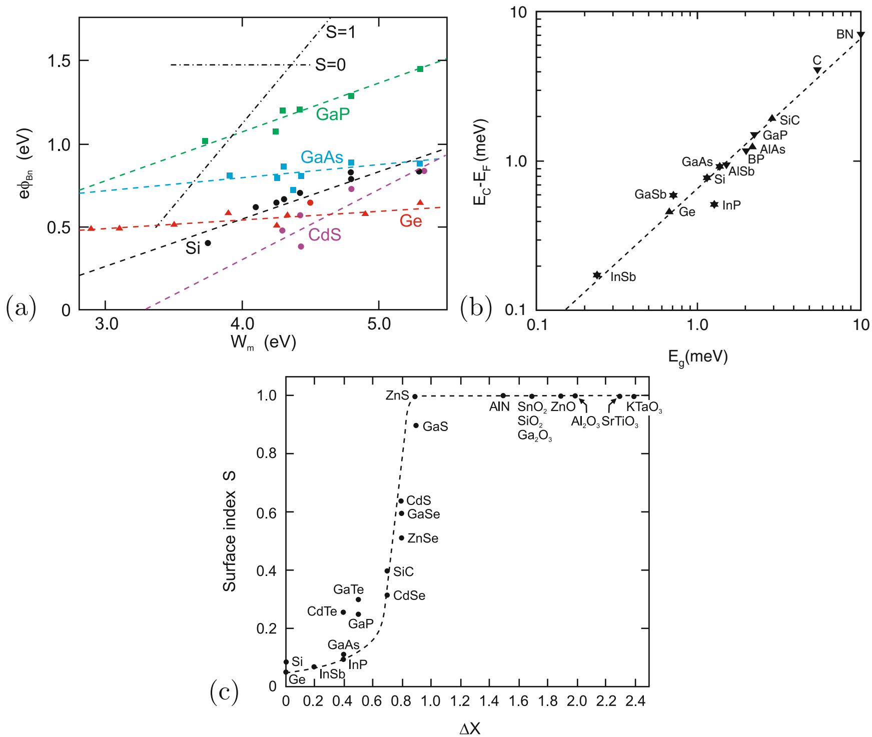

Fig. 20.5. (**a**) Experimental Schottky barrier heights F_{Bn} vs. metal work function $\mathrm{W_m}$ for various metal–semiconductor junctions as labeled. *Dashed lines* are guides to the eye, *dash-dotted lines* indicate dependencies for $S = 1$ and $S = 0$. Data from [1121, 1122]. (**b**) $E_C - E_F$ at the metal–semiconductor interface vs. the band gap E_g for Au Schottky contacts on various semiconductors. The *dashed line* represents $E_C - E_F = 2E_g/3$. Data from [1123]. (**c**) Surface index S vs. the electronegativity difference ΔX between the species of compound semiconductors. *Dashed line* is a guide to the eye. Data from [1122, 1124]

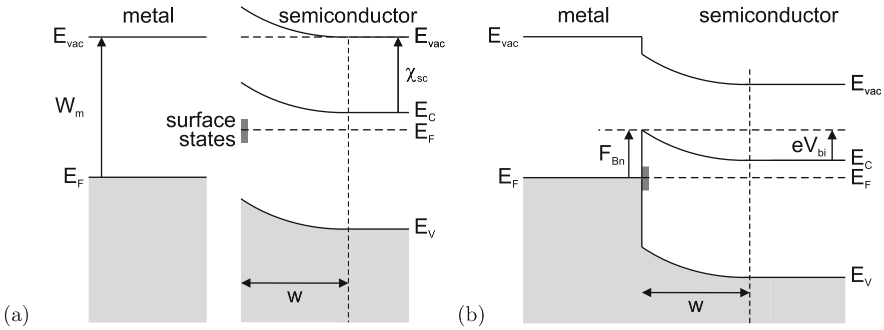

Fig. 20.6. Schematic band structure of a metal–semiconductor junction that is dominated by surface properties of the semiconductor. (**a**) no contact; due to pinning of the Fermi level at surface states of the semiconductor, a depletion-layer of width w is already present. (**b**) Metal and semiconductor in contact

If the semiconductor has a large density of states at its surface ($\gtrsim 10^{12}$ cm^{-2}), there is a space-charge region already without the metal [1126]. Surface traps are filled up to the Fermi level (Fig. 20.6a). The size of the band bending in the semiconductor will be denoted as F_{Bn} since it will turn out below as the Schottky barrier height. If the density of surface states is very high, the charge carriers moving from the semiconductor into the metal upon contact formation are accommodated in the surface states and the position of the Fermi level at the semiconductor surface changes only very little. Thus, the space-charge region is not modified and it is identical to the surface depletion region. The Schottky barrier height is then given by the band bending at the (bare) semiconductor surface F_{Bn} (Fig. 20.6d) and does not depend on the metal work function at all (Bardeen model)). For this limiting case we find for the surface index $S = \partial F_{\mathrm{Bn}}/\partial W_{\mathrm{m}} = 0$.

For actual metal–semiconductor contacts the surface index S takes values between 0 and 1. A theory involving the semiconductor band structure and midgap (surface) states (MIGS) is needed [488, 1127]. For Si, the experimental result is $S = 0.27$; the corresponding density of surface states is $D_{\mathrm{s}} = 4 \times 10^{13}\,\mathrm{cm}^{-2}\,\mathrm{eV}^{-1}$.

20.2.2 Space-Charge Region

The width w of the space-charge region is calculated next. First, we make the so-called abrupt approximation. In this approximation (Schottky–Mott model), the charge density ρ in the space-charge region ($0 \leq x \leq w$) is given by the doping, i.e. $\rho = +eN_{\mathrm{D}}$. Outside the space-charge region the semiconductor is neutral, i.e. $\rho = 0$ and the electric field is zero, i.e. $\mathrm{d}\varphi/\mathrm{d}x = 0$. As further boundary conditions the potential at the interface is $\varphi(0) = -V_{\mathrm{bi}} < 0$. The potential drop in the space-charge region is determined by the one-dimensional Poisson equation

$$\frac{d^2\varphi}{dx^2} = -\frac{\rho}{\epsilon_s} , \tag{20.6}$$

where $\epsilon_s = \epsilon_r \, \epsilon_0$ is the static dielectric constant of the semiconductor. Using the ansatz $\varphi(x) = \varphi_0 + \varphi_1 x + \varphi_2 x^2$ we find

$$\varphi(x) = -V_{bi} + \frac{e\,N_D}{\epsilon_s}\left(w_0\,x - \frac{1}{2}\,x^2\right) , \tag{20.7}$$

w_0 being the depletion layer width at zero bias.

The electric field strength is

$$\mathcal{E}(x) = -\frac{e\,N_D}{\epsilon_s}(w_0 - x) = \mathcal{E}_m + \frac{e\,N_D}{\epsilon_s}\,x , \tag{20.8}$$

with the maximum field strength $\mathcal{E}_m = -eN_D\,w_0/\epsilon_s$ at $x = 0$. From the condition $\varphi(w_0) = 0$ we obtain w_0 as

$$w_0 = \sqrt{\frac{2\epsilon_s}{eN_D}V_{bi}} . \tag{20.9}$$

The charge density and the potential in the abrupt approximation are shown in Fig. 20.7 for GaAs material parameters.

Beyond the abrupt approximation, the thermal distribution of the majority carriers must be treated with more care. The dependence of the charge density $\rho = e(N_D^+ - n)$ on the potential φ (within the Boltzmann approximation) is ($\beta = e/kT$)

$$\rho = eN_D\,[1 - \exp(\beta\,\varphi)] . \tag{20.10}$$

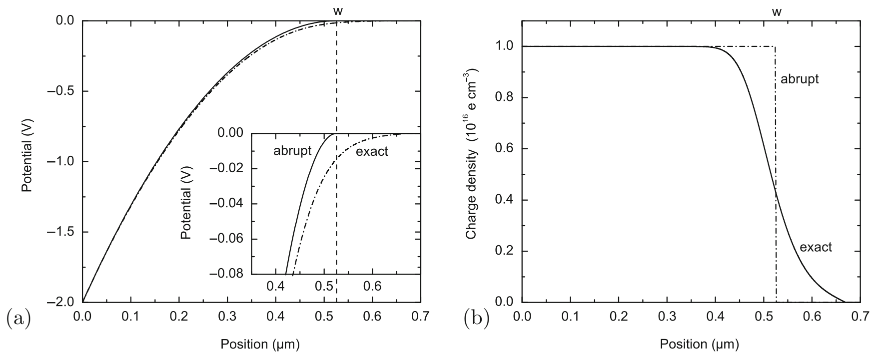

Fig. 20.7. (**a**) Potential φ and (**b**) charge density ρ across the depletion layer of a Schottky n-GaAs diode. Calculation parameters are $\epsilon_s = 12.5\,\epsilon_0$, $V_{bi} - V_{ext} = 2\,V$ (small reverse bias), $N_D = 1 \times 10^{16}\,cm^{-3}$, $T = 300\,K$. Abrupt approximation is shown as *solid lines*, exact (numerical) calculation as *dash-dotted line*. *Dashed line* in (**a**) indicates depletion layer width w_0 in the abrupt approximation

The actual charge density and the potential, obtained from a numerical solution of (20.6), are shown in Fig. 20.7 in comparison with the abrupt approximation. Clearly, at the Schottky depletion layer width w_0, the charge varies continuously and the potential does not drop to zero.

We note that for the depletion layer $\varphi \leq 0$ and $n \leq N_{\rm D}$. The charge difference $\Delta\rho$ (due to the tail of the thermal distribution of the majority charge carriers in the depletion layer) between the real distribution (20.10) to the abrupt approximation model with constant charge density ($\rho_0 = eN_{\rm D}$) in the depletion layer is

$$\Delta\rho(x) = \rho(x) - \rho_0 = -e\, N_{\rm D}\, \exp\left(\beta\, \varphi(x)\right) \,. \tag{20.11}$$

The integration of $\Delta\rho$ over the depletion layer yields that the voltage drop $V_{\rm bi}$ across the depletion layer needs to be corrected by ΔV

$$\Delta\varphi = \int_0^{w_0} \left[\int_0^x \frac{-\Delta\rho(x')}{\epsilon_{\rm s}}\, {\rm d}x'\right] {\rm d}x = \frac{1}{\beta}\left[1 - \exp(-\beta\, V_{\rm bi})\right] \approx \beta^{-1} \,. \tag{20.12}$$

The approximation is valid for $\beta V_{\rm bi} \gg 1$. Therefore, (20.9) is corrected to

$$w_0 = \sqrt{\frac{2\,\epsilon_{\rm s}}{e\, N_{\rm D}}\left(V_{\rm bi} - \beta^{-1}\right)} \,. \tag{20.13}$$

When a potential difference $V_{\rm ext}$ is applied externally to the diode, (20.13) is modified by the change in the interface boundary condition, $\varphi(0) = -V_{\rm bi} + V_{\rm ext}$. The band structure is shown schematically in Fig. 20.4a for a forward bias and in Fig. 20.4c for a reverse bias. Therefore, we obtain for the depletion-layer width (within the abrupt approximation)

$$w(V_{\rm ext}) = \sqrt{\frac{2\,\epsilon_{\rm s}}{e\, N_{\rm D}}\left(V_{\rm bi} - V_{\rm ext} - \beta^{-1}\right)} \,. \tag{20.14}$$

Now we can also give explicitly the value of the maximum electric field (at $x = 0$)

$$\begin{aligned}\mathcal{E}_{\rm m} &= -\sqrt{\frac{2\, e\, N_{\rm D}}{\epsilon_{\rm s}}\left(V_{\rm bi} - V_{\rm ext} - \beta^{-1}\right)} \\ &= -\frac{2}{w}\left(V_{\rm bi} - V_{\rm ext} - \beta^{-1}\right) \,.\end{aligned} \tag{20.15}$$

We note that so far the barrier height is independent of the applied bias voltage. In the next section, it is shown that this is actually not the case.

20.2.3 Schottky Effect

The barrier height is reduced by the image-charge effect that has been neglected so far. An electron (charge $q = -e$) at position x in the semiconductor

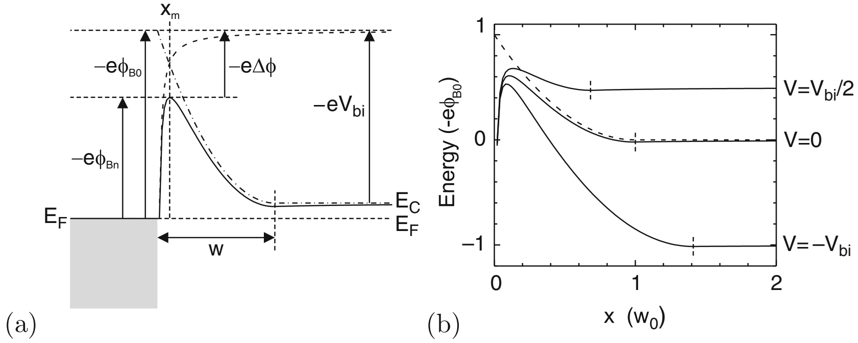

Fig. 20.8. (**a**) Energy of a particle with respect to the metal surface (*dashed line*), conduction band in semiconductor depletion layer (*dash-dotted line*) and combined effect (*solid line*). The image charge energy lowers the potential barrier F_{B_0} by the amount ΔF_{B} to F_{Bn}. (**b**) Conduction band on the semiconductor side of a metal–semiconductor junction at various bias voltages ($V = 0$, $V = +V_{\mathrm{bi}}/2$, and $V = -V_{\mathrm{bi}}$ as labeled) taking into account the Schottky effect. The width of the depletion layer is indicated with a *short vertical dashed line*. The barrier height without Schottky effect is F_{B0}. The *dashed line* is the situation without Schottky effect for zero bias

is facing a metal surface. The metal surface is at zero position (Fig. 20.8a). The potential distribution of the free charge is modified since the metal surface is an equipotential surface. The potential distribution outside the metal is identical to that if an *image* charge $-q$ were located at $-x$. This image charge exerts a force (image force F_{if}) on the electron

$$F_{\mathrm{if}} = -\frac{q^2}{16\,\pi\,\epsilon_{\mathrm{s}}\,x^2}\ , \tag{20.16}$$

where ϵ_{s} is the relative dielectric constant of the semiconductor. In order to bring an electron to x from infinity the work E_{if}

$$E_{\mathrm{if}} = \int_{\infty}^{x} F_{\mathrm{if}}\,\mathrm{d}x = -\frac{q^2}{16\,\pi\,\epsilon_{\mathrm{s}}\,x} \tag{20.17}$$

is needed. This image potential energy is shown in Fig. 20.8a. The total energy E_{tot} (solid line in Fig. 20.8a) of the electron in the presence of an electric field $\mathcal{E}$ is given by

$$E_{\mathrm{tot}} = q\,\mathcal{E}x - \frac{q^2}{16\,\pi\,\epsilon_{\mathrm{s}}x}\ . \tag{20.18}$$

The maximum of this function ($\mathrm{d}E_{\mathrm{tot}}/\mathrm{d}x = 0$) is at x_{m}

$$x_{\mathrm{m}} = \sqrt{\frac{e}{16\,\pi\,\epsilon_{\mathrm{s}}\,\mathcal{E}}}\ . \tag{20.19}$$

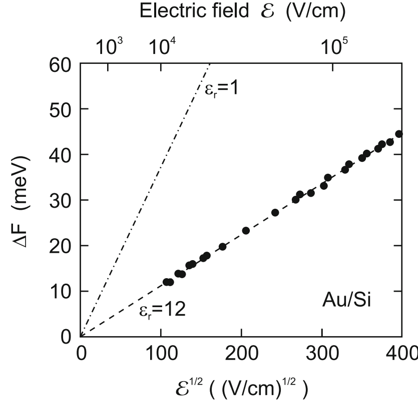

Fig. 20.9. Electric-field dependence of the image charge lowering of the Schottky barrier. *Dash-dotted* line is for vacuum dielectric constant, *dashed line* is (20.20) for $\epsilon_r = 12$. Adapted from [1129]

The energy barrier (20.2) (without image charge effect now labeled as F_{B_0}) is reduced by ΔF_B given by

$$\Delta F_B^{\text{if}} = e \sqrt{\frac{e\,\mathcal{E}}{4\,\pi\epsilon_s}} = 2\,e\,\mathcal{E}\,x_m \,. \tag{20.20}$$

With the field in the vicinity of the interface given by $\mathcal{E}_m$ from (20.16), the barrier reduction is[5] [1128]

$$\Delta F_B^{\text{if}} = e \left[\frac{e^3\,N_D}{8\,\pi^2\,\epsilon_0^3\,\epsilon_s^3} \left(V_{bi} - V_{ext} - \beta^{-1}\right) \right]^{1/4} \,. \tag{20.21}$$

For $\epsilon_s = \epsilon_0$ (vacuum) and a field strength of 10^5 V/cm the maximum position is at $x_m = 6$ nm and the barrier reduction is $\Delta F_B^{\text{if}} = 0.12$ eV. For 10^7 V/cm $x_m = 1$ nm and $\Delta F_B^{\text{if}} = 1.2$ eV. For semiconductors with $\epsilon_r \sim 10$ the effect is smaller (Fig. 20.9). The Schottky effect depends on the bias voltage as visualized in Fig. 20.8b and therefore the barrier height depends on the applied bias voltage.

20.2.4 Capacitance

The total space charge Q (per unit area) in the semiconductor is ($V = V_{ext}$)

$$Q(V) = e\,N_D\,w = \sqrt{2\,e\,N_D\,\epsilon_s\,(V_{bi} - V - \beta^{-1})} \,. \tag{20.22}$$

and depends on the external voltage.

[5] The term ϵ_s^3 is technically $\epsilon_s \epsilon_d^2$ where ϵ_d is the image-force dielectric constant. ϵ_d is equal to ϵ_s if the transit time of an electron from the metal to the maximum of the potential energy is sufficiently long to build up the dielectric polarization of the semiconductor [1116].

For measurement of the depletion layer capacitance first the external dc bias voltage V is set which defines the extension of the depletion layer. The (differential) capacitance is probed by an ac voltage with small amplitude $\delta V \ll V$. First we assume that the ac frequency ω is small compared to characteristic time constants of the electrically active impurities (quasi-static capacitance) and discuss the bias dependence $C(V)$. Following we discuss the frequency and temperature dependence of the capacitance[6] $C(\omega, T)$, in particular when the measurement frequency is in the range of the (temperature dependent) electron capture or emission rate (10.51).

Bias Dependence

From (20.22) the capacitance $C = |\mathrm{d}Q/\mathrm{d}V|$ (per unit area) of the space charge region is given by

$$C = \sqrt{\frac{e\, N_\mathrm{D}\, \epsilon_\mathrm{s}}{2\,(V_\mathrm{bi} - V - \beta^{-1})}} = \frac{\epsilon_\mathrm{s}}{w} \ . \tag{20.23}$$

Equation (20.23) can also be written as

$$\frac{1}{C^2} = \frac{2\left(V_\mathrm{bi} - V - \beta^{-1}\right)}{e\, N_\mathrm{D}\, \epsilon_\mathrm{s}} \ . \tag{20.24}$$

If $1/C^2$ is measured as a function of the bias voltage (C–V spectroscopy), it should be linearly dependent on the bias voltage if the doping concentration is homogeneous (Fig. 20.10a). The doping concentration can be determined from the slope via

$$N_\mathrm{D} = -\frac{2}{e\,\epsilon_\mathrm{s}} \left[\frac{\mathrm{d}}{\mathrm{d}V}\left(\frac{1}{C^2}\right)\right]^{-1} \ , \tag{20.25}$$

(see Fig. 20.10b) and the built-in voltage V_bi from the extrapolation to $V = V'$ such that $1/C^2 = 0$, $V_\mathrm{bi} = V' + kT$. Using (20.4) the Schottky barrier height can be determined from this [1130] via

$$F_{\mathrm{B}_n} = e\,V' - e\,V_\mathrm{n} + kT - \Delta F_\mathrm{B}^\mathrm{if} \ , \tag{20.26}$$

where $\Delta F_\mathrm{B}^\mathrm{if}$ is the barrier lowering (20.21) due to the image force effect between the flat-band and the zero-bias cases.

We note that for inhomogeneous doping the depth profile of the doping can be determined by C–V spectroscopy. The $1/C^2$ vs. bias curve is then no longer a straight line and exhibits a varying slope. $N_\mathrm{D}(w)$ is evaluated according to (20.25) using $w = \epsilon_\mathrm{s}/C$ from (20.23) [1131],

---

[6] Probing the capacitance as a function of the ac frequency is called admittance spectroscopy.

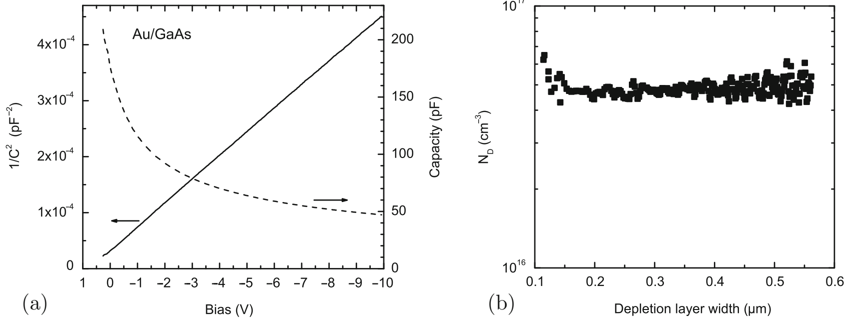

Fig. 20.10. (**a**) Capacitance C (*dashed line*) and $1/C^2$ (*solid line*) vs. bias voltage dependence for an Au/GaAs Schottky diode (2-µm MOVPE-grown GaAs:Si on a n-GaAs substrate) at room temperature. From the extrapolation to $1/C^2 = 0$ and (20.24) we obtain $V_{\mathrm{bi}} = 804\pm3\,\mathrm{mV}$. (**b**) Donor concentration ($N_{\mathrm{D}} = 4.8\times10^{16}\,\mathrm{cm}^{-3}$) determined via (20.25) from the $1/C^2$ plot vs. the depletion layer width (calculated using (20.23))

$$N_{\mathrm{D}}\left(w = \frac{\epsilon_{\mathrm{s}}}{C}\right) = -\frac{2}{e\epsilon_{\mathrm{s}}}\left[\frac{\mathrm{d}}{\mathrm{d}V}\left(\frac{1}{C^2}\right)\right]^{-1}, \tag{20.27}$$

Using functional integration, the capacitance of a depletion layer can be expressed in terms of $\varphi(0) = V_{\mathrm{bi}} - V$ without explicit knowledge of the potential $\varphi(x)$ [1132].[7] In the approximation $e\varphi(0) \gg kT$ we obtain for homogeneous doping as refinement of (20.23)

$$C = \sqrt{\frac{e\,N_{\mathrm{D}}\,\epsilon_{\mathrm{s}}}{2\left(V_{\mathrm{bi}} - V - \beta^{-1}\left(\frac{n_0}{N_{\mathrm{D}}} - \ln\frac{n_0}{N_{\mathrm{D}}}\right)\right)}}, \tag{20.28}$$

where n_0 is the electron concentration in the neutral region. Within this general treatment, the validity of (20.25) has been confirmed. Also, C does not diverge in the flatband case, for $V \to V_{\mathrm{bi}}$, as for the abrupt approximation but exhibits a maximum [1132].

At a given bias voltage, the charge (ionized donors or acceptors) at the boundary of the space-charge region is tested by the capacitance measurement. However, this principle works only if the depth of the space-charge region actually changes with the bias voltage. The method can therefore not be applied to such systems like δ-doped layers or quantum wells.

Frequency and Temperature Dependence

The release of carriers from (and capture on) a donor occurs with a characteristic emission rate g_{c} (10.51) (capture rate r_{c}). This is true similarly

[7] This is valid as long as $\varphi(x)$ is strictly monotonous.

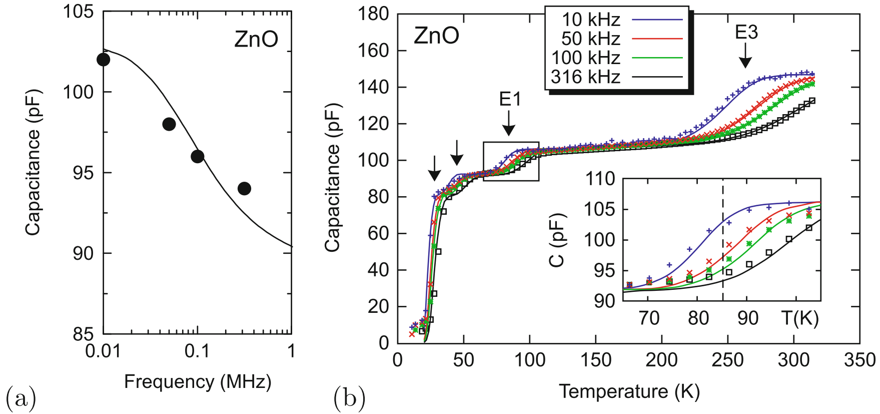

Fig. 20.11. (**a**) Capacitance vs. probing frequency f for a Pd/ZnO Schottky diode (zero bias) at $T = 85\,\mathrm{K}$. Theoretical dependence (*solid line*) and experimental data (*circles*). (**b**) Capacitance of the same diode as a function of temperature (thermal admittance spectroscopy, TAS) for four different probing frequencies f =10, 50, 100 and 316 kHz (ac amplitude 50 mV). *Arrows* denote the release of carriers from four different defect levels, two shallow ones and the well-known defects E1 and E3 [523, 1136]. The *inset* shows the contribution of the E1 defect, indicated by a *rectangle* in the main graph, in more detail. *Symbols* are experimental data, *lines* are fit with four-level model (E1: $E_\mathrm{D} = 116\,\mathrm{meV}$, E3: $E_\mathrm{D} = 330\,\mathrm{meV}$) [1137]

for acceptors. Therefore, the capacitance depends on the sampling frequency (Fig. 20.11a). If the capacitance is probed with a frequency much smaller than the release rate, the system appears to be in equilibrium and has the (quasi-)static capacitance C_0. If the probe frequency is much higher, the system cannot follow and the donor does not contribute to the capacitance. The characteristic frequency $\hat{f}$ at the turning point of $C(f)$ is [718]

$$2\pi\,\hat{f} = 2\,g_\mathrm{c}\ , \tag{20.29}$$

with corrections of the simple factor of 2 discussed in [1133]. Since the emission rate depends exponentially on temperature, for a given frequency the capacitance depends on temperature [1134]. This is shown in Fig. 20.11b for ZnO which exhibits several donor levels. At low temperature shallow levels release their carriers, at higher temperature the deeper levels start to contribute. The DX center in AlGaAs (see Sect. 7.7.6) has been investigated in [1135] with this technique.

20.2.5 Current–Voltage Characteristic

The current transport through a metal–semiconductor junction is dominated by the majority charge carriers, i.e. electrons (holes) in the case of an n-type (p-type) semiconductor, respectively.

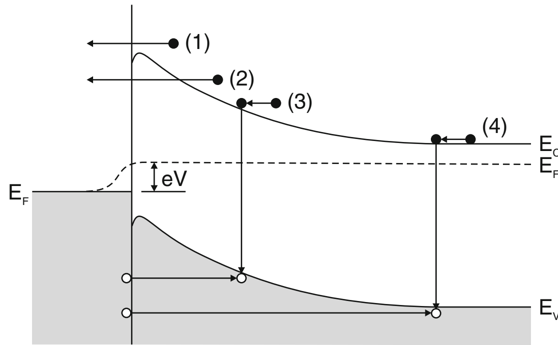

Fig. 20.12. Transport mechanisms at metal–semiconductor junctions. (1) Thermionic emission ('above' the barrier) (2) tunneling ('through' the barrier), (3) recombination in the depletion layer, (4) hole injection from metal

In Fig. 20.12, the possible transport mechanisms are visualized for an n-type semiconductor. Thermionic emission 'above' the barrier involves the hot electrons from the thermal distribution and will be important at least at high temperatures. Tunneling 'through' the barrier will be important for thin barriers, i.e. at high doping ($w \propto N_\mathrm{D}^{-1/2}$, cf. (20.14)). 'Pure' tunneling for electrons close to the (quasi-) Fermi level, also called field emission, and thermionic field emission, i.e. tunneling of electrons with higher energies, are distinguished. Also, recombination in the depletion layer and hole injection from the metal are possible.

The transport of electrons above the barrier can be described with diffusion theory [1138, 1139] or thermionic-emission theory [1140]. In both cases the barrier height is large compared to kT. For thermionic emission (typically relevant for semiconductors with high mobility) the current is limited by the emission process and an equilibrium (constant electron quasi-Fermi level) is established throughout the depletion layer and ballistic transport is considered. In diffusion theory (for low mobility) a thermal equilibrium between metal and semiconductor electrons is established in the interface plane and the current is limited by diffusion and drift in the depletion region.

Thermionic Emission

The current density per unit area $j_{\mathrm{s}\to\mathrm{m}}$ of electrons that flow from the semiconductor into the metal is due to the hot electrons from the thermal distribution function

$$j_{\mathrm{s}\to\mathrm{m}} = \int_{E_\mathrm{F} - e\,F_\mathrm{Bn}}^{\infty} (-e)\, v_\mathrm{x}\, \mathrm{d}n \; . \tag{20.30}$$

The integral starts at the lowest possible energy, the top of the Schottky barrier (no tunneling allowed in this model!). The electron density dn in a small energy interval dE is

$$\mathrm{d}n = D(E)\, f(E)\, \mathrm{d}E \,. \tag{20.31}$$

The carrier velocity is obtained from

$$E = E_\mathrm{C} + \frac{1}{2}\, m^*\, v^2 \,. \tag{20.32}$$

For a bulk semiconductor and the Boltzmann distribution ($eF_\mathrm{B} \gg kT$)

$$\mathrm{d}n = 2 \left(\frac{m^*}{h}\right) \exp\left(\beta V\right) \exp\left(-\frac{m^* v^2}{2\, kT}\right) 4\pi v^2 \,\mathrm{d}v \,. \tag{20.33}$$

Using $4\pi v^2\, \mathrm{d}v = \mathrm{d}v_\mathrm{x}\, \mathrm{d}v_\mathrm{y}\, \mathrm{d}v_\mathrm{z}$ and integrating over all velocities in y and z directions and v_x from the minimum velocity necessary to pass the barrier $v_\mathrm{min,x} = \sqrt{2e\,(V_\mathrm{bi} - V)/m^*}$ to ∞, the current density is found to be

$$j_{\mathrm{s}\to\mathrm{m}} = A^*\, T^2 \exp\left(-\frac{F_\mathrm{Bn}}{kT}\right) \exp\left(\beta V\right) \,, \tag{20.34}$$

with A^* being the Richardson constant given by

$$A^* = \frac{4\pi e\, m^*\, k_\mathrm{B}^2}{h^3} = \frac{e\, N_\mathrm{C}\, \bar{v}}{4T^2} \,, \tag{20.35}$$

where $\bar{v}$ is the average thermal velocity in the semiconductor. A^* for electrons in vacuum is $120\,\mathrm{A\,cm^{-2}\,K^{-2}}$. A similar result is obtained for the thermionic emission of electrons from a metal into vacuum. Since F_Bn is positive, the saturation current increases with increasing temperature.

If the bias is changed, the current from the semiconductor to the metal increases in the forward direction because the energy difference between the quasi-Fermi level and the top of the barrier is reduced. The current is reduced for reverse bias. The barrier from the metal into the semiconductor remains constant (except for the Schottky effect whose impact on the current–voltage characteristic is discussed next). Therefore the current from the metal into the semiconductor is constant and can be obtained from the condition $j = 0$ for zero bias. Therefore the current–voltage characteristic in the thermionic-emission model is

$$\begin{aligned} j &= A^*\, T^2 \exp\left(-\frac{F_\mathrm{Bn}}{kT}\right) \left[\exp\left(\beta V\right) - 1\right] \\ &= j_\mathrm{s} \left[\exp\left(\beta V\right) - 1\right] \,. \end{aligned} \tag{20.36}$$

The pre-factor

$$j_\mathrm{s} = A^*\, T^2 \exp\left(-\frac{F_\mathrm{Bn}}{kT}\right) \tag{20.37}$$

is called the saturation current density. This dependence is the ideal diode characteristic and is shown in Fig. 20.13. The temperature dependence of the saturation current j_s can be written as

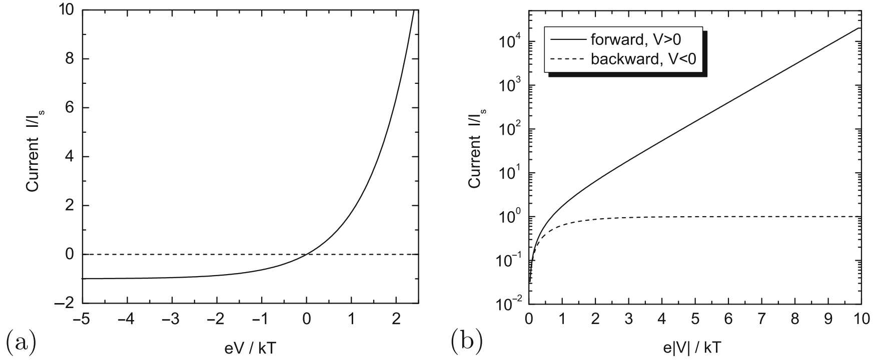

Fig. 20.13. Ideal diode I–V characteristics $I = I_s\,(\exp(eV/kT) - 1)$ (**a**) in linear plot and (**b**) semilogarithmic plot

$$\ln\left(\frac{j_s}{T^2}\right) = \ln A^* - \frac{F_{Bn}}{kT} \tag{20.38}$$

by transforming (20.37). The plot of $\ln\left(j_s/T^2\right)$ to vs. $1/T$ is called a Richardson plot and allows the barrier height and the Richardson constant to be determined from a linear fit.

Ideality Factor

If the Schottky (image force) effect, i.e. the change of barrier height with bias voltage, is considered, the semilogarithmic slope of the forward I–V characteristic is no longer $V_0^{-1} = e/kT$ but can be expressed as $V_0^{-1} = e/nkT$, n being a dimensionless parameter termed the ideality factor,[8]

$$j = j_s\left[\exp\left(\frac{e\,V}{n\,kT}\right) - 1\right] . \tag{20.39}$$

n is given by

$$n = \left(1 - \frac{1}{e}\frac{\partial F_B}{\partial V}\right)^{-1} \approx 1 + \frac{1}{e}\frac{\partial F_B}{\partial V} . \tag{20.40}$$

Values for n_{if} due to the image force effect [1128] (using (20.21) and the image force barrier lowering $\Delta F_B^{if,0}$ at zero bias),

$$n_{if} = 1 + \frac{\Delta F_B^{if,0}}{4\,e\,V_{bi}} , \tag{20.41}$$

are smaller than 1.03. For GaAs and $N_D = 10^{17}\,cm^{-3}$, $n = 1.02$. With regard to V_0 and its temperature dependence, we refer also to Fig. 20.15 and the related discussion.

[8]Obviously $n = 1$ for the ideal characteristic (20.36). Otherwise $n \geq 1$.

Laterally Inhomogeneous Barrier

In [1141] the effect of a spatial inhomogeneity of the diffusion voltage and thus the barrier height is investigated. The barrier height $F_{\mathrm{Bn}}(x, y)$ across the contact area is assumed to have a Gaussian probability distribution $p(F_{\mathrm{Bn}})$ with a mean value $\bar{F}_{\mathrm{Bn}}$ and a standard deviation σ_F, It turns out that the barrier height $F_{\mathrm{Bn}}^{\mathrm{C}}$ responsible for the capacitance, and thus the diffusion voltage determined by C–V spectroscopy, is given by the spatial average, i.e. $F_{\mathrm{Bn}}^{\mathrm{C}} = \bar{F}_{\mathrm{Bn}}$. The barrier height $F_{\mathrm{Bn}}^{\mathrm{j}}$ determining the current–voltage characteristics (cf. (20.36)) via

$$
\begin{aligned}
j &= A^* T^2 \left[\exp(\beta V) - 1\right] \int \exp\left(-\frac{F_{\mathrm{Bn}}}{kT}\right) p(F_{\mathrm{Bn}})\, \mathrm{d}F_{\mathrm{Bn}} \qquad (20.42)\\
&= A^* T^2 \exp\left(-\frac{F_{\mathrm{Bn}}^{\mathrm{j}}}{kT}\right) \left[\exp(\beta V) - 1\right]
\end{aligned}
$$

is given by

$$
F_{\mathrm{Bn}}^{\mathrm{j}} = \bar{F}_{\mathrm{Bn}} - \frac{\sigma_{\mathrm{F}}^2}{2\,kT} \,. \qquad (20.43)
$$

Thus, the barrier height determined from the current–voltage characteristic underestimates the spatial average of the barrier height.[9] The Richardson plot (20.38) is now modified (and is nonlinear in $1/T$) to

$$
\ln\left(\frac{j_{\mathrm{s}}}{T^2}\right) = \ln A^* - \frac{F_{\mathrm{Bn}}}{kT} + \frac{\sigma_{\mathrm{F}}^2}{2\,k^2\,T^2} \,. \qquad (20.44)
$$

Temperature Dependence

Figure 20.14a shows the temperature-dependent I–V characteristics of a Pd/ZnO Schottky diode. A straightforward evaluation according to (20.36) results in a barrier height of about 700 meV and a Richardson constant that is orders of magnitude smaller than the theoretical value of $32\,\mathrm{A\,K^{-2}\,cm^{-2}}$ (for $m_{\mathrm{e}}^* = 0.27$). A fit of the temperature-dependent data with (20.43), as shown in Fig. 20.14b, results in $\bar{F}_{\mathrm{Bn}} = 1.1\,\mathrm{eV}$, in agreement with the (temperature-independent) value obtained from CV spectroscopy, and $\sigma_F = 0.13\,\mathrm{eV}$ [1142].

The temperature dependence of the ideality factor n is given by [1143]

$$
n = \frac{1}{1 - \rho_2 + \rho_3/(2kT)} \,, \qquad (20.45)
$$

where ρ_2 (ρ_3) is the (temperature-independent) proportionality coefficient of the bias dependence of the mean barrier height (standard deviation), i.e.

[9] This phenomenon is similar to the red-shift of luminescence lines (Stokes shift) due to thermalization in the presence of disorder, see Sect. 11.4.

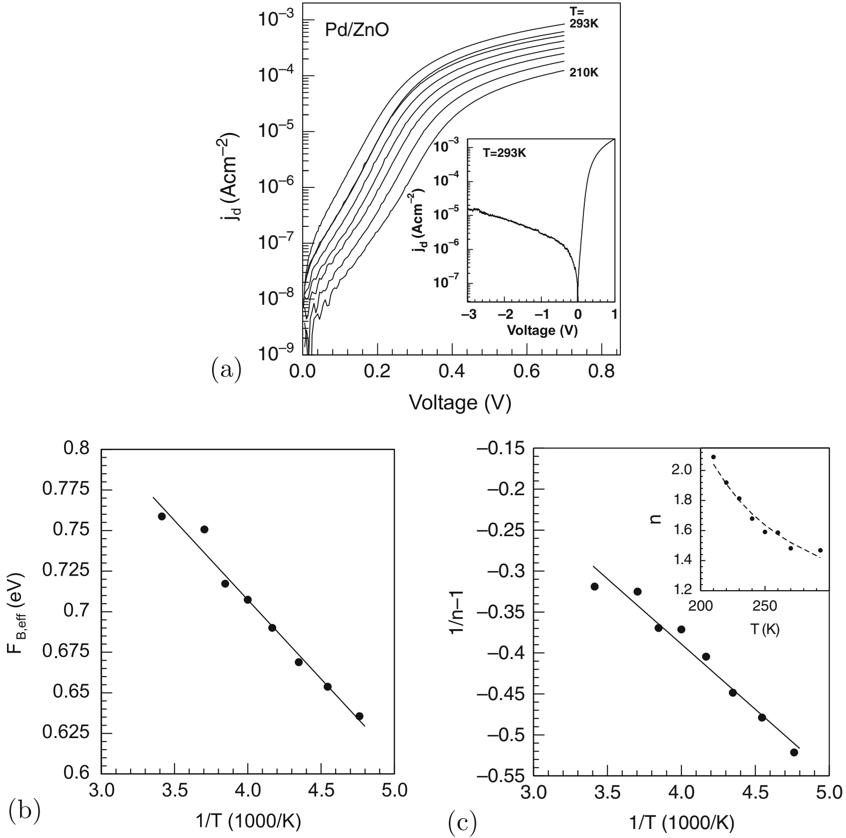

Fig. 20.14. (**a**) Forward I–V characteristic of Pd/ZnO Schottky diodes for various temperatures. Diode temperatures are 210 K, 220 K, 230 K, 240 K, 250 K, 260 K, 270 K, and 293 K. The *inset* shows the current density vs. voltage for 293 K on a semilogarithmic scale. (**b**) Effective barrier height $F^{\mathrm{j}}_{\mathrm{Bn}}$ vs. the inverse temperature. The *solid line* is a linear fit according to (20.43) yielding the standard deviation $\sigma_F = 0.13\,\mathrm{eV}$ and the mean barrier height $\bar{F}_{\mathrm{Bn}} = 1.1\,\mathrm{eV}$. (**c**) Plot of $1/n - 1$ vs. the inverse temperature. The *solid line* is a linear fit of the data yielding the voltage deformation coefficients $\rho_2 = -0.025$ and $\rho_3 = -0.028\,\mathrm{eV}$. The *inset* shows the experimentally determined n factors and the n factors calculated from (20.45) using the voltage-deformation coefficients obtained from the linear fit (*dashed line*). Adapted from [1142]

$$\rho_2 = \frac{1}{e}\,\frac{\partial \bar{F}_{\mathrm{Bn}}}{\partial V} \tag{20.46a}$$

$$\rho_3 = \frac{1}{e}\,\frac{\partial\, \sigma_F^2}{\partial V}\;. \tag{20.46b}$$

The fit of $1/n - 1$ vs. $1/T$ in Fig. 20.14c yields $\rho_2 = -0.025$ and $\rho_3 = -0.028\,\mathrm{eV}$ for the ZnO diodes under investigation.

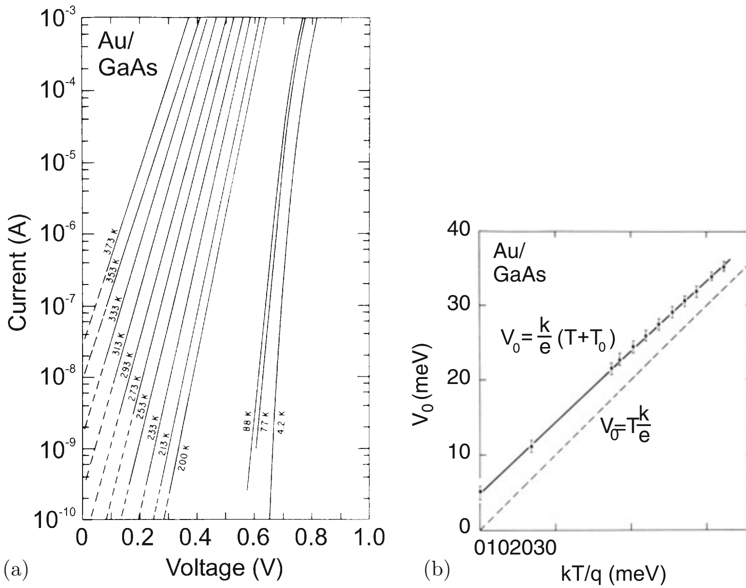

Fig. 20.15. (**a**) Forward I–V characteristic of Au/GaAs diode for various temperatures. (**b**) Temperature dependence of the voltage V_0. The experimental data are fitted with $T_0 = 45 \pm 8\,\text{K}$. Adapted from [1144]

The forward I–V characteristic of an Au/GaAs Schottky diode reported in [1144, 1145] is shown in Fig. 20.15a at various temperatures. The current amplitude decreases with decreasing temperature due to the temperature dependence of the saturation current (20.36). Also, the slope V_0^{-1} of the characteristic $j = j_s \exp(V/V_0)$ varies with temperature. Looking at the temperature dependence of V_0, it is described as $V_0 = k(T + T_0)/e$ rather than with an ideality factor n in the form of $V_0 = nkT/e$. In other words, the ideality factor follows a temperature dependence $n = 1 + T_0/T$. In view of (20.45), such behavior means for small T_0 that $n \approx 1/(1 - T_0/T)$ and thus $\rho_2 = 0$ and $\rho_3 = 2kT_0$. For $T_0 = 45\,\text{K}$, ρ_3 is 0.008 eV, which is a fairly small value. Thus, the temperature behavior of the diode is due to the narrowing of the Gaussian distribution of barrier height with bias voltage [1141].

Correlation of Barrier Height and Ideality Factor

In a set of similar diodes with varying magnitude of barrier inhomogeneities, it is found that the effective barrier height and the ideality factor correlate [1146]. The extrapolation to $n = n_{\text{if}}$ yields the limit of the barrier height for a homogeneous barrier (Fig. 20.16). For silicon, it is found that the surface orientation has a minor influence on the Schottky barrier height (Fig. 20.16b)

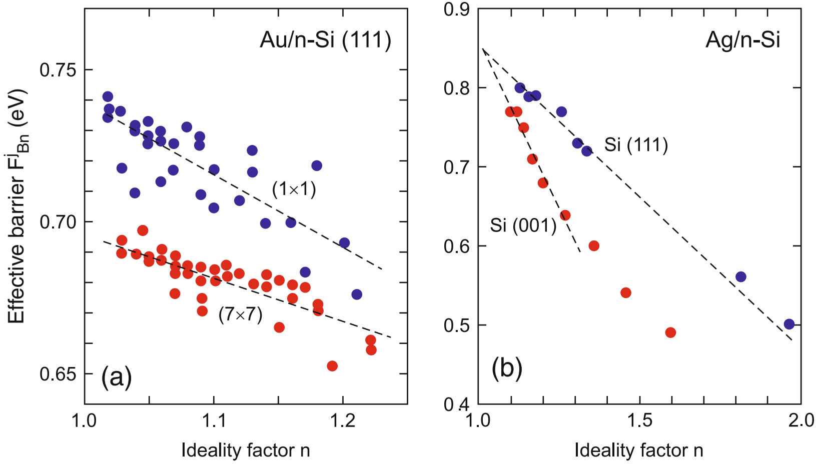

Fig. 20.16. (**a**) Effective barrier height vs. ideality factor for Ag/n-Si Schottky diodes prepared on Si(111) surface with (7 × 7) reconstruction or unreconstructed (1 × 1) as labeled. The more ideal (1 × 1) surface exhibits the higher barrier. The *dashed lines* are linear fits. (**b**) Effective barrier height vs. ideality factor for Au/n-Si Schottky diodes prepared on HF-dipped (1×1) unreconstructed (001) and (111) surfaces. The *dashed lines* are linear fits and extrapolation to $n = n_{\mathrm{if}}$. Both surface orientations exhibit the same extrapolated homogeneous barrier height. Based on data compiled in [1146]

for an unreconstructed surface. The presence of a reconstruction lowers the barrier height[10] (Fig. 20.16a).

Diffusion Theory

In diffusion theory the current density is considered in the presence of a carrier-density and electric-field gradient. In the Boltzmann approximation the electron current is given by (8.57a). In stationary equilibrium the current density is constant, i.e. independent of x. Assuming that the carrier density has its equilibrium values at $x = 0$ and $x = w$, we find after integration and using (20.7)

$$\begin{aligned} j &= -e\,\mu_n\,N_{\mathrm{C}}\,\mathcal{E}_{\mathrm{m}}\,\exp\left(-\frac{F_{\mathrm{Bn}}}{kT}\right)[\exp(\beta V)-1] \\ &= j_{\mathrm{s}}\,[\exp(\beta V)-1]\ . \end{aligned} \tag{20.47}$$

[10] Reconstructions are accompanied by redistributions of the valence charge with respect to the undisturbed bulk. The subsequent extra interface dipoles alter the barrier heights of reconstructed interfaces [1146].

Therefore, also in this case the ideal diode characteristic is obtained, however, with a different saturation current. The ideality factor in diffusion theory is $n = 1.06$ (for $F_{\mathrm{Bn}} \gtrsim 15\, kT$) [1118].

Combined Theory

A combination of both theories [1147] considers both mechanisms to be in series. The current can then be expressed as

$$
\begin{aligned}
j &= \frac{eN_{\mathrm{C}} v_{\mathrm{r}}}{1 + v_{\mathrm{r}}/v_{\mathrm{D}}} \exp\left(-\frac{F_{\mathrm{Bn}}}{kT}\right) [\exp(\beta V) - 1] && (20.48a)\\
&= A^{**}\, T^2 [\exp(\beta V) - 1] && (20.48b)\\
&= j_{\mathrm{s}} [\exp(\beta V) - 1] \ .
\end{aligned}
$$

Here $v_{\mathrm{r}} = \bar{v}/4$ is a ‘recombination velocity’ [1148] at the top of the barrier according to $j = v_{\mathrm{r}}(n - n_0)$, n_0 being the equilibrium electron density at the top of the barrier and $\bar{v}$ is the average thermal velocity in the semiconductor. v_{D} is an effective diffusion velocity describing the transport of electrons from the edge of the depletion layer ($x = w$) to the top of the barrier ($x = x_{\mathrm{m}}$). It is defined as

$$
v_{\mathrm{D}} = \left[\int_{x_{\mathrm{m}}}^{w} \frac{-e}{\mu_n kT} \exp\left(-\frac{F_{\mathrm{Bn}} - E_{\mathrm{C}}(x)}{kT}\right) \mathrm{d}x\right]^{-1} . \qquad (20.49)
$$

In [1147] μ_n has been assumed to be independent of the electric field. This assumption is potentially not realistic. If $v_{\mathrm{D}} \gg v_{\mathrm{r}}$, thermionic theory applies and we obtain (20.36). The case $v_{\mathrm{r}} \gg v_{\mathrm{D}} \sim \mu_n \mathcal{E}_{\mathrm{m}}$ relates to diffusion theory and we recover (20.47).

The constant A^{**} in (20.48b) is called the effective Richardson constant. Its calculated dependence on the electric field is shown in Fig. 20.17 for Si. At room temperature for most Ge, Si and GaAs Schottky diodes the thermionic emission of majority carriers is the dominating process.

Tunneling Current

At high doping the width of the depletion layer becomes small and tunneling processes become more probable. Also at low temperatures, when thermionic emission is very small, tunneling processes can dominate the transport between metal and semiconductor. One process is tunneling of electrons close to the Fermi level of the semiconductor. This process is called field emission (F) and is at least important for degenerate semiconductors at very low temperatures. If the temperature is raised, electrons are excited to higher energies where they encounter a thinner barrier. The tradeoff between thermal energy and barrier width selects an electron energy E_{m} above the conduction-band edge for which the current is largest. This process is known as thermionic field

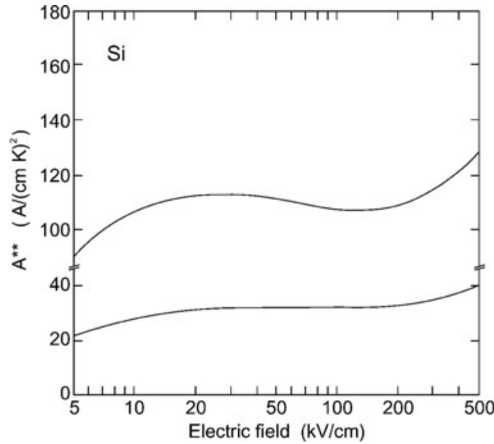

Fig. 20.17. Calculated effective Richardson constant A^{**} as a function of the electric field for a metal–Si diode at $T = 300\,\mathrm{K}$ for a (n-type or p-type) doping of $10^{16}\,\mathrm{cm}^{-3}$. Adapted from [1149]

emission (TF). For very high temperatures enough carriers can overcome the barrier completely and we are back in the thermionic emission regime. The validity of the two regimes is shown in Fig. 20.18 for Au/GaAs Schottky diodes as a function of doping concentration (n-type) and temperature.

In the field-emission regime the forward current is given by

$$j = j_{\mathrm{s}} \exp\left(\frac{eV}{E_{00}}\right) , \tag{20.50}$$

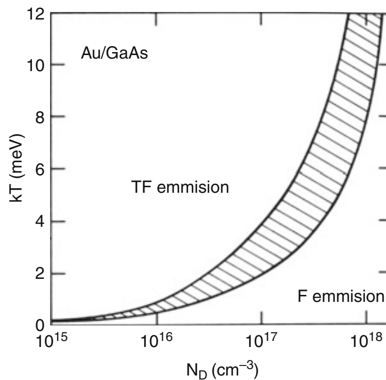

Fig. 20.18. Calculated conditions for thermionic field ('TF') and field ('F') emission in a Au/GaAs Schottky diode as a function of temperature and doping concentration. Adapted from [1118]

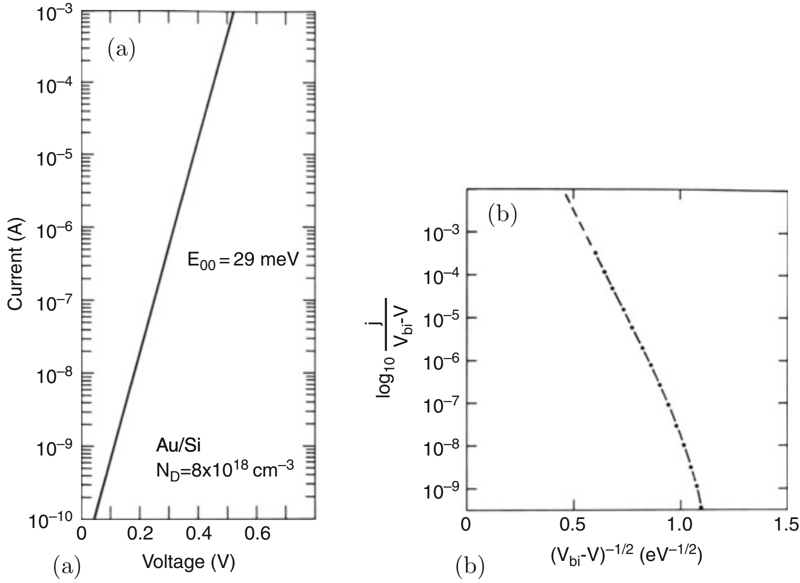

Fig. 20.19. (**a**) Forward and (**b**) reverse I–V characteristic of a Au/Si Schottky diode at 77 K. The doping concentration of the Si was $N_{\mathrm{D}} = 8 \times 10^{18}\,\mathrm{cm}^{-3}$. Adapted from [1118]

with the characteristic energy parameter E_{00} given by

$$E_{00} = \frac{e\hbar}{2} \sqrt{\frac{N_{\mathrm{D}}}{m^* \epsilon_{\mathrm{s}}}} \, . \tag{20.51}$$

The saturation current is

$$j_{\mathrm{s}} \propto \exp\left(-F_{\mathrm{Bn}}/E_{00}\right) \, . \tag{20.52}$$

In Fig. 20.19, the forward characteristic of a highly doped Au/Si is shown. The experimental value of $E_{00} = 29\,\mathrm{meV}$ agrees well with the theoretical expectation of $E_{00} = 29.5\,\mathrm{meV}$.

In the reverse direction the I–V characteristic under field emission is given by

$$j = \frac{4e\pi m^*}{h^3} \, E_{00}^2 \, \frac{e(V_{\mathrm{bi}} - V)}{F_{\mathrm{Bn}}} \, \exp\left(- \frac{2F_{\mathrm{Bn}}^{3/2}}{3E_{00}\sqrt{e(V_{\mathrm{bi}} - V)}} \right) \, . \tag{20.53}$$

From Fig. 20.19b, a barrier height of 0.79 eV is deduced.

In the TF-emission regime the current–voltage characteristic is given by

$$j = j_{\mathrm{s}} \exp\left(\frac{eV}{E_0}\right) \, , \tag{20.54}$$

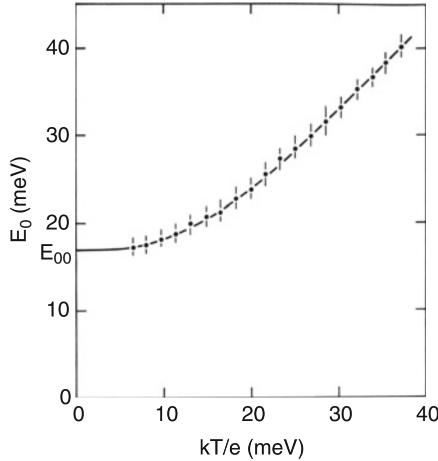

Fig. 20.20. Temperature dependence of E_0 of an Au/GaAs diode with $N_D = 5 \times 10^{17}\,\mathrm{cm}^{-3}$. The *solid line* is the theoretical dependence for thermionic emission according to (20.55) with $N_D = 6.5\times10^{17}\,\mathrm{cm}^{-3}$ and $m^* = 0.07$. Adapted from [1118]

with

$$E_0 = E_{00} \coth\left(\frac{E_{00}}{kT}\right) , \tag{20.55}$$

where E_{00} is given by (20.51). The energy for maximum TF emission E_m is given by $E_m = e(V_{bi} - V)/\cosh^2(E_{00}/kT)$. The coth-dependence of E_0 is shown in Fig. 20.20 for an Au/GaAs diode.

A Schottky diode can suffer from nonideality such as series and parallel ohmic resistance [1143]. These effects are discussed in some detail below for pn-diodes in Sect. 20.4.4 and apply similarly to Schottky diodes.

20.2.6 Ohmic Contacts

Although an ohmic contact does not have a diode characteristic, it can be understood from the previous remarks. An ohmic contact will have a small contact resistance for both current directions. The voltage drop across the contact will be small compared to the voltage drop in the active layer (somewhere else). The contact resistance R_c is defined as the differential resistance at $V = 0$

$$R_c = \left(\frac{\partial I}{\partial V}\right)^{-1}_{V=0} . \tag{20.56}$$

At low doping, the transport is dominated by thermionic emission (20.36). In this case R_c is given by

$$R_c = \frac{k}{eA^* T} \exp\left(\frac{F_{Bn}}{kT}\right) . \tag{20.57}$$

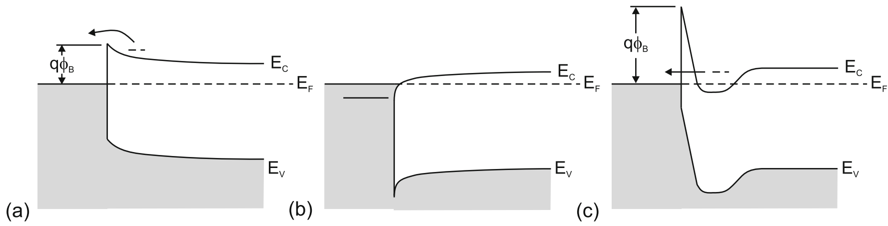

Fig. 20.21. Schematic conditions for the formation of an Ohmic contact, (**a**) low barrier height, (**b**) accumulation layer (**c**) high doping (thin depletion layer)

A small barrier height (Fig. 20.21a) will lead to small contact resistance. A negative Schottky barrier height, i.e. $W_{\mathrm{m}} < E_{\mathrm{vac}} - E_{\mathrm{F}}$ for a n-type semiconductor, leads to an accumulation layer without a barrier for carrier transport (Fig. 20.21b).

For high doping R_{c} is determined by the tunneling current (Fig. 20.21c) and is proportional to

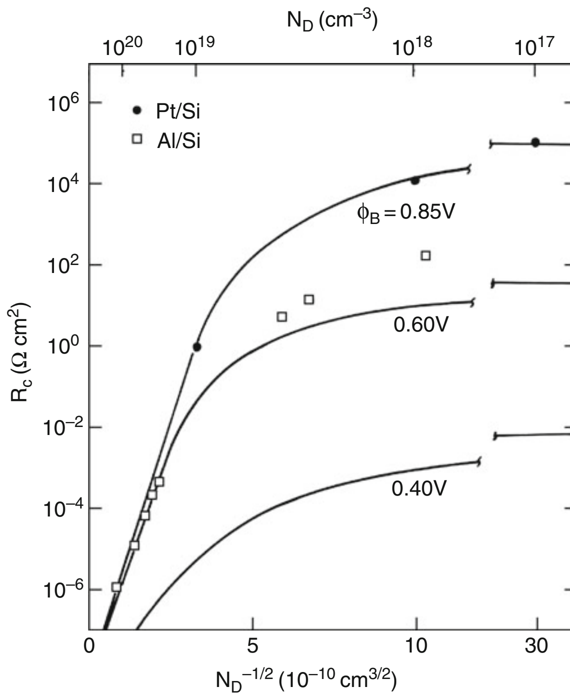

Fig. 20.22. Theoretical and experimental values of specific contact resistances at $T = 300\,\mathrm{K}$ for Al/n-Si [1152] and PtSi/n-Si [1153] contacts as a function of donor concentration. *Solid lines* are theoretical dependencies for different values of the barrier height as labeled. Adapted from [384]

$$R_c \propto \exp\left(\frac{F_{\mathrm{Bn}}}{E_{00}}\right) . \tag{20.58}$$

The contact resistance decreases exponentially with the doping. A theoretical calculation and experimental data are compared in Fig. 20.22 for contacts on Si.

The three mechanisms, low barrier height, accumulation layer and high doping, for the formation of Ohmic contacts are summarized schematically in Fig. 20.21. Ohmic contacts on wide band gap semiconductors are difficult, since metals with sufficiently small (large) work function for contacting n-type (p-type) material are mostly not available.

Although Schottky contact devices have their place in semiconductor technology, Ohmic contacts are indispensable for almost all devices.[11] Ohmic contacts are typically prepared by evaporating a contact metal containing the doping material for the semiconductor, e.g. Au/Zn for a contact on p-type GaAs [1150] and Au/Ge for a contact [1151] on n-type GaAs. The contact is alloyed around 400–500 °C (see Fig. 20.23) above the eutectic temperature of $T_{\mathrm{eu}} = 360\,°\mathrm{C}$ (for Au/Ge) to form a eutectic liquid in which the dopant can quickly diffuse. When the eutectic liquid cools it forms a solid, a highly doped semiconductor layer underneath the metal. The liquid-phase reactions can lead to inhomogeneous contacts. On n-type GaAs Pd/Ge/Au contacts

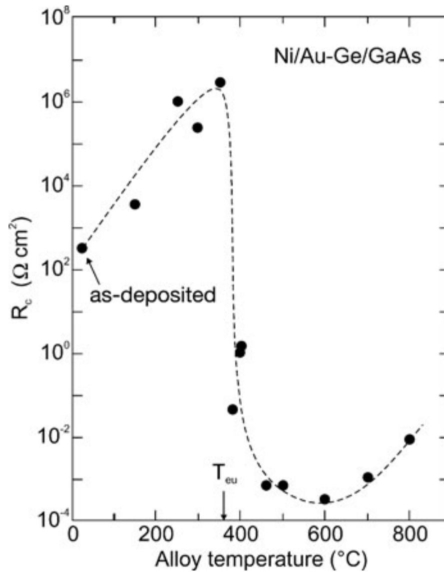

Fig. 20.23. Specific contact resistance for Ni/Au-Ge on n-type epitaxial GaAs for varying alloying temperatures (2 min). *Arrow* at T_{eu} denotes the eutectic temperature of Au-Ge. Adapted from [1157]

[11] Also a Schottky diode has an Ohmic back contact.

have been reported to have superior structural quality [1154]. Ohmic contacts for a number of different semiconductors are reviewed in [1155, 1156].

20.2.7 Metal Contacts to Organic Semiconductors

Also, for organic semiconductors the metal contact plays a vital role, either for carrier injection or for manipulation of the space-charge region. The position of the Fermi level has been determined for various organic semiconductors as shown in Fig. 20.24. These data have been obtained from measurements on metal–semiconductor–metal structures (MSM, see also Sect. 21.3.5) as shown in Fig. 20.25a. The thin (50 nm) organic layer is fully depleted, thus the built-in field inside the semiconductor is constant. The built-in field is measured by applying an external dc bias and finding the external potential at which the electroabsorption signal vanishes. Figure 20.25b shows the mea-

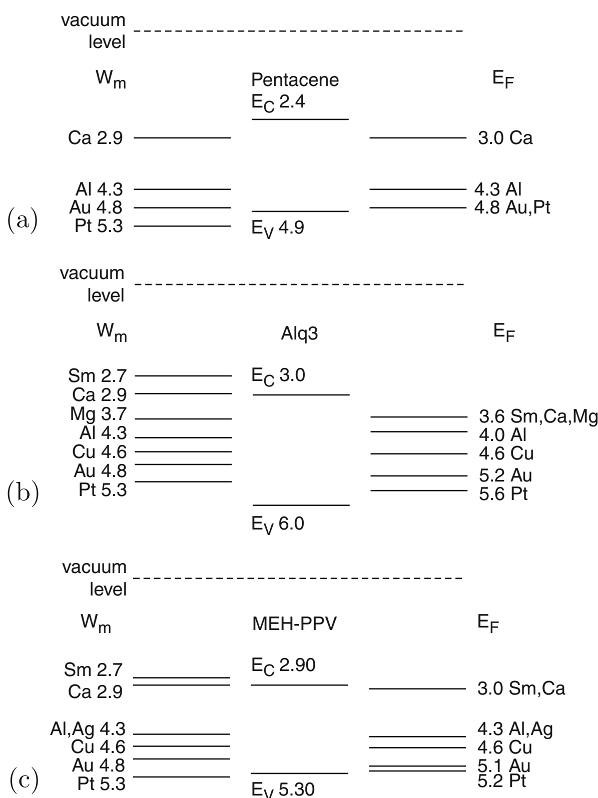

Fig. 20.24. Measured Fermi energies E_{F} (*labeled data* in eV) and the work functions W_{m} of various metals contacting (**a**) pentacene, (**b**) $\mathrm{Alq_3}$ and (**c**) MEH-PPV. E_{C} (E_{V}) denotes the energy position of the electron (hole) polaron. Measured data for E_{F} for MEH-PPV from [1159], other from [1160]. Data for W_{m} from Table 20.1

sured electroabsorption signal $\Delta T/T$ (relative change of transmission T) and the optical density of an MEH-PPV film as a function of photon energy for an Al/MEH-PPV/Al structure. The exciton absorption peak is found at 2.25 eV. The bias at which the built-in field vanishes can then be determined for various other metals in metal/MEH-PPV/Al structures. Figure 20.24 summarizes such results for various metals and three organic semiconductors. The plot of the Fermi level position vs. the metal work function (Figs. 20.25d,e) shows that the metals investigated do not introduce interface states in the

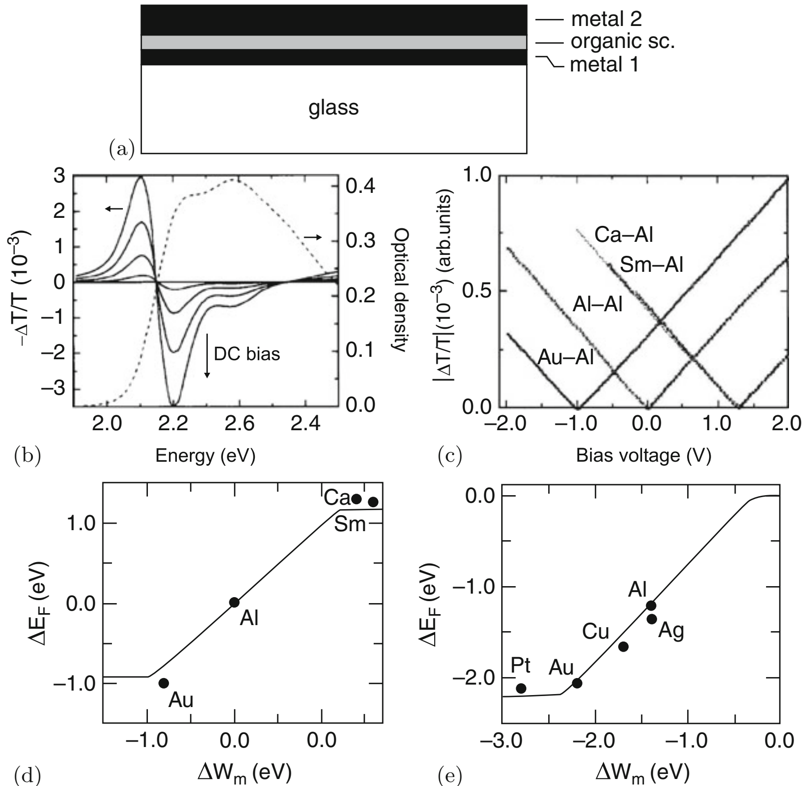

Fig. 20.25. (**a**) Schematic MSM structure with organic semiconductor (sc.) on transparent glass substrate. Metal 1 is thin and semitransparent. Thickness of organic semiconductor (polymer or small molecules) is about 50 nm. (**b**) Electroabsorption spectra of Al/MEH-PPV/Al structure at four dc bias voltages (*solid lines*) and optical density spectrum (*dashed line*). (**c**) Magnitude of the electroabsorption response at 2.1 eV as a function of bias for metal/MEH-PPV/Al structures. (**d**,**e**) Calculated (*solid lines*) and experimental (*points*) potential difference across (**d**) metal/MEH-PPV/Al structures and (**e**) metal/MEH-PPV/Ca structures as a function of the work-function difference of the contacts. Parts (**b**)–(**e**) adapted from [1159]

single-particle gap that pin the Schottky barrier (see Fig. 20.5 for inorganic semiconductors). An electron trap, such as C_{60} in MEH-PPV, can pin the Fermi level of the n-contact metal and leads to a change of the built-in potential [1158].

20.3 Metal–Insulator–Semiconductor Diodes

In a metal–insulator–semiconductor (MIS) diode an insulator is sandwiched between the metal and the semiconductor. Subsequently, a MIS contact has zero dc conductance. The semiconductor typically has an ohmic back contact. As insulator, often the oxide of the respective semiconductor, is used. In particular SiO_2 on Si has been technologically advanced (Fig. 20.26). In the latter case, the diode is called a MOS (metal–oxide–semiconductor) diode. This structure has great importance for the investigation of semiconductor surfaces and overwhelming importance for semiconductor technology (planar integration of electronic circuits, CMOS technology). Also, CCDs (Sect. 21.3.8) are based on MIS diodes.

20.3.1 Band Diagram for Ideal MIS Diode

An ideal MIS diode has to fulfill the following three conditions:

(i) (as shown in Fig. 20.27) without external bias the energy difference ϕ_{ms} between the work function of the metal and the semiconductor

$$\phi_{\mathrm{ms}} = W_{\mathrm{m}} - \left(\chi_{\mathrm{sc}} + \frac{E_{\mathrm{g}}}{2} \pm e\Psi_{\mathrm{B}} \right) \tag{20.59}$$

is zero ($\phi_{\mathrm{ms}} = 0$). The '+' ('−') sign in (20.59) applies to a p-type, Fig. 20.27b (n-type, Fig. 20.27a) semiconductor. Ψ_{B} is the potential difference between the intrinsic and actual Fermi level, $\Psi_{\mathrm{B}} = |E_{\mathrm{i}} - E_{\mathrm{F}}|/e > 0$.

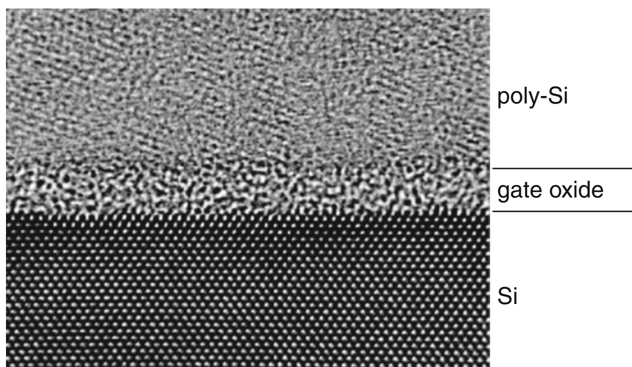

Fig. 20.26. High-resolution transmission electron microscopy image of a 1.6-nm thick gate oxide between poly-Si (cf. Sect. 23.5.4) and crystalline Si. From [1161]

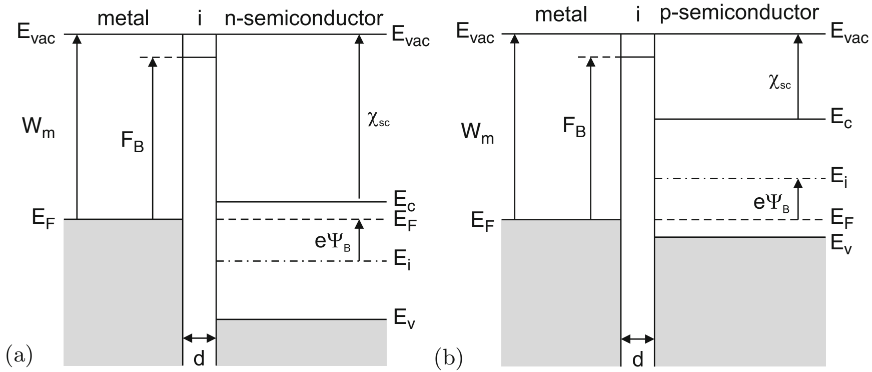

Fig. 20.27. Band diagram of an ideal MIS diode with (**a**) n- and (**b**) p-type semiconductor at external bias $V = 0$. The insulator ('i') thickness is d as labeled. The *dash-dotted line* represents the intrinsic Fermi level E_{i}

(ii) The only charges present are those in the semiconductor and the opposite charge is on the metal surface close to the insulator.
(iii) There is no dc current between the metal and the semiconductor, i.e. the conductivity of the insulator is zero.

When an ideal MIS diode is biased, three general cases – accumulation, depletion and inversion – can occur (Fig. 20.28). We discuss these first for the p-type semiconductor.

Figure 20.28d shows the accumulation case for a negative voltage at the metal.[12] Part of the voltage drops across the insulator, the rest across the semiconductor. The valence band is bent upwards towards the Fermi level. The quasi-Fermi level in the semiconductor, however, is constant since no dc current flows.[13]

Since the charge-carrier (hole) density depends exponentially on the energy separation $E_{\mathrm{F}} - E_{\mathrm{V}}$, a charge accumulation (of holes) occurs in the (p-type) semiconductor in the vicinity of the interface to the insulator.

In Fig. 20.28e the depletion case is shown. Now a moderate reverse voltage, i.e. a positive bias to the metal, is applied. A depletion of majority charge carriers occurs in the semiconductor close to the insulator. The quasi-Fermi level in the semiconductor remains beneath the intrinsic level ($E_{\mathrm{i}} \approx E_{\mathrm{C}} + E_{\mathrm{g}}/2$), i.e. the semiconductor remains p-type everywhere. If the voltage is

[12]This poling is a forward bias of the respective Schottky diode since the positive pole is at the p-type semiconductor.

[13]We note that in order to reach the situations shown in Fig. 20.28 from the zero bias case of Fig. 20.27, a current must have flowed since charge carriers are redistributed. Figure 20.28 depicts the stationary equilibrium after transient voltage switch-on effects have subsided. The time, however, that is needed in order to reach such stationary equilibrium from zero bias (thermal equilibrium) may be very long (e.g. days, cf. Sect. 21.3.8).

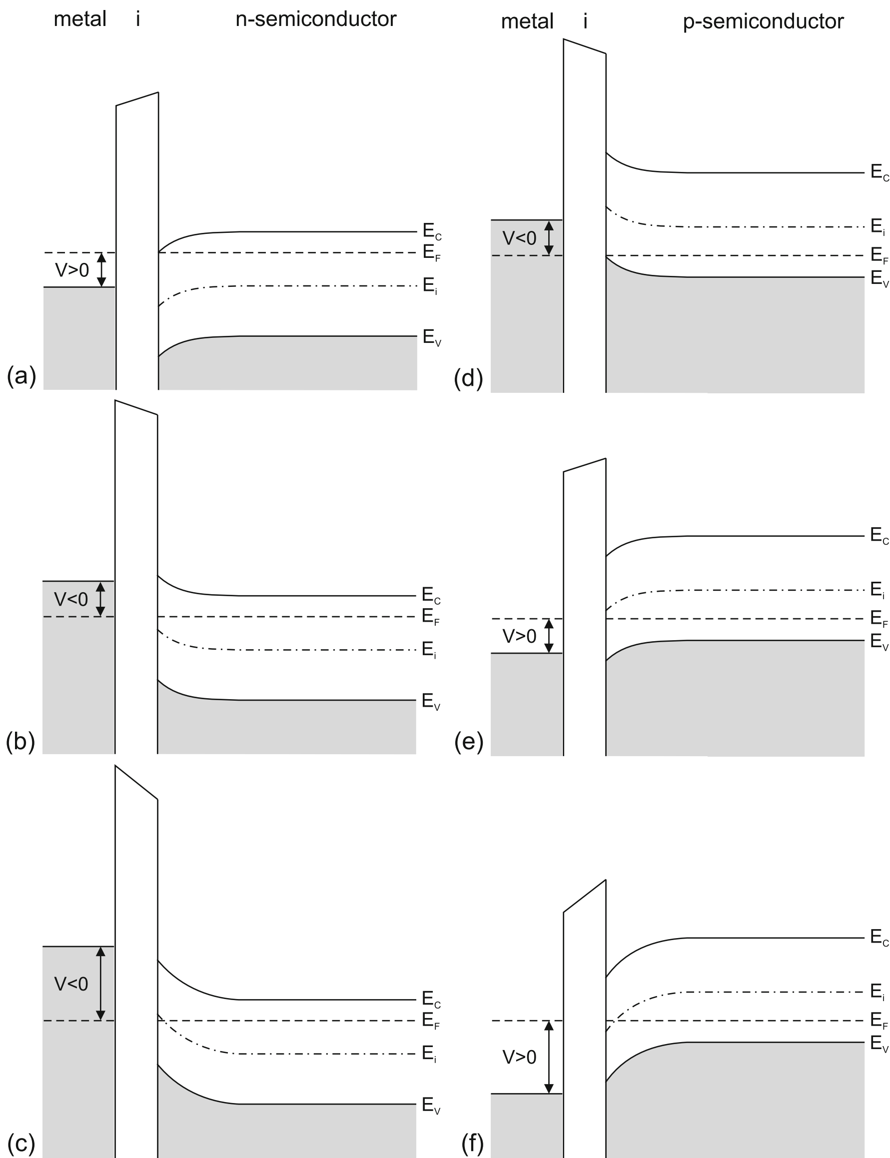

Fig. 20.28. Band diagram of ideal MIS diodes with (**a**,**b**,**c**) n-type and (**d**,**e**,**f**) p-type semiconductors for $V \neq 0$ in stationary equilibrium for the cases (**a**,**d**) accumulation, (**b**,**e**) depletion and (**c**,**f**) inversion

increased further to large values, the quasi-Fermi level intersects the intrinsic level and lies *above* E_i close to the insulator (Fig. 20.28f). In this region, the electron concentration becomes larger than the hole concentration and we have the inversion case. The inversion is called 'weak' if the Fermi level is still close to E_i. The inversion is called 'strong' when the Fermi level lies close to the conduction-band edge.

The corresponding phenomena occur for n-type semiconductors for the opposite signs of the voltage with electron accumulation and depletion. In the inversion case, $p > n$ close to the insulator (Figs. 20.28a–c).

20.3.2 Space-Charge Region

Now we calculate the charge and electric field distribution in an ideal MIS diode, following the treatment in [1162]. We introduce the potential Ψ that measures the separation of the intrinsic bulk Fermi level and the actual intrinsic level E_i, i.e. $-e\Psi(x) = E_\mathrm{i}(x) - E_\mathrm{i}(x \to \infty)$ (see Fig. 20.29). Its value at the surface is termed Ψ_s, the surface potential. The value is positive, i.e. $\Psi_\mathrm{s} > 0$, if the intrinsic Fermi level at the surface is below the bulk Fermi level.

The electron and hole concentrations are given (for a p-type semiconductor) as

$$n_\mathrm{p} = n_{\mathrm{p}_0} \exp(\beta\Psi) \tag{20.60a}$$

$$p_\mathrm{p} = p_{\mathrm{p}_0} \exp(-\beta\Psi) \ , \tag{20.60b}$$

where n_{p_0} (p_{p_0}) are the bulk electron (hole) concentrations, respectively, and $\beta = e/kT > 0$.

Therefore, the net free charge is given by

$$n_\mathrm{p} - p_\mathrm{p} = n_{\mathrm{p}_0} \exp(\beta\Psi) - p_{\mathrm{p}_0} \exp(-\beta\Psi) \ . \tag{20.61}$$

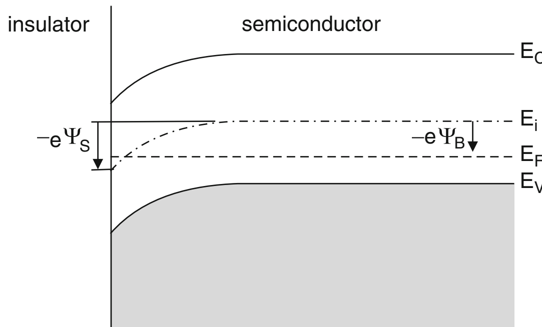

Fig. 20.29. Band diagram at the surface of a p-type semiconductor of a MIS diode. Accumulation occurs for $\Psi_\mathrm{s} < 0$, depletion for $\Psi_\mathrm{s} > 0$ and inversion (as shown here) for $\Psi_\mathrm{s} > \Psi_\mathrm{B} > 0$

The electron and hole concentrations at the surface are denoted with an index ‘s’ and are given by[14]

$$n_{\rm s} = n_{\rm p_0}\, \exp(\beta \Psi_{\rm s}) \tag{20.62a}$$

$$p_{\rm s} = p_{\rm p_0}\, \exp(-\beta \Psi_{\rm s})\ . \tag{20.62b}$$

We use the Poisson equation $\frac{{\rm d}^2\Psi}{{\rm d}x^2} = -\frac{\rho}{\epsilon_{\rm s}}$ with the charge given by

$$\rho(x) = e\left[p(x) - n(x) + N_{\rm D}^{+}(x) - N_{\rm A}^{-}(x)\right]\ . \tag{20.63}$$

As boundary condition we employ that far away from the surface (for $x \to \infty$) there is charge neutrality (cf. (7.47)), i.e.

$$n_{\rm p_0} - p_{\rm p_0} = N_{\rm D}^{+} - N_{\rm A}^{-}\ , \tag{20.64}$$

and that $\Psi = 0$. We note that $N_{\rm D}^{+} - N_{\rm A}^{-}$ must be constant throughout the completely ionized, homogeneous semiconductor. Therefore (20.64) (but not charge neutrality) holds everywhere in the semiconductor. Using (20.61) the Poisson equation reads

$$\frac{\partial^2\Psi}{\partial x^2} = -\frac{e}{\epsilon_{\rm s}}\{p_{\rm p_0}\left[\exp(-\beta\Psi) - 1\right] - n_{\rm p_0}\left[\exp(\beta\Psi) - 1\right]\}\ . \tag{20.65}$$

The Poisson equation is integrated and with the notations

$$\mathcal{F}(\Psi) = \left[(\exp(-\beta\Psi) + \beta\Psi - 1) + \frac{n_{\rm p_0}}{p_{\rm p_0}}(\exp(\beta\Psi) - \beta\Psi - 1)\right]^{1/2} \tag{20.66a}$$

$$L_{\rm D} = \sqrt{\frac{\epsilon_{\rm s} kT}{e^2 p_{\rm p_0}}} = \sqrt{\frac{\epsilon_{\rm s}}{e\beta p_{\rm p_0}}}\ , \tag{20.66b}$$

with $L_{\rm D}$ being the Debye length for holes, the electric field can be written as

$$\mathcal{E} = -\frac{\partial\Psi}{\partial x} = \pm\frac{\sqrt{2}kT}{eL_{\rm D}}\mathcal{F}(\Psi)\ . \tag{20.67}$$

The positive (negative) sign is for $\Psi > 0$ ($\Psi < 0$), respectively. At the surface, $\Psi_{\rm s}$ will be taken as the value for Ψ. The total charge $Q_{\rm s}$ per unit area creating the surface field

$$\mathcal{E}_{\rm s} = -\frac{\partial\Psi}{\partial x} = \pm\frac{\sqrt{2}kT}{eL_{\rm D}}\mathcal{F}(\Psi_{\rm s}) \tag{20.68}$$

is given by Gauss’s law as $Q_{\rm s} = -\epsilon_{\rm s}\mathcal{E}_{\rm s}$.

---

[14] $\Psi_{\rm s}$ represents the voltage drop across the semiconductor that will be discussed in more detail in Sect. 20.3.3. In this sense, $\Psi_{\rm s}$ for the MIS diode is related to $V_{\rm bi} - V$ for the Schottky contact.

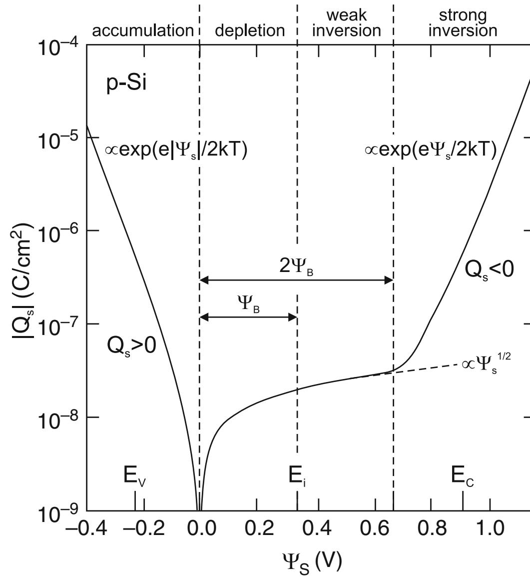

Fig. 20.30. Dependence of the space charge on the surface potential Ψ_s for p-type silicon with $N_\mathrm{A} = 4 \times 10^{15}\,\mathrm{cm}^{-3}$ at $T = 300\,\mathrm{K}$. The flat-band condition is present for $\Psi_\mathrm{s} = 0$

The dependence of the space-charge density from the surface potential[15] is depicted in Fig. 20.30. If Ψ_s is negative, $\mathcal{F}$ is dominated by the first term in (20.66a) and the space charge is positive (accumulation) and proportional to $Q_\mathrm{s} \propto \exp(-\beta|\Psi|/2)$. For $\Psi_\mathrm{s} = 0$ the (ideal) MIS diode has the flat-band condition and the space charge is zero. For $0 \leq \Psi_\mathrm{s} \leq \Psi_\mathrm{B}$ the space charge is negative (depletion) and $\mathcal{F}$ is dominated by the second term in (20.66a), i.e. $\Psi_\mathrm{s} \propto \sqrt{\Psi_\mathrm{s}}$. For $\Psi_\mathrm{s} \gg \Psi_\mathrm{B}$ we are in the (weak) inversion regime and the space charge is dominated by the fourth term in (20.66a), $Q_\mathrm{s} \propto -\exp(-\beta\Psi/2)$. Strong inversion starts at about $\Psi_\mathrm{s}^\mathrm{inv} \approx 2\Psi_\mathrm{B} = (2kT/e)\ \ln(N_\mathrm{A}/n_\mathrm{i})$.

For the case of strong inversion the band diagram is shown in Fig. 20.31 together with the charge, field and potential. The total voltage drop V across the MIS diode is

$$V = V_\mathrm{i} + \Psi_\mathrm{s}\ , \tag{20.69}$$

with V_i being the voltage drop across the insulator. In the case of inversion, the charge (per unit area) in the space-charge region

$$Q_\mathrm{s} = Q_\mathrm{d} + Q_\mathrm{n} \tag{20.70}$$

[15] We note that we discuss the space-charge region now only with regard to Ψ_s, the voltage drop across the semiconductor, and the dependence of Ψ_s on the bias of the diode will be discussed in the next section.

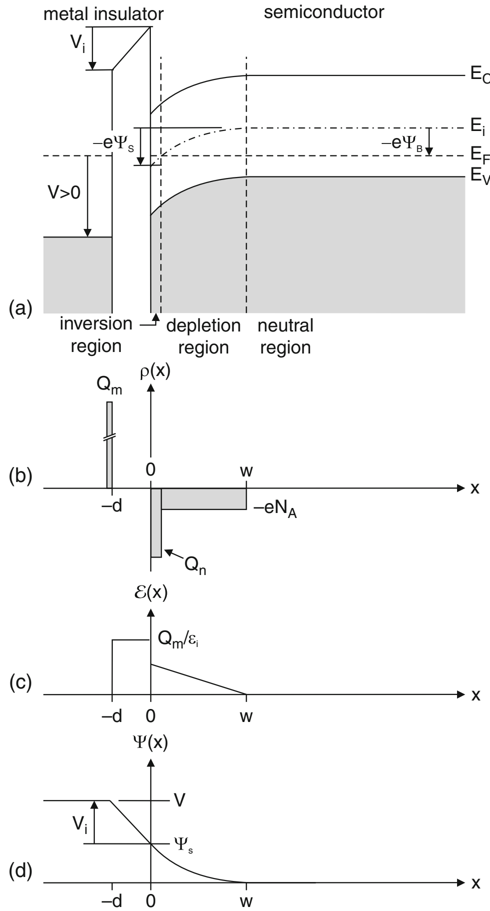

Fig. 20.31. Ideal MIS diode at inversion: (**a**) band diagram, (**b**) charge distribution, (**c**) electric field and (**d**) potential

is composed of the depletion charge (ionized acceptors)

$$Q_{\mathrm{d}} = -ewN_{\mathrm{A}} \;, \tag{20.71}$$

with w being the width of the depletion region, and the inversion charge Q_{n}, which is present only close to the interface.

The metal surface carries the opposite charge

$$Q_{\mathrm{m}} = -Q_{\mathrm{s}} \tag{20.72}$$

due to global charge neutrality. The insulator itself does not contribute charges in the case of an ideal MIS diode.

20.3.3 Capacitance

The insulator represents a capacitor with the dielectric constant ϵ_{i} and a thickness d. Therefore, the capacitance is

$$C_{\mathrm{i}} = \frac{\epsilon_{\mathrm{i}}}{d} \,. \tag{20.73}$$

Between the charges $-Q_{\mathrm{s}}$ and Q_{s} the field strength $\mathcal{E}_{\mathrm{i}}$ in the insulator is

$$\mathcal{E}_{\mathrm{i}} = \frac{|Q_{\mathrm{s}}|}{\epsilon_{\mathrm{i}}} \,. \tag{20.74}$$

The voltage drop V_{i} across the insulator is given by

$$V_{\mathrm{i}} = \mathcal{E}_{\mathrm{i}}\, d = \frac{|Q_{\mathrm{s}}|}{C_{\mathrm{i}}} \,. \tag{20.75}$$

The total capacitance C of the MIS diode is given by the insulator capacitance in series with the capacitance C_{d} of the depletion layer

$$C = \frac{C_{\mathrm{i}}\, C_{\mathrm{d}}}{C_{\mathrm{i}} + C_{\mathrm{d}}} \,. \tag{20.76}$$

The capacitance of the space-charge region varies with the applied bias (Fig. 20.32). For forward bias (accumulation), the capacitance of the space-charge region is high. Therefore, the total capacitance of the MIS diode is given by the insulator capacitance $C \approx C_{\mathrm{i}}$. When the voltage is reduced, the capacitance of the space-charge region drops to $C_{\mathrm{d}} = \epsilon_{\mathrm{s}}/L_{\mathrm{D}}$ for the flat-band case ($\Psi_{\mathrm{s}} = 0$). For a high reverse voltage, the semiconductor is inverted at the surface and the space-charge region capacitance is high again. In this case, the total capacitance is given by $C \approx C_{\mathrm{i}}$ again.

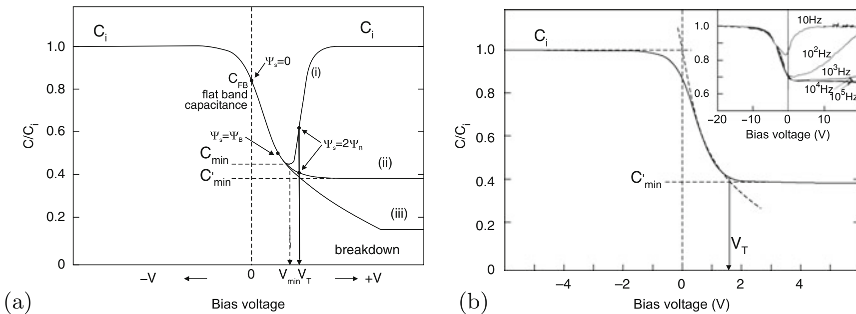

Fig. 20.32. (**a**) Schematic dependence of the capacitance of a MIS diode on the bias for (i) low frequencies, (ii) high frequencies and (iii) deep depletion. (**b**) High-frequency capacitance of a Si/SiO_2 diode. The *inset* shows the frequency dependence. Adapted from [1163]

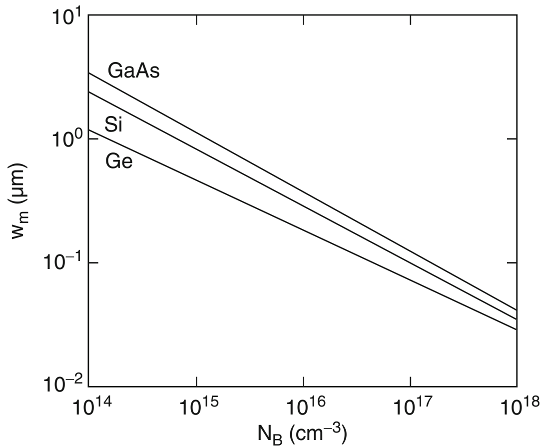

Fig. 20.33. Maximum width of the depletion layer w_{m} (20.77) at room temperature for deep depletion for GaAs, Si and Ge diodes as a function of bulk doping level

The previous consideration assumes that the charge density in the semiconductor can follow changes of the bias sufficiently fast.[16] The inversion charge must disappear via recombination that is limited by the recombination time constant τ. For frequencies around τ^{-1} or faster, the charge in the inversion layer cannot follow and the capacitance of the semiconductor is given by the value $C_{\mathrm{d}} \cong \epsilon_{\mathrm{s}}/w_{\mathrm{m}}$. w_{m} (Fig. 20.33) is the maximum depletion-layer width present at the beginning of inversion (cf. (20.9))

$$w_{\mathrm{m}} \cong \sqrt{\frac{2\epsilon_{\mathrm{s}}}{eN_{\mathrm{A}}}\Psi_{\mathrm{s}}^{\mathrm{inv}}} = \sqrt{\frac{4\epsilon_{\mathrm{s}}kT\,\ln(N_{\mathrm{A}}/n_{\mathrm{i}})}{e^2 N_{\mathrm{A}}}}\,. \tag{20.77}$$

For further increased voltage (into the inversion regime), the electric field is screened by the inversion charge and the width of the depletion layer remains constant. Therefore, the total capacitance in the inversion regime is given by

$$C \cong \frac{\epsilon_{\mathrm{i}}}{d + w_{\mathrm{m}}\,\epsilon_{\mathrm{i}}/\epsilon_{\mathrm{s}}}\,. \tag{20.78}$$

20.3.4 Nonideal MIS Diode

In a real, i.e. nonideal, MIS diode, the difference ϕ_{ms} in the work functions of the metal and semiconductor (cf. (20.59)) is no longer zero. Therefore, the capacitance vs. voltage relation is shifted with respect to the ideal MIS diode characteristic by the *flat-band voltage shift* V_{FB}

[16] Typically, a dc bias voltage V is set and the capacitance is sampled with a small ac voltage of amplitude ΔV, with $\delta V \ll V$.

$$V_{\mathrm{FB}} = \phi_{\mathrm{ms}} - \frac{Q_{\mathrm{ox}}}{C_{\mathrm{i}}} \,. \tag{20.79}$$

Additionally, the flat-band voltage can be shifted by charges Q_{ox} in the oxide that have been neglected so far. Such charges can be trapped, i.e. fixed with regard to their spatial position, or mobile, e.g. ionic charges such as sodium.

For Al as metal ($\phi_{\mathrm{m}} = 4.1\,\mathrm{eV}$) and n-type Si ($\phi_{\mathrm{s}} = 4.35\,\mathrm{eV}$), the flat-band voltage shift is $\phi_{\mathrm{ms}} = -0.25\,\mathrm{V}$, as shown schematically in Fig. 20.34a for zero bias. V_{FB} is split into 0.2 eV and 0.05 eV for the oxide and the silicon, respectively. In Fig. 20.34b, the dependence of ϕ_{ms} on the doping, conductivity type and metal is shown for various SiO_2–Si MIS diodes. An Au-SiO_2–Si diode with p-type Si and $N_{\mathrm{A}} \approx 10^{15}\,\mathrm{cm}^{-3}$ fulfills the condition of an ideal MIS diode with regard to $\phi_{\mathrm{ms}} = 0$.

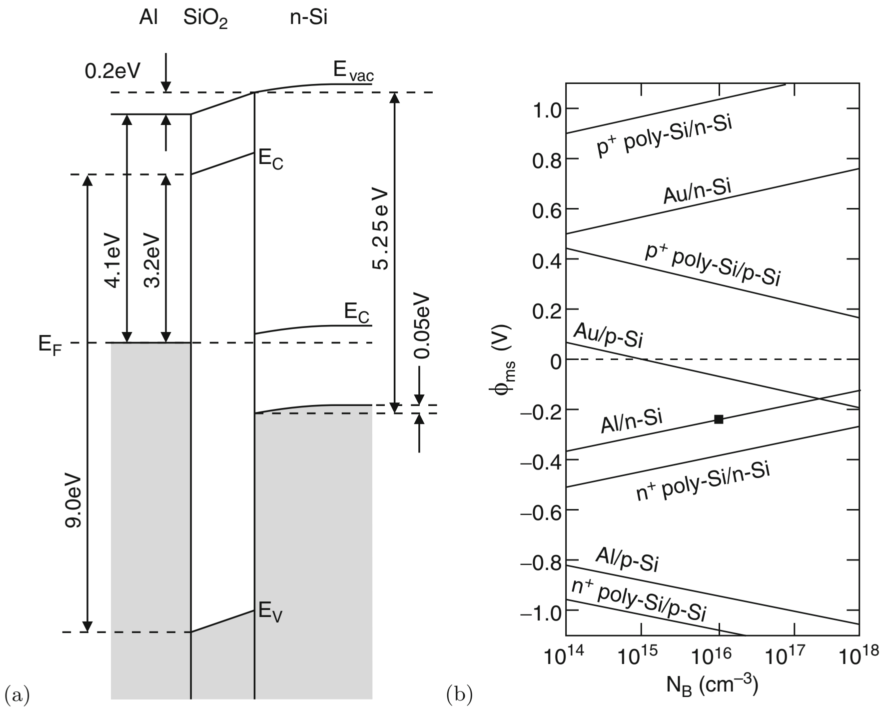

Fig. 20.34. (**a**) Schematic band diagram of an Al–SiO_2–Si (n-type) diode with 50 nm oxide thickness and $N_{\mathrm{D}} = 10^{16}\,\mathrm{cm}^{-3}$ for zero bias. Based on data from [1164]. (**b**) Difference of work functions ϕ_{ms} for SiO_2–Si MIS diodes and various doping levels and electrode materials (Al, Au and polycrystalline Si). The *square* represents the situation depicted in panel (**a**). Based on data from [1165]

20.4 Bipolar Diodes

A large class of diodes is based on pn-junctions. In a homo pn-junction an n-doped region is next to a p-doped region of the same semiconductor. Such a device is called *bipolar*. At the junction a depletion region forms. The transport properties are determined by the minority carriers. An important variation is the pin-diode in which an intrinsic (or lowly doped) region is between the doped region (Sect. 20.5.8). If the differently doped regions belong to different semiconductor materials, the diode is a heterostructure pn-diode (Sect. 20.5.12). Various schemes have been used to fabricate pn diodes (Fig. 20.35).

20.4.1 Band Diagram

If the doping profile is arbitrarily sharp, the junction is called *abrupt* (Fig. 20.36b). This geometry is the case for epitaxial pn-junctions where the differently doped layers are grown on top of each other.[17] For junctions that are fabricated by diffusion, the abrupt approximation is suitable for alloyed, ion-implanted and shallow-diffused junctions. For deep-diffused junctions a linearly graded approximation is better (Fig. 20.36d), which is treated in more detail in [384]. If one doping level is much higher that the other, the junction is termed a *one-sided* (abrupt) junction. If $n \gg p$ ($p \gg n$), the junction is denoted as an n^+p-diode (p^+n-diode).

The thermodynamical equilibrium of a pn-diode is considered here only for the electronic system. The thermodynamic stability of the atomic doping distribution is discussed in [1166]. Typically, thermodynamics works to randomize the chemical concentration gradient; the existence of a pn-junction is due to the extremely low diffusion coefficient of dopants in the semiconductor lattice. Elevated temperatures can cause the destruction of the pn-diode via enhanced dopant diffusion (Sect. 4.2.3). However, a thermodynamically stable concentration gradient and thus a built-in field can exist in a multicomponent system [1166].

20.4.2 Space-Charge Region

In thermodynamical equilibrium, i.e. without external bias, no net current flows. The electron current is given by (8.52a)

$$\mathbf{j}_\mathrm{n} = -e\mu_\mathrm{n} n \mathcal{E} - \mu_\mathrm{n} n \nabla E_\mathrm{F} \ , \tag{20.80}$$

and therefore in the absence of external electric fields and zero net electron and hole currents the Fermi energy is constant:

[17] The choices of dopant and the growth conditions, in particular the temperature, need to be made such that no interdiffusion of the dopants takes place.

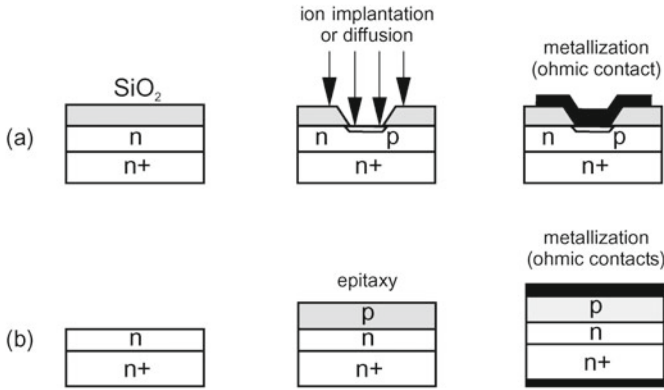

Fig. 20.35. Schematic fabrication technologies for bipolar diodes: (**a**) Planar junction with local impurity incorporation (diffusion from gas phase or ion implantation) through mask and contact metallization, (**b**) epitaxial junction

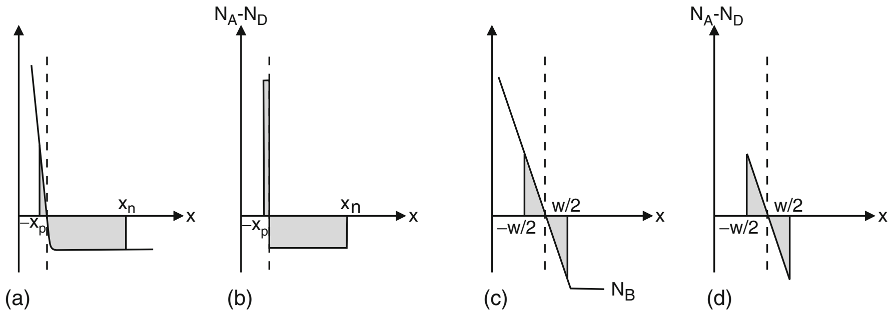

Fig. 20.36. Description of doping distribution with (**a**,**b**) abrupt approximation and with (**c**,**d**) linearly graded junction. (**a**,**c**) show real impurity concentration, (**b**,**d**) idealized doping profile

$$\nabla E_{\mathrm{F}} = 0 \, . \tag{20.81}$$

The built-in voltage V_{bi} is given by (see Fig. 20.37c)

$$eV_{\mathrm{bi}} = E_{\mathrm{g}} + eV_{\mathrm{n}} + eV_{\mathrm{p}} \, , \tag{20.82}$$

where V_{n} is the difference between conduction band and Fermi level on the n-side, $-eV_{\mathrm{n}} = E_{\mathrm{C}} - E_{\mathrm{F}}$. V_{p} is the difference between valence band and Fermi level on the p-side, $-eV_{\mathrm{p}} = E_{\mathrm{F}} - E_{\mathrm{V}}$. For the nondegenerate semiconductor $V_{\mathrm{n}}, V_{\mathrm{p}} < 0$ and (using (7.17), (7.15) and (7.16))

$$
\begin{aligned}
eV_{\mathrm{bi}} &= kT\,\ln\left(\frac{N_{\mathrm{C}}N_{\mathrm{V}}}{n_{\mathrm{i}}^2}\right) - \left[kT\,\ln\left(\frac{N_{\mathrm{C}}}{n_{\mathrm{n}_0}}\right) + kT\,\ln\left(\frac{N_{\mathrm{V}}}{p_{\mathrm{p}_0}}\right)\right] \\
&= kT\,\ln\left(\frac{p_{\mathrm{p}_0}n_{\mathrm{n}_0}}{n_{\mathrm{i}}^2}\right) = kT\,\ln\left(\frac{p_{\mathrm{p}_0}}{p_{\mathrm{n}_0}}\right) = kT\,\ln\left(\frac{n_{\mathrm{n}_0}}{n_{\mathrm{p}_0}}\right) \qquad (20.83\mathrm{a}) \\
&\cong kT\,\ln\left(\frac{N_{\mathrm{A}}N_{\mathrm{D}}}{n_{\mathrm{i}}^2}\right)\,. \qquad (20.83\mathrm{b})
\end{aligned}
$$

The electron and hole densities on either side of the junction (n_{p_0} and p_{p_0} at $x=-x_{\mathrm{p}}$ and n_{n_0} and p_{n_0} at $x=x_{\mathrm{n}}$) are related to each other by (from rewriting (20.83a))

$$
n_{\mathrm{p}_0} = n_{\mathrm{n}_0}\,\exp\left(-\beta V_{\mathrm{bi}}\right) \qquad (20.84\mathrm{a})
$$

$$
p_{\mathrm{n}_0} = p_{\mathrm{p}_0}\,\exp\left(-\beta V_{\mathrm{bi}}\right)\,. \qquad (20.84\mathrm{b})
$$

Microscopically, the equilibration of the Fermi levels on the n- and p-side occurs via the diffusion of electrons and holes to the p- and n-side, respectively. The electrons and holes recombine in the depletion layer. Therefore, on the n-side the ionized donors and on the p-side the ionized acceptors remain (Fig. 20.37a). These charges build up an electric field (Fig. 20.37d) that works against the diffusion current. At thermal equilibrium the diffusion and drift currents cancel and the Fermi level is constant.

Values for the built-in potential are depicted in Fig. 20.38 for Si and GaAs diodes. The spatial dependence of the potential in the depletion layer is determined by the Poisson equation.

We assume here the complete ionization of the donors and acceptors. Also, we neglect at first majority carriers in the depletion layers on the n- and p-sides.[18] With these approximations, the Poisson equation in the depletion layers on the n- and p-side reads

$$
\frac{\partial^2 V}{\partial x^2} = \frac{eN_{\mathrm{D}}}{\epsilon_{\mathrm{s}}},\ 0 \le x \le x_{\mathrm{n}} \qquad (20.85\mathrm{a})
$$

$$
\frac{\partial^2 V}{\partial x^2} = -\frac{eN_{\mathrm{A}}}{\epsilon_{\mathrm{s}}},\ -x_{\mathrm{p}} \le x \le 0\,. \qquad (20.85\mathrm{b})
$$

One integration yields (together with the boundary conditions that the field is zero at the boundaries of the depletion layer) the electric field in the two regions

$$
\mathcal{E}(x) = \frac{e}{\epsilon_{\mathrm{s}}}\,N_{\mathrm{D}}\,(x-x_{\mathrm{n}}),\ 0 \le x \le x_{\mathrm{n}} \qquad (20.86\mathrm{a})
$$

$$
\mathcal{E}(x) = -\frac{e}{\epsilon_{\mathrm{s}}}\,N_{\mathrm{A}}\,(x+x_{\mathrm{p}}),\ -x_{\mathrm{p}} \le x \le 0\,. \qquad (20.86\mathrm{b})
$$

[18] An abrupt decrease of the majority carrier density at the border of the space-charge region corresponds to zero temperature.

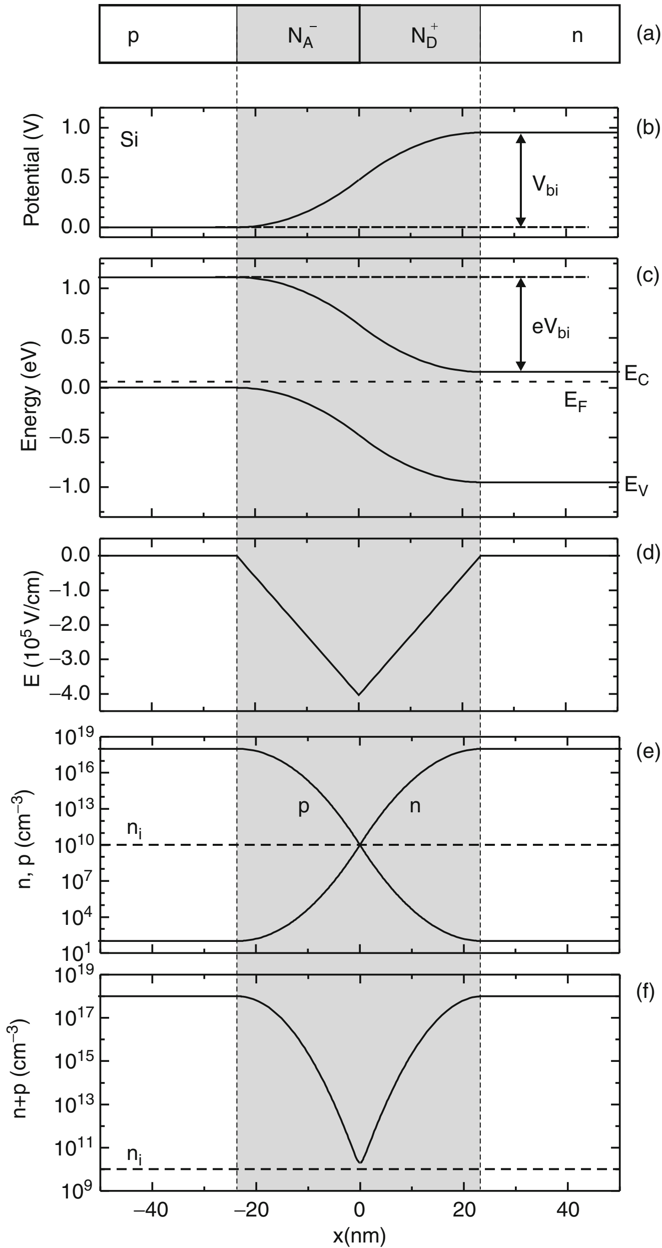

Fig. 20.37. pn-junction (abrupt approximation) in thermal equilibrium (zero bias) for Si at room temperature and $N_\mathrm{A} = N_\mathrm{D} = 10^{18}\,\mathrm{cm}^{-3}$. (**a**) Schematic representation of p-doped and n-doped region with depletion layer (*grey area*) and fixed space charges, (**b**) diffusion potential, (**c**) band diagram with Fermi level (*dashed line*), (**d**) electric field, (**e**) free-carrier concentrations n and p and (**f**) total free-carrier density $n + p$

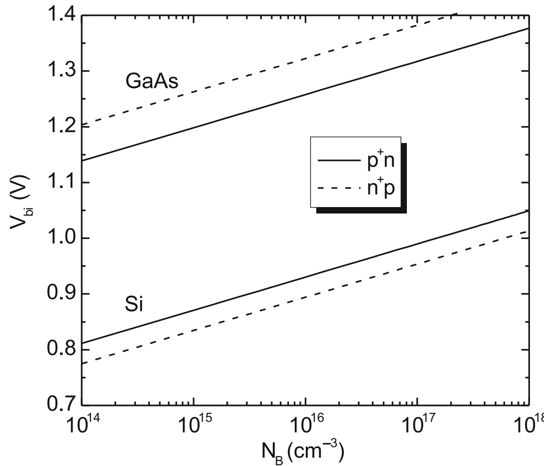

Fig. 20.38. Built-in voltage as a function of doping for one-sided Si and GaAs pn-diodes

The maximum field strength $\mathcal{E}_{\mathrm{m}}$ is present at $x = 0$ and is given by

$$\mathcal{E}_{\mathrm{m}} = -\frac{eN_{\mathrm{D}}x_{\mathrm{n}}}{\epsilon_{\mathrm{s}}} = -\frac{eN_{\mathrm{A}}x_{\mathrm{p}}}{\epsilon_{\mathrm{s}}} \,. \tag{20.87}$$

The continuity of the field at $x = 0$ is equivalent to the overall charge neutrality

$$N_{\mathrm{D}}\, x_{\mathrm{n}} = N_{\mathrm{A}}\, x_{\mathrm{p}} \,. \tag{20.88}$$

Another integration yields the potential (setting $V(x = 0) = 0$)

$$V(x) = -\mathcal{E}_{\mathrm{m}} \left(x - \frac{x^2}{2x_{\mathrm{n}}} \right), \; 0 \leq x \leq x_{\mathrm{n}} \tag{20.89a}$$

$$V(x) = -\mathcal{E}_{\mathrm{m}} \left(x + \frac{x^2}{2x_{\mathrm{p}}} \right), \; -x_{\mathrm{p}} \leq x \leq 0 \,. \tag{20.89b}$$

The built-in potential $V_{\mathrm{bi}} = V(x_{\mathrm{n}}) - V(-x_{\mathrm{p}}) > 0$ is related to the maximum field via

$$V_{\mathrm{bi}} = -\frac{1}{2}\, \mathcal{E}_{\mathrm{m}}\, w \,, \tag{20.90}$$

where $w = x_{\mathrm{n}} + x_{\mathrm{p}}$ is the total width of the depletion layer. The elimination of $\mathcal{E}_{\mathrm{m}}$ from (20.87) and (20.90) yields

$$w = \sqrt{\frac{2\epsilon_{\mathrm{s}}}{e} \left(\frac{N_{\mathrm{A}} + N_{\mathrm{D}}}{N_{\mathrm{A}} N_{\mathrm{D}}} \right) V_{\mathrm{bi}}} \,. \tag{20.91}$$

For $\mathrm{p}^+\mathrm{n}$ and $\mathrm{n}^+\mathrm{p}$ junctions, the width of the depletion layer is determined by the lowly doped side of the junction

$$w = \sqrt{\frac{2\epsilon_s}{eN_B} V_{bi}} \,, \tag{20.92}$$

where N_B denotes the doping of the lowly doped side, i.e. N_A for a n^+p diode and N_D for a p^+n diode.

If the spatial variation of the majority carrier density is considered in more detail (and for finite temperature, cf. (20.12)), an additional term $-2kT/e = -2/\beta$ is added [1162] to V_{bi}

$$w = \sqrt{\frac{2\epsilon_s}{e} \left(\frac{N_A + N_D}{N_A N_D}\right) \left(V_{bi} - V - \frac{2kT}{e}\right)} \,. \tag{20.93}$$

Also, the external bias V has been included in the formula. If w_0 denotes the depletion layer width at zero bias, the depletion layer width for a given voltage V can be written as

$$w(V) = w_0 \sqrt{1 - \frac{V}{V_{bi} - 2/\beta}} \approx w_0 \sqrt{1 - \frac{V}{V_{bi}}} \,. \tag{20.94}$$

Using the Debye length (cf. (20.66b))

$$L_D = \sqrt{\frac{\epsilon_s kT}{e^2 N_B}} \,, \tag{20.95}$$

the depletion layer width for a one-sided diode can be written as (with $\beta = e/kT$)

$$w = L_D \sqrt{2(\beta V_{bi} - \beta V - 2)} \,. \tag{20.96}$$

The Debye length is a function of the doping level and is shown for Si in Fig. 20.39. For a doping level of $10^{16}\,\mathrm{cm}^{-3}$ the Debye length in Si is 40 nm at room temperature. For one-sided junctions the depletion layer width is about $6\,L_D$ for Ge, $8\,L_D$ for Si and $10\,L_D$ for GaAs.

The external bias is counted positive if the '+' ('−') pole is at the p-side (n-side). The reverse voltage has opposite polarity. If a reverse bias is applied, the depletion layer width is increased (Fig. 20.40).

20.4.3 Capacitance

The capacitance of the depletion layer is the charge change upon a change of the external bias. It is given as

$$C = \left|\frac{\mathrm{d}Q}{\mathrm{d}V}\right| = \frac{\mathrm{d}(eN_B w)}{\mathrm{d}(w^2 e N_B / 2\epsilon_s)} = \frac{\epsilon_s}{w} = \frac{\epsilon_s}{\sqrt{2} L_D} \sqrt{\beta V_{bi} - \beta V - 2} \,. \tag{20.97}$$

Therefore, the capacitance of the depletion layer is inversely proportional to the depletion-layer width (see the two scales in Fig. 20.40). A detailed treatment has been given in [1167]. $1/C^2$ is proportional to the external bias

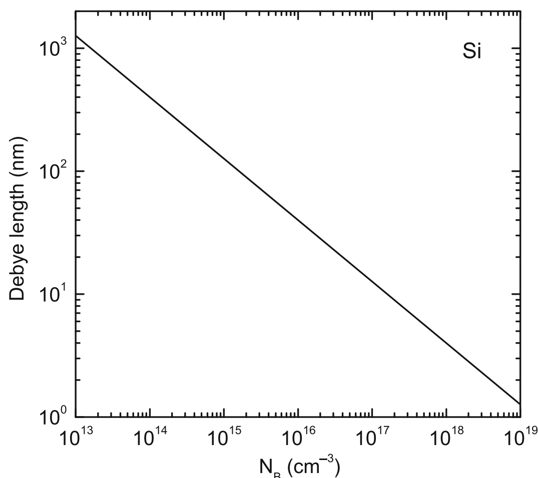

Fig. 20.39. Debye length in Si at room temperature as a function of the doping level N_B according to (20.95)

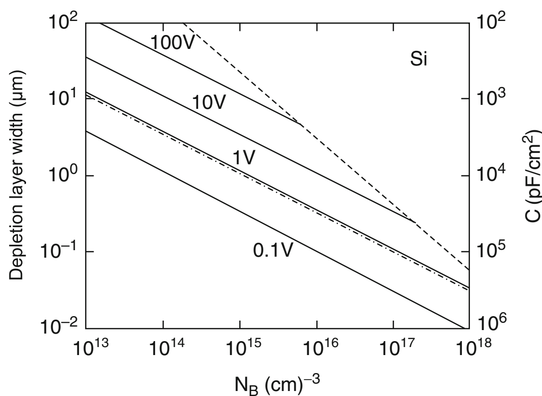

Fig. 20.40. Width of the depletion layer and capacitance per area for one-sided, abrupt Si junctions for various values of $V_{\mathrm{bi}} - V - 2kT/e$ as labeled. The *dash-dotted line* is for zero bias, the *dashed line* is the limit due to avalanche breakdown. Adapted from [384]

$$\frac{1}{C^2} = \frac{2L_{\mathrm{D}}^2}{\epsilon_{\mathrm{s}}^2} \left(\beta V_{\mathrm{bi}} - \beta V - 2\right) . \tag{20.98}$$

From C–V spectroscopy the doping level can be obtained from the slope

$$\frac{\mathrm{d}(1/C^2)}{\mathrm{d}V} = \frac{2\beta L_{\mathrm{D}}^2}{\epsilon_{\mathrm{s}}^2} = \frac{2}{e\,\epsilon_{\mathrm{s}}\,N_{\mathrm{B}}} . \tag{20.99}$$

From the extrapolation to the voltage for which $1/C^2 = 0$ the built-in voltage can be obtained.

20.4.4 Current–Voltage Characteristics

Ideal Current–Voltage Characteristics

Now, the currents in thermodynamical equilibrium ($V = 0$) and under bias are discussed. A diode characteristic will be obtained. We work at first with the following assumptions: abrupt junction, Boltzmann approximation, low injection, i.e. the injected minority-carrier density is small compared to the majority-carrier density, and zero generation current in the depletion layer, i.e. the electron and hole currents are constant throughout the depletion layer. In the presence of a bias, electrons and holes have quasi-Fermi levels and the carrier densities are given by (cf. (7.61a and b))

$$n = N_\mathrm{C}\,\exp\left(\frac{F_\mathrm{n} - E_\mathrm{C}}{kT}\right) \tag{20.100a}$$

$$p = N_\mathrm{V}\,\exp\left(-\frac{F_\mathrm{p} - E_\mathrm{V}}{kT}\right)\ . \tag{20.100b}$$

Using the intrinsic carrier concentration, we can write

$$n = n_\mathrm{i}\,\exp\left(\frac{F_\mathrm{n} - E_\mathrm{i}}{kT}\right) = n_\mathrm{i}\,\exp\left[\beta(\psi - \phi_\mathrm{n})\right] \tag{20.101a}$$

$$p = n_\mathrm{i}\,\exp\left(-\frac{F_\mathrm{p} - E_\mathrm{i}}{kT}\right) = n_\mathrm{i}\,\exp\left[\beta(\phi_\mathrm{p} - \psi)\right]\ , \tag{20.101b}$$

where ϕ and ψ are the potentials related to the (quasi-) Fermi level and the intrinsic Fermi levels, $-e\phi_{\mathrm{n,p}} = F_{\mathrm{n,p}}$ and $-e\psi = E_\mathrm{i}$. The potentials ϕ_n and ϕ_p can also be written as

$$\phi_\mathrm{n} = \psi - \beta^{-1}\ln\left(\frac{n}{n_\mathrm{i}}\right) \tag{20.102a}$$

$$\phi_\mathrm{p} = \psi + \beta^{-1}\ln\left(\frac{p}{p_\mathrm{i}}\right)\ . \tag{20.102b}$$

The product np is given by

$$np = n_\mathrm{i}^2\exp\left[\beta(\phi_\mathrm{p} - \phi_\mathrm{n})\right]\ . \tag{20.103}$$

Of course, at thermodynamical equilibrium (zero bias) $\phi_\mathrm{p} = \phi_\mathrm{n}$ and $np = n_\mathrm{i}^2$. For forward bias $\phi_\mathrm{p} - \phi_\mathrm{n} > 0$ (Fig. 20.41a) and $np > n_\mathrm{i}^2$. For reverse bias $\phi_\mathrm{p} - \phi_\mathrm{n} < 0$ (Fig. 20.41b) and $np < n_\mathrm{i}^2$.

The electron current density (per unit area) is given by (8.57a) that reads here with $\mathbf{E} = \nabla\psi$ and n given by (20.101a) as[19]

$$\mathbf{j}_\mathrm{n} = -e\mu_\mathrm{n}\left(n\mathbf{E} + \beta^{-1}\nabla n\right) = en\mu_\mathrm{n}\nabla\phi_\mathrm{n}\ . \tag{20.104}$$

[19] We remind the reader that μ_n was defined as a negative number.

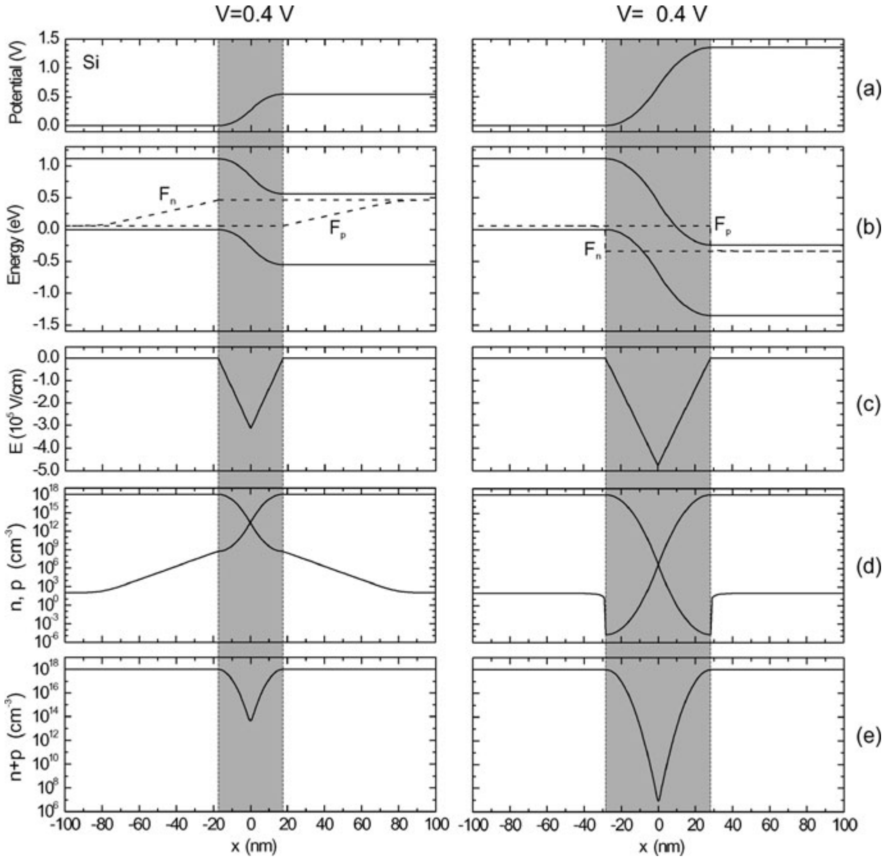

Fig. 20.41. (**a**) Diffusion potential, (**b**) band diagram, (**c**) electric field, (**d**) electron and hole concentrations and (**e**) $n + p$ under forward bias +0.4 V (*left panel*) and reverse bias (*right panel*) −0.4 V for a silicon pn-diode at room temperature with $N_{\mathrm{A}} = N_{\mathrm{D}} = 10^{18}\,\mathrm{cm}^{-3}$ (same as in Fig. 20.37). The *dashed lines* in (b) are the electron and hole quasi-Fermi levels F_{n} and F_{p}. The depletion layer is shown as the *grey area*. The diffusion length in the n- and p-type material is taken as 4 nm. This value is much smaller than the actual diffusion length (µm-range) and is chosen here only to show the carrier concentration in the depletion layer and the neutral region in a single graph

Similarly, we obtain for the hole current density (using (8.57b) and (20.101b))

$$\mathbf{j}_{\mathrm{p}} = e\mu_{\mathrm{p}} \left(p\mathbf{E} - \beta^{-1} \nabla p \right) = -ep\mu_{\mathrm{p}} \nabla \phi_{\mathrm{p}} \, . \tag{20.105}$$

The current through the depletion layer is constant (since no recombination/generation was assumed). The gradient of the quasi-Fermi levels in the depletion layer is very small and the quasi-Fermi levels $\phi_{\mathrm{n,p}}$ are practically constant. The electron and hole currents are shown in Fig. 20.42 together

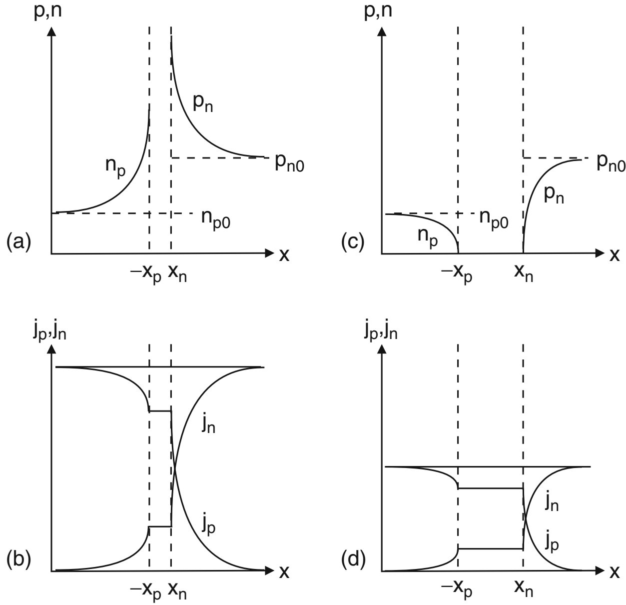

Fig. 20.42. Carrier densities (**a**,**c**) and current densities (**b**,**d**) (linear scales) in a pn-diode under (**a**,**b**) forward bias and (**c**,**d**) reverse bias

with the carrier densities. The change of carrier density is mostly due to the variation of ψ (or E_i).

Therefore, the voltage drop across the depletion layer is $V = \phi_\mathrm{p} - \phi_\mathrm{n}$ and (20.103) reads

$$np = n_\mathrm{i}^2 \exp(\beta V) \ . \qquad (20.106)$$

The electron density at the boundary of the depletion layer on the p-side (at $x = -x_\mathrm{p}$) is (using (20.106))

$$n_\mathrm{p} = \frac{n_\mathrm{i}^2}{p_\mathrm{p}} \exp(\beta V) = n_{\mathrm{p}_0} \exp(\beta V) \ . \qquad (20.107)$$

Similarly, the hole density on the n-side at $x = x_\mathrm{n}$ is given by

$$p_\mathrm{n} = p_{\mathrm{n}_0} \exp(\beta V) \ . \qquad (20.108)$$

From the continuity equation and the boundary condition that far away from the depletion layer the hole density is p_{n_0}, the hole density on the n-side is given by

$$p_\mathrm{n}(x) - p_{\mathrm{n}_0} = p_{\mathrm{n}_0} \left[\exp(\beta V) - 1\right] \exp\left(-\frac{x - x_\mathrm{n}}{L_\mathrm{p}}\right) \ , \qquad (20.109)$$

where $L_\mathrm{p} = \sqrt{D_\mathrm{p} \tau_\mathrm{p}}$ is the hole (minority-carrier) diffusion length.

The hole current density at the boundary of the depletion layer on the n-side is

$$j_{\mathrm{p}}(x_{\mathrm{n}}) = -eD_{\mathrm{p}} \frac{\partial p_{\mathrm{n}}}{\partial x}|_{x_{\mathrm{n}}} = \frac{eD_{\mathrm{p}} p_{\mathrm{n}_0}}{L_{\mathrm{p}}} \left[\exp\left(\beta V\right) - 1\right] . \tag{20.110}$$

Similarly, the electron current in the depletion layer is

$$j_{\mathrm{n}}(-x_{\mathrm{p}}) = \frac{eD_{\mathrm{n}} n_{\mathrm{p}_0}}{L_{\mathrm{n}}} \left[\exp\left(\beta V\right) - 1\right] . \tag{20.111}$$

The total current due to diffusion is

$$j_{\mathrm{d}} = j_{\mathrm{p}}(x_{\mathrm{n}}) + j_{\mathrm{n}}(-x_{\mathrm{p}}) = j_{\mathrm{s}} \left[\exp\left(\beta V\right) - 1\right] , \tag{20.112}$$

with the saturation current given by

$$j_{\mathrm{s}}^{\mathrm{d}} = \frac{eD_{\mathrm{p}} p_{\mathrm{n}_0}}{L_{\mathrm{p}}} + \frac{eD_{\mathrm{n}} n_{\mathrm{p}_0}}{L_{\mathrm{n}}} . \tag{20.113}$$

This dependence is an ideal diode characteristic and the famous result from Shockley. For a one-sided ($\mathrm{p}^+\mathrm{n}$-) diode, the saturation current is

$$j_{\mathrm{s}}^{\mathrm{d}} \cong \frac{eD_{\mathrm{p}} p_{\mathrm{n}_0}}{L_{\mathrm{p}}} \cong e \left(\frac{D_{\mathrm{p}}}{\tau_{\mathrm{p}}}\right)^{1/2} \frac{n_{\mathrm{i}}^2}{N_{\mathrm{B}}} . \tag{20.114}$$

The saturation depends via $D_{\mathrm{p}}/\tau_{\mathrm{p}}$ weakly on the temperature. The term n_{i}^2 depends on T, proportional to $T^3 \exp(-E_{\mathrm{g}}/kT)$, which is dominated by the exponential function.

If the minority carrier lifetime is given by the radiative recombination (10.19), the hole diffusion length is

$$L_{\mathrm{p}} = \sqrt{\frac{D_{\mathrm{p}}}{B n_{\mathrm{n}_0}}} . \tag{20.115}$$

For GaAs (Tables 8.2 and 10.1) with $N_{\mathrm{D}} = 10^{18}\,\mathrm{cm}^{-3}$, we find $\tau_{\mathrm{p}} = 10\,\mathrm{ns}$ and $L_{\mathrm{p}} \approx 3\,\mu\mathrm{m}$. For L_{n} we find $14\,\mu\mathrm{m}$, however, the lifetime at room temperature can be significantly shorter due to nonradiative recombination and subsequently also the diffusion length will be shorter (by about a factor of 10). For $L \sim 1\,\mu\mathrm{m}$, the diffusion saturation current is $j_{\mathrm{s}}^{\mathrm{d}} \sim 4 \times 10^{-20}\,\mathrm{A/cm}^2$.

The radiative recombination rate (band–band recombination, b–b) in the neutral n-region (as relevant for LEDs, see Sect. 22.3) is $B(np - n_{\mathrm{i}}^2) \approx B n_{\mathrm{n}_0}(p_{\mathrm{n}}(x) - p_{\mathrm{n}_0})$. Therefore, the recombination current $j_{\mathrm{d,n}}^{\mathrm{b-b}}$ in the neutral n-region is (using (20.109))

$$\begin{aligned} j_{\mathrm{d,n}}^{\mathrm{b-b}} &= e \int_{x_{\mathrm{n}}}^{\infty} B n_{\mathrm{i}}^2 \left[\exp\left(\beta V\right) - 1\right] \exp\left(-\frac{x - x_{\mathrm{n}}}{L_{\mathrm{p}}}\right) \mathrm{d}x \\ &= eBL_{\mathrm{p}} n_{\mathrm{i}}^2 \left[\exp\left(\beta V\right) - 1\right] . \end{aligned} \tag{20.116}$$

For the neutral region on the p-side a similar expression results. The total radiative recombination current from the neutral regions is

$$j_{\mathrm{d}}^{\mathrm{b-b}} = eB(L_{\mathrm{n}} + L_{\mathrm{p}})n_{\mathrm{i}}^2 \left[\exp\left(\beta V\right) - 1\right] . \tag{20.117}$$

For GaAs, the saturation current for the radiative recombination in the neutral region

$$j_{\mathrm{s}}^{\mathrm{r,b-b}} = eB\left(L_{\mathrm{n}} + L_{\mathrm{p}}\right) n_{\mathrm{i}}^2 \tag{20.118}$$

is (Tables 7.1 and 10.1) for a diffusion length of 1 µm of $j_{\mathrm{s}}^{\mathrm{r,b-b}} \sim 4 \times 10^{-21}\,\mathrm{A/cm^2}$.

Since the (radiative) minority-carrier lifetime is inversely proportional to the majority-carrier density, the relevant diffusion length is that of the side with the lower doping level and is given by

$$L = \frac{1}{n_{\mathrm{i}}} \sqrt{\frac{D_{\mathrm{B}}\, N_{\mathrm{B}}}{B}} , \tag{20.119}$$

where D_{B} is the minority-carrier diffusion coefficient on the lowly doped side. The radiative recombination current from the neutral region can be written as

$$j_{\mathrm{d}}^{\mathrm{b-b}} = e\,\sqrt{B D_{\mathrm{B}} N_{\mathrm{B}}}\; n_{\mathrm{i}}\, \left[\exp\left(\beta V\right) - 1\right] . \tag{20.120}$$

The I–V characteristic for pn-diodes from two semiconductors with different band gap are shown in Fig. 20.43 (for Ge and Si). Both forward characteristics are exponential functions. The Si diode seems to have the steeper slope, however, the difference is only the smaller saturation current. The saturation current increases at higher temperature (Fig. 20.44).

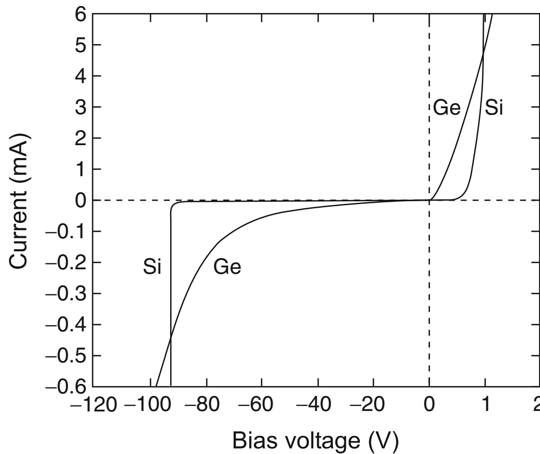

Fig. 20.43. Comparison of the characteristics of Ge and Si diodes at room temperature. Note the different scales in the forward and reverse regime

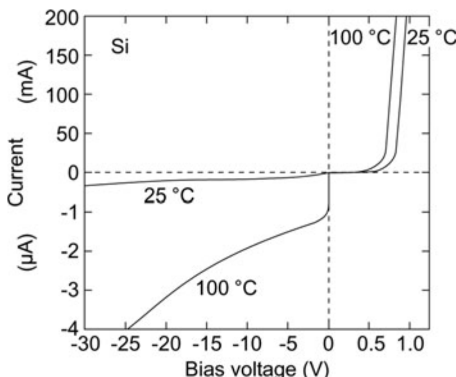

Fig. 20.44. Characteristics of a Si power diode at two temperatures, 25 °C and 100 °C

Real *I*–*V* Characteristics

The ideal *I*–*V* characteristics are not observed for real diodes due to several reasons:

- besides the diffusion current, also a generation–recombination (G–R) current is present
- already for fairly small forward voltages, high injection conditions are present, i.e. $p_\mathrm{n} \ll n_\mathrm{n}$ is no longer valid
- the series resistance R_s of the diode is finite (ideally $R_\mathrm{s} = 0$)
- the diode has a finite parallel (shunt) resistance R_p (ideally $R_\mathrm{p} = \infty$)
- at high reverse voltage the junction breaks down; this phenomenon is treated in Sect. 20.4.5

First, we consider the generation–recombination current due to band–impurity (b–i) processes (see Sect. 10.9). Such recombination is nonradiative or at least does not produce photons with an energy close to the band gap. The net rate is given by (10.54). For reverse voltage, the generation dominates the G–R current. For $n < n_\mathrm{i}$ and $p < n_\mathrm{i}$, the net recombination rate r is

$$r \cong \frac{\sigma_\mathrm{n}\,\sigma_\mathrm{p}\,v_\mathrm{th}\,N_\mathrm{t}}{\sigma_\mathrm{n}\,\exp\left(\frac{E_\mathrm{t}-E_\mathrm{i}}{kT}\right) + \sigma_\mathrm{p}\,\exp\left(\frac{E_\mathrm{i}-E_\mathrm{t}}{kT}\right)}\,n_\mathrm{i} \equiv \frac{n_\mathrm{i}}{\tau_\mathrm{e}}\,, \tag{20.121}$$

where τ_e is the effective electron lifetime. The generation current density is given by

$$j_\mathrm{g} = \frac{e\,n_\mathrm{i}\,w}{\tau_\mathrm{e}}\,. \tag{20.122}$$

Since the width of the depletion layer varies with the applied reverse bias V, we expect a dependence

$$j_\mathrm{g} \propto \sqrt{V_\mathrm{bi} + |V|}\,. \tag{20.123}$$

The saturation current is given by the sum of the diffusion and generation parts

$$j_{\mathrm{s}} = e\sqrt{\frac{D_{\mathrm{p}}}{\tau_{\mathrm{p}}}}\frac{n_{\mathrm{i}}^2}{N_{\mathrm{D}}} + \frac{e\,n_{\mathrm{i}}\,w}{\tau_{\mathrm{e}}} \ . \tag{20.124}$$

In semiconductors with large n_{i} (narrow band gap, e.g. Ge) the diffusion current will dominate; in Si (larger band gap) the generation current can dominate.

The maximum of the recombination rate is present for $E_{\mathrm{t}} \approx E_{\mathrm{i}}$ (10.58). Then $n_{\mathrm{t}} = p_{\mathrm{t}} = n_{\mathrm{i}}$ in (10.54). Assuming $\sigma = \sigma_{\mathrm{n}} = \sigma_{\mathrm{p}}$, the recombination rate is

$$r_{\mathrm{b-i}} = \sigma\, v_{\mathrm{th}}\, N_{\mathrm{t}}\, \frac{np - n_{\mathrm{i}}^2}{n + p + 2n_{\mathrm{i}}} \ . \tag{20.125}$$

Using (20.103) we can write

$$r_{\mathrm{b-i}} = \sigma\, v_{\mathrm{th}}\, N_{\mathrm{t}}\, n_{\mathrm{i}}\, \frac{n_{\mathrm{i}}}{n + p + 2n_{\mathrm{i}}}\, \left[\exp\left(\beta V\right) - 1\right] \ . \tag{20.126}$$

The term $\zeta = \frac{n_{\mathrm{i}}}{n+p+2n_{\mathrm{i}}}$ is maximal for $n = p$, which is given (from (20.106)) by

$$n_{\mathrm{mr}} = p_{\mathrm{mr}} = n_{\mathrm{i}}\, \exp\left(\beta V/2\right) \ . \tag{20.127}$$

The function $\zeta(x)$ cannot be analytically integrated. In order to evaluate the integral of ζ over the depletion layer

$$\chi = \int_{-x_{\mathrm{p}}}^{x_{\mathrm{n}}} \zeta \, \mathrm{d}x \ , \tag{20.128}$$

the maximum rate

$$\zeta_{\mathrm{mr}} = \frac{n_{\mathrm{i}}}{n_{\mathrm{mr}} + p_{\mathrm{mr}} + 2n_{\mathrm{i}}} = \frac{1}{2}\,\frac{1}{1 + \exp\left(\frac{eV}{2kT}\right)} \tag{20.129}$$

can be integrated over the depletion layer as an approximation [384], $\chi \approx \zeta_{\mathrm{mr}}\, w$. This approach yields a recombination current

$$j_{\mathrm{mr}} = \frac{e\sigma v_{\mathrm{th}} N_{\mathrm{t}} w n_{\mathrm{i}}}{2}\,\frac{\exp\left(\beta V\right) - 1}{\exp\left(\frac{eV}{2kT}\right) + 1} \cong j_{\mathrm{s}}^{\mathrm{mr}}\, \exp\left(\frac{eV}{2kT}\right) \ , \tag{20.130}$$

with $j_{\mathrm{s}}^{\mathrm{mr}} = e\sigma v_{\mathrm{th}} N_{\mathrm{t}} w n_{\mathrm{i}}/2$ and the approximation being valid for $eV/kT \gg 1$. Thus the nonradiative band–impurity recombination is often said to cause an ideality factor of $n = 2$.

For a better approximation of χ, the dependence of the potential $\varphi(x)$ can be approximated as linear (constant-field approximation), i.e. using the local field $\mathcal{E}_{\mathrm{mr}}$ at the position where $n = p$ [1168]. For a symmetric diode with $n_{\mathrm{n}_0} = p_{\mathrm{p}_0}$, this position is at $x = 0$; for a one-sided junction on the lower-doped side. $\mathcal{E}_{\mathrm{mr}}$ is given for $p_{\mathrm{p}_0} \leq n_{\mathrm{n}_0}$ by

$$\mathcal{E}_{\mathrm{mr}} = -\left(V_{\mathrm{bi}} - V\right) \sqrt{1 + \frac{1}{\beta\left(V_{\mathrm{bi}} - V\right)} \ln \frac{p_{\mathrm{p_0}}}{n_{\mathrm{n_0}}}} \sqrt{1 + \frac{p_{\mathrm{p_0}}}{n_{\mathrm{n_0}}}} \frac{\sqrt{2}}{w} . \tag{20.131}$$

For a symmetric diode (20.132a) holds, for a one-sided diode the approximation in (20.132b) holds

$$\mathcal{E}_{\mathrm{mr}} = -\frac{2}{w}\left(V_{\mathrm{bi}} - V\right) \propto \sqrt{V_{\mathrm{bi}} - V} \tag{20.132a}$$

$$\mathcal{E}_{\mathrm{mr}} \cong -\frac{\sqrt{2}}{w}\left(V_{\mathrm{bi}} - V\right) \propto \sqrt{V_{\mathrm{bi}} - V} . \tag{20.132b}$$

We note that for zero bias ($V = 0$), (20.90) is recovered from (20.132a). Using the above approximation ζ is given by

$$\zeta(x) = \frac{1}{2} \frac{1}{1 + \exp\left(\beta V/2\right) \cosh(\beta \mathcal{E}_{\mathrm{mr}} x)} , \tag{20.133}$$

with $\beta = e/kT$. Since ζ decreases sufficiently fast within the depletion layer, the integration over the depletion layer can be extended to $\pm\infty$ and we obtain

$$\chi = \frac{2}{\beta \mathcal{E}_{\mathrm{mr}}} \frac{1}{\sqrt{\exp(\beta V) - 1}} \arctan\left[\sqrt{\frac{\exp(\beta V/2) - 1}{\exp(\beta V/2) + 1}}\right] . \tag{20.134}$$

We note that for $V = 0$, the integral takes the value $\chi = (\beta \mathcal{E}_{\mathrm{mr}})^{-1}$. The recombination current is now given by [1168]

$$j_{\mathrm{r,b-i}} = \frac{2\sigma v_{\mathrm{th}} N_{\mathrm{t}} n_{\mathrm{i}} kT}{\mathcal{E}_{\mathrm{mr}}} \arctan\left[\sqrt{\frac{\exp(\beta V/2) - 1}{\exp(\beta V/2) + 1}}\right] \sqrt{\exp\left(\beta V\right) - 1} . \tag{20.135}$$

For large voltage the arctan term becomes $\pi/4$. For $eV/kT \gg 1$ the nonradiative recombination current can be written as

$$j_{\mathrm{r,b-i}} = j_{\mathrm{s}}^{\mathrm{r,b-i}} \exp\left(\frac{eV}{nkT}\right) , \tag{20.136}$$

with $j_{\mathrm{s}}^{\mathrm{r,b-i}} = e\sigma v_{\mathrm{th}} N_{\mathrm{t}} n_{\mathrm{i}} kT\pi/(2\mathcal{E}_{\mathrm{mr}})$. The voltage-dependent ideality factor n (semilogarithmic slope $n = \beta j_{\mathrm{r}}(V)/j_{\mathrm{r}}'(V)$) is close but not identical to 2 and is shown in Fig. 20.45 for various values of V_{bi}. The built-in voltage influences the logarithmic slope via the factor $1/\mathcal{E}_{\mathrm{mr}}$ in (20.135).

In the case of radiative band–band (b–b) recombination, the recombination rate is given by (10.14). Together with (20.106) and integrated over the depletion layer, the recombination current in the depletion layer is given by (cf. (20.117))

$$j_{\mathrm{r,b-b}} = e\, B\, w\, n_{\mathrm{i}}^2 \left[\exp\left(\beta V\right) - 1\right] , \tag{20.137}$$

and exhibits an ideality factor of $n = 1$. Comparing (20.117) and (20.137), the dominating radiative-recombination current is determined by the ratio of

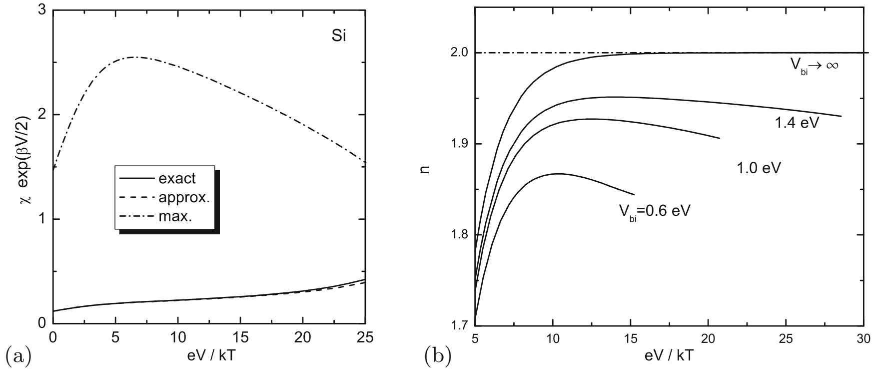

Fig. 20.45. (**a**) Integral χ (20.128) multiplied by $\exp(\beta V/2)$ in order to extract the differences on a linear scale. *Solid line*: Exact numerical calculation, *dash-dotted line*: standard approximation with constant maximum rate, *dashed line*: this work (approximation with constant field). As material parameters we have used room temperature and $n_\mathrm{i} = 10^{10}\,\mathrm{cm}^{-3}$ (Si), $n_{\mathrm{n}_0} = 10^{18}\,\mathrm{cm}^{-3}$ and $p_{\mathrm{p}_0} = 10^{17}\,\mathrm{cm}^{-3}$. (**b**) Logarithmic slope of band–impurity recombination current in the forward bias regime for various values of the built-in voltage $V_\mathrm{bi} = 0.6$, 1.0, and 1.4 eV and in the limit $V_\mathrm{bi} \to \infty$. Adapted from [1168]

w and $L_\mathrm{n}+L_\mathrm{p}$. Since in the forward direction, the depletion-layer width tends towards zero (for flat-band conditions), the radiative-recombination current is dominated by the recombination in the neutral region(s).

For high injection current (under forward bias), the injected minority-carrier density can become comparable with the majority-carrier density. In this case, diffusion *and* drift need to be considered. At large current density, the voltage drop across the junction is small compared to the ohmic voltage drop across the current path. In the simulation (Fig. 20.46), the high-injection effects start on the n-doped side because it has been modeled with the lower doping ($N_\mathrm{D} < N_\mathrm{A}$).

The series resistance R_s (typically a few Ohms) also effects the characteristic at low injection. The voltage drop across the junction is reduced by $R_\mathrm{s}\,I$. Thus, the I–V characteristic taking into account the effect of the series resistance is

$$I = I_\mathrm{s} \exp\left[\frac{e(V - R_\mathrm{s} I)}{nkT}\right] . \tag{20.138}$$

This equation is implicit with regard to I and can only be solved numerically. At high current, the resistance of the junction becomes very small (Fig. 20.47a) and the I–V characteristic is dominated by the series resistance and becomes linear.

The diode can also exhibit a parallel (shunt) resistance R_p, e.g. due to surface conduction between the contacts. Including the shunt resistance, the diode characteristic is

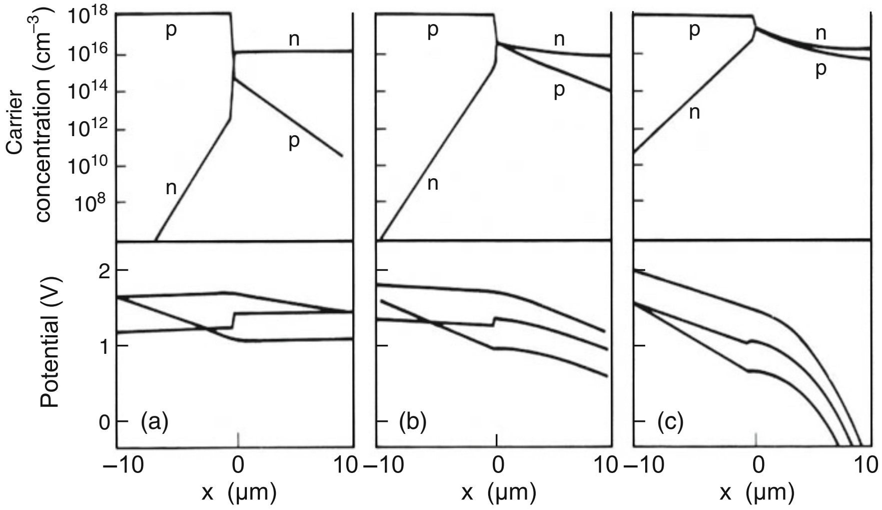

Fig. 20.46. Theoretical modeling of charge-carrier concentration, intrinsic Fermi level (potential) ψ and quasi-Fermi levels (with arbitrary offset) for a Si p$^+$n diode for various current densities: (**a**) $10\,\mathrm{A\,cm^{-2}}$, (**b**) $10^3\,\mathrm{A\,cm^{-2}}$ and (**c**) $10^4\,\mathrm{A\,cm^{-2}}$. $N_\mathrm{A} = 10^{18}\,\mathrm{cm^{-3}}$, $N_\mathrm{D} = 10^{16}\,\mathrm{cm^{-3}}$, $\tau_\mathrm{n} = 0.3\,\mathrm{ns}$, $\tau_\mathrm{p} = 0.84\,\mathrm{ns}$. Adapted from [1169]

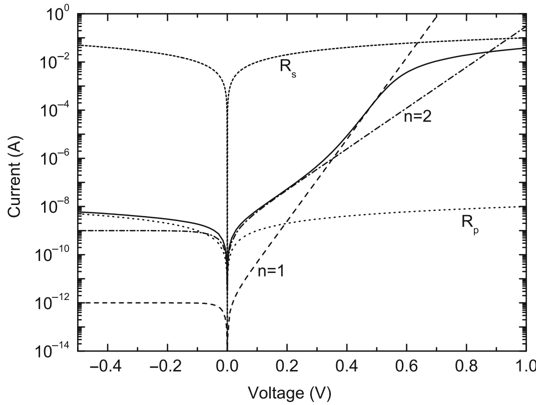

Fig. 20.47. Theoretical I–V characteristic of a diode at room temperature with saturation currents for the $n = 1$ and $n = 2$ processes of $I_\mathrm{s}^{n=1} = 10^{-12}\,\mathrm{A}$ and $I_\mathrm{s}^{n=2} = 10^{-9}\,\mathrm{A}$ and resistances $R_\mathrm{s} = 10\,\Omega$, $R_\mathrm{p} = 100\,\mathrm{M\Omega}$. *Dashed line*: Ideal diode with $n = 1$ characteristic only, *dash-dotted line*: only $n = 2$ process, *dotted line*: only parallel ohmic resistance, *short dashed line*: only series resistance, *solid line*: all effects combined as in (20.140)

$$I = I_{\mathrm{s}} \exp\left[\frac{e(V - R_{\mathrm{s}}I)}{nkT}\right] + \frac{V - R_{\mathrm{s}}I}{R_{\mathrm{p}}} \ . \tag{20.139}$$

The shunt resistance can be evaluated best from the differential conductance in the reverse-voltage regime [1143]. Due to a high surface-state density, the passivation of GaAs diodes can be difficult. Si can be very well passivated with low leakage current and high reliability.

Often, a clear distinction between the $n = 1$ and $n = 2$ regimes cannot be made. In this case, an intermediate ideality factor $1 \leq n \leq 2$ is fitted to the I–V characteristic as in (20.139). If the current can be separated into a $n = 1$ (diffusion) and a $n = 2$ (recombination–generation) process, the characteristic is given by (see Fig. 20.47)

$$I = I_{\mathrm{s}}^{n=1} \exp\left[\frac{e(V - R_{\mathrm{s}}I)}{kT}\right] + I_{\mathrm{s}}^{n=2} \exp\left[\frac{e(V - R_{\mathrm{s}}I)}{2kT}\right] + \frac{V - R_{\mathrm{s}}I}{R_{\mathrm{p}}} \ . \tag{20.140}$$

In summary, the pn-diode has the equivalent circuit given in Fig. 20.48; the photocurrent source I_{ph} is discussed below in Sect. 21.3.

20.4.5 Breakdown

If a large voltage is applied in the reverse direction, the pn-junction breaks down. At breakdown, a small voltage increase leads to a dramatic increase of the current. There are three mechanisms that lead to breakdown: thermal instability, tunneling, and avalanche multiplication [1170–1172]. Defects cause localized pre-breakdown sites [1172, 1173].

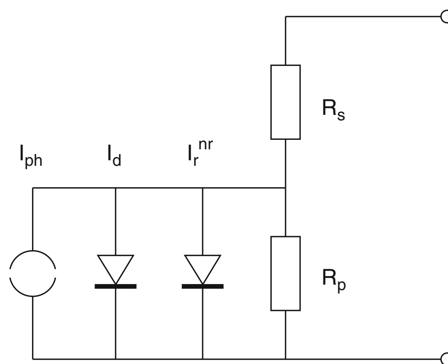

Fig. 20.48. Equivalent circuit of a pn-diode. Serial (R_{s}) and parallel (R_{p}) resistance and diode currents: I_{d} (due to diffusion, $n \approx 1$), $I_{\mathrm{r}}^{\mathrm{nr}}$ (nonradiative recombination due to band–impurity recombination, $n \approx 2$) and an ideal current source due to photogeneration (as discussed in Sect. 21.3)

Thermal Instability

The reverse current at large applied voltage leads to a power dissipation and heating of the junction. This temperature increase leads to a further increase of the saturation current (20.114). If the heat sink, e.g. the mounting of the chip, is not able to transport the heat away from the device, the current increases indefinitely. If not limited by a resistor, such a current can destroy the device. The thermal instability is particularly important for diodes with high saturation current, e.g. Ge at room temperature.

Tunneling

At large reverse bias, charge carriers can tunnel between conduction and valence band through the junction. A more detailed discussion will be given below in Sect. 20.5.9 about the tunneling diode. Since for the tunneling effect a thin barrier is necessary, breakdown due to tunneling is important for diodes where both sides are highly doped. For Si and Ge diodes, tunneling dominates the breakdown if the breakdown voltage V_{br} is $V_{\mathrm{br}} < 4E_{\mathrm{g}}/e$. For $V_{\mathrm{br}} > 6E_{\mathrm{g}}/e$ avalanche multiplication dominates. The intermediate regime is a mixed case.

With increasing temperature, the tunneling current can be achieved already with a smaller field (since the band gap decreases with increasing temperature), thus the breakdown voltage *decreases* (negative temperature coefficient).

Avalanche Multiplication

Avalanche multiplication due to impact ionization is the most important mechanism for the breakdown of pn-diodes. It limits the maximum reverse voltage for most diodes and also the collector voltage in a bipolar transistor or the drain voltage in a field-effect transistor. Avalanche multiplication can be used for the generation of microwave radiation or for photon counting (cf. Sect. 21.3.6).

Impact ionization was discussed in Sect. 8.5.4. The most important parameters are the electron and hole ionization coefficients α_{n} and α_{p}. For discussion of the diode breakdown, we assume that at $x = 0$ a hole current I_{p_0} enters the depletion layer. This current is amplified by the field in the depletion layer and impact ionization. At the end of the depletion layer ($x = w$), it is $M_{\mathrm{p}} I_{\mathrm{p}_0}$, i.e. $M_{\mathrm{p}} = I_{\mathrm{p}}(w)/I_{\mathrm{p}}(0)$. Similarly, an electron current is increased on its way from w to $x = 0$. The incremental change of the hole current due to electron–hole pairs generated along a line element dx is

$$\mathrm{d}I_{\mathrm{p}} = (I_{\mathrm{p}}\alpha_{\mathrm{p}} + I_{\mathrm{n}}\alpha_{\mathrm{n}})\,\mathrm{d}x \; . \tag{20.141}$$

The total current in the depletion layer is $I = I_{\mathrm{p}} + I_{\mathrm{n}}$ and is constant in stationary equilibrium. Therefore,

$$\frac{\mathrm{d}I_\mathrm{p}}{\mathrm{d}x} - (\alpha_\mathrm{p} - \alpha_\mathrm{n})\; I_\mathrm{p} = \alpha_\mathrm{n}\, I\;. \tag{20.142}$$

The solution is

$$I_\mathrm{p}(x) = I\,\frac{\frac{1}{M_\mathrm{p}} + \int_0^x \alpha_\mathrm{n}\, \exp\left[-\int_0^x (\alpha_\mathrm{p} - \alpha_\mathrm{n})\, \mathrm{d}x'\right]\, \mathrm{d}x}{\exp\left[-\int_0^x (\alpha_\mathrm{p} - \alpha_\mathrm{n})\, \mathrm{d}x'\right]}\;. \tag{20.143}$$

For $x = w$ we find for the multiplication factor

$$1 - \frac{1}{M_\mathrm{p}} = \int_0^w \alpha_\mathrm{n}\, \exp\left[-\int_0^x (\alpha_\mathrm{p} - \alpha_\mathrm{n})\, \mathrm{d}x'\right]\, \mathrm{d}x\;. \tag{20.144}$$

Avalanche breakdown is reached for $M_\mathrm{p} \to \infty$, i.e. when

$$\int_0^w \alpha_\mathrm{n}\, \exp\left[-\int_0^x (\alpha_\mathrm{p} - \alpha_\mathrm{n})\, \mathrm{d}x'\right]\, \mathrm{d}x = 1\;. \tag{20.145}$$

A corresponding and equivalent equation is obtained when the consideration is started with the electron current. If $\alpha_\mathrm{p} = \alpha_\mathrm{n} = \alpha$, (20.145) simplifies to

$$\int_0^w \alpha\, \mathrm{d}x = 1\;. \tag{20.146}$$

This means that per transit of one carrier through the depletion layer, on average another carrier is created such that the process just starts to diverge. The breakdown voltage for various semiconductor materials is shown in Fig. 20.49a as a function of the doping level. The depletion-layer width w at breakdown and the maximum electric field $\mathcal{E}_\mathrm{m}$ are depicted in Fig. 20.49b. The average impact ionization coefficient α has been given as [1174]

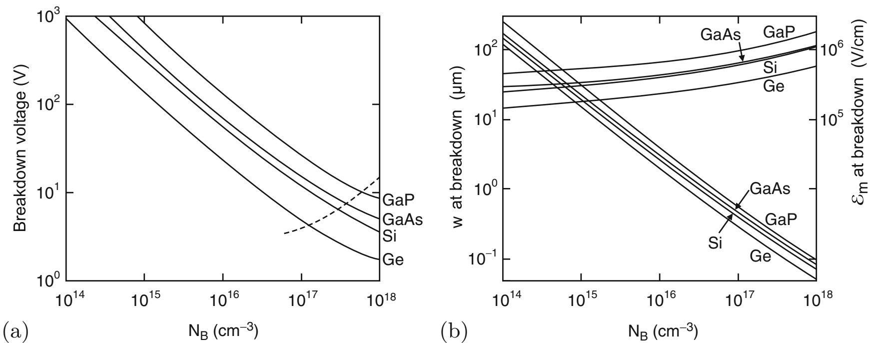

Fig. 20.49. (**a**) Avalanche breakdown voltage for one-sided abrupt junctions in Ge, Si, (100)-GaAs and GaP at $T = 300\,\mathrm{K}$. The *dashed line* indicates the limit of avalanche breakdown at high doping due to tunneling breakdown. (**b**) Depletion-layer width w at breakdown and maximum electric field $\mathcal{E}_\mathrm{m}$ for the same junctions. Adapted from [1175]

$$\alpha = A\,\mathcal{E}^7\,. \tag{20.147}$$

for silicon with $A = 1.8 \times 10^{-35}\,(\mathrm{cm/V})^7\ \mathrm{cm}^{-1}$. For the breakdown condition (20.146), using (20.8) and (20.147) the depletion layer width at breakdown w_B (w_B in cm, N_D in cm^3) is found to be

$$w_\mathrm{B} = 2.67 \times 10^{10}\,N_\mathrm{D}^{-7/8}\,. \tag{20.148}$$

From this the breakdown voltage can be calculated with (20.14) (V_B in V, N_D in cm^3) [1176]

$$V_\mathrm{B} = 6.40 \times 10^{13}\,N_\mathrm{D}^{-3/4}\,. \tag{20.149}$$

In GaAs, the impact-ionization coefficients and therefore the breakdown voltage are direction dependent. At a doping of $N_\mathrm{B} = 10^{16}\,\mathrm{cm}^{-3}$, the breakdown voltage is the same for (001) and (111) orientation; for smaller doping the breakdown voltage of (001)-oriented GaAs is smaller, for larger doping that of GaAs (111) [1177].

At higher temperatures, the charge carriers release their excess energy faster to the lattice.[20] Thus, less energy is available for impact ionization and the required electric field is higher. Therefore, the breakdown voltage *increases* with the temperature (Fig. 20.50). This behavior is opposite to tunneling diodes and the two processes can be distinguished in this way.

In planar structures (Fig. 20.51a), high electric fields as present in high power devices will occur at the parts with large curvature. At these sites breakdown will occur first and at much lower voltages than expected for a perfectly planar (infinite) structure [1179, 1180]. For devices that require

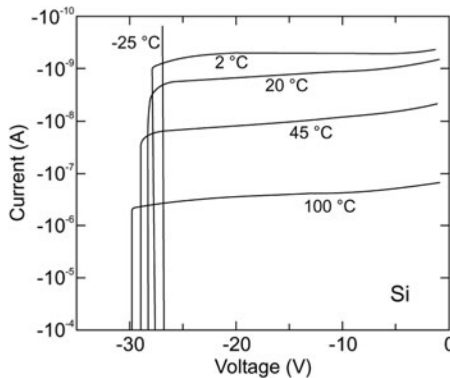

Fig. 20.50. Temperature dependence of a n$^+$p Si-diode with $N_\mathrm{B} = 2.5 \times 10^{16}\,\mathrm{cm}^{-3}$ and a guard-ring structure (see Fig. 20.51d). The temperature coefficient $\partial V_\mathrm{br}/\partial T$ is 0.024 V/K. Adapted from [1178]

[20] The scattering rate becomes higher with increasing temperature and, e.g., the mobility decreases, see Sect. 8.3.9, and the drift saturation velocity decreases, see Sect. 8.5.1.

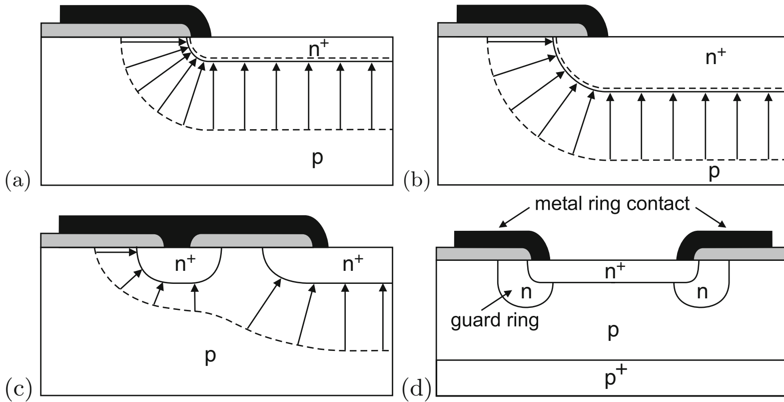

Fig. 20.51. (**a**) Large electric fields at large curvatures in a shallow junction. Avoidance of regions with large electric fields by (**b**) deep junction and (**c**) field-ring structure. (**d**) shows a guard-ring structure with circular, low-doped n region. *Grey area* denotes insulating material, arrows indicate field lines and the *dashed lines* indicate the extension of the depletion layers

high breakdown voltage, design changes have to be made. These include deep junctions (Fig. 20.51b) with a smaller curvature, a field-ring structure (Fig. 20.51c) in which an additional depletion layer is used to smooth the field lines and the often used guard ring (Fig. 20.51d) for which a circular region of low doping (and thus high breakdown voltage) is incorporated.

The decrease of breakdown voltage in a junction with cylindrical and spherical geometry has been numerically calculated as a function of curvature [1181] (Fig. 20.52). Analytical formulas in terms of the ratio of radius

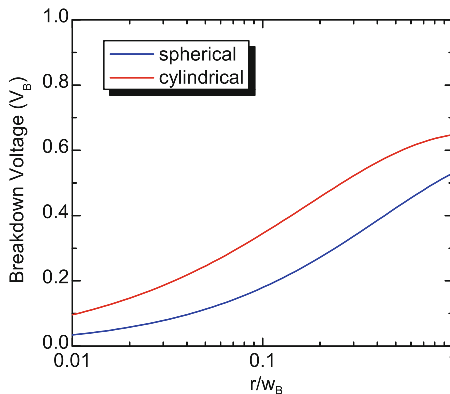

Fig. 20.52. Breakdown voltage (in units of the breakdown voltage V_{B} of a plane junction) for cylindrical and spherical junctions as a function of the curvature radius (in units of the depletion layer width at breakdown W_{B} for a plane junction). Data from [1176]

of curvature and the depletion layer width at breakdown for a plane junction r/w_{B} have been given later [1176].

Defects

In material with extended defects such as polycrystalline silicon breakdown can occur locally at lower voltage than in the corresponding defect-free bulk material ('pre-breakdown') [1173]. This effect typically occurs at certain grain boundaries and probably involves mid-gap states. It is also accompanied with electroluminescence by which it can be detected with high spatial resolution (Fig. 20.53).

20.4.6 Organic Semiconductor Diodes

A bipolar diode from organic semiconductors consists of the p-conductive hole transport layer (HTL) and the n-conductive electron transport layer (ETL). The low conductivity of organic semiconductors causes the applied

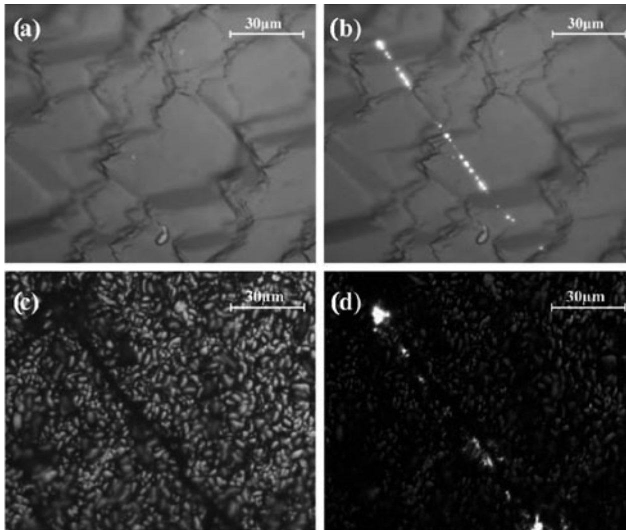

Fig. 20.53. Microscopic (**a**) forward bias electroluminescence and (**b**) microscopic reverse bias electroluminescence (μ-ReBEL) image of an alkaline texturized solar cell (cmp. Fig. 21.57) in a region without specific surface features at $U = -17\,\mathrm{V}$. The bulk defects at these positions are revealed topographically in the neighboring acidic texturized solar cell in the microscopic (**c**) image. Their ReBEL pattern appears similarly in the corresponding EL image (**d**). Adapted from [1173]

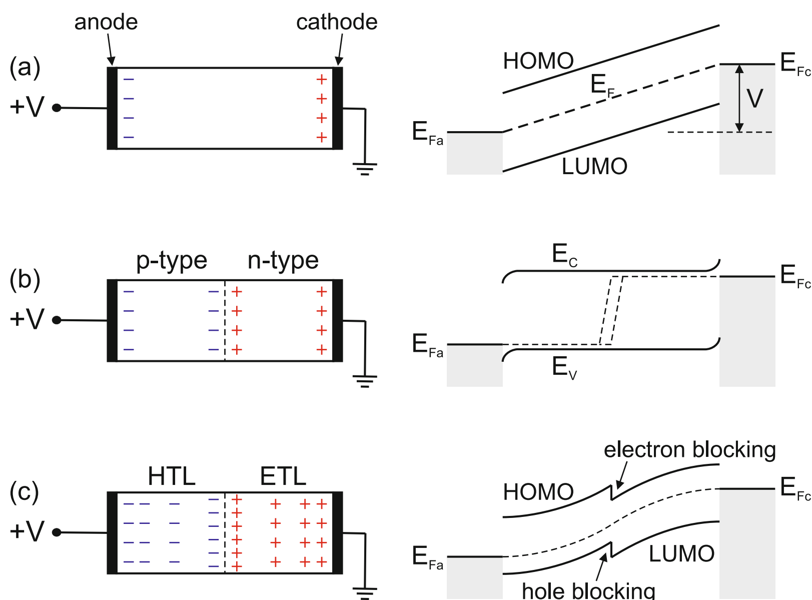

Fig. 20.54. Schematic sample geometry and charge distribution (*left*) and energy diagram (*right*) for (**a**) an ideal insulator, (**b**) a typical inorganic semiconductor pn-diode and (**c**) a double layer organic diode under forward bias V. Adapted from [1184]

voltage to drop over the entire structure [1182–1184] (Fig. 20.54c) while in a typical silicon diode for sufficient forward bias (and moderate injection, cmp. Fig. 20.46) flat-band conditions are present (Fig. 20.54b). The first organic homodiode was reported only in 2005 for zinc-phthalocyanine (ZnPc) doped with $[\mathrm{Ru(terpy)_2}]^0$ (n-type) and F_4-TCNQ (p-type, cmp. Fig. 16.7b) [1185]. Deviation from ideal Shockley behavior is discussed in this report.

The hole injecting contact is often made from ITO, the electron injection contact from low work function metals such as Al, Mg or Ca. Specially designed layers for efficient charge injection (HIL, hole injection layer [1186] and EIL, electron injection layer [1187]) can be introduced between the contact metal and the transport layers (Fig. 20.55c). The particular level lineup of the HTL and HTL as shown in Fig. 20.54c (also Fig. 20.55a) leads to a barrier for electrons and holes. The hole and/or electron blocking is beneficial for recombination in the vicinity of the interface and prevents exciton diffusion to the contacts. In organic light emitting diodes (Sect. 22.3.7) an additional layer (EML, emission layer) designed for efficient radiative recombination (Sect. 16.5) is introduced between HTL and ETL (Fig. 20.55b).

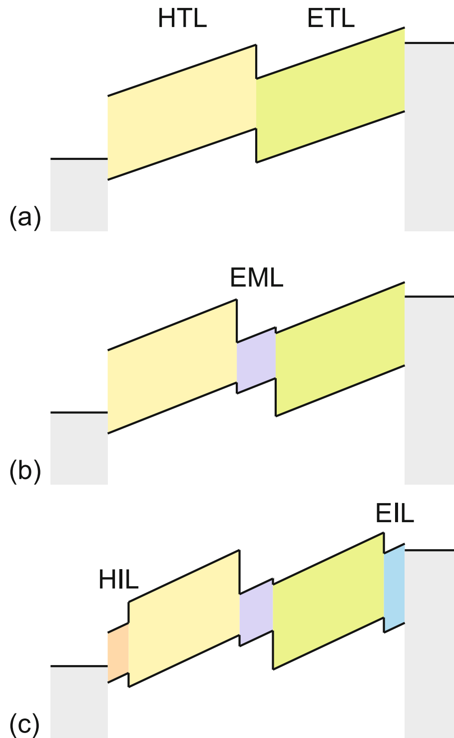

Fig. 20.55. Schematic energy diagram for (**a**) dual layer organic diode (HTL, ETL), (**b**) with additional emission layer (EML) and (**c**) with further hole and electron injection layers (HIL, EIL)

20.5 Applications and Special Diode Devices

In the following, various electronic applications of diodes are discussed. The most important special diode types are introduced. Optoelectronic applications (involving absorption and emission of photons) are treated below (Sect. 21).

20.5.1 Rectification

In a rectifier, the diode has to supply a high resistivity for one polarity of the bias and a low one to the other polarity. In Fig. 20.56a, a single-path rectification method is shown. Only the positive half-wave can pass the load resistor R_L (Fig. 20.56b). In Fig. 20.56c, the characteristic of a Si diode is shown. Of course, the voltage drop across the diode can only range in the 1-V regime. In order to make the setup work, the load resistor has to be

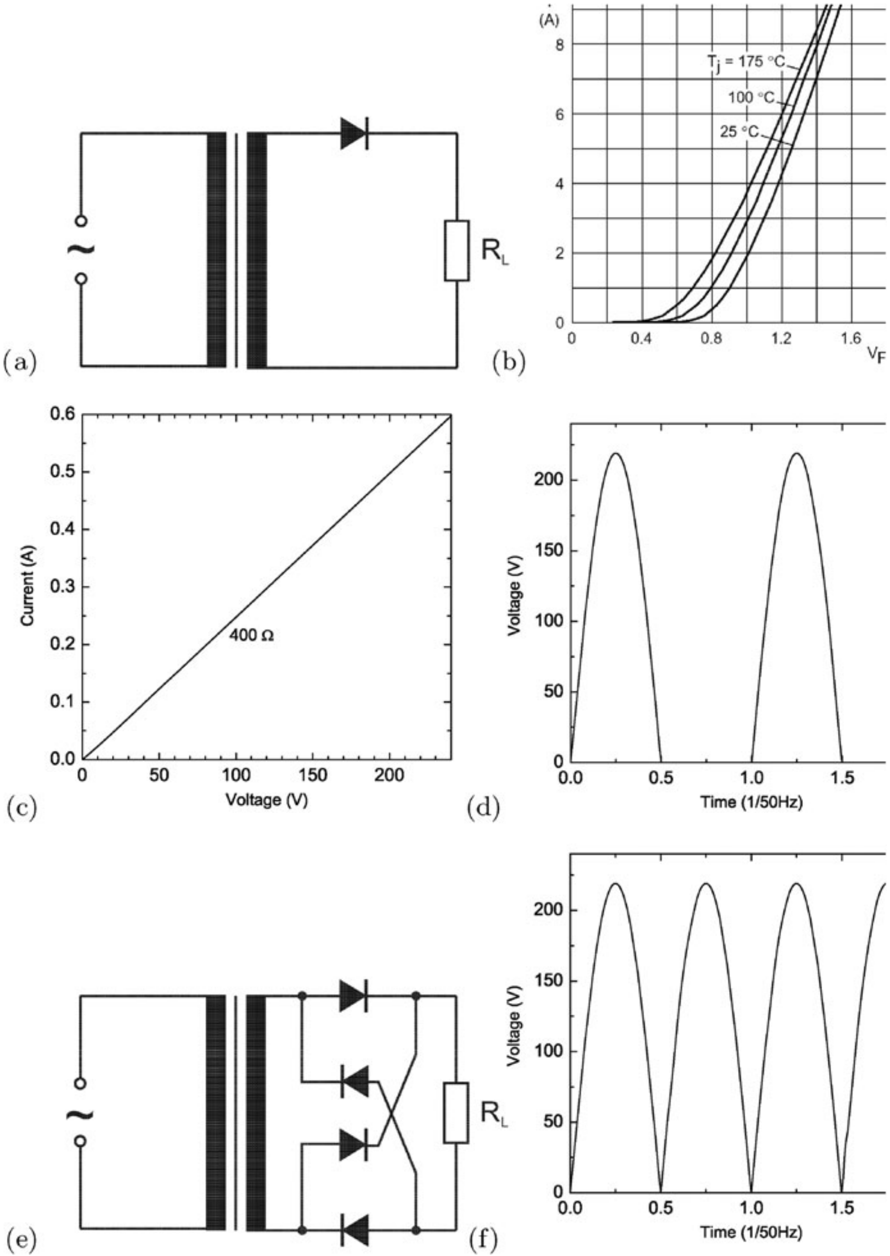

Fig. 20.56. (**a**) Single-path mains rectifier, (**b**) characteristics of Si diode (BYD127, Philips), (**c**) load characteristics of the mains rectifier ($R_L = 400\,\Omega$), (**d**) voltage output of single-path mains rectifier. (**e**) depicts the schematic circuit of a bridge rectifier that works for both half-waves, (**f**) the resulting voltage output

considered. The total current is given by $I = I_s\left[\exp\left(eU_d/nkT\right) - 1\right]$. The total voltage U is split between the voltage drop across the diode U_d and that over the load resistance $U_L = R_L I$. The current is therefore given by

$$I = \frac{U - U_d}{R_L} \ . \tag{20.150}$$

For sizeable currents the voltage drop across the diode U_d is between 0.7 and 1 V. The characteristic is linear between about 1 and 220 V (Fig. 20.56d). Typically, the voltage U_L is low-pass filtered with a capacitor parallel to the load resistor. The effective voltage is the peak voltage divided by 2.

The drawback of the single diode rectifier is that only the positive half-wave contributes to a dc signal. The setup in Fig. 20.56e (bridge rectifier) allows both half-waves to contribute to the dc signal. The effective voltage in this case is the peak voltage divided by $\sqrt{2}$.

The forward resistance in the static (R_f) and dynamic (r_f) case are (for $\beta V_f > 3$)

$$R_f = \frac{V_f}{I_f} \cong \frac{V_f}{I_s} \exp\left(-\frac{eV_f}{nkT}\right) \tag{20.151a}$$

$$r_f = \frac{\partial V_f}{\partial I_f} = \frac{nkT}{eI_s} \exp\left(\frac{eV_f}{nkT}\right) \cong \frac{nkT}{eI_f} \ . \tag{20.151b}$$

For reverse bias we have ($\beta|V_r| > 3$)

$$R_r = \frac{V_r}{I_r} \cong \frac{V_r}{I_s} \tag{20.152a}$$

$$r_r = \frac{\partial V_r}{\partial I_r} = \frac{nkT}{eI_s} \exp\left(\frac{e|V_r|}{nkT}\right) \ . \tag{20.152b}$$

Thus, the dc and ac rectifications ratios are given by

$$\frac{R_r}{R_f} = \exp\left(\frac{eV_f}{nkT}\right) \tag{20.153a}$$

$$\frac{r_r}{r_f} = \frac{I_f}{I_s \exp\left(\frac{e|V_r|}{nkT}\right)} \ . \tag{20.153b}$$

Rectifiers generally have slow switching speeds. A significant time delay arises from the necessary charge-carrier recombination when the diode switches from low (forward) to high (reverse) impedance. This poses typically no problem for line-frequency (50–60 Hz) applications. For fast applications, however, the minority-carrier lifetime needs to be reduced, e.g. by doping Si with Au (see Sect. 10.9).

20.5.2 Frequency Mixing

The nonlinear characteristic of the diode allows the mixing of frequencies, e.g. for second- (or higher-) harmonic generation, upconversion or demodulating of radio-frequency (RF) signals. A single balanced mixer is shown in

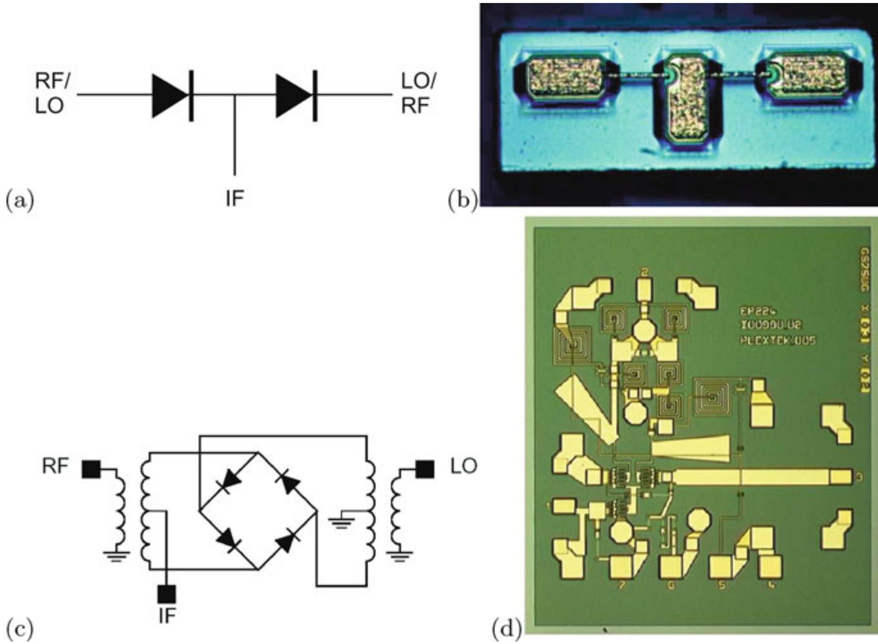

Fig. 20.57. (**a**) Schematic circuit of single balanced mixer with input (RF: radio frequency, LO: local oscillator) and output (IF: intermediate frequency). (**b**) Optical plan-view image ($300 \times 125\,\mu\mathrm{m}^2$) of a high-speed single balanced mixer with two GaAs Schottky diodes with opposite poling. The device properties are $R_\mathrm{s} = 5\,\Omega$, for $I = 1\,\mu\mathrm{A}$ a forward and reverse voltage of 0.7 and 6 V, respectively; the capacitance of each diode is 8 fF. Reprinted with permission from [1188]. (**c**) Schematic circuit of a double balanced mixer. (**d**) Optical image ($1.65\,\mathrm{mm}^2$) of 40–45 GHz MMIC (Gilbert cell) mixer on GaAs basis using pHEMTs. Reprinted with permission from [1189]

Figs. 20.57a and b. The RF signal consists of a RF carrier frequency f_0 modulated with an intermediate frequency (IF) signal $f_\mathrm{IF}(t)$. It is mixed with a local oscillator (LO) that has a constant frequency f_LO outside the RF modulation bandwidth $f_0 \pm f_\mathrm{IF}$. The IF signal can be detected from the setup in Fig. 20.57a if filtered through a low-pass filter to avoid loss of power to the IF amplifier. The temperature dependence of the diode characteristic (via j_s and β) on mixing efficiency is typically less than 0.5 dB for a 100-K change in temperature.

Problems of single-diode mixers are the radiation of local-oscillator power from the RF input port,[21] loss of sensitivity by absorption of input power in the local oscillator circuit, loss of input power in the intermediate frequency

[21] that in military applications could make the mixer detectable by the enemy.

amplifier, and the generation of spurious output frequencies by harmonic mixing. Some of these problems can be solved by circuit techniques, but these circuits often introduce new problems. Most mixers therefore use multiple-diode techniques to provide a better solution of these problems. In Fig. 20.57c, the circuit diagram of a double balance mixer is shown. Even-order harmonics of both the LO and the signal frequency are rejected. This mixer does not require a low-pass filter to isolate the IF circuit. The three ports are isolated from each other by the symmetry of the circuit. These mixers usually cover a broader frequency band than the others. Ratios as high as 1000:1 are available. Microwave equivalents (working at $f \gg 1\,\mathrm{GHz}$) of such mixer circuits are available. Bandwidth ratios as high as 40:1 are available at microwave frequencies in MMICs (millimeter-wave integrated circuits).

The common drawback of MMIC diodes is that they are obtained from the Schottky barriers used in field-effect transistors, that have inferior performance compared to discrete diodes. The use of pHEMT technology[22] for millimeter-wave applications provides diodes that differently from regular Schottky diodes, since they consist of a Schottky barrier in series with a heterojunction. In Fig. 20.57d, a MMIC 45 GHz mixer is shown using fast GaAs-based pHEMTs.

20.5.3 Voltage Regulator

In a voltage regulator, the large variation of resistance with applied bias is used. This effect occurs in the forward direction and close to the breakdown voltage.

In Fig. 20.58a, a simple circuit is shown. When the input voltage V_{in} is increased, the current increases. The preresistor $R_1 = 5\,\mathrm{k\Omega}$ and the load resistor represent a voltage divider with $V_{\mathrm{in}} = I R_1 + V_{\mathrm{out}}$. The total current I is given by the two currents through the diode and the load resistor $I = I_{\mathrm{s}}\left[\exp(\beta V_{\mathrm{out}}/n) - 1\right] + V_{\mathrm{out}}/R_{\mathrm{L}}$. Therefore, the output voltage is implicitly given by

$$V_{\mathrm{out}}\left(1 + \frac{R_1}{R_{\mathrm{L}}}\right) = V_{\mathrm{in}} - R_1\, I_{\mathrm{s}}\left[\exp\left(\frac{\beta V_{\mathrm{out}}}{n}\right) - 1\right] . \tag{20.154}$$

A large current change is related to a fairly small change of the voltage across the diode, which at the same time is the output voltage. Therefore, a change in the input voltage causes only a small change in the output voltage.

We assume a diode with $n = 1$ and $I_{\mathrm{S}} = 10^{-14}\,\mathrm{A}$ with the characteristic shown in Fig. 20.58a. The numerical example in Fig. 20.58c is calculated for $R_{\mathrm{L}} = 2\,\mathrm{k\Omega}$ and $4\,\mathrm{k\Omega}$, respectively. The output voltage varies by about 0.02 V if the input varies between 5 and 9 V. In Fig. 20.58d, the differential voltage change $\alpha = \frac{V_{\mathrm{in}}}{V_{\mathrm{out}}}\frac{\partial V_{\mathrm{out}}}{\partial V_{\mathrm{in}}}$ is shown.

[22] pseudomorphic high electron mobility transistors, cf. Sect. 23.5.8.

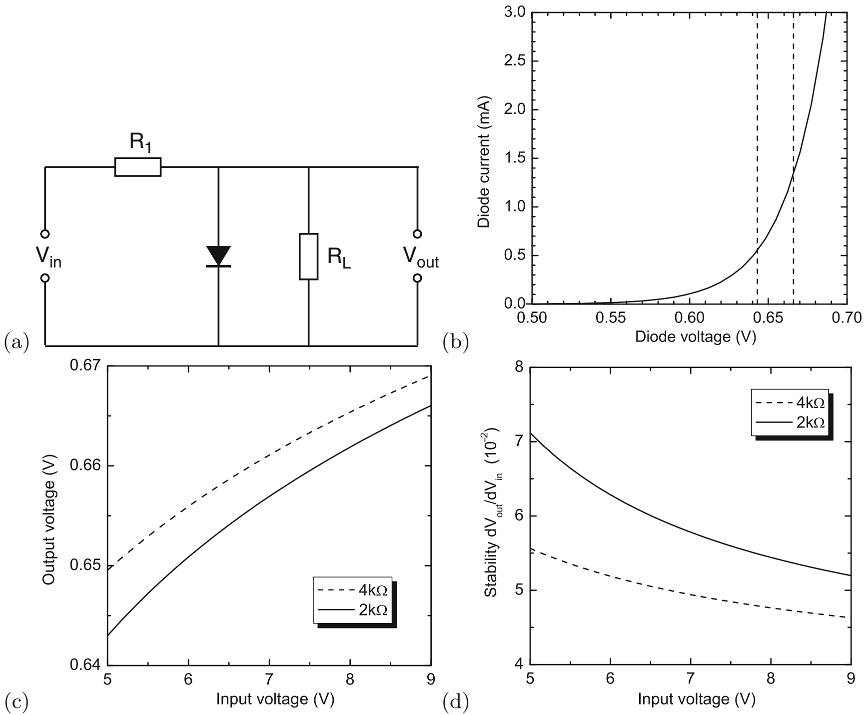

Fig. 20.58. (**a**) Circuit diagram of a voltage regulator, (**b**) diode characteristic ($n = 1$). The *vertical dashed lines* show the operation conditions for $R_{\mathrm{L}} = 2\,\mathrm{k}\Omega$ and $U_{\mathrm{E}} = 5$ and $9\,\mathrm{V}$ and thus the principle of voltage stabilization. (**c**) Output vs. input voltage and (**d**) stability (differential voltage ratio α, see text) for input voltage between 5 and 9 V

In this way, voltage peaks can be filtered from the input voltage. If two antiparallel diodes are used, this principle works for both polarities. Instead of a diode in the forward direction, the very steep slope of the diode I–V characteristic at the breakdown can be used. Just before breakdown, the diode has a high resistance and the voltage drops at the load resistor. If the input voltage increases a little, the diode becomes conductive and shorts the additional voltage (the maximum allowed breakdown current needs to be observed!). Due to its small saturation current, typically Si diodes are used. The breakdown voltage can be designed via the diode parameters. Such diodes with defined breakdown voltage are called Z- or Zener diodes (see next section).

If the breakdown is due to tunneling (avalanche multiplication), the breakdown voltage decreases (increases) with temperature. If two diodes with positive and negative temperature coefficient are put in series, a very good temperature stability of the breakdown voltage of 0.002%/K can be achieved. Such diodes can be used to realize a reference voltage.

20.5.4 Zener Diodes

A Zener diode is designed to have a defined breakdown voltage. Zener diodes are available with a number of different standard breakdown voltages. Their characteristic is shown for reverse bias with the current shown positive. The characteristics of various Zener diodes for different breakdown voltages are shown in Fig. 20.59.

20.5.5 Varactors

A diode exhibits a voltage-dependent capacitance. This effect can be used to tune an oscillator using the diode bias (voltage-controlled oscillator, VCO). The equivalent circuit is shown in Fig. 20.60. The capacitance consists of a parasitic capacitance C_p due to mounting and bonding. This effect also causes a parasitic inductance. The series resistance due to mounting can typically be neglected. The variable junction capacitance C_j and the ohmic resistance R_s are bias dependent.

The $C(V)$ dependence has generally a power law with an exponent γ (which itself may depend on the bias voltage)

$$C = \frac{C_0}{(1 + V/V_\mathrm{bi})^\gamma} , \tag{20.155}$$

where C_0 is the-zero bias capacitance. Since the frequency f of an LC oscillator circuit depends on $C^{-1/2}$ the frequency, f depends on the voltage as $f \propto V^{\gamma/2}$. Therefore, a $\gamma = 2$ dependence is most desirable.

For uniformly doped profiles, the capacitance depends with an inverse square root law on the applied voltage (20.98), i.e. $\gamma = 0.5$. Hyperabrupt junctions are typically made by ion implantation or epitaxy with graded impurity

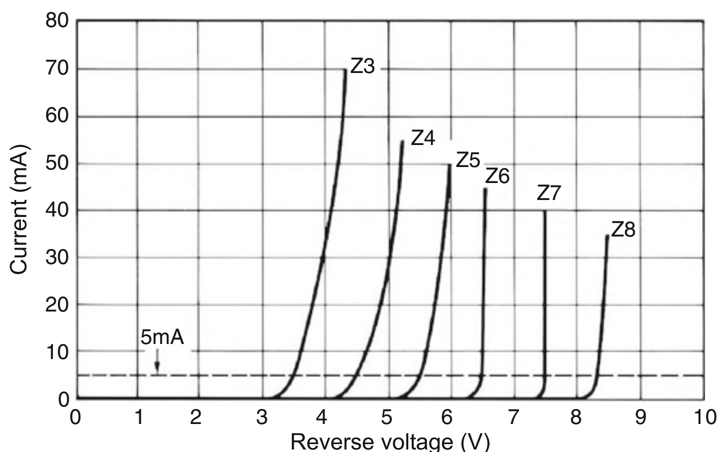

Fig. 20.59. Characteristics of a field of Zener diodes (at room temperature)

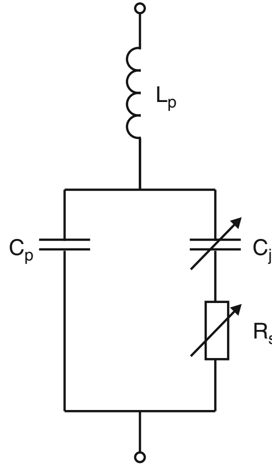

Fig. 20.60. Equivalent circuit of a varactor diode with parasitic capacitance C_p and inductance L_p and variable capacitance C_j and resistance R_s

incorporation to create a special nonuniform doping profile (Fig. 20.61a). For a doping profile

$$N_\mathrm{B}(z) = \hat{N}_\mathrm{B} \left(\frac{z}{z_0}\right)^m \tag{20.156}$$

the capacitance is given as

$$C = \left[\frac{e\,\hat{N}_\mathrm{B}\,\epsilon_\mathrm{s}^{m+1}}{(m+2)\,z_0^m\,(V_\mathrm{bi}-V)}\right]^{\frac{1}{m+2}} = \frac{C_0}{(1+V/V_\mathrm{bi})^{1/(m+2)}}\,. \tag{20.157}$$

Ideally, $m = -3/2$ results is a linear frequency vs. voltage relation. The C–V characteristic of an implanted, hyperabrupt diode exhibits a part that has an exponent $\gamma = 2$ (Fig. 20.61b). A $\gamma = 2$ $C(V)$ dependence and therefore a linear $f(V)$ curve can be achieved over more than one octave using computer-controlled variable epitaxial-layer doping (Fig. 20.61c).

20.5.6 Fast-Recovery Diodes

Fast-recovery diodes are designed for high switching speeds. The switching speed from the forward to the reverse regime is given by the time $t_0 = t_1 + t_2$ with t_1 being the time to reduce the minority carrier density to the equilibrium value (e.g. $p_\mathrm{n} \rightarrow p_{\mathrm{n}_0}$) and t_2 being the time in which the current decreased exponentially (Fig. 20.62). The time t_1 can be drastically reduced by incorporation of deep levels that act as recombination centers. A prominent example is Si:Au. However, this concept is limited since the reverse generation current, e.g. (20.135), depends on the trap density. For direct

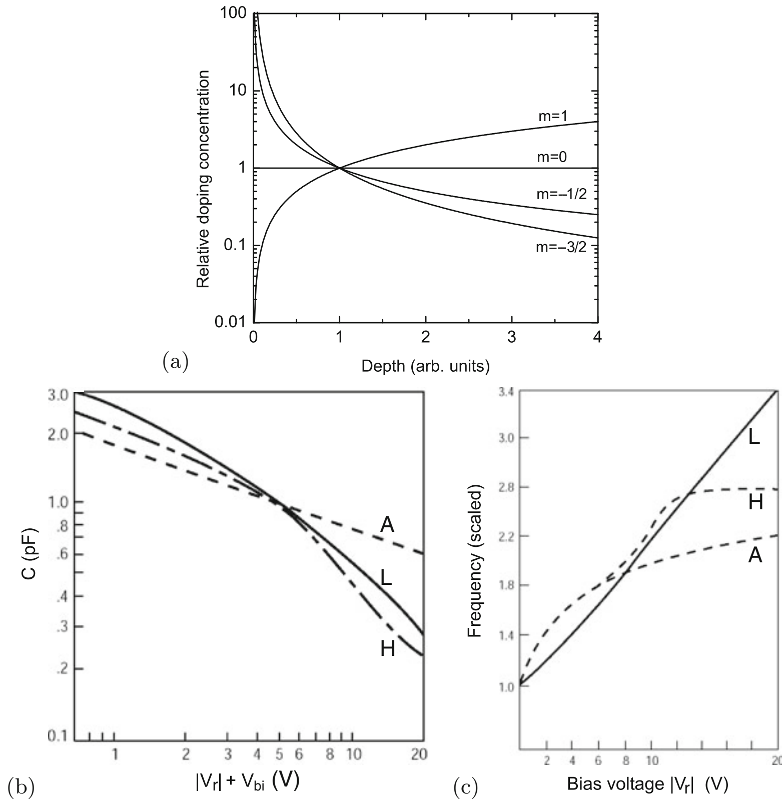

Fig. 20.61. (**a**) Donor-doping profile according to (20.156) in p^+n or Schottky diodes for $m = 0$ (abrupt junction), $m = 1$ (linearly graded junction) and two values with $m < 0$ (hyperabrupt junctions). (**b**) Bias dependence of capacitance for diodes with abrupt junction ('A', $\gamma = 0.5$), hyperabrupt junction ('H', $\gamma > 0.5$) and 'epilinear' junction ('L', $\gamma = 2$). (**c**) Frequency–voltage tuning characteristics (scaled to 1.0 for $V = 0$) for the three diode types. Parts (**b**) and (**c**) adapted from [1190], reprinted with permission.

semiconductors, recombination times are short, e.g. 0.1 ns or less for GaAs. In silicon, they can be extremely long (up to ms) or at least 1–5 ns. Schottky diodes are suitable for high-speed applications since they are majority-carrier devices and minority-charge carrier storage can be neglected.

20.5.7 Step-Recovery Diodes

This type of diode is designed to store charge in the forward direction. If polarity is reversed, the charge will allow conductance for a short while, ideally until a current peak is reached (Fig. 20.63a), and then cutoff the current very rapidly during the so-called snapback time T_s (Fig. 20.63b).

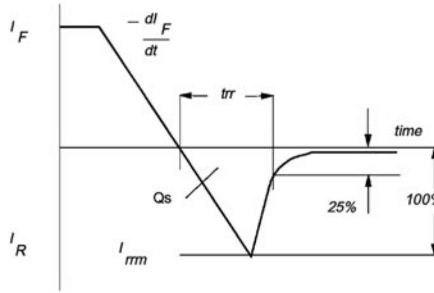

Fig. 20.62. Current vs. time trace for a (soft) fast-recovery diode. Reprinted with permission from [1191]

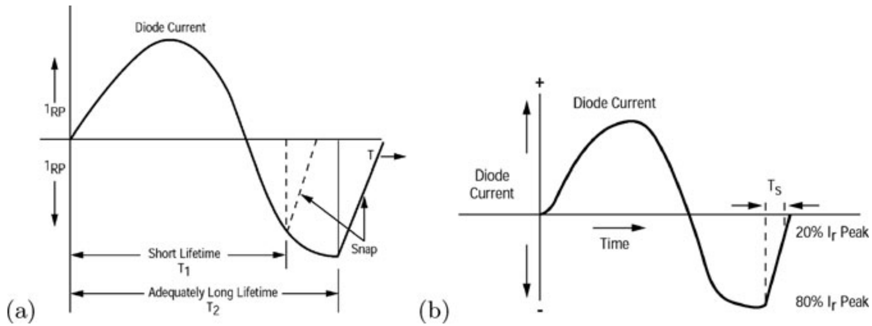

Fig. 20.63. (**a**) Current vs. time trace for a step-recovery diode and sinusoidal voltage input. The lifetime must be sufficiently large such that a current peak is reached. (**b**) Definition of the snapback time T_s. Reprinted with permission from [1192]

The cutoff can be quite rapid, in the ps regime. These properties are used for pulse (comb) generation or as a gate in fast sampling oscilloscopes. In Si, only 0.5–5 µs are reached (fast-recovery diode, see previous section) while GaAs diodes can be used in the several tens of GHz regime.

Using a heterostructure GaAs/AlGaAs diode (cf. Sect. 20.5.12), as shown schematically in Fig. 20.64a, a steepening of a 15-V, 70-ps (10% to 90%) pulse to a fall time of 12 ps was observed (Fig. 20.64c). The forward current of the diode was 40 mA, supplied via a bias tee.

20.5.8 pin-Diodes

In a pin-diode, an intrinsic (i), i.e. undoped region (with higher resistivity) is located between the n- and the p-regions (Fig. 20.65). Often, also a region with low n- or p-doping is used. In this case, the center region is denoted as a ν- or π-region, respectively. The fabrication of arbitrary doping profiles and an intrinsic region poses little problem for epitaxial diodes.

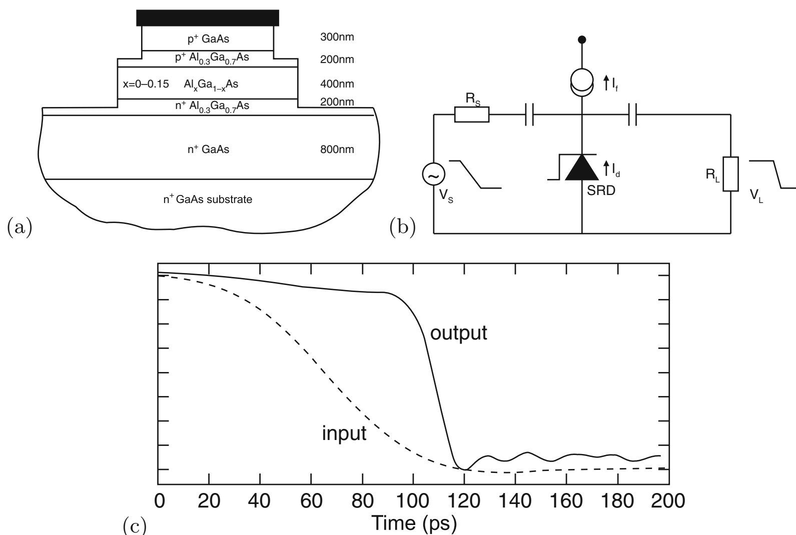

Fig. 20.64. (**a**) Schematic layer sequence for fast GaAs/AlGaAs step-recovery diode. (**b**) Circuit with input and output pulse. (**c**) Input (*dashed line*) and output (*solid line*) waveforms. Vertical division is 2 V. Adapted from [1193]

Via the Poisson equation, the charge in the intrinsic layer is related to the electric field. If no dopants are present, there is a constant (maximum) field in the i-region at zero bias. If there is low doping, a field gradient exists.

The capacitance for reverse bias is $\epsilon_s A/w$ and is constant starting at fairly small reverse bias (10 V). The series resistance is given by $R_s = R_i + R_c$. The contact resistance R_c dominates the series resistance for large forward bias.

20.5.9 Tunneling Diodes

For the invention of the tunneling diode and the explanation of its mechanism the 1973 Nobel Prize in Physics was awarded to L. Esaki. Eventually, the tunneling diode did not make the commercial breakthrough due to its high basis capacitance. It is used for special microwave applications with low power consumption, for frequency stabilization and possibly in tunneling field-effect transistors (Sect. 23.5.6).

First, the tunneling diode is a pn-diode. While the tunnel effect [1194] has already been discussed for Schottky diodes, it has not yet been considered by us for pn–diodes. We expect the tunnel effect to be important if the depletion-layer is thin, i.e. when the doping of both sides is high.

The doping is so high that the quasi-Fermi levels lie within the respective bands (Fig. 20.66). The degeneracy is typically several kT and the depletion layer width is in the 10 nm range.

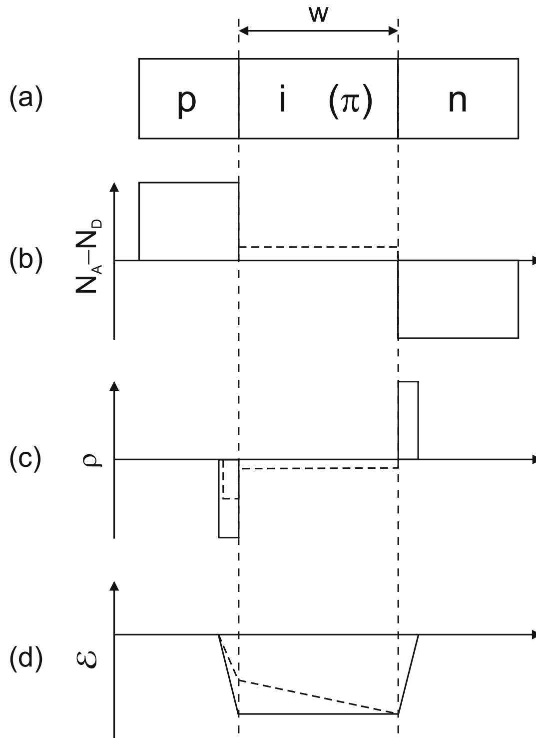

Fig. 20.65. (**a**) Schematic layer sequence of pin-diode ('i': intrinsic, 'π': lowly p-doped), (**b**) net impurity distribution $N_\mathrm{A} - N_\mathrm{D}$, (**c**) space charge and (**d**) electric field in a pin (*solid lines*) and a p–π–n (*dashed lines*) diode

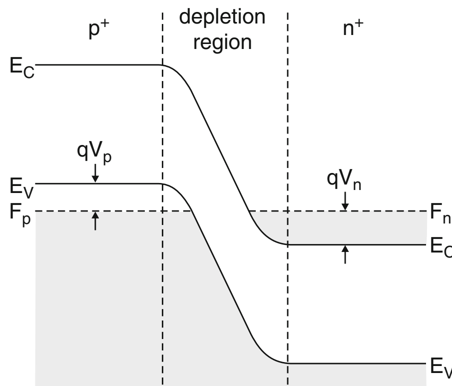

Fig. 20.66. Band diagram of a tunneling diode in thermodynamic equilibrium ($V = 0$). V_n and V_p characterize the degeneracies on the n- and p-side, respectively

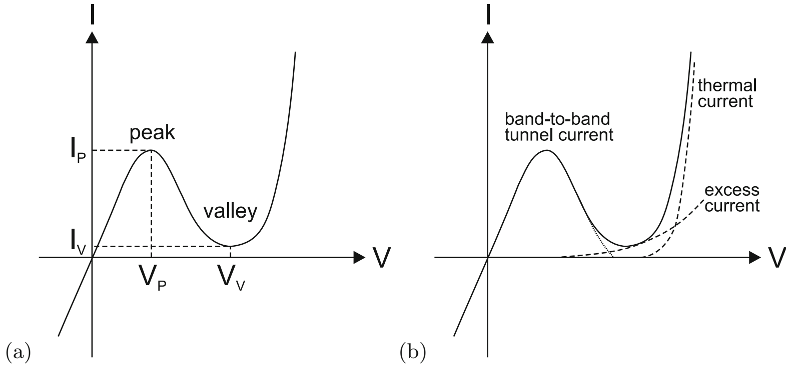

Fig. 20.67. (**a**) Static current–voltage characteristics of a typical tunneling diode. Peak and valley current and voltage are labeled. (**b**) The three components of the current (*short dashed*: band-to-band tunnel current, *dashed*: excess current, *dash-dotted*: thermal current) are shown separately. Adapted from [383], ©1981 Wiley

In the forward direction, the I–V characteristic of the tunneling diode exhibits a maximum followed by a minimum and subsequently an exponential increase (Fig. 20.67a). As shown in Fig. 20.67b, the total current consists of three currents, the band-to-band tunneling current, the excess current and the thermal (normal thermionic diode) current.

The $V = 0$ situation is again shown in Fig. 20.68b. Upon application of a small forward bias, electrons can tunnel from populated conduction-band states on the n-doped side into empty valence-band states (filled with holes)

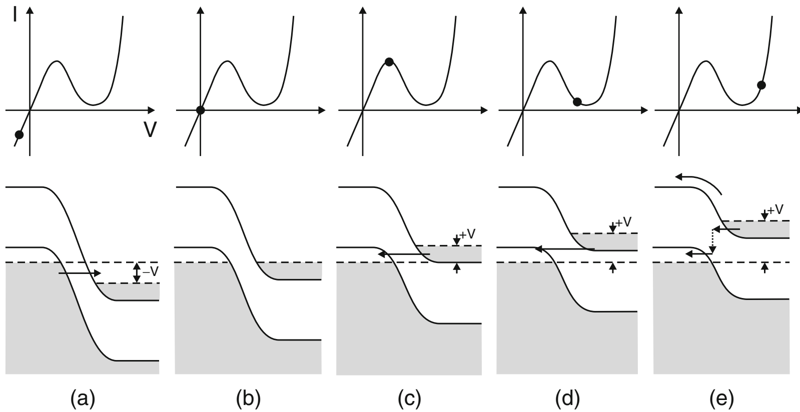

Fig. 20.68. I–V characteristics (*upper row*) and simplified band structure (*lower row*) of a tunneling diode at various bias voltages as indicated with a *dot* in the I–V plot. (**a**) Reverse bias, (**b**) in thermodynamic equilibrium ($V = 0$), (**c**) in the maximum of the tunneling current, (**d**) close to the valley and (**e**) forward bias with dominating thermal current. The tunneling current is indicated with *straight arrows*. In (**e**) the thermionic emission current (*curved arrow*) and the excess current with inelastic tunneling (*dotted arrow*) are shown.

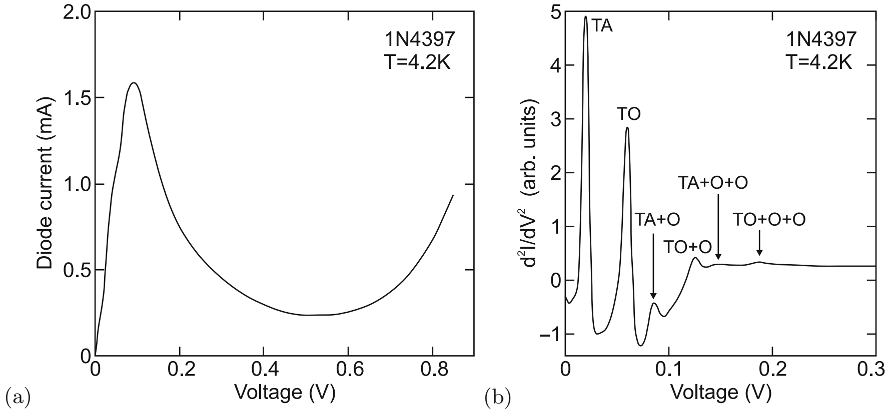

Fig. 20.69. (**a**) Current–voltage characteristic of silicon tunneling diode (model 1N4397 from American Microsemiconductor) at low temperature ($T = 4.2\,\mathrm{K}$). (**b**) $\mathrm{d}^2I/\mathrm{d}V^2$ for small forward voltages, exhibiting characteristic phonon energies. Adapted from [1198]

on the p-doped side (Fig. 20.68c). We note that this tunneling process is usually considered elastic. However, signatures at characteristic phonon and multi-phonon energies are found (at low temperature) in the forward current [1195, 1196] and are best seen in a $\mathrm{d}^2I/\mathrm{d}V^2$-plot [1197, 1198] (Fig. 20.69).

A similar situation, now with electrons tunneling for the valence band on the p-side into the conduction band on the n-side, is present for small reverse bias (Fig. 20.68a). Thus the rectifying behavior of the diode is lost. For larger forward bias, the bands are separated so far that the electrons coming from the n-doped side do not find final states on the p-doped side. Thus the tunneling current ceases (Fig. 20.68d). The current minimum is at a voltage $V = V_\mathrm{n} + V_\mathrm{p} > 0$. The thermal current is the normal diode diffusion current (Fig. 20.68e). Therefore, a minimum is present in the I–V characteristic. The excess current is due to inelastic tunneling processes through states in the band gap and causes the minimum to not drop down to almost zero current.

The peak (V_p, I_p) and valley (V_v, I_v) structure of the characteristic leads to a region of negative differential resistance (NDR). $I_\mathrm{p}/I_\mathrm{v}$ is termed the peak-to-valley ratio (Fig. 20.70). Peak-to-valley ratios of 8 (Ge), 12 (GaSb, GaAs), 4 (Si), 5 (InP) or 2 (InAs) have been reported (all at room temperature).

20.5.10 Backward Diodes

When the doping in a tunneling diode is nearly or not quite degenerate, the peak-to-valley ratio can be very small. Then the tunnel current flows mostly in the reverse direction (low resistance) and the forward direction has a higher resistance (with or without the NDR regime). Such diodes are called backward diodes. Since there is no minority-charge carrier storage, such diodes are useful for high-frequency applications.

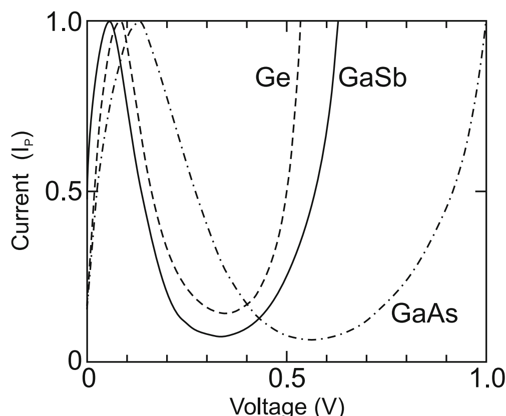

Fig. 20.70. Comparison of tunneling characteristic (room temperature) of diodes based on Ge, GaSb and GaAs. Peak-to-valley ratios are 8 (Ge) and 12 (GaSb, GaAs). Adapted from [384]

20.5.11 Gunn Diodes

The Gunn diode is not really a diode and thus more appropriately called *Gunn element*. It allows to generate microwave radiation in the frequency range of 1–100 GHz [1199] and beyond [1200] using GaAs and in the THz-regime using GaN [1201]. Extracting higher harmonics, frequencies of several 100 GHz can be realized [1202, 1203].

The Gunn element relies on the negative differential resistance (NDR) occurring in semiconductors with two valleys of different mobility such as GaAs or InP (cmp. Sect. 8.5.2). At high fields, the electrons are scattered from the Γ-valley into the upper valley (L for most materials). Accordingly, the Gunn element is also called 'transferred electron device' (TED).

The Gunn effect was discovered by and named after J.B. Gunn [87]. The spontaneous oscillation of current in a n-type semiconductor occurs when a sufficiently large voltage (pulse) is applied that causes the electric field in the semiconductor to reach the NDR regime (Fig. 20.71). The applied average field of $\mathcal{E} = 16\,\mathrm{V}/25\,\mu m = 6.4\,\mathrm{kV/cm}$ [87] is larger than the threshold field of $\mathcal{E}_{\mathrm{T}} = 3.2\,\mathrm{kV/cm}$ for NDR in GaAs (Table 8.4).

The self-started oscillations are due the inherent instability introduced by NDR. A homogeneous (uniform) electric field and electron distribution is unstable and a thin high-field domain with bipolar charge distribution (Gunn domain, predicted in [541]) can develop and drift through the device. After reaching the anode, another domain can form, causing a periodically fluctuating current. The highest frequencies can be achieved with the so-called limited-space-charge accumulation (LSA) mode which operates without domains. Optical performance requires non-homogeneous doping profiles. A detailed discussion of the various oscillation mechanisms can be found in [542, 1199, 1204].

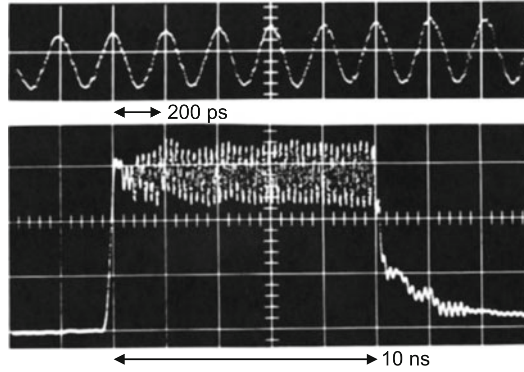

Fig. 20.71. Current traces upon excitation of a 25 µm thick piece of n-type GaAs with a voltage pulse (amplitude 16 V and duration 10 ns). The upper trace is an expanded view of the lower trace. The oscillation period is 4.5 GHz. Adapted from [87]

20.5.12 Heterostructure Diodes

In a heterostructure diode, the n- and p-regions are made of different semiconductors. Such a diode is important in particular as an injection (emitter–base) diode in transistors. In Fig. 20.72, the band diagram is shown for a type-I heterostructure with the n (p) region having the larger (smaller) band gap. Additionally to the built-in voltage, the barrier in the valence band is

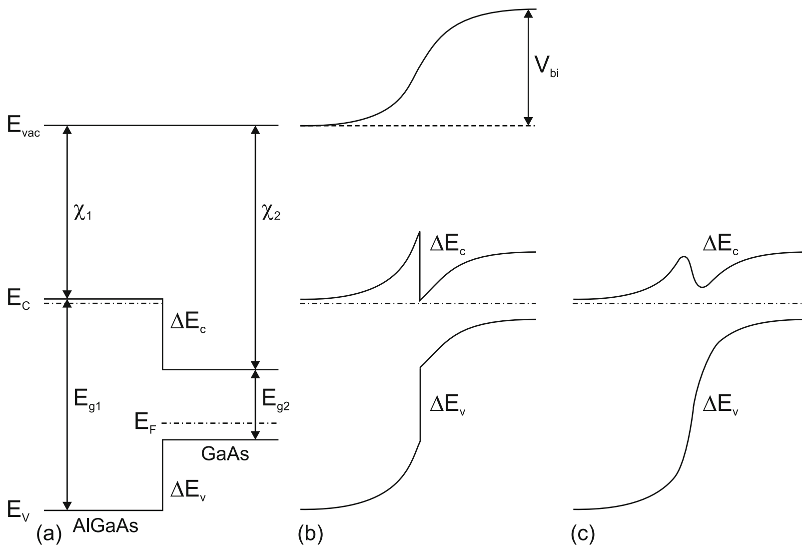

Fig. 20.72. Schematic band diagram of a n-AlGaAs/p-GaAs diode (**a**) without contact of the n- and p-materials, (**b**) in thermodynamic equilibrium, and (**c**) with graded Al composition at the heterointerface

increased. In this case, the (mostly undesired) hole current from the p- to the n-side is reduced. The peak in the conduction band poses potentially a greater barrier than the diffusion potential itself. The spike can be reduced by grading the materials across the heterojunction and creating a smooth transition of E_{g} between the materials. The effect of grading on the properties of the heterojunction is discussed in detail in [1205].

21 Light-to-Electricity Conversion

21.1 Photocatalysis

The absorption of light in a semiconductor across the band gap creates free electrons and holes. In particular, for small particle size in powders[1] these charge carriers can reach the surface of the semiconductor. At the surface they can react with chemicals. The hole can form $\bullet$OH radicals from OH^- attached to the bead. The electron can form $O_2\bullet^-$. These radicals can subsequently attack and detoxify, e.g., noxious organic pollutants in the solution surrounding the semiconductor. Such photocatalytic activity has been found, e.g., for TiO_2 and ZnO powders. A review of photocatalysis, in particular with TiO_2 particles and their surface modifications with metals and other semiconductors, is found in [1206].

The efficiency of the photocatalytic activity depends on the efficiency of the charge separation (Fig. 21.1). Any electron–hole pair that recombines within the bulk or the surface of the particle is lost for the catalytic activity. Thus, surfaces must exhibit a small density of recombination centers. Surface traps, however, can be beneficial for charge-carrier separation when they 'store' the charge-carrier rather than letting it recombine. Small particles are expected to exhibit more efficient charge-carrier separation than larger ones. Electrons at the surface can be donated and reduce an electron acceptor, typically oxygen, $A \rightarrow A^-$. A hole at the surface can oxidize a donor species, $D \rightarrow D^+$.

An example of increased photocatalytic activity are TiO_2 powders with deposited metal particles (such as Pt) for H_2 evolution and metal-oxide particles (such as RuO_2) for O_2 evolution. Such a system behaves as a short-circuited microscopic photoelectrochemical cell in which Pt is the cathode and RuO_2 is the anode [1207]. Excitation with light energy above the band gap in the TiO_2 particle (3.2 eV) injects electrons into the Pt particles and holes into the RuO_2 particles. Trapped electrons in Pt reduce water to hydrogen and trapped holes in RuO_2 oxidize water to oxygen.

The photocatalytic activity is also tied to the geometrical shape of the semiconductor. Generally, powders with nanosized grains have much higher

[1] 'Small' is here in relation to the diffusion length and does not need to be in the range where quantization effects (quantum dots) are present.

M. Grundmann, *The Physics of Semiconductors*, 2nd ed., Graduate Texts in Physics, DOI 10.1007/978-3-642-13884-3_21,

© Springer-Verlag Berlin Heidelberg 2010

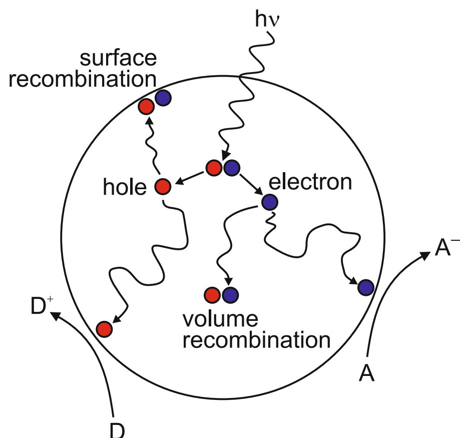

Fig. 21.1. Principle of photocatalytic activity. Light absorption creates an electron–hole pair. The electron and hole diffuse and can recombine in the bulk or at the surface. Free carriers can react at the surface with species from the surrounding solution, reducing an electron acceptor or oxidizing a donor species. Adapted from [1206]

activity than those with microsized particles [1208]. In Fig. 21.2 it is shown that nanosized objects with high surface-to-volume ratio are more effective catalysts than rather compact surfaces.

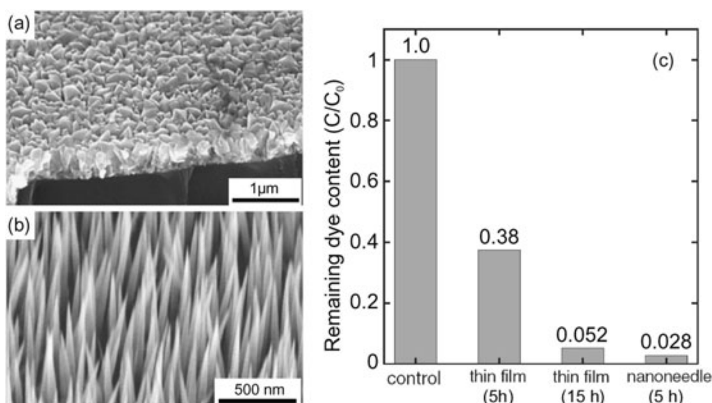

Fig. 21.2. SEM images of MOCVD-grown (**a**) ZnO thin film and (**b**) ZnO nanoneedle layer. (**c**) Comparison of the photocatalytic activity (decoloration of the dye Orange II in aqueous solution) of the ZnO thin film (irradiation with a Hg lamp for 5 h and 15 h) and the ZnO nanoneedles (irradiation 5 h). The sample labeled 'control' (scaled to 100%) is the start situation (absorption of the dye Orange II) without photocatalytic process. Adapted from [1209], reprinted with permission

In sun-protection cream only the UV absorption is wanted in UVA (330–420 nm) and UVB (260–330 nm) ranges. Subsequent photocatalysis on the skin and the presence of radicals are unwanted. Thus the semiconductor particles (∼10–200 nm diameter) are encapsulated in microbeads (∼1–10 µm diameter) of silica, PMMA or urethane, also improving ease of dispersion, aggregation, stability and skin feel.

21.2 Photoconductors

21.2.1 Introduction

Charge carriers can be generated in the semiconductor through the absorption of light with a photon energy above or below the band gap (Fig. 21.3). Absorption involving impurities occurs typically in the mid- and far-infrared spectral regimes (cf. Sect. 9.6). The additional charge carriers cause an increase in the conductivity (8.11).

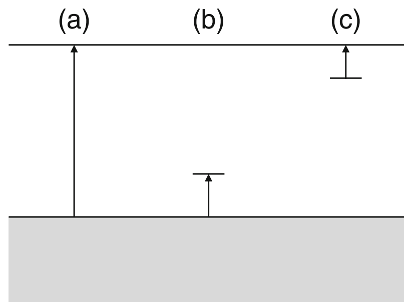

Fig. 21.3. Absorption and charge-carrier generation in a photoconductor: (**a**) band–band transition, (**b**) valence-band to acceptor and (**c**) donor to conduction-band transition

21.2.2 Photoconductivity Detectors

In stationary equilibrium for constant illumination of power P_{opt} and photon energy $E = h\nu$ the generation rate G is given by

$$G = \frac{n}{\tau} = \eta \, \frac{P_{\mathrm{opt}}/h\nu}{V} \, , \tag{21.1}$$

where V is the volume ($V = wdL$, see Fig. 21.4) and τ denotes the charge-carrier lifetime. η is the quantum efficiency, i.e. the average number of electron–hole pairs generated per incoming photon. The photocurrent between the electrodes is

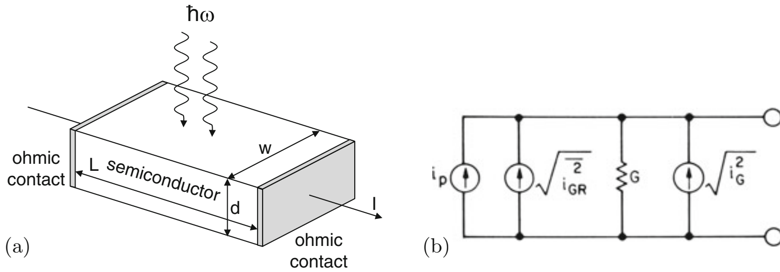

Fig. 21.4. (**a**) Scheme of photoconductor. (**b**) Equivalent circuit of photoconductor

$$I_{\mathrm{ph}} = \sigma \mathcal{E} w d \approx e \mu_{\mathrm{n}} n \mathcal{E} w d \, , \tag{21.2}$$

assuming that $\mu_{\mathrm{n}} \gg \mu_{\mathrm{p}}$ and with $\mathcal{E} = V/L$ denoting the electric field in the photoconductor, V being the voltage across the photoconductor. We can then also write

$$I_{\mathrm{ph}} = e \left(\eta \, \frac{P_{\mathrm{opt}}}{h\nu} \right) \left(\frac{\mu_{\mathrm{n}} \tau \mathcal{E}}{L} \right) . \tag{21.3}$$

With the primary photocurrent $I_{\mathrm{p}} = e \left(\eta \, \frac{P_{\mathrm{opt}}}{h\nu} \right)$ we deduce a gain

$$g = \frac{\mu_{\mathrm{n}} \tau \mathcal{E}}{L} = \frac{\tau}{t_{\mathrm{r}}} \, , \tag{21.4}$$

where $t_{\mathrm{r}} = L/v_{\mathrm{d}}$ is the transit time through the photoconductor.

Now we consider a modulated light intensity

$$P(\omega) = P_{\mathrm{opt}} \left[1 + m \exp(\mathrm{i}\omega t) \right] \, , \tag{21.5}$$

where m is between 0 and 1. For $m = 0$ it is a constant light power, for $m = 1$ the intensity is sinusoidally modulated between 0 and $P_{\mathrm{max}} = 2P_{\mathrm{opt}}$. The rms optical power[2] is given by $\sqrt{2} m P_{\mathrm{opt}}$. In the case of $m = 1$ this is equal to $P_{\mathrm{max}}/\sqrt{2}$.

The rms photocurrent is

$$i_{\mathrm{ph}} \approx \frac{e \, \eta \, m \, P_{\mathrm{opt}}}{\sqrt{2} h\nu} \, \frac{\tau}{t_{\mathrm{r}}} \, \frac{1}{\sqrt{1 + \omega^2 \tau^2}} \, . \tag{21.6}$$

The thermal noise at a conductivity G is

$$i_{\mathrm{G}}^2 = 4kTGB \, , \tag{21.7}$$

with B being the bandwidth over which the noise is integrated. The generation–recombination noise (shot noise) is

[2] The rms value is the square root of the time average of the square of the power, $\sqrt{\langle P^2 \rangle}$.

$$i_{\mathrm{GR}}^2 = \frac{\tau}{t_\mathrm{r}} \frac{4qI_0}{1+\omega^2\tau^2} B \tag{21.8}$$

for the modulation frequency ω and I_0 being the current in stationary equilibrium. The equivalent circuit with the ideal photocurrent source and the noise currents is depicted in Fig. 21.4b.

The signal-to-noise ratio of the power is then given by

$$S/N = \frac{i_{\mathrm{ph}}^2}{i_{\mathrm{G}}^2 + i_{\mathrm{GR}}^2} = \frac{\eta m^2 (P_{\mathrm{opt}}/h\nu)}{8B} \left[1 + \beta^{-1} \frac{t_\mathrm{r}}{\tau} (1+\omega^2\tau^2) \frac{G}{I_0}\right]^{-1} . \tag{21.9}$$

An important quantity is the noise equivalent power (NEP). This is the light power $(mP_{\mathrm{opt}}/\sqrt{2})$ for which the S/N ratio is equal to 1 (for $B=1$). For infrared detectors the typical figure of merit is the detectivity D^* that is defined by

$$D^* = \frac{\sqrt{A\,B}}{\mathrm{NEP}} . \tag{21.10}$$

A denotes the area of the detector. The unit of D^* is $\mathrm{cm\,Hz^{1/2}\,W^{-1}}$. It should be given together with the modulation frequency. It can be given for monochromatic radiation of a particular wavelength λ or a blackbody spectrum of given temperature T_0.

21.2.3 Electrophotography

The principle of the Xerox copy machine is based on a photoconductive layer (Fig. 21.5). This layer is normally insulating such that both sides of the layer

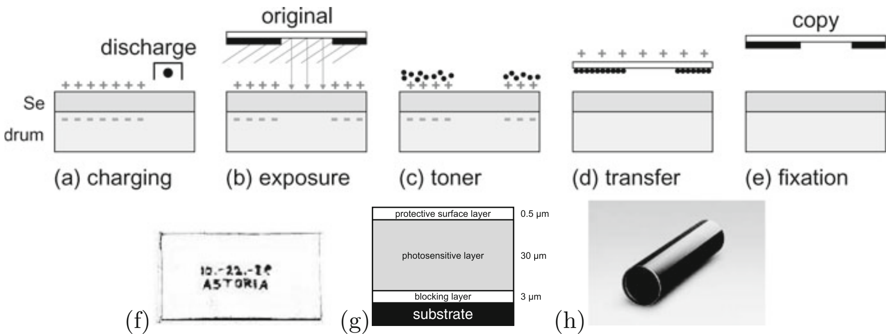

Fig. 21.5. Principle of xerography: (**a**) charging of the selenium-covered drum, (**b**) (reflection) exposure of the Se, exposed areas become uncharged, (**c**) toner addition, (**d**) toner transfer to paper for copy, and (**e**) fixation of the toner on the copy and preparation of drum for the next cycle. (**f**) First xerox copy (Oct. 22nd 1938). (**g**) Schematic cross section of coating of photosensitive drum. The indicated thicknesses are approximate. (**h**) Image of drum with photosensitive layer made from amorphous silicon. Part (**h**) from [1210]

can be oppositely charged. If light hits the layer it becomes photoconductive and neutralizes locally. This requires a small lateral diffusion of charge carriers. Initially amorphous selenium ($E_g = 1.8$ eV) was used. The conductivity in the dark of a-Se is $10^{16}\,\Omega$/cm. Se was subsequently replaced by organic material. The highest performance is currently achieved with amorphous silicon.

On the charged areas of the photosensitive layer toner can be attached. The toner pattern is subsequently transferred to the copy sheet and fixated. A copy takes typically more than one rotation of the drum. The principle was invented in 1938 by Chester F. Carlson (1906–1968) with sulfur as the photoconductor.[3]

21.2.4 QWIPs

Quantum-well intersubband photodetectors (QWIPs) are based on the absorption of photons between two quantum well subbands (Fig. 21.6). A review can be found in [1211]. Quantized electron or hole states can be used. Besides an oscillator strength for this transition, the lower level must be populated and the upper level must be empty in order to allow this process. The Fermi level is typically chosen by appropriate doping such that the lower subband is populated.

For infinite barrier height the energy separation between the first and second quantized levels (in the effective-mass theory) is (cf. (11.5))

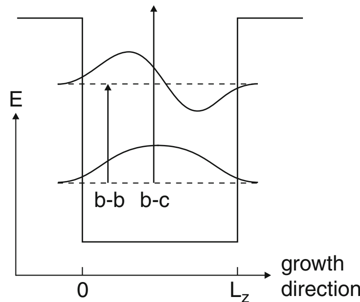

Fig. 21.6. Schematic level diagram of a quantum well. Optical intersubband transitions between the first and second quantized level (b–b) and the ground state and the continuum (b–c)

[3]In 1947 the Haloid company bought the rights to this process, renamed itself XeroX and brought the first copy machine to the market in 1958 based on amorphous selenium. The word 'xerography' stems from the Greek word $\xi\acute{\epsilon}\rho o\varsigma$ (dry). The last 'X' in XeroX was added to mimic the name of the KodaK corporation.

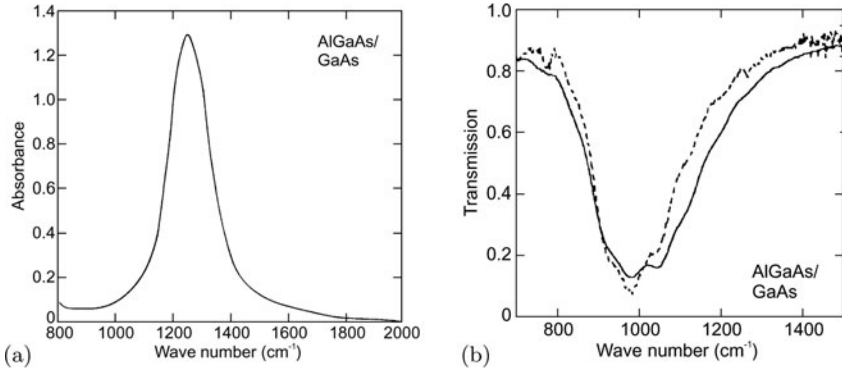

Fig. 21.7. (**a**) AlGaAs/GaAs QWIP absorption spectrum for multiple reflection geometry. Adapted from [1211]. (**b**) Transmission of AlGaAs/GaAs QWIP (100 QWs) in double reflection geometry (45° angle of incidence). The well doping is $1.0 \times 10^{12}\,\mathrm{cm}^{-2}$ (*dashed line*) and $1.5 \times 10^{12}\,\mathrm{cm}^{-2}$ (*solid line*). Adapted from [1212]

$$E_2 - E_1 = 3\,\frac{\hbar^2}{2m^*}\,\frac{\pi^2}{L_\mathrm{z}^2}\,. \tag{21.11}$$

For real materials the barrier height determines the maximum transition energy. Typical absorption and transmission spectra of a QWIP structure are shown in Fig. 21.7. The spectral response is in the mid- or far-infrared.

The dipole matrix element $\langle z \rangle = \langle \Psi_2 | z | \Psi_1 \rangle$ can be easily calculated to be

$$\langle z \rangle = \frac{16}{9\pi^2}\,L_\mathrm{z}\,. \tag{21.12}$$

The oscillator strength is about 0.96. The polarization selection rule causes the absorption to vary $\propto \cos^2\phi$, where ϕ is the angle between the electric-field vector and the z direction (Fig. 21.8). This means that for vertical incidence ($\phi = 90°$) the absorption vanishes. Thus schemes have been developed to allow for skew entry of the radiation (Fig. 21.9a). The strict selection rule can be relaxed by using asymmetric potential wells (breaking of mirror symmetry/parity), strained materials (band mixing) or quantum dots (lateral confinement). Also, a grating can be used to create a finite angle of incidence (Fig. 21.9b).

Besides a useful detectivity ($2 \times 10^{10}\,\mathrm{cm\,Hz}^{1/2}/\mathrm{W}$ at 77 K) QWIPs have the advantage, e.g. against HgCdTe interband absorbers, that the highly developed GaAs planar technology is available for the fabrication of focal plane arrays (FPA) as shown in Fig. 21.10. A FPA is an image sensor (in the focal plane of an imaging infrared optics) and is used, e.g., for the detection of heat leaks in buildings or night surveillance. In particular, night vision support in cars may become a major market. A competing technology are bolometric arrays with thermally insulated pixels based on MEMS technology.

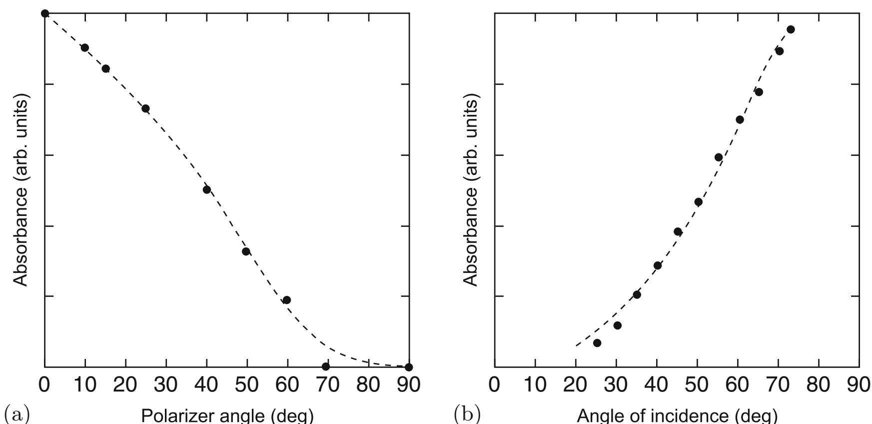

Fig. 21.8. Dependence of the QWIP response on (**a**) polarization and (**b**) angle of incidence. *Dashed lines* are guides to the eye. Adapted from [1211]

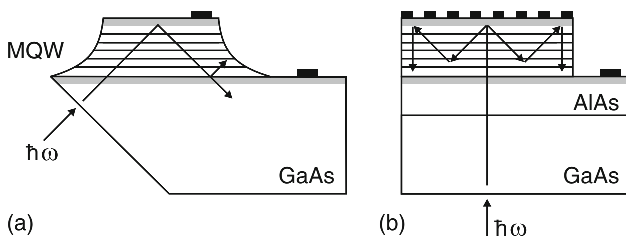

Fig. 21.9. QWIP geometries: (**a**) 45° edge coupled with multiple quantum-well (MQW) absorber and (**b**) grating coupled with GaAs substrate, AlAs reflector and metal grating on top. *Grey areas* are highly n-doped contact layers

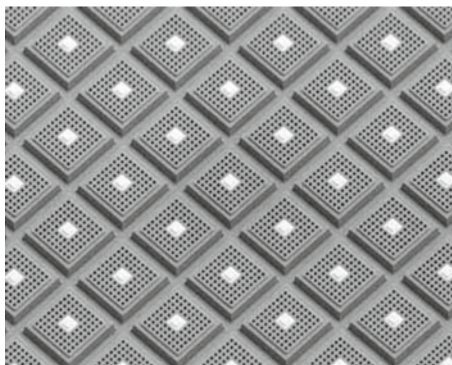

Fig. 21.10. Part of a 256×256 QWIP focal plane array (FPA) with grating coupler (area of one pixel: $37\,\mu\mathrm{m}^2$). From [1213]

The carriers that have been optically excited into the upper state leave the QW by tunneling or thermionic emission. Also, a QWIP can be made based on the direct transfer from the (populated) subband into the continuum.

The incoming infrared radiation creates a photocurrent density of

$$i_{\mathrm{ph}} = e\,\eta_{\mathrm{w}}\,\Phi\;, \tag{21.13}$$

where η_{w} is the quantum efficiency of a single quantum well (including the escape rate) and Φ is the photon flux per time and unit area. During the transport of the charge carriers through the barrier they can be (re-)captured by the QW with the probability p_{c}. The capture probability decreases exponentially with the applied bias. The total photocurrent (including generation and recapture) is

$$I_{\mathrm{ph}} = (1-p_{\mathrm{c}})I_{\mathrm{ph}} + i_{\mathrm{ph}} = \frac{i_{\mathrm{ph}}}{p_{\mathrm{c}}}\;. \tag{21.14}$$

If the quantum efficiency is small, the efficiency of N_{w} quantum wells $\eta \approx N_{\mathrm{w}} \times \eta_{\mathrm{w}}$. With this approximation the total photocurrent of N_{w} quantum wells is given by

$$I_{\mathrm{ph}} = e\,\eta\,\Phi\,g\;, \tag{21.15}$$

where g is termed the gain of the structure and is given by

$$g = \frac{1}{p_{\mathrm{c}}}\,\frac{\eta_{\mathrm{w}}}{\eta} \approx \frac{1}{N_{\mathrm{w}}\,p_{\mathrm{c}}}\;. \tag{21.16}$$

The dark current can be calculated from thermionic emission and agrees fairly well with experiment (Fig. 21.11a). When the voltage is increased further, avalanche multiplication can occur while the carriers are transported

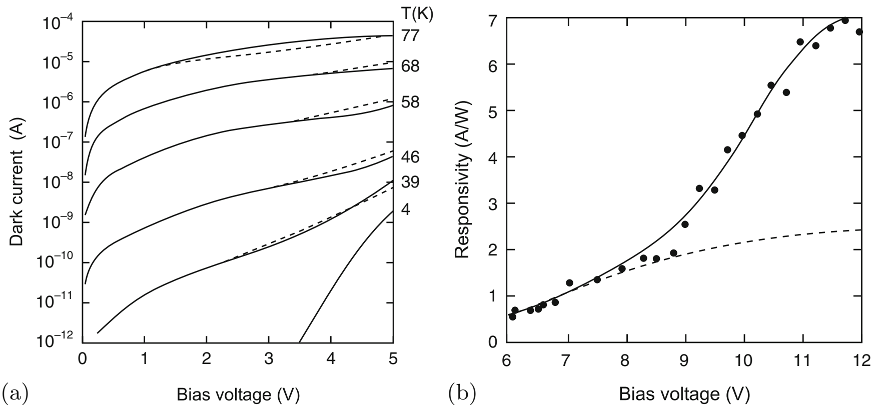

Fig. 21.11. (**a**) Dark current of a QWIP at 10.7 µm, experimental (*solid lines*) and theoretical (*dashed lines*) response. (**b**) QWIP responsivity as a function of the applied voltage. The *solid line* (*dashed line*) is the theoretical dependence with (without) the effect of avalanche multiplication. Adapted from [1211]

through the barrier(s). This mechanism provides further gain as shown in Fig. 21.11b.

21.2.5 Blocked Impurity-Band Detectors

Impurity absorption allows photoconductivity detectors in the mid- and far-infrared regions to be made. In particular, for THz spectroscopy in medicine and astronomy the extension to longer wavelengths is interesting. For conventional photoconductors the impurity concentration is well below the critical dopant concentration (cf. Sect 7.5.6). Long-wavelength response can be achieved by going to impurity/host systems with smaller ionization energy, such as Si:B (45 meV) → Ge:As (12.7 meV) → GaAs:Te (5.7 meV). By applying stress to Ge the energy separation between impurity and conduction bands can be lowered and subsequently the detector response is shifted towards longer wavelengths.

For high doping the impurity level broadens to an impurity band and thus allows smaller ionization energy and thus stronger long-wavelength detector response. However, conduction in the impurity band leads to dark current and makes such detectors unfeasible. In a blocked impurity band (BIB) detector [1214, 1215] an additional intrinsic blocking layer is sandwiched between the absorption layer and the contact (Fig. 21.12a). Such a structure is

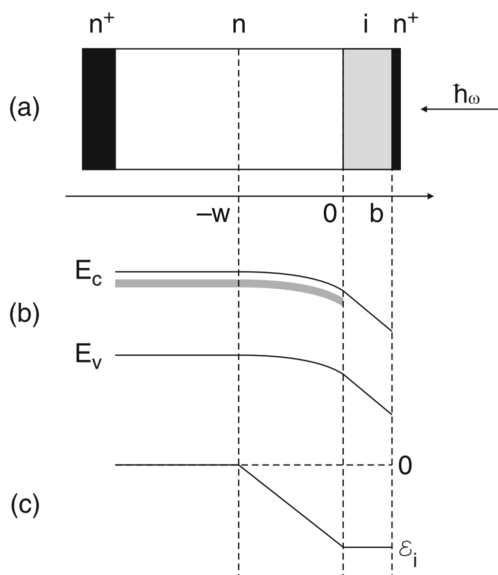

Fig. 21.12. (**a**) Structure of BIB photodetectors. Highly doped contact layers (*black*), doped semiconductor (*white*) and blocking (intrinsic) layer (*grey*). (**b**) Band diagram under small forward bias. *Shaded area* represents the donor impurity band. (**c**) Electric field in the structure

similar to a MIS diode, the insulator being the intrinsic semiconductor. We assume in the following an n-type semiconductor, such as Si:As or GaAs:Te, but also p-type BIBs can be made, e.g., from Ge:Ga.

The semiconductor is highly doped (N_{D}) and partly compensated (N_{A}). Typically, the acceptor concentration must be small, about $10^{12}\,\mathrm{cm}^{-3}$, and controls the formation of the electric field as shown below. The doping is so high that the impurities form an impurity band. Some of the electrons recombine with the acceptors $N_{\mathrm{A}}^{-} = N_{\mathrm{A}}$ and leave some donors charged $N_{\mathrm{D}}^{+} = N_{\mathrm{A}}$. For GaAs, e.g., the donor concentration in the doped semiconductor is $> 10^{16}\,\mathrm{cm}^{-3}$ and $\sim 10^{13}\,\mathrm{cm}^{-3}$ in the i-layer.

Under an external forward bias V, i.e. the positive pole is at the insulator, part of the applied voltage drops over the blocking layer of thickness b. If ideally no charges are present here, the electric field is constant. In the n-doped material electrons move in the impurity band towards the insulator, forming neutral donors in an electron accumulation layer of thickness w in the presence of the charged acceptors N_{A}^{-}. This layer is the absorption layer. The mechanism can also be considered as if positive charge (the charged donors, N_{D}^{+}) moves (via hopping conduction) towards the back contact. In the literature the layer close to the insulator is thus also termed a 'depletion layer'. The band diagram and the electric field are shown in Fig. 21.12b,c. Due to the blocking layer the carriers on the donors in the n-type material cannot spill via the impurity band into the contact but must be lifted (by photoabsorption) into the conduction band.

From the Poisson equation the electric field is given by

$$\mathcal{E}(x) = -\frac{e}{\epsilon_{\mathrm{s}}} N_{\mathrm{A}}\,(w + x)\,,\ -w \le x \le 0 \tag{21.17a}$$

$$\mathcal{E}(x) = -\frac{e}{\epsilon_{\mathrm{s}}} N_{\mathrm{A}} w = \mathcal{E}_{\mathrm{i}},\ 0 \le x \le b\,. \tag{21.17b}$$

The voltage drops across the blocking layer V_{b} and the doped semiconductor V_{s} fulfill

$$V = V_{\mathrm{b}} + V_{\mathrm{s}}\,. \tag{21.18}$$

Integration of the fields yields

$$V_{\mathrm{s}} = \frac{e}{\epsilon_{\mathrm{s}}}\, N_{\mathrm{A}}\, \frac{w^2}{2} \tag{21.19a}$$

$$V_{\mathrm{b}} = \frac{e}{\epsilon_{\mathrm{s}}}\, N_{\mathrm{A}} w b\,. \tag{21.19b}$$

Substituting (21.19a,b) into (21.18) results in the width of the 'depletion layer'

$$w = \sqrt{\frac{2\epsilon_{\mathrm{s}} V}{e N_{\mathrm{A}}} + b^2} - b\,. \tag{21.20}$$

The high dopant concentration allows for much thinner absorption layers than in a conventional photoconductivity detector, making it less susceptible

to background high-energy cosmic radiation. The recombination in the depletion layer is negligible. Detector performance is modeled in [1216].

21.3 Photodiodes

21.3.1 Introduction

The principle of the photodiode is the interband absorption of light in the depletion layer of a diode (or the i-zone of a pin-diode) and the subsequent separation of electrons and holes by the electric field. There are opposite requirements for fast detectors (thin depletion layer) and efficient detectors

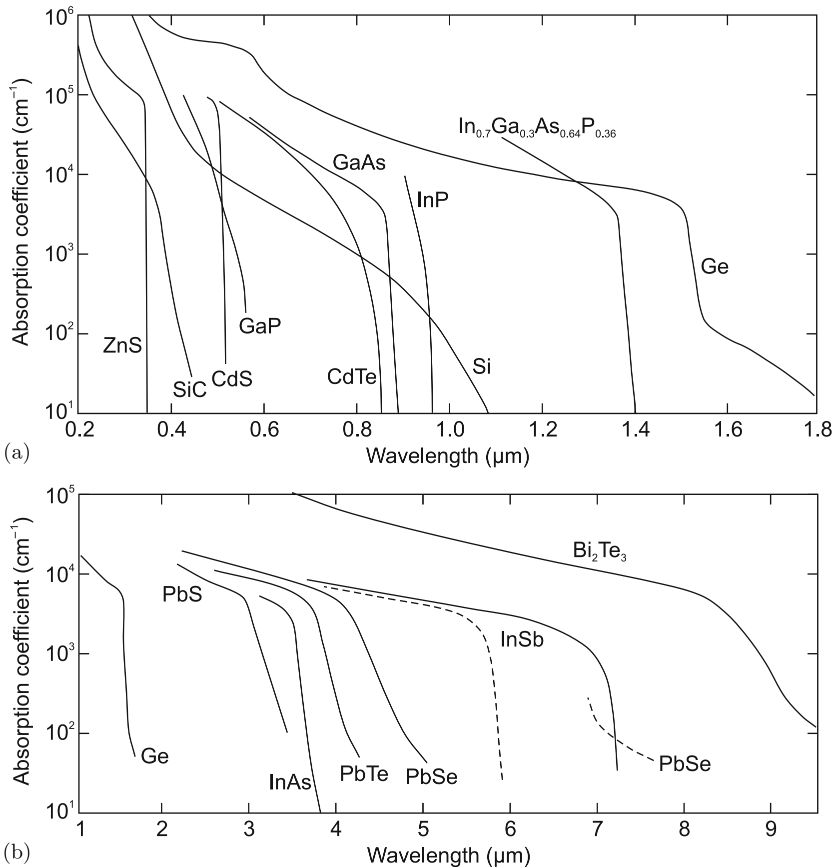

Fig. 21.13. Optical absorption coefficient of various semiconductor materials (as labeled) used for photodetectors (**a**) in the UV, visible and near-infrared range (at room temperature) and (**b**) in the mid-infrared spectral range at room temperature (*solid lines*) and at 77 K (*dashed lines*). Based on [1217]

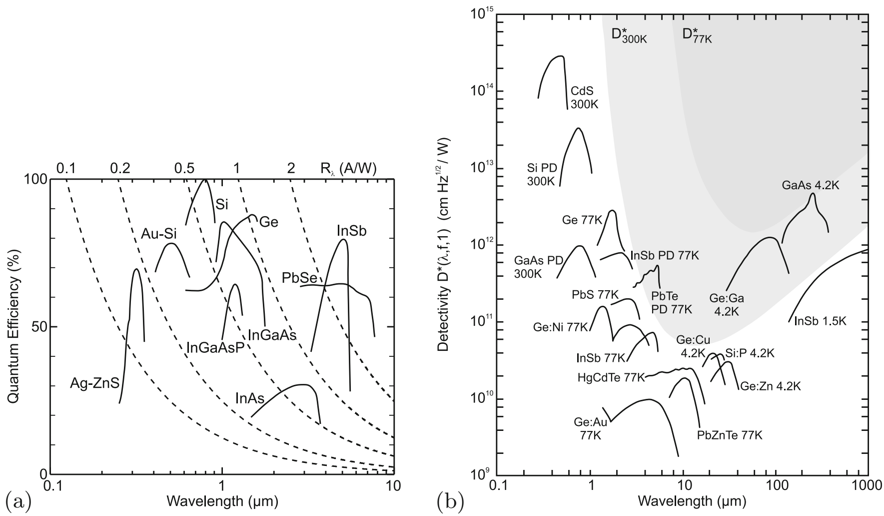

Fig. 21.14. (**a**) Quantum efficiency of various photodetectors. The *dashed lines* depict lines of equal responsivity (R_λ in A/W) as labeled on top of the panel. (**b**) Detectivity D^* of various photoconductors and photodiodes (PD). The *lighter* (*darker*) *shaded area* indicates the range unachievable at 300 K (77 K) due to background radiation. Adapted from [383]

(complete light absorption, sufficiently thick depletion layer). For this reason generally semiconductors with high absorption coefficient are most suited (Fig. 21.13). In Fig. 21.14 the quantum efficiency and detectivity D^* of various semiconductor detectors are compared.

A diode can be operated without bias (photovoltaic mode) using the built-in field. An improvement in the speed of a pn-diode is achieved with a reverse bias since it increases the field strength in the depletion layer. However, the reverse bias is below the breakdown voltage. Operation near breakdown is exploited in the avalanche photodiode (APD). In the following we will discuss pn-, pin-, MS- (Schottky-), MSM- and heterostructure-diodes and APDs.

21.3.2 pn Photodiodes

The most important figures of merit are the quantum efficiency, responsivity, noise equivalent power (NEP) and the response speed.

If the depletion layer is hit by a photon flux with a generation rate G_0 (i.e. electron–hole pairs per unit volume per unit time) the photogenerated current is added to the diffusion current. The photocurrent density j_p (per unit area) is

$$j_\mathrm{p} = -e\,G_0\,L_\mathrm{p} \tag{21.21}$$

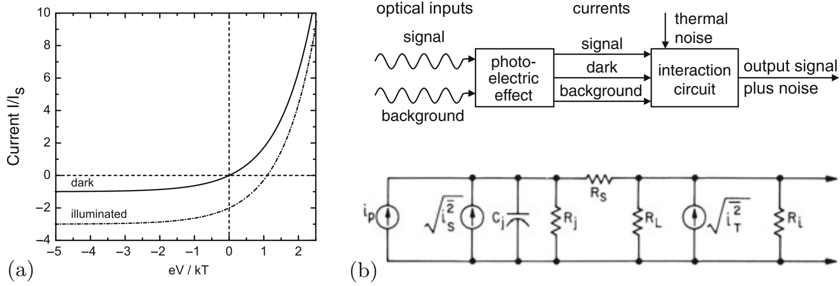

Fig. 21.15. (**a**) Schematic dark and illuminated I–V-characteristics of a photodiode (for the case $j_\mathrm{p} = -2j_\mathrm{s}$). (**b**) Schematic representation of currents in a photodiode and equivalent circuit. Part (**b**) adapted from [1218]

for a p$^+$n-diode. In order to obtain this result the diffusion and continuity equations have to be solved for the depletion region[4]. Equation (21.21) means that the dark I–V characteristic is shifted by j_p as shown in Fig. 21.15a. The number of electron–hole pairs that are generated per photon of energy $h\nu$ by the absorption of the (monochromatic) light power P_opt is

$$\eta = \frac{I_\mathrm{ph}/e}{P_\mathrm{opt}/(h\nu)} , \tag{21.22}$$

where $I_\mathrm{ph} = Aj_\mathrm{ph}$ is the photogenerated current over the surface A. The *responsivity* R_λ of the photodiode (for monochromatic radiation) is defined as

$$R_\lambda = \frac{I_\mathrm{ph}}{P_\mathrm{opt}} = \frac{e}{h\nu}\,\eta \approx \frac{\lambda}{1.24\,\mu\mathrm{m}}\,\eta . \tag{21.23}$$

For a modulated light intensity P_opt must be replaced by $mP_\mathrm{opt}/\sqrt{2}$. The equivalent circuit including noise sources for a photodiode is shown in Fig. 21.15b.

Random processes lead to shot noise $\langle i_\mathrm{S}^2 \rangle$. Besides the photocurrent I_ph itself, the background radiation (I_B, in particular for infrared detectors) and the thermal generation (dark current, I_D) of carriers contribute:

$$\langle i_\mathrm{S}^2 \rangle = 2e\,(I_\mathrm{ph} + I_\mathrm{B} + I_\mathrm{D})\,B , \tag{21.24}$$

with B being the bandwidth. Additionally, the parallel resistances cause thermal noise

$$\langle i_\mathrm{T}^2 \rangle = 4\,kT\,B/R_\mathrm{eq} . \tag{21.25}$$

The resistance R_eq is given by the resistance of the depletion layer (junction) R_j, the load R_L and the input of the amplifier R_i as $R_\mathrm{eq}^{-1} = R_\mathrm{j}^{-1} + R_\mathrm{L}^{-1} + R_\mathrm{i}^{-1}$. The series resistance R_s of the photodiode can be usually ignored in this context.

[4]This derivation is done in Sect. 21.3.3. Equation (21.21) is obtained from (21.32) for vanishing thickness w and $\alpha L_\mathrm{p} \ll 1$.

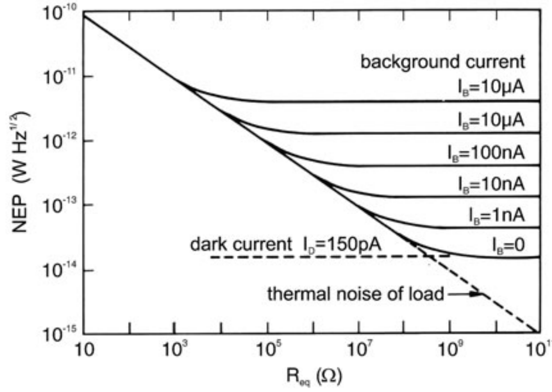

Fig. 21.16. NEP as a function of the resistance R_{eq} for a Si photodiode. From [1218]

For a fully modulated signal the signal-to-noise ratio of the photodiode is given by

$$S/N = \frac{i_{\mathrm{ph}}^2}{\langle i_{\mathrm{S}}^2 \rangle^2 + \langle i_{\mathrm{T}}^2 \rangle^2} = \frac{\left(e\eta P_{\mathrm{opt}}/h\nu\right)^2/2}{2e\left(I_{\mathrm{ph}} + I_{\mathrm{B}} + I_{\mathrm{D}}\right)B + 4kTB/R_{\mathrm{eq}}} \,. \tag{21.26}$$

Therefore the NEP is given by

$$\mathrm{NEP} = \frac{2h\nu B}{\eta}\left[1 + \sqrt{1 + \frac{I_{\mathrm{eq}}}{eB}}\right] \,. \tag{21.27}$$

The current I_{eq} is given by $I_{\mathrm{eq}} = I_{\mathrm{B}} + I_{\mathrm{D}} + 2kT/(eR_{\mathrm{eq}})$. If $I_{\mathrm{eq}}/eB \ll 1$, the NEP is determined by the shot noise of the signal itself. In the other limit $I_{\mathrm{eq}}/eB \gg 1$ the detection is limited by the background radiation or thermal noise. In this case, the NEP is (for $B = 1\,\mathrm{Hz}$, in $\mathrm{W\,cm^2\,Hz^{1/2}}$)

$$\mathrm{NEP} = \sqrt{2}\,\frac{h\nu}{\eta}\sqrt{\frac{I_{\mathrm{eq}}}{e}} \,. \tag{21.28}$$

In Fig. 21.16 the situation is shown for a silicon photodiode as a function of R_{eq}. The diode has a quantum efficiency of 75% at $\lambda = 0.77\,\mu\mathrm{m}$. A high value of $R_{\mathrm{eq}} \sim 1\,\mathrm{G}\Omega$ is necessary to ensure detection limited by dark current.

21.3.3 pin Photodiodes

The depletion layer in pn-diodes is relatively thin such that the incident light is not completely absorbed. An almost complete absorption of light can be achieved by using a thick intrinsic absorption layer. The field in the intrinsic region is constant or slowly varying linearly (Fig. 20.65). The generation rate per unit area decreases exponentially following the Lambert–Beer law (9.8) as shown in Fig. 21.17c:

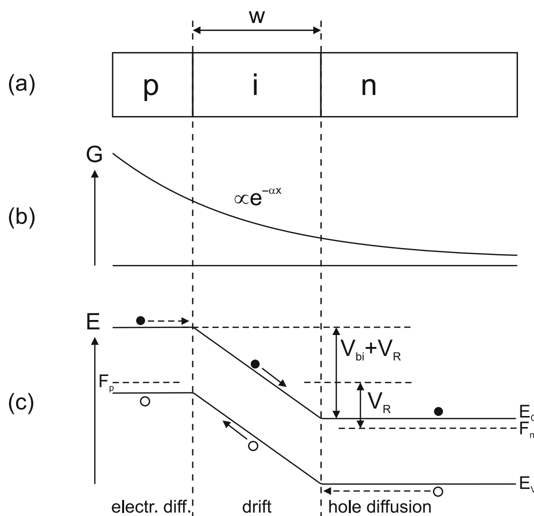

Fig. 21.17. (**a**) Schematic cross section of pin-diode, (**b**) profile of carrier generation due to light absorption and (**c**) schematic band structure under reverse bias. The generation of three electron-hole pairs is shown; subsequent drift (diffusive) transport is indicated with *solid* (*dashed*) *arrows*

$$G(x) = G_0 \exp(-\alpha x) . \qquad (21.29)$$

The initial generation rate $G_0 = \Phi_0 \alpha$ is given by the incident photon flux per unit area Φ_0 and the reflectance of the surface R as $\Phi_0 = P_{\mathrm{opt}}(1-R)/(Ah\nu)$.

The drift current in the i-region collects all those carriers (if recombination in the depletion layer is neglected). The electron drift current is given by

$$j_{\mathrm{dr}} = -e \int_0^w G(x)\,\mathrm{d}x = e\,\Phi_0\,[1 - \exp(-\alpha w)] \;, \qquad (21.30)$$

with w being the thickness of the depletion layer that is approximately the same as the thickness of the i-region. In the bulk (neutral) region ($x > w$) the minority-carrier density is determined by drift and diffusion[5] (10.75). The diffusion current density at $x = w$ is thus given by

$$j_{\mathrm{diff}} = e\,\Phi_0 \exp(-\alpha w)\,\frac{\alpha L_{\mathrm{p}}}{1 + \alpha L_{\mathrm{p}}} + e\,p_{\mathrm{n}_0}\,\frac{D_{\mathrm{p}}}{L_{\mathrm{p}}} \;. \qquad (21.31)$$

The first term is due to the diffusion current of photo-generated carriers (10.75), the second term due to thermally generated carriers (20.114). The total current $j_{\mathrm{tot}} = j_{\mathrm{diff}} + j_{\mathrm{dr}}$ is given by

[5] At the edge of the depletion layer, $x = w$, all photo-generated carriers are transported away instantly, thus the excess carrier density from photo-generated carriers is zero there and (10.75) applies.

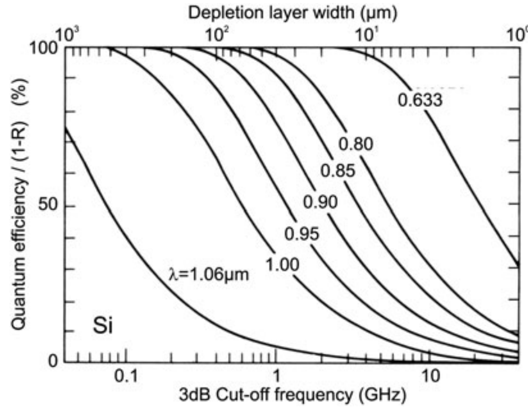

Fig. 21.18. Quantum efficiency and 3 dB cutoff frequency of a Si pin-diode at $T = 300$ K for various wavelengths of input radiation. Adapted from [1218]

$$j_{\mathrm{tot}} = e\,\Phi_0 \left[1 - \frac{\exp(-\alpha w)}{1+\alpha L_{\mathrm{p}}}\right] + e\,p_{\mathrm{n_0}}\,\frac{D_{\mathrm{p}}}{L_{\mathrm{p}}}\ . \tag{21.32}$$

The first term is due to the photocurrent, the second term is due to the diffusion current known from the p^+n-diode. In normal operation, the second can be neglected compared to the first. The quantum efficiency is

$$\eta = \frac{j_{\mathrm{tot}}/e}{P_{\mathrm{opt}}/h\nu} = (1-R)\left[1 - \frac{\exp(-\alpha w)}{1+\alpha L_{\mathrm{p}}}\right]\ . \tag{21.33}$$

For a high quantum efficiency, of course low reflectance and high absorption coefficient, i.e. $\alpha w \gg 1$, are necessary.

However, for $w \gg 1/\alpha$ the transit time through the depletion layer $t_{\mathrm{r}} \approx w/v_{\mathrm{s}}$ (at sufficiently high field, v_{s} being the drift-saturation velocity) increases too much. The 3 dB cutoff frequency $f_{3\,\mathrm{dB}}$ (Fig. 21.18) is

$$f_{3\,\mathrm{dB}} \cong \frac{2.4}{2\pi t_{\mathrm{r}}} \cong \frac{0.4\,v_{\mathrm{s}}}{w}\ . \tag{21.34}$$

Therefore a tradeoff exists between the quantum efficiency and the response speed of the pin-photodiode (Fig. 21.18). Choosing $w \cong 1/\alpha$ is a good compromise.

21.3.4 Position-Sensing Detector

In a position-sensing detector (PSD) two electrodes are placed at opposite edges of a photodetector. The current output depends linearly on the beam position in between the electrodes, similar to a voltage divider. If two pairs of

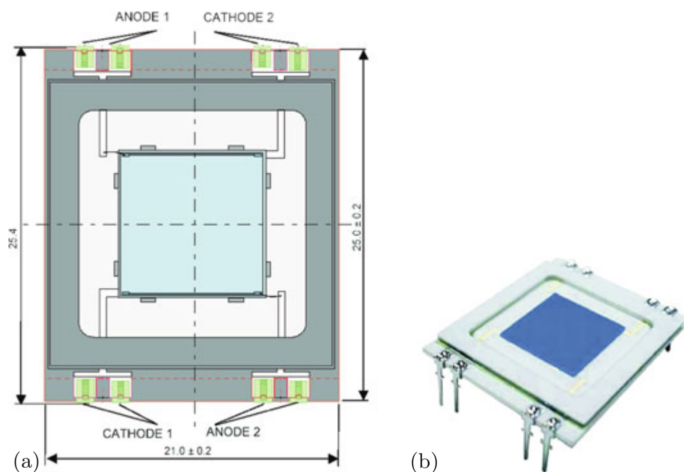

Fig. 21.19. (**a**) Scheme of two-dimensional position-sensing detector (PSD), (**b**) image of PSD. From [1219]

electrodes, one on the front and one on the back of the detector, are fabricated in orthogonal directions (Fig. 21.19a), the beam position can be measured in both x and y directions.

21.3.5 MSM Photodiodes

A MSM photodiode consists of a piece of semiconductor between two Schottky contacts (MS contacts). These are typically arranged laterally (as shown in Fig. 21.24b) but will first be considered at the front and back of the semiconductor [1220]. The band structure in thermodynamic equilibrium is shown in Fig. 21.20.

In the general case two different metals with two different barriers ϕ_{n1}, ϕ_{n2} and built-in voltage V_{D1}, V_{D2} are considered. If a voltage is applied across the MSM diode, one of the junctions is biased in the forward, the other in the reverse direction. We assume in Fig. 21.21 that the voltage biases the first contact in the reverse direction, i.e. the '+' pole is on the left contact. The applied voltage V is split between the two contacts, the larger voltage will drop at the reverse-biased contact (here: $V_1 > V_2$)

$$V = V_1 + V_2 \; . \tag{21.35}$$

The electron current arises from thermionic emission at contact 2. Due to current continuity (without recombination since we inject majority charge carriers) this is also the current through contact 1, i.e.

$$j_{n1} = j_{n2} \; . \tag{21.36}$$

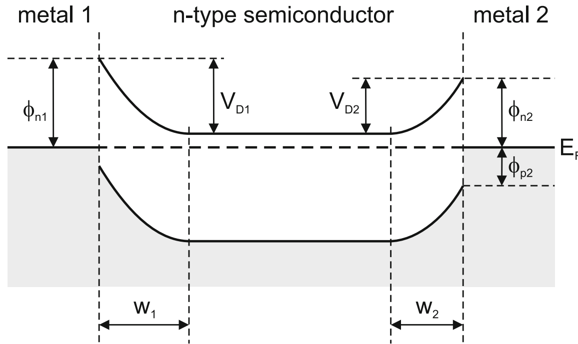

Fig. 21.20. Band diagram of a MSM structure with an n-type semiconductor in thermal equilibrium. In the general case, two different metals cause two different Schottky barrier heights and related depletion layer widths. Adapted from [1220]

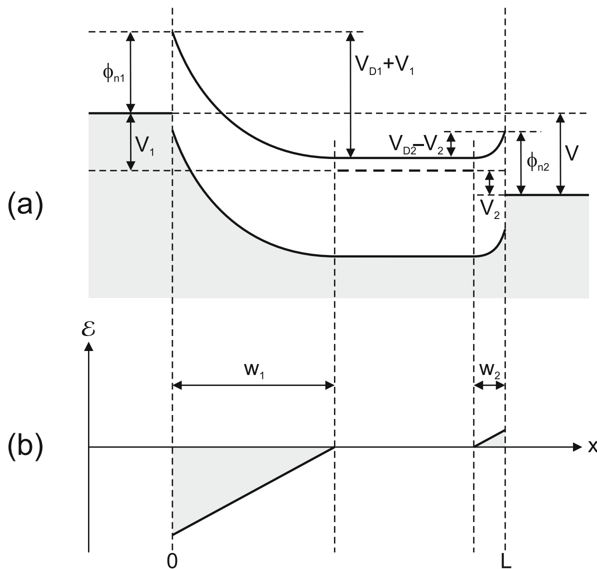

Fig. 21.21. (**a**) Band diagram for a MSM structure under bias ($V < V_{\mathrm{RT}}$), (**b**) electric field distribution. Adapted from [1220]

The reverse current at contact 1 is

$$j_{\mathrm{n1}} = A_{\mathrm{n}}^* T^2 \exp\left(-\beta \phi_{\mathrm{n1}}\right) \exp\left(\beta \Delta\phi_{\mathrm{n1}}\right) \left[1 - \exp\left(-\beta V_1\right)\right] \ , \tag{21.37}$$

where $\Delta\phi_{\mathrm{n1}}$ is the barrier reduction due to the Schottky effect (Sect. 20.2.3 and (20.21)). The forward current at contact 2 is

$$j_{\mathrm{n2}} = -A_{\mathrm{n}}^* T^2 \exp\left(-\beta \phi_{\mathrm{n2}}\right) \exp\left(\beta \Delta\phi_{\mathrm{n2}}\right) \left[1 - \exp\left(\beta V_2\right)\right] \ . \tag{21.38}$$

For a symmetric structure, i.e. $\phi_{n1} = \phi_{n2}$ and $V_{D1} = V_{D2} = V_D$, (21.36)–(21.38) yield together with (20.21)

$$\left(\frac{e^3 N_D}{8\pi^2 \epsilon_s^3}\right)^{1/4} \left[(V_D + V_1)^{1/4} - (V_D - V_2)^{1/4}\right] = \frac{1}{\beta} \ln \left[\frac{\exp(\beta V_2) - 1}{1 - \exp(-\beta V_1)}\right] . \tag{21.39}$$

Together with (21.35) a numerical or graphical solution can be found. Initially (for small voltages) the injected hole current (from contact 2) is much smaller than the electron current and diffusion occurs in the neutral region.

The reach-through voltage V_{RT} is reached when the width of the neutral region is reduced to zero (Fig. 21.22a). At the juncture of the two depletion regions inside the semiconductor material the electric field is zero and changes sign. For a larger voltage V_{FB} flat-band conditions are present at contact 2, i.e. the electric field is zero at contact 2 (Fig. 21.22b). At even larger voltage V_B breakdown occurs.

At $V = V_{RT}$ we have

$$w_1 = \left[\frac{2\epsilon_s}{eN_D}(V_1 + V_{D1})\right]^{1/2} \tag{21.40a}$$

$$w_2 = \left[\frac{2\epsilon_s}{eN_D}(V_{D2} - V_2)\right]^{1/2} \tag{21.40b}$$

$$L = w_1 + w_2 , \tag{21.40c}$$

and therefore (with (21.35))

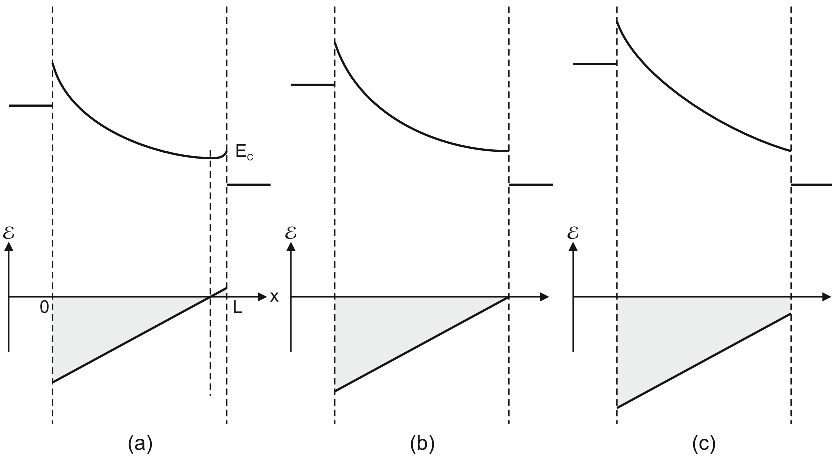

Fig. 21.22. Band diagram (*upper parts*) and electric field distribution (*lower parts*) in a MSM diode for various bias conditions: (**a**) at reach-through voltage V_{RT}, (**b**) at flat-band voltage V_{FB} and (**c**) for $V > V_{FB}$. Adapted from [1220]

$$V_{\mathrm{RT}} = \frac{eN_{\mathrm{D}}}{2\epsilon_{\mathrm{s}}} L^2 - L \left[\frac{2eN_{\mathrm{D}}}{\epsilon_{\mathrm{s}}} \left(V_{\mathrm{D2}} - V_2 \right) \right] - \Delta V_{\mathrm{D}} \;, \tag{21.41}$$

with $\Delta V_{\mathrm{D}} = (V_{\mathrm{D1}} - V_{\mathrm{D2}})$, vanishing for a symmetric MSM structure. At and after reach-through the electric field varies linearly from 0 to L within the semiconductor. The point of zero electric field shifts towards contact 2. At the flat-band voltage this point has reached the contact 2 and the width of the depletion layer at contact 2 is zero. This condition leads (as long as no breakdown occurred) to

$$V_{\mathrm{FB}} = \frac{eN_{\mathrm{D}}}{2\epsilon_{\mathrm{s}}} L^2 - \Delta V_{\mathrm{D}} \;. \tag{21.42}$$

The maximum electric field is at contact 1 and is given (for $V > V_{\mathrm{FB}}$) by

$$\mathcal{E}_{\mathrm{m1}} = \frac{V + V_{\mathrm{FB}} + 2\Delta V_{\mathrm{D}}}{L} \;. \tag{21.43}$$

If in a part of the structure the critical field $\mathcal{E}_{\mathrm{B}}$ for impact ionization is reached (this will be at contact 1, since the field is highest there), the diode breaks down. Therefore the breakdown voltage is given by

$$V_{\mathrm{B}} \approx \mathcal{E}_{\mathrm{B}} L - V_{\mathrm{FB}} - 2\Delta V_{\mathrm{D}} \;. \tag{21.44}$$

The current–voltage characteristic for a Si-MSM structure is shown in Fig. 21.23. At small voltages only small currents flow since one contact is in reverse bias. The hole current is much smaller than the electron current. Only those holes that diffuse through the neutral region contribute to the hole current. After reach-through the barrier $\phi_{\mathrm{p2}} + V_{\mathrm{D2}} - V_2$ for hole injection is strongly reduced that leads to strong hole injection. Beyond the flat-band voltage the hole current increases only weakly since a lowering of the barrier occurs only via the Schottky effect. For high fields ($V > V_{\mathrm{FB}}$, before breakdown) the hole current is

$$j_{\mathrm{p1}} = A_{\mathrm{p}}^* T^2 \exp\left(-\beta\phi_{\mathrm{p2}}\right) \exp\left(\beta\Delta\phi_{\mathrm{p2}}\right) = j_{\mathrm{p,s}} \exp\left(\beta\Delta\phi_{\mathrm{p2}}\right) \;, \tag{21.45}$$

and the total current is

$$j = j_{\mathrm{n,s}} \exp\left(\beta\Delta\phi_{\mathrm{n1}}\right) + j_{\mathrm{p,s}} \exp\left(\beta\Delta\phi_{\mathrm{p2}}\right) \;, \tag{21.46}$$

with $j_{\mathrm{n,s}} = A_{\mathrm{n}}^* T^2 \exp\left(-\beta\phi_{\mathrm{n1}}\right)$ and $j_{\mathrm{p,s}} = A_{\mathrm{p}}^* T^2 \exp\left(-\beta\phi_{\mathrm{p2}}\right)$.

In a MSM photodetector the metal contacts are typically formed in an interdigitated structure on the semiconductor surface (Fig. 21.24). These contacts shield some of the active area from photons. An increase in quantum efficiency can be achieved with transparent contacts (e.g. ZnO or ITO) and an antireflection (AR) coating.

The dark current is given by (21.46) and is minimal when electron and hole saturation currents are identical. This conditions leads to the optimal barrier height

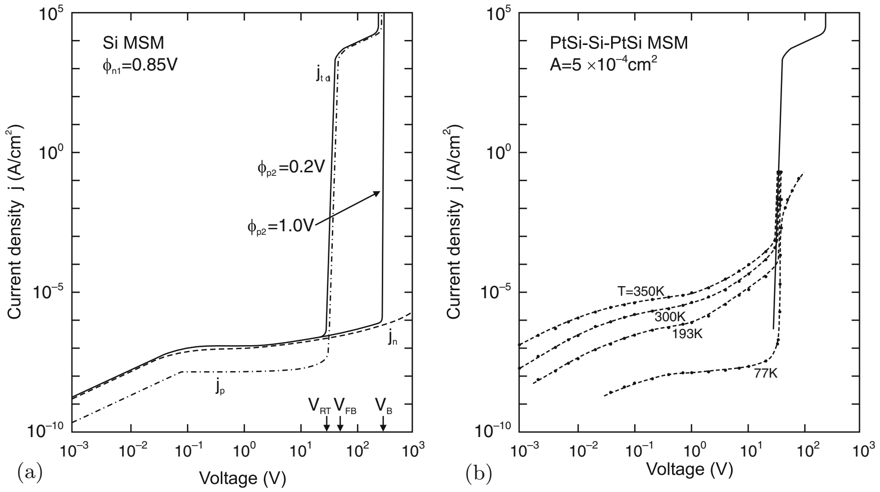

Fig. 21.23. Current–voltage characteristics of a Si MSM structure, $N_{\mathrm{D}} = 4 \times 10^{14}\,\mathrm{cm}^{-3}$, $L = 12\,\mu\mathrm{m}$ (thin, polished, ⟨111⟩-oriented wafer), $T = 300\,\mathrm{K}$. (**a**) Theory for two different values of ϕ_{p_2}, (**b**) experiment (for $\phi_{\mathrm{p}_2} = 0.2\,\mathrm{V}$). Adapted from [1220]

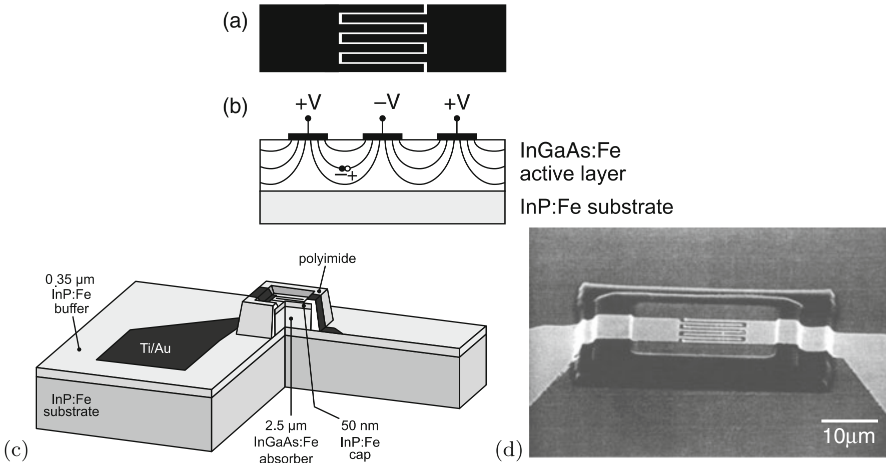

Fig. 21.24. Scheme of MSM photodetector with interdigital contacts in (**a**) plan view and (**b**) cross section. In part (**b**), the electric field lines are shown schematically together with an electron–hole pair ready to be separated. (**c**) Scheme of a MSM mesa structure, (**d**) SEM image of an InGaAs/InP MSM mesa photodetector. Parts (**c**) and (**d**) adapted from [1221]

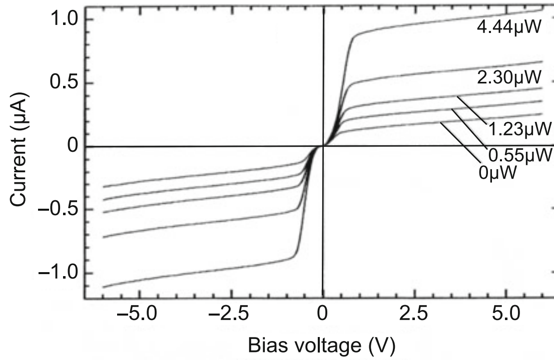

Fig. 21.25. dc I–V characteristic of an InGaAs/InP MSM photodetector (InP:Fe/InGaAs:Fe/InP:Fe, finger separation 1 µm, $\lambda = 1.3$ µm) under illumination for dark environment (0 µW) and various illumination levels as labeled. Adapted from [1221]

$$\phi_{\mathrm{n}} = E_{\mathrm{g}} - \phi_{\mathrm{ph}} = \frac{1}{2}\beta^{-1} \ln\left(\frac{m_{\mathrm{e}}}{m_{\mathrm{hh}}}\right) + \frac{1}{2}E_{\mathrm{g}} \tag{21.47}$$

close to middle of the band gap. For InP and optimal barrier $\phi_{\mathrm{n}} = 0.645$ eV a dark current of 0.36 pA/cm^2 is expected for a field of 10 V/µm. For deviating barrier height the current increases exponentially. The current–voltage characteristic of an InGaAs:Fe MSM photodetector is shown in Fig. 21.25 for a dark environment and various illumination levels.

The time-dependent response of a MSM photodetector depends on the drift time of the carriers, i.e. the time that a created electron and hole need to arrive at their respective contacts. In Fig. 21.26 a simulation is shown for a MSM detector. The current has two components, a fast one due to

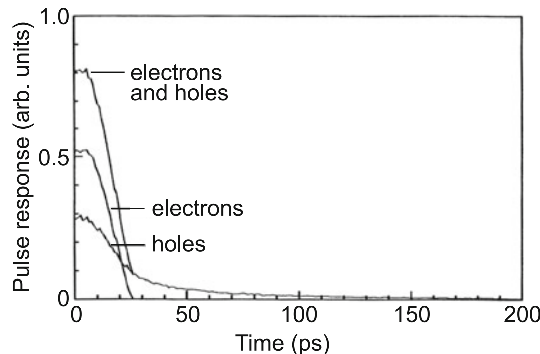

Fig. 21.26. Simulation of the time-dependent response of an InGaAs:Fe MSM photodetector to a short light pulse. Adapted from [1221]

the electrons and a slow one due to the holes that have the lower mobility and smaller drift saturation velocity. A similar dependence is found in experiment (Fig. 21.27a). For longer wavelengths the detector is slower since they penetrate deeper into the material and thus the charge carriers have a longer path to the contacts (cf. scheme in Fig. 21.24b). An important role is played by the finger separation; smaller finger separation ensures a more rapid carrier collection (Fig. 21.27b). In [1222] a bandwidth of 300 GHz was demonstrated for 100 nm/100 nm finger width and separation for LT-GaAs[6] and bulk GaAs, limited by the *RC* time constant. For 300 nm/300 nm fingers and a LT-GaAs a bandwidth of 510 GHz (pulsewidth of 0.87 ps) was reported, which is faster than the intrinsic transit time (1.1 ps) and not limited by the *RC* time constant (expected pulse width 0.52 ps), due to the recombination time (estimated to be 0.2 ps).

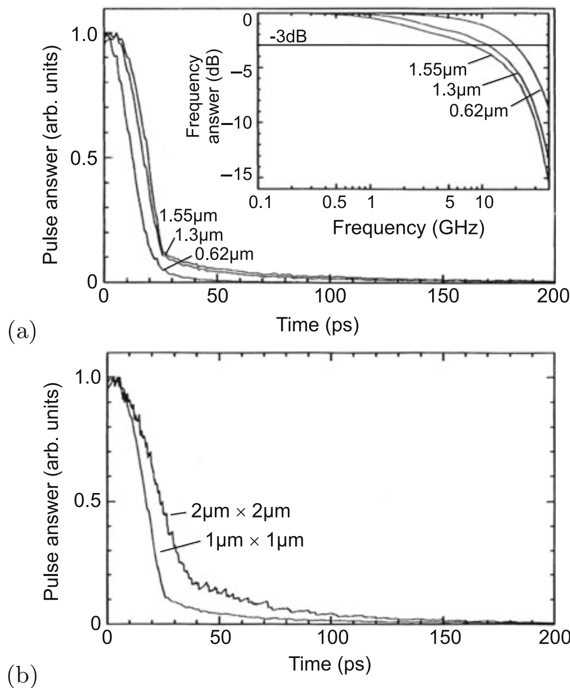

Fig. 21.27. (**a**) Experimental time-dependent response of an InGaAs:Fe MSM photodetector to a short light pulse for three different wavelengths, *inset* shows the frequency response from a Fourier transform. (**b**) Response of the MSM for two different finger widths and separations (both 1 or 2 µm, respectively), InGaAs layer thickness 2 µm, $\lambda = 1.3$ µm and bias voltage 10 V. Adapted from [1221]

[6]LT: grown at *low temperature*, i.e. containing many defects that reduce the carrier lifetime.

21.3.6 Avalanche Photodiodes

In an avalanche photodiode (APD) intrinsic amplification due to carrier multiplication (through impact ionization) in a region with high electric field is used to increase the photocurrent. The field is generated by a high reverse bias in the diode. In an ideal APD only one type of carrier is multiplied, resulting in the lowest noise. If electrons are injected into the field region at $x = 0$ (Fig. 21.28a), the multiplication factor for electrons is

$$M_{\rm n} = \exp(\alpha_{\rm n} w) \,, \tag{21.48}$$

for $\alpha_{\rm p} = 0$. Typically, both carrier types suffer multiplication. If the electron and hole impact ionization coefficients are the same ($\alpha_{\rm n} = \alpha_{\rm p} = \alpha$), the multiplication factor for electrons and holes M is given by

$$M = \frac{1}{1 - \alpha w} \,. \tag{21.49}$$

The rms value of the current noise is the same as in the case of the pn-diode (21.24), only that now the gain M is added

$$\langle i_{\rm S}^2 \rangle = 2e \left(I_{\rm ph} + I_{\rm B} + I_{\rm D} \right) \langle M^2 \rangle B \,. \tag{21.50}$$

The term $\langle M^2 \rangle$ is written as $\langle M \rangle^2 \, F(M)$ with $F(M) = \langle M^2 \rangle / \langle M \rangle^2$ being the excess noise factor that describes the additional noise introduced by the random nature of the impact ionization. For multiplication started with electron injection, it is given by

$$F(M) = kM + (1 - k) \left(2 - \frac{1}{M} \right) \,, \tag{21.51}$$

with $k = \alpha_{\rm p}/\alpha_{\rm n}$. For hole injection starting the multiplication (21.51) holds with k substituted by $k' = \alpha_{\rm n}/\alpha_{\rm p}$. In Fig. 21.29a the excess noise factor is shown vs. the average multiplication for various values of k and k'.

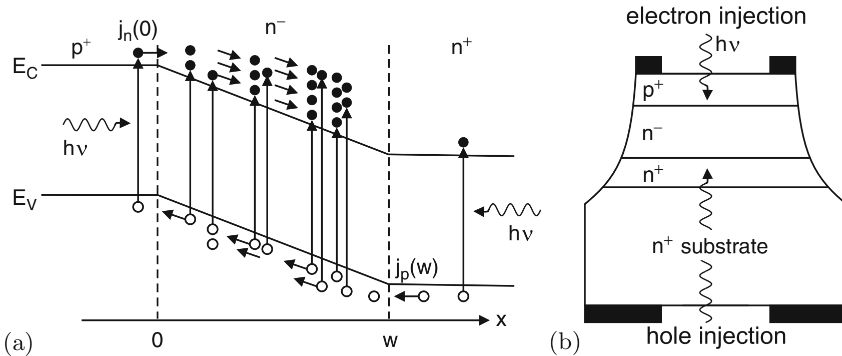

Fig. 21.28. Schematic band structure (**a**) and schematic device setup (**b**) of an avalanche photodiode (APD). From [795]

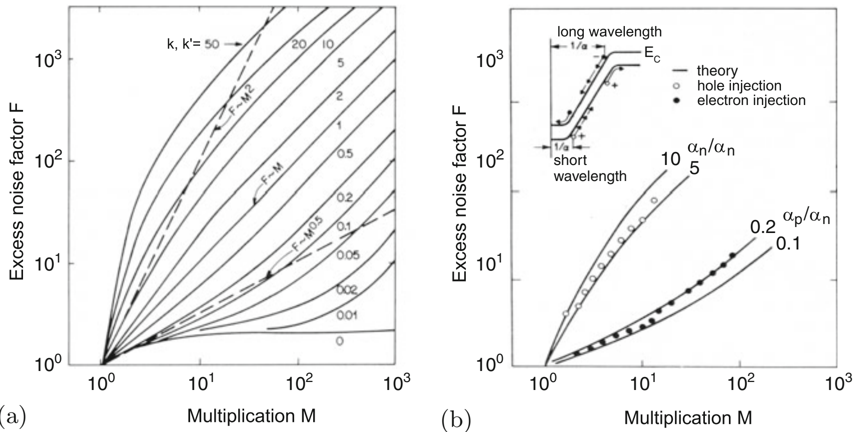

Fig. 21.29. (**a**) Excess noise factor for various values of the ratio of ionization coefficients k or k'. Adapted from [1223]. (**b**) Experimental results for F for a Si APD with 0.1 μA primary current. The *empty* (*full*) symbols are for short (long) wavelengths [primary hole (electron) current]. The *inset* shows the schematic band diagram of the np-diode under reverse bias. Adapted from [1224]

Experimental data are shown in Fig. 21.29b for a Si APD. For short wavelengths absorption is preferential at the surface (n-region) and we have the case of hole injection. The data for the excess noise factor are fairly well fit with $k' \approx 5$. For longer wavelengths, the data for electron injection are fit by $k \approx 0.2 = 1/k'$.

For a fully modulated signal the signal-to-noise ratio is given by

$$S/N = \frac{(e\eta P_{\mathrm{opt}}/h\nu)^2/2}{2e\,(I_{\mathrm{ph}} + I_{\mathrm{B}} + I_{\mathrm{D}})\,F(M)B + 4kTB/(R_{\mathrm{eq}}M^2)}\,. \tag{21.52}$$

If S/N is limited by thermal noise, the APD concept leads to a drastic improvement of noise.

A particular APD structure is known as a *solid-state multiplier*. It has separate absorption and amplification regions (SAM structure). In the low-field region the light is absorbed. One type of carrier is transported with the drift field $\mathcal{E}_{\mathrm{d}}$ to the multiplication region in which a large field $\mathcal{E}_{\mathrm{m}}$ is present and multiplication occurs. In Fig. 21.30a a homo-APD with SAM structure is shown. Regions with different electric field are created by a special doping profile.[7] A π-p-π structure leads to regions with homogeneous low and high field strengths.

In the case of a heterostructure-APD with SAM structure (Fig. 21.30b) absorption (of light with sufficiently long wavelength with an energy smaller the the InP band gap) takes place only in the InGaAs layer. Since no light is

[7]Employing Poisson's equation $\partial(\epsilon_{\mathrm{s}}(x)\mathcal{E}(x))/\partial x = \rho(x)$.

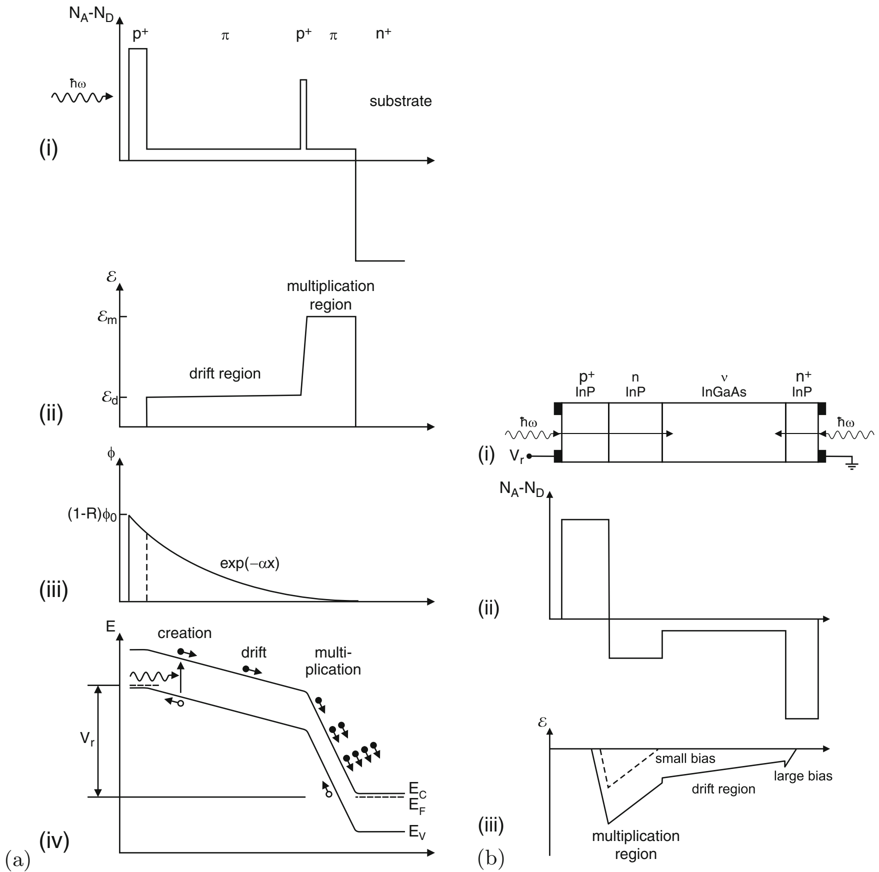

Fig. 21.30. (**a**) Homo-APD with SAM structure. (**i**) doping profile, (**ii**) electric field, (**iii**) photon flux or electron–hole pair generation rate and (**iv**) schematic band diagram under reverse voltage V_r with charge-carrier transport. The multiplication is for $\alpha_n \gg \alpha_p$. Adapted from [384]. (**b**) (**i**) Scheme of an InP/InGaAs hetero-APD with SAM structure, (**ii**) doping profile and (**iii**) electric field for small (*dashed line*) and large (*solid line*) reverse bias V_r. Adapted from [795]

absorbed in the multiplication region, the device functions similarly for front and back illumination.

21.3.7 Traveling-Wave Photodetectors

In a standard photodetector there was a tradeoff between the thickness of the absorption layer and the speed of the detector. In a traveling-wave photodetector the light absorption occurs in a waveguide such that for sufficient length L all incident light is absorbed. Complete absorption is achieved ('long' waveguide) if $L \gg (\Gamma\alpha)^{-1}$, α being the absorption coefficient and $\Gamma \leq 1$

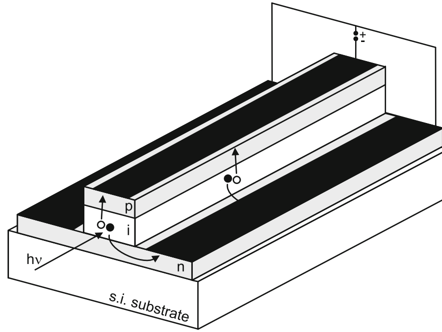

Fig. 21.31. Scheme of a traveling-wave photodetector with pin structure and coplanar contacts

being the optical confinement factor, the geometrical overlap of the optical mode with the cross section of the absorbing medium (cf. also Sect. 22.4.4).

The electrical connections are designed along this waveguide on the sides (coplanar layout, Fig. 21.31). The bandwidth limitation due to a RC time constant is now replaced by the velocity match of the light wave $v_{\mathrm{opt}} = c/n$ and the traveling electric wave in the contact lines $v_{\mathrm{el}} \approx 1/\sqrt{LC}$. While the two waves travel along the waveguide, energy is transferred from the light wave to the electric wave. The 3 dB bandwidth due to velocity mismatch B_{vm} (for impedance- matched, long waveguides) is given by

$$B_{\mathrm{vm}} = \frac{\Gamma\alpha}{2\pi} \frac{v_{\mathrm{opt}}\, v_{\mathrm{el}}}{v_{\mathrm{opt}} - v_{\mathrm{el}}} \; . \tag{21.53}$$

For a MSM structure, whose electrode separation has been designed with a self-aligned process (without extensive effort in lateral patterning) by an etch

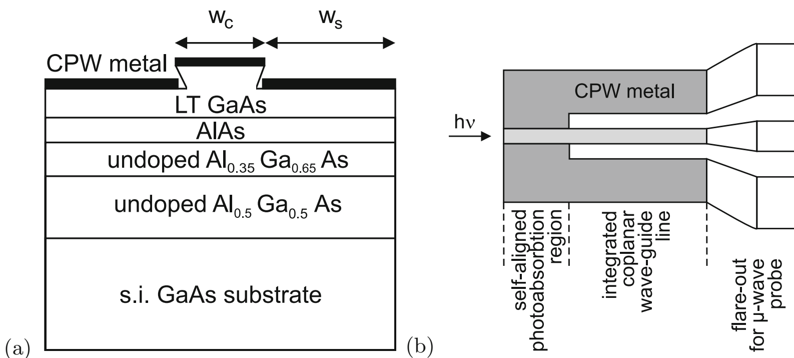

Fig. 21.32. Scheme of a MSM traveling-wave photodetector in (**a**) cross section and (**b**) plan view. Adapted from [1227]

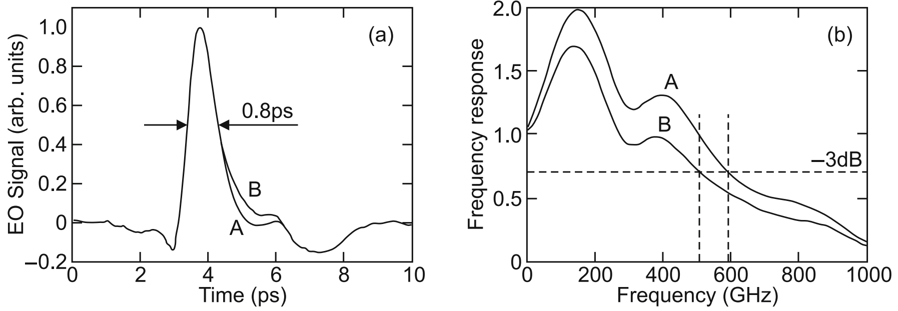

Fig. 21.33. (**a**) Pulse response (FWHM=0.8 ps) and (**b**) frequency response (Fourier transform of time response) of a MSM traveling-wave photodetector (bias 5 V) for various illumination intensities, A: 1 mW, B: 2.2 mW. Adapted from [1227]

depth of a few 100 nm (Fig. 21.32), 3 dB cutoff frequencies beyond 500 GHz have been achieved (Fig. 21.33). The quantum efficiency of this detector was still 8.1%.

21.3.8 Charge Coupled Devices

The concept of the charge coupled device (CCD), an array of connected photodetectors serving as an image sensor, was devised by W.S. Boyle and G.E. Smith [1225] (Fig. 21.34). As textbook for further details [1226] may serve.

A MIS diode (mostly a silicon-based MOS diode) can be designed as a light detector. The diode is operated in deep depletion. When a large reverse voltage is applied, initially a depletion layer is formed and the bands are

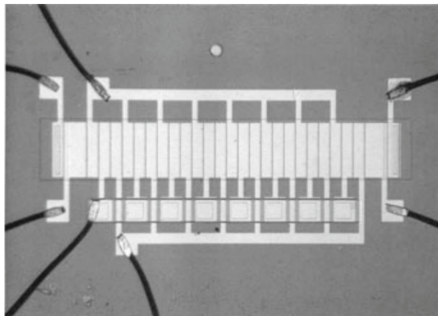

Fig. 21.34. First 8-bit charge coupled device (1970). The chip (size: $1.5 \times 2.5\,\mathrm{mm}^2$) consists of 24 closely packed MOS capacitors (narrow rectangles in the center grid). The thick rectangles at either end of the grid are input/output terminals

strongly bent as shown in Fig. 21.35b. We note that in this situation the semiconductor is not in thermodynamic equilibrium (as it is in Fig. 21.35d) when the quasi-Fermi level is constant throughout the semiconductor. The inversion charge has yet to build up.

There are three mechanisms to generate the inversion charge. (a) generation–recombination, (b) diffusion from the depletion-layer boundary and (c) carrier generation by light absorption. Mechanisms (a) and (b) represent dark currents for the photodetector. The conductivity due to these two processes is shown in Fig. 21.36 and slowly builds up the inversion charge. Two temperature regimes are obvious; at low temperatures the generation dominates ($\propto n_\mathrm{i} \propto \exp\left(-E_\mathrm{g}/2kT\right)$), at high temperatures the diffusion ($\propto n_\mathrm{i}^2 \propto \exp\left(-E_\mathrm{g}/kT\right)$). The latter process can be strongly suppressed by cooling the device.

The gate voltage V_G and the surface potential Ψ_s are related to each other via

$$V_\mathrm{G} - V_\mathrm{FB} = V_\mathrm{i} + \Psi_\mathrm{s} = \frac{eN_\mathrm{A}w}{C_\mathrm{i}} + \frac{eN_\mathrm{A}w^2}{2\epsilon_\mathrm{s}} , \qquad (21.54)$$

where w is the width of the depletion layer. w will be larger than w_m in thermodynamic equilibrium. The first term in the sum is $|Q_\mathrm{s}|/C_\mathrm{i}$ and the second is obtained by integrating the Poisson equation for the constant charge density $-eN_\mathrm{A}$ across the depletion layer. The elimination of w yields

$$V_\mathrm{G} - V_\mathrm{FB} = \Psi_\mathrm{s} + \frac{1}{C_\mathrm{i}}\sqrt{2e\epsilon_\mathrm{s}N_\mathrm{A}\Psi_\mathrm{s}} . \qquad (21.55)$$

If light is absorbed in the depletion layer (process (c)), the hole (for p-Si) drifts towards the bulk material. The electron is stored as part of the signal charge Q_sig close to the oxide semiconductor interface (Fig. 21.35b).

$$V_\mathrm{G} - V_\mathrm{FB} = \frac{Q_\mathrm{sig}}{C_\mathrm{i}} + \frac{eN_\mathrm{A}w}{C_\mathrm{i}} + \Psi_\mathrm{s} . \qquad (21.56)$$

As a consequence of the increase in signal charge the potential well becomes shallower (21.56). For each gate voltage there is a maximum charge (well capacity). The maximum signal charge is reached for $\Psi_\mathrm{s} \approx 2\Psi_\mathrm{B}$ (Fig. 21.37).

In a charge coupled device (CCD) many light-sensitive MIS diodes, as described above, are fabricated in matrix form to create an image sensor. Upon application of a gate voltage they accumulate charge depending on the local exposure to light. The read out of this charge occurs by shifting the charge through the array to a read-out circuit. Therefore charge is transferred from one pixel to the next. Several schemes have been developed for this task. The three-phase clocking is shown schematically in Fig. 21.38. Other clocking schemes involve four, two or only one electrode per pixel [1230].

Since the CCD sensor has many pixels (e.g. up to 4096) along a line, the charge transfer must be highly efficient. The transfer of charge carriers occurs

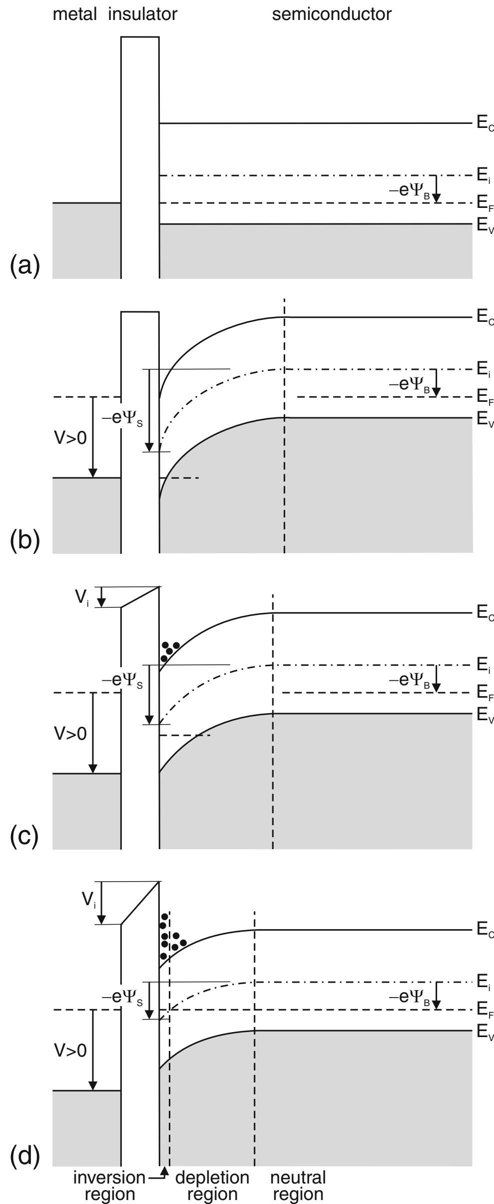

Fig. 21.35. Ideal MIS-diode (with p-type semiconductor) as photodetector (principle of a CCD pixel). (**a**) Without bias (see Fig. 20.27b). (**b**) Immediately after an external (reversely poled) voltage $V > 0$ has been applied, the surface potential is $\Psi_\mathrm{s} = V$ and no charges have moved yet. (**c**) Strong depletion (still not in thermodynamic equilibrium) with signal charge and reduced surface potential $\Psi_\mathrm{s} < V$. (**d**) The semiconductor in equilibrium (E_F is constant) with depletion and inversion layer (see Fig. 20.31). For all diagrams, $V = V - \mathrm{i} + \Psi_\mathrm{s}$

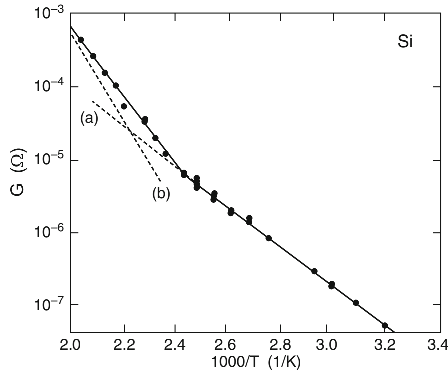

Fig. 21.36. Conductivity of a n-Si/SiO$_2$-diode as a function of temperature ($1/T$). The slope of the *dashed lines* is (a) $\sim 0.56\,\mathrm{eV}$ ($\approx E_\mathrm{g}/2$) and (b) $\sim 1.17\,\mathrm{eV}$ ($\approx E_\mathrm{g}$). Adapted from [1228]

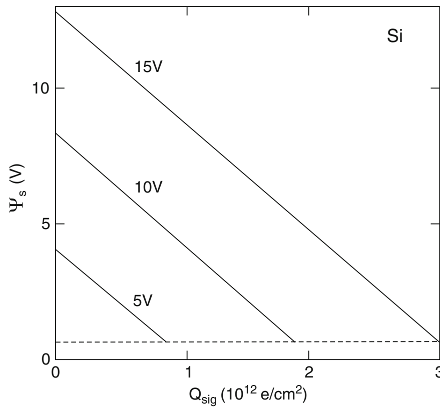

Fig. 21.37. Surface potential as a function of the signal charge Q_sig for various values of the bias $V_\mathrm{G} - V_\mathrm{FB}$ as labeled for a SiO$_2$/p-Si diode with $N_\mathrm{A} = 10^{15}\,\mathrm{cm}^{-3}$ and an oxide thickness of 100 nm. The *dashed line* represents the limit for inversion given by $\Psi_\mathrm{s} = 2\Psi_\mathrm{B} \approx 0.6\,\mathrm{V}$. Adapted from [1229]

via thermal (regular) diffusion, self-induced drift and the effect of the fringing field (inset of Fig. 21.39). The time constant with which the charge carriers move due to diffusion (in a p-type semiconductor) is

$$\tau_\mathrm{th} = \frac{4L^2}{\pi^2 D_\mathrm{n}} \,, \tag{21.57}$$

where L is the length of the electrode. For a sufficiently large charge packet the self-induced drift due to Coulomb repulsion is important. The decay of charge is then given by

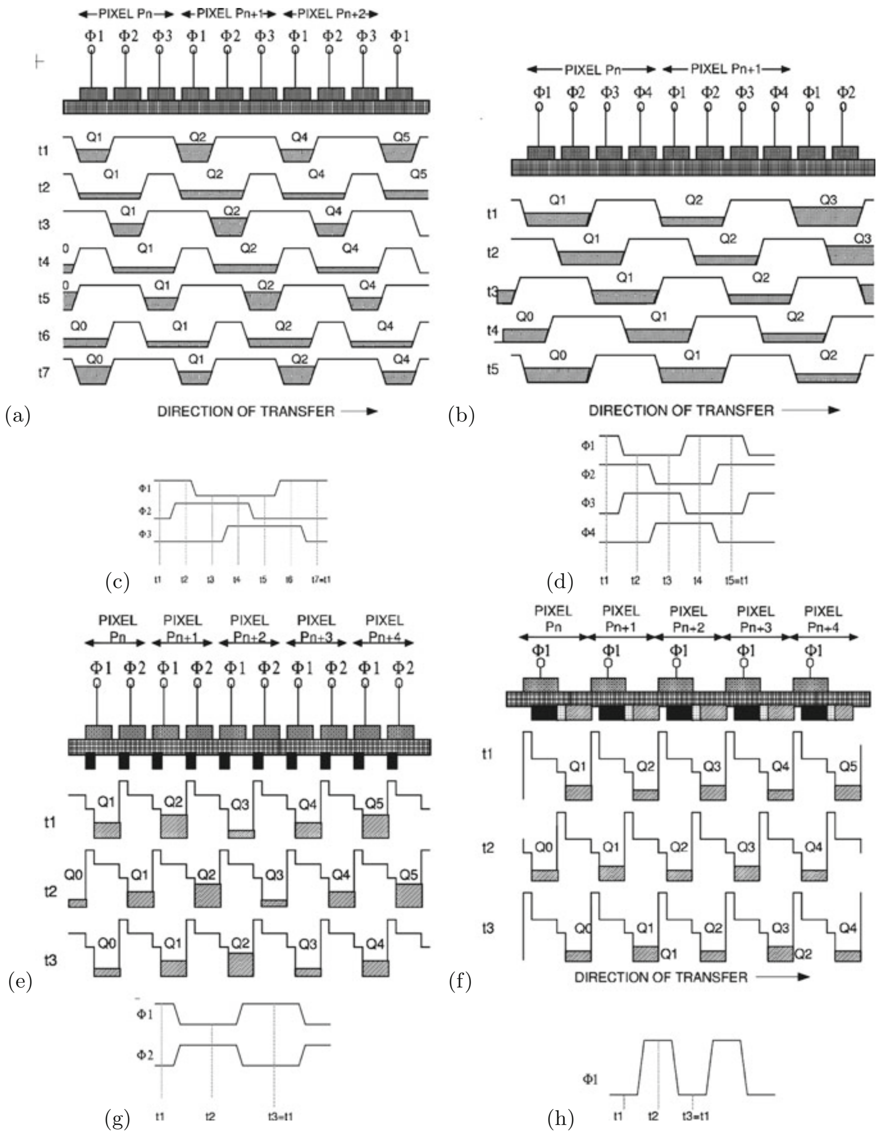

Fig. 21.38. (**a**) Three-phase CCD. Each pixel has three electrodes that can be switched independently (phases 1–3). (**b**,**e**,**f**) Schematic of CCDs with four, two or one phase, respectively. (**c**) (t_1) Charge accumulated after light exposure. A lateral potential well is formed along the row of pixels by the voltages at the three electrodes, e.g. $P_1 = P_3 = 5\,\mathrm{V}$, $P_2 = 10$,V. (t_2–t_7) transfer of charge, (t_7) has the same voltages as (t_1), the charge has been moved one pixel to the right. (**d**,**g**,**h**) Timing schemes for 4-, 2- and 1-phase CCDs, respectively. From [1230]

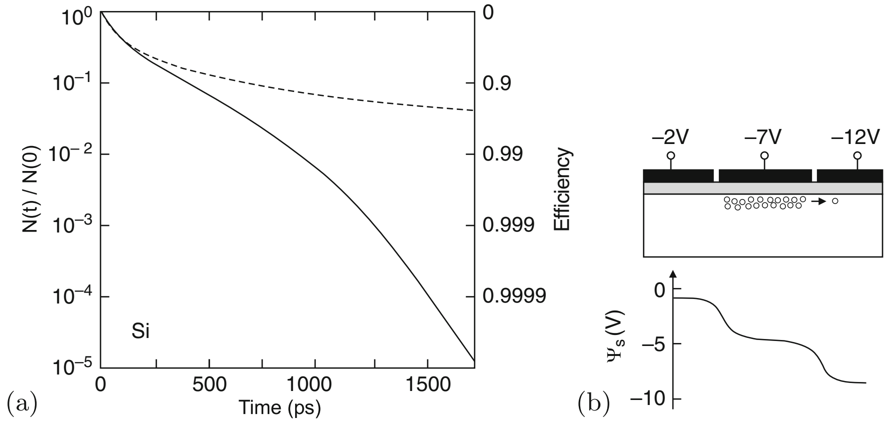

Fig. 21.39. (**a**) Efficiency of charge transfer with (*solid* line) and without (*dashed* line) the effect of the fringing field. (**b**) Schematic plot of the CCD electrodes and bias with the fringing field for a three-electrode CCD, oxide thickness 200 nm, doping $N_\mathrm{D} = 10^{15}\,\mathrm{cm}^{-3}$. The electrode pitch is 4 μm and the gap between electrodes is 200 nm wide. Adapted from [1231]

$$\frac{Q(t)}{Q(0)} = \frac{t_0}{t + t_0} \,, \tag{21.58}$$

with $t_0 = \pi L^3 W_\mathrm{e} C_\mathrm{i}/(2\mu_\mathrm{n} Q(0))$. W_e is the width of the electrode. This dependence is shown as a dashed line in Fig. 21.39a. The last electrons are efficiently transferred by the drift induced by the fringing field of the electrodes (solid line in Fig. 21.39a). The origin of the fringing field is schematically shown in Fig. 21.39b; the minimum fringing field shown is 2×10^3 V/cm. In about 1–2 ns practically all $(1 - 10^{-5})$ charges are transferred. This enables clock rates of several 10 MHz.

For the clocking of the CCD the lateral variation of potential depth with the applied gate voltage is used. In Fig. 21.40 it is shown how a lateral

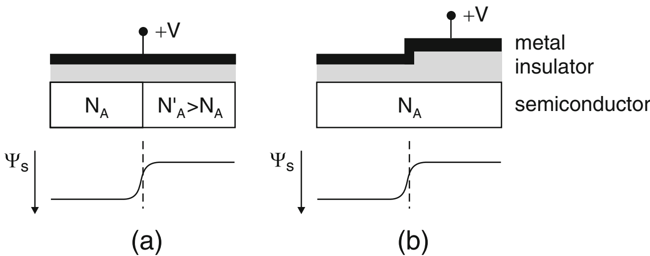

Fig. 21.40. Creation of a lateral potential well (barrier) in a MIS structure with (**a**) varying doping via diffusion or implantation and (**b**) varying (stepped) oxide thickness. *Upper row* shows schematic geometry, *lower row* depicts schematic lateral variation of the surface potential

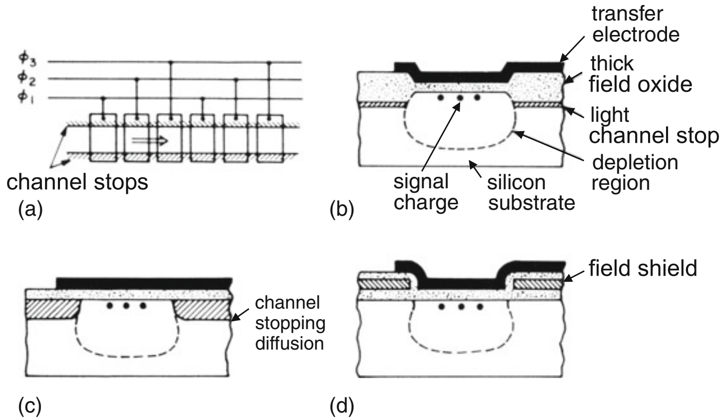

Fig. 21.41. (**a**) Schematic image of channel isolation. Cross section for channel isolation by (**b**) variation of oxide thickness, (**c**) highly doped region and (**d**) field effect. Adapted from [1232]

variation of doping or oxide thickness creates a lateral potential well. Such structures are used to confine the row of pixels against the neighboring rows (channel stops, Fig. 21.41). In order to avoid carrier loss at the interface between the oxide and the semiconductor a buried-channel structure is used (Fig. 21.42).

For front illumination parts of the contact electrodes shield the active area of the device. Higher sensitivity (in particular in the UV) is achieved for back illumination. For this purpose the chip is thinned (polished). This process is expensive and makes the chip mechanically less stable. For red/infrared wavelengths typically interference fringes occur for such thinned chips due to the small thickness. An increase in efficiency for front illumination can be achieved with an onchip microlens (Fig. 21.43).

For color imaging the CCD is covered with a three-color Bayer mask [1235] (Fig. 21.44a). On average there are one blue and one red pixel and two green pixels since green is the most prominent color in typical lighting situations. Thus each pixel delivers monochromatic information; RGB images are generated using suitable image software. Alternatives in high-end products are the use of a beam splitter, static color filters and three CCD chips, one for each color (Fig. 21.44b), or the time-sequential recording of three monochromatic images using one CCD chip and a rotating color-filter wheel (Fig. 21.44c).

21.3.9 Photodiode Arrays

An array of photodiodes is also suitable to create an image sensor. During illumination each diode charges a capacitor that is read out with suitable electronics. Based on CMOS technology (cf. Sect. 23.5.4) cheap image sensors

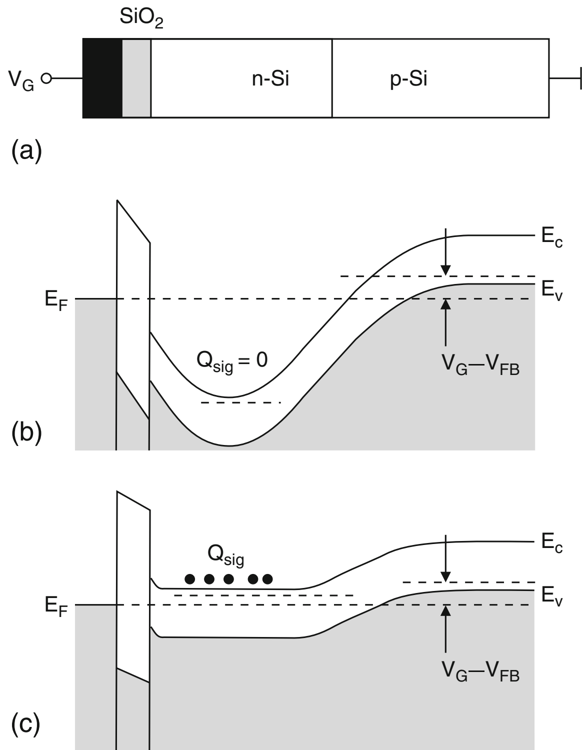

Fig. 21.42. (**a**) Schematic layers of MIS diode with buried-channel structure. Band diagram (**b**) after application of reverse voltage V_G and (**c**) with signal charge Q_{sig}. Adapted from [1233]

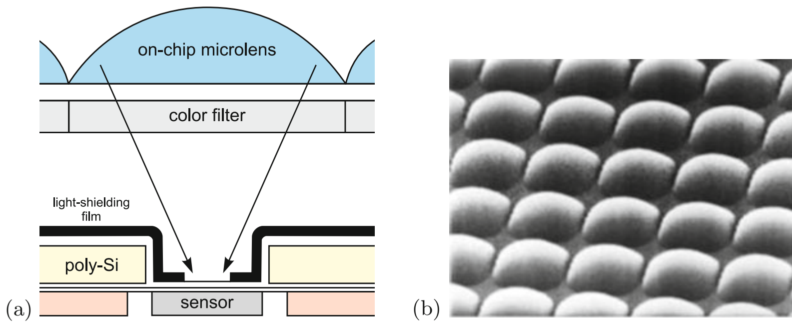

Fig. 21.43. (**a**) Scheme for enhancement of CCD efficiency for front illumination by application of an onchip microlens. (**b**) SEM image of an array of such microlenses. From [1235]

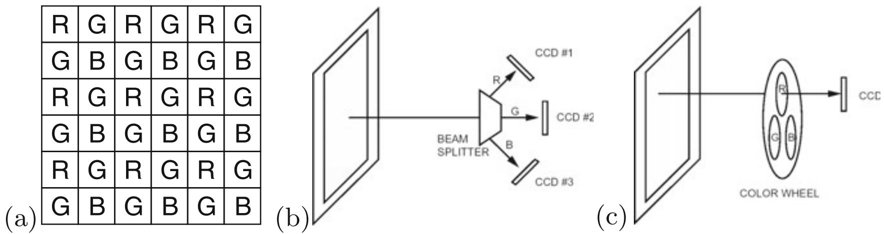

Fig. 21.44. (**a**) Arrangement of colors in a CCD Bayer [1235] color filter ('R': red, 'G': green, 'B': blue). Color splitting with (**b**) static color filters and (**c**) rotating color wheel. Parts (**b**) and (**c**) from [1230]

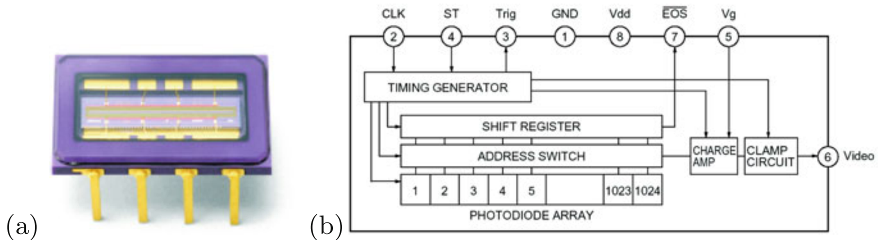

Fig. 21.45. (**a**) CMOS linear array sensor in a 8-pin package. (**b**) Block diagram, the built-in timing generator allows operation only with start and clock pulse inputs. Reprinted with permission from [1234]

can be made that show currently, however, inferior performance to CCDs. The built-in electronics allows simple outward connections (Fig. 21.45).

The three-color CCD image sensor did not offer RGB color information at each pixel. Therefore the spatial resolution of a color image is not directly given by the pixel distance. This is not a very dramatic drawback since human vision is more sensitive to intensity contrast than color contrast. However, RGB color information for each pixel would be desirable, giving higher resolution, in particular in professional photography. Such a sensor has been fabricated employing the wavelength dependence of the silicon absorption coefficient (Fig. 21.13). Blue light has the shortest and red light the largest penetration depth. By stacking three photodiodes on top of each other (Fig. 21.46) photocurrents at different penetration depth are recorded that can be used to generate a RGB value for each pixel.

In Fig. 21.47a a 16-channel array of silicon avalanche photodiodes is shown. It features a quantum efficiency of $> 80\%$ between 760 and 910 nm. The pixel size is $648 \times 208\,\mu\text{m}^2$ on a $320\,\mu$m pitch. The gain is 100 and the rise time 2 ns.

The InGaAs photodiode array in Fig. 21.47b is hybridized with CMOS read-out integrated circuits. It is useful for detection in the spectral range

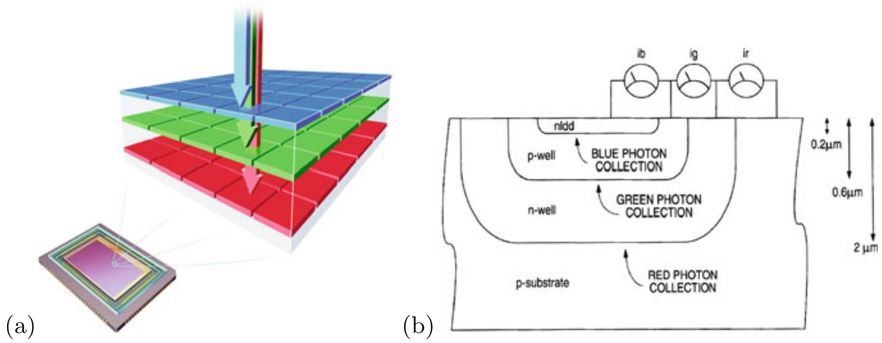

Fig. 21.46. (**a**) Scheme of image sensor with depth-dependent light detection. From [1237]. (**b**) Schematic layer sequence for three-color pixel. i_b, i_g and i_r denote the photocurrents for blue, green and red light, respectively. Adapted from [1238]

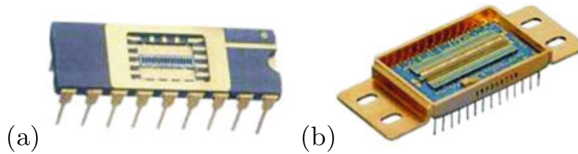

Fig. 21.47. (**a**) Array of 16 silicon APDs. From [1239]. (**b**) 1024-pixel InGaAs photodiode array. From [1240]

0.8–1.7 µm. The asymmetric diode size of 25 × 500 µm is designed for use in the focal plane of a monochromator.

Another special type of photodiode array is the four-quadrant detector. A light beam generates four photocurrents I_a, I_b, I_c, I_d of the respective parts (Fig. 21.48a). A beam deviation in the horizontal or vertical direction can be

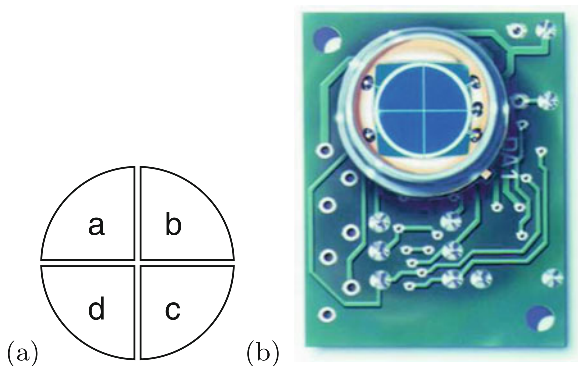

Fig. 21.48. (**a**) Scheme of four-quadrant photodetector with sections 'a', 'b', 'c' and 'd', (**b**) image of four-quadrant silicon photodetector with circuit board. Part (**b**) from [1241]

detected from the (signed) signals $(I_\mathrm{a}+I_\mathrm{d})-(I_\mathrm{b}+I_\mathrm{c})$ or $(I_\mathrm{a}+I_\mathrm{b})-(I_\mathrm{c}+I_\mathrm{d})$, respectively. We note that these signals can also be normalized to the total beam intensity $I_\mathrm{a}+I_\mathrm{b}+I_\mathrm{c}+I_\mathrm{d}$.

21.4 Solar Cells

Solar cells are light detectors, mostly photodiodes, that are optimized for the (large-area) conversion of solar radiation (light) into electrical energy. A 1993 review of the historic development of photovoltaics is given in [1242]. The latest data on solar cell efficiencies are compiled in the Solar Cell Efficiency Tables [1243].

21.4.1 Solar Radiation

The sun has three major zones, the core with a temperature of 1.56×10^7 K and a density of $100\,\mathrm{g/cm^3}$ in which 40% of the mass is concentrated and 90% of the energy is generated, the convective zone with a temperature of 1.3×10^5 K and a density of $0.07\,\mathrm{g/cm^3}$, and the photosphere with a temperature of 5800 K and low density ($\sim 10^{-8}$ $\mathrm{g/cm^3}$). The radius is 6.96×10^8 m and is about 100 times larger than that of the earth (6.38×10^6 m). The distance sun–earth is 1.496×10^{11} m. The angle under which the sun disk appears on earth is 0.54°. An energy density of $1367 \pm 7\,\mathrm{W/m^2}$ arrives at the earth in front of its atmosphere.

This value and the according spectrum of the sun's emission, which is similar to a blackbody with temperature 5800 K (Fig. 21.49), is termed air mass zero (AM0). The total energy that reaches the earth from the sun is 1.8×10^{17} W per year. This value is 10^4 times the world's primary energy need.

Air mass zero (AM0) is important for solar cells in satellites. When the solar spectrum passes the earth's atmosphere, it is changed with regard to its shape and the total energy density due to gas absorption (ozone, water, CO_2, ...). Depending on the meridian of the sun γ (Fig. 21.50), the spectrum on the surface of the earth is termed AMx with $x = 1/\sin\gamma$. In spring and fall (March 21st and September 21st), Leipzig (51°42′N latitude) has about AM1.61. At the summer (June 21st) and winter (December 21st) solstices the air mass in Leipzig is AM1.13 ($\gamma = 61.8°$) and AM3.91 ($\gamma = 14.8°$), respectively. Additionally, the duration of sunshine and thus the light power density is regionally different across the earth due to climate and weather (Fig. 21.51). For AM1.5, the incident power density is 844 $\mathrm{W/m^2}$.

The global radiation reaching a photovoltaic cell has three components: (i) the direct radiation, (ii) diffuse radiation and (iii) reflected radiation. The relative amounts and their spectra depend on details such as the climate (e.g. humidity) or the environment (e.g. outdoors vs. urban).

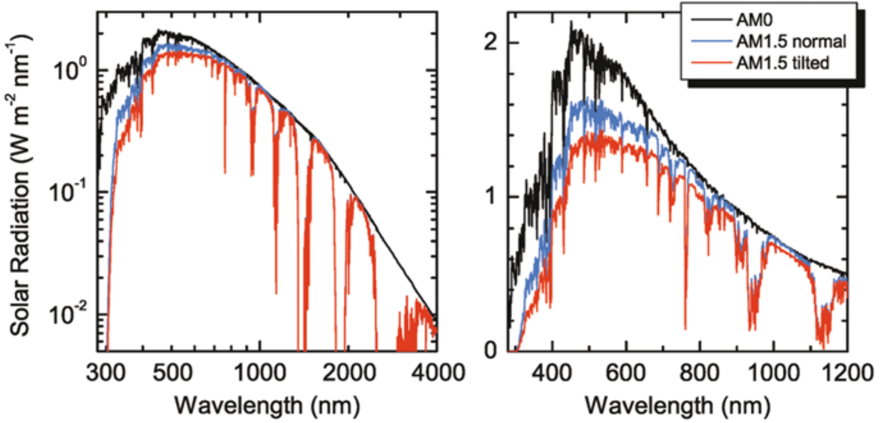

Fig. 21.49. Solar spectra (power per area and wavelength interval) for AM0 (*black line*, extraterrestrial irradiance) and AM1.5 (sun at 41.8° elevation above horizon) for direct normal irradiance (*blue line*) and global total irradiance (*red line*) on a sun facing surface (tilted 37° towards the equator). Left (right) graph in log-log (linear) scales

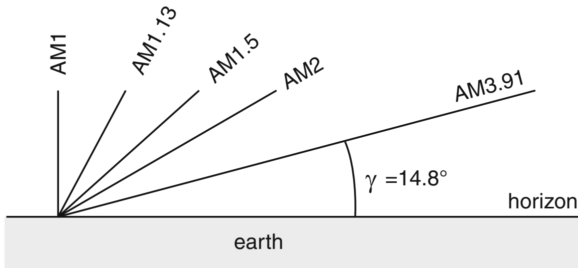

Fig. 21.50. Schematic path of sunlight through the atmosphere and definition of the air mass AMx

21.4.2 Ideal Solar Cells

When a solar cell made from a semiconductor with a band gap E_g is irradiated by the sun, only photons with $h\nu > E_\mathrm{g}$ contribute to the photocurrent and the output power. The I–V characteristic under illumination (Fig. 21.52) is given by

$$I = I_\mathrm{s} \left[\exp\left(\beta V\right) - 1\right] - I_\mathrm{L} \;, \tag{21.59}$$

with I_L being the current due to generation of excess carriers by the absorption of the sunlight. Assuming a simple n$^+$p-diode solar cell model, the current consists of two components: the depletion layer current j_DL from carriers absorbed in the depletion layer (field region) and the diffusion current j_D from absorption in the neutral region ($j = I/A$).

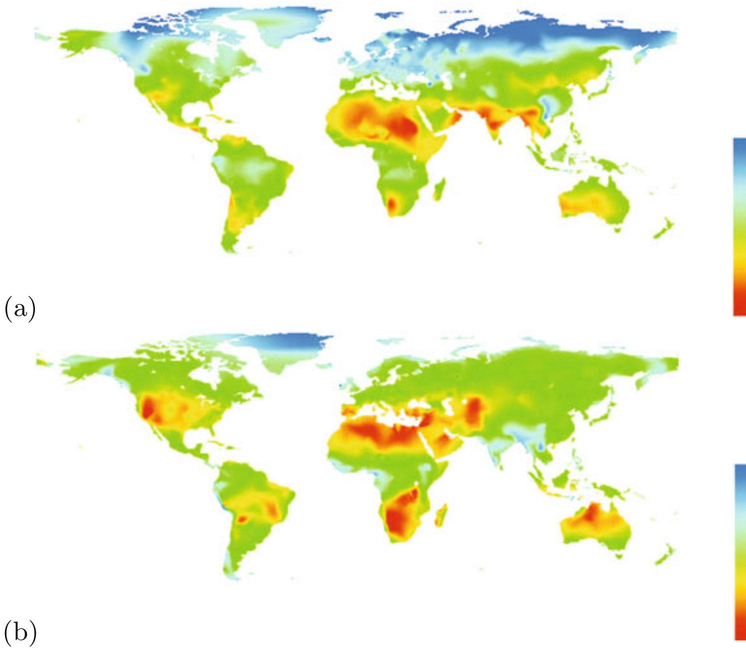

Fig. 21.51. Global sunshine distribution in (**a**) January and (**b**) July. The sunshine fraction is the actual number of bright sunshine hours over the potential number, and is thus expressed as a percentage figure. The color scale reaches from 0 to 100%. The sunshine data are in a 0.5 degree grid based on data from [1244]

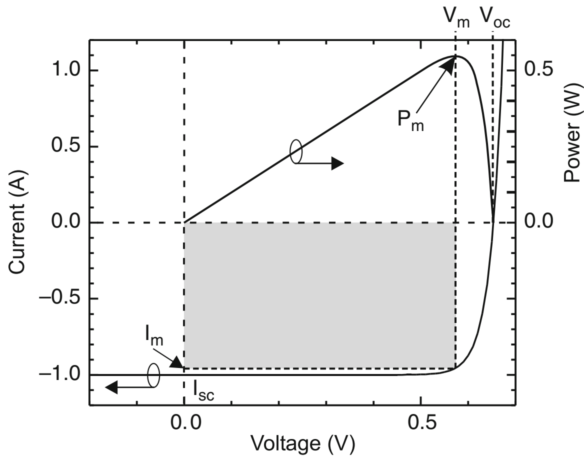

Fig. 21.52. Schematic I–V characteristics of a solar cell under illumination (*left scale*) and extracted power (*right scale*). The *grey area* is the maximum power rectangle with $P_{\mathrm{m}} = I_{\mathrm{m}} V_{\mathrm{m}}$.

For the drift current out of the depletion layer of width w it can be assumed that it is collected fast and recombination plays no role. Thus (cmp. (21.30))

$$j_{\mathrm{DL}}(\lambda) = e\, n_{\mathrm{ph}}(\lambda)\, [1 - R(\lambda)]\, [1 - \exp(-\alpha(\lambda) w)] \;, \tag{21.60}$$

where λ is the wavelength of the incident radiation, R the reflectance of the surface, α the absorption coefficient and $n_{\mathrm{ph}}(\lambda)$ the photon flux (number of photons per area and time) at the given wavelength. For a solar spectrum, an integral needs to be performed over the spectral distribution:

$$j_{\mathrm{DL}} = \int j_{\mathrm{DL}}(\lambda)\, \mathrm{d}\lambda \;, \tag{21.61}$$

the total photon flux being $n_{\mathrm{ph}} = \int n_{\mathrm{ph}}(\lambda)\, \mathrm{d}\lambda$.

The diffusion current collected at the back contact is obtained from solving (10.70) (now for electrons in p-type material) with the appropriate boundary conditions (reversely bias depletion layer, $n_{\mathrm{p}}(w) = 0$, $\Delta n_{\mathrm{p}}(\infty) = n_{\mathrm{p}}(\infty) - n_{\mathrm{p}_0} = 0$ [1245]):

$$j_{\mathrm{D}}(\lambda) = e\, n_{\mathrm{ph}}(\lambda)\, [1 - R(\lambda)]\, \frac{\alpha L_{\mathrm{n}}}{1 + \alpha L_{\mathrm{n}}}\, \exp(-\alpha w) + e\, n_0\, \frac{D_{\mathrm{n}}}{L_{\mathrm{n}}} \;, \tag{21.62}$$

Dropping the wavelength dependence and neglecting the dark term, the usual formula is obtained,

$$j_{\mathrm{L}} = e\, n_{\mathrm{ph}}\, [1 - R] \left[1 - \frac{\exp(-\alpha w)}{1 + \alpha L_{\mathrm{n}}}\right] \;, \tag{21.63}$$

The last bracket represents the quantum efficiency [1246]. The model can be extended for taking into account a non-zero surface recombination velocity at the back contact at finite distance [1247].

Here a voltage *independent* photo-generated current I_{L} is assumed. If the diffusion length is small compared to the transport path, the carrier collection efficiency η_{c} becomes voltage dependent [1246]. The reduction of the diffusion potential for forward voltage decreases the carrier collection efficiency [1248], possibly to zero close to the built-in voltage.

The saturation current density is given by (20.113) and (20.114)

$$j_{\mathrm{s}} = I_{\mathrm{s}}/A = e N_{\mathrm{C}} N_{\mathrm{V}} \left[\frac{1}{N_{\mathrm{A}}}\sqrt{\frac{D_{\mathrm{n}}}{\tau_{\mathrm{n}}}} + \frac{1}{N_{\mathrm{D}}}\sqrt{\frac{D_{\mathrm{p}}}{\tau_{\mathrm{p}}}}\right] \exp\left(-\frac{E_{\mathrm{g}}}{kT}\right) \;, \tag{21.64}$$

with A being the cell area.

The voltage at $I = 0$ is termed the *open-circuit* voltage V_{oc}, the current at $V = 0$ is termed the *short-circuit* current $I_{\mathrm{sc}} = I_{\mathrm{L}}$ (Fig. 21.52). Only a part of the rectangle $I_{\mathrm{sc}} \times V_{\mathrm{oc}}$ can be used for power conversion. By choice

of the load resistance R_L, the work point is set. At I_m and V_m, the generated power $P_m = I_m V_m$ is maximal. The filling factor F is defined as the ratio

$$F = \frac{I_m V_m}{I_{sc} V_{oc}} \ . \tag{21.65}$$

The open-circuit voltage is given by

$$V_{oc} = \beta^{-1} \ln \left(\frac{I_L}{I_s} + 1 \right) \cong \beta^{-1} \ln \left(\frac{I_L}{I_s} \right) \tag{21.66}$$

and increases with increasing light power and decreasing dark current. The output power is

$$P = IV = I_s V \left[\exp\left(\beta V\right) - 1 \right] - I_L V \ . \tag{21.67}$$

The condition $\mathrm{d}P/\mathrm{d}V = 0$ yields the optimal voltage at which the solar cell has to be operated and is given by the implicit equation

$$V_m = \frac{1}{\beta} \ln \left(\frac{I_L/I_s + 1}{1 + \beta V_m} \right) = V_{oc} - \frac{1}{\beta} \ln\left(1 + \beta V_m\right) \ . \tag{21.68}$$

The current at maximum power is

$$I_m = I_L \left(1 - \frac{1 - \beta V_m I_s/I_L}{1 + \beta V_m} \right) \cong I_L \left(1 - \frac{1}{\beta V_m} \right) \ . \tag{21.69}$$

E_m is the energy that is delivered per photon at the load resistor at the power maximum. The maximum power is $P_m = I_L E_m/e$ and E_m is given by

$$E_m \cong e \left[V_{oc} - \frac{1}{\beta} \ln\left(1 + \beta V_m\right) - \frac{1}{\beta} \right] \ . \tag{21.70}$$

The ideal solar cell has a (power) conversion efficiency $\eta = P_m/P_{in}$ that can be determined from Fig. 21.53a.

The right curve (1) in Fig. 21.53a shows the integral number n_{ph} of photons in the solar spectrum (per area and time) with an energy larger than a given one (E_g). For a given value of n_{ph}, the left curve (2) represents the value of E_m. The efficiency is the ratio of $E_m n_{ph}$ and the area under curve (1). The efficiency as a function of the band gap is shown in Fig. 21.54a. It has a fairly broad maximum such that many semiconductors can be used for solar cells, in principle. The maximum theoretical efficiency for a single junction is 31% for nonconcentrated sunlight (AM1.5). This limit corresponds to the classic Shockley–Queisser limit [1250–1252], assuming radiative recombination as the only charge-carrier recombination mechanism. In [1253], the limit for a single material is found to be 43% for an optimally tailored band structure that allows carrier multiplication by optically excited hot carriers. The solar cell as a heat engine is discussed in [1254].

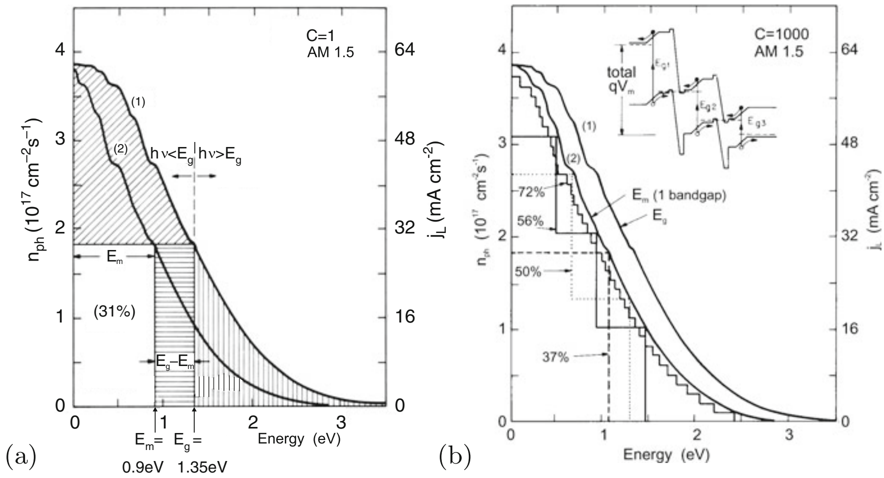

Fig. 21.53. (**a**) Number of photons n_{ph} per area and time in the sun spectrum (AM1.5, $C = 1$ sun) with an energy larger than a cutoff energy (*curve* 1) and graphical method to determine the quantum efficiency (from *curve* 2). Adapted from [1249]. (**b**) Number of photons in concentrated solar spectrum (AM1.5, $C = 1000$ sun) with an energy larger than a given energy and graphical method to determine the quantum efficiency of multijunction solar cells. Adapted from [384] after [1249]

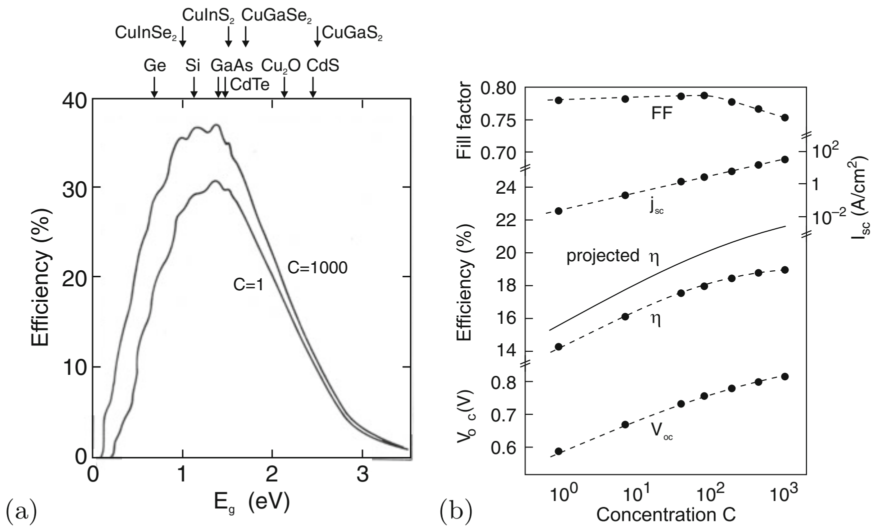

Fig. 21.54. (**a**) Ideal quantum efficiency of solar cells (single junction) as a function of band gap and light concentration C. The band gaps of some important semiconductors are denoted by *arrows*. Adapted from [1249]. (**b**) Properties of a silicon solar cell (water cooled) as a function of light concentration. *Solid line* is theoretically projected efficiency, *dashed lines* are guides to the eye. Adapted from [384]

When the sunlight is concentrated, e.g. by a lens, the efficiency increases (Fig. 21.54b). The short-circuit current increases linearly. The effect is mostly due to the increase of the open-circuit voltage. For $C = 1000$, the maximum theoretical efficiency for a single-junction solar cell is 38%.

A further increase of efficiency can be achieved with multiple junctions using various materials for absorption. In a tandem cell (two junctions), the upper layer absorbs the higher-energy photons in a wide band gap material. The material with the lower band gap makes use of the low-energy photons. Thus, the cell works with two different values of E_{m} (Fig. 21.53b). With band gaps of 1.56 eV and 0.84 eV, an efficiency of 50% can be reached theoretically. With three materials 56%, and for a large number of materials 72% is the limit. Between the junctions, tunneling diodes (Sect. 20.5.9) must be used to allow carrier transport through the entire structure. It is a nontrivial task to fabricate multiple heterojunctions due to incompatibilities of the lattice constants. Besides heteroepitaxy, wafer bonding can also be used for fabrication. A lattice-matched InGaP/GaAs/InGaAsN cell seems a viable solution for high-efficiency solar cells.

21.4.3 Real Solar Cells

For a real solar cell, the effect of parallel resistance R_{sh} (shunt resistance due to leakage current, e.g. by local shorts of the solar cell) and serial resistance R_{s} (due to ohmic loss) must be considered. The I–V characteristic is then (cf. (20.139))

$$\ln\left(\frac{I + I_{\mathrm{L}}}{I_{\mathrm{s}}} - \frac{V - IR_{\mathrm{s}}}{I_{\mathrm{s}} R_{\mathrm{sh}}} + 1\right) = \beta\,(V - IR_{\mathrm{s}}) \ . \tag{21.71}$$

The serial resistance affects the efficiency more strongly than the shunt resistance (Fig. 21.55). Therefore, it is frequently enough to consider R_{s} only and use (cf. Fig. 20.138)

$$I = I_{\mathrm{s}}\,\exp\left(\beta(V - IR_{\mathrm{s}})\right) - I_{\mathrm{L}} \ . \tag{21.72}$$

In the example of Fig. 21.55, a serial resistance of $5\,\Omega$ reduces the filling factor by a factor of about four.

21.4.4 Design Refinements

In order to collect electrons most efficiently, a back surface field is used (Fig. 21.56). A higher-doped region at the back contact creates a potential barrier and reflects electrons back to the front contact.

An important point for optimization is the management of the reflection at the solar cell surface. First, a dielectric antireflection (AR) layer (or multilayers) can be used. These layers should have a broad AR spectrum. Additionally, a textured surface reduces reflection (Fig. 21.57d), giving reflected photons a second chance for penetration (Fig. 21.57c). The reflectance of

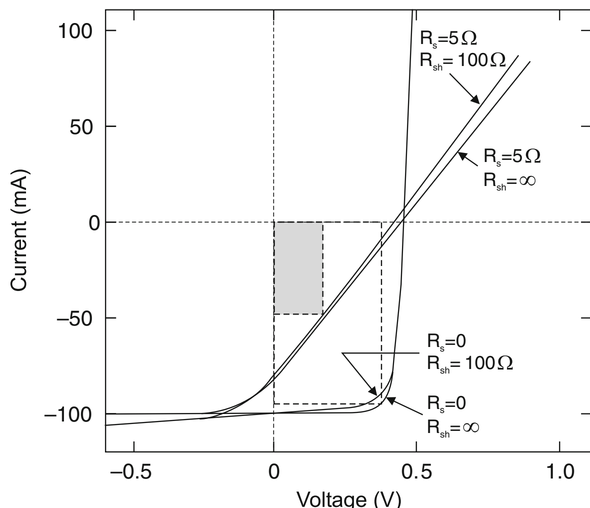

Fig. 21.55. *I–V* characteristics of a solar cell considering shunt and series resistances R_s and R_{sh}, respectively. The efficiency of the real cell (*shaded* power rectangle) is less than 30% of that of the ideal cell. Adapted from [1256]

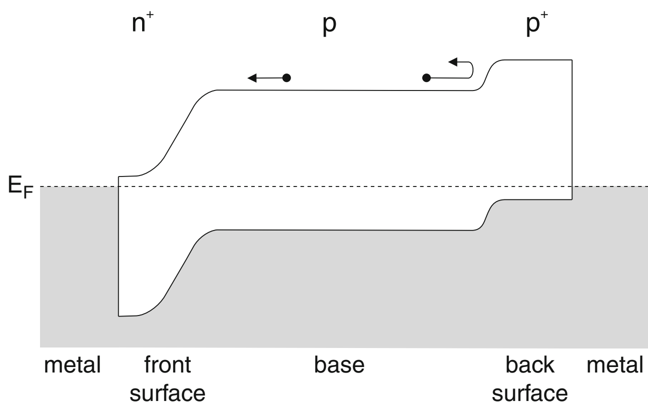

Fig. 21.56. Increase of the carrier collection efficiency by a back surface field. Adapted from [1257]

bare Si, 35%, can be reduced to 2%. An AM0 efficiency of over 15% was reached using textured multi-crystalline cells. Alkaline KOH-based etches attack Si (001) anisotropically and yield pyramidal structures (Fig. 21.57b) with {111} facets. Recently an acidic HF/HNO_3-based process has been established [1255], resulting in a worm-like surface pattern on multi-crystalline silicon wafers (Fig. 21.57a) with superior anti-reflection properties.

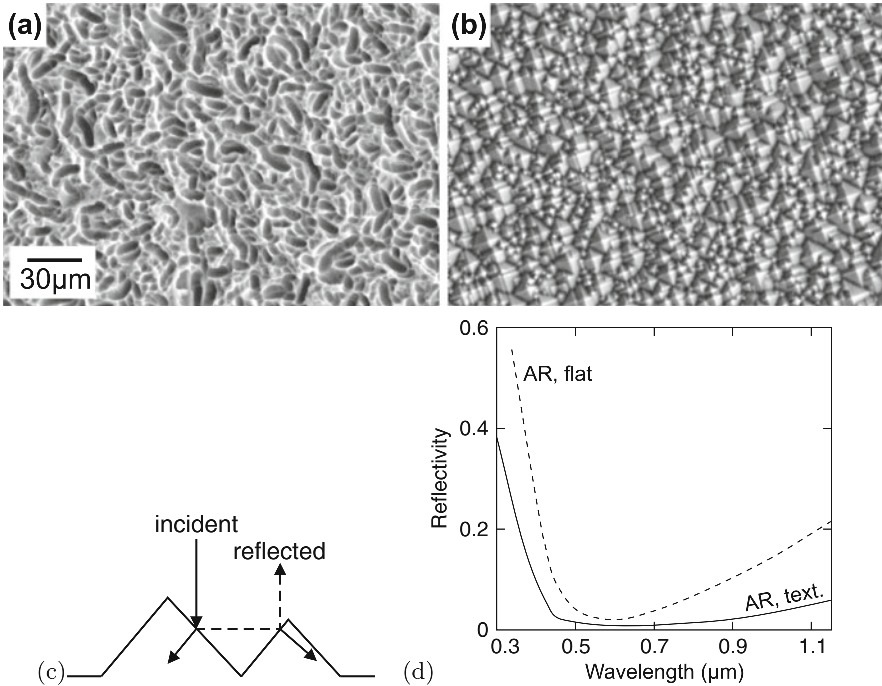

Fig. 21.57. (**a**) SEM image of topology of acidically etched multi-crystalline silicon wafer. (**b**) SEM image of alkaline etched mono-crystalline silicon wafer. (**c**) Exemplary light path. (**d**) Reflectance of antireflection-coated flat (*dashed line*) and textured (*solid line*) surface). Parts (**a**) and (**b**) adapted from [1260], part (**d**) adapted from [1261]

During its course over the sky during the day, the sun changes its angle towards a fixed solar cell.[8] A tracking mechanism can optimize the angle of incidence during the day and increase the overall efficiency of the solar cell (Fig. 21.58).

21.4.5 Modules

In order to cover a large area and supply certain values of output voltage and current, several solar cells are connected into modules. Arrays are built up from several modules (Fig. 21.59). If solar cells are connected in parallel, the total current increases; if they are connected in series, the output voltage increases. We note that in partially shadowed modules the reverse characteristics of solar cells are important [1258, 1259]; local breakdown can lead to hot spots and irreversible degradation.

[8] We are of course aware that the earth rather rotates around the sun.

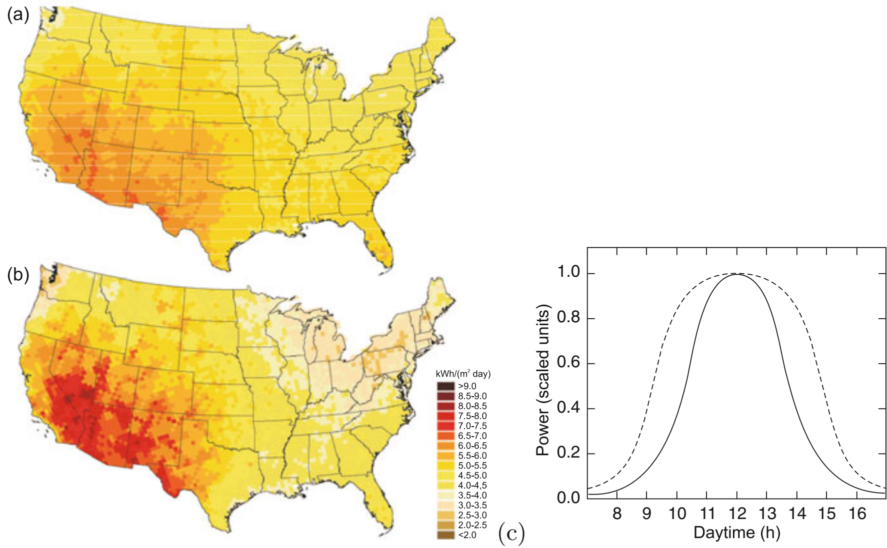

Fig. 21.58. Annual average solar energy (in kWh/(m^2 day)) for (**a**) an optimally tilted south-facing fixed panel and (**b**) an optimally two-axis tracked panel (in mainland US). Adapted from [1266]. (**c**) Power generation of a solar cell vs. time (in daytime hours) for a stationary setup facing the sun at constant angle (*solid line*) and mounting with tracking (*dashed line*) to optimize the angle towards the sun. Adapted from [1267]

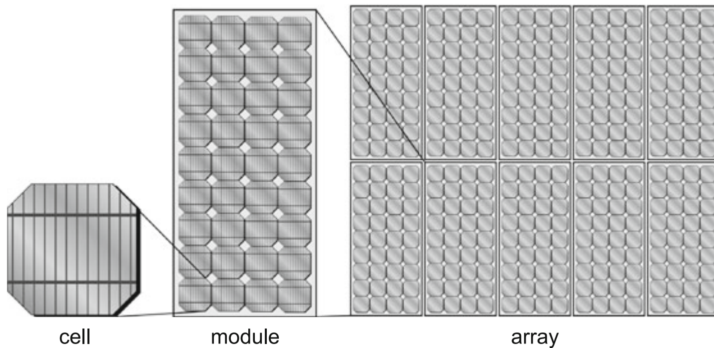

Fig. 21.59. Schematic drawing of a solar cell (with contact grid), a module (36 cells) and an array of ten modules

21.4.6 Solar-Cell Types

First Generation Photovoltaics

Silicon is the most frequently used material for solar cells. Cells based on single-crystalline silicon (wafers) have the highest efficiency but are the most

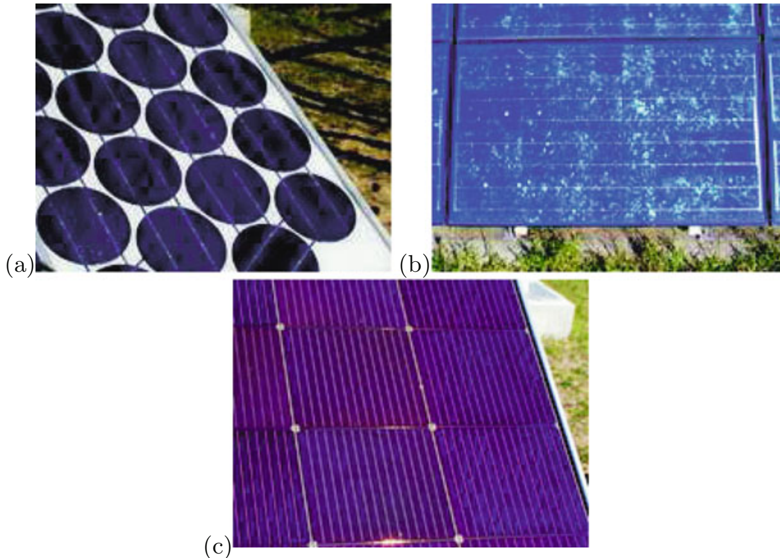

Fig. 21.60. Various types of solar cells: (**a**) monocrystalline silicon solar cell, (**b**) polycrystalline solar cell, (**c**) amorphous silicon solar cell. From [1267]

Table 21.1. Record efficiency of various solar cells (AM1.5, 1000W/cm^2, 25° unless noted otherwise). Most data from [1243], additional data for 3J (conc.) from [1268]

cell material/type	efficiency (%)	V_{oc} (V)	j_{sc} (mA/cm^2)	FF (%)	date m/y
Si (crystalline)	24.7 ± 0.5	0.706	42.2	82.8	3/1999
Si (polycrystalline)	20.3 ± 0.5	0.664	37.7	80.9	5/2004
Si (amorphous)	9.3 ± 0.5	0.859	17.5	63.0	4/2003
GaAs (crystalline)	25.9 ± 0.8	1.038	29.4	84.7	12/2007
GaAs (thin film)	24.5 ± 0.5	1.029	28.8	82.5	5/2005
GaAs (polycrystalline)	18.2 ± 0.5	0.994	23.0	79.7	11/1995
2J (GaInP/GaAs)	30.3	2.488	14.22	85.6	4/1996
3J (GaInP/GaAs/Ge)	32.0 ± 1.5	2.622	14.4	85.0	1/2003
3J (conc., 240 suns)	40.7 ± 2.4	2.911	3832	87.5	9/2006
CIGS	19.2 ± 0.6	0.716	33.3	80.3	1/2008
CdTe	16.5 ± 0.5	0.845	25.9	75.5	9/2001
dye sensitized	10.4 ± 0.3	0.729	21.8	65.2	8/2005
organic polymer	5.15 ± 0.3	0.876	9.4	62.5	12/2006

expensive (Fig. 21.60a). The efficiencies of various solar cells are compiled in Table 21.1. Polycrystalline (for large grains also called multi-crystalline) silicon (Fig. 21.60b) is cheaper but offers less performance. Material design is oriented towards increasing the grain size and/or reducing their elec-

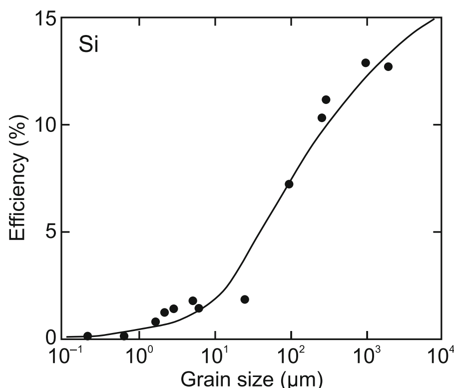

Fig. 21.61. Theoretical dependence of the effect of grain size on efficiency of polycrystalline solar cells (*solid line*) with experimental data points (*circles*). Adapted from [1264]

trical activity. Grain boundaries act as recombination centers with a surface (i.e. interface) recombination velocity of 10^2 cm/s [1262] for particular, electrically fairly inactive grain boundaries, several 10^3 cm/s [1263], several 10^4 cm/s [1264] or even 10^5–10^7 cm/s [1265]. The grain boundaries reduce the effective diffusion length and thus carriers recombine before they can reach the contacts. A detailed theory of solar cell performance for polycrystalline material has been worked out in [1264] and explains the reduction of efficiency with decreasing grain size as shown in Fig. 21.61.

These solar cells are also called 'first-generation' photovoltaics. Thin sheets of crystalline silicon drawn from a melt between two seed crystals in a modified CZ growth (sheet silicon or ribbon silicon) allow cheaper production compared to cells based on 'traditional' polished wafers cut from a large silicon rod. Silicon made particularly for solar cell use is called 'solar-grade' silicon.

Second Generation Photovoltaics

Even cheaper are solar cells from amorphous silicon (Fig. 21.61c). Since silicon is an indirect semiconductor, a fairly thick layer is needed for light absorption. If direct band gap semiconductors are used, a thin layer ($d \approx 1\,\mu$m) is sufficient for complete light absorption. Such cells are called thin-film solar cells. A typical material class used in this type of cell are chalcopyrites, such as $CuInSe_2$ (CIS). The band gap is around 1 eV, which is not optimal. An improvement can be achieved by adding Ga and/or S which increases the band gap, $Cu(In,Ga)(Se,S)_2$ (CIGS), to 1.2–1.6 eV. Using CIGS, an efficiency of over 19% has been reported in laboratory samples; 12–13% seeming realistic for production [1269]. Also CdTe is a viable absorber mostly sputtered on glass with over 16% efficiency demonstrated and 9–10% realistic in produc-

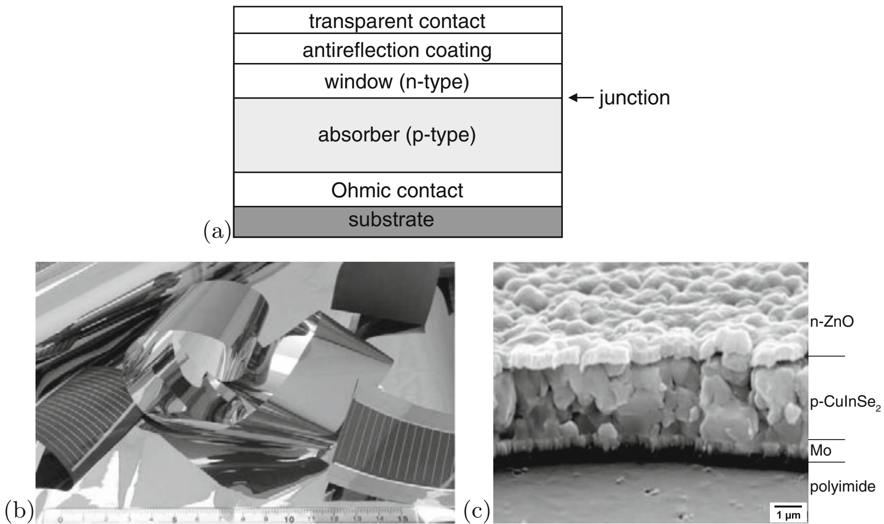

Fig. 21.62. (**a**) Schematic cross section of a polycrystalline thin-film solar cell. (**b**) Rolled sheets of CIS thin film solar cell on flexible Kapton foil. (**c**) SEM cross section of CIS thin-film solar cell. Parts (**b**) and (**c**) reprinted with permission from [1275]

tion. Thin-film solar cells can be fabricated on glass substrate or on flexible polymer substrate such as Kapton[9] (Fig. 21.62a,b). Also here, optimization of the grain size is important (Fig. 21.62b). As the front contact, a transparent conductive oxide (TCO), such as ITO ($InSnO_2$) or ZnO:Al, is used. If the front surface is given by the glass substrate, as can be the case for CdTe/glass solar cells, the glass is actually termed 'superstrate'. Thin-film and amorphous silicon solar cells are also termed 'second-generation' photovoltaics. Also organic materials can be used for solar cells [1270], promising low-cost production at acceptable performance, in 2004 2.5% [1271] and in 2006 about 4% maximum efficiency [1272].

Third Generation Photovoltaics

'Third-generation' photovoltaics attempt to go beyond the 30% limit and comprise of multijunction solar cells, concentration of sunlight, use of hot-carrier excess energy as discussed above and possibly other concepts including photon conversion [1274, 1275], intermediate band absorption [1276, 1278], multi-exciton generation [1279] or the use of quantum dots [1280].

In multijunction cells the different absorber layers are stacked on the substrate with increasing band gap and connected via (highly doped) tunneling junctions (Sect. 20.5.9). Under 500-fold AM1.5 illumination a three junction (3J) cell (GaInP/GaInAs/Ge) is expected to exhibit up to 41% efficiency, for

[9]Kapton® is a polyimide and a product and registered trademark of DuPont.

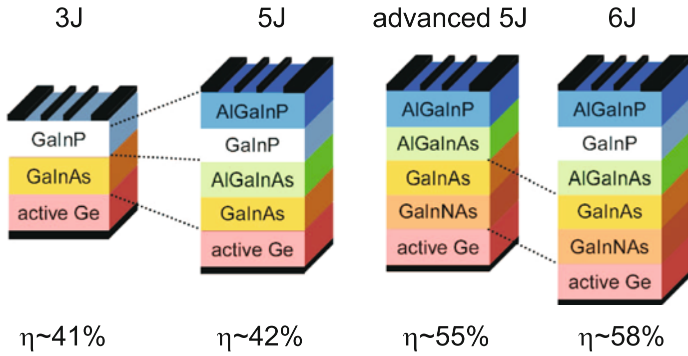

Fig. 21.63. Schematic layer stacking of multijunction solar cells and expected efficiency. Adapted from [1281]

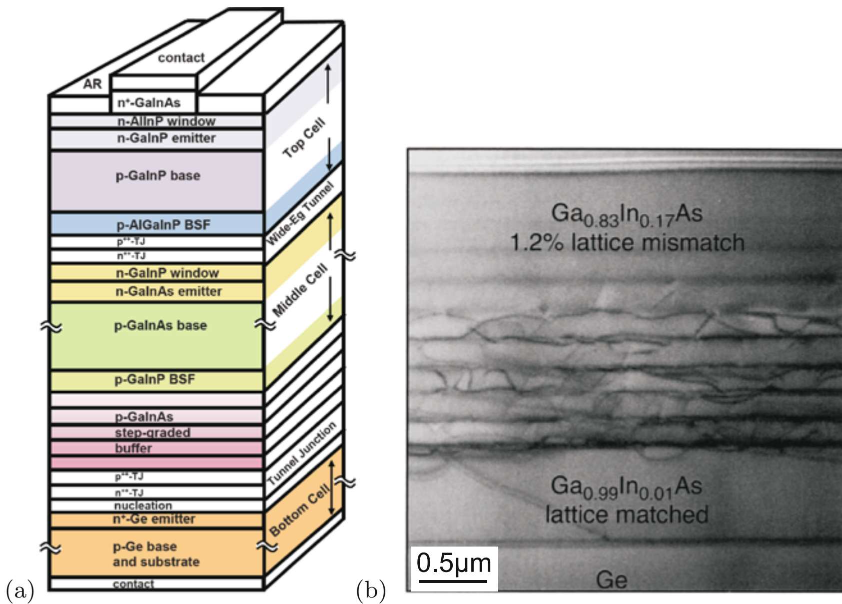

Fig. 21.64. (**a**) Schematic layer stacking of three-junction (3J) solar cell. The step-graded buffer (metamorphic buffer) changes the in-plane lattice constant for the following layers. Adapted from [1284]. (**b**) Cross-section TEM image of metamorphic InGaAs buffer on Ge. Adapted from [1285]

5J 42% or up to 55% using GaInNAs and with 6J up to 59% [1281, 1282] (Fig. 21.63). For a 3J cell the record efficiency is 40.7% (240 suns) using the layer structure as shown in Fig. 21.64 [1268]. Details on modeling of III–V multijunction solar cells can be found in [1283]. In a monolithic cell the absorbers must be tuned such that the same current (Kirchhoff's law) can pass

through all layers. Multijunction solar cells are heteroepitaxial devices and thus expensive; the use of concentration is economically mandatory.

21.4.7 Commercial Issues

The cost[10] of producing photovoltaic (PV) modules, in constant dollars, has fallen from as much as $50 per peak watt in 1980 to as little as $3 per peak watt in 2004. A projected cost of 0.2 €/kWh in 2020, a third of the current cost, is realistic and competitive in many applications. In 2002, photovoltaic power of 560 MW was installed worldwide. By the end of 2003, a total photovoltaic power of about 350 MW was installed in Germany. Thus, the PV power is 0.33% of the total installed electric power of 106 GW in Germany. The current market growth of 30% (worldwide) is driven by crystalline silicon cells (95% in 2002).

The energy payback period is also dropping rapidly. For example, it takes today's typical crystalline silicon module about 4 years to generate more energy than went into making the module in the first place. The next generation of silicon modules, which will employ a different grade of silicon and use thinner layers of semiconductor material, will have an energy payback of about 2 years. And thin-film modules will soon bring the payback down to one year or less. However, market growth of thin-film modules is currently slow. This means that these modules will produce 'free' and clean energy for the remaining 29 years of their expected life.

PV technology can meet electricity demand on any scale. The solar energy resource in a 100 mile-square area of Nevada could supply the United States with all its electricity (about 800 GW), using modestly efficient (10%) commercial PV modules. A more realistic scenario involves distributing these same PV systems throughout the 50 states. Currently available sites, such as vacant land, parking lots, and rooftops, could be used. The land requirement to produce 800 GW would average out to be about 17×17 miles per state. Alternatively, PV systems built in the 'brownfields', the estimated 5 million acres of abandoned industrial sites in the US, could supply 90% of America's current electricity. Solar power is expected to contribute 10% of the US energy need in 2030. For Germany, more than 2% in 2020 is probable.

In 2001, PV module shipments in the US approached the 400 MW mark, representing a $2.5 to $3 billion market. The US-based industry itself is now approaching $1 billion per year and provides 25,000 jobs. It is expected to grow to the $10–$15 billion level in the next 20 years, providing 3,00,000 jobs by 2025.

[10]The following information is taken from [1286] and [1287].

22 Electricity-to-Light Conversion

22.1 Radiometric and Photometric Quantities

22.1.1 Radiometric Quantities

The radiometric quantities are derived from the radiant flux (power) Φ_{e} (or usually simply Φ) that is the total power (energy per time) emitted by a source, measured in Watts. The radiant intensity I_{e} is the radiant flux emitted by a point source into a solid angle,[1] measured in Watts per steradian (or W/sr). The irradiance E_{e} is the radiant flux per area incident on a given plane, measured in $\mathrm{W/m^2}$. The radiance L_{e} is the radiant flux per area and solid angle as, e.g., emitted by an extended source, measured in $\mathrm{W/(m^2\,sr)}$.

22.1.2 Photometric Quantities

The photometric quantities are related to the visual impression and are derived from the radiometric quantities by weighting them with the $V(\lambda)$ curve.

The luminous flux (luminosity or visible brightness) Φ_{v} of a source with the radiant flux (spectral power distribution) $\Phi(\lambda)$ is given by

$$\Phi_{\mathrm{v}} = K_{\mathrm{m}} \int_0^\infty \Phi(\lambda) V(\lambda) \mathrm{d}\lambda \,, \tag{22.1}$$

with $K_{\mathrm{m}} = 683\,\mathrm{lm/W}$. This formula is also the definition of the unit 'lumen'. In Fig. 22.1b, the conversion function[2] $V(\lambda)$ is shown for light and dark adapted vision.[3]

[1] A solid angle Ω is the ratio of the spherical surface area A and the square of the sphere's radius r, i.e. $\Omega = A/r^2$.

[2] The $V(\lambda)$ curve has been experimentally determined by letting several observers adjust (decrease) the perceived brightness of a monochromatic light source at 555 nm to that of light sources of the same absolute radiation power at other wavelengths with so-called heterochromatic flicker photometry. The 'relative sensitivity curve for the CIE Standard Observer' was determined in 1924. The 'standard observer' is neither a real observer nor an average human observer. The curve has shortcomings, e.g., due to the used spectral band width (20–30 nm) of the light sources and the comparison of spectral power instead of the photon flux.

[3] While photopic vision is due to cones, the scotopic (dark-adapted) vision is due to rods. Rods are more than one thousand times as sensitive as the cones and

M. Grundmann, *The Physics of Semiconductors*, 2nd ed., Graduate Texts in Physics, DOI 10.1007/978-3-642-13884-3_22,

© Springer-Verlag Berlin Heidelberg 2010

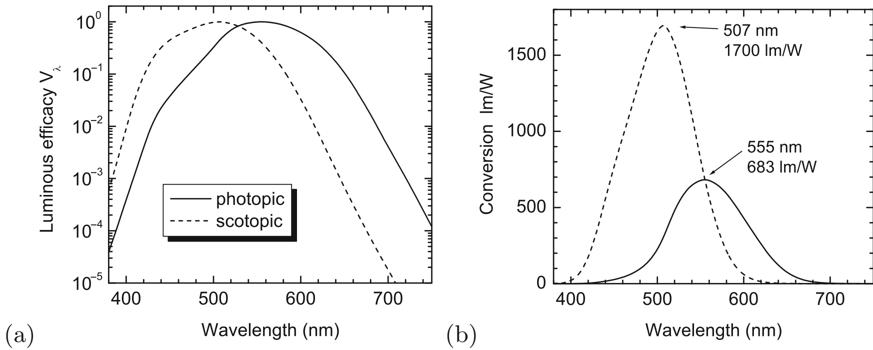

Fig. 22.1. (**a**) Relative eye sensitivity curves for photopic (light adapted, *solid line*) and (dark adapted, *dashed line*) vision. (**b**) Conversion of lumen to Watt for light- and dark-adapted vision

Further derived photometric quantities are luminous intensity (luminous flux per solid angle), measured in candela (cd), the illuminance (luminous flux per area), measured in lux (lx), and the luminance (luminous flux per area and solid angle). The latter is particularly important if the radiation enters an optical system, e.g. for refocusing. The radiometric and photometric quantities are summarized in Table 22.1.

Table 22.1. Radiometric and photometric quantities and units. The photometric units are lumen (lm), lux (lx=lm/m^2) and candela (cd=lm/sr)

Radiometric			Photometric		
quantity	symbol	unit	quantity	symbol	unit
radiant flux	Φ_e	W	luminous flux	Φ_v	lm
radiant intensity	I_e	W/sr	luminous intensity	I_v	cd
irradiance	E_e	W/m^2	illuminance	E_v	lx
radiance	L_e	W/m^2/sr	luminance	L_v	lm/m^2/sr

22.2 Scintillators

A scintillator (or phosphor) is a material that converts impacting high-energy radiation into photons [1288]. Besides a high conversion efficiency, the spectrum and decay time constant of the scintillator are important for display applications. For display purposes, the photons are directly used for forming

can reportedly be triggered by individual photons under optimal conditions. Rods predominate in the peripheral vision and are not color sensitive.

the image for the observer. For radiation detection, the photons are fed to a photomultiplier tube and counted.

The most prominent applications, involving the conversion of electrons, are the screens of cathode ray tubes (CRT) (acceleration voltage $> 10\,\mathrm{kV}$) and of flat panel devices, such as field-effect displays (using a low voltage for excitation, typically $< 1\,\mathrm{kV}$) or plasma displays (using the UV light from the discharge of a plasma placed between two electrodes for excitation). Further details on electroluminescent displays can be found in [1289]. Other forms of radiation detected with scintillators are α-, β-, and γ-radiation, X-rays and neutrons [1290]. Different excitation conditions require different phosphors for optimal performance.

22.2.1 CIE Chromaticity Diagram

The CIE[4] procedure converts the spectral power distribution (SPD) of light from an object into a brightness parameter Y and two chromaticity coordinates x and y. The chromaticity coordinates map the color[5] with respect to hue and saturation on the two-dimensional CIE chromaticity diagram. The procedure for obtaining the chromaticity coordinates for a given colored object involves determination of its spectral power distribution $P(\lambda)$ at each wavelength, multiplication by each of the three color-matching functions $\bar{x}(\lambda)$, $\bar{y}(\lambda)$, and $\bar{z}(\lambda)$ (Fig. 22.2a) and integration (or summation) of the three tristimulus values X, Y, Z

$$X = \int_{380\,\mathrm{nm}}^{780\,\mathrm{nm}} P(\lambda)\bar{x}(\lambda)\mathrm{d}\lambda \tag{22.2a}$$

$$Y = \int_{380\,\mathrm{nm}}^{780\,\mathrm{nm}} P(\lambda)\bar{y}(\lambda)\mathrm{d}\lambda \tag{22.2b}$$

$$Z = \int_{380\,\mathrm{nm}}^{780\,\mathrm{nm}} P(\lambda)\bar{z}(\lambda)\mathrm{d}\lambda\ . \tag{22.2c}$$

Y gives the brightness. The tristimulus values are normalized to yield the chromaticity coordinates, e.g. $x = X/(X+Y+Z)$. x and y obtained in this way are the chromaticity coordinates. The third coordinate $z = 1 - x - y$

[4]Commission Internationale de l'Éclairage. The color space can be described by different coordinate systems, and the three most widely used color systems, Munsell, Ostwald, and CIE, describe the color space with different parameters. The Munsell system uses hue, value, and chroma and the Ostwald system uses dominant wavelength, purity, and luminance. The more precise CIE system uses a parameter Y to measure brightness and parameters x and y to specify the chromaticity that covers the properties hue and saturation on a two-dimensional chromaticity diagram.

[5]This definition is motivated by the color vision of the eye. Two light sources will have the same color, even if they have different SPDs, when they evoke the same color impression to the human eye.

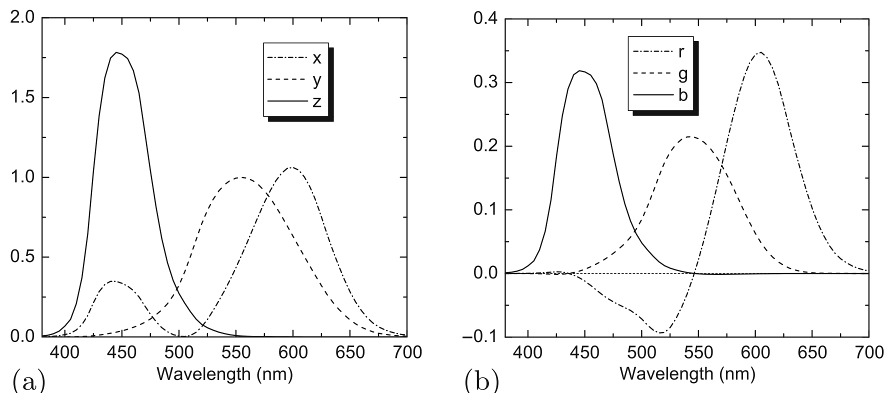

Fig. 22.2. (**a**) Color-matching functions $\bar{x}$, $\bar{y}$, and $\bar{z}$ for the calculation of the CIE chromaticity, (**b**) color-matching functions $\bar{r}$, $\bar{g}$, and $\bar{b}$ for the calculation of RGB values

offers no additional information and is redundant. Therefore, the color is represented in a two-dimensional diagram, the CIE chromaticity diagram[6] as shown in Fig. 22.3a. White is represented by $x = y = z = 1/3$. In order to relate the differences between colors as perceived by the human eye more closely to the geometrical distance in the chart, a revision was made (Fig. 22.3b) with new coordinates

$$u' = 4x/(-2x + 12y + 3) \tag{22.3a}$$

$$v' = 9y/(-2x + 12y + 3) \; . \tag{22.3b}$$

For CRTs the red-green-blue (RGB) color space is used.[7] The color matching functions for RGB values are shown in Fig. 22.2b. The RGB values are related to the XYZ values according to

$$\begin{pmatrix} R \\ G \\ B \end{pmatrix} = \begin{pmatrix} 2.36461 & -0.89654 & -0.46807 \\ -0.51517 & 1.42641 & 0.08876 \\ 0.00520 & -0.01441 & 1.00920 \end{pmatrix} \begin{pmatrix} X \\ Y \\ Z \end{pmatrix} \; . \tag{22.4}$$

[6]The coloring of the chart is provided for an understanding of color relationships. CRT monitors and printed materials cannot reproduce the full gamut of the color spectrum as perceived in human vision. The color areas that are shown only depict rough categories and are not precise statements of color.

[7]RGB is an additive color system. However, printing devices use a subtractive color system. This means that the ink absorbs a particular color, and the visible impression stems from what is reflected (not absorbed). When inks are combined, they absorb a combination of colors, and hence the reflected colors are reduced, or subtracted. The subtractive primaries are cyan, magenta and yellow (CMY) and are related to RGB via $(C, M, Y) = (1 - R, 1 - G, 1 - B)$.

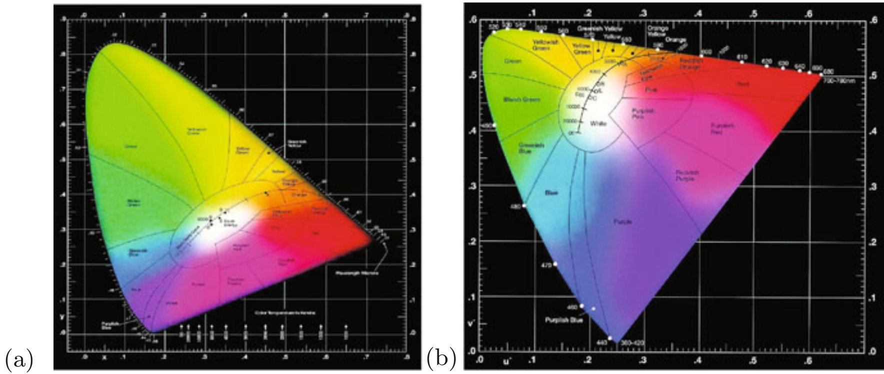

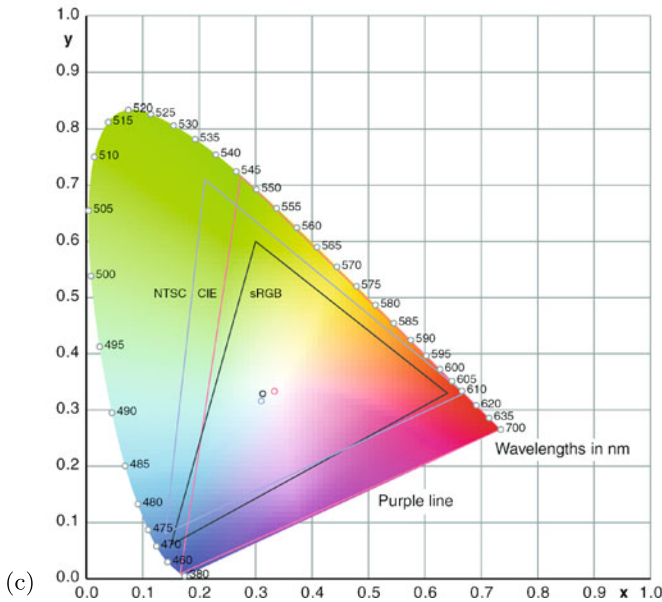

Fig. 22.3. CIE chromaticity diagram from 1931 (**a**) in the coordinates x and y and from 1976 (**b**) in the coordinates u' and v' (22.3b). The curved upper boundary is called the 'spectrum locus' and contains monochromatic colors, the straight line at the lower left is termed the 'purple boundary'. In the graph also the color of blackbody radiation is given, $T = 5440\,\text{K}$ corresponds to $x = y = 1/3$. 'A', 'B', 'C', and 'E' are standard illuminants, 'D65' denotes daylight with color temperature $T = 6500\,\text{K}$. (**c**) CIE chart with the color ranges of sRGB, CIE and NTSC. Part (**c**) adapted from [1291]

The CIE RGB primaries from 1931 are at 700, 546.1, and 435.8 nm with the relative intensities 1.0, 4.5907, and 0.0601. A display device using three phosphors can only display colors in the triangular area of the CIE chart

Table 22.2. Primaries and white points for sRGB, CIE and NTSC

primary	red		green		blue		white	
CIE	0.73467	0.26533	0.27376	0.71741	0.16658	0.00886	0.33333	0.33333
NTSC	0.6700	0.3300	0.2100	0.7100	0.1400	0.0800	0.3100	0.3160
sRGB	0.6400	0.3300	0.3000	0.6000	0.1500	0.0600	0.3127	0.3290

between the three chromaticity coordinates. For sRGB[8], the 1931 CIE primaries and the NTSC[9] norm the coordinates are given in Table 22.2 and visualized in Fig. 22.3c. An optimal coverage of the CIE chart involves monochromatic sources (for laser TV or LED displays) at about 680, 520 and 440 nm.

22.2.2 Display Applications

The once ubiquitous amber-colored monochrome displays are mostly fabricated using ZnS:Mn [1289], having broad emission (540–680 nm) with its spectral peak at 585 nm ($x = 0.50$, $y = 0.50$) with an efficiency of 2–4 lm/W. In color television (and similar applications such as color computer monitors, tubes for aviation use, projection television) the image is reproduced by selective and time-multiplexed cathode excitation of three phosphors (blue, green and red) deposited on the internal face of the screen. The chromaticity coordinates of the standard CRT phosphors P-22B, P-22G and P-22R are given in Table 22.3. They cover about the color range labeled 'sRGB' in Fig. 22.3c. For blue and green ZnS:Ag ($x = 0.157$, $y = 0.069$), ZnS:Ag,Cl, ZnS:Ag,Al and ZnS:Cu,Al ($x = 0.312$, $y = 0.597$), ZnS:Cu,Au,Al are used as phosphors, respectively. Y_2O_2S:Eu ($x = 0.624$, $y = 0.337$) activated with trivalent europium (Eu^{3+}) facilitated such a gain in the brilliance of red over ZnS:Ag (more than doubled it) that it has totally replaced it at about one fifth of the cost. For reproducible image quality, precise grain-size control (median size for CRT phosphors is about 8 µm), dispersion control and surface treatment

Table 22.3. CIE color coordinates, peak emission wavelength and decay time (10%) of standard CRT phosphors

phosphor	x	y	λ_p (nm)	decay time
P-22B	0.148	0.062	440	∼20 µs
P-22G	0.310	0.594	540	∼60 µs
P-22R	0.661	0.332	625	1 ms

[8]Standard RGB color space as defined mainly by Hewlett-Packard and Microsoft, almost identical to PAL/SECAM European television phosphors.

[9]National television standard colors, US norm.

are necessary. Flat-panel displays with their lower excitation voltage require different phosphors for optimal efficiency.

22.2.3 Radiation Detection

The most commonly used scintillation detector for alpha measurements is ZnS activated with silver, ZnS:Ag. This material is not very transparent to light and is usually prepared as a large number of crystals with sub-mm size attached with an adhesive to a flat piece of plastic or other material. The flat screen is optically coupled to a photomultiplier tube that is attached to associated electronics. The voltage and discriminator levels are selected so that the detector is sensitive to the rather large pulses from alpha interactions but insensitive to beta- or gamma-induced pulses. The alpha particles deposit all of their energies in a small thickness of material compared to beta and gamma radiations.

Scintillation detectors for beta radiation are often made from organic materials. In an organic scintillator, the light emission occurs as a result of fluorescence when a molecule relaxes from an excited level following excitation by energy absorption from ionizing radiation. Molecules such as anthracene, trans-stilbene, para-terphenyl, and phenyl oxazole derivatives are among the many organic species that have useful scintillation properties. The organic molecules are dissolved in organic solvents and used as liquid scintillators. A classic application is in the measurement of low-energy beta radiation from, e.g. tritium, ^{14}C, or ^{35}S. In such cases, the sample containing the radioactive beta emitter is dissolved in, or in some cases suspended in, the liquid scintillation solution. The emitted beta radiation transfers energy through the solvent to the scintillator molecule that emits light, subsequently detected by photomultiplier tubes. Organic scintillator molecules can also be dissolved in an organic monomer that can then be polymerized to produce a plastic scintillator in a wide variety of shapes and sizes. Very thin scintillators have been used for alpha detection, somewhat thicker scintillators for beta detection. Large-volume plastic scintillators have been used in gamma detection, particularly for dose-related measurements.

Other inorganic crystalline scintillators, especially sodium iodide activated with thallium, NaI:Tl, have been used for gamma-ray energy measurements. Such detectors can be grown as large single crystals that have a reasonably high efficiency for absorbing all of the energy from incident gamma rays. There exists a rather large number of inorganic scintillators; some examples of these include cesium iodide activated with thallium, CsI:Tl, bismuth germanate, $Bi_4Ge_3O_{12}$, and barium fluoride, BaF_2. These are mostly used for gamma measurements but can also be prepared with thin windows and have been used for charged particle (e.g. alpha and beta) counting. A number of scintillator materials including tungstates like $CdWO_4$ has been reviewed in [1292].

Table 22.4. Emission peak wavelength and decay time of various scintillator materials

material	λ_p (nm)	decay time
Zn_2SiO_4:Mn	525	24 ms
ZnS:Cu	543	35–100 µs
$CdWO_4$	475	5 µs
CsI:Tl	540	1 µs
CsI:Na	425	630 ns
$Y_3Al_5O_{12}$:Ce	550	65 ns
Lu_2SiO_5:Ce	400	40 ns
$YAlO_3$:Ce	365	30 ns
ZnO:Ga	385	2 ns

In Table 22.4, the peak emission wavelength and the characteristic decay time are listed for a variety of scintillator materials. Direct semiconductors, although not offering the highest efficiency, are particularly useful for high time resolution in, e.g., time-of-flight measurements or fast scanning electron microscopy.

22.2.4 Luminescence Mechanisms

Self-trapped Excitons

In a strongly ionic crystal, such as NaI, a hole becomes localized to an atomic site via the polaron effect. A spatially diffuse electron is attracted, and a self-trapped exciton is formed that can recombine radiatively.

Self-activated Scintillator

In such material, the luminescent species is a constituent of the crystal. The emission involves an intraionic transition, e.g. 6p→6s in Bi^{3+} of $Bi_4Ge_3O_{12}$, or a charge-transfer transition in the case of $(WO_4)^{2-}$ in $CaWO_4$. At room temperature, nonradiative competing processes limit the efficiency.

Activator Ions

For dopant ions such as Eu^{2+} in YO_2S:Eu, Ce^{3+} in $YAlO_3$:Ce or Tl^+ in NaI:Tl, the hole and electron excited by the radiation are sequentially trapped by the same ion that then undergoes a radiative transition, in the case of Eu and Ce[10] 5d→4f, for Tl $^3P_{0,1} \rightarrow S_0$. CsI:Tl has one of the highest efficiencies of 64.8 photons/keV [1293].

[10] This transition is dipole allowed for Ce and partially forbidden for Eu.

Core–Valence Luminescence

In some materials, e.g., BaF_2, CsF, $BaLu_2F_8$ the energy gap between the valence band and the top core band is less than the fundamental band gap. A radiative transition occurs when an electron from the valence band fills a hole in the top core band that has been created by the radiation. The light yield is limited to about 2 photons/keV.

Semiconductor Recombination Processes

Free excitons or excitons bound to impurities can recombine radiatively. This process is most efficient at low temperatures. At room temperature, the emission is typically much weaker ($\gtrsim 10\times$) since excitons become unbound or dissociated. Highly doped n-type semiconductors, e.g. CdS:In, exhibit recombination between donor-band electrons and holes. ZnO:Ga has an efficiency of about 15 photons/keV and a fast response (with 2.4 photons/keV emitted in the first 100 ps). Luminescence can also stem from donor–acceptor pair transitions, e.g. in PbI_2 with an efficiency of 3 photons/keV at 10 K. Isoelectronic impurities such as nitrogen in GaP:N and tellurium in CdS:Te attract an electron and subsequently a hole. In ZnS:Ag and ZnS:Cu (conduction) band to trap recombination is dominant. In a codoping scheme like CdS:In,Te, In supplies electrons in an impurity band that can recombine with holes trapped at Te.

22.3 Light-Emitting Diodes

22.3.1 Introduction

Light-emitting diodes (LEDs) are semiconductor devices in which injected carriers recombine radiatively. The recombination process leading to light emission can be of intrinsic nature, i.e. band–band recombination, or extrinsic, e.g. impurity-bound excitons. Impurity-related luminescence can also be excited via impact excitation. For an extensive treatment of LEDs see [1294], for a review of the early field [1295] and for recent reviews [1296, 1297]. Mostly LEDs are pn-diodes although also some MIS-based devices have been reported [1298, 1299].

22.3.2 Spectral Ranges

Applications for LEDs can be sorted by the color of emission. In Fig. 22.4, the standard sensitivity $V(\lambda)$ of the human eye is shown (see Fig. 22.1a). In the visible spectral region (about 400–750 nm) the perceived brightness of the LED depends on the eye sensitivity. It is largest in the green (at 555 nm) and drops strongly towards the red and blue.

Fig. 22.4. Spectral coverage by various semiconductor materials. Reprinted with permission from [384], ©1981 Wiley

The most important spectral regions and applications are:

- infrared ($\lambda > 800$ nm): remote controls, optocouplers, low-cost data transmission, IR interface
- visible: indicator LED, lighting[11] (room, buildings, cars), white LED for broad spectrum
- ultraviolet ($\lambda < 400$ nm): pumping of phosphors for white LEDs, biotechnology

In Fig. 22.4, potentially useful semiconductors for the various spectral regions are shown. The semiconductors that are currently used for the various colors of the visible spectrum are

- red–yellow: GaAsP/GaAs, now AlInGaP/GaP
- yellow–green: GaAsP:N, GaP:N
- green–blue: SiC, now GaN, InGaN
- violet: GaN
- ultraviolet: AlGaN

22.3.3 Quantum Efficiency

The *external* (or total) quantum efficiency η_{ext} is the number of photons emitted from the device per injected electron–hole pair. It is given by the product of the *internal* quantum efficiency η_{int} and the light extraction efficiency χ_{ex}:

[11] Penetration of white LEDs into the general lighting market could translate (globally) into cost savings of \$ 10^{11} or a reduction of power generation capacity of 120 GW.

$$\eta_{\text{ext}} = \chi_{\text{ex}}\, \eta_{\text{int}} \ . \tag{22.5}$$

The internal quantum efficiency is the number of photons generated (inside the semiconductor) per injected electron–hole pair. High material quality, low defect density and low trap concentration are important for a large value of η_{int}. The recombination current in the pn-diode has been already given in (20.117). The light extraction efficiency is ratio of the number of photons leaving the device and the total number of generated photons. The geometry of the LED is of prime importance to optimize χ_{ex}.

Due to the large index of refraction of the semiconductors ($n_{\text{s}} \sim 2.5$–3.5), light can leave the semiconductor only under a small angle θ_{c} from the surface normal due to total reflection (cf. (9.3) and see right part of Fig. 9.2). Against air ($n_1 \approx 1$) the critical angle is

$$\theta_{\text{c}} = \sin^{-1}(1/n_{\text{s}}) \ . \tag{22.6}$$

The critical angle for total reflection is 16° for GaAs and 17° for GaP. Additionally, a portion of the photons that do not suffer total reflection is reflected back from the surface with the reflectance R given by (cf. (9.7))

$$R = \left(\frac{n_{\text{s}} - 1}{n_{\text{s}} + 1}\right)^2 \ . \tag{22.7}$$

We note that the above formula is valid strictly for vertical incidence. For the GaAs/air interface, the surface reflectance (for normal incidence) is about 30%. Thus, the light extraction efficiency for a LED is given by (1–R) and the critical angle by

$$\chi_{\text{ex}} \cong \frac{4 n_1 n_{\text{s}}}{(n_1 + n_{\text{s}})^2}\,(1 - \cos\theta_{\text{c}}) \approx \frac{4 n_{\text{s}}}{(n_{\text{s}} + 1)^2}\,(1 - \cos\theta_{\text{c}}) \ . \tag{22.8}$$

The latter approximation is valid when the outer medium is air. For GaAs, the light extraction efficiency is $0.7 \times 4\% \approx 2.7\%$. Thus, typically only a small fraction of generated photons can leave the device and contribute to the LED emission.

22.3.4 Device Design

In the following subsections the strategies that have allowed significant improvement of the extraction efficiency (Fig. 22.5) and thus LED performance are briefly discussed.

Nonplanar Surfaces

With curved surfaces, the problem of total reflection can be (partially) circumvented (Fig. 22.6). Spherically polished chips are feasible, but, very expensive. The epoxy seal of the standard LED case (Fig.22.7a) and its shape play a similar role, however, with a smaller index of refraction than the semiconductor, and are important for the beam shape.

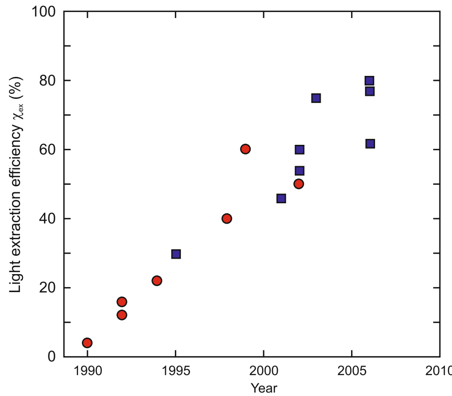

Fig. 22.5. Historic development of maximum light extraction efficiency for AlGaInP (*red circles*) and InGaN (*blue squares*) LEDs. Adapted from [1297]

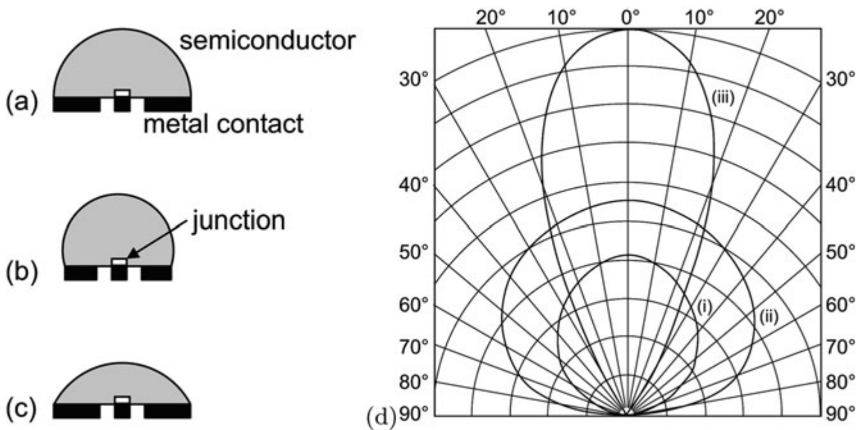

Fig. 22.6. Form of various LED casings with (**a**) hemispherical, (**b**) truncated sphere and (**c**) parabolic geometry. Adapted from [1300]. (**d**) Emission characteristics for rectangular (**i**), hemispheric (**ii**) and parabolic (**iii**) geometry. Adapted from [1301]

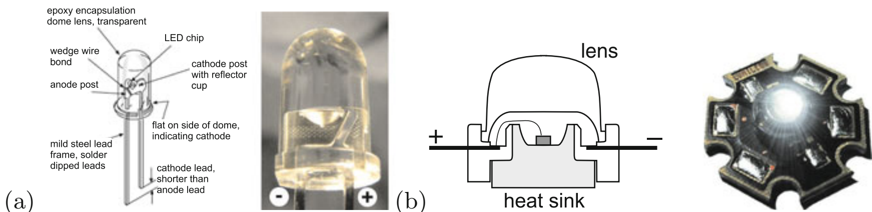

Fig. 22.7. (**a**) Standard LED casing (schematic drawing and macrophoto), (**b**) high-power mounting (schematic drawing and image of Luxeon® LED)

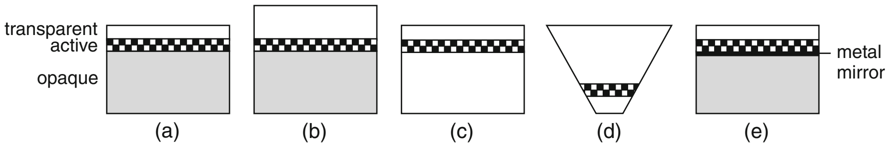

Fig. 22.8. (**a**) Standard LED layer sequence with opaque substrate (*grey*), active layer (*checkered*) and transparent top, (**b**) thick window design with thick top layer (50–70 µm). (**c**) Transparent substrate (by rebonding, see Fig. 22.9, (**d**) chip shaping (cf. also Fig. 22.11). (**e**) Thin-film LED with metal mirror (*black*) and rebonding (cf. also Fig. 22.12)

Thick-Window Chip Geometry

An increase in light extraction efficiency to about 10–12% can be achieved if the top layer is fabricated with a much larger thickness (Fig. 22.8b) of 50–70 µm instead of a few µm. However, such approach is not scalable since larger device area would demand even larger thickness.

Transparent Substrate

Reflection of photons is not so detrimental if they are not lost later due to absorption in the substrate. In Fig. 22.8, the evolution of LED chip design is shown schematically. In Fig. 22.9, the light path is compared for opaque and transparent substrates. The latter provides higher light extraction efficiency due to the 'photon recycling' effect. Efficiencies of 20–25% are possible. In Fig. 22.10, the technological steps are shown to fabricate a GaP LED with an AlGaInP active layer. The active layer is initially grown on GaAs due to lattice-match conditions.

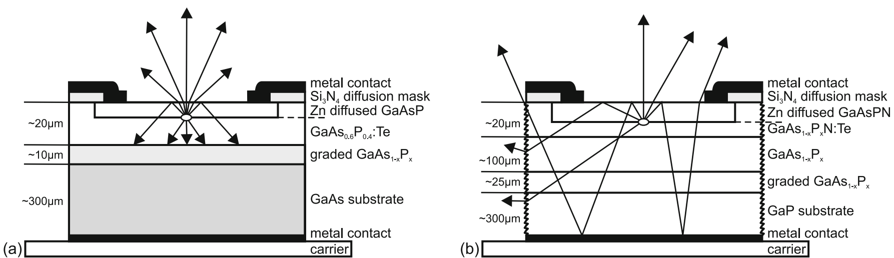

Fig. 22.9. Comparison of light paths in a GaAsP-based LED with (**a**) opaque (GaAs) and (**b**) transparent (GaP) substrate (side facets roughened). Adapted from [1302]

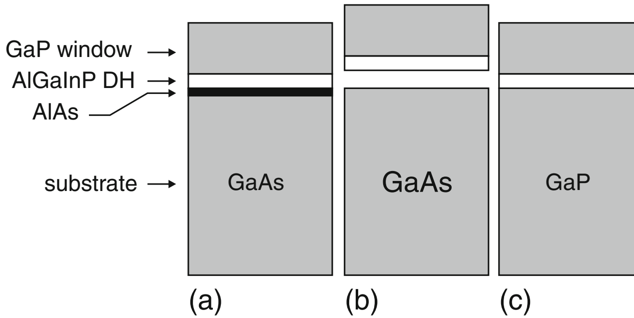

Fig. 22.10. Scheme of fabrication for red high brightness LED: (**a**) AlGaInP double heterostructure (DH) with GaP window on GaAs substrate (growth with MOCVD). (**b**) Lift-off using HF etch of sacrificial AlAs layer. (**c**) Wafer bonding on GaP (transparent for red light)

Nonrectangular Chip Geometry

If the chip is made with an inverted structure and mounted on a mirror, a high light extraction efficiency ($> 50\%$) can be achieved. Typical commercial designs are shown in Fig. 22.11.

The increase in quantum efficiency allows the devices to run on much higher output power. While initially LEDs delivered power only in the mW regime, now output power in the ~ 1 W regime is possible (high brightness LEDs). The higher currents made a redesign of the LED mount towards better heat sinks necessary (Fig. 22.7b). While the standard case has a thermal resistance of 220 K/W (chip size $(0.25\,\mathrm{mm})^2$ for 0.05–0.1 W and 0.2–2 lm), the high-power case has 15 K/W (chip size $(0.5\,\mathrm{mm})^2$ for 0.5–2 W and 10–100 lm). An epoxy-free technique for encapsulation also enhances the color uniformity and maintains the brightness.

Thin-Film LED

In the thin-film LED design [1303], as schematically shown in Fig. 22.12a, a metal mirror is evaporated on the LED layers. Subsequently, the metal side is wafer bonded to another metallized substrate and the original substrate is removed. Additionally, the LED surface can be patterned (before bonding) into an (hexagonal) array of (hexagonal) microprism mesas with an insulating (e.g. silicon nitride) layer with openings in order to optimize the current path. The microprisms are optimized to allow efficient reflection of light towards the emitting surface. This technology is scalable to large areas without loss in efficiency.

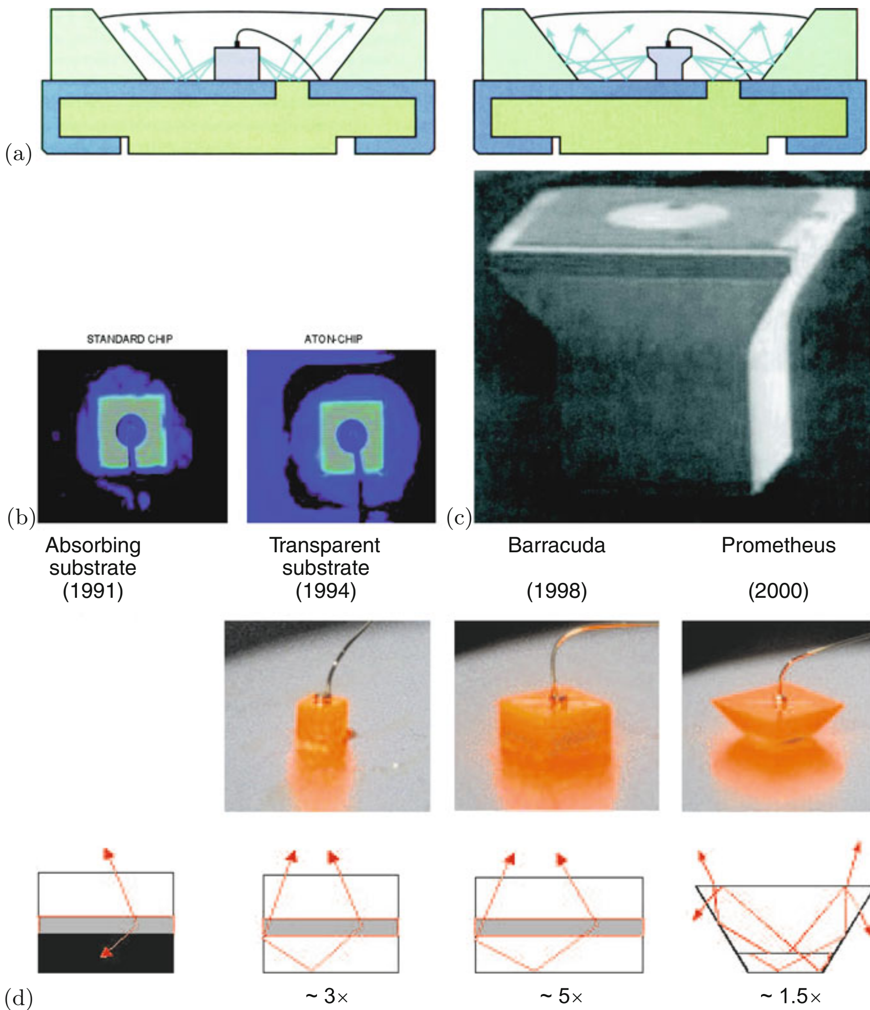

Fig. 22.11. Optimization of light exit by 3D design of the LED chip, (**a**) scheme, (**b**) emission pattern comparison and (**c**) SEM image of the ATON chip. Reprinted with permission from [1304]. (**d**) Development stages towards the truncated inverted pyramid (Prometheus) chip. From [1305]

Historic Development

In Fig. 22.13, the historic development of the LED luminous efficacy (luminous flux per electrical input power) is shown for various material systems. While the luminosity has increased by a factor of 20 per decade in the last 40 years, the price has decreased by a factor of ten per decade (Fig. 22.14). Currently, there is a need for the development of efficient LEDs in the green

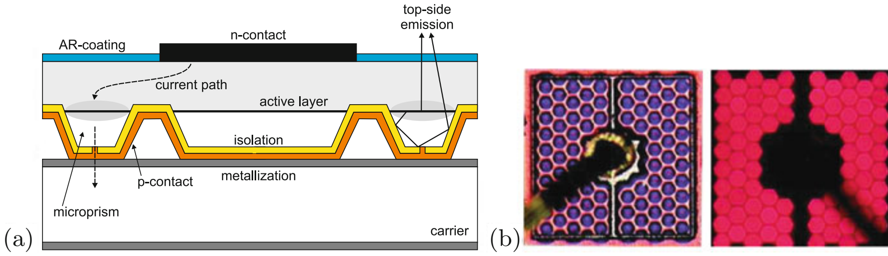

Fig. 22.12. (**a**) Scheme of thin-film LED with microprisms. (**b**) image and luminescence image of thin film AlInGaP LED (chip length: 320 µm). Reprinted with permission from [1306]

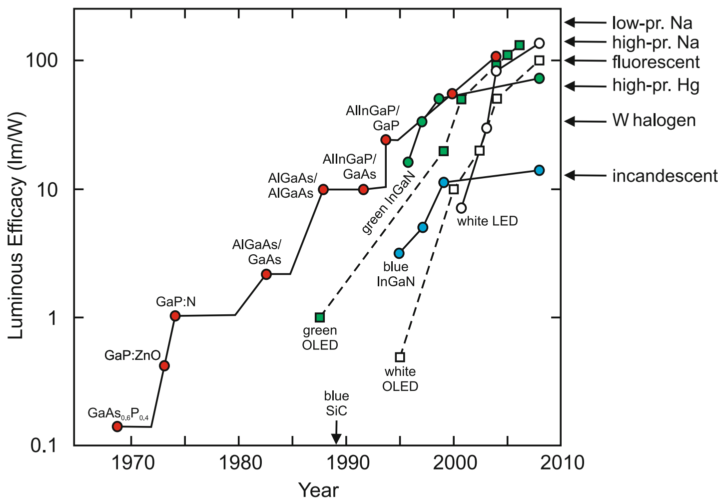

Fig. 22.13. Historic development of the luminous efficacy of semiconductor LEDs and OLEDs. Based on [1307] with the addition of data on OLEDs and recent data on LEDs. The arrows on the right indicate efficacy of various other light sources

spectral range since their luminosity is small compared to devices for the blue and red spectral regions (Fig. 22.15).

22.3.5 White LEDs

There are different possibilities to generate white light with an LED as shown schematically in Fig. 22.16. The highest color gamut and a tunable white point can be achieved by combining a red, a green and a blue LED (Fig. 22.16a). Using a blue LED and a yellow phosphor (Figs. 22.16b and 22.17a,b), a white spectrum can be achieved that is, however, not very close

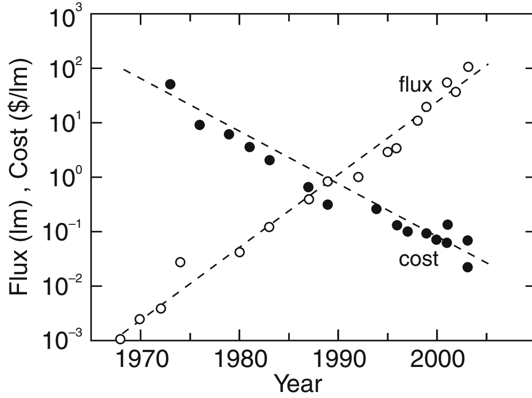

Fig. 22.14. Historic development of the flux (in lumen) and cost (in $/lm) for semiconductor LEDs. Data from [1305]

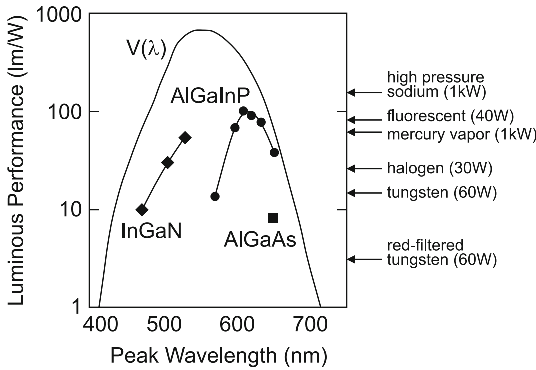

Fig. 22.15. Luminous performance of various LED materials in comparison with other light sources. Adapted from [1307]

to a blackbody spectrum (Fig. 22.17c). A better color rendering can be obtained with the combination of two phosphors [1308]. With an UV LED that is itself invisible (and must be shielded so no UV radiation leaves the LED), phosphors with various colors can be pumped (Fig. 22.16c). The mix of phosphors determines the white point.

Using a blue-emitting LED based on InGaN material, phosphors (similar to those used in fluorescence lamps) can be pumped. Blue light is converted into green, yellow or red light such that the resulting total spectrum appears white to the human eye. Also, a broad range of other colors can be designed (color on demand), e.g. pink or particular corporate colors.

The color of a white LED depends on the operation conditions. In Fig. 22.18a the intensity vs. dc driving current characteristic of a white LED is shown. In Fig. 22.18b the chromaticity coordinates are shown for various

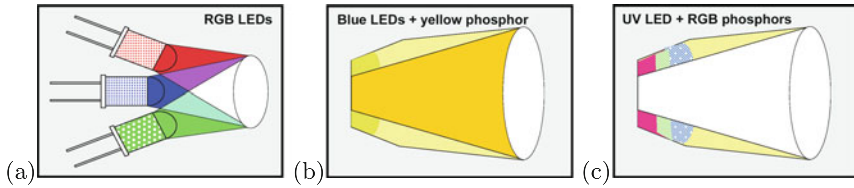

Fig. 22.16. Different strategies to generate white light with LEDs. (**a**) Addition of R, G, and B LEDs, (**b**) blue LED and yellow phosphor, (**c**) UV LED (invisible) and R, G, and B phosphors. From [1305]

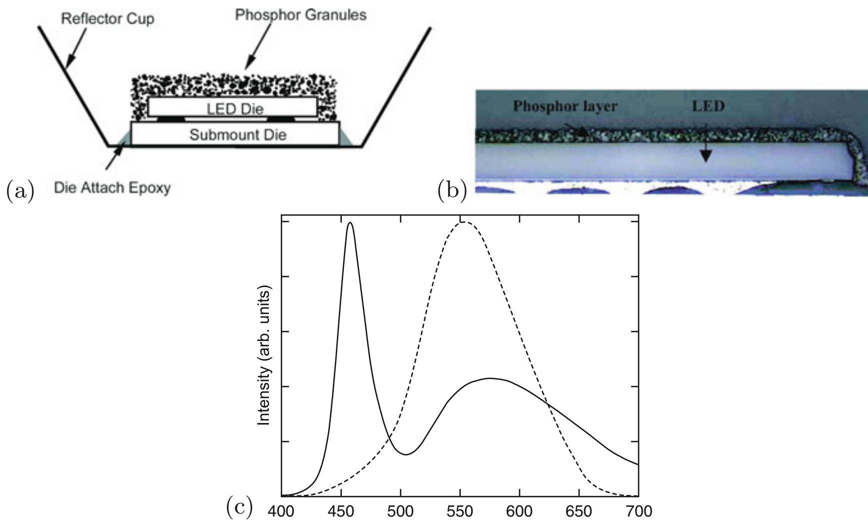

Fig. 22.17. (**a**) Scheme and (**b**) image of color conversion Luxeon® LED. From [1305]. (**c**) Spectrum (*solid line*) of white LED with blue LED pumping a yellow phosphor together with eye-sensitivity curve $V(\lambda)$ (*dashed line*). Adapted from [1306]

dc currents. In order to avoid this effect, the LED is driven with pulses of a fixed amplitude and a repetition frequency that is high enough to provide a flicker-free image to the human eye, e.g. 100 Hz. The intensity of the LED is modulated via the pulse width, i.e. between 0–10 ms in this case (PWM, pulsewidth modulation).

A major advantage of LEDs for display and lighting applications is their long lifetime compared to halogen (about 2000 h), xenon (10,000 h) or fluorescent (6000–10,000 h) lights. Philips Lumileds projects (for white LUXEON® K2 LEDs) 70% lumen maintenance at given current (1 A) at 50,000 h for junction temperature $T_{\mathrm{j}} \leq 120°$ [1309]. Similar values are given by OSRAM [1310] for white high power LEDs (Fig. 22.19).

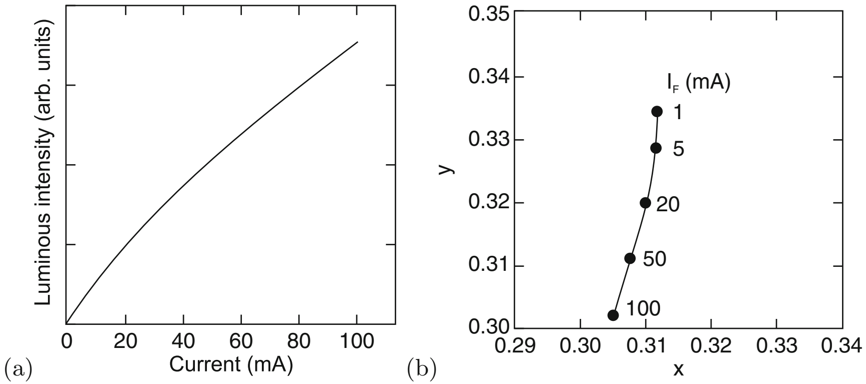

Fig. 22.18. (**a**) Luminous intensity of white LED (NSCW215) vs. dc forward current. (**b**) CIE chromaticity coordinates for various dc driving conditions as labeled. Data taken from [1311]

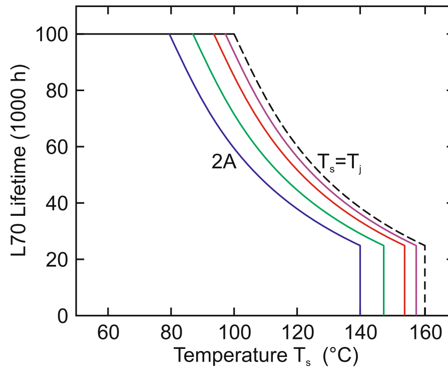

Fig. 22.19. Lifetime for 70% lumen as a function of solder temperature T_s (for white Diamond Dragon® LED) for various driving currents (0.3, 0.7, 1.4 and 2.0 A, *solid lines* from right to left). The *dashed line* is for low driving current and $T_\mathrm{s} = T_\mathrm{j}$. Adapted from [1310]

22.3.6 Quantum Dot LED

Quantum dots are an interesting active medium for LEDs due to their spectroscopic properties (Sect. 13.3.4).

Ultranarrow Spectral Emission

A LED based on a single QD exhibits a rather unique spectrum consisting of a single spectral line, at least at low temperatures [1312], due to exciton recombination as shown in Fig. 22.20. Such device can deliver single photons on demand and be a photon source for quantum cryptographic communication.

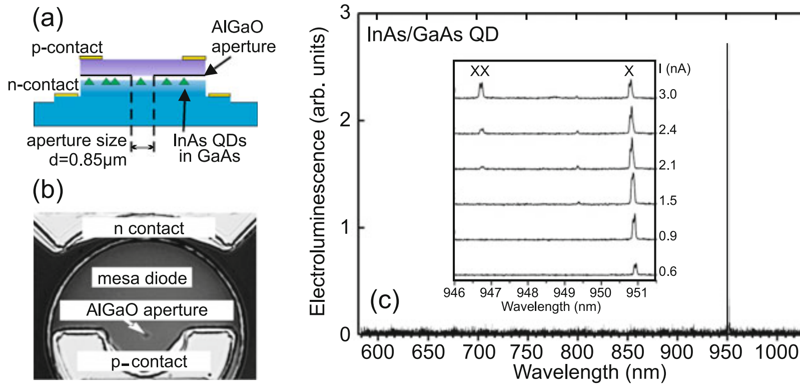

Fig. 22.20. (**a**) Schematic cross-section of QD LED. Current is fed to a single QD via an oxide aperture. (**b**) Plan-view SEM image of QD LED. (**c**) Electroluminescence (EL) spectrum ($T = 10\,\mathrm{K}$, $U = 1.65\,\mathrm{V}$, $I = 0.87\,\mathrm{nA}$) of single InGaAs/GaAs QD LED (diameter of oxide aperture 0.85 µm, thickness 60 nm). The single line is due to (neutral) exciton recombination. The *inset* shows dependence of EL spectrum on injection current; at higher currents a second peak due to biexciton recombination (XX→X) appears. Adapted from [1316]

At higher current also biexciton recombination appears. In [1313, 1314] the triggered emission of photon pairs from cascade-like XX and X recombination in a single dot and their polarization entanglement is reported. Entanglement is related to degenerate X and XX emission energy [1315] (cmp. Fig. 13.33).

Ultrabroad Spectral Emission

An LED based on the emission from a quantum dot ensemble exhibits a fairly broad spectrum because of inhomogeneous broadening due to size fluctuations of the quantum dots (cmp. Fig. 13.36). Additionally several ensembles of QDs with different mean emission wavelength can be incorporated in a device, e.g. in stacked layers [1317]. This way ultrabroad electroluminescence spectra can be realized (Fig. 22.21). Also emission on the ground and excited state can be used for broad spectral emission.

22.3.7 Organic LED

An organic light emitting diode (OLED) is made from organic semiconductors. The pioneering work was made by Tang and Van Slyke [1186, 1318]. Typical layer sequences are depicted in Fig. 20.55. The light emission occurs through the anode (and the transparent ITO layer) while the metal cathode is opaque. Two major configurations are possible, emission through the transparent substrate (glass) or top emission (Fig. 22.22).

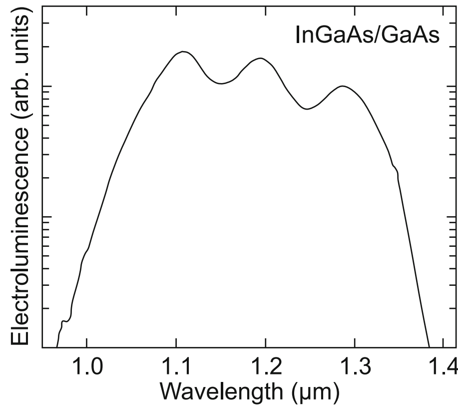

Fig. 22.21. Electroluminescence spectrum of a quantum dot LED designed for broad spectral range (at 5 kA/cm^2). Adapted from [1319]

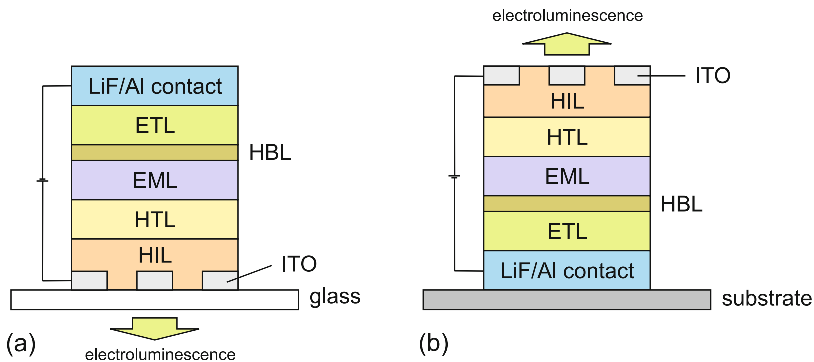

Fig. 22.22. Typical OLED design for (**a**) bottom and (**b**) top emission

The optimization of materials for the various functional layers is ongoing. The emission layer (EML) is optimized for efficient radiative recombination for the design wavelength or wavelength range. The highest efficacy of over 100 lm/W (Fig. 22.13) is achieved using phosphorescent materials (Sect. 16.5). The contacts are optimized for high carrier injection efficiency and the transport layers are optimized for high conductivity.

End of 2007 a transparent white OLED panel was introduced [1320] (Fig. 22.23a). Its transparency is 55% and shall be improved in the future. A crucial point is the protection of the organic films against moisture and air. The encapsulation by glass is very good. Flexible OLED panels with polymer substrate and encapsulation have been demonstrated (Fig. 22.23b). OLED technology is currently used for small displays in digital cameras and cellular phones. It enables very thin TV panels, only a few mm thick (Fig. 22.23c)

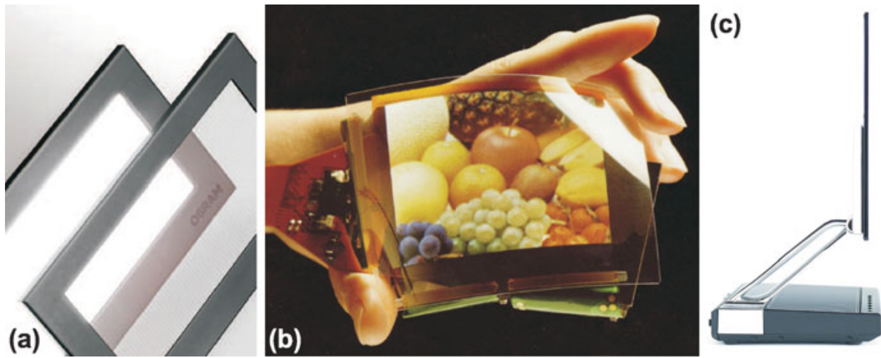

Fig. 22.23. (**a**) Transparent OLED panel. From [1320]. (**b**) Flexible OLED display. From [1321]. (**c**) 3 mm thin, 11 inch diagonal OLED TV. From [1322]

entering the mass market in 2010. An increase of the lifetime from 30,000 to beyond 50,000 hours is expected.

22.4 Lasers

22.4.1 Introduction

Semiconductor lasers[12] [1323, 1324] contain a zone (mostly called the *active layer*) that has gain if sufficiently pumped and that overlaps with an optical wave. The wave bounces back and forth in an optical cavity that leads to optical feedback. The part of the wave that exits the semiconductor forms the laser beam. Some of the first semiconductor lasers and a mounting design are shown in Fig. 22.24.

Generally, two main geometrical laser types, *edge* emitters (Fig. 22.25a) and *surface* emitters (Fig. 22.25b), are distinguished. The emission of the edge emitter exits through cleaved $\{110\}$ side facets[13] ($\approx 30\%$ reflectance), of which an opposite pair acts as a Fabry–Perot optical cavity. The surface emission is directed along (001), since this is the (standard) growth direction of the heterostructure sequence making up the laser. The mirrors in a vertical-cavity surface-emitting laser (VCSEL) are made from dielectric Bragg mirrors

[12]The term 'laser' is an acronym for 'light amplification by stimulated emission of radiation'. The amplification relies on stimulated emission, theoretically predicted by Einstein in 1917. The laser concept was first explored in the microwave wavelength region (1954, MASER using ammonia, Ch.H. Townes, Nobel prize 1964). The first optical laser (1958, US patent No. 2,929,922 awarded 1960, A.L. Schawlow, Ch.H. Townes) was the ruby laser developed in 1960 by Th. Maiman. A device is a laser when it emits stimulated light. This light must neither be monochromatic nor be emitted in a narrow, directed beam.

[13]Or etched facets in possibly any direction.

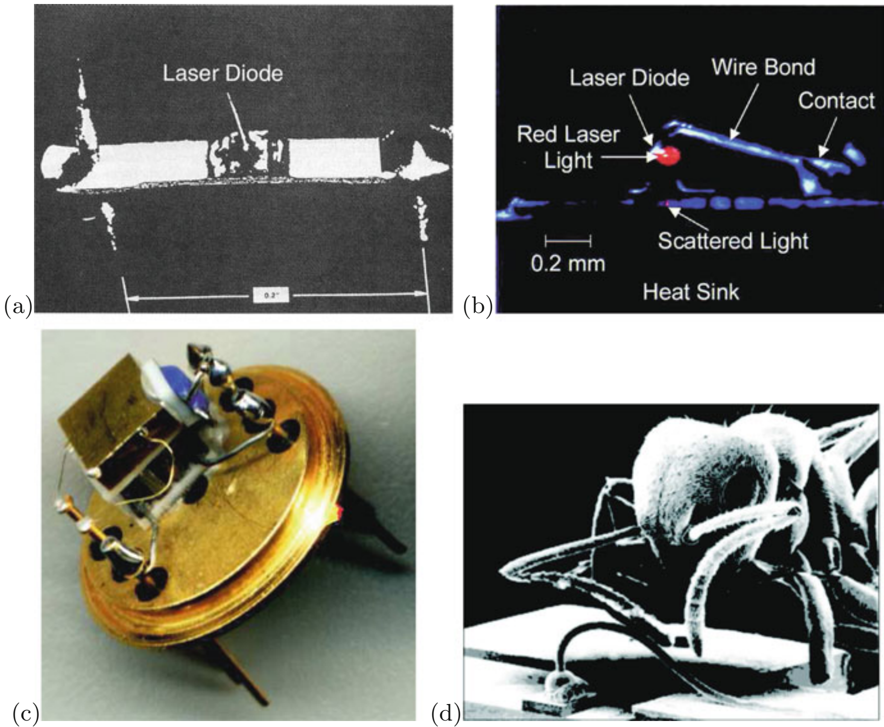

Fig. 22.24. Images of the first semiconductor lasers, 1962: (**a**) GaAs laser, Lincoln Laboratories and (**b**) GaInP laser, N. Holonyak and S.F. Bevacqua, Urbana Champaign. (**c**) Laser (at the end of gold bond wire) mounted on Peltier heat sink and a TO chip, Universität Leipzig. (**d**) Size comparison of an ant with a laser chip (underneath the bond wire)

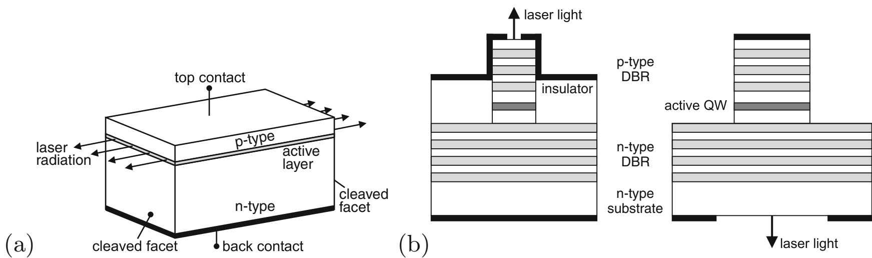

Fig. 22.25. (**a**) Schematic drawing of edge-emitting semiconductor laser. (**b**) Schematic drawings of vertical-cavity surface-emitting lasers with top emission (*left*) and emission through the substrate (*right*). *Black areas* are metal contacts

(cf. Sect. 18.1.4) with typically $R > 99.6\%$. Using antireflection coating on one facet, semiconductor lasers can be set up with an external cavity.[14] If both facets are antireflection coated, feedback is missing and the chip can be used as an optical amplifier (cf. Sect. 22.5).

Most lasers are pn-diodes and are then called laser diodes. They rely on the gain of interband transitions and the emission wavelength is determined and (more or less) given by the band gap of the semiconductor. The cascade laser [1325] (Sect. 22.4.16) is a unipolar structure with a superlattice as active layer. Here, the intersubband transitions (mostly in the conduction band but also in the valence band) carry the gain. The emission wavelength depends on the subband separation and lies typically in the far- and mid-infrared. Extensions to the THz regime and also to shorter wavelengths are possible. A third type of laser is the 'hot-hole' laser (Sect. 22.4.17), typically fabricated with p-doped Ge, which can be viewed as unipolar and functions only in a magnetic field; its emission is in the THz regime.

22.4.2 Applications

In Fig. 22.26, the revenue in the worldwide diode laser market is shown. The drop after 2000 is due to the burst of the 'internet bubble'. Nondiode laser (gas, ruby, excimer, ...) revenue is currently stable at around 2 billion US$, thus semiconductor lasers account for the largest share of all laser types sold.

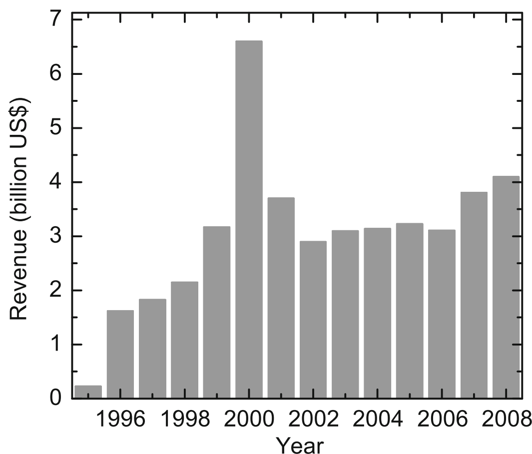

Fig. 22.26. Revenue in worldwide diode laser market. Based on numbers from [1326]

[14] Such external cavities can be used for manipulation of the laser properties such as wavelength tuning.

The following applications rely on semiconductor lasers:

- optical communication, mostly optical fiber based (senders), typically at 10 GBit/s, in special situations also 40 GBit/s data rate.
- optical information storage and retrieval (CD, DVD, BD[15]) with as short of a wavelength as possible, as shown in Fig. 22.27, currently 405 nm.
- pumping of solid-state lasers, typically 910 or 940 nm for pumping Nd:YAG
- portable projectors, laser TV, entertainment.
- laser pointers, see Fig. 22.28. A red laser pointer simply uses the collimated red emission of a GaAs-based diode. In a green laser pointer, an infrared diode pumps a Nd:YAG or Nd:YVO_4 crystal. The emitted beam is then frequency doubled, typically with a $KTiOPO_4$ (KTP) crystal.
- medical instruments with a variety of wavelengths in ophthalmology, dermatology, cosmetics (hair removal, tattoo removal).
- various other uses, such as remote control, position detection, distance measurement, printing, scientific instrumentation.

The market for photonic devices is much more dynamic than the electronics market. An example is the rapid change of dominating laser applications. For diode lasers, the two most prominent applications are telecommunication (77% market share in 2000, 25% in 2003, 45% in 2008) and optical data storage (17% market share in 2000, 60% in 2003, 44% in 2008).

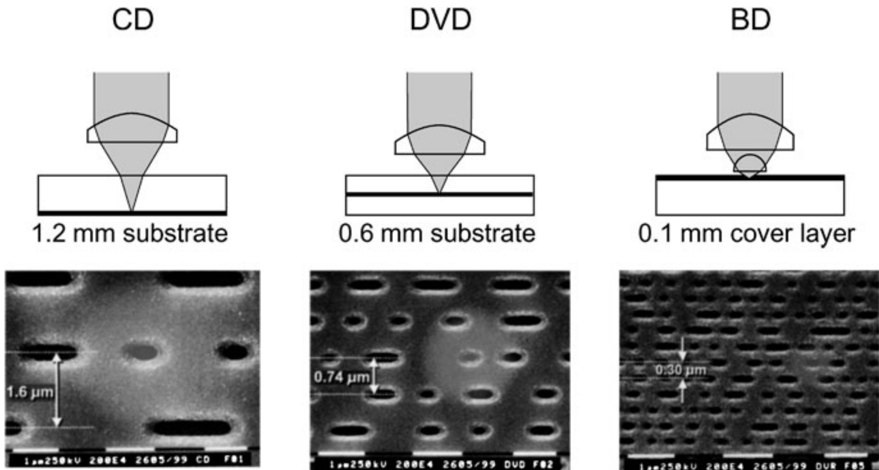

Fig. 22.27. Evolution of optical data storage technology, 'CD': compact disk (laser: 780 nm, pitch: 1.6 µm, capacity: 0.7 GB), 'DVD': digital versatile disk (laser: 635–650 nm, pitch: 0.74 µm, capacity: 4.7 GB for one layer), 'BD': 'Blu-ray' disk (laser: 405 nm, pitch: 0.32 µm, capacity: 27 GB for one layer)

[15]Sixteen million 405 nm laser diodes were shipped in 2006–2008. Eighty five percent of those are built into SONY's PS3, the rest into HD-DVD and other Blu-ray™disc (BD) players.

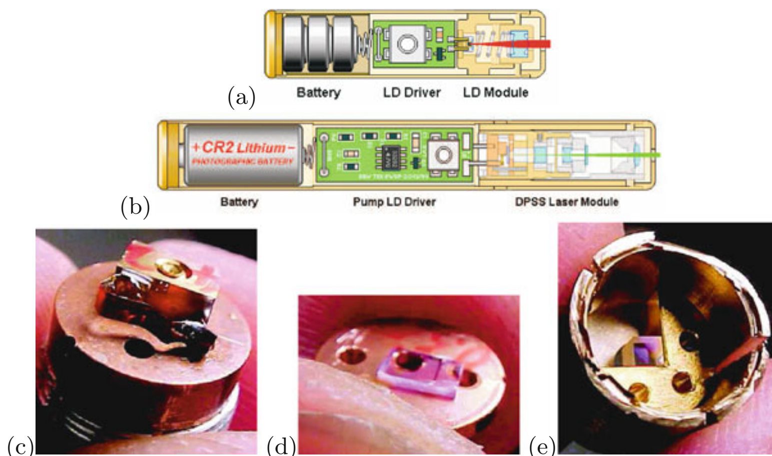

Fig. 22.28. (**a**) Scheme of red laser pointer, (**b**) scheme of green laser pointer. Parts of a green laser pointer: (**c**) pump laser diode, (**d**) YVO_4 crystal, (**e**) KTP doubler

22.4.3 Gain

Due to current injection,[16] a nonequilibrium carrier distribution is created. After fast thermalization processes (phonon scattering), it can mostly described by quasi-Fermi levels. Sufficiently strong pumping leads to inversion, i.e. conduction-band states are more strongly populated with electrons than valence-band states (Fig. 22.29). In this case, the stimulated emission rate is stronger than the absorption rate (cf. Sect. 10.2.6). The thermodynamic laser condition (cf. (10.23)) requires the difference of the quasi-Fermi levels to be larger than the band gap.

$$F_{\mathrm{n}} - F_{\mathrm{p}} > E_{\mathrm{g}} \tag{22.9}$$

The gain is defined as the (frequency-dependent) coefficient $g(\hbar\omega)$ that describes the light intensity along a path L according to

$$I(L) = I(0) \exp{(gL)} \ . \tag{22.10}$$

The gain spectrum as a function of the photon energy $\hbar\omega$ is given for non-k-conserving recombination by (cf. (10.5) and (10.6))

$$g(\hbar\omega) = \int_0^{\hbar\omega - E_{\mathrm{g}}} D_{\mathrm{e}}(E) D_{\mathrm{h}}(E') \left[f_{\mathrm{e}}(E) f_{\mathrm{h}}(E') - (1 - f_{\mathrm{e}}(E))(1 - f_{\mathrm{h}}(E')) \right] \mathrm{d}E \ , \tag{22.11}$$

[16] Or due to optical pumping. If electrical contacts are not available, the laser action can be invoked by supplying a high-intensity light beam, possibly in a stripe-like shape. For optically pumped semiconductor lasers see Sect. 22.4.15.

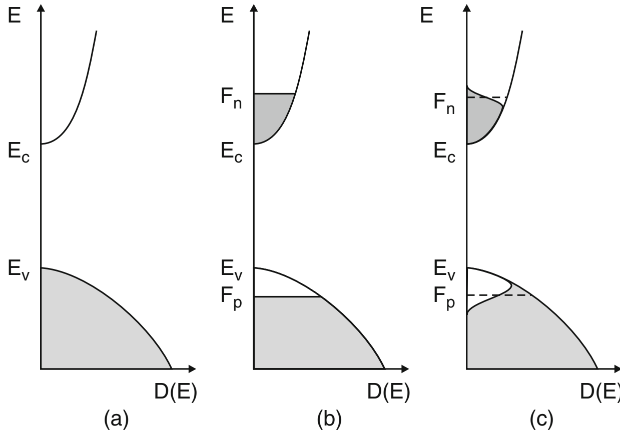

Fig. 22.29. Population (**a**) in thermodynamic equilibrium $T = 0\,\mathrm{K}$, (**b**) under inversion for $T = 0\,\mathrm{K}$, (**c**) under inversion for $T > 0\,\mathrm{K}$. *Shaded areas* are populated with electrons

with $E' = \hbar\omega - E_\mathrm{g} - E$. The gain is positive for those photon energies for which light is amplified and negative for those that are absorbed. In Fig. 22.30a, the electron and hole concentrations are shown for GaAs as a function of the quasi-Fermi energies. In Fig. 22.30b, the difference of the quasi-Fermi energies is shown as a function of the carrier density (for neutrality $n = p$). The gain spectrum is shown in Fig. 22.30c for a simple two-band model.[17] For a more elaborate discussion of such matters we refer to [1327]. In the case of inversion, the gain is positive for energies between E_g and $F_\mathrm{n} - F_\mathrm{p}$. At $\hbar\omega = F_\mathrm{n} - F_\mathrm{p}$, the gain is zero (transparency) and for larger energies negative (positive absorption coefficient). The agreement of experimental gain spectra of quantum wells with theoretical considerations, including carrier collision effects at the level of quantum kinetic theory in the Markovian limit, is very good (Fig. 22.31a) [1328].

For a given fixed energy, the gain increases with increasing pumping and increasing carrier density n (Fig. 22.30d). For very small density, it is given as $g(n \to 0) = -\alpha$. The gain rises around transparency approximately linearly with the pumping intensity. At transparency carrier density n_tr, the gain is zero. Therefore, the relation $g(n)$ can be approximated as (linear gain model)

$$g(n) \cong \hat{\alpha} \frac{n - n_\mathrm{tr}}{n_\mathrm{tr}} \,. \tag{22.12}$$

For large carrier density, the gain saturates (at a value similar to α). The onset of positive gain is related to the separation of the quasi-Fermi levels

[17] One electron and one hole band are considered; the heavy and light hole bands are taken into account via the mass according to (7.14).

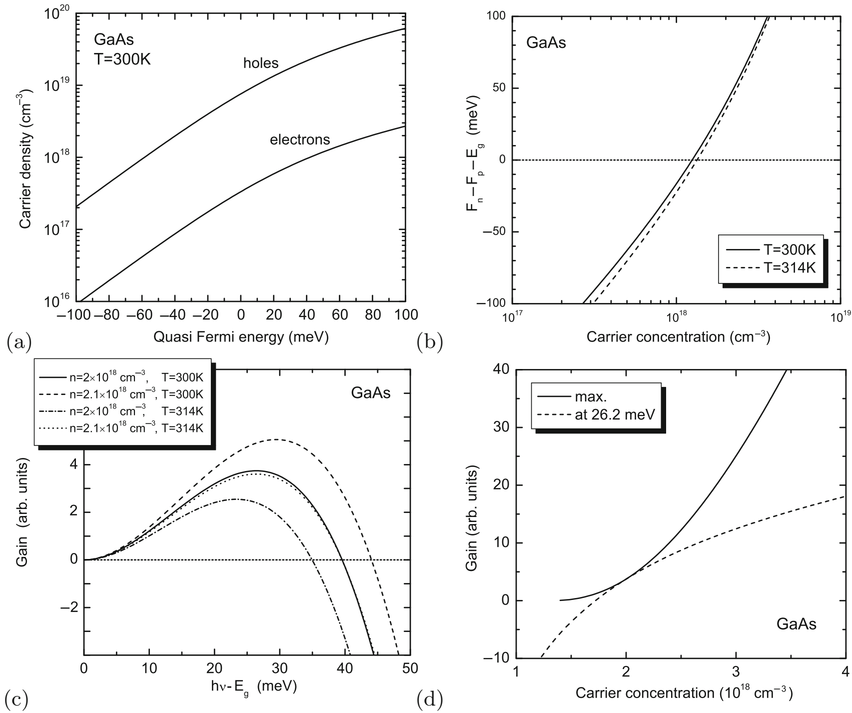

Fig. 22.30. Gain in the two-band model for GaAs. (**a**) Electron and hole concentrations at $T = 300\,\mathrm{K}$ as a function of the quasi-Fermi energies counted relative to the band edges, i.e. $F_\mathrm{n} - E_\mathrm{C}$ and $E_\mathrm{V} - F_\mathrm{p}$. (**b**) Difference of quasi-Fermi levels as a function of carrier concentration ($n = p$) for GaAs at two different temperatures. (**c**) Gain spectra according to (22.11) for $n = 2 \times 10^{18}$ and $T = 300\,\mathrm{K}$ (*solid line*), increased carrier density $n = 2.1 \times 10^{18}$ and $T = 300\,\mathrm{K}$ (*dashed line*), higher temperature $n = 2 \times 10^{18}$ and $T = 314\,\mathrm{K}$ (*dash-dotted line*) and same difference of the quasi-Fermi levels as for the *solid line*, $n = 2.1 \times 10^{18}$ and $T = 314\,\mathrm{K}$ (*dotted line*). (**d**) Maximum gain (*solid line*) and gain at a particular energy (*dashed line*, for photon energy $E_\mathrm{g} + 26.2\,\mathrm{meV}$ for which the gain is maximal for $n = 2 \times 10^{18}$ and $T = 300\,\mathrm{K}$, see *solid line* in part (**c**))

being larger than the band gap (22.9), Fig. 22.31b. The gain in quantum dot lasers [1329] has been discussed in [1330].

22.4.4 Optical Mode

The light wave that is amplified must be guided in the laser. An optical cavity is needed to provide optical feedback such that the photons travel several times through the gain medium and contribute to amplification. We explain the light-wave management for the edge emitter first:

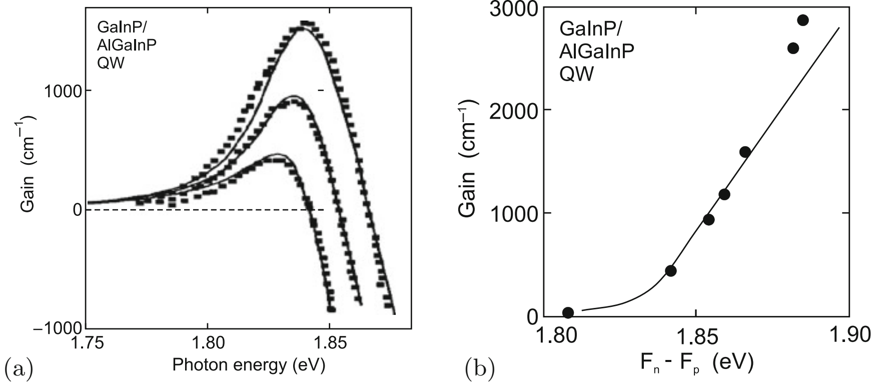

Fig. 22.31. (**a**) Gain spectra of a 6.8 nm thick $Ga_{0.41}In_{0.59}P/\ (Al_{0.5}\ Ga_{0.5})_{0.51}In_{0.49}P$ quantum well, experimental data (*symbols*) and theory (*lines*) for three different sheet carrier densities $n_{2D} = 2.2$, 2.7, and $3.2 \times 10^{12}\,cm^{-2}$. (**b**) Maximum gain as a function of the separation of the quasi-Fermi levels, experimental data (*symbols*) and theory (*lines*). Adapted from [1328]

Vertical Mode Guiding

In the course of the historical development of the semiconductor laser, the most significant improvements (reduction of lasing threshold current) have been achieved through the improvement of the overlap of the optical wave with the gain medium, as shown in Fig. 22.32. From homojunctions over the single heterojunction, eventually the double heterostructure (DHS) design could reduce the laser threshold current density to the $1\,kA/cm^2$ level.

The band diagram of a double heterostructure is shown in Fig. 22.33 for zero and forward bias. In the DHS, the optical mode is guided by total reflection within the low band gap center layer, which has a larger index of refraction than the outer, large band gap layer.[18] When the layer thickness is in the range of λ/n_r, the form of the optical mode must be determined from the (one-dimensional) wave equation (Helmholtz equation)

$$\frac{\partial^2 \mathcal{E}_z}{\partial z^2} + \omega^2 \mu\, \epsilon(z) \mathcal{E}_z = 0\,. \tag{22.13}$$

In Fig. 22.34a, the shape of the optical mode for $GaAs/Al_{0.3}Ga_{0.7}As$ DHS with different GaAs thickness is shown.

The optical confinement factor Γ is the part of the wave that has geometrical overlap with the gain medium, i.e. is subject to amplification. It is shown for $GaAs/Al_xGa_{1-x}As$ DHS with different GaAs thickness and different Al concentration in Fig. 22.34b. The modal gain g_{mod} that is responsible

[18] A smaller band gap coincides for many cases with a larger index of refraction.

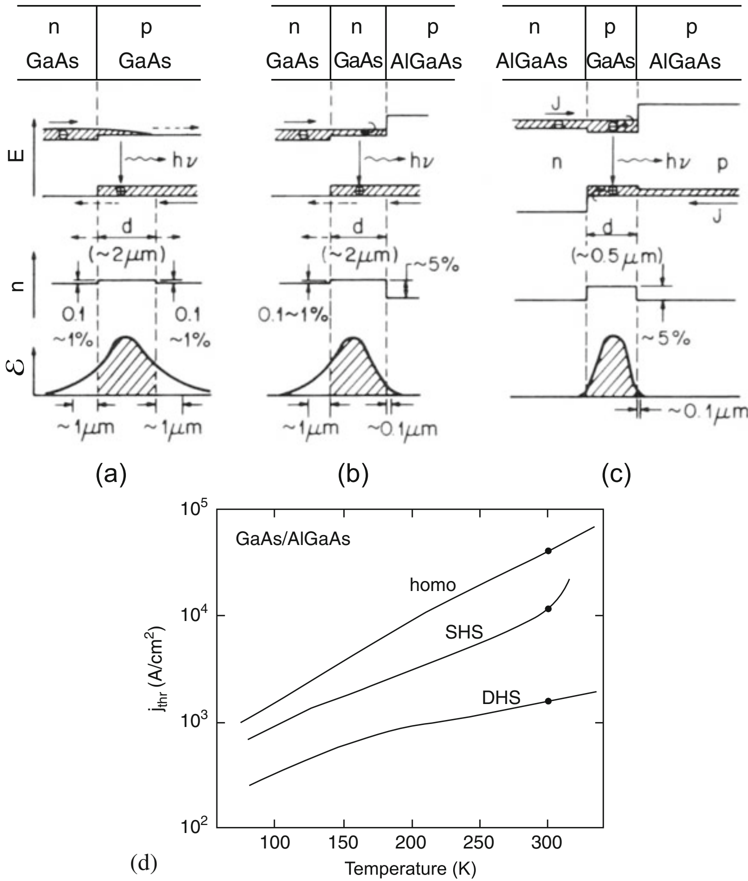

Fig. 22.32. Laser with (**a**) homojunction, (**b**) single heterostructure (SHS), (**c**) double heterostructure ('DHS'), (**d**) reduction of threshold current with design progress ('SHS': d =2 μm, 'DHS': d =0.5 μm). Adapted from [1331]

for light amplification in the cavity consists of the material gain g_{mat} due to inversion and the optical confinement factor.

$$g_{\mathrm{mod}} = \Gamma g_{\mathrm{mat}} \ . \tag{22.14}$$

In order to allow simultaneous optimization of the light mode and the carrier confinement, the separate confinement heterostructure (SCH) has been designed. Here, a single or multiple quantum well of a third material with even smaller band gap is the active medium (Fig. 22.35a,b,d). A single quantum well has an optical confinement factor of a few per cent only. It offers, however, efficient carrier capture and efficient radiative recombination. An increase in the carrier capture efficiency can be achieved using a graded index in the barrier (GRINSCH, Fig. 22.35c).

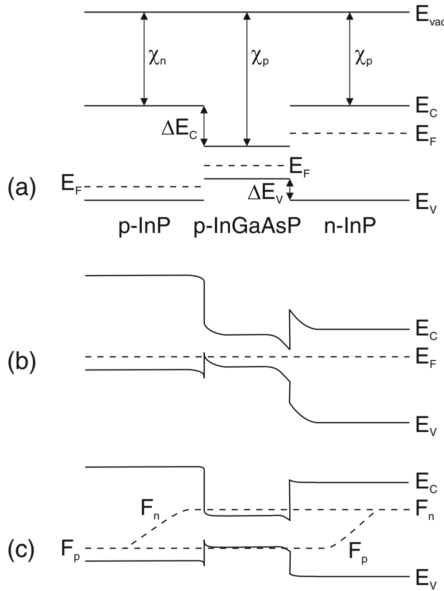

Fig. 22.33. Schematic band diagram of a pn double heterostructure (DHS) diode (InP/InGaAsP/InP) (**a**) before contact of the materials, (**b**) in thermodynamic equilibrium (zero bias, *dashed line* is Fermi level E_F = const.), (**c**) with forward bias close to flat-band conditions, *dashed lines* are quasi-Fermi levels

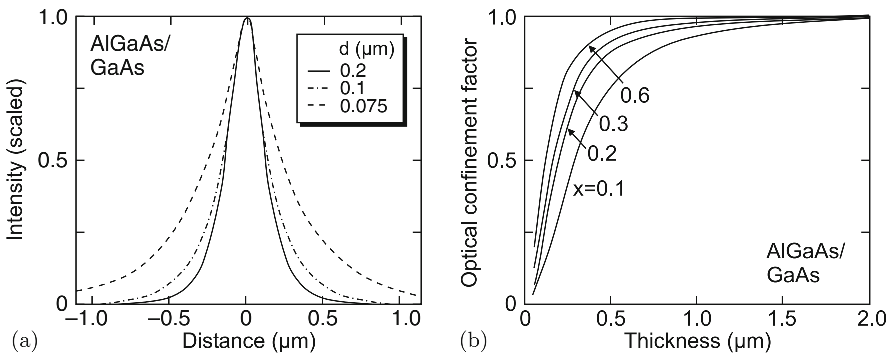

Fig. 22.34. (**a**) Optical mode (relative intensity) for various values of the thickness d of the active layer as labeled of a GaAs/$Al_{0.3}Ga_{0.7}As$ DHS laser, (**b**) Optical confinement factor Γ as a function of the thickness of the active layer and the Al concentration x of the barrier as labeled in a GaAs/$Al_xGa_{1-x}As$ DHS laser. Adapted from [1323]

The thin wave-guiding layer leads to large divergence of the laser beam along the vertical direction, typically about 90°. The strong confinement of light also limits the maximum achievable output power due to catastrophic

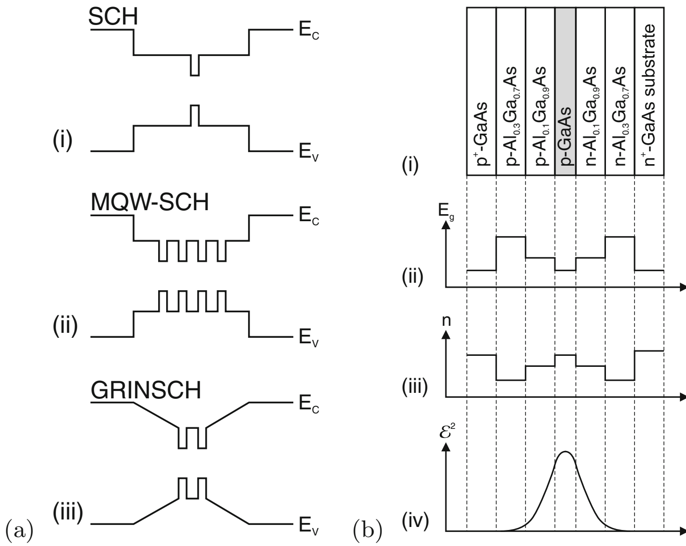

Fig. 22.35. (**a**) Various geometries of the active layer of a DHS laser with quantum wells as active medium, (**i**) single QW (separate confinement heterostructure, SCH), (**ii**) multiple QW SCH, and (**c**) GRINSCH (graded-index SCH) structure. (**b**) Layer sequence for a separate confinement heterostructure laser

optical damage (COD). Several ideas have been realized to overcome this problem and achieve much smaller divergence of about 18°. The waveguide can be designed to be very thick (large optical cavity, LOC) that leads to an increase of threshold. Other schemes are insertion of a low-index layer into the confinement layer, insertion of a high-index layer into the cladding layer or the use of high-index quarter-wavelength reflecting layers [1333].

Lateral Mode Guiding

Lateral waveguiding can be achieved with gain guiding and index guiding (or a mixture of the two). In the gain-guiding scheme (Fig. 22.36), the current path that is defined by the stripe contact and the current spreading underneath it, defines the gain region and therefore the volume of amplification that guides the optical wave. Since a high carrier density reduces the index of refraction, a competing antiguiding effect can occur. For index guiding, the lateral light confinement is caused by a lateral increase of the index of refraction. This index modulation can be achieved by using a mesa-like contact stripe (Fig. 22.37a). A shallow mesa reaches down into the upper cladding, a deep mesa reaches down into or through the active layer. Possible problems with surface recombination can be avoided by regrowth of the structure (Fig. 22.37b) with a wide band gap material (compared to the active layer). Optimization of regrowth is targeted to achieve a well-defined surface for

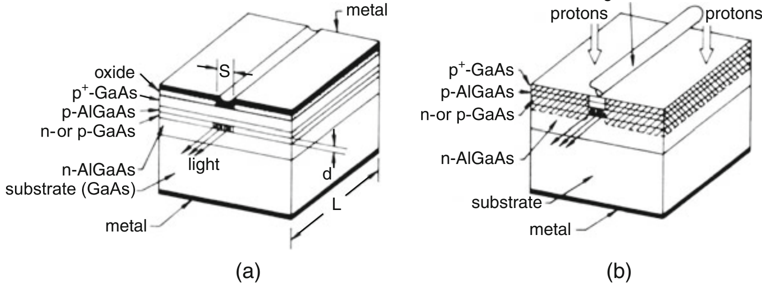

Fig. 22.36. Scheme of gain-guided lasers with stripe contact: (**a**) oxide stripe, (**b**) proton implanted with shadow mask from tungsten wire ($\sim 10\,\mu$m). Adapted from [1332]

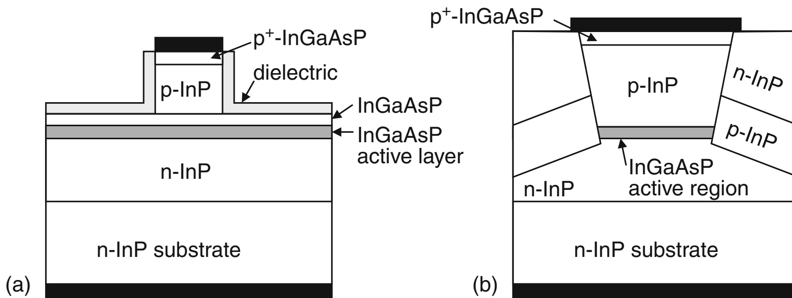

Fig. 22.37. Schematic cross section of index-guided lasers: (**a**) shallow ridge, (**b**) deep etch and regrowth. *Black areas* are metal contacts

subsequent contact processing. A lateral pn-diode can be incorporated that avoids current spreading in the upper part of the structure.

Depending on the width of the lateral mode, it can be monomode or multimode (Fig. 22.38a). For laterally monomode lasers, the stripe width may only be a few µm. In particular for such lasers, the current spreading must be controlled. Problems can arise for wide stripe widths due to current filamentation and inhomogeneous laser emission from the facet. Since the optical mode is typically more confined in the growth direction than in the lateral direction, the far field is asymmetric (Fig. 22.38c). The vertical axis has the higher divergence and is called the fast axis. The lateral axis is called the slow axis. The asymmetric beam shape is detrimental when the laser needs to be coupled into an optical fiber or a symmetric beam profile is needed for subsequent optics. The beam can be made symmetric using special optic components such as anamorphic prisms (Fig. 22.38d) and graded-index lenses. The beam from a laterally monomode laser is diffraction limited and can therefore generally be refocused efficiently (beam quality $M^2 \gtrsim 1$).

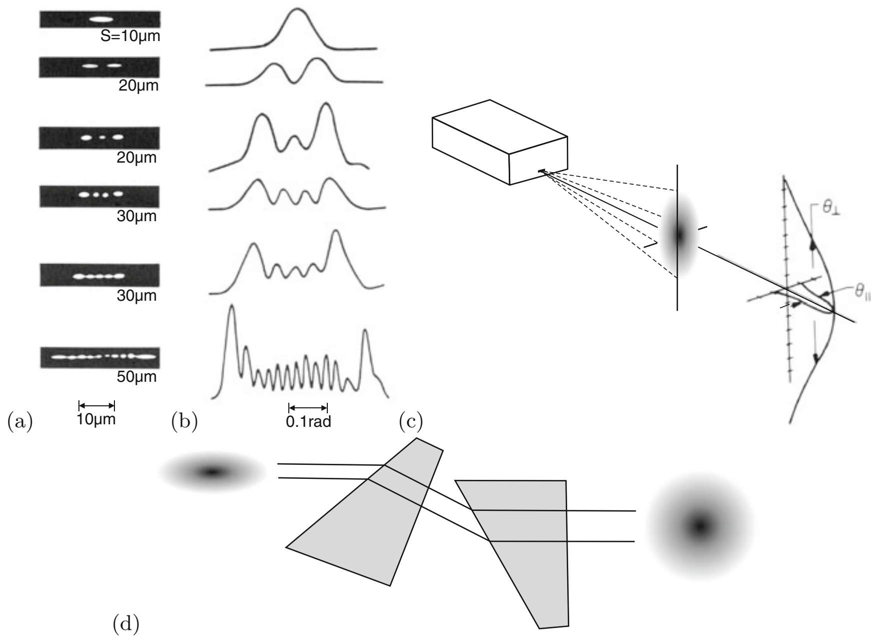

Fig. 22.38. Lateral near field (**a**) and far field (**b**) of lasers with various width S of the injection stripe as labeled. Adapted from [1334]. (**c**) Typical asymmetric far field of an edge emitter. Adapted from [384]. (**d**) Correction of asymmetric far field with a pair of anamorphic prisms

Longitudinal Modes

The spectral positions of the laser modes for a cavity with length L is given by the condition (cf. (18.34))

$$L = \frac{m\,\lambda}{2n_{\mathrm{r}}(\lambda)}\ , \tag{22.15}$$

where m is a natural number and $n(\lambda)$ is the dispersion of the index of refraction. The distance of neighboring modes is given by (for large m)

$$\Delta\lambda = \frac{\lambda^2}{2n_{\mathrm{r}}L\left(1 - \frac{\lambda}{n_{\mathrm{r}}}\frac{\mathrm{d}n_{\mathrm{r}}}{\mathrm{d}\lambda}\right)}\ . \tag{22.16}$$

The dispersion $\mathrm{d}n_{\mathrm{r}}/\mathrm{d}\lambda$ can sometimes be neglected.

The facets of edge-emitting lasers are typically cleaved. Cleaving bears the danger of mechanical breakage and tends to have poor reproducibility, low yield and therefore high cost. Etched facets are another possibility to form the cavity mirror. The etch process, typically reactive ion dry etching, must yield sufficiently smooth surfaces to avoid scattering losses. A highly

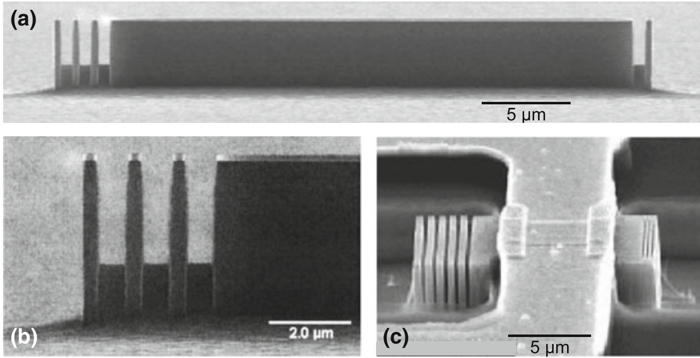

Fig. 22.39. SEM image of (**a**) an InP microlaser with third-order Bragg mirrors, (**b**) magnified view of the front facet with three slabs, (**c**) a 12-µm long microlaser with five third-order mirrors on the rear side and three first-order mirrors on the front side with top contact. From [1336]; part (**b**) reprinted with permission from [1335], ©2001 AIP

efficient distributed Bragg mirror (cf. Sect. 18.1.4) with only a few periods can be created by using the large index contrast between the semiconductor and air. As shown in Fig. 22.39, slabs can be etched that make a Bragg mirror with the air gaps [1335]. In this way, very short longitudinal cavities can be made ($\approx 10\,\mu$m).

22.4.5 Loss Mechanisms

While the light travels through the cavity, it is not only amplified but it also suffers losses. The internal loss $\alpha_{\rm i}$ and the mirror loss $\alpha_{\rm m}$ contribute to the total loss $\alpha_{\rm tot}$

$$\alpha_{\rm tot} = \alpha_{\rm i} + \alpha_{\rm m} \,. \tag{22.17}$$

The internal loss is due to absorption in the cladding, scattering at waveguide inhomogeneities and possibly other processes. It can be written as

$$\alpha_{\rm i} = \alpha_0 \mathit{\Gamma} + \alpha_{\rm g}(1 - \mathit{\Gamma}) \,, \tag{22.18}$$

where α_0 is the loss coefficient in the active medium and $\alpha_{\rm g}$ is the loss coefficient outside the active medium.

The mirror loss is due to the incomplete reflection of the optical wave at the laser facets. This condition is necessary, however, to observe a laser beam outside the cavity. R_1 and R_2 are the values of reflectance of the two facets, respectively. An as-cleaved facet has a reflectance of about 30% (cf. (22.7)). Using dielectric layers on the facets, the reflectance can be increased (high reflection, HR-coating) or decreased (antireflection, AR-coating). One round-trip through the cavity of length L has the length $2L$. The intensity loss due to reflection at the facets is expressed via $\exp(-2\alpha_{\rm m}L) = R_1\,R_2$

$$\alpha_{\rm m} = \frac{1}{2L} \ln\left(\frac{1}{R_1 R_2}\right) . \tag{22.19}$$

If both mirrors have the same reflectance R, we have $\alpha_{\rm m} = -L^{-1} \ln R$. For $R = 0.3$ a 1-mm cavity has a loss of $12\,{\rm cm}^{-1}$. For the internal loss a typical value is $10\,{\rm cm}^{-1}$, very good waveguides go down to 1–$2\,{\rm cm}^{-1}$.

Lasing is only possible if the gain overcomes all losses (at least for one wavelength), i.e.

$$g_{\rm mod} = g_{\rm mat} \Gamma \geq \alpha_{\rm tot} . \tag{22.20}$$

22.4.6 Threshold

When the laser reaches threshold, the (material) gain is pinned at the threshold value

$$g_{\rm thr} = \frac{\alpha_{\rm i} + \alpha_{\rm m}}{\Gamma} . \tag{22.21}$$

Since $g \propto n$, the carrier density is also pinned at its threshold value and does not increase further with increasing injection current. Instead, additional carriers are quickly converted into photons by stimulated emission. The threshold carrier density is (using the linear gain model, cf. (22.12))

$$n_{\rm thr} = n_{\rm tr} + \frac{\alpha_{\rm i} + \alpha_{\rm m}}{\hat{\alpha} \Gamma} . \tag{22.22}$$

For an active layer of thickness d, the threshold current density is

$$j_{\rm thr} \cong \frac{e d n_{\rm thr}}{\tau(n_{\rm thr})} , \tag{22.23}$$

where $\tau_{\rm e}(n_{\rm thr})$ is the minority carrier lifetime at the threshold carrier density:

$$\tau(n_{\rm thr}) = \frac{1}{A + B n_{\rm thr} + C n_{\rm thr}^2} . \tag{22.24}$$

Using (22.22), we can write (for $R = R_1 = R_2$)

$$j_{\rm thr} = j_{\rm tr} + \frac{e d}{\tau \hat{\alpha} \Gamma} \left(\alpha_{\rm i} - \ln R \frac{1}{L}\right) , \tag{22.25}$$

where the transparency current density is $j_{\rm tr} = e d n_{\rm tr}/\tau$. Thus, the plot of $j_{\rm thr}$ vs. $1/L$ (or the optical loss) should be linear and can be extrapolated towards the transparency current density (cf. Fig. 22.40a).

Any additional increase of the current j leads to stimulated emission with the rate

$$r_{\rm st} = d v_{\rm g} g_{\rm thr} N_{\rm ph} , \tag{22.26}$$

where $v_{\rm g}$ is the group velocity (mostly $c_0/n_{\rm r}$) and $N_{\rm ph}$ is the photon density (per length) in the cavity. The photon density increases linearly beyond the threshold

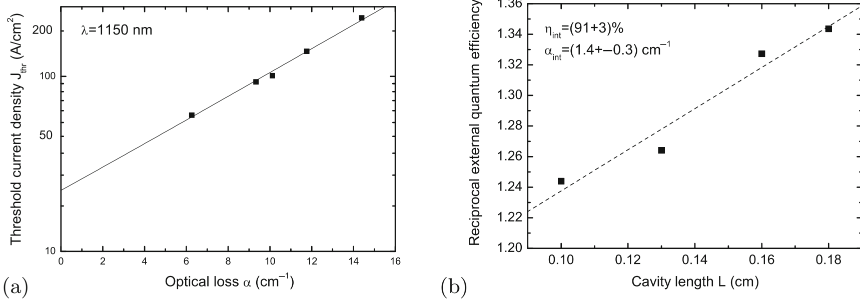

Fig. 22.40. (**a**) Threshold current density for (three-fold InGaAs/GaAs QD stack) laser ($\lambda = 1150\,\mathrm{nm}$) at 10°C with different cavity length vs. the optical loss ($\propto 1/L$). The extrapolated transparency current density is $21.5 \pm 0.9\,\mathrm{A/cm^2}$. (**b**) Inverse external quantum efficiency vs. cavity length. The internal quantum efficiency determined from the plot is 91% and the internal loss is $1.4\,\mathrm{cm}^{-1}$

$$N_{\mathrm{ph}} = \frac{1}{e d v_{\mathrm{g}} g_{\mathrm{thr}}} \left(j - j_{\mathrm{thr}} \right) \ . \tag{22.27}$$

The photon lifetime

$$\frac{1}{\tau_{\mathrm{ph}}} = v_{\mathrm{g}} \left(\alpha_{\mathrm{i}} + \alpha_{\mathrm{m}} \right) = v_{\mathrm{g}} \Gamma g_{\mathrm{thr}} \tag{22.28}$$

is introduced that describes the loss rate of photons. $v_{\mathrm{g}} \alpha_{\mathrm{m}}$ describes the escape rate of photons from the cavity into the laser beam(s). Therefore,

$$N_{\mathrm{ph}} = \frac{\tau_{\mathrm{ph}} \Gamma}{e d} \left(j - j_{\mathrm{thr}} \right) \ . \tag{22.29}$$

Since the threshold depends on the carrier density, it is advantageous to reduce the active volume further and further. In this way, the same *amount* of injected carriers creates a larger carrier *density*. Figure 22.41 shows the historic development of laser threshold due to design improvements.

22.4.7 Spontaneous Emission Factor

The spontaneous emission factor β is the fraction of spontaneous emission (emitted into all angles) that is emitted into laser modes. For Fabry–Perot lasers, β is typically in the order of 10^{-4}–10^{-5}. The design of a microcavity can increase β drastically by several orders of magnitude to ≈ 0.1 [1337] or above and thus reduce the threshold current. The photon number as a function of the pump current can be calculated from the laser rate equations and is depicted in Fig. 22.42. For $\beta = 1$, all emitted power goes into the laser mode regardless of whether emission is spontaneous or stimulated. The definition of threshold in such 'nonclassical' lasers with large β is discussed in detail in [1338].

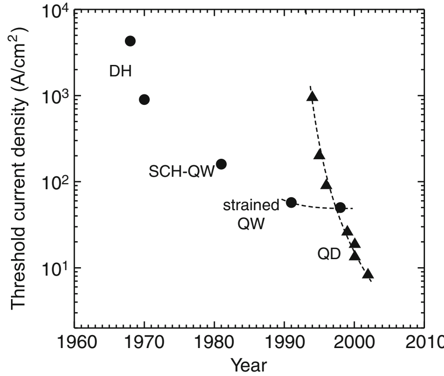

Fig. 22.41. Historic development of threshold current density (at room temperature, extrapolated for infinite cavity length and injection stripe width) for various laser designs, 'DH': double heterostructure, 'SCH–QW': separate confinement heterostructure with quantum wells. 'QD': quantum dots. *Dashed lines* are guides to the eye

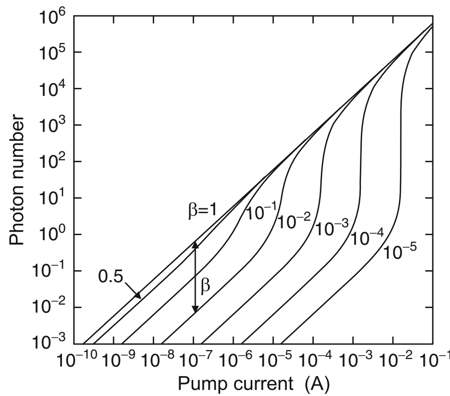

Fig. 22.42. Photon number vs. pump current for a model laser. Adapted from [1339]

22.4.8 Output Power

The output power is given by the product of photon energy, the photon density in the cavity, the effective mode volume and the escape rate:

$$P_{\mathrm{out}} = \hbar\omega N_{\mathrm{ph}} \frac{Lwd}{\Gamma} v_{\mathrm{g}} \alpha_{\mathrm{m}} \; . \tag{22.30}$$

Thus, it is given by

$$P_{\mathrm{out}} = \hbar\omega v_{\mathrm{g}} \alpha_{\mathrm{m}} \frac{\tau_{\mathrm{ph}}}{e} Lw \left(j - j_{\mathrm{thr}}\right) = \frac{\hbar\omega}{e} \frac{\alpha_{\mathrm{m}}}{\alpha_{\mathrm{m}} + \alpha_{\mathrm{i}}} \left(I - I_{\mathrm{thr}}\right) \; . \tag{22.31}$$

To this equation, the factor η_{int} must be added. The internal quantum efficiency describes the efficiency of the conversion of electron–hole pairs into photons:

$$\eta_{\mathrm{int}} = \frac{Bn^2 + v_{\mathrm{g}} g_{\mathrm{thr}} N_{\mathrm{ph}}}{An + Bn^2 + Cn^3 + v_{\mathrm{g}} g_{\mathrm{thr}} N_{\mathrm{ph}}} \,. \tag{22.32}$$

All in all, now (see Fig. 22.43a)

$$P_{\mathrm{out}} = \frac{\hbar\omega}{e} \frac{\alpha_{\mathrm{m}}}{\alpha_{\mathrm{m}} + \alpha_{\mathrm{i}}} \eta_{\mathrm{int}} \left(I - I_{\mathrm{thr}}\right) \,. \tag{22.33}$$

The differential (or slope) quantum efficiency, also called the external quantum efficiency η_{ext}, is the slope of the P_{out} curve vs. the current in the lasing regime. It is given by

$$\eta_{\mathrm{ext}} = \frac{\mathrm{d}P_{\mathrm{out}}/\mathrm{d}I}{\hbar\omega/e} = \eta_{\mathrm{int}} \frac{\alpha_{\mathrm{m}}}{\alpha_{\mathrm{m}} + \alpha_{\mathrm{i}}} \,. \tag{22.34}$$

The external quantum efficiency can also be written as

$$\frac{1}{\eta_{\mathrm{ext}}} = \frac{1}{\eta_{\mathrm{int}}} \left(1 + \frac{\alpha_{\mathrm{i}}}{\alpha_{\mathrm{m}}}\right) = \frac{1}{\eta_{\mathrm{int}}} \left[1 - 2\alpha_{\mathrm{i}} L \ln\left(R_1 R_2\right)\right] \,. \tag{22.35}$$

Therefore, if η_{ext}^{-1} is plotted for similar lasers with different cavity length (see Fig. 22.40b), a straight line should arise from which the internal quantum efficiency (extrapolation to $L \to 0$) and the internal loss ($\propto$ slope) can be determined experimentally.

The threshold current for a given laser is determined from the P–I characteristic via extrapolation of the linear regime as shown in Fig. 22.43a. Record values for the threshold current density are often given for the limit $L \to \infty$.

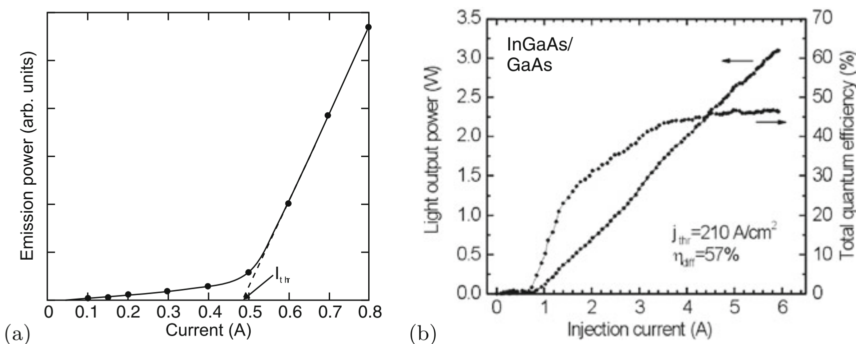

Fig. 22.43. (**a**) Typical P–I characteristic of a semiconductor laser. Adapted from [384]. (**b**) Output power and total quantum efficiency of a quantum dot laser (3 stacks of InGaAs/GaAs QDs, $L = 2\,\mathrm{mm}$, $w = 200\,\mu\mathrm{m}$, $\lambda = 1100\,\mathrm{nm}$, $T = 293\,\mathrm{K}$) vs. injection current

Due to current spreading, the threshold current density also depends on the width of the injection stripe. Record low thresholds are therefore often given for the limit $w \to \infty$.

The total quantum efficiency is given by

$$\eta_{\mathrm{tot}} = \frac{P_{\mathrm{out}}/I}{\hbar\omega/e} \ . \tag{22.36}$$

This quantity is shown in Fig. 22.43b for a laser as a function of the current. For a linear P–I lasing characteristic, the total quantum efficiency converges towards the external quantum efficiency for high currents because the low quantum efficiency subthreshold regime no longer plays any role. Another important figure of merit is the wall-plug efficiency η_{w} that describes the power conversion:

$$\eta_{\mathrm{w}} = \frac{P_{\mathrm{out}}}{U\,I} \ . \tag{22.37}$$

Additionally to the current balance discussed so far, typically a leakage current exists that flows without contributing to recombination or lasing. Carriers not captured into or escaping from the active layers can contribute to this current. The present record for wall-plug efficiency of high-power laser diodes is above 70% [1340, 1341], employing careful control of band alignment (graded junctions, avoiding voltage barriers), optical losses, Joule heating, spontaneous emission and carrier leakage. It seems possible to achieve η_{w} of 80%.

The P–I characteristic is not linear to arbitrary high currents. Generally, the output power will saturate or even decrease for increasing current. These effects can be due to increasing leakage current, increasing internal loss at high current or temperature effects, e.g. an increase of threshold with increasing temperature (cf. Sect. 22.4.9) and therefore a reduction of total efficiency. All nonradiative losses will eventually show up as heat in the laser that must be managed with a heat sink.

A radical effect is catastrophical optical damage (COD) at which the laser facet is irreversible (partially) destructed. Antioxidation or protective layers can increase the damage threshold to $> 20\,\mathrm{MW/cm^2}$. The record power from a single edge emitter is $\sim 12\,\mathrm{W}$ (200 µm stripe width). For a lateral monomode laser, cw power of about 1.2 W has been reached from a 1480-nm InGaAsP/InP double quantum-well lasers with 3–5 µm stripes and 3 mm cavity length [1342]. About 500 mW can be coupled into a single-mode fiber [1343].

22.4.9 Temperature Dependence

The threshold of a laser typically increases with increasing temperature as shown in Fig. 22.44a. Empirically, in the vicinity of a temperature T_1 the threshold follows an exponential law (see Fig. 22.44b)

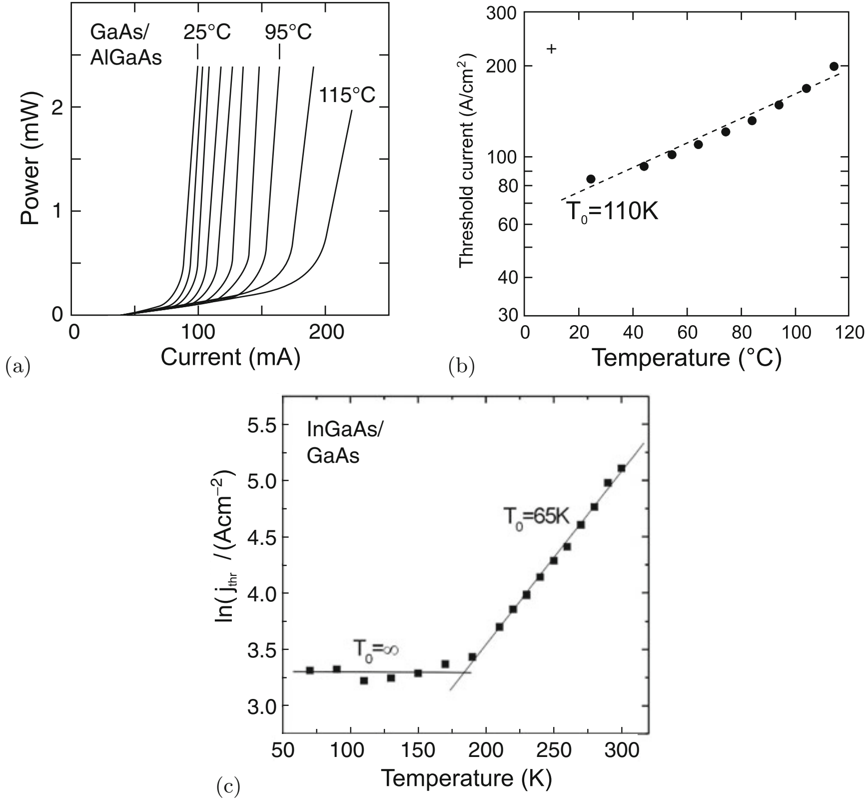

Fig. 22.44. (**a**) *P–I* characteristic (cw output power per mirror facet) of stripe-buried heterostructure laser at various temperatures of the heat sink between 25 °C and 115 °C in steps of 10 K. (**b**) Threshold current (in logarithmic scale) of this laser as a function of heat-sink temperature and exponential fit (*dashed line*) with $T_0 = 110\,\mathrm{K}$. Parts (**a**) and (**b**) adapted from [1344]. (**c**) Temperature dependence of the threshold current density of a quantum dot laser (3 stacks of InGaAs/GaAs QDs, $\lambda = 1150\,\mathrm{nm}$) with T_0 (*solid lines* are fits) given in the figure

$$j_{\mathrm{thr}}(T) = j_{\mathrm{thr}}(T_1)\exp\left(\frac{T-T_1}{T_0}\right) \propto \exp\left(\frac{T}{T_0}\right) , \qquad (22.38)$$

with T_0 being the so-called characteristic temperature.[19] It is the inverse logarithmic slope, $T_0^{-1} = \mathrm{d}\ln j_{\mathrm{thr}}/\mathrm{d}T$.

T_0 summarizes the temperature-dependent loss and the carrier redistribution in **k**-space due to the change of the Fermi distribution with temperature. With increasing temperature, populated states below the quasi-Fermi level become unpopulated and nonlasing states become populated. Therefore, the gain decreases with increasing temperature. This redistribution must be compensated by an increase of the quasi-Fermi energy, i.e. stronger pumping.

[19] Since T_0 has the dimension of a temperature difference, it can be expressed in °C or K. For the sake of unambiguity it should be given in K.

This effect is present for (even ideal) bulk, quantum well and quantum wire lasers. Only for quantum dots with a δ-like density of states is the change of Fermi distribution irrelevant as long as excited states are energetically well separated from the (lasing) ground state. In Fig. 22.44c, the threshold of a quantum dot laser is indeed temperature independent ($T_0 = \infty$) as long as excited states are not thermally populated (for $T < 170\,\mathrm{K}$ for the present laser).

22.4.10 Mode Spectrum

In Fig. 22.45a, the mode spectrum of a typical edge-emitting laser is shown. Below threshold, the amplified spontaneous emission (ASE) spectrum exhibits a comb-like structure due to the Fabry–Perot modes. Above threshold, some modes grow much faster than others, possibly resulting in single longitudinal mode operation at high injection. The relative strength of the strongest side mode is expressed through the side-mode suppression ratio (SSR) in dB

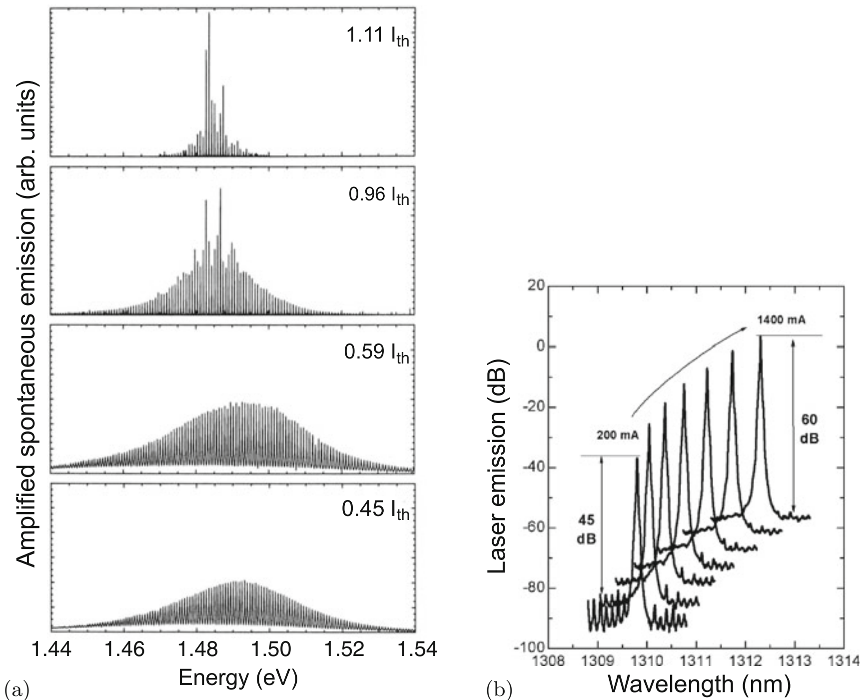

Fig. 22.45. (**a**) Mode spectra of a Fabry–Perot laser, under, at and above threshold ($I_{\mathrm{thr}} = 13.5\,\mathrm{mA}$). Adapted from [795]. (**b**) Mode spectra of a cw DFB InGaAs/InP laser with 2 mm cavity length at various currents of 200, 400, ..., 1400 mA ($I_{\mathrm{thr}} = 65\,\mathrm{mA}$), SSR>40 dB at $T = 293\,\mathrm{K}$. Adapted from [1350], reproduced with permission from SPIE

$$SSR = 10 \log \left(\frac{I_{\mathrm{mm}}}{I_{\mathrm{sm}}} \right) , \tag{22.39}$$

where I_{mm} (I_{sm}) is the intensity of the maximum (strongest side) mode in the lasing spectrum.

As a tendency a DHS or QW semiconductor laser above threshold develops a narrow spectrum since the pump power is channeled into one or few modes with large gain. A quantum dot laser behaves differently when pumped largely above threshold. Since the gain of individual QDs in an inhomogeneously broadened ensemble (due to different QD sizes) is independent, a broad gain spectrum is present [1345]. The lasing spectrum takes a hat-like shape when homogeneous broadening is small compared to the inhomogeneous broadening [1346, 1347] (Fig. 22.46) as predicted theoretically [1345, 1348].

22.4.11 Longitudinal Single-Mode Lasers

In order to achieve a high SSR or single longitudinal mode lasing, the feedback must offer a higher wavelength selectivity than a simple mirror. A preferential feedback for certain modes can be obtained using a periodic dielectric structure that 'fits' to a particular wavelength, similar to a Bragg mirror.

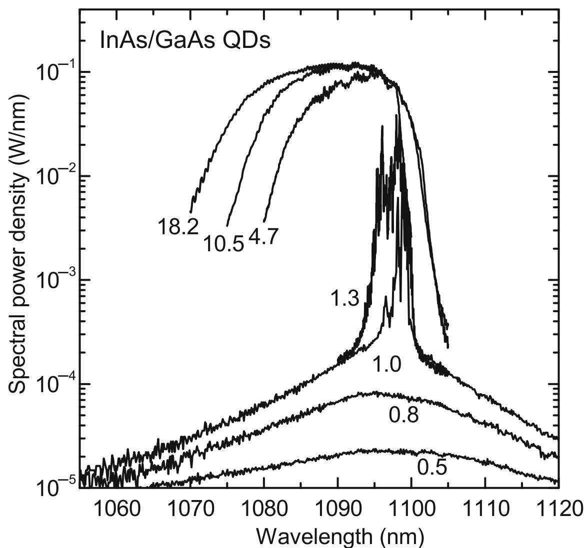

Fig. 22.46. Lasing spectra of quantum dot laser ($L = 1.2$ mm, stripe width $w = 75\,\mu$m) at room temperature. The active medium is a three-fold stack of InGaAs/GaAs QDs. The current density as labeled is given in units of the threshold current density ($j_{\mathrm{thr}} = 230\,\mathrm{A/cm^2}$). Adapted from [1347]

The periodic modulation of the refractive index can be made within the cavity (distributed feedback, DFB, Fig. 22.47a) or at the mirror (distributed reflection, DBR, Fig. 22.47b). In this way, monochromatic lasers with SSR $\gg 30$ dB are possible (Fig. 22.45b).

It is possible to couple several hundred mW optical power of a laterally and spectrally monomode laser into a monomode optical fiber [1349] (Fig. 22.48).

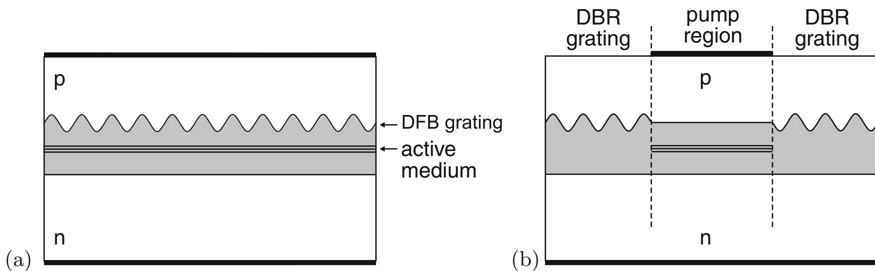

Fig. 22.47. Schematic drawing of (**a**) DFB (distributed feedback) and (**b**) DBR (distributed Bragg reflection) lasers. The active medium is schematically shown as a triple quantum well, the waveguide is shown as a *grey area*

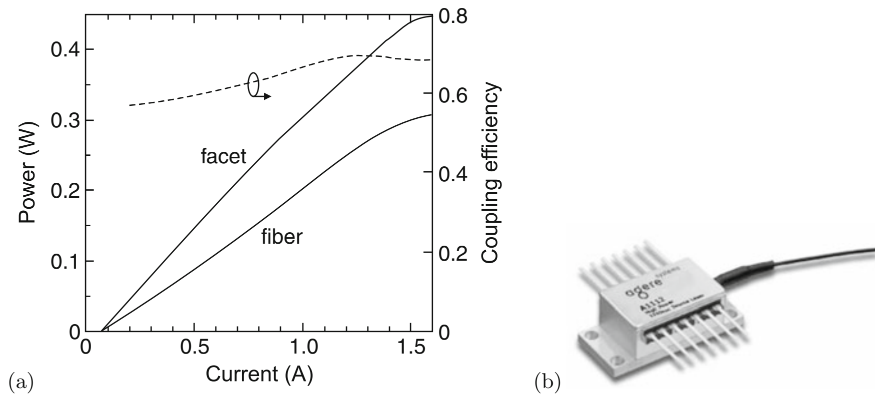

Fig. 22.48. (**a**) Output power of an InGaAsP/InP cw single-mode DFB laser at 1427 nm with 2 mm cavity length from the facet and coupled to a single-mode fiber vs. driving current ($T = 293$ K). The *dashed* line represents the coupling efficiency to the fiber (right scale). Adapted from [1349]. (**b**) Package with pigtail of fiber coupled 1550 nm DFB laser with 40 mW output power in the fiber. From [1352]

22.4.12 Tunability

The tunability of the emission wavelength [1351] is important for several applications such as wavelength division multiplexing[20] and spectroscopy.

The simplest possibility to tune a laser is to vary its temperature and thus its band gap. This method is particularly used for lead salt lasers in the mid-infrared region,[21] as shown in Fig. 22.49.

For monomode lasers, mode hopping, i.e. the discontinuous shift of lasing wavelength (or gain maximum) from one mode to the next, poses a problem for continuous tuning, as shown in Fig. 22.50. The continuous shift of emission wavelength is due to the temperature dependence of the index of refraction and subsequently the longitudinal modes. The index of refraction increases with increasing temperature at typically $\sim 3 \times 10^{-4}\,\mathrm{K}^{-1}$. Generally, a red-shift is the consequence.

Another possibility to vary the index of refraction (and thus the optical path length) is a variation of the carrier density. The coefficient $\mathrm{d}n_\mathrm{r}/\mathrm{d}n$ is about $-10^{-20}\,\mathrm{cm}^3$. In a two-section laser, separate regions (with separately controlled currents) for gain and tuning are present. The regions are separated with deep-etched trenches to avoid crosstalk. The tuning range is limited to about 10 nm. For a mode-hopping free tuning, the control of the phase in the cavity is important and requires an additional section for the phase control.

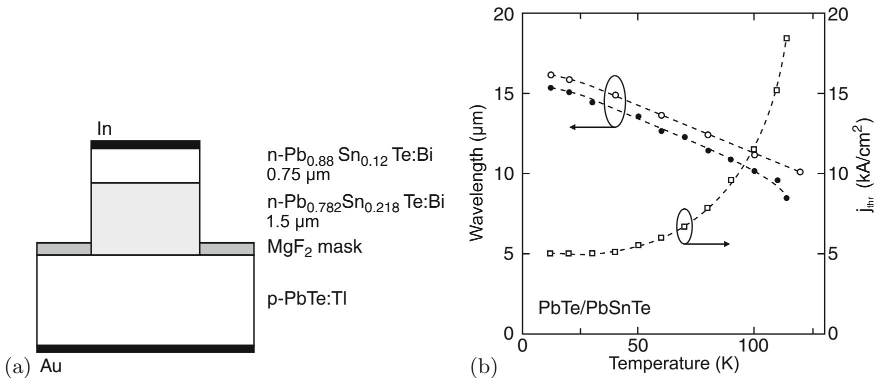

Fig. 22.49. (**a**) Schematic drawing of PbTe lead salt laser. (**b**) Tuning characteristics of such laser: Emission wavelength (*left scale*, *filled circles*: emission wavelength at cw threshold, *empty circles*: emission maximum under pulsed operation) and cw threshold current density (*right scale*) as a function of the heat-sink temperature. *Symbols* are experimental data, *dashed lines* are guides to the eye. Adapted from [1353]

[20] In order to make better use of the high bandwidth of the optical fiber several information channels with closely lying wavelengths are transmitted.

[21] Note the anomalous positive coefficient $\mathrm{d}E_\mathrm{g}/\mathrm{d}T$ as discussed in Sect. 6.7.

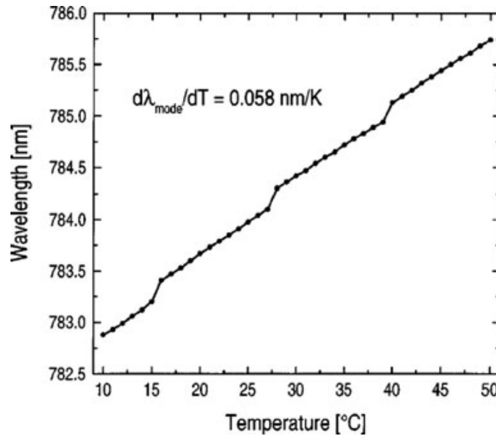

Fig. 22.50. Wavelength as a function of temperature (with mode hopping) for a GaAs-based DFB laser

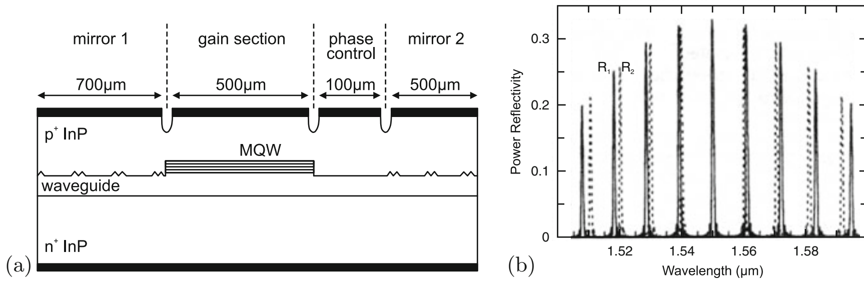

Fig. 22.51. (**a**) Schematic representation of SGDBR (sampled-grating DBR) laser with four sections. Adapted from [1354]. (**b**) Reflectance of two sampled gratings DBR mirrors

Such a three-section laser has separate regions (and current control) for the reflection, phase and amplification (or gain) region.

Using sampled gratings, the tuning range can be strongly increased to about 100 nm. A sampled grating is a nonperiodic lattice that has several ($\sim$ 10) reflection peaks. The laser structure has four sections (Fig. 22.51) with two mirrors that have slightly different sampled gratings. Via the carrier densities in the two mirror sections, different maxima can be brought to overlap (Vernier effect) and the position of the selected maximum can be tuned over a wide spectral range (Fig. 22.52).

22.4.13 Modulation

For transmission of information, the laser intensity must be modulated. This can be accomplished by direct modulation, i.e. modulation of the injection

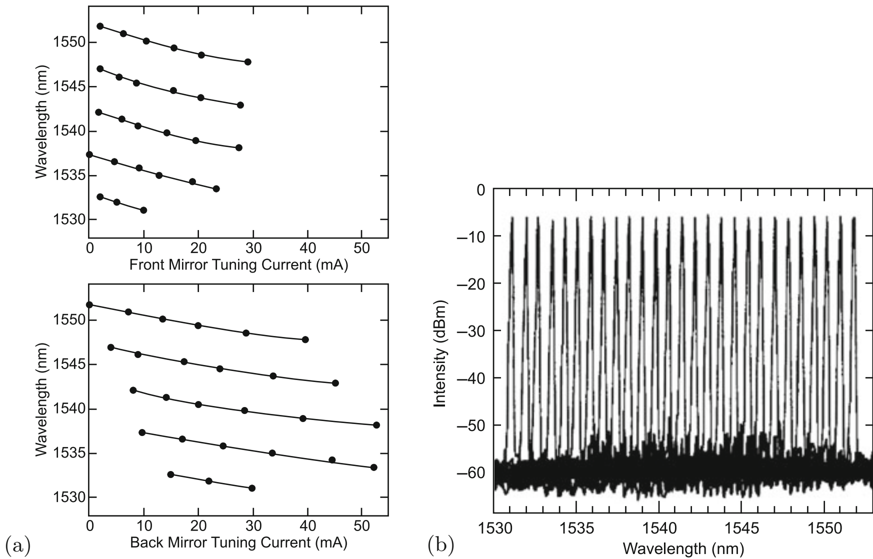

Fig. 22.52. (**a**) Tuning curves of two sampled gratings DBR mirrors for the front and back mirror current. (**b**) 27 wavelength channels (1531.12 to 1551.72 nm) with a channel separation of 1 nm. Adapted from [1355]

current, or external modulators, e.g. using, e.g., the voltage-induced shift of the absorption spectrum due to QCSE (cf. Sect. 12.1.2). For direct modulation, small- and large-signal modulation are distinguished.

Large-Signal Modulation

If a current pulse is fed to the laser, the laser radiation is emitted with a short time delay, the so-called turn-on delay (TOD) time. This time is needed to build up the carrier density for inversion. The time dependence of the density is (neglecting the density dependence of the lifetime)

$$n(t) = \frac{I\tau}{eAd}\left[1 - \exp\left(-\frac{t}{\tau}\right)\right] . \tag{22.40}$$

The TOD time to reach the threshold density (using (22.23)) is

$$\tau_{\mathrm{TOD}} = \tau \ln\left(\frac{I}{I - I_{\mathrm{thr}}}\right) . \tag{22.41}$$

We note that $\tau_{\mathrm{TOD}} > 0$ for $I > I_{\mathrm{thr}}$. Such a dependence is found experimentally (Fig. 22.53). The turn-on delay time decreases with increasing pump current but typically is at least 1 ns. In order to circumvent this limitation for more than about 1 GHz pulse repetition rate, the laser is biased slightly below threshold.

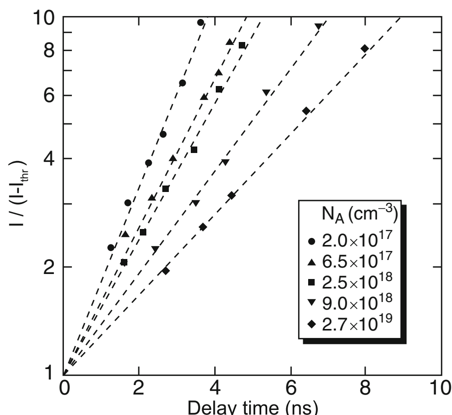

Fig. 22.53. Variation of turn-on delay time with the injected current for a laser at room temperature. Adapted from [1356]

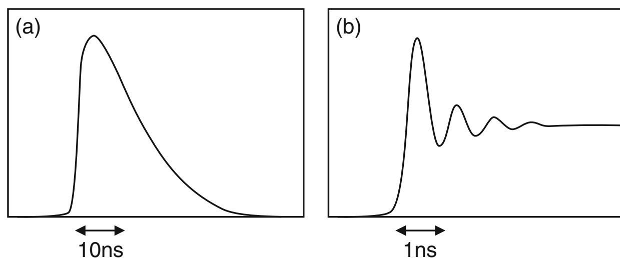

Fig. 22.54. Schematic response of (**a**) LED to current pulse and (**b**) of laser to current step

In Fig. 22.54a, the response (light emission) of a LED to a short current pulse is shown schematically. The monotonously decreasing transient (that is more or less exponential) corresponds to the carrier recombination dynamics. When a laser is excited with a steep (long) current pulse, the response exhibits so-called relaxation oscillations (RO) before the steady-state (cw) intensity level is reached (Fig. 22.54b).

In the laser, first the carrier density is built up. It surpasses the threshold density that leads to a build-up of the photon density. The laser pulse depletes the carrier density faster below threshold than the current can supply further carriers. Therefore, the laser intensity drops below the cw level. From the coupled rate equations for the electron and photon densities n and N_{ph}, the relaxation oscillations have a frequency of

$$f_{\mathrm{RO}} = \frac{1}{2\pi} \left(\frac{v_{\mathrm{g}} g' S_0}{\tau_{\mathrm{ph}}} \right)^{1/2} , \tag{22.42}$$

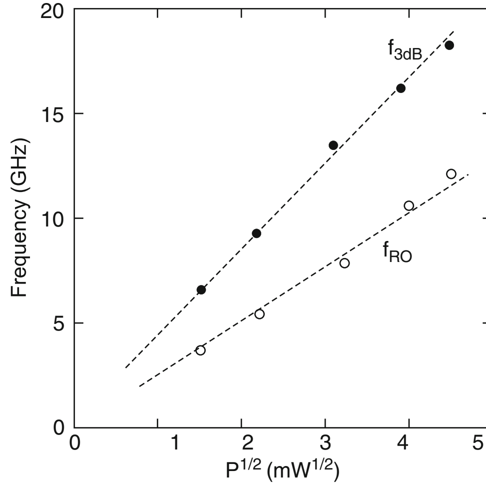

Fig. 22.55. Dependence of small-signal 3 dB cutoff frequency $f_{3\mathrm{dB}}$ (*filled symbols*) and relaxation oscillation frequency f_{RO} (*empty symbols*) on the square root of the output power P for a DFB-laser. Adapted from [1357]

where g' is the differential gain $g' = \mathrm{d}g/\mathrm{d}n$ ($g(n) = g_0 + g'(n - n_0)$) and S_0 is the photon density per volume that is proportional to the laser intensity. The dependence $f_{\mathrm{RO}} \propto S_0^{1/2}$ is also found experimentally (Fig. 22.55).

For digital data transmission, the laser is driven with pulse sequences. The response to a random bit pattern is called an 'eye pattern' and is shown in Fig. 22.56. The pattern consists of traces of the type shown in Fig. 22.54b. A clear distinction with well-defined trigger thresholds between 'on'- and 'off'-states can only be made if the eye formed by the overlay of all possible traces remains open. From the eye patterns in Fig. 22.56, it can be seen that the RO overshoot can be suppressed by driving the laser with a dc offset current well above threshold.

Small-Signal Modulation

In small-signal modulation, the injection current I is varied periodically by a small amount δI with $\delta I \ll I$ in the lasing regime. The current modulation leads to a corresponding variation of the output intensity. The frequency response is limited by the differential gain and the gain compression coefficient ϵ. The latter describes the saturation of gain with increasing photon density S_0 according to

$$g(n) = g_0 + \frac{g'(n - n_0)}{1 + \epsilon S_0} \,. \tag{22.43}$$

The frequency response shifts to higher frequency with increasing laser power as shown in Fig. 22.57b.

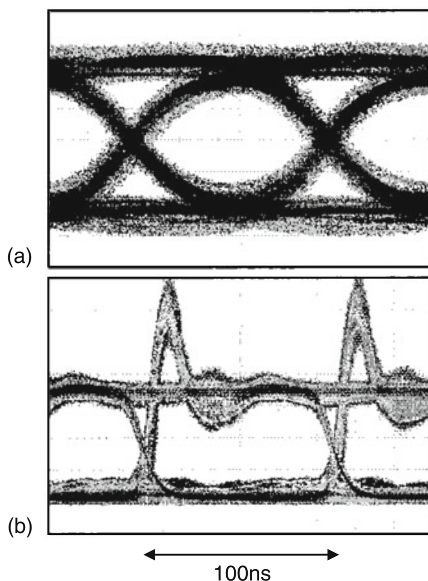

Fig. 22.56. Eye pattern of a single-mode VCSEL in response to a 10 Gb/s random bit pattern. The patterns are measured (**a**) with an offset current well above threshold and (**b**) with an offset current above but close to threshold. Adapted from [1358], reprinted with permission, ©2002 IEEE

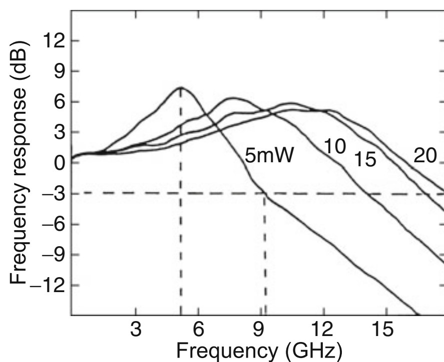

Fig. 22.57. Frequency response of a DFB-laser for various output powers as labeled. Adapted from [1357]

α factor

Another important quantity is the α factor, also called the linewidth enhancement factor [1359, 1360]. Due to the coupling of amplitude and phase fluctuations in the laser, the linewidth Δf is larger than expected.

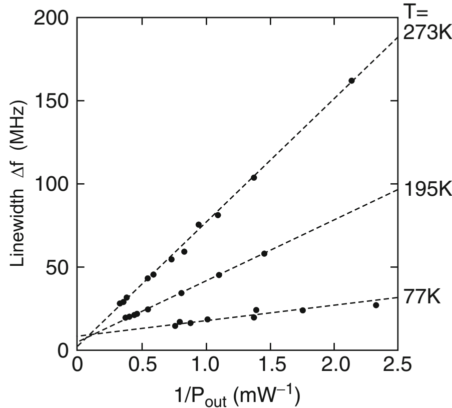

Fig. 22.58. Linewidth Δf of a cw GaAs/AlGaAs semiconductor laser at various temperatures as a function of the inverse output power $P_{\rm out}^{-1}$. At room temperature $\alpha \approx 5$. Adapted from [1361]

$$\Delta f = \frac{\hbar \omega v_{\rm g} R_{\rm spont} \ln R}{8\pi P_{\rm out} L} (1+\alpha^2) \ . \tag{22.44}$$

The linewidth enhancement is described via $(1+\alpha^2)$ with

$$\alpha = \frac{{\rm d}n_{\rm r}/{\rm d}n}{{\rm d}\kappa/{\rm d}n} = -\frac{4\pi}{\lambda} \frac{{\rm d}n_{\rm r}/{\rm d}n}{g'} \ , \tag{22.45}$$

where κ denotes the imaginary part of the index of refraction ($n^* = n_{\rm r} + {\rm i}\kappa$). Typical values for α are between 1 and 10. The linewidth is inversely proportional to the output power (Fig. 22.58).

22.4.14 Surface-Emitting Lasers

Surface-emitting lasers emit their beam normal to the surface. They can be fabricated from horizontal (edge-) emitters by reflecting the beam with a suitable mirror into the surface direction. This technology requires tilted facets or micro-optical components but allows for high power per area. In Fig. 22.59, a schematic cross section of a horizontal-cavity surface-emitting laser (HCSEL) and the light emission from an array of 220 such lasers are shown. The laser contains a 45° mirror that steers the light through the substrate and a Bragg mirror to provide the cavity mirror. The facet can also be fabricated such that the emission is to the top surface (Fig. 22.60). Another possibility to couple the beam out of a horizontal cavity is a surface grating.

Now, surface-emitting lasers with vertical-cavity (VCSEL), as shown in Fig. 22.25b, will be discussed. A detailed treatment can be found in [1363].

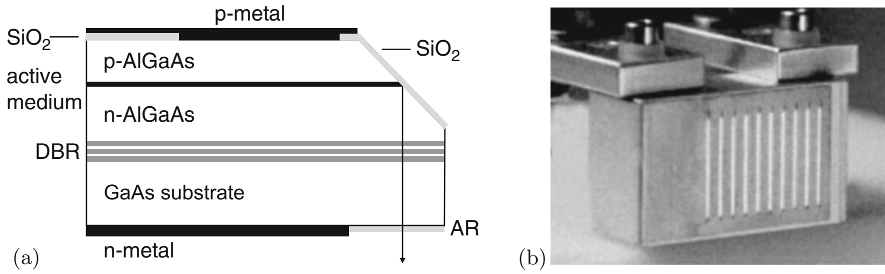

Fig. 22.59. (**a**) Principle of a surface-emitting laser. Light generated in the active region is internally reflected by the 45° angled mirror and directed through the substrate; 'AR': antireflection coating, 'DBR': epitaxial Bragg mirror. (**b**) Light emission from a 10 × 22 surface-emitting diode array. The light emission appears as stripes due to the broad beam divergence in the vertical direction. Part (**b**) reprinted with permission from [1362]

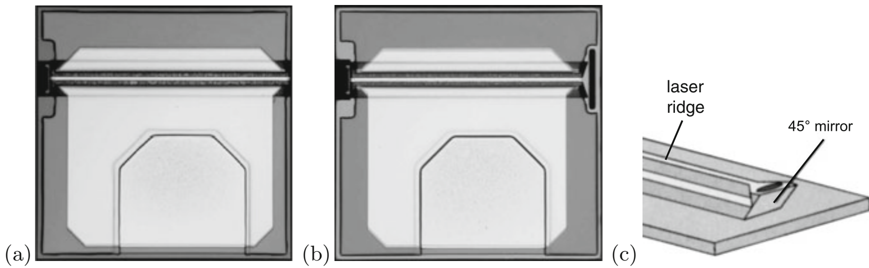

Fig. 22.60. (**a**) Horizontal Fabry–Perot cavity InP-based laser with 1310 nm emission length and 10 mW output power for modulation at 2.5 GB/s. The right facet is formed as DBR, emission is to the left. The trapezoid area in the center bottom of the image is the bond pad for the top contact. (**b**) Horizontal-cavity surface-emitting laser. Compared to (**a**), the right facet is replaced with a 45° mirror, leading to surface emission. (**c**) Schematic drawing of the tilted facet. Parts (**a**) and (**b**) from [1364]

VCSELs are of increasing importance after many issues regarding their technology and fabrication have been solved. VCSEL fabrication is essentially a planar technology and VCSELs can be fabricated as arrays (Fig. 22.61). An on-wafer test of their properties is possible. They offer a symmetrical (or possibly a controlled asymmetrical) beam profile (Fig. 22.62) with possible polarization control or fixation.

The cavity is formed by two highly reflecting Bragg mirrors with a distance of $\lambda/2$ or $3\lambda/2$ forming a microcavity (see Sect. 18.1.7). A high index contrast can be obtained from GaAs/AlAs Bragg mirrors in which the AlAs layers have been selectively oxidized in a hot moist atmosphere. Pure semiconductor Bragg mirrors suffer typically from small index contrast and require many pairs. This poses a problem, e.g. for InP-based VCSELs. In Fig. 22.63,

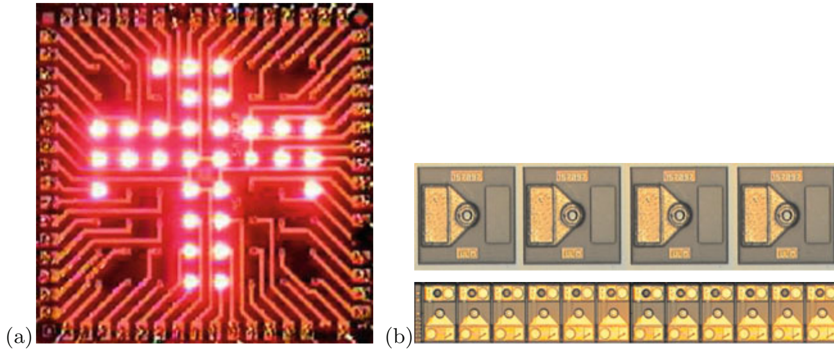

Fig. 22.61. (**a**), (**b**) VCSEL arrays. Part (**a**) reprinted from [1365] with permission, part (**b**) reprinted from [1366] with permission

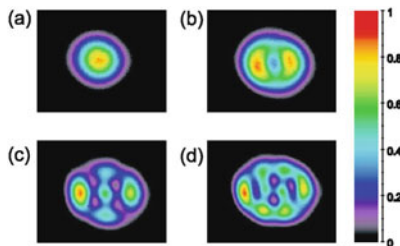

Fig. 22.62. In-plane near field of a VCSEL with 6 μm oxide aperture at various currents, (**a**) 3.0 mA, (**b**), 6.2 mA, (**c**) 14.7 mA, (**d**) 18 mA

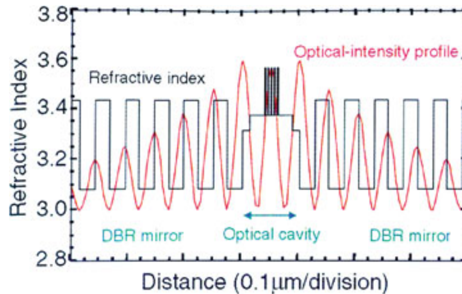

Fig. 22.63. Simulation of the longitudinal distribution of the optical field in a VCSEL structure. The active medium are five quantum wells in the center. Reproduced from [1368] by permission from the MRS Bulletin

the distribution of light intensity along a $3\lambda/2$ cavity is shown. In the stop band of the mirrors, there is only one optical mode, the cavity mode, that can propagate along the vertical (z) direction.

The current path through the active layer can be defined with an oxide aperture. This aperture is fabricated by selective oxidation of an AlAs layer,

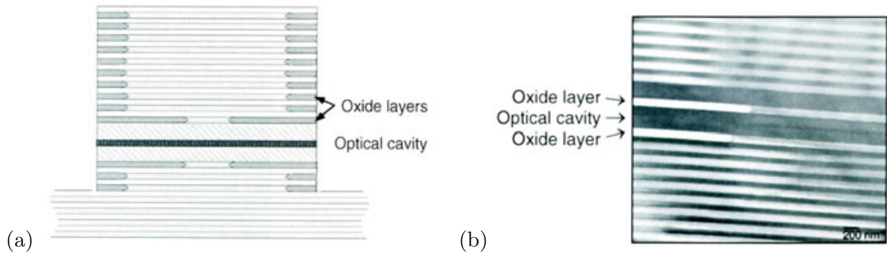

Fig. 22.64. (**a**) Schematic cross section of VCSEL with oxide aperture, (**b**) TEM image of cross section. Reproduced from [1368] by permission from the MRS Bulletin

leaving a circular opening in the center of the VCSEL pillar as shown in Fig. 22.64. The current can be injected through the mirrors if they are doped. Alternatively, the current can be directly fed to the active layer by so-called intracavity contacts.

The emission wavelength of a VCSEL can be shifted via a variation of temperature or pump power. Tuning of the VCSEL emission can also be accomplished by leaving an air gap between the cavity and the upper mirror [1367]. Applying a voltage to the lever arm with the top mirror, the width of the air gap can be varied. This variation leads to a shift of the cavity mode

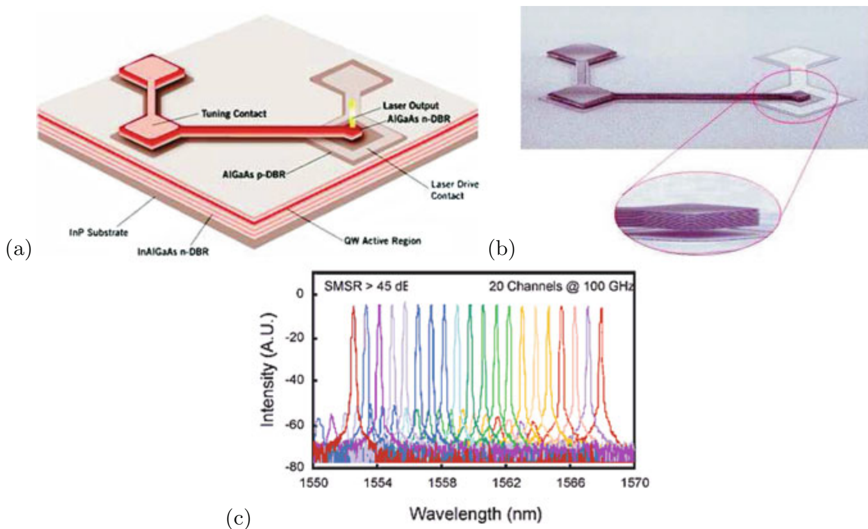

Fig. 22.65. (**a**) Schematic setup and (**b**) SEM image of VCSEL with air gap between active layer and top Bragg mirror, (**c**) spectra for different tuning conditions (width of air gap). From [1372]

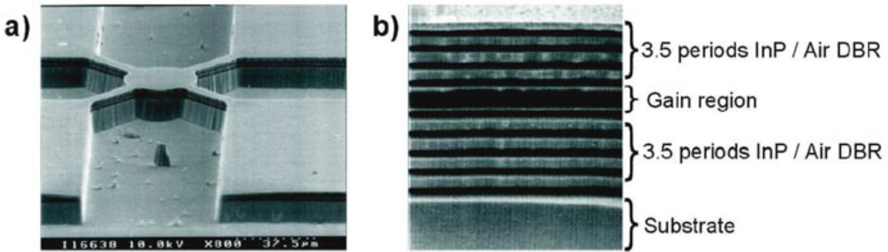

Fig. 22.66. (**a**) VCSEL with air gap and (**b**) Bragg mirror with high dielectric contrast InP/air interfaces. Reprinted with permission from [1373], ©2002 IEEE

and therefore of the laser emission wavelength (Fig. 22.65). A VCSEL with air gap and particularly a high contrast Bragg mirror is achieved with InP/air as shown in Fig. 22.66.

22.4.15 Optically Pumped Semiconductor Lasers

An easy way to pump semiconductor lasers is optical pumping. This technique is similar to diode-pumped solid-state lasers (DPSS). A (semiconductor) pump diode illuminates a suitable semiconductor structure (Fig. 22.67). The resonator is built between the bottom Bragg mirror of the semiconductor and the output coupler. The semiconductor structure contains suitable absorption layers (barriers) that absorb the pump light and quantum wells that emit laser radiation. This radiation is intracavity frequency doubled. In order to reach, e.g., a 488-nm output laser beam, a standard 808-nm pump

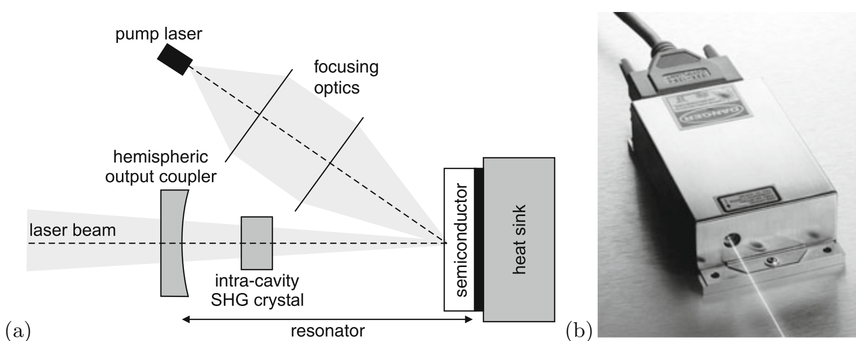

Fig. 22.67. (**a**) Schematic setup of optically pumped semiconductor laser (OPSL). The semiconductor chip consists of a Bragg mirror on the bottom, multiple quantum wells and an antireflection coating on the top. Adapted from [1368]. (**b**) OPSL source (488 nm, 20 mW, footprint: 125 × 70 mm^2). Reprinted with permission from [1374]

diode is employed. The InGaAs/GaAs quantum wells are designed to emit at 976 nm. Other design wavelengths of the quantum wells allow for other output wavelengths. This technology allows compact lasers with little heat dissipation [1369]. The optically pumped semiconductor laser (OPSL) is also known as a semiconductor disc laser.

22.4.16 Quantum Cascade Lasers

In a quantum cascade laser (QCL), the gain stems from an intersubband transition. The concept was conceived in 1971 [1370, 1371] and realized in 1994 [1325]. In Fig. 22.68a, the schematic conduction-band structure at operation is shown. The injector supplies electrons into the active region. The electron is removed quickly from the lower level in order to allow inversion. The electron is then extracted into the next injector. The laser medium consists of several such units as shown in Fig. 22.68b. Since every unit can deliver

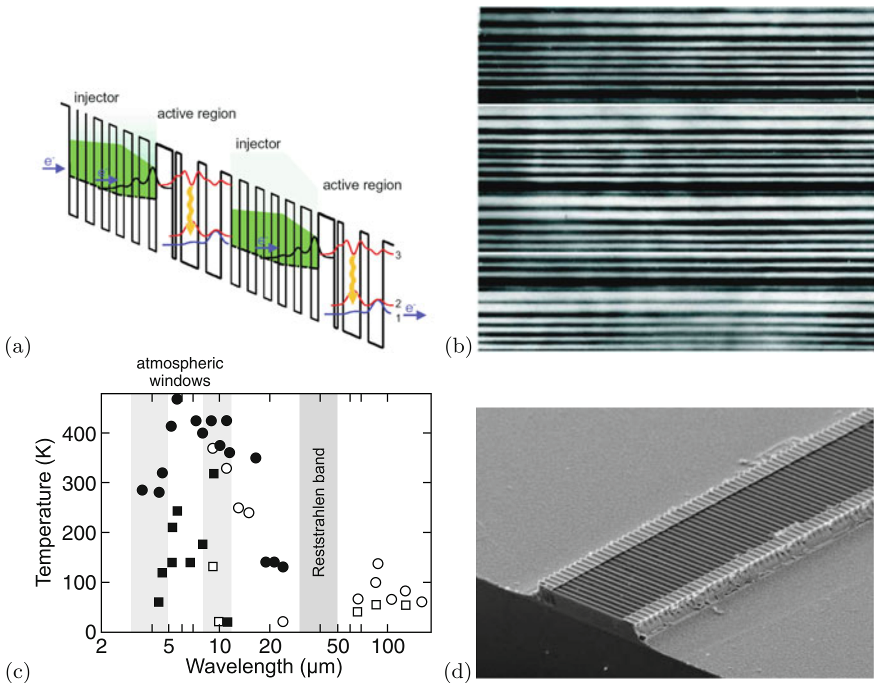

Fig. 22.68. (**a**) Schematic band diagram of quantum cascade laser. (**b**) Cross sectional TEM of cascade layer sequence. The periodicity of the vertical layer sequence is 45 nm. From [1375]. (**c**) Laser emission wavelengths and operation temperatures for various realized quantum cascade lasers (*squares*: cw, *circles*: pulsed operation, *solid symbols*: InP-, *empty symbols*: GaAs-based). Data from [1376]. (**d**) SEM image of a quantum cascade DFB laser (grating period: 1.6 µm). From [1376]

a photon per electron (with efficiency η_1), the total quantum efficiency of N units $\eta = N\,\eta_1$ can be larger than 1.

The emission wavelength is in the far- or mid-infrared, depending only on the designed layer thicknesses and *not* on the band gap of the material (Fig. 22.68d). In the mid-infrared, room-temperature operation has been achieved while operation in the far-infrared requires cooling so far. Extensions to the THz-range and the infrared spectral region (telecommunication wavelengths of 1.3 and 1.55 μm) seem feasible. The cascade laser concept can also be combined with the DFB technology to create single-mode laser emission (Fig. 22.68d).

22.4.17 Hot-Hole Lasers

The hot-hole laser, which is mostly realized with p-doped Ge, is based on a population inversion between the light- and heavy-hole valence subbands. The laser operates with crossed electric and magnetic fields (Voigt configuration, typically E = 0.5–3 kV/cm, B = 0.3–2 T) and at cryogenic temperatures (T = 4–40 K) [1377–1379].

A significant scattering process of hot carriers is interaction with optical phonons, mainly optical phonon emission. This process has a threshold in carrier energy given by the optical phonon energy. For sufficiently high electric fields and at low temperature, hot carriers accelerate without acoustical phonon interaction (ballistic transport) along the crystallographic direction in which the electric field is applied. These hot carriers reach the optical phonon energy and lose all their energy due to emission of an optical phonon. They accelerate again, repeating this directional motion in momentum space. This motion is called *streaming motion*.

For $|E/B|$ ratios of about 1.5 kV/cmT, the heavy holes are accelerated up to energies above the optical phonon energy (37 meV in germanium) and consequently are scattered strongly by these phonons. Under these conditions, a few per cent of the heavy holes are scattered into the light-hole band. The light holes remain at much lower energies and are accumulated at the bottom of the light-hole band below the optical phonon energy as sketched in Fig. 22.69. The continuous pumping of heavy holes into the light-hole band can lead to a population inversion. Consequently, laser radiation is emitted from optical (radiative) intervalence-band transitions (cf. Sect. 9.5.5). The emission wavelength is in the far-infrared around 100 μm. Typical p-Ge lasers span the frequency range 1–4 THz (300–70 μm) [1380] and deliver 1–10 W peak output power for 1 cm^3 typical active volume.

Since the applied electric field causes considerable heating, the temperature of the laser crystal rises quickly, within a few μs, up to 40 K. Then the laser action stops. Thus the duration of the electric-field excitation is limited to 1–5 μs (limiting the emission power) and the repetition frequency is only a few Hertz due to the necessary cooling. Research is underway towards

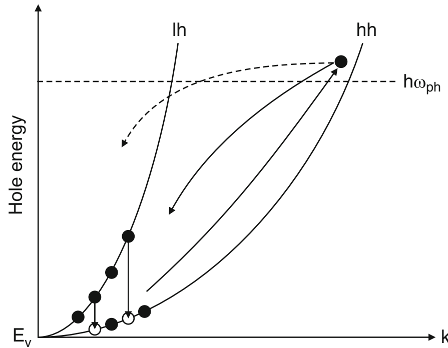

Fig. 22.69. Schematic cycle of hole motion in a hot-hole laser. *Filled* (*empty*) circles represent populated (unpopulated) hole states. The *solid lines* represent streaming motion of heavy hole, the *dashed line* represents scattering into the light hole band. *Arrows* denote radiative intervalence-band transitions

high duty cycle (possibly cw) operation by using smaller volumes and planar vertical-cavities [1381, 1382].

22.5 Semiconductor Optical Amplifiers

If the facets of a laser cavity are antireflection coated, a laser gain medium can be used as a semiconductor optical amplifier (SOA). A textbook on this subject is [1383]. Optical feedback from facets can also be avoided using tilted facets [1384].

A tapered amplifier geometry, as shown in Fig. 22.70a, allows for laterally monomode input and a preservation of the lateral beam quality during the propagation of the optical wave through the gain medium. The active medium

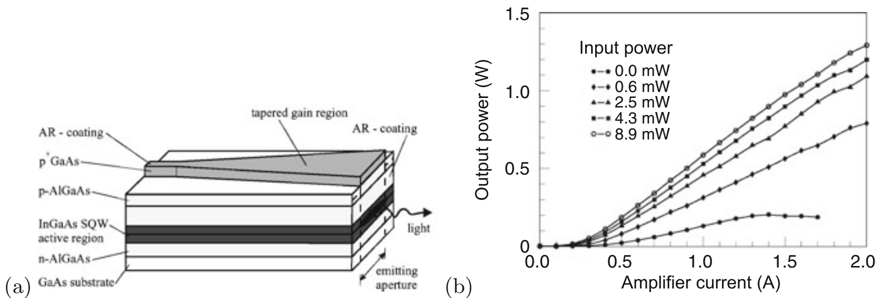

Fig. 22.70. (**a**) Schematic geometry of tapered semiconductor amplifier. (**b**) Optical output power vs. amplifier current for various values of the optical input power, taper angle was 5°. For zero input power only spontaneous and amplified spontaneous emission is observed. Reprinted with permission from [1385]

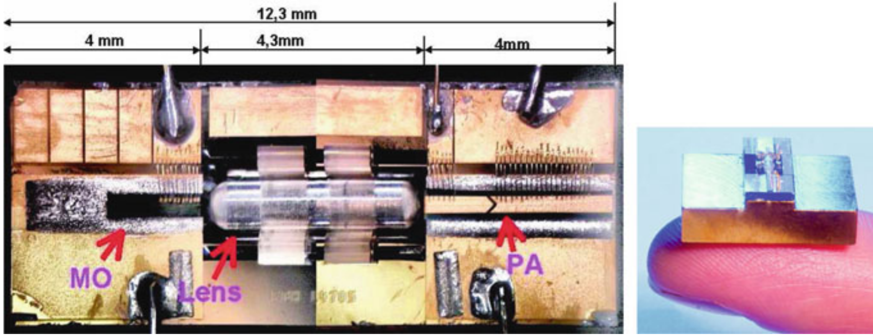

Fig. 22.71. Photographs of a MOPA arrangement of a laser (master oscillator, 'MO'), glass lens and tapered amplifier (power amplifier, 'PA') on a silicon micro-optical 'bench'. Reprinted with permission from [1386]

is an 8-nm compressively strained InGaAs quantum well. A typical taper angle is 5–10°. The input aperture is between 5 and 7-µm. The amplifier length is 2040 µm. More than 20 dB optical amplification can be obtained (Fig. 22.70b). The self-oscillation is suppressed for currents up to 2 A by AR facet coating of 10^{-4} in a 70-nm band. The wall-plug efficiency of the discussed amplifier is up to over 40%. If such an amplifier is arranged together with a seed laser diode (master oscillator), the setup is called MOPA (master oscillator power amplifier), as shown in Fig. 22.71. A modulated input also leads to a modulated output.

Quantum dot arrays can be a useful gain medium in a SOA [1387, 1388] due to their fast gain dynamics [1389] and broad spectrum (Sect. 22.3.6).

23 Transistors

23.1 Introduction

Transistors[1] are the key elements for electronic circuits such as amplifiers, memories and microprocessors. Transistors can be realized in bipolar technology (Sect. 23.2) or as unipolar devices using the field effect (Sect. 23.3). The equivalent in vacuum-tube technology to the transistor is the triode (Fig. 23.1a). Transistors can be optimized for their properties in analog circuits such as linearity and frequency response or their properties in digital circuits such as switching speed and power consumption. Early commercial models are shown in Fig. 23.2.

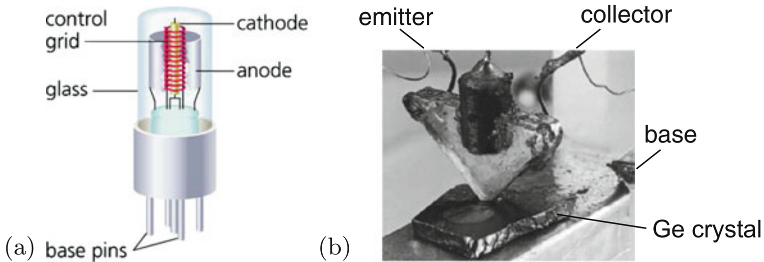

Fig. 23.1. (**a**) Schematic image of a vacuum triode. The electron current flows from the heated cathode to the anode when the latter is at a positive potential. The flow of electrons is controlled with the grid voltage. (**b**) Bell Laboratories' first (experimental) transistor, 1947

[1]The term 'transistor' was coined from the combination of 'transconductance' or 'transfer' and 'varistor' after initially such devices were termed 'semiconductor triodes'. The major breakthrough was achieved in 1947 when the first transistor was realized that showed gain (Figs. 1.6 and 23.1b).

M. Grundmann, *The Physics of Semiconductors*, 2nd ed., Graduate Texts in Physics, DOI 10.1007/978-3-642-13884-3_23,
© Springer-Verlag Berlin Heidelberg 2010

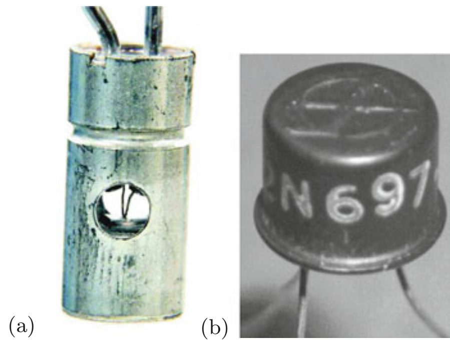

Fig. 23.2. (**a**) First commercial, developmental (point contact) transistor from BTL (Bell Telephone Laboratories) with access holes for adjustment of the whiskers pressing on a piece of Ge, diameter 7/32"=5 mm, 1948. (**b**) First high-performance silicon transistor (npn mesa technology), model 2N697 from Fairchild Semiconductor, 1958 (at $200, in 1960 $28.50). The product number is still in use (now $0.95)

23.2 Bipolar Transistors

Bipolar transistors consist of a pnp or npn sequence (Fig. 23.3). The layers (or parts) are named emitter (highly doped), base (thin, highly doped) and collector (normal doping level). The transistor can be considered to consist of two diodes (emitter–base and base–collector) back to back. However, the important point is that the base is sufficiently thin (in relation to its minority carrier diffusion length) and carriers from the emitter (which are minority carriers in the base) can dominantly reach the collector by diffusion.

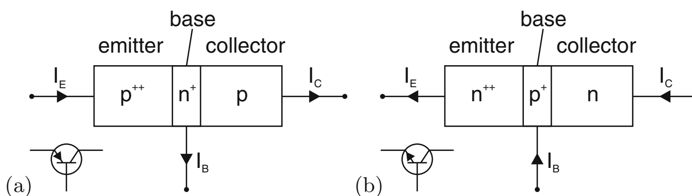

Fig. 23.3. Schematic structure and circuit symbol for (**a**) pnp and (**b**) npn transistors

In Fig. 23.4, the three basic circuits with a transistor are shown. They are classified by the common contact for the input and output circuit. The space charges and band diagram for a pnp transistor in the base circuit configuration are depicted in Fig. 23.5. The emitter–base diode is switched in the forward direction to inject electrons into the base. The base–collector

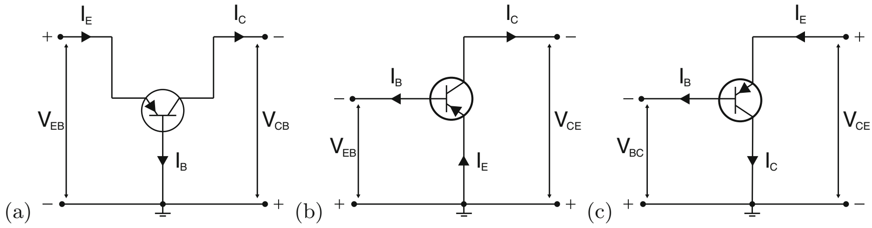

Fig. 23.4. Basic transistor circuits, named after the common contact: (**a**) Common base circuit, (**b**) common emitter circuit and (**c**) common collector circuit

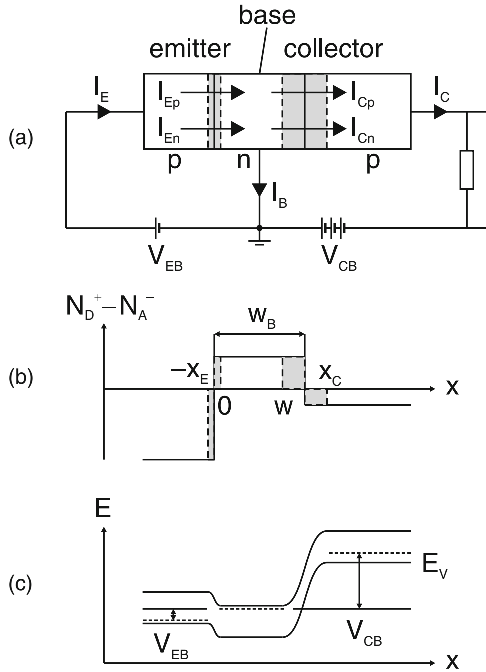

Fig. 23.5. pnp transistor in (**a**) base circuit. (**b**) Doping profile and space charges (abrupt approximation) and (**c**) band diagram for typical operation conditions

diode is switched in the reverse direction. The electrons that diffuse through the base and reach the neutral region of the collector are transported by the high drift field away from the base.

23.2.1 Carrier Density and Currents

The modeling of transistors is a complex topic. We treat the transistor on the level of the abrupt junction. As an approximation, we assume that all voltages

drop at the junctions. Series resistances, capacities and stray capacities and other parasitic impedances are neglected at this point.

The major result is that the emitter–base current from the forward-biased emitter–base diode will be transferred to the collector. The current flowing from the base contact is small compared to the collector current. This explains the most prominent property of the transistor, the current amplification.

For the neutral part of the base region of a pnp transistor, the stationary equations for diffusion and continuity are

$$0 = D_{\mathrm{B}} \frac{\partial^2 p}{\partial x^2} - \frac{p - p_{\mathrm{B}}}{\tau_{\mathrm{B}}} \tag{23.1a}$$

$$j_{\mathrm{p}} = -e D_{\mathrm{B}} \frac{\partial p}{\partial x} \tag{23.1b}$$

$$j_{\mathrm{tot}} = j_{\mathrm{n}} + j_{\mathrm{p}} \ , \tag{23.1c}$$

where p_{B} is the equilibrium minority carrier density in the base. From the discussion of the pn-diode, we know that at the boundary of the depletion layer the minority carrier density is increased by $\exp(eV/kT)$ (cf. (20.84a,b)). At the boundaries of the emitter–base diode (for geometry see Fig. 23.5a)

$$\delta p(0) = p(0) - p_{\mathrm{B}} = p_{\mathrm{B}} \left[\exp\left(\beta V_{\mathrm{EB}}\right) - 1\right] \tag{23.2a}$$

$$\delta n(-x_{\mathrm{E}}) = n(-x_{\mathrm{E}}) - n_{\mathrm{E}} = n_{\mathrm{E}} \left[\exp\left(\beta V_{\mathrm{EB}}\right) - 1\right] \ , \tag{23.2b}$$

where n_{E} and p_{B} are the equilibrium minority-carrier densities in the emitter and base, respectively. Accordingly, at the boundaries of the base–collector diode we have

$$\delta p(w) = p(w) - p_{\mathrm{B}} = p_{\mathrm{B}} \left[\exp\left(\beta V_{\mathrm{CB}}\right) - 1\right] \tag{23.3a}$$

$$\delta n(x_{\mathrm{C}}) = n(x_{\mathrm{C}}) - n_{\mathrm{C}} = n_{\mathrm{C}} \left[\exp\left(\beta V_{\mathrm{CB}}\right) - 1\right] \ . \tag{23.3b}$$

These are the boundary conditions for the diffusion equations in the p-doped layers and in the neutral region of the n-doped base. For the p-layers (with infinitely long contacts), the solution is (similar to (20.109)) for $x < -x_{\mathrm{E}}$ and $x > -x_{\mathrm{C}}$, respectively

$$n(x) = n_{\mathrm{E}} + \delta n(-x_{\mathrm{E}}) \exp\left(\frac{x + x_{\mathrm{E}}}{L_{\mathrm{E}}}\right) \tag{23.4a}$$

$$n(x) = n_{\mathrm{C}} + \delta n(-x_{\mathrm{C}}) \exp\left(-\frac{x - x_{\mathrm{C}}}{L_{\mathrm{C}}}\right) \ . \tag{23.4b}$$

L_{E} and L_{C} are the minority carrier (electron) diffusion lengths in the emitter and collector, respectively. The solution for the hole density in the neutral region in the base ($0 < x < w$) is

$$\begin{aligned} p(x) = p_{\mathrm{B}} &+ \left[\frac{\delta p(w) - \delta p(0) \exp\left(-w/L_{\mathrm{B}}\right)}{2 \sinh\left(w/L_{\mathrm{B}}\right)}\right] \exp\left(\frac{x}{L_{\mathrm{B}}}\right) \\ &- \left[\frac{\delta p(w) - \delta p(0) \exp\left(w/L_{\mathrm{B}}\right)}{2 \sinh\left(w/L_{\mathrm{B}}\right)}\right] \exp\left(-\frac{x}{L_{\mathrm{B}}}\right) \ . \end{aligned} \tag{23.5}$$

We shall denote the excess hole density at $x = 0$ and $x = w$ as $\delta p_\mathrm{E} = \delta p(0)$ and $\delta p_\mathrm{C} = \delta p(w)$, respectively. Typical ('normal') operation condition in the common base circuit is that $\delta p_\mathrm{C} = 0$ (Fig. 23.8a). In the 'inverted' configuration, the role of emitter and collector are reversed and $\delta p_\mathrm{E} = 0$. We can write (23.5) also as

$$p(x) = p_\mathrm{B} + \delta p_\mathrm{E} \frac{\sinh\left[(w-x)/L_\mathrm{B})\right]}{\sinh\left[w/L_\mathrm{B}\right]} + \delta p_\mathrm{C} \frac{\sinh\left[x/L_\mathrm{B})\right]}{\sinh\left[w/L_\mathrm{B}\right]} \,. \tag{23.6}$$

If the base is thick, i.e. $w \to \infty$, or at least large compared to the diffusion length ($w/L_\mathrm{B} \gg 1$), the carrier concentration is given by

$$p(x) = p_\mathrm{B} + \delta p(0) \exp\left(\frac{-x}{L_\mathrm{B}}\right) \tag{23.7}$$

and does not depend on the collector. In this case there is no transistor effect. A 'coupling' between emitter and collector currents that are given by the derivative $\partial p/\partial x$ at 0 and w, respectively, is only present for a sufficiently thin base.

From (23.6), the hole current densities at $x = 0$ and $x = w$ are given as[2]

$$j_\mathrm{Ep} = j_\mathrm{p}(0) = e\frac{D_\mathrm{B}}{L_\mathrm{B}}\left[\delta p_\mathrm{E} \coth\left(\frac{w}{L_\mathrm{B}}\right) - \delta p_\mathrm{C} \,\mathrm{csch}\left(\frac{w}{L_\mathrm{B}}\right)\right] \tag{23.8a}$$

$$j_\mathrm{Cp} = j_\mathrm{p}(w) = e\frac{D_\mathrm{B}}{L_\mathrm{B}}\left[\delta p_\mathrm{E} \,\mathrm{csch}\left(\frac{w}{L_\mathrm{B}}\right) - \delta p_\mathrm{C} \coth\left(\frac{w}{L_\mathrm{B}}\right)\right] \,. \tag{23.8b}$$

From (23.4a,b), the electron current densities at $x = -x_\mathrm{E}$ and $x = x_\mathrm{C}$ are given (with $\delta n_\mathrm{E} = \delta n(-x_\mathrm{E})$ and $\delta n_\mathrm{C} = \delta n(x_\mathrm{C})$) by

$$j_\mathrm{En} = j_\mathrm{n}(-x_\mathrm{E}) = e\frac{D_\mathrm{E}}{L_\mathrm{E}}\,\delta n_\mathrm{E} \tag{23.9a}$$

$$j_\mathrm{Cn} = j_\mathrm{n}(x_\mathrm{C}) = -e\frac{D_\mathrm{C}}{L_\mathrm{C}}\,\delta n_\mathrm{C} \,. \tag{23.9b}$$

The emitter current density is (similar to (20.112))

$$j_\mathrm{E} = j_\mathrm{p}(0) + j_\mathrm{n}(-x_\mathrm{E}) = e\frac{D_\mathrm{B}}{L_\mathrm{B}}\left[\delta p_\mathrm{E} \coth\left(\frac{w}{L_\mathrm{B}}\right) - \delta p_\mathrm{C} \,\mathrm{csch}\left(\frac{w}{L_\mathrm{B}}\right)\right] + e\frac{D_\mathrm{E}}{L_\mathrm{E}}\,\delta n_\mathrm{E} \,. \tag{23.10}$$

The collector current density is given as

$$j_\mathrm{C} = j_\mathrm{p}(w) + j_\mathrm{n}(x_\mathrm{C}) = e\frac{D_\mathrm{B}}{L_\mathrm{B}}\left[\delta p_\mathrm{E} \,\mathrm{csch}\left(\frac{w}{L_\mathrm{B}}\right) - \delta p_\mathrm{C} \coth\left(\frac{w}{L_\mathrm{B}}\right)\right] - e\frac{D_\mathrm{C}}{L_\mathrm{C}}\,\delta n_\mathrm{C} \,. \tag{23.11}$$

[2] $\coth x \equiv \cosh x/\sinh x$, $\mathrm{csch} x \equiv 1/\sinh x$.

In these equations, only the diffusion currents are considered. Additionally, the recombination currents in the depletion layers must be considered, in particular at small junction voltages.

23.2.2 Current Amplification

The emitter current consists of two parts, the hole current I_{pE} injected from the base and the electron current I_{nE} that flows from the emitter to the base (Fig. 23.5a). Similarly, the collector current is made up from the hole and electron currents I_{pC} and I_{pC}, respectively.

The total emitter current splits into the base and collector currents

$$I_{\mathrm{E}} = I_{\mathrm{B}} + I_{\mathrm{C}} \ . \tag{23.12}$$

The amplification (gain) in common base circuits

$$\alpha_0 = h_{\mathrm{FB}} = \frac{\partial I_{\mathrm{C}}}{\partial I_{\mathrm{E}}} = \frac{\partial I_{\mathrm{pE}}}{\partial I_{\mathrm{E}}} \frac{\partial I_{\mathrm{pC}}}{\partial I_{\mathrm{pE}}} \frac{\partial I_{\mathrm{C}}}{\partial I_{\mathrm{pC}}} = \gamma \alpha_{\mathrm{T}} M \ , \tag{23.13}$$

where γ is the emitter efficiency, α_{T} the base transport factor and M the collector multiplication factor. Since the collector is normally operated below the threshold for avalanche multiplication, $M = 1$.

The current amplification in the common emitter circuit is

$$\beta_0 = h_{\mathrm{FE}} = \frac{\partial I_{\mathrm{C}}}{\partial I_{\mathrm{B}}} \ . \tag{23.14}$$

Using (23.12), we find

$$\beta_0 = \frac{\partial I_{\mathrm{E}}}{\partial I_{\mathrm{B}}} - 1 = \frac{\partial I_{\mathrm{E}}}{\partial I_{\mathrm{C}}} \frac{\partial I_{\mathrm{C}}}{\partial I_{\mathrm{B}}} - 1 = \frac{1}{\alpha_0} \beta_0 - 1 = \frac{\alpha_0}{1 - \alpha_0} \ . \tag{23.15}$$

Since α_0 is close to 1 for a well-designed transistor, β_0 is a large number, e.g. $\beta_0 = 99$ for $\alpha_0 = 0.99$.

The emitter efficiency is (A denotes the device area)

$$\gamma = \frac{A \partial j_{\mathrm{p}}}{\partial I_{\mathrm{E}}} |_{x=0} = \left[1 + \frac{n_{\mathrm{E}}}{p_{\mathrm{B}}} \frac{D_{\mathrm{E}}}{D_{\mathrm{B}}} \frac{L_{\mathrm{B}}}{L_{\mathrm{E}}} \tanh\left(\frac{w}{L_{\mathrm{B}}} \right) \right]^{-1} \ . \tag{23.16}$$

The base transport factor, i.e. the ratio of minority carriers reaching the collector and the total number of injected minority carriers, is

$$\alpha_{\mathrm{T}} = \frac{j_{\mathrm{p}}(w)}{j_{\mathrm{p}}(0)} = \frac{\partial p / \partial x|_{x=w}}{\partial p / \partial x|_{x=0}} = \frac{1}{\cosh\left(w / L_{\mathrm{B}}\right)} \approx 1 - \frac{w^2}{2 L_{\mathrm{B}}^2} \ . \tag{23.17}$$

The approximation is valid if α_{T} is close to 1. If the base length is a tenth of the diffusion length, the base transport factor is $\alpha_{\mathrm{T}} > 0.995$. Then

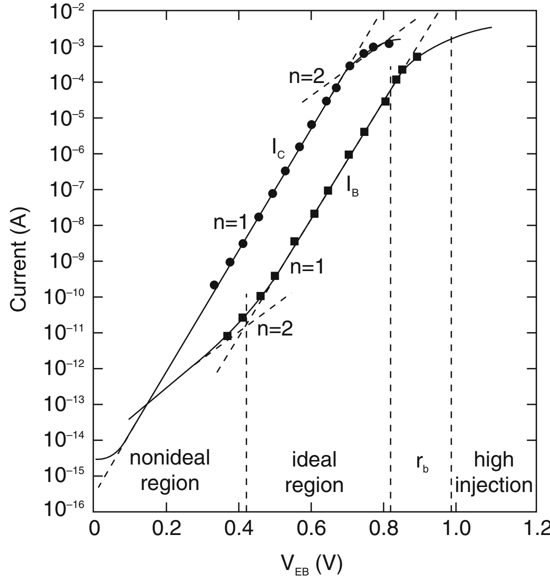

Fig. 23.6. Collector current I_C and base current I_B as a function of the emitter–base voltage V_{EB}. Adapted from [1390]

$$\beta_0 = h_{FE} \cong \frac{\gamma}{1-\gamma} \propto \frac{N_E}{w\, N_B} \,, \tag{23.18}$$

with N_E and N_B being the doping levels in the emitter and base, respectively. The base and collector current are shown in Fig. 23.6 as a function of the emitter–base voltage, i.e. the voltage at the injection diode. The collector current is close to the emitter–base diode current and displays a dependence $\propto \exp(eV_{EB}/kT)$. The base current shows a similar slope but is orders of magnitude smaller in amplitude. For small forward voltages of the emitter–base diode, the current is typically dominated by a nonradiative recombination current that flows through the base contact and has an ideality factor (m in Fig. 23.6) close to 2.

23.2.3 Ebers–Moll Model

The Ebers–Moll model (Fig. 23.7) was developed in 1954 and is a relatively simple transistor model that needs, at its simplest level (Fig. 23.7a) just three parameters. It can (and must) be refined (Figs. 23.7b,c). The model considers two ideal diodes ('F' (forward) and 'R' (reverse)) back to back, each feeding a current source. The F diode represents the emitter–base diode and and the R diode the collector–base diode. The currents are

$$I_F = I_{F0} \left[\exp\left(\beta V_{EB}\right) - 1\right] \tag{23.19a}$$

$$I_R = I_{R0} \left[\exp\left(\beta V_{CB}\right) - 1\right] \,. \tag{23.19b}$$

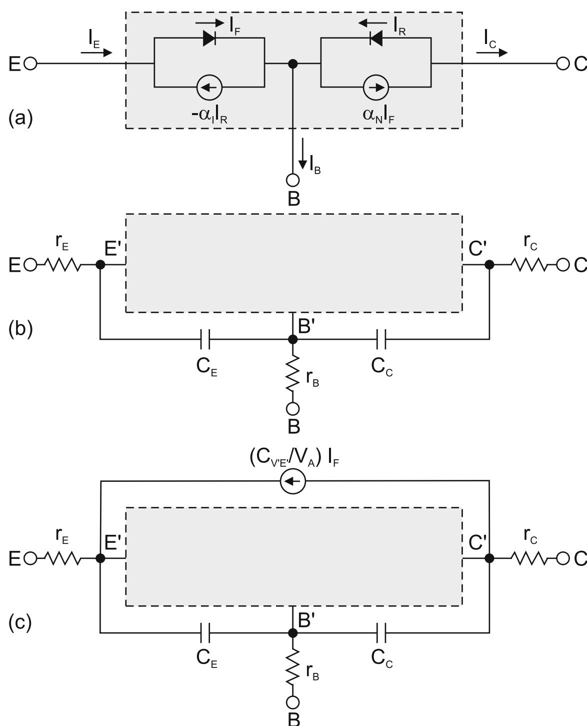

Fig. 23.7. Ebers–Moll model of a transistor, 'E': emitter, 'C': collector and 'B': base. Currents are shown for a pnp transistor. (**a**) Basic model (*grey area* in (**b**,**c**)), (**b**) model with series resistances and depletion-layer capacitances, (**c**) model additionally including the Early effect (V_A: Early voltage)

Using (23.8a,b)–(23.11), the emitter and collector currents are

$$\begin{aligned} I_E &= \hat{a}_{11} \left[\exp\left(\beta V_{EB}\right) - 1\right] + \hat{a}_{12} \left[\exp\left(\beta V_{CB}\right) - 1\right] \\ I_C &= \hat{a}_{21} \left[\exp\left(\beta V_{EB}\right) - 1\right] + \hat{a}_{22} \left[\exp\left(\beta V_{CB}\right) - 1\right] \ , \end{aligned}$$

with

$$\hat{a}_{11} = eA \left[p_B \frac{D_B}{L_B} \coth\left(\frac{w}{L_B}\right) + n_E \frac{D_E}{L_E} \right] \tag{23.21a}$$

$$\hat{a}_{12} = -eAp_B \frac{D_B}{L_B} \operatorname{csch}\left(\frac{w}{L_B}\right) \tag{23.21b}$$

$$\hat{a}_{21} = eAp_B \frac{D_B}{L_B} \operatorname{csch}\left(\frac{w}{L_B}\right) = -\hat{a}_{12} \tag{23.21c}$$

$$\hat{a}_{22} = -eA \left[p_B \frac{D_B}{L_B} \coth\left(\frac{w}{L_B}\right) + n_C \frac{D_C}{L_C} \right] \ . \tag{23.21d}$$

The currents at the three contacts are

$$I_{\mathrm{E}} = I_{\mathrm{F}} - \alpha_{\mathrm{I}} I_{\mathrm{R}} \tag{23.22a}$$

$$I_{\mathrm{C}} = \alpha_{\mathrm{N}} I_{\mathrm{F}} - I_{\mathrm{R}} \tag{23.22b}$$

$$I_{\mathrm{B}} = (1 - \alpha_{\mathrm{N}}) I_{\mathrm{F}} + (1 - \alpha_{\mathrm{I}}) I_{\mathrm{R}} \; . \tag{23.22c}$$

The last equation is obtained from (23.22a,b) using (23.12). By comparison with (23.19a,b) and (23.21a–d) we find

$$I_{\mathrm{F0}} = \hat{a}_{11} \tag{23.23a}$$

$$I_{\mathrm{R0}} = -\hat{a}_{22} \tag{23.23b}$$

$$\alpha_{\mathrm{I}} = \hat{a}_{12} / I_{\mathrm{R0}} \tag{23.23c}$$

$$\alpha_{\mathrm{N}} = \hat{a}_{21} / I_{\mathrm{F0}} = -\hat{a}_{12} / I_{\mathrm{F0}} = -\alpha_{\mathrm{I}} I_{\mathrm{R0}} / I_{\mathrm{F0}} \; . \tag{23.23d}$$

The constants α_{N} and α_{I} are the forward ('normal') ($\alpha_{\mathrm{N}} = \alpha_0$ from (23.13)) and reverse ('inverted') gains in the common base circuit, respectively. Both constants are larger than zero. Typically, $\alpha_{\mathrm{N}} \approx 0.98 \ldots 0.998 \lessapprox 1$ and $\alpha_{\mathrm{I}} \approx 0.5 \ldots 0.9 < \alpha_{\mathrm{N}}$. The model has three independent parameters, e.g. α_{N}, I_{F0} and I_{R0}. Equations (23.22a,b) can be rewritten as

$$I_{\mathrm{E}} = \alpha_{\mathrm{I}} I_{\mathrm{C}} + (1 - \alpha_{\mathrm{I}} \alpha_{\mathrm{N}}) I_{\mathrm{F}} \tag{23.24a}$$

$$I_{\mathrm{C}} = \alpha_{\mathrm{N}} I_{\mathrm{E}} - (1 - \alpha_{\mathrm{I}} \alpha_{\mathrm{N}}) I_{\mathrm{R}} \; . \tag{23.24b}$$

Under normal operation we have

$$I_{\mathrm{E}} = I_{\mathrm{F}} \tag{23.25a}$$

$$I_{\mathrm{C}} = \alpha_{\mathrm{N}} I_{\mathrm{E}} \; . \tag{23.25b}$$

The model can be refined and made more realistic by including the effect of series resistances and depletion-layer capacitances, increasing the number of parameters to eight. The Early effect (see p. 723) can be included by adding a further current source. This level is the 'standard' Ebers–Moll model with a total of nine parameters. Further parameters can be added. However, as is always the case with simulations, there is a tradeoff between the simplicity of the model and to what detail a real situation is approximated.

23.2.4 Current–Voltage Characteristics

In Fig. 23.8, the hole density in the base (of a pnp transistor) is shown for various voltage conditions. In Fig. 23.9, the I–V characteristics of a bipolar transistor in common base and common collector circuit are shown. In the common base circuit (Fig. 23.9a), the collector current is practically equal to the emitter current and is almost independent of the collector–base voltage. From (23.24b), the dependence of the collector current on the collector–base voltage is given (within the Ebers–Moll model) as

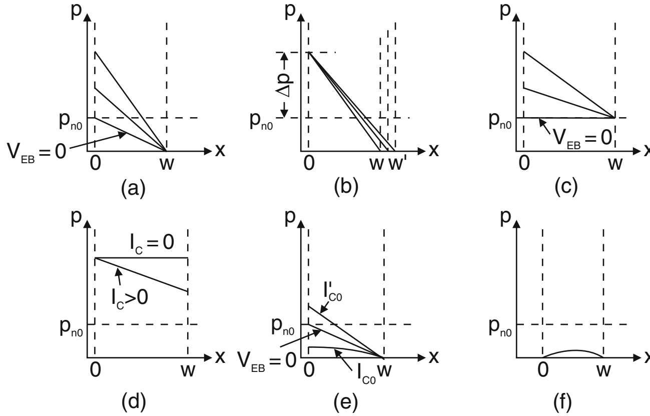

Fig. 23.8. Hole density (linear scale) in the base region (the neutral part of the base ranges from 0 to w) of a pnp transistor for various voltages. (**a**) normal voltages, V_{CB} = const. and various V_{EB} (in forward direction). (**b**) V_{EB} = const. and various values of V_{CB}. (**c**) Various values of $V_{\mathrm{EB}} > 0$, $V_{\mathrm{CB}} = 0$. (**d**) Both pn-junctions in forward direction. (**e**) Conditions for I_{C0} and I'_{C0}. (**f**) both junctions in reverse direction. Adapted from [384]

$$I_{\mathrm{C}} = \alpha_{\mathrm{N}} I_{\mathrm{E}} - (1 - \alpha_{\mathrm{I}} \alpha_{\mathrm{N}}) I_{\mathrm{R0}} \left[\exp\left(\beta V_{\mathrm{CB}}\right) - 1\right] \, . \tag{23.26}$$

V_{CB} is in the reverse direction. Therefore, the second term is zero for normal operating conditions. Since $\alpha_{\mathrm{N}} \lessapprox 1$, the collector current is almost equal to the emitter current.

Even at $V_{\mathrm{CB}} = 0$ (the case of (Fig. 23.8c), holes are extracted from the base since $\partial p/\partial x|_{x=w} > 0$. A small forward voltage must be applied to the collector–base diode in order to make the current zero, i.e. $\partial p/\partial x|_{x=w} = 0$

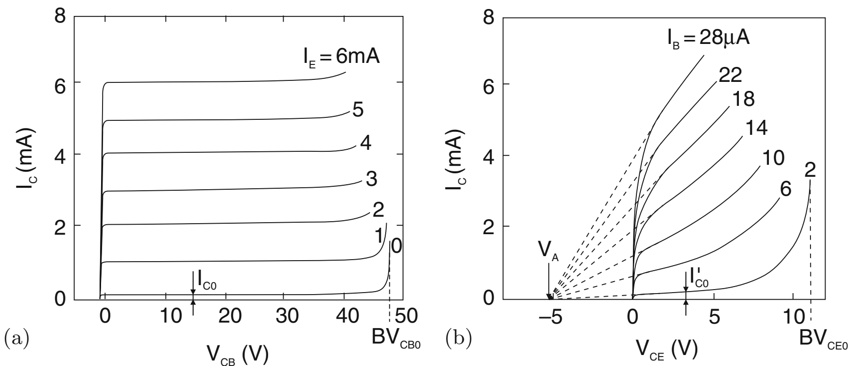

Fig. 23.9. Characteristics (I_{C} vs. V_{CB}) of a pnp transistor in (**a**) common base (CB) circuit (Fig. 23.4a) for various values of the emitter current as labeled. Adapted from [1391]. (**b**) Characteristics in common emitter (CE) circuit (Fig. 23.4b). Adapted from [1392]

(Fig. 23.8d). The collector saturation current I_{C0} is measured with an open emitter side. This current is smaller than the saturation current of the CB diode, since at the emitter side of the basis a vanishing gradient of the hole density is present (Fig. 23.8e). This reduces the gradient (and thus the current) at the collector side. The current I_{C0} is therefore smaller than the collector current for shorted emitter–base contact ($V_{EB} = 0$). At high collector voltage, the current increases rapidly at BV_{CB0} due to breakdown of the collector–base diode. It can also occur that the width of the neutral base region w becomes zero (punch-through). In this case, the emitter and collector are short-circuited.

In the common emitter circuit (Fig. 23.9b), there is a high current amplification I_C/I_B. Note that the collector current is given in mA and the base current in μA. The current increases with increasing V_{CE} because the base width w decreases and β_0 increases. There is no saturation of the I–V characteristics (Early effect). Instead, the I–V curves look as if they start at a negative collector–emitter voltage, the so-called Early voltage V_A. In the linear regime, the characteristic can be approximated by

$$I_C = \left(1 + \frac{V_{CE}}{V_A}\right) \beta_0 I_B \ . \tag{23.27}$$

The physical reason for the increase of the collector current with increasing V_{CE} is the increasing reverse voltage at the collector–base diode that causes a so-called 'base-width modulation', as shown in Fig. 23.8b. This causes an expansion of the CB depletion layer and subsequently a reduction of the neutral base width w. w will be smaller and smaller compared to the geometrical base width w_B. When w is reduced, the base transfer factor α_T (23.17) becomes closer to 1 and the current gain β_0 (23.15) increases. Therefore, the collector current increases for a given (fixed) base current. For transistors for which the geometrical base width is much larger than the width of the depletion layers, the Early voltage is

$$V_A \approx \frac{e}{\epsilon_s} N_B w_B^2 \ . \tag{23.28}$$

For small collector–emitter voltage, the current quickly drops to zero. V_{CE} is typically split in such a way that the emitter–base diode is well biased forward and the CB diode has a high reverse voltage. If V_{CE} drops below a certain value ($\approx 1\,\text{V}$ for silicon transistors), there is no longer any bias at the CB diode. A further reduction of V_{CE} biases the CB diode in the forward direction and quickly brings the collector current down to zero.

23.2.5 Basic Circuits

Common Base Circuit

In the common base configuration, there is no current amplification since the currents flowing through emitter and base are almost the same. However,

there is voltage gain since the collector current causes a large voltage drop across the load resistor.

Common Emitter Circuit

The input resistance of the common emitter circuit (Fig. 23.10a) depends on the emitter–base diode and varies between a value of the order of 100 kΩ at small current and a few Ω at larger current and high V_{EB}. The voltage gain is

$$r_{\mathrm{V}} = \frac{V_{\mathrm{CE}}}{V_{\mathrm{EB}}} = \frac{I_{\mathrm{C}}}{V_{\mathrm{EB}}} R_{\mathrm{L}} \ , \tag{23.29}$$

where R_{L} is the load resistance in the output circuit (see Fig. 23.4b). The ratio $g_{\mathrm{m}} = I_{\mathrm{C}}/V_{\mathrm{EB}}$ is called the forward transconductance. Also, the differential transconductance $g'_{\mathrm{m}} = \partial I_{\mathrm{C}}/\partial V_{\mathrm{EB}}$ is used. The voltage gain of the common emitter circuit is typically 10^2–10^3. Since current *and* voltage are amplified, this circuit has the highest power gain.

If the input voltage V_{EB} (U_1 in Fig. 23.10a) is increased, the collector current rises. This increase causes an increase of the voltage drop across the load resistance R_{L} and a decrease of the output voltage U_2. Therefore, the phase of the input signal is reversed and the amplifier is inverting.

Common Collector Circuit

In Fig. 23.10c, the collector is connected to mass for alternating currents. Input and output current flow through the load resistance at which part of the input voltage drops. The input voltage is divided between the load resistor R_{L} and the emitter–base diode. At the transistor, the voltage $V_{\mathrm{BE}} = V_1 - V_{\mathrm{RL}}$ is applied. If the input voltage is increased, I_2 increases. This leads to a larger voltage drop at the load resistor and therefore to a decrease of V_{BE}, working against the original increase. The input resistance R_1 is large despite a small load resistance, $R_1 \approx \beta_0 R_{\mathrm{L}}$. The input voltage is larger than V_{RL}, thus no voltage gain occurs (actually it is a little smaller than 1).

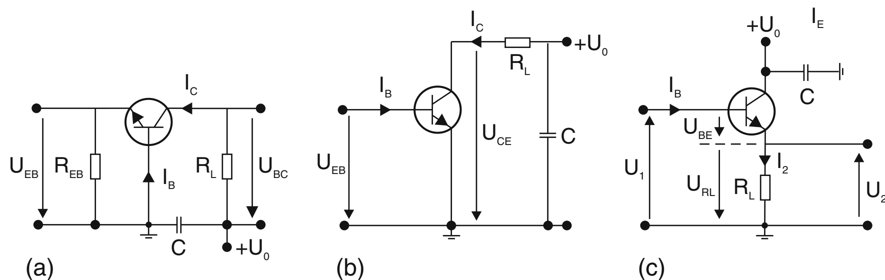

Fig. 23.10. (**a**) Common base, (**b**) common emitter and (**c**) common collector circuits with external loads

The current amplification is $(\beta+1)$. The output resistance R_2 is small, $R_2 = U_2/I_2 \approx R_L/\beta_0$. Therefore, this circuit is also called an impedance amplifier that allows high-impedance sources to be connected low-impedance loads. Since an increase of the input voltage leads to an increase of the output voltage that is present at the emitter, this circuit is a direct amplifier and is also called an emitter follower.

23.2.6 High-Frequency Properties

Transistors for amplification of high-frequency signals are typically chosen as npn transistors since electrons, the minority carriers in the base, have higher mobility than holes. The active area and parasitic capacitance must be minimized. The emitter is formed in the shape of a stripe, nowadays in the 100 nm regime. The base width is in the 10 nm range. High p-doping of GaAs with low diffusion of the dopant is accomplished with carbon. Defects that would short emitter and collector at such thin base width must be avoided.

An important figure of merit is the cutoff frequency f_T for which h_{FE} is unity in the common emitter configuration. The cutoff frequency is related to the emitter–collector delay time τ_{EC} by

$$f_T = \frac{1}{2\pi\tau_{EC}} . \tag{23.30}$$

The delay time is determined by the charging time of the emitter–base depletion layer, the base capacitance, and the transport through the base–collector depletion layer. It is favorable if all times are short and similar. It does not help to minimize only one or two of the three processes since the longest time determines the transistor performance.

Another important figure of merit is the maximum frequency with which the transistor can oscillate in a feedback circuit with zero loss. This frequency is denoted by f_{max}. Approximately,

$$f_{max} \simeq \sqrt{\frac{f_T}{8\pi R_B C_{CB}}} , \tag{23.31}$$

where R_B is the base resistance and C_{CB} is the collector–base capacitance. f_{max} is larger than f_T, by a factor of the order of three.

23.2.7 Heterobipolar Transistors

In a heterojunction bipolar transistor (HBT), the emitter–base diode is formed with a heterostructure diode. The desired functionality is obtained when the emitter is made from the higher-bandgap material and the base from the lower-bandgap material. The schematic band diagram is shown in Fig. 23.11 (see Fig. 20.72c for the emitter–base diode).

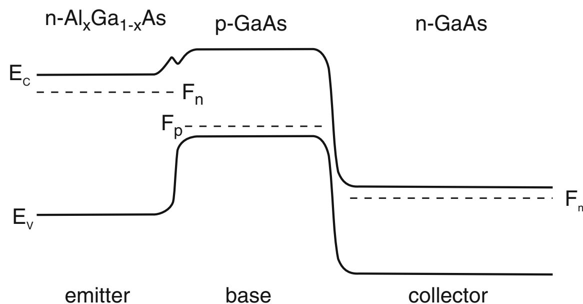

Fig. 23.11. Schematic band diagram of a heterojunction bipolar transistor

The higher discontinuity in the valence band, compared to a homojunction with the base material, provides a higher barrier for hole transport from the base to the emitter. Thus, the emitter efficiency is increased. Another advantage is the possibility for higher doping of the base without loss of emitter efficiency. This reduces the base series resistance and leads to better high-frequency behavior due to higher current gain and a smaller RC time constant. Also, operation at higher temperature is possible when the emitter has a larger band gap. Current InP/InGaAs-based HBTs have cutoff frequencies beyond 30 GHz, SiGe-HBTs beyond 80 GHz. The high-frequency performance is influenced by the velocity-overshoot effect (cf. Sect. 8.5.3) [1393].

In Fig. 23.12, an InAlAs/InGaAs HBT is shown [1394]. The cutoff frequency is 90 GHz. For the layer design, a fairly thick collector with low doping was chosen. This design allows a broad depletion layer with fairly small maximum electric field and thus a high breakdown voltage of $BV_{\mathrm{CE0}} > 8.5\,\mathrm{V}$. The base is not too thin (80 instead of maybe 60 nm) to reduce the series resistance. A graded region between emitter and base was chosen to avoid a spike occurring in the conduction band (Fig. 20.72b) and keep the turn-on voltage low.

23.2.8 Light-Emitting Transistors

The base current has two components. One is the recombination current in the neutral region of the emitter; this current can be suppressed in the HBT. The other is the recombination in the base region itself.[3] If quantum wells are introduced into the base region, this recombination can occur radiatively between electrons and holes captured into the quantum well (Fig. 23.13). The spectrum exhibits two peaks from the QWs and the GaAs barrier.

[3] Also, a recombination current in the emitter–base depletion region is possible. However, since in normal operating conditions this diode is forward biased, the depletion layer is short and the associated recombination current is small, cf. p. 573.

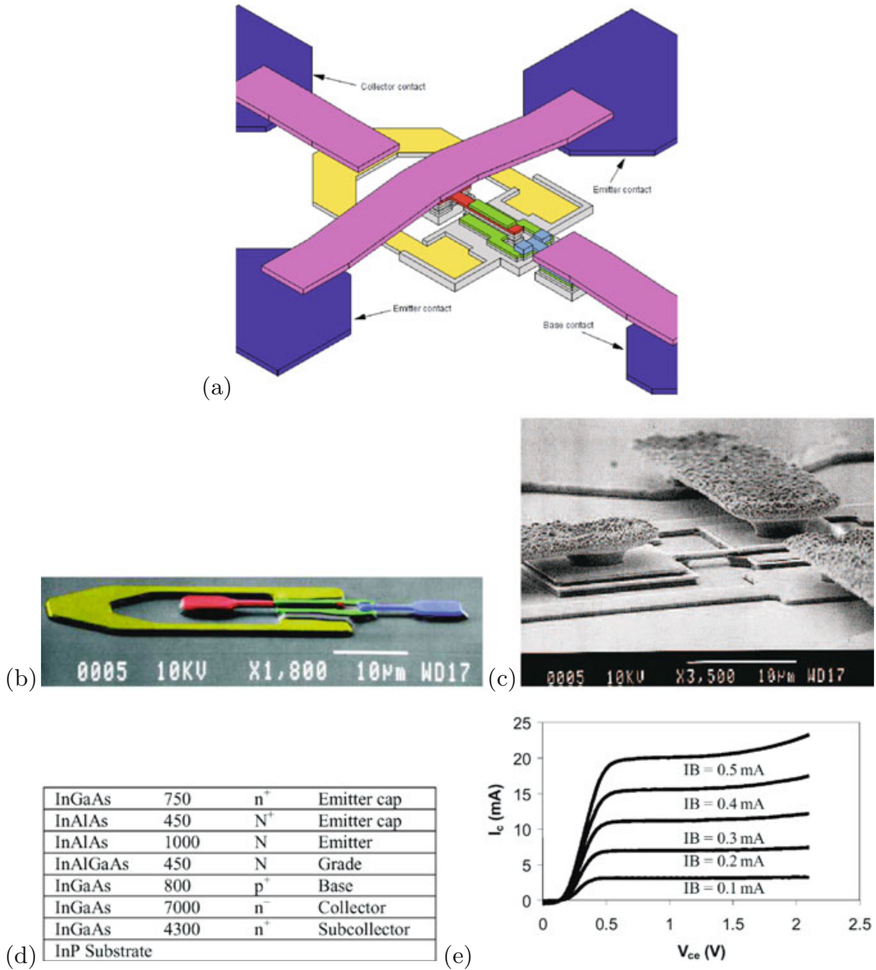

InGaAs	750	n^+	Emitter cap
InAlAs	450	N^+	Emitter cap
InAlAs	1000	N	Emitter
InAlGaAs	450	N	Grade
InGaAs	800	p^+	Base
InGaAs	7000	n^-	Collector
InGaAs	4300	n^+	Subcollector
InP Substrate			

Fig. 23.12. (**a**) Schematic layout of a high-frequency HBT and SEM images (**b**) without and (**c**) with contacts. (**d**) Epitaxial layer sequence and (**e**) static performance data. Parts (**a**,**b**) from [1395], parts (**d**,**e**) from [1394]

23.3 Field-Effect Transistors

Next to the bipolar transistors, the field-effect transistors (FET) are another large class of transistors. FETs were conceptualized first but due to technological difficulties with semiconductor surfaces, realized second. The principle is fairly simple: A current flows through a channel from source to drain. The current is varied via the channel conductivity upon the change of the gate voltage. The gate needs to make a nonohmic contact to the semiconductor. Since the conductivity in the channel is a property related to the majority charge carriers, FETs are called unipolar transistors. FETs feature a higher

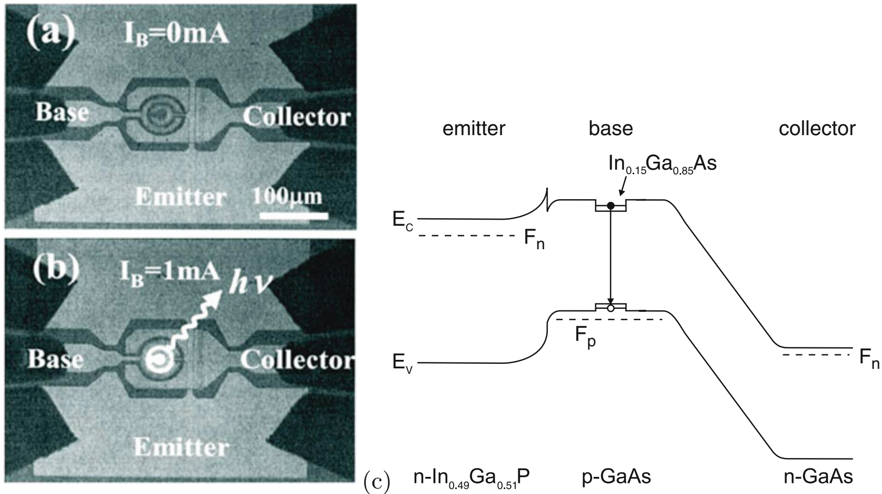

Fig. 23.13. Microscopic image of an InGaP/GaAs HBT with two 5-nm InGaAs/GaAs QWs in the 30-nm wide base at (**a**) zero base current and (**b**) at 1 mA base current in the common emitter configuration with Si CCD image of light emission. (**c**) Schematic band diagram of a HBT with a single InGaAs/GaAs quantum well in the base. Parts (**a**,**b**) from [1396], part (**c**) adapted from [1396]

input impedance than bipolar transistors, a good linearity, and a negative temperature coefficient and thus a more homogeneous temperature distribution. According to the structure of the gate diode we distinguish JFETs, MESFETs and MOSFETs, as discussed in the following:

In the junction FET (JFET), the variation of channel conductivity is accomplished via the extension of the depletion layer of the pn-junction formed by the gate and the channel material (Fig. 23.14a). The JFET was analyzed by Schottky in 1952 [69] and realized by Dacey and Ross in 1953 [70].

In a MESFET, a metal–semiconductor diode (Schottky diode) is used as rectifying contact instead of a pn-diode. Otherwise, the principle is the same as that of the JFET. After the proposal by Mead in 1966 [89], the first (epitaxial) GaAs MESFET was realized by Hooper and Lehrer in 1967 [90]. The MESFET offers some advantages, such as the fabrication of the metal gate at lower temperature than necessary for the (diffusion or epitaxy of the) pn-diode, lower resistance, good thermal contact. The JFET can be made with a heterostructure gate to improve the frequency response.

In a MISFET, the gate diode is a metal–insulator–semiconductor diode (Fig. 23.14b). If the insulator is an oxide, the related FET is a MOSFET. When the gate is put at a positive voltage (for a p-channel), an inversion layer is formed close to the insulator–semiconductor interface. This layer is an n-conducting channel allowing conduction between the two oppositely biased pn-diodes. It can carry a high current. The MOSFET was theoretically

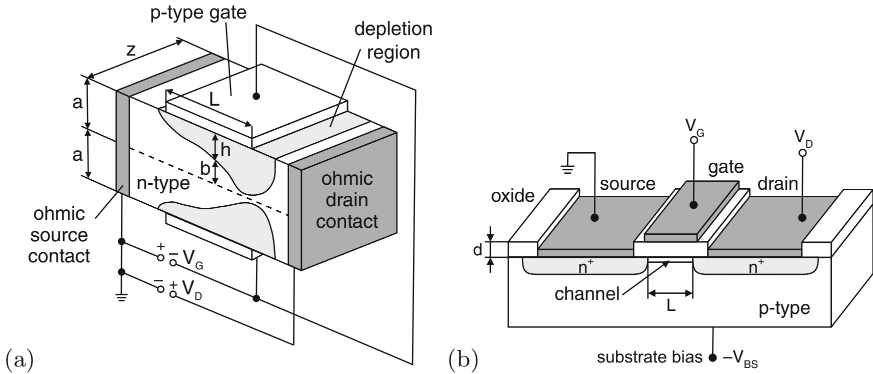

Fig. 23.14. (**a**) Shockley's model of a JFET. The *dashed line* represents the middle of the symmetric channel of total thickness $2a$. The *light grey area* is the depletion layer with thickness h. The gate length is L. The *dark grey* areas are ohmic metal contacts. Based on [70]. (**b**) Scheme of a MOSFET with channel length L and oxide thickness d. The *dark grey* areas are ohmic metal contacts. Adapted from [384]

envisioned early by Lilienfeld in 1925 [34] and realized only in 1960 by Kahng and Atalla [80].

FETs come in 'n' and 'p' flavors, depending on the conductivity type of the channel. For high-frequency applications, typically an n-channel is used due to the higher mobility or drift velocity. In CMOS (complementary MOS) technology, both n-FETs and p-FETs are integrated in high density, allowing the effective realization of logic gates with minimized power consumption.

23.4 JFET and MESFET

23.4.1 General Principle

The principal characteristic of a JFET is shown in Fig. 23.15. At $V_{\mathrm{D}} = 0$ and $V_{\mathrm{G}} = 0$, the transistor is in thermodynamic equilibrium and there are no net currents. Underneath the gate diode, a depletion layer is present. If for zero gate voltage the source–drain voltage is applied to the channel, the current increases linearly. The positive voltage at the drain contact causes the expansion of the depletion layer of the (reversely biased) gate–drain pn-diode. When the two (the upper and the lower) depletion regions meet (pinch-off), the current saturates. The respective source–drain voltage is denoted as $V_{\mathrm{D,sat}}$. For high gate–drain (reverse) voltage V_{D}, breakdown occurs with a strong increase of the source–drain current. A variation of the gate voltage V_{G} leads to a variation of the source–drain current. A reverse voltage leads to a reduction of the saturation current and saturation at lower source–drain voltage. For a certain gate voltage V_{P}, the pinch-off voltage, no current can flow in the channel any longer since pinch-off exists even for $V_{\mathrm{D}} = 0$.

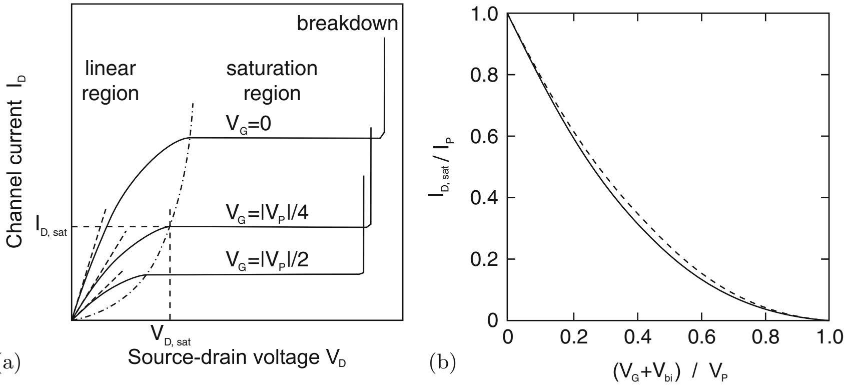

Fig. 23.15. (**a**) Principal characteristics of a JFET. The channel current I_{D} is shown as a function of the source–drain voltage V_{D} for three different values of the (absolute value of the) gate voltage V_{G}. The saturation values $V_{\mathrm{D,sat}}$ and $I_{\mathrm{D,sat}}$ are indicated for one curve. The intersections with the *dash-dotted* line yield the saturation voltage. Adapted from [384] (**b**) Transfer behavior of a JFET for two different carrier distributions, homogeneous (*solid* line) and δ-like (*dashed* line). Adapted from [384] after [1397, 1398]

23.4.2 Static Characteristics

Here, we will calculate the general static behavior outlined in the previous section. We assume a long channel ($L \gg a$), the abrupt approximation for the depletion layer, the gradual channel approximation, i.e. the depletion layer depth changes slowly along x, and a field-independent, constant mobility. In this case, the two-dimensional Poisson equation for the potential distribution V can be used by solving it along the y direction (channel depth) for all x-positions (adiabatic approximation),

$$\frac{\partial^2 V}{\partial y^2} = -\frac{\rho(y)}{\epsilon_{\mathrm{s}}} \; . \tag{23.32}$$

The geometry is shown in the inset of Fig. 23.15b.

The depth h of the depletion layer in the abrupt approximation is given by (cf. (20.92), reverse voltages are counted as positive here)

$$h = \left[\frac{2\epsilon_{\mathrm{s}}}{e N_{\mathrm{D}}} \left(V_{\mathrm{bi}} + V_{\mathrm{G}} + V(x) \right) \right]^{1/2} \; . \tag{23.33}$$

Here, we have assumed homogeneous doping, i.e. N_{D} does not depend on y (or x). The built-in voltage (for a p*n gate diode) is given by $V_{\mathrm{bi}} = \beta^{-1} \ln \left(\frac{N_{\mathrm{D}}}{n_{\mathrm{i}}} \right)$ (20.83a). The voltage V is the applied source–drain voltage in relation to the source. The depth of the depletion layer at $x = 0$ (source) and $x = L$ (drain) is given by

$$y_1 = h(0) = \left[\frac{2\epsilon_s}{eN_D}(V_{bi} + V_G)\right]^{1/2} \quad (23.34a)$$

$$y_2 = h(L) = \left[\frac{2\epsilon_s}{eN_D}(V_{bi} + V_G + V_D)\right]^{1/2} . \quad (23.34b)$$

The maximum value of h is a. Therefore, the pinch-off voltage V_P, at which $V_P = V_{bi} + V_G + V_D$ is such that $h = a$, is given by

$$V_P = \frac{ea^2 N_D}{2\epsilon_s} . \quad (23.35)$$

The (drift) current density along x is given by (cf. (8.51a))

$$j_x = -eN_D\mu_n\mathcal{E}_x = eN_D\mu_n\frac{\partial V}{\partial x} \quad (23.36)$$

for the neutral part of the semiconductor. Therefore, the current in the upper half of the channel is given by

$$I_D = eN_D\mu_n\frac{\partial V(x)}{\partial x}[a - h(x)]\, Z , \quad (23.37)$$

where Z is the width of the channel (Fig. 23.14a). Although it seems that I_D depends on x, it is of course constant along the channel due to Kirchhoff's law.[4] Using the triviality $\int_0^L I_D \mathrm{d}x = LI_D$ and $\frac{\partial V}{\partial x} = \frac{\partial V}{\partial h}\frac{\partial h}{\partial x}$ with $\frac{\partial V}{\partial h} = eN_D h/\epsilon_s$ from (23.33), we find from (23.37)

$$I_D = \frac{e^2\mu_n N_D Z a^3}{6\epsilon_s L}\left[\frac{3}{a^2}\left(y_2^2 - y_1^2\right) - \frac{2}{a^3}\left(y_1^3 - y_2^3\right)\right] . \quad (23.38)$$

This equation can also be written, using (23.35) and

$$I_P = \frac{e^2\mu_n N_D Z a^3}{6\epsilon_s L} , \quad (23.39)$$

as

$$I_D = I_P\left[\frac{3V_D}{V_P} - 2\frac{(V_{bi} + V_G + V_D)^{3/2} - (V_{bi} + V_G)^{3/2}}{V_P^{3/2}}\right] . \quad (23.40)$$

The saturation current is reached for $y_2 = a$ or $V_{bi} + V_G + V_D = V_P$ and is given by

$$I_{D,sat} = I_P\left[1 - 3\frac{V_{bi} + V_G}{V_P} + 2\left(\frac{V_{bi} + V_G}{V_P}\right)^{3/2}\right] . \quad (23.41)$$

[4] We neglect recombination, in particular since the current is a majority-carrier current.

The dependence of the saturation current on $(V_G + V_{bi})/V_P$ is depicted in Fig. 23.15b. We note that for $V_{bi} + V_G = V_P$, the saturation current is zero since then $V_D = 0$. The gate voltage at which a certain saturation current is reached can be determined graphically from Fig. 23.15b or numerically from (23.41). Letting γ be the saturation current in units of I_P, i.e. $\gamma = I_{D,sat}/I_P$, the gate voltage at the saturation point $V_{G,sat}$ is given by[5]

$$V_{G,sat} = V_P \left[\frac{3}{4} - \frac{8^{-1} \mathrm{i}(\sqrt{3} - \mathrm{i})(1 + 8\gamma)}{\hat{\gamma}} + 8^{-1} \mathrm{i}(\sqrt{3} + \mathrm{i}) \hat{\gamma} \right] - V_{bi} \quad (23.42)$$

$$\hat{\gamma} = \left[-1 + 8(\gamma - 1)^{3/2} + 20\gamma + 8\gamma^2 \right]^{1/3} .$$

The source–drain voltage at the saturation point decreases with decreasing saturation current as $V_{D,sat} = V_P - V_{bi} - V_{G,sat}$ (dashed parabola-like line in Fig. 23.15a).

If the charge-carrier distribution differs from the homogeneous distribution assumed so far, a change of transistor properties arises, as shown in Fig. 23.15b for a δ-like carrier distribution. The I–V characteristic is slightly less curved, but not linear. A linear characteristic is only achievable in the drift velocity saturation regime (cf. Sect. 23.4.4).

For high source–drain voltage $V_D > V_P - V_{bi} - V_G$, the current remains essentially at its saturation value. For very high source–drain voltage, breakdown in the gate–drain diode can occur, when the maximum voltage, which is given by $V_G + V_D$ at the end of the channel, is equal to the breakdown voltage V_B.

The forward transconductance g_m and the drain transconductance g_D are given by

$$g_m = \frac{\partial I_D}{\partial V_G} = g_{max} \left[\left(\frac{V_{bi} + V_G}{V_P} \right)^{1/2} - \left(\frac{V_{bi} + V_G + V_D}{V_P} \right)^{1/2} \right] \quad (23.43)$$

$$g_D = \frac{\partial I_D}{\partial V_D} = g_{max} \left[1 - \left(\frac{V_{bi} + V_G + V_D}{V_P} \right)^{1/2} \right] , \quad (23.44)$$

where

$$g_{max} = \frac{3 I_P}{V_P} = \frac{e N_D a \mu Z}{L} . \quad (23.45)$$

The drain transconductance for $V_D \to 0$ (linear regime, dashed straight lines in Fig. 23.15a) is given by

$$g_{D0} = g_{max} \left[1 - \left(\frac{V_{bi} + V_G}{V_P} \right)^{1/2} \right] = g_{m,sat} , \quad (23.46)$$

[5] Although the arguments are complex, the result is real for $0 \leq \gamma \leq 1$.

which is equal[6] to the forward transconductance in the saturation regime $g_{\mathrm{m,sat}} = \partial I_{\mathrm{D,sat}}/\partial V_{\mathrm{G}}$.

23.4.3 Normally On and Normally Off FETs

The JFET discussed so far had an n-conductive channel and was conductive at $V_{\mathrm{G}} = 0$. It is termed an 'n-type, normally on' (or depletion) FET. If the channel is p-conductive, the FET is called 'p-type'. A FET that has a nonconductive channel at $V_{\mathrm{G}} = 0$ is called 'normally off' (or accumulation) FET. In this case, the built-in voltage must be large enough to cause pinch-off. For a positive gate voltage (in the forward direction of the gate–drain diode), current begins to flow. The I–V characteristics of the four FET-types are depicted in Fig. 23.16. The circuit symbols for the four different FET types are shown in Fig. 23.17.

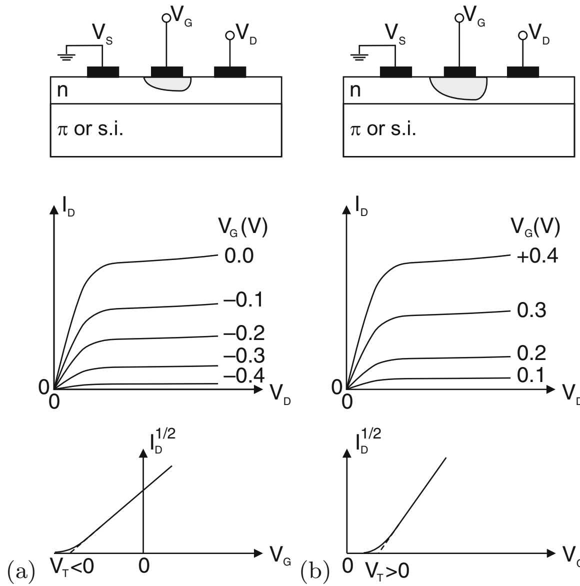

Fig. 23.16. Scheme (*top*), I_{D} vs. V_{D} (*center*) and $I_{\mathrm{D}}^{1/2}$ vs. V_{G} (*bottom*) I–V characteristics for (**a**) normally on (depletion) and (**b**) normally off (accumulation) n-type JFET. Adapted from [384]

[6] Technically, here $g_{\mathrm{D0}} = -g_{\mathrm{m,sat}}$, however, we had counted V_{G} positive for the reverse direction.

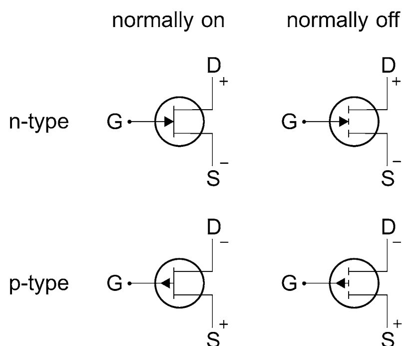

Fig. 23.17. Circuit symbols for various types of FETs

23.4.4 Field-Dependent Mobility

So far, we have considered FETs with long channels ($L \gg a$). This situation is often not the case, in particular for high-integration or high-frequency applications. For short channels, the I–V characteristics exhibit changes. The theory needs to be modified to take into account, among other effects, the electric-field dependence of the mobility (Fig. 8.12) that was discussed in Sect. 8.5.1.

Drift-Velocity Saturation

A material without negative differential mobility, such as Si or Ge, can be described with a drift-velocity model

$$v_\mathrm{d} = \mu \mathcal{E} \, \frac{1}{1 + \mu \mathcal{E} / \mu_\mathrm{s}} \; . \tag{23.47}$$

In this model, μ denotes the low-field (ohmic) mobility and v_s the drift-saturation velocity reached for $\mathcal{E} \gg v_\mathrm{s}/\mu$. The fraction in (23.47) describes the drift-velocity saturation.

By inserting (23.47) into (23.37), we obtain

$$I_\mathrm{D} = e N_\mathrm{D} \mu \mathcal{E}(x) \, \frac{1}{1 + \mu \mathcal{E}(x) / \mu_\mathrm{s}} \, [a - h(x)] \, Z \; , \tag{23.48}$$

and after a short calculation the drain current is given by (cf. (23.40))

$$I_\mathrm{D} = I_\mathrm{P} \left(1 + \frac{\mu V_\mathrm{G}}{v_\mathrm{s} L} \right)^{-1} \left[\frac{3 V_\mathrm{D}}{V_\mathrm{P}} - 2 \frac{(V_\mathrm{bi} + V_\mathrm{G} + V_\mathrm{D})^{3/2} - (V_\mathrm{bi} + V_\mathrm{G})^{3/2}}{V_\mathrm{P}^{3/2}} \right] \; . \tag{23.49}$$

The factor $1/(1+z)$ with $z = \mu V_\mathrm{G} / v_\mathrm{s} L$ reduces the channel current due to the drift saturation effect. The effect of the parameter z is depicted in

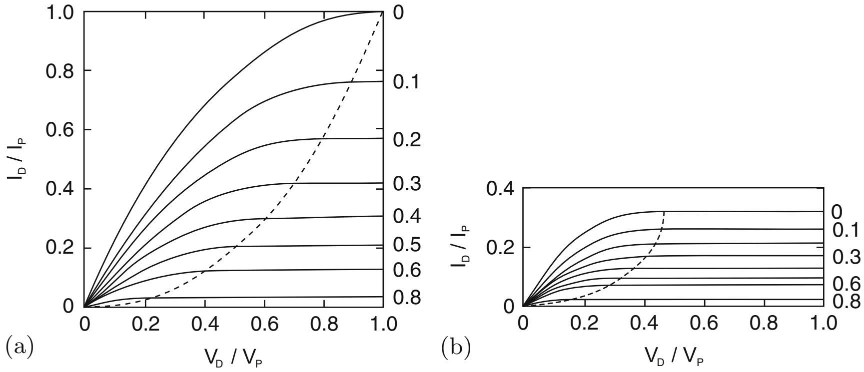

Fig. 23.18. I–V characteristic (**a**) without consideration of drift saturation ($z = 0$) and (**b**) with drift saturation ($z = 3$) for various values of $(V_G + V_{bi})/V_P$ =0, 0.1, 0.2, 0.3, 0.4, 0.5, 0.6, 0.8 as indicated at the right side. The intersections of the *dashed line* and the *solid lines* indicate the beginning of saturation. Adapted from [1399]

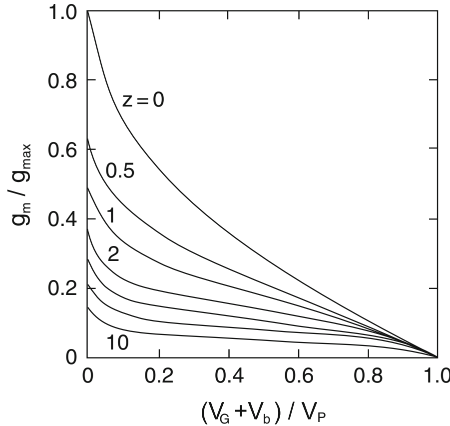

Fig. 23.19. Decrease of (saturated) forward conductance with gate voltage (according to (23.46)) and parametric dependence on z for z = 0, 0.5, 1, 2, 3, 5 and 10. Adapted from [1399]

Fig. 23.18 in comparison to $z = 0$, i.e. without the drift saturation effect (or $v_s \to \infty$). The forward conductance $g_{m,sat}$ decreases with increasing z, as shown in Fig. 23.19.

Two-Region Model

In order to model the GaAs drift velocity vs. field characteristic, a two-region model is used. In the front region of the channel (region I), the field is small enough and a constant mobility μ is used. In the back region of the channel (region II) is the high-field region where a constant drift velocity v_s is used.

With increasing source–drain voltage, the region II (I) increases (decreases) in length. The relative width of region II is also increased with decreasing channel length.

Saturated-Drift Model

Here, the drift velocity is taken everywhere as v_{s}, i.e. complete drift saturation. This is a good approximation for short channels (high fields) that are in current saturation. In this case, the current is given by

$$I_{\mathrm{D}} = e N_{\mathrm{D}} v_{\mathrm{s}} \left[a - h(x)\right] Z \; . \tag{23.50}$$

Equation (23.50) is valid for homogeneous doping. For other doping profiles, the current is given by

$$I_{\mathrm{D}} = v_{\mathrm{s}} Z \int_h^a \rho(y) \mathrm{d}y \; . \tag{23.51}$$

The forward conductance is given by

$$g_{\mathrm{m}} = \frac{v_{\mathrm{s}} Z \epsilon_{\mathrm{s}}}{h(V_{\mathrm{G}})} \; . \tag{23.52}$$

The transistor is more linear if the depletion-layer depth only weakly depends on the gate voltage. This can be accomplished with a doping profile with increasing doping with depth. An increase with a power law and a stepwise or exponential increase lead to a more linear $I(V)$-dependence. In the limit of δ-like doping, a linear $I_{\mathrm{D,sat}}$ vs. V_{G} relation develops. Indeed, FETs with graded or stepped doping profiles exhibit improved linearity and are used for analog circuits.

Nonequilibrium Velocity

Below the electric field for which the drift velocity in GaAs peaks, the carriers can be considered to be in equilibrium. If the field is higher, velocity overshoot (Sect. 23.4.4 and Fig. 8.15) occurs. The carriers have a higher velocity (and ballistic transport) before they relax to the lower equilibrium (or steady-state) velocity after intervalley scattering. This effect will shorten the transit time in short-channel FETs.

23.4.5 High-Frequency Properties

Two factors limit the high-frequency performance of a FET: The transit time and the RC time constant. The transit time t_{r} is the time that the carrier needs to go from source to drain. For the case of constant mobility (long

channel) and constant drift velocity (short channel), the transit time is given by (23.53a and b), respectively.

$$t_{\mathrm{r}} = \frac{L}{\mu \mathcal{E}} \approx \frac{L^2}{\mu V_{\mathrm{G}}} \tag{23.53a}$$

$$t_{\mathrm{r}} = \frac{L}{v_{\mathrm{s}}} \,. \tag{23.53b}$$

For a 1-µm long gate in a GaAs FET, the transit time is of the order of 10 ps. This time is typically small compared to the RC time constant due to the capacitance C_{GS} and transconductance. The cutoff frequency is given by

$$f_{\mathrm{T}} = \frac{g_{\mathrm{m}}}{2\pi C_{\mathrm{GS}}} \,. \tag{23.54}$$

23.5 MOSFETs

The MOSFET has four terminals. In Fig. 23.14b, two n-type regions (source and drain) are within a p-type substrate. The n-type channel (length L) forms underneath a MIS diode. A forth electrode sets the substrate bias. The source electrode is considered to be at zero potential. The important parameters are the substrate doping N_{A}, the insulator thickness d and the depth r_{j} of the n-type regions. Around the MOSFET structure is an oxide to insulate the transistor from neighboring devices.

23.5.1 Operation Principle

When there is no applied gate voltage, only the saturation current of the pn-diode(s) between source and drain flows. In thermodynamic equilibrium (Fig. 23.20c), the necessary surface potential for inversion at the MIS diode is $\Psi_{\mathrm{s}}^{\mathrm{inv}} \approx 2\Psi_{\mathrm{B}}$. If there is a finite drain voltage, a current flows and there is no longer equilibrium. In this case, the quasi-Fermi level of the electrons (or generally of the minority carriers) is lowered and a higher gate voltage is needed to create inversion. The situation at the drain is depicted in Fig. 23.21.

In nonequilibrium, the depletion layer width is a function of the drain voltage V_{D}. In order to reach strong inversion at the drain, the surface potential must be at least $\Psi_{\mathrm{s}}^{\mathrm{inv}} \approx V_{\mathrm{D}} + 2\Psi_{\mathrm{B}}$.

If the gate voltage is such that an inversion channel is present from source to drain, a current will flow for a small drain voltage (Fig. 23.22a). Initially, the current will increase linearly with V_{D}, depending on the conductivity of the channel. With increasing drain voltage, the quasi-Fermi level of the electrons is lowered until, finally at $V_{\mathrm{D}} = V_{\mathrm{D,sat}}$, the inversion channel depth becomes zero (pinch-off at the point denoted with an arrow in Fig. 23.22b). The current at this condition is denoted as $I_{\mathrm{D,sat}}$. For a further increase of V_{D}, the pinch-off point moves closer to the source contact and the channel

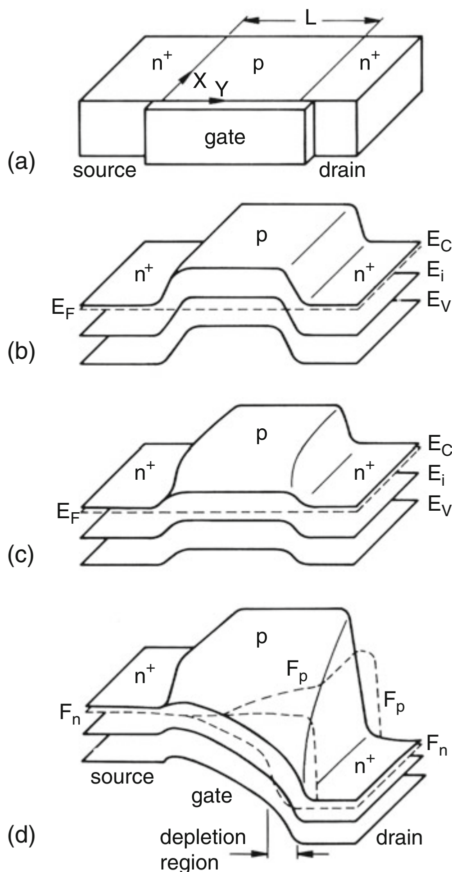

Fig. 23.20. (**a**) Schematic geometry of a MOSFET and its band diagram for (**b**) flat-band conditions for zero gate voltage (and $V_\mathrm{D} = 0$), (**c**) thermodynamic equilibrium with reverse gate voltage (weak inversion, still $V_\mathrm{D} = 0$) and (**d**) nonequilibrium with nonzero drain voltage and gate voltages (with most of the channel being inverted, the depletion region is indicated). Adapted from [1400]

length (inverted region) is shortened (arrow in Fig. 23.22c). The voltage at the pinch-off point remains $V_\mathrm{D,sat}$ and thus the current in the channel remains constant at $I_\mathrm{D,sat}$.

23.5.2 Current–Voltage Characteristics

We assume now that the potential $V(y)$ varies along the channel from $V = 0$ at $y = 0$ to $V = V_\mathrm{D}$ at $y = L$. In the gradual-channel approximation, the voltage drop V_i across the oxide is

$$V_\mathrm{i}(y) = V_\mathrm{G} - \Psi_\mathrm{s}(y) \; , \tag{23.55}$$

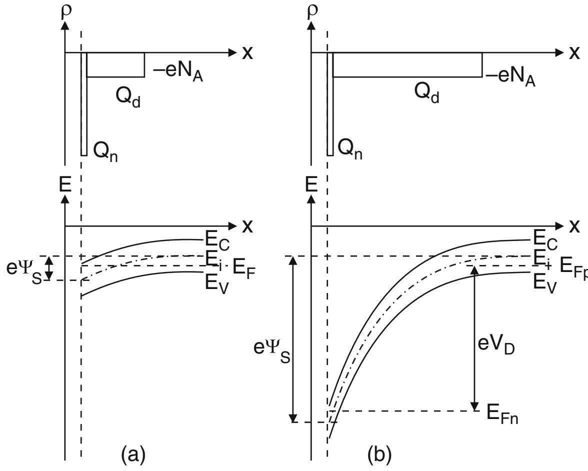

Fig. 23.21. Charge-carrier distribution (*top*) and band diagram (*bottom*) at the inverted p-region of a MOSFET for (**a**) thermodynamic equilibrium ($V_\mathrm{D} = 0$) and (**b**) nonequilibrium at drain

where Ψ_s is the surface potential in the semiconductor (see Fig. 20.31). The total charge induced in the semiconductor (per unit area) is, using (20.72), given by

$$Q_\mathrm{s}(y) = -\left[V_\mathrm{G} - \Psi_\mathrm{s}(y)\right] C_\mathrm{i} \, , \tag{23.56}$$

with C_i being the insulator capacitance (per unit area), as given in (20.73).

The inversion surface potential can be approximated by $\Psi_\mathrm{s}(y) \approx 2\Psi_\mathrm{B} + V(y)$ (see Fig. 23.21). Using (20.71) and (20.77), the depletion-layer charge is

$$Q_\mathrm{d}(y) = -eN_\mathrm{A} w_\mathrm{m} = -\left(2\epsilon_\mathrm{s} e N_\mathrm{A} \left[2\Psi_\mathrm{B} + V(y)\right]\right)^{1/2} \, , \tag{23.57}$$

such that, using (23.56), the inversion layer charge is

$$\begin{aligned} Q_\mathrm{n}(y) &= Q_\mathrm{s}(y) - Q_\mathrm{d}(y) \\ &= -\left[V_\mathrm{G} - V(y) - 2\Psi_\mathrm{B}\right] C_\mathrm{i} + \left(2\epsilon_\mathrm{s} e N_\mathrm{A} \left[2\Psi_\mathrm{B} + V(y)\right]\right)^{1/2} \, . \end{aligned} \tag{23.58}$$

For the calculation of the drain current, we consider the increase of channel resistance $\mathrm{d}R(y)$ along a line element $\mathrm{d}y$ of the channel. The integral of the conductivity over the cross section A of the channel (width Z) is

$$\iint_A \sigma(x,z)\mathrm{d}x\,\mathrm{d}z = -e\mu_\mathrm{n} \iint_A n(x,z)\mathrm{d}x\,\mathrm{d}z = Z\mu_\mathrm{n}|Q_\mathrm{n}(y)| \, . \tag{23.59}$$

Therefore,

$$\mathrm{d}R(y) = \mathrm{d}y \frac{1}{Z\mu_\mathrm{n}|Q_\mathrm{n}(y)|} \, . \tag{23.60}$$

Here we have assumed that the mobility is constant along the channel, i.e. not field dependent. The change of voltage across the line element $\mathrm{d}x$ is

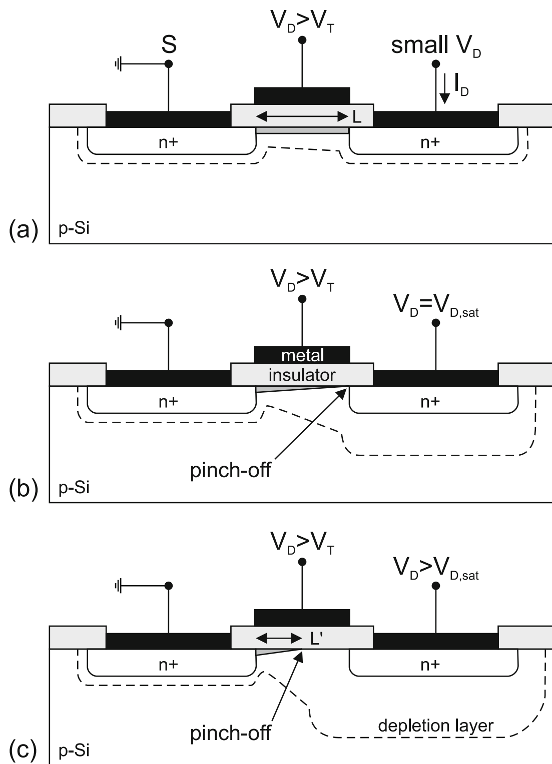

Fig. 23.22. (**a**) MOSFET with inverted channel (*dark grey*) of length L for small source–drain voltage V_{D} in linear regime, (**b**) at the start of saturation at pinch-off, (**c**) in the saturation regime with reduced channel length L'. The pinch-off point is denoted by an arrow in (**b**) and (**c**). The *dashed lines* denote the extension of the depletion region. Adapted from [384]

$$\mathrm{d}V(y) = I_{\mathrm{D}}\,\mathrm{d}R = \frac{I_{\mathrm{D}}\,\mathrm{d}y}{Z\mu_{\mathrm{n}}|Q_{\mathrm{n}}(y)|}\,. \tag{23.61}$$

We note the drain current is independent of x. Using (23.58) and performing the integral of (23.61) from $V(y=0)=0$ to $V(y=L)=V_{\mathrm{D}}$, we find

$$I_{\mathrm{D}} = \mu_{\mathrm{n}} C_{\mathrm{i}} \frac{Z}{L} \left\{ \left(V_{\mathrm{G}} - 2\Psi_{\mathrm{B}} - \frac{V_{\mathrm{D}}}{2} \right) - \frac{2}{3} \frac{(2e\epsilon_{\mathrm{s}} N_{\mathrm{A}})^{1/2}}{C_{\mathrm{i}}} \left[(V_{\mathrm{D}} + 2\Psi_{\mathrm{B}})^{3/2} - (2\Psi_{\mathrm{B}})^{3/2} \right] \right\}. \tag{23.62}$$

This characteristic is depicted in Fig. 23.23a. In the linear regime (small drain voltage, $V_{\mathrm{D}} \ll (V_{\mathrm{G}} - V_{\mathrm{T}})$), the drain current is given by

$$I_{\mathrm{D}} \cong \mu_{\mathrm{n}} C_{\mathrm{i}} \frac{Z}{L} (V_{\mathrm{G}} - V_{\mathrm{T}})\, V_{\mathrm{D}}\,. \tag{23.63}$$

The threshold voltage V_T, i.e. the gate voltage for which the channel is opened and a current can flow, is given for small drain voltage (linear regime) by

$$V_\mathrm{T} = 2\Psi_\mathrm{B} + \frac{(4e\epsilon_\mathrm{s} N_\mathrm{A} \Psi_\mathrm{B})^{1/2}}{C_\mathrm{i}} \ . \tag{23.64}$$

The transconductances in the linear regime are easily obtained as

$$g_\mathrm{m} = \mu_\mathrm{n} C_\mathrm{i} \frac{Z}{L} V_\mathrm{D} \tag{23.65a}$$

$$g_\mathrm{D} = \mu_\mathrm{n} C_\mathrm{i} \frac{Z}{L} (V_\mathrm{G} - V_\mathrm{T}) \ . \tag{23.65b}$$

The saturation current (for constant mobility) is approximately

$$I_\mathrm{D,sat} \cong \mu_\mathrm{n} C_\mathrm{i} \frac{mZ}{L} (V_\mathrm{G} - V_\mathrm{T})^2 \ , \tag{23.66}$$

where m depends on the doping concentration and is about 0.5 for low doping. For low p-doping of the substrate, the threshold voltage in (23.66) for the saturation regime is also given by (23.64). At higher doping, the threshold voltage becomes dependent on the gate voltage. C_i denotes the insulator capacitance

$$C_\mathrm{i} = \epsilon_\mathrm{i} / d_\mathrm{i} \ . \tag{23.67}$$

The forward transconductance in the saturation regime is

$$g_\mathrm{m,sat} = \mu_\mathrm{n} C_\mathrm{i} \frac{2mZ}{L} (V_\mathrm{G} - V_\mathrm{T}) \ . \tag{23.68}$$

For constant drift velocity (Fig. 23.23b for field-dependent mobility), the saturation current is given by

$$I_\mathrm{D,sat} = Z C_\mathrm{i} v_\mathrm{s} (V_\mathrm{G} - V_\mathrm{T}) \ , \tag{23.69}$$

and the forward transconductance in the saturation regime is

$$g_\mathrm{m,sat} = Z C_\mathrm{i} v_\mathrm{s} \ . \tag{23.70}$$

We note that the transistor properties depend on and can be separated into the geometry factor (Z/L) and the material properties $(\mu\, C_\mathrm{i} = \mu\, \epsilon_\mathrm{i}/d_\mathrm{i})$.

The threshold voltage can be changed by the substrate bias V_BS as $(\beta = e/kT)$

$$\Delta V_\mathrm{T} = \frac{a}{\sqrt{\beta}} \left[(2\Psi_\mathrm{B} + V_\mathrm{BS})^{1/2} - (2\Psi_\mathrm{B})^{1/2} \right] \ , \tag{23.71}$$

with (L_D being the Debye length (cf. 20.66b))

$$a = 2 \frac{\epsilon_\mathrm{s}}{\epsilon_\mathrm{i}} \frac{d}{L_\mathrm{D}} \ . \tag{23.72}$$

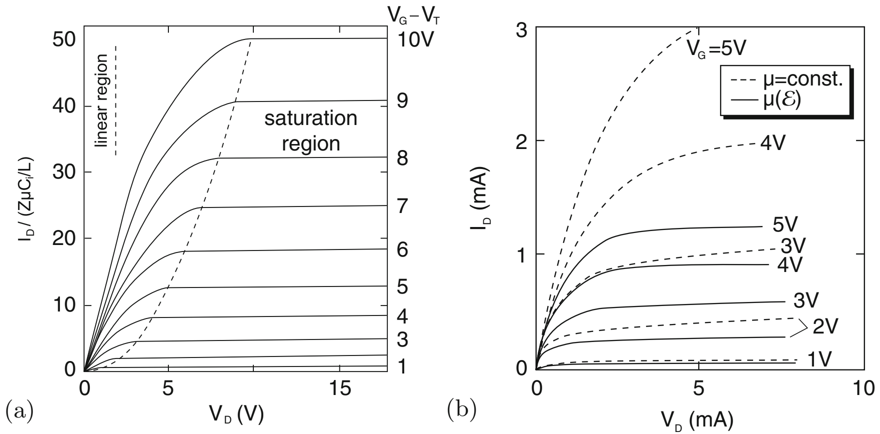

Fig. 23.23. (**a**) Idealized I–V characteristics for a MOSFET with constant mobility. The *dashed line* visualizes the drain (saturation) voltage for which the current is equal to $I_{\mathrm{D,sat}}$. The *solid lines* are for various values of the gate voltage $V_{\mathrm{G}} - V_{\mathrm{T}}$ =1–10 V. Adapted from [384] (**b**) I–V characteristics taking into account the effect of field-dependent mobility (*solid lines*) in comparison to the constant-mobility model (*dashed lines*) for various gate voltages as labeled. Adapted from [1401]

Experimental data are shown in Fig. 23.24. For a Si/SiO$_2$ gate diode, $a = 1$ for, e.g., $d_{\mathrm{i}} = 10\,\mathrm{nm}$ and $N_{\mathrm{A}} = 10^{16}\,\mathrm{cm}^{-3}$. For gate voltages below V_{T}, the current is given by the diffusion current, similar to a npn transistor. This regime is important for low-voltage, low-power conditions. The related drain current is termed the *subthreshold* current and is given by

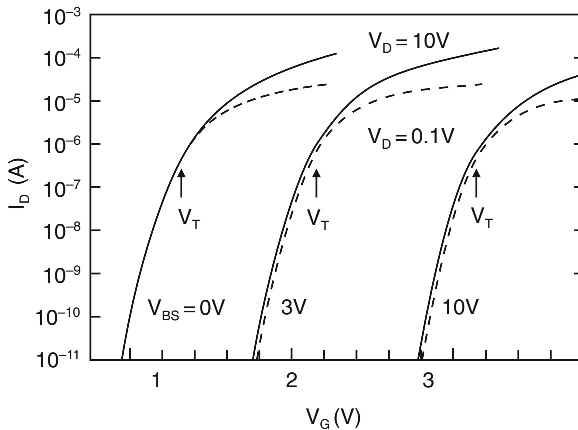

Fig. 23.24. Experimental subthreshold I–V characteristic of a MOSFET device with long channel (15.5 µm). *Solid lines* for $V_{\mathrm{D}} = 10\,\mathrm{V}$, *dashed lines* for $V_{\mathrm{D}} = 0.1\,\mathrm{V}$. Adapted from [1402]

$$I_{\mathrm{D}} = \mu_{\mathrm{n}} \frac{ZaC_{\mathrm{i}}n_{\mathrm{i}}^2}{2L\beta^2 N_{\mathrm{A}}^2} \left[1 - \exp\left(-\beta V_{\mathrm{D}}\right)\right] \exp\left(-\beta \Psi_{\mathrm{s}}\right) \left(\beta \Psi_{\mathrm{s}}\right)^{-1/2} . \quad (23.73)$$

The drain current therefore increases exponentially with V_{G}, as shown in Fig. 23.24. V_{G} is roughly proportional to Ψ_{B}:

$$\Psi_{\mathrm{s}} = (V_{\mathrm{G}} - V_{\mathrm{FB}}) - \frac{a^2}{2\beta} \left\{ \left[1 + \frac{4}{a^2} \left(\beta V_{\mathrm{G}} - \beta V_{\mathrm{FB}} - 1\right) \right]^{1/2} - 1 \right\} , \quad (23.74)$$

where V_{FB} is the flat-band voltage of the gate MIS diode. The drain current is independent of V_{D} for $V_{\mathrm{D}} \gtrsim 3kT/e$.

23.5.3 MOSFET Types

MOSFETs can have an n-type channel (on a p-substrate) or a p-channel (on an n-type substrate). So far, we have discussed the normally off MOSFET. If there is a conductive channel even without a gate voltage, the MOSFET is normally on. Here, a negative gate voltage must be applied to close the channel. Therefore, similar to the JFET, a total of four different types of MOSFET exist, see Fig. 23.25.

23.5.4 Complementary MOS

Complementary metal–oxide–semiconductor technology (CMOS) is the dominating technology for highly integrated circuits. In such devices, MOSFETs with n-channel (NMOS) and p-channel (PMOS) are used on the same chip. The basic structure of logic circuits, the inverter, can be realized with a pair of NMOS and PMOS transistors, as shown in Fig. 23.26a with two normally off transistors. The load capacitor represents the capacitance of the following elements.

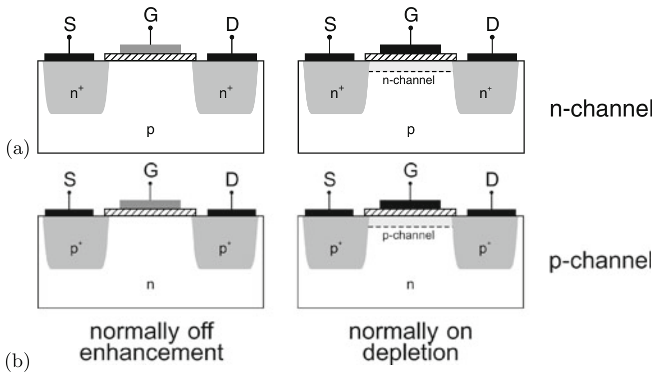

Fig. 23.25. The four MOSFET types. (**a**) Enhancement and (**b**) depletion type with n-channel (*top row*) and p-channel (*bottom row*)

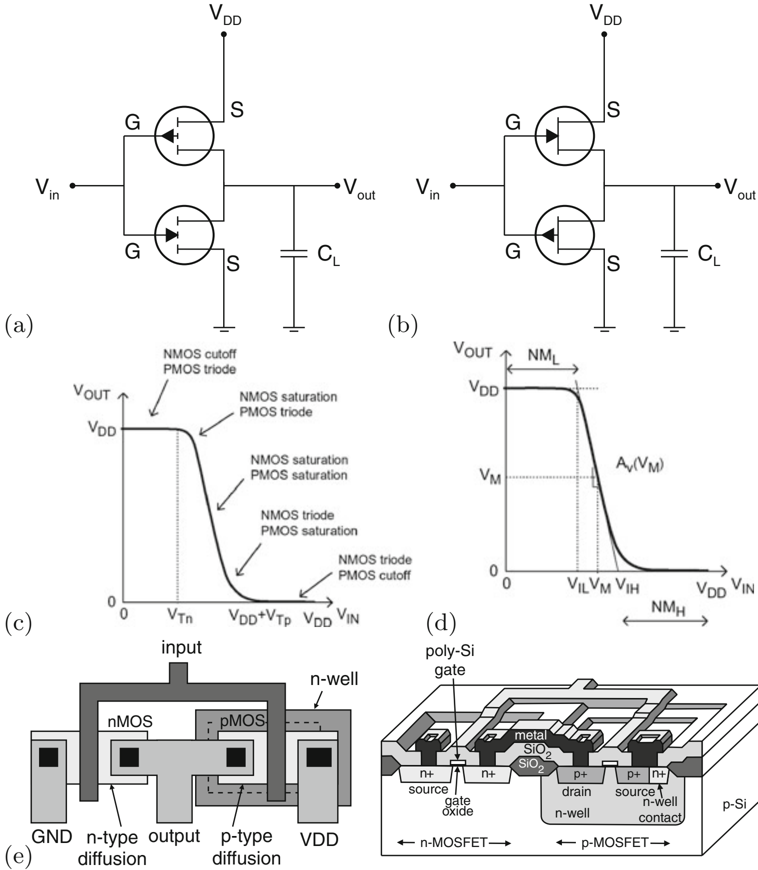

Fig. 23.26. Circuit diagram of (**a**) inverter with n-type (bottom) and p-type (normally off, enhancement mode) FETs and (**b**) inverter with p-type (bottom) and n-type (normally on, depletion mode) FETs. (**c**) Inverter characteristic with the transistor thresholds indicated, (**d**) inverter characteristic with middle voltage V_{M} indicated. $\mathrm{NM}_{\mathrm{L,H}}$ denotes the low- and high-noise margins, respectively, i.e. the voltage by which the input voltage can fluctuate without leading to switching. (**e**) Composite layout (*left panel*) and cross-sectional view (*right panel*) of CMOS inverter. Part (**e**) adapted from [1403]

If the input voltage is $V_{\mathrm{in}} = 0$, the NMOS transistor is nonconductive ('off'). The (positive) voltage V_{DD} is at the PMOS transistor source, thus the gate is negative in relation to the source and the transistor is conductive ('on') since $-V_{\mathrm{DD}} = V_{\mathrm{Gp}} < V_{\mathrm{Tp}} < 0$ (see Fig. 23.25). The current flows through the capacitor that becomes charged to $V_{\mathrm{out}} = V_{\mathrm{DD}}$. The current then subsides, since V_{D} at the PMOS becomes zero. If the input voltage is set to V_{DD}, the NMOS transistor has a positive gate–source voltage larger than the threshold $V_{\mathrm{Tn}} < V_{\mathrm{Gn}} = V_{\mathrm{DD}}$ and becomes conductive. The charge from the capacitor

flows over the NMOS to ground. The PMOS transistor has zero gate–source voltage and is in the 'off' state. In this case, the voltage V_{DD} drops entirely across the PMOS and the capacitor is uncharged with $V_{\mathrm{out}} = 0$.

In both its logic states, the CMOS inverter does not consume power. No current[7] flows in either of the two steady states since one of the two transistors is in both cases in the 'off' state. Current flows only during the switching operation. Therefore, the CMOS scheme allows for low power consumption.

The middle voltage for which $V_{\mathrm{in}} = V_{\mathrm{out}}$ can be calculated from the MOSFET characteristics. Both are, for this condition, in saturation and the currents are given by (cf. (23.66))

$$I_{\mathrm{Dn}} = \mu_{\mathrm{n}} C_{\mathrm{ox}} \frac{Z_{\mathrm{n}}}{2L_{\mathrm{n}}} \left(V_{\mathrm{M}} - V_{\mathrm{Tn}}\right)^2 \tag{23.75a}$$

$$I_{\mathrm{Dp}} = \mu_{\mathrm{p}} C_{\mathrm{ox}} \frac{Z_{\mathrm{p}}}{2L_{\mathrm{p}}} \left(V_{\mathrm{DD}} - V_{\mathrm{M}} - V_{\mathrm{Tp}}\right)^2 \ . \tag{23.75b}$$

With $\gamma = \frac{Z_{\mathrm{p}}}{Z_{\mathrm{n}}} \frac{L_{\mathrm{n}}}{L_{\mathrm{p}}} \frac{\mu_{\mathrm{p}}}{(-\mu_{\mathrm{n}})}$, we find from $I_{\mathrm{Dn}} = -I_{\mathrm{Dp}}$,

$$V_{\mathrm{M}} = \frac{V_{\mathrm{Tn}} + \gamma \left(V_{\mathrm{DD}} + V_{\mathrm{Tp}}\right)}{1 + \gamma} \ . \tag{23.76}$$

As gate material, often polycrystalline silicon (poly-Si) is used (cf. Fig. 20.26). It is used instead of metals because its work function matches that of silicon closely. Also, poly-Si is more resistant to temperature. Despite its high doping, the resistance of poly-Si is two orders of magnitude larger than that of metals. Since it is easily oxidized, it cannot be used with high-k oxide dielectrics.[8]

For optimized ohmic contacts on the n- and p-Si, different metals are used to create a small barrier height (Fig. 20.21a) and low contact resistance (cf. Sect. 20.2.6). Figure 23.27 visualizes the band edges of silicon in relation to the work functions of various metals (see Table 20.1). For example, the work function of titanium matches the electron affinity of n-Si closely. However, a direct deposition of Ti on Si results in a Schottky barrier of 0.5 eV [1121]. A surface passivation with a group-VI element such as Se can help reduce this value to 0.19 eV [1404].

In the latest generation of CMOS ICs the PMOS (NMOS) device has a built-in compressive (tensile) channel strain for modifying the effective mass (cf. Sect. 6.10.2), both allowing higher drive current due to higher mobility.

[7] Except for the subthreshold current and other leakage currents. These need to be reduced further since the dissipated power limits chip performance (speed and device density) and battery lifetime in handheld applications.

[8] The term 'high-k dielectric' means a dielectric material with large dielectric constant ϵ.

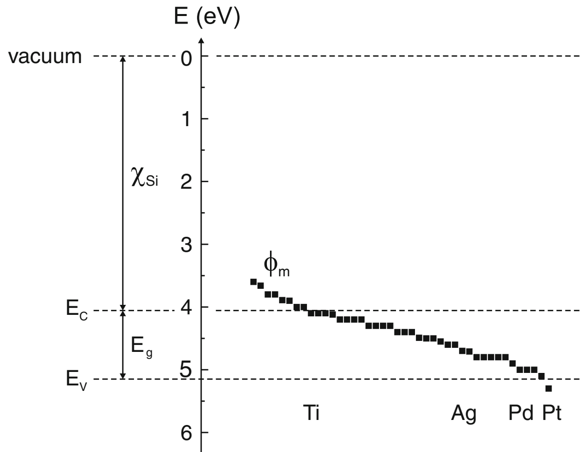

Fig. 23.27. Silicon band edges in relation to different metals and their work functions

23.5.5 Large-Scale Integration

Historic Development

Compared to the first computers on the basis of vacuum tubes (triodes), e.g. ENIAC (Fig. 23.28), today's devices are extremely miniaturized and need many orders of magnitude less power per operation. ENIAC needed 174 kW of power. A comparable computing power was reached in 1971 with the few cm^2 large Intel 4004 microprocessor (Fig. 23.29b) consuming only several Watts with 2300 transistors. In 2004 about 42 million transistors were integrated in the Pentium 4 microprocessor (Fig. 23.30). Also, memory chips started to become highly integrated (Fig. 23.29a).

The development of electronic circuit integration is empirically described by Moore's 'law' [1405] that has been valid since the 1970s. According to this law, the number of transistors doubles every 20 months (Fig. 23.31a). At the

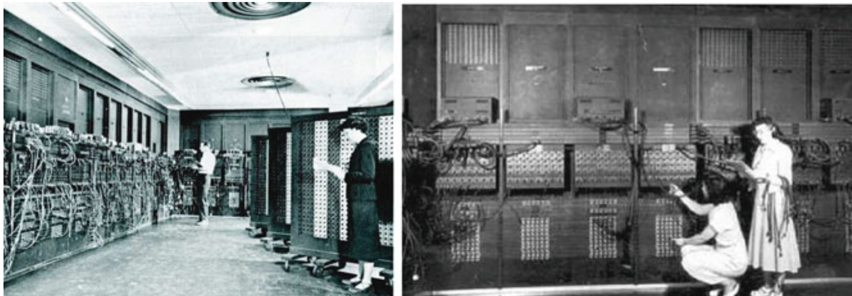

Fig. 23.28. ENIAC, the first electronic computer (J.P. Eckert, J.W. Mauchly, 1944/5). The images show only a small part of the 18,000 vacuum tubes

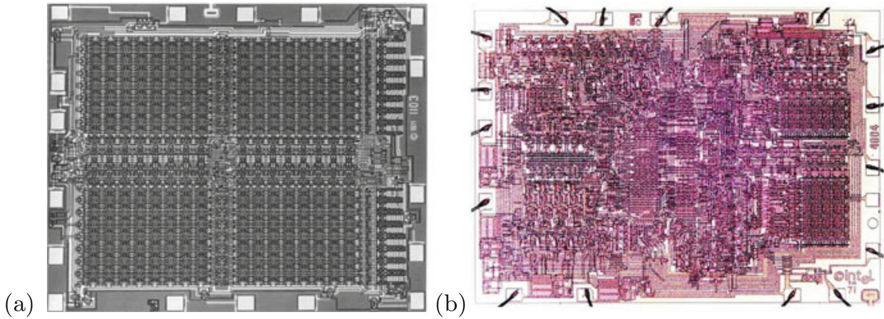

Fig. 23.29. (**a**) Intel^{TM} 1103 1 KByte (1024 memory cells) dynamic random access memory (RAM), arranged in four grids with 32 rows and columns (1970), chip size: 2.9×3.5 mm^2. (**b**) Intel^{TM} 4004 microprocessor (1971), chip size: 2.8×3.8 mm^2, circuit lines: 10 µm, 2,300 MOS transistors, clock speed: 108 kHz

same time, the performance has been improved by an increase of the clock speed (Fig. 23.31b).[9]

Interconnects

Moore's second law says that the cost of production also doubles for each new chip generation and is currently (2004) in the multi-billion US$ range. Most of the cost saved by integration is due to efficient *wiring* (interconnects) of the components, in 2004 (65 nm node) in eight layers above the active elements (transistors and capacitors) (Fig. 23.32), in 2008 (45 nm node) in eleven layers. Plane-view images of the first three layers of the interconnects are shown in Fig. 23.33. The Cu interconnects are fabricated with the so-called damascene process [1406–1408]. Barrier layers (e.g. TaN or TiN) are required to avoid out-diffusion of Cu into the silicon or other parts of the circuit. Three effects limit the conductivity: The interconnect metal line width and height approaches the mean free path of carriers ($d_{\mathrm{Cu}} \approx 40$ nm) [503, 1409], grain boundary scattering can limit mobility since grain size is reduced for thinner lines, and the (high resistivity) barrier reduces space for the conductive part of the metal line. In Fig. 23.34 the increase of the resistivity of copper with reduced dimension is shown as a function of film thickness t and for a 100 nm-film as a function of line width w. In a simplified approach, the line resistivity ρ_{line} is given as [1409]

$$\frac{\rho_{\mathrm{line}}}{\rho_0} = 1 + \frac{3}{8}\,(1-p)\left(\frac{d}{t} + \frac{d}{w}\right) , \qquad (23.77)$$

[9] After year 2003 data for maximum clock rate are not for highest integration density processors.

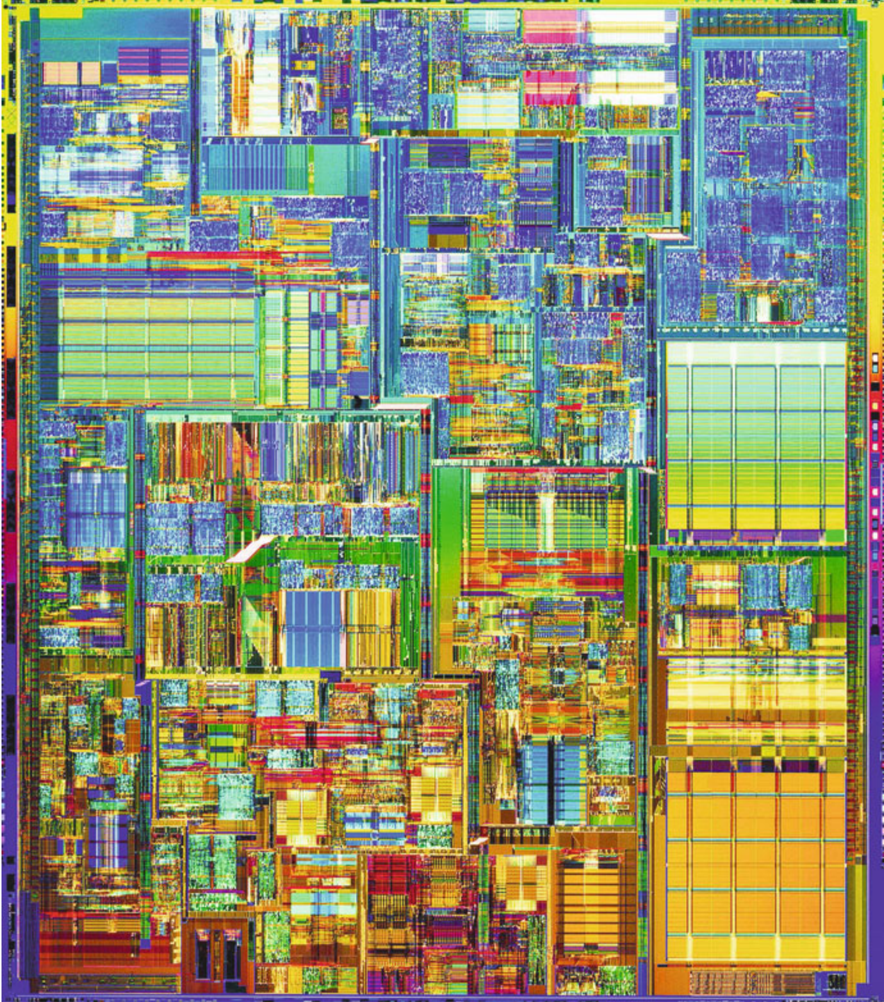

Fig. 23.30. The Intel™ Pentium 4 microprocessor (2000), circuit lines: 0.18 μm, 42 million transistors, clock speed: 1.5 GHz

ρ_0 denoting the bulk resistivity (1.7 μΩ cm for Cu), d being the mean free path (8.6) and p being the electron scattering parameter ($p = 0$ for diffuse scattering).

In order to achieve the best high frequency performance the material between the metal interconnects should have low dielectric constant ('low-k' dielectric). Alternative materials to the standard SiO_2 ($\epsilon_r \approx 4.1$) are investigated such as SiOF (≈ 3.8), SiCOH (≈ 3.0), porous materials (≈ 2.5) and air gaps [1410].

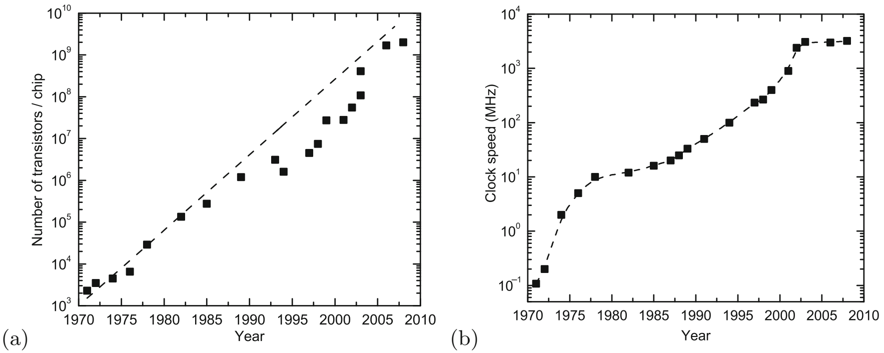

Fig. 23.31. (**a**) Moore's law on the exponential increase of transistors per chip (for Intel$^{\rm TM}$ processor chips). *Dashed line* corresponds to doubling in 20 months. (**b**) Historical increase of maximum clock speed, *dashed line* is guide to the eye. Note the almost constant rate of 10 MHz from the mid-1970s to the mid-1980s and another plateau developing after 2000

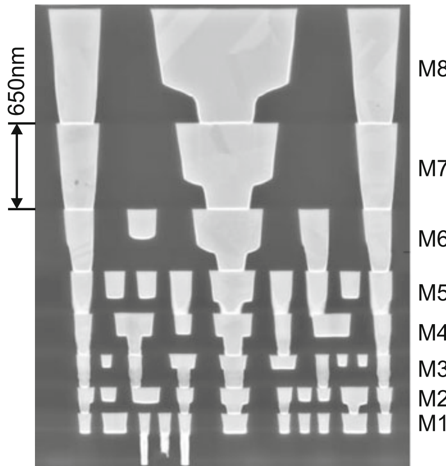

Fig. 23.32. Cross section through a logic chip (65 nm technology, 35 nm gate length) with eight layers of dual damascene Cu interconnects (M1–M8) with low-k carbon-doped oxide ($\epsilon_{\rm r} = 2.9$) inter-level dielectric above the active elements. Adapted from [1411]

CMOS Scaling

Using planar technologies, LSI (large-scale integration), VLSI (very large-scale integration), ULSI (ultra large-scale integration) and further generations of devices have been conceived, driven by high-density electronic memory devices. Subsequently also logic devices are produced with reduced device size.

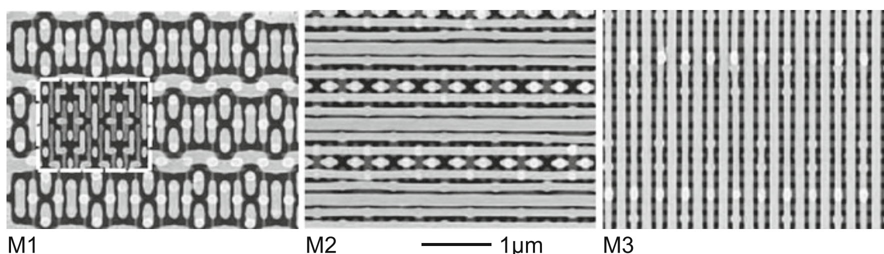

Fig. 23.33. Plane-view of the first three interconnect layers of a 45 nm node SRAM array (Intel® Xeon®). In the image of the M1 layer the gate layer metal connects are shown in the *inset*, framed with a *white dashed line*. Adapted from [1412]

The increase of the number of transistors per area requires the scaling of their geometrical properties. This impacts many other properties of the transistor and their scaling needs to be considered as well. From a general perspective, the physical properties scale while the thermal energy kT remains constant for room-temperature electronics.

If channel width Z and channel length L of a transistor are scaled down by a factor of $s > 1$, $Z' = Z/s$ and $L' = L/s$, the area obviously scales as $A' = A/s^2$. In subsequent transistor generations $s = \sqrt{2}$, i.e. doubling of the number of devices per area. In order to maintain the aspect ratio of the device also the oxide thickness (d_i) is scaled, $t'_\mathrm{ox} = t_\mathrm{ox}/s$ (‘classical scaling’).

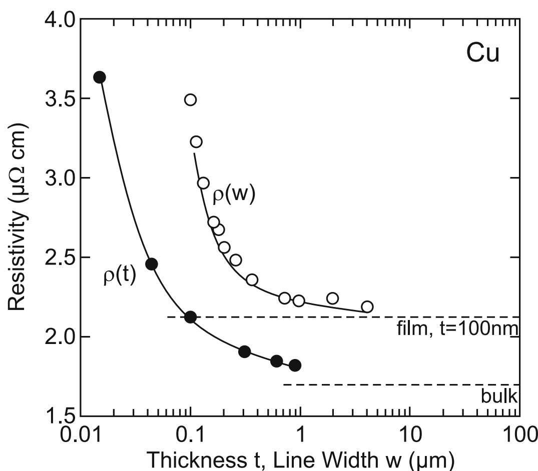

Fig. 23.34. Resistivity of copper at room temperature for various film thickness (*solid circles*), and for a 100 nm-film as a function of line width w (*empty circles*). *Solid lines* are theoretical dependence according to (23.77). The *dashed lines* indicate the limits for bulk material ($t \to \infty$) and for large line thickness ($d = 100$ nm, $w \to \infty$). Adapted from [1409]

The ultimate design criteria are maximum temperature and maximum power loss. The maximum temperature needs to be obeyed, the worst case usually taken as 100°C. The power loss per area, e.g. heating, needs to stay constant at an appropriate maximum level around 200 kW/m^2 (Fig. 23.35b) unless higher (and more expensive) efforts on cooling are made. At the same time the device performance needs to be maintained if not improved, e.g. for lower power dissipation in battery operated devices. Very important is the reduction of operation voltage V_{DD} in order to keep electric fields and power consumption small enough (Fig. 23.35). The power consumption in stand-by mode P_{off} depends on V_{DD} and the subthreshold (off) current

$$P_{\mathrm{off}} = W_{\mathrm{tot}}\, V_{\mathrm{DD}}\, I_{\mathrm{off}} \;, \tag{23.78}$$

where W_{tot} is the total width of the turned-off devices and I_{off} is the average off-current per device per width. The latter increases exponentially with reduced threshold voltage V_{T},

$$I_{\mathrm{off}} = I_0 \, \exp\left(-\frac{eV_{\mathrm{T}}}{nkT}\right) \;, \tag{23.79}$$

with ideality factor $n \approx 1.2$ and $I_0 \approx 1$–$10\,\mu$A/μm [1413]. A well-functioning MOSFET requires a ratio of $V_{\mathrm{T}}/V_{\mathrm{DD}}$ of < 0.3.

The power consumption in active mode P_{ac} depends also on the clock speed (frequency f) that increases with higher integration due to shorter gate length,

$$P_{\mathrm{ac}} = C_{\mathrm{sw}}\, V_{\mathrm{DD}}^2\, f \;, \tag{23.80}$$

where C_{sw} is the total node capacitance being charged and decharged in a clock cycle.

Historically the oxide thickness has been reduced less than the channel length [1413] (Fig. 23.35a) leading to increased local fields. The reduction of the physical gate oxide thickness is limited due to gate leakage through tunneling [1415]. While for a gate voltage of 1.5 V and oxide thickness $t_{\mathrm{ox}} = 3.6$ nm the leakage current is only about 10^{-8} A/cm^2, it is about 1 A/cm^2 for $t_{\mathrm{ox}} = 2.0$ nm and about 10^4 A/cm^2 for $t_{\mathrm{ox}} = 1.0$ nm. Obviously variations of oxide thickness are more harmful at small average thickness. 1.2 nm physical SiO_2 thickness has been used in the 90 nm (gate length) logic node.

The technological solution for further reduction of oxide thickness is the use of geometrically thicker layers, to suppress tunneling, with higher dielectric constant ('high-k dielectrics'), e.g. HfO_2 [1416], to maintain reasonable gate capacitance per gate width

$$C_{\mathrm{G}} = \frac{\epsilon_{\mathrm{ox}}}{t_{\mathrm{ox}}}\, L \;, \tag{23.81}$$

(cmp. (23.67)) at a value of about 1.0–1.5 fF/μm (Fig. 23.35)b. For the 45 nm technology node a 0.7-fold reduction in electrical oxide thickness was achieved while reducing gate leakage 1000× for the PMOS and 25× for the NMOS transistors [1417].

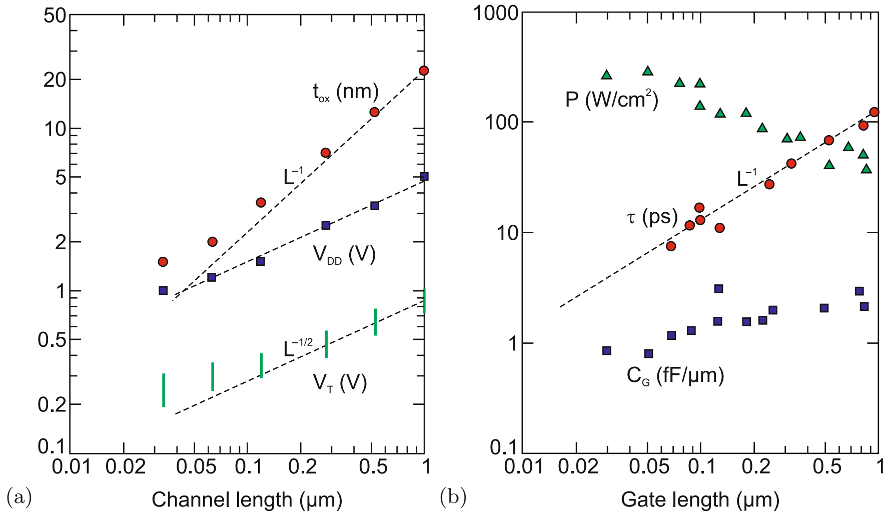

Fig. 23.35. Scaling of MOSFET parameters gate oxide thickness t_{ox}, power supply voltage V_{DD} (across source–drain), threshold voltage V_{T}, total power loss per area P, gate capacitance per channel width C_{G} and inverter delay τ, the time required to propagate a transition through a single inverter driving a second, identical inverter, commonly used as a means of gauging the speed of CMOS transistors. Data for (**a**) from [1413] and for (**b**) selected from [1414]

Materials

The electronics industry is based on silicon as the material for transistors. However, many other materials are incorporated in the technology. Traditionally silicon dioxide gate oxide is used, silicon nitride for insulation layers and polysilicon for gate contacts. For wiring aluminum has been used. Silicides were introduced as contact materials around 1986.

Progress was made with copper interconnects (IBM, 1997), replacing aluminum. The better electrical and heat conductivity could previously not be used since Cu is a deep level in Si (cf. Fig. 7.6). The key to success was an improved barrier technology based on amorphous TaN- or TiN-based barrier layers to prevent the diffusion of Cu into the silicon and dielectric layers. The first chip from series production, incorporating the Cu technology, was the PowerPC 750 (400 MHz) in 1998. Since 2000 high-k, i.e. large ϵ_{r}, Hf-containing gate dielectrics are used (Fig. 23.36). HfO_2 has a dielectric constant of 25–30. 45 nm node technology probably uses HfZrO, HfSiO or HfSiON [1418] gate dielectrics with $k \sim 12$ and an electrical thickness of $t_{\mathrm{ox}}\, \epsilon_{\mathrm{SiO_2}}/\epsilon_{\mathrm{ox}} = 1.0\,\mathrm{nm}$.

Germanium is reintroduced into mainstream semiconductor technology via SiGe stressors in the source and drain for PMOS. Uniaxial compressive strain in the channel region leads to 30% increased saturation current [1420]

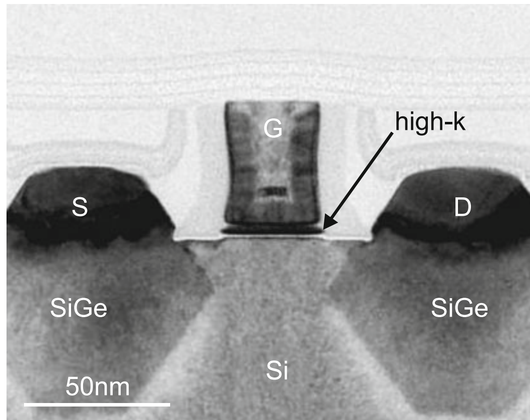

Fig. 23.36. Cross-section TEM image of 45 nm node PMOS transistor with high-k Hf-containing gate oxide (*dark*) above a thin SiO_2 layer (*white*). The role of the stressor SiGe pockets is explained in Fig. 23.35. Adapted from [1419]

mostly due to reduced effective masses [526, 1421, 1422] (Sect. 8.3.11) for 90 nm transistors. Similarly, uniaxial tensile strain in NMOS, introduced by SiN caps or more recently tensile trench contacts [1417], allows for 10% higher saturation current [1420] (Fig. 23.37). The enhanced electron mobility is due to strain-induced splitting of the X-valley and change of electron mass [1423]. Further improvement to 18% (NMOS) and 50% (PMOS) increase in $I_{\mathrm{D,sat}}$ compared to unstrained Si have been made in 65 nm transistors [1411].

The end of the miniaturization has been theoretically predicted many times and for various feature sizes. Today, only fundamental limits such as the size of an atom seems to limit circuit design.[10] Such limits (and the effects in nanostructures in the few-nm regime) will be reached beyond 2010, projected at about 2020. Up to then, it is probable that at least a few companies will follow the road map for further miniaturization, as laid out by the Semiconductor Industry Association[11] (SIA).

23.5.6 Tunneling FETs

A decisive parameter for FET performance is low leakage current. With shrinking device dimensions it increases rapidly for conventional FET design. A novel type of FET has thus been conceptualized, the tunneling FET (TFET) [1426]. It is a lateral p-i-n diode with a MOS gate (Fig. 23.38). The leakage current is minimized due to the reverse biased p-i-n structure.

[10] Only commercial profit, rather than testing physical limits, drives the miniaturization. Insufficient economic advantages or low yield of further chip generations possibly can limit or slow down large-scale integration.

[11] www.semichips.org

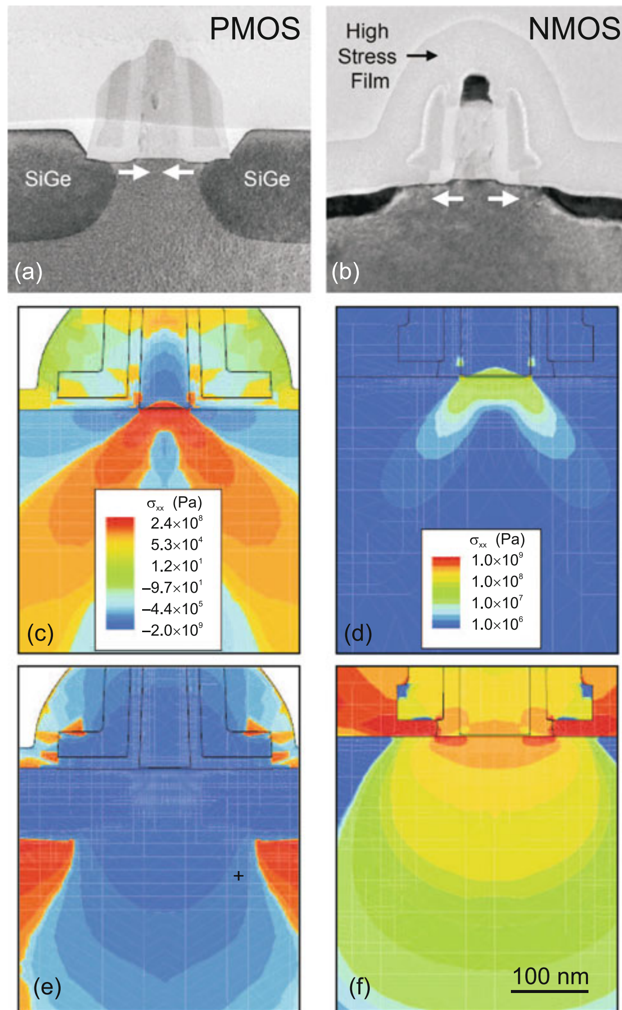

Fig. 23.37. Cross-section TEM images of strained (**a**) PMOS and (**b**) NMOS transistors. Adapted from [1424]. (**c**–**f**) Modelling of strain distribution: PMOS without (**c**) and with (**e**) $Si_{0.83}Ge_{0.17}$ pockets, NMOS without (**d**) and with (**f**) tensile cap layer. Adapted from [1425]

A low leakage current (per gate width) of less than 10^{-14} A/μm has been realized [1427, 1428]. The channel current is due to band-to-band tunneling as in an Esaki diode (Sect. 20.5.9) and can be controlled by the gate voltage [1429]. The surface tunneling junction is close to the source electrode. The use of germanium instead of silicon allows further performance enhancements [1430].

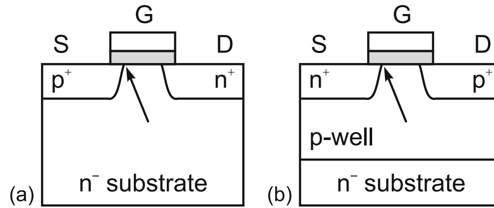

Fig. 23.38. Schematic of a (**a**) n-type and (**b**) p-type tunneling FET (TFET). D is reversely biased, i.e. positive for NTFET and negative for PTFET. The *grey areas* represent the gate oxide, the *arrows* denote the spatial position of tunneling (surface tunneling junction) for sufficient (NTFET: positive, PTFET: negative) gate voltage

23.5.7 Nonvolatile Memories

Floating Gate Memories

When the gate electrode of a MOSFET is modified in such a way that a (semi-)permanent charge can be stored in the gate, a nonvolatile electronic memory can be fabricated. In the floating-gate structure (Fig. 23.39a), an insulator–metal–insulator structure is used where charge is stored in the metal and cannot escape through the insulating barriers. The 'metal' is often realized by poly-Si. In the MIOS structure (Fig. 23.39b), the insulator–oxide interface is charged. The charge can be removed by UV light (EPROM, erasable programmable read-only memory) or by a sufficient voltage across the oxide at which the charge carriers can tunnel out (Fowler–Nordheim tunneling) (EEPROM, E^2PROM, electrically erasable programmable read-only memory).

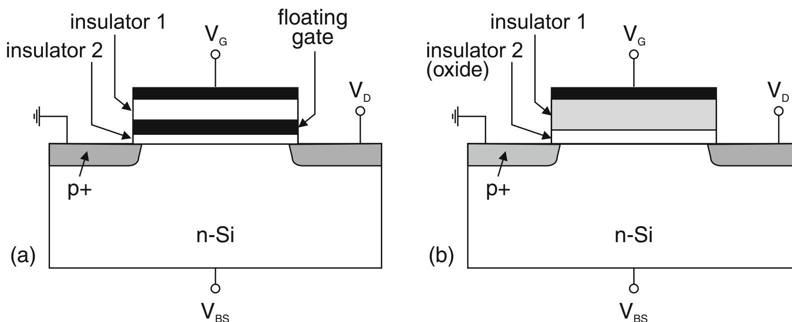

Fig. 23.39. MOSFET with (**a**) floating gate and (**b**) MIOS structure

Nowadays, a special type of EEPROM is used for the so-called *flash* memories. The stored gate charge causes a change in the MOSFET threshold voltage and is designed to switch between the on and off state. The storage time of

the charge can be of the order of 100 years. Since tunneling limits the charge retention, the oxide must be sufficiently thick. In Fig. 23.40 a cross section of a 4 Gb, 73 nm SLC (single-level cell) flash memory is shown. The lower insulator (tunneling oxide at the channel) consist of 7.2 nm SiO_2, the upper insulator (insulator 1 in Fig. 23.39a) is a 18 nm thick oxide/nitride/oxide (ONO) stack. The floating gate has a $90 \times 90\,\mathrm{nm}^2$ footprint, is about 86 nm high and consists of two polysilicon layers.

In a SLC memory the floating gate has two states, a certain charge value and the erased state. In a MLC (multi-level cell) the gate can store several charge states which can be sensed as different logic states, e.g. $2^2 = 4$ states. This increases the storage density, lowering cost per bit, but also increases the complexity. SLC cells so far have the higher endurance (possible number of read–write cycles) and lower power consumption. Generally SLC flash memory is considered industrial grade and MLC flash is considered consumer grade.

Typical endurance is at least 10^6 program–erase cycles. The ultimate limit, explored currently, is to use a single electron charge to cause such an effect in the single-electron transistor (SET).

Future Concepts

Memory concepts beyond the storage of free charges include information storage via

- the static polarization in a ferroelectric material (either crystalline or polymer) (FeRAM [1431], Fig. 23.41a) which can be switched by an electric field.

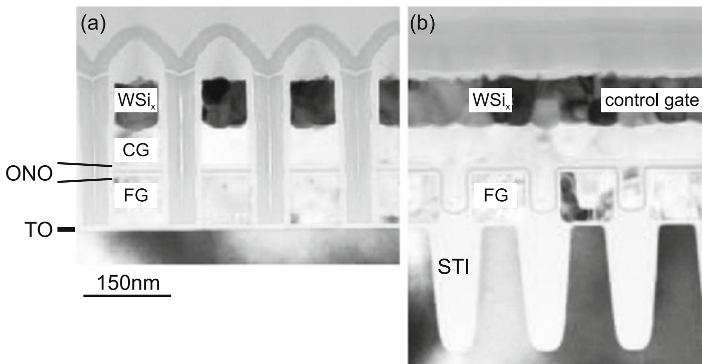

Fig. 23.40. Cross sections (**a**) perpendicular and (**b**) parallel to the control gate line of a 4 Gb, 73 nm SLC flash memory (Samsung K9F4G08U0M). 'CG' denotes the control gate, 'FG' the floating gate, 'TO' the tunneling oxide, 'ONO' the oxide/nitride/oxide insulator stack, and 'STI' the shallow trench insulation. Adapted from [1412]

- the phase change between amorphous and polycrystalline phases in a chalcogenide layer (typically GeSb [1432] or $Ge_2Sb_2Te_5$, GST [1433, 1434] with an $\alpha \leftrightarrow$ c transition, Fig. 23.42) upon local heating (similar to a rewritable DVD) and the related change is resistivity (PCM, phase change memory).
- the storage of magnetization direction (MRAM [1435, 1436]) and subsequent resistance change of a magneto-tunneling junction (MTJ) whose resistance depends on the relative magnetization (parallel or perpendicular) of two magnetic layers separated by a thin tunneling insulator (Fig. 23.41b). The largest TMR (tunnel-magnetoresistance) effect has been achieved with MgO as insulator [1436]. The magnetization of the bottom magnetic layer of the MTJ is fixed. The magnetization directions $\pm 45°$ are written into the free layer with the magnetic fields of two perpendicular high current wires in two subsequent back-end interconnect layers sandwiching the MTJ.
- resistance change based on solid electrolytes (PMC, programmable metallization cell memory). The lowering of the resistance is attained by the reduction of ions in a fairly high resistivity electrolyte (e.g. from the system Cu,Ag–Ge–Se,S,O [1437, 1438] or oxides [1439]) to form a conducting bridge between the electrodes. The resistance is returned to the high value via the application of a reverse bias that results in the breaking of the conducting pathway.
- resistance change in transition metal oxides such as perovskites, e.g. $SrTiO_3$:Cr [1440, 1441] or NiO:Ti (RRAM). Electrical pulses of opposite polarity switch the resistance reversibly between a high- and a low-resistance state. Oxygen-vacancy drift modulates the valence of the mixed-valence transition-metal ion (e.g. Ti^{3+}–Ti^{4+}) and thus the conducting state [1442].
- a molecular configuration change (e.g. redox reaction) between crossed wire lines (molecular electronics [1443–1445].

23.5.8 Heterojunction FETs

Several types of field-effect transistors have been devised that use heterojunctions (HJFET).

HIGFET

As conducting channel, the two-dimensional electron gas at an undoped heterointerface is used. Such a transistor is called a heterojunction insulating gate FET (HIGFET). With forward or backward gate voltage, an electron or hole gas can be created (channel enhancement mode), as visualized in Fig. 23.43. Thus, a complementary logic can be realized. However, the p-channel suffers from low hole mobility.

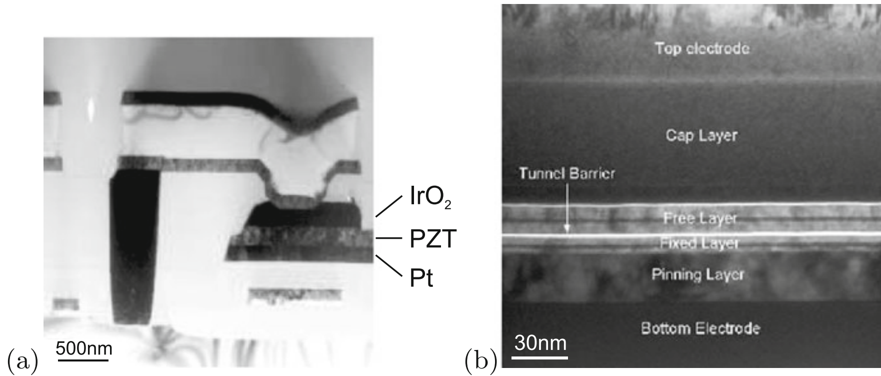

Fig. 23.41. (**a**) Cross-section TEM image of a cell from a Ramtron 4 Mb FeRAM. The information is stored in the electric polarization of a polycrystalline $Pb(Ti_xZr_{1-x})O_3$ (PZT) island, contacted on the bottom and top with platinum and iridium oxide, respectively. Adapted from [1412]. (**b**) Cross-section TEM of the magnetic tunneling junction from a Freescale 4.2 Mb MRAM, located between the M4 and M5 interconnect layers. The magnetization of the free layer can be switched, that of the fixed layer remains constant. Adapted from [1412]

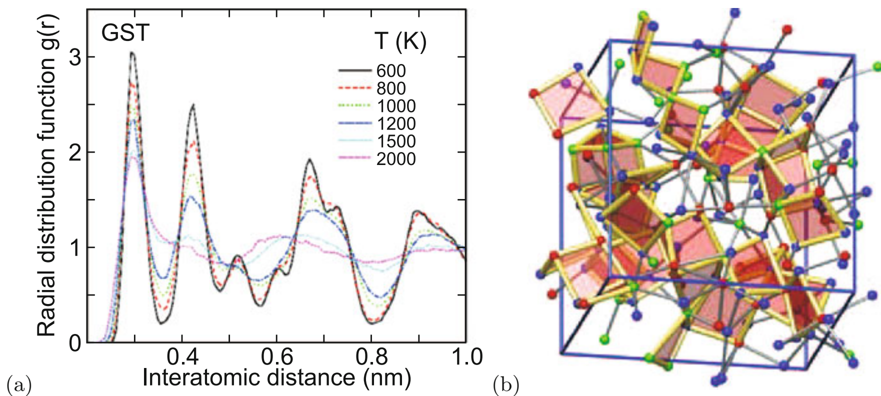

Fig. 23.42. (**a**) Radial distribution function of ions in $Ge_2Sb_2Te_5$ (GST) for various temperatures (cmp. Fig. 3.14b). Adapted from [1433]. (**b**) Atom arrangement in the amorphous phase of GST with square units highlighted that nucleate crystallization. Adapted from [1434]

HEMT

If the top wide-bandgap layer is n-doped, a modulation-doped FET (MODFET) is made (see Sect. 11.3.4). This structure is also called a HEMT (high electron mobility transistor) or TEGFET (two-dimensional electron gas FET) (Fig. 23.44). A thin undoped AlGaAs spacer layer is introduced between the doped AlGaAs and the undoped GaAs to reduce impurity scattering from

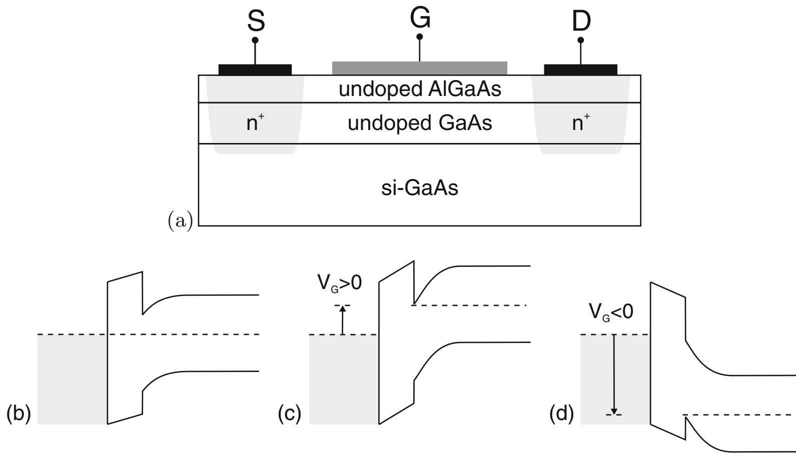

Fig. 23.43. (**a**) Scheme of a HIGFET structure with metal gate and undoped AlGaAs/GaAs heterointerface on semi-insulating GaAs. The source and drain contacts are n-doped such that this structure can be used as an n-HIGFET (see part (**c**)). (**b**) Band diagram for zero gate voltage. (**c**) Band diagram for positive gate voltage and n-channel, (**d**) for negative gate voltage and p-channel

carriers that tunnel into the barrier. With increasing gate voltage, a parallel conduction channel in the AlGaAs is opened. The natural idea would be to increase the Al fraction in the AlGaAs to increase the quantum-well barrier height. Unfortunately, the barrier height is limited to 160 meV for an aluminum concentration of about 20%. For Al content higher than about 22%, the DX center (cf. Sect. 7.7.6) forms a deep level such that the apparent ionization energy increases drastically and no shallow donors can be used for modulation doping. An improvement for the barrier conduction problem is the use of δ-doping [1446], i.e. the introduction of a highly doped thin (mono-)layer (Fig. 23.45), which results in higher channel carrier concentration.

Pseudomorphic HEMTs

Instead of increasing the height of the barrier, the depth of the well can be increased by using a low-bandgap material. On GaAs substrate, InGaAs is used (Fig. 23.46). However, strain is introduced in this case and the InGaAs layer thickness is limited by the onset of dislocation formation (cf. Sect. 5.3.7) (which reduces the channel mobility and the device reliability). For $In_{0.15}Ga_{0.85}As$ (thickness about 10–20 nm), a total barrier height of about 400 meV can be obtained. A barrier height of 500 meV can be reached with an InAlAs/InGaAs structure on InP (Fig. 23.47). The InAlAs does not suffer from the problem related to DX centers. The channel indium concentration is typically 50%. The mobility increases with increasing indium concentration.

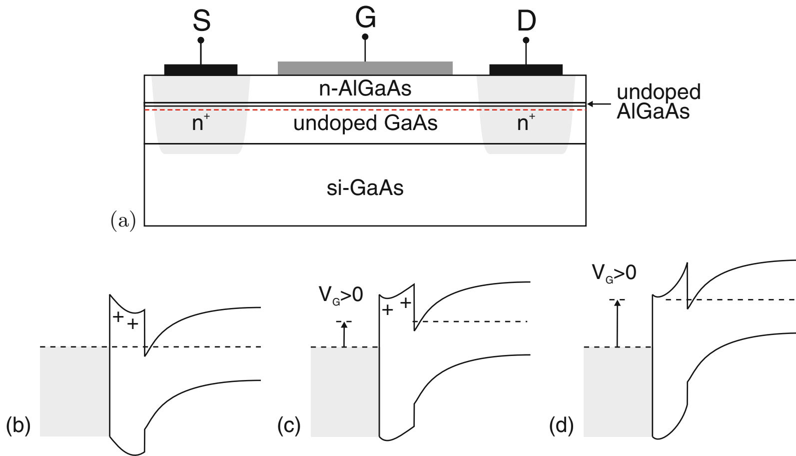

Fig. 23.44. (**a**) Scheme of a HEMT structure with n-AlGaAs/GaAs heterointerface on semi-insulating GaAs. The source and drain contacts are n-doped such that this structure can be used as an n-channel (normally-on) HEMT. The *horizontal dashed line* represents schematically the position of the 2DEG at the heterointerface on the GaAs side. (**b**) Band diagram at zero gate voltage. (**c**) Band diagram at positive gate voltage, increase of channel carrier concentration. (**d**) Band diagram at even larger positive gate voltage, formation of conducting channel in the AlGaAs layer

This InP-based HEMT structure is widely used in satellite receivers for its excellent high-speed and low-noise properties in the 100–500 GHz range and beyond.

However, the InP technology is economically less favorable than GaAs due to smaller available substrate size and higher cost (2001: 4” InP substrate: \$1000, 6” GaAs substrate: \$450).

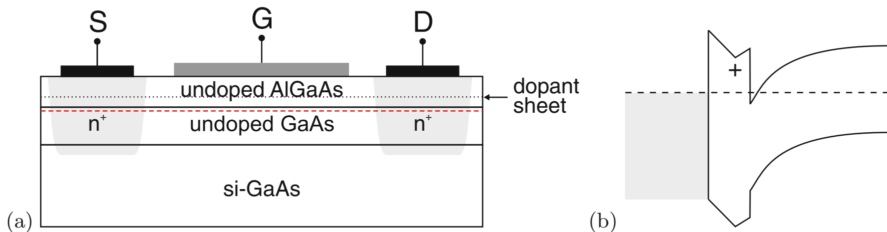

Fig. 23.45. (**a**) Scheme of a δ-doped HEMT structure with AlGaAs/GaAs heterointerface on semi-insulating GaAs. The source and drain contacts are n-doped such that this structure can be used as an n-channel HEMT. The *horizontal dashed line* represents schematically the position of the 2DEG in the GaAs layer. (**b**) Band diagram at zero gate voltage

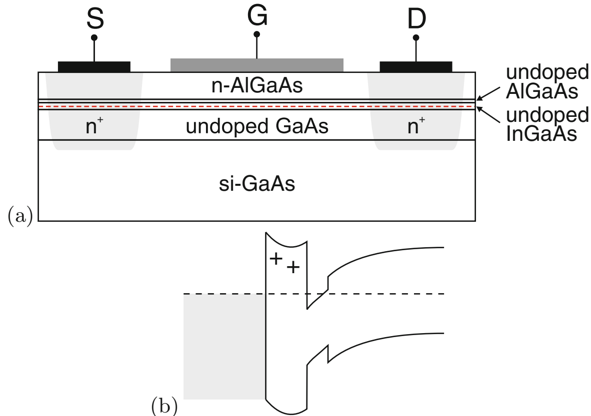

Fig. 23.46. (**a**) Scheme of a PHEMT structure with n-AlGaAs/InGaAs heterointerface on semi-insulating GaAs. The source and drain contacts are n-doped such that this structure can be used as an n-channel HEMT. The *horizontal dashed line* represents schematically the position of the 2DEG in the InGaAs layer. (**b**) Band diagram at zero gate voltage

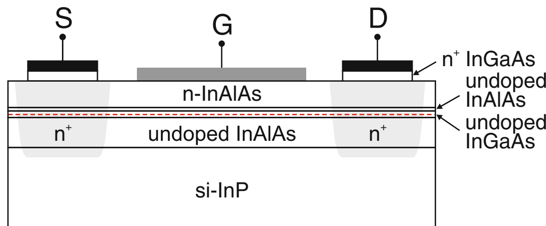

Fig. 23.47. Scheme of a PHEMT structure with n-AlInAs/InGaAs/InAlAs structure on semi-insulating InP. The source and drain contacts (with a highly doped InGaAs contact layer) are an n-doped such that this structure can be used as an n-channel HEMT. The *horizontal dashed line* represents schematically the position of the 2DEG in the InGaAs layer.

Metamorphic HEMTs

A unification of the InAlAs/InGaAs structure with the best figure of merit and the GaAs substrate is achieved with the metamorphic HEMT (MHEMT). Here, a relaxed buffer is used to bring the in-plane lattice constant from that of GaAs to about that of InP. It is key that the defects occurring are confined to the relaxed buffer and do not enter the active device structure (see Fig. 23.48). The relaxed buffer is typically about 1 µm thick. It can be grown, e.g., with a graded $\mathrm{In}_x(\mathrm{Ga,Al})_{1-x}\mathrm{As}$ layer with x =0–42% or with a stepped structure with piecewise constant indium concentration in each layer. It is important that a smooth interface of the channel is achieved inorder to

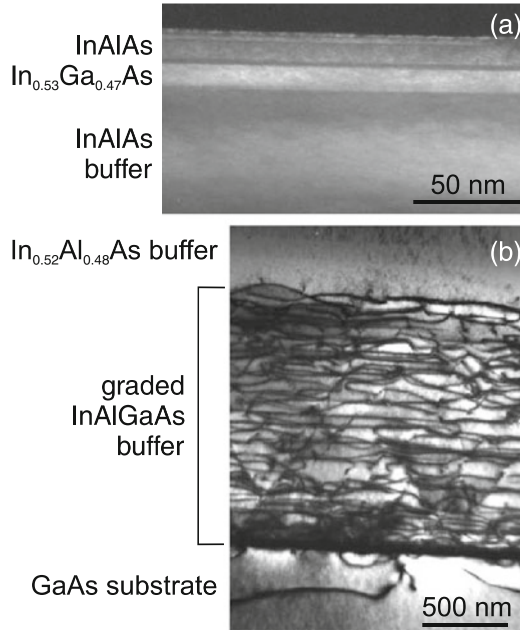

Fig. 23.48. Cross-sectional TEM image of an InAlAs/InGaAs MHEMT: (**a**) Active layer with rms surface roughness of 2.0 nm (from AFM), (**b**) graded InGaAlAs buffer layer (1.5 µm) on GaAs substrate. Adapted from [1453]

avoid additional scattering mechanisms. For high-frequency operation, the fabrication of a small gate length is important, as shown in Fig. 23.49 for a 70-nm gate of a f_{T} =293 GHz, $f_{\max}$ = 337 GHz transistor [1447]. SiGe

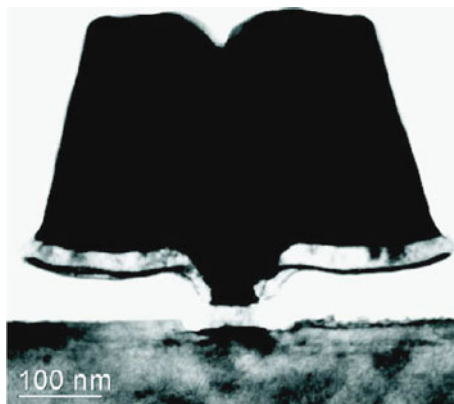

Fig. 23.49. Cross-sectional TEM image of the 70-nm gate of an InAlAs MHEMT on GaAs substrate. From [1447]

channels, providing higher mobility than pure Si, can be fabricated using graded or stepped SiGe buffer layers on Si substrate. With such Si-based MHEMTs frequencies up to 100 GHz can be achieved.

23.6 Thin-Film Transistors

Thin-film transistors (TFTs) are field-effect transistors typically fabricated as large-area arrays from thin layers of polycrystalline or amorphous silicon [1448] or organic semiconductors [1449–1452] on cheap substrates such as glass. Their most prominent use is driving pixels in active-matrix displays such as electroluminescence (EL) displays or twisted nematic liquid crystal displays (LCD) [1454]. Various gates and gate geometries have been reported as depicted in Fig. 23.50.

23.6.1 Annealing of Amorphous Silicon

Since the mobility in polycrystalline silicon is much higher (up to several hundred cm^2/Vs depending on grain size, see Sect. 8.3.8) than in amorphous silicon ($< 1\,cm^2/Vs$), such material is much more desirable as channel in TFTs. However, it requires high deposition temperatures. In order to achieve polycrystalline silicon with large grain size from amorphous silicon films that can be deposited at low temperature (down to room temperature) several schemes have been developed, the most important being thermal annealing and (excimer) laser annealing (ELA). Crystallization occurs by thermally activated nucleation and growth processes [1455]. Polycrystalline layers will small grain size can be made amorphous with implantation of Si (self-implantation) and a subsequent optimized (re-)crystallization processes.

In laser annealing energy is locally introduced during short pulses (several 10 ns or even fs); subsequent material change occurs on a sub-µs time scale [1456]. Laser induced crystallization enables the use of inexpensive low-temperature substrates, such as plastic or glass, since it involves the ultrafast melting and resolidification of the near-surface region of the sample, and

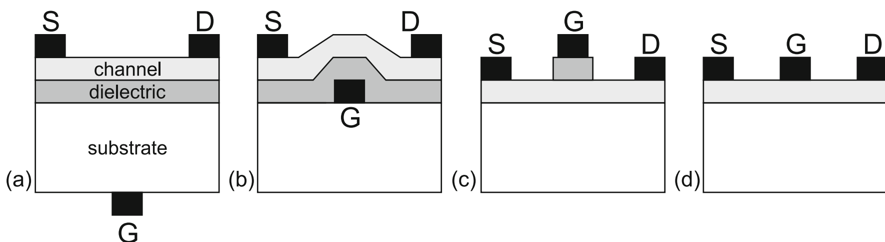

Fig. 23.50. Schematic geometries of TFTs: (**a**-**c**) MISFETs, (**d**) MESFET with (**a**, **b**) bottom gate and (**c**, **d**) top gate. Semiconductor channel layer (*light grey*), insulating dielectric (*dark grey*) and metals (*black*)

minimal heating of the substrate. Local processing is also possible using laser crystallization.

In Fig. 23.51 the effect of thermal annealing of amorphous silicon is shown. The annealing time necessary to convert the amorphous phase completely to polycrystalline, e.g. 10 h at 640°C, depends largely on temperature as detailed in [1457, 1458] (Fig. 23.51a) with a large activation energy of 3.9 eV. Also the final grain size is temperature dependent (Fig. 23.51b).

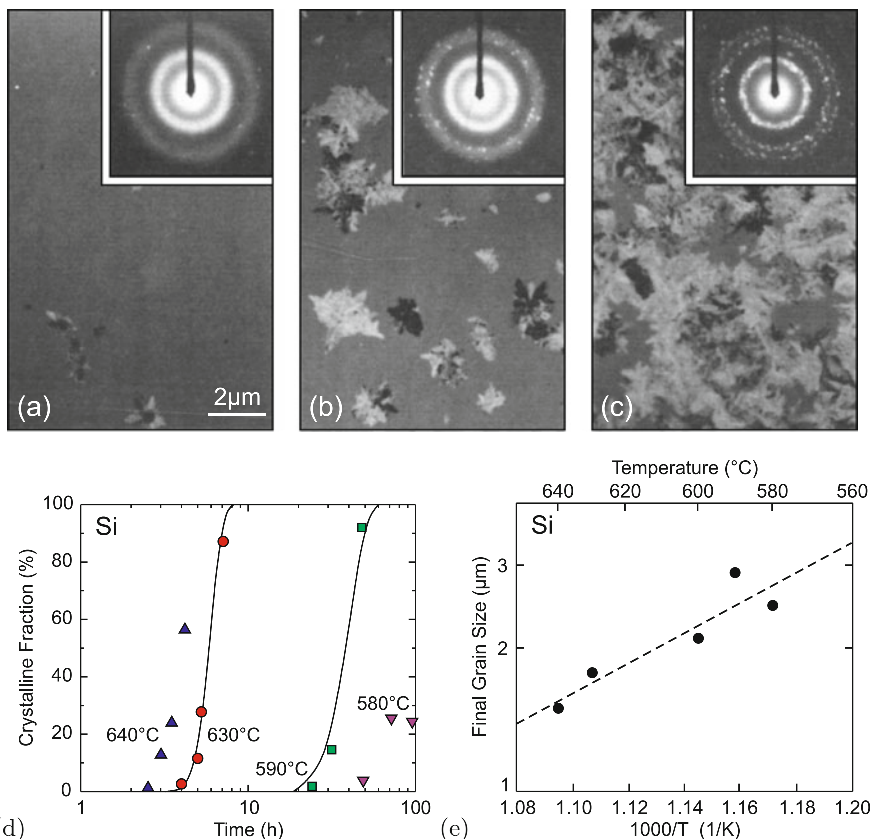

Fig. 23.51. Thermal annealing of 100 nm thick film of amorphous silicon (fabricated from LPCVD and amorphized by 100 keV Si^+ implantation with a dose of $5 \times 10^{15}\,\mathrm{cm}^{-2}$). TEM images and diffraction patterns (*insets*) for amorphized Si after (**a**) 4 h, (**b**) 5.25 h and (**c**) 7.1 h annealing at $T = 630°\mathrm{C}$. The crystalline fractions are 2%, 28% and 87%, respectively. (**d**) Crystalline fraction as a function of annealing time for various annealing temperatures as labeled. *Symbols* are experimental data, *solid lines* depict theory considering grain nucleation and growth. (**e**) Final grain size for various annealing temperature. *Dashed line* is exponential with a slope of 0.6 eV. Adapted from [1457]

The introduction of certain metals like Pd [1459], Al [1460], Au [1461] or Ni [1462] induces crystallization and allows for much lower annealing temperatures. Pd and Ni create silicides that play an important role for the grain nucleation or growth front. Au and Al are solved in the bulk but have a similar effect. For example, using Pd complete crystallization of a 150 nm thick a-Si film deposited at 480°C can be achieved by thermal annealing after 10 h at only 500°C [1463] (using metal-induced lateral crystallization, MILC).

23.6.2 TFT Devices

A schematic cross section of an amorphous silicon-based TFT is shown in Fig. 23.52a. Carriers in amorphous silicon have a low mobility typically less than 1 cm^2/Vs [1464, 1465]. As-grown polycrystalline silicon has a mobility of typically less than 10 cm^2/Vs. With the use of laser irradiation or thermal annealing, amorphous or small-grain polycrystalline silicon layers can be recrystallized, increasing the mobility up to several 100 cm^2/Vs, improving transistor performance [1464, 1466, 1467]. However, for display applications a mobility of 10 cm^2/Vs is large enough.

The main optimization criteria for thin-film transistors are high on-off ratio, long-term stability, good uniformity and reproducibility, and low cost. Recently, flexible (on polymer substrate) and transparent TFTs (TFET, transparent FET), e.g. with polycrystalline ZnO or GaInZnO (GIZO) channel (Fig. 23.52b), are being investigated for advanced applications such as all-transparent electronics and displays [1111, 1468–1471]. A compilation of recent results on transparent semiconducting oxide (TSO) channel FETs can be found in [1472]. In Fig. 23.53 performance data for various TSO channel FETs are visualized. In Fig. 23.54 a transparent inverter based on ZnO-MESFETs is depicted [1473].

23.6.3 OFETs

Organic field effect transistors (OFETs) [1474–1477] are transistors for which at least the channel consists of an organic material. Most work is done on thin

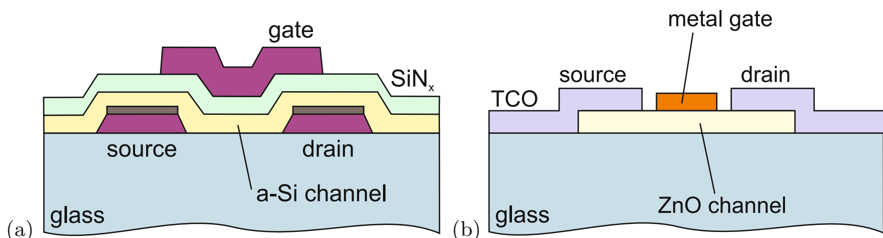

Fig. 23.52. (**a**) Schematic cross section of a top-gate amorphous silicon (a-Si) thin-film transistor (MISFET) on glass substrate. (**b**) Schematic cross section of a transparent ZnO thin-film transistor (MESFET)

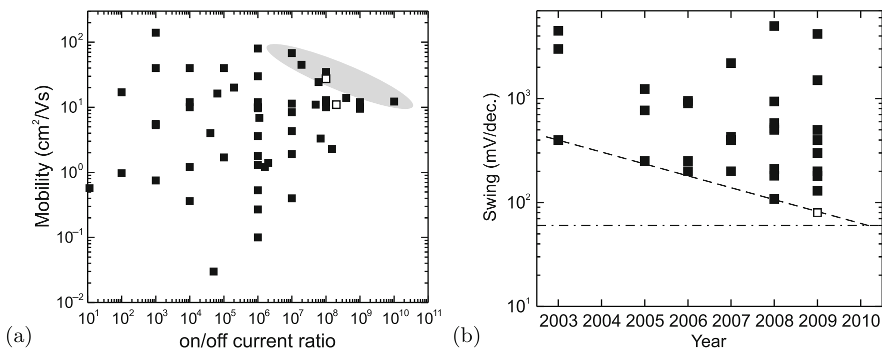

Fig. 23.53. (**a**) Field effect mobility and on/off current ratio for oxide channel transistors. *Filled squares* represent MISFET transistors; *open squares* are for MESFETs from Ref. [1471]. The *shaded area* indicates best performance. (**b**) Voltage swing for MISFETs (*filled squares*, subthreshold voltage swing) and MESFET (*empty square*, above turn-on voltage from Ref. [1471]) with TSO channels. The *dashed line* is guide to the eyes for the trend of best performance. The *dash-dotted line* indicates the thermodynamic limit of about 60 meV/decade for the swing [1480]. Adapted from [1472]

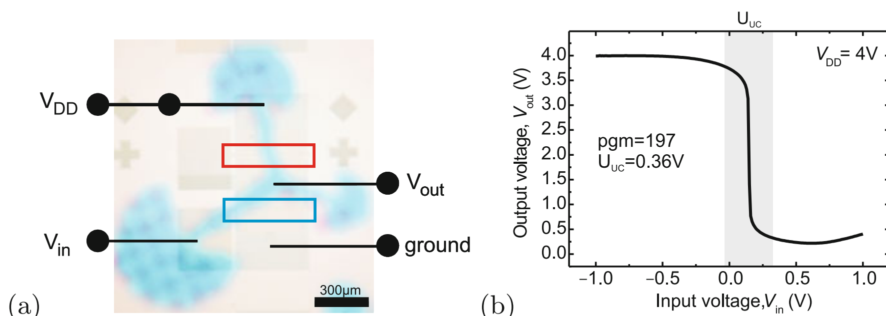

Fig. 23.54. (**a**) Optical image of transparent MESFET inverter based on ZnO. The *two rectangles* indicate the two gates. (**b**) Transfer characteristic for supply voltage V_{DD}=4 V

film transistors, although some work on OFETs using bulk organic semiconductors has been reported [1478, 1479]. Organic materials are also used for the insulator and the contact materials. Often organic and flexible substrates are used. Applications are in low cost electronics, e.g. for driving display pixels or RFID tags (typically operating at 13.56 MHz or 900 MHz). Processes like spin-on and printing can be used. Due to their larger chemical stability against oxidation, mostly p-type channel materials are used. The highest mobilities are reached for pentacene (6 cm^2/Vs) and sexithiophene (1 cm^2/Vs); n-type organic semiconductors exhibit field mobility below 0.1 cm^2/Vs [1475].

Part IV

Appendices

A Tensors

Introduction

A physical quantity $T_{ij\ldots m}$ with a total of k indices that is independent of translations of the coordinate system and transforms with respect to all indices like a vector is called a tensor of rank k.

Often, Einstein's sum convention is used; a sum is built over indices with the same symbol. For example, $x'_i = D_{ij} x_j$ shall be read as $x'_i = \sum_{j=1}^{3} D_{ij} x_j$.

Rotation of Coordinate System

A rotation of the coordinate system is a transformation $\mathbf{x} \rightarrow \mathbf{x}'$ that is written in components as

$$x'_i = D_{ij} x_j \ . \tag{A.1}$$

$\mathbf{D}$ is called the rotation matrix. The inverse of the rotation matrix is $\mathbf{D}^{-1}$ with

$$D^{-1}_{kl} = D_{lk} \ , \tag{A.2}$$

i.e. it is the transposed matrix $\mathbf{D}$. The inverse transformation is $x_j = D_{ij} x'_i$. Thus,

$$D_{ij} D_{kj} = \delta_{ij} \ . \tag{A.3}$$

A simple example is the azimuthal rotation around the z-axis by an angle ϕ (in the mathematically positive direction)

$$\mathbf{D} = \begin{pmatrix} \cos\phi & -\sin\phi & 0 \\ \sin\phi & \cos\phi & 0 \\ 0 & 0 & 1 \end{pmatrix} \ . \tag{A.4}$$

For the description of a general rotation $(x, y, z) \rightarrow (X, Y, Z)$, generally three angles are necessary. Typically, the Euler angles (ϕ, θ, ψ) are used (Fig. A.1). First, the system is rotated by ϕ around the z-axis. The y-axis becomes the u-axis. Then, the system is tilted by θ around the u-axis and the z-axis becomes the Z-axis. Finally, the system is rotated by ψ around the Z-axis.

M. Grundmann, *The Physics of Semiconductors*, 2nd ed., Graduate Texts in Physics, DOI 10.1007/978-3-642-13884-3_24,

© Springer-Verlag Berlin Heidelberg 2010

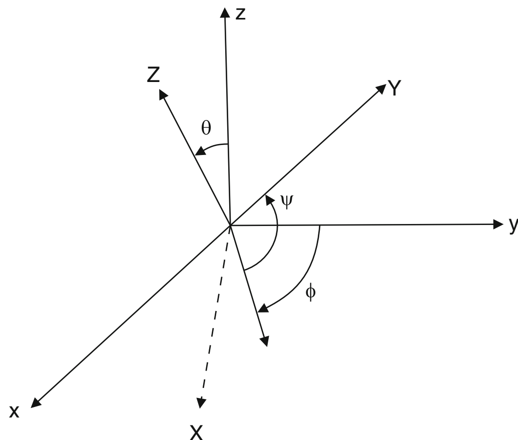

Fig. A.1. Rotation of a coordinate system (x, y, z) by the Euler angles (ϕ, θ, ψ) into the system (X, Y, Z)

The matrix for the general rotation by the Euler angles is

$$\begin{pmatrix} \cos\psi\cos\theta\cos\phi - \sin\psi\sin\phi & -\sin\psi\cos\theta\cos\phi - \cos\psi\sin\phi & \sin\theta\cos\phi \\ \cos\psi\cos\theta\sin\phi + \sin\psi\cos\phi & -\sin\psi\cos\theta\sin\phi + \cos\psi\cos\phi & \sin\theta\sin\phi \\ -\cos\psi\sin\theta & \sin\psi\sin\theta & \cos\theta \end{pmatrix} . \tag{A.5}$$

Rank-n Tensors

Rank-0 Tensors

A tensor of rank 0 is also called a scalar. For example, the length $v_1^2 + v_2^2 + v_3^2$ of the vector $\mathbf{v} = (v_1, v_2, v_3)$ is a scalar since it is invariant under rotation of the coordinate system. However, 'scalar' is not equivalent to 'number' since, e.g. the number $v_1^2 + v_2^2$ is not rotationally invariant.

Rank-1 Tensors

A tensor of rank 1 is a vector. It transforms under coordinate rotation $\mathbf{D}$ as

$$v_i' = D_{ij} v_j \ . \tag{A.6}$$

Rank-2 Tensors

A tensor of rank 2 is also called a dyade and is a 3×3 matrix $\mathbf{T}$ that transforms under coordinate rotation as

$$T_{ij}' = D_{ik} D_{jl} T_{kl} \ . \tag{A.7}$$

The physical meaning is the following: Two vectors $\mathbf{s}$ and $\mathbf{r}$ shall be related to each other via $s_i = T_{ij} r_j$. This could be, e.g., the current $\mathbf{j}$ and the electric field $\mathbf{E}$ that are connected via the tensor of conductivity σ, i.e. $j_i = \sigma_{ij} E_j$.

Such an equation only makes physical sense if it is also valid in a (any) rotated coordination system. The tensor $\mathbf{T}'$ in the rotated coordinate system must fulfill $s'_i = T'_{ij} r'_j$. This implies the transformation law (A.7). $s'_k = D_{ki} s_i = D_{ki} T_{ij} r_j$ and also $s'_k = T'_{km} r'_m = T'_{km} D_{mj} r_j$. Thus, $T'_{km} D_{mj} = D_{ki} T_{ij}$ since the previous relations are valid for arbitrary $\mathbf{r}$. Multiplication by D_{lj} yields $T'_{km} D_{mj} D_{lj} = T'_{km} \delta_{ml} = T'_{kl} = D_{ki} D_{lj} T_{ij}$.

The trace of a rank-2 tensor is defined as $\mathrm{tr}\mathbf{T} = T_{ii} = T_11 + T_22 + T_33$. It is a scalar, i.e. invariant under coordinate rotation, since $T'_{kk} = D_{ki} D_{kj} T_{ij} = \delta_{ij} T_{ij} = T_{ii}$.

A rank-2 tensor can be separated into a symmetric part $\mathbf{T}^S$ and an antisymmetric part $\mathbf{T}^A$, i.e. $T^S_{ji} = T^S_{ij}$ and $T^A_{ji} = -T^A_{ij}$ with

$$\mathbf{T} = \mathbf{T}^S + \mathbf{T}^A \tag{A.8a}$$

$$T^S_{ij} = \frac{T_{ij} + T_{ji}}{2} \tag{A.8b}$$

$$T^A_{ij} = \frac{T_{ij} - T_{ji}}{2} \ . \tag{A.8c}$$

A rank-2 tensor can be separated into an isotropic (spherical) part $\mathbf{T}^I$ and a deviatoric part $\mathbf{T}^D$. The isotropic part is invariant under coordinate rotation.

$$\mathbf{T} = \mathbf{T}^I + \mathbf{T}^D \tag{A.9a}$$

$$T^I_{ij} = \delta_{ij} \frac{\mathrm{tr}\mathbf{T}}{3} \tag{A.9b}$$

$$T^D_{ij} = T_{ij} - \delta_{ij} \frac{\mathrm{tr}\mathbf{T}}{3} \ . \tag{A.9c}$$

The trace of $\mathbf{T}$ is the same as that of $\mathbf{T}^I$. The trace of $\mathbf{T}^D$ is zero.

Rank-3 Tensors

A tensor of rank 3 transforms according to

$$T'_{ijk} = D_{il} D_{jm} D_{kn} T_{lmn} \ . \tag{A.10}$$

An example is the tensor $\mathbf{e}$ of piezoelectric constants that relates the rank-2 tensor of the strains ϵ with the polarization vector $\mathbf{P}$, i.e. $P_i = e_{ijk} \epsilon_{jk}$.

Rank-4 Tensors

A tensor of rank 4 transforms according to

$$T'_{ijkl} = D_{im} D_{jn} D_{ko} D_{lp} T_{mnop} \ . \tag{A.11}$$

An example is the tensor $\mathbf{C}$ of elastic constants that relates the rank 2 tensors ϵ and σ of the elastic strains and stresses, i.e. $\sigma_{ij} = C_{ijkl} \epsilon_{kl}$.

B Space Groups

The space groups of crystallography have been introduced in Sect. 3.3.3. Here, a complete list of all 230 space groups and their standard international notation is given.

M. Grundmann, *The Physics of Semiconductors*, 2nd ed., Graduate Texts in Physics, DOI 10.1007/978-3-642-13884-3_25,
© Springer-Verlag Berlin Heidelberg 2010

Table B.1. Space group numbers and corresponding space group symbols

1	P1	2	$P\bar{1}$	3	P2	4	$P2_1$	5	C2
6	Pm	7	Pc	8	Cm	9	Cc	10	P2/m
11	$P2_1/m$	12	C2/m	13	P2/c	14	$P2_1/c$	15	C2/c
16	P222	17	$P222_1$	18	$P2_12_12$	19	$P2_12_12_1$	20	$C222_1$
21	C222	22	F222	23	I222	24	$I2_12_12_1$	25	Pmm2
26	$Pmc2_1$	27	Pcc2	28	Pma2	29	$Pca2_1$	30	Pnc2
31	$Pmn2_1$	32	Pba2	33	$Pna2_1$	34	Pnn2	35	Cmm2
36	$Cmc2_1$	37	Ccc2	38	Amm2	39	Abm2	40	Ama2
41	Aba2	4_2	Fmm2	43	Fdd2	44	Imm2	45	Iba2
46	Ima2	47	Pmmm	48	Pnnn	49	Pccm	50	Pban
51	Pmma	52	Pnna	53	Pmna	54	Pcca	55	Pbam
56	Pccn	57	Pbcm	58	Pnnm	59	Pmmn	60	Pbcn
61	Pbca	62	Pnma	63	Cmcm	64	Cmca	65	Cmmm
66	Cccm	67	Cmma	68	Ccca	69	Fmmm	70	Fddd
71	Immm	72	Ibam	73	Ibca	74	Imma	75	P4
76	$P4_1$	77	$P4_2$	78	$P4_3$	79	I4	80	$I4_1$
81	$P\bar{4}$	82	$I\bar{4}$	83	P4/m	84	$P4_2/m$	85	P4/n
86	$P4_2/n$	87	I4/m	88	$I4_1/a$	89	P422	90	$P42_12$
91	P4122	92	$P412_12$	93	$P4_222$	94	$P4_22_12$	95	$P4_322$
96	$P4_32_12$	97	I422	98	$I4_122$	99	P4mm	100	P4bm
101	$P4_2cm$	102	$P4_2nm$	103	P4cc	104	P4nc	105	$P4_2mc$
106	$P4_2bc$	107	I4mm	108	I4cm	109	$I4_1md$	110	$I4_1cd$
111	$P\bar{4}2m$	112	$P\bar{4}2c$	113	$P\bar{4}2_1m$	114	$P\ \bar{4}2_1c$	115	$P\bar{4}m2$
116	$P\bar{4}c2$	117	$P\bar{4}b2$	118	$P\bar{4}n2$	119	$I\bar{4}m2$	120	$I\bar{4}c2$
121	$I\bar{4}2m$	122	$I\bar{4}2d$	123	P4/mmm	124	P4/mcc	125	P4/nbm
126	P4/nnc	127	P4/mbm	128	P4/mnc	129	P4/nmm	130	P4/ncc
131	$P4_2/mmc$	132	$P4_2/mcm$	133	$P4_2/nbc$	134	$P4_2/nnm$	135	$P4_2/mbc$
136	$P4_2/mnm$	137	$P4_2/nmc$	138	$P4_2/ncm$	139	I4/mmm	140	I4/mcm
141	$I4_1/amd$	142	$I4_1/acd$	143	P3	144	$P3_1$	145	$P3_2$
146	R3	147	$P\bar{3}$	148	$R\bar{3}$	149	P312	150	P321
151	$P3_112$	152	$P3_121$	153	$P3_212$	154	$P3_221$	155	R32
156	P3m1	157	P31m	158	P3c1	159	P31c	160	R3m
161	R3c	162	$P\bar{3}1m$	163	$P\bar{3}1c$	164	$P\bar{3}m1$	165	$P\bar{3}c1$
166	$R\bar{3}m$	167	$R\bar{3}c$	168	P6	169	$P6_1$	170	$P6_5$
171	$P6_2$	172	$P6_4$	173	$P6_3$	174	$P\bar{6}$	175	P6/m
176	$P6_3/m$	177	P622	178	$P6_122$	179	$P6_522$	180	$P6_222$
181	$P6_422$	182	$P6_322$	183	P6mm	184	P6cc	185	$P6_3cm$
186	$P6_3mc$	187	$P\bar{6}m2$	188	$P\bar{6}c2$	189	$P\bar{6}2m$	190	$P\bar{6}2c$
191	P6/mmm	192	P6/mcc	193	$P6_3/mcm$	194	$P6_3/mmc$	195	P23
196	F23	197	I23	198	$P2_13$	199	$I2_13$	200	$Pm\bar{3}$
201	$Pn\bar{3}$	202	$Fm\bar{3}$	203	$Fd\bar{3}$	204	$Im\bar{3}$	205	$Pa\bar{3}$
206	$Ia\bar{3}$	207	P432	208	$P4_232$	209	F432	210	$F4_132$
211	I432	212	$P4_332$	213	$P4_132$	214	$I4_132$	215	$P\bar{4}3m$
216	$F\bar{4}3m$	217	$I\bar{4}3m$	218	$P\bar{4}3n$	219	$F\bar{4}\ 3c$	220	$I\bar{4}3d$
221	$Pm\bar{3}m$	222	$Pn\bar{3}n$	223	$Pm\bar{3}n$	224	$Pn\bar{3}m$	225	$Fm\bar{3}m$
226	$Fm\bar{3}c$	227	$Fd\bar{3}m$	228	$Fd\bar{3}c$	229	$Im\bar{3}m$	230	$Ia\bar{3}d$

C Kramers–Kronig Relations

The Kramers–Kronig relations (KKR) are relations between the real and imaginary part of the dielectric function. They are of a general nature and are based on the properties of a complex, analytical response function $f(\omega) = f_1(\omega) + \mathrm{i} f_2(\omega)$ fulfilling the following conditions:[1]

- The poles of $f(\omega)$ are below the real axis.
- The integral of $f(\omega)/\omega$ along a semicircle with infinite radius in the upper half of the complex plane vanishes.
- The function $f_1(\omega)$ is even and the function $f_2(\omega)$ is odd for real values of the argument.

The integral of $f(s)/(s-\omega)\mathrm{d}s$ along the real axis and an infinite semicircle in the upper half of the complex plane is zero because the path is a closed line. The integral along a semicircle above the pole at $s = \omega$ yields $-\pi \mathrm{i} f(\omega)$, the integral over the infinite semicircle is zero. Therefore the value of $f(\omega)$ is given by[2]

$$f(\omega) = \frac{1}{\pi \mathrm{i}} \,\mathrm{Pr}\!\int_{-\infty}^{\infty} \frac{f(s)}{s-\omega} \mathrm{d}s \,. \tag{C.1}$$

Equating the real and imaginary parts of (C.1) yields for the real part

$$f_1(\omega) = \frac{1}{\pi} \,\mathrm{Pr}\!\int_{-\infty}^{\infty} \frac{f_2(s)}{s-\omega} \mathrm{d}s \,. \tag{C.2}$$

Splitting the integral into two parts $\int_0^\infty$ and $\int_{-\infty}^0$, going from s to $-s$ in the latter and using $f_2(-\omega) = -f_2(\omega)$ and $\frac{1}{s-\omega} + \frac{1}{s+\omega} = \frac{2s}{s^2-\omega^2}$ yields (C.3a)

$$f_1(\omega) = \frac{2}{\pi} \,\mathrm{Pr}\!\int_{0}^{\infty} \frac{s f_2(s)}{s^2-\omega^2} \mathrm{d}s \tag{C.3a}$$

$$f_2(\omega) = -\frac{2}{\pi} \,\mathrm{Pr}\!\int_{0}^{\infty} \frac{f_1(s)}{s^2-\omega^2} \mathrm{d}s \,. \tag{C.3b}$$

[1] The requirements for the function f to which the KKR apply can be interpreted as that the function must represent the Fourier transform of a linear and causal physical process.

[2] The Cauchy principal value Pr of the integral is the limit for $\delta \to 0$ of the sum of the integrals over $-\infty < s < \omega - \delta$ and $\omega + \delta < s < \infty$.

M. Grundmann, *The Physics of Semiconductors*, 2nd ed., Graduate Texts in Physics, DOI 10.1007/978-3-642-13884-3_26,

© Springer-Verlag Berlin Heidelberg 2010

In a similar way, (C.3b) is obtained. These two relations are the Kramers–Kronig relations [1481, 1482]. They are most often applied to the dielectric function ϵ. In this case, they apply to the susceptibility, i.e. $f(\omega) = \chi(\omega) = \epsilon(\omega)/\epsilon_0 - 1$. The susceptibility can be interpreted as the Fourier transform of the time-dependent polarization in the semiconductor after an infinitely short pulsed electric field, i.e. the impulse response of the polarization. For the dielectric function $\epsilon = \epsilon_1 + \mathrm{i}\epsilon_2$, the following KKR relations hold:

$$\epsilon_1(\omega) = \epsilon_0 + \frac{2}{\pi}\,\mathrm{Pr}\!\int_0^\infty \frac{s\epsilon_2(s)}{s^2-\omega^2}\mathrm{d}s \tag{C.4a}$$

$$\epsilon_2(\omega) = -\frac{2\omega}{\pi}\,\mathrm{Pr}\!\int_0^\infty \frac{\epsilon_1(s)-\epsilon_0}{s^2-\omega^2}\mathrm{d}s\ . \tag{C.4b}$$

The static dielectric constant is thus given by

$$\epsilon(0) = \epsilon_0 + \frac{2}{\pi}\,\mathrm{Pr}\!\int_0^\infty \frac{\epsilon_2(s)}{s}\mathrm{d}s\ . \tag{C.5}$$

The integral does not diverge since ϵ_2 is an odd function and zero at $\omega = 0$. Generally the j–th momentum M_j of the imaginary part of the dielectric function is

$$M_j = \int_0^\infty \epsilon_2(\omega)\omega^j\,\mathrm{d}\omega\ . \tag{C.6}$$

Thus, $M_{-1} = \pi[\epsilon(0) - \epsilon_0]/2$.

Other KKRs are, e.g., the relation between the index of refraction n_r and the absorption coefficient α:

$$n_\mathrm{r}(\lambda) = \frac{1}{\pi}\,\mathrm{Pr}\!\int_0^\infty \frac{\alpha(s)}{1-s^2/\lambda^2}\mathrm{d}s\ . \tag{C.7}$$

If the imaginary (real) part of the dielectric function is known (for all frequencies), the real (imaginary) part can be calculated via the KKR. If the dependence is not known for the entire frequency range, assumptions about the dielectric function in the unknown spectral regions must be made that limits the reliability of the transformation.

D Oscillator Strength

The response of an oscillator to an electric field $\mathbf{E}$ is formulated with the dielectric function. The resulting polarization $\mathbf{P}$ is related to the electric field via

$$\mathbf{P} = \epsilon_0 \chi \mathbf{E} \,, \tag{D.1}$$

with χ being the electric susceptibility, and the displacement field $\mathbf{D}$ is given by

$$\mathbf{D} = \epsilon_0 \mathbf{E} + \mathbf{P} = \epsilon_0 \epsilon \mathbf{E} \,. \tag{D.2}$$

Thus the (relative) dielectric constant is

$$\epsilon = 1 + \chi \,. \tag{D.3}$$

We assume a harmonic oscillator model for an electron, i.e. an equation of motion for the amplitude $x = x_0 \exp(\mathrm{i}\omega t)$

$$m\ddot{x} = -Cx \,. \tag{D.4}$$

The resonance frequency is $\omega_0^2 = C/m$. The presence of a harmonic electric field E of frequency ω and amplitude E_0 adds a force eE. Thus,

$$-m\omega^2 x = -m\omega_0^2 x + eE \,. \tag{D.5}$$

The polarization ex_0 is given by

$$ex_0 = \frac{e^2}{m} \frac{1}{\omega_0^2 - \omega^2} E_0 = \frac{e^2}{m\omega_0^2} \frac{1}{1 - \frac{\omega^2}{\omega_0^2}} E_0 \,. \tag{D.6}$$

The pre-factor is called the (dimensionless) *oscillator strength* and will be denoted as

$$f = \frac{e^2}{\epsilon_0 m \omega_0^2} \tag{D.7}$$

in the following. The frequency-dependent dielectric function of the resonance is thus

$$\epsilon(\omega) = 1 + \frac{f}{1 - \frac{\omega^2}{\omega_0^2}} \,. \tag{D.8}$$

M. Grundmann, *The Physics of Semiconductors*, 2nd ed., Graduate Texts in Physics, DOI 10.1007/978-3-642-13884-3_27,

© Springer-Verlag Berlin Heidelberg 2010

In the low-frequency limit, the dielectric function is $\epsilon(0) = 1 + f$, in the high-frequency limit $\epsilon(\infty) = 1$. The oscillator strength is the difference of ϵ for frequencies below and above the resonance.

For all systems, the high-frequency limit of ϵ is 1. This means that $\chi = 0$, i.e. there are no more oscillators to be polarized. The low-frequency limit includes all possible oscillators. If there are further oscillators between frequencies well above ω_0 and $\omega \to \infty$, these are summarized as the high-frequency dielectric constant $\epsilon_\infty > 1$. Equation (D.8) then reads

$$\epsilon(\omega) = \epsilon(\infty) + \frac{\hat{f}}{1 - \frac{\omega^2}{\omega_0^2}} \ . \tag{D.9}$$

The limit $\epsilon \to \epsilon(\infty)$ is only valid for frequencies above ω_0 but smaller than the next resonance(s) at higher frequencies.[1] Another common form is to include the background dielectric constant via

$$\epsilon(\omega) = \epsilon(\infty) \left[1 + \frac{f}{1 - \frac{\omega^2}{\omega_0^2}} \right] \ . \tag{D.10}$$

Obviously, $f = \hat{f}/\epsilon(\infty)$, making the two forms equivalent.

In order to discuss the lineshape, not only for ϵ but also for the index of refraction $n^* = n_\mathrm{r} + \mathrm{i}\kappa = \sqrt{\epsilon}$, we introduce damping to our calculation by adding a term $-m\Gamma\dot{x}$ to the left side of (D.5). This term is something like a 'friction' and would cause the oscillation amplitude to decay exponentially with a time constant $\tau = 2/\Gamma$ without external stimulus. The dielectric constant is

$$\epsilon(\omega) = \epsilon(\infty) \left[1 + \frac{f}{1 - \frac{\omega^2 + \mathrm{i}\omega\Gamma}{\omega_0^2}} \right] = \epsilon' + \mathrm{i}\epsilon'' \ . \tag{D.11}$$

The real and imaginary part fulfill the Kramers–Kronig relations (C.3a) and (C.3b). For the oscillator strength, the regimes of large oscillator strength ($f \sim 1$) and small oscillator strength ($f \ll 1$) are distinguished. For the damping, two regimes should be distinguished: Small damping ($\Gamma \ll \omega_0$) and strong damping ($\Gamma \gtrsim \omega_0$). Typical lineshapes are shown in Figs. D.1 and D.2.

For small oscillator strength, i.e. $f \ll 1$, the index of refraction $n^* = \sqrt{\epsilon} = n_\mathrm{r} + \mathrm{i}\kappa$ is given by ($n_\infty = \sqrt{\epsilon(\infty)}$)

$$n_\mathrm{r} = n_\infty \left[1 + \frac{f}{2} \frac{\omega_0^2(\omega_0^2 - \omega^2)}{(\omega_0^2 - \omega^2)^2 + \Gamma^2\omega^2} \right] \tag{D.12a}$$

$$\kappa = n_\infty \frac{f}{2} \frac{\Gamma\omega_0(\omega_0^2 - \omega^2)}{(\omega_0^2 - \omega^2)^2 + \Gamma^2\omega^2} \ . \tag{D.12b}$$

---

[1] For ω going to infinite values (beyond the X-ray regime), ϵ always goes towards one.

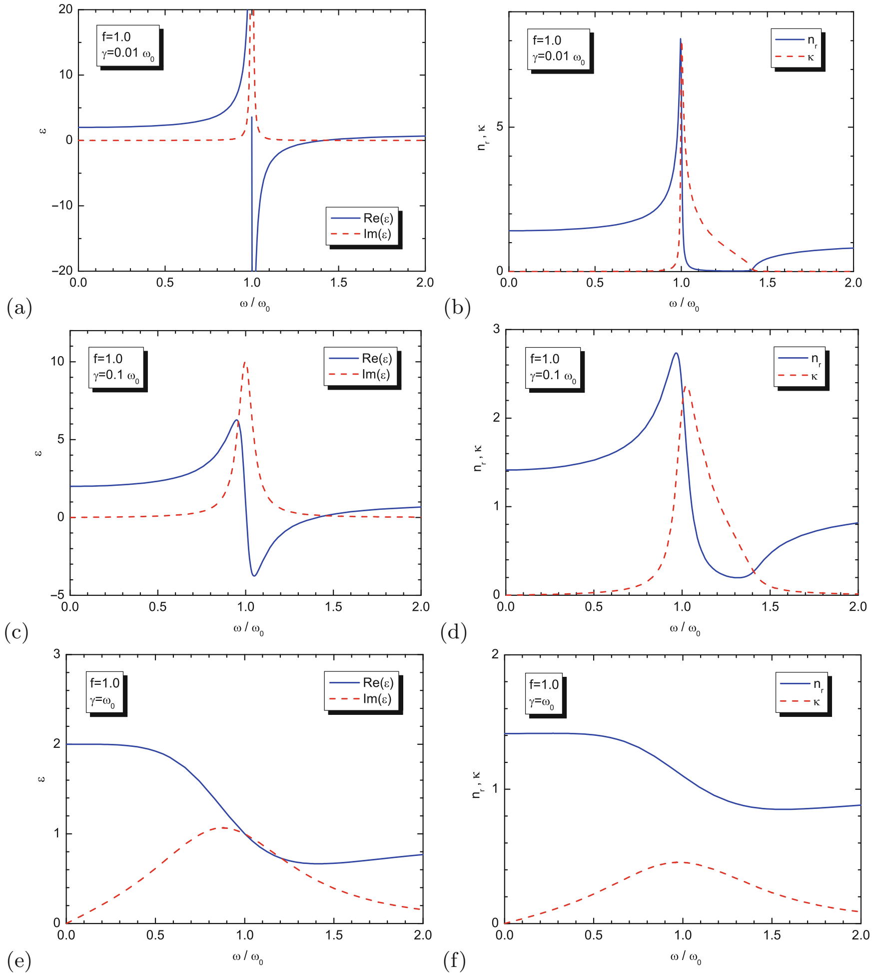

Fig. D.1. Real (*solid lines*) and imaginary (*dashed lines*) parts of the dielectric constant (**a**,**c**,**e**) and index of refraction (**b**,**d**,**f**) (D.11) for oscillator strength $f = 1$ and various values of damping: (**a**,**b**) $\Gamma = 10^{-2}\omega_0$, (**c**,**d**) $\Gamma = 10^{-1}\omega_0$, and (**e**,**f**) $\Gamma = \omega_0$

For small detuning from the resonance frequency, i.e. $\omega = \omega_0 + \delta\omega$ with $|\delta\omega|/\omega_0 \ll 1$, the index of refraction is given by

$$n_{\mathrm{r}} = n_\infty \left[1 - \frac{f}{4} \frac{\omega_0\, \delta\omega}{(\delta\omega)^2 + \Gamma^2/4} \right] \tag{D.13a}$$

$$\kappa = n_\infty \frac{f}{4} \frac{\omega_0\, \Gamma/2}{(\delta\omega)^2 + \Gamma^2/4} \; . \tag{D.13b}$$

The maximum absorption is given as

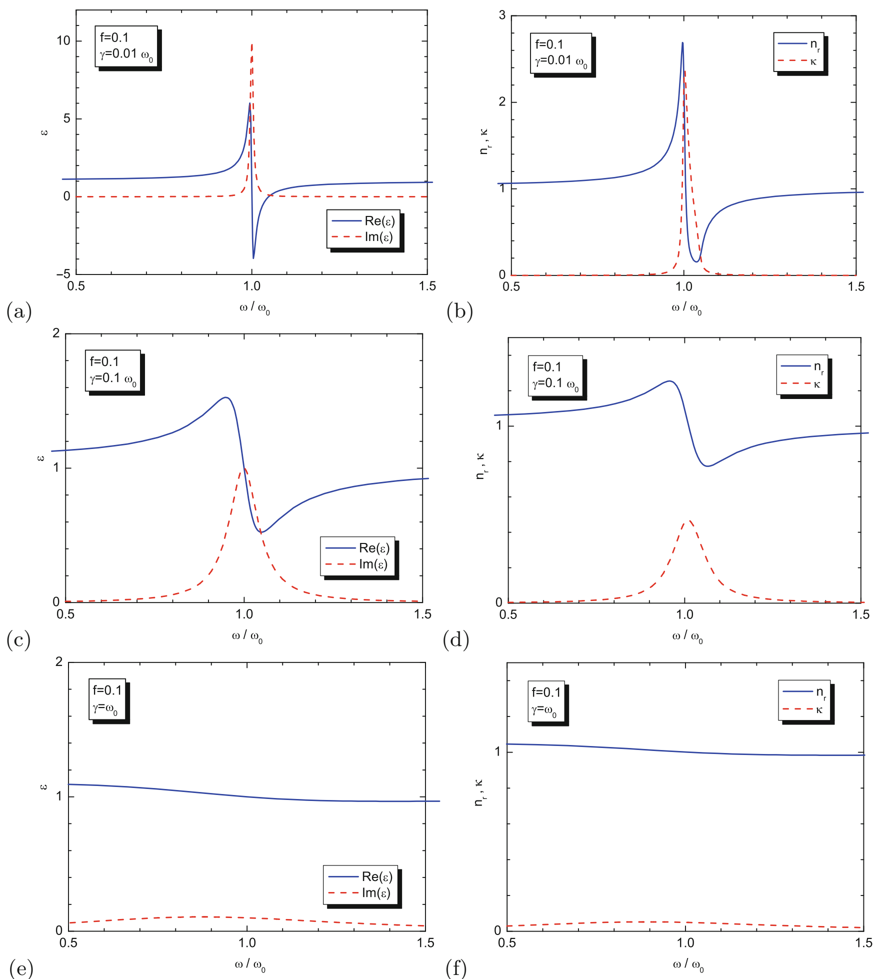

Fig. D.2. Real (*solid lines*) and imaginary (*dashed lines*) parts of the dielectric constant (**a**,**c**,**e**) and index of refraction (**b**,**d**,**f**) (D.11) for oscillator strength $f = 10^{-1}$ and various values of damping: (**a**,**b**) $\Gamma = 10^{-2}\omega_0$, (**c**,**d**) $\Gamma = 10^{-1}\omega_0$, and (**e**,**f**) $\Gamma = \omega_0$

$$\alpha_{\mathrm{m}} = 2\frac{\omega_0}{c}\kappa(\omega_0) = f\,\frac{\omega_0^2}{\Gamma}\frac{n_\infty}{c}\ . \tag{D.14}$$

For zero damping, the dielectric function has a zero at

$$\omega_0' = \sqrt{1+f}\,\omega_0 \approx \omega_0\left(1+\frac{f}{2}\right)\ . \tag{D.15}$$

The latter approximation is valid for $f \ll 1$. In the region between ω_0 and ω_0', the real part of the index of refraction is very small (for the physically

unrealistic case of $\Gamma \equiv 0$ it is exactly zero since $\epsilon < 0$). The reflectance (for vertical incidence $R = [(1-n^*)/(1+n^*)]^2$) in this region (width: $f\omega_0/2$) is thus very high. For larger damping (and small oscillator strength), this effect is washed out.

The frequency $\omega_{\epsilon'',\max}$ of the maximum of the imaginary part of ϵ'' of the dielectric function ($\hat{\Gamma} = \Gamma/\omega_0$) is

$$\omega^2_{\epsilon'',\max} = \frac{2 - \hat{\Gamma}^2 + \sqrt{16 - 4\hat{\Gamma}^2 + \hat{\Gamma}^4}}{6}\,\omega_0^2 \approx \omega_0^2 \left[1 - \left(\frac{\Gamma}{2\omega_0}\right)^2\right] . \tag{D.16}$$

The approximation is valid for small damping $\Gamma \ll \omega_0$. In this case, the detuned frequency of the maximum is close to ω_0 (Fig. D.3). The frequency position of the maximum of $\tan\delta = \epsilon''/\epsilon'$ is

$$\begin{aligned} \omega^2_{\tan\delta,\max} &= \frac{2 + f - \hat{\Gamma}^2 + \Lambda^2}{6}\,\omega_0^2 \\ \Lambda^2 &= \sqrt{12\,(1+f) + \left(2 + f - \hat{\Gamma}^2\right)^2} . \end{aligned} \tag{D.17}$$

The value of $\tan\delta$ at its maximum is (Λ has the same meaning as in (D.17))

$$(\tan\delta)_{\max} = \frac{-3\sqrt{\frac{3}{2}}\,f\,\hat{\Gamma}\,\sqrt{2 + f - \hat{\Gamma}^2 + \Lambda^2}}{-8 - 8\,f + f^2 - 4\,\hat{\Gamma}^2 - 2\,f\,\hat{\Gamma}^2 + \hat{\Gamma}^4 + \left(2 + f - \hat{\Gamma}^2\right)\Lambda^2} . \tag{D.18}$$

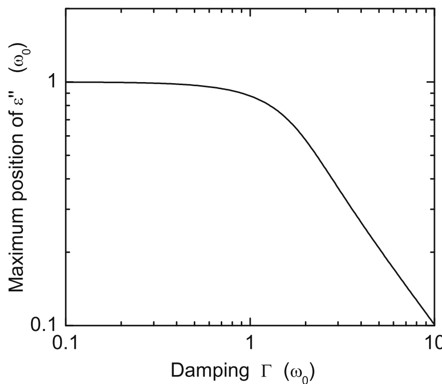

Fig. D.3. Frequency position of the maximum of ϵ'' as a function of the damping

E Quantum Statistics

Introduction

Bosons are particles with integer spin $s = n$, fermions are particles with spin $s = n + 1/2$ with n being an integer including zero. The fundamental quantum-mechanical property of the wavefunction of a system with N such particles is that under exchange of any two particles, the wavefunction is symmetric in the case of bosons and antisymmetric in the case of fermions. For two particles, these conditions read

$$\Psi(q_1, q_2) = \Psi(q_2, q_1) \tag{E.1a}$$

$$\Psi(q_1, q_2) = -\Psi(q_2, q_1) \ , \tag{E.1b}$$

where (E.1a) holds for bosons and (E.1b) holds for fermions. The variables q_i denote the coordinates and spin of the i-th particle. The Pauli principle allows bosons to populate the same single particle state with an arbitrary number of particles (at least more than one). For fermions, the exclusion principle holds that each single particle state can only be populated once.

Partition Sum

We consider a gas of N identical particles in a volume V in equilibrium at a temperature T. The possible quantum-mechanical states of a particle is denoted as r. The energy of a particle in the state r is ϵ_r, the number of particles in the state r is n_r.

For vanishing interaction of the particles, the total energy of the gas in the state R (with n_r particles in the state r) is

$$E_R = \sum_r n_r \epsilon_r \ . \tag{E.2}$$

The sum runs over all possible states r. The total number of particles imposes the condition

$$N = \sum_r n_r \ . \tag{E.3}$$

M. Grundmann, *The Physics of Semiconductors*, 2nd ed., Graduate Texts in Physics, DOI 10.1007/978-3-642-13884-3_28,

© Springer-Verlag Berlin Heidelberg 2010

In order to calculate the thermodynamic potentials, the partition sum Z needs to be calculated

$$Z = \sum_R \exp(-\beta E_R) \; , \tag{E.4}$$

with $\beta = 1/(kT)$. The sum runs over all possible microscopic states R of the gas, i.e. all combinations of the n_r that fulfill (E.3). The probability P_S to find the system in a particular state S is given by (canonical ensemble)

$$P_S = \frac{\exp(-\beta E_S)}{Z} \; . \tag{E.5}$$

The average number $\bar{n}_s$ of particles in a state s is given by

$$\bar{n}_s = \frac{\sum_R n_s \exp(-\beta E_R)}{Z} = -\frac{1}{\beta Z}\frac{\partial Z}{\partial \epsilon_\mathrm{s}} = -\frac{1}{\beta}\frac{\partial \ln Z}{\partial \epsilon_\mathrm{s}} \; . \tag{E.6}$$

We note that the average deviation $\overline{(\Delta n_s)^2} = \overline{n_s^2 - \bar{n}_s^2} = \overline{n_s^2} - \bar{n}_s^2$ is given by

$$\overline{(\Delta n_s)^2} = \frac{1}{\beta^2}\frac{\partial^2 \ln Z}{\partial \epsilon_\mathrm{s}^2} = -\frac{1}{\beta}\frac{\partial \bar{n}_s}{\partial \epsilon_\mathrm{s}} \; . \tag{E.7}$$

In the Bose–Einstein statistics (for bosons), the particles are fundamentally indistinguishable. Thus, a set of $(n_1, n_2, \ldots)$ uniquely describes the system. In the case of fermions, for each state n_r is either 0 or 1. In both cases, (E.3) needs to be fulfilled.

Photon Statistics

This case is the Bose–Einstein statistics (cf. (E.22)) with undefined particle number. We rewrite (E.6) as

$$\bar{n}_s = \frac{\sum_{n_s} n_s \exp(-\beta n_s \epsilon_\mathrm{s}) \sum^{(s)}_{n_1,n_2,\ldots} \exp(-\beta(n_1\epsilon_1 + n_2\epsilon_2 + \ldots))}{\sum_{n_s} \exp(-\beta n_s \epsilon_\mathrm{s}) \sum^{(s)}_{n_1,n_2,\ldots} \exp(-\beta(n_1\epsilon_1 + n_2\epsilon_2 + \ldots))} \; , \tag{E.8}$$

where $\sum^{(s)}$ denotes a summation that does not include the index s. In the case of photons, the values n_r can take any value (integers including zero) without restriction and therefore the sums $\sum^{(s)}$ in the numerator and denominator of (E.8) are identical. After some calculation we find

$$\bar{n}_s = -\frac{1}{\beta}\frac{\partial}{\partial \epsilon_\mathrm{s}} \ln\left(\sum_{n_s=0}^{\infty} \exp(-\beta n_s \epsilon_\mathrm{s})\right) \; . \tag{E.9}$$

The argument of the logarithm is a geometrical series with the limit $[1- \; \exp(-\beta\epsilon_\mathrm{s})]^{-1}$. This leads to the so-called Planck distribution

$$\bar{n}_s = \frac{1}{\exp(\beta\epsilon_\mathrm{s}) - 1} \; . \tag{E.10}$$

Fermi–Dirac Statistics

Now, the particle number is fixed to N. For the sum $\sum^{(s)}$ from (E.6), we introduce the term $Z_S(M)$

$$Z_s(M) = \sum_{n_1,n_2,\ldots}^{(s)} \exp(-\beta(n_1\epsilon_1 + n_2\epsilon_2 + \ldots)) \; , \tag{E.11}$$

when M particles are to be distributed over all states except s ($\sum_r^{(s)} n_r = M$). M is either $N-1$ if $n_s = 1$ and N if $n_s = 0$. Using Z_s, we can write

$$\bar{n}_s = \frac{1}{\frac{Z_s(N)}{Z_s(N-1)} \exp(\beta\epsilon_\mathrm{s}) + 1} \; . \tag{E.12}$$

We evaluate $Z_s(N-1)$

$$\ln Z_s(N - \Delta N) = \ln Z_s(N) - \frac{\partial \ln Z_s}{\partial N}|_N \, \Delta N \; , \tag{E.13}$$

or

$$Z_s(N - \Delta N) = Z_s(N) \exp(-\gamma_s \Delta N) \; , \tag{E.14}$$

with

$$\gamma_s = \frac{\partial \ln Z_s}{\partial N} \; . \tag{E.15}$$

Since Z_s runs over many states, the derivative is approximately equal to

$$\gamma = \frac{\partial \ln Z}{\partial N} \; , \tag{E.16}$$

as will be shown below. Thus, we obtained so far

$$\bar{n}_s = \frac{1}{\exp(\gamma + \beta\epsilon_\mathrm{s}) + 1} \; . \tag{E.17}$$

Equation (E.3) holds also for the average values $\bar{n}_s$, i.e.

$$N = \sum_r \bar{n}_r = \sum_r \frac{1}{\exp(\gamma + \beta\epsilon_\mathrm{s}) + 1} \; , \tag{E.18}$$

from which the value of γ can be calculated. Given that the free energy is given as $F = -kT \ln Z$, we find that

$$\gamma = -\frac{1}{kT}\frac{\partial F}{\partial N} = -\beta\mu \; , \tag{E.19}$$

where μ is the chemical potential by definition. Therefore, the distribution function for the Fermi–Dirac statistics (also called the Fermi function) is

$$\bar{n}_s = \frac{1}{\exp(\beta(\epsilon_\mathrm{s} - \mu)) + 1} \; . \tag{E.20}$$

Now, we briefly revisit the approximation $\gamma = \gamma_s$. Exactly, γ fulfills

$$\gamma = \gamma_s - n_s \frac{\partial \gamma}{\partial N} \; . \tag{E.21}$$

Thus, the approximation is valid if $n_s \frac{\partial \gamma}{\partial N} \ll \gamma$. Since $n_s < 1$, this means that the chemical potential does not change significantly upon addition of another particle.

Bose–Einstein Distribution

Executing (E.8) with the approximation $\gamma = \gamma_s$, the Bose–Einstein distribution is found to be

$$\bar{n}_s = \frac{1}{\exp(\beta(\epsilon_{\mathrm{s}} - \mu)) - 1} \; . \tag{E.22}$$

F The $\mathbf{k} \cdot \mathbf{p}$ Perturbation Theory

The solutions of the Schrödinger equation (cf. Sect. 6.2.1)

$$H\Psi_{n\mathbf{k}}(\mathbf{r}) = \left(-\frac{\hbar^2}{2m}\nabla^2 + U(\mathbf{r})\right)\Psi_{n\mathbf{k}}(\mathbf{r}) = E_n(\mathbf{k})\Psi_{n\mathbf{k}}(\mathbf{r}) \;, \tag{F.1}$$

with a lattice periodic potential U, i.e. $U(\mathbf{r}) = U(\mathbf{r}+\mathbf{R})$ for direct lattice vectors $\mathbf{R}$, are Bloch waves of the form

$$\Psi_{n\mathbf{k}}(\mathbf{r}) = \mathrm{e}^{\mathrm{i}\mathbf{k}\mathbf{r}} u_{n\mathbf{k}}(\mathbf{r}) \;, \tag{F.2}$$

with the lattice periodic Bloch function $u_{n\mathbf{k}}(\mathbf{r}) = u_{n\mathbf{k}}(\mathbf{r}+\mathbf{R})$.

Inserting the Bloch wave into (F.1), the following equation is obtained for the periodic Bloch function:

$$\left(-\frac{\hbar^2}{2m}\nabla^2 + U(\mathbf{r}) + \frac{\hbar}{m}\mathbf{k}\cdot\mathbf{p}\right)u_{n\mathbf{k}}(\mathbf{r}) = \left(E_n(\mathbf{k}) - \frac{\hbar^2 k^2}{2m}\right)u_{n\mathbf{k}}(\mathbf{r}) \;. \tag{F.3}$$

For simplicity, we assume a band edge $E_n(0)$ at $\mathbf{k}=0$. In its vicinity, the $\mathbf{k}\cdot\mathbf{p}$ term can be treated as a perturbation. The dispersion for a nondegenerate band[1] is given up to second order in k

$$E_n(\mathbf{k}) = E_n(0) + \sum_{i,j=1}^{3}\left(\frac{\hbar^2}{2m}\delta_{ij} + \frac{\hbar^2}{m}\sum_{l\neq n}\frac{p_{nl}^i\, p_{ln}^j}{E_n(0)-E_l(0)}\right)k_i\, k_j \;, \tag{F.4}$$

with l running over other, so-called *remote* bands. The momentum matrix element is given by $p_{nl}^i = \langle u_{n0}|p_i|u_{l0}\rangle$ (cf. (6.38)). The coefficients in front of the quadratic terms are the components of the dimensionless inverse effective-mass tensor (cf. (6.42))

$$\left(\frac{m}{m^*}\right)_{ij} = \delta_{ij} + \frac{2}{m}\sum_{l\neq n}\frac{p_{nl}^i\, p_{ln}^j}{E_n(0)-E_l(0)} \;. \tag{F.5}$$

For degenerate bands, the $p_{nn'}^i$ vanish when n and n' belong to the degenerate set and also the first-order correction is zero. In the Löwdin perturbation

[1] apart from the spin degeneracy

M. Grundmann, *The Physics of Semiconductors*, 2nd ed., Graduate Texts in Physics, DOI 10.1007/978-3-642-13884-3_29,

© Springer-Verlag Berlin Heidelberg 2010

theory [1483], the bands are separated into the close-by degenerate or nearly degenerate bands and the remote bands. The effect of the remote bands is taken into account by an effective perturbation

$$\mathbf{k} \cdot \mathbf{p} + \mathbf{k} \cdot \mathbf{p} \sum_{l \neq n} \frac{|l\rangle\langle l|}{E_n(0) - E_l(0)} \mathbf{k} \cdot \mathbf{p} \,, \tag{F.6}$$

with the index l running over all bands not being in the degenerate set. The dispersion relation is obtained by diagonalization of the Hamiltonian (F.3) in the degenerate basis but with the perturbation given by (F.6).

The spin-orbit interaction [964] adds an additional term

$$H_{\mathrm{so}} = \frac{\hbar}{4m^2c^2} \left(\boldsymbol{\sigma} \times \nabla U\right) \mathbf{p} \tag{F.7}$$

to the Hamiltonian, where $\boldsymbol{\sigma}$ are the Pauli spin matrices and c the vacuum speed of light. In the Schrödinger equation for the Bloch functions two new terms arise:

$$\begin{aligned} &\left(-\frac{\hbar^2}{2m} \nabla^2 + U(\mathbf{r}) + \frac{\hbar}{4m^2c^2} \left(\boldsymbol{\sigma} \times \nabla U\right) \mathbf{p} + \right. \\ &\left. \frac{\hbar}{m} \mathbf{k} \left[\mathbf{p} + \frac{\hbar}{4m^2c^2} \left(\boldsymbol{\sigma} \times \nabla U\right) \right] \right) u_{n\mathbf{k}}(\mathbf{r}) = \left(E_n(\mathbf{k}) - \frac{\hbar^2 k^2}{2m} \right) u_{n\mathbf{k}}(\mathbf{r}) \,. \end{aligned} \tag{F.8}$$

The linear term in $\mathbf{k}$ is again treated as a perturbation. The first spin-orbit term in (F.8) is lattice periodic, thus the solutions at $\mathbf{k} = 0$ are still periodic Bloch functions, however, different ones from previously. If the band edge is not degenerate, the momentum operator in (F.3) is simply replaced by

$$\boldsymbol{\pi} = \mathbf{p} + \frac{\hbar}{4m^2c^2} \left(\boldsymbol{\sigma} \times \nabla U\right) \,, \tag{F.9}$$

and the band edge is still parabolic. For a degenerate band edge, the effect can be more profound, in particular it can lead to the lifting of a degeneracy.

In the 8-band Kane model [335], four bands (lowest conduction band, heavy, light and split-off hole band) are treated explicitly and the others through Löwdin perturbation theory. The basis is chosen to be diagonal in the spin-orbit interaction leaving the spin-orbit interaction Δ_0 as parameter. The band- edge Bloch functions are denoted as $|i \uparrow\rangle$, where the index $i = s, x, y, z$ labels the symmetry of the different bands. The linear combinations that diagonalize the spin-orbit interaction are given in Table F.1. The band gap and the spin-orbit interaction are given by

$$E_{\mathrm{g}} = E_{\Gamma_6} - E_{\Gamma_8} \tag{F.10a}$$

$$\Delta_0 = E_{\Gamma_8} - E_{\Gamma_7} \,. \tag{F.10b}$$

The Hamiltonian in the basis states of Table F.1 is given by

Table F.1. Basis set that diagonalizes the spin-orbit interaction

$\lvert J, m_j\rangle$	wavefunction	symmetry
$\lvert\frac{1}{2},\frac{1}{2}\rangle$	$\mathrm{i}\lvert s\uparrow\rangle$	Γ_6
$\lvert\frac{1}{2},-\frac{1}{2}\rangle$	$\mathrm{i}\lvert s\downarrow\rangle$	Γ_6
$\lvert\frac{3}{2},\frac{3}{2}\rangle$	$\frac{1}{\sqrt{2}}\lvert(x+\mathrm{i}y)\uparrow\rangle$	Γ_8
$\lvert\frac{3}{2},\frac{1}{2}\rangle$	$\frac{1}{\sqrt{6}}\lvert(x+\mathrm{i}y)\downarrow\rangle-\sqrt{\frac{2}{3}}\lvert z\uparrow\rangle$	Γ_8
$\lvert\frac{3}{2},-\frac{1}{2}\rangle$	$-\frac{1}{\sqrt{6}}\lvert(x-\mathrm{i}y)\uparrow\rangle-\sqrt{\frac{2}{3}}\lvert z\downarrow\rangle$	Γ_8
$\lvert\frac{3}{2},-\frac{3}{2}\rangle$	$\frac{1}{\sqrt{2}}\lvert(x-\mathrm{i}y)\uparrow\rangle$	Γ_8
$\lvert\frac{1}{2},\frac{1}{2}\rangle$	$\frac{1}{\sqrt{3}}\lvert(x+\mathrm{i}y)\downarrow\rangle+\sqrt{\frac{1}{3}}\lvert z\uparrow\rangle$	Γ_7
$\lvert\frac{1}{2},-\frac{1}{2}\rangle$	$-\frac{1}{\sqrt{3}}\lvert(x-\mathrm{i}y)\uparrow\rangle+\sqrt{\frac{1}{3}}\lvert z\downarrow\rangle$	Γ_7

$$\begin{bmatrix}
k^2+E_{\mathrm{g}} & 0 & \sqrt{2}Pk_+ & -\sqrt{\frac{2}{3}}Pk_z & -\sqrt{\frac{2}{3}}Pk_- & 0 & \sqrt{\frac{1}{3}}Pk_z & -\sqrt{\frac{4}{3}}Pk_- \\
0 & k^2+E_{\mathrm{g}} & 0 & \sqrt{\frac{2}{3}}Pk_+ & -\sqrt{\frac{2}{3}}Pk_z & \sqrt{2}Pk_- & \sqrt{\frac{4}{3}}Pk_+ & \sqrt{\frac{1}{3}}Pk_z \\
\sqrt{2}Pk_- & 0 & k^2 & 0 & 0 & 0 & 0 & 0 \\
-\sqrt{\frac{2}{3}}Pk_z & \sqrt{\frac{2}{3}}Pk_- & 0 & k^2 & 0 & 0 & 0 & 0 \\
-\sqrt{\frac{2}{3}}Pk_+ & -\sqrt{\frac{2}{3}}Pk_z & 0 & 0 & k^2 & 0 & 0 & 0 \\
0 & \sqrt{2}Pk_+ & 0 & 0 & 0 & k^2 & 0 & 0 \\
\sqrt{\frac{1}{3}}Pk_z & \sqrt{\frac{4}{3}}Pk_- & 0 & 0 & 0 & 0 & k^2-\Delta_0 & 0 \\
-\sqrt{\frac{4}{3}}Pk_+ & \sqrt{\frac{1}{3}}Pk_z & 0 & 0 & 0 & 0 & 0 & k^2-\Delta_0
\end{bmatrix} \tag{F.11}$$

with the energy measured from the valence-band edge in units of $\hbar^2/(2m)$ and

$$\frac{1}{2}\mathrm{i}\hbar P = \langle s|\pi_x|x\rangle = \langle s|\pi_y|y\rangle = \langle s|\pi_z|z\rangle \tag{F.12a}$$

$$k_\pm = k_x \pm \mathrm{i}k_y\ . \tag{F.12b}$$

The inclusion of remote bands renormalizes the above Hamiltonian to

$$\begin{bmatrix}
Dk^2+E_{\mathrm{g}} & 0 & \sqrt{2}Pk_+ & -\sqrt{\frac{2}{3}}Pk_z & -\sqrt{\frac{2}{3}}Pk_- & 0 & \sqrt{\frac{1}{3}}Pk_z & -\sqrt{\frac{4}{3}}Pk_- \\
0 & Dk^2+E_{\mathrm{g}} & 0 & \sqrt{\frac{2}{3}}Pk_+ & -\sqrt{\frac{2}{3}}Pk_z & \sqrt{2}Pk_- & \sqrt{\frac{4}{3}}Pk_+ & \sqrt{\frac{1}{3}}Pk_z \\
\sqrt{2}Pk_- & 0 & H_{\mathrm{h}} & R & S & 0 & \frac{\mathrm{i}}{\sqrt{2}}R & -\mathrm{i}\sqrt{2}S \\
-\sqrt{\frac{2}{3}}Pk_z & \sqrt{\frac{2}{3}}Pk_- & R^* & H_{\mathrm{l}} & 0 & S & \frac{H_{\mathrm{h}}-H_{\mathrm{l}}}{\sqrt{2}\mathrm{i}} & \mathrm{i}\sqrt{\frac{3}{2}}R \\
-\sqrt{\frac{2}{3}}Pk_+ & -\sqrt{\frac{2}{3}}Pk_z & S^* & 0 & H_{\mathrm{l}} & -R & -\mathrm{i}\sqrt{\frac{3}{2}}R^* & \frac{H_{\mathrm{h}}-H_{\mathrm{l}}}{\sqrt{2}\mathrm{i}} \\
0 & \sqrt{2}Pk_+ & 0 & S^* & -R^* & H_{\mathrm{h}} & -\mathrm{i}\sqrt{2}S^* & -\frac{\mathrm{i}}{\sqrt{2}}R^* \\
\sqrt{\frac{1}{3}}Pk_z & \sqrt{\frac{4}{3}}Pk_- & -\frac{\mathrm{i}}{\sqrt{2}}R^* & -\frac{H_{\mathrm{h}}-H_{\mathrm{l}}}{\sqrt{2}\mathrm{i}} & \mathrm{i}\sqrt{\frac{3}{2}}R & \mathrm{i}\sqrt{2}S & \frac{H_{\mathrm{h}}+H_{\mathrm{l}}}{\sqrt{2}}-\Delta_0 & 0 \\
-\sqrt{\frac{4}{3}}Pk_+ & \sqrt{\frac{1}{3}}Pk_z & \mathrm{i}\sqrt{2}S^* & -\mathrm{i}\sqrt{\frac{3}{2}}R^* & -\frac{H_{\mathrm{h}}-H_{\mathrm{l}}}{\sqrt{2}\mathrm{i}} & \frac{\mathrm{i}}{\sqrt{2}}R & 0 & \frac{H_{\mathrm{h}}+H_{\mathrm{l}}}{\sqrt{2}}-\Delta_0
\end{bmatrix} \tag{F.13}$$

with

$$D = 1 + \frac{2}{m}\sum_{l\neq n}\frac{|\langle s|\pi_x|l\rangle|^2}{E_\mathrm{g} - E_l(0)} \tag{F.14a}$$

$$\gamma_1' = \left[1 + \frac{2}{m}\sum_{l\neq n}\frac{|p_{xl}^x|^2}{E_n(0) - E_l(0)}\right] - \frac{2P^2}{3E_\mathrm{g}} \tag{F.14b}$$

$$\gamma_2' = \left[1 + \frac{2}{m}\sum_{l\neq n}\frac{|p_{xl}^y|^2}{E_n(0) - E_l(0)}\right] - \frac{P^2}{3E_\mathrm{g}} \tag{F.14c}$$

$$\gamma_3' = \left[\frac{2}{m}\sum_{l\neq n}\frac{p_{xl}^x p_{ly}^y + p_{xl}^y p_{ly}^x}{E_n(0) - E_l(0)}\right] - \frac{P^2}{3E_\mathrm{g}} \tag{F.14d}$$

$$H_\mathrm{h} = (\gamma_1' + \gamma_2')(k_x^2 + k_y^2) + (\gamma_1' - 2\gamma_2')k_z^2 \tag{F.14e}$$

$$H_\mathrm{l} = (\gamma_1' - \gamma_2')(k_x^2 + k_y^2) + (\gamma_1' + 2\gamma_2')k_z^2 \tag{F.14f}$$

$$R = -2\sqrt{3}\gamma_3' k_- k_z \tag{F.14g}$$

$$S = \sqrt{3}\gamma_2'(k_x^2 - k_y^2) + 2\sqrt{3}\gamma_3' \mathrm{i} k_x k_y \; . \tag{F.14h}$$

The Hamiltonian in the presence of inhomogeneous strain is given in Ref. [361]. The hole bands decouple from the conduction band for $E_\mathrm{g} \to \infty$ (six-band model [831]). The heavy and light holes can be treated separately for $\Delta_0 \to \infty$ (Luttinger Hamiltonian). For the Γ_8 states, the Hamiltonian is then given by

$$\begin{bmatrix} H_\mathrm{h} & R & S & 0 \\ R^* & H_\mathrm{l} & 0 & S \\ S^* & 0 & H_\mathrm{l} & -R \\ 0 & S^* & -R^* & H_\mathrm{h} \end{bmatrix} \; . \tag{F.15}$$

G Effective-Mass Theory

The effective-mass theory or approximation (EMA), also termed the envelope function approximation, is widely used for calculating the electronic properties of carriers in potentials in an otherwise periodic crystal. The strength of the method is that the complexities of the periodic potential are hidden in the effective-mass tensor m^*_{ij}. The effective-mass theory is a useful approximation for the treatment of shallow impurities (Sect. 7.5) or quantum wells (Sect. 11.3.2) with a potential that is slowly varying with respect to the scale of the lattice constant.

For the lattice-periodic potential, the Schrödinger equation

$$H_0 \Psi_{n\mathbf{k}} = E_n(\mathbf{k}) \Psi_{\mathrm{n}\mathbf{k}} \tag{G.1}$$

is solved by the Bloch wave $\Psi_{n\mathbf{k}}$. With a perturbing potential V, the Schrödinger equation reads

$$(H_0 + V)\, \Psi_{n\mathbf{k}} = E_n(\mathbf{k}) \Psi_{\mathrm{n}\mathbf{k}} \; . \tag{G.2}$$

According to Wannier's theorem [1484], the solution is approximated by the solution of the equation

$$[E_n(-\mathrm{i}\nabla) + V]\, \Phi_n = E\, \Phi_n \; . \tag{G.3}$$

The dispersion relation is expanded to second order as described in Appendix F. The function Φ_n is termed the *envelope function* since it varies slowly compared to the lattice constant and the exact wavefunction is approximated (in lowest order) by

$$\Psi(\mathbf{r}) = \Phi_n(\mathbf{r}) \, \exp\left(\mathrm{i}\mathbf{k}\mathbf{r}\right) u_{n0}(\mathbf{r}) \; . \tag{G.4}$$

M. Grundmann, *The Physics of Semiconductors*, 2nd ed., Graduate Texts in Physics, DOI 10.1007/978-3-642-13884-3_30,
© Springer-Verlag Berlin Heidelberg 2010

References

1. J.M. Bishop, *How to Win the Nobel Prize* (Harvard University Press, Cambridge, 2003)
2. G. Busch, *Early history of the physics and chemisty of semiconductors - from doubts to fact in a hundred years.* Eur. J. Phys. **10**, 254–264 (1989)
3. K.C. Handel, Anfänge der halbleiterforschung und -entwicklung. Dargestellt an den Biographien von vier deutschen Halbleiterpionieren, PhD thesis, RWTH Aachen (1999)
4. P.R. Morris, *A History of the World Semiconductor Industry*, IEE History of Technology Series, Vol. 12 (Peter Peregrinus Ltd., London, 1990)
5. D. Holbrook, W.M. Cohen, D.A. Hounshell, S. Klepper, The Nature, Sources, and Consequences of Firm Differences in the Early History of the semiconductor Industry. Strat. Mgmt. J. **21**, 1017–1041 (2000)
6. A. Volta, Del modo di render sensibilissima la più debole Elettricità sia Naturale, sia Artificiale. Phil. Trans. R. Soc. Lond. **72**, 237–80 (1782). (followed by an English translation of the Method of rendering very sensible the weakest Natural and Artificial Electricity)
7. T.J. Seebeck, Magnetische Polarisation der Metalle und Erze durch Temperaturdifferenz, Abhandl. Deut. Akad. Wiss. Berlin, 265–373 (1822)
8. M. Faraday, *Experimental Researches in Electricity*, Series IV, (1833), p. 433
9. W. Smith, J. Soc. Tel. Engrs. **2**, 31 (1873), Nature **7** (issue of 20 February 1873), 303 (1873)
10. S. Bidwell, Proc. Phys. Soc. London **7**, 129 (1885)
11. S. Bidwell, Proc. Phys. Soc. London **13**, 552 (1894)
12. F. Braun, Über die Stromleitung durch Schwefelmetalle, J.C. Poggendorf (ed.), Ann. Phys. Chem. **153**, 556 (1874)
13. W. Schreier, Ferdinand Braun in Leipzig, Zum 150. Geburtstag des Entdeckers des Halbleitereffektes und des Erfinders der Kathodenstrahlröhre, NTM Zeitschrift für Geschichte der Wissenschaften, Technik und Medizin **8**, 201–08 (2000)
14. W.G. Adams, R.E. Day, Proc. Roy. Soc. London A **25**, 113 (1876)
15. W. Siemens, On the influence of light upon the conductivity of crystalline Selenium. Phil. Mag. **50**(332), 416 (1875)
16. Ch.E. Fritts, On a new form of Selenium cell, and some electrical discoveries made by its use. Am. J. Sci. **26**, 465 (1883)
17. E.H. Hall, Amer. J. Math. **2**, 287 (1879)
18. E.H. Hall, Philos. Mag. **9**, 225 (1879)
19. H.A. Rowland, Philos. Mag. **9**, 432 (1880)
20. J.Z. Buchwald, Centaurus **23**, 51–99 (1979)

M. Grundmann, *The Physics of Semiconductors*, 2nd ed., Graduate Texts in Physics, DOI 10.1007/978-3-642-13884-3,

© Springer-Verlag Berlin Heidelberg 2010

21. J.Z. Buchwald, Centaurus **23**, 118–62 (1979)
22. J.C. Bose, Detector for electrical disturbances, US patent 755,860, filed 1901, awarded 1904
23. G.W. Pickard, Means for receiving intelligence communicated by electric waves, US patent 836,531, filed 1906, awarded 1906
24. G.W. Pickard, Oscillation-receiver, US patent 888,191, filed 1907, awarded 1908
25. T. Jenkins, A brief history of semiconductors. Phys. Educat. **40**, 430 (2005)
26. H.J. Round, A note on carborundum. Electron. World **19**, 309 (1907)
27. K. Bädeker, Über die elektrische Leitfähigkeit und die thermoelektrische Kraft einiger Schwermetallverbindungen, Ann. Physik **327**, 749–66 (1907), Habilitationsschrift, Universität Leipzig
28. W. Kaiser, Centaurus **22**, 187 (1979)
29. J. Weiss, Experimentelle Beiträge zur Elektronentheorie aus dem Gebiet der Thermoelektrizität, PhD Thesis, Albert-Ludwigs Universität Freiburg i.Br., 1910
30. J. Königsberger, J. Weiss, Ann. Physik **35**, 1 (1911)
31. Th. Thomas, New Scientist (issue of March 29 1997), p. 55 (1997)
32. C. Kleint, Progr. Surf. Sci. **57**, 253–327 (1998)
33. J.E. Lilienfeld, Method and apparatus controlling electric currents, US patent1,745,175, filed 1926, awarded 1930
34. J.E. Lilienfeld, Device for controlling electric current, US patent 1,900,018, filed 1928, awarded 1933
35. J.E. Lilienfeld, Amplifier for electric currents, US patent 1,877,140, filed 1928, awarded 1932
36. A. Schleede, H. Buggisch, Untersuchungen am Bleiglanz- und Pyritdetektor, Z. Anorg. Allg. Chemie **161**, 85–107 (1927)
37. E. Körner, Über die Darstellungsmethoden und die Lumineszenzfähigkeit reinsten Zinksulfids und Zinkoxydes, PhD Thesis, Universität Greifswald, 1930
38. A. Schleede, Über den Strukturellen Bau der Leuchtzentren in den Zink- und Cadmium-Sulfid-Leuchtstoffen, Chem. Ber. 90, 1162–75 (1957)
39. F. Bloch, Über die Quantenmechanik der Elektronen in Kristallgittern. Z. Phys. **52**, 555–60 (1928)
40. R. Peierls, Zur Theorie der galvanomagnetischen Effekte, Zeitschr. f. Physik **53**, 255–66 (1929)
41. R.E. Peierls, Zur Theorie des Hall-Effekts. Phys. Z. **30**, 273–74 (1929)
42. W. Heisenberg, Zum Paulischen Ausschließungsprinzip. Ann. Physik **402**, 888–904 (1931)
43. R. de L. Kronig, W.G. Penney, Proc. Roy. Soc. London A **130**, 499 (1931)
44. A.H. Wilson, The theory of electronic semiconductors. Proc. Roy. Soc. London A **133**, 458 (1931)
45. C. Zener, Proc. Roy. Soc. London A **130**, 499 (1931)
46. C. Wagner, Theorie der geordneten Mischphasen. Z. Phys. Chem. B 22, 181–94 (1933)
47. H.H. von Baumbach, C. Wagner, Die elektrische Leitfähigkeit von Zinkoxyd und Cadmiumoxyd. Z. Phys. Chem. B **22**, 199–211 (1933)
48. J. Frenkel, Phys. Z. Sowjetunion 9, 158 (1936)

49. B.I. Davydov, Dokl. Acad. Nauk SSSR (C.R. Acad. Sci. USSR) **20**, 283 (1938)
50. W. Schottky, Naturwissenschaften **26**, 843 (1938)
51. N.F. Mott, Proc. Camb. Philos. Soc. **34**, 568 (1938)
52. R. Hilsch, R.W. Pohl, Steuerung von Elektronenströmen mit einem Dreielektrodenkristall und ein Modell einer Sperrschicht. Z. Phys. **111**, 399–408(1938)
53. R.S. Ohl, Light-sensitive electric device, US patent 2,402,662, filed 1941, awarded 1946
54. J.H. Scaff, The role of metallurgy in the technology of electronic materials. Metall. Transact. **1**, 561–73 (1970)
55. M. Riordan, L. Hoddeson, The origins of the pn junction. IEEE Spectrum. **34**, 46 (1997)
56. R.S. Ohl, Alternating current rectifier, US patent 2,402,661, filed 1941, awarded 1946
57. K. Clusius, E. Holz, H. Welker, Elektrische Gleichrichteranordnung mit Germanium als Halbleiter und Verfahren zur Herstellung von Germanium für eine solche Gleichrichteranordnung, German patent DBP 966 387, 21g,11/02 (1942)
58. H. Welker, Halbleiteranordnung zur kapazitiven Steuerung von Strömen in einem Halbleiterkristall, German patent DBP 980 084, 21g, 11/02 (1945)
59. J. Bardeen, W.H. Brattain, Three-electrode circuit element utilizing semiconductor materials, US patent 2,524,035, filed 1948, awarded 1950
60. M. Riordan, L. Hoddeson, C. Herring, The invention of the transistor. Rev. Mod. Phys. **71**, S336–S345 (1999)
61. J. Bardeen, W.H. Brattain, Physical principles involved in transistor action. Phys. Rev. **75**, 1208 (1949)
62. J. Bardeen, W.H. Brattain, The transistor, a semiconductor triode. Phys. Rev. **74**, 230 (1948)
63. W.F. Brinkman, D.E. Haggan, W.W. Troutman, IEEE J. Solid-State Circ. SC-32, 1858–65 (1997)
64. W.B. Shockley, Circuit Element Utilizing Semiconductor Material, US patent 2,569,347, filed 1948, awarded 1951
65. H. Welker, Verfahren zur Herstellung eines Halbleiterkristalls mit Zonen verschiedenen Leitungstyps bei A III – B V - Verbindungen, German patent DBP 976 709, 21g, 11/02 (1952)
66. H.Welker, Verfahren zur Herstellung eines Halbleiterkristalls aus einer A III – B V - Verbindung mit Zonen verschiedenen Leitungstyps, German patent DBP 976 791, 12c, 2 (1952)
67. H. Welker, Semiconductor devices and methods of their manufacture, US patent 2,798,989, filed 1952, awarded 1957
68. H. Welker, Z. Naturf. 7a, 744 (1952)
69. W. Shockley, A unipolar “field-effect” transistor. Proc. IRE **40**, 1365–76 (1952)
70. G.C. Dacey, I.M. Ross, Unipolar “field-effect” transistor. Proc. IRE **41**, 970 (1953)
71. D.M. Chapin, C.S. Fuller, G.L. Pearson, J. Appl. Phys. **25**, 676 (1954)
72. J.S. Kilby, Miniaturized electronic circuits, US patent 3,138,743, filed 1959, awarded 1964

73. R.N. Noyce, Semiconductor device-and-lead structure, US patent 2,981,877, filed 1959, awarded 1961
74. A.N. Saxena, *Invention of Integrated Circuits – Untold Important Facts* (World Scientific, Singapore, 2009)
75. J.A. Hoerni, Method of manufacturing semiconductor devices, US patent 3,025,589, filed 1959, awarded 1962
76. J.A. Hoerni, Semiconductor device, US patent 3,064,167, filed 1959, awarded 1962
77. J.A. Hoerni, Planar silicon diodes and transistors. IRE Trans. Electron Devices, Mar. 8, p. 178 (1961); also presented at Professional Group on Electron Devices Meeting, Washington, D.C., Oct. 1960
78. M. Riordan, The silicon dioxide solution: how physicist Jean Hoerni built the bridge from the transistor to the integrated circuit. IEEE Spectrum, 50–6 (Dec. 2007)
79. G. Mortenson, D.O. Relin, *Three Cups of Tea* (Penguin, New York, 2006)
80. D. Kahng, M.M. Atalla, Silicon-silicon dioxide field induced surface device, IRE Solid-State Device Research Conference, Carnegie Institute of Technology, Pittsburgh, PA, 1960
81. D. Kahng, Electric field controlled semiconductor device, US patent 3,102,230, filed 1960, awarded 1963
82. R.N. Hall, G.E. Fenner, J.D. Kingsley, T.J. Soltys, R.O. Carlson, Phys. Rev. Lett. **9**, 366 (1962)
83. M.I. Nathan, W.P. Dumke, G. Burns, F.H. Dill Jr., G. Lasher, Appl. Phys. Lett. **1**, 62 (1962)
84. N. Holonyak, S.F. Bevacqua, Appl. Phys. Lett. **1**, 82 (1962)
85. Zh.I. Alferov, R.F. Kasarinov, Inventor's Certificate No. 181737 [in Russian], Application No. 950840 (1963)
86. H. Kroemer, Proc. IEEE **51**, 1782 (1963)
87. J.B. Gunn, Solid State Commun. **1**, 88 (1963)
88. Zh.I. Alferov, V.I. Korol'kov, V.I. Maslov, A.V. Litina M.K. Krukan, A.A. Yakovenko, Fizika i Tekn. Poluprovodn. **1**, 260 (1967)
89. C.A. Mead, Proc. IEEE **54**, 307 (1966)
90. W.W. Hooper, W.I. Lehrer, Proc. IEEE **55**, 1237 (1967)
91. Zh.I. Alferov, V.M. Andreev, E.L. Portnoi, M.K. Trukan, Fizika i. Tekn. Poluprovodn. **3**, 1328 (1969)
92. I. Hayashi, IEEE Trans. Electron Devices ED-31, 1630 (1969)
93. R.A. Logan, H.G. White, W. Wiegmann, Appl. Phys. Lett. **13**, 139 (1968)
94. R.M. Potter, J.M. Blank, A. Addamiano, J. Appl. Phys. **40**, 2253 (1969)
95. R.S. Pengelly, J.A. Turner, Electr. Lett. **12**, 251 (1976)
96. S. Nakamura, M. Senoh, N. Iwasa, S. Nagahama, Jpn. J. Appl. Phys. **34**, L797 (1995)
97. M. Dayah, www.dayah.com
98. N. Bernstein, M.J. Mehl, D.A. Papaconstantopoulos, N.I. Papanicolaou, M.Z. Bazant, E. Kaxiras, Phys. Rev. B **62**, 4477 (2000)
99. P. Evers, Die wundersame Welt der Atomis: 10 Jahre in den Physikalischen Blättern (Wiley-VCH, Weinheim, 2002)
100. M.T. Yin, M.L. Cohen, Phys. Rev. Lett. **45**, 1004 (1980)
101. J. Bardeen, W. Shockley, Phys. Rev. **80**, 72 (1950)
102. G.E. Kimball, J. Chem. Phys. **3**, 560 (1935)

103. Royston M. Roberts, *Serendipidty, Accidental Discoveries in Science* (John Wiley & Sons, New York, 1989), pp. 75–81
104. H.J.F. Jansen, A.J. Freeman, Phys. Rev. B **33**, 8629 (1986)
105. T. Soma, T. Umenai, Phys. Stat. Sol. (b) **78**, 229 (1976)
106. J.C. Phillips, *Bonds and Bands in Semiconductors* (Academic Press, New York, 1973)
107. J.A. Van Vechten, Phys. Rev. **182**, 891 (1969)
108. J.C. Phillips, J.A. Van Vechten, Phys. Rev. Lett. **22**, 705 (1969)
109. H.B. Callen, Phys. Rev. **76**, 1394 (1949)
110. J.C. Phillips, J.A. Van Vechten, Phys. Rev. Lett. **23**, 1115 (1969)
111. S. Takeuchi, K. Suzuki, Phys. Stat. Sol. (A) **171**, 99 (1999)
112. M.S. Dresselhaus, G. Dresselhaus, A. Jorio, *Group Theory, Application to the Physics of Condensed Matter* (Springer, Berlin, 2008)
113. G. Burns, A.M. Glazer, *Space Groups for Solid State Scientists* (Academic Press, San Diego, 1990)
114. B. Kramer, Electronic properties of amorphous solids. Adv. Solid State Phys. (Festkörperprobleme) **12**, 133 (1972)
115. R.E. Proano, D.G. Ast, J. Appl. Phys. **66**, 2189 (1989)
116. M.H. Brodsky (ed.), *Amorphous Semiconductors.* Topics in Applied Physics, vol 36 (Springer, Berlin, 1979)
117. A.J. Haq, P.R. Munroe, J. Mater. Res. **24**, 1967 (2009)
118. G.A. Busch, R. Kern, Semiconducting properties of gray tin. Solid State Phys. **11**, 1 (1960)
119. J.R. Chelikowski, Phys. Rev. B **34**, 5295 (1986)
120. J.M. Besson, J.P. Itié, A. Polian, G. Weill, J.L. Mansot, J. Gonzalez, Phys. Rev. B **44**, 4214 (1991)
121. P. Lawaetz, Phys. Rev. B **5**, 4039 (1972)
122. R.F. Davis, M.S. Shur, *GaN-based Materials and Devices: Growth, Fabrication, Characterization & Performance* (World Scientific, Singapore, 2004)
123. C. Jaggadish, S.J. Pearton (eds.), *Zinc Oxide Bulk, Thin Films and Nanostructures: Processing, Properties and Applications* (Elsevier, Amsterdam, 2006)
124. M. Shur, S. Rumyantsev, M. Levinshtein (eds.), *SiC Materials And Devices* (World Scientific, Singapore, 2006)
125. S. Siebentritt, U. Rau (eds.), *Wide-Gap Chalcopyrites* (Springer, Berlin, 2006)
126. J.L. Shay, J.H. Wernick, *Ternary Chalcopyrites* (Pergamon, Oxford, 1975)
127. A. Zunger, Appl. Phys. Lett. **50**, 164 (1987)
128. J.E. Jaffe, A. Zunger, Phys. Rev. B **29**, 1882 (1984)
129. J.E. Jaffe, R.A. Bachorz, M. Gutowski, Phys. Rev. B **72**, 144107 (2005)
130. P. Duwez, F.H. Brown, Jr., F. Odell, J. Electrochem. Soc. **98**, 356 (1951)
131. R. Ruh, K.S. Mazdiyasni, P.G. Valentine, H.O. Bielstein, J. Am. Ceram. Soc. **67**, C-190 (1984)
132. X. Nie, S.-H. Wei, S.B. Zhang, Phys. Rev. Lett. **88**, 066405 (2002)
133. C.Y. Yang, Z.R. Huang, W.H. Yang, Y.Q. Zhou, K.K. Fung, Acta Cryst. A **47**, 703 (1991)
134. A. Guivarc'h, R. Guérin, J. Caulet, A. Poudoulec, J. Appl. Phys. **66**, 2129 (1989)

135. S. Yoshioka, H. Hayashi, A. Kuwabara, F. Oba, K. Matsunaga, I. Tanaka, J. Phys.: Condens. Matter **19**, 346211 (2007)
136. H.F. Liu, S.W. Wong, S.J. Chua, E-MRS 2008 (Straßburg), Symp. G, P2.1 (2008)
137. K.-W. Park, Y.-H. Yun, S.-C. Choi, Solid State Ionics **177**, 1875 (2006)
138. T. Maitra, R. Valentí, J. Phys.: Condens. Matter **17**, 7417 (2005)
139. E.S. Dana, W.E. Ford, *A Textbook of Mineralogy with an Extended Treatise on Crystallography and Physical Mineralogy* (JohnWiley & Sons, New York, 1932)
140. W. Borchardt-Ott, *Kristallographie: Eine Einführung für Naturwissenschaftler*, 7th edn. (Springer, Berlin, 2008)
141. W. Borchardt-Ott, R.O. Gould, *Crystallography*, 2nd edn. (Springer, Berlin, 2004)
142. Th. Hahn (ed.), International Tables for Crystallography. *Volume a: Space Group Symmetry: A*, 5th edn. (Springer, Dordrecht, 2002)
143. cst-www.nrl.navy.mil/lattice
144. P.F. Fewster, *X-Ray Scattering from Semiconductors* (Imperial College Press, London, 2003)
145. Th. Höche, private communication (2008)
146. Y. Lifshitz, X.F. Duan, N.G. Shang, Q. Li, L.Wan, I. Bello, S.T. Lee, Nature **412**, 404 (2001)
147. M.J. Kozielski, J. Cryst. Growth **30**, 86 (1975)
148. K.-J. Chao, Ch.-K. Shih, D.W. Gotthold, B.G. Streeman, Phys. Rev. Lett. **79**, 4822 (1997)
149. J.F. Zheng, J.D. Walker, M.B. Salmeron, E.R. Weber, Phys. Rev. Lett. **72**, 2414 (1994)
150. C. Bundesmann, M. Schubert, D. Spemann, A. Rahm, H. Hochmuth, M. Lorenz, M. Grundmann, Appl. Phys. Lett. **85**, 905 (2004)
151. M.M. Kreitman, D.L. Barnett, J. Chem. Phys. **43**, 364 (1965)
152. O. Okada, J. Phys. Soc. Jpn. **48**, 391 (1980)
153. S.-H. Wei, L.G. Ferreira, A. Zunger, Phys. Rev. B **41**, 8240 (1990)
154. I.-H. Ho, G.B. Stringfellow, Appl. Phys. Lett. **69**, 2701 (1996)
155. J.C. Mikkelsen Jr., J.B. Boyce, Phys. Rev. Lett. **49**, 1412 (1982)
156. J.C. Mikkelsen Jr., J.B. Boyce, Phys. Rev. B **28**, 7130 (1983)
157. A. Zunger, S. Mahajan, Atomic Ordering and Phase Separation in III–V Alloys in *Handbook of Semiconductors*, vol. 3 (Elsevier, Amsterdam, 1994), pp. 1399–513
158. O. Ambacher, M. Eickhoff, A. Link, M. Hermann, M. Stutzmann, F. Bernardini, V. Fiorentini, Y. Smorchkova, J. Speck, U. Mishra, W. Schaff, V. Tilak, L.F. Eastman, Phys. Stat. Sol. (C) **0**, 1878 (2003)
159. H.S. Lee, J.Y. Lee, T.W. Kim, D.U. Lee, D.C. Choo, H.L. Park, Appl. Phys. Lett. **79**, 1637 (2001)
160. C. Domke, Ph. Ebert, M. Heinrich, K. Urban, Phys. Rev. Lett. **54**, 10288 (1996)
161. Ph. Ebert, X. Chen, M. Heinrich, M. Simon, K. Urban, M.G. Lagally, Phys. Rev. Lett. **76**, 2089 (1996)
162. R.M. Feenstra, J.M. Woodall, G.D. Pettit, Phys. Rev. Lett. **71**, 1176 (1993)
163. R.B. Capaz, K. Cho, J.D. Joannopoulos, Phys. Rev. Lett. **75**, 1811 (1995)

164. R. Jones, A. Carvalho, J.P. Goss, P.R. Briddon, Mat. Sci Engin. B **159**, 112 (2008)
165. S.J. Clark, Complex structure in tetrahedral semiconductors, PhD Thesis, University of Edinburgh, 1994
166. M. Lannoo, J. Bourgoin, *Point Defects in Semiconductors I* (Springer, Berlin, 1981)
167. S. Lee, G.S. Hwang, Phys. Rev. B **78**, 125310 (2008)
168. H. Bracht, N.A. Stolwijk, H. Mehrer, Phys. Rev. B **52**, 16542 (1995)
169. V. Ranki, K. Saarinen, Phys. Rev. Lett. **93**, 255502 (2004)
170. J. Gebauer, M. Lausmann, F. Redmann, R. Krause-Rehberg, H.S. Leipner, E.R. Weber, Ph. Ebert, Phys. Rev. B **67**, 235207 (2003)
171. F. Morehead, N. Stolwijk, W. Meyberg, U. Gösele, Appl. Phys. Lett. **42**, 690 (1983)
172. S. Dannefaer, P. Mascher, D. Kerr, Phys. Rev. Lett. **56**, 2195 (1986)
173. P.M. Fahey, P.B. Griffin, J.D. Plummer, Rev. Mod. Phys. **61**, 289–384 (1989)
174. P. Pichler, *Intrinsic Point Defects, Impurities, and Their Diffusion in Silicon* (Springer, Berlin, 2004)
175. G.D. Watkins, J. Appl. Phys. **103**, 106106 (2008)
176. Y. Shimizu, M. Uematsu, K.M. Itoh, Phys. Rev. Lett. **98**, 095901 (2007)
177. C.S. Nichols, C.G. Van der Walle, S.T. Pantelides, Phys. Rev. B **40**, 5484 (1989)
178. A. Ural, P.B. Griffin, J.D. Plummer, J. Appl. Phys. **85**, 6440 (1999)
179. J.-W. Jeong, A. Oshiyama, Phys. Rev. B **64**, 235204 (2001)
180. W. Windl, Appl. Phys. Lett. **92**, 202104 (2008)
181. K.-S. Yoon, C.-O. Wang, J.-H. Yoo, T. Won, J. Korean Phys. Soc. **48**, 535 (2006)
182. X.-Y. Liu, W. Windl, K.M. Beardmore, M.P. Masquelier, Appl. Phys. Lett. **82**, 1839 (2003)
183. L. Rayleigh, Philos. Mag. **4**, 521 (1902)
184. C.H. Li, J. Phys. D: Appl. Phys. **7**, 155 (1974)
185. W. Zulehner, Metrologia **31**, 255 (1994)
186. I. Yonenaga, T. Ayuzawa, J. Cryst. Growth **297**, 14 (2006)
187. W.G. Pfann, Techniques of zone melting and crystal growing. Solid State Phys. **4**, 423 (1957)
188. W.C. O'Mara, R.B. Herring, L.P. Hunt (eds.), *Handbook of Semiconductor Silicon Technology* (Noyes, Berkshire, 1990)
189. J.J. Dowd, R.L. Rouse, Proc. Phys. Soc. B **66**, 60 (1953)
190. W.W. Tyler, R. Newman, H.H. Woodbury, Phys. Rev. **98**, 461 (1955)
191. W.C. Dunlap, Jr., Phys. Rev. **97**, 614 (1955)
192. Landolt-Börnstein, in *New Series, Semiconductors*, ed. by O. Madelung, M. Schulz, H. Weiss. Numerical Data and Functional Relationships in Science and Technology, vol. 17 (Springer, Berlin, 1982)
193. M. Nastasi, J.W. Mayer, *Ion Implantation and Synthesis of Materials* (Springer, Berlin, 2006)
194. A. Benninghoven, F.G. Rudenauer, H.W. Werner (eds.), *Secondary Ion Mass Spectrometry* (John Wiley & Sons, New York, 1987)
195. S. Uppal, A.F.W. Willoughby, J.M. Bonar, A.G.R. Evans, N.E.B Cowern, R. Morris, M.G. Dowsett, J. Appl. Phys. **90**, 4293 (2001)
196. R.F. Lever, K.W. Brannon, J. Appl. Phys. **69**, 6369 (1991)

197. www.srim.org
198. J.F. Ziegler, J.P. Biersack, M.D. Ziegler, *SRIM – The Stopping and Range of Ions in Matter* (Lulu Press, Morrisville, 2006)
199. K. Kimura, Y. Oota, K. Nakajima, T.H. Büyüklimanli, Curr. Appl. Phys. **3**, 9 (2003)
200. R.Wittmann, Miniaturization Problems in CMOS Technology: Investigation of Doping Profiles and Reliability, PhD Thesis, TU Wien, 2007
201. J. Yokota, J. Phys. Soc. Jpn. **19**, 1487 (1964)
202. J.A. Vergés, D. Glötzel, M. Cardona, O.K. Andersen, Phys. Stat. Sol. (B) **113**, 519 (1982)
203. M. Cardona, N.E. Christensen, Phys. Rev. B **35**, 6182 (1987)
204. D.A.W. Soarez, C.A. Pimentel, J. Appl. Cryst. **16**, 486 (1983)
205. H.R. Vydyanath, J.S. Lorenzo, F.A. Kröger, J. Appl. Phys. **49**, 5928 (1978)
206. P. Deák, A. Gali, A. Sólynom, A. Buruzs, Th. Fraunheim, J. Phys.: Condens. Matter **17**, S2141–2153 (2005) and references therein
207. B.P. Uberuaga, G. Henkelman, H. Jónsson, S.T. Dunham, W. Windl, R. Stumpf, Phys. Stat. Sol. (B) **233**, 24 (2002)
208. M.J. Caturla, M.D. Johnson, T.D. de la Rubia, Appl. Phys. Lett. **72**, 2736 (1998)
209. F.A. Trumbore, Bell Syst. Tech. J. **39**, 205–33 (1960)
210. V.E. Borisenko, S.G. Yudin, Phys. Stat. Sol. (A) **101**, 123 (1987)
211. J. Adey, R. Jones, P.R. Briddon, J. Phys.: Condens. Matter **16**, 9117 (2004)
212. S. Fischler, J. Appl. Phys. **33**, 1615 (1962)
213. F.S. Shishiyanu, V.G. Gheorghiu, S.K. Palazov, Phys. Stat. Sol. (A) **40**, 29 (1977)
214. M. Luysberg, R. Göbel, H. Janning, J. Vac. Sci. Technol. B **12**, 2305 (1984)
215. N.A. Smith, I.R. Harris, B. Cockayne, W.R. MacEwan, J. Cryst. Growth **68**, 517 (1984)
216. J.P. Hirth, A brief history of dislocation theory. Metall. Mat. Transact. A **16**, 2085–90 (1985)
217. S. Kret, Pawel Dłużewski, Piotr Dłużewski, J.-Y. Laval, Philos. Mag. **83**, 231 (2003). Also at info.ifpan.edu.pl/SL-1/sl14sub/dys1.htm
218. A.R. Smith, V. Ramachandran, R.M. Feenstra, D.W. Greve, M.-S. Shin, M. Skowronski, J. Neugebauer, J.E. Northrup, J. Vac. Sci. Technol. A **16**, 1641 (1998)
219. S.N.G. Chu, W.T. Tsang, T.H. Chiu, A.T. Macrander, J. Appl. Phys. **66**, 521 (1989)
220. J.G. Grabmaier, C.B. Watson, Phys. Stat. Sol. **32**, K13 (1969)
221. M. Horn-von Hoegen, F.K. LeGoues, M. Copel, M.C. Reuter, R.M. Tromp, Phys. Rev. Lett. **67**, 1130 (1991)
222. R.B. Heimann, *Auflösung von Kristallen* (Springer, Wien, 1975)
223. K. Sato, M. Shikida, T. Yamashiro, K. Asaumi, Y. Iriye, M. Yamamoto, Sens. Actuat. **73**, 131 (1999)
224. A.F. Bogenschütz, *Ätzpraxis für Halbleiter* (Carl Hanser, München, 1967) (in German)
225. K. Ishida, H. Kawano, Phys. Stat. Sol. (A) **98**, 175 (1986)
226. J.L. Weyher, J. van de Ven, J. Cryst. Growth **78**, 191–217 (1986)
227. M. Köhler, *Etching in Microsystem Technology* (Wiley-VCH, Weinheim, 1999)

228. J. Frühauf, *Shape and Functional Elements of the Bulk Silicon Microtechnique: A Manual of Wet-Etched Silicon Structures* (Springer, Berlin, 2005)
229. D.M. Manos, D.L. Flamm (eds.), *Plasma Etching: An Introduction* (Academic Press, San Diego, 1988)
230. G.S. May, C.J. Spanos, *Fundamentals of Semiconductor Manufacturing and Process Control* (John Wiley & Sons, Hoboken, 2006)
231. J.W. Coburn, *Plasma etching and reactive ion etching: Fundamentals and Applications*. American Vacuum Society Monograph Series (AVS, New York, 1982)
232. V. Smaminathan, A.S. Jordan, Dislocations in III/V compounds, Semicond. Semimet. **38**, 294 (1993)
233. T. Kamejima, J. Matsui, Y. Seki, H. Watanabe, J. Appl. Phys. **50**, 3312 (1979)
234. L. Wang, W. Jie, Y. Yang, G. Xu, L. Fu, J. Cryst. Growth **310** 2810 (2008)
235. S. Mader, A.E. Blakeslee, Appl. Phys. Lett. **25**, 365 (1974)
236. M. Sato, K. Sumino, K. Hiraga, Phys. Stat. Sol. (A) **68**, 567 (1981)
237. D.J.H. Cockayne, P.B. Hirsch, V. Vitek, Philos. Mag. **31**, 105 (1975)
238. D. Gerthsen, C.B. Carter, Phys. Stat. Sol. (A) **136**, 29 (1993)
239. P. Pirouz, D.J.H. Cockayne, N. Shimada, P. Hirsch, A.R. Lang, Proc. Roy. Soc. London A **386**, 241 (1983)
240. H. Gottschalk, G. Patzer, H. Alexander, Phys. Stat. Sol. (A) **45**, 207 (1978)
241. S. Takeuchi, K. Suzuki, K. Maeda, Philos. Mag. A **50**, 171 (1984)
242. NREL, www.nrel.gov/measurements/trans.html
243. Z. Liliental-Weber, H. Sohn, J. Washburn, Structural defects in epitaxial III/V layers, Semicond. Semimet. **38**, 397 (1993)
244. Y. Hao, G. Meng, Zh.L. Wang, Ch. Ye, L. Zhang, Nano Lett. **6**, 1650 (2006)
245. S. Amelinckx, W. Dekeyser, The structure and properties of grain boundaries. Solid State Phys. **8**, 325 (1959)
246. C.R.M. Grovenor, J. Phys. C: Solid State Phys. **18**, 4079–119 (1985)
247. C. Fontaine, D.A. Smith, Appl. Phys. Lett. **40**, 153 (1982)
248. H. Sawada, H. Ichinose, M. Kohyama, J. Electron Microsc. **51**, 353 (2002)
249. F.L. Vogel, W.G. Pfann, H.E. Corey, E.E. Thomas, Phys. Rev. **90**, 489 (1953)
250. H. Föll, www.tf.uni-kiel.de/matwis/amat/def en/index.html
251. H. Föll, D. Ast, Philos. Mag. A **40**, 589 (1979)
252. F. Wolf, W. Mader, Optik 110, Suppl. 8 (1999)
253. M. Grundmann, A. Krost, D. Bimberg, J. Cryst. Growth **107**, 494 (1991)
254. W. Mader, private communication (2006)
255. G.P. Srivastava, *The Physics of Phonons* (Taylor & Francis, New York, 1990)
256. J.L.T. Waugh, G. Dolling, Phys. Rev. **132**, 2410 (1963)
257. S. Bağcı, S. Duman, H.M. Tütüncü, G.P. Srivastava, G. Uğur, Diamond Relat. Mater. **15**, 1161 (2006)
258. E. Ruiz, S. Alvarez, P. Alemany, Phys. Rev. B **49**, 7115 (1994)
259. A. Göbel, T. Ruf, A. Fischer, K. Eberl, M. Cardona, J.P. Silveira, F. Briones, Phys. Rev. B **59**, 12612 (1999)
260. M. Schubert, Universität Leipzig, private communication (2006)
261. A.S. Barker, A.J. Sievers, Rev. Mod. Phys. **47**, Suppl. No. 2, S1 (1975)
262. R.C. Newman, Semicond. Semimet. **38**, 118 (1993)
263. M. Stavola, Semicond. Semimet. B **51**, 153 (1999)

264. M.D. McCluskey, J. Appl. Phys. **87**, 3593 (2000)
265. L. Hoffmann, J.C. Bach, B. Bech Nielsen, P. Leary, R. Jones, S. Öberg, Phys. Rev. B **55**, 11167 (1997)
266. F. Thompson, R.C. Newman, J. Phys. C: Solid State Phys. **4**, 3249 (1971)
267. M. Vandevyver, D.N. Talwar, Phys. Rev. B **21**, 3405 (1980)
268. I.F. Chang, S.S. Mitra, Phys. Rev. **172**, 924 (1968)
269. L.I. Deych, A. Yamilov, A.A. Lisyansky, Phys. Rev. B **62**, 6301 (2000)
270. M. Born, I. Huang, *Dynamical Theory of Crystal Lattices* (Clarendon Press, Oxford, 1960)
271. H.M. Kayaga, T. Soma, Phys. Stat. Sol. (B) **129**, K5 (1985)
272. A.S. Saada, *Elasticity, Theory and Applications* (Pergamon, New York, 1974)
273. P.N. Keating, Phys. Rev. **145**, 637 (1966)
274. A.-B. Chen, A. Sher, W.T. Yost, Semicond. Semimet. **37**, 1 (1992)
275. R.S. Lakes, Science **235**, 1038 (1987)
276. K.E. Evans, M.A. Nkansah, I.J. Hutchinson, S.C. Rogers, Nature **353**, 124 (1991)
277. R.H. Baughman, Nature **425**, 667 (2003)
278. R. Gatt, J.N. Grima, Phys. Stat. Sol. RRL **2**, 236 (2008)
279. R.M. Martin, Phys. Rev. B **6**, 4546 (1972)
280. K. Kim, W.R.L. Lambrecht, B. Segall, Phys. Rev. B **53**, 16310 (1996)
281. R.M. Martin, Phys. Rev. B **1**, 4005 (1970)
282. Ch.G. Van de Walle, Phys. Rev. B **39**, 1871 (1989)
283. J.D. Eshelby, Proc. Roy. Soc. London A **241**, 376 (1957)
284. A. Polian, M. Grimsditch, I. Grzegory, J. Appl. Phys. **79**, 3343 (1996)
285. L.E. McNeil, M. Grimsditch, R.H. French, J. Am. Ceram. Soc. **76**, 1132 (1993)
286. C.F. Cline, H.L. Dunegan, G.W. Henderson, J. Appl. Phys. **38**, 1944 (1967)
287. G. Carlotti, D. Fioretto, G. Socino, E. Verona, J. Phys.: Condens. Matter **7**, 9147 (1995)
288. M. Grundmann, O. Stier, D. Bimberg, Phys. Rev. B **52**, 11969 (1995)
289. L.B. Freund, J.A. Floro, E. Chason, Appl. Phys. Lett. **74**, 1987 (1999)
290. M. Grundmann, Appl. Phys. Lett. **83**, 2444 (2003)
291. G.G. Stoney, Proc. R. Soc. London, Ser. A **82**, 172 (1909)
292. R. Beresford, J. Yin, K. Tetz, E. Chason, J. Vac. Sci. Technol. B **18**, 1431 (2000)
293. V.Y. Prinz, V.A. Seleznev, A.K. Gutakovsky, *Proc. 24th Int. Conf. Semicond. Physics, Jerusalem, Israel*, World Scientific, Singapore, 1998, Th3-D5
294. B. Schmidt, Calc. Var. **30**, 477 (2007)
295. J. Zang, F. Liu, Appl. Phys. Lett. **92**, 021905 (2008)
296. O.G. Schmidt, N. Schmarje, C. Deneke, C. Müller, N.-Y. Jin-Phillipp, Adv. Mater. **13**, 756 (2001)
297. S. Mendach, University of Hamburg, private communication (2006)
298. J.C. Bean, L.C. Feldman, A.T. Fiory, S. Nakahara, I.K. Robinson, J. Vac. Sci. Technol. A **2**, 436 (1984)
299. R. Hull, J.C. Bean, J. Vac. Sci. Technol. A **7**, 2580 (1989)
300. J.W. Matthews, A.E. Blakeslee, J. Cryst. Growth **27**, 118 (1974)
301. R. People, J.C. Bean, Appl. Phys. Lett. **47**, 322 (1985)

302. F.C. Frank, J. van der Merwe, Proc. R. Soc. A **198**, 216 (1949); ibid **198**, 2205
303. J.H. van der Merwe, J. Appl. Phys. **34**, 123 (1962)
304. J.R. Willis, S.C. Jain, R. Bullough, Philos. Mag. A **62**, 115 (1990)
305. B.W. Dodson, J.Y. Tsao, Appl. Phys. Lett. **51**, 1325 (1987)
306. E. Kasper, H.J. Herzog, H. Kibbel, Appl. Phys. **8**, 199 (1975)
307. K.L. Kavanagh, M.A. Capano, L.W. Hobbs, J.C. Barbour, P.M.J. Marée, W. Schaff, J.W. Mayer, D. Pettit, J.M. Woodall, J.A. Stroscio, R.M. Feenstra, J. Appl. Phys. **64**, 4843 (1988)
308. M. Grundmann, U. Lienert, D. Bimberg, A. Fischer-Colbrie, J.N. Miller, Appl. Phys. Lett. **55**, 1765 (1989)
309. P. Quadbeck, Ph. Ebert, K. Urban, J. Gebauer, R. Krause-Rehberg, Appl. Phys. Lett. **76**, 300 (2000)
310. Ch. Kittel, *Quantum Theory of Solids* (John Wiley & Sons, New York, 1963)
311. J.R. Chelikowsky, M.L. Cohen, Phys. Rev. B **14**, 556 (1976)
312. R. Dalven, Electronic structure of PbS, PbSe, and PbTe. Solid State Phys. **28**, 179 (1973)
313. J.E. Jaffe, A. Zunger, Phys. Rev. B **28**, 5822 (1983)
314. S. Limpijumnong, S.N. Raskkeev, W.R.L. Lambrecht, MRS Internet J. Nitride Semicond. Res. **4S1**, G6.11 (1999)
315. R. Ahuja, O. Eriksson, B. Johansson, J. Appl. Phys. **90**, 1854 (2001)
316. J.E. Bernard, A. Zunger, Phys. Rev. B **26**, 3199 (1987)
317. E.W. Williams, V. Rehn, Phys. Rev. **172**, 798 (1968)
318. K.-R. Schulze, H. Neumann, K. Unger, Phys. Stat. Sol. (B) **75**, 493 (1976)
319. B. Kramer, Phys. Stat. Sol. **41**, 649 (1970)
320. R. Braunstein, A.R. Moore, F. Herman, Phys. Rev. **109**, 695 (1958)
321. D.J. Wolford, W.Y. Hsu, J.D. Dow, B.G. Streetman, J. Lumin. **18/19**, 863 (1978)
322. R. Schmidt, B. Rheinländer, M. Schubert, D. Spemann, T. Butz, J. Lenzner, E.M. Kaidashev, M. Lorenz, M. Grundmann, Appl. Phys. Lett. **82**, 2260 (2003)
323. R. Schmidt-Grund, A. Carstens, B. Rheinländer, D. Spemann, H. Hochmut, G. Zimmermann, M. Lorenz, M. Grundmann, C.M. Herzinger, M. Schubert, J. Appl. Phys. **99**, 123701 (2006)
324. S. Larach, R.E. Shrader, C.F. Stocker, Phys. Rev. **108**, 587 (1957)
325. S. Merita, T. Krämer, B. Mogwitz, B. Franz, A. Polity, B.K. Meyer, Phys. Stat. Sol. (C) **3**, 960 (2006)
326. B. Kramer, Phys. Stat. Sol. (B) **47**, 501 (1971)
327. B. Seraphin, Z. Naturf. **9a**, 450 (1954)
328. N. Garro, A. Cantarero, M. Cardona, A. Göbel, T. Ruf, K. Eberl, Phys. Rev. B **54**, 4732 (1996)
329. J.A. van Vechten, *A Simple Man's View of the Thermochemistry of Semiconductors*. Handbook on Semiconductors, vol. 3, 1–111 (North Holland, Amsterdam, 1982)
330. Y.W. Tsang, M.L. Cohen, Phys. Rev. B **3**, 1254 (1971)
331. J. Hartung, L.Å. Hansson, J. Weber, *Proc. of the 20th Int. Conf. on the Physics of Semiconductors*, Thessaloniki, Greece, ed. by E.M. Anastassakis, J.D. Joannopoulos (World Scientific, Singapore, 1990), p. 1875
332. Y. Varshni, Physica **34**, 149 (1967)

333. K.P. O'Donnell, X. Chen, Appl. Phys. Lett. **58**, 2924 (1991)
334. R. Pässler, Phys. Rev. B **66**, 085201 (2002)
335. E.O. Kane, J. Phys. Chem. Solids **1**, 249 (1957)
336. C. Hermann, C. Weisbuch, Phys. Rev. B **15**, 823 (1977)
337. Y.-N. Xu, W.Y. Ching, Phys. Rev. B **48**, 4335 (1993)
338. M. Oshikiri, F. Aryasetiawan, Y. Imanaka, G. Kido1, Phys. Rev. B **66**, 125204 (2002)
339. G. Dresselhaus, A.F. Kip, C. Kittel, Phys. Rev. **98**, 368 (1955)
340. S. Shokhovets, G. Gobsch, O. Ambacher, Superlatt. Microstruct. **39**, 299 (2006)
341. W.S. Baer, R.N. Dexter, Phys. Rev. **135**, A1388 (1964)
342. W. Shockley, Phys. Rev. **90**, 491 (1953)
343. H. Fröhlich, H. Pelzer, S. Zienau, Philos. Mag. **41**, 221 (1950)
344. J. Appel, Polarons. Solid State Phys. **21**, 193 (1968)
345. R.P. Feynman, Phys. Rev. B **97**, 660 (1955)
346. G.D. Mahan, *Many-Particle Physics* (Plenum Press, New York, 1981)
347. T.D. Schultz, Phys. Rev. **116**, 526 (1959)
348. S. Adachi, *Properties of Group-IV, III–V and II–VI Semiconductors* (John Wiley & Sons, Chichester, 2005)
349. P. Pfeffer, W. Zawadzki, Phys. Rev. B **41**, 1561 (1990)
350. M. Cardona, N.E. Christensen, G. Fasol, Phys. Rev. B **38**, 1806 (1988)
351. G. Ottaviani, L. Reggiani, C. Canali, F. Nava, A. Alberigi-Quaranta, Phys.Rev. B **12**, 3318 (1975)
352. D. Bimberg, private communication, original authorship unknown
353. M. Cardona, F.H. Pollak, Phys. Rev. **142**, 530 (1966)
354. M.I. Eremets, Semicond. Sci. Technol. **6**, 439 (1991)
355. J.J. Hopfield, J. Phys. Chem. Solids **15**, 97 (1960)
356. G. Bastard, J. Phys. C: Solid State Phys. **14**, 839 (1981)
357. J.L. Shay, B. Tell, L.M. Schiavone, H.M. Kasper, F. Thiel, Phys. Rev. B **9**, 1719 (1974)
358. G.L. Bir, G.E. Pikus, *Symmetry and Strain-Induced Effects in Semiconductors* (John Wiley & Sons, New York, 1974)
359. G.E. Pikus, G.L. Bir, Fiz. Tverd. Tela **1**, 1642 (1956) [Sov. Phys. Solid State **1**, 1502 (1959)]
360. N.E. Christensen, Phys. Rev. B **30**, 5753 (1984)
361. Y. Zhang, Phys. Rev. B **49**, 14352 (1994)
362. A.R. Goñi, K. Strössner, K. Syassen, M. Cardona, Phys. Rev. B **36**, 1581 (1987)
363. W. Shan, W. Walukiewicz, J.W. Ager III, E.E. Haller, J.F. Geisz, D.J. Friedman, J.M. Olson, S.R. Kurtz, Phys. Rev. Lett. **82**, 1221 (1999)
364. S.L. Chuang, C.S. Chang, Phys. Rev. B **54**, 2491 (1996)
365. M. Kumagai, S.L. Chuang, H. Ando, Phys. Rev. B **57**, 15303 (1998)
366. C. Herring, E. Vogt, Phys. Rev. **101**, 944 (1956)
367. M.V. Fischetti, S.E. Laux, J. Appl. Phys. **80**, 2234 (1996)
368. D. Aspnes, M. Cardona, Phys. Rev. B **17**, 726 (1978)
369. P.R.C. Kent, A. Zunger, Phys. Rev. B **64**, 115208 (2001)
370. J. Chelikowsky, D.J. Chadi, M.L. Cohen, Phys. Rev. B **8**, 2786 (1973)

371. W. Pauli 1931 in a letter from New York to R. Peierls, in: Pauli, Briefwechsel II, 1985, Nr. 287, p. 94; cf. G. Busch, Condens. Matter News **2**, 15 (1993). Lateron Pauli complains to Peierls "...daß Sie immer noch nicht von der Physik des festen Körpers losgekommen sind." (in: Pauli an Peierls, 22. Mai 1933, in: Pauli, Briefwechsel II, 1985, Nr. 310, p. 163)
372. W. Shockley, *Electrons and Holes in Semiconductors* (D. van Nostrand, New York, 1950)
373. X. Aymerich-Humet, F. Serra-Mestres, J. Millán, Solid State Electron. **24**, 981 (1981)
374. D. Bednarczyk, J. Bernarczyk, Phys. Lett. A **64**, 409 (1978)
375. K. Unger, Phys. Stat. Sol. (A) **149**, K141 (1988)
376. J. McDougall, E.C. Stoner, Philos. Trans. Roy. Soc. London **237**, 67 (1938)
377. A.J. MacLeod, ACM Trans. Math. Softw. **24**, 1 (1998)
378. A.B. Sproul, M.A. Green, J. Zhao, Appl. Phys. Lett. **57**, 255 (1990)
379. A.B. Sproul, M.A. Green, J. Appl. Phys. **73**, 1214 (1993)
380. M.A. Green, J. Appl. Phys. **67**, 2944 (1990)
381. K. Misiakos, D. Tsamakis, J. Appl. Phys. **74**, 3293 (1993)
382. B. Gudden, Sitzungsber. Phys.-Med. Soz. Erlangen **62**, 289 (1930)
383. E.F. Schubert, *Doping in III–V Semiconductors* (Cambridge University Press, Cambridge, 1993)
384. S.M. Sze, *Physics of Semiconductor Devices, 2nd edn.* (John Wiley & Sons, New York, 1981)
385. W. Kohn, J.M. Luttinger, Phys. Rev. **98**, 915 (1955)
386. G. Feher, D.K. Wilson, E.A. Gere, Phys. Rev. Lett. **3**, 25 (1959)
387. R. Kalish, The search for donors in diamond. Diamond Relat. Mater. **10**, 1749–55 (2001)
388. V.A. Karasyuk, D.G.S. Beckett, M.K. Nissen, A. Villemarie, T.W. Steiner, M.L.W. Thewalt, Phys. Rev. B **49**, 16381 (1994)
389. U. Kaufmann, J. Schneider, Adv. Electron. Electr. Phys. **58**, 81 (1982)
390. W. Götz, N.M. Johnson, C. Chen, H. Liu, C. Kuo, W. Imler, Appl. Phys. Lett. **68**, 3144 (1996)
391. A.J. Ptak, L.J. Holbert, L. Ting, C.H. Swartz, M. Moldovan, N.C. Giles, T.H. Myersa, P. Van Lierde, C. Tian, R.A. Hockett, S. Mitha, A.E. Wickenden, D.D. Koleske, R.L. Henry, Appl. Phys. Lett. **79**, 2740 (2001)
392. S. Teitler, R.F. Wallis, J. Phys. Chem. Solids **16**, 71 (1960)
393. B. Šantić, Superlatt. Microstruct. **36**, 445 (2004)
394. R.M. Dickstein, S.L. Titcomb, R.L. Anderson, J. Appl. Phys. **66**, 2437 (1989)
395. J.S. Blakemore, Phys. Rev. **163**, 809 (1967)
396. H.B. Bebb, Phys. Rev. B **5**, 4201 (1972)
397. E.M. Conwell, Phys. Rev. **99**, 1195 (1955)
398. A.T. Collins, A.W.S. Williams, J. Phys. C: Solid State Phys. **4**, 1789 (1971)
399. K. Thonke, The boron acceptor in diamond. Semicond. Sci. Technol. **18**, S20–S26 (2003)
400. G.W. Brown, H. Grube, M.E. Hawley, Phys. Rev. B **70**, 121301 (2004)
401. W. Kohn, Solid State Phys. **5**, 257 (1957)
402. K.Ya. Shtivel'man, R.G. Useinov, Russian Phys. J. **17**, 1439 (1974)
403. H. Alves, Defects, Doping and Compensation in Wide Bandgap Semiconductors, PhD Thesis, Universität Giessen, 2003

404. S. Fischer, C. Wetzel, E.E. Haller, B.K. Meyer, Appl. Phys. Lett. **67**, 1298 (1995)
405. D.C. Look, *Electrical Characterization of GaAs Materials and Devices* (John Wiley & Sons, New York, 1989)
406. E.E. Haller, W.L. Hansen, F.S. Goulding, Adv. Phys. **30**, 93–138 (1981)
407. M.B. Johnson, O. Albrektsen, R.M. Feenstra, H.W.M. Salemink, Appl. Phys. Lett. **63**, 2923 (1993) and Erratum Appl. Phys. Lett. **64**, 1454 (1994)
408. A.M. Yakunin, A.Yu. Silov, P.M. Koenraad, J.H. Wolter, W. Van Roy, J. De Boeck, J.-M. Tang, M.E. Flatté, Phys. Rev. Lett. **92**, 216806 (2004)
409. J.-M. Tang, M. Flatté, Phys. Rev. Lett. **92**, 047201 (2004)
410. J.S. Blakemore, *Semiconductor Statistics* (Pergamon Press, Oxford, 1962)
411. N.B. Hannay (ed.), *Semiconductors* (Reinhold Publ. Corp., New York, 1959)
412. E. Ziegler, W. Siegel, Crystal Res. & Technol. **17**, 1015 (1982)
413. H.-J. Hoffmann, Appl. Phys. **19**, 307 (1979)
414. G. Leibiger: $A^{III}B^{V}$-Mischkristallbildung mit Stickstoff und Bor, PhD Thesis, Universität Leipzig, 2003
415. M. Tao, J. Appl. Phys. **87**, 3554 (2000)
416. G. Weyer, J.W. Peterson, S. Damgaard, H.L. Nielsen, J. Heinemeier, Phys. Rev. Lett. **44**, 155 (1980)
417. E. Antoncik, B.L. Gu, Hyperfine Interact. **14**, 257 (1983)
418. R. Noufi, R. Axton, C. Herrington, S.K. Deb, Appl. Phys. Lett. **45**, 668 (1994)
419. N.F. Mott, *Metal-Insulator Transitions* (Taylor & Francis, London, 1990)
420. V.I. Fistul, *Highly Doped Semiconductors* (Plenum, New York, 1969)
421. P.P. Debye, E.M. Conwell, Phys. Rev. **93**, 693 (1954)
422. B.L. Crowder, W.N. Hammer, Phys. Rev. **150**, 541 (1966)
423. G.L. Pearson, J. Bardeen, Phys. Rev. **75**, 865 (1949)
424. G.E. Stillman, L.W. Cook, T.J. Roth, T.S. Low, B.J. Skromme, in *GaInAsP Alloy Semiconductors*, ed. by T.P. Pearsall (John Wiley & Sons, New York, 1982), p. 121
425. H. Kato, A. Ogawa, H. Kotani, M. Sano, T. Yao, MRS Fall Meeting 2006, Boston, Symp. K ('Zinc Oxide and Related Materials'), K5.6 (2006)
426. M.L. Young, S.J. Bass, J. Phys. D: Appl. Phys. **4**, 995 (1971)
427. H.C. Casey, Jr., F. Ermanis, K.B. Wolfstirn, J. Appl. Phys. **40**, 2945 (1969)
428. K. Pakula, M.Wojdak, M. Palczewska, B. Suchanek, J.M. Baranowski, MRS Internet J. Nitride Semicond. Res. **3**, 34 (1998)
429. G.R. James, A.W.R. Leitch, F. Omnès, M.C. Wagener, M. Leroux, J. Appl. Phys. **96**, 1047 (2004)
430. M. Brandt, H. von Wenckstern, C. Meinecke, T. Butz, H. Hochmuth, M. Lorenz, M. Grundmann, J. Vac. Sci. Technol. B **27** (2009)
431. M.C. Wu, Y.K. Su, K.Y. Cheng, C.Y. Chang, Solid State Electron. **31**, 251 (1988)
432. M. Ogawa, T. Baba, Jpn. J. Appl. Phys. **24**, L572 (1985)
433. T. Yamada, E. Tokumitsu, K. Saito, T. Akatsuka, M. Miyauchi, M. Konagai, K. Takahashi, J. Cryst. Growth **95**, 145 (1989)
434. J.L. Lievin, F. Alexandre, C. Dubon-Chevaillier, in *Properties of Impurity States in Superlattice Semiconductors*, ed. by C.Y. Fong, I.P. Batra, S. Ciraci (Plenum, New York, 1988), p. 19

435. J. Bourgoin, M. Lannoo, *Point Defects in Semiconductors II* (Springer, Berlin, 1983)
436. S.T. Pantelides (ed.), *Deep Centers in Semiconductors*, (Gordon & Breach, New York, 1986)
437. J.-W. Chen, A.G. Milnes, Energy levels in silicon. Ann. Rev. Mat. Sci. **10**, 157–228 (1980)
438. K. Lischka, Deep level defects in narrow gap semiconductors. Phys. Stat. Sol. (B) **133**, 17–46 (1986)
439. J.-M. Spaeth, H. Overhof, *Point Defects in Semiconductors and Insulators, Determination of Atomic and Electronic Structure from Paramagnetic Hyperfine Interactions* (Springer, Berlin, 2003)
440. P.T. Landsberg, J. Phys. D: Appl. Phys. **10**, 2467 (1977)
441. H.I. Ralph, J. Appl. Phys. **49**, 672 (1978)
442. R. Kassing, L. Cohausz, P. van Staa, W. Mackert, H.J. Hoffman, Appl. Phys. A **34**, 41 (1984)
443. H.H. Woodbury, G.W. Ludwig, Phys. Rev. **117**, 102 (1960)
444. S. Greulich-Weber, J.R. Niklas, E.R. Weber, J.M. Spaeth, Phys. Rev. B **30**, 6292 (1984)
445. H. Feichtinger, J. Waltl, A. Gschwandtner, Solid State Commun. **27**, 867 (1978)
446. Y.H. Lee, R.L. Kleinhenz, J.W. Corbett, Appl. Phys. Lett. **31**, 142 (1977)
447. H.G. Grimmeiss, E. Janzén, H. Ennen, O. Schirmer, J. Schneider, R.Wörner, C. Holm, E. Sirtl, P. Wagner, Phys. Rev. B **24**, 4571 (1981)
448. H.G. Grimmeiss, L. Montelius, K. Larsson, Phys. Rev. B **37**, 6916 (1988)
449. R.K. Franks, J.B. Robertson, Solid State Commun. **5**, 479 (1967)
450. U. Kaufmann, J. Schneider, R.Wörner, T.A. Kennedy, N.D.Wilsey, J. Phys. C: Solid State Phys. **14**, L951 (1981)
451. R.J. Wagner, J.J. Krebs, G.H. Strauss, A.M. White, Solid State Commun. **36**, 15 (1980)
452. R.O. Carlson, Phys. Rev. **108**, 1390 (1957)
453. W.W. Tyler, H.H. Woodbury, Phys. Rev. **102**, 647 (1956)
454. M.D. Sturge, The Jahn-Teller effect in solids. Solid State Phys. **20**, 92 (1967)
455. G.D. Watkins, Adv. Solid State Phys. (Festkörperprobleme) **24**, 163 (1984)
456. G.D. Watkins, J.R. Troxell, Phys. Rev. Lett. **44**, 593 (1980)
457. P.W. Anderson, Phys. Rev. Lett. **34**, 953 (1975)
458. R.D. Harris, J.L. Newton, G.D. Watkins, Phys. Rev. B **36**, 1094 (1987)
459. G.A. Baraff, E.O. Kane, M. Schlüter, Phys. Rev. B **21**, 5662 (1980)
460. M. Sprenger, S.H. Muller, E.G. Sieverts, C.A.J. Ammerlaan, Phys. Rev. B **35**, 1566 (1987)
461. A.F. Wright, Phys. Rev. B **74**, 165116 (2006)
462. A. Fazzio, A. Janotti, A.J.R. da Silva, Phys. Rev. B **61**, R2401 (2000)
463. P.M. Mooney, N.S. Caswell, S.L. Wright, J. Appl. Phys. **62**, 4786 (1987)
464. P.M. Mooney, J. Appl. Phys. **67**, R1 (1990)
465. J.C. Bourgoin (ed.), Physics of DX Centers in GaAs Alloys, (Sci-Tech, Lake Isabella, CA, 1990)
466. D.V. Lang, R.A. Logan, Phys. Rev. Lett. **39**, 635 (1977)
467. J. Mäkinen, T. Laine, K. Saarinen, P. Hautojärvi, C. Corbel, V.M. Araksinen, J. Nagle, Phys. Rev. B **52**, 4870 (1995)
468. J. Dabrowski, M. Scheffler, Phys. Rev. B **40**, 10391 (1989)

469. J.S. Blakemore, J. Appl. Phys. **53**(10), R123-R181 (1982)
470. A. Rohatgi, R.H. Hopkins, J.R. Davis, R.B. Campbell, H.C. Mollenkopf, J.R. McCormick, Solid State Electron. **23**, 1185 (1980)
471. G.M. Martin, Appl. Phys. Lett. **39**, 747 (1981)
472. D.C. Look, J. Appl. Phys. **48**, 5141 (1977)
473. O. Mizuno, H. Watanabe, Electron. Lett. **11**, 118 (1975)
474. Y. Toudic, B. Lambert, R. Coquille, G. Grandpierre, M. Gauneau, Semicond. Sci. Technol. **3** 464 (1988)
475. R.P. Tapster, M.S. Skolnick, R.G. Humphreys, P.J. Dean, B. Cockayne, W.T. MacEwan, J. Phys. C: Solid State Phys. **14**, 5069 (1981)
476. A. Juhl, A. Hoffmann, D. Bimberg, H.J. Schulz, Appl. Phys. Lett. **50**, 1292 (1987)
477. A.M. Hennel, Transition metals in III/V compounds. Semicond. Semimet. **38**, 189 (1993)
478. H.J. Schulz, J. Cryst. Growth **59**, 65 (1982)
479. J. Cheng, S.R. Forrest, B. Tell, D. Wilt, B. Schwartz, P.D. Wright, J. Appl. Phys. **58**, 1780 (1985)
480. D.G. Knight, B. Watt, R. Bruce, D.A. Clark, in *Semi-Insulating III–V Materials*, ed. by A. Milnes, C.J. Miner (Bristol, 1990), p. 83
481. D. Söderström, G. Fornuto, A. Buccieri, *Proc. 10th European Workshop on MOVPE*, Lecce (Italy), PS.IV.01, 2003
482. A. Dadgar, O. Stenzel, A. Näser, M. Zafar Iqbal, D. Bimberg, H. Schumann, Appl. Phys. Lett. **73**, 3878 (1998)
483. R.A. Faulkner, Phys. Rev. **175**, 991 (1968)
484. P.J. Dean, J. Lumin. **1–2**, 398 (1970)
485. R. Schwabe, W. Seifert, F. Bugge, R. Bindemann, V.F. Agekyan, S.V. Pogarev, Solid State Commun. **55**, 167–173 (1985)
486. X. Liu, M.-E. Pistol, L. Samuelson, Phys. Rev. B **42**, 7504 (1990)
487. B. Gil, J.P. Albert, J. Camassel, H. Mathieu, C. Benoit á la Guillaume, Phys. Rev. B **33**, 2701 (1986)
488. W. Mönch, *Semiconductor Surfaces and Interfaces* (Springer, Berlin, 2001)
489. Y. Rosenwaks, R. Shikler, Th. Glatzel, S. Sadewasser, Phys. Rev. B **70**, 085320 (2004)
490. D.G. Thomas, J.J. Hopfield, Phys. Rev. **150**, 680 (1966)
491. E. Mollwo, Z. Phys. **138**, 478 (1954)
492. J.I. Pankove, N.M. Johnson (eds.), Hydrogen in semiconductors. Semicond. Semimet. **34**, (1991)
493. S.J. Pearton, J.W. Corbett, M. Stavola, *Hydrogen in Crystalline Semiconductors* (Springer, Berlin, 1992)
494. T. Sakurai, H.D. Hagstrom, J. Vac. Sci. Technol. **13**, 807 (1976)
495. J.I. Pankove, Appl. Phys. Lett. **32**, 812 (1978)
496. M.H. Brodsky, M. Cardona, J.J. Cuomo, Phys. Rev. B **16**, 3556 (1977)
497. P.J.H. Denteneer, C.G. Van de Walle, S.T. Pantelides, Phys. Rev. B **39**, 10809 (1989)
498. C.P. Herrero, M. Stutzmann, Phys. Rev. B **38**, 12668 (1988)
499. M. Stavola, K. Bergmann, S.J. Pearton, J. Lopata, Phys. Rev. Lett. **61**, 2786 (1988)
500. V.P. Markevich, L.I. Murin, M. Suezawa, J.L. Lindström, J. Coutinho, R. Jones, P.R. Briddon, S. Öberg, Phys. Rev. B **61**, 12964 (2000)

501. V.P. Markevich, A.R. Peaker, J. Coutinho, R. Jones, V.J.B. Torres, S.Öberg, P.R. Briddon, L.I. Murin, L. Dobaczewski, N.V. Abrosimov, Phys. Rev. B **69**, 125218 (2004)
502. A.S. Yapsir, P. Deak, R.K. Singh, L.C. Snyder, J.W. Corbett, T.-M. Lu, Phys. Rev. B **38**, 9936 (1988)
503. H.-D. Liu, Y.-P. Zhao, G. Ramanath, S.P. Murarka, G.-C. Wang, Thin Solid Films **384**, 151 (2001)
504. C. Jacoboni, L. Reggiani, Adv. Phys. **28**, 493–553 (1979)
505. E.M. Conwell, V. Weisskopf, Phys. Rev. **77**, 388 (1950)
506. H. Brooks, Phys. Rev. **83** 879 (1951)
507. B.K. Ridley, J. Phys. C: Solid State Phys. **10** 1589 (1977)
508. D.C. Chattopadhyay, H.J. Queisser, Rev. Mod. Phys. **53**, 745 (1981)
509. B.K. Ridley, *Quantum Processes in Semiconductors*, 2nd edn. (Clarendon, Oxford, 1988)
510. J.H. You, H.T. Johnson, Effect of dislocations on electrical and optical properties of GaAs and GaN. Solid State Phys. **61**, 143–261 (2009)
511. G.L. Pearson, W.T. Read, F.J. Morin, Phys. Rev. **93**, 666 (1954)
512. W.T. Read, Philos. Mag. **45**, 775 (1954)
513. W.T. Read, Philos. Mag. **46**, 111 (1954)
514. B. Pödör, Phys. Stat. Sol. **16**, K167 (1966)
515. H.W. Choi, J. Zhang, S.J. Chua, Mat. Sci. Semicond. Process. **4**, 567 (2001)
516. J.Y.W. Seto, J. Appl. Phys. **46**, 5247 (1975)
517. C.H. Seager, T.G. Castner, J. Appl. Phys. **49**, 3879 (1978)
518. M.R. Murti, K.V. Reddy, Phys. Stat. Sol. (A) **119**, 237 (1990)
519. J.W. Orton, M.J. Powell, Rep. Prog. Phys. **43**, 1263–1307 (1980)
520. N. Gupta, B.P. Tyagi, Phys. Scripta **71**, 225 (2005)
521. R.L. Petritz, Phys. Rev. **104**, 1508 (1956)
522. C.M. Wolfe, G.E. Stillman, W.T. Lindley, J. Appl. Phys. **41**, 3088 (1970)
523. H. V. Wenckstern, S. Weinhold, G. Biehne, R. Pickenhain, H. Schmidt, H. Hochmuth, M. Grundmann, Adv. Solid State Phys. (Festkörperprobleme) **45**, 263 (2005)
524. H.K. Sy, D.K. Desai, C.K. Ong, Phys. Stat. Sol. (B) **130**, 787 (1985)
525. G. Masetti, M. Severi, S. Solmi, IEEE Trans. Electron Devices **30**, 764 (1983)
526. C.S. Smith, Phys. Rev. B **94**, 42 (1954)
527. R.W. Keyes, The effect of elastic deformation on the electrical conductivity of semiconductors. Solid State Phys. **11**, 149–221 (1960)
528. Y. Ohmura, Phys. Rev. B **42**, 9178 (1990)
529. M. Zerbst, Z. Naturforschung **17a**, 649 (1962)
530. A. Sagar, Phys. Rev. **112**, 1533 (1958)
531. Y. Kanda, IEEE Trans. Electron Devices **ED-29**, 64 (1982)
532. L.J. van der Pauw, Philips Res. Repts. **13**, 1 (1958)
533. L.J. van der Pauw, Philips Tech. Rev. **20**, 220 (1958)
534. D.S. Perloff, Four-Point sheet resistance correction factors for thin rectangular samples. Solid State Electron. **20**, 681 (1977)
535. O. Breitenstein, M. Langenkamp, *Lock-in Thermography, Basics and Use for Functional Diagnostics of Electronic Components*. Springer Series in Advanced Microelectronics, vol. 10 (Springer, Heidelberg, 2003)
536. O. Madelung, H. Weiss, Z. Naturf. **9a**, 527 (1954)

537. J. Antoszweski, D.J. Seymour, L. Faraone, J.R. Meyer, C.A. Hoffmann, J. Appl. Phys. **84**, 4966 (1998)
538. J. Rothman, J. Meilhan, G. Perrais, J.-P. Belle, O. Gravrand, J. Electr. Mat. **35**, 1174 (2006)
539. E.M. Conwell, *High Field Transport in Semiconductors* (Academic Press, New York, 1967)
540. C. Canali, C. Jacoboni, F. Nava, G. Ottaviani, A. Alberigi-Quaranta, Phys. Rev. B **12**, 2265 (1975)
541. B.K. Ridley, T.B. Watkins, Proc. Phys. Soc. **78**, 293 (1961)
542. P.N. Butcher, The gunn effect. Rep. Prog. Phys. **30**, 97–148 (1967)
543. C. Jacoboni, C. Canali, G. Ottaviani, A. Alberigi-Quaranta, Solid State Electron. **20**, 77 (1977)
544. C. Jacoboni, F. Nava, C. Canali, G. Ottaviani, Phys. Rev. B **24**, 1014 (1981)
545. T. Gonzalez Sanchez, J.E. Velazquez Perez, P.M. Gutierrez Conde, D. Pardo, Semicond. Sci. Technol. **7**, 31 (1992)
546. V. Balynas, A. Krotkus, A. Stalnionis, A.T. Gorelionok, N.M. Shmidt, J.A. Tellefsen, Appl. Phys. A **51**, 357 (1990)
547. J.D. Albrecht, P.P. Ruden, S. Limpijumnong, W.R. Lambrecht, K.F. Brennan, J. Appl. Phys. **86**, 6864 (1999)
548. T.K. Ishii (ed.), *Handbook of Microwave Technology* (Academic Press, San Diego, 1995)
549. S. Sridharan, P.D. Yoder, IEEE Electr. Dev. Lett. **29**, 1190 (2008)
550. J. Pozhela, A. Reklaitis, Solid State Electron. **23**(9) 927–33 (1980)
551. B. Kramer, A. Mircea, Appl. Phys. Lett. **26**, 623 (1975)
552. A. Kuligk, N. Fitzer, R. Redmer, Phys. Rev. B **71**, 085201 (2005)
553. P.T. Landsberg, Proc. Roy. Soc. London A **213**, 226 (1952)
554. N.G. Nilsson, Phys. Stat. Sol. (A) **19**, K75 (1973)
555. E. Spenke, *Elektronische Halbleiter* (Springer, Berlin, 1956)
556. F.A. Lindholm, R.W. Ayers, Proc. IEEE **56**, 371 (1968)
557. H.S. Carslaw, J.C. Jaeger, *Conduction of Heat in Solids* (Clarendon Press, Oxford, 1959)
558. T.H. Geballe, G.W. Hull, Phys. Rev. **110**, 773 (1958)
559. W.S. Capinski, H.J. Maris, E. Bauser, I. Silier, M. Asen-Palmer, T. Ruf, M. Cardona, E. Gmelin, Appl. Phys. Lett. **71**, 2109 (1997)
560. T. Ruf, R.W. Henn, M. Asen-Palmer, E. Gmelin, M. Cardona, H.J. Pohl, G.G. Devyatykh, P.G. Sennikov, Solid State Commun. **115**, 243 (2000)
561. G.O. Mahan, Good thermoelectrics. Solid State Phys. **51**, 81 (1997)
562. H. Boettner, G. Chen, R. Venkatasubramanian, MRS Bull. **31**, 211 (2006)
563. T.H. Geballe, G.W. Hull, Phys. Rev. **98**, 940 (1955)
564. M. Bouguer, *Essai d'optique sur la gradation de la lumiere* (Claude Jombert, Paris, 1729)
565. A. Beer, Ann. Phys. Chem. **86**, 78 (1852)
566. Ch.M. Wolfe, N. Holonyak, Jr., G.E. Stillman, *Physical Properties of Semiconductors* (Prentice Hall, Englewood Cliffs, NJ, 1989)
567. B. Jogai, Solid State Commun. **116**, 153 (2000)
568. M. Cardona, Modulation spectroscopy. Solid State Phys. Suppl. 11 (1969)
569. P.J. Dean, D.G. Thomas, Phys. Rev. **150**, 690 (1966)
570. L.H. Hall, J. Bardeen, F.J. Blatt, Phys. Rev. **95**, 559 (1954)
571. M.D. Sturge, Phys. Rev. **127**, 768 (1962), Phys. Rev. **129**, 2835 (1963)

572. R.G. Ulbrich, Adv. Solid State Phys. (Festkörperprobleme) **25**, 299 (1985)
573. J. Geist, A. Migdall, H.P. Baltes, Appl. Opt. **27**, 3777 (1988)
574. G.G. Macfarlane, V. Roberts, Phys. Rev. **97**, 1714 (1955)
575. G.G. Macfarlane, T.P. McLean, J.E. Quarrington, V. Roberts, Phys. Rev. **111**, 1245 (1958)
576. B.N. Brockhouse, Phys. Rev. Lett. **2**, 256 (1959)
577. J.I. Pankove, P. Aigrain, Phys. Rev. **126**, 956 (1962)
578. G.A. Cox, G.G. Roberts, R.H. Tredgold, Br. J. Appl. Phys. **17**, 743 (1966)
579. F. Urbach, Phys. Rev. **92**, 1324 (1953)
580. T.S. Moss, T.D.F. Hawking, Infrared Phys. **1**, 111 (1961)
581. S.R. Johnson, T. Tiedje, J. Appl. Phys. **78**, 5609 (1995)
582. M. Beaudoin, A.J.G. DeVries, S.R. Johnson, H. Laman, T. Tiedje, Appl. Phys. Lett. **70**, 3540 (1997)
583. R. Braunstein, E.O. Kane, J. Phys. Chem. Solids **23**, 1423 (1962)
584. J. Struke, J. Non-Cryst. Solids **4**, 1 (1970)
585. A. Baldereschi, N.O. Lipari, Phys. Rev. B **3**, 439 (1971)
586. N.O. Lipari, M. Altarelli, Phys. Rev. B **15**, 4883 (1977)
587. N.O. Lipari, Phys. Rev. B **4**, 4535 (1971)
588. D. Birkedal, J. Singh, V.G. Lyssenko, J. Erland, J. M. Hvam, Phys. Rev. Lett. **76**, 762 (1996)
589. E.F. Gross, Usp. Fiz. Nauk **76**, 433 (1962) [Sov. Phys.-Usp. **5**, 195 (1962)]
590. R.J. Elliott, Phys. Rev. **108**, 1384 (1957)
591. S. Rudin, T.L. Reinecke, B. Segall, Phys. Rev. B **42**, 11218 (1990)
592. Ch. Uihlein, D. Fröhlich, R. Kenklies, Phys. Rev. B **23**, 2731 (1981)
593. A.K. Viswanath, J.I. Lee, D. Kim, C.R. Lee, J.Y. Leem, Phys. Rev. B **58**, 16333 (1998)
594. A.J. Fischer, W. Shan, J.J. Song, Y.C. Chang, R. Horning, B. Goldenberg, Appl. Phys. Lett. **71**, 1981 (1997)
595. A.J. Fischer, D.S. Kim, J. Hays, W. Shan, J.J. Song, D.B. Eason, J. Ren, J.F. Schetzina, H. Luo, J.K. Furdyna, Z.Q. Zhu, T. Yao, W. Schäfer, Phys. Rev. Lett. **73**, 2368 (1994)
596. D.-S. Kim, J. Shah, J.E. Cunnigham, T.C. Damen, W. Schäfer, M. Hartmann, S. Schmitt-Rink, Phys. Rev. Lett. **68**, 1006 (1992)
597. R. Hauschild, H. Priller, M. Decker, J. Brückner, H. Kalt, C. Klingshirn, Phys. Stat. Sol. (C) **3**, 976 (2006)
598. A. Shikanai, T. Azuhata, T. Sota, S. Chichibu, A. Kuramata, K. Horino, S. Nakamura, J. Appl. Phys. **81**, 417 (1997)
599. J.J. Hopfield, D.G. Thomas, Phys. Rev. Lett. **15**, 22 (1965)
600. J.J. Hopfield, Phys. Rev. **182**, 945 (1969)
601. A.A. Maradudin, D.L. Mills, Phys. Rev. B **7**, 2787 (1973)
602. Y. Toyozawa, Prog. Theor. Phys., Suppl. 12, 111 (1959)
603. U. Heim, P. Wiesner, Phys. Rev. Lett. **24**, 1205 (1973)
604. I. Broser, M. Rosenzweig, Phys. Rev. B **22**, 2000 (1980)
605. M. Rosenzweig, Exzitonische Polaritonen in CdS – Optische Eigenschaften räumlich dispersiver Medien, PhD Thesis, Technische Universität Berlin, 1982
606. B. Gil, Phys. Rev. B **64**, 201310 (2001)
607. T. Soma, H.-M. Kagaya, Phys. Stat. Sol. (B) **118**, 245 (1983)

608. A. Göldner, Nichtstrahlende Relaxationsprozesse bandkantennaher Zustände in II-VI- und III-V-Halbleiterstrukturen, PhD Thesis, TU Berlin, Wissenschaft und Technik Verlag, Berlin, 2000
609. G. Blattner, G. Kurtze, G. Schmieder, C. Klingshirn, Phys. Rev. B **25**, 7413 (1982)
610. B. Gil, A. Hoffmann, S. Clur, L. Eckey, O. Briot, R.-L. Aulombard, J. Cryst. Growth **189/190**, 639 (1998)
611. C. Weisbuch, R. Ulbrich, J. Lumin. **18/19**, 27 (1979)
612. A.E. Yunovich, Radiative recombination and optical properties of GaP in *Radiative Recombination in Semiconductors*, ed. by Ya. E. Pokrovskii (Moscow, 1972) (in Russian); A.E. Yunovich, Strahlende Rekombination und optische Eigenschaften von GaP, Fortschritte der Physik **23**, 317–98 (1975) (in German)
613. E. Burstein, Phys. Rev. **93**, 632 (1954)
614. T.S. Moss, Proc. Phys. Soc. London B **76**, 775 (1954)
615. V. Vashishta, R.K. Kalia, Phys. Rev. B **25**, 6492 (1982)
616. J.P. Löwenau, S. Schmitt-Rink, H. Haug, Phys. Rev. Lett. **49**, 1511 (1982)
617. L.V. Keldysh, *Proc. of the 9th Int. Conf. on the Physics of Semiconductors, Moscow*, Nauka, Leningrad, 1968, p. 1303
618. W.F. Brinkman, T.M. Rice, P.W. Anderson, S.T. Chui, Phys. Rev. Lett. **28**, 961 (1972)
619. R. Zimmermann, Phys. Stat. Sol. (B) **146**, 371 (1988)
620. H.-E. Swoboda, M. Sence, F.A. Majumder, M. Rinker, J.-Y. Bigot, J.B. Grun, C. Klingshirn, Phys. Rev. B **39**, 11019 (1989)
621. G.A. Thomas, T.M. Rice, J.C. Hensel, Phys. Rev. Lett. **33**, 219 (1974)
622. T.L. Reinecke, S.C. Ying, Phys. Rev. Lett. **35**, 311 (1975)
623. R.S. Markienwicz, J.P. Wolfe, C.D. Jeffries, Phys. Rev. B **15**, 1988 (1977)
624. L.V. Butov, C.W. Lai, A.L. Ivanov, A.C. Gossard, D.S. Chemla, Nature **417**, 47 (2002)
625. L.V. Butov, A.C. Gossard, D.S. Chemla, Nature **418**, 751 (2002)
626. K.E. O. Hara, L.O. Suilleabhain, J.P. Wolfe, Phys. Rev. B **60**, 10565 (1999)
627. M. Skolnick, A.I. Tartakovskii, R. Butté, R.M. Stevenson, J.J. Baumberg, D.M. Whittaker, High occupancy effects and condensation phenomena in semiconductor microcavities and bulk semiconductors in *Nano-Optoelectronics, Concepts, Physics and Devices*, ed. by M. Grundmann (Springer, Berlin, 2002), p. 273
628. J.P. van der Ziel, Phys. Rev. B **16**, 2775 (1977)
629. H. Mahr, in *Quantum Electronics*, ed. by H. Rabin, C.L. Tang, vol. IA (Academic, New York, 1975), p. 285
630. H.J. Fossum, D.B. Chang, Phys. Rev. B **8**, 2842 (1973)
631. Sh.M. Kogan, T.M. Lifshits, Phys. Stat. Sol. (A) **39**, 11 (1977)
632. C.J. Summers, R. Dingle, D.E. Hill, Phys. Rev. B **1**, 1603 (1970)
633. R.A. Cooke, R.A. Hoult, R.F. Kirkman, R.A. Stradling, J. Phys. D: Appl. Phys. **11**, 945 (1978)
634. L.T. Ho, A.K. Ramdas, Phys. Rev. B **5**, 462 (1972)
635. M. Kleverman, K. Bergmann, H.G. Grimmeiss, Semicond. Sci. Technol. **1**, 49 (1986)
636. B.L. Cardozo, E.E. Haller, L.A. Reichertz, J.W. Beemann, Appl. Phys. Lett. **83**, 3990 (2003)

637. U. Fano, Nuovo Cimento **12**, 156 (1935)
638. G. Breit, E. Wigner, Phys. Rev. **49**, 519 (1936)
639. C.R. Pidgeon, *Free carrier optical properties of semiconductors*, Handbook on Semiconductors, vol. 2, 223–328 (North Holland, Amsterdam, 1982)
640. H.Y. Fan, Effects of free carriers on the optical properties. Semicond. Semimet. **3**, 409 (1967)
641. H.R. Chandrasekhar, A.K. Ramdas, Phys. Rev. B **21**, 1511 (1980)
642. R. Zallen, *Crystal Structures*, Handbook on Semiconductors, vol. 1 (North Holland, Amsterdam, 1982), pp. 3–27
643. W.G. Spitzer, Multiphonon lattice absorption. Semicond. Semimet. **3**, 17 (1967)
644. E.S. Koteles, W.R. Datars, Can. J. Phys. **54**, 1676 (1976)
645. A. Mooradian, G.B. Wright, Phys. Rev. Lett. **16**, 999 (1966)
646. P.T. Landsberg, *Recombination in Semiconductors* (Cambridge University Press, Cambridge, 1991)
647. G. Göbel, Appl. Phys. Lett. **24**, 492 (1974)
648. W. Michaelis, M. Pilkuhn, Phys. Stat. Sol. **36**, 311 (1969)
649. X. Sun, J. Liu, L.C. Kimerling, J. Michel, Appl. Phys. Lett. **95**, 011911 (2009)
650. R.N. Hall, Phys. Rev. **87**, 387 (1952)
651. W. Shockley, W.T. Read, Phys. Rev. **87**, 835 (1952)
652. V.K. Malyutenko, Physica E **20**, 553 (2004)
653. J.F. Muth, J.H. Lee, I.K. Shmagin, R.M. Kolbas, H.C. Casey, Jr., B.P. Keller, U.K. Mishra, S.P. DenBaars, Appl. Phys. Lett. **71** 2572 (1997)
654. W. Gerlach, H. Schlangenotto, H. Maeder, Phys. Stat. Sol. (A) **13**, 277 (1972)
655. A. Galeskas, J. LSiCros, V. Grivickas, U. Lindefelt, C. Hallin, *Proc. of the 7th International Conference on SiC, III-Nitrides and Related Materials*, Stockholm (Sweden), 1997, pp. 533–36
656. V. Palankovski Simulation of Heterojunction Bipolar Transistors, PhD Thesis, Technische Universität Wien, 2002
657. R.K. Akrenkiel, Minority-Carrier lifetime in III-V semiocnductors. Semicond. Semimet. **39**, 39–150 (1993)
658. P.J. Dean, J.R. Haynes, W.F. Flood, Phys. Rev. **161**, 711 (1967)
659. G. Davies, The optical properties of luminescence centres in silicon, Phys. Rep. **176**, 83 (1989)
660. G.D. Gilliland, Photoluminescence spectroscopy of crystalline semiconductors. Mat. Sci Engin. R **18**, 99–400 (1997)
661. P.J. Dean, *Luminescence of Crystals, Molecules and Solutions*, ed. by F. Williams (Plenum, New York, 1973), p. 523
662. S. Permogorov, A. Reznitsky, A. Naumov, H. Stolz, W. von der Osten, J. Phys.: Condens. Matter **1**, 5125 (1989)
663. T. Skettrup, M. Suffczynski, W. Gorzkowski, Phys. Rev. B **4**, 512 (1971)
664. J.R. Haynes, Phys. Rev. Lett. **4**, 361 (1960)
665. B. K. Meyer, H. Alves, D.M. Hofmann,W. Kriegseis, D. Forster, F. Bertram, J. Christen, A. Hoffmann, M. Straßburg, M. Dworzak, U. Haboeck, A.V. Rodina, Phys. Stat. Sol. (B) **241**, 231 (2004)
666. P.J. Dean, M. Skolnick, J. Appl. Phys. **54**, 346 (1983)

667. F.A.J.M. Driessen, H.G.M. Lochs, S.M. Olsthoorn, L.J. Giling, J. Appl. Phys. **69**, 906 (1991)
668. R.G. Ulbrich, Solid State Electron. **21**, 51 (1978)
669. D.E. Hill, Phys. Rev. B **1**, 1863 (1970)
670. D.C. Reynolds, D.C. Look, B. Jogai, V.M. Phanse, R.P. Vaudo, Solid State Commun. **103**, 533 (1997)
671. N. Nepal, M.L. Nakarmi, K.B. Nam, J.Y. Lin, H.X. Jiang, Appl. Phys. Lett. **85**, 2271 (2004)
672. D.G. Thomas, J.J. Hopfield, Phys. Rev. **128**, 2135 (1962)
673. J.L. Merz, H. Kukimoto, K. Nassau, J.W. Shiever, Phys. Rev. B **6**, 545 (1972)
674. P.J. Dean, D.C. Herbert, C.J. Werkhoven, B.J. Fitzpatrick, R.N. Bhargava, Phys. Rev. B **23**, 4888 (1981)
675. B.K. Meyer, J. Sann, S. Lautenschläger, M.R. Wagner, A. Hoffmann, Phys. Rev. B **76**, 184120 (2007)
676. D. Karaiskaj, M.L.W Thewalt, T. Ruf, M. Cardona, H.-J. Pohl, G.G. Deviatych, P.G. Senniko, H. Riemann, Phys. Rev. Lett. **86**, 6010 (2001)
677. D. Karaiskaj, M.L.W Thewalt, T. Ruf, M. Cardona, M. Konuma, Phys. Rev. Lett. **89**, 016401 (2002)
678. S. Müller, D. Stichtenoth, M. Uhrmacher, H. Hofsäss, C. Ronning, J. Röder, Appl. Phys. Lett. **90**, 012107 (2007)
679. V.A. Karasyuk, M.L.W Thewalt, S. An, E.C. Lightowlers, A.S. Kaminskii, Phys. Rev. B **54**, 10 543 (1996)
680. M.L.W. Thewalt, A. Yang, M. Steger, D. Karaiskaj, M. Cardona, H. Riemann, N.V. Abrosimov, A.V. Gusev, A.D. Bulanov, I.D. Kovalev, A.K. Kaliteevskii, O.N. Godisov, P. Becker, H.J. Pohl, E.E. Haller, J.W. Ager III, K.M. Itoh, J. Appl. Phys. **101**, 081724 (2007)
681. J.D. Cuthbert, D.G. Thomas, Phys. Rev. **154**, 763 (1967)
682. J.P. Laurenti, P. Roentgen, K. Wolter, K. Seibert, H. Kurz, J. Camassel, Phys. Rev. B **37**, 4155 (1988)
683. D. Bimberg, M. Sondergeld, E. Grobe, Phys. Rev. B **4**, 3451 (1971)
684. V.D. Kulakovskiĭ, G.E. Pikus, V.B. Timofeev, Sov. Phys. Usp. **24**, 815 (1981)
685. A.S. Kaminskiĭ, Ya.E. Pokrovskiĭ, Pis'ma Zh. Eksp. Teor. Fiz. **11**, 381 (1970) [JETP Lett. 11, 255 (1970)]
686. M.L.W. Thewalt, Can. J. Phys. **55**, 1463 (1977)
687. M.L.W. Thewalt, J.A. Rostworowski, G. Kirczenow, Can. J. Phys. **57**, 1898 (1979)
688. D.G. Chtchekine, Z.C. Feng, S.J. Chua, G.D. Gilliland, Phys. Rev. B **63**, 125211 (2001)
689. O. Goede, L. John, D. Hennig, Phys. Stat. Sol. (B) **89**, K183 (1978)
690. E.F. Schubert, E.O. Göbel, Y. Horikoshi, K. Ploog, H.J. Queisser, Phys. Rev. B **30**, 813 (1984)
691. S. Heitsch, G. Zimmermann, D. Fritsch, C. Sturm, R. Schmidt-Grund, C. Schulz, H. Hochmuth, D. Spemann, G. Benndorf, B. Rheinländer, Th. Nobis, M. Lorenz, M. Grundmann, J. Appl. Phys. **101**, 083521 (2007)
692. R. Zimmermann, J. Cryst. Growth **101**, 346 (1990)
693. J.M Langer, R. Buczko, A.M. Stoneham, Semicond. Sci. Technol. **7**, 547 (1992)
694. M. Grundmann, C.P. Dietrich, J. Appl. Phys. **106**, 123521 (2009)

695. A. Müller, M. Stölzel, G. Benndorf, M. Lorenz, M. Grundmann, J. Appl. Phys. **107**, 013704 (2010)
696. M.C. Wagener, G.R. James, A.W.R. Leitch, F. Omnès, Phys. Stat. Sol. (C) **1**, 2322 (2004)
697. B. Segall, G.D. Mahan, Phys. Rev. **171**, 935 (1968)
698. J. Conradi, R.R. Haering, Phys. Rev. Lett. **20**, 1344 (1968)
699. Y.S. Park, J.R. Schneider, Phys. Rev. Lett. **21**, 798 (1968)
700. D. Kovalev, B. Averboukh, D. Volm, B.K. Meyer, H. Amano, I. Akasaki, Phys. Rev. B **54**, 2518 (1996)
701. S. Permogorov, Optical Emission due to Exciton Scattering by LO Phonons in Semiconductors in *Excitons*, ed. by E.I. Rashba, M.D. Sturge (North-Holland, 1982)
702. M. Wojdak, A. Wysmołek, K. Pakuła, J.M. Baranowski, Phys. Stat. Sol. (B) **216**, 95 (1999)
703. R. Dingle, Phys. Rev. Lett. **23**, 579 (1969)
704. Th. Agne, Identifikation und Untersuchung von Defekten in ZnO Einkristallen, PhD Thesis, Universität des Saarlandes, Saarbrücken, 2004
705. K. Huang, A. Rhys, Proc. Roy. Soc. London A **204**, 406 (1950)
706. J.J. Hopfield, J. Phys. Chem. Solids **10**, 110 (1959)
707. M. Lax, J. Chem. Phys. **20**, 1752 (1952)
708. J.L. Merz, Phys. Rev. **176**, 961 (1968)
709. C. Klingshirn, Phys. Stat. Sol. (B) **71**, 547 (1975)
710. P.J. Dean, C.H. Henry, C.J. Frosch, Phys. Rev. **168**, 812 (1968)
711. W.H. Koschel, U. Kaufmann, S.G. Bishop, Solid State Commun. **21**, 1069 (1977)
712. A. Juhl, Calorimetrische Absorptionsspektroskopie (CAS) – Eine neue Methode zur Charakterisierung der optischen Eigenschaften von Halbleitersystemen, PhD Thesis, Technische Universität Berlin, 1987
713. M. Takeshima, Phys. Rev. B **23**, 6625 (1981)
714. M. Takeshima, Phys. Rev. B **30**, 3302 (1984)
715. P.C. Findlay, C.R. Pidgeon, H. Pellemans, R. Kotitschke, B.N. Murdin, T. Ashley, A.D. Johnson, A.M. White, C.T. Elliott, Semicond. Sci. Technol. **14**, 1026 (1999)
716. D. Vignaud, J.F. Lampin, E. Lefebvre, M. Zaknoune, F. Mollot, Appl. Phys. Lett. **80**, 4151 (2002)
717. D.B. Laks, G.F. Neumark, S.T. Pantelides, Phys. Rev. B **42**, 5176 (1990)
718. P. Blood, J. Orton, *The Electrical Characterization of Semiconductors: Majority Carriers and Electron States* (Academic Press, San Diego, 1992)
719. D. Macdonald, A. Cuevas, Phys. Rev. B **67**, 075203 (2003)
720. D.H. Auston, Semicond. Semimet. **28**, 85 (1990)
721. A.A. Istratov, E.R. Weber, Appl. Phys. A **66**, 123 (1998)
722. A.A. Istratov, H. Hieslmair, E.R. Weber, Appl. Phys. A **69**, 13–44 (1999)
723. A.A. Istratov, H. Hieslmair, E.R. Weber, Appl. Phys. A **70**, 489–534 (2000)
724. J.S. Blakemore, Phys. Rev. **110**, 1301 (1958)
725. M.S. Tyagi, R. van Overstraeten, Solid State Electron. **26**, 577 (1983)
726. G. Bemski, Phys. Rev. **100**, 523 (1955)
727. J. Frenkel, Phys. Rev. **54**, 647 (1938)
728. S. Bothra, S. Tyagi, S. K. Chandhi, J. M. Borrego, Solid State Electron. **34**, 47 (1991)

729. K. Kurita, T. Shingyouji, Jpn. J. Appl. Phys. (Part 1) **38**, 5710 (1999)
730. M.J. Kerr, J. Schmidt, A. Cuevas, J.H. Bultman, J. Appl. Phys. **89**, 3821 (2001)
731. O. Hahneiser, M. Kunst, J. Appl. Phys. **85**, 7741 (1999)
732. D.E. Aspnes, Surf. Sci. **132**, 406 (1983)
733. C. Donolato, J. Appl. Phys. **54**, 1314 (1983)
734. T. Kieliba, S. Riepe, W. Warta, J. Appl. Phys. **100**, 063706 (2006)
735. J. Palm, J. Appl. Phys. **74**, 1169 (1993)
736. A.D. Kurtz, S.A. Kulin, B.L. Averbach, Phys. Rev. **101**, 1285 (1956)
737. E.A. Fitzgerald, D.G. Ast, P.D. Kirchner, G.D. Pettit, J.M. Woodall, J. Appl. Phys. **63**, 693 (1988)
738. M. Grundmann, J. Christen, D. Bimberg, A. Fischer-Colbrie, R. Hull, J. Appl. Phys. **66**, 2214 (1989)
739. T.F. Ciszek, T.H. Wang, R.W. Burrows, X. Wu, J. Alleman, Y.S. Tsuo, T. Bekkedahl, 23th IEEE Photovoltaic Specialists Conf. Rec., IEEE, New York, 1993, p. 101
740. R. Corkish, T. Puzzer, A.B. Sproul, K.L. Luke, J. Appl. Phys. **84**, 5473 (1998)
741. J.Y. Tsao, *Materials Fundamentals of Molecular Beam Epitaxy* (Academic Press, San Diego, 1993)
742. M.L. Hitchman, K.F. Jensen (eds.), *Chemical Vapor Deposition* (Academic Press, San Diego, 1993)
743. P. George, *Chemical Vapor Deposition* (VDM Verlag Dr. Mueller, Saarbrücken, 2008)
744. G. Stringfellow, *Organometallic Vapor-Phase Epitaxy: Theory and Practice* (Academic Press, San Diego, 1999)
745. R. Eason (ed.), *Pulsed Laser Deposition of Thin Films: Applications-Led Growth of Functional Materials* (John Wiley & Sons, Hoboken, 2006)
746. P. Capper, M. Mauk (eds.), *Liquid Phase Epitaxy of Electronic, Optical and Optoelectronic Materials* (John Wiley & Sons, Chichester, 2007)
747. B.A. Joyce, J.H. Neave, P.J. Dobson, P.K. Larsen, Phys. Rev. B **29**, 814 (1984)
748. J.-T. Zettler, W. Richter, K. Ploska, M. Zorn, J. Rumberg, C. Meyne, M. Pristovsek, *Real Time Diagnostics of Semiconductor Surface Modifications by Reflectance Anisotropy Spectroscopy in Semiconductor Characterization – Present Status and Future Needs*, ed. by W. Bullis, D. Seiler, A. Diebold (AIP Press, Woodbury, New York, 1996), p. 537
749. J.-T. Zettler, Prog. Cryst. Growth Charact. Mater. **35**, 27 (1997)
750. W. Zulehner, Status and future of silicon crystal growth. Mat. Sci Engin. B **4**, 1–10 (1989)
751. W. Zulehner, Historical overview of silicon crystal pulling development. Mat. Sci Engin. B **73**, 7–15 (2000)
752. B. Depuydt, A. Theuwis, I. Romandie, Mat. Sci. Semicond. Process. **9**, 437 (2006)
753. Virgina Semiconductor, www.virginiasemi.com
754. G.K. Teal, J.B. Little, Phys. Rev. **78**, 647 (1950)
755. W.G. Pfann, *Zone Melting* (John Wiley & Sons, New York, 1966)
756. H.J. Scheel, T. Fukuda (eds.), *Crystal Growth Technology* (JohnWiley & Sons, New York, 2004)

757. Siltronic AG, Hanns-Seidel-Platz 4 81737 München, Germany
758. K.A. Reinhardt, W. Kern, *Handbook of Silicon Wafer Cleaning Technology* (William Andrew, New York, 2008)
759. W. Kern, Semiconductor International, April 1984, p. 94
760. A. Ishizaka, Y. Shiraki, J. Electrochem. Soc. **133**, 666 (1986)
761. J.C. Kim, J.-Y. Ji, J.S. Kline, J.R. Tucker, T.-C. Shen, Appl. Surf. Sci. **220**, 293 (2003)
762. H. Hartnagel, B.L. Weiss, J. Mat. Sci. **8**, 1061 (1973)
763. Z.F. Tomashik, N.V. Kusyak, V.N. Tomashik, Inorg. Mat. **38**, 434 (2002)
764. H. von Wenckstern, H. Schmidt, C. Hanisch, M. Brandt, C. Czekalla, G. Benndorf, G. Biehne, A. Rahm, H. Hochmuth, M. Lorenz, M. Grundmann, Phys. Stat. Sol. RRL **1**, 129 (2007)
765. C. Weisbuch, Fundamental properties of III–V semiconductor two-dimensional quantized structures: the basis for optical and electronic device applications, Semicond. Semimet. **24**, 1–133 (1987)
766. F.C. Frank, J.H. van der Merwe, Proc. Roy. Soc. London A **198**, 205 (1949)
767. M. Volmer, A. Weber, Z. Phys. Chem. **119**, 277 (1926)
768. I.N. Stranski, L. Krastanow, Sitzungsberichte d. Akad. d. Wissenschaften in Wien, Abt. IIb, Band **146**, 797 (1937)
769. E. Bauer, Z. Kristallogr. **110**, 372 (1958)
770. T. Shitara, D.D. Vvedensky, M.R. Wilby, J. Zhang, J.H. Neave, B.A. Joyce, Phys. Rev. B **46**, 6815 (1992)
771. A. Pimpinelli, J. Villain, *Physics of Crystal Growth* (Cambridge University Press, Cambridge, 1999)
772. E. Ohshima, H. Ogino, I. Niikura, K. Maeda, M. Sato, M. Ito, T. Fukuda, J. Cryst. Growth **260**, 16 (2004)
773. M. Grundmann, T. Böntgen, M. Lorenz, Phys. Rev. Lett. **105**, 14 (2010)
774. J. Ohta, H. Fujioka, M. Oshima, K. Fujiwara, A. Ishii, Appl. Phys. Lett. **83**, 3075 (2003)
775. P.J. Schuck, M.D. Mason, R.D. Grober, O. Ambacher, A.P. Lima, C. Miskys, R. Dimitrov, M. Stutzmann, Appl. Phys. Lett. **79**, 952 (2001)
776. S. Heitsch, C. Bundesmann, G. Wagner, G. Zimmermann, A. Rahm, H. Hochmuth, G. Benndorf, H. Schmidt, M. Schubert, M. Lorenz, M. Grundmann, Thin Solid Films **496**, 234 (2006)
777. A. Strittmatter, S. Rodt, L. Reißmann, D. Bimberg, H. Schröder, E. Obermeier, T. Riemann, J. Christen, A. Krost, Appl. Phys. Lett. **78**, 727 (2001)
778. B.J. Rodriguez, A. Gruveman, A.I. Kingon, R.J. Nemanich, O. Ambacher, Appl. Phys. Lett. **80**, 4166 (2002)
779. A. Dadgar, J. Bläsing, A. Diez, A. Alam, M. Heuken, A. Krost, Jpn. J. Appl. Phys. **39**, L1183 (2000)
780. J. Bläsing, A. Reiher, A. Dadgar, A. Dietz, A. Krost, Appl. Phys. Lett. **81**, 2722 (2002)
781. Y.H. Lo, Appl. Phys. Lett. **59**, 2311 (2005)
782. J.E. Ayers, J. Electr. Mat. **37**, 1511–23 (2008)
783. C. Lynch, E. Chason, R. Beresford, L.B. Freund, K. Tetz, K.W. Schwarz, J. Appl. Phys. **98**, 073532 (2005)
784. K. Sakamoto, T. Sakamoto, S. Nagao, G. Hashiguchi, K. Kuniyoshi, Y. Bando, Jpn. J. Appl. Phys. **26**, 666 (1987)

785. P.M.J. Marée, K. Nakagawa, F.M. Mulders, J.F. van der Veen, Surf. Sci. **191**, 305 (1987)
786. M. Copel, M.C. Reuter, E. Kaxiras, R.M. Tromp, Phys. Rev. Lett. **63**, 632 (1989)
787. D. Kandel, E. Kaxiras, Solid State Phys. **54**, 219 (2000)
788. M. Ilg, D. Eißler, C. Lange, K. Ploog, Appl. Phys. A **56**, 397 (1993)
789. X. Yang, M.J. Jurkovic, J.B. Heroux, W.I. Wang, Electron. Lett. **35**, 1081 (1999)
790. T. Kageyama, T. Miyamoto, M. Ohta, T. Matsuura, Y. Matsui, T. Furuhata, F. Koyama, Appl. Phys. Lett. **96**, 44 (2004)
791. H.J. Osten, J. Klatt, G. Lippert, B. Dietrich, E. Bugiel, Phys. Rev. Lett. **69**, 450 (1992)
792. Ch. G. van der Walle, J. Neugebauer, Nature **423**, 626 (2003)
793. V. Gottschalch, G. Wagner, University of Leipzig, private communication (2006)
794. P. Offermans, Study of III-V semiconductor nanostructures by crosssectional scanning tunneling microscopy, PhD Thesis, Technische Universiteit Eindhoven, 2005
795. S.L. Chuang, *Physics of Optoelectronic Devices* (John Wiley & Sons, New York, 1995)
796. Y.C. Chang, J.N. Schulman, Phys. Rev. B **31**, 2069 (1985)
797. R.C. Miller, D.A. Kleinman, A.C. Gossard, Phys. Rev. B **29**, 7085 (1984)
798. R.C. Miller, A.C. Gossard, W.T. Tsang, O. Munteanu, Phys. Rev. B **25**, 3871 (1982)
799. W.T. Masselink, Y.-Ch. Chang, H. Morkoç, Phys. Rev. B **28**, 7373 (1983)
800. D.B. Tran Thoai, R. Zimmermann, M. Grundmann, D. Bimberg, Phys. Rev. B **42**, 5906 (1990)
801. M.J.L.S. Haines, N. Ahmed, S.J.A. Adams, K. Mitchell, I.R. Agool, C.R. Pidgeon, B.C. Cavenett, E.P. O'Reilly, A. Ghiti, M.T. Emeny, Phys. Rev. B **43**, 11944 (1991)
802. K.J. Moore, G. Duggan, K. Woodbridge, C. Roberts, Phys. Rev. B **41**, 1090 (1990)
803. L. Esaki in *Recent Topics in Semiconductor Physics*, ed. by H. Kamimura, Y. Toyozawa (World Scientific, Singapore, 1983), pp. 1–71
804. R. Dingle, A.C. Gossard, W. Wiegmann, Phys. Rev. Lett. **34**, 1327 (1975)
805. A.L. Efros, F.G. Pikus, G.G. Samsonidze, Phys. Rev. B **41**, 8295 (1990)
806. F. Stern, S. Das Sarma, Phys. Rev. B **30**, 840 (1984)
807. J. Christen, D. Bimberg, Phys. Rev. B **42**, 7213 (1990)
808. L. Pfeiffer, K.W. West, Physica E **20**, 57 (2003)
809. M.S. Skolnick, J.M. Rorison, K.J. Nash, D.J. Mowbray, P.R. Tapster, S.J. Bass, A.D. Pitt, Phys. Rev. Lett. **58**, 2130 (1987)
810. D. Gammon, S. Rudin, T.L. Reinecke, D.S. Katzer, C.S. Kyono, Phys. Rev. B **51**, 16785 (1995)
811. E. Runge, R. Zimmermann, Adv. Solid State Phys. (Festkörperprobleme) **38**, 251 (1998)
812. E. Runge, Solid State Phys. **57**, 149 (2002)
813. M.S. Skolnick, E.G. Scott, B.Wakefield, G.J. Davies, Semicond. Sci. Technol. **3**, 365 (1988)

814. M. Grassi Alessi, F. Fragano, A. Patané, M. Capizzi, E. Runge, R. Zimmermann, Phys. Rev. B **61**, 10985 (2000)
815. Q. Li, S.J. Xu,W.C. Cheng, M.H. Xie, S.Y. Tong, C.M. Che, H. Yang, Appl. Phys. Lett. **79**, 1810 (2001)
816. J. Hegarty, L. Goldner, M.D. Sturge, Phys. Rev. B **30**, 7346 (1984)
817. N.F. Mott, E.A. Davies, *Electronic Processes in Noncrystalline Materials*, 2nd edn. (Oxford University Press, New York, 1979)
818. T. Takeuchi, S. Sota, M. Katsuragawa, M. Komori, H. Takeuchi, H. Amano, I. Akasaki, Jpn. J. Appl. Phys. Part. 1 **36**, L382 (1997)
819. S.F. Chichibu, A.C. Abare, M.S. Minsky, S. Keller, S.B. Fleicher, J.E. Bowers, E. Hu, U.K. Mishra, L.A. Coldern, S.P. DenBaars, Appl. Phys. Lett. **73**, 2005 (1998)
820. C. Morhain, T. Bretagnon, P. Lefebvre, X. Tang, P. Valvin, T. Guillet, B. Gil, T. Taliercio, M. Teisseire-Doninelli, B. Vinter, C. Deparis, Phys. Rev. B **72**, 241305(R) (2005)
821. J.A. Davis, L.V. Dao, X. Wen, C. Ticknor, P. Hannaford, V.A. Coleman, H.H. Tan, C. Jagadish, K. Koike, S. Sasa, M. Inoue, M. Yano, Nanotechnology **19**, 055205 (2008)
822. J. Spitzer, T. Ruf, M. Cardona, W. Dondl, R. Schorer, G. Abstreiter, E.E. Haller, Phys. Rev. Lett. **72**, 1565 (1994)
823. E. Berkowicz, D. Gershoni, G. Bahir, E. Lakin, D. Shilo, E. Zolotoyabko, A.C. Abare, S.P. Denbaars, L.A. Coldren, Phys. Rev. B **61**, 10994 (2000)
824. N. Akopian, G. Bahir, D. Gershoni, M.D. Craven, J.S. Speck, S.P. DenBaars, Appl. Phys. Lett. **86**, 202104 (2005)
825. Q.-Y. Tong, U. Gösele, *Semiconductor Wafer Bonding* (John Wiley & Sons, New York, 1998)
826. M. Alexe, U. Gösele (eds.), *Wafer Bonding* (Springer, Berlin, 2004)
827. A. Reznicek, R. Scholz, S. Senz, U. Gösele, Mater. Chem. Phys. **81**, 277 (2003)
828. P. Kopperschmidt, S. Senz, G. Kästner, D. Hesse, U.M. Gösele, Appl. Phys. Lett. **72**, 3181 (1998)
829. A. Jager, Exzitonen und Franz–Keldysh-Effekt im quaternären Halbleiter In-GaAsP/InP, PhD Thesis, Phillips-Universität Marburg, 1997
830. D.A.B. Miller, D.S. Chemla, T.C. Damen, A.C. Gossard, W. Wiegmann, T.H. Wood, C.A. Burrus, Phys. Rev. B **32**, 1043 (1985)
831. J.M. Luttinger, Phys. Rev. **102**, 1030 (1956)
832. N. Miura, *Physics of Semiconductors in High Magnetic Fields* (Oxford University Press, Oxford, 2008)
833. M. Oestreich, S. Hallstein, A.P. Heberle, K. Eberl, E. Bauser, W.W. Rühle, Phys. Rev. B **53**, 7911 (1996)
834. M.J. Snelling, E. Blackwood, C.J. McDonagh, R.T. Harley, C.T.B. Foxon, Phys. Rev. B **45**, 3922 (1992)
835. M. Schubert, *Infrared Ellipsometry on Semiconductor Layer Structures: Phonons, Plasmons and Polaritons* (Springer, Heidelberg, 2004)
836. M. Schubert, T. Hofmann, C.M. Herzinger, J. Opt. Soc. Am. A **20**, 347 (2003)
837. B. Lax, J.G. Mavroid, H.J. Zeiger, R.J. Keys, Phys. Rev. **122**, 31 (1961)
838. W. Zawadski, R. Lassnig, Solid State Commun. **50**, 537 (1984)

839. H.L. Störmer, R. Dingle, A.C. Gossard, W. Wiegmann, R.A. Logan, Conf. Ser. – Inst. Phys. **43**, 557 (1979)
840. A.B. Fowler, F.F. Fang, W.E. Howard, P.J. Stiles, Phys. Rev. Lett. **16**, 901 (1966)
841. M.A. Paalanen, D.C. Tsui, A.C. Gossard, Phys. Rev. B **25**, 5566 (1982)
842. Physikalisch-Technische Bundesanstalt
843. K. V. Klitzing, G. Dorda, M. Pepper, Phys. Rev. Lett. **45**, 494 (1980)
844. G. Landwehr, Physica E **20**, 1 (2003)
845. E.O. Göbel, Semiconductor applications in metrology. Adv. Solid State Phys. (Festkörperprobleme) **39**, 1–12 (1999)
846. H. Bachmair, E.O. Göbel, G. Hein, J. Melcher, B. Schumacher, J. Schurr, L. Schweitzer, P. Warnecke, Physica E **20**, 14 (2003)
847. J.K. Jain, *Composite Fermions* (Cambridge University Press, 2007, Cambridge)
848. R.E. Prange, Phys. Rev. B **23**, 4802 (1981)
849. M. Büttiker, Phys. Rev. B **38**, 9375 (1988)
850. H. Aoki, T. Ando, Solid State Commun. **38**, 1079 (1981)
851. E. Ahlswede, P. Weitz, J. Weis, K. V. Klitzing, K. Eberl, Physica E **298**, 562 (2001)
852. K. Lier, R.R. Gerhardts, Phys. Rev. B **50**, 7757 (1994)
853. R.B. Laughlin, Phys. Rev. B **23**, 5632 (1981)
854. J.P. Eisenstein, H.L. Störmer, Science **248**, 1510 (1990)
855. J.K. Jain, Phys. Rev. Lett. **63**, 199 (1983)
856. J.K. Jain, Phys. Rev. B **41**, 7653 (1990)
857. H.L. Störmer, D. Tsui, A.C. Gossard, Rev. Mod. Phys. **71**, S298 (1999)
858. D. Weiss, M.L. Roukes, A. Menschig, P. Frambow, K. V. Klitzing, G. Weimann, Phys. Rev. Lett. **66**, 2790 (1991)
859. R.P. Feynman, There's Plenty of Room at the Bottom. After-dinner speech on December 29, 1959 at the annual meeting of the American Physical Society at the California Institute of Technology
860. D. Bimberg, M. Grundmann, N.N. Ledentsov, *Quantum Dot Heterostructures* (John Wiley & Sons, Chichester, 1999)
861. M. Grundmann (ed.), *Nano-Optoelectronics, Concepts, Physics and Devices*, (Springer, Heidelberg, 2002)
862. E. Kapon, M. Walther, J. Christen, M. Grundmann, C. Caneau, D.M. Hwang, E. Colas, R. Bhat, G.H. Song, D. Bimberg, Superlatt. Microstruct. **12**, 491 (1992)
863. M. Grundmann, J. Christen, M. Joschko, O. Stier, D. Bimberg, E. Kapon, Semicond. Sci. Technol. **9**, 1939 (1994)
864. L. Pfeiffer, K.W. West, H.L. Störmer, J.P. Eisenstein, K.W. Baldwin, D. Gershoni, J. Spector, Appl. Phys. Lett. **56**, 1697 (1990)
865. M. Grundmann, D. Bimberg, Phys. Rev. B **55**, 4054 (1997)
866. W. Wegscheider, G. Schedelbeck, G. Abstreiter, M. Rother, M. Bichler, Phys. Rev. Lett. **79**, 1917 (1997)
867. A.P. Levitt (ed.), *Whisker Technology* (John Wiley & Sons, New York, 1970)
868. Zh.L. Wang (ed.), *Nanowires and Nanobelts – Materials, Properties and Devices.* Metal and Semiconductor Nanowires, vol. I and Nanowires and Nanobelts of Functional Materials, vol. II (Kluwer Academic, Boston, 2004)

869. M.T. Björk, B.J. Ohlsen, T. Sass, A.I. Perrson, C. Thelander, M.H. Magnusson, K. Deppert, L.R. Wallenberg, L. Samuelson, Appl. Phys. Lett. **80**, 1058 (2002)
870. M.H. Huang, S. Mao, H. Feick, H. Yan, Y.Wu, H. Kind, E.Weber, R. Russo, P. Yang, Science **292**, 1897 (2001)
871. X. Duan, Y. Huang, R. Agarwal, C. Lieber, Nature **421**, 241 (2003)
872. Zh.L. Wang, J. Song, Science **312**, 242 (2006)
873. M. Lorenz, J. Lenzner, E.M. Kaidashev, H. Hochmuth, M. Grundmann, Ann. Physik **13**, 39 (2004)
874. B.Q. Cao, J. Zúñiga-Pérez, N. Boukos, C. Czekalla, H. Hilmer, J. Lenzner, A. Travlos, M. Lorenz, M. Grundmann, Nanotechnology **20**, 305701 (2009)
875. M.V. Barton, J. Appl. Mech. **8**, A97 (1941)
876. E. Ertekin, P.A. Greaney, D.C. Chrzan, T.D. Sands, J. Appl. Phys. **97**, 114325 (2005)
877. F. Glas, Phys. Rev. B **74**, 121302 (2006)
878. X.Y. Kong, Zh.L. Wang, Appl. Phys. Lett. **84**, 975 (2004)
879. Zh.L. Wang, J. Phys.: Conf. Ser. **26**, 1 (2006)
880. M. Grundmann, E. Kapon, J. Christen, D. Bimberg, Electronic and optical properties of quasi one-dimensional carriers in quantum wires, J. Nonlinear Opt. Phys. and Mater. **4**, 99 (1995)
881. H.J. Xiang, J. Yang, J.G. Hou, Q. Zhu, Appl. Phys. Lett. **89**, 223111 (2006)
882. M. Grundmann, O. Stier, D. Bimberg, Phys. Rev. B **58**, 10557 (1998)
883. O. Stier, M. Grundmann, D. Bimberg, Phys. Rev. B **59**, 5688 (1999)
884. R. Santoprete, B. Koiller, R.B. Capaz, P. Kratzer, Q.K.K. Liu, M. Scheffler, Phys. Rev. B **68**, 235311 (2003)
885. Th. Maltezopoulos, A. Bolz, C. Meyer, C. Heyn, W. Hansen, M. Morgenstern, R. Wiesendanger, Phys. Rev. Lett. **91**, 196804 (2003)
886. O. Stier, Theory of the optical properties of InGaAs/GaAs quantum dots in *Nano-Optoelectronics, Concepts, Physics, Devices*, ed. by M. Grundmann (Springer, Berlin, 2002)
887. L.P. Kouwenhoven, N.C. van der Vaart, A.T. Johnson, W. Kool, C.J.P.M. Harmans, J.G. Williamson, A.A.M. Staring, C.T. Foxon, Z. Phys. B **85**, 367–73 (1991)
888. S. Tarucha, D.G. Austing, T. Honda, R.J. van der Hage, L.P. Kouwenhoven, Phys. Rev. Lett. **77**, 3613 (1996)
889. N. Horiguchi, T. Futatsugi, Y. Nakata, N. Yokoyama, Appl. Phys. Lett. **70**, 2294 (1997)
890. A. Forchel, R. Steffen, M. Michel, A. Pecher, T.L. Reinecke, *Proc. 23rd Int. Conf. on the Physics of Semiconductors*, Berlin (Germany), ed. by M. Scheffler, R. Zimmermann (World Scientific, Singapore, 1996), p. 1285
891. K.C. Rajkumar, K. Kaviani, J. Chen, P. Chen, A.Madhukar, D. Rich, Mater. Res. Soc. Symp. Proc. **263**, 163 (1992)
892. W. Weller, private communication (2006)
893. M. Grundmann, Adv. Solid State Phys. (Festkörperprobleme) **35**, 123 (1996)
894. V.A. Shchukin, N.N. Ledentsov, D. Bimberg, *Epitaxy of Nanostructures* (Springer, Heidelberg, 2004)
895. V.A. Shchukin, D. Bimberg, Phys. Rev. Lett. **75**, 2968 (1995)
896. N. Moll, M. Scheffler, E. Pehlke, Phys. Rev. B **58**, 4566 (1998)

897. D. Leonard, M. Krishnamurthy, C.M. Reaves, S.P. Denbaars, P.M. Petroff, Appl. Phys. Lett. **63**, 3203 (1993)
898. D.M. Bruls, P.M. Koenraad, H.W.M. Salemink, J.H. Wolter, M. Hopkinson, M.S. Skolnick, Appl. Phys. Lett. **82**, 3758 (2003)
899. Q. Xie, A. Madhukar, P. Chen, N. Kobayashi, Phys. Rev. Lett. **75**, 2542 (1995)
900. S. Facsko, T. Dekorsy, C. Koerdt, C. Trappe, H. Kurz, A. Vogt, H.L. Hartnagel, Science **285**, 1551 (1999)
901. F. Frost, A. Schindler, F. Bigl, Phys. Rev. Lett. **85**, 4116 (2000)
902. R. Gago, L. Vásquez, R. Cuerno, M. Varela, C. Ballesteros, J.M. Albella, Appl. Phys. Lett. **78**, 3316 (2001)
903. R. Gago, L. Vásquez, O. Plantevin, T.H. Metzger, J. Muñoz-García, R. Cuerno, M. Castro, Appl. Phys. Lett. **89**, 233101 (2006)
904. B. Ziberi, F. Frost, B. Rauschenbach, Th. Höche, Appl. Phys. Lett. **87**, 033113 (2005)
905. W.L. Chan, E. Chason, J. Appl. Phys. **101**, 121301–1-46 (2007)
906. B. Ziberi, F. Frost, Th. Höche, B. Rauschenbach, Phys. Rev. B **72**, 235310 (2005)
907. O. Stier, A. Schliwa, R. Heitz, M. Grundmann, D. Bimberg, Phys. Stat. Sol. (B) **224**, 115 (2001)
908. D.J.P. Ellis, R.M. Stevenson, R.J. Young, A.J. Shields, P. Atkinson, D.A. Ritchie, Appl. Phys. Lett. **90**, 011907 (2007)
909. B. Urbaszek, R.J. Warburton, K. Karrai, B.D. Gerardot, P.M. Petroff, J.M. Garcia, Phys. Rev. Lett. **90**, 247403 (2003)
910. R.J. Warburton, C. Schäflein, D. Haft, F. Bickel, A. Lorke, K. Karrai, J.M. Garcia, W. Schoenfeld, P.M. Petroff, Nature **405**, 926 (2000)
911. F. Findeis, A. Zrenner, G. Böhm, G. Abstreiter, Solid State Commun. **114**, 227 (2000)
912. L. Besombes, Y. Léger, L. Maingault, D. Ferrand, H. Mariette, Phys. Rev. Lett. **93**, 207403–1 (2004)
913. M. Fiebig, Revival of the magnetoelectric effect. J. Phys. D: Appl. Phys. **38**, R123–R152 (2005)
914. W. Eerenstein, N.D. Mathur, J.F. Scott, Multiferroic and magnetoelectric materials. Nature **442**, 759 (2006)
915. V.M. Fridkin, *Ferroelectric Semiconductors* (translated from Russian) (Plenum, New York, 1980)
916. Y. Xu, *Ferroelectric Materials and Their Applications* (North Holland, Amsterdam, 1991)
917. K. Rabe, Ch. H. Ahn, J.-M. Triscone (eds.), *Physics of Ferroelectrics.* Topics in Applied Physics, vol. 105 (Springer, Berlin, 2007)
918. Nils Ashcroft, Cornell University, private communication (2006)
919. R. Comes, M. Lambert, A. Guinier, Solid State Commun. **6**, 715 (1968)
920. R.E. Cohen, Nature **358**, 136 (1992)
921. G. Shirane, S. Hoshino, J. Phys. Soc. Jpn. **6**, 265 (1951)
922. W.J. Merz, Phys. Rev. **76**, 1221 (1949)
923. D.K. Agrawal, C.H. Perry, Phys. Rev. B **4**, 1893 (1971)
924. G. Rupprecht, R.O. Bell, Phys. Rev. **135**, A748 (1964)
925. M.E. Lines, Phys. Rev. **177**, 819 (1969)
926. W.J. Merz, Phys. Rev. **91**, 513 (1953)

927. P.W. Forsbergh, Jr., Phys. Rev. **76**, 1187 (1949)
928. C. Gähwiller, Phys. Condens. Mater. **6**, 269 (1967)
929. G. Arlt, P. Quadflieg, Phys. Stat. Sol. **25**, 323 (1968)
930. M. Grundmann, O. Stier, D. Bimberg, Phys. Rev. B **50**, 14187 (1994)
931. D.L. Smith, C. Mailhiot, J. Appl. Phys. **63**, 2717 (1988)
932. A. Al-Yacoub, L. Bellaiche, S.-H Wei, Phys. Rev. Lett. **89**, 057601 (2002)
933. J.G. Gualtieri, J.A. Kosinski, A. Ballato, IEEE Trans. Ultrason. Ferroelectr. Freq. Control **41**, 53 (1994)
934. O. Ambacher, private communication (2005)
935. P. Waltereit, O. Brandt, A. Trampert, H.T. Grahn, J. Menniger, M. Ramsteiner, M. Reiche, K.H. Ploog, Nature **406**, 865 (2000)
936. C.Q. Chen, V. Adivarahan, J.W. Yang, M. Shatalov, E. Kuokstis, M.A. Khan, Jpn. J. Appl. Phys. Part 2 **42**, L1039 (2003)
937. R. Sharma, P.M. Pattison, H. Masui, R.M. Farrel, T.J. Baker, B.A. Haskell, F.Wu, S.P. DenBaars, J.S. Speck, S. Nakamura, Appl. Phys. Lett. **87**, 231110 (2005)
938. S.-H. Park, J. Appl. Phys. **91**, 9904 (2002)
939. H. Sato, R.B. Chung, H. Hirasawa, N. Fellows, H. Masui, F. Wu, M. Saito, K. Fujito, J.S. Speck, S.P. DenBaars, S. Nakamura, Appl. Phys. Lett. **92**, 221110 (2008)
940. A.D. Andreev, E.P. O'Reilly, Phys. Rev. B **62**, 15851 (2000)
941. J.K. Furdyna, J. Kossut (eds.), Diluted magnetic semiconductors, Semicond. Semimet. **25** (1988)
942. D. Awshalom, D. Loss, N. Samarth (eds.), *Semiconductor Spintronics and Quantum Computation.* Nanoscience and Technology (Springer, Berlin, 2002)
943. S.J. Pearton, C.R. Abernathy, M.E. Overberg, G.T. Thaler, D.P. Norton, N. Theodoropoulou, A.F. Hebard, Y.D. Park, F. Ren, J. Kim, L.A. Boatner, J. Appl. Phys. **93**, 1 (2003)
944. I. Tsubokawa, J. Phys. Soc. Jpn. **15**, 1664 (1960)
945. B.T. Matthias, R.M. Bozorth, J.H. van Vleck, Phys. Rev. Lett. **7**, 160 (1961)
946. G. Güntherodt, Phys. Cond. Matter **18**, 37–78 (1974)
947. P.G. Steeneken, New light on EuO thin films: preparation, transport, magnetism and spectroscopy of a ferromagnetic semiconductor, PhD Thesis, Rijksuniversiteit Groningen, 2002
948. P.Wachter, in *Handbook on the Physics and Chemistry of Rare Earths*, ed. by K.A. Gschneider Jr., L. Eyring, Chap. 19, (1979), p. 507
949. T. Fukumura, H. Toyosaki, Y. Yamada, Semicond. Sci. Technol. **20**, S103 (2005)
950. W. Giriat, J.K. Furdyna, Crystal structure, composition, and materials preparation of diluted magnetic semiconductors in Ref. [934], p. 1
951. C. Rigaux, Magnetooptics in narrow gap diluted magnetic semiconductors in Ref. [934], p. 229
952. C. Domb, N.W. Dalton, Proc. Phys. Soc. London **89**, 859 (1966)
953. C. Zener, Phys. Rev. **81**, 440 (1951)
954. H. Akai, Phys. Rev. Lett. **81**, 3002 (1998)
955. T. Dietl, H. Ohno, F. Matsukura, J. Cibert, D. Ferrand, Science **287**, 1019 (2000)

956. H. Munekata, H. Ohno, S. von Molnár, A. Segmüller, L.L. Chang, L. Esaki, Phys. Rev. Lett. **63**, 1849 (1989)
957. H. Ohno, M. Munekata, T. Penney, S. von Molnár, L.L. Chang, Phys. Rev. Lett. **68**, 2664 (1992)
958. H. Ohno, A. Shen, F. Matsukura, A. Oiwa, A. Endo, S. Katsumoto, Y. Iye, Appl. Phys. Lett. **69**, 363 (1996)
959. Y.-J. Zhao, P. Mahadevan, A. Zunger, Appl. Phys. Lett. **84**, 3753 (2004)
960. H. Ohno, D. Chiba, F. Matsukura, T. Omiya, E. Abe, T. Dietl, Y. Ohno, K. Ohtani, Nature **408**, 944 (2000)
961. S.T.B. Goennenwein, Th.A. Wassner, H. Huebl, M.S. Brandt, J.B. Philipp, M. Opel, R. Gross, A. Koeder, W. Schoch, A. Waag, Phys. Rev. Lett. **92**, 227202 (2004)
962. P. Sharma, A. Gupta, K. V. Rao, F.J. Owens, R. Sharma, R. Ahuja, J.M. Osorio Guillen, B. Johansson, G.A. Gehring, Nature Mater. **2**, 673–77 (2003)
963. M. Diaconu, H. Schmidt, H. Hochmuth, M. Lorenz, G. Benndorf, D. Spemann, A. Setzer, P. Esquinazi, A. Pöppl, H. von Wenckstern, K.-W. Nielsen, R. Gross, H. Schmid, W. Mader, G. Wagner, M. Grundmann, J. Magn. and Magn. Mat. **307**, 212 (2006)
964. E.I. Rashba, Physica E **20**, 189 (2004)
965. M.I. Dyakonov, V.I. Perel, Sov. Phys. Solid State **13**, 3023 (1972)
966. S. Datta, B. Das, Appl. Phys. Lett. **56**, 665 (1990)
967. A.T. Kanbicki, O.M.J. van 't Erve, R. Magno, G. Kioseoglou, C.H. Li, B.T. Jonker, Appl. Phys. Lett. **82**, 4092 (2003)
968. B.T. Jonker, S.C. Erwin, A. Petrou, A.G. Petukhov, MRS Bull. **28**(10), 740 (2003)
969. C.L. Braun, *Organic Semiconductors*. Handbook on Semiconductors, vol. 3 (North Holland, Amsterdam, 1982), pp. 857–73
970. W. Brütting (ed.), *Physics of Organic Semiconductors* (Wiley-VCH, Weinheim, 2005)
971. Th.U. Kampen, *Low Molecular Weight Organic Semiconductors* (Wiley-VCH, Weinheim, 2009)
972. D. Braun, A. Heeger, Appl. Phys. Lett. **58**, 1982 (1991)
973. A. McL. Mathieson, J. Monteath Robertson, V.C. Sinclair, Acta Cryst. **3**, 245 (1950)
974. N. Karl, High purity organic molecular crystals in *Crystals: Growth, Properties and Applications*, vol. 4, ed. by H.C. Freyhardt (Springer, Berlin, 1980), p. 1
975. N. Karl, J. Cryst. Growth **99**, 1009 (1990)
976. Ch. Kloc, P.G. Simpkins, T. Siegrist, R. A. Laudise, J. Cryst. Growth **182**, 416 (1997)
977. R.A. Laudise, Ch. Kloc, P.G. Simpkins, T. Siegrist, J. Cryst. Growth **187**, 449 (1998)
978. M. Mas-Torrent, M. Durkut, P. Hadley, X. Ribas, C. Rovira, J. Am. Chem. Soc. **126**, 984 (2004)
979. M. Campione, R. Ruggerone, S. Tavazzi, M. Moret, J. Mat. Chem. **15**, 2437 (2005)
980. A. Curioni, W. Andreoni, R. Treusch, F.J. Himpsel, E. Haskal, P. Seidler, C. Heske, S. Kakar, T. van Buuren, L.J. Terminello, Appl. Phys. Lett. **72**, 1575 (1998)

981. J. Monteath Robertson, V.C. Sinclair, J. Trotter, Acta Cryst. **14**, 697 (1961)
982. M. Oehzelt, A. Aichholzer, R. Resel, G. Heimel, E. Venuti, R.G. Della Valle, Phys. Rev. B **74**, 104103 (2006)
983. A. Kahn, N. Koch, W. Gao, J. Polymer Sc.: Part B: Polymer Phys. **41**, 2529–48 (2003)
984. B.A. Gregg, S.-G. Chen, H.M. Branz, Appl. Phys. Lett. **84**, 1707 (2004)
985. M. Pfeiffer, A. Beyer, T. Fritz, K. Leo, Appl. Phys. Lett. **73**, 3202 (1998)
986. B.A. Gregg, S.-G. Chen, R.A. Cormier, Chem. Mater. **16**, 4586 (2004)
987. G.F. Neumark, Phys. Rev. B **5**, 408 (1972)
988. A.J. Heeger, S. Kivelson, J.R. Schrieffer, W.-P. Su, Rev. Mod. Phys. **60**, 781 (1988)
989. P.W.M. Blom, M.C.J.M. Vissenberg, Mat. Sci Engin. **27**, 53 (2000)
990. L.B. Schein, Phys. Rev. B **15**, 1024 (1977)
991. L.B. Schein, C.B. Duke, A.R. McGhie, Phys. Rev. Lett. **40**, 197 (1978)
992. L. Li, G. Meller, H. Kosina, Microelectr. J. **38**, 47 (2007)
993. Y. Kawasumi, I. Akai, T. Karasawa, Int. J. Mod. Phys. B **15**, 3825 (2001)
994. M.A. Baldo, S.R. Forrest, Phys. Rev. B **62**, 10958 (2000)
995. W. Humbs, H. Zhang, M. Glasbeek, Chem. Phys. **254**, 319 (2000)
996. Z. Vardeny, E. Ehrenfreund, J. Shinar, F. Wudl, Phys. Rev. B **35**, 2498 (1987)
997. J.-W. van der Horst, P.A. Bobbert, M.A.J. Michels, Phys. Rev. B **66**, 035206 (2002)
998. A. Baldo, D.F. O'Brien, M.E. Thompson, S.R. Forrest, Phys. Rev. B **60**, 14422 (1999)
999. M.A. Baldo, M.E. Thompson, S.R. Forrest, Nature **403**, 750 (2000)
1000. M.A. Baldo, S. Lamansky, P.E. Burrows, M.E. Thompson, S.R. Forrest, Appl. Phys. Lett. **75**, 4 (1999)
1001. A. Baldo, D.F. O'Brien, Y. You, A. Shoustikov, S. Sibley, M.E. Thompson, S.R. Forrest, Nature **395**, 151 (1998)
1002. C. Adachi, M.A. Baldo, M.E. Thompson, S.R. Forrest, J. Appl. Phys. **90**, 5048 (2001)
1003. T. Förster, Discuss. Faraday Soc. **27**, 7–17 (1959)
1004. K.S. Novoselov, A.K. Geim, S.V. Morozov, D. Jiang, Y. Zhang, S.V. Dubonos, I.V. Grigorieva, A.A. Firsov, Science **306**, 666 (2004)
1005. K.S. Novoselov, D. Jiang, F. Schedin, T.J. Booth, V.V. Khotkevich, S.V. Morozov, A.K. Geim, PNAS **102**, 10451 (2005)
1006. J.S. Bunch, A.M. van der Zande, S.S. Verbridge, I.W. Frank, D.M. Tanenbaum, J.M. Parpia, H.G. Craighead, P.L. McEuen, Science **315**, 490 (2007)
1007. Ch.L. Kane, Nature **438**, 168 (2005)
1008. K.S. Novoselov, A.K. Geim, S.V. Morozov, D. Jiang, M.I. Katsnelson, I.V. Grigorieva, S.V. Dubonos, A.A. Firsov, Nature **438**, 197 (2005)
1009. onnes.ph.man.ac.uk/ kostya/Graphene.html
1010. P.R. Wallace, Phys. Rev. **71**, 622 (1947)
1011. R. Saito, G. Dresselhaus, M.S. Dresselhaus, *Physical Properties of Carbon Nanotubes* (Imperial, London, 1998)
1012. S. Reich, J. Maultzsch, C. Thomsen, P. Ordejón, Phys. Rev. B **66**, 035412 (2002)
1013. L. Wirtz, A. Rubio, Solid State Commun. **131**, 141 (2004)

1014. 1107. A. Bostwick, T. Ohta, Th. Seyller, K. Horn, E. Rotenberg, Nature Physics **3**, 36 (2006)
1015. B. Partoens, F.M. Peeters, Phys. Rev. B **74**, 075404 (2006)
1016. T. Ohta, A. Bostwick, Th. Seyller, K. Horn, E. Rotenberg, Science **313**, 951 (2006)
1017. S.V. Vonsovsky, M.I. Katsnelson, *Quantum Solid State Physics* (Springer, New York, 1989)
1018. M.S. Sercheli, Y. Kopelevich, R. Ricardo da Silva, J.H.S. Torres, C. Rettori, Solid State Commun. **121**, 579 (2002)
1019. K.I. Bolotin, K.J. Sikes, Z. Jiang, M. Klima, G. Fudenberg, J. Hone, P. Kim, H.L. Störmer, Solid State Commun. **146**, 351 (2008)
1020. K.S. Novoselov, Z. Jiang, Y. Zhang, S.V. Morozov, H.L. Störmer, U. Zeitler, J.C. Maan, G.S. Boebinger, P. Kim, A.K. Geim, Science Express 15 Feb 2007, 1, 2007
1021. O. Klein, Z. Phys. **53**, 157 (1929)
1022. A. Calogeracos, N. Dombey, History and physics of the Klein paradox. Contemp. Phys. **40**, 313–21 (1999)
1023. M.I. Katsnelson, K.S. Novoselov, A.K. Geim, Nature Physics **2**, 620 (2006)
1024. Y. Miyamoto, M.L. Cohen, S.G. Louie, Phys. Rev. B **52**, 14971 (1995)
1025. S. Iijima, Nature **354**, 56 (1991)
1026. S. Iijima, T. Ichihasi, Nature **363**, 603 (1993)
1027. S. Reich, C. Thomsen, J. Maultzsch, *Carbon Nanotubes: Basic Concepts and Physical Properties* (Wiley-VCH, Berlin, 2004)
1028. J. Kïti, V. Zólyomi, M. Kertesz, G. Sun, New J. Phys. **5**, 125 (2003)
1029. R. Saito, M. Fujita, G. Dresselhaus, M.S. Dresselhaus, Appl. Phys. Lett. **60**, 2204 (1992)
1030. M.-F. Yu, B.S. Files, S. Arepalli, R.S. Ruoff, Phys. Rev. Lett. 84, 5552 (2000)
1031. S. Ogata, Y. Shibutani, Phys. Rev. B **68**, 165409 (2003)
1032. R. Saito, M. Fujita, G. Dresselhaus, M.S. Dresselhaus, MRS Symp. Proc. **247**, 333 (1992)
1033. J.W. Mintmire, C.T. White, Phys. Rev. Lett. **81**, 2506 (1989)
1034. N. Hamada, S.-I. Sawada, A. Oshiyama, Phys. Rev. Lett. **68**, 1579 (1992)
1035. X. Blase, Lorin X. Benedict, Eric L. Shirley, S.G. Louie, Phys. Rev. Lett. **72**, 1878 (1994)
1036. N.G. Chopra, R.J. Luyken, K. Cherrey, V.H. Crespi, M.L. Cohen, S.G. Louie, A. Zettl, Science **269**, 966 (1995)
1037. R.S. Lee, J. Gavillet, M.L. de la Chapelle, A. Loiseau, J.-L. Cochon, D. Pigache, J. Thibault, F. Willaime, Phys. Rev. B **64**, 121405(R) (2001)
1038. A. Rubio, J.L. Corkill, M.L. Cohen, Phys. Rev. B **49**, 5081 (1994)
1039. L. Wirtz, V. Olevano, A.G. Marinopoulos, L. Reining, A. Rubio, AIP Conf. Proc. **685**, 406 (2003)
1040. A. Grüneis, R. Saito, G.G. Samsonidze, T. Kimura, M.A. Pimenta, A. Jorio, A.G. Souza Filho, G. Dresselhaus, M.S. Dresselhaus, Phys. Rev. B **67**, 165402 (2003)
1041. S.M. Bachilo, M.S. Strano, C. Kittrell, R.H. Hauge, R.E. Smalley, R.B. Weisman, Science **298**, 2361 (2002)
1042. H. Telg, J. Maultzsch, S. Reich, F. Hennrich, C. Thomsen, Phys. Rev. Lett. **93**, 177401 (2004)

1043. C. Thomsen, S. Reich, Raman Scattering in Carbon Nanotubes, *Light Scattering in Solids IX*, ed. by M. Cardona, R. Merlin, Topics Appl. Phys. vol. 108 (Springer, Berlin, 2007), p. 115
1044. R.R. Willey, *Practical Design and Production of Optical Thin Films* (CRC Press, London, 2002)
1045. J.M. Bendickson, J.P. Dowling, M. Scalora, Phys. Rev. E **53**, 4107 (1996)
1046. J. Gottmann, A. Husmann, T. Klotzbücher, E.W. Kreutz, Surf. Coat. Tech. **100–101**, 415 (1998)
1047. J. Sellmann, Ch. Sturm, R. Schmidt-Grund, Ch. Czekalla, J. Lenzner, H. Hochmuth, B. Rheinländer, M. Lorenz, M. Grundmann, Phys. Stat. Sol. (C) **5**, 1240 (2008)
1048. C.M. Soukoulis (ed.), *Photonic Crystals and Light Localization in the 21st Century*, NATO Science Series C, vol. 563 (Kluwer Academic Publishers, Dordrecht, 1996)
1049. J.D. Joannopoulos, R.D. Meade, J.N. Winn, *Photonic Crystals* (Princeton University Press, Princeton, NJ, 1995)
1050. K. Busch, S. Lölkes, R.B. Wehrspohn, H. Föll (eds.), Photonic Crystals (Wiley-VCH, Berlin, 1994)
1051. E.-X. Ping, J. Appl. Phys. **76**, 7188 (1994)
1052. B. Rauschenbach, Leibniz-Institut für Oberflächenmodifizierung, Leipzig, private communication (2006)
1053. N. Kaiser, Fraunhofer-Institute for Applied Optics, Jena, Germany
1054. K.M. Ho, C.T. Chan, C.M. Soukoulis, Phys. Rev. Lett. **65**, 3152 (1990)
1055. O. Toader, S. John, Science **292**, 1133 (2001)
1056. S.R. Kennedy, M.J. Brett, O. Toader, S. John, Nano Lett. **2**, 59 (2002)
1057. K. Busch, S. John, Phys. Rev. E **58**, 3896 (1998)
1058. E. Yablonovitch, T.J. Gmitter, K.M. Leung, Phys. Rev. Lett. **67**, 2295 (1991)
1059. K.M. Ho, C.T. Chan, C.M. Soukoulis, R. Biswas, M. Sigalas, Solid State Commun. **89**, 413 (1994)
1060. A. Chutinan, S. Noda, Phys. Rev. B **57**, R2006 (1998)
1061. S. Fan, P.R. Villeneuve, R.D. Meade, J.D. Joannopoulos, Appl. Phys. Lett. **65**, 1466 (1994)
1062. H.S. Sözüer, J.W. Haus, J. Opt. Soc. Am. B **10**, 296 (1993)
1063. H.S. Sözüer, J.W. Haus, R. Inguva, Phys. Rev. B **45**, 13962 (1992)
1064. S. John, K. Busch, J. Lightw. Techn. **17**, 1931 (1999)
1065. F. Garcia-Santamaria, C. López, F. Meseguer, F. López-Tejeira, J. Sánchez-Dehesa, H.T. Miyazaki, Appl. Phys. Lett. **79**, 2309 (2001)
1066. A. Blanco, E. Chomski, S. Grabtchak, M. Ibisate, S. John, S.W. Leonard, C. Lopez, F. Meseguer, H. Miguez, J.P. Mondia, G.A. Ozin, O. Toader, H.M. van Driel, Nature **405**, 437 (2000)
1067. A.F. Koenderink, A. Lagendijk, W.L. Vos, Phys. Rev. B **72**, 153102 (2005)
1068. Y. Zhu, Q. Wu, S. Morin, T.W. Mossberg, Phys. Rev. Lett. **65**, 1200 (1990)
1069. C. Weisbuch, M. Nishioka, A. Ishikawa, Y. Arakawa, Phys. Rev. Lett. **69**, 3314 (1992)
1070. M. Lončar, D. Nedeljković, T. Doll, J. Vučović, A. Scherer, T.P. Pearsall, Appl. Phys. Lett. **77**, 1937 (2000)
1071. V. Savona, Z. Hadril, A. Quattropani, P. Schwendimann, Phys. Rev. B **49**, 8774 (1994)

1072. G. Khitrova, H.M. Gibbs, F. Jahnke, M. Kira, S.W. Koch, Rev. Mod. Phys. **71**, 1591 (1999)
1073. M.S. Skolnick, T.A. Fisher, D.M. Whittaker, Semicond. Sci. Technol. **13**, 645 (1998)
1074. P.J. Klar, G. Rowland, P.J.S. Thomas, A. Onischenko, T.E. Sale, T.J.C. Hosea, R. Grey, Phys. Rev. B **59**, 2894 (1999)
1075. J.J. Baumberg, P.G. Savvidis, R.M. Stevenson, A.I. Tartakovskii, M.S. Skolnick, D.M. Whittaker, J.S. Roberts, Phys. Rev. B **62**, R16247 (2000)
1076. A. Kavokin, G. Malpuech, B. Gil, MRS Internet J. Nitride Semicond. Res. **8**, 3 (2003)
1077. Le Si Dang, D. Heger, R. André, F. Boeuf, R. Romestain, Phys. Rev. Lett. **81**, 3920 (1998)
1078. A. Pawlis, D.J. As, D. Schikora, J. Schörmann, K. Lischka, Phys. Stat. Sol. (C) **1**, 202 (2004)
1079. T. Tawara, H. Gotoh, T. Akasaka, N. Kobayashi, T. Saitoh, Phys. Rev. Lett. **92**, 256402 (2004)
1080. N. Antoine-Vincent, F. Natali, D. Byrne, P. Disseix, A. Vasson, J. Leymarie, F. Semond, J. Massies, Superlatt. Microstruct. **36**, 599 (2004)
1081. E. Feltin, G. Christmann, R. Butté, J.-F. Carlin, M. Mosca, N. Grandjean, Appl. Phys. Lett. **89**, 071107 (2006)
1082. F. Semond, I. R. Sellers, F. Natali, D. Byrne, M. Leroux, J. Massies, N. Ollier, J. Leymarie, P. Disseix, A. Vasson, Appl. Phys. Lett. **87**, 021102 (2005)
1083. R. Schmidt-Grund, B. Rheinländer, C. Czekalla, G. Benndorf, H. Hochmuth, M. Lorenz, M. Grundmann, Appl. Phys. B **93**, 331 (2008)
1084. P.G. Savvidis, J.J. Baumberg, R.M. Stevenson, M.S. Skolnick, D.M. Whittaker, J.S. Roberts, Phys. Rev. Lett. **84**, 1547 (2000)
1085. S.L. McCall, A.F.J. Levi, R.E. Slusher, S.J. Pearton, R.A. Logan, Appl. Phys. Lett. **60**, 289 (1992)
1086. R.P. Wang, M.-M. Dumitrescu, J. Appl. Phys. **81**, 3391 (1997)
1087. A.F.J. Levi, R.E. Slusher, S.L. McCall, J.L. Glass, S.J. Pearton, R.A. Logan, Appl. Phys. Lett. **62**, 561 (1993)
1088. S.-K. Kim, S.-H. Kim, G.-H. Kim, H.-G. Park, D.-J. Shin, Y.-H. Lee, Appl. Phys. Lett. **84**, 861 (2004)
1089. E. Peter, P. Senellart, D. Martrou, A. Lemaître, J. Hours, J. M. Gérard, J. Bloch, Phys. Rev. Lett. **95**, 067401 (2005)
1090. J.M. Gérard, B. Sermage, B. Gayral, B. Legrand, E. Costard, V. Thierry-Mieg, Phys. Rev. Lett. **81**, 1110 (1998)
1091. E.M. Purcell, Phys. Rev. **69**, 681 (1946)
1092. A. Kiraz, P. Michler, C. Becher, B. Gayral, A. Imamoğlu, Lidong Zhang, E. Hu, W.V. Schoenfeld, P.M. Petroff, Appl. Phys. Lett. **78**, 3932 (2001)
1093. J.U. Nöckel, A.D. Stone, Nature **385**, 45 (1997)
1094. C. Gmachl, F. Capasso, E.E. Narimanov, J.U. Nöckel, A.D. Stone, J. Faist, D.L. Sivco, A.Y. Cho, Science **280**, 1556 (1998)
1095. G.D. Chern, H.E. Tureci, A. Douglas Stone, R.K. Chang, M. Kneissl, N.M. Johnson, Appl. Phys. Lett. **83**, 1710 (2003)
1096. S.-Y. Lee, S. Rim, J.-W. Ryu, T.-Y. Kwon, M. Choi, C.-M. Kim, Phys. Rev. Lett. **93**, 164102 (2004)

1097. M. Kneissl, M. Teepe, N. Miyashita, N.M. Johnson, G.D. Chern, R.K. Chang, Appl. Phys. Lett. **84**, 2485 (2004)
1098. T. Nobis, E.M. Kaidashev, A. Rahm, M. Lorenz, M. Grundmann, Phys. Rev. Lett. **93**, 103903 (2004)
1099. F. Leiter, H. Zhou, F. Henecker, A. Hofstaetter, D.M. Hofmann, B.K. Meyer, Physica B **908**, 308–310, (2001)
1100. J. Wiersig, Phys. Rev. A **67**, 023807 (2003)
1101. C. Czekalla, C. Sturm, R. Schmidt-Grund, B. Cao, M. Lorenz, M. Grundmann, Appl. Phys. Lett. **92**, 241102 (2008)
1102. F. Streintz, Ann. Physik **314**, 854 (1902)
1103. H.L. Hartnagel, A.L. Dawar, A.K. Jain, C. Jagadish, *Semiconducting Transparent Thin Films* (Institute of Physics Publishing, Philadelphia, 1995)
1104. MRS Bulletin, August 2000 issue
1105. T. Minami, Semicond. Sci. Technol. **20**, S35–S44 (2005)
1106. R.G. Gordon, MRS Bull. **8**, 52 (2000)
1107. H. Kawazoe, M. Yasukawa, H. Hyodo, M. Kurita, H. Yanagi, H. Hosono, Nature **389**, 939 (1997)
1108. M. Marezio, Acta Cryst. **20**, 723 (1966)
1109. S.H. Brewer, S. Franzen, Chem. Phys. **300**, 285 (2004)
1110. O.N. Mryasov, A.J. Freeman, Phys. Rev. B **64**, 233111 (2001)
1111. K. Nomura, H. Ohta, A. Takagi, T. Kamiya, M. Hirano, H. Hosono, Nature **432**, 488 (2004)
1112. H. Agura, A. Suzuki, T. Matsushita, T. Aoki, M. Okuda, Thin Solid Films **445**, 263 (2003)
1113. T. Minami, S. Suzuki, T. Miyata, Mat. Res. Soc. Symp. Proc. **666**, F1.3.1 (2001)
1114. D.S. Ginley, C. Bright, MRS Bull. **8**, 15 (2000)
1115. J.R. Bellingham, W.A. Phillips, C.J. Adkins, J. Mat. Sci. Lett. 11, 263 (1992)
1116. H.K. Henisch, Rectifying Semiconductor Contacts (Oxford University Press (Clarendon), London, 1957)
1117. J.R. Macdonald, Solid State Electron. **5**, 11 (1962)
1118. F.A. Padovani, The voltage–current characteristic of metal–semiconductor contacts. Semicond. Semimet. **7**, 75 (1971)
1119. E.H. Rhoderick, Inst. Phys. Conf. Ser. **22**, 3 (1974)
1120. E.H. Rhoderick, R.H. Williams, *Metal-Semiconductor Contacts* (Oxford Press, 1988)
1121. A.M. Cowley, S.M. Sze, J. Appl. Phys. **36**, 3212 (1965)
1122. A. Dimoulas, P. Tsipas, A. Sotiropoulos, E.K. Evangelou, Appl. Phys. Lett. **89**, 252110 (2006)
1123. C.A. Mead, *Ohmic Contacts to Semiconductors*, ed. by B. Schwartz (Electrochemical Society, New York, 1969), pp. 3–16
1124. S. Kurtin, T.C. McGill, C.A. Mead, Phys. Rev. Lett. **22**, 1433 (1969)
1125. C.A. Mead, Phys. Lett. **18**, 218 (1965)
1126. J. Bardeen, Phys. Rev. **71**, 717 (1947)
1127. W. Mönch, 125 years of metal-semiconductor contacts: where do we stand? Adv. Solid State Phys. (Festkörperprobleme) **39**, 13–24 (1999)
1128. W. Schottky, Phys. Z. **15**, 872 (1914)
1129. S.M. Sze, C.R. Crowell, D. Kahng, J. Appl. Phys. **35**, 2534 (1964)
1130. A.M. Goodman, J. Appl. Phys. **34**, 329 (1963)

1131. C. Opdorp, Solid State Electron. **11**, 397 (1968)
1132. M. Schmidt, R. Pickenhain, M. Grundmann, Solid State Electron. **51**, 1002 (2007)
1133. S. Dueñas, M. Jaraiz, J. Vicente, E. Rubio, L. Bailón, J. Barbolla, J. Appl. Phys. **61**, 2541 (1987)
1134. D.L. Losee, J. Appl. Phys. **46**, 2204 (1975)
1135. M.P. Verkhovodov, H.P Peka, D.A. Pulemyotov, Semicond. Sci. Technol. **8**, 1842 (1993)
1136. F.D. Auret, J.M. Nela, M. Hayesa, L. Wua, W. Weschb, E. Wendlerb, Superlatt. Microstruct. **39**, 17 (2006)
1137. M. Schmidt, M. Ellguth, C. Czekalla, H. von Wenckstern, R. Pickenhain, M. Grundmann, G. Brauer, W. Skorupa, M. Helm, Q. Gu, Ch.Ch. Ling, J. Vac. Sci. Technol. B **27**, 1597 (2009)
1138. C. Wagner, Phys. Z **32**, 641 (1931)
1139. W. Schottky, E. Spenke, Wiss. Veröff. Siemens Werke **18**, 225 (1939)
1140. H.A. Bethe, MIT Radiation Lab. Report 43–12 (1942)
1141. J.H. Werner, H.H. Güttler, J. Appl. Phys. **69**, 1522 (1991)
1142. H. von Wenckstern, G. Biehne, R. Abdel Rahman, H. Hochmuth, M. Lorenz, M. Grundmann, Appl. Phys. Lett. **88**, 092102 (2006)
1143. J.H. Werner, Appl. Phys. A **47**, 291 (1988)
1144. F.A. Padovani, G.G. Summer, J. Appl. Phys. **36**, 3744 (1965)
1145. F.A. Padovani, R. Stratton, Solid State Electron. **9**, 695 (1966)
1146. W. Mönch, J. Vac. Sci. Technol. B **17**, 1867 (1999)
1147. C.R. Crowell, S.M. Sze, Solid State Electron. **9**, 1035 (1966)
1148. C.R. Crowell, M. Beguwala, Solid State Electron. **14**, 1149 (1971)
1149. J.M. Andrews, M.P. Lepselter, Solid State Electron. **13**, 1011 (1970)
1150. T. Sanada, O. Wada, Jpn. J. Appl. Phys. **49**, L491 (1980)
1151. N. Braslau, J.B. Gunn, J.L. Staples, Solid State Electron. **10**, 381 (1967)
1152. A.Y.C. Yu, Solid State Electron. **13**, 239 (1970)
1153. C.Y. Chang, Y.K. Fang, S.M. Sze, Solid State Electron. **14**, 541 (1971)
1154. C.L. Chen, L.J. Mahoney, M.C. Finn, R.C. Brooks, A. Chu, J.G. Mavroides, Appl. Phys. Lett. **48**, 535 (1986)
1155. V.L. Rideout, Solid State Electron. **18**, 541 (1975)
1156. B.C. Sharma, Ohmic contacts to III–V compound semiconductors. Semicond. Semimet. **15**, 1–38 (1981)
1157. G.Y. Robinson, Solid State Electron. **18**, 331 (1975)
1158. C.M. Heller, I.H. Campbell, D.L. Smith, N.N. Barashkov, J.P. Ferraris, J. Appl. Phys. **81**, 3227 (1997)
1159. I.H. Campbell, T.W. Hagler, D.L. Smith, J.P Ferraris, Phys. Rev. Lett. **76**, 1900 (1996)
1160. I.H. Campbell, D.L. Smith, Physics of organic electronic devices, Solid State Phys. **55**, 1 (2001)
1161. Frieder Baumann, Lucent Technologies Bell Labs.
1162. C.G.B. Garrett, W.H. Brattain, Phys. Rev. **99**, 376 (1955)
1163. A.S. Grove, B.E. Deal, E.H. Snow, C.T. Shah, Solid State Electron. **8**, 145 (1965)
1164. B.E. Deal, E.H. Snow, C.A. Mead, J. Phys. Chem. Solids **27**, 1873 (1966)
1165. W.M. Werner, Solid State Electron. **17**, 769 (1974)

1166. J.F. Guilleomoles, I. Lubomirsky, I. Riess, D. Cahen, J. Phys. Chem. **99**, 14486 (1995)
1167. W.F. O'Hearn, Y.F. Chang, Solid State Electron. **13**, 473 (1970)
1168. M. Grundmann, Solid State Electron. **49**, 1446 (2005)
1169. H.K. Gummel, Solid State Electron. **10**, 209 (1967)
1170. J.L. Moll, *Physics of Semiconductors* (McGraw-Hill, New York, 1964)
1171. M.J.O. Strutt, *Semiconductor Devices*, vol. 1 (Academic, New York, 1966), Chap. 2
1172. S. Mahadevan, S.M. Hardas, G. Suryan, Phys. Stat. Sol. (A) **8**, 335 (1971)
1173. D. Lausch, K. Petter, H. von Wenckstern, M. Grundmann, Phys. Stat. Sol. RRL **3**, 70 (2009)
1174. W. Fulop, Solid State Electron. **10**, 39 (1967)
1175. S.M. Sze, G. Gibbons, Appl. Phys. Lett. **8**, 111 (1966)
1176. B.J. Baliga, S.K. Ghandhi, Solid State Electron. **19**, 739 (1976)
1177. M.H. Lee, S.M. Sze, Solid State Electron. **23**, 1007 (1980)
1178. A. Goetzberger, B. McDonald, R.H. Haitz, R.M. Scarlet, J. Appl. Phys. **34**, 1591 (1963)
1179. B.J. Baliga, *Modern Power Devices* (John Wiley & Sons, New York, 1987)
1180. B.J. Baliga, *Fundamentals of Power Semiconductor Devices* (Springer, Berlin, 2008)
1181. S.M. Sze, G. Gibbons, Solid State Electron. **9**, 831 (1966)
1182. J. Yang, J. Shen, J. Appl. Phys. **85**, 2699 (1999)
1183. J. Staudigel, M. Stößel, F. Steuber, J. Simmerer, J. Appl. Phys. **86**, 3895 (1999)
1184. J. Blochwitz, Organic light-emitting diodes with doped charge transport layers, PhD Thesis, Technische Universität Dresden, 2001
1185. K. Harada, A.G. Werner, M. Pfeiffer, C.J. Bloom, C.M. Elliott, K. Leo, Phys. Rev. Lett. **94**, 036601 (2005)
1186. S.A. Van Slyke, C.H. Chen, C.W. Tang, Appl. Phys. Lett. **69**, 2160 (1996)
1187. T. Oyamada, H. Yoshizaki, H. Sasabe, C. Adachi, Chem. Lett. **33**, 1034 (2004)
1188. Virginia Diodes, Inc., www.virginiadiodes.com
1189. A. Dearn, L. Devlin, Plextek Ltd., UK
1190. *Tuning varactors*, Application Note, MicroMetrics Inc., Londonderry, NH, USA
1191. *BY329 Product Specifications*, Philips Semiconductors (1998)
1192. *Step recovery diodes*, Application Note, MicroMetrics Inc., Londonderry, NH, USA
1193. M.R.T. Tan, S.Y. Yang, D.E. Mars, J.L. Moll, Hewlett Packard, Palo Alto, CA, USA (1991)
1194. E.O. Kane, J. Phys. Chem. Solids **12**, 181 (1959)
1195. L. Esaki, Y. Miyahara, Solid State Electron. **1**, 13 (1960)
1196. N. Holonyak Jr., I.A. Lesk, R.N. Hall, J.J. Tiemann, H. Ehrenreich, Phys. Rev. Lett. **3**, 167 (1959)
1197. A.G. Chynoweth, R.A. Logan, D.E. Thomas, Phys. Rev. **125**, 877 (1962)
1198. M. Bao, K.L. Wang, IEEE Trans. Electron Devices **53**, 2564 (2006)
1199. P.J. Bulmann, G.S. Hobson, B.S: Taylor, *Transferred Electron Devices* (Academic, New York, 1972)

1200. A. Khalid, N.J. Pilgrim, G.M. Dunn, M.C. Holland, C.R. Stanley, I.G. Thayne, D.R.S. Cumming, IEEE Electr. Dev. Lett. **28**, 849 (2007)
1201. V.N. Sokolov, K.W. Kimb, V.A. Kochelap, D.L. Woolard, J. Appl. Phys. **98**, 064507 (2005)
1202. A. Rdyberg, IEEE Electr. Dev. Lett. **11**, 439 (1990)
1203. H. Eisele, Electron. Lett. **42**, 358 (2006)
1204. R. Van Zyl, W. Perold, R. Botha, *The Gunn-Diode: Fundamentals and Fabrication*, Proc. 1998 South African Symposium on Communications and Signal Processing, 1998, pp. 407–12
1205. H.J.A. Bluyssen, L.J. van Ruyven, F. Williams, Solid State Electron. **22**, 573 (1979)
1206. A.L. Linsebigler, G. Lu, J.T. Yates, Chem. Rev. **95**, 735–58 (1995)
1207. D. Duonghong, E. Borgarello, M. Grätzel, J. Am. Chem. Soc. **103**, 4685 (1981)
1208. K.Y. Jung, Y.Ch. Kang, S.B. Park, J. Mater. Sci. Lett. **16**, 1848 (1997)
1209. J.L. Yang, S.J. An, W.I. Park, G.-Ch. Yi, W. Choi, Adv. Mater. **16**, 1661 (2004)
1210. Canon Inc., www.canon.com/technology
1211. B.F. Levine, J. Appl. Phys. **74**, R1 (1993)
1212. H.C. Liu, R. Dudek, A. Shen, E. Dupont, C.Y. Song, Z.R. Wasilewski, M. Buchanan, Appl. Phys. Lett. **79**, 4237 (2001)
1213. Fraunhofer-Institut für Angewandte Festkörperphysik, Freiburg, www.iaf.fraunhofer
1214. M.D. Petroff, M.G. Stapelbroek, Blocked impurity band detectors, US Patent 4,568,960, filed 1980, awarded 1986
1215. N.M. Haegel, Proc. SPIE **4999**, 182 (2003)
1216. F. Szmulowicz, F.L. Madarsz, J. Appl. Phys. **62**, 2533 (1987)
1217. H.Melchior, *Demodulation and Photodetection Techniques*, ed. by F.T. Arecchi, E.O. Schulz-Dubois. Laser Handbook, vol. 1 (North-Holland, Amsterdam, 1972), p. 725–835
1218. G.E. Stillman, C.M. Wolfe, Semicond. Semimet. **12**, 291 (1977)
1219. Datasheet Position Sensitive Photodiodes, DL-100–7-KER pin (2002), Silicon Sensor GmbH, Berlin (Germany), www.silicon-sensor.com
1220. S.M. Sze, D.J. Coleman, A. Loya, Solid State Electron. **14**, 1209 (1971)
1221. D. Kuhl, Herstellung und Charakterisierung von MSM Detektoren, PhD Thesis, Technische Universität Berlin, 1992
1222. S.Y. Chou, M.Y. Liu, IEEE J. Quantum Electr. **QE-28**, 2358 (1992)
1223. R.J. McIntyre, IEEE Trans. Electron Devices **ED-13**, 164 (1966)
1224. R.D. Baertsch, IEEE Trans. Electron Devices **ED-13**, 987 (1966)
1225. W.S. Boyle, G.E. Smith, Bell Syst. Tech. J., **49**, 587 (1970)
1226. J.D.E. Beynon, D.R. Lamb (eds.), *Charge-Coupled Devices and Their Applications* (McGraw-Hill, Maidenhead, 1977)
1227. J.-W. Shi, K.-G. Gan, Y.-J. Chiu, Y.-H. Chen, C.-K. Sun, Y.-J. Yang, J.E. Bowers, IEEE Phot. Technol. Lett. **16**, 623 (2001)
1228. A. Goetzberger, E.H. Nicollian, Bell Syst. Tech. J. **46**, 513 (1967)
1229. J.D.E. Beynon, Microelectron. **7**, 7 (1975)
1230. Charge-coupled device (CCD) image sensors, MTD/PS-0218, Rev. 1 (2001), Eastman Kodak Company, Rochester, NY, www.kodak.com/go/ccd

1231. J.E. Carnes, W.F. Kosonocky, E.G. Ramberg, IEEE Trans. Electron Devices **ED-19**, 798 (1972)
1232. C.H. Sequin, M.F. Tompsett, *Charge Transfer Devices* (Academic, New York, 1975)
1233. D.J. Burt, Int. Conf. Technol. Appl. CCD, University of Edinburgh, 1974, p. 1
1234. SONY Corporation, www.sony.net
1235. B.E. Bayer, Color imaging array, US Patent 3,971,065, filed 1975, awarded 1976
1236. Datasheet *CMOS linear image sensor*, S9226 (2003), www.hamamatsu.com
1237. Foveon Inc., www.foveon.com
1238. R.B. Merrill, Color separation in an active pixel cell imaging array using a triple-well structure, US Patent 5,965,875, filed 1998, awarded 1999
1239. Datasheet *Avalanche Photodiode Array*, AD-LA-16–9-DIL 18 (2002), Silicon Sensor GmbH, Berlin, Germany, www.silicon-sensor.com
1240. Datasheet *InGaAs Linear Photodiode Array*, SU1024LE-1.7 (2003), Sensors Unlimited, Inc., www.sensorsinc.com
1241. Datasheet *Quadrant Photodiode with Position Sensing*, QD50–0-SD (2004), Centrovision, OSI Systems, Inc., Newbury Park, CA, USA, www.centrovision.com
1242. J.J. Loferski, *The First Forty Years: A Brief History of the Modern Photovoltaic Age*. Progress in Photovoltaics, vol. 1, (1993), pp. 67–78
1243. Published in 'Progress in Photovoltaics: Research and Applications'. The latest tables (version 33) can be found in M.A. Green, K. Emery, Y. Hishikawa, W. Warta, Prog. Photovolt: Res. Appl. **17**, 85 (2009)
1244. R. Leemans, W. Cramer, *The IIASA database for mean monthly values of temperature, precipitation and cloudiness on a global terrestrial grid*, Research Report RR-91–18. International Institute of Applied Systems Analyses, Laxenburg, (1991), pp. 61
1245. W.W. Gärtner, Phys. Rev. **116**, 84 (1959)
1246. X. Liu, J. Sites, J. Appl. Phys. **75**, 577 (1994)
1247. H.H. Hovel, Semicond. Semimet. **11**, 8 (1975)
1248. S. Hegedus, D. Desai, C. Thompson, Prog. Photovolt: Res. Appl. **15**, 587–602 (2007)
1249. C.H. Henry, J. Appl. Phys. **51**, 4494 (1980)
1250. W. Shockley, H.-J. Queisser, J. Appl. Phys. **32**, 510 (1961)
1251. H.-J. Queisser, Mat. Sci Engin. B **159**, 322 (2008)
1252. Th. Kirchartz, U. Rau, Phys. Stat. Sol. (A) **205**, 2737 (2008)
1253. J.H. Werner, S. Kolodinski, H.-J. Queisser, Phys. Rev. Lett. **72**, 3851 (1994)
1254. T. Markvart, Phys. Stat. Sol. (A) **205**, 2752 (2008)
1255. A. Hauser, I. Melnyk, P. Fath, S. Narayanan, S. Roberts, T.M. Bruton, *Proc. of 3rd World Conference on Photovoltaic Energy Conversion*, vol. 2, 1447 (2003)
1256. M.B. Prince, J. Appl. Phys. **26**, 534 (1955)
1257. J. Mandelkorn, J.H. Lamneck, Conf. Rec. 9th IEEE Photovoltaic Spec. Conf. (IEEE, New York, 1972), p. 83
1258. A. Woyte, J. Nijs, R. Belmans, Sol. Energy **74**, 217 (2003)
1259. J. W. Bishop, Solar Cells **25**, 73 (1988)
1260. K. Wambach, S. Schlenker, I. Röver, Deutsche Solar AG, Freiberg

1261. R.A. Arndt, J.F. Allison, J.G. Haynos, A. Meulenberg Jr., Conf. Rec. 11th IEEE Photovoltaic Spec. Conf. (IEEE, New York, 1975), p. 40
1262. J.H. Werner, K. Taretto, U. Rau, Solid State Phenom. **80–81**, 299 (2001)
1263. M. Imaizumi, T. Ito, M. Yamaguchi, K. Kaneko, J. Appl. Phys. **81**, 7635 (1997)
1264. A.K. Ghosh, C. Fishman, T. Feng, J. Appl. Phys. **51**, 446 (1980)
1265. K.R. Taretto: Modeling and characterization of polycrystalline silicon for solar cells and microelectronics, PhD Thesis, Universität Stuttgart, 2003
1266. NREL, www.nrel.gov/gis/solar.html
1267. Australian CRC for Renewable Energy Ltd. (ACRE), acre.murdoch.edu.au
1268. R.R. King, D.C. Law, K.M. Edmondson, C.M. Fetzer, G.S. Kinsey, H. Yoon, R.A. Sherif, N.H. Karam, Appl. Phys. Lett. **90**, 183516 (2007)
1269. V. Probst, J. Palm, S. Visbeck, T. Niesen, R. Tölle, A. Lerchenberger, M. Wendl, H. Vogt, H. Calwer, W. Stetter, F. Karg, Sol. Energy Mater. Sol. Cells **90**, 3115 (2006)
1270. H. Hoppe, N.S. Sariciftci, J. Mater. Res. **19**, 1924 (2004)
1271. S.E. Shaheen, C.J. Brabec, N.S. Sariciftci, F. Padinger, T. Fromherz, J.C. Hummelen, Appl. Phys. Lett. **78**, 841 (2001)
1272. V. Shrotriya, G. Li, Y. Yao, T. Moriarty, K. Emery, Y. Yang, Adv. Funct. Mater. **16**, 2016 (2006)
1273. Solarion GmbH, Leipzig (Germany), www.solarion.de
1274. T. Trupke, M.A. Green, P. Würfel, J. Appl. Phys. **92**, 1668 (2002)
1275. T. Trupke, M.A. Green, P. Würfel, J. Appl. Phys. **92**, 4117 (2002)
1276. A. Luque, A. Martí, Phys. Rev. Lett. **78**, 5014 (1997)
1277. K.M. Yu, W. Walukiewicz, J. Wu, W. Shan, J.W. Beeman, M.A. Scarpulla, O.D. Dubon, P. Becla, Phys. Rev. Lett. **91**, 246403 (2003)
1278. A. Franceschetti, S. Lanya, G. Bester, Low-dimensional systems and nanostructures. Physica E **41**, 15 (2008)
1279. A. Luque, A. Martí, A.J. Nozik, MRS Bull. **32**, 236 (2007)
1280. S. Suraprapapich, S. Thainoi, S. Kanjanachuchai, S. Panyakeow, Sol. Energy Mater. Sol. Cells **90**, 2968 (2006)
1281. F. Dimroth, Physica Status Solidi (C) **3**, 373 (2006)
1282. R.R. King, D.E. Joslin, H. Karam, Multijunction photovoltaic cell with thin 1st (top) subcell and thick 2nd subcell of same or similar semiconductor material, US patent 6,316,715, filed 2000, awarded 2001
1283. Gergö Létay, Modellierung von III–V Solarzellen, PhD Thesis, Universität Konstanz, 2003
1284. Spectrolab, www.spectrolab.com
1285. F. Dimroth, S. Kurtz, MRS Bull. **32**, 230 (2007)
1286. US Department of Energy, www.eere.energy.gov/solar
1287. J.H. Werner, Adv. Solid State Phys. (Festkörperprobleme) **44**, 51 (2004)
1288. S.E. Derenzo, M.J. Weber, E. Bourret-Courchesne, M.K. Klintenberg, Nucl. Instrum Methods **A505**, 111–117 (2003)
1289. Y.A. Ono, *Electroluminescent Displays* (World Scientific, Singapore, 1995)
1290. Glenn F. Knoll, *Radiation Detection and Measurement*, 3rd edn. (JohnWiley & Sons, New York, 2000)
1291. G. Hoffmann, FH Emden, Private Communication (2006)
1292. M. Nikl, V.V. Laguta, A. Vedda, Phys. Stat. Sol. (B) 245, 1701 (2008)

1293. S.E. Derenzo, W.W. Moses, M.J. Weber, A.C.West, Mater. Res. Soc. Symp. **348**, 39 (1994)
1294. E.F. Schubert, *Light-emitting Diodes* (Cambridge University Press, 2003)
1295. A.A. Bergh, P.J. Dean, Proc. IEEE **60**, 156–223 (1972)
1296. M.R. Krames, O.B. Shchekin, R. Mueller-Mach, G.O. Mueller, L. Zhou, G. Harbers, M.G. Craford, IEEE J. Displ. Technol. **3**, 160 (2007)
1297. R.D. Dupuis, M.R. Krames, History, development, and applications of high-brightness visible light-emitting diodes. IEEE J. Lightw. Techn. **26**, 1154 (2008)
1298. H.P.Maruska, D.A. Stevenson, J.I. Pankove, Appl. Phys. Lett. **22**, 303 (1973)
1299. N. Koide, H. Kato, S. Yamasaki, K. Manabe, M. Hashimoto, H. Amano, K. Hiramatsu, I. Aksaki, J. Cryst. Growth **115**, 639 (1991)
1300. W.N. Carr, Infrared Phys. **6**, 1 (1966)
1301. S.V. Galginaitis, J. Appl. Phys. **36**, 460 (1965)
1302. M.G. Craford, IEEE Trans. Electron Devices **ED-24**, 935 (1977)
1303. V. Haerle, B. Hahn, S. Kaiser, A. Weimar, S. Bader, F. Eberhard, A. Plössl, D. Eisert, Phys. Stat. Sol. (A) **201**, 2736 (2004)
1304. OSRAM Opto Semiconductors GmbH (2001), Regensburg, Germany, www.osram-os.com
1305. LumiLeds Lighting, www.lumileds.com
1306. OSRAM Opto Semiconductors GmbH (2003), Regensburg, Germany, www.osram-os.com
1307. M.G. Craford, MRS Bull. **25**(10), 27 (2000)
1308. R. Mueller-Mach, G. Mueller, M.R. Krames, H.A. Höppe, F. Stadler, W. Schnick, Th. Juestel, P. Schmidt, Phys. Stat. Sol. (A) **202**, 1727 (2005)
1309. Technical Datasheet DS51 (6/08) for Luxeon K2 (2008), www.philipslumileds.com
1310. S. Weise, Th. Zahner, Th. Lutz, A. Stich, *Reliability of the DRAGON® Product Family*, Application Note Feb. 2009, www.osram-os.com
1311. Application note STS-KSE3692, Nichia Corp. (2004)
1312. A. Lochmann, E. Stock, O. Schulz, F. Hopfer, D. Bimberg, V.A. Haisler, A.I. Toropov, A.K. Bakarov, A.K. Kalagin, Electron. Lett. **42**, 774 (2006)
1313. R.M. Stevenson, R.J. Young, P. Atkinson, K. Cooper, D.A. Ritchie, A.J. Shields, Nature **439**, 179 (2006)
1314. R.J. Young, R.M. Stevenson, P. Atkinson, D.A. Ritchie, A.J. Shields, New J. Phys. **8**, 29 (2006)
1315. A.J. Shields, Semiconductor quantum light sources, Nat. Photonics **1**, 215 (2007)
1316. A. Lochmann, E. Stock, O. Schulz, F. Hopfer, D. Bimberg, V.A. Haisler, A.I. Toropov, A.K. Bakarov, M. Scholz, S. Büttner, O. Benson, Phys. Stat. Sol. (C) **4**, 547 (2007)
1317. S.K. Ray, K.M. Groom, M.D. Beattie, H.Y. Liu, M. Hopkinson, R.A. Hogg, IEEE Phot. Technol. Lett. **18**, 58 (2006)
1318. C.W. Tang, S.A. Van Slyke, Appl. Phys. Lett. **51**, 913 (1987)
1319. E.U. Rafailov, M.A. Cataluna, W. Sibbett, Nat. Photonics **1**, 395 (2007)
1320. OSRAM Opto Semiconductors GmbH (2007), Regensburg, Germany, www.osram-os.com
1321. www.pioneerelectronics.com
1322. Model XEL-1 (2009), www.sony.com

1323. H.C. Casey, M.B Panish, *Heterostructure Lasers*, 1st edn. (Academic Press, New York, 1978) (Two volumes. Part A: Fundamental Principles and Part B: Materials and Operating Characteristics.)
1324. H. Kressel, J. Butler, *Semiconductor Lasers and LEDs* (Academic Press, New York, 1st edn., 1977)
1325. J. Faist, F. Capasso, D.L. Sivco, C. Sirtori, A.L. Hutchinson, A.Y. Cho, Science **264**, 553 (1994)
1326. Lasers and Photonics Marketplace Seminar 2008
1327. H. Haug, S.W. Koch, *Quantum Theory of the Optical and Electronic Properties of Semiconductors* (World Scientific, Singapore, 1994)
1328. W.W. Chow, P.M. Smowton, P. Blood, A. Girndt, F. Jahnke, S.W. Koch, Appl. Phys. Lett. **71**, 157 (1997)
1329. N. Kirstaedter, N.N. Ledentsov, M. Grundmann, D. Bimberg, V.M. Ustinov, S.S. Ruvimov, M.V. Maximov, P.S. Kop'ev, Zh.I. Alferov, U. Richter, P. Werner, U. Gösele, J. Heydenreich, Electron. Lett. **30**, 1416 (1994)
1330. M. Grundmann, Physica E **5**, 167 (2000)
1331. M.B. Panish, I. Hayashi, S. Sumski, Appl. Phys. Lett. **16**, 326 (1970)
1332. L.A. D'Asaro, J. Lumin. **7**, 310 (1973)
1333. H. Wenzel, F. Bugge, G. Erbert, R. Hülsewede, R. Staske, G. Tränkle, Electron. Lett. **37**, 351 (2001)
1334. H. Yonezu, I. Sakuma, K. Kobayashi, T. Kamejima, M. Ueno, Y. Nannichi, Jpn. J. Appl. Phys. **12**, 1585 (1973)
1335. M. Kamp, J. Hofmann, A. Forchel, S. Lourdudoss, Appl. Phys. Lett. **78**, 4074 (2001)
1336. M. Kamp, private communication (2006)
1337. M. Fujite, R. Ushigome, T. Baba, IEEE Phot. Technol. Lett. **13**, 403 (2001)
1338. G. Björk, A. Karlsson, Y. Yamamoto, Phys. Rev. A **50**, 1675 (1994)
1339. Y. Yamamoto, S. Machida, G. Björk, Phys. Rev. A **44**, 657 (1991)
1340. N.A. Pikhtin, S.O. Slipchenko, Z.N. Sokolova, A.L. Stankevich, D.A. Vinokurov, I.S. Tarasov, Zh.I. Alferov, Electron. Lett. **40**, 1413 (2004)
1341. A. Knigge, G. Erbert, J. Jonsson, W. Pittroff, R. Staske, B. Sumpf, M. Weyers, G. Tränkle, Electron. Lett. **41**, 250 (2005)
1342. D. Garbuzov, I. Kudryashov, A. Komissarov, M. Maiorov, W. Roff, J. Connolly, Optical Fiber Communication Conference, OSA Technical Digest Series, WD1 (Optical Society of America, Washington, D.C., 2003)
1343. T. Kimura, M. Nakae, J. Yoshida, S. Iizuka, A. Sato, *Optical Fiber Digest Series*, ThN5 485–486 (Optical Society of America, Washington, D.C., 2002)
1344. W.T. Tsang, R.A. Logan, J.P. Van der Ziel, Appl. Phys. Lett. **34**, 644 (1979)
1345. M. Grundmann, Appl. Phys. Lett. **77**, 1428 (2000)
1346. F. Heinrichsdorff, C. Ribbat, M. Grundmann, D. Bimberg, Appl. Phys. Lett. **76**, 556 (2000)
1347. M. Grundmann, O. Stier, S. Bognár, C. Ribbat, F. Heinrichsdorff, D. Bimberg, Phys. Stat. Sol. (A) **178**, 255 (2000)
1348. Ch. Ribbat, R. Sellin, M. Grundmann, D. Bimberg, Phys. Stat. Sol. (B) **224**, 819 (2000)
1349. D. Garbuzov, I. Kudryashov, A. Tsekoun, A. Komissarov, W. Roff, M. Maiorov, R. Menna, A. Lunev, J. Connolly, Optical Fiber Communication Conference 2002, Technical Digest: ThN6 (2002)

1350. D. Garbuzov, M. Maiorov, R. Menna, A. Komissarov, V. Khalfin, I. Kudryashov, A. Lunev, L. DiMarco, J. Connolly, Proc. SPIE **4651**, 92 (2002)
1351. M.-C. Amann, J. Buus, *Tunable Laser Diodes* (Artech House, Boston, 1998)
1352. Datasheet *High-Power 1550 nm DFB Source Lasers, A1112*, Agere Systems (2001), www.agere.com
1353. J.N. Walpole, A.R. Calawa, T.C. Harman, S.H. Groves, Appl. Phys. Lett. **28**, 552 (1976)
1354. S.-L. Lee, I.-F. Jang, C.-T. Pien, C.-Y. Wang, T.-T. Shih, IEEE Phot. Technol. Lett. **11**, 955 (1999)
1355. B. Mason, G.A. Fish, S.P. DenBaars, L.A. Coldren, IEEE Phot. Technol. Lett. **10**, 1211 (1998)
1356. C.J. Hwang, J.C. Dyment, J. Appl. Phys. **44**, 3240 (1973)
1357. N.K. Dutta, S.J. Wang, A.B. Piccirilli, R.F. Karlicek Jr., R.L. Brown, M. Washington, U.K. Chakrabarti, A. Gnauck, J. Appl. Phys. **66**, 4640 (1989)
1358. J.S. Gustavsson, Å. Haglund, J. Bengtsson, A. Larsson, IEEE J. Quantum Electr. **QE-38**, 1089 (2002)
1359. C.H. Henry, IEEE J. Quantum Electr. **QE-18**, 259 (1982)
1360. Y. Yamamoto, H.A. Haus, Phys. Rev. A **41**, 5164 (1990)
1361. D. Welford, A. Mooradian, Appl. Phys. Lett. **40**, 865 (1982); Appl. Phys. Lett. **41**, 1007 (1982) (erratum)
1362. Quintessence Photonics Corporation, www.qpc.cc
1363. K. Iga, *Vertical-cavity Surface-emitting Laser Devices* (Springer, Berlin, 2003)
1364. BinOptics Corporation, Ithaca, NY, www.binoptics.com
1365. Sandia National Laboratories, www.sandia.gov
1366. www.ulm-photonics.de
1367. C.J. Chang-Hasnain, Tunable VCSELs, IEEE J. Sel. Topics Quantum Electron. **6**, 978 (2000)
1368. K.D. Choquette, MRS Bull. **27**(7), 507 (2002)
1369. M. Schulze, J.-M. Pelaprat, Photon. Spectra **5** (2001)
1370. R.F. Kazarinov, R.A. Suris, Fiz. Tekh. Poluprovodn, **5**, 797 (1971)
1371. F. Capasso, K. Mohammed, A.Y. Cho, IEEE J. Quantum Electr. **22**, 1853 (1986)
1372. Bandwidth 9, www.bw9.com
1373. F. Römer, C. Prott, J. Daleiden, S. Irmer, M. Strassner, A. Tarraf, H. Hillmer, IEEE LEOS International Semiconductor Laser Conference, Garmisch/Germany (2002)
1374. Datasheet *Sapphire*™ *488–20 laser* (2004), Coherent Inc.
1375. F. Capasso, www.bell-labs.com
1376. J. Faist, www.qoe.ethz.ch
1377. H. Krömer, Phys. Rev. **109**, 1856 (1958)
1378. A.A. Andronov, I.V. Zverev, V.A. Kozlov, Yu.N. Nozdrin, S.A. Pavlov, V. N. Shastin, Pis'ma Zh. Eksp. Teor. Fiz. **40**, 69 (1984) [JETP Lett. **40**, 804 (1984)]
1379. Opt. Quantum Electron. 23, Special Issue *Far-infrared Semiconductor Lasers*, ed. by E. Gornik, A.A. Andronov (Chapman and Hall, London, 1991)

1380. E. Bründermann, Widely tunable far infrared hot hole semiconductor lasers, in *Long-Wavelength Infrared Semiconductor Lasers* ed. by H.K. Choi (John Wiley & Sons, New York, 2004), pp. 279–350
1381. E. Bründermann, A.M. Linhart, H.P. Röser, O.D. Dubon, W.L. Hansen, E.E. Haller, Appl. Phys. Lett. **68**, 1359 (1996)
1382. E. Bründermann, D.R. Chamberlin, E.E. Haller, Appl. Phys. Lett. **76**, 2991 (2000)
1383. N.K. Dutta, Q. Wang, *Semiconductor Optical Amplifiers* (World Scientific, Singapore, 2006)
1384. A.J. Collar, G.D. Henshall, J. Farré, B. Mikkelsen, Z. Wang, L. Eskildsen, D.S. Olesen, K.E. Stubkjaer, IEEE Phot. Technol. Lett. **2**, 553 (1990)
1385. G. Jost, University of Ulm, Department of Optoelectronics, Annual Report 1998, p. 64
1386. Ferdinand-Braun-Institut für Höchstfrequenztechnik, Berlin, www.fbh-berlin.de
1387. M. Sugawara, N. Hatori, M. Ishida, H. Ebe, Y. Arakawa, T. Akiyama, K. Otsubo, T. Yamamoto, Y. Nakata, J. Phys. D: Appl. Phys. **38**, 2126–34 (2005)
1388. N. Yasuko, K. Kawaguchi, H. Ebe, T. Akiyama, M. Ekawa, K. Morito, M. Sugawara, Y. Arakawa, Phys. Rev. Lett. **20**, 1908 (2008)
1389. P. Borri, S. Schneider, W. Langbein, U. Woggon, A.E. Zhukov, V.M. Ustinov, N.N. Ledentsov, Zh.I. Alferov, D. Ouyang, D. Bimberg, Appl. Phys. Lett. **79**, 2633 (2001)
1390. P.G.A Jespers, Measurements for Bipolar Devives in *Process and Device Modelling for Integrated Circuit Design*, ed. by F. van de Wiele, W.L. Engl, P.G. Jespers (Noordhoff, Leyden, 1977)
1391. M.J. Morant, *Introduction to Semiconductor Devices* (Addison-Wesley, Reading, MA, 1964)
1392. H.K. Gummel, H.C. Poon, Bell Syst. Tech. J. **49**, 827 (1970)
1393. D.C. Herbert, Semicond. Sci. Technol. **10**, 682 (1995)
1394. D. Cui, D. Sawdai, D. Pavlidis, S.H. Hsu, P. Chin, T. Block, *Proc. of the 12th Int. Conf. on Indium Phosphide and Related Materials*, 2000, p. 473
1395. Solid State Electronics Laboratory, University of Michigan, www.eecs.umich.edu
1396. M. Feng, N. Holonyak Jr., R. Chan, Appl. Phys. Lett. **84**, 1952 (2004)
1397. R.R. Bockemuehl, IEEE Trans. Electron Devices **ED-10**, 31 (1963)
1398. R.D. Middlebrook, I. Richer, Solid State Electron. **6**, 542 (1963)
1399. K. Lehovec, R. Zuleeg, Solid State Electron. **13**, 1415 (1970)
1400. H.C. Pao, C.T. Sah, Solid State Electron. **9**, 927 (1966)
1401. K. Yamaguchi, IEEE Trans. Electron Devices **ED-26**, 1068 (1979)
1402. R.R. Troutman, IEEE J. Solid-State Circ. **SC-9**, 55 (1974)
1403. W. Maly, *Atlas of IC technologies – An Introduction to VLSI Processes* (Benjamin/Cummings Publishing Company, San Francisco, 1987)
1404. D. Udeshi, E. Maldonado, Y. Xu, M. Tao, W.P. Kirk, J. Appl. Phys. **95**, 4219 (2004)
1405. G.E. Moore, Cramming more components onto integrated circuits. Electronics **38**(8) April 19th (1965)
1406. M. Fayolle, F. Romagna, Microelectron. Eng. **37/38**, 135 (1997)

1407. Z. Stavreva, D. Zeidler, M. Ploetner, K. Drescher, Appl. Surf. Sci. **108**, 39 (1997)
1408. C.-H. Tung, G.T.T. Sheng, C.-Y. Lu, *ULSI Semiconductor Technology Atlas* (John Wiley & Sons, Hoboken, 2003)
1409. K. Hinode, Y. Hanaoka, K.-I. Takeda, S. Kondo, Jpn. J. Appl. Phys. **40**, L1097 (2001)
1410. T. Harada, A. Ueki, K. Tomita, K. Hashimoto, J. Shibata, H. Okamura, K. Yoshikawa, T. Iseki, M. Higashi, S. Maejima, K. Nomura, K. Goto, T. Shono, S. Muranaka, N. Torazawa, S. Hirao, M. Matsumoto, T. Sasaki, S. Matsumoto, S. Ogawa, M. Fujisawa, A. Ishii, M. Matsuura, T. Ueda, International Interconnect Technology Conference (IITC), IEEE 2007, pp. 141–43
1411. P. Bai, C. Auth, S. Balakrishnan, M. Bost, R. Brain, V. Chikarmane, R. Heussner, M. Hussein, J. Hwang, D. Ingerly, R. James, J. Jeong, C. Kenyon, E. Lee, S.-H. Lee, N. Lindert, M. Liu, Z. Ma, T. Marieb, A. Murthy, R. Nagisetty, S. Natarajan, J. Neirynck, A. Ott, C. Parker, J. Sebastian, R. Shaheed, S. Sivakumar, J. Steigerwald, S. Tyagi, C. Weber, B. Woolery, A. Yeoh, K. Zhang, M. Bohr, IEDM Technical Digest, p. 657 (2004)
1412. www.chipworks.com
1413. Y. Taur, IBM J. Res. & Dev. **46**, 213 (2002)
1414. E.J. Nowak, IBM J. Res. & Dev. **46**, 169 (2002)
1415. S.-H. Lo, D.A. Buchanan, Y. Taur, W. Wang, IEEE Electron Device Lett. **18**, 209 (1997)
1416. G.D. Wilk, R.M. Wallace, J.M. Anthony, J. Appl. Phys. **87**, 484 (2000)
1417. Ch. Auth, M. Buehler, A. Cappellani, C.-H. Choi, G. Ding, W. Han, S. Joshi, B. McIntyre, M. Prince, P. Ranade, J. Sandford, Ch. Thomas, Intel Techn. J. **12**, 77 (2008)
1418. M.A. Quevedo-Lopez, S.A. Krishnan, D. Kirsch, C.H.J. Li, J.H. Sim, C. Huffman, J.J. Peterson, B.H. Lee, G. Pant, B.E. Gnade, M.J. Kim, R.M. Wallace, D. Guo, H. Bu, T.P. Ma, IEDM Technical Digest, p. 425 (2005)
1419. K. Mistry, C. Allen, C. Auth, B. Beattie, D. Bergstrom, M. Bost, M. Brazier, M. Buehler, A. Cappellani, R. Chau, C.-H. Choi, G. Ding, K. Fischer, T. Ghani, R. Grover, W. Han, D. Hanken, M. Hattendorf, J. He, J. Hicks, R. Heussner, D. Ingerly, P. Jain, R. James, L. Jong, S. Joshi, C. Kenyon, K. Kuhn, K. Lee, H. Liu, J. Maiz, B. McIntyre, P. Moon, J. Neirynck, S. Pae, C. Parker, D. Parsons, C. Prasad, L. Pipes, M. Prince, P. Ranade, T. Reynolds, J. Sandford, L. Shifren, J. Sebastian, J. Seiple, D. Simon, S. Sivakumar, P. Smith, C. Thomas, T. Troeger, P. Vandervoorn, S. Williams, K. Zawadzki, IEDM Technical Digest, p. 247 (2007)
1420. K. Mistry, M. Armstrong, C. Auth, S. Cea, T. Coan, T. Ghani, T. Hoffmann, A. Murthy, J. Sandford, R. Shaheed, K. Zawadzki, K. Zhang, S. Thompson, M. Bohr, Symp. VLSI Technology Digest of Technical Papers, pp. 50–51 (2004)
1421. T. Krishnamohan, C. Jungemann, D. Kim, E. Ungersboeck, S. Selberherr, A.-T. Pham, B. Meinerzhagen, P. Wong, Y. Nishi, K.C. Saraswat, Microelectr. Eng. **84**, 2063 (2007)
1422. T. Guillaume, M. Mouis, Solid State Electron. **50**, 701 (2006)
1423. E. Ungersboeck, S. Dhar, G. Karlowatz, H. Kosina, S. Selberherr, J. Comput. Electron. **6**, 55 (2007)

1424. M. Bohr, *The Invention of Uniaxial Strained Silicon Transistors at Intel*, Intel (2007)
1425. Synopsys, Inc., www.synopsys.com
1426. W. Hansch, C. Fink, J. Schulze, I. Eisele, Thin Solid Films **369**, 287 (2000)
1427. P.-F. Wang, K. Hilsenbeck, Th. Nirschl, M. Oswald, Ch. Stepper, M. Weis, D. Schmitt-Landsiedel, W. Hansch, Solid State Electron. **48**, 2281 (2004)
1428. W.M. Reddick, G.A.J. Amaratunga, Appl. Phys. Lett. **67**, 494 (1995)
1429. P.-F.Wang, T. Nirschl, D. Schmitt-Landsiedel, W. Hansch, Solid State Electron. **47**, 1187 (2003)
1430. E.-H. Toh, G.H. Wang, G. Samudra, Y.-C. Yeo, J. Appl. Phys. **103**, 104504 (2008)
1431. G.R. Fox, R.Bailey, W.B. Kraus, F. Chu, S. Sun, T. Davenport, The Current Status of FeRAM in *Ferroelectric Random Access Memories*, Topics in Applied Physics 93, ed. by H. Ishiwara, M. Okuyama, Y. Arimoto, (Springer, Berlin, 2004), pp. 139–49
1432. Y.C. Chen, C.T. Rettner, S. Raoux, G.W. Burr, S.H. Chen, R.M. Shelby, M. Salinga, W.P. Risk, T.D. Happ, G.M. McClelland, M. Breitwisch, A. Schrott, J.B. Philipp, M.H. Lee, R. Cheek, T. Nirschl, M. Lamorey, C.F. Chen, E. Joseph, S. Zaidi, B. Yee, H.L. Lung, R. Bergmann, C. Lam, IEDM Technical Digest (2006), p. 777
1433. Zh. Sun, J. Zhou, R. Ahuja, Phys. Rev. Lett. **98**, 055505 (2007)
1434. J. Hegedüs, S.R. Elliott, Nature Mater. **7**, 399 (2008)
1435. P.K. Naji, ISSCC Digest of Technical Papers (2001), p. 122
1436. W.J. Gallagher, S.S.P. Parkin, IBM J. Res. & Dev. **50**, 5 (2006)
1437. M.N. Kozicki, C. Gopalan, M. Balakrishnan, M. Park, M. Mitkova, IEEE Non-Volatile Memory Technology Symposium (2004), pp. 10–17
1438. M.N. Kozicki, P. Mira, M. Mitkova, IEEE Trans. Nanotechnol. **4**, 331–338 (2005)
1439. K. Szot, W. Speier, G. Bihlmayer, R. Waser, Nature Mater. **5**, 312 (2006)
1440. A. Beck, J.G. Bednorz, Ch. Gerber, C. Rossel, D.Widmer, Appl. Phys. Lett. **77**, 139 (2000)
1441. S. Karg, G. I. Meijer, D. Widmer, R. Stutz, J. G. Bednorz, Ch. Rettner, IEEE NVSMW Monterey, California (2007), pp. 68
1442. M. Janousch, G.I. Meijer, U. Staub, B. Delley, S.F. Karg, B.P. Andreasson, Adv. Mater. **19**, 2232 (2007)
1443. M. A. Reed, C. Zhou, C.J. Muller, T.P. Burgin, J.M. Tour, Science **278**, 252 (1997)
1444. J.R. Heath, P.J. Kuekes, G.S. Snider, R.S. Williams, Science **280**, 1716 (1998)
1445. A. Aviram, M. Ratner (eds.), Molecular electronics: science and technology. Ann. N. Y. Acad. Sci. **852** (1998)
1446. E.F. Schubert, Delta-doping of semiconductors: electronic, optical and structural properties of materials and devices. Semicond. Semimet. **40**, 1–151 (1994)
1447. M. Schlechtweg, A. Tessmann, A. Leuther, C. Schwörer, M. Lang, U. Nowotny, O. Kappeler, *Proc. of the European Gallium Arsenide and other Compound Semiconductors Application Symposium* (GAAS 2003) (Horizon House, London, 2003), pp. 465–68

1448. Y. Kuo (ed.), *Thin Film Transistors: Materials and Processes* (Springer, Netherlands, 2003)
1449. G. Horowitz, Adv. Mater. **10**, 365–77 (1998)
1450. C.D. Dimitrakopoulos, P.R.L. Malenfant, Adv. Mater. **14**, 99 (2002)
1451. B.Ch. Shekar, J. Lee, S.-W. Rhee, Korean J. Chem. Eng. **21**, 267–85 (2004)
1452. Y.M. Sun, Y.Q. Liu, D.B. Zhu, J. Mater. Chem. **15**, 53–65 (2005)
1453. D. Lubyshev, W.K. Liu, T.R. Stewart, A.B. Cornfeld, X.M. Fang, X. Xu, P. Specht, C. Kisielowski, M. Naidenkova, M.S. Goorsky, C.S. Whelan, W.E. Hoke, P.F. Marsh, J.M. Millunchick, S.P. Svensson, J. Vac. Sci. Technol. B **19**, 1510 (2001)
1454. C.T. Liu, Revolution of the TFT LCD technology, J. Displ. Technol. **3**, 342 (2007)
1455. U. Köster, Phys. Stat. Sol. (A) **48**, 313 (1978)
1456. D. Toet, P.M. Smith, T.W. Sigmon, T. Takehara, C.C. Tsai, W.R. Harshbarger, M.O. Thompson, J. Appl. Phys. **85**, 7914 (1999)
1457. R.B. Iverson, R. Reif, J. Appl. Phys. **62**, 1675 (1987)
1458. N. Yamauchi, R. Reif, J. Appl. Phys. **75**, 3235–57 (1994)
1459. G. Liu, S.J. Fonash, Appl. Phys. Lett. **62**, 2554 (1993)
1460. M.S. Haque, H.A. Naseem, W.D. Brown, J. Appl. Phys. **79**, 7529 (1996)
1461. L.H. Lee, Y.K. Fang, S.H. Fan, Electron. Lett. **35**, 1108 (1999)
1462. T.K. Kim, T.H. Ihn, B.I. Lee, S.K. Joo, Jpn. J. Appl. Phys. **37**, 4244 (1998)
1463. S.-W. Lee, Y.-C. Jeon, S.-K. Joo, Appl. Phys. Lett. **66**, 1671 (1995)
1464. K. Sera, F. Okumura, H. Uchida, S. Itoh, S. Kaneko, K. Hotta, IEEE Trans. Electron Devices **36**, 2868 (1989)
1465. H. Gleskova, S. Wagner, Appl. Phys. Lett. **79**, 3347 (2001)
1466. N. Yamauchi, N. Kakuda, T. Hisaki, IEEE Trans. Electron Devices **41**, 1882 (1994)
1467. M. Zaghdoudi, R. Rogel, N. Alzaied, M. Fathallah, T. Mohammed-Brahim, Mat. Sci Engin. C **28**, 1010 (2008)
1468. J.F. Wager, Science **300**, 1245 (2003)
1469. K. Nomura, H. Ohta, K. Ueda, T. Kamiya, M. Hirano, H. Hosono, Science **300**, 1269 (2003)
1470. E.M.C. Fortunato, P.M.C. Barquinha, A. Pimentel, A.M.F. Gonçalves, A.J.S. Marques, L.M.N. Pereira, R.F.P. Martins, Adv. Mater. **17**, 590 (2005)
1471. H. Frenzel, A. Lajn, M. Brandt, H. von Wenckstern, G. Biehne, H. Hochmuth, M. Lorenz, M. Grundmann, Appl. Phys. Lett. **92**, 192108 (2008)
1472. M. Grundmann, H. Frenzel, A. Lajn, M. Lorenz, F. Schein, H. von Wenckstern, Phys. Stat. Sol. (A) **207**, 1437–1449 (2010)
1473. H. Frenzel, A. Lajn, H. von Wenckstern, M. Grundmann, J. Appl. Phys. **107**, 114515 (2010)
1474. S.R. Forrest, Chem. Rev. **97**, 1793 (1997)
1475. G. Horowitz, J. Mater. Res. **19**, 1946 (2004)
1476. Z. Bao, J. Locklin (eds.), *Organic Field-Effect Transistors*, (CRC Press, New York, 2007)
1477. Ch.Wöll (ed.), Physical and Chemical Aspects of Organic Electronics (Wiley-VCH, Weinheim, 2009)
1478. G. Horowitz, F. Garnier, A. Yassar, R. Hajlaoui, F. Kouki, Adv. Mater. **8**, 52 (1996)

1479. H.E. Katz, C. Kloc, V. Sundar, J. Zaumseil, A.L. Briseno, Z. Bao, J. Mater. Res. **19**, 1995 (2004)
1480. S. Jit, P.K. Pandey, P.K. Tiwari, Solid State Electron. **53**, 57 (2009)
1481. H.A. Kramers, Nature **117**, 775 (1926)
1482. R. de L. Kronig, J. Opt. Soc. Am. **12**, 547 (1926)
1483. P.O. Löwdin, J. Chem. Phys. **19**, 1396 (1951)
1484. G.H. Wannier, Phys. Rev. **52**, 191 (1937)

Index

Absorption, 265, 311, 314, 585, 605, 610, 628
atmospheric, 637
band–band, 271
bleaching, 226
bound exciton, 288
free-carrier, 269, 299, 383
impurity, 296
intravalence-band, 278
lattice, 303
negative, 293
optical, 225
schematic spectrum, 268
selfabsorption, 330
spectrum, 273, 373, 380
two-photon, 282, 294
Absorption edge, 277
optical, 151
shift, 293
Acceleration, 161
Acceptor, 193, 200, 202
binding energy, 203
charged, 202
double, 219
energy, 203
neutral, 204, 331
Accumulation, 549
Admittance spectroscopy, 530
Air gap, 706
Air mass, 637
Alkali halogenides, 167
Alloy, 63, 102, 231, 441, 545
quaternary, 65
random, 63, 323
ternary, 57, 65, 153
Amplification, 315, 680, 698, 711
light, 674
region, 624
Amplifier
optical, 676, 710
power, 711
Angle
Brewster, 267
critical, 266, 663
Euler, 769
taper, 711
Anharmonicity, 428
Annealing, 73
laser, 763
thermal, 763
Anode, 519
Anticrossing, 287, 363, 497, 498
Antidot, 394
Approximation
abrupt, 525, 558, 730
adiabatic, 33, 730
Boltzmann, 186, 187, 199, 539
Born–Oppenheimer, 33, 329
electric dipole, 269
envelope function, 361
gradual channel, 730
harmonic, 103
quasi-cubic, 174
relaxation time, 236, 257, 299
two-band, 295
virtual crystal, 68, 153
WKB, 340
Atmosphere, 637
Auger process, 333
Autocompensation, 208
Avalanche multiplication, 576, 607, 718

Background radiation, 612
Band
alignment, 359
bending, 369, 523, 525, 549

conduction, 22, 147, 340
minimum, 147, 153
diagram, 714
diode, 520, 548
discontinuity, 359, 362
edge, 296
filled, 168, 190
gap, 22, 144, 147, 152, 156, 162, 191, 399, 433
engineering, 360
fundamental, 276
negative, 175
photonic, 481–499
renormalization, 292
temperature dependence, 158
zero, 444
impurity, 211
lineup, 359
mixing, 176, 363, 409, 605
parabolic, 273
remote, 787
splitting, 28
staggered lineup, 359
straddled lineup, 359
tail, 278
tilted, 379
valence, 22, 147, 709
fine structure, 173
Band structure, 139–179, 270, 459
chalcopyrites, 149
delafossites, 151
direct, 148, 153
extrema, 180
indirect, 147, 153, 294
lead salt, 149
multivalley, 253
perovskites, 152
photonic, 488
strained, 176
theory, 5
Bandwidth, 602, 612, 626
Bardeen model, 520, 525
Barrier, 339, 362, 366
Coulomb, 410
finite, 364
height, 362, 536
reduction, 529
Schottky, 522
triangular, 340
Base, 36, 714
diatomic, 36, 120
monoatomic, 36
width, 723
Beam profile, 685, 704
Benzene, 23, 451
Biexciton, 290, 420
Binodal, 66
Birefringence, 300, 384
Blackbody, 603
Bloch's theorem, 140
Bohr radius, 193
Bond
angle, 45
breaking, 138
covalent, 19
dangling, 47
elastic, 103
electron pair, 19
homopolar, 27
ionic, 25
length, 27, 45, 68, 74, 126, 153
metallic, 30
mixed, 27
partially ionic, 119
sp^2, 23
sp^3, 19
strength, 156
strong, 352
tetrahedral, 22, 193
van-der-Waals, 30
Bose–Einstein
statistics, 784
Boson, 783
Bottleneck, 287
Boule, 349
Boundary
additional ∼ condition, 288
antiphase domain, 101
condition, 104, 142, 343, 362, 397, 408, 484, 525, 552, 560, 716
depletion layer, 628, 716
inversion domain, 101, 353
periodic ∼ condition, 104
sample, 393
Bow-tie, 204, 504
Bowing, 69
parameter, 153
Bragg mirror, 485, 674, 687, 704

Breakdown, 575, 611, 618, 723
Brightness, 655
  high, 666
  perceived, 661
  visible, 653
Brillouin zone, 62, 103, 105, 141, 459
  cubic
    body-centered, 63
    face centered, 63
    simple, 63
  hexagonally close packed, 63
  orthorhombic, 63, 150
  paths, 62
  size, 273
Broadening
  alloy, 323
  inhomogeneous, 371, 392, 422
  phonon, 283
  Stark, 297
Buffer, 352
  graded, 762
  metamorphic, 650
  relaxed, 761
Burger's vector, 87, 135
Burstein–Moss shift, 291

Capacitance, 530, 536, 555, 563
  parasitic, 725
Capture, 400
  barrier, 225
  cross section, 336
Carrier
  capture, 217, 335
  concentration, 187
    intrinsic, 191
  density, 309, 384
    equilibrium, 313
    excess, 313, 342
    nonequilibrium, 314
  excess, 334, 400
  excess ∼ profile, 342
  free, 300
  freeze-out, 198
  hot, 641
  injection, 215, 309
  itinerant charge, 445
  majority, 519, 532
  minority, 519, 558
  release, 335
  threshold ∼ density, 688
Catalysis, 348
Catastrophical optical damage, 684, 692
Cathodoluminescence, 399
Cavity
  empty, 497
  external, 676
  Fabry–Perot, 497, 674
  hexagonal, 505
  mirror, 497
  mode, 497
  optical, 674
  resonance, 502
  short, 687
Cell
  central ∼ correction, 211, 296
  elementary, 36
  internal parameter, 50, 69, 427
  photoelectrochemical, 599
  primitive elementary, 36
  primitive unit, 57
  tandem, 643
  unit, 36, 425
  Wigner–Seitz, 36, 62
Chalcogenide, 51, 757
  atoms, 219
  europium, 441
  glass, 221
  impurity, 220
  lead, 149
Channel, 448, 727
  buried, 633
  depth, 730
  edge, 393
  inversion, 737
  isolation, 633
  length, 729, 750
  long, 737
  short, 736
  stop, 633
  strain, 745
  n-type, 743
  p-type, 743
  width, 731, 750
Charge
  conservation, 337
  deficit, 394
  density, 369

effective, 28
elementary, 217
excess, 309
fixed, 193
image, 366, 527
inversion, 554, 628
ionic, 557
maximum, 628
neutrality, 552
packet, 630
polarization, 425
relative shift, 425
retention, 756
sign, 384
signal, 628
state, 217
storage, 590
surface, 522
transfer, 368
Charge coupled device, 11, 627–635
Chemical shift, 296
Chromaticity, 655
Circuit
common base, 714, 721, 723
common collector, 721, 724
common emitter, 718, 723, 724
equivalent, 575, 588, 603, 612
feedback, 725
integrated, 8, 11, 743
millimeter-wave, 586
open, 261, 640
optoelectronic integrated, 494
read-out, 628, 635
short, 262, 640
Cleaving, 137, 401, 686
Clock speed, 751
Cluster, 63
size, 444
Clustering, 64, 102
CMOS technology, 633, 743–753
Coating
antireflection, 619, 687, 710
high-reflection, 687
Coefficient
absorption, 268, 273, 274, 301, 343, 635, 776
Auger recombination, 334
bimolecular recombination, 312
diffusion, 228, 257
distribution, 81, 86
elastic, 122
electron ionization, 256
gain compression, 701
hole ionization, 256
impact ionization, 623
negative temperature, 728
Peltier, 261
sign, 262
segregation, 81
stiffness, 123
temperature, 576, 578, 587
thermal expansion, 122, 130, 159, 354
transmission, 482
two-photon absorption, 295
Collector, 714
Colloid, 415, 423
Commensurability, 395
Compensation, 206, 227, 331
Composite fermion, 394
Compound
binary, 28
carbon, 23, 451
I–VII, 25
II–VI, 27
ionic, 27
Condensation, 294
Bose–Einstein, 294
bosonic, 294
Conduction
heat, 259–260
hole, 204
intrinsic, 190, 200
ohmic, 191
n-type, 204
p-type, 204
Conductivity, 185, 236–238, 457, 601, 628
channel, 410, 727
complex, 257, 299
heat, 259
longitudinal, 392
metal, 237
one-dimensional, 393
type, 211
zero-field, 389
Configuration
atomic, 217
coordinate, 222

Confinement
  spatial, 274
Constant
  Boltzmann, 186
  damping, 257
  dielectric, 120, 193, 304, 366
    high frequency, 120
    negative, 302
    static, 120
  effective Richardson, 540
  elastic, 104, 124
  fine-structure, 391
  force, 106, 109, 114, 116, 221
  Fröhlich coupling, 166
  normalization, 140
  Poisson, 131
  Richardson, 534, 536
  spring, 104
  static dielectric, 526
  stiffness, 125
  von-Klitzing, 390
Contact
  back, 643
  base, 716
  intracavity, 706
  lines, 626
  metal–semiconductor, 5, 520–547
  nonohmic, 727
  Ohmic, 520, 543–545, 745
  resistance, 520, 543
  Schottky, 5, 56, 616
  transparent, 619
Continuity equation, 259
Convolution, 373
Coordination number, 36
Coulomb
  blockade, 410
  charging energy, 411
  correlation, 282
  staircase, 410
Coupling, 717
  antiferromagnetic, 442
  capacitive, 410
  ferromagnetic, 445
  intervalley, 296
  nanostructures, 397
  phonon–plasmon, 307
  strong, 497
  weak, 497
Crack, 95, 354
Crescent, 398
Crystal
  class, 40
  nobel gas, 30
  structure, 10
Curie–Weiss law, 431
Current
  amplification, 718
  dark, 607, 612, 619, 628, 641
  diffusion, 257, 611
  divergence, 259
  excess, 594, 595
  gain, 723
  leakage, 643
  particle, 257
  photo-, 601, 638
  photogenerated, 611
  saturation, 534, 542, 732
  short-circuit, 640
  spreading, 692
  transparency, 688
  tunneling, 205, 540, 594
Curvature, 130, 146, 161, 167, 286, 338, 399, 578, 663
C–V spectroscopy, 530, 536
Cyclotron
  frequency, 248, 383
  motion, 236, 382, 395
  orbit, 385, 395
  resonance, 164

De Broglie wavelength, 397
De Haas–van Alphén effect, 385
Debye length, 552, 563, 741
Decay
  hyperbolic, 314
  time, 314
Defect, 63, 73–102, 134
  acceptor, 202
  annihilation, 95
  antisite, 74, 219, 226
  area, 73
  density, 354
  diffusion, 79
  donor, 193
  double acceptor, 219
  double donor, 218
  EL2, 226

electronic states, 185–233
etching induced, 413
Frenkel, 73
interstitial, 73, 211, 218, 226, 232
isoelectronic, 228
line, 73, 87, 494
metastable, 73
nucleation, 359
pair, 85, 206
passivation, 231
point, 73, 211, 338, 494
symmetry, 221
thermodynamics, 74
vacancy, 74
Deformation
volume, 153
Degeneracy, 77, 108, 202, 223, 386, 410
holes, 363
Kramer's, 147
spin, 180, 197, 204, 390, 468
valley, 188, 197, 388, 468
Demodulation, 584
Density of modes, 486, 487, 502
Density of states, 179–183, 187, 363, 367, 385, 386, 397, 458
band-edge, 337
conduction-band edge, 188
joint, 271, 373
δ-like, 391
surface, 520, 525
two-dimensional, 182
valence-band edge, 188
Depletion, 549
deep, 627
Depletion layer, 191, 522, 610
width, 527, 562
Depolarization, 425
Deposition
chemical vapor, 347
pulsed laser, 348
Detailed balance, 309, 312
Detectivity, 603, 605, 611
Deuterium, 446
Device
cooling, 235
high-power, 235
high-speed, 227
optoelectronic, 265
performance, 191
photonic, 265
reliability, 759
two-terminal, 519
Diffraction, 266–269
reflection high energy electron, 348
Diffusion, 235, 257–258, 400, 533, 539, 560, 628, 630, 714
equation, 342
lateral, 373, 604
length, 343
pair $\sim$ mechanism, 79
point defects, 78
surface, 348
Diode, 235, 519–597
backward, 595
bipolar, 519, 558–579
I–V characteristics, 565–575
fast-recovery, 589
Gunn, 253, 596
heterostructure, 558, 591, 597, 725
ideal characteristic, 534
light-emitting, 347, 661–669
application, 662
white, 668
metal–insulator–semiconductor, 520, 548–557
metal–oxide–semiconductor, 389, 548
metal–semiconductor, 519
nonideal MIS, 556
pin, 591
pn-junction, 519
Schottky, 421, 520
I–V characteristics, 532–543
step-recovery, 590
tunneling, 592
unipolar, 519
Zener, 587, 588
Dipole moment, 381
Dirac particle, 472
Direction
growth $\sim$, 674
polar, 99
surface $\sim$, 703
Dislocation, 87, 348
60°, 89
α, β, 90
core, 87, 136
density, 136
edge, 89

half-loop, 135
line, 87
misfit, 90, 134, 356
partial, 90, 95
screw, 89
spacing, 97
threading, 135
Disorder, 45, 68, 102, 153, 180, 278, 386, 536
cation, 53
configurational, 76
isotope, 319, 323
Dispersion
free electron, 161
linear, 286
quadratic, 287
spatial, 285
Dispersion relation, 144, 161, 302, 363, 483
branch, 106, 110, 306
free electron, 141
hole, 169
lattice vibration, 103
linear chain, 105, 108
parabolic, 146
Displacement, 87, 103, 129, 226, 241, 427
atomic, 221
ion, 165
parameter, 51
Display, 654
application, 658
electroluminescence, 763
field-effect, 655
liquid crystal, 763
plasma, 655
Distortion
tetragonal, 133, 416
Distribution
binomial, 323
Boltzmann, 186
Bose–Einstein, 240, 312, 786
degenerate, 187, 291
Fermi–Dirac, 185, 370, 785
Gaussian, 373, 536
nondegenerate, 186
Planck, 784
spectral power, 655
Domain
antiphase, 99
inversion, 99
polarization, 432
Donor, 193
–acceptor pair, 331
binding energy, 193
deep, 226
double, 218
empty, 197
fine structure, 198
ionization energy, 193, 199
ionized, 196
neutral, 196, 331
populated, 197
shallow, 193
Dopant, 335, 369
Doping, 74, 193–215, 301, 633
concentration, 530
depth profile, 530
glass, 415
modulation, 243, 369, 386, 759
profile, 589, 736
Drain, 727
Drift, 235, 533, 614, 628
self-induced, 630
time, 621
Droplet, 416
Drude theory, 383, 389
DX center, 224, 759

Early effect, 721, 723
Ebers–Moll model, 719, 721
Effect
field, 339
polaronic, 165
thermoelectric, 261
Effective-mass
impurity, 195, 216
theory, 193, 791
Efficiency
conversion, 641, 654
differential, 691
emitter, 718
external, 691
external quantum, 662
internal quantum, 662, 691
light extraction, 662
maximum solar cell, 641
quantum, 413, 601, 611

total quantum, 662, 692
wall-plug, 692, 711
Einstein relation, 258
Elasticity, 122–137
Electroabsorption, 546
Electroluminescence, 3, 763
Electromagnetic spectrum, 265
Electron
affinity, 521
conduction, 30
configuration, 19, 441
density, 187
dispersion, 161
distribution function, 185
equation of motion, 161
trap, 336
valence, 30, 139
wave packet, 161
Electron gas
free, 180
one-dimensional, 183
three-dimensional, 182, 384
two-dimensional, 182, 239, 368, 386, 395
Electron–hole droplet, 293
Electronegativity, 27, 304
Electrophotography, 603
Ellipsometry, 384
Emission
amplified spontaneous, 694
directional, 495
field, 533, 540
pattern, 504
probability, 339
spontaneous, 309, 481
stimulated, 270, 311, 314
thermally activated, 339
thermionic, 533, 607
thermionic field, 541
Emitter, 714
follower, 725
Energy
activation, 79, 232
barrier, 221
capture, 224
charging, 224
confinement, 362
conservation, 274
correlation, 293
Coulomb, 222
defect formation, 73
density, 235
Dirac, 469, 471
dissipation, 391
elastic, 122
electrostatic, 410
exchange, 293
free, 217, 430
gap, 22, 24, 145
ionization, 193, 339
kinetic, 145
loss, 252
Madelung, 26
optoelectronic, 380
parameter, 163
radiation, 497
Rydberg, 194, 280
surface, 416
thermal, 241
zero-point, 31
Enthalpy, 76
formation, 76, 78, 218
free, 74, 218
migration, 78
mixing, 66
Entropy, 76, 223, 430
configurational, 66
disorder, 77
formation, 76
Epitaxial relationship, 352
Epitaxy
liquid phase, 348
metalorganic vapor phase, 347
molecular beam, 347
thin film, 348
Equilibrium
state, 309
stationary, 539
thermodynamic, 185, 186, 191, 215, 216, 312, 313, 333, 336, 368, 520
Etch, 92, 350
pit, 93
RCA, 350
Shiraki, 350
Etching, 413
anisotropic, 101, 397
plasma, 94
reactive ion, 94, 413, 686

thermal, 350
wet chemical, 413
Euler angles, 125
Excitation
external, 309
neutral, 314
optical, 225
Exciton, 5, 268, 280–284, 459
binding energy, 280, 366
bound, 288
bright, 285
charged, 290, 420
correlation, 381
dark, 285
delocalized, 373
dynamics, 373
free, 315, 323
Frenkel, 459
interchain, 460
intrachain, 460
ionization, 381, 382
localized, 373
longitudinal, 285
ortho-, 285
oscillator strength, 281
para-, 285
polariton, 285
radius, 280
recombination, 315
scattering states, 282
self-trapped, 660
transverse, 285
volume, 323
Exclusion principle, 783
Exhaustion, 200
regime, 208
Eye pattern, 701

Facet
cleaved, 401, 674
etched, 686
laser, 687
side, 398
tilted, 703
Factor
base transport, 718
collector multiplication, 718
fractional filling, 393
ideality, 535, 536, 719
linewidth enhancement, 702
optical confinement, 626
quality, 494, 502
Sommerfeld, 282
spontaneous emission, 689
Fano resonance, 299
Far field, 685
Feedback
distributed, 696
loop, 348
optical, 674
Fermi
energy, 385
integral, 187, 188, 258
intrinsic ∼ level, 192, 204, 551
level, 186, 198, 200, 204, 207, 291, 337, 368, 389, 421, 520, 547
gradient, 258
liquid, 294
local quasi ∼ level, 216
quasi ∼ level, 215, 312, 315, 533, 628, 737
sphere, 236
surface, 385
vector, 384
Fermi's golden rule, 269, 481, 502
Fermi–Dirac statistics, 217, 218, 785
Fermion, 783
Ferroelectricity, 425, 427
Ferromagnet
Heisenberg, 441
Fick's law, 257
Field
built-in, 546
crossed electric and magnetic, 709
crystal, 227
displacement, 777
displacment, 120
drift, 715
electric, 161, 166, 235, 256, 257, 300, 379, 526
electromagnetic, 269
external, 379
fringing, 630
high magnetic, 389
homogeneous, 381
internal electric, 235
macroscopic electric, 119

magnetic, 161, 164, 236, 247, 274, 297, 382
static, 300
piezoelectric, 241, 409
ring, 579
strength, 624
strong electric, 339
surface, 552
time dependent electric, 299
transverse electric, 247
Filling factor, 44, 641
Finesse, 494
Flip-flop, 8
Flow
heat, 259
Fluctuation, 67, 324, 373
amplitude, 702
phase, 702
quantum dot size, 422
vacuum, 481
Fluorescence, 458
Flux
luminous, 653
radiant, 653
Focal plane array, 605
Force, 161
dissipative, 257
image, 528
Lorentz, 247, 389
restoring, 122, 428
van-der-Waals, 26
Fourier
coefficient, 144, 145
series, 144
transform, 775
transformation, 57
Franck–Condon principle, 329
Freeze-out
regime, 200
Frequency
cutoff, 725
high, 725, 736, 762
mixing, 584
Fresnel formulas, 267, 485
Friction, 236
Function
Bessel, 408
Bloch, 140, 163, 216, 270, 285, 362, 365, 787
Boltzmann, 373
color matching, 655
dielectric, 120, 121, 270, 300, 498, 775
envelope, 362, 791
error-, 373
Fermi, 185, 312, 785
Hankel, 408
spherical harmonic, 407
static dielectric, 429

Gain, 607, 674, 693
differential, 701
maximum, 697
Gate, 410, 727
charge, 755
contact, 448
voltage, 389, 410, 628
Gauge invariance, 393
Generation–recombination, 628
g-factor, 383
Gibbs-Thomson effect, 416
Ginzburg–Landau theory, 429
Glide plane, 87
Glide reflection, 40
Grain
boundary, 35, 97, 231
boundary, small-angle, 97
size, 649, 658, 763
Graphene, 465
Grating, 605
sampled, 698
Group
point, 37
space, 39, 352
theory, 35
Growth
Czochralski, 348
Frank-van der Merwe, 351
kinetics, 210
methods, 347
mode, 351
pseudomorphic, 130
spiral, 89
Stranski-Krastanow, 351, 415
template, 415
Volmer-Weber, 351
Guard ring, 579

Halbleiter, 4
Hall
  bar, 389, 394
  coefficient, 248, 389
    sign, 250
  constant, 249
  current, 393
  effect, 225, 247–251
    electrical, 384
    fractional quantum, 393
    integral quantized, 389
    optical, 384
    quantized, 10, 11, 389
    quantum, 347
  factor, 251
  plateau, 390, 393
  quantum ∼ liquid, 393
  resistivity, 392, 395
Hayne's rule, 318
Heat
  capacity, 430
  latent, 430
  sink, 263, 666, 675, 692
Helmholtz equation, 482
Heteroepitaxy, 122, 127, 435
Heterointerface, 386
  graded, 598
Heterojunction, 643, 757
Heterostructure, 11, 347–378, 390, 415, 500
  type-I, 359
  type-II, 359
Hexagonality index, 57
Hole, 168–175
  capture, 337
  concept, 168
  density, 187, 204
  dispersion, 168, 363
  effective mass, 169
  gas, 445
  heavy, 169, 363
  light, 169, 363
  split-off, 169, 254, 274, 278
HOMO, 24
Hopping, 167
Hund's rule, 442
Hybridization
  p–d, 446
  sp^2, 23, 451, 465
  sp^3, 20
Hydrogen, 193, 231, 318, 446
  atom, 381
  model, 280
  molecule, 19, 290
  problem, 195
Hydrogenation, 47
Hysteresis, 425, 432, 446

Illuminance, 654
Illumination, 601, 621, 625, 633, 638
Image sensor, 605, 628, 633
Impact ionization, 254, 333, 576, 623
Impedance, 584, 626
  amplifier, 725
  input, 728
Impurity, 73, 94, 185, 231, 296, 317, 335
  amphoteric, 210
  background, 206
  binding energy, 366
  charged, 297
  concentration, 185
  hardening, 94
  incorporation, 210
  isoelectronic, 288, 661
  isovalent, 73
  magnetic, 442
  shallow, 193
In-situ
  control, 348
  monitoring, 348
Incompressible, 393
Index of refraction, 266, 301, 776
Interaction
  antiferromagnetic, 445
  atom–cavity, 497
  Coulomb, 26, 193, 280, 366, 393, 397
  dipole–dipole, 30
  double exchange, 445
  electron–phonon, 33, 158, 166, 269–271
  electrostatic, 26, 32
  exchange, 285, 294
  gap, 444
  hyperfine, 195, 217, 222
  indirect exchange, 445
  London, 30
  many-body, 393
  nearest-neighbor, 441

parameter, 66
Ruderman–Kittel–Kasuya–Yoshida, 445
spin-orbit, 169, 383, 448, 461, 788
superexchange, 441, 444
van-der-Waals, 30, 451
Interconnect, 747
Interface, 134, 366, 426, 435, 549, 628
flat, 374
geometry, 347
heterostructure, 520
planar, 266, 347
plane, 363, 533
single hetero-, 360, 368
state, 547
Inversion, 38, 101, 147, 549, 709
center, 434
strong, 553
weak, 553
Inverted opal, 490
Inverter, 745
Ionicity, 28, 126, 156, 304
Ionization, 297, 560
photothermal, 297
Iron, 87, 101, 218, 228
Irradiance, 653
Irradiation, 338
Island growth, 415
Isomer shift, 210
Isotope, 102, 210, 260, 319
effect on phonon, 111

Jahn–Teller effect, 74, 221, 222
dynamic, 221
Joule heating, 261, 262
Junction
deep, 579
graded, 692
hyperabrupt, 588
multiple, 643
one-sided, 558

Kane model, 788
Keating criterion, 125
Kick-out mechanism, 79
Kirchhoff's law, 731
Klein paradox, 472
k · **p** theory, 162, 787–790
Kramers–Kronig relation, 271, 775–776, 778
Kronig–Penney model, 142, 157, 366

Lambert–Beer's law, 268, 613
Lamé's constant, 126
Large scale integration, 746
Laser, 9, 235, 347, 674–710
cascade, 676
condition
thermodynamic, 315
diode, 676
double heterostructure, 9
edge emitting, 674
horizontal cavity surface-emitting, 703
hot hole, 709
lead salt, 697
modulation, 698
monochromatic, 696
monomode, 696
multisection, 698
optically pumped, 707
output power, 690
quantum cascade, 708
surface-emitting, 674, 703
tunable, 697, 706
two-section, 697
vertical-cavity surface-emitting, 497, 703
zero-threshold, 481
Lasing, 314
Lattice
body-centered cubic, 42
Bravais, 35, 40
constant, 68, 103, 109, 130, 157
1D Bravais, 103
2D Bravais, 40
3D Bravais, 40
empty, 141
expansion, 158
face-centered cubic, 42
hexagonally close packed, 44
ionic, 165
match, 153
mismatch, 122, 130, 356
period, 395
point, 36, 105
reciprocal, 57–63, 140

relaxation, 74, 221, 225
simple cubic, 41
site, 210
temperature, 252, 294
vibration, 103–122
Lattice matched, 356
Laughlin theory, 394
Layer
active, 674
amorphous, 352
inversion, 389, 390, 728
nucleation, 354
semi-insulating, 217
sequence, 360
space-charge, 522
spacer, 758
wetting, 352
Level
deep, 193, 216, 299, 589
Landau, 384, 386, 389, 390, 393, 444
midgap, 338, 340
occupancy, 222
quantized, 362
Lifetime, 314, 339, 373
carrier, 601
minority carrier, 314, 337
minority-carrier, 584
photon, 689
Lift-off, 132
Linear chain
diatomic, 106
monoatomic, 103
Lithography, 413
Localization, 393
light, 494
Löwdin perturbation theory, 787
Loss, 687
internal, 687
mirror, 687
Luminance, 654
Luminescence, 323, 458
decay, 503
impurity, 661
mechanism, 660
negative, 313
Luminosity, 653
LUMO, 24
Luttinger Hamiltonian, 790
Lyddane–Sachs–Teller relation, 121, 304

Madelung constant, 26, 27
Magnetic moment, 443
Magnetoresistance, 385, 388
Magnetotransport, 382, 395
Mask, 354
Mass, 103, 109
anisotropic, 296, 382
carrier, 384
density of states, 188
effective, 147, 161, 168, 193, 239, 336, 362, 363
electron, 163
hole, 171
isotropic, 164
longitudinal, 164
nonparabolicity, 167
polaron, 165
reduced, 304, 379
strain effect, 179
transverse, 164, 363
Mass-action law, 190
Matrix element, 269, 270, 312, 365, 413
bulk momentum, 163
dipole, 605
k-dependence, 163
momentum, 162, 270, 787
Matthiesen rule, 239
Maxwell's equations, 266, 489
Mean free path, 237, 395
Memory, 713, 746
flash, 755
nonvolatile, 755
Metalorganic, 348, 461
Microcavity, 294, 494, 503, 689, 704
Microdisc, 500
Micropillar, 503
Microscopy
scanning tunneling, 201, 204
secondary electron, 399
Midgap level, 295
Miller indices, 60
wurtzite, 62
Miniband, 367
Minigap, 367
Mirror operation, 37
Miscibility gap, 63

Mobility, 238, 369, 384, 395, 533, 725, 763
  channel, 759
  edge, 373, 392
  extremely high, 347
  high, 389
  high electron, 239
  hole, 238
  metal, 239
  negative differential, 734
  optical carrier, 383
  surface, 352
  temperature dependence, 243
Mode
  chaotic, 504
  defect, 493, 495
  evanescent, 503
  gap, 118
  hopping, 697
  localized vibrational, 76, 114–117, 232
  longitudinal phonon plasmon, 307
  normal, 31
  optical, 108, 481
  out of plane, 465
  single longitudinal, 694
  soft phonon, 428
  spectrum, 694
  stretching, 459
  volume, 502
  whispering gallery, 501, 503, 505
Modulation
  large-signal, 699
  pulsewidth, 670
  small-signal, 701
Momentum
  angular, 274, 363, 407
  conservation, 270
  cyrstal, 161
  orbital, 296
  orbital angular, 169
  total angular, 169
Monolayer, 347, 360, 374
Moore's law, 746
Multiexciton, 420
Multiferroics, 425
Multiplication
  region, 625
Nanobelt, 403
Nanolaser, 402
Nanoscroll, 132, 133
Nanostructure, 397–423, 753
Nanotube, 132
  BN, 476
  carbon, 473
  metallic, 475
Nanowhisker, 401, 405
negative-U center, 221
Neutrality, 190
  condition, 191, 200, 206
  constraint, 217
Newton's law, 161
Nobel Prize, 10, 12, 347, 592
Noise
  equivalent power, 603, 611
  excess, 623
  generation–recombination, 602
  shot, 602, 612
  source, 612
  thermal, 602, 612, 624
Nonequilibrium, 215, 309
  thermodynamic, 216
Nonlinear optics, 295, 432, 482
Nonparabolicity, 381
Nonpolar, 240, 438
Nucleation, 352, 353, 763
  dislocation, 135
Number
  atomic order, 73, 323
  complexion, 77
  order number, 48

Ohm's law, 237
Orbital, 21
  antibinding, 22
  antisymmetric, 19
  bonding, 22
  highest populated, 24
  lowest unoccupied, 24
  overlap, 103
  symmetric, 19
Order
  antiferromagnetic long-range, 445
  long-range, 45
  spontaneous magnetic, 441
  stacking, 49, 57
Ordering, 69

CuAu, 69
CuPt, 69
in-plane, 418
Orientation, 232
random in-plane, 352
Oscillation
Bloch, 236
Franz–Keldysh, 380
Shubnikov–de Haas, 385, 387
Weiss, 394
Oscillator, 8, 253
harmonic, 32, 103, 384, 407, 412, 777
local, 585
master, 711
strength, 118, 271, 285, 304, 604, 777–781
voltage-controlled, 588
Ostwald ripening, 416
Overgrowth
cleaved-edge, 401
epitaxial lateral, 354
Overlap
geometrical, 626
Oxide
aperture, 705
high-k dielectrics, 745
transparent conductive, 4, 511–515

Parabola, 167
Paramagnetic ion, 441
Parameter
s, 28, 97
Heisenberg exchange, 441
Huang–Rhys, 328
Luttinger, 171
Partition sum, 783
Peak-to-valley ratio, 595
Peltier effect, 235, 262
Periodic system, 11, 19, 193
Phase, 87, 101, 109, 698
Bloch, 484
change, 757
cubic, 427
diagram, 66, 294
factor, 142, 484
ferroelectric, 427, 430
metastable, 57, 149
opposite, 119
ordered, 102
orthorhombic, 427, 432
paraelectric, 427, 429
paramagnetic, 445
rhombohedral, 432
separation, 66
shift, 394
spin glass, 445
tetragonal, 152, 427, 432
transition, 45, 50, 153, 293, 427, 429
first-order, 431
second-order, 429
trigonal, 427
Phonon, 33, 103, 114, 274
absorption, 340
acoustic, 109, 240, 287
alloy, 116
one-mode, 118
two-mode, 118
average temperature, 160
Bose–Einstein model, 160
broadening, 283
dispersion, 110, 160
emission, 333
energy, 375
infrared active, 268
LA, 108
LO, 108, 122, 166, 241
long wavelength, 121
optical, 109, 160, 304, 307
emission, 252
replica, 459
soft, 428
TA, 108
TO, 121
Phosphor, 654, 669
Phosphorescence, 458
Photocatalysis, 599
Photoconductivity
persistent, 225
Photoconductor, 601, 604
Photodetector, 217, 235
FIR, 296
quantum well intersubband, 604
traveling wave, 625
Photodiode, 610–637
array, 633
avalanche, 611, 623–625, 635
bipolar, 611
metal–semiconductor–metal, 616

pin, 613
stacking, 635
Photometry, 653
Photon
counting, 576
Photoresistor, 519
Piezoelectricity, 425, 433
Pinch-off, 729, 731, 733, 737, 740
Planar technology, 8, 519, 605, 704, 749
Planck's law, 312
Plasma, 655
frequency, 301, 307, 383
Plasmon, 302
Plastic flow, 135
Pnictide, 51
Point
critical, 272
crossover, 224
Dirac, 465, 470, 475
F, 151
Γ, 62, 105, 108, 109, 147, 152, 276
K, 62
L, 62, 147–149, 153
M, 152
saddle, 272
X, 62, 108, 147, 153
Poisson equation, 369, 525, 552, 560, 730
Poisson ratio, 125
Polariton, 294, 304
lower branch, 287
Polarizability, 304
Polarization, 120, 267, 285, 365, 605, 776
circular, 274, 448
electric, 241, 425
ferroelectric, 55
light, 295
p, 266
s, 266
spin, 445
spontaneous, 69, 425
TE, 366
time-dependent, 119
TM, 366
Polaron, 165, 457, 660
Poling, 432, 549
periodic, 432
Polyhedra, 37
Polymer, 23
chain, 454
Polytypism, 57
Poole–Frenkel effect, 339
Population, 336
inverted, 315
Position sensing detector, 615
Potential
asymmetric, 103, 605
atomic interaction, 103
built-in, 523
chemical, 218, 785
confinement, 362
Coulomb, 144
crystal, 144
distribution, 528
double well, 157
external, 527
fluctuation, 373
hard wall, 142
harmonic, 103
hydrostatic deformation, 176, 240
inversion surface, 739
ion core, 193
lateral ~ well, 633
Lennard–Jones, 30
long-range Coulomb, 339
minimum, 373
optical deformation, 176
periodic, 5, 139, 193
piezoelectric, 438
pure Coulomb, 296
screened Coulomb, 239
short range, 193
triangular, 368
two-dimensional well, 404
well
three-dimensional, 407
Power
maximum, 641
output, 641
thermoelectric, 261
total, 653
Pre-breakdown, 575
Precipitate, 208
Precursor, 348
Pressure, 76, 122
high, 10
hydrostatic, 50

partial, 210
vapor, 416
Process
activation, 221
causal, 775
Processing temperature, 512
Propagation
direction, 365
Punch-through, 723
Purcell effect, 497, 502
Purity, 185
Pyroelectricity, 425
Pyrolysis, 348

Quadrupole, 438, 504
Quantum
dot, 128, 183, 373, 397, 407–423, 502, 605
charge tunable, 420
cleaved-edge overgrowth, 401
cubic, 408
lens-shape, 413
pyramidal, 409
self-assembled, 412, 413
spherical, 408
stack, 417
electrodynamics, 497
magnetic flux, 393
well, 182, 294, 360, 381, 726
coupled, 367
energy level, 361
multiple, 360
sidewall, 398
vertical, 400
wire, 128, 183, 397–406
cleaved-edge overgrowth, 401
T-shaped, 401
V-groove, 397
Quantum statistics, 783–786
Quarter-wave stack, 485

Rabi frequency, 497, 498
Radiance, 653
Radiometry, 653
Radius
self-limited, 398
Random bit pattern, 701
Random walk, 257
Rashba effect, 448
Rate
Auger recombination, 333
capture, 336
emission, 336, 339
escape, 607, 689
generation, 259, 309, 601
growth, 348
net recombination, 312
pulling, 348
recombination, 259, 312
thermal Auger generation, 333
thermal generation, 312
tunneling, 340
Recombination, 206, 309–344, 449, 459, 533, 556, 584, 599, 726
Auger, 333
band–band, 309
band–impurity, 335
bimolecular, 312
bound-exciton, 317
center, 338, 589
current, 340, 663
donor–acceptor pair, 331
dynamics, 313
excitons, 315
free-exciton, 315
lineshape, 371
nonradiative, 217, 719
quantum well, 369
radiative, 347, 661
spectrum, 420
spontaneous, 309
surface, 340–341
velocity, 540
Rectification, 2, 5, 582
Rectifier
metal–semiconductor, 5
point contact, 5
Reflectance, 267, 304
Reflection, 265–269, 698
anisotropy spectroscopy, 348
distributed, 696
low, 615
total, 266, 504, 663
Region
space-charge, 522
Relaxation
carrier, 309
plastic, 134, 416

Resharpening, 398
Resistance
  negative differential, 595
  serial, 643
  shunt, 643
Resistivity, 237
  high, 227
  negative differential, 252
  transverse, 389
Resonator
  deformed, 502, 503
  microscopic, 500–508
  spiral, 504
Responsivity, 612
Reststrahlenbande, 304, 307
Rotation, 37, 101, 240
  general, 769
  improper, 38
Roughness, 351, 503

Saturation
  electron density, 199
Scattering, 382, 391
  deformation potential, 240
  elastic ∼ process, 240
  grain boundary, 243
  hot-carrier, 709
  impurity, 758
  inelastic, 241
  intervalley, 736
  ionized impurity, 239, 369
  matrix, 483
  microscopic process, 239
  orbit, 395
  phonon, 299
  piezoelectric potential, 241
  polar optical, 241
  process, 236
  Rutherford, 239
  spin, 448
  theory, 481
  time, 250
Schönfließ notation, 37
Schottky effect, 527
Schottky–Mott model, 520
Schrödinger equation, 139, 145, 362, 369, 379, 397, 482, 787
Scintillation detector, 659
Scintillator, 654
Scrolling, 132
  direction, 133
Second harmonic generation, 432
Second-harmonic generation, 584
Seebeck effect, 235, 261
Selection rule, 274, 364
  optical, 366
  polarization, 605
Self-assembly, 415
Self-consistent, 369
Semiconductor, 4
  alloy, 153
  amorphous, 35, 45–46, 180, 231, 279, 763
  compound, 7, 49, 148
  diluted magnetic, 441–447
  doped, 191
  elemental, 147, 156
  ferroelectric, 428
  history, 1
  II–VI, 156, 241
  III–V, 156
  indirect, 276, 335
  inhomogeneous, 235
  intrinsic, 190
  lead salts, 159
  magnetic, 56, 441–449
  nonpolar, 240
  organic, 23, 451–460, 546
  oxide, 347
  polarized, 425–439
  polycrystalline, 35, 45–46
  properties, 14
  semi-insulating, 227
  small band gap, 239
  small-gap, 191
  wide band gap, 191, 441, 446, 545
  wide-gap, 191
Semipolar, 438
Shockley-Read-Hall kinetics, 312, 335
Shubnikov–de Haas effect, 388
Side-mode suppression ratio, 694
Signal-to-noise ratio, 603, 613, 624
Singularity, 130, 180, 272
  Fermi-edge, 370
  van-Hove, 180, 272
Snapback time, 590
Snellius' law, 266
Sol-gel process, 415

Solar
cell, 235, 637–651
spectrum, 637
Solid-state multiplier, 624
Solubility, 67, 85, 86, 214, 228
Source, 727
Space-charge region, 525, 551, 558
capacitance, 530, 555
Spectroscopy
deep level transient, 226
Mössbauer, 210
Raman, 375
Spin, 147, 169, 274, 443
alignment, 449
glass, 445
LED, 448
nuclear, 195, 320
rotation, 448
total, 285
transistor, 448
Spinodal, 66
decomposition, 66
Spintronics, 441, 448
Splitting, 221, 320
crystal field, 174
Rabi, 498
spin, 383, 390
valley-orbit, 320
Zeeman, 297, 320
Stacking, 44
vertical, 398, 417
Stacking fault, 90, 95
energy, 97
extrinsic, 95
intrinsic, 95
Stark effect
quantum confined, 381, 436, 699
second-order, 381
State
edge, 393
extended, 393
localized, 393
macroscopic quantum, 393
midgap surface, 525
Step
monoatomic, 101
surface, 350
Stirling's formula, 77
Stoichiometry, 64, 211
Stokes shift, 373, 536
Stoney's formula, 132
Strain, 123, 241, 356, 605
bending, 132
biaxial, 127, 130, 176
compressive, 127, 176
distribution, 129, 409
energy, 122, 133, 137, 416
homogeneous, 176
hydrostatic, 176, 179
in-plane, 435
inhomogeneous, 176, 294, 790
large, 176
management, 132
microscopic, 53
misfit, 136
plastic relaxation, 90
random, 320
relaxation, 356, 416
shear, 127, 176, 434
small, 176
tensile, 127, 176
tensile surface, 417
tensor, 240
three-dimensional, 128, 409
Streaming motion, 709
Stress, 123, 232, 356
–strain relation, 126
external, 425
superposition, 129
uniaxial, 435
Structure
chalcopyrite, 51
CsCl, 48
delafossite, 54
diamond, 48, 137, 153
dielectric, 481–508
field-ring, 579
fluorite, 53
interdigitated, 619
NiAs, 56
orthorhombic, 27
periodically poled, 432
perovskite, 55, 427
pseudomorphic, 356
rocksalt, 27, 47, 56, 153
shell, 412, 521
tetragonal, 27
wurtzite, 50, 153

zincblende, 27, 49, 101, 138, 153, 157
Subband, 182, 386, 604
edge, 363, 365, 367
Sublattice, 49, 331, 441
anion, 49
cation, 49
Substrate
bending, 127, 130
compliant, 356
hetero-, 352
homo-, 352
polished, 350
rotation, 348
transparent, 665
Sun, 637
Superconductivity, 33
Superlattice, 63, 236, 360, 363, 366–368, 676
buffer layer, 350
isotope, 375
Surface
index, 525
Susceptibility
electric, 777
magnetic, 385
nonlinear third-order electric dipole, 295
Switch, 217
Symmetry
inversion, 147
mirror, 381
reduction, 221
tetrahedral, 296
time reversal, 147
trigonal, 224

Tail
carrier distribution, 527
exponential, 379
states, 387, 392
Taylor series, 258
Temperature
blackbody, 603
characteristic, 693
Curie, 429, 441, 446
Curie–Weiss, 432
Debye, 241
gradient, 235, 259
local, 216
Tensor, 771
conductivity, 389
dielectric
magneto-optic, 384
dielectric function, 300
effective-mass, 161, 195
nonlinear third-order electric dipole susceptibility, 295
resistivity, 389
Theory
perturbation, 221
time-dependent perturbation, 269
Thermal instability, 576
Thermalization, 373, 536
incomplete, 373
Thickness
barrier, 144, 366
critical, 133–137, 356, 402
film, 136
oxide, 633
quantum well, 361, 373
Thomson heating, 262
Threshold, 688
Tilt, 97
Time constant, 309, 314, 530, 556, 630, 726
decay, 654
LO phonon emission, 252
RC, 626
relaxation, 236, 239
reorientation, 221
Transconductance, 724, 732, 741
differential, 724
Transistor, 6, 235, 713–766
bipolar, 8, 714–727
effect, 10
field effect, 5
field-effect, 4, 727
heterobipolar, 347, 725
high electron mobility, 347, 758
JFET, 8
junction field effect, 729
junction field-effect, 5
light-emitting, 726
MESFET, 5, 9, 729
MOSFET, 4, 9, 390, 737
organic, 765
planar, 9
point contact, 6

thin film, 765
Transit time, 615, 736
Transition
band–band, 271
dipole, 285
direct, 272
displacement, 428
donor–acceptor pair, 331, 661
forbidden, 282
indirect, 274
intersubband, 708
metal, 442
metal–insulator, 212
Mott, 373
optical, 163, 174, 268, 296, 309, 419, 502
probability, 269
Transmission, 265
Transparency, 688
Transport, 235–263, 410
ballistic, 236, 533, 709
charge, 235
coupled heat and charge, 261
diode current, 532
heat, 259
heat energy, 235
high frequency, 257
high-field, 251
hopping, 457
low-field, 238
Trap, 339
filled, 336
multilevel, 339
surface, 525
Trion, 290, 420, 421
Tuning range, 698
Tunneling, 10, 362, 366, 373, 533, 540, 576, 580, 607
assisted, 340
current, 410
direct, 340
Fowler–Nordheim, 755
inelastic, 595
phonon-assisted, 340
photon-assisted, 340, 380
Zener, 5
Turn-on delay time, 699
Twin, 95
boundary, 95
lamella, 95
Twist, 97, 404
Two-electron satellite, 318
Two-photon process, 269

Umklapp process, 114
Unit cell
volume, 163
Urbach tail, 278

Vacancy, 73, 211, 217, 223, 226
Vacuum, 401
level, 521
tube, 2, 4, 519, 713, 746
ultrahigh, 348
Valley
current, 413, 594
L, 253
X, 296
Van-der-Pauw geometry, 247
Varactor, 588
Varshi's formula, 159
Vector
antiphase, 99
displacment, 122
in-plane wave, 365
line, 87
potential, 129, 269
reciprocal lattice, 141
translation, 35
wave, 145
Vegard's law, 68
Velocity, 393
average carrier, 236
drift saturation, 251, 615, 732
effective diffusion, 540
group, 105, 161, 482
light, 300
match, 626
maximum, 236
maximum drift, 252
mismatch, 626
overshoot, 254
phase, 105
sound, 105, 240
surface recombination, 340, 344
thermal, 336, 534
Vernier effect, 698
Void, 74

Voltage
bias, 529
breakdown, 577, 586, 619, 726
built-in, 530, 559
diffusion, 523
inhomogeneity, 536
Early, 723
flat-band, 556, 619
gain, 724
maximum reverse, 576
open-circuit, 640
pinch-off, 729
reach-through, 618
reference, 587
regulator, 586
threshold, 741
turn-on, 726
Vortex, 394

Wafer, 348
bonding, 377, 643, 666
diameter, 349
epiready, 351
flat, 349
Wannier's theorem, 791
Warping, 169, 202
Wave
acoustic, 105
compression, 240
electromagnetic, 299
equation, 144, 300, 482
longitudinal, 104
plane, 105, 140, 379
shear, 240, 241
sound, 105
standing, 106, 145
transverse, 104
traveling, 625
vector, 300
Wavefunction
d, 205
many-electron, 394
overlap, 366, 397, 413
strongly localized, 216
Waveguide, 488, 494, 495, 625, 684, 688, 696
plasmon, 302
Well capacity, 628
Wiedemann–Franz law, 259
Work function, 520, 524, 547, 548

Young's modulus, 125, 126

Zone
boundary, 108, 144, 145, 236
vicinity, 146
reduced scheme, 140
scheme, 140